Published in Journals: Biomolecules, Cells, International Journal of Molecular Sciences, Metabolites and Molecules

Topic Reprint

Bioactive Compounds and Therapeutics

Molecular Aspects, Metabolic Profiles, and Omics Studies

Edited by
Giovanni N. Roviello and Michele Costanzo

mdpi.com/topics

MDPI

Bioactive Compounds and Therapeutics: Molecular Aspects, Metabolic Profiles, and Omics Studies

Bioactive Compounds and Therapeutics: Molecular Aspects, Metabolic Profiles, and Omics Studies

Topic Editors

Giovanni N. Roviello
Michele Costanzo

MDPI

Basel • Beijing • Wuhan • Barcelona • Belgrade • Novi Sad • Cluj • Manchester

Topic Editors

Giovanni N. Roviello
Institute of Biostructures and Bioimaging (IBB)
National Research Council of Italy (CNR)
Naples
Italy

Michele Costanzo
Department of Molecular Medicine and Medical Biotechnology
University of Naples Federico II
Naples
Italy

Editorial Office

MDPI AG
Grosspeteranlage 5
4052 Basel, Switzerland

This is a reprint of the Topic, published open access by the journals *Biomolecules* (ISSN 2218-273X), *Cells* (ISSN 2073-4409), *International Journal of Molecular Sciences* (ISSN 1422-0067), *Metabolites* (ISSN 2218-1989) and *Molecules* (ISSN 1420-3049), freely accessible at: www.mdpi.com/topics/LL4H8331Z3.

For citation purposes, cite each article independently as indicated on the article page online and as indicated below:

Lastname, A.A.; Lastname, B.B. Article Title. *Journal Name* **Year**, *Volume Number*, Page Range.

ISBN 978-3-7258-6570-3 (Hbk)
ISBN 978-3-7258-6571-0 (PDF)
https://doi.org/10.3390/books978-3-7258-6571-0

© 2026 by the authors. Articles in this reprint are Open Access and distributed under the Creative Commons Attribution (CC BY) license. The reprint as a whole is distributed by MDPI under the terms and conditions of the Creative Commons Attribution-NonCommercial-NoDerivs (CC BY-NC-ND) license (https://creativecommons.org/licenses/by-nc-nd/4.0/).

Contents

About the Editors . . . . . **ix**

Preface . . . . . **xi**

Michele Costanzo and Giovanni N. Roviello
Precision Therapeutics Through Bioactive Compounds: Metabolic Reprogramming, Omics Integration, and Drug Repurposing Strategies
Reprinted from: *Int. J. Mol. Sci.* **2025**, *26*, 10047, https://doi.org/10.3390/ijms262010047 . . . . . **1**

Sujata B. Walunj, Geetanjali Mishra, Kylie M. Wagstaff, Swati Patankar and David A. Jans
The Ivermectin Related Compound Moxidectin Can Target Apicomplexan Importin α and Limit Growth of Malarial Parasites
Reprinted from: *Cells* **2025**, *14*, 39, https://doi.org/10.3390/cells14010039 . . . . . **5**

Nlandu Roger Ngatu, Akram Hossain, Nao Maruo, Steeve Akumwami, Asadur Md. Rahman, Masamitsu Eitoku, et al.
NBF2, an Algal Fiber-Rich Formula, Reverses Diabetic Dyslipidemia and Hyperglycemia In Vivo
Reprinted from: *Int. J. Mol. Sci.* **2024**, *25*, 10828, https://doi.org/10.3390/ijms251910828 . . . . . **20**

Man Zhao, Yali Cui, Fengxia Wang, Fengyang Wu, Chong Li, Shudong Liu and Baojiang Chen
Ursolic Acid Regulates Immune Balance, Modulates Gut Microbial Metabolism, and Improves Liver Health in Mice
Reprinted from: *Int. J. Mol. Sci.* **2024**, *25*, 10623, https://doi.org/10.3390/ijms251910623 . . . . . **32**

Yanchun Li, Hong Yu, Maria F. Lopes-Virella and Yan Huang
GPR40/GPR120 Agonist GW9508 Improves Metabolic Syndrome-Exacerbated Periodontitis in Mice
Reprinted from: *Int. J. Mol. Sci.* **2024**, *25*, 9622, https://doi.org/10.3390/ijms25179622 . . . . . **49**

Anoopjit Singh Kooner, Hai Yu, Shani Leviatan Ben-Arye, Vered Padler-Karavani and Xi Chen
Broad-Spectrum Legionaminic Acid-Specific Antibodies in Pooled Human IgGs Revealed by Glycan Microarrays with Chemoenzymatically Synthesized Nonulosonosides
Reprinted from: *Molecules* **2024**, *29*, 3980, https://doi.org/10.3390/molecules29163980 . . . . . **66**

Kumudesh Mishra, Sahar Sweetat, Saja Baraghithy, Uri Sprecher, Monzer Marisat, Sultan Bastu, et al.
The Autophagic Activator GHF-201 Can Alleviate Pathology in a Mouse Model and in Patient Fibroblasts of Type III Glycogenosis
Reprinted from: *Biomolecules* **2024**, *14*, 893, https://doi.org/10.3390/biom14080893 . . . . . **85**

Xinyu Shen and Xiaoqin Mu
Systematic Insights into the Relationship between the Microbiota–Gut–Brain Axis and Stroke with the Focus on Tryptophan Metabolism
Reprinted from: *Metabolites* **2024**, *14*, 399, https://doi.org/10.3390/metabo14080399 . . . . . **101**

Meiqi Liu, Fushuai Gong, Wang Yu, Kun Cao, Hongwei Xu and Xiaofu Zhou
The Rhododendron Chrysanthum Pall.s' Acetylation Modification of Rubisco Enzymes Controls Carbon Cycling to Withstand UV−B Stress
Reprinted from: *Biomolecules* **2024**, *14*, 732, https://doi.org/10.3390/biom14060732 . . . . . **130**

Nikolina Elez-Burnjaković, Lejla Pojskić, Anja Haverić, Naida Lojo-Kadrić, Maida Hadžić Omanović, Ajla Smajlović, et al.
Halogenated Boroxine $K_2[B_3O_3F_4OH]$ Modulates Metabolic Phenotype and Autophagy in Human Bladder Carcinoma 5637 Cell Line
Reprinted from: *Molecules* **2024**, *29*, 2919, https://doi.org/10.3390/molecules29122919 . . . . . **147**

Maximilian Penkl, Johannes A. Mayr, René G. Feichtinger, Ralf Reilmann, Otfried Debus, Manfred Fobker, et al.
Anaplerotic Therapy Using Triheptanoin in Two Brothers Suffering from Aconitase 2 Deficiency
Reprinted from: *Metabolites* **2024**, *14*, 238, https://doi.org/10.3390/metabo14040238 . . . . . **161**

Albatul S. Almousa, Pandurangan Subash-Babu, Ibrahim O. Alanazi, Ali A. Alshatwi, Huda Alkhalaf, Eman Bahattab, et al.
Hemp Seed Oil Inhibits the Adipogenicity of the Differentiation-Induced Human Mesenchymal Stem Cells through Suppressing the Cannabinoid Type 1 (CB1)
Reprinted from: *Molecules* **2024**, *29*, 1568, https://doi.org/10.3390/molecules29071568 . . . . . **173**

Mei Yang, Qian Xie, Yintao Xiao, Minglong Xia, Jiashun Chen, Bi-E Tan and Yulong Yin
Dietary Methionine Restriction Improves Gut Health and Alters the Plasma Metabolomic Profile in Rats by Modulating the Composition of the Gut Microbiota
Reprinted from: *Int. J. Mol. Sci.* **2024**, *25*, 3657, https://doi.org/10.3390/ijms25073657 . . . . . **189**

Alin Finkelshtein, Hala Khamesa-Israelov and Daniel A. Chamovitz
Overexpression of *S30* Ribosomal Protein Leads to Transcriptional and Metabolic Changes That Affect Plant Development and Responses to Stress
Reprinted from: *Biomolecules* **2024**, *14*, 319, https://doi.org/10.3390/biom14030319 . . . . . **206**

Yung-Husan Chen, Qiaoqiao Zhu, Jingyi Li, Rong Yang, Jingwen Zhang, Minxin You, et al.
Optimization of Fermentation Process for New Anti-Inflammatory Glycosylceramide Metabolite from *Aspergillus* sp.
Reprinted from: *Metabolites* **2024**, *14*, 99, https://doi.org/10.3390/metabo14020099 . . . . . **220**

Yan Xu and Makoto Komiyama
G-Quadruplexes in Human Telomere: Structures, Properties, and Applications
Reprinted from: *Molecules* **2024**, *29*, 174, https://doi.org/10.3390/molecules29010174 . . . . . **239**

Cheng Yang, Mingzhen Xue, Yifei He, Hanwei Yin, Chen Yang, Dafang Zhong, et al.
Absorption, Distribution, Metabolism, and Excretion of [^{14}C]BS1801, a Selenium-Containing Drug Candidate, in Rats
Reprinted from: *Molecules* **2023**, *28*, 8102, https://doi.org/10.3390/molecules28248102 . . . . . **257**

Fushuai Gong, Wang Yu, Qingpan Zeng, Jiawei Dong, Kun Cao, Hongwei Xu and Xiaofu Zhou
Rhododendron chrysanthum's Primary Metabolites Are Converted to Phenolics More Quickly When Exposed to UV-B Radiation
Reprinted from: *Biomolecules* **2023**, *13*, 1700, https://doi.org/10.3390/biom13121700 . . . . . **274**

Sidsel Madsen, Steffen Yde Bak, Christian Clement Yde, Henrik Max Jensen, Tine Ahrendt Knudsen, Cecilie Bæch-Laursen, et al.
Unravelling Effects of Rosemary (*Rosmarinus officinalis* L.) Extract on Hepatic Fat Accumulation and Plasma Lipid Profile in Rats Fed a High-Fat Western-Style Diet
Reprinted from: *Metabolites* **2023**, *13*, 974, https://doi.org/10.3390/metabo13090974 . . . . . **296**

Yukyung Park, Huddar Srigouri and Dongwon Kim
Novel Quinazoline Derivative Induces Differentiation of Keratinocytes and Enhances Skin Barrier Functions against Th2 Cytokine-Mediated Signaling
Reprinted from: *Molecules* **2023**, *28*, 6119, https://doi.org/10.3390/molecules28166119 . . . . . **317**

Xianmei Gou, Lin Qin, Di Wu, Jian Xie, Yanliu Lu, Qianru Zhang and Yuqi He
Research Progress of Takeda G Protein-Coupled Receptor 5 in Metabolic Syndrome
Reprinted from: *Molecules* **2023**, *28*, 5870, https://doi.org/10.3390/molecules28155870 . . . . . **330**

Nathan Calzadilla, Aisha Qazi, Anchal Sharma, Kai Mongan, Shane Comiskey, Jahnavi Manne, et al.
Mucosal Metabolomic Signatures in Chronic Colitis: Novel Insights into the Pathophysiology of Inflammatory Bowel Disease
Reprinted from: *Metabolites* **2023**, *13*, 873, https://doi.org/10.3390/metabo13070873 . . . . . **345**

Mathilde Coulet, Sylvie Lachkar, Marion Leduc, Marc Trombe, Zelia Gouveia, Franck Perez, et al.
Identification of Small Molecules Affecting the Secretion of Therapeutic Antibodies with the Retention Using Selective Hook (RUSH) System
Reprinted from: *Cells* **2023**, *12*, 1642, https://doi.org/10.3390/cells12121642 . . . . . **364**

Bamaprasad Dutta, Shining Loo, Antony Kam, Siu Kwan Sze and James P. Tam
Ginsentide TP1 Protects Hypoxia-Induced Dysfunction and ER Stress-Linked Apoptosis
Reprinted from: *Cells* **2023**, *12*, 1401, https://doi.org/10.3390/cells12101401 . . . . . **382**

About the Editors

Giovanni N. Roviello

Giovanni Roviello holds a master's degree with honors in Chemistry and a Ph.D. in Biotechnology. He works as a senior researcher at the Institute of Biostructure and Bioimaging (IBB) of the Italian National Council for Research (CNR) in Naples, Italy. He has been a visiting researcher in the US (Coastal Carolina University, Gupta Science College November 2025), Germany (IMB Jena, Georg-August University, FAU University Erlangen), the UK (University of Greenwich), and Ireland (UCD Dublin), specializing in bioorganic chemistry. He has strong academic ties with AMU University of Poznan (Poland), where he lectured on nucleic acids for Ph.D. students in 2021, and with YSU (Armenia) and Geomedi University (Georgia), where he was appointed honorary professor in medicinal chemistry in 2012. Dr. Roviello is the principal investigator for CNR on various international projects, including EU- and the Royal Society (UK)-funded projects. He serves as an academic editor for several international journals and has authored more than 150 scientific papers (Scopus h-index: 33). Since 2021, he has been consistently listed among the top 2% of scientists in Stanford University's global author rankings, including the 2024 Author Database (Ioannidis, J. P. A., Updated Science-Wide Author Databases, 2025).

Michele Costanzo

Michele Costanzo is a Researcher of Biochemistry in the Department of Molecular Medicine and Medical Biotechnology at the University of Naples Federico II. He graduated with honors in Genetic Sciences and Technologies and obtained his Ph.D. in Molecular Medicine and Medical Biotechnology in 2020. He has carried out international research projects as a visiting researcher at the Proteomics facility of Necker Hospital/INSERM U24 in Paris (2017), and at the Leibniz-Institute of Analytical Sciences (ISAS) in Dortmund (2019). Dr. Costanzo's activity has focused on the development of innovative methodologies in clinical proteomics, metabolomics, and lipidomics. He has extensive experience in mass spectrometry–based technologies and in the analysis of large-scale omics datasets. His current research has a strong translational focus on rare human diseases and inborn errors of metabolism, leveraging integrative multi-omics approaches and advanced bioinformatics pipelines. He has contributed as academic editor for international peer-reviewed journals and has an extensive publication record (Scopus h-index: 23). Since 2025, he has been a member of the Directive Board of the Italian Proteomics Association.

Preface

Bioactive compounds represent one of the most dynamic and interdisciplinary frontiers in contemporary biomedical research. Their ability to modulate molecular pathways, reshape metabolic networks, and influence cellular homeostasis places them at the intersection of natural product chemistry, pharmacology, and systems biology. This reprint, developed within the Topic 'Bioactive Compounds and Therapeutics: Molecular Aspects, Metabolic Profiles, and Omics Studies', offers an integrated overview of recent scientific advances, highlighting how mechanistic studies and omics-driven approaches are transforming our understanding of therapeutic action.

More in detail, the contributions collected here span a wide spectrum of biological models and disease contexts, including metabolic dysfunction, cancer, infectious diseases, immune imbalance, as well as neurological or vascular disorders.

The volume encompasses investigations on phytochemicals, synthetic molecules, drug repurposing strategies, and innovative chemical entities, illustrating the breadth of therapeutic potential emerging from both natural and engineered bioactive structures. A recurring theme across the articles is the integration of metabolomics, proteomics, transcriptomics, and advanced biochemical assays to decode metabolic reprogramming, signaling cascades, and adaptive responses triggered by these compounds. We believe this reprint is particularly valuable for researchers, as it provides methodological insights, mechanistic frameworks, and omics-based strategies that can inspire new hypotheses and experimental designs. For clinicians, the collection highlights translational implications, emerging therapeutic candidates, and molecular evidence that may inform future precision-medicine approaches. For other readers, including students and early-career scientists, the volume serves as an accessible entry point into a rapidly evolving field, offering clear examples of how multidisciplinary research can bridge fundamental biology and therapeutic innovation.

By bringing together diverse perspectives and cutting-edge findings, this work demonstrates the importance of integrative science in identifying new drug targets, understanding disease mechanisms, and advancing the rational development of bioactive compounds. Moreover, it aims to support the scientific community in navigating the complexity of modern therapeutics and in shaping the next generation of biomedical discoveries.

Giovanni N. Roviello and Michele Costanzo
Topic Editors

International Journal of
Molecular Sciences

MDPI

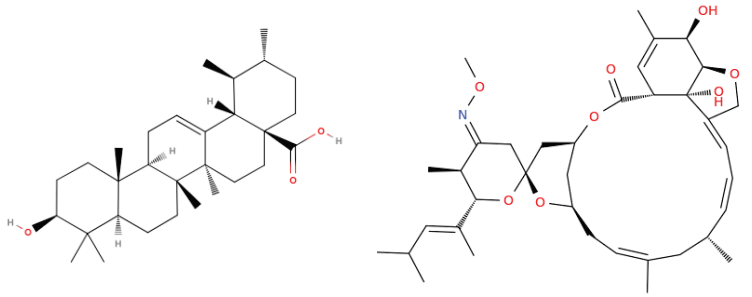
Editorial

Precision Therapeutics Through Bioactive Compounds: Metabolic Reprogramming, Omics Integration, and Drug Repurposing Strategies

Michele Costanzo [1,2,*] and Giovanni N. Roviello [3,*]

[1] Department of Molecular Medicine and Medical Biotechnology, University of Naples Federico II, 80131 Naples, Italy
[2] CEINGE—Biotecnologie Avanzate Franco Salvatore, 80145 Naples, Italy
[3] CNR Institute of Biostructures and Bioimaging, Via Tommaso De Amicis 95, 80145 Naples, Italy
* Correspondence: michele.costanzo@unina.it (M.C.); giovanni.roviello@cnr.it (G.N.R.); Tel.: +39-0812203415 (G.N.R.)

Bioactive compounds, whether derived from nature or synthetically produced, continue to redefine the landscape of therapeutic innovation. Integrating bioactive compounds with omics technologies [1,2] and metabolic profiling [3] unlocks transformative insights for precision medicine [4], drug repurposing [5], and systems-level therapeutic innovation. Remarkably, the pursuit of cutting-edge therapies for socially impactful diseases, especially neurodegenerative pathologies [6,7], centers on molecular platforms that integrate both natural and synthetic compounds, ranging from phytomolecules, amino acids, and peptides to synthetic heteroaromatic compounds [8–11]. Their ability to modulate molecular pathways, restore metabolic balance, and interact with complex biological systems positions them as key agents in the interest of precision medicine. The Topic "Bioactive Compounds and Therapeutics: Molecular Aspects, Metabolic Profiles, and Omics Studies" (https://www.mdpi.com/topics/LL4H8331Z3 accessed on 1 October 2025) brings together a diverse collection of 23 studies that explore the therapeutic potential of bioactive molecules through the lens of molecular biology, metabolic profiling, and omics technologies (Table 1). Natural products such as ursolic acid (Figure 1), rosemary extract, and hemp seed oil demonstrate promising effects on immune regulation, lipid metabolism, and adipogenesis [12,13].



Ursolic acid **Moxidectin**

Figure 1. Structural representations of ursolic acid and moxidectin [12,13]. Moxidectin is a macrocyclic lactone with antiparasitic activity. Ursolic acid is a triterpenoid known for its anti-inflammatory and anticancer effects.

Table 1. Summary of the research collection on bioactive compounds.

Category	Examples	Therapeutic Focus
Natural Products	Ursolic acid, rosemary extract, hemp seed oil	Immune regulation, lipid metabolism, adipogenesis
Synthetic Derivatives	Halogenated boroxine, quinazoline compounds	Cancer cell autophagy, skin barrier function
Drug Repurposing	Moxidectin, GHF-201	Antimalarial activity, autophagic activation in glycogenosis
Metabolic Modulators	Methionine restriction, algal fiber-rich formulas, GPR40/GPR120 agonists	Gut health, metabolic syndrome, inflammation-linked periodontitis
Omics-Based Approaches	Glycan microarrays, metabolomic and proteomic signatures	Systems-level understanding of therapeutic mechanisms
Other Investigations	Plant stress responses, telomere biology, drug pharmacokinetics	Environmental biology, structural biology, molecular profiling
Methodologies Used	In vitro assays, in vivo models, in silico simulations	Multidisciplinary exploration from molecular insight to clinical relevance

Synthetic derivatives like halogenated boroxine [14] and novel quinazoline compounds reveal targeted actions on cancer cell autophagy and skin barrier function. The repositioning of existing drugs, exemplified by moxidectin's antimalarial activity and GHF-201′s autophagic activation [15] in glycogenosis, underscores the value of drug repurposing in rare and infectious diseases. Several studies delve into the gut–brain axis [16–22], microbiota modulation, and metabolic syndrome, highlighting the systemic impact of bioactive agents. For instance, dietary methionine restriction [23] and algal fiber-rich formulas show metabolic improvements in animal models, while GPR40/GPR120 agonists [24] alleviate inflammation-linked periodontitis. The integration of omics approaches, such as glycan microarrays [25–28], metabolomic signatures in colitis [29], and proteomic insights into antibody secretion [30], provides a systems-level understanding of therapeutic mechanisms in some disease conditions. Research into bioactive compounds continues to evolve beyond traditional boundaries, encompassing not only human health but also environmental and structural biology. In particular, investigations into plant stress responses [31–33], telomere biology [34,35], and drug pharmacokinetics [36–41] exemplify this expanded scope, revealing how bioactivity influences diverse biological systems across species and contexts. These studies underscore the interconnectedness of molecular mechanisms that govern resilience, aging, and therapeutic efficacy.

Together, these insights illuminate the path from molecular understanding to clinical relevance by bridging bioactivity with omics technologies and metabolic profiling, thereby fostering a deeper understanding of how therapeutic agents can be harnessed for targeted, effective, and personalized interventions across a wide spectrum of biological systems, disease models, and therapeutic contexts, ultimately advancing precision medicine through integrative approaches that combine molecular characterization, functional analysis, and translational application.

Author Contributions: Conceptualization, M.C. and G.N.R.; writing—review and editing, M.C. and G.N.R. All authors have read and agreed to the published version of the manuscript.

Funding: This research received no external funding.

Institutional Review Board Statement: Not applicable.

Informed Consent Statement: Not applicable.

Data Availability Statement: Not applicable.

Conflicts of Interest: The authors declare no conflicts of interest.

References

1. Vailati-Riboni, M.; Palombo, V.; Loor, J.J. What are omics sciences? In *Periparturient Diseases of Dairy Cows: A Systems Biology Approach*; Springer: Berlin/Heidelberg, Germany, 2017; pp. 1–7.
2. Karczewski, K.J.; Snyder, M.P. Integrative omics for health and disease. *Nat. Rev. Genet.* **2018**, *19*, 299–310. [CrossRef]
3. Want, E.J.; Wilson, I.D.; Gika, H.; Theodoridis, G.; Plumb, R.S.; Shockcor, J.; Holmes, E.; Nicholson, J.K. Global metabolic profiling procedures for urine using UPLC–MS. *Nat. Protoc.* **2010**, *5*, 1005–1018. [CrossRef]
4. Ashley, E.A. Towards precision medicine. *Nat. Rev. Genet.* **2016**, *17*, 507–522. [CrossRef]
5. Pushpakom, S.; Iorio, F.; Eyers, P.A.; Escott, K.J.; Hopper, S.; Wells, A.; Doig, A.; Guilliams, T.; Latimer, J.; McNamee, C. Drug repurposing: Progress, challenges and recommendations. *Nat. Rev. Drug Discov.* **2019**, *18*, 41–58. [CrossRef] [PubMed]
6. Vicidomini, C.; Roviello, G.N. Therapeutic Convergence in Neurodegeneration: Natural Products, Drug Repurposing, and Biomolecular Targets. *Biomolecules* **2025**, *15*, 1333. [CrossRef] [PubMed]
7. Dugger, B.N.; Dickson, D.W. Pathology of neurodegenerative diseases. *Cold Spring Harb. Perspect. Biol.* **2017**, *9*, a028035. [CrossRef] [PubMed]
8. Simonyan, H.; Palumbo, R.; Vicidomini, C.; Scognamiglio, P.L.; Petrosyan, S.; Sahakyan, L.; Melikyan, G.; Saghyan, A.; Roviello, G.N. Binding of G-quadruplex DNA and serum albumins by synthetic non-proteinogenic amino acids: Implications for c-Myc-related anticancer activity and drug delivery. *Mol. Ther. Nucleic Acids* **2025**, *36*, 102478. [CrossRef]
9. Mittova, V.; Pirtskhalava, M.; Tsetskhladze, Z.R.; Makalatia, K.; Loladze, A.; Bebiashvili, I.; Barblishvili, T.; Gogoladze, A.; Roviello, G.N. Antioxidant Potential and Antibacterial Activities of Caucasian Endemic Plants Sempervivum transcaucasicum and Paeonia daurica subsp. mlokosewitschii Extracts and Molecular In Silico Mechanism Insights. *J. Xenobiotics* **2025**, *15*, 109. [CrossRef]
10. Ferrara, B.T.; Thompson, E.P.; Roviello, G.N.; Gale, T.F. C-Terminal Analogues of Camostat Retain TMPRSS2 Protease Inhibition: New Synthetic Directions for Antiviral Repurposing of Guanidinium-Based Drugs in Respiratory Infections. *Int. J. Mol. Sci.* **2025**, *26*, 6761. [CrossRef]
11. Roviello, G.N.; Roviello, G.; Musumeci, D.; Capasso, D.; Di Gaetano, S.; Costanzo, M.; Pedone, C. Synthesis and supramolecular assembly of 1, 3-bis (1′-uracilyl)-2-propanone. *RSC Adv.* **2014**, *4*, 28691–28698. [CrossRef]
12. Hinney, B.; Wiedermann, S.; Kaiser, W.; Krücken, J.; Joachim, A. Eprinomectin and moxidectin resistance of trichostrongyloids on a goat farm in Austria. *Pathogens* **2022**, *11*, 498. [CrossRef]
13. Mlala, S.; Oyedeji, A.O.; Gondwe, M.; Oyedeji, O.O. Ursolic acid and its derivatives as bioactive agents. *Molecules* **2019**, *24*, 2751. [CrossRef]
14. Hadzic, M.; Pojskic, L.; Lojo-Kadric, N.; Haveric, A.; Ramic, J.; Galic, B.; Haveric, S. Novel boron-containing compound, halogenated boroxine, induces selective cytotoxicity through apoptosis triggering in UT-7 leukemia. *J. Biochem. Mol. Toxicol.* **2022**, *36*, e23005. [CrossRef]
15. Mishra, K.; Sweetat, S.; Baraghithy, S.; Sprecher, U.; Marisat, M.; Bastu, S.; Glickstein, H.; Tam, J.; Rosenmann, H.; Weil, M. The Autophagic Activator GHF-201 Can Alleviate Pathology in a Mouse Model and in Patient Fibroblasts of Type III Glycogenosis. *Biomolecules* **2024**, *14*, 893. [CrossRef]
16. Bercik, P.; Collins, S.; Verdu, E. Microbes and the gut-brain axis. *Neurogastroenterol. Motil.* **2012**, *24*, 405–413. [CrossRef]
17. Chen, X.; D'Souza, R.; Hong, S.-T. The role of gut microbiota in the gut-brain axis: Current challenges and perspectives. *Protein Cell* **2013**, *4*, 403–414. [CrossRef] [PubMed]
18. Kraimi, N.; Ross, T.; Pujo, J.; De Palma, G. The gut microbiome in disorders of gut–brain interaction. *Gut Microbes* **2024**, *16*, 2360233. [CrossRef] [PubMed]
19. Mayer, E.A. Gut feelings: The emerging biology of gut–brain communication. *Nat. Rev. Neurosci.* **2011**, *12*, 453–466. [CrossRef] [PubMed]
20. Góralczyk-Bińkowska, A.; Szmajda-Krygier, D.; Kozłowska, E. The Microbiota–Gut–Brain Axis in Psychiatric Disorders. *Int. J. Mol. Sci.* **2022**, *23*, 11245. [CrossRef]
21. Doroszkiewicz, J.; Groblewska, M.; Mroczko, B. The Role of Gut Microbiota and Gut–Brain Interplay in Selected Diseases of the Central Nervous System. *Int. J. Mol. Sci.* **2021**, *22*, 10028. [CrossRef]
22. Hamamah, S.; Aghazarian, A.; Nazaryan, A.; Hajnal, A.; Covasa, M. Role of Microbiota-Gut-Brain Axis in Regulating Dopaminergic Signaling. *Biomedicines* **2022**, *10*, 436. [CrossRef]
23. Orgeron, M.L.; Stone, K.P.; Wanders, D.; Cortez, C.C.; van Nancy, T.; Gettys, T.W. The Impact of Dietary Methionine Restriction on Biomarkers of Metabolic Health. In *Glucose Homeostatis and the Pathogenesis of Diabetes Mellitus*; Elsevier: Amsterdam, The Netherlands, 2014; pp. 351–376.

24. Bianchini, G.; Nigro, C.; Sirico, A.; Novelli, R.; Prevenzano, I.; Miele, C.; Beguinot, F.; Aramini, A. A new synthetic dual agonist of GPR120/GPR40 induces GLP-1 secretion and improves glucose homeostasis in mice. *Biomed. Pharmacother.* **2021**, *139*, 111613. [CrossRef] [PubMed]
25. Rillahan, C.D.; Paulson, J.C. Glycan microarrays for decoding the glycome. *Annu. Rev. Biochem.* **2011**, *80*, 797–823. [CrossRef]
26. Kim, Y.; Hyun, J.Y.; Shin, I. Glycan microarrays from construction to applications. *Chem. Soc. Rev.* **2022**, *51*, 8276–8299. [CrossRef] [PubMed]
27. Heimburg-Molinaro, J.; Song, X.; Smith, D.F.; Cummings, R.D. Preparation and analysis of glycan microarrays. *Curr. Protoc. Protein Sci.* **2011**, *64*, 12.10.1–12.10.29. [CrossRef] [PubMed]
28. Gao, C.; Wei, M.; McKitrick, T.R.; McQuillan, A.M.; Heimburg-Molinaro, J.; Cummings, R.D. Glycan microarrays as chemical tools for identifying glycan recognition by immune proteins. *Front. Chem.* **2019**, *7*, 833. [CrossRef]
29. Liu, M.; Guo, S.; Wang, L. Systematic review of metabolomic alterations in ulcerative colitis: Unveiling key metabolic signatures and pathways. *Ther. Adv. Gastroenterol.* **2024**, *17*, 17562848241239580. [CrossRef]
30. Xu, N.; Ou, J.; Si, Y.; Goh, K.Y.; Flanigan, D.D.; Han, X.; Yang, Y.; Yang, S.-T.; Zhou, L.; Liu, X.M. Proteomics insight into the production of monoclonal antibody. *Biochem. Eng. J.* **2019**, *145*, 177–185. [CrossRef]
31. Shulaev, V.; Cortes, D.; Miller, G.; Mittler, R. Metabolomics for plant stress response. *Physiol. Plant.* **2008**, *132*, 199–208. [CrossRef]
32. Sunkar, R.; Li, Y.-F.; Jagadeeswaran, G. Functions of microRNAs in plant stress responses. *Trends Plant Sci.* **2012**, *17*, 196–203. [CrossRef]
33. Mittler, R.; Zandalinas, S.I.; Fichman, Y.; Van Breusegem, F. Reactive oxygen species signalling in plant stress responses. *Nat. Rev. Mol. Cell Biol.* **2022**, *23*, 663–679. [CrossRef]
34. Oeseburg, H.; De Boer, R.A.; Van Gilst, W.H.; Van Der Harst, P. Telomere biology in healthy aging and disease. *Pflügers Arch.-Eur. J. Physiol.* **2010**, *459*, 259–268. [CrossRef]
35. Xu, L.; Li, S.; Stohr, B.A. The role of telomere biology in cancer. *Annu. Rev. Pathol. Mech. Dis.* **2013**, *8*, 49–78. [CrossRef]
36. Ruiz-Garcia, A.; Bermejo, M.; Moss, A.; Casabo, V.G. Pharmacokinetics in drug discovery. *J. Pharm. Sci.* **2008**, *97*, 654–690. [CrossRef] [PubMed]
37. Benedetti, M.S.; Whomsley, R.; Poggesi, I.; Cawello, W.; Mathy, F.-X.; Delporte, M.-L.; Papeleu, P.; Watelet, J.-B. Drug metabolism and pharmacokinetics. *Drug Metab. Rev.* **2009**, *41*, 344–390. [CrossRef] [PubMed]
38. Coelho, M.M.; Fernandes, C.; Remião, F.; Tiritan, M.E. Enantioselectivity in Drug Pharmacokinetics and Toxicity: Pharmacological Relevance and Analytical Methods. *Molecules* **2021**, *26*, 3113. [CrossRef] [PubMed]
39. Dobrek, L. Chronopharmacology in Therapeutic Drug Monitoring—Dependencies between the Rhythmics of Pharmacokinetic Processes and Drug Concentration in Blood. *Pharmaceutics* **2021**, *13*, 1915. [CrossRef]
40. Karaźniewicz-Łada, M.; Główka, A.K.; Mikulska, A.A.; Główka, F.K. Pharmacokinetic Drug–Drug Interactions among Antiepileptic Drugs, Including CBD, Drugs Used to Treat COVID-19 and Nutrients. *Int. J. Mol. Sci.* **2021**, *22*, 9582. [CrossRef]
41. Rombolà, L.; Scuteri, D.; Marilisa, S.; Watanabe, C.; Morrone, L.A.; Bagetta, G.; Corasaniti, M.T. Pharmacokinetic Interactions between Herbal Medicines and Drugs: Their Mechanisms and Clinical Relevance. *Life* **2020**, *10*, 106. [CrossRef]

Disclaimer/Publisher's Note: The statements, opinions and data contained in all publications are solely those of the individual author(s) and contributor(s) and not of MDPI and/or the editor(s). MDPI and/or the editor(s) disclaim responsibility for any injury to people or property resulting from any ideas, methods, instructions or products referred to in the content.

cells

MDPI

Article

The Ivermectin Related Compound Moxidectin Can Target Apicomplexan Importin α and Limit Growth of Malarial Parasites

Sujata B. Walunj [1,2,†], Geetanjali Mishra [2], Kylie M. Wagstaff [1], Swati Patankar [2] and David A. Jans [1,*]

[1] Nuclear Signaling Laboratory, Monash Biomedicine Discovery Institute, Department of Biochemistry and Molecular Biology, Monash University, Clayton, VIC 3800, Australia; sujatawlnj@gmail.com (S.B.W.); kylie.wagstaff@monash.edu (K.M.W.)
[2] Molecular Parasitology Laboratory, Department of Biosciences and Bioengineering, IIT Bombay, Powai, Mumbai 400076, India; geetanjali_m0012@iitb.ac.in (G.M.); patankar@iitb.ac.in (S.P.)
* Correspondence: david.jans@monash.edu
† Current address: UCSF Helen Diller Family Comprehensive Cancer Center, San Francisco, CA 94158, USA.

Abstract: Signal-dependent transport into and out of the nucleus mediated by members of the importin (IMP) superfamily is crucial for eukaryotic function, with inhibitors targeting IMPα being of key interest as anti-infectious agents, including against the apicomplexan *Plasmodium* species and *Toxoplasma gondii*, causative agents of malaria and toxoplasmosis, respectively. We recently showed that the FDA-approved macrocyclic lactone ivermectin, as well as several other different small molecule inhibitors, can specifically bind to and inhibit *P. falciparum* and *T. gondii* IMPα functions, as well as limit parasite growth. Here we focus on the FDA-approved antiparasitic moxidectin, a structural analogue of ivermectin, for its IMPα-targeting and anti-apicomplexan properties for the first time. We use circular dichroism and intrinsic tryptophan fluorescence measurements to show that moxidectin can bind directly to apicomplexan IMPαs, thereby inhibiting their key binding functions at low μM concentrations, as well as possessing anti-parasitic activity against *P. falciparum* in culture. The results imply a class effect in terms of IMPα's ability to be targeted by macrocyclic lactone compounds. Importantly, in the face of rising global emergence of resistance to approved anti-parasitic agents, the findings highlight the potential of moxidectin and possibly other macrocyclic lactone compounds as antimalarial agents.

Keywords: *Plasmodium falciparum*; malaria; *Toxoplasma gondii*; toxoplasmosis; importins; nuclear transport inhibitors

1. Introduction

Signal-dependent transport of molecules into and out of the cell nucleus facilitated by multiple distinct members of the importin (IMP) superfamily of α and β types is central to eukaryotic cell function [1]. The best understood nuclear import pathway is that mediated by a heterodimer of IMPα and IMPβ1, where IMPα binds specifically to IMPβ1 and to the nuclear localisation signal (NLS) of cargo proteins [2–5]. IMPβ1 within the complex then mediates passage through the nuclear pore into the nucleus and subsequent release in the nucleus via distinct binding interactions with various other components of the nuclear transport machinery [1–5].

Dysregulation of nucleocytoplasmic transport can severely impact cell function [1,6–8], with the inhibition of transport through the use of small molecules a promising therapeutic strategy for cancer and infectious diseases [1,4,9]. Various inhibitors of IMPα

such as the macrocyclic lactone ivermectin [10] have been a focus of interest as antiviral agents [1,4,9,11–16], and more recently as agents to combat the apicomplexan *Plasmodium* species and *Toxoplasma gondii* [17,18], the causative agents of malaria and toxoplasmosis, respectively [19–24].

With 249 million cases and 608,000 deaths in 2022 worldwide alone, malaria is a global concern (WHO Malaria Report, 2023), with growing resistance to artemisinin-based combination therapies highlighting the need for new antiparasitic approaches [19–21]. Toxoplasmosis, caused by *T. gondii*, potentially afflicts one-third of humans asymptomatically, with immunocompromised individuals and children facing severe complications; the limitations of current therapies for toxoplasmosis, including drug resistance, emphasize the compelling need to develop new therapeutic strategies [22–25].

We recently showed that distinct inhibitors targeting IMPα can limit the growth of *P. falciparum* and *T. gondii* in culture [17,18], validating IMPα from these parasites as viable therapeutic targets [26–29]. These inhibitors included the US Food and Drug Administration (FDA)-approved anti-helminthic ivermectin [10,30], which is active against a range of different viruses, including SARS-CoV2 [9,12–16,31–33], and has been clinically investigated in an anti-malarial context [34,35]. Of a number of structural homologues of ivermectin that belong to the macrocyclic lactone class of compounds and possess anti-parasitic properties, moxidectin is also FDA-approved for human use [36,37]. Both moxidectin and ivermectin possess the ability to target glutamate-gated chloride channels [37], with moxidectin showing longer half-life/sustained release into the bloodstream that may be part of the basis of its more potent and prolonged anti-parasitic effect compared to ivermectin [38].

Although moxidectin has demonstrated efficacy against various parasites in animals [37–40], its specific activity against apicomplexan parasites, or apicomplexan IMPα, has not previously been examined. The present study addresses this directly for the first time, comparing the effects of moxidectin with those of ivermectin on IMPα from *P. falciparum* and *T. gondii*, as well as its anti-parasitic activity. Moxidectin shows a robust ability to interact with and inhibit the functions of apicomplexan IMPα, as well as limit malarial-parasite growth in culture. The results imply a class effect of macrocyclic lactones in this context, opening up the intriguing possibility of using these compounds more widely in the context of malaria and toxoplasmosis.

2. Materials and Methods

2.1. Protein Expression and Purification

P. falciparum IMPα (PfIMPα, PlasmoDB ID: Pf3D7_0812400), *T. gondii* IMPα (TgIMPα, ToxoDB ID: TGGT1_252290), *Mus musculus* IMPα (Kpna2/Rch1/pendulin/PTAC58 NCBI ID: 16647) abbreviated here to MmIMPα; MmIMPα deleted for the IMPβ1-binding domain (IBB) (MmΔIBBIMPα); and *M. musculus* IMPβ1 (MmIMPβ1, NCBI ID: 16211) GST fusion proteins were all expressed and purified as previously [14,16–18]. The His-tagged green fluorescent protein (GFP) fusion proteins T-ag-NLS-GFP and TGS1-NLS-GFP, as well as PfIMPα and TgIMPα proteins, were all purified using nickel-affinity chromatography as described [14,16–18]. GST-fusion proteins were biotinylated using the Sulfo-NHS-Biotin reagent (Pierce, Rockford, IL, USA) as previously [14,17].

2.2. Compounds

Moxidectin and ivermectin were from Sigma-Aldrich (St. Louis, MO, USA); 10 mM stock solutions were prepared in 100% DMSO.

2.3. AlphaScreen

IC_{50} analysis was performed in quadruplicate using an AlphaScreen binding assay as previously [16–18], using bacterially expressed glutathione S-transferase (GST)-C-terminally tagged PfIMPα and TgIMPα proteins [17], as well as SV40 T-ag-NLS-GFP fusion protein and MmIMPβ1 [11,41]. As previously, nickel-acceptor and streptavidin-donor beads were used [17,18]. The AlphaScreen signal was measured on a Perkin Elmer plate reader, and IC_{50} plots drawn using GraphPad Prism 9.0.2 (San Diego, CA, USA).

2.4. Circular Dichroism (CD) Spectroscopy

CD spectroscopy experiments were carried out to assess direct binding of moxidectin and ivermectin to different IMPαs as described [17,18]. CD spectra at 90.15 mg/mL protein concentration were recorded from 200–260 nm using a Jasco CD spectrometer (Jasco, Easton, MD, USA) in the absence and presence of 30 or 80 μM ivermectin or moxidectin, with percentage α-helix content estimated from the ellipticity at 222 nm as described [16,42] using the CD Multivariate secondary structure estimation analysis program.

2.5. Intrinsic Tryptophan Fluorescence Assays

Tryptophan fluorescence spectroscopy experiments were performed using a JASCO Fluorescence Spectrophotometer (JASCO, Hachioji, Tokyo, Japan) (0.5 mL quartz cuvette), with a fixed excitation wavelength of 295 nm and emission spectra collected between 310 and 400 nm with a slit width of 5 nm at 25 °C. Increasing concentrations of compounds in DMSO were incubated with the IMPαs (1 μM) in PBS for 5 min at room temperature prior to measurement. Data from three independent experiments were analysed using GraphPad Prism 10 (San Diego, CA, USA). Non-linear regression analysis was used to fit the one-site binding curves using the equation: y = Bmax * x/(Kd + x), where Bmax represents the maximum binding capacity and Kd is the dissociation constant, reflecting the concentration of ligand at which half-maximal binding is achieved.

2.6. P. falciparum Culture

The *P. falciparum* 3D7 strain was cultured and maintained according to the standard procedures [43] with minor modifications. Cultures were maintained in RPMI 1640 (GibcoTM, Waltham, MA, USA) supplemented with 0.5% Albumax (GibcoTM), 50 mg/L hypoxanthine (Sigma-Aldrich), 2 gm/L D-glucose (Sigma-Aldrich), 2 gm/L sodium bicarbonate (Sigma-Aldrich), and 56 mg/L of gentamicin (Abbott, Chicago, IL, USA). Blood for parasite cultures was procured from volunteer blood donors with approval from the Institute Ethical Committee.

2.7. Drug Susceptibility Assays for P. falciparum Using HRP2 (Histidine-Rich Protein 2) ELISA

Samples from the continuous culture of *P. falciparum* were synchronised to obtain predominant rings of 0.25% parasitemia at 3% haematocrit. Compounds were made at a stock concentration of 10 mM in 100% DMSO, with the FDA-approved antimalarial dihydroartemisinin (a kind gift from IPCA Laboratories, Mumbai, India) as a control. Compound dilutions were made in RPMI 1640 to obtain the desired final test concentrations for the IC_{50} analysis.

The HRP2-sandwich ELISA assay was performed according to the standard protocol [16,17,44,45]. Briefly, the PfHRP2 protein concentration in the culture wells, indicative of the level of parasitemia, is measured using a sandwich ELISA technique. Serial 2-fold dilutions of compounds (25 μL/well) were manually dispensed into standard 96-well microculture plates (Eppendorf). Subsequently, 200 μL of *P. falciparum* culture at 0.25% parasitemia (3% haematocrit) was added to each well. The plates were then incubated

for 72 h at 37 °C in 5% CO_2 in a humidified incubator. Plates were then subjected to freeze–thaw to achieve complete haemolysis. PfHRP2 levels in control and test samples were measured using a horseradish peroxidase enzyme-linked immunosorbent assay at 450 nm. GraphPad Prism 9.2.0 was used to perform non-linear regression analysis to determine the IC_{50} values [16,17].

2.8. T. gondii Tachyzoite Culture and Growth Inhibition Assay

A *T. gondii* RH strain expressing a luciferase reporter (RH-Fluc) [16] was used to assess the effect of the inhibitors on growth as described. *T. gondii* tachyzoites were maintained and cultured at 37 °C in 5% CO_2 in a humidified incubator using primary human foreskin fibroblasts (HFF, ATCC) maintained in Dulbecco's modified Eagle medium (DMEM) (GibcoTM, Waltham, MA, USA) supplemented with 3.7 g/L sodium bicarbonate and 2.38 g/L HEPES, 10% Cosmic Calf serum (HycloneTM, Logan, UT, USA) and 20 mg/L gentamicin [46,47]. Growth inhibition was monitored by luminescence [16], where 100 µL of culture medium without or with inhibitors, followed by 100 µL of DMEM containing 5000 parasites, were added to confluent monolayers of HFF cells in 96-well culture dishes (Eppendorf, Hamburg, Germany). After 48 h, 150 µL of the culture medium was discarded from each well, and 10 µL lysis buffer was added to lyse the parasites, followed by 50 µL of 2× luciferase assay reagent (Promega, Madison, WI, USA). Luminescence was then measured directly for 10 s using a Varioskan™ LUX multimode microplate reader (Thermo Fisher Scientific, Waltham, MA, USA).

2.9. MTT Assay for Host Cell Cytotoxicity

The MTT assay was used to measure the cytotoxicity of the small molecules against the HFF cells as described [48]. Briefly, freshly confluent HFF cells were incubated for 48 h in a 96-well culture plate at 37 °C in a humidified incubator (5% CO_2 atmosphere) in the presence of increasing concentrations of compounds (total volume 200 uL). A 10 µL quantity of MTT reagent (Sigma Aldrich) prepared in complete DMEM medium was then added to each well, and incubation continued for a further 3 h. 150 µL of the medium containing the MTT reagent was then removed from each well and replaced with 150 µL DMSO. Plates were then incubated room temperature in the dark for 20 min, after which absorbance for each well was measured at 570 nm. Data were analysed in GraphPad Prism 9 software.

2.10. Statistical Analysis

Non-linear regression analysis was performed in GraphPad Prism 9.2.0 (San Diego, CA, USA) to fit four parameter dose–response curves using the formula: $y = a + ((b - a)/(1 + 10^{(Log(c) - x)} \times d))$, where a and b are the minimum and maximum asymptotes respectively, c is the half-maximal inhibitory concentration value (IC_{50}), and d is the slope at the steepest part of the curve (the Hill slope).

3. Results

3.1. Moxidectin Can Block NLS Recognition by Apicomplexan IMPαs

Structurally related to ivermectin (see Figure 1a), the anti-parasitic agent moxidectin was approved for the treatment/prevention of river blindness (onchocerciasis) in humans by the FDA in 2018 [36–38]. It appears to have a longer half-life/higher efficacy against *Onchocerca volvulus* than ivermectin in animals and humans [38,49,50]. We recently showed that as for mammalian nuclear transport systems [11,12,15,16], ivermectin can block the interaction of apicomplexan IMPα proteins with NLSs as well as IMPβ1 [17]. Here, we set

out for the first time to test whether moxidectin had comparable activity, performing IC_{50} analysis using an established AlphaScreen binding assay [16,17].

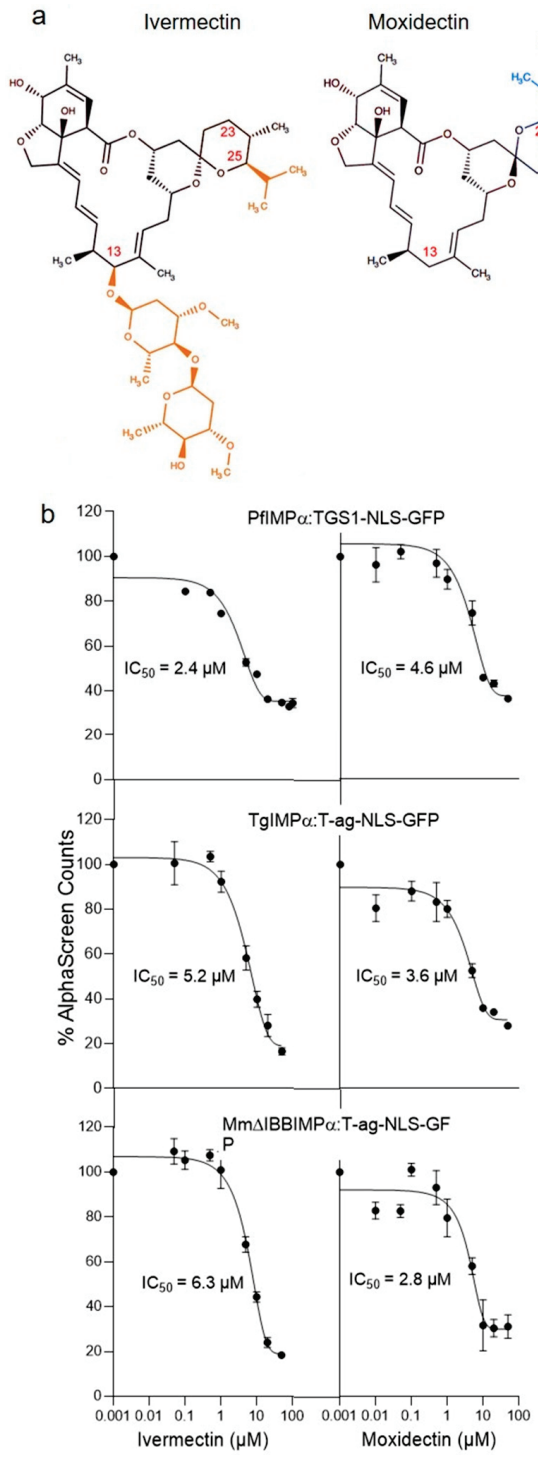


Figure 1. Close similarities of ivermectin and moxidectin in structure and IMPα inhibitory properties. (**a**). Structures of ivermectin and moxidectin are shown, with the shared chemical scaffold in black, and distinct groups highlighted in colour; an example is the C13 residue that is attached to sugar groups in the case of avermectins such as ivermectin, but is protonated in moxidectin and other members of the milbemycin family. (**b**). AlphaScreen technology was used to determine the IC_{50} values for inhibition of the binding of various IMPαs (5 nM) to NLS-containing proteins (30 nM) by ivermectin and moxidectin. Data represent the mean ± SEM for quadruplet wells from a single experiment, from a series of 3 independent experiments (see Table 1 for pooled data).

Table 1. Summary of IC_{50} analysis for inhibition of IMPα binding interactions by moxidectin and ivermectin.

	IC_{50} (μM) *	
Binding Interaction	**Ivermectin**	**Moxidectin**
PfIMPα:TGS1-NLS-GFP	5.0 ± 1.3	4.8 ± 0.4
TgIMPα:Tag-NLS-GFP	4.9 ± 0.2	3.8 ± 0.8
MmΔIBBIMPα:Tag-NLS-GFP	6.2 ± 0.2	3.6 ± 0.5
PfIMPα:MmIMPβ1	1.9 ± 0.2	3.4 ± 0.4
TgIMPα:MmIMPβ1	6.9 ± 1.2	2.7 ± 0.2
MmIMPα:MmIMPβ1	3.1 ± 0.5	4.0 ± 0.4

* Results represent the mean ± SEM (n = 3) for the values measured, as per Figures 1 and 2.

In contrast to mammalian systems where there are multiple different IMPα forms [2–4], *P. falciparum* and *T. gondii* both retain a single, essential form of IMPα, the amino acid sequences of which are 63 and 59% similar (43 and 41% identical), respectively, to that of MmIMPα (Kpna1/Rch1—see Section 2.1) used here. As previously [16–18], we first analysed the MmΔIBBIMPα (truncated) form of IMPα, which is not autoinhibited and hence can bind NLSs with high affinity in the absence of MmIMPβ1 [51,52]. We found that ivermectin inhibited MmΔIBBIMPα recognition of the well-characterised simian virus SV40 large tumour antigen (T-ag) in the context of a bacterially expressed GFP fusion protein (T-ag-NLS-GFP) at low μM concentration (Figure 1b bottom left; IC_{50} value of c. 6 μM—see Table 1), consistent with previous studies [11,16,18,41]. Strikingly, moxidectin showed similar inhibitory activity (Figure 1b bottom right) with an IC_{50} of 3–4 μM (Table 1). As previously [18], ivermectin inhibited NLS binding by PfIMPα (TGS1-NLS-GFP fusion protein) and TgIMPα (SV40:T-ag-NLS-GFP fusion protein) at low μM concentration (Figure 1b, top left and middle left panels), with IC_{50} values of c. 5 μM (Table 1). Moxidectin showed very similar ability to inhibit both apicomplexan IMPαs (Figure 1b top right/middle right panels), with comparable IC_{50} values (4–5 μM, Table 1). Clearly, moxidectin strongly resembled ivermectin in being able to inhibit NLS binding by IMPαs, including those from apicomplexans, at low μM concentrations.

Apicomplexan IMPβ1 has not been characterized as yet, but previous studies [16,18] show that apicomplexan IMPαs are able to interact with mammalian IMPβ1 with high affinity, and that ivermectin is able to inhibit this interaction through its ability to bind to IMPα to alter structure/conformation. Accordingly, we used the AlphaScreen binding assay to assess the ability of moxidectin to inhibit binding of IMPα from *Mus musculus*, *P. falciparum* and *T. gondii* to mammalian IMPβ1. Binding of full-length MmIMPα to MmIMPβ1 was inhibited by moxidectin with an IC_{50} of c. 4 μM, very similar to that of ivermectin (Figure 2, Table 1). Strikingly, it also inhibited binding of PfIMPα and TgIMPα to MmIMPβ1 with IC_{50} values of c. 3 μM, very similar to those of ivermectin (IC_{50} values of 2–7 μM; Figure 2, Table 1). Clearly, moxidectin resembles ivermectin in being able to inhibit IMPβ1 recognition by mammalian and apicomplexan IMPαs at low μM concentrations.

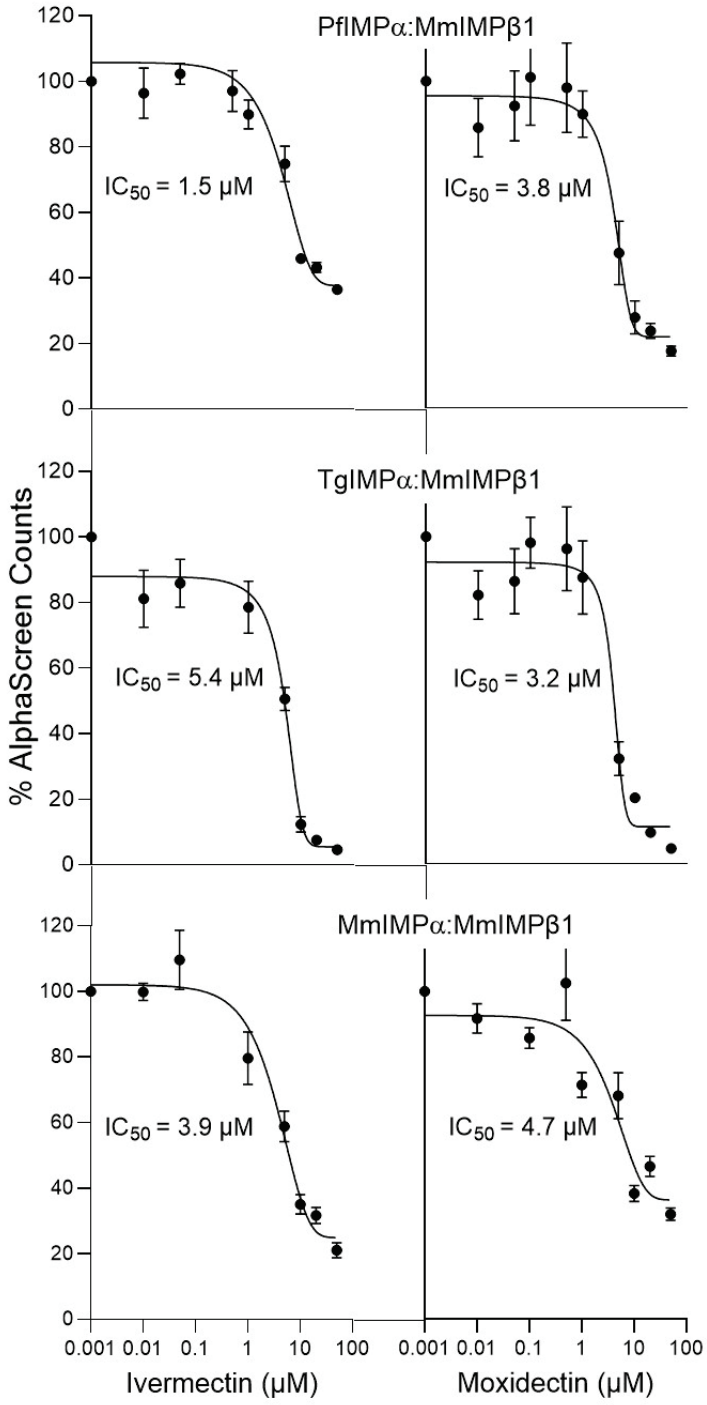


Figure 2. Like ivermectin, moxidectin can inhibit IMPα–IMPβ1 binding. AlphaScreen technology was used to determine the IC_{50} for inhibition by ivermectin and moxidectin of binding of MmIMPβ1 (30 nM) to various IMPαs (30 nM). Data represent the mean ± SEM for quadruplet wells from a single typical experiment, from a series of three independent experiments (see Table 1 for pooled data).

3.2. Moxidectin Can Bind Directly to Apicomplexan IMPα Proteins

We employed far-UV CD spectroscopy, as previously [14,18], to assess the potential of moxidectin to bind directly to IMPα proteins. The CD spectra of PfIMPα, TgIMPα, and MmIMPα all showed double minima at 208 and 222 nm (Figure 3a), consistent with the predominantly α-helical structure of IMPα (see [51]). Quantitative estimation indicated that apicomplexan IMPαs were c. 60% α-helical, compared to c. 70% for MmIMPα (Figure 3b). The CD spectra of the proteins in the presence of increasing concentrations of ivermectin

and moxidectin revealed a concentration-dependent reduction in α-helicity (Figure 3a,b), indicating that, like ivermectin, moxidectin appears to be able to bind to the IMPαs directly to perturb structure.

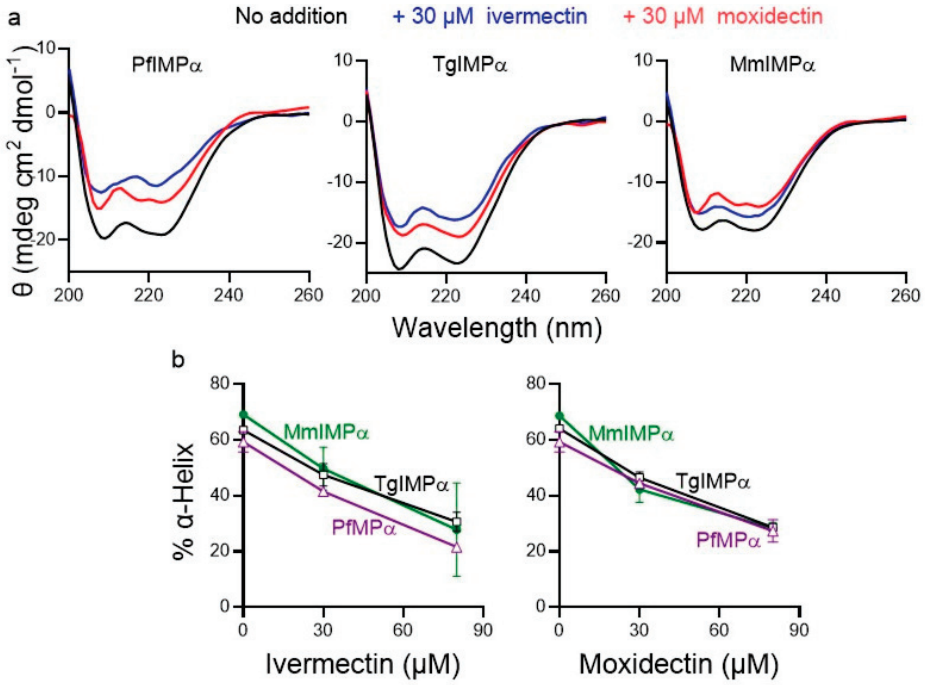


Figure 3. CD spectra for apicomplexan and mammalian IMPαs in the absence and presence of moxidectin and ivermectin. CD spectra were collected for PfIMPα, TgIMPα, and MmIMPα in the absence or presence of 30 or 80 μM ivermectin or moxidectin. (**a**). Spectra are shown from a single experiment, representative of 2 independent experiments for IMPαs without or with 30 μM ivermectin or moxidectin. Note: θ is ellipticity in mdeg cm^2 $dmol^{-1}$. (**b**). The α-helical content of the respective IMPαs was estimated as previously (see Section 2.4) from spectra as per Figure 3a. Results represent the mean ± SD for 2 independent experiments.

We built on these results using an intrinsic tryptophan fluorescence assay. Tryptophan residues within proteins have an intrinsic fluorescence, a change in the microenvironment of which, through ligand binding or other interactions by the protein, can alter the intrinsic fluorescence intensity [53]. We recorded tryptophan fluorescence emission spectra for the IMPαs, all of which showed a fluorescence maximum at 340 nm.

The addition of increasing concentrations of ivermectin or moxidectin resulted in a concentration-dependent decrease in fluorescence intensity at 340 nm (Figure 4a), enabling estimation of dissociation constants (Figure 4b). Moxidectin and ivermectin showed low μM IC_{50} values for mammalian IMPα (3 μM and 4 μM) and PfIMPα (6.4 μM and 7.8 μM). In contrast, IC_{50} values of moxidectin and ivermectin were higher for TgIMPα (24 μM and 19 μM). As NLS binding sites in IMPα have conserved tryptophan residues, these results suggest that moxidectin and ivermectin bind to conserved tryptophan residues on apicomplexan IMPα proteins and impact their conformation; the significance of the possibility that TgIMPα may be slightly less sensitive in this respect is not clear.

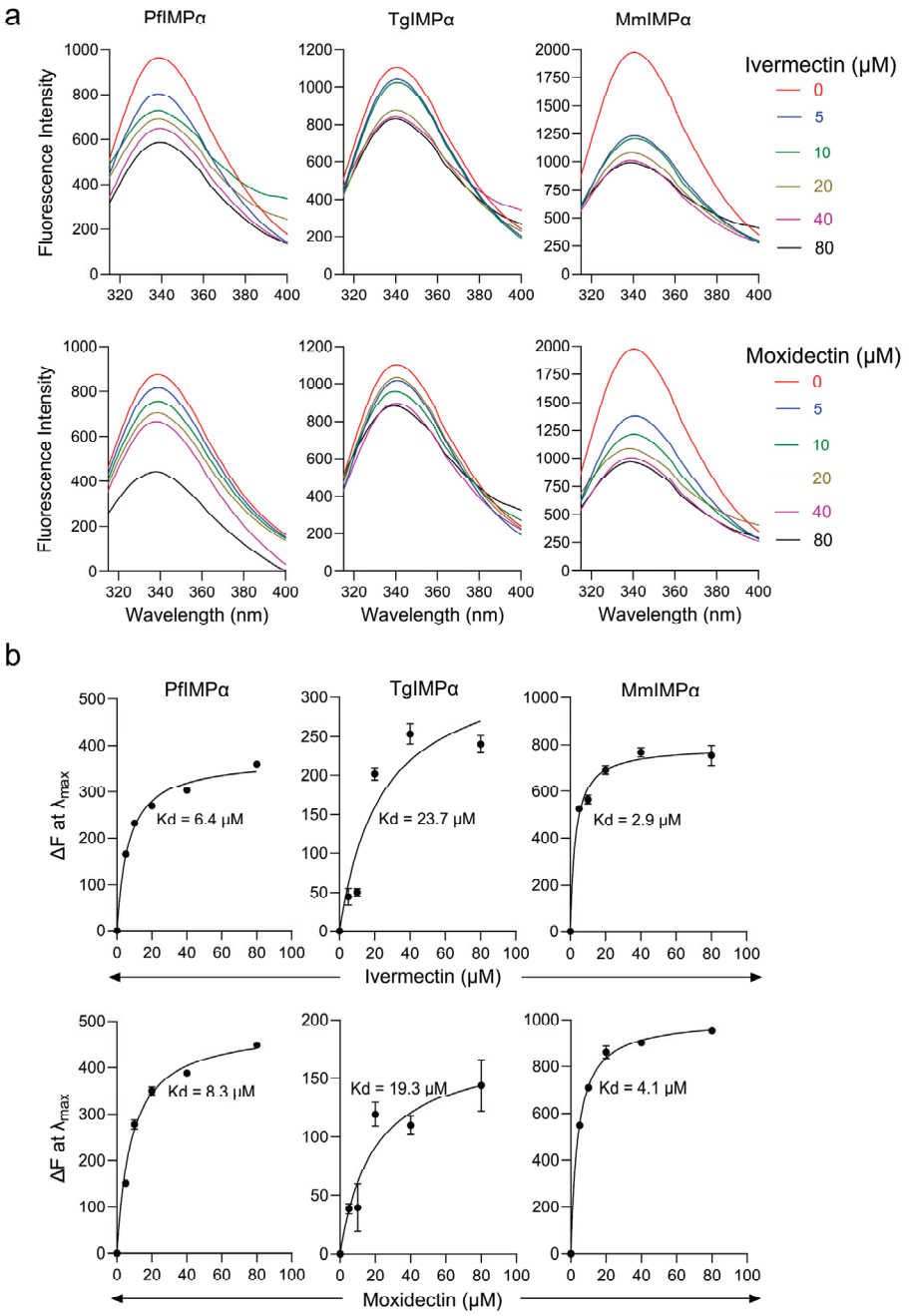


Figure 4. Intrinsic tryptophan fluorescence assay to study the interaction between moxidectin and ivermectin with PfIMPα, TgIMPα, and MmIMPα. (**a**) Intrinsic tryptophan fluorescence spectra of PfIMPα, TgIMPα, and MmIMPα were collected (excitation wavelength: 295 nm and emission from 315 nm to 400 nm) in the presence or absence of moxidectin and ivermectin in the indicated concentration ranges. (**b**). Changes in fluorescence intensity at 340 nm (λmax) from (**a**) with increasing concentrations of compound were plotted using GraphPad prism for a single typical set of measurements, representative of a series of 3 independent experiments (see Table 2).

Table 2. Summary of Kd estimations measured using intrinsic tryptophan fluorescence measurements.

Protein	Kd (μM) *	
	Ivermectin	Moxidectin
PfIMPα	6.4 ± 0.3	7.8 ± 1.2
TgIMPα	24 ± 1.4	19 ± 2.2
MmIMPα	2.9 ± 0.4	4.1 ± 0.2

* Results represent the mean ± SEM (n = 3) for the values measured as per Figure 4b.

3.3. Like Ivermectin, Moxidectin Can Limit Proliferation of P. falciparum

Since moxidectin appears to bind to PfIMPα and thereby inhibit NLS- and IMPβ1-binding, we carried out drug susceptibility assays for moxidectin and ivermectin against *P. falciparum* parasites using an established ELISA technique [16,17,44,45], with the clinically prescribed drug dihydroartemisinin (DHA) used as a positive control. In similar fashion to ivermectin, moxidectin showed an IC_{50} value of 1 μM against *P. falciparum* asexual stages in culture (Figure 5, Table 3), supporting the idea that moxidectin, like ivermectin, has antimalarial activity.

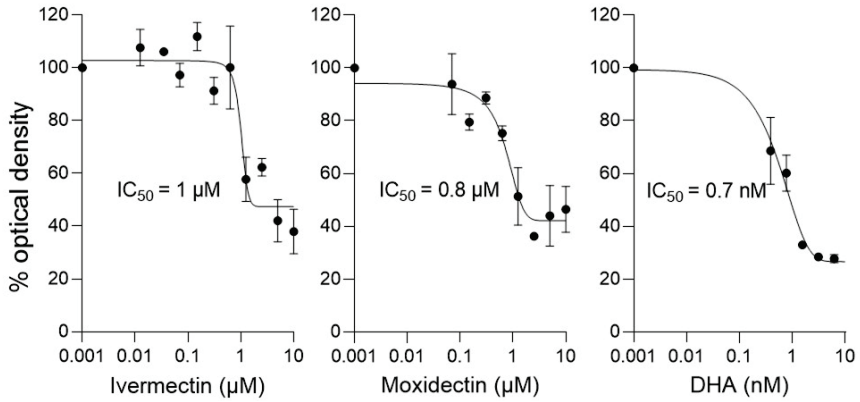


Figure 5. Ivermectin and moxidectin inhibit *P. falciparum* parasites in culture at low μM concentrations. *P. falciparum* cultures (0.25% parasitemia) were treated with increasing concentrations of the indicated compounds for 72 h, after which the HRP2-based sandwich ELISA was used to measure the HRP2 levels, determined by optical density. The results shown are from a single typical experiment performed in duplicate (SD shown), representative of a series of three independent experiments (see Table 3 for pooled data).

Table 3. Summary of the IC_{50} values for inhibition of *P. falciparum* parasites by moxidectin and ivermectin in culture.

Compound	IC_{50} (μM) *
Ivermectin	0.7 ± 0.1
Moxidectin	0.9 ± 0.1
DHA	0.001 ± 0.0005

* Results represent the mean ± SD (n = 3) for IC_{50} analysis as per Figure 5.

We also tested the effect of moxidectin on the growth of *T. gondii* tachyzoites constitutively expressing luciferase in HFF host cells [54]. IC_{50} analysis indicated values in the 30–35 μM range, comparable to that for ivermectin (see Table 4). Analysis of the potential cytotoxic effects of the compounds on the HFF cells in the infectious system using the MTT assay, however, revealed that both ivermectin and moxidectin have CC_{50} values for HFF cells of c. 10 μM (Table 4). Clearly, it cannot be excluded that the observed inhibitory effects

of ivermectin/moxidectin on *T. gondii* tachyzoites in the HFF cell infectious system are attributable to cytotoxic effects on the host cells.

Table 4. Summary of IC_{50}/CC_{50} values for effects of moxidectin and ivermectin on *T. gondii* parasites in culture.

Compound	IC_{50} (μM) *	CC_{50} (μM) +
Ivermectin	29 ± 0.7	8 ± 1.8
Moxidectin	35 ± 3.1	10 ± 0.8

* Results represent the mean ± SD (n = 3). + Results represent the mean ± SD (n = 2).

4. Discussion

This study is the first to show that the macrocyclic lactone moxidectin shows promise as an inhibitor of IMPα, and accordingly has potential as an anti-parasitic agent. Through its chemical scaffold shared with ivermectin (see Figure 1a), moxidectin exhibits similar inhibitory effects on mammalian and apicomplexan IMPα proteins. Both compounds effectively inhibit NLS recognition and binding to IMPβ1 with IC_{50} values of 3–7 μM (Table 1; Figures 1 and 2); based on the fluorescence quenching and structural perturbations observed in the tryptophan fluorescence and CD spectroscopy assays here (Figures 3 and 4), conserved tryptophan residues within the IMPαs likely play a critical role in these interactions. Consistent with this, moxidectin's activity against the asexual stages of *P. falciparum* was confirmed in culture (IC_{50} of 1 μM; Figure 5). Thus, taken together our novel findings suggest that moxidectin, like ivermectin, targets/binds to conserved structural motifs in IMPα, disrupting their conformation and inhibiting key protein–protein interactions; this is likely the basis of its antimalarial activity. As it is approved by the FDA to treat helminthic infections, moxidectin's pharmacokinetic properties/safety are well documented in human studies (see [36,40,49,50]), but of course, rigorous testing of the antimalarial action of moxidectin in clinical studies, initially along the lines of those already carried out for ivermectin [34,35], will be required in the future to assess properly its true therapeutic potential against apicomplexan disease.

As mentioned, moxidectin and ivermectin share key chemical scaffolds (Figure 1a) that enable them to target glutamate-gated chloride channels in helminths/insects [54–58]. Based on the results here using CD and intrinsic tryptophan fluorescence measurements, as well as previous studies [16], it would appear that moxidectin/ivermectin's shared chemical scaffolds enable them to bind directly to specific regions of IMPα, thereby impacting key protein–protein interactions central to the nuclear transport process. Understanding the precise binding site of these compounds on apicomplexan and mammalian IMPα is crucial for the development of agents that selectively target apicomplexan without affecting mammalian host IMPα. This understanding holds the potential to pave the way for the development of a novel class of antimalarials that are selective and efficacious.

A key implication of this study is that other macrocyclic lactones related to ivermectin and moxidectin (avermectins, milbemycins etc.) may conceivably have similar properties. Although moxidectin is structurally related to ivermectin, it has distinct features (see Figure 1a and legend), which appear to be the basis of its improved stability and efficacy as an anti-parasitic compared to ivermectin in mammalian systems [38,49]. It is an intriguing possibility that other distinct avermectins/milbemycins, such as selamectin, eprinomectin, abamectin, doramectin, etc., which are currently in veterinary/agricultural use may also prove to have the same general properties. Direct experimentation is of course required to test this possibility, but in the important quest to continue to develop new strategies to combat apicomplexan disease, especially in the context of emerging resistance to existing treatments, this may well prove worthwhile. Moxidectin here showed antimalarial activity

at low μM concentrations; combined with its reported longer half-life and sustained release in mammalian systems compared to ivermectin [38,49], it appears to be a more compelling candidate for further exploration in the development of anti-parasitic drugs than ivermectin. Future investigations should focus on optimising moxidectin's selectivity, exploring its efficacy in vivo, and potentially its specific targets within the parasites.

In summary, the study presented here emphasizes the exciting potential of repurposing existing drugs, such as moxidectin and ivermectin, to address the urgent need for novel and effective treatments against malaria.

Author Contributions: Conceptualisation: D.A.J., S.P., S.B.W. and K.M.W. Analysis and investigation: S.B.W. Methodology: S.B.W. and G.M. Writing original draft: S.B.W. Writing—review and editing: D.A.J., S.P. and K.M.W. Supervision: D.A.J., S.P. and K.M.W. Project administration: D.A.J. and S.P. Funding acquisition: D.A.J. and S.P. All authors have read and agreed to the published version of the manuscript.

Funding: The authors acknowledge the financial support of the National Health and Medical Research Council Australia (Senior Principal Research Fellowship APP1002486/APP1103050) to D.A.J. and the Department of Science and Technology (DST), Science and Engineering Research Board (SERB Core Research Grant CRG/2018/000129), India to S.P. S.B.W. acknowledges the support of a PhD scholarship from IITB/Monash University and support from the Department of Biotechnology, India, for project IMURA 0716 (IITB-Monash Research Academy).

Institutional Review Board Statement: Not applicable.

Informed Consent Statement: Not applicable.

Data Availability Statement: The original contributions presented in this study are included in the article. Further inquiries can be directed to the corresponding author.

Acknowledgments: The authors acknowledge IIT Bombay Hospital, staff, and volunteers for their help in the blood collection for *P. falciparum* cultures and Sanjeeva Srivastava and Prakriti Tayalia for the use of plate readers for the anti-parasitic assays.

Conflicts of Interest: The authors declare no conflicts of interest. The funders had no role in the design of the study, in the collection, analyses, or interpretation of data, in the writing of the manuscript, or in the decision to publish the results.

References

1. Kosyna, F.K.; Depping, R. Controlling the Gatekeeper: Therapeutic Targeting of Nuclear Transport. *Cells* **2018**, *7*, 221. [CrossRef] [PubMed]
2. Fulcher, A.J.; Jans, D.A. Regulation of Nucleocytoplasmic Trafficking of Viral Proteins: An Integral Role in Pathogenesis? *Biochim. Biophys. Acta-Mol. Cell Res.* **2011**, *1813*, 2176–2190. [CrossRef] [PubMed]
3. Köhler, M.; Speck, C.; Christiansen, M.; Bischoff, F.R.; Prehn, S.; Haller, H.; Hartmann, E. Evidence for Distinct Substrate Specificities of Importin α Family Members in Nuclear Protein Import. *Mol. Cell. Biol.* **1999**, *16*, 7782–7791. [CrossRef]
4. Jans, D.A.; Martin, A.J.; Wagstaff, K.M. Inhibitors of Nuclear Transport. *Curr. Opin. Cell Biol.* **2019**, *58*, 50–60. [CrossRef]
5. Stewart, M. Molecular Mechanism of the Nuclear Protein Import Cycle. *Nat. Rev. Mol. Cell Biol.* **2007**, *8*, 195–208. [CrossRef]
6. Dunn, J.; McCuaig, R.D.; Tan, A.H.Y.; Tu, W.; Wu, F.; Wagstaff, K.M.; Zafar, A.; Ali, S.; Diwakar, H.; Dahlstrom, J.E.; et al. Selective Targeting of Protein Kinase C (PKC)-θ Nuclear Translocation Reduces Mesenchymal Gene Signatures and Reinvigorates Dysfunctional $CD8^+$ T Cells in Immunotherapy-Resistant and Metastatic Cancers. *Cancers* **2022**, *14*, 1596. [CrossRef]
7. Gajewska, K.; Lescesen, H.; Ramialison, M.; Wagstaff, K.M.; Jans, D.A. Nuclear transporter Importin-13 plays a key role in the oxidative stress transcriptional response. *Nat. Commun.* **2021**, *12*, 5904. [CrossRef] [PubMed]
8. Zhang, S.Y.; Williamson, N.A.; Duvick, L.; Lee, A.; Orr, H.T.; Korlin-Downs, A.; Yang, P.; Mok, Y.-F.; Jans, D.A.; Bogoyevitch, M.A. The ataxin-1 interactome reveals direct connection with multiple disrupted nuclear transport pathways. *Nat. Commun.* **2020**, *11*, 3343. [CrossRef] [PubMed]
9. Martin, A.J.; Jans, D.A. Antivirals that target the host IMPα/β1-virus interface. *Biochem. Soc. Trans.* **2021**, *49*, 281–295. [CrossRef] [PubMed]

10. Crump, A.; Omura, S. Ivermectin, wonder drug from Japan: The human use perspective. *Proc. Jpn. Acad.* **2011**, *87*, 13–28. [CrossRef] [PubMed]
11. Wagstaff, K.M.; Sivakumaran, H.; Heaton, S.M.; Harrich, D.; Jans, D.A. Ivermectin Is a Specific Inhibitor of Importin α/β -Mediated Nuclear Import Able to Inhibit Replication of HIV-1 and Dengue Virus. *Biochem. J.* **2012**, *856*, 851–856. [CrossRef] [PubMed]
12. Caly, L.; Druce, J.D.; Catton, M.G.; Jans, D.A.; Wagstaff, K.M. The FDA-Approved Drug Ivermectin Inhibits the Replication of SARS-CoV-2 in Vitro. *Antivir. Res.* **2020**, *178*, 104787. [CrossRef]
13. Thomas, D.R.; Lundberg, L.; Pinkham, C.; Shechter, S.; Debono, A.; Baell, J.; Wagstaff, K.M.; Hick, C.A.; Kehn-hall, K.; Jans, D.A. Identification of Novel Antivirals Inhibiting Recognition of Venezuelan Equine Encephalitis Virus Capsid Protein by the Importin α/β1 Heterodimer through High-Throughput Screening. *Antivir. Res.* **2018**, *151*, 8–19. [CrossRef] [PubMed]
14. Yang, S.N.Y.; Atkinson, S.C.; Fraser, J.E.; Wang, C.; Maher, B.; Roman, N.; Forwood, J.K.; Wagstaff, K.M.; Borg, N.A.; Jans, D.A. Novel Flavivirus Antiviral That Targets The Host Nuclear Transport Importin α/β1 Heterodimer. *Cells* **2019**, *8*, 281. [CrossRef] [PubMed]
15. Shechter, S.; Thomas, D.R.; Lundberg, L.; Pinkham, C.; Lin, S.; Wagstaff, K.M.; Debono, A.; Kehn-hall, K.; Jans, D.A. Novel Inhibitors Targeting Venezuelan Equine Encephalitis Virus Capsid Protein Identified Using In Silico Structure-Based-Drug-Design. *Sci. Rep.* **2017**, *7*, 17705. [CrossRef]
16. Yang, S.N.Y.; Atkinson, S.C.; Wang, C.; Lee, A.; Bogoyevitch, M.A.; Borg, N.A.; Jans, D.A. The Broad Spectrum Antiviral Ivermectin Targets the Host Nuclear Transport Importin α/b1 Heterodimer. *Antivir. Res.* **2020**, *177*, 104760. [CrossRef]
17. Walunj, S.B.; Dias, M.M.; Kaur, C.; Wagstaff, K.M.; Dey, V.; Hick, C.; Patankar, S.; Jans, D.A. High-Throughput Screening to Identify Inhibitors of *Plasmodium falciparum* Importin α. *Cells* **2022**, *11*, 1201. [CrossRef]
18. Walunj, S.B.; Wang, C.; Wagstaff, K.M.; Patankar, S.; Jans, D.A. Conservation of Importin a Function in Apicomplexans: Ivermectin and GW5074 Target *Plasmodium falciparum* Importin a and Inhibit Parasite Growth in Culture. *Int. J. Mol. Sci.* **2022**, *23*, 13899. [CrossRef] [PubMed]
19. Greenwood, B.M.; Fidock, D.A.; Kyle, D.E.; Kappe, S.H.I.; Alonso, P.L.; Collins, F.H.; Duffy, P.E. Malaria: Progress, Perils, and Prospects for Eradication. *J. Clin. Investig.* **2008**, *118*, 1266–1276. [CrossRef]
20. Tse, E.G.; Korsik, M.; Todd, M.H. The Past, Present and Future of Antimalarial Medicines. *Malar. J.* **2019**, *18*, 93. [CrossRef]
21. Blasco, B.; Leroy, D.; Fidock, D.A. Antimalarial Drug Resistance: Linking *Plasmodium falciparum* Parasite Biology to the Clinic. *Nat. Med.* **2017**, *23*, 917–928. [CrossRef] [PubMed]
22. Montazeri, M.; Mikaeili Galeh, T.; Moosazadeh, M.; Sarvi, S.; Dodangeh, S.; Javidnia, J.; Sharif, M.; Daryani, A. The Global Serological Prevalence of *Toxoplasma gondii* in Felids during the Last Five Decades (1967–2017): A Systematic Review and Meta-Analysis. *Parasites Vectors* **2020**, *13*, 82. [CrossRef]
23. Sabin, A.B. Toxoplasmic encephalitis in children. *J. Am. Med. Assoc.* **1941**, *116*, 801–807. [CrossRef]
24. Alday, P.H.; Doggett, J.S. Drugs in Development for Toxoplasmosis: Advances, Challenges, and Current Status. *Drug Des. Dev. Ther.* **2017**, *11*, 273–293. [CrossRef] [PubMed]
25. Montazeri, M.; Mehrzadi, S.; Sharif, M.; Sarvi, S.; Tanzifi, A.; Aghayan, S.A.; Daryani, A. Drug Resistance in *Toxoplasma gondii*. *Front. Microbiol.* **2018**, *9*, 2587. [CrossRef]
26. Frankel, M.B.; Knoll, L.J. Functional Analysis of Key Nuclear Trafficking Components Reveals an Atypical Ran Network Required for Parasite Pathogenesis. *Mol. Microbiol.* **2008**, *70*, 410–420. [CrossRef] [PubMed]
27. Frankel, M.B.; Knoll, L.J. The Ins and Outs of Nuclear Trafficking: Unusual Aspects in Apicomplexan Parasites. *DNA Cell Biol.* **2009**, *28*, 277–284. [CrossRef]
28. Zhang, M.; Wang, C.; Otto, T.D.; Oberstaller, J.; Liao, X.; Adapa, S.R.; Udenze, K.; Bronner, I.F.; Casandra, D.; Mayho, M.; et al. Uncovering the Essential Genes of the Human Malaria Parasite *Plasmodium falciparum* by Saturation Mutagenesis. *Science* **2018**, *360*, eaap7847. [CrossRef] [PubMed]
29. Sidik, S.M.; Huet, D.; Ganesan, S.M.; Huynh, M.H.; Wang, T.; Nasamu, A.S.; Thiru, P.; Saeij, J.P.J.; Carruthers, V.B.; Niles, J.C.; et al. A Genome-Wide CRISPR Screen in Toxoplasma Identifies Essential Apicomplexan Genes. *Cell* **2016**, *166*, 1423–1435.e12. [CrossRef]
30. González Canga, A.; Sahagún Prieto, A.M.; Diez Liébana, M.J.; Fernández Martínez, N.; Sierra Vega, M.; García Vieitez, J.J. The pharmacokinetics and interactions of ivermectin in humans—A mini-review. *AAPS J.* **2008**, *10*, 42–46. [CrossRef]
31. Jans, D.A.; Wagstaff, K.M. Ivermectin as a Broad-Spectrum Host-Directed Antiviral: The Real Deal? *Cells* **2020**, *9*, 2100. [CrossRef]
32. Ooi, E.E. Repurposing Ivermectin as an Anti-Dengue Drug. *Clin. Infect. Dis.* **2021**, *72*, e594–e595. [CrossRef] [PubMed]
33. Bryant, A.; Lawrie, T.A.; Dowswell, T.; Fordham, E.J.; Mitchell, S.; Hill, S.R.; Tham, T.C. Ivermectin for Prevention and Treatment of COVID-19 Infection: A Systematic Review, Meta-Analysis, and Trial Sequential Analysis to Inform Clinical Guidelines. *Am. J. Ther.* **2021**, *28*, e434–e460. [CrossRef]

34. Foy, B.D.; Alout, H.; Seaman, J.A.; Rao, S.; Magalhaes, T.; Wade, M.; Parikh, S.; Soma, D.; Sagna, B.; Fournet, F.; et al. Efficacy and Risk of Harms of Repeat Ivermectin Mass Drug Administrations for Control of Malaria (RIMDAMAL): A Cluster-Randomised Trial. *Lancet* **2019**, *393*, 1517–1526. [CrossRef] [PubMed]
35. Ouédraogo, A.L.; Bastiaens, G.J.H.; Tiono, A.B.; Guelbéogo, W.M.; Kobylinski, K.C.; Ouédraogo, A.; Barry, A.; Bougouma, E.C.; Nebie, I.; Ouattara, M.S.; et al. Efficacy and Safety of the Mosquitocidal Drug Ivermectin to Prevent Malaria Transmission after Treatment: A Double-Blind, Randomized, Clinical Trial. *Clin. Infect. Dis.* **2015**, *60*, 357–365. [CrossRef] [PubMed]
36. Sprecher, V.P.; Hofmann, D.; Savathdy, V.; Xayavong, P.; Norkhankhame, C.; Huy, R.; Khieu, V.; Sayasone, S.; Hattendorf, J.; Keiser, J. Efficacy and Safety of Moxidectin Compared with Ivermectin against Strongyloides Stercoralis Infection in Adults in Laos and Cambodia: A Randomised, Double-Blind, Non-Inferiority, Phase 2b/3 Trial. *Lancet Infect. Dis.* **2023**, *24*, 196–205. [CrossRef]
37. Cobb, R.; Boeckh, A. Moxidectin: A Review of Chemistry, Pharmacokinetics and Use in Horses. *Parasit. Vectors* **2009**, *2*, S5. [CrossRef] [PubMed]
38. Prichard, R.K.; Geary, T.G. Perspectives on the Utility of Moxidectin for the Control of Parasitic Nematodes in the Face of Developing Anthelmintic Resistance. *Int. J. Parasitol. Drugs Drug Resist.* **2019**, *10*, 69–83. [CrossRef]
39. Tang, M.; Hu, X.; Wang, Y.; Yao, X.; Zhang, W.; Yu, C.; Cheng, F.; Li, J.; Fang, Q. Ivermectin, a Potential Anticancer Drug Derived from an Anti-parasitic Drug. *Pharmacol. Res.* **2021**, *163*, 105207. [CrossRef]
40. Cotreau, M.M.; Warren, S.; Ryan, J.L.; Fleckenstein, L.; Vanapalli, S.R.; Brown, K.R.; Rock, D.; Chen, C.Y.; Schwertschlag, U.S. The Anti-parasitic Moxidectin: Safety, Tolerability, and Pharmacokinetics in Humans. *J. Clin. Pharmacol.* **2003**, *43*, 1108–1115. [CrossRef]
41. Wagstaff, K.M.; Jans, D.A. Intramolecular Masking of Nuclear Localization Signals: Analysis of Importin Binding Using a Novel AlphaScreen-Based Method. *Anal. Biochem.* **2006**, *348*, 49–56. [CrossRef]
42. Oshokoya, O.O.; Roach, C.A.; Jiji, R.D. Quantification of Protein Secondary Structure Content by Multivariate Analysis of Deep-Ultraviolet Resonance Raman and Circular Dichroism Spectroscopies. *Anal. Methods* **2014**, *6*, 1691–1699. [CrossRef]
43. Trager, W.; Jensen, J.B. Human Malaria Parasites in Continuous Culture. *Science* **1976**, *193*, 673–675. [CrossRef]
44. Kurth, F.; Pongratz, P.; Bélard, S.; Mordmüller, B.; Kremsner, P.G.; Ramharter, M. In Vitro Activity of Pyronaridine against *Plasmodium falciparum* and Comparative Evaluation of Antimalarial Drug Susceptibility Assays. *Malar. J.* **2009**, *8*, 79. [CrossRef] [PubMed]
45. Noedl, H.; Bronnert, J.; Yingyuen, K.; Attlmayr, B.; Kollaritsch, H.; Fukuda, M. Simple Histidine-Rich Protein 2 Double-Site Sandwich Enzyme-Linked Immunosorbent Assay for Use in Malaria Drug Sensitivity Testing. *Antimicrob. Agents Chemother.* **2005**, *49*, 3575–3577. [CrossRef]
46. Jacot, D.; Meissner, M.; Sheiner, L.; Soldati-Favre, D.; Striepen, B. Genetic Manipulation of *Toxoplasma gondii*. In *Toxoplasma Gondii: The Model Apicomplexan—Perspectives and Methods*, 2nd ed.; Academic Press: Cambridge, MA, USA, 2013; pp. 577–611. [CrossRef]
47. Striepen, B.; Soldati, D. Genetic Manipulation of *Toxoplasma gondii*. In *Toxoplasma Gondii*; Academic Press: Cambridge, MA, USA, 2007; pp. 391–418. [CrossRef]
48. Riss, T.L.; Moravec, R.A.; Niles, A.L.; Duellman, S.; Benink, H.A.; Worzella, T.J.; Minor, L. Cell Viability Assays. In *Assay Guidance Manual [Internet]*; Markossian, S., Grossman, A., Arkin, M., Auld, D., Austin, C., Baell, J., Brimacombe, K., Chung, T.D.Y., Coussens, N.P., Dahlin, J.L., et al., Eds.; Eli Lilly & Company and the National Center for Advancing Translational Sciences: Bethesda, MD, USA, 2016.
49. Hürlimann, E.; Hofmann, D.; Keiser, J. Ivermectin and Moxidectin against Soil-Transmitted Helminth Infections. *Trends Parasitol.* **2023**, *39*, 272–284. [CrossRef]
50. Tan, B.; Opoku, N.; Attah, S.K.; Awadzi, K.; Kuesel, A.C.; Lazdins-Helds, J.; Rayner, C.; Ryg-Cornejo, V.; Sullivan, M.; Fleckenstein, L. Pharmacokinetics of Oral Moxidectin in Individuals with *Onchocerca Volvulus* Infection. *PLoS Negl. Trop. Dis.* **2022**, *16*, e0010005. [CrossRef] [PubMed]
51. Kobe, B. Autoinhibition by an Internal Nuclear Localization Signal Revealed by the Crystal Structure of Mammalian Importin α. *Nat. Struct. Biol.* **1999**, *6*, 388–397. [CrossRef]
52. Fanara, P.; Hodel, M.R.; Corbett, A.H.; Hodel, A.E. Quantitative Analysis of Nuclear Localization Signal (NLS)-Importin a Interaction through Fluorescence Depolarization. Evidence for auto-inhibitory regulation of NLS binding. *J. Biol. Chem.* **2000**, *275*, 21218–21223. [CrossRef]
53. Sindrewicz, P.; Li, X.; Yates, E.A.; Turnbull, J.E.; Lian, L.Y.; Yu, L.G. Intrinsic Tryptophan Fluorescence Spectroscopy Reliably Determines Galectin-Ligand Interactions. *Sci. Rep.* **2019**, *9*, 11851. [CrossRef]
54. Prichard, R.; Ménez, C.; Lespine, A. Moxidectin and the Avermectins: Consanguinity but Not Identity. *Int. J. Parasitol. Drugs Drug Resist.* **2012**, *2*, 134–153. [CrossRef] [PubMed]
55. Atif, M.; Estrada-Mondragon, A.; Nguyen, B.; Lynch, J.W.; Keramidas, A. Effects of glutamate and ivermectin on single glutamate-gated chloride channels of the parasitic nematode *H. contortus*. *PLoS Pathog.* **2017**, *13*, e1006663. [CrossRef] [PubMed]
56. Hibbs, R.; Gouaux, E. Principles of activation and permeation in an anion-selective Cys-loop receptor. *Nature* **2011**, *474*, 54–60. [CrossRef] [PubMed]

57. Lynagh, T.; Lynch, J.W. A glycine residue essential for high ivermectin sensitivity in Cys-loop ion channel receptors. *Int. J. Parasitol.* **2010**, *40*, 1477–1481. [CrossRef] [PubMed]
58. Lynagh, T.; Webb, T.I.; Dixon, C.L.; Cromer, B.A.; Lynch, J.W. Molecular Determinants of Ivermectin Sensitivity at the Glycine Receptor Chloride Channel. *J. Biol. Chem.* **2011**, *286*, 43913–43924. [CrossRef] [PubMed]

Disclaimer/Publisher's Note: The statements, opinions and data contained in all publications are solely those of the individual author(s) and contributor(s) and not of MDPI and/or the editor(s). MDPI and/or the editor(s) disclaim responsibility for any injury to people or property resulting from any ideas, methods, instructions or products referred to in the content.

International Journal of
Molecular Sciences

MDPI

Article

NBF2, an Algal Fiber-Rich Formula, Reverses Diabetic Dyslipidemia and Hyperglycemia In Vivo

Nlandu Roger Ngatu [1,*], Akram Hossain [2], Nao Maruo [3], Steeve Akumwami [4], Asadur Md. Rahman [2], Masamitsu Eitoku [3], Kanae Kanda [1], Akira Nishiyama [2], Narufumi Suganuma [3] and Tomohiro Hirao [1,*]

[1] Department of Public Health, Kagawa University Faculty of Medicine, Kagawa 761-0793, Japan; kanda.kanae@kagawa-u.ac.jp
[2] Department of Medical Pharmacology, Kagawa University Faculty of Medicine, Kagawa 761-0793, Japan; akram.hossain@kagawa-u.ac.jp (A.H.); rahman.md.asadur@kagawa-u.ac.jp (A.M.R.); nishiyama.akira@kagawa-u.ac.jp (A.N.)
[3] Department of Environmental Medicine, Kochi University School of Medicine, Nankoku 783-8505, Japan; jm-n.maruo@kochi-u.ac.jp (N.M.); meitoku@kochi-u.ac.jp (M.E.); nsuganuma@kochi-u.ac.jp (N.S.)
[4] Department of Anesthesiology, Kagawa University Faculty of Medicine, Kagawa 761-0793, Japan; s21d703@kagawa-u.ac.jp
* Correspondence: ngatu.nlandu@kagawa-u.ac.jp (N.R.N.); hirao.tomohiro@kagawa-u.ac.jp (T.H.)

Abstract: *Ulva prolifera*, known as Aonori in Japan, is an edible alga species that is mass-cultivated in Japan. Supplementation with Aonori-derived biomaterials has been reported to enhance metabolic health in previous studies. This was an experimental study that evaluated the metabolic health effects of NBF2, a formula made of algal and *junos Tanaka citrus*-derived biomaterials, on obesity and type 2 diabetes (T2DM). We used 18 obese and hyperglycemic Otsuka Long-Evans Tokushima Fatty (OLETF) rats that were assigned randomly to three groups of six animals: a high-dose NBF2 drink (20 mg/kg) group, a low-dose (10 mg/kg) NBF2 drink group and the control group that received 2 mL of tap water daily for a total of six weeks. We also used eight LETO rats as the normal control group. In addition to the glucose tolerance test (OGTT), ELISA and real-time PCR assays were performed. High-dose and lowdose NBF2 improved insulin sensitivity, as well as glycemic and lipid profiles, as compared with control rats. The OGTT showed that both NBF2 groups and LETO rats had normalized glycemia by the 90-min time-point. NBF2 up-regulated PPARα/γ-mRNA and Sirt2-mRNA gene expressions in BAT and improved the blood pressure profile. These findings suggest that the NBF2 formula, which activates PPAR-α/γ mRNA and Sirt2-mRNA, may reverse dyslipidemia and hyperglycemia in T2DM.

Keywords: algal formula; dyslipidemia; hyperglycemia; peroxisome proliferation-activated receptor; sirtuin; type 2 diabetes

1. Introduction

Drugs that are agonists of peroxisome proliferation-activated receptors (PPARs) may be effective in the management of lifestyle-related metabolic disorders such as dyslipidemia and type 2 diabetes mellitus (T2DM) [1]. The latter condition is characterized by an inadequate pancreatic beta cell response to insulin resistance. Recently, T2DM management has undergone a major conceptual change, with more emphasis on a patient-centered care approach and the safety profile of antihyperglycemic agents [1–3]. In T2DM, the loss of insulin function is reported to be closely related to adiponectin (APN) deficiency. Thus, APN replenishment in T2DM patients might reverse this condition and improve their metabolic health. APN, a protein produced by adipocytes, has been reported to stimulate fatty acid oxidation, improve insulin sensitivity and inhibit neoglucogenesis, resulting in an improvement in energy homeostasis [4]. The insulin-sensitizing effect of APN has been linked to PPAR activation [5,6]. APN also plays a role in tissue regeneration [7,8].

The up-regulation of APN production to correct its deficiency and the restoration of the function of cells involved in energy homeostasis have motivated our research. Natural compounds from *Radix astragali* [9,10] and omega-3 poly-unsaturated fatty acids have been reported to modulate APN production and improve the metabolic health markers of high-risk subjects [11]. We discovered APN-modulating biomaterials (Ngatu Bio Formulas or NBF) containing edible green marine algal species mass-cultivated in Japan, known as Aonori and Aosanori, with beneficial metabolic health effects [12,13].

This study evaluated the effects of NBF2, a formula composed of Aonori alga and *Junos citrus* peel-derived biomaterials, on metabolic health markers in obesity and T2DM model rats.

2. Results

2.1. Obesity and Diabetic Hyperglycemia Establishment in OLETF Rat Model and Effects of Daily Intake of NBF2 on Body Weight (BW) and Fasting Blood Glucose (FBG)

As shown in Figure 1, treatment with NBF2 significantly reduced weight gain in OLETF rats that received both high and low doses of NBF2 versus vehicle-treated OLETF controls ($p < 0.05$) (Figure 1A). Additionally, both low- and high-dose NBF2-treated OLETF rats had reduced fasting blood glucose (FBG) as compared with OLETF controls ($p < 0.01$), which was normalized within the third week of treatment (Figure 1B).

In this study, an oGTT was performed by administering 0.002g of glucose/1g body weight); FBG was measured at baseline (T0), 15 min (T15), 30 min (T30), 60 min (T60), and 120 min (T120). Moreover, the decrease in FBG was greater in high- ($p < 0.01$) and low-dose ($p < 0.05$) NBF2-treated rat groups, as well as in normal rats ($p < 0.001$; vs. controls) (Figure 1C).

Furthermore, only the normal (LETO) rat group had a significantly lower daily calorie intake (vs. control group; $p = 0.000$). No significant difference was observed when comparing NBF2-treated rats and the controls (Supplementary Table S1).

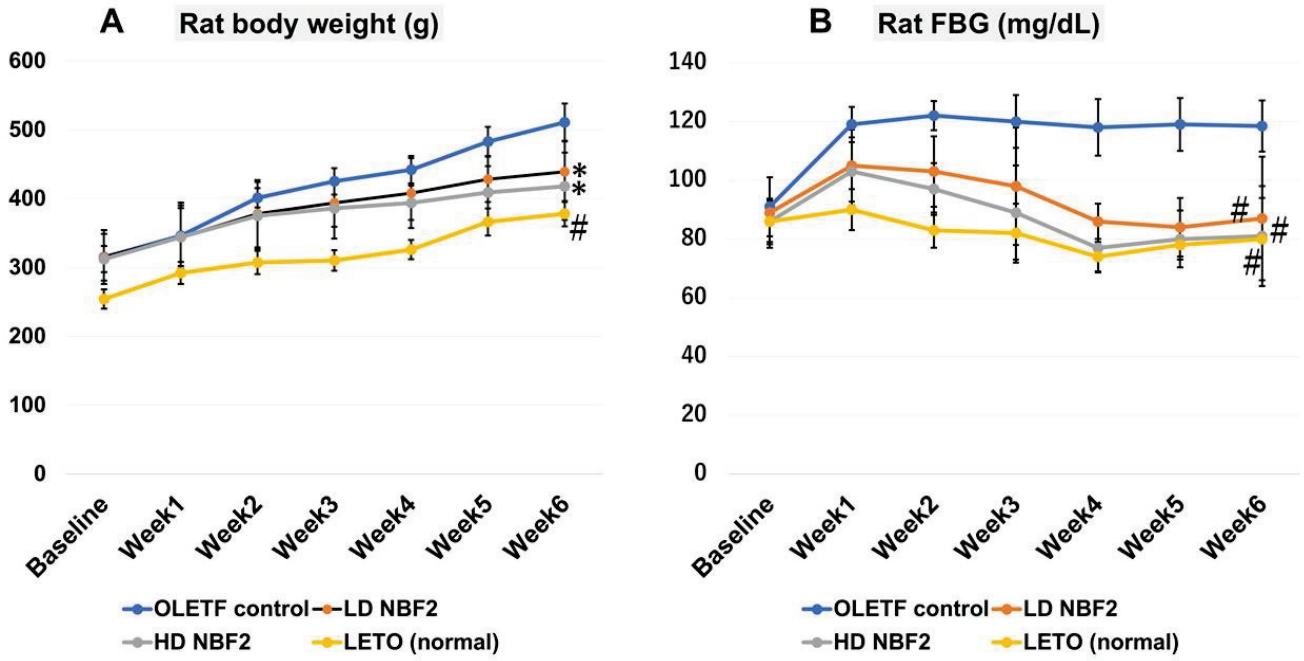


Figure 1. *Cont.*

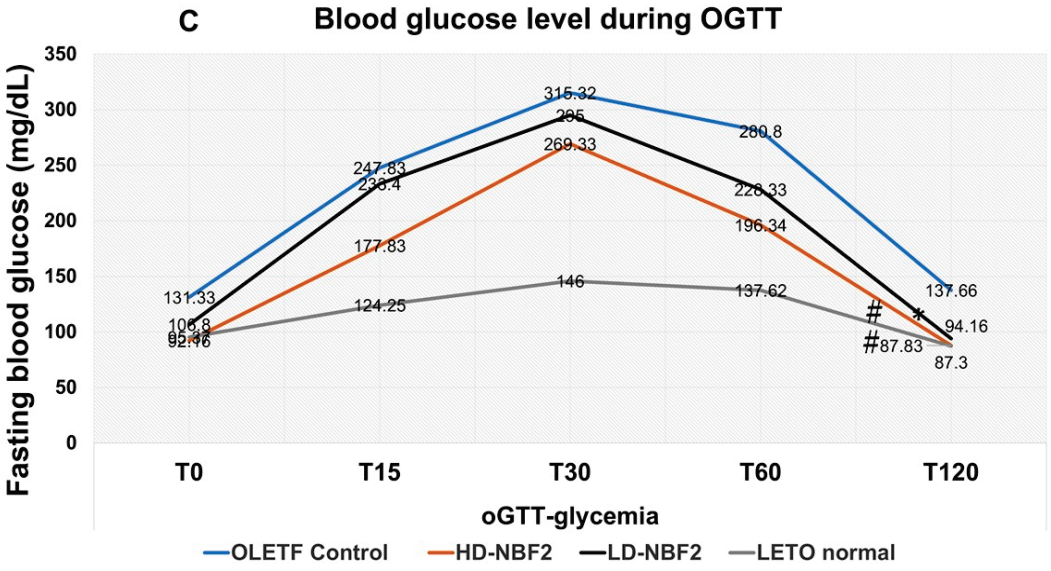


Figure 1. (**A**–**C**): The trend in rat body weight (**A**) and fasting blood glucose across the study period (**B**) and the blood glucose level during the glucose tolerance test (oGTT) (**C**) (N = 26). **Legend**: *, p-value less than 0.05; #, p-value less than 0.01 (by one-way ANOVA); OLETF, Otsuka Long-Evans Tokushima Fatty rats; LETO, Long-Evans Tokushima Otsuka rats.

2.2. Effects of NBF2 on Plasma Cholesterol, Triglycerides, Adiponectin, Insulin Resistance and Blood Pressure Profile

Figure 2 shows the plasma levels of cholesterols, triglycerides (TGs) and the blood pressure profile. The high-dose NBF2 group had significantly lower total cholesterol (Figure 2A), LDL-c ($p < 0.05$) (Figure 2B) and TG levels ($p < 0.01$) (Figure 2C) compared to the control group. Similarly, the low-dose NBF2 group also showed significantly reduced total cholesterol, TGs and LDL-c ($p < 0.05$). On the other hand, the HDL-c level was significantly higher in the high-dose NBF2 group (vs. control group; $p < 0.05$). Furthermore, significantly reduced blood pressure was observed in the high- and low-dose NBF2 groups for DBP and MBP compared to the control group ($p < 0.05$) (Figure 2E–G).

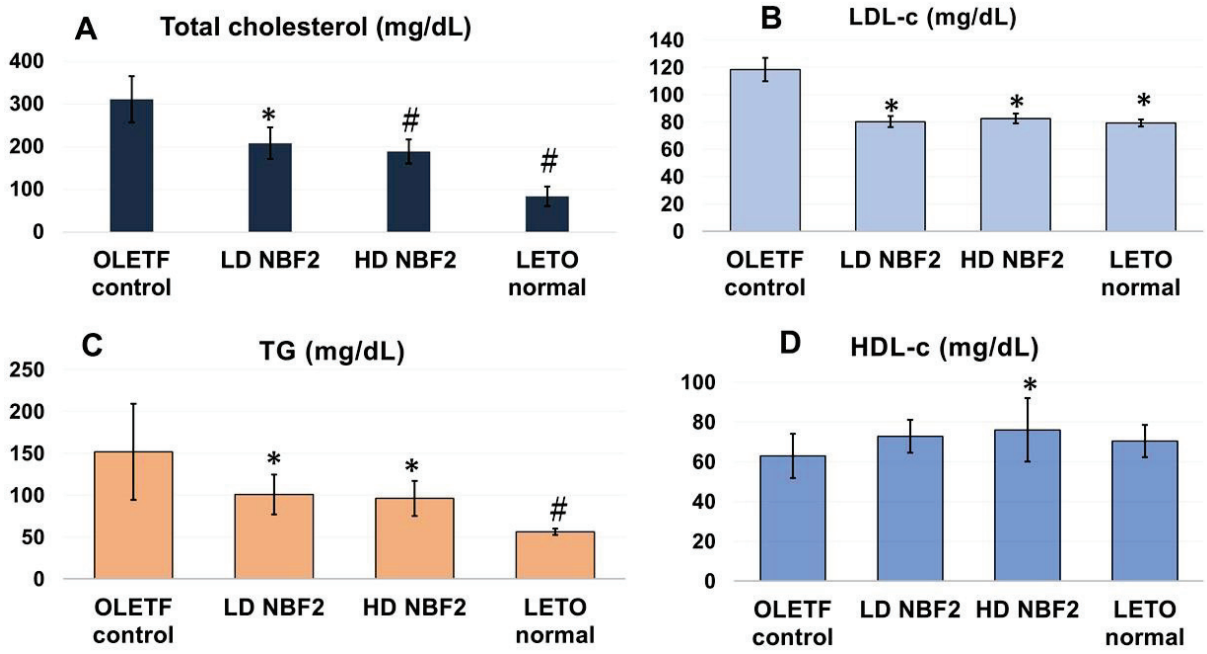


Figure 2. *Cont.*

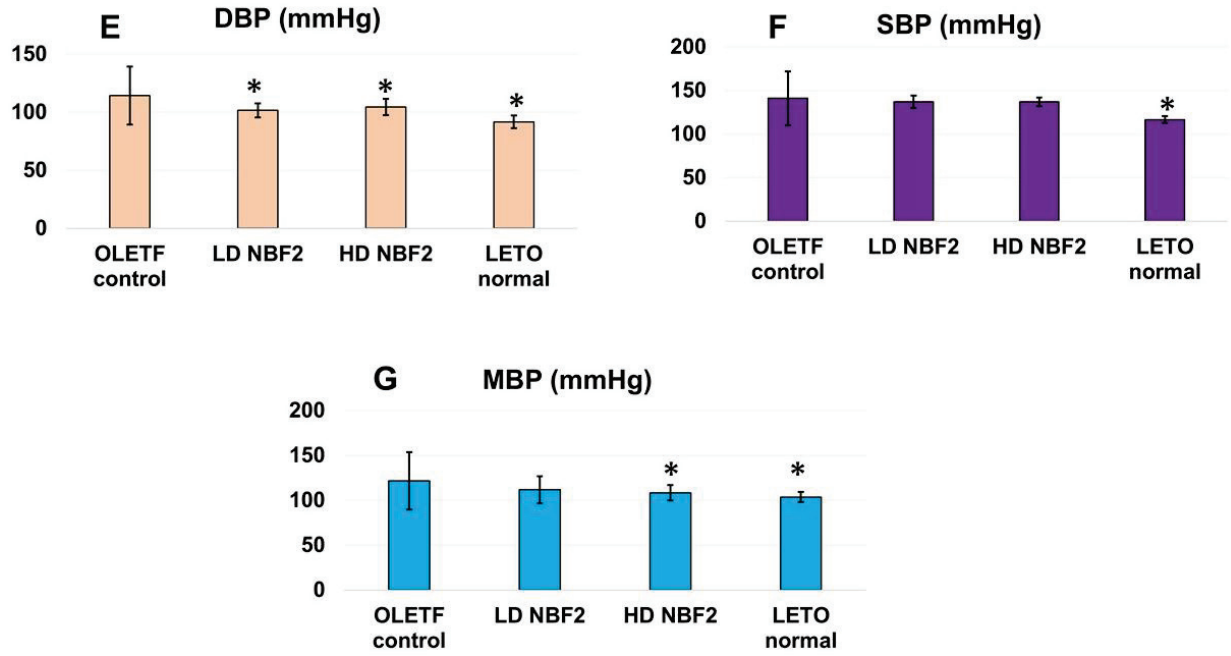


Figure 2. (**A**–**G**) Blood lipid and blood pressure profiles in rats (N = 26). **Legend**: *, p-value less than 0.05; #, p-value less than 0.01 (by one-way ANOVA); OLETF, Otsuka Long-Evans Tokushima Fatty rats; LETO, Long-Evans Tokushima Otsuka rats; T-chol, total cholesterol; LDL-c, low-density lipoprotein cholesterol; HDL-c, high-density lipoprotein cholesterol; TG, triglyceride.

ELISA assays showed significantly higher APN levels in both NBF2 groups compared to the control group ($p < 0.05$). Regarding plasma insulin, a relatively low level was observed in NBF2-treated rats but this was not significant (Figure 3A,B). Furthermore, a significant reduction in HOMA-IR was observed in the NBF2-treated groups compared to the control group (−17% versus −3% change, respectively; $p < 0.05$) (Figure 3C).

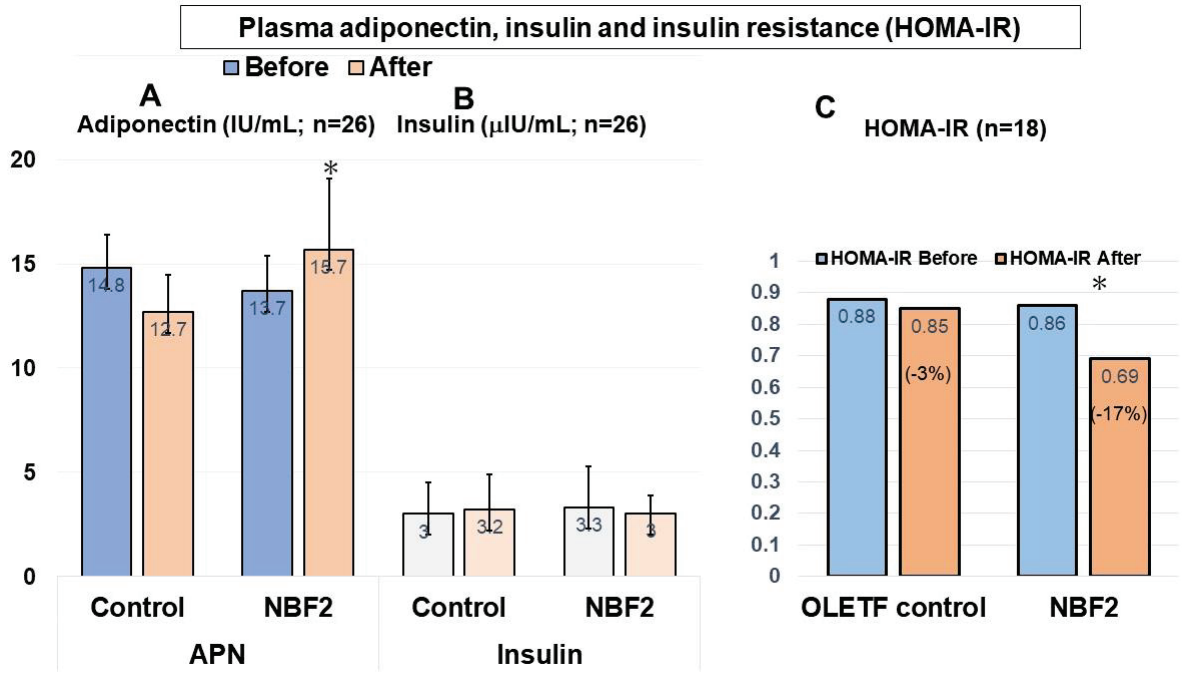


Figure 3. (**A**–**C**) Plasma adiponectin (**A**), insulin (**B**) and HOMA-IR (**C**) (N = 24). **Legend**: *, $p < 0.05$; IU, international unit; APN, adiponectin; NBF, Ngatu Bio Formula; HOMA-IR, homeostasis model assessment for insulin resistance.

3. Messenger RNA (mRNA) Gene Expression Levels of Metabolic Biomarkers

Real-time PCR assays were performed to determine the mRNA gene expression levels of metabolic biomarkers. Table 1 presents the list of primers of rat biomarkers and the corresponding mRNA gene sequences. Leptin and fatty acid synthase (FASN) are linked to the development of obesity and related metabolic disorders. It was observed that rats treated with NBF2 had significantly reduced leptin mRNA expression in brown (BAT) and white adipose tissue (WAT) and liver specimens, as compared with vehicle-treated OLETF controls ($p < 0.05$) (Figure 4A–C). Similarly, NBF2-treated rats had reduced FASN mRNA gene expression in both BAT and WAT specimens (Figure 4D), suggesting an inhibitory effect of NBF2 on fat accumulation.

Unlike FASN and leptin, sirtuin 2 (Sirt2) and the peroxisome proliferator-activated receptors alpha and gamma (PPAR-α/γ) are known to improve obesity-associated metabolic disorders and are considered therapeutic targets for diseases such as T2DM. We observed that treatment with NBF2 caused a marked increase in Sirt2-mRNA expression in the rat BAT ($p < 0.01$) and WAT ($p < 0.05$), as well as an increase in PPAR–γ and PPAR–α mRNA expressions in OLETF rat BAT as compared with the vehicle in the control rats (Figure 4G,H). The lowdose NBF2 group also had reduced APN-mRNA gene expression in BAT and APN-mRNA gene expression in WAT. ATPase sarcoplasmic/endoplasmic reticulum Ca^{2+}, also known as ATPase 2a2 or SERCA2, is an enzyme that plays an important metabolic role as a glucose transport regulator; it is down-regulated in the adipocytes of diabetic animals and humans. We found that BAT ATP2a2-mRNA expression was up-regulated in NBF2-treated rats (Figure 4M–O) (vs. control group; $p < 0.05$). Consequently, the dual PPARα/γ and Sirt2 modulatory effects of NBF2 observed in this study suggest an improvement in lipid and glucose metabolism.

Table 1. List of primers used and corresponding biomarkers' nucleic acid sequences.

Name	Primer (5′→3′)	Length	GC%	Tm	Target Gene	Amplified Size (bp)	Amplified Area
PPAR-[F]	GAGGGCACACGCTAGGAAG	19	63	60	XM_006242152.4	72	GAGGGCACACGCTAGGAAGG GCACACGCGTGCGACTTTCGG GGCCCCTGGAACTGTCCGCTA CTTCGA GTCC
PPAR-[R]	GGACTCGAAGTAGCGGACAG	20	60	60			
PPAR-[F]	GCCGCCTCAGATTTGAAAGAA	21	48	59	XM_006237009.4	142	GCCGCCTCAGATTTGAAAGAA GCTGTGAACCACTAATATCCA AGGACATTTTTGAAAACAAGG ACTACCCTTTACTGAAATTACC ATGGTTGACACAGAGATGCCA TTCTGGCCCACCAACTTCGGA ATCAGCTCTGTGGAC
PPAR-[R]	GTCCACAGAGCTGATTCCGA	20	55	60			
APN [F]	CAAGCGCTCCTGTTCCTCTT	20	55	62	XM_039087986.1	228	CAAGCGCTCCTGTTCCTCTTAA TCCTGCCCAGTCATGAAGGGA TTACTGCAACCGAAGGGCCAG GAGCTTTGGTCCCTCCACCCA AGGAAACTTGTGCAGGTTGGA TGGCAGGCATCCCAGGATATC CTGGTCACAATGGGATACCGG GCCGTGATGGCAGAGATGGCA CTCCTGGAGAGAAGGGAGAG AAGGGAGACGCAGGTGTTCT TGGTCCTAAGGGTGACCCA
APN [R]	TGGGTCACCCTTAGGACCAA	20	55	62.6			
Sirtuin 2 [F]	GACGAGCTGACCCTTGAAG	19	58	63	NM_001399630.1	148	GACGAGCTGACCCTTGAAG GAGTGACACGCTACATGCA GAGCGAGCGCTGTCGCAG GGTCATCTGTTTGGTGGGA GCTGGAATCTCCACATCCG CAGGAATCCCTGACTTCCG CTCCCCATCCACTGGCCTC TATGCAAACTTGGAGA
Sirtuin 2 [R]	TCTCCAAGTTTGCATAGAGGC	21	48	63			

Table 1. *Cont.*

Name	Primer (5′→3′)	Length	GC%	Tm	Target Gene	Amplified Size (bp)	Amplified Area
Atp2a2 [F]	TTTGGGCAGGATGAGGATG	19	53	66	NM_001110139.2	128	TTTGGGCAGGATGAGGA TGTGACATCAAAGGCTTT TACAGGGCGAGAATTTGA TGAATTAGCCCCTCAGCC CAGAGAGACGCCTGCTT AAATGCCCGTTGTTTTGCT CGAGTTGAACCTTCCCACAA
Atp2a2 [R]	TTGTGGGAAGGTTCAACTCG	20	50	65			
Fasn [F]		20	55	64	NM_017332.2	214	TCGCTCATGGGTGTGGA AGTGCGCCAGATCCTGG AACGTGAACATGATCTGG TGCTACCCATTCGTGAAG TACGGCAACTCACACTGC GGAAGCTTCAGGAAATGT CCTCCAAGGCTGGCTCAG ACACTGAGTTGGCAGCCC CCAAGTCCAAGAATGATAC ATCCCTGAAGCAGGCCCA GCTGAATCTGAGTATCCTG CTGGTGAACCCTGA
Fasn [R]		20	55	63			
Leptin [F]	GAGACCCCTGTGTCGGTTC	19	63	60	NM_013076.3	139	GAGACCCCTGTGCCGGT TCCTGTGGCTTTGGTCC TATCTGTCCTATGTTCAA GCTGTGCCTATCCACAA AGTCCAGGATGACACCA AAACCCTCATCAAGACC ATTGTCACCAGGATCAA TGACATTTCACACACGCAG
Leptin [R]	CTGCGTGTGTGAAATGTCATTG	22	45	59			
rGapdh [F]	TGATTCTACCCACGGCAAGT	20	50	64	NM_017008.4	142	TGACTCTACCCACGGCA AGTTCAACGGCACAGTC AAGGCTGAGAATGGGAA GCTGGTCATCAACGGGA AACCCATCACCATCTTCC AGGAGCGAGATCCCGCTA ACATCAAATGGGGTGATGCT
rGapdh [R]	AGCATCACCCCATTTGATGT	20	45	65			

Notes: APN, adiponectin; F, forward; R, reverse; %, percent.

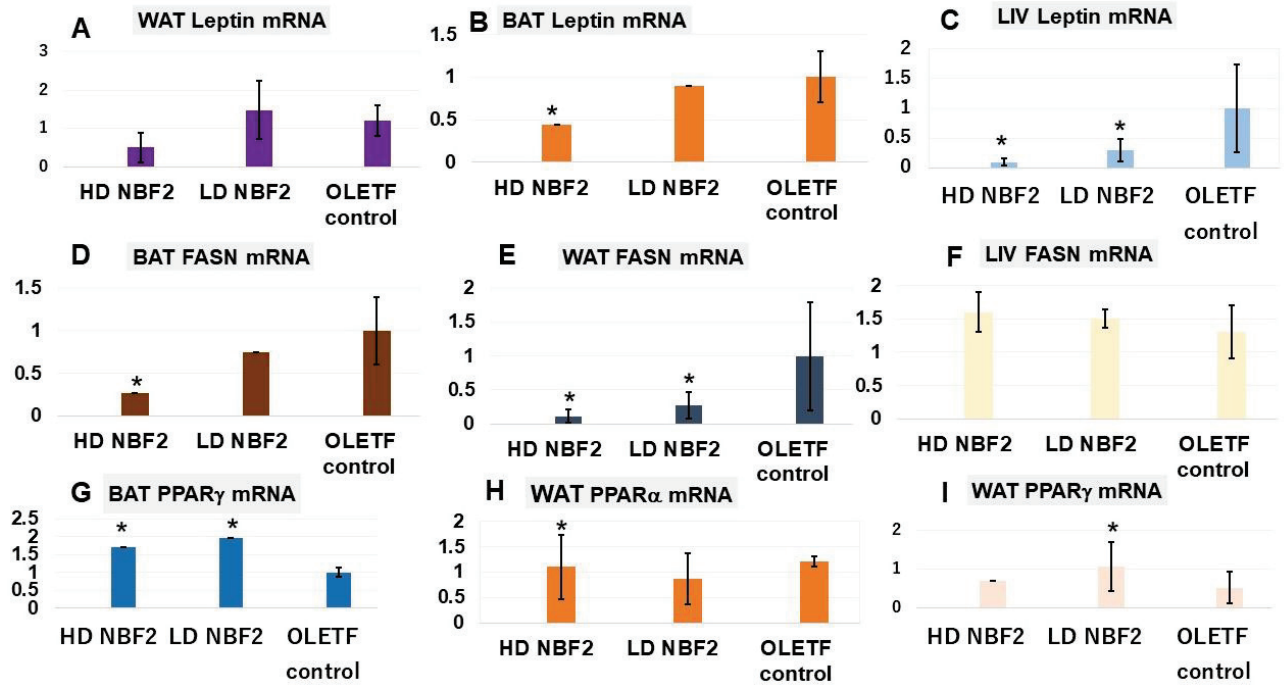


Figure 4. *Cont.*

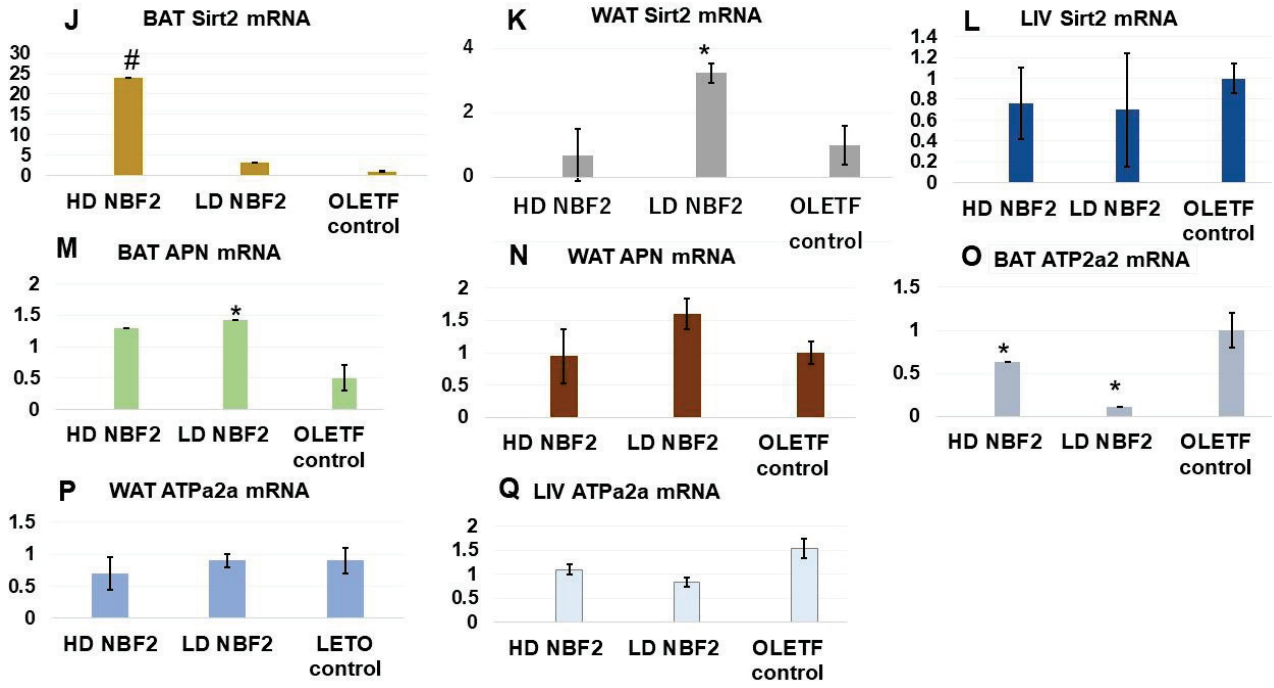


Figure 4. Messenger RNA (mRNA) gene expression of biomarkers in white/brown adipose tissue and liver biopsies (N = 20). **Legend**: *, *p*-value less than 0.05; #, *p*-value less than 0.01 (vs. OLET control; by Student's *t* test); OLETF, Otsuka Long-Evans Tokushima Fatty rats; LETO, Long-Evans Tokushima Otsuka rats; mRNA, messenger ribonucleic acid; BAT, brown adipose tissue; WAT, white adipose tissue; LIV, liver tissue; APN, adiponectin; FASN, fatty acid synthase; PPAR, peroxisome proliferator-activated receptor; Sirt2; sirtuin 2; ATPa2a or SERCA2, ATPase sarcoplasmic/endoplasmic reticulum Ca^{2+}. The unit used is the percentage (%) of the relative mRNA gene expression level for each biomarker.

In the histopathological examination, white adipose tissue (WAT) and liver sections showed the following results: Large adipocytes were mostly observed in WAT specimens from OLETF control rats (Supplementary Figure S1C,D) compared to in specimens from normal rats (Supplementary Figure S1A,B) and NBF2-treated animals (Supplementary Figure S1E,F). Regarding BAT specimens, the presence of smaller adipocytes mixed with large adipocytes was observed in OLETF controls (Supplementary Figure S1I,J), but larger ones were predominant in BAT from rats treated with NBF2 (Supplementary Figure S1K,L) and in LETO rats (Supplementary Figure S1G,H). Images of blood sinusoidal dilation and hepatic steatosis with lipid droplets were mostly observed in liver specimens from OLETF control rats (Supplementary Figure S1O,P), whereas these changes were either reduced and inexistent in liver specimens from NBF2-treated OLETF (Supplementary Figure S1Q,R) and normal rats (Supplementary Figure S1M,N).

4. Discussion

In the present experimental study, we explored the metabolic health effects of low and high (normal) doses of NBF2, a formula containing marine Aonori alga and *junos* Tanaka *citrus*-derived biomaterials, on lipid and glucose metabolism in obese and hyperglycemic OLETF rats. NBF2 treatment increased APN production.

Previously, we reported that algal biomaterial (NBF1), which represents 60% of NBF2, induced a 2- to 3-fold increase in APN in human subjects [12]. On the other hand, *junos citrus* peel, another component of NBF2 that represents 40%, is mainly composed of a potent anti-inflammatory compound, limonene [14]. Thus, the formula used in this study can be considered a potent PPAR modulator, an APN modulator and an anti-inflammatory agent that exerts beneficial effects on glucose and lipid metabolism.

In our study, NBF2 intake prevented weight gain in OLETF rats compared to the vehicle. Moreover, NBF2 could improve insulin sensitivity and also normalize blood glucose in OLETF rats to a level similar to that of lean LETO rats across the experiment. The latter finding can be explained by the increased brown fat mass, the relatively low FASN mRNA expression and the enhanced APN production in NBF2-treated OLETF rats. APN is known to ameliorate insulin resistance and glucose intolerance. By restoring insulin sensitivity through the up-regulation of APN production, NBF2 could reverse hyperglycemia. Recently, we have reported that in addition to its anti-inflammatory effect, NBF-containing algal biomaterial has a potential to improve the glycemic profile in individuals with a high cardiometabolic risk and in diabetic patients as well [13].

This study also showed an enhanced lipid metabolism and BP profile in obese and hyperglycemic rats treated with NBF2. The observed improvement in lipid profile, possibly intertwined with Sirt2 activation, may explain the slowing of weight gain and the improved BP. Recently, evidence has been accumulated suggesting that not only PPARs but also sirtuin activators can be utilized as novel therapeutic targets for metabolic disorders [15,16]. Sirt2, known as an NAD+-dependent deacetylase and which was activated by NBF2 in our study, plays an important role in terms of lipid metabolism regulation and improving liver function [17–19].

Compared to WAT, BAT has been reported to produce a larger amount of circulating APN. On the other hand, PPARs are known to induce the browning of white fat and regulate brown adipocyte thermogenic function [20,21]. The fiber-rich algal component of NBF2 has displayed a good safety profile, has exerted anti-inflammatory activity in humans in previous studies [22,23] and seems to have influenced PPAR activity in BAT in the present study. This suggests that NBF2 could be a potential natural agent with beneficial metabolic health effects. Further investigations are needed to clarify the relationship between NBF2 and PPARs.

Nonetheless, this study has some limitations. The effects of NBF2 on other metabolic markers such as glucagon-like protein-1 receptor (GLP-1R) have not been explored. Drugs that inhibit GLP-1R have recently emerged as effective therapeutic agents for T2DM, as they stimulate insulin secretion, causing a decrease in blood glucose [24].

Taken together, the findings from this study suggest that the NBF2 formula, which increased BAT, improved glucose tolerance and alleviated insulin resistance in this experiment, has a potential to reverse dyslipidemia and hyperglycemia in T2DM.

5. Materials and Methods

5.1. Animals and Intervention

The experimental protocol, as well as the animal care procedures, were carried out according to the guidelines for the care and use of animals of the Experimental Animal Center of Kagawa University (ethical approval number: 20656-1), Japan. Six-week-old male Otsuka Long-Evans Tokushima Fatty (OLETF) and genetic control Long-Evans Tokushima Otsuka (LETO) rats were purchased from Japan SLC Inc. (Shizuoka, Japan) and maintained under a controlled temperature (24 ± 2 °C) and humidity (55 ± 5%), with a 12 h light/dark cycle, at the Animal Center of Kagawa University in Japan. The rats were fed with MF chow and had access to tap water ad libitum. They were used when they reached 10 weeks of age. It has been reported that OLETF rats exhibit metabolic syndrome and prediabetes from the age of 10 weeks of age and, later on, the type 2 diabetic phase.

The NBF2-based drink was a gift from Kochi Ice Co., Ltd. (Kochi, Japan), a food processing factory located in Kochi prefecture, Japan. It is a food-based formula containing 60% ulvan-rich alga powder and 40% *Junos* Tanaka *citrus* peel powder. The chemical composition of the two biomaterials that make up the NBF2 formula is as follows:

(1) The Aonori (*Ulva prolifera*) algal biomaterial used in this study is rich in fiber (~65%), and its main bioactive component is ulvan [12], followed by protein (9~14%), omega-3 and omega-6 fatty acids (10.4~10.9%), and small amounts of flavonoids, carotenoids and minerals;

(2) The *junos citrus* peel biomaterial is rich in limonene (68~70%), other terpenoids such as γ-terpinene (11.4~12.5%), β–phellandrene (4.6~5.4%), myrcene (3.0~3.2%) and α−pinene (2.3~21.7%), and small amounts of aromatic compounds [12,15].

5.2. Experimental Protocol

In this experiment, a total of 26 rats were used, including 18 OLETF and 8 LETO (normal) rats. LETO rats were used as normal controls; prediabetic OLETF rats were randomly divided into 3 groups at week 10 of age (baseline) based on body weight and fasting blood glucose (FBG) (Figure 5):

(1) Group 1: 2 mL H_2O (vehicle)-treated OLETF rats or OLETF controls (n = 6);
(2) Group 2: 20 mg/kg/day NBF2-treated OLETF rats (n = 6);
(3) Group 3: 10 mg/kg/day NBF2-treated OLETF rats (n = 6).

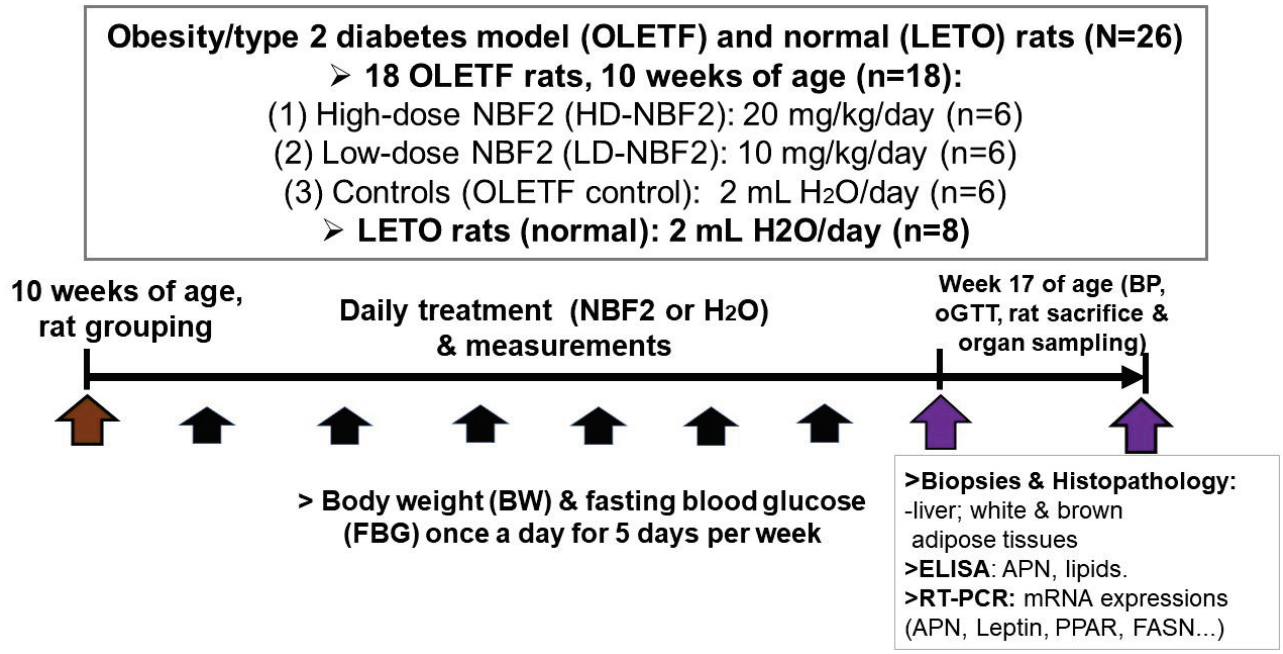


Figure 5. The experimental protocol. Figure 1 shows the procedures used in this study and the measurements performed to obtain the clinical, laboratory (ELISA, RT-PCR assays) and pathological data. **Legend**: APN, adiponectin; PPAR, peroxisome proliferator-activated receptor; FASN, fatty acid synthetase; mRNA, messenger ribonucleic acid; oGTT, glucose tolerance test. Brown arrow shows that start of experiment; purple arrows indicate the week where oGTT and biospecimen sampling were performed for bioassays, black arrows indicate the period in which daily measurements of body weight and blood glucose were carried out.

Daily calorie intake was measured on a weekly basis starting from week 10 of age; the mean value of calorie intake calculated for each group was estimated based on the energy provided by the MF chow and NBF2-containing nutrients. Furthermore, fasting blood glucose (FBG) was measured with the use of a freestyle glucose meter (Glucotest AI, Sanwa Biochemical Research Center, Kanagawa, Japan) from the tip of the rat tail once a week. Body weight was also measured on a weekly basis.

5.3. Measurements

The oral glucose tolerance test (OGTT) was carried out in duplicate within the last week of the experiment when the rats were 16 weeks old, as described previously [14]. Briefly, the rats were fasted for 12 h, and 0 min blood glucose was measured. Then, the rats were each fed 2 g/kg of 50% glucose solution by gavage; blood glucose was measured again at 30, 60 and 120 min.

Blood pressure (BP) and heart rate (HR) were measured using an automatic device (BP-98A, Softron, Tokyo, Japan), following the tail-cuff method. Briefly, a photo-elective sensor, which is attached to the animal tail by a piece of rubber tubing, detects the pulse volume oscillations through the cuff pressure and pulse waves. The pulse waves are detected as systolic BP (SBP) and mean BP (MBP); these two values are used to calculate the diastolic BP (DBP) automatically with the use of the following formula: DBP = (3 × MBP − SBP)/2. The homeostatic model assessment of insulin resistance (HOMA-IR) was calculated according to the following formula:

$$\text{HOMA-IR} = \text{glycemia (mg/dL)} \times \text{plasma insulin (UI/mL)}/405.$$

5.4. Biospecimen Sampling, Histological Examination and Real-Time PCR

On the day of animal sacrifice, the rats were fasted for 12 h and anesthetized; blood was drawn. Blood lipids were measured using a portable lipid analyzer MLA-1 (Changsha Zealson Biotech Co., Ltd., Changsha, China). Plasma adiponectin and insulin measurements were performed by using the enzyme-linked immunosorbent assay (ELISA; SRL biochemical company, Kobe, Japan). Brown adipose tissue (BAT) was collected from the scapula area, whereas white adipose tissue (WAT) was collected from the mesenteric, retroperitoneal and epididymal spaces. All necessary organs taken from the rats were weighted and stored at −80 °C prior to histological examination. The latter was performed by a pathologist. Visceral adipose tissue and liver specimens were formalin-fixed and paraffin-embedded. They were stained with hematoxylin–eosin (HE) prior to observation of the specimen with an all-in-one fluorescence microscope BZ-X800. (Keyence Corp., Osaka, Japan).

The collected adipose tissues were snap-frozen in liquid nitrogen, then stored at −80 °C until processing for RNA extraction. Real-time reverse transcription PCR (RT-PCR) was performed at the laboratory unit of the department of Environmental Medicine, Kochi University Medical School, Japan. RNA was isolated from WAT, FAT and liver tissue by using the phenol–chloroform extraction method, and cDNA was prepared. Messenger RNA (mRNA) expressions of PPAR−α, PPAR−γ, leptin and APN were analyzed in adipose tissue, whereas those of the three markers of lipid metabolism, namely fatty acid synthase (FAS), sirtuin2 (Sirt2) and ATPase sarcoplasmic/endoplasmic reticulum Ca^{2+} transporting 2 (ATP2a2), were analyzed in liver tissue by RT-PCR using ABI Prism 7000 with Power SYBR Green PCR Master Mix (Invitrogen, Tokyo, Japan) and primer sequences from Eurofins genomics (Japan). Group comparisons for mRNA gene expressions of different biomarkers were performed using the relative quantification of genes.

5.5. Ethical Considerations and Statistical Analysis of Collected Data

The study protocol was approved by the Ethical Review Board of the Experimental Animal Center of Kagawa University (approval number: 20656-1). All of the procedures were performed according to internationally adopted guidelines for the care and use of laboratory animals. Mean (SD) values were used to present continuous data. Furthermore, Student's t test was used when comparing two groups of normally distributed data related to the outcome variables. Analysis of variance (ANOVA) for repeated measures or one-way ANOVA, followed by a post hoc Tukey's test, was used when appropriate. The significance level was set at a *p*-value less than 0.05. Stata statistical software version 15 was used for all statistical analyses (SataCorp, College Station, TX, USA).

6. Conclusions

The present study, which is related to one of the newly discovered alga-based adiponectin-modulating formulas, NBF2, showed that its intake caused Sirt2 and dual PPAR activation, up-regulated APN, and improved glucose and lipid metabolism in a rodent model of obesity and T2DM. These findings suggest that NBF2 may be beneficial in preventing and reversing hyperlipidemia and hyperglycemia in at-risk subjects and T2DM patients.

Supplementary Materials: The following supporting information can be downloaded at: https://www.mdpi.com/article/10.3390/ijms251910828/s1.

Author Contributions: Conceptualization, N.R.N., A.H., A.M.R. and A.N.; methodology, N.R.N., T.H., K.K. and M.E.; investigation and interpretation of data, N.R.N., N.M. and N.S.; writing manuscript draft, N.R.N., S.A. and M.E.; final approval of manuscript, all authors. All authors have read and agreed to the published version of the manuscript.

Funding: No funding was received. This study was conducted with internal funds of the department of public health, Kagawa University Faculty of Medicine, Japan.

Institutional Review Board Statement: This study was conducted in accordance with the Helsinki Declaration, and the animal study protocol was approved by the Ethical Review Board of the Experimental Animal Center of Kagawa University (approval number: 20656-1).

Informed Consent Statement: Not applicable.

Data Availability Statement: The datasets used in this study are available from the corresponding authors.

Acknowledgments: We thank the manager of Kochi Ice company (Kochi, Japan), Daniel Ton-duangu from the Faculty of Medicine of Kinshasa University in D.R. Congo, Yukimi Nakamura from Takamatsu Health Center in Japan, and Joel Ngoie, President of FICE (Congo Diaspora Forum) international, for supporting this research project.

Conflicts of Interest: The authors declare no conflicts of interest.

References

1. Luo, W.; Guo, Z.; Wu, M.; Hao, C.; Hu, X.; Zhou, Z.; Yao, X.; Zhang, L.; Lui, J. Association of peroxisome proliferator-activated receptor $\alpha/\delta/\gamma$ with obesity, and gene-gene interaction, in the Chinese Han population. *J. Epidemiol.* **2013**, *23*, 187–194. [CrossRef] [PubMed]
2. American Diabetes Association. Pharmacologic approaches to glycemic treatment: Standards of medical care in diabetes-2021. *Diabetes Care* **2021**, *44*, S111–S124. [CrossRef] [PubMed]
3. Lingvay, I. Obesity management as a primary treatment goal for type 2 diabetes: Time to reframe the conversation. *Lancet* **2022**, *399*, 394–405. [CrossRef] [PubMed]
4. Kadowaki, T.; Yamauchi, T.; Kubota, N.; Hara, K.; Ueki, K.; Tobe, K. Adiponectin and adiponectin receptors in insulin resistance, diabetes, and the metabolic syndrome. *J. Clin. Investig.* **2006**, *116*, 1784–1792. [CrossRef]
5. Kersten, S.; Desvergne, B.; Wahli, W. Roles of PPARs in health and disease. *Nature* **2000**, *405*, 421–424. [CrossRef]
6. Yamauchi, T.; Kamon, J.; Minokoshi, Y.; Ito, Y.; Waki, H.; Yochida, S.; Uchida, S.; Yamashita, S.; Noda, M.; Kita, S.; et al. Adiponectin stimulates glucose utilization and fatty acid oxidation by activating AMP-activated protein kinase. *Nat. Med.* **2002**, *8*, 1288–1295. [CrossRef]
7. Karbowska, J.; Kochan, Z. Role of adiponectin in the regulation of carbohydrate and lipid metabolism. *J. Physiol. Pharmacol.* **2006**, *57*, 103–113. Available online: https://www.jpp.krakow.pl/journal/archive/11_06_s6/pdf/103_11_06_s6_article.pdf (accessed on 12 February 2024). [PubMed]
8. Fiaschi, T.; Magherini, F.; Gamberi, T.; Modesti, P.A.; Modesti, A. Adiponectin as a tissue regenerating hormone: More than a metabolic function. *Cell Mol. Life Sci.* **2014**, *71*, 1917–1925. [CrossRef]
9. Xu, A.; Wang, H.; Hoo, R.L.C.; Sweeney, G.; Vanhoutte, P.M.; Wang, Y.; Wu, D.; Chu, W.; Qin, G.; Lam, K.S.L. Selective elevation of adiponectin production by the natural compounds derived from medicinal herb alleviates insulin resistance and glucose intolerance in obese mice. *Endocrinology* **2009**, *150*, 625–633.
10. Hoo, R.L.C.; Wong, J.Y.L.; Qiao, C.F.; Xu, A.; Xu, H.X.; Lam, K.S.L. The effective fraction isolated from Radix astragali alleviates glucose intolerance, insulin resistance and hyperglyceridemia in diabetic db/db mice through its anti-inflammatory activity. *Nutr. Metab.* **2010**, *7*, 67–79. [CrossRef]
11. O'Mahony, L.L.; Matu, J.; Price, O.J.; Birch, K.M.; Ajjan, R.A.; Farrar, D.; Tapp, R.; West, D.J.; Deighton, K.; Campbell, M.D. Omega-3 polyunsaturated fatty acids favourably modulate cardiometabolic biomarkers in type 2 diabetes: A meta-analysis and meta-regression of randomized controlled trials. *Cardiovasc. Diabetol.* **2018**, *17*, 98–110. [CrossRef] [PubMed]
12. Ngatu, R.N.; Ikeda, M.; Watanabe, H.; Tanaka, M.; Inoue, M.; Kanbara, S.; Nojima, S. Uncovering adiponectin replenishing property of Sujiaonori algal biomaterial in humans. *Mar. Drugs* **2017**, *15*, 32–41. [CrossRef] [PubMed]
13. Ngatu, R.N.; Ikeda, M.; Tonduangu, D.K.; Nangana, S.L.; Hirao, T. Modulatory effects of NBF1 algal-rich bioformula on adiponectin and c-reactive protein levels and its therapeutic prospects for metabolic syndrome and type 2 diabetes. *Biomedicines* **2022**, *10*, 272–2581. [CrossRef] [PubMed]

14. Hossain, A.; Yamaguchi, F.; Hirose, K.; Matsunaga, T.; Sui, L.; Hirata, Y.; Noguchi, C.; Katagi, A.; Kamitori, K.; Dong, Y.; et al. Rare sugar d-psicose prevents progression and development of diabetes in T2DM model Otsuka Long-Evans Tokushima Fatty rats. *Drug Des. Devel. Ther.* **2015**, *9*, 525–535. [CrossRef] [PubMed]
15. Watanabe, H.; Inata, Y.; Kimura, K.; Matsumoto, M.; Kaneko, S.; Kasuga, M.; Inoue, H. Sirt2 facilitates hepatic glucose uptake by deacetylating glucokinase regulatory protein. *Nat. Commun.* **2018**, *9*, 30. [CrossRef]
16. Ren, H.; Hu, F.; Wang, D.; Kang, X.; Feng, X.; Zhang, L.; Zhou, B.; Liu, S.; Yuan, G. Sirtuin 2 prevents liver steatosis and metabolic disorders by deacetylation of hepatocyte nuclear factor 4a. *Hepatology* **2021**, *74*, 723–740. [CrossRef]
17. Park, S.Y.; Chung, M.J.; Son, J.Y.; Yun, H.H.; Park, J.M.; Yim, J.H.; Jung, S.J.; Lee, S.H.; Jeong, K.S. The role of sirtuin2 in sustaining functional integrity of the liver. *Life Sci.* **2021**, *285*, 119997–120004. [CrossRef]
18. Kim, S.H.; Hong, S.H.; Park, Y.J.; Sung, J.H.; Lee, K.W.; Jung, K.; Lim, C.; Kim, J.H.; Kim, H.; Kim, H.; et al. MD001, a novel peroxisome proliferator-activated receptor α/γ agonist, improves glucose and lipid metabolism. *Sci. Rep.* **2019**, *9*, 1656–1667. [CrossRef]
19. Jain, N.; Bhansali, S.; Kurpad, A.V.; Hawkins, M.; Sharma, A.; Kaur, S.; Rastogi, A.; Bhansali, A. Effect of a dual PPAR α/γ agonist on insulin sensitivity in patients of type 2 diabetes with hyperglycemia–randomized double-blind placebo-controlled trial. *Sci. Rep.* **2019**, *9*, 19017–19026. [CrossRef]
20. Kroon, T.; Harms, M.; Mauer, S.; Ida, B.; Alexandersson, I.; Lindblom, A.; Ahnmark, A.; Nilsson, D.; Gennemark, P.; O'Mahony, G.; et al. PPARg and PPARa synergize to induce robust browning of white fat in vivo. *Mol. Metab.* **2020**, *36*, 100964. [CrossRef]
21. Shen, Y.; Su, Y.; Silva, F.J.; Weller, A.H.; Sostre-Colon, J.; Titchenell, P.M.; Steger, D.J.; Seale, P.; Soccio, P.E. Sahred PPARα/γ target genes regulate brown adipocyte thermogenic function. *Cell Rep.* **2020**, *9*, 3079–3091.e5. [CrossRef] [PubMed]
22. Gallwitz, B. Clinical perspectives on the use of the GIP/GLP-1 receptor agonist tirzepatide for the treatment of type-2 diabetes and obesity. *Front. Endocrinol.* **2022**, *13*, 1004044. [CrossRef] [PubMed]
23. Hirota, R.; Ngatu-Nlandu, R.; Nakamura, H.; Songo, H.S.; Sawamura, M. Anti-inflammatory effects of limonene from yuzu (citrus junos Tanaka) essential oil on eosinophils. *J. Food Sci.* **2010**, *75*, 87–92. [CrossRef] [PubMed]
24. Dosoky, N.S.; Setzer, W.N. Biological activities and safety of *Citrus* spp. Essential oils. *Int. J. Mol. Sci.* **2018**, *19*, 1966–1991. [CrossRef]

Disclaimer/Publisher's Note: The statements, opinions and data contained in all publications are solely those of the individual author(s) and contributor(s) and not of MDPI and/or the editor(s). MDPI and/or the editor(s) disclaim responsibility for any injury to people or property resulting from any ideas, methods, instructions or products referred to in the content.

International Journal of
Molecular Sciences

MDPI

Article

Ursolic Acid Regulates Immune Balance, Modulates Gut Microbial Metabolism, and Improves Liver Health in Mice

Man Zhao [1,†], Yali Cui [2,†], Fengxia Wang [1], Fengyang Wu [1], Chong Li [1], Shudong Liu [1] and Baojiang Chen [1,*]

[1] College of Animal Science and Technology, Hebei Agricultural University, Baoding 071051, China
[2] College of Traditional Chinese Veterinary Medicine, Hebei Agricultural University, Baoding 071051, China
* Correspondence: 199051@hebau.edu.cn
† These authors contributed equally to this work.

Abstract: Ursolic acid (UA) has demonstrated significant immunomodulatory and hepatoprotective effects; however, the underlying mechanisms remain unclear. This study aims to analyze the impact of UA on the gut microbiome, metabolome, and liver transcriptome, investigate UA's role in maintaining gut immune homeostasis and liver health, and evaluate the potential contributions of gut microbes and their metabolites to these beneficial effects. Our findings indicate that UA enhances immune balance in the jejunum, fortifies intestinal barrier function, and promotes overall gut health. UA modulates the intestinal microbiota and its metabolic processes, notably increasing the abundance of beneficial bacteria such as *Odoribacter* and *Parabacteroides*, along with their metabolites, including ornithine and lactucin. Additionally, UA inhibits the expression of interleukin-1 receptor 1 (*IL1R1*) and calcium (Ca^{2+}) voltage-gated channel auxiliary subunit beta 2 (*CACNB2*) while enhancing the synthesis pathways of retinol and ascorbic acid, thereby exerting a protective influence on liver function. In summary, UA enhances intestinal immune homeostasis and promotes liver health, with these advantageous effects potentially mediated by beneficial bacteria (*Odoribacter* and *Parabacteroides*) and their metabolites (ornithine and lactucin).

Keywords: ursolic acid; gut health; liver protection; gut microbiota; metabolism; liver transcriptome

1. Introduction

Body health is closely related to gut health, relying on moderate immunity, an intact gut barrier, and a stable gut microbe. The gut harbors a diverse array of immune cells, including T helper (Th) cells and T regulatory (Treg) cells, which work together to maintain the balance of the body's immune response [1]. An overproduction of immune-related cytokines, such as interleukin (IL)-6, IL-1β, and IL-17A, can lead to intestinal cell damage and compromise the integrity of the gut barrier, consequently triggering systemic inflammation. In contrast, cytokines such as IL-10 and transforming growth factor-β (TGF-β) play a role in inhibiting inflammation [1]. Ursolic acid (UA) is a naturally occurring pentacyclic triterpene carboxylic acid found in various plants, either in free acid form or as an aglycone of triterpene saponins [2]. In recent years, there has been a surge of interest in UA, primarily concerning its pharmacological properties, which include antioxidant [3], antitumor [4], anti-inflammatory [5], and antimicrobial [2] effects. Our previous meta-analysis confirmed that UA can reduce levels of pro-inflammatory cytokines like IL-1β and IL-6 [6]. Furthermore, UA has been shown to activate the immune system and enhance the proliferation of immune cells [7]. Nevertheless, the regulatory mechanisms by which UA influences intestinal immune homeostasis and gut health remain unclear.

The gut microbiota plays a critical role in maintaining intestinal immune homeostasis and barrier function [8–10]. Research has demonstrated that gut microbes can modulate immune equilibrium through the regulation of Th17/Treg cell dynamics. For example, *Lactobacillus rhamnosus GG* is capable of modulating Th17/Treg homeostasis, thus aiding in

the preservation of host intestinal health [11]. Similarly, *Bacteroides fragilis* enhances Treg cell activation by increasing *Foxp3* expression [12]. UA has exhibited significant regulatory effects on the gut microbiota [13–15]. Consequently, understanding how UA influences immune balance and gut health via the modulation of gut microbes presents a compelling area of investigation. Additionally, UA has been shown to mitigate liver damage by modulating enterohepatic axis homeostasis [13] and is recognized as a contributing factor to the hepatoprotective properties of various foods and medicinal plants [13,16]. The gut microbiota, a key component of the gut–liver axis (GLA), is also closely associated with liver health [8]. Studies indicate that *Lactobacillus* and *Bifidobacterium* can enhance metabolic processes in rats through the GLA [17]. However, the specific mechanisms through which UA exerts protective effects on the liver necessitate further exploration.

To address these questions, this study utilizes a multi-omics approach to analyze the effects of UA on the intestinal microbiota, metabolome, and liver transcriptome in mice. We evaluate the role of UA in immune balance and liver protection, elucidating the potential contributions of gut microbes and their metabolites to these processes.

2. Results

2.1. Effect of UA on Immune-Related Cytokines in Mice

As shown in Figure 1A, the body weight (BW) of mice in the UA 5 and UA 25 groups was significantly higher than that of the CON group ($p < 0.05$). Compared to the CON group, the UA 5 and UA 25 groups had significantly lower levels of interleukin (IL)-1β, IL-6, and tumor necrosis factor (TNF)-α ($p < 0.05$) and higher levels of transforming growth factor (TGF)-β and IL-10 ($p < 0.05$) (Figure 1B–G).

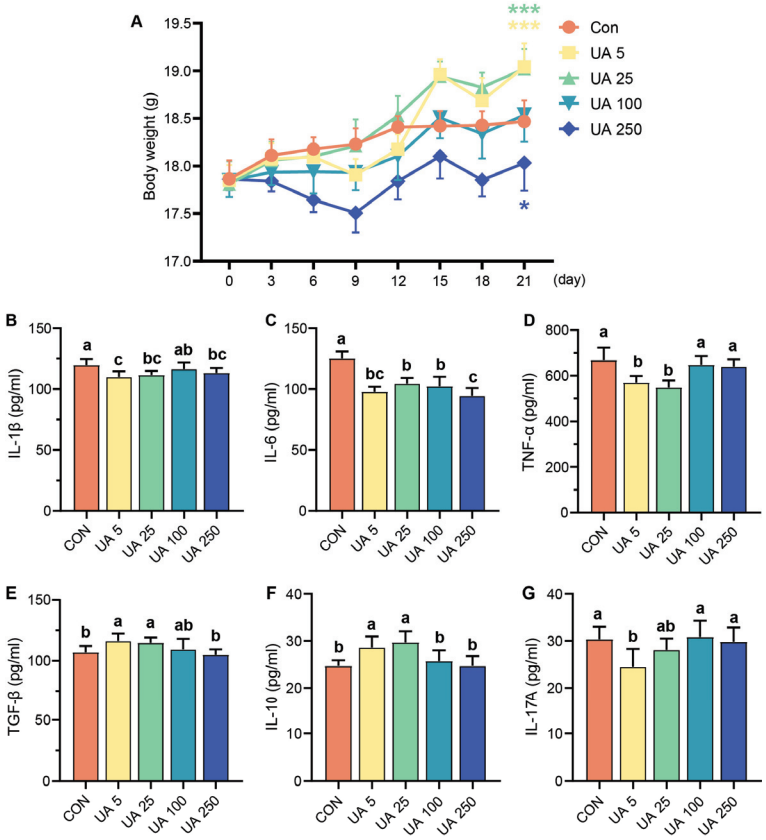


Figure 1. Effects of ursolic acid on body weight and immune-related cytokines in mice. (**A**) Body weight (*, $p < 0.05$, and ***, $p < 0.001$). (**B**) IL-1β, (**C**) IL-6, (**D**) TNF-α, (**E**) TGF-β, (**F**) IL-10, and (**G**) IL-17A cytokine levels in serum. Values with different letters (a, b, and c) differed significantly within a mice trial ($p < 0.05$). Data are shown as mean ± SD. $n = 6$.

2.2. UA Promotes Intestinal Development, Intestinal Epithelial Barrier Integrity, and Immune Balance in Mice

Mouse intestinal tissues (duodenum, jejunum, and ileum) were stained with H&E to explore the effect of UA on intestinal development in mice (Figure 2A–F). The results indicated that UA treatment (UA 5 and UA 100) significantly increased duodenal villus length (V), while (UA 5, UA 25, and UA 100) significantly increased duodenal crypt depth (C), (UA 5, UA 25, UA 100, and UA 250) significantly increased duodenal wall thickness ($p < 0.05$), and (UA 5, UA 25, UA 100, and UA 250) significantly increased duodenal crypt depth. However, there was no significant effect on the V/C ratio ($p > 0.05$). Compared to the CON group, UA treatment (UA 5, UA 25, UA 100, and UA 250) significantly increased jejunal villus length, (UA 25) crypt depth, and (UA 25) V/C and (UA 5 and UA 250) intestinal wall thickness ($p < 0.05$). UA treatment had no significant effect on the intestinal morphology (villus length, crypt depth, V/C, and intestinal wall thickness) of the ileum ($p > 0.05$). It is concluded that the effect of UA on the small intestine is mainly concentrated in the jejunum, with the optimal dose being the UA 25 group. Based on this, we further investigated the effects of optimal UA treatment (UA 25) on the intestinal barrier and immune balance in mice. The results showed that UA treatment significantly increased the mRNA expression of zonula occludens-1 (*ZO-1*) and *Occludin* in the jejunum of mice ($p < 0.05$) but had no significant effect on the mRNA expression of *Claudin1* ($p > 0.05$) (Figure 2G–I). Compared with the CON group, the UA-treated group had significantly higher forkhead box P3 (*Foxp3*) mRNA expression levels and significantly lower signal transducer and activator of transcription 3 (*Stat3*) mRNA expression levels ($p < 0.05$). UA had no significant effect on retinoid-related orphan receptor gamma t (*RORγt*) mRNA expression ($p > 0.05$) (Figure 2J–L) based on the optimal effects of the UA 25 group on body weight, serum immune factor levels, and intestinal tissue morphology, as well as beneficial effects on genes related to the intestinal barrier and immune balance. We selected the UA 25 group (UA group) for the omics study.

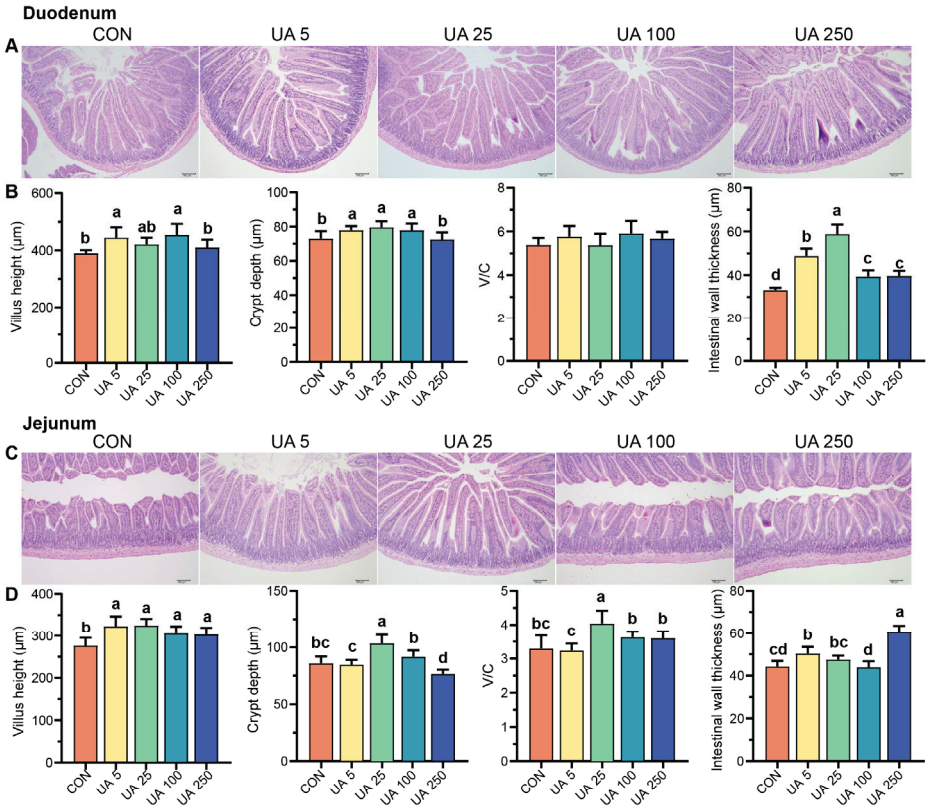


Figure 2. *Cont.*

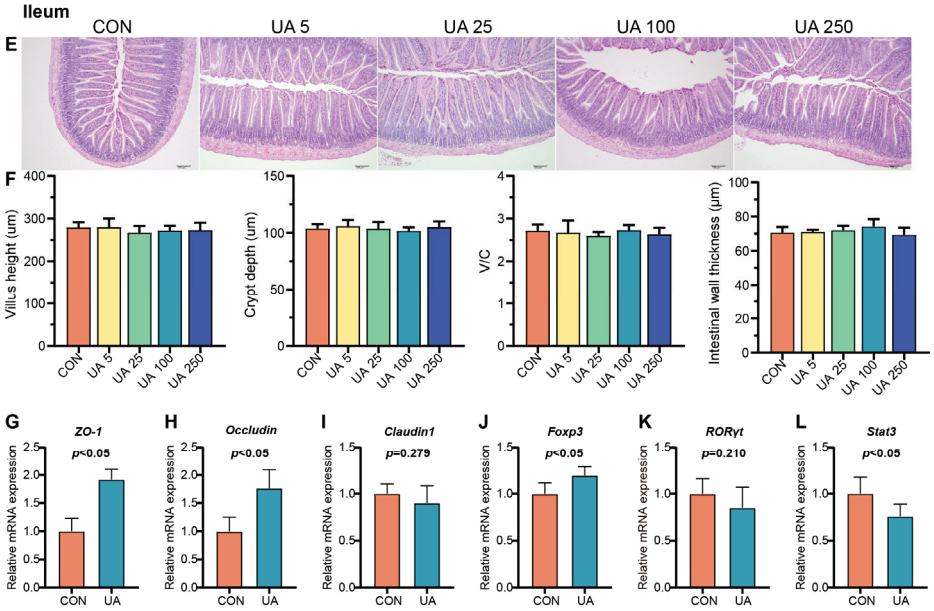


Figure 2. Effect of ursolic acid on the intestinal health of mice. Effect of ursolic acid on the intestinal morphology of the duodenum (**A**,**B**), jejunum (**C**,**D**), and ileum (**E**,**F**) in mice. Effects of ursolic acid on the expression of genes related to the intestinal barrier (**G**–**I**) and Th17/Treg cell-related factor (**J**–**L**) in the jejunum of mice. Values with different letters (a, b, c, and d) differed significantly within a mice trial ($p < 0.05$). Data are shown as mean ± SD. $n = 6$. Scale bars in (**A**,**C**,**E**) = 100 μm.

2.3. UA Changes the Composition and Structure of the Gut Microbiota in Mice

To explore whether the physiological effects of UA were related to the gut microbiota, we further investigated the effects of UA on the gut microbiota. Figure S1A–C illustrates the rank abundance curves, rarefaction curves, and Shannon curves derived from this gene sequencing. There was no significant difference in the Shannon index between the two groups ($p > 0.05$) (Figure 3A). The results of principal coordinate analysis (PCoA) indicated that the first principal component explained 42.32% of the variance between groups, and the second principal component explained 25.31% of the variance between groups. The results of the Adonis analysis demonstrated that UA treatment significantly regulated the structure of intestinal flora in mice ($p < 0.05$) (Figure 3B). Figure S1D,E presents the top 10 bacteria with relative abundance at the phylum level and the top 15 bacteria with relative abundance at the genus level. UA significantly reduced the relative abundance of *Romboutsia* and significantly increased the relative abundance of *Odoribacter*, *Coriobacteriaceae_UCG-002*, *Parabacteroides*, *Anaeroplasma*, and *Norank_f__Eggerthellaceae* ($p < 0.05$) (Figure 3C). Linear discriminant analysis (LDA) effect size (LEfSe) was employed to identify the core taxa (LDA ≥ 3, $p < 0.05$) that were most likely to explain the differences between groups. The results revealed that there were six taxa-marker bacteria in the CON group and nine taxa-marker bacteria in the UA group (Figures 3D and S1F). Notably, *Romboutsia* was further identified as the marker bacteria in the CON group, while *Odoribacter*, *Coriobacteriaceae_UCG-002*, and *Parabacteroides* were identified as the marker bacteria in the UA group.

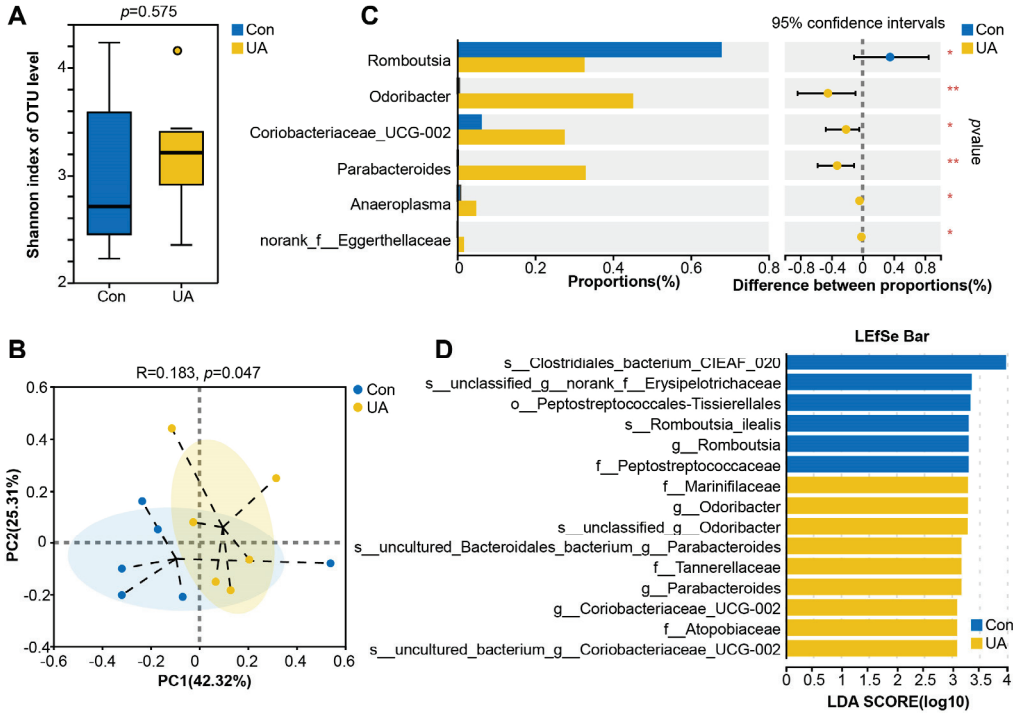


Figure 3. Effect of ursolic acid on gut microbiota in mice. (**A**) The comparison of microbiota diversity (Shannon index) and the Adonis analysis. Boxes denote the interquartile (IQR) between the first and third quartiles (25th and 75th percentiles, respectively) and the line inside denotes the median. (**B**) Principal coordinate analysis (PCoA) based on Bray–Curtis distance. (**C**) Comparison of differences in the relative abundance of bacteria at the genus level (*, $p < 0.05$, and **, $p < 0.01$). (**D**) Differentiating bacteria identified by LEfSe with LDA effect size ≥ 3. $n = 6$.

2.4. UA Also Altered Metabolism of Gut Microbiota

A total of 355 metabolites were identified in the mouse fecal metabolome. Partial least squares discriminant analysis (PLS-DA) indicated that the mice in the CON group and the UA group exhibited different metabolic characteristics (Figure S2A,B). Sixteen metabolites were significantly different between the two groups, among which indole carboxylic acid sulfate and cholic acid were significantly enriched in the CON group. Dihydroconiferyl alcohol, 5′-phosphoribosyl-N-formylglycinamide, 5-hydroperoxypent-1-enylbenzene, Asn Asn Leu Asn Val, 3-hydroxy-N^6,N^6,N^6-trimethyl-L-lysine, ornithine, lactucin, D-erythro-sphingosine C-17, dodemorph, wyerone, neoporrigenin B, Xi-4-hydroxy-4-methyl-2-cyclohexen-1-one, prolylglycine, and PA(24:0/22:6(5Z,8E,10Z,13Z,15E,19Z)-2OH(7S, 17S)) were significantly enriched in the UA group (variable importance in projection (VIP) > 1, $p < 0.05$) (Figure 4A). Kyoto Encyclopedia of Genes and Genomes (KEGG) enrichment analysis based on the 16 differential metabolites showed that three pathways were significantly enriched. It includes D-amino acid metabolism, arginine biosynthesis, and biosynthesis of various other secondary metabolites (Benjamini–Hochberg false discovery rate (FDR) < 0.05) (Figure 4B).

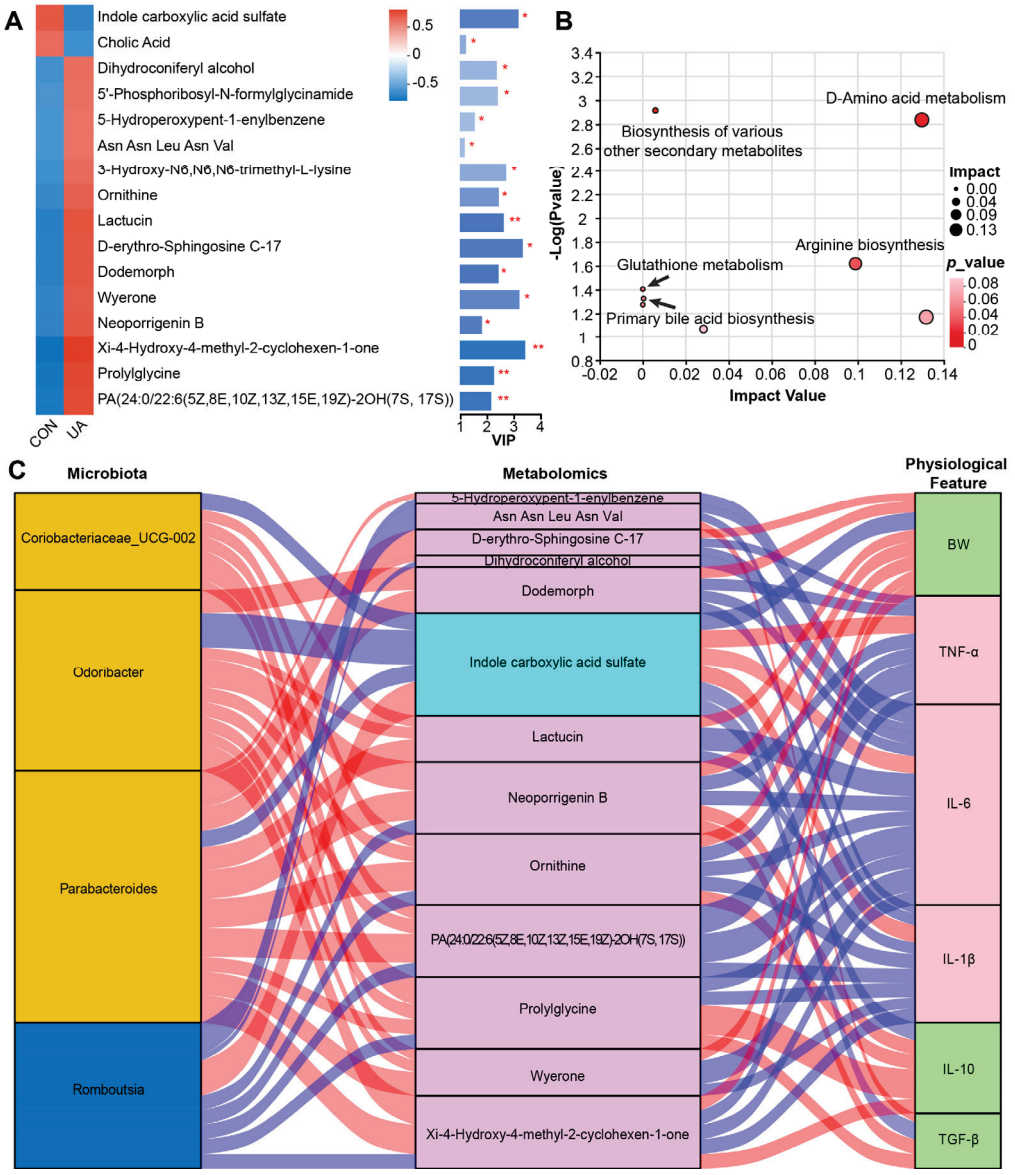


Figure 4. Effect of ursolic acid on the fecal metabolism of mice. (**A**) Heatmap of 16 different metabolites. The right side shows the variable importance in the projection (VIP) bar graph of the metabolite. The color of the bars indicates the significant difference in metabolites between the two groups of samples, and the smaller the *p*-value, the darker the color (*, $p < 0.05$; **, $p < 0.01$). (**B**) KEGG pathway enrichment analysis of differential metabolites. (**C**) Interrelationship between microbiota, metabolomics, and physiological features. Red connections indicate a positive correlation (Spearman correlation test, $|R| > 0.6$, $p < 0.05$,), while blue connections show correlations that were negative (Spearman correlation test, $|R| > 0.6$, $p < 0.05$). In the microbiota column, the orange stratum represents bacteria that were highly enriched in the UA group, and the stratum-colored blue was increased in the control group. In the metabolomics column, the purple stratum represents metabolites that were highly enriched in the UA group, and the stratum-colored ice blue was increased in the control group. In the physiological feature column, the green stratum represents bacteria that were highly enriched in the UA group, and the pink stratum was increased in the control group. $n = 6$.

2.5. UA Treatment Alters the Gut Microbiota and Its Metabolic Characteristics and Affects the Host Phenotype

Subsequently, we evaluated the correlation among gut microbiota, serum metabolites, and host phenotype to further explore the possible regulatory mechanisms between gut mi-

crobiota characteristics and host phenotype following UA treatment. As indicated by spearman's correlation coefficient, the four bacteria identified as marker bacteria were significantly correlated with 13 differential metabolites. These metabolites were further associated with BW, TNF-α, IL-6, IL-1β, IL-10, and TGF-β (representing the physiological features of mice) ($|R| > 0.6$, $p < 0.05$) (Figure 4C). *Odoribacter*, *Coriobacteriaceae_UCG-002,* and *Parabacteroides*, which were identified as the marker bacteria of the UA group, were positively correlated with metabolites (lactucin, ornithine, PA(24:0/22:6(5Z,8E,10Z,13Z,15E,19Z)-2OH(7S, 17S), prolylglycine, and wyerone) enriched in the UA group and were negatively correlated with Indole carboxylic acid sulfate enriched in the CON group. *Romboutsia*, which was identified as the marker bacteria in the CON group, was negatively correlated with 5-hydroperoxypent-1-enylbenzene, Asn Asn Leu Asn Val, dihydroconiferyl alcohol, neoporrigenin B, ornithine, and PA(24:0/22:6(5Z,8E,10Z,13Z,15E,19Z)-2OH(7S, 17S). Prolylglycin and Xi-4-hydroxy-4-methyl-2-cyclohexen-1-one) enriched in the UA group were positively correlated with indole carboxylic acid sulfate enriched in the CON group. Lactucin was negatively correlated with IL-6 and IL-1β and positively correlated with BW. Ornithine was negatively correlated with TNF-α, IL-6, and IL-1β, and positively correlated with BW and IL-10. In addition, there was a direct correlation between the differential bacteria and the host phenotype. *Odoribacter* and *Parabacteroides* were significantly negatively correlated with TNF-α, IL-6, and IL-1β and significantly positively correlated with BW, TGF-β, and IL-10 (Figure S3). *Coriobacteriaceae_UCG-002* was negatively correlated with IL-6 and IL-1β ($p < 0.05$) but positively correlated with IL-10 ($p < 0.05$). *Romboutsia* was significantly positively correlated with IL-6 and negatively correlated with IL-10.

2.6. UA Alters the Liver Transcriptome

To investigate the effects of UA on the mouse liver, we conducted RNA-seq analysis. A total of 29,094 genes were identified in the mouse liver. The results of the PCA analysis indicated a clear separation between the two groups of samples. The first principal component explained 48.12% of the variance between the two groups, and the second principal component explained 15.22% of the variance (Figure 5A). According to the filter threshold $|\log2FC| \geq 1$ and FDR < 0.05, we identified 636 differentially expressed genes (DEGs) in the UA vs. CON group. Compared to the CON group, there were 167 up-regulated DEGs and 469 down-regulated DEGs in the UA group (Figure 5B). In addition, the expression results of eight random mRNAs detected by qRT-PCR are presented (Figure S4A). The results of RNA-Seq (log2 fold change) and qRT-PCR (log2 fold change) were significantly positively correlated (correlation value = 0.84, $p < 0.01$) (Figure S4B). This indicates the high accuracy of both the sequencing and differential expression analysis results. Gene Ontology (GO) enrichment analysis was performed separately for down-regulated and up-regulated DEGs, and the results showed that the down-regulated genes were significantly enriched to 47 GO terms, such as cell projection organization, chemical synaptic transmission, anterograde trans-synaptic signaling, neuromuscular junction development, centrosome, and triplet codon-amino acid adaptor activity (Figure S5A). The up-regulated genes were significantly enriched in 191 GO terms, including myofilament, skeletal muscle thin filament assembly, and FATZ binding (Figure S5B).

The up-regulated and down-regulated genes were further subjected to KEGG pathway analysis to determine the functional categories. The results showed that there were no significantly enriched pathways among the down-regulated genes, but the pathway with the most enriched genes was the MAPK signaling pathway (DEGs = 11, FDR > 0.05) (Figure 5C). The top five significantly enriched pathways of up-regulated genes were retinol metabolism (DEGs = 6), ascorbate and aldarate metabolism (DEGs = 4), oxidative phosphorylation (DEGs = 7), chemical carcinogenesis-reactive oxygen species (DEGs = 9), and arginine and proline metabolism (DEGs = 5) (FDR < 0.01) (Figure 5D). Based on all DEGs, we further constructed the regulatory mechanism of UA on the ko04010, ko04668, ko00053, and ko00190 pathways (Figure 5E). Interestingly, all DEGs involved in the ko04010

and ko04668 pathways were down-regulated genes (Figure S6A), and all DEGs involved in the ko00053 (Figure S6B) and ko00190 (Figure S6C) pathways were up-regulated genes.

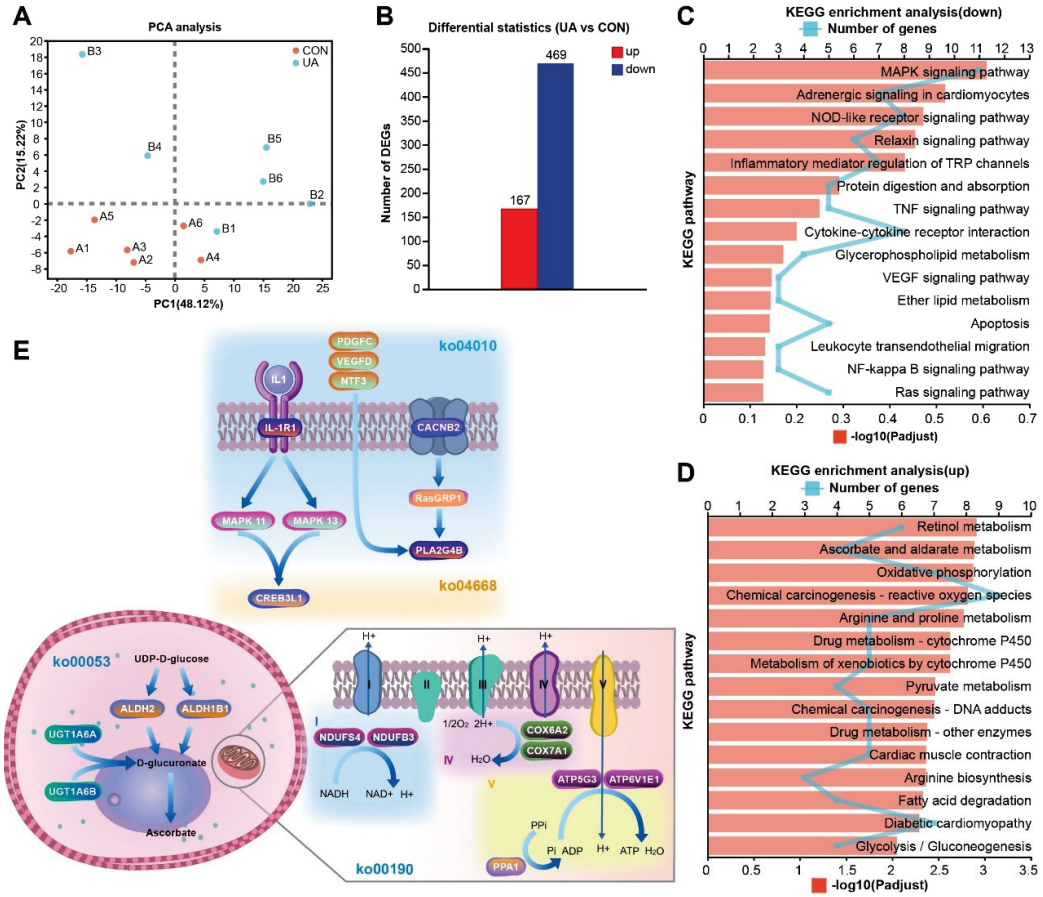


Figure 5. Effect of ursolic acid on the liver transcriptome of mice. (**A**) PCA analysis. (**B**) The number of differentially expressed genes (DEGs). KEGG enrichment pathways of down-regulated (**C**) and up-regulated (**D**) DEGs. (**E**) DEGs related to enrichment pathways (ko04010, ko04668, ko00053, and ko00190). ko04010, MAPK signaling pathway; ko04668, TNF signaling pathway; ko00053, Ascorbate and aldarate metabolism; and ko00190, Oxidative phosphorylation; I, Nicotinamide adenine dinucleotide (NADH) dehydrogenase; II, Succinate dehydrogenase; III, Cytochrome C Reductase; IV, Cytochrome c oxidase; V, ATP synthase. $n = 6$.

2.7. Multi-Omics Integrated Analysis Reveals the Possible Regulatory Mechanism of UA

Connections between bacteria, metabolites, liver genes, gut genes, and host phenotypes were established through an association study (Spearman correlation coefficient, $|R| > 0.6$, $p < 0.05$) (Figure 6). BW was positively correlated with intestinal barrier-related genes (*Occludin* and *ZO-1*) and negatively correlated with inflammation-related genes (Mitogen-activated protein kinase (*MAPK)13*, *MAPK11*, Interleukin-1 receptor 1 (*IL1R1*), Neurotrophic factor-3 (*NTF3*), and Calcium (Ca^{2+}) voltage-gated channel auxiliary subunit beta 2 (*CACNB2*)). The immune-related cytokines (IL-1β, IL-6, and TNF-α) were negatively correlated with the intestinal barrier-related genes (*Occludin* and *ZO-1*), and all of them were positively correlated with the inflammation-related gene (*CACNB2*). In addition, IL-1β and TNF-α exhibited a strong positive correlation with *IL1R1*, of which IL-1β had the strongest correlation with *IL1R1* ($R = -0.799$). *Stat3*, an immune balance-related gene, inhibited the expression of TGF-β and promoted the expression of IL-17A, while *Foxp3* facilitated the expression of TGF-β. *Odoribacter* and *Parabacteroides* were positively correlated with *Foxp3* and *Parabacteroides* was negatively correlated with *Stat3*. *Coriobacteriaceae_UCG-002*, *Odoribacter*, *Parabacteroides*, wyerone, ornithine, and lactucin could enhance intestinal barrier function

by promoting the expression of *Occludin* and *ZO-1*. *Odoribacter*, wyerone, ornithine, and dodemorph showed significant negative correlations with *IL1R1* and *CACNB2*. Notably, *Odoribacter* (16 correlations: 3 negative and 13 positive), *Parabacteroides* (15 correlations: 3 negative and 12 positive), ornithine (10 correlations: 4 negative and 6 positive), wyerone (8 correlations: 4 negative and 4 positive), and lactucin (7 correlations: 4 negative and 3 positive) had the highest number of correlations, suggesting that they may serve as crucial connections in the anti-inflammatory pathway of UA.

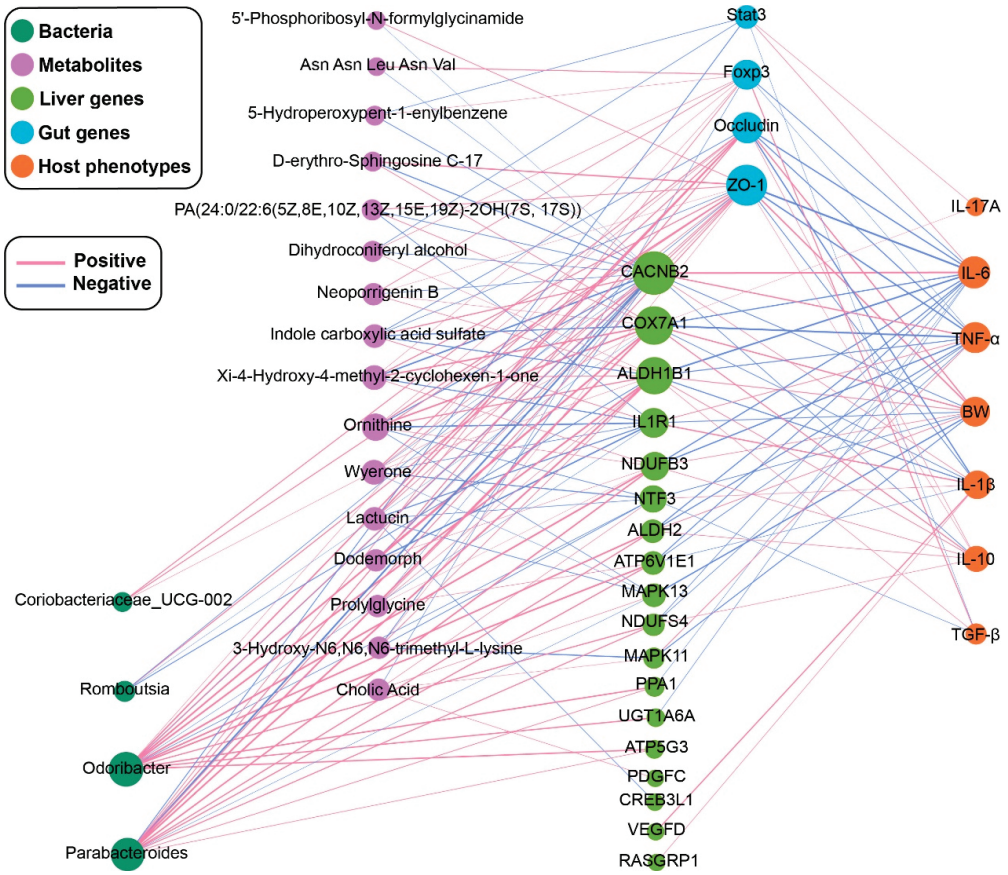


Figure 6. Spearman correlation network among the bacteria, metabolites, liver genes, gut genes, and host phenotypes ($|R| > 0.6$, $p < 0.05$). The width of the edges is proportional to the correlation strength. The color of the edges: red, positive; blue, and negative, $n = 6$.

3. Discussion

UA has garnered considerable attention for its array of pharmacological benefits [6,15,18,19]. In this study, the significant effects of UA in the jejunum were observed, including a notable increase in the V/C ratio and enhancement of intestinal barrier function. These findings highlight UA's role in promoting digestion and absorption as well as in improving gut health in mice. Th17 and Treg cells, which differentiate from $CD4^+$ T cells, are pivotal in the immune response and synergistically contribute to intestinal immune function [20]. The balance between Th17 and Treg cells is crucial for maintaining intestinal immune homeostasis [21]. Disruption of this balance can adversely affect nutrient digestion and absorption, thus compromising overall health [1,21,22].

IL-6-mediated Stat3 signaling stimulates the differentiation of Th17 cells by inducing the nuclear receptor RORγt, leading to the production of the inflammatory cytokine IL-17A [23]. Subsequently, IL-17A can enhance the secretion of other pro-inflammatory cytokines, including TNF-α, IL-6, and IL-1β [24]. Conversely, TGF-β promotes the transcription of Foxp3, facilitating the differentiation of Treg cells and the production of anti-inflammatory cytokines such as IL-10 and TGF-β [25]. Moreover, Foxp3 can inhibit the

differentiation of Th17 cells by restricting their transcriptional potential [23]. Our results indicate that UA treatment resulted in the down-regulation of *Stat3* mRNA expression, up-regulation of *Foxp3* mRNA expression, and increased levels of TGF-β and IL-10 in mice. These findings suggest that UA can improve intestinal immune homeostasis.

The gut microbiota serves as a critical link between environmental factors and host health [26,27]. Investigating whether UA's functional role is connected to intestinal microbiota composition has become a topic of interest [13,15,28]. In our study, UA treatment significantly altered the composition and metabolites of the gut microbiota. Notably, the abundance of *Odoribacter* and *Parabacteroides* was significantly increased in the UA-treated mice. *Odoribacter*, a potential probiotic, is known to enhance mucosal immunity and maintain intestinal homeostasis [29]. Its colonization can augment Foxp3/RORγt regulatory T cells (Treg cells) and induce IL-10 production, thereby mitigating colitis in mice [30,31]. Numerous studies have highlighted the immunomodulatory effects of *Parabacteroides* [32–34], which have also been shown to promote $CD4^+$ T cell differentiation toward the CD4/Foxp3/IL-10 regulatory pathway [35,36]. Our correlation analysis demonstrated associations between *Odoribacter*, *Parabacteroides*, and key immune factors, including *Foxp3*, *Occludin*, *ZO-1*, IL-1β, IL-6, TNF-α, and IL-10. These observations suggest that UA's effects on immune balance and intestinal barrier function may be mediated by *Odoribacter* and *Parabacteroides*.

Furthermore, gut microbiota-derived ornithine has been shown to stimulate RORγt (+) IL-22 (+) cells and promote gut mucus formation, playing a vital role in maintaining intestinal homeostasis [37]. Previous research has demonstrated that lactucin can modulate gut microbiota and restore intestinal barrier function in inflammatory rat models [38]. Our findings revealed that both ornithine and lactucin were significantly enriched in UA-treated mice, indicating that these metabolites may be key factors in UA-mediated immune balance and intestinal barrier enhancement.

Additionally, our study investigates the effects of UA on liver health in mice. The MAPK signaling pathway is integral to regulating immune responses and plays a critical role in innate immunity [39]. Genes such as *IL1R1*, *MAPK11*, and *MAPK13*, expressed by immune or inflammatory cells, are crucial for inflammatory signaling [40,41]. Ras-guanine nucleotide-releasing protein 1 (RasGRP1) serves as a key regulator of the inflammatory response and is implicated in various inflammatory diseases [42]. Calcium (Ca^{2+}) voltage-gated channel auxiliary subunit beta 2 (CACNB2) may contribute to aberrant RAS-MAPK activation [43]. Our study found that *IL1R1*, *MAPK11*, *MAPK13*, *CACNB2*, and *RasGRP1* expression levels were significantly downregulated in the livers of mice in the UA group, suggesting that UA may lower the risk of liver inflammation and improve liver homeostasis. Moreover, the upregulated genes in the UA group were significantly enriched in pathways related to retinol metabolism, ascorbic acid and aldarate metabolism, and oxidative phosphorylation. Retinol, a form of vitamin A, plays an unexpected but crucial role in regulating immune responses [44]. Ascorbate, or vitamin C, acts as a potent antioxidant that supports various immune functions and enhances immune defenses [45]. Mitochondrial oxidative phosphorylation is responsible for generating the majority of ATP, which is essential for sustaining life and maintaining metabolic homeostasis [46]. These results imply that UA may enhance liver health by promoting the synthesis of retinol and ascorbic acid, thereby regulating metabolic homeostasis in the liver.

Interestingly, we observed that the *IL1R1* and *CACNB2* genes, which are associated with the MAPK signaling pathway, are broadly linked to immune-related factors, bacteria (*Odoribacter* and *Parabacteroides*), and metabolites (ornithine and lactucin). *Parabacteroides distasonis* has been shown to reduce liver damage and inflammation by inhibiting the NF-κB/MAPK pathway and activating the Nrf2 pathway, which may be related to the improvement in amino acid and bile acid metabolism in intestinal microorganisms [47]. *Parabacteroides distasonis* has a protective effect against non-alcoholic steatohepatitis (NASH) in mice by producing beneficial metabolites from dietary fiber [48]. In addition, *Odoribacter* has also been shown to be significantly negatively associated with measures of NASH

progression [49]. Previous studies suggest that the liver-protective mechanism of ornithine may involve its conversion into the antioxidant glutathione and the nitric oxide precursor L-arginine, both of which are crucial for improving liver microcirculation [50,51]. Additionally, lactucin has been shown to downregulate the MAPK pathway, further enhancing liver health [52,53]. Lactucin may also enhance GLA circulation and reduce liver inflammation [38]. These observations suggest that the effects of UA on liver health may be mediated by regulating gut microbiome composition and its metabolism. However, our correlation analysis offers only indicative and predictive insights and does not definitively establish causal relationships between metabolites and hepatoprotective effects. Further studies are required to validate the relationship between these metabolites and liver health.

Our data can help us understand the function of UA in regulating immune homeostasis and improving liver health and identify the key role that gut microbiota and its metabolites may play in this process. However, we acknowledge that some limitations should be noted. We did not assess changes in gut microbial function and its association with inflammation in UA-treated mice. Further systematic studies, such as metagenomic, metatranscriptomic, or other multi-omics investigations, are needed to identify the function of gut microbiota and further explain the impact of changes in microbial metabolic function on inflammation.

In conclusion, UA can improve immune balance and enhance intestinal barrier function in mice. UA is able to increase beneficial bacteria (*Odoribacter* and *Parabacteroides*) and their metabolites (ornithin and lactucin). UA can inhibit the expression of *IL1R1* and *CACNB2* mRNA in the liver, upregulate the synthesis pathway of retinol and ascorbic acid in the liver, and promote liver health.

4. Materials and Methods

4.1. Ethics Statement

All experiments were performed in accordance with the ARRIVE guidelines and were carried out in accordance with the U.K. Animals (Scientific Procedures) Act, 1986 and associated guidelines, EU Directive 2010/63/EU for animal experiments, and approved by the Ethics Committee of Animal Experimentation of Hebei Agricultural University (Protocol 2023058).

4.2. Animals and Experimental Design

Eight-week-old female C57BL/6J mice were purchased from SPF Biotechnology Co., Ltd. (Beijing, China) and housed in pathogen-free facilities with a 12-h light and 12-h dark cycle at 22 °C.

After acclimatization to the laboratory conditions for 1 week, mice were randomly divided into 5 groups (n = 6 per group), including the control (CON) group, the UA 5, UA 25, UA 100, and UA 250 groups. Mice in the CON group were provided with a daily oral administration of 100 μL of PBS. Mice from the UA 5, UA 25, UA 100, and UA 250 groups received 5, 25, 100, and 250 mg/kg body weight of UA (purity $\geq$ 98%, Shenniu Pharmaceutical Co., Ltd., Dezhou, China; Figure S7) added to 100 μL PBS by daily gavage for 21 days. All group mice were administered menstruum, which was isovolumetric with 0.5% sodium carboxymethyl cellulose and 1% Tween 80. UA was dissolved in that menstruum (the menstruum and UA were administered directly into the stomach using an oral gavage needle).

Body weight was measured every three days throughout the study. On the 21st day, the mice were anesthetized with ether, the eyeballs were removed, blood samples were taken in 1.5 mL centrifuge tubes, and serum was separated by centrifugation for 15 min (3500× g, 4 °C), after which the mice were sacrificed. Fecal samples from all mice were collected aseptically and stored at −80 °C for microbiome and metabolomic analyses. The middle segments (0.5 cm) of the duodenum, jejunum, and ileum were flushed with PBS and fixed in a 10% formaldehyde solution for histological observation. Jejunum and liver tissue were washed with PBS, cut into slices, snap-frozen in liquid nitrogen, and stored at −80 °C for future analysis.

4.3. Enzyme-Linked Immunosorbent Assay (ELISA)

Serum samples were measured for the levels of IL-1β (MM-0040M2), IL-6 (MM-0163M2), TNF-α (MM-0132M2), TGF-β (MM-0689M2), IL-10 (MM-0176M2), and IL-17A (MM-0759M2) according to the instructions of specific ELISA kits (Jiangsu Meimian Industrial Co., Ltd., Yancheng, China).

4.4. Histological Analysis

The fixed duodenum, jejunum, and ileum samples were embedded in paraffin and stained with hematoxylin–eosin to obtain cross-sectional sections. In each section, intact and representative villi were selected, and intestinal morphology was measured. The images were evaluated using the ImageJ software 1.53j (US National Institutes of Health, Bethesda, MD, USA). Villus height (VH), crypt depth (CD), and intestinal wall thickness were measured. The ratio of villus height to crypt depth (V/C) was calculated.

4.5. Quantitative Reverse Transcription-Polymerase Chain Reaction (qRT-PCR)

Total RNA extraction and quantitative real-time PCR were performed as described previously. The extracted RNA was dissolved in RNase-free water and quantified using a NanoDrop-2000 spectrophotometer (Thermo Fisher Scientific, Waltham, MA, USA). RNA purity was evaluated by measuring the absorbance ratio at 260:280 nm, while RNA integrity was confirmed by the detection of the 18S and 28S bands after electrophoresis in 1% agarose gels. The primer sequences are shown in Table S1. The standard curve was drawn for each gene, and the linear relationship and amplification efficiency were calculated. Primers were confirmed as follows: correlation coefficient (R^2) > 0.98; the slope of the standard curve: -3–-3.5; and the amplification efficiency: 0.9–1.2. The mRNA levels of target genes were normalized to *β-actin* mRNA. Based on the cycle threshold (CT) value, the *β-actin* mRNA level was stable across the treatments in this study ($p > 0.1$) (Figure S8). The results of the relative mRNA expression of genes were calculated using the $2^{-\Delta\Delta CT}$ method [54].

4.6. 16S rRNA Gene Sequencing

Microbial genomic DNA was isolated from fecal specimens utilizing the E.Z.N.A.® soil DNA kit (Omega Bio-tek, Norcross, GA, USA). The V3-V4 hypervariable region of the bacterial 16S rRNA gene underwent amplification with the primer combinations 338F (5′-ACTCCTACGGGAGGCAGCAG-3′) and 806R (5′-GGACTACHVGGGTWTCTAAT-3′) via the T100 Thermal Cycler PCR thermocycler (BIO-RAD, Hercules, CA, USA). Subsequently, the purified amplicons were combined in equimolar proportions and subjected to paired-end sequencing on an Illumina PE300 platform (Illumina, San Diego, CA, USA) in accordance with standard operating procedures established by Majorbio Bio-Pharm Technology Co., Ltd. (Shanghai, China).

4.7. Microbiota Data Analysis

Initial sequencing data underwent quality filtering using Fastp version 0.19.6, followed by read merging using FLASH version 1.2.11. Subsequently, the sequences were optimized and grouped into operational taxonomic units (OTUs) at a 97% sequence similarity threshold utilizing UPARSE 11. The taxonomic classification of each OTU representative sequence was conducted, employing RDP Classifier version 2.13 against the Silva v138 16S rRNA gene database, with a confidence threshold set at 0.7.

Analysis of fecal microbiota data was executed on the Majorbio Cloud platform (https://cloud.majorbio.com (accessed on 15 April 2024)). Rarefaction curves and alpha diversity indices were computed using Mothur v1.30.1. Principal coordinate analysis (PCoA) and Adonis analysis, based on Bray–Curtis dissimilarity, were employed to assess the similarity among microbial communities across different samples, facilitated by the "Vegan" package. The statistical significance of non-parametric relative abundance profiles was evaluated utilizing the Mann–Whitney test. Additionally, linear discriminant analysis

(LDA) effect size (LEfSe) analysis was conducted to identify significantly enriched bacterial taxa among distinct groups (LDA score > 3, $p < 0.05$).

4.8. Liquid Chromatograph–Mass Spectrometer Analysis (LC–MS Analysis)

A solid sample weighing 50 mg underwent metabolite extraction utilizing 400 µL of a 4:1 (*v*:*v*) methanol–water extract solution. LC–MS/MS analysis was performed on a SCIEX UPLC-Triple TOF 6600 system featuring an ACQUITY HSS T3 column (100 mm × 2.1 mm i.d., 1.8 µm; Waters, Milford, MA, USA) at Majorbio Bio-Pharm Technology Co., Ltd. (Shanghai, China). Mobile phase A is 95% water + 5% acetonitrile (containing 0.1% formic acid); mobile phase B is 47.5% acetonitrile + 47.5% isopropyl alcohol + 5% water (containing 0.1% formic acid). The flow rate was 0.40 mL/min, the sample size was 10 µL, and the column temperature was 45 °C. Positive ion mode separation gradient 0–3 min and mobile phase B increased from 0% to 20%; in 3–4.5 min, mobile phase B increased from 20% to 35%; in 4.5–5 min, mobile phase B increased from 35% to 100%; at 5–6.3 min, mobile phase B remained 100%; and in 6.3–6.4 min, mobile phase B decreased from 100% to 0%. At 6.4–8 min, mobile phase B maintained 0%. Negative ion mode separation gradient: 0–1.5 min, mobile phase B from 0 to 5%; 1.5–2 min, mobile phase B increased from 5% to 10%; 2–4.5 min, mobile phase B increased from 10% to 30%; 4.5–5 min, mobile phase B increased from 30% to 100%; and at 5–6.3 min, the linearity of mobile phase B remained 100%. In 6.3–6.4 min, mobile phase B decreases from 100% to 0%. The linearity of mobile phase B remained at 0% from 6.4–8 min. Positive and negative ion scanning modes are used to collect the sample quality spectrum signal, and the quality scanning range is 50–1200 m/z. The spray gas flow rate is 50 psi, the auxiliary gas flow rate is 50 psi, the curtain gas flow rate is 35 psi, the ion source temperature is 500 °C, the positive mode ion spray voltage is set to 5500 V, the negative mode ion spray voltage is set to −4500 V, and the ion transfer tube temperature is 325 °C. Normalized collision energy is 20-40-60 eV cyclic collision energy. DDA mode was used to collect data.

Raw UHPLC–MS data were processed using Progenesis QI 2.3 software (Nonlinear Dynamics, Waters, USA) for peak detection and alignment. Metabolic features detected in at least 80% of samples were retained, and minimum imputation was applied to samples falling below the quantitation limit. The normalization of each metabolic feature was conducted by sum and quality control. Variables with relative standard deviation (RSD) exceeding 30% of QC samples were excluded, and log10 transformation was performed to obtain the final data matrix.

Conduct variance analysis on the processed data matrix file. The "ropls" R package (Version 1.6.2) was utilized for partial least squares discriminant analysis (PLS-DA). Metabolites with a variable importance in projection (VIP) value exceeding 1 and a significance level of $p < 0.05$ were deemed significantly different. Differential metabolites between the two groups were subjected to metabolic enrichment and pathway analysis based on the Kyoto Encyclopedia of Genes and Genomes (KEGG) database (http://www.genome.jp/kegg/ (accessed on 15 April 2024)) to map their biochemical pathways.

4.9. RNA Extraction, Library Construction, and Sequencing

Total RNA was isolated from the tissue using TRIzol® Reagent as per the manufacturer's protocol. Subsequently, RNA integrity was assessed using a 5300 Bioanalyser (Agilent, Santa Clara, CA, USA) and quantification was carried out using the ND-2000 (NanoDrop Technologies, Wilmington, DE, USA). RNA purification, reverse transcription, library preparation, and sequencing procedures were conducted at Shanghai Majorbio Bio-pharm Biotechnology Co., Ltd. (Shanghai, China) following the guidelines provided by Illumina (San Diego, CA, USA). The RNA-seq transcriptome library was constructed using Illumina® Stranded mRNA Prep and Ligation Kit from Illumina (San Diego, CA, USA), utilizing 1 µg of total RNA. Libraries underwent size selection for cDNA fragments of 300 bp on 2% low-range ultra-agarose, followed by PCR amplification with Phusion DNA polymerase (NEB) for 15 PCR cycles. Following quantification with Qubit 4.0, paired-end

RNA-seq libraries were sequenced using the NovaSeq 6000 sequencer (Illumina, San Diego, CA, USA) (2 × 150 bp read length).

The raw paired-end reads underwent trimming and quality control using Fastp with default parameters. Subsequently, clean reads were individually aligned to the reference genome in orientation mode employing HISAT2 software 2.2.1. The mapped reads of each sample were assembled by StringTie v2.1.4 utilizing a reference-based approach.

To identify differential expression genes (DEGs) between distinct samples, the expression level of each transcript was quantified utilizing the transcripts per million reads (TPM) method via RSEM. Differential expression analysis was conducted using DESeq2 (version 1.12.3), with DEGs meeting the criteria of $|\log2FC| \geq 1$ and false discovery rate (FDR) < 0.05 considered significantly differentially expressed genes. Additionally, functional enrichment analysis, encompassing Gene Ontology (GO) and KEGG pathways, was performed to discern which DEGs were enriched in GO terms and metabolic pathways.

4.10. Correlation Analysis

Given the extensive diversity, dimensional complexity, and discontinuous distribution of omics data, we applied the Spearman correlation examination in this investigation to investigate the associations among the bacteria, metabolites, liver genes, gut genes, and host phenotypes. A threshold of $|R| > 0.6$, with $p < 0.05$, was utilized to discern noteworthy correlations. Cytoscape version 3.9.0 was employed for network construction. Visualization of the interrelations between microbiome, metabolome, and physiological attributes was accomplished utilizing the R package "ggplot2".

4.11. Statistical Analysis

The body weight, ELISA, and histological observation data were analyzed and one-way analysis of variance (ANOVA) by Statistical Package for the Social Sciences (SPSS) version 26; the differences between means were compared by Duncan's multiple range test. Gene relative expression was compared using the *t*-test. The results were expressed as mean ± standard deviation (SD). The significance was set at $p < 0.05$.

Supplementary Materials: The supporting information can be downloaded at https://www.mdpi.com/article/10.3390/ijms251910623/s1.

Author Contributions: M.Z.: Conceptualization, Data curation, Formal analysis, Funding acquisition, Investigation, Methodology, Visualization, Writing—original draft, and Writing—review and editing. Y.C.: Data curation, Formal analysis, Methodology, and Writing—original draft. F.W. (Fengxia Wang): Data curation, Formal analysis, Methodology, and Writing—original draft. F.W. (Fengyang Wu): Data curation, Validation, and Methodology. C.L.: Data curation, Validation, and Methodology. S.L.: Data curation, Validation, and Methodology. B.C.: Conceptualization, Funding acquisition, Project administration, Resources, Supervision, and Writing—review and editing. All authors have read and agreed to the published version of the manuscript.

Funding: This research was funded by the Modern Agriculture Industry Technology System of Rabbit, China (CARS-43-B-2) and the Postgraduate Innovation Funding project of Hebei Province (CXZZBS2024075).

Institutional Review Board Statement: All experiments were performed in accordance with the ARRIVE guidelines and were carried out in accordance with the U.K. Animals (Scientific Procedures) Act, 1986, associated guidelines, EU Directive 2010/63/EU for animal experiments and approved by the Ethics Committee of Animal Experimentation of Hebei Agricultural University (Protocol 2023058).

Informed Consent Statement: Not applicable.

Data Availability Statement: The data presented in this study are openly available in the NCBI Sequence Read Archive (SRA), reference number PRJNA1115940.

Conflicts of Interest: The authors declare no conflicts of interest.

References

1. Ma, Z.; Akhtar, M.; Pan, H.; Liu, Q.; Chen, Y.; Zhou, X.; You, Y.; Shi, D.; Liu, H. Fecal microbiota transplantation improves chicken growth performance by balancing jejunal Th17/Treg cells. *Microbiome* **2023**, *11*, 137. [CrossRef] [PubMed]
2. Cargnin, S.T.; Gnoatto, S.B. Ursolic acid from apple pomace and traditional plants: A valuable triterpenoid with functional properties. *Food Chem.* **2017**, *220*, 477–489. [CrossRef] [PubMed]
3. Fu, Y.; Liu, T.; He, S.; Zhang, Y.; Tan, Y.; Bai, Y.; Shi, J.; Deng, W.; Qiu, J.; Wang, Z.; et al. Ursolic acid reduces oxidative stress injury to ameliorate experimental autoimmune myocarditis by activating Nrf2/HO-1 signaling pathway. *Front. Pharmacol.* **2023**, *14*, 1189372. [CrossRef] [PubMed]
4. Gou, W.; Luo, N.; Yu, B.; Wu, H.; Wu, S.; Tian, C.; Guo, J.; Ning, H.; Bi, C.; Wei, H.; et al. Ursolic Acid Derivative UA232 Promotes Tumor Cell Apoptosis by Inducing Endoplasmic Reticulum Stress and Lysosomal Dysfunction. *Int. J. Biol. Sci.* **2022**, *18*, 2639–2651. [CrossRef] [PubMed]
5. Wan, Y.; Zhang, W.; Huang, C.; Jian, J.; Zhang, Y.; Liu, Q.; Chen, P.; Zhu, X. Ursolic acid alleviates Kupffer cells pyroptosis in liver fibrosis by the NOX2/NLRP3 inflammasome signaling pathway. *Int. Immunopharmacol.* **2022**, *113*, 109321. [CrossRef]
6. Zhao, M.; Wu, F.; Tang, Z.; Yang, X.; Liu, Y.; Wang, F.; Chen, B. Anti-inflammatory and antioxidant activity of ursolic acid: A systematic review and meta-analysis. *Front. Pharmacol.* **2023**, *14*, 1256946. [CrossRef]
7. Zhang, B.C.; Lai, C.M.; Luo, B.Y.; Shao, J.W. Triterpenoids-templated self-assembly nanosystem for biomimetic delivery of CRISPR/Cas9 based on the synergy of TLR-2 and ICB to enhance HCC immunotherapy. *Acta Pharm. Sin. B* **2024**, *14*, 3205–3217. [CrossRef]
8. Larabi, A.; Barnich, N.; Nguyen, H.T.T. New insights into the interplay between autophagy, gut microbiota and inflammatory responses in IBD. *Autophagy* **2020**, *16*, 38–51. [CrossRef]
9. Singh, V.; Yeoh, B.S.; Walker, R.E.; Xiao, X.; Saha, P.; Golonka, R.M.; Cai, J.; Bretin, A.C.A.; Cheng, X.; Liu, Q.; et al. Microbiota fermentation-NLRP3 axis shapes the impact of dietary fibres on intestinal inflammation. *Gut* **2019**, *68*, 1801–1812. [CrossRef]
10. Cheng, H.; Guan, X.; Chen, D.; Ma, W. The Th17/Treg Cell Balance: A Gut Microbiota-Modulated Story. *Microorganisms* **2019**, *7*, 583. [CrossRef]
11. Zhang, L.L.; Xu, J.Y.; Xing, Y.; Wu, P.; Jin, Y.W.; Wei, W.; Zhao, L.; Yang, J.; Chen, G.C.; Qin, L.Q. *Lactobacillus rhamnosus* GG alleviates radiation-induced intestinal injury by modulating intestinal immunity and remodeling gut microbiota. *Microbiol. Res.* **2024**, *286*, 127821. [CrossRef] [PubMed]
12. Yan, J.-B.; Luo, M.-M.; Chen, Z.-Y.; He, B.-H. The Function and Role of the Th17/Treg Cell Balance in Inflammatory Bowel Disease. *J. Immunol. Res.* **2020**, *2020*, 8813558. [CrossRef] [PubMed]
13. Yan, X.; Ren, X.; Liu, X.; Wang, Y.; Ma, J.; Song, R.; Wang, X.; Dong, Y.; Fan, Q.; Wei, J.; et al. Dietary Ursolic Acid Prevents Alcohol-Induced Liver Injury via Gut–Liver Axis Homeostasis Modulation: The Key Role of Microbiome Manipulation. *J. Agric. Food Chem.* **2021**, *69*, 7074–7083. [CrossRef]
14. Sheng, Q.; Li, F.; Chen, G.; Li, J.; Li, J.; Wang, Y.; Lu, Y.; Li, Q.; Li, M.; Chai, K. Ursolic Acid Regulates Intestinal Microbiota and Inflammatory Cell Infiltration to Prevent Ulcerative Colitis. *J. Immunol. Res.* **2021**, *2021*, 6679316. [CrossRef]
15. Nie, Y.; Liu, Q.; Zhang, W.; Wan, Y.; Huang, C.; Zhu, X. Ursolic acid reverses liver fibrosis by inhibiting NOX4/NLRP3 inflammasome pathways and bacterial dysbiosis. *Gut Microbes* **2021**, *13*, 1972746. [CrossRef]
16. Kashyap, D.; Tuli, H.S.; Sharma, A.K. Ursolic acid (UA): A metabolite with promising therapeutic potential. *Life Sci.* **2016**, *146*, 201–213. [CrossRef]
17. Chen, C.; Gao, K.; Chen, Z.; Zhang, Q.; Ke, X.; Mao, B.; Fan, Q.; Li, Y.; Chen, S. The supplementation of the multi-strain probiotics WHHPRO™ alleviates high-fat diet-induced metabolic symptoms in rats via gut-liver axis. *Front. Nutr.* **2023**, *10*, 1324691. [CrossRef]
18. Li, J.; Li, N.; Yan, S.; Liu, M.; Sun, B.; Lu, Y.; Shao, Y. Ursolic acid alleviates inflammation and against diabetes-induced nephropathy through TLR4-mediated inflammatory pathway. *Mol. Med. Rep.* **2018**, *18*, 4675–4681. [CrossRef] [PubMed]
19. Li, H.; Yu, Y.; Liu, Y.; Luo, Z.; Law, B.Y.K.; Zheng, Y.; Huang, X.; Li, W. Ursolic acid enhances the antitumor effects of sorafenib associated with Mcl-1-related apoptosis and SLC7A11-dependent ferroptosis in human cancer. *Pharmacol. Res.* **2022**, *182*, 106306. [CrossRef]
20. Knochelmann, H.M.; Dwyer, C.J.; Bailey, S.R.; Amaya, S.M.; Elston, D.M.; Mazza-McCrann, J.M.; Paulos, C.M. When worlds collide: Th17 and Treg cells in cancer and autoimmunity. *Cell. Mol. Immunol.* **2018**, *15*, 458–469. [CrossRef]
21. Liu, Y.J.; Tang, B.; Wang, F.C.; Tang, L.; Lei, Y.Y.; Luo, Y.; Huang, S.J.; Yang, M.; Wu, L.Y.; Wang, W.; et al. Parthenolide ameliorates colon inflammation through regulating Treg/Th17 balance in a gut microbiota-dependent manner. *Theranostics* **2020**, *10*, 5225–5241. [CrossRef] [PubMed]
22. Zhong, Y.; Liu, W.; Xiong, Y.; Li, Y.; Wan, Q.; Zhou, W.; Zhao, H.; Xiao, Q.; Liu, D. Astragaloside IV alleviates ulcerative colitis by regulating the balance of Th17/Treg cells. *Phytomedicine* **2022**, *104*, 154287. [CrossRef] [PubMed]
23. Chung, Y.; Chang, S.H.; Martinez, G.J.; Yang, X.O.; Nurieva, R.; Kang, H.S.; Ma, L.; Watowich, S.S.; Jetten, A.M.; Tian, Q.; et al. Critical regulation of early Th17 cell differentiation by interleukin-1 signaling. *Immunity* **2009**, *30*, 576–587. [CrossRef] [PubMed]
24. Noack, M.; Miossec, P. Th17 and regulatory T cell balance in autoimmune and inflammatory diseases. *Autoimmun. Rev.* **2014**, *13*, 668–677. [CrossRef]
25. Wang, J.; Zhao, X.; Wan, Y.Y. Intricacies of TGF-β signaling in Treg and Th17 cell biology. *Cell. Mol. Immunol.* **2023**, *20*, 1002–1022. [CrossRef]

26. Kamada, N.; Seo, S.-U.; Chen, G.Y.; Núñez, G. Role of the gut microbiota in immunity and inflammatory disease. *Nat. Rev. Immunol.* **2013**, *13*, 321–335. [CrossRef]
27. Wu, Z.; Huang, S.; Li, T.; Li, N.; Han, D.; Zhang, B.; Xu, Z.Z.; Zhang, S.; Pang, J.; Wang, S.; et al. Gut microbiota from green tea polyphenol-dosed mice improves intestinal epithelial homeostasis and ameliorates experimental colitis. *Microbiome* **2021**, *9*, 184. [CrossRef]
28. Hao, W.; Kwek, E.; He, Z.; Zhu, H.; Liu, J.; Zhao, Y.; Ma, K.Y.; He, W.S.; Chen, Z.Y. Ursolic acid alleviates hypercholesterolemia and modulates the gut microbiota in hamsters. *Food Funct.* **2020**, *11*, 6091–6103. [CrossRef]
29. Zhou, J.; Li, M.; Chen, Q.; Li, X.; Chen, L.; Dong, Z.; Zhu, W.; Yang, Y.; Liu, Z.; Chen, Q. Programmable probiotics modulate inflammation and gut microbiota for inflammatory bowel disease treatment after effective oral delivery. *Nat. Commun.* **2022**, *13*, 3432. [CrossRef]
30. Lima, S.F.; Gogokhia, L.; Viladomiu, M.; Chou, L.; Putzel, G.; Jin, W.B.; Pires, S.; Guo, C.J.; Gerardin, Y.; Crawford, C.V.; et al. Transferable Immunoglobulin A–Coated *Odoribacter splanchnicus* in Responders to Fecal Microbiota Transplantation for Ulcerative Colitis Limits Colonic Inflammation. *Gastroenterology* **2021**, *162*, 166–178. [CrossRef]
31. Xing, C.; Wang, M.; Ajibade, A.A.; Tan, P.; Fu, C.; Chen, L.; Zhu, M.; Hao, Z.Z.; Chu, J.; Yu, X.; et al. Microbiota regulate innate immune signaling and protective immunity against cancer. *Cell Host Microbe* **2021**, *29*, 959–974.E7. [CrossRef] [PubMed]
32. Kverka, M.; Zakostelska, Z.; Klimesova, K.; Sokol, D.; Hudcovic, T.; Hrncir, T.; Rossmann, P.; Mrazek, J.; Kopecny, J.; Verdu, E.F.; et al. Oral administration of *Parabacteroides distasonis* antigens attenuates experimental murine colitis through modulation of immunity and microbiota composition. *Clin. Exp. Immunol.* **2011**, *163*, 250–259. [CrossRef]
33. Koh, G.Y.; Kane, A.V.; Wu, X.; Crott, J.W. *Parabacteroides distasonis* attenuates tumorigenesis, modulates inflammatory markers and promotes intestinal barrier integrity in azoxymethane-treated A/J mice. *Carcinogenesis* **2020**, *41*, 909–917. [CrossRef]
34. Sun, H.; Guo, Y.; Wang, H.; Yin, A.; Hu, J.; Yuan, T.; Zhou, S.; Xu, W.; Wei, P.; Yin, S.; et al. Gut commensal *Parabacteroides distasonis* alleviates inflammatory arthritis. *Gut* **2023**, *72*, 1664–1677. [CrossRef]
35. Cuffaro, B.; Assohoun, A.L.W.; Boutillier, D.; Súkeníková, L.; Desramaut, J.; Boudebbouze, S.; Salomé-Desnoulez, S.; Hrdý, J.; Waligora-Dupriet, A.J.; Maguin, E.; et al. In Vitro Characterization of Gut Microbiota-Derived Commensal Strains: Selection of *Parabacteroides distasonis* Strains Alleviating TNBS-Induced Colitis in Mice. *Cells* **2020**, *9*, 2104. [CrossRef] [PubMed]
36. Ezeji, J.C.; Sarikonda, D.K.; Hopperton, A.; Erkkila, H.L.; Cohen, D.E.; Martinez, S.P.; Cominelli, F.; Kuwahara, T.; Dichosa, A.E.K.; Good, C.E.; et al. *Parabacteroides distasonis*: Intriguing aerotolerant gut anaerobe with emerging antimicrobial resistance and pathogenic and probiotic roles in human health. *Gut Microbes* **2021**, *13*, 1922241. [CrossRef]
37. Qi, H.; Li, Y.; Yun, H.; Zhang, T.; Huang, Y.; Zhou, J.; Yan, H.; Wei, J.; Liu, Y.; Zhang, Z.; et al. Lactobacillus maintains healthy gut mucosa by producing L-Ornithine. *Commun. Biol.* **2019**, *2*, 171. [CrossRef] [PubMed]
38. Han, C.; Wu, X.; Zou, N.; Zhang, Y.; Yuan, J.; Gao, Y.; Chen, W.; Yao, J.; Li, C.; Hou, J.; et al. *Cichorium pumilum* Jacq Extract Inhibits LPS-Induced Inflammation via MAPK Signaling Pathway and Protects Rats from Hepatic Fibrosis Caused by Abnormalities in the Gut-Liver Axis. *Front. Pharmacol.* **2021**, *12*, 683613. [CrossRef]
39. Krishna, M.; Narang, H. The complexity of mitogen-activated protein kinases (MAPKs) made simple. *Cell. Mol. Life Sci.* **2008**, *65*, 3525–3544. [CrossRef]
40. Kyriakis, J.M.; Avruch, J. Mammalian MAPK signal transduction pathways activated by stress and inflammation: A 10-year update. *Physiol. Rev.* **2012**, *92*, 689–737. [CrossRef]
41. Petrasek, J.; Bala, S.; Csak, T.; Lippai, D.; Kodys, K.; Menashy, V.; Barrieau, M.; Min, S.Y.; Kurt-Jones, E.A.; Szabo, G. IL-1 receptor antagonist ameliorates inflammasome-dependent alcoholic steatohepatitis in mice. *J. Clin. Investig.* **2012**, *122*, 3476–3489. [CrossRef] [PubMed]
42. Wang, C.; Li, X.; Xue, B.; Yu, C.; Wang, L.; Deng, R.; Liu, H.; Chen, Z.; Zhang, Y.; Fan, S.; et al. RasGRP1 promotes the acute inflammatory response and restricts inflammation-associated cancer cell growth. *Nat. Commun.* **2022**, *13*, 7001. [CrossRef] [PubMed]
43. Pandian, V.D.; Giovannucci, D.R.; Vazquez, G.; Kumarasamy, S. CACNB2 is associated with aberrant RAS-MAPK signaling in hypertensive Dahl Salt-Sensitive rats. *Biochem. Biophys. Res. Commun.* **2019**, *513*, 760–765. [CrossRef]
44. Mora, J.R.; Iwata, M.; von Andrian, U.H. Vitamin effects on the immune system: Vitamins A and D take centre stage. *Nat. Rev. Immunol.* **2008**, *8*, 685–698. [CrossRef]
45. Carr, A.C.; Maggini, S. Vitamin C and Immune Function. *Nutrients* **2017**, *9*, 1211. [CrossRef]
46. Wilson, D.F. Oxidative phosphorylation: Regulation and role in cellular and tissue metabolism. *J. Physiol.* **2017**, *595*, 7023–7038. [CrossRef] [PubMed]
47. Wang, L.; Zheng, W.; Sun, Y.; Ren, X.; Yan, C.; Song, S.; Ai, C. Fucoidan ameliorates alcohol-induced liver injury in mice through Parabacteroides distasonis-mediated regulation of the gut-liver axis. *Int. J. Biol. Macromol.* **2024**, *279*, 135309. [CrossRef]
48. Zhao, Q.; Dai, M.Y.; Huang, R.Y.; Duan, J.Y.; Zhang, T.; Bao, W.M.; Zhang, J.Y.; Gui, S.Q.; Xia, S.M.; Dai, C.T.; et al. Parabacteroides distasonis ameliorates hepatic fibrosis potentially via modulating intestinal bile acid metabolism and hepatocyte pyroptosis in male mice. *Nat. Commun.* **2023**, *14*, 1829. [CrossRef]
49. Shu, Y.; Huang, Y.; Dong, W.; Fan, X.; Sun, Y.; Chen, G.; Zeng, X.; Ye, H. The polysaccharides from Auricularia auricula alleviate non-alcoholic fatty liver disease via modulating gut microbiota and bile acids metabolism. *Int. J. Biol. Macromol.* **2023**, *246*, 125662. [CrossRef]

50. Canbay, A.; Sowa, J.P. L-Ornithine L-Aspartate (LOLA) as a Novel Approach for Therapy of Non-alcoholic Fatty Liver Disease. *Drugs* **2019**, *79* (Suppl. 1), 39–44. [CrossRef]
51. Ding, Y.; Koda, Y.; Shashni, B.; Takeda, N.; Zhang, X.; Tanaka, N.; Nishikawa, Y.; Nagasaki, Y. An orally deliverable ornithine-based self-assembling polymer nanomedicine ameliorates hyperammonemia in acetaminophen-induced acute liver injury. *Acta Biomater.* **2023**, *168*, 515–528. [CrossRef] [PubMed]
52. Imam, K.M.S.U.; Tian, Y.; Xin, F.; Xie, Y.; Wen, B. Lactucin, a Bitter Sesquiterpene from *Cichorium intybus*, Inhibits Cancer Cell Proliferation by Downregulating the MAPK and Central Carbon Metabolism Pathway. *Molecules* **2022**, *27*, 7358. [CrossRef] [PubMed]
53. Dang, T.; Zheng, G.; Zhang, Q.; Jin, P.; Zhang, H.; Su, L.; Qin, D.; Yao, G. Sesquiterpenoids with diverse carbon skeletons from the roots of *Cichorium glandulosum* and their anti-inflammatory activities. *Fitoterapia* **2019**, *136*, 104170. [CrossRef] [PubMed]
54. Zhou, W.; Zhang, H.; Huang, L.; Sun, C.; Yue, Y.; Cao, X.; Jia, H.; Wang, C.; Gao, Y. Disulfiram with Cu^{2+} alleviates dextran sulfate sodium-induced ulcerative colitis in mice. *Theranostics* **2023**, *13*, 2879–2895. [CrossRef]

Disclaimer/Publisher's Note: The statements, opinions and data contained in all publications are solely those of the individual author(s) and contributor(s) and not of MDPI and/or the editor(s). MDPI and/or the editor(s) disclaim responsibility for any injury to people or property resulting from any ideas, methods, instructions or products referred to in the content.

International Journal of
Molecular Sciences

MDPI

Article

GPR40/GPR120 Agonist GW9508 Improves Metabolic Syndrome-Exacerbated Periodontitis in Mice

Yanchun Li [1], Hong Yu [2], Maria F. Lopes-Virella [1] and Yan Huang [1,*]

[1] Division of Endocrinology, Diabetes and Metabolic Diseases, Department of Medicine, College of Medicine, Medical University of South Carolina, Charleston, SC 29425, USA; liyya@musc.edu (Y.L.); virellam@musc.edu (M.F.L.-V.)
[2] Department of Biomedical & Community Health Sciences, The James B. Edwards College of Dental Medicine, Medical University of South Carolina, Charleston, SC 29425, USA; yuho@musc.edu
* Correspondence: huangyan@musc.edu

Abstract: G protein-coupled receptor (GPR)40 and GPR120 are receptors for medium- and long-chain free fatty acids. It has been well documented that GPR40 and GPR120 activation improves metabolic syndrome (MetS) and exerts anti-inflammatory effects. Since chronic periodontitis is a common oral inflammatory disease initiated by periodontal pathogens and exacerbated by MetS, we determined if GPR40 and GPR120 activation with agonists improves MetS-associated periodontitis in animal models in this study. We induced MetS and periodontitis by high-fat diet feeding and periodontal injection of lipopolysaccharide, respectively, and treated mice with GW9508, a synthetic GPR40 and GPR120 dual agonist. We determined alveolar bone loss, osteoclast formation, and periodontal inflammation using micro-computed tomography, osteoclast staining, and histology. To understand the underlying mechanisms, we further performed studies to determine the effects of GW9508 on osteoclastogenesis and proinflammatory gene expression in vitro. Results showed that GW9508 improved metabolic parameters, including glucose, lipids, and insulin resistance. Results also showed that GW9508 improves periodontitis by reducing alveolar bone loss, osteoclastogenesis, and periodontal inflammation. Finally, in vitro studies showed that GW9508 inhibited osteoclast formation and proinflammatory gene secretion from macrophages. In conclusion, this study demonstrated for the first time that GPR40/GPR120 agonist GW9508 reduced alveolar bone loss and alleviated periodontal inflammation in mice with MetS-exacerbated periodontitis, suggesting that activating GPR40/GPR120 with agonist GW9508 is a potential anti-inflammatory approach for the treatment of MetS-associated periodontitis.

Keywords: fatty acid receptors; periodontitis; metabolic syndrome; inflammation

1. Introduction

Periodontitis, a bacteria-induced chronic inflammatory disease, is characterized by progressive destruction of tooth-supporting connective tissue and periodontal alveolar bone, leading to tooth loss [1,2]. It has been well-established that diabetes exacerbates periodontitis [3]. Interestingly, clinical studies have further demonstrated that metabolic syndrome (MetS), which is commonly associated with prediabetes, also increases the prevalence and severity of periodontitis [4–9]. MetS is defined as a cluster of cardiovascular risk factors, including obesity, high blood pressure, lipid abnormalities such as high triglycerides and low HDL, insulin resistance, and increased plasma glucose [10,11]. A recent systematic review and meta-analyses showed a dose-response relationship between the number of cardiovascular risk factors in MetS and the occurrence of periodontitis [9]. Another meta-analysis also showed that MetS is positively associated with the severity of periodontitis [12].

The findings of the relationship between MetS and periodontitis are important since 34% of the US population have MetS as contrasted to 9.3% of the US population having

diabetes [13]. Given that MetS worsens periodontitis, it is important to carefully evaluate and effectively treat periodontitis in patients with MetS as patients with diabetes. Indeed, early treatment of periodontitis in MetS patients who also have prediabetes is likely to reduce the severity of periodontitis when prediabetes progresses to diabetes [14]. More importantly, patients with MetS may also have life-threatening complications such as cardiovascular disease [15], nonalcoholic fatty liver disease [16], and Alzheimer's disease [17], and increasing studies have shown that periodontitis worsens these MetS complications via periodontitis-promoted systemic inflammation [18–20]. Therefore, the development of novel and effective therapeutics for MetS-exacerbated periodontitis is essential to reduce not only tooth loss but also the severity of MetS and MetS complications.

To study the pathogenesis of MetS-associated periodontitis, our lab has developed several mouse models with both MetS and periodontitis [21–23]. In these animal models, MetS was induced by high-fat diet (HFD) feeding for 20 weeks, and periodontitis was induced by periodontal LPS injection, ligature placement around the tooth, or oral inoculation of *Porphyromonas gingivalis* [21–23]. Using these animal models, we demonstrated that MetS worsened periodontitis by increasing macrophage infiltration and the production of inflammatory cytokines in periodontal tissue and promoting osteoclastogenesis, which led to alveolar bone loss [21,22]. Obviously, MetS, as a systemic disorder, worsens periodontitis by augmenting periodontal inflammation. Hence, we hypothesized that compounds that are capable of not only improving MetS but also inhibiting tissue inflammation may have the potential to treat periodontitis in patients with MetS as an adjunctive therapy to scaling and root planning (SRP), the gold standard treatment of chronic periodontitis [24–26]. By combining anti-inflammatory therapy with SRP, the treatment of periodontitis in patients with MetS can be more effective.

In recent years, it has been well established that G protein-coupled receptor (GPR)40 and GPR120 as fatty acid (FA) receptors play important roles in not only uptaking FAs but also mediating anti-inflammatory signaling [27–29]. It has been shown that GRP40 or GPR120 activation in animal models improved inflammation-associated metabolic disorders such as diabetes and MetS [28,30]. It has also been shown that omega-3 (ω-3) FAs such as docosahexaenoic acid (DHA) and eicosapentaenoic acid (EPA) as natural agonists for both GPR40 and GPR120 [31,32] have beneficial effects on periodontitis [33,34]. To increase potency and specificity, several synthetic agonists for GPR40 or GPR120, as well as dual agonists for both GPR40 and GPR120, have been developed [35–38]. A large number of studies have shown that these agonists have therapeutic potential for many chronic diseases, including MetS and atherosclerosis, through anti-inflammatory mechanisms [32,39,40]. Since GPR40/GPR120 agonists are capable of not only improving MetS but also acting as potent anti-inflammatory agents, they may have beneficial effects on MetS-exacerbated periodontitis. However, whether activation of GPR40/GPR120 by agonists improves MetS-associated periodontitis remains unknown. In this study, we hypothesized that GPR40/GPR120 dual agonist GW9508 is capable of inhibiting the progression of periodontitis exacerbated by MetS. Our specific objectives include the following: 1. To determine the effect of GW9508 on alveolar bone loss and periodontal inflammation in a mouse model for MetS-associated periodontitis; 2. To explore the potential molecular mechanisms involved in GW9508-attenuated alveolar bone loss and periodontal inflammation.

2. Results

2.1. GW9508 Treatment Improves MetS

We first determined the effects of GW9508 on HFD-induced MetS. As shown in Figure 1, compared with control mice that were fed a low-fat diet (LFD), MetS mice that were fed HFD had increased bodyweight, fasting glucose, cholesterol, free fatty acid, insulin, and homeostatic model assessment for insulin resistance (HOMA-IR). Periodontitis (PD) induced by periodontal LPS injection had no significant effect on these metabolic parameters in LFD-fed control mice but reduced insulin and insulin resistance in HFD-fed mice. Interestingly, GW9508 treatment significantly reduced MetS-increased fasting glucose,

cholesterol, and free fatty acids (FFA) in mice, suggesting that GW9508 as a GPR40/GPR120 agonist improves MetS.

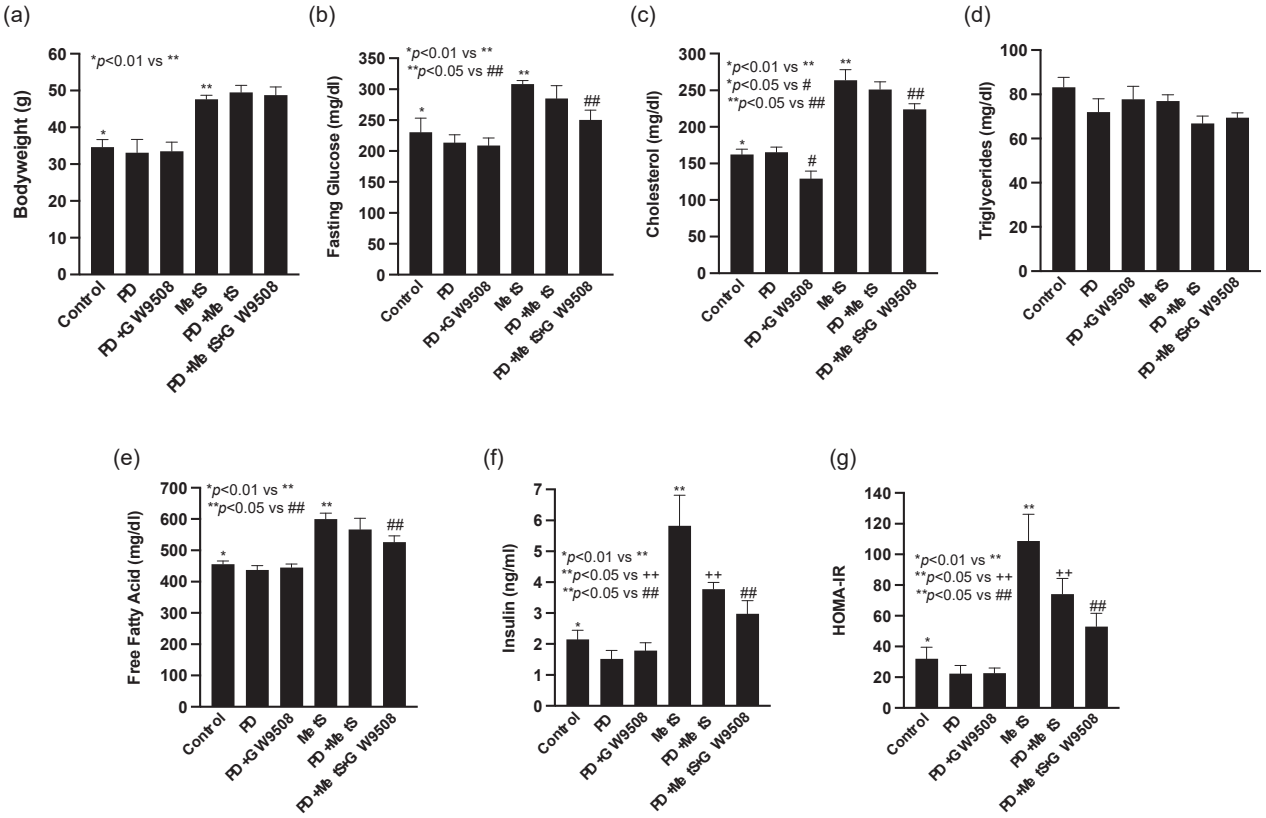


Figure 1. The effects of GW9508 on the metabolic parameters for control (LFD-fed) or MetS (HFD-fed) mice with or without LPS-induced periodontitis (PD). Eight-week-old male C57BL/6 mice were fed LFD or HFD for 20 weeks and periodontally injected with PBS or LPS in the last 4 weeks. Some of the mice were treated with GW9508 by intraperitoneal injection during the last 4 weeks. At the end of the experiment, the metabolic parameters, including bodyweight (**a**), fasting glucose (**b**), cholesterol (**c**), triglycerides (**d**), free fatty acids (**e**), insulin (**f**), and HOMA-IR (**g**) were determined. The data are presented as mean ± SD (n = 6). Group symbols: * Control, ** MetS, ++ PD+MetS, # PD+GW9508, ## PD+MetS+GW9508.

2.2. GW9508 Reduces Alveolar Bone Loss in Mice with MetS-Associated Periodontitis

At the end of the animal experiment, the mouse maxillae were dissected and scanned by micro-computed tomography (μCT) for bone volume fraction (BVF) quantification. As shown in Figure 2a and Table 1, periodontitis or MetS alone reduced BVF significantly, and the combination of periodontitis and MetS further reduced BVF. In contrast, GW9508 significantly reversed the loss of BVF in mice with both periodontitis and MetS. We also measured the distance between the cemento–enamel junction (CEJ) and alveolar bone crest (ABC) since CEJ–ABC distance is positively associated with alveolar bone loss [22]. Results showed that periodontitis or MetS significantly increased CEJ–ABC distance, and the combination of periodontitis and MetS further increased CEJ–ABC distance. Consistent with the findings from the mCT study, GW9508 significantly reduced CEJ–ABC distance in mice with both periodontitis and MetS (Figure 2b–d).

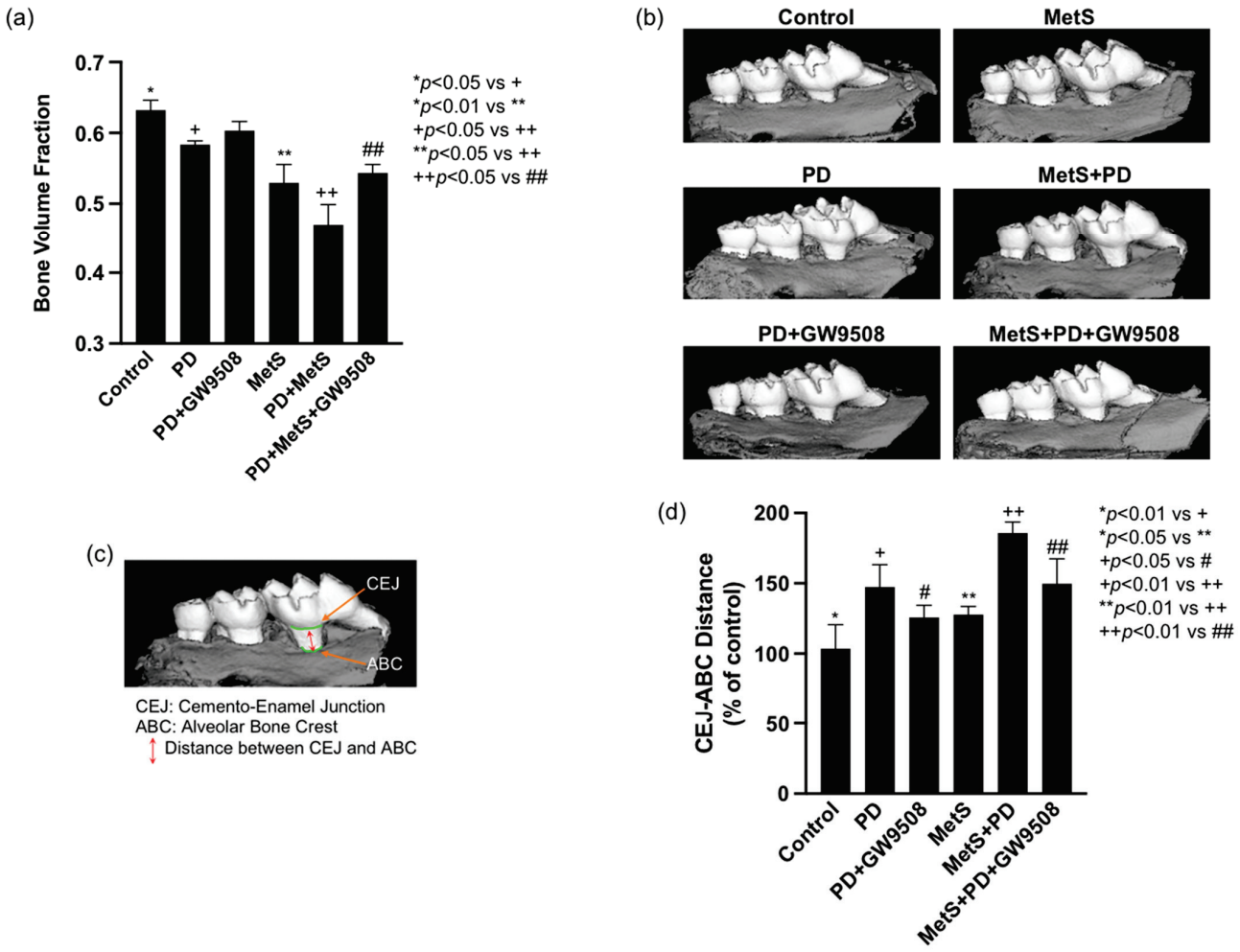


Figure 2. The effect of GW9508 on alveolar bone loss in mice with periodontitis (PD) alone or with MetS and PD. Male C57BL/6 mice were fed LFD or HFD and periodontally injected with LPS. After the treatment, the maxillae were scanned by mCT, and bone volume fraction was quantified (**a**,**b**). Additionally, the distance from CEJ to ABC was measured for the first and second molars (**b**–**d**). The data are presented as means ± SD (n = 6). Group symbols: * Control, ** MetS, + PD, ++ PD+MetS, # PD+GW9508, ## PD+MetS+GW9508.

Table 1. The effect of GW9508 on bone volume fraction (BVF) in mice with periodontitis (PD) and/or metabolic syndrome (MetS).

	BVF (Mean SD)	% BVF Reduction Compared to Control Mice	% BVF Increase by GW9508 Treatment
Control	0.632 ± 0.014	-	
PD	0.583 ± 0.005	7.75%	
PD+GW9508	0.603 ± 0.013	4.59%	3.16%
MetS	0.530 ± 0.026	16.14%	
PD+MetS	0.470 ± 0.029	25.63%	
PD+MetS+GW9508	0.544 ± 0.012	13.92%	11.71%

2.3. GW9508 Inhibits Osteoclastogenesis in Mice with MetS-Associated Periodontitis

To understand how GW9508 reduced alveolar bone loss in mice with MetS-associated periodontitis, we performed Tartrate-resistant acid phosphatase (TRAP) staining on tis-

sue sections of the maxillae to detect osteoclasts. We focused on the area of periodontal ligaments which connects the tooth root and alveolar bone. Results showed that periodontitis or MetS increased osteoclast formation on the surface of alveolar bones, and the combination of periodontitis and MetS further increased osteoclast formation (Figure 3a,b). However, GW9508 treatment significantly reduced the number of osteoclasts in mice with periodontitis and MetS (Figure 3a,b).

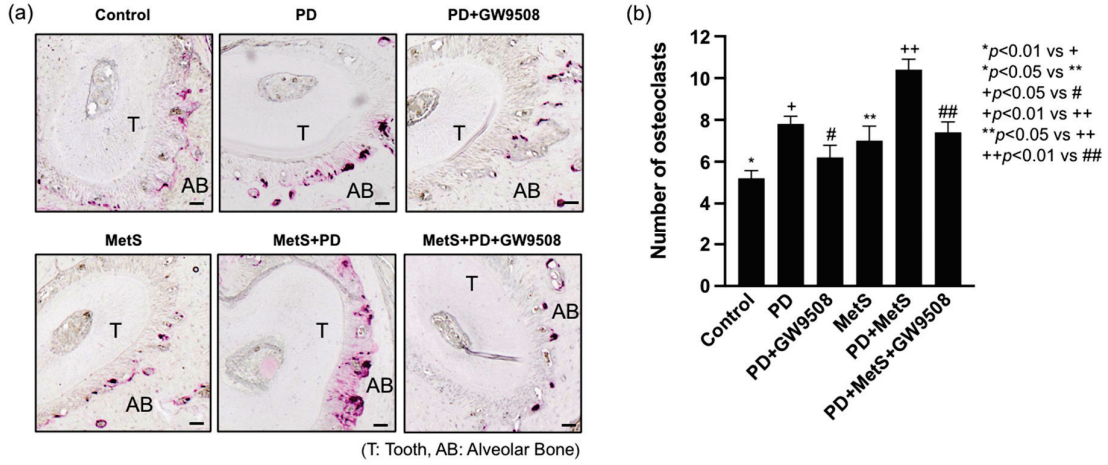


Figure 3. The effect of GW9508 on osteoclastogenesis in mice with periodontitis (PD) alone or with MetS and PD. After the maxillae were examined by mCT, as described in Figure 2, they were decalcified and sectioned. Tartrate-resistant acid phosphatase (TRAP) staining to detect osteoclasts was performed on the tissue sections. Representative tissue images from 6 groups of mice were shown (scale bar = 100 μm) (**a**), and multinucleated TRAP-positive osteoclasts per field of view were quantified and compared among the groups (**b**). The data are presented as mean ± SD (n = 6). Group symbols: * Control, + PD, # PD+GW9508, ** MetS, ++ PD+MetS, ## PD+MetS+GW9508.

2.4. GW9508 Inhibits Osteoclastogenesis Enhanced by LPS Plus Palmitic Acid (PA) In Vitro

In this study, we used a receptor activator of nuclear factor kappa-B ligand (RANKL) to induce osteoclast formation from RAW264.7 macrophages and determined the effect of GW9508 on osteoclast formation. Since we have found previously that LPS and palmitic acid (PA), a saturated fatty acid, cooperatively enhanced RANKL-induced osteoclast formation in vitro [22], we also determine the effect of GW9508 on osteoclast formation enhanced by LPS, PA, or LPS plus PA. Consistent with our previous observations [22], results showed that while either LPS or PA increased osteoclast number and area, the combination of LPS and PA further augmented osteoclast number and area (Figure 4a–c). Results also showed that GW9508 treatment significantly inhibited the osteoclast number and area enhanced by LPS plus PA in vitro (Figure 4a–c), which is consistent with the findings from our animal study shown in Figure 3.

2.5. GW9508 Reduces Periodontal Inflammation in Mice with MetS-Associated Periodontitis

Histological analysis of maxillae with a focus on the area of periodontal ligaments between the tooth root and alveolar bone was performed, and inflammatory scoring was made according to the criteria described in Materials and Methods to assess the effect of GW9508 on periodontal inflammation and bone resorption in mice. Results showed that while periodontitis increased the inflammatory scores as evidenced by increased leukocyte infiltration and bone resorption, the combination of MetS and periodontitis further increased the inflammatory score in mice (Figure 5a,b). In contrast, GW9508 treatment reduced the inflammatory scores in mice with MetS-associated periodontitis as determined by decreased leukocyte infiltration and bone resorption (Figure 5a,b).

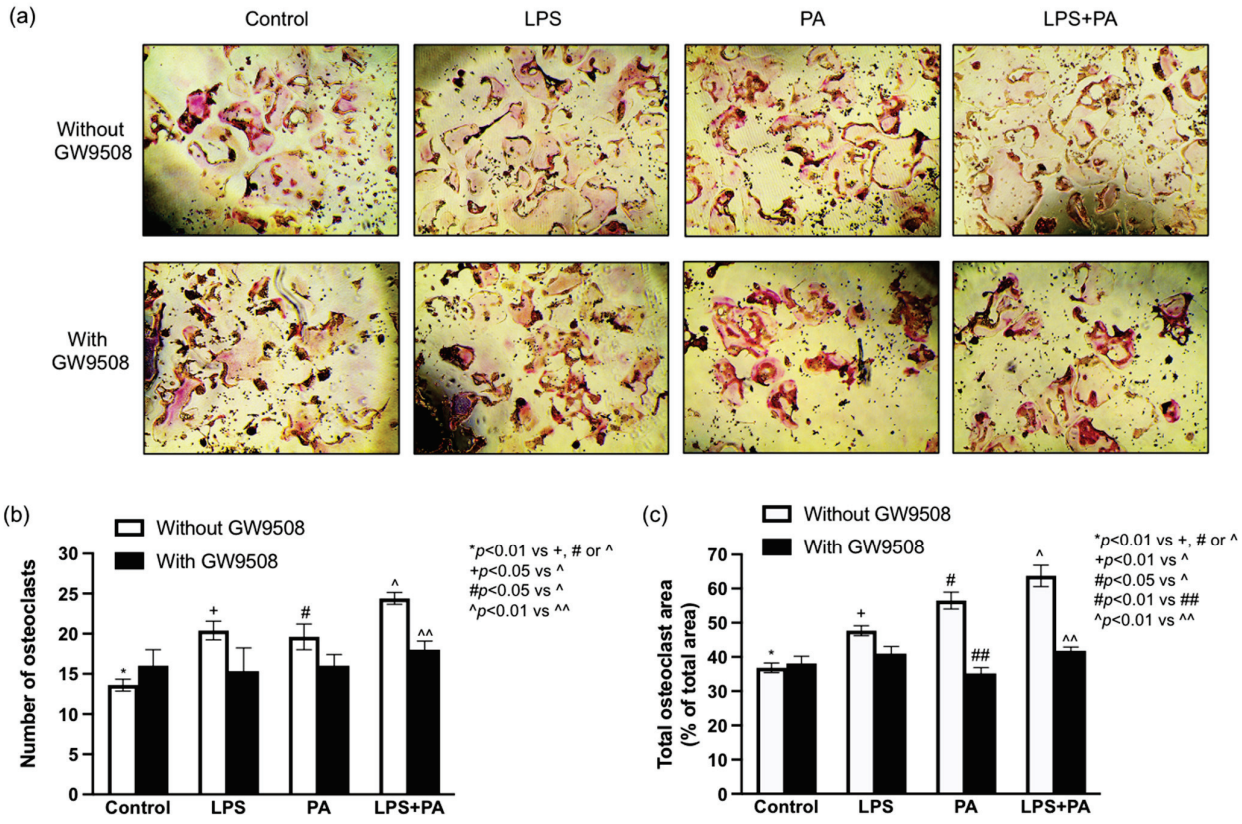


Figure 4. The effect of GW9508 on osteoclast formation stimulated by LPS, PA, or both LPS and PA. RAW264.7 macrophages were treated with 100 ng/mL of RANKL alone (control) or with RANKL plus 1 ng/mL of LPS, 100 mM of PA, or both LPS and PA for 3 days. After changing the medium, the macrophages were treated with RANKL alone or RANKL plus LPS, PA, or LPS and PA in the absence or presence of 1 mM of GW9508 for 2 days, and cells were then fixed. TRAP staining was carried out, and the osteoclasts, which were positively stained and contained more than three nuclei, were identified (**a**), counted, and compared among different groups (**b**). The total osteoclast area was also quantified as % of the total area and compared among different groups (**c**). The data are presented as mean ± SD (n = 3). Group symbols: * Control cells without GW9508 treatment, + LPS treatment without GW9508, # PA treatment without GW9508, ## PA treatment with GW9508, ^ LPS+PA without GW9508, ^^ LPS+PA with GW9508.

2.6. GW9508 Inhibits Proinflammatory Cytokine Secretion from Macrophages In Vitro

To explore the mechanisms by which GW9508 reduced periodontal inflammation in mice, we tested our hypothesis that GW9508 inhibits the secretion of proinflammatory cytokines from macrophages, which are immune cells known to play a pivotal role in periodontal inflammation [41]. Since LPS is released by Gram-negative bacteria that play a critical role in periodontitis, while PA is the most common saturated fatty acid in humans [42] and associated with MetS [43], we determined the effect of GW9508 on inflammatory cytokine secretion from macrophages stimulated by LPS and PA. We have shown previously that LPS and PA have a synergy on proinflammatory cytokine upregulation in macrophages [44]. Results showed that while LPS potently induced secretion of IL-6, tumor necrosis factor (TNF)a, and monocyte chemoattractant protein (MCP)-1, PA augmented the LPS-induced secretions (Figure 6). However, GW9508 significantly inhibited the cytokine secretion stimulated by LPS and PA (Figure 6).

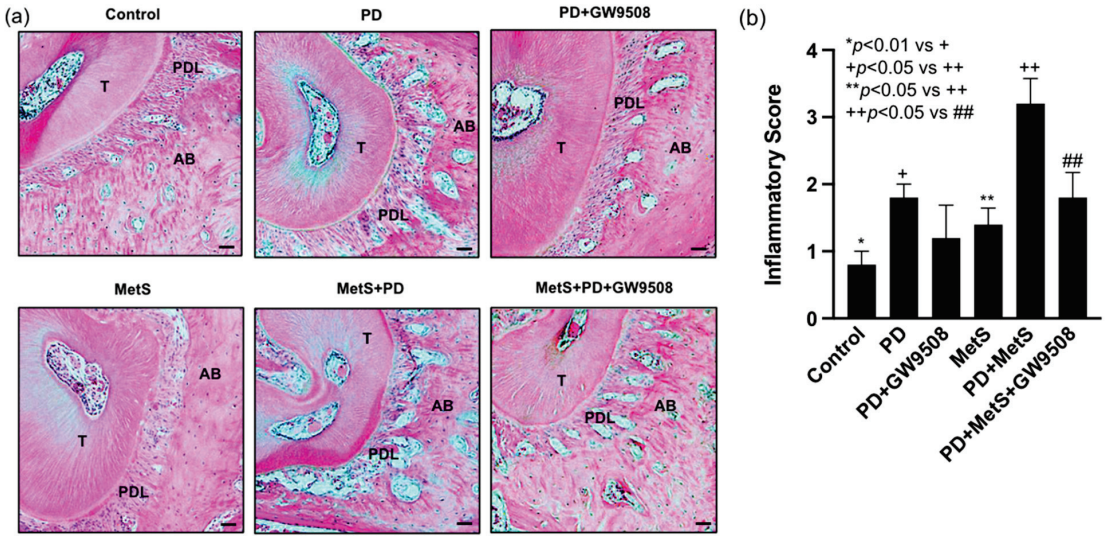


Figure 5. The effect of GW9508 on periodontal inflammation and bone resorption in mice with periodontitis (PD) or with MetS and PD. The periodontal tissue sections were stained with hematoxylin and eosin, and histologic analysis was performed. Representative photomicrographs focused on the area of periodontal ligament (PDL) along with tooth root (T) and alveolar bone (AB) were shown (scale bar = 100 μm) (**a**). The inflammatory scoring for leukocyte infiltration and bone resorption in all groups were made (**b**) according to the criteria as described in Methods. The data are presented as means ± SD (n = 6). Group symbols: * Control, + PD, ** MetS, ++ PD+MetS, ## PD+MetS+GW9508.

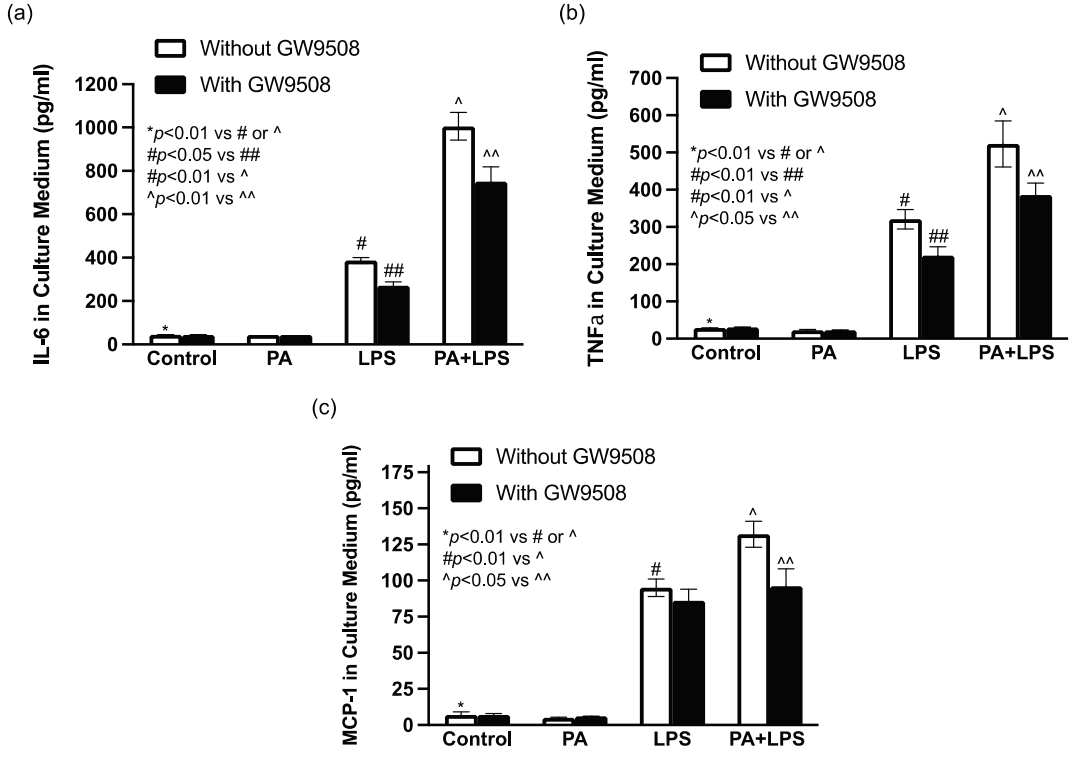


Figure 6. The effect of GW9508 on proinflammatory cytokine secretion from macrophages. RAW264.7 macrophages were treated with 1 ng/mL of LPS, 100 μM of palmitic acid (PA), or both LPS and PA in the absence or presence of 1 μM of GW9508 for 24 h. After the treatment, IL-6 (**a**), TNFa (**b**), and monocyte chemoattractant protein (MCP)-1 (**c**) in a culture medium were quantified with ELISA. The data presented as means ± SD are from one of three experiments with similar results. Group symbols: * Control cells without GW9508, # PA treatment without GW9508, ## PA treatment with GW9508, ^ LPS+PA without GW9508, ^^ LPS+PA with GW9508.

3. Discussion

GPR40 and GPR120 are G protein-coupled receptors for medium- and long-chain FAs [45,46]. It has been well documented that GPR40 is highly expressed in pancreatic β cells, and its activation enhances glucose-induced insulin secretion [47]. It has been further shown that GPR40 is involved in metabolic homeostasis [48]. In addition to pancreatic β cells, GPR40 is also expressed by many other types of cells, such as macrophages [49], osteoclasts [50], vascular endothelial cells [51,52], and hepatocytes [53], and has anti-inflammatory properties [54–58]. Park et al. showed that treatment of bone marrow-derived macrophages with GPR40 agonist TAK875 or AMG1638 suppressed the activation of the NLRP3 inflammasome by IL-1b and IL-18 via NFkB and sarco/endoplasmic reticulum Ca^{2+}-ATPase [59]. Our lab also showed recently that loss of GPR40 in mice worsened MetS-associated periodontal inflammation and that GPR40 agonists downregulated proinflammatory molecules in macrophages [23].

Similar to GPR40, GPR120 is also capable of promoting glucose homeostasis through incretin-dependent insulin secretion [60]. Furthermore, studies have shown that GPR120 is expressed by several types of immune cells, such as macrophages and $CD4^+$ T cells [61,62]. GPR120 activation suppresses proinflammatory cytokine expression and enhances anti-inflammatory cytokine expression [63]. All the above findings suggest that GPR40 or GPR120 agonists may have favorable effects on diabetes or MetS and its inflammation-related complications.

The findings that DHA and EPA, as natural dual agonists of GPR40 and GPR120, exert anti-inflammatory effects are consistent with the beneficial role of GPR40 and GPR120 in inflammatory diseases [31,64–66]. DHA and EPA have similar potencies (pEC_{50}) to GPR40 and GPR120 [32]. In addition to anti-inflammatory properties, DHA and EPA also have favorable effects on lipid metabolism and blood pressure [39]. To increase the specificity and potency, synthetic agonists for GPR40 or GPR120 and dual agonists for both GPR40 and GPR120 have been developed [37,67]. Interestingly, studies have suggested that the simultaneous activation of both GPR40 and GPR120 with a dual agonist may be more therapeutically useful than the activation of only one of them with a specific agonist. Satapati et al. reported that a dual agonist of GPR40 and GPR120 achieved superior glycemic control compared with a GPR40 selective agonist by improving insulin resistance in ob/ob mice [38], and it has been well documented that periodontitis and insulin resistance have a bidirectional relationship [68]. Furthermore, Huang et al. demonstrated that GW9508, a dual agonist of GPR40 and GPR120, has a dual effect of inhibiting osteoclastogenesis and promoting osteogenesis [69], which is closely related to periodontal health.

GW9508 is a well-characterized dual agonist with pEC_{50} of 7.32 and 5.46 for GPR40 and GPR120, respectively [70]. Studies have well documented that GW9508 is anti-inflammatory [55] and thereby exerts beneficial effects on many inflammation-related diseases, including nonalcoholic steatohepatitis [71], Alzheimer's disease [72], bacterial infection [73], and atherosclerosis [32,39,40]. In the current study, we reported for the first time that GW9508 also improved periodontitis in animal models with MetS by alleviating alveolar bone loss and periodontal inflammation.

Given that MetS exacerbates periodontitis, we first investigated the effect of GW9508 on HFD-induced MetS in this study. Results showed that GW9508 reduced metabolic parameters, including fasting glucose, cholesterol, and FFAs, clearly indicating that GW9508 improves MetS. These findings are consistent with the previous reports that GW9508 alleviates hyperglycemia [74], hyperlipidemia [71], and insulin resistance [75] in various animal models. Since it is known that MetS-related cardiovascular risk factors, including hyperglycemia, hyperlipidemia, and insulin resistance, are associated with periodontitis [21], the above results have revealed an important mechanism by which GW9508 mitigates MetS-associated periodontitis by modulating metabolic parameters.

In addition to MetS, we also investigated the effect of GW9508 on osteoclastogenesis. Results showed that GW9508 treatment strongly inhibited osteoclast formation in mice with periodontitis and MetS, indicating that GW9508 reduces alveolar bone loss by inhibiting

osteoclastogenesis. To further elucidate the molecular mechanism whereby GW9508 reduced alveolar bone loss in mice with both periodontitis and MetS, we used an in vitro cell model to demonstrate that GW9508 inhibited osteoclastogenesis induced by RANKL and enhanced by LPS and PA. It is well known that LPS is increased by periodontitis [76], and PA is associated with MetS [77]. Furthermore, we demonstrated previously that LPS and PA had a cooperative effect on osteoclastogenesis [22]. Therefore, the findings from the above in vitro study indicate that the inhibition of the LPS-PA cooperation on osteoclastogenesis by GW9508 is likely a molecular mechanism involved in GW9508-reduced alveolar bone loss in mice with MetS-associated periodontitis.

In this study, we further assessed the effect of GW9508 on periodontal inflammation since it is well-known that periodontal inflammation is critically involved in osteoclastogenesis [76,78]. To test our hypothesis that GW9508 attenuated the periodontal inflammation in mice with both periodontitis and MetS, we performed histological analysis on the area of the periodontal ligament and ligament-connected tooth root and alveolar bone. Results showed that GW9508 treatment reduced leukocyte infiltration in the area in mice with both periodontitis and MetS. We also performed an in vitro study to demonstrate that GW9508 inhibited the secretion of proinflammatory cytokines such as IL-6, TNFa, and MCP-1 from macrophages stimulated by LPS and PA. Since it is well-known that proinflammatory cytokines are potent stimulators of osteoclast precursor proliferation, osteoclast formation, and bone resorption in vivo [79,80], these findings suggest that the inhibition of proinflammatory cytokine secretion by GW9508 plays a pivotal role in GW9508-reduced osteoclastogenesis and subsequent alveolar bone loss.

In the animal models for human periodontitis, the oral bacterial gavage model, periodontal bacteria or LPS inoculation model, and ligature model are commonly used mouse models [81]. All these mouse models are good models for human periodontitis [81] and were used in our research [23,82]. In the current study, we utilized the periodontal LPS inoculation model for the following reasons. We have reported previously that MetS exacerbates periodontal inflammation and bone loss in a mouse model with periodontitis induced by periodontal LPS inoculation [21]. We have also reported that LPS and PA have a synergistic stimulation on the expression of proinflammatory cytokines in macrophages [44]. In the current study, based on the above findings, we hypothesized that GW9508 attenuates the progression of periodontitis in animal models and the inhibition of the synergistic effect of LPS and PA on proinflammatory cytokine expression by GW9508 is a mechanism involved in the attenuation of periodontitis progression by GW9508. To be consistent with our hypothesis, we used the periodontal LPS inoculation model in the current study.

A limitation of this study is that only male mice were used since it is known that female C57BL/6 mice are protected against HFD-induced MetS [83]. However, clinical studies have shown that the incidence of MetS in women is similar to that in men [84]. Although it is known that periodontitis has a documented higher prevalence in men (56.4%) compared to women (38.4%) [85], the incidence of 38.4% in women is still very high. Therefore, it is important to determine the effect of GW9508 on MetS-related periodontitis in both male and female mice to understand how targeting GPR40/GPR120 affects MetS-associated periodontitis in animal models with different genders. The findings will help the development of relevant gender-based treatment options for patients with MetS-associated periodontitis. To address the effect of GW9508 on MetS-associated periodontitis in female animals, LDL receptor-deficient (LDLR $-/-$) mice may be used as an animal model with MetS [86,87]. Wall et al. reported that female LDLR $-/-$ mice fed an HFD developed a MetS phenotype, which is similar to that in male mice [86]. These female mice had increased bodyweight, blood glucose, glucose intolerance, and lipids, including triglycerides and cholesterol.

Similar to GPR40 and GPR120, CD36, also called fatty acid translocase (FAT), is also a receptor for long-chain free fatty acids [88]. However, CD36 is different from GPR40 and GPR120 as it is a multifunctional membrane receptor involved in macrophage foam cell formation, oxidative stress, tissue degradation, and apoptosis [88]. We have shown

previously that CD36 expression in periodontal tissue is upregulated by MetS in mouse models of both periodontitis and MetS and upregulated in vitro by LPS and saturated fatty acids such as PA in macrophages [89]. Since CD36 is markedly upregulated by PA, PA is likely to bind to CD36 to stimulate the expression of proinflammatory molecules such as IL-6, MCP-1, and TNFa in macrophages [90,91]. We have also shown that PA and LPS have a synergy in activating pro-inflammatory signaling and upregulating pro-inflammatory gene expression [44].

As illustrated in Figure 7, the current study showed, for the first time, that the synthetic dual GPR40/GPR120 agonist GW9508 alleviated alveolar bone loss and periodontal inflammation in mice with MetS-associated periodontitis. The investigations on the underlying mechanisms demonstrated that GW9508 inhibited osteoclastogenesis and inflammatory cytokine secretion stimulated by LPS and PA from macrophages. All these results strongly indicate that targeting GPR40/GPR120 with agonists is a potential anti-inflammatory approach in the treatment of MetS-associated periodontitis.

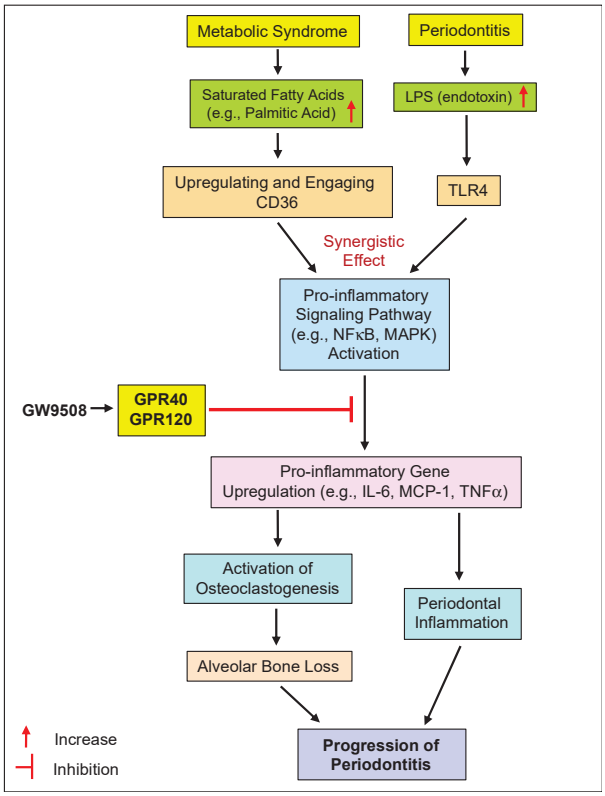


Figure 7. The potential mechanisms involved in the alleviation of alveolar bone loss and periodont inflammation by GPR40/GPR120 agonist GW9508 in mice with both MetS and periodontitis.

4. Materials and Methods

4.1. Animals

The Institutional Animal Care and Use Committee at the Medical University of South Carolina approved all experimental protocols. The study was performed in accordance with the Guidelines of ARRIVE. All mice were maintained on a 12-h light-dark cycle in a pathogen-free environment and had ad libitum access to water and food. MetS and periodontitis were induced by HFD feeding and periodontal LPS injection, respectively, and part of the mice were treated with GW9508 by intraperitoneal injection. Eight-week-old male C57BL/6 mice were randomly divided into 6 groups (n = 6): 1. Control; 2. Periodontitis; 3. Periodontitis with GW9508 treatment; 4. MetS; 5. MetS and periodontitis; 6. MetS and periodontitis with GW9508 treatment.

4.2. Induction of MetS

Mice were fed either LFD (D12450B) or HFD (D12492) (Research Diet Inc., New Brunswick, NJ, Canada) for 20 weeks. D12492 is a lard-based HFD containing 60% kcal fat, 20% kcal protein, and 20% kcal carbohydrate. For fat, it contains 254.5 g/kg fatty acid, 81.5 g/kg saturated fatty acid (SFA) and 51 g/kg PA. D12450B is a control LFD for D12492 containing 10% kcal fat, 20% kcal protein, and 70% kcal carbohydrate. For fat, it contains 43.7 g/kg fatty acid, 9.9 g/kg SFA and 1.1 g/kg PA.

4.3. Induction of Periodontitis and Treatment with GW9508

During the last 4 weeks of LFD or HFD feeding, some of the mice were injected with LPS isolated from *A.* actinomycetemcomitans (strain Y4, serotype B) [92] (0.2 mg/kg) through both left and right sides of the palatal gingiva between the maxillary 1st and 2nd molars, twice a week, for 4 weeks [93,94]. *A.* actinomycetemcomitans is one of the oral pathogens involved in chronic periodontitis [95]. For control, mice were periodontally injected with phosphate-buffered saline (PBS), the vehicle for LPS. Some of the mice were treated with GW9508 at 50 mg/kg/day by intraperitoneal injection (IP) during the last 4 weeks of LFD or HFD feeding when periodontal LPS injection was performed. The above dose of GW9508 was selected since it had been shown that treatment with GW9508 at the dose of 50 mg/kg/day through IP in C57BL/6 mice inhibited diabetes-induced neuropathy [96] and improved glucose homeostasis and insulin sensitivity [75]. The mice with IP of PBS were used as controls for GW9508 treatment.

4.4. Metabolic Measurements

Blood samples were obtained under the fasted condition, and glucose level was determined using a Precision QID glucometer (MediSense Inc., Bedford, MA, USA). Serum cholesterol was measured using the Cholestech LDX Lipid Monitoring System (Fisher Scientific, Pittsburgh, PA, USA). Serum triglycerides were measured using EnzyChrom™ Triglyceride Assay Kit (BioAssay Systems, Hayward, CA, USA). Serum FFAs were determined using the EnzyChrom™ free fatty acid kit (BioAssay systems (Hayward, CA, USA)). Serum fasting insulin was assayed using the Ultra Sensitive Insulin ELISA Kit (Crystal Chem, Inc., Downers Grove, IL, USA). Fasting whole-body insulin sensitivity was estimated with the HOMA-IR according to the formula [fasting plasma glucose (mg/dL) $\times$ fasting plasma insulin (mU/mL)]/405.

4.5. Micro-Computed Tomography (μCT), Analysis of Bone Volume Fraction (BVF), and Measurement of Cementoenamel Junction (CEJ)-Alveolar Bone Crest (ABC) Distance

Maxillae were dissected and fixed in 10% phosphate-buffered formalin for 24 h, washed with PBS, and stored in 70% ethanol. Maxillae were scanned at 55 kVp, 145 μA, 16 μm voxel resolution using Scanco Medical 40 mCT scanner (Scanco Medical, Brüttisellen, Switzerland) as described previously [97]. Three-dimensional images were generated and reconstructed for each specimen. These images were rotated with a standard orientation and threshold to discern mineralized and non-mineralized tissue. The region of interest (ROI) was indicated by the contour height of molars at the CEJ as the width and the molar cusp tips to root apices as the height. Depth was equal to the buccolingual size of the teeth plus 1.0 mm^3. BVF was calculated as the percentage of bone within the ROI using AnalyzePro software (AnalyzeDirect, Inc., Overland Park, KS, USA), https://analyzedirect.com/analyzepro-support/ (accessed on 27 August 2024). A well-trained and experienced research specialist who was blinded to the treatment groups performed the mCT analysis. Data are reported in accordance with standardized nomenclature [98]. Additionally, three-line measurements of the distance from CEJ to ABC were taken for the first and second molars, as previously described [99].

4.6. Tartrate-Resistant Acid Phosphatase (TRAP) Staining and Quantification of Osteoclasts

Formalin-fixed maxillae were decalcified in a 10% EDTA solution for 4 weeks at 4 °C. The EDTA solution was changed three times per week. The maxillae were paraffin-embedded, and 7-μm sagittal sections were prepared. TRAP staining was performed in tissue sections using a leukocyte acid phosphatase kit (Sigma Aldrich, St. Louis, MO, USA). The tissue sections were counterstained with hematoxylin after TRAP staining. Pictures were taken with a Nikon Eclipse TS-100 inverted microscope. Active osteoclasts were defined as multinucleated TRAP-positive cells in contact with the bone surface. TRAP-positive osteoclasts under the first and the second molar on the surface of the alveolar bone were counted.

4.7. Histological Study of Periodontal Inflammation

For pathological evaluation, the above tissue sections were stained with hematoxylin and eosin. The tissue inflammation and bone resorption were evaluated according to the criteria for scoring tissue inflammation and bone resorption: 0 = within normal limits; 1 = focal some leukocyte infiltration, no significant bone resorption; 2 = moderate leukocyte infiltration with mild bone resorption; 3 = severe leukocyte infiltration with moderate bone resorption; and 4 = severe leukocyte infiltration with extensive bone resorption [100].

4.8. Cell Culture

RAW 264.7 macrophages were purchased from the American Type Culture Collection (Manassas, VA, USA) and grown in DMEM (American Type Culture Collection, Manassas, VA, USA) supplemented with 10% heat-inactivated fetal calf serum (HyClone, Logan, UT, USA). The cells were maintained in a 37 °C, 90% relative humidity, 5% CO_2 environment.

4.9. PA Preparation

To prepare PA solution for cell treatments, PA (Sigma, St. Louis, MO, USA) was dissolved in 0.1 N NaOH and 70% ethanol at 70 °C to make PA with a stock concentration of 50 mM. The solution was kept at 55 °C for 10 min, mixed, and brought to room temperature.

4.10. Enzyme-Linked Immunosorbent Assay (ELISA)

Cytokines in the medium were quantified using a sandwich ELISA kit according to the protocol provided by the manufacturer (BioLegend, San Diego, CA, USA).

4.11. In Vitro Study of Osteoclast Formation

RAW264.7 macrophages were treated with 100 ng/mL of receptor activator of RANKL alone (control) or with RANKL plus 1 ng/mL of LPS, 100 mM of PA, or both LPS and PA for 3 days. The medium was then changed, and the macrophages were treated with RANKL alone or RANKL plus LPS, PA, or LPS plus PA in the absence or presence of 1 mM of GW9508 for 2 days. The RAW264.7 macrophages were treated with GW9508 during the last two days since it has been reported previously that significant changes in osteoclast differentiation induced by RANKL started on day 3 after RAW264.7 macrophages were exposed to RANKL [101]. After the treatment, cells were fixed with 4% paraformaldehyde in PBS for 10 min at room temperature. TRAP staining was carried out in accordance with the manufacturer's instructions (Sigma Aldrich, St. Louis, MO, USA). Cells were observed under light microscopy, and those containing more than three nuclei were considered osteoclasts. The means of osteoclast number per well were counted and compared among different groups. The total area of multinuclear osteoclasts was measured with ImageJ software, version 2.0.0.-rc-43/1.52n (NIH, Bethesda, MD, USA) and presented as a % of the total area per field.

4.12. Statistical Analysis

GraphPad Prism 8 (v. 8.4.3) (GraphPad Software, Inc., La Jolla, CA, USA) was used for statistical analysis. The one-way analysis of variance (ANOVA) with the post hoc test

was used to determine whether there were any statistically significant differences between the means of three or more independent groups. A Student's *t*-test was performed for comparison between the two groups when data had a normal distribution. For data without normal distribution, nonparametric analysis using the Mann–Whitney test. For the in vitro study of osteoclast formation, the osteoclast numbers in three random fields per well viewed under the light microscope were counted, and the mean of the osteoclast numbers per well was calculated. The means of three wells were then compared between different groups. When an experiment was repeated, statistical analysis was also performed to compare their variances. The values were expressed as mean ± SD, and a value of $p < 0.05$ was considered significant.

Author Contributions: Conceptualization, Y.H.; methodology, Y.L. and H.Y.; supervision, Y.H. and M.F.L.-V.; analysis, Y.L., H.Y. and Y.H.; fund acquisition, Y.H.; writing—original draft preparation, Y.H.; writing—review and editing, Y.H., M.F.L.-V. and H.Y. All authors have read and agreed to the published version of the manuscript.

Funding: This work was supported by grant DE027070 funded by National Institute of Dental and Craniofacial Research (NIDCR), National Institutes of Health (NIH) of United States.

Institutional Review Board Statement: The animal study was conducted in accordance with the Declaration of Helsinki and approved by the Institutional Animal Care and Use Committee at the Medical University of South Carolina (certification no. 01154; date of approval: 13 April 2022).

Informed Consent Statement: Not applicable.

Data Availability Statement: All data generated or analyzed during the current study are available from the corresponding author upon reasonable request.

Acknowledgments: This study utilized the facilities and resources of the Center for Oral Health Research in the James B. Edwards College of Dental Medicine at the Medical University of South Carolina.

Conflicts of Interest: The authors declare no conflicts of interest.

References

1. Beck, J.; Garcia, R.; Heiss, G.; Vokonas, P.S.; Offenbacher, S. Periodontal disease and cardiovascular disease. *J. Periodontol.* **1996**, *67* (Suppl. S10), 1123–1137. [CrossRef]
2. Offenbacher, S. Periodontal diseases: Pathogenesis. *Ann. Periodontol.* **1996**, *1*, 821–878. [CrossRef] [PubMed]
3. Zheng, M.; Wang, C.; Ali, A.; Shih, Y.A.; Xie, Q.; Guo, C. Prevalence of periodontitis in people clinically diagnosed with diabetes mellitus: A meta-analysis of epidemiologic studies. *Acta Diabetol.* **2021**, *58*, 1307–1327. [CrossRef] [PubMed]
4. Katz, P.P.; Wirthlin, M.R., Jr.; Szpunar, S.M.; Selby, J.V.; Sepe, S.J.; Showstack, J.A. Epidemiology and prevention of periodontal disease in individuals with diabetes. *Diabetes Care* **1991**, *14*, 375–385. [CrossRef]
5. Yalda, B.; Offenbacher, S.; Collins, J.G. Diabetes as a modifier of periodontal disease expression. *Periodontology 2000* **1994**, *6*, 37–49. [CrossRef] [PubMed]
6. Nibali, L.; Tatarakis, N.; Needleman, I.; Tu, Y.K.; D'Aiuto, F.; Rizzo, M.; Donos, N. Clinical review: Association between metabolic syndrome and periodontitis: A systematic review and meta-analysis. *J. Clin. Endocrinol. Metab.* **2013**, *98*, 913–920. [CrossRef] [PubMed]
7. Gomes-Filho, I.S.; das Merces, M.C.; de Santana Passos-Soares, J.; da Cruz, S.S.; Ladeia, A.M.T.; Trindade, S.C.; de Moraes Marcilio Cerqueira, E.; Coelho, J.M.F.; Monteiro, F.M.M.; Barreto, M.L.; et al. Severity of Periodontitis and Metabolic Syndrome: Is There an Association? *J. Periodontol.* **2016**, *87*, 357–366. [CrossRef]
8. Gobin, R.; Tian, D.; Liu, Q.; Wang, J. Periodontal Diseases and the Risk of Metabolic Syndrome: An Updated Systematic Review and Meta-Analysis. *Front. Endocrinol.* **2020**, *11*, 336. [CrossRef]
9. Campos, J.R.; Martins, C.C.; Faria, S.F.S.; Carvalho, A.P.; Pereira, A.G.; Costa, F.O.; Cota, L.O.M. Association between components of metabolic syndrome and periodontitis: A systematic review and meta-analysis. *Clin. Oral Investig.* **2022**, *26*, 5557–5574. [CrossRef]
10. Grundy, S.M.; Brewer, H.B., Jr.; Cleeman, J.I.; Smith, S.C., Jr.; Lenfant, C.; National Heart, Lung, and Blood Institute (NHLBI). Definition of metabolic syndrome: Report of the National Heart, Lung, and Blood Institute/American Heart Association conference on scientific issues related to definition. *Circulation* **2004**, *109*, 433–438. [CrossRef] [PubMed]

11. Alberti, K.G.; Eckel, R.H.; Grundy, S.M.; Zimmet, P.Z.; Cleeman, J.I.; Donato, K.A.; Fruchart, J.C.; James, W.P.; Loria, C.M.; Smith, S.C., Jr.; et al. Harmonizing the metabolic syndrome: A joint interim statement of the International Diabetes Federation Task Force on Epidemiology and Prevention; National Heart, Lung, and Blood Institute; American Heart Association; World Heart Federation; International Atherosclerosis Society; and International Association for the Study of Obesity. *Circulation* **2009**, *120*, 1640–1645. [CrossRef] [PubMed]
12. Rosário-Dos-Santos, H.L.; Miranda, S.S.; Gomes-Filho, I.S.; Cruz, S.S.D.; Figueiredo, A.; Souza, E.S.; Hintz, A.M.; Loomer, P.M.; Passos-Soares, J.S. Periodontitis severity relationship with metabolic syndrome: A systematic review with meta-analysis. *Oral Dis.* **2023**, *29*, 2512–2520. [CrossRef]
13. Day, C. Metabolic syndrome, or What you will: Definitions and epidemiology. *Diabetes Vasc. Dis. Res.* **2007**, *4*, 32–38. [CrossRef] [PubMed]
14. Srivastava, M.C.; Srivastava, R.; Verma, P.K.; Gautam, A. Metabolic syndrome and periodontal disease: An overview for physicians. *J. Family Med. Prim. Care* **2019**, *8*, 3492–3495. [CrossRef]
15. Benetti, E.; Patel, N.S.; Collino, M. The role of PPARβ/δ in the management of metabolic syndrome and its associated cardiovascular complications. *Endocr. Metab. Immune Disord.-Drug Targets* **2011**, *11*, 273–284. [CrossRef]
16. Bogdanova, K.; Poczatkova, H.; Uherkova, L.; Riegrova, D.; Rypka, M.; Feher, J.; Marchesini, G.; Vesely, J. Non-alcoholic fatty liver disease (NAFLD)—A novel common aspect of the metabolic syndrome. *Biomed. Pap.-Palacky Univ. Olomouc* **2006**, *150*, 101–104. [CrossRef] [PubMed]
17. Rojas-Gutierrez, E.; Muñoz-Arenas, G.; Treviño, S.; Espinosa, B.; Chavez, R.; Rojas, K.; Flores, G.; Díaz, A.; Guevara, J. Alzheimer's disease and metabolic syndrome: A link from oxidative stress and inflammation to neurodegeneration. *Synapse* **2017**, *71*, e21990. [CrossRef]
18. Persson, G.R.; Persson, R.E. Cardiovascular disease and periodontitis: An update on the associations and risk. *J. Clin. Periodontol.* **2008**, *35* (Suppl. S8), 362–379. [CrossRef]
19. Alakhali, M.S.; Al-Maweri, S.A.; Al-Shamiri, H.M.; Al-Haddad, K.; Halboub, E. The potential association between periodontitis and non-alcoholic fatty liver disease: A systematic review. *Clin. Oral Investig.* **2018**, *22*, 2965–2974. [CrossRef]
20. Dioguardi, M.; Crincoli, V.; Laino, L.; Alovisi, M.; Sovereto, D.; Mastrangelo, F.; Russo, L.L.; Muzio, L.L. The Role of Periodontitis and Periodontal Bacteria in the Onset and Progression of Alzheimer's Disease: A Systematic Review. *J. Clin. Med.* **2020**, *9*, 495. [CrossRef]
21. Li, Y.; Lu, Z.; Zhang, X.; Yu, H.; Kirkwood, K.L.; Lopes-Virella, M.F.; Huang, Y. Metabolic syndrome exacerbates inflammation and bone loss in periodontitis. *J. Dent. Res.* **2015**, *94*, 362–370. [CrossRef]
22. Lu, Z.; Li, Y.; Yu, H.; Lopes-Virella, M.F.; Huang, Y. High-fat diet-induced metabolic syndrome increases ligature-induced alveolar bone loss in mice. *Oral Dis.* **2023**, *29*, 1312–1323. [CrossRef]
23. Li, Y.; Lu, Z.; Kirkwood, C.L.; Kirkwood, K.L.; Wank, S.A.; Li, A.J.; Lopes-Virella, M.F.; Huang, Y. GPR40 deficiency worsens metabolic syndrome-associated periodontitis in mice. *J. Periodontal Res.* **2023**, *58*, 575–587. [CrossRef] [PubMed]
24. Van Ravensteijn, M.M.; Timmerman, M.F.; Brouwer, E.A.G.; Slot, D.E. The effect of omega-3 fatty acids on active periodontal therapy: A systematic review and meta-analysis. *J. Clin. Periodontol.* **2022**, *49*, 1024–1037. [CrossRef] [PubMed]
25. Dos Santos, N.C.C.; Furukawa, M.V.; Oliveira-Cardoso, I.; Cortelli, J.R.; Feres, M.; Van Dyke, T.; Rovai, E.S. Does the use of omega-3 fatty acids as an adjunct to non-surgical periodontal therapy provide additional benefits in the treatment of periodontitis? A systematic review and meta-analysis. *J. Periodontal Res.* **2022**, *57*, 435–447. [CrossRef] [PubMed]
26. Stańdo-Retecka, M.; Piatek, P.; Namiecinska, M.; Bonikowski, R.; Lewkowicz, P.; Lewkowicz, N. Clinical and microbiological outcomes of subgingival instrumentation supplemented with high-dose omega-3 polyunsaturated fatty acids in periodontal treatment—A randomized clinical trial. *BMC Oral Health* **2023**, *23*, 290. [CrossRef] [PubMed]
27. Hara, T.; Kimura, I.; Inoue, D.; Ichimura, A.; Hirasawa, A. Free fatty acid receptors and their role in regulation of energy metabolism. *Rev. Physiol. Biochem. Pharmacol.* **2013**, *164*, 77–116. [CrossRef]
28. Miyamoto, J.; Kasubuchi, M.; Nakajima, A.; Kimura, I. Anti-Inflammatory and Insulin-Sensitizing Effects of Free Fatty Acid Receptors. *Free Fat. Acid Recept.* **2017**, *236*, 221–231. [CrossRef]
29. Talukdar, S.; Olefsky, J.M.; Osborn, O. Targeting GPR120 and other fatty acid-sensing GPCRs ameliorates insulin resistance and inflammatory diseases. *Trends Pharmacol. Sci.* **2011**, *32*, 543–550. [CrossRef]
30. Miyamoto, J.; Hasegawa, S.; Kasubuchi, M.; Ichimura, A.; Nakajima, A.; Kimura, I. Nutritional Signaling via Free Fatty Acid Receptors. *Int. J. Mol. Sci.* **2016**, *17*, 450. [CrossRef]
31. Kumari, P.; Inoue, A.; Chapman, K.; Lian, P.; Rosenbaum, D.M. Molecular mechanism of fatty acid activation of FFAR1. *Proc. Natl. Acad. Sci. USA* **2023**, *120*, e2219569120. [CrossRef] [PubMed]
32. Christiansen, E.; Watterson, K.R.; Stocker, C.J.; Sokol, E.; Jenkins, L.; Simon, K.; Grundmann, M.; Petersen, R.K.; Wargent, E.T.; Hudson, B.D.; et al. Activity of dietary fatty acids on FFA1 and FFA4 and characterisation of pinolenic acid as a dual FFA1/FFA4 agonist with potential effect against metabolic diseases. *Br. J. Nutr.* **2015**, *113*, 1677–1688. [CrossRef] [PubMed]
33. Miroult, C.; Lasserre, J.; Toma, S. Effects of Omega-3 as an adjuvant in the treatment of periodontal disease: A systematic review and meta-analysis. *Clin. Exp. Dent. Res.* **2023**, *9*, 545–556. [CrossRef]
34. Ma, J.; Kitaura, H.; Ohori, F.; Noguchi, T.; Marahleh, A.; Kinjo, R.; Kanou, K.; Ren, J.; Miura, M.; Narita, K.; et al. Generating Bone Marrow Chimeric Mouse Using GPR120 Deficient Mouse for the Study of DHA Inhibitory Effect on Osteoclast Formation and Bone Resorption. *Int. J. Mol. Sci.* **2023**, *24*, 17000. [CrossRef] [PubMed]

35. Rodrigues, D.A.; Pinheiro, P.S.M.; Ferreira, T.; Thota, S.; Fraga, C.A.M. Structural basis for the agonist action at free fatty acid receptor 1 (FFA1R or GPR40). *Chem. Biol. Drug Des.* **2018**, *91*, 668–680. [CrossRef]
36. Milligan, G.; Alvarez-Curto, E.; Watterson, K.R.; Ulven, T.; Hudson, B.D. Characterizing pharmacological ligands to study the long-chain fatty acid receptors GPR40/FFA1 and GPR120/FFA4. *Br. J. Pharmacol.* **2015**, *172*, 3254–3265. [CrossRef]
37. Bianchini, G.; Nigro, C.; Sirico, A.; Novelli, R.; Prevenzano, I.; Miele, C.; Beguinot, F.; Aramini, A. A new synthetic dual agonist of GPR120/GPR40 induces GLP-1 secretion and improves glucose homeostasis in mice. *Biomed. Pharmacother.* **2021**, *139*, 111613. [CrossRef]
38. Satapati, S.; Qian, Y.; Wu, M.S.; Petrov, A.; Dai, G.; Wang, S.P.; Zhu, Y.; Shen, X.; Muise, E.S.; Chen, Y.; et al. GPR120 suppresses adipose tissue lipolysis and synergizes with GPR40 in antidiabetic efficacy. *J. Lipid Res.* **2017**, *58*, 1561–1578. [CrossRef]
39. Liu, Y.X.; Yu, J.H.; Sun, J.H.; Ma, W.Q.; Wang, J.J.; Sun, G.J. Effects of Omega-3 Fatty Acids Supplementation on Serum Lipid Profile and Blood Pressure in Patients with Metabolic Syndrome: A Systematic Review and Meta-Analysis of Randomized Controlled Trials. *Foods* **2023**, *12*, 725. [CrossRef]
40. Suski, M.; Kiepura, A.; Wiśniewska, A.; Kuś, K.; Skałkowska, A.; Stachyra, K.; Stachowicz, A.; Gajda, M.; Korbut, R.; Olszanecki, R. Anti-atherosclerotic action of GW9508—Free fatty acid receptors activator—In apoE-knockout mice. *Pharmacol. Rep.* **2019**, *71*, 551–555. [CrossRef]
41. Wang, W.; Zheng, C.; Yang, J.; Li, B. Intersection between macrophages and periodontal pathogens in periodontitis. *J. Leukoc. Biol.* **2021**, *110*, 577–583. [CrossRef] [PubMed]
42. Carta, G.; Murru, E.; Banni, S.; Manca, C. Palmitic Acid: Physiological Role, Metabolism and Nutritional Implications. *Front. Physiol.* **2017**, *8*, 902. [CrossRef]
43. Walchuk, C.; Wang, Y.; Suh, M. The impact of EPA and DHA on ceramide lipotoxicity in the metabolic syndrome. *Br. J. Nutr.* **2021**, *125*, 863–875. [CrossRef]
44. Jin, J.; Zhang, X.; Lu, Z.; Perry, D.M.; Li, Y.; Russo, S.B.; Cowart, L.A.; Hannun, Y.A.; Huang, Y. Acid sphingomyelinase plays a key role in palmitic acid-amplified inflammatory signaling triggered by lipopolysaccharide at low concentrations in macrophages. *Am. J. Physiol. Endocrinol. Metab.* **2013**, *305*, E853–E867. [CrossRef] [PubMed]
45. Trzaskowski, B.; Latek, D.; Yuan, S.; Ghoshdastider, U.; Debinski, A.; Filipek, S. Action of molecular switches in GPCRs—Theoretical and experimental studies. *Curr. Med. Chem.* **2012**, *19*, 1090–1109. [CrossRef]
46. Itoh, Y.; Kawamata, Y.; Harada, M.; Kobayashi, M.; Fujii, R.; Fukusumi, S.; Ogi, K.; Hosoya, M.; Tanaka, Y.; Uejima, H.; et al. Free fatty acids regulate insulin secretion from pancreatic beta cells through GPR40. *Nature* **2003**, *422*, 173–176. [CrossRef]
47. Paul, A.; Nahar, S.; Nahata, P.; Sarkar, A.; Maji, A.; Samanta, A.; Karmakar, S.; Maity, T.K. Synthetic GPR40/FFAR1 agonists: An exhaustive survey on the most recent chemical classes and their structure-activity relationships. *Eur. J. Med. Chem.* **2023**, *264*, 115990. [CrossRef]
48. Al Mahri, S.; Malik, S.S.; Al Ibrahim, M.; Haji, E.; Dairi, G.; Mohammad, S. Free Fatty Acid Receptors (FFARs) in Adipose: Physiological Role and Therapeutic Outlook. *Cells* **2022**, *11*, 750. [CrossRef] [PubMed]
49. Relling, I.; Akcay, G.; Fangmann, D.; Knappe, C.; Schulte, D.M.; Hartmann, K.; Muller, N.; Turk, K.; Dempfle, A.; Franke, A.; et al. Role of wnt5a in metabolic inflammation in humans. *J. Clin. Endocrinol. Metab.* **2018**, *103*, 4253–4264. [CrossRef]
50. Cornish, J.; MacGibbon, A.; Lin, J.M.; Watson, M.; Callon, K.E.; Tong, P.C.; Dunford, J.E.; van der Does, Y.; Williams, G.A.; Grey, A.B.; et al. Modulation of osteoclastogenesis by fatty acids. *Endocrinology* **2008**, *149*, 5688–5695. [CrossRef]
51. Wang, S.; Awad, K.S.; Elinoff, J.M.; Dougherty, E.J.; Ferreyra, G.A.; Wang, J.Y.; Cai, R.; Sun, J.; Ptasinska, A.; Danner, R.L. G Protein-coupled Receptor 40 (GPR40) and Peroxisome Proliferator-activated Receptor gamma (PPARgamma): An Integrated Two-Receptor Signaling Pathway. *J. Biol. Chem.* **2015**, *290*, 19544–19557. [CrossRef] [PubMed]
52. Lu, Z.; Li, Y.; Jin, J.; Zhang, X.; Hannun, Y.A.; Huang, Y. GPR40/FFA1 and neutral sphingomyelinase are involved in palmitate-boosted inflammatory response of microvascular endothelial cells to LPS. *Atherosclerosis* **2015**, *240*, 163–173. [CrossRef] [PubMed]
53. Suh, H.N.; Huong, H.T.; Song, C.H.; Lee, J.H.; Han, H.J. Linoleic acid stimulates gluconeogenesis via Ca^{2+}/PLC, cPLA2, and PPAR pathways through GPR40 in primary cultured chicken hepatocytes. *Am. J. Physiol. Cell Physiol.* **2008**, *295*, C1518–C1527. [CrossRef]
54. Li, S.; Yu, Y.; Wang, B.; Qiao, S.; Hu, M.; Wang, H.; Fu, C.; Dong, B. Overexpression of G protein-coupled receptor 40 protects obesity-induced cardiomyopathy through the SIRT1/LKB1/AMPK pathway. *Hum. Gene Ther.* **2022**, *33*, 598–613. [CrossRef] [PubMed]
55. Xiao, J.; Cai, T.; Fang, Y.; Liu, R.; Flores, J.J.; Wang, W.; Gao, L.; Liu, Y.; Lu, Q.; Tang, L.; et al. Activation of GPR40 attenuates neuroinflammation and improves neurological function via PAK4/CREB/KDM6B pathway in an experimental GMH rat model. *J. Neuroinflamm.* **2021**, *18*, 160. [CrossRef]
56. Shen, X.; Fan, B.; Hu, X.; Luo, L.; Yan, Y.; Yang, L. Metformin Reduces Lipotoxicity-Induced Meta-Inflammation in β-Cells through the Activation of GPR40-PLC-IP3 Pathway. *J. Diabetes Res.* **2019**, *2019*, 7602427. [CrossRef]
57. Dragano, N.R.V.; Solon, C.; Ramalho, A.F.; de Moura, R.F.; Razolli, D.S.; Christiansen, E.; Azevedo, C.; Ulven, T.; Velloso, L.A. Polyunsaturated fatty acid receptors, GPR40 and GPR120, are expressed in the hypothalamus and control energy homeostasis and inflammation. *J. Neuroinflamm.* **2017**, *14*, 91. [CrossRef]
58. Gras, D.; Chanez, P.; Urbach, V.; Vachier, I.; Godard, P.; Bonnans, C. Thiazolidinediones induce proliferation of human bronchial epithelial cells through the GPR40 receptor. *Am. J. Physiol. Lung Cell Mol. Physiol.* **2009**, *296*, L970–L978. [CrossRef]

59. Park, J.; Lee, M.Y.; Seo, Y.S.; Kang, B.; Lim, S.C.; Kang, K.W. GPR40 agonist inhibits NLRP3 inflammasome activation via modulation of nuclear factor-κB and sarco/endoplasmic reticulum Ca^{2+}-ATPase. *Life Sci.* **2021**, *287*, 120127. [CrossRef]
60. Ghislain, J.; Poitout, V. Targeting lipid GPCRs to treat type 2 diabetes mellitus—Progress and challenges. *Nat. Rev. Endocrinol.* **2021**, *17*, 162–175. [CrossRef]
61. Oh, D.Y.; Talukdar, S.; Bae, E.J.; Imamura, T.; Morinaga, H.; Fan, W.; Li, P.; Lu, W.J.; Watkins, S.M.; Olefsky, J.M. GPR120 is an omega-3 fatty acid receptor mediating potent anti-inflammatory and insulin-sensitizing effects. *Cell* **2010**, *142*, 687–698. [CrossRef] [PubMed]
62. Yang, W.; Liu, H.; Xu, L.; Yu, T.; Zhao, X.; Yao, S.; Zhao, Q.; Barnes, S.; Cohn, S.M.; Dann, S.M.; et al. GPR120 Inhibits Colitis Through Regulation of $CD4^+$ T Cell Interleukin 10 Production. *Gastroenterology* **2022**, *162*, 150–165. [CrossRef] [PubMed]
63. Di Petrillo, A.; Kumar, A.; Onali, S.; Favale, A.; Fantini, M.C. GPR120/FFAR4: A Potential New Therapeutic Target for Inflammatory Bowel Disease. *Inflamm. Bowel Dis.* **2023**, *29*, 1981–1989. [CrossRef]
64. Petermann, A.B.; Reyna-Jeldes, M.; Ortega, L.; Coddou, C.; Yévenes, G.E. Roles of the Unsaturated Fatty Acid Docosahexaenoic Acid in the Central Nervous System: Molecular and Cellular Insights. *Int. J. Mol. Sci.* **2022**, *23*, 5390. [CrossRef] [PubMed]
65. Karmokar, P.F.; Moniri, N.H. Oncogenic signaling of the free-fatty acid receptors FFA1 and FFA4 in human breast carcinoma cells. *Biochem. Pharmacol.* **2022**, *206*, 115328. [CrossRef]
66. Jin, J.; Lu, Z.; Li, Y.; Cowart, L.A.; Lopes-Virella, M.F.; Huang, Y. Docosahexaenoic acid antagonizes the boosting effect of palmitic acid on LPS inflammatory signaling by inhibiting gene transcription and ceramide synthesis. *PLoS ONE* **2018**, *13*, e0193343. [CrossRef]
67. Mizuta, K.; Zhang, Y.; Mizuta, F.; Hoshijima, H.; Shiga, T.; Masaki, E.; Emala, C.W., Sr. Novel identification of the free fatty acid receptor FFAR1 that promotes contraction in airway smooth muscle. *Am. J. Physiol. Lung Cell Mol. Physiol.* **2015**, *309*, L970–L982. [CrossRef] [PubMed]
68. Islam, S.K.; Seo, M.; Lee, Y.S.; Moon, S.S. Association of periodontitis with insulin resistance, β-cell function, and impaired fasting glucose before onset of diabetes. *Endocr. J.* **2015**, *62*, 981–989. [CrossRef]
69. Huang, F.; Liu, X.; Fu, X.; Chen, Y.; Jiang, D.; Wang, T.; Hu, R.; Zou, X.; Hu, H.; Liu, C. 3D-Printed Bioactive Scaffold Loaded with GW9508 Promotes Critical-Size Bone Defect Repair by Regulating Intracellular Metabolism. *Bioengineering* **2023**, *10*, 535. [CrossRef]
70. Briscoe, C.P.; Peat, A.J.; McKeown, S.C.; Corbett, D.F.; Goetz, A.S.; Littleton, T.R.; McCoy, D.C.; Kenakin, T.P.; Andrews, J.L.; Ammala, C.; et al. Pharmacological regulation of insulin secretion in MIN6 cells through the fatty acid receptor GPR40: Identification of agonist and antagonist small molecules. *Br. J. Pharmacol.* **2006**, *148*, 619–628. [CrossRef] [PubMed]
71. Li, M.; Meng, X.; Xu, J.; Huang, X.; Li, H.; Li, G.; Wang, S.; Man, Y.; Tang, W.; Li, J. GPR40 agonist ameliorates liver X receptor-induced lipid accumulation in liver by activating AMPK pathway. *Sci. Rep.* **2016**, *6*, 25237. [CrossRef] [PubMed]
72. Gong, Y.; Li, Y.; Liu, X.; He, L. GW9508 ameliorates cognitive dysfunction via the external treatment of encephalopathy in $A\beta_{1\text{-}42}$ induced mouse model of Alzheimer's disease. *Eur. J. Pharmacol.* **2021**, *909*, 174362. [CrossRef]
73. Souza, P.R.; Walker, M.E.; Goulding, N.J.; Dalli, J.; Perretti, M.; Norling, L.V. The GPR40 Agonist GW9508 Enhances Neutrophil Function to Aid Bacterial Clearance during *E. coli* Infections. *Front. Immunol.* **2020**, *11*, 573019. [CrossRef]
74. McKillop, A.M.; Miskelly, M.G.; Moran, B.M.; Flatt, P.R. Incretins play an important role in FFA4/GPR120 regulation of glucose metabolism by GW-9508. *Life Sci.* **2023**, *318*, 121475. [CrossRef] [PubMed]
75. Ou, H.Y.; Wu, H.T.; Hung, H.C.; Yang, Y.C.; Wu, J.S.; Chang, C.J. Multiple mechanisms of GW-9508, a selective G protein-coupled receptor 40 agonist, in the regulation of glucose homeostasis and insulin sensitivity. *Am. J. Physiol. Endocrinol. Metab.* **2013**, *304*, E668–E676. [CrossRef]
76. AlQranei, M.S.; Chellaiah, M.A. Osteoclastogenesis in periodontal diseases: Possible mediators and mechanisms. *J. Oral Biosci.* **2020**, *62*, 123–130. [CrossRef] [PubMed]
77. Kien, C.L. Dietary interventions for metabolic syndrome: Role of modifying dietary fats. *Curr. Diab Rep.* **2009**, *9*, 43–50. [CrossRef]
78. Baloul, S.S. Osteoclastogenesis and Osteogenesis during Tooth Movement. *Front. Oral Biol.* **2016**, *18*, 75–79. [CrossRef]
79. Zhao, B. Does TNF Promote or Restrain Osteoclastogenesis and Inflammatory Bone Resorption? *Crit. Rev. Immunol.* **2018**, *38*, 253–261. [CrossRef]
80. Lee, S.K.; Lorenzo, J. Cytokines regulating osteoclast formation and function. *Curr. Opin. Rheumatol.* **2006**, *18*, 411–418. [CrossRef]
81. Rojas, C.; García, M.P.; Polanco, A.F.; González-Osuna, L.; Sierra-Cristancho, A.; Melgar-Rodríguez, S.; Cafferata, E.A.; Vernal, R. Humanized Mouse Models for the Study of Periodontitis: An Opportunity to Elucidate Unresolved Aspects of Its Immunopathogenesis and Analyze New Immunotherapeutic Strategies. *Front. Immunol.* **2021**, *12*, 663328. [CrossRef] [PubMed]
82. Lu, Z.; Li, Y.; Chowdhury, N.; Yu, H.; Syn, W.K.; Lopes-Virella, M.; Yilmaz, Ö.; Huang, Y. The Presence of Periodontitis Exacerbates Non-Alcoholic Fatty Liver Disease via Sphingolipid Metabolism-Associated Insulin Resistance and Hepatic Inflammation in Mice with Metabolic Syndrome. *Int. J. Mol. Sci.* **2023**, *24*, 8322. [CrossRef]
83. Pettersson, U.S.; Waldén, T.B.; Carlsson, P.O.; Jansson, L.; Phillipson, M. Female mice are protected against high-fat diet induced metabolic syndrome and increase the regulatory T cell population in adipose tissue. *PLoS ONE* **2012**, *7*, e46057. [CrossRef] [PubMed]
84. Bentley-Lewis, R.; Koruda, K.; Seely, E.W. The metabolic syndrome in women. *Nat. Clin. Pract. Endocrinol. Metab.* **2007**, *3*, 696–704. [CrossRef]
85. Ioannidou, E. The Sex and Gender Intersection in Chronic Periodontitis. *Front. Public Health* **2017**, *5*, 189. [CrossRef]

86. Wall, V.Z.; Barnhart, S.; Kanter, J.E.; Kramer, F.; Shimizu-Albergine, M.; Adhikari, N.; Wight, T.N.; Hall, J.L.; Bornfeldt, K.E. Smooth muscle glucose metabolism promotes monocyte recruitment and atherosclerosis in a mouse model of metabolic syndrome. *JCI Insight* **2018**, *3*, e96544. [CrossRef] [PubMed]
87. Ferreira, D.F.; Fiamoncini, J.; Prist, I.H.; Ariga, S.K.; de Souza, H.P.; de Lima, T.M. Novel role of TLR4 in NAFLD development: Modulation of metabolic enzymes expression. *Biochim. Biophys. Acta* **2015**, *1851*, 1353–1359. [CrossRef]
88. Karunakaran, U.; Elumalai, S.; Moon, J.S.; Won, K.C. CD36 Signal Transduction in Metabolic Diseases: Novel Insights and Therapeutic Targeting. *Cells* **2021**, *10*, 1833. [CrossRef]
89. Lu, Z.; Li, Y.; Brinson, C.W.; Kirkwood, K.L.; Lopes-Virella, M.F.; Huang, Y. CD36 is upregulated in mice with periodontitis and metabolic syndrome and involved in macrophage gene upregulation by palmitate. *Oral Dis.* **2017**, *23*, 210–218. [CrossRef]
90. Kim, D.H.; Cho, Y.M.; Lee, K.H.; Jeong, S.W.; Kwon, O.J. Oleate protects macrophages from palmitate-induced apoptosis through the downregulation of CD36 expression. *Biochem. Biophys. Res. Commun.* **2017**, *488*, 477–482. [CrossRef]
91. Urso, C.J.; Zhou, H. Role of CD36 in Palmitic Acid Lipotoxicity in Neuro-2a Neuroblastoma Cells. *Biomolecules* **2021**, *11*, 1567. [CrossRef] [PubMed]
92. Yu, H.; Li, Q.; Herbert, B.; Zinna, R.; Martin, K.; Junior, C.R.; Kirkwood, K.L. Anti-inflammatory effect of MAPK phosphatase-1 local gene transfer in inflammatory bone loss. *Gene Ther.* **2011**, *18*, 344–353. [CrossRef]
93. Rogers, J.E.; Li, F.; Coatney, D.D.; Rossa, C.; Bronson, P.; Krieder, J.M.; Giannobile, W.V.; Kirkwood, K.L. Actinobacillus actinomycetemcomitans lipopolysaccharide-mediated experimental bone loss model for aggressive periodontitis. *J. Periodontol.* **2007**, *78*, 550–558. [CrossRef] [PubMed]
94. Jin, J.; Zhang, X.; Lu, Z.; Li, Y.; Lopes-Virella, M.F.; Yu, H.; Haycraft, C.J.; Li, Q.; Kirkwood, K.L.; Huang, Y. Simvastatin inhibits lipopolysaccharide-induced osteoclastogenesis and reduces alveolar bone loss in experimental periodontal disease. *J. Periodontal Res.* **2014**, *49*, 518–526. [CrossRef]
95. Silva, N.; Dutzan, N.; Hernandez, M.; Dezerega, A.; Rivera, O.; Aguillon, J.C.; Aravena, O.; Lastres, P.; Pozo, P.; Vernal, R.; et al. Characterization of progressive periodontal lesions in chronic periodontitis patients: Levels of chemokines, cytokines, matrix metalloproteinase-13, periodontal pathogens and inflammatory cells. *J. Clin. Periodontol.* **2008**, *35*, 206–214. [CrossRef]
96. Königs, V.; Pierre, S.; Schicht, M.; Welss, J.; Hahnefeld, L.; Rimola, V.; Lütjen-Drecoll, E.; Geisslinger, G.; Scholich, K. GPR40 Activation Abolishes Diabetes-Induced Painful Neuropathy by Suppressing VEGF-A Expression. *Diabetes* **2022**, *71*, 774–787. [CrossRef] [PubMed]
97. Steinkamp, H.M.; Hathaway-Schrader, J.D.; Chavez, M.B.; Aartun, J.D.; Zhang, L.; Jensen, T.; Shojaee Bakhtiari, A.; Helke, K.L.; Stumpo, D.J.; Alekseyenko, A.V.; et al. Tristetraprolin Is Required for Alveolar Bone Homeostasis. *J. Dent. Res.* **2018**, *97*, 946–953. [CrossRef]
98. Bouxsein, M.L.; Boyd, S.K.; Christiansen, B.A.; Guldberg, R.E.; Jepsen, K.J.; Muller, R. Guidelines for assessment of bone microstructure in rodents using micro-computed tomography. *J. Bone Miner. Res.* **2010**, *25*, 1468–1486. [CrossRef]
99. Park, C.H.; Abramson, Z.R.; Taba, M., Jr.; Jin, Q.; Chang, J.; Kreider, J.M.; Goldstein, S.A.; Giannobile, W.V. Three-dimensional micro-computed tomographic imaging of alveolar bone in experimental bone loss or repair. *J. Periodontol.* **2007**, *78*, 273–281. [CrossRef]
100. Jin, J.; Machado, E.R.; Yu, H.; Zhang, X.; Lu, Z.; Li, Y.; Lopes-Virella, M.F.; Kirkwood, K.L.; Huang, Y. Simvastatin inhibits LPS-induced alveolar bone loss during metabolic syndrome. *J. Dent. Res.* **2014**, *93*, 294–299. [CrossRef]
101. Pengjam, Y.; Madhyastha, H.; Madhyastha, R.; Yamaguchi, Y.; Nakajima, Y.; Maruyama, M. NF-κB pathway inhibition by anthrocyclic glycoside aloin is key event in preventing osteoclastogenesis in RAW264.7 cells. *Phytomedicine* **2016**, *23*, 417–428. [CrossRef] [PubMed]

Disclaimer/Publisher's Note: The statements, opinions and data contained in all publications are solely those of the individual author(s) and contributor(s) and not of MDPI and/or the editor(s). MDPI and/or the editor(s) disclaim responsibility for any injury to people or property resulting from any ideas, methods, instructions or products referred to in the content.

molecules

MDPI

Article

Broad-Spectrum Legionaminic Acid-Specific Antibodies in Pooled Human IgGs Revealed by Glycan Microarrays with Chemoenzymatically Synthesized Nonulosonosides

Anoopjit Singh Kooner [1], Hai Yu [1], Shani Leviatan Ben-Arye [2], Vered Padler-Karavani [2,*] and Xi Chen [1,*]

[1] Department of Chemistry, University of California, Davis, CA 95616, USA; akooner@ucdavis.edu (A.S.K.); hyu@ucdavis.edu (H.Y.)

[2] Department of Cell Research and Immunology, The Shmunis School of Biomedicine and Cancer Research, The George S. Wise Faculty of Life Sciences, Tel Aviv University, Tel Aviv 69978, Israel; leviata@tauex.tau.ac.il

* Correspondence: vkaravani@tauex.tau.ac.il (V.P.-K.); xiichen@ucdavis.edu (X.C.); Tel.: +972-3-640-6737 (V.P.-K.); +1-530-754-6037 (X.C.)

Abstract: The presence and the level of antibodies in human sera against bacterial glycans are indications of prior encounters with similar antigens and/or the bacteria that express them by the immune system. An increasing number of pathogenic bacteria that cause human diseases have been shown to express polysaccharides containing a bacterial nonulosonic acid called 5,7-di-*N*-acetyllegionaminic acid (Leg5,7Ac_2). To investigate the immune recognition of Leg5,7Ac_2, which is critical for the fight against bacterial infections, a highly effective chemoenzymatic synthon strategy was applied to construct a library of α2–3/6-linked Leg5,7Ac_2-glycans via their diazido-derivatives (Leg5,7diN_3-glycans) formed by efficient one-pot three-enzyme (OP3E) synthetic systems from a diazido-derivative of a six-carbon monosaccharide precursor. Glycan microarray studies using this synthetic library of a Leg5,7Ac_2-capped collection of diverse underlying glycan carriers and their matched sialoside counterparts revealed specific recognition of Leg5,7Ac_2 by human IgG antibodies pooled from thousands of healthy donors (IVIG), suggesting prior human encounters with Leg5,7Ac_2-expressing pathogenic bacteria at the population level. These biologically relevant Leg5,7Ac_2-glycans and their immune recognition assays are important tools to begin elucidating their biological roles, particularly in the context of infection and host–pathogen interactions.

Keywords: bacterial nonulosonic acid; carbohydrate; chemoenzymatic synthesis; legionaminic acid; human antibodies

1. Introduction

Human sera contain protective antibodies against a large range of carbohydrate epitopes expressed by different species [1–4]. These antibodies are developed either naturally or in response to infections, vaccinations, or other exposures to antigens. Human antibodies recognizing bacterial glycans have been revealed by profiling human sera and pooled human immunoglobulins against bacterial surface carbohydrate antigens immobilized on glycan microarrays [5]. Synthetic glycans with defined structures are important probes for these studies. Access to such synthetic glycans, especially those with complex structures that are challenging to obtain either by purification from natural sources or by chemical synthesis, is greatly facilitated by the development of efficient chemoenzymatic methods. Glycans and glycoconjugates containing nine-carbon α-keto acids called nonulosonic acids (NulOs) [6] are among the challenging synthetic targets [7]. The most well-known NulOs are sialic acids (Sias) based on a neuraminic acid (Neu) or a 2-keto-3-deoxy-nononic acid (Kdn) backbone in the deuterostome lineage of animals and in certain bacteria. In vertebrates, Sias are often presented on the termini of glycans on cell surface glycoconjugates

and *N*-acetylneuraminic acid (Neu5Ac, **1**, Figure 1) is the most common and well-studied sialic acid form.

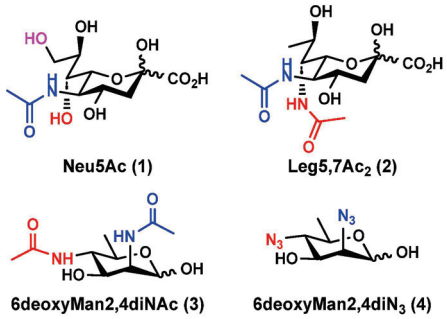


Figure 1. Structures of *N*-acetylneuraminic acid (Neu5Ac, **1**); 5,7-di-*N*-acetyllegionaminic acid (Leg5,7Ac$_2$, **2**); Leg5,7Ac$_2$ precursor 6deoxyMan2,4diNAc (**3**); and Leg5,7Ac$_2$ chemoenzymatic synthon 6deoxyMan2,4diN$_3$ (**4**).

Bacterial nonulosonic acid (NulO) 5,7-di-*N*-acetyllegionaminic acid (Leg5,7Ac$_2$, **2**) (Figure 1), or 5,7-diacetamido-3,5,7,9-tetradeoxy-D-*glycero*-D-*galacto*-non-2-ulosonic acid [6,8], is an analog of Neu5Ac (**1**). Leg5,7Ac$_2$ and Neu5Ac share an identical D-*glycero*-D-*galacto*-backbone configuration but differ for the functional groups at C7 and C9 positions. Leg5,7Ac$_2$ is the 7-acetamido-7,9-dideoxy derivative of Neu5Ac by replacing its C7-OH with an acetamido group and its C9-OH with a hydrogen atom (Figure 1) [9,10].

Chemical synthesis of Leg5,7Ac$_2$ from 2,4-diacetamido-2,4,6-trideoxy-D-mannose (6deoxyMan2,4diNAc, **3**) (Figure 1) and oxalacetic acid under basic conditions was initially reported in 2001 [11,12]. The synthetic Leg5,7Ac$_2$ was used to facilitate the identification and the correction of Leg5,7Ac$_2$-containing bacterial lipopolysaccharide (LPS) structures including those from *Legionella pneumophila* serogroup 1, a pathogen known to cause Legionnaire's disease; *Acinetobacter baumannii*, a causative agent of fatal bacteremia; and *Pseudomonas fluorescens*, *Vibrio salmonicida*, and *Vibrio alginolyticus* [11,12]. Leg5,7Ac$_2$ derivatives with variations on the stereochemistry of C4 and/or C8 and substitutions at C5 and/or C7 were also identified from bacterial sources [6,8,11,13].

The synthesis of glycans containing Leg5,7Ac$_2$ and derivatives [14] by chemical methods has been challenging [15]. The chemical synthetic strategies reported involved long routes, low overall yields, and a lack of stereochemical control for the formation of the biologically relevant α-legionaminic acid glycosyl linkage found in several bacterial polysaccharides [15]. In addition, the obtained products were limited to monosaccharides [11,12,16] or glycosides of either monosaccharides [15,17] or disaccharides [18,19].

The biosynthetic processes for Leg5,7Ac$_2$ and its cytidine 5′-monophosphate (CMP)-activated donor CMP-Leg5,7Ac$_2$ for the presumed legionaminyltransferases were reported from *Legionella pneumophila* [20] and *Campylobacter jejuni* [21] in 2008 and 2009, respectively. Both processes formed 6deoxyMan2,4diNAc (**3**, Figure 1) as a key intermediate despite the differences in using its uridine 5′-diphosphate (UDP) [20] or guanosine 5′-diphosphate (GDP) [21]-activated precursor in these two bacteria. The related enzymes had been expressed in *E. coli* for the production of Leg5,7Ac$_2$ and CMP-Leg5,7Ac$_2$ [22,23]. Recently, a metabolic labeling method using azide-modified Leg precursors led to the identification of Maf4 as a putative flagellin legionaminyltransferase from *Campylobacter jejuni* [24]. Nevertheless, information regarding legionaminyltransferases is very limited in general.

Recombinant sialyltransferases identified from bacterial and mammalian sources have been used for enzymatic and/or chemoenzymatic synthesis of Leg5,7Ac$_2$-glycans and derivatives. For example, bacterial *Pasteurella multocida* multifunctional α2–3-sialyltransferase PmST1 (previously named as tPm0188Ph [25]) [26] and *Neisseria meningitidis* MC58 α2–3-sialyltransferase [27], as well as porcine ST3Gal-I [26], were found to be efficient in forming α2–3-linked glycosides terminated with Leg5,7Ac$_2$. In comparison, bacterial *Photobacterium damselae* α2–6-sialyltransferase was less efficient in the formation of α2–6-linked glyco-

sides terminated with Leg5,7Ac_2 [26] but its A235M mutant [27] had improved activity. Porcine ST3Gal-I was used to catalyze the transfer of Leg5,7Ac_2 from CMP-Leg5,7Ac_2 to a glycolipid GM1a to form a GD1a analog containing a terminal Leg5,7Ac_2, which was not recognized by an Neu5Ac-terminated GD1a-binding protein, myelin-associated glycoprotein (MAG or Siglec-4) [28]. Porcine ST3Gal-I and human ST6Gal-I were suitable for catalyzing the transfer of Leg5,7Ac_2 from CMP-Leg5,7Ac_2 to the O-glycans and N-glycans, respectively, on the therapeutic glycoproteins interferon-α2b and α1-antitrypsin [28]. We previously reported the chemical synthesis of the important biosynthetic intermediate 6deoxyMan2,4diNAc (**3**) and its application as an enzymatic precursor for the direct formation of Leg5,7Ac_2-glycosides [9] using a one-pot three-enzyme (OP3E) system containing *Pasteurella multocida* (PmAldolase), *Legionella pneumophila* CMP-Leg5,7Ac_2 synthetase (LpCLS), and an α2–3-sialyltransferase such as *Pasteurella multocida* multifunctional α2–3-sialyltransferase 1 (PmST1) or its M144D mutant (PmST1_M144D) with decreased sialidase and donor hydrolysis activities [10]. Nevertheless, the production of Leg5,7Ac_2-glycosidases by directly transferring Leg5,7Ac_2 from CMP-Leg5,7Ac_2 to appropriate acceptors using known sialyltransferases can be restricted by the types of acceptors that can be tolerated by a given sialyltransferase and the decreased efficiency in using CMP-Leg5,7Ac_2 as the donor substrate.

To overcome the challenges, we developed a chemoenzymatic synthon strategy for the highly efficient synthesis of Leg5,7Ac_2-glycosides [9]. In this strategy, a chemoenzymatic synthon 2,4-diazido-2,4,6-trideoxy-D-mannose (6deoxyMan2,4diN_3, **4**) (Figure 1) was chemically synthesized from commercially available D-fucose in eight steps with an overall 59.5% yield. It was a well-suited precursor for the synthesis of the corresponding 5,7-diazido-legionaminic acid (Leg5,7diN_3)-glycosides in 71–98% yields using a one-pot three-enzyme (OP3E) system containing PmAldolase, *Neisseria meningitidis* CMP-sialic acid synthetase (NmCSS), and an α2–3-sialyltransferase such as PmST1_M144D or an α2–6-sialyltransferase such as *Photobacterium* species α2–6-sialyltransferase (Psp2,6ST) [9]. The resulting Leg5,7diN_3-glycosides were conveniently converted to the corresponding target Leg5,7Ac_2-glycosides in 69–88% yields by treating with thioacetic acid in the presence of saturated sodium bicarbonate in aqueous solution [9]. Herein, we explore the application of the chemoenzymatic synthon 6deoxyMan2,4diN_3 (**4**) for the synthesis of a comprehensive library of α2–3- and α2–6-linked Leg5,7Ac_2-glycosides containing different underlying glycans. Glycan microarrays printed with this comprehensive collection of synthetic α2–3- and α2–6-linked Leg5,7Ac_2-glycosides and their related sialoside pairs demonstrate that pooled human IgGs are rich with antibodies that selectively recognize this broad spectrum of Leg5,7Ac_2-glycosides.

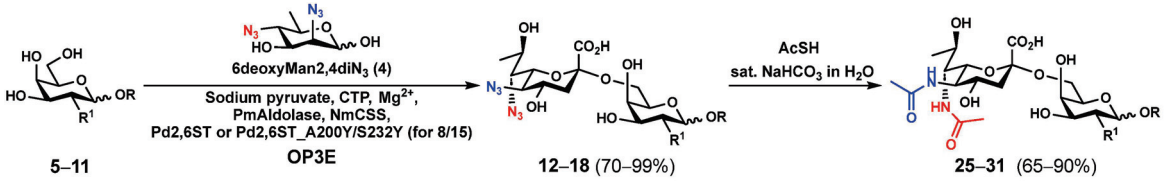
2. Results and Discussion

2.1. Chemoenzymatic Synthesis of Leg5,7Ac_2-Glycosides

Our synthetic targets were α2–3- and α2–6-linked Leg5,7Ac_2-glycosides containing different underlying glycans with an aglycon linker that can be used for immobilization on slides for glycan microarray assays. A propylamine aglycon was chosen as a well-suited design for the purpose. To produce the 5,7-diazido-legionaminic acid (Leg5,7diN_3)-glycosides efficiently from the chemoenzymatic synthon 6-deoxyMan2,4diN_3 (**4**) using OP3E sialyation systems [9] and allow efficient product purification, glycosides containing a hydrophobic carboxybenzyl (Cbz)-protected propylamine aglycon (ProNHCbz) [29] were chosen as sialyltransferase acceptors. Seven Cbz-tagged glycosides [30] including GalNAcαProNHCbz (Tn antigen, **5**), LacβProNHCbz (**6**), LacNAcβProNHCbz (**7**), Galβ1–3GalNAcβProNHCbz (**8**), Galβ1–3GalNAcαProNHCbz (Core 1, **9**), Galβ1–3GlcNAcβProNHCbz (Type I glycan, **10**), and Galβ1–3GlcNAcαProNHCbz (**11**) were used as sialyltransferase acceptors for OP3E sialylation reactions. The UV-detectability and the hydrophobicity of the ProNHCbz [29] in the glycoside acceptors and the resulting Leg5,7diN_3-glycosylated products facilitate the reaction monitoring and product purification processes.

As shown in Scheme 1, the OP3E system containing PmAldolase, NmCSS, and *Photobacterium damselae* α2–6-sialyltransferase (Pd2,6ST) or its A200Y/S232Y double mutant (Pd2,6ST_A200Y/

S232Y) [31] was used to synthesize α2–6-linked Leg5,7diN$_3$-glycosides (**12**–**18**) from 6deoxyMan2, 4diN$_3$ (**4**) and glycoside acceptors **5**–**11**. In this system, 6deoxyMan2,4diN$_3$ (**4**) reacted with pyruvate by a PmAldolase-catalyzed reaction to form Leg5,7diN$_3$, which was activated by NmCSS in the presence of cytidine 5′-triphosphate (CTP) and magnesium (Mg^{2+}) cation to form the corresponding CMP-activated sugar nucleotide CMP-Leg5,7diN$_3$ to allow the transfer of Leg5,7diN$_3$ to the sialyltransferase acceptor used in the OP3E reaction to form the desired α2–6-linked Leg5,7diN$_3$-glycoside. The target glycosides **12**–**18** (Table 1) were obtained with yields ranging from 70 to 99%, each was purified from the OP3E reaction with a single C18-cartridge purification process. When Galβ1–3GalNAcβProNHCbz (**8**) was used as the acceptor for Pd2,6ST in the OP3E, an undesired additional Leg5,7diN$_3$ could be added to the penultimate GalNAc moiety in the acceptor substrate, which caused complications in purifying the desired product Leg5,7diN$_3$α2–6Galβ1–3GalNAcβProNHCbz (**15**) and led to low yields. To our delight, the Pd2,6ST_A200Y/S232Y double mutant [31] was capable of adding Leg5,7diN$_3$ regio-selectively to the terminal galactose (Gal) of **8** to produce **15** in an excellent 96% yield. On the other hand, Pd2,6ST in the OP3E was efficient in synthesizing other α2–6-linked Leg5,7diN$_3$-glycoside targets (**12**–**14**, **16**–**18**). Treatment of the azido-containing glycosides (**12**–**18**) with thioacetic acid and saturated sodium bicarbonate aqueous solution [9,30] produced the target α2–6 linked Leg5,7Ac$_2$-glycosides (**25**–**31**) in 65–90% yields.

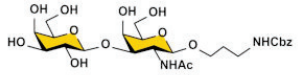
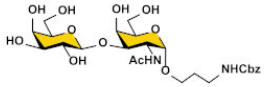
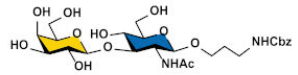
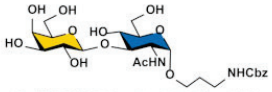


Scheme 1. Chemoenzymatic synthesis of α2–6-linked Leg5,7Ac$_2$-glycosides (**25**–**31**) via OP3E produced α2–6-linked Leg5,7diN$_3$-glycosides (**12**–**18**).

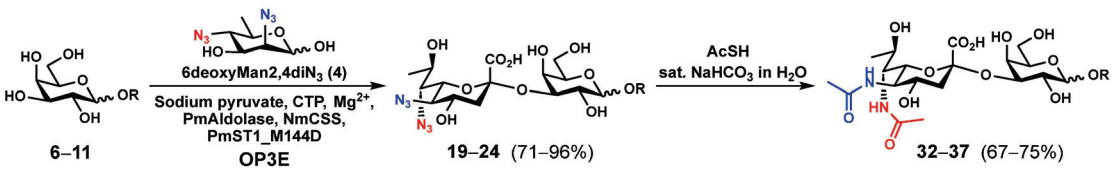
Table 1. Structures of the OP3E sialyltransferase acceptors and yields of Leg5,7diN$_3$-glycosides (**12**–**24**) and Leg5,7Ac$_2$-glycosides (**25**–**37**) products.

Acceptors (**5**–**11**)	OP3E Products Leg5,7diN$_3$-glycosides (**12**–**24**)		Leg5,7Ac$_2$-glycosides (**25**–**37**)	
	12–**18** (70–99%)	**19**–**24** (71–96%)	**25**–**31** (65–90%)	**32**–**37** (67–75%)
GalNAcαProNHCbz (**5**) R = αProNHCbz, R^1 = NHAc	**12** (99%)	-	**25** (65%)	-
LacβProNHCbz (**6**) R = β4GlcβProNHCbz, R^1 = OH	**13** (75%)	**19** (74%)	**26** (78%)	**32** (68%)
LacNAcβProNHCbz (**7**) R = β4GlcNAcβProNHCbz, R^1 = OH	**14** (70%)	**20** (71%)	**27** (68%)	**33** (67%)

Table 1. *Cont.*

 Galβ3GalNAcβProNHCbz (**8**) R = β3GalNAcβProNHCbz, R^1 = OH	**15** (93%)	**21** (96%)	**28** (90%)	**34** (67%)
 Galβ3GalNAcαProNHCbz (**9**) R = β3GalNAcαProNHCbz, R^1 = OH	**16** (77%)	**22** (77%)	**29** (68%)	**35** (69%)
 Galβ3GlcNAcβProNHCbz (**10**) R = β3GlcNAcβProNHCbz, R^1 = OH	**17** (81%)	**23** (80%)	**30** (78%)	**36** (75%)
 Galβ3GlcNAcαProNHCbz (**11**) R = β3GlcNAcαProNHCbz, R^1 = OH	**18** (99%)	**24** (96%)	**31** (71%)	**37** (72%)

Similarly, the OP3E system containing PmAldolase, NmCSS, and PmST1_M144D [32] was used for the efficient synthesis of α2–3-linked Leg5,7diN_3-glycosides (**19**–**24**) from galactosides **6**–**11**, respectively, in 71–96% yields (Scheme 2). They were readily converted to the desired α2–3-linked Leg5,7Ac_2-glycosides (**32**–**37**) in 67–75% yields using thioacetic acid in saturated sodium bicarbonate aqueous solution.



Scheme 2. Chemoenzymatic synthesis of α2–3-linked Leg5,7Ac_2-glycosides (**32**–**37**) via OP3E produced α2–3-linked Leg5,7diN_3-glycosides (**19**–**24**).

The Cbz group in Leg5,7Ac_2-glycosides (**25**–**37**) was conveniently and completely removed by catalytic hydrogenation [33] to produce Leg5,7Ac_2-glycosides containing a primary amino group on the propylamine aglycon, which was ready for immobilization on *N*-hydroxysuccinimide (NHS)-ester-coated [34,35] or epoxy-coated surface [36–39] for glycan microarray studies. It could also be coupled to other molecules such as proteins [40] and/or biotin [41] for various functional studies.

2.2. Glycan Microarray Binding Studies Reveal a Broad Spectrum of Human IgG Antibodies against Leg5,7Ac_2-Glycosides

A previously reported glycan microarray study using β-glycosides of a Leg5,7Ac_2 monosaccharide and its derivative that was chemically synthesized from D-threonine showed that human IgGs in three different samples of pooled human sera recognize the β-glycoside of Leg5,7Ac_2 but not its 7-amino-derivative [15]. We used glycan microarrays to characterize the immune recognition of the biologically relevant propylamine aglycon-containing Leg5,7Ac_2-α-glycosides obtained from **25**–**37** by catalytic hydrogenation to remove the Cbz group. These α-glycosides were fabricated onto epoxide-activated glass slides together with their matched pairs of sialoglycans synthesized previously, including those

containing Neu5Ac [25,42], 9-*O*-acetyl-Neu5Ac (Neu5,9Ac_2) [40,42], *N*-glycolylneuraminic acid (Neu5Gc) [40,42,43], 9-*O*-acetyl-Neu5Gc (Neu5Gc9Ac) [40,42,43], or 7-acetamido-7-deoxy-*N*-acetylneuraminic acid (Neu5Ac7NAc) [30]. Non-sialylated glycosides were also printed as control glycan probes. The resulting glycan microarrays were used to investigate the binding profiles of several antibodies and lectins (Figures 2 and 3). Binding profiles of anti-Neu5Gc chicken immunoglobulin Y (IgY) [44], SiaFindα2–6, and *Maackia amurensis* lectin II (MAL-II) confirmed recognition of their known targets Neu5Gc-glycans, Siaα2–6-glycans, and Siaα2–3-glycans, respectively (Figure 2a). Interestingly, SiaFindα2–6 recognized all α2–6-linked glycans, including those with a terminal Leg5,7Ac_2 or Neu5Ac7NAc, except those linked to GalNAc that were less preferred. In contrast, MAL-II preferred sialyl T-antigen (Siaα2–3Core1). Its binding was much reduced against Neu5Ac7NAc and completely lost against terminal Leg5,7Ac_2 (Figure 2a). Similarly, most of the other lectins did not bind to Leg5,7Ac_2-glycans, except for *Lycopersicon esculentum* (tomato) lectin (LEL, TL) that recognized α2–3LacNAc glycans with terminal Sia/Leg5,7Ac_2 (Figure 2a). Importantly, human intravenous immunoglobulin G (IVIG; human IgG) pooled from thousands of individual donors, from two different sources (Privigen, OMRIgG-AR), showed strong binding to all Leg5,7Ac_2-glycans, Neu5Gc-glycans, and non-sialylated glycans, but very low binding to Neu5Ac-glycans or Neu5Ac7NAc-glycans (Figure 2a). IVIG bound most non-sialylated glycans, but the least to LacNAc (ID-45). Among sialylated glycans, IVIG showed a strong preference for Neu5Gc over Neu5Ac, which was clear by comparing binding to the matched pairs of glycans that differ only by the single additional oxygen in C5 *N*-glycolyl versus *N*-acetyl (Figure 2a). While Neu5Gc is foreign to humans, Neu5Ac is a protective self-glycan and is not normally recognized by human antibodies, as previously described [45,46]. IVIG showed stronger binding to all Leg5,7Ac_2-glycans compared to uncapped non-Sia underlying glycan counterparts. In contrast, there was no binding to their matched pairs of Neu5Ac7NAc-glycans, irrespective of their underlying glycan structures (Figure 2a,b). Thus, like human IgG preference toward Neu5Gc > Neu5Ac, binding of IVIG to Leg5,7Ac_2 > Neu5Ac7NAc occurs despite their difference in only a single oxygen atom at the C9 position in Neu5Ac7NAc that is absent in Leg5,7Ac_2 (Figure 2a,b). Together, these findings suggest that while Neu5Ac7NAc is less immunogenic, Leg5,7Ac_2 is perceived as foreign, as indicated by human IgG binding, thus likely representing secondary immune responses after previous encounters with Leg5,7Ac_2-expressing pathogens.

Sialic acids are known to belong to 'self-associated molecular patterns' (SAMPs) that provide a protective shield for glycoconjugates and cells [47], including from circulating antibodies [46]. To investigate human IgG immune recognition of Leg5,7Ac_2 within the context of 'pathogen-associated molecular patterns' (PAMPs), enzymatic cleavage of these sialic acids analogs on the arrays was evaluated by two sialidases, *Arthrobacter ureafaciens* sialidase (AUS) and *Clostridium perfringens* neuraminidase (NCP), that peel-off terminal sialic acid moieties from glycans printed on the array. Both sialidases effectively removed Neu5Ac and Neu5Gc, exposing the underlying de-capped glycans to a robust binding of IVIG anti-glycan antibodies. However, all Leg5,7Ac_2-glycans and Neu5Ac7NAc-glycans were found to be resistant to such cleavage by these two bacterial sialidases (Figure 3a), which correlated well with our previous results [9,48]. Despite the close similarity between Neu5Ac and Leg5,7Ac_2, the glycans capped with the latter become resistant to sialidase cleavage, potentially providing an immunological advantage to a human invading pathogen that would be coated with such PAMP glycans. This is further supported by recent studies of *Campylobacter jejuni*, the leading cause of foodborne bacterial gastroenteritis, revealing that expression of legionaminic acid on its bacterial flagellin serves as a virulence factor supporting enhanced biofilm formation, auto-agglutination, and host colonization [24,49]. On the other hand, pathogens also commonly use SAMPs as a molecular mimicry mechanism to evade host immunity, particularly by sialic acid sugar coating (e.g., on lipooligosaccharide; LOS) using sialyltransferases that they express. LOS sialylation shields bacteria from complement and cationic peptides and also engages inhibitory siglec receptors on host immune cells to dampen inflammatory responses [50,51].

Unlike the molecular mimicry properties of Neu5Ac used by pathogenic bacteria such as *Neisseria gonorrhoeae,* which causes sexually transmitted gonorrhea infection, incorporating Leg5,7Ac$_2$ instead of Neu5Ac to the LOS by *Neisseria gonorrhoeae* had been found to make the bacterium sensitive to complement and human serum [51,52]. Therefore, applying CMP-Leg5,7Ac$_2$, which can be used by some human pathogens to decorate their LOS with Leg5,7Ac$_2$, has been proposed as a novel therapeutic approach to address the global threat of multidrug-resistant bacteria [51–53]. Nevertheless, the host–pathogen interplay involving sialic acids and other nonulosonic acids with sialidases, siglecs, complement, cationic antimicrobial peptides, serum antibodies, and the complement system is complex and warrants further investigation.

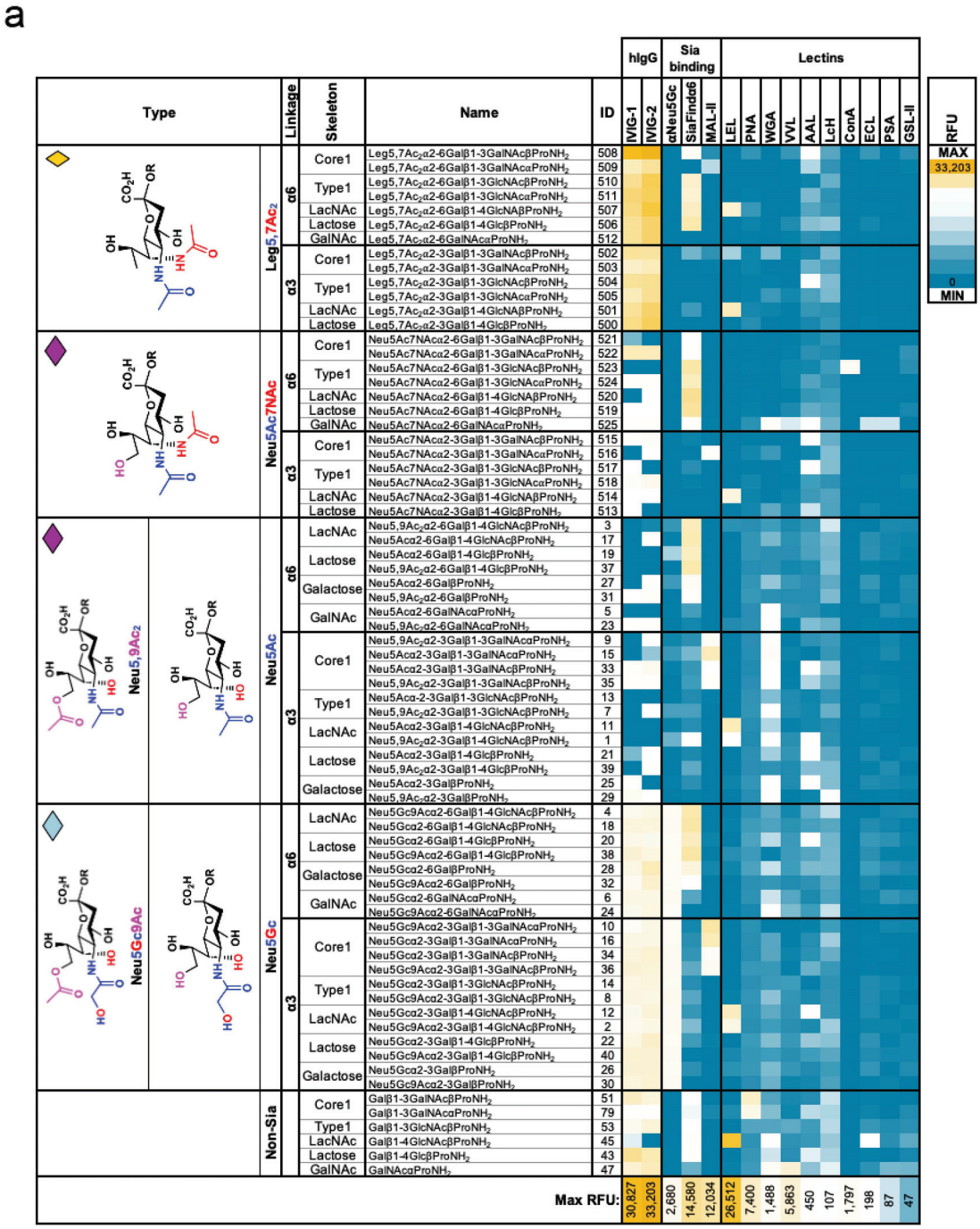


Figure 2. *Cont.*

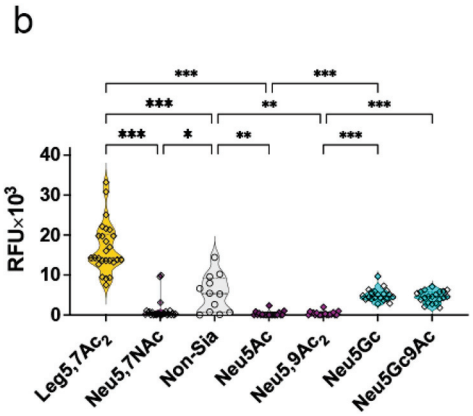


Figure 2. Glycan microarray binding studies against Leg5,7Ac_2-glycans and sialoglycan counterparts. (**a**) Glycan microarrays fabricated with Leg5,7Ac_2-glycans and sialoglycans (Neu5Gc/Neu5Ac/Neu5Ac7NAc-glycans) were examined with IVIG (IVIG-1 Privigen or IVIG-2 OMRIgG-AR; 50 μg/sub-array), anti-Neu5Gc IgY (αNeu5Gc; 1:7000), SiaFindα2-6 (0.25 μg), and 11 biotinylated plant lectins (2 μg each: MAL-II, LEL, PNA, WGA, VVL, AAL, LcH, ConA, ECL, PSA, and GSL-II) at 100 μL/subarray in blocking buffer (PBS, 1% ovalbumin; the assay buffers for plant lectins also contained divalent cations, see ESI), then detected with Cy3-anti-human IgG (0.4 ng/μL) for IVIG, Cy3-anti-chicken IgY (0.375 ng/μL) for IgY, and Cy3-sterptavidin (1.2 ng/μL) for Sia-Find and Lectins, at each 200 μL/sub-array. Slides were scanned and analyzed for Relative Fluorescence Units (RFU), which were plotted as a heatmap. (**b**) Binding of IVIG (average IVIG-1 and IVIG-2) to Leg5,7Ac_2-glycans compared to Neu5Ac7NAc-glycans, non-Sia glycans, and glycans terminated with Neu5Ac, Neu5,9Ac2, Neu5Gc, and Neu5Gc9Ac (mixed effects analysis, with the Geisser-Greenhouse correction and individual variances computed for each comparison using uncorrected Fisher's LSD; * $p = 0.04$, ** $p = 0.001$, *** $p < 0.001$).

To gain further insight into human IgG immune recognition of Leg5,7Ac_2, binding of IVIG to Leg5,7Ac_2-glycans on the glycan microarray was examined in the presence of selected competing glycans, including methyl α-*N*-glycolylneuraminoside (2-*O*-methyl-αNeu5Gc, or Gc2Me), glycopeptides of diverse *N*/*O*-glycans produced from mice sera digestion (mGP) [46], and the glycans that showed top preference of binding on the arrays including glycans ID-51, ID-502, ID-508 (Core1β; Leg5,7Ac_2α3Core1β; and Leg5,7Ac_2α6Core1β, respectively; Figure 3a). This analysis revealed that only αNeu5Gc (Gc2Me) did not affect IVIG binding to Leg5,7Ac_2-glycans, while all other glycans inhibited its binding (Figure 3b). Particularly, while IVIG binding to all Leg5,7Ac_2-glycans was inhibited by 50% with Core1β (ID-51) and by 80% with mGP, the competing Leg5,7Ac_2α3/6Core1β-glycans (ID-502/508) completely abolished it (Figure 3b,c). This suggests that human IgG is enriched with antibodies that recognize diverse Leg5,7Ac_2-glycans, in which the Leg5,7Ac_2 moiety is critical for their recognition, although with some promiscuity with the variation in the underlying glycans including Core1/Lactose/LacNAc. Based on these inhibition studies together with previous structural studies of antibodies against sialyl-Tn [54] and sialyl Lewis a (sLe^a) [55], it is plausible that the Leg5,7Ac_2 moiety is buried within the binding pocket of these anti-Leg5,7Ac_2 IgG antibodies.

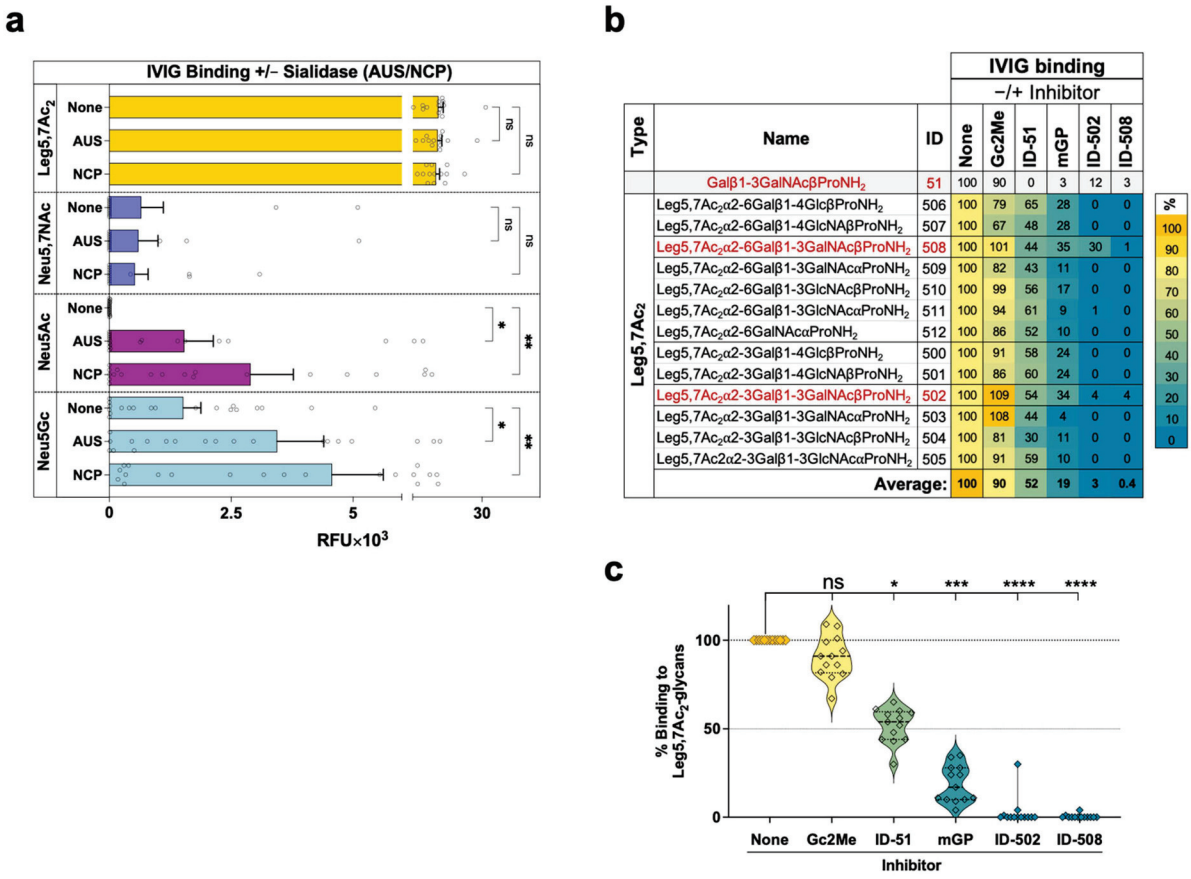


Figure 3. Characterization of IVIG binding to Leg5,7Ac$_2$-glycans. (**a**) Binding of IVIG-2 (OMRIgG-AR) to glycan microarray at 50 μg/sub-array, after pre-treatment of the arrays with/without 10 mU sialidase (*Arthrobacter ureafaciens* sialidase, AUS; *Clostridium perfringens* neuraminidase; NCP) for 2 h at 37 °C, then detected with 0.4 ng/μL Cy3-anti-human IgG. Slides were scanned, analyzed, and RFU-plotted (mixed-effects analysis, with the Geisser-Greenhouse correction, and individual variances computed for each comparison using uncorrected Fisher's LSD; ns = non-significant $p > 0.05$ ($p = 0.6132$, 0.3334, 0.7287, 0.7454 None vs AUS/NCP in Leg/Neu, respectively), * $p = 0.02$, ** $p < 0.003$). (**b**) Averaged binding of IVIG-1 and IVIG-2 to Leg5,7Ac$_2$-glycans on glycan microarrays in the presence of selected competing glycans. IVIG (IVIG-1 Privigen or IVIG-2 OMRIgG-AR, 50 μg/sub-array) were pre-incubated for 2 h on ice with various inhibitors on each sub-array, including 2-*O*-methyl-αNeu5Gc (Gc2Me; 4 mM), glycan ID-51 (Core1β, 2 mM), mouse serum glycopeptides (mGP, containing *N*/*O*-glycans [46], 0.45 mM), glycan ID-502 (Leg5,7Ac$_2$α3Core1β, 1 mM), and glycan ID-508 (Leg5,7Ac$_2$α6Core1β; 1 mM). Then, binding of the pre-complexed IVIG was examined and detected with 0.4 ng/μL Cy3-anti-human IgG. Slides were scanned, analyzed, and RFU results were plotted. Percent binding to each glycan was calculated as a ratio to binding of IVIG without inhibitor (none, 100% binding). (**c**) Statistical analysis of inhibition of IVIG binding to Leg5,7Ac$_2$-glycans of data presented in (**b**) (Friedman test with uncorrected Dunn's test; ns $p = 0.4631$, * $p = 0.0159$, *** $p = 0.0002$, and **** $p < 0.0001$).

3. Materials and Methods

3.1. Materials and Instruments

Chemicals were purchased and used without further purification. Nuclear magnetic resonance (NMR) spectra were recorded in the NMR facility of the University of California, Davis on 600 MHz and 800 MHz Bruker Avance III-NMR spectrometers and a 400 MHz Bruker Avance III HD Nanobay spectrometer (Bruker, Billerica, MA, USA). Chemical shifts are reported in parts per million (ppm) on the δ scale. High-resolution electrospray ionization (ESI) mass spectra were obtained using a Thermo Electron LTQ-

Orbitrap Hybrid mass spectrometer (Thermo Fisher Scientific, Waltham, MA, USA) at the mass spectrometry facility at the University of California, Davis. Column chromatography was performed using a CombiFlash® Rf 200i system (Teledyne ISCO, Lincoln, NE, USA) with either Redi*Sep* Rf silica columns or an ODS-SM (C18) column (51 g, 50 μm, 120 Å, Yamazen, Osaka, Japan) or manually using columns packed with silica gel 60 Å (230–400 mesh, Sorbent Technologies, Norcross, GA, USA). Thin layer chromatography (TLC) was performed on silica gel plates (Sorbent Technologies) using anisaldehyde sugar stain or 5% sulfuric acid in ethanol stain for detection. Gel filtration chromatography was performed with a column (100 cm × 2.5 cm) packed with Bio-Gel P-2 Fine resins (Bio-Rad, Hercules, CA, USA). Neu5GcaOMe (Gc2Me) was synthesized as reported previously [46]. *Pasteurella multocida* sialic acid aldolase (PmAldolase) [56], *Neisseria meningitidis* CMP-sialic acid synthetase (NmCSS) [57], *Pasteurella multocida* α2–3-sialyltransferase 1 (PmST1) [25], *Photobacterium damselae* α2–6-sialyltransferase (Pd2,6ST) [42], and Pd2,6ST_A200Y/S232Y were expressed and purified as described previously. PBSx10 was purchased from Hy-labs (Rehovot, Israel), ethanolamine from Fisher Scientific (Waltham, MA, USA), ovalbumin grade V from Sigma-Aldrich (St. Louis, MO, USA), SiaFindα2-6 from LectenzBio (Athens, GA, USA), anti-Neu5Gc IgY from BioLegend (San Diego, CA, USA), the lectins MAL-II, AAL, ConA, ECL, GSL-II, LcH, LEL, PNA, PSA, VVL, and WGA were purchased from Vector Laboratories (Newark, CA, USA), and ChromPure Human IgG whole molecule, Cy3-AffiniPure goat-anti-human IgG H+L, Cy3-sreptavidin, and Cy3-anti-chicken IgY from Jackson ImmunoResearch (West Grove, PA, USA). AlexaFlour-555-Hydraside from Invitrogen (Waltham, MA, USA). Pooled human IgG were IVIG-1 (Privigen from CSL Behring USA, King of Prussia, PA, USA) and IVIG-2 (OMRIgG-AM clinical remnants).

*3.2. General Procedures for One-Pot Three-Enzyme (OP3E) Preparative-Scale Synthesis of Leg5,7diN$_3$α2–6-Linked Nonulosonosides (***12**–**18***)*

Acceptors [30] (GalNAcαProNHCbz **5**, LacβProNHCbz **6**, LacNAcβProNHCbz **7**, Galβ1–3GalNAcβProNHCbz **8**, Galβ1–3GalNAcαProNHCbz **9**, Galβ1–3GlcNAcβProNHCbz **10**, or Galβ1–3GlcNAcαProNHCbz **11**) (0.10–0.20 mmol), 6deoxyMan2,4diN$_3$ [9] (**4**, 0.15–0.30 mmol, 1.5 eq.), sodium pyruvate (7.5 eq), and CTP (1.5 eq) were dissolved in water in a 50 mL centrifuge tube containing Tris-HCl buffer (100 mM, pH 8.5) and $MgCl_2$ (20 mM). After adding sialic acid aldolase (1–3 mg), NmCSS (0.5–1.0 mg), and Pd2,6ST (1–4 mg, for acceptors **5**–**7**, **9**–**11**) or Pd2,6ST_A200Y/S232Y28 (2 mg, for acceptor **8**), water was added to bring the final concentration of acceptor to 10 mM. The reaction mixture was incubated at 30 °C for 24–36 h. The reaction progress was monitored using TLC (ethyl acetate:methanol:water = 6:1:1, by volume, was used as the developing solvent) and mass spectrometry. The reaction mixture was diluted with the same volume of ethanol and incubated at 4 °C for 30 min. The mixture was then centrifuged and concentrated, which was purified by an automated flash chromatograph using a C18 column (acetonitrile in water gradient was used as running solvents) to obtain the desired nonulosonosides.

Leg5,7diN$_3$α2–6GalNAcαProNHCbz (**12**). A total of 110 mg, 99% yield, white amorphous solid. ^{1}H NMR (800 MHz, D_2O) δ 7.46–7.36 (m, 5H), 5.15–5.07 (m, 2H), 4.12 (dd, *J* = 11.0, 3.8 Hz, 1H), 4.02–3.81 (m, 7H), 3.78–3.62 (m, 3H), 3.58–3.52 (m, 2H), 3.46 (dt, *J* = 10.8, 5.9 Hz, 1H), 3.31–3.16 (m, 2H), 2.75 (dd, *J* = 12.5, 4.5 Hz, 1H), 2.01 (s, 3H), 1.97 (s, 3H), 1.94 (s, 3H), 1.80 (p, *J* = 6.4 Hz, 2H), 1.65 (t, *J* = 12.1 Hz, 1H), 1.15 (d, *J* = 6.3 Hz, 3H). ^{13}C{^{1}H} NMR (200 MHz, D_2O) δ 174.4, 174.1, 157.8, 136.5, 128.6, 128.1, 127.6, 101.4, 97.1, 72.1, 69.4, 69.0, 67.8, 67.6, 66.6, 66.1, 65.7, 65.3, 63.8, 61.4, 59.3, 49.9, 40.2, 37.5, 28.9, 22.0, 19.2. HRMS (ESI) *m*/*z* calculated for $C_{28}H_{39}N_8O_{13}^-$ $[M - H]^-$ 695.2642, found 695.2611.

Leg5,7diN$_3$α2–6LacβProNHCbz (**13**). A total of 57 mg, 75% yield, white amorphous solid. ^{1}H NMR (800 MHz, D_2O) δ 7.50 7.32 (m, 5H), 5.11 (s, 2H), 4.44 (d, *J* = 8.1 Hz, 1H), 4.40 (d, *J* = 7.9 Hz, 1H), 4.20–4.11 (m, 1H), 3.98–3.89 (m, 4H), 3.81–3.66 (m, 8H), 3.64 (dd, *J* = 10.0, 3.4 Hz, 1H), 3.61–3.50 (m, 6H), 3.46 (dd, *J* = 8.8, 2.4 Hz, 1H), 3.31 (t, *J* = 8.7 Hz, 1H), 3.29–3.19 (m, 2H), 2.71 (dd, *J* = 12.6, 4.8 Hz, 1H), 1.85–1.74 (m, 3H), 1.38 (d, *J* = 6.3 Hz, 3H). ^{13}C{^{1}H} NMR (200 MHz, D_2O) δ 173.0, 158.4, 136.6, 128.8, 128.3, 127.7, 103.3, 102.0, 100.8, 79.9, 74.6,

74.6, 73.6, 72.6, 72.4, 72.0, 70.8, 69.4, 68.3, 67.7, 66.8, 66.5, 65.8, 63.5, 63.3, 60.3, 59.3, 39.9, 37.3, 28.8, 18.9. HRMS (ESI) *m*/*z* calculated for $C_{32}H_{46}N_7O_{18}^-$ [M − H]$^-$ 816.1905, found 816.1880.

Leg5,7diN$_3$α2–6LacNAcβProNHCbz (**14**). A total of 26 mg, 70% yield, white amorphous solid. ^{1}H NMR (600 MHz, D_2O) δ 7.50–7.39 (m, 5H), 5.17–5.11 (m, 2H), 4.53 (d, *J* = 8.1 Hz, 1H), 4.42 (d, *J* = 7.9 Hz, 1H), 4.25–4.15 (m, 1H), 4.00–3.91 (m, 3H), 3.85–3.76 (m, 3H), 3.75 (s, 1H), 3.73–3.52 (m, 9H), 3.46–3.35 (m, 2H), 3.25–3.12 (m, 2H), 2.68 (dd, *J* = 12.6, 4.7 Hz, 1H), 2.06 (s, 3H), 1.83–1.71 (m, 3H), 1.40 (d, *J* = 6.3 Hz, 3H). ^{13}C{^{1}H} NMR (150 MHz, D_2O) δ 174.2, 173.0, 158.3, 136.6, 128.8, 128.4, 127.6, 103.5, 100.8, 100.6, 80.8, 74.5, 73.6, 72.5, 72.5, 72.0, 70.8, 69.2, 68.3, 67.6, 66.8, 66.3, 65.5, 63.8, 63.4, 60.4, 59.3, 55.0, 39.9, 37.3, 28.7, 22.2, 18.9. HRMS (ESI) *m*/*z* calculated for $C_{34}H_{49}N_8O_{18}^-$ [M − H]$^-$ 857.3170, found 857.3141.

Leg5,7diN$_3$α2–6Galβ1–3GalNAcβProNHCbz (**15**). A total of 73 mg, 93% yield, white amorphous solid. ^{1}H NMR (600 MHz, D_2O) δ 7.47–7.40 (m, 5H), 5.14–5.08 (m, 2H), 4.41 (d, *J* = 7.8 Hz, 1H), 4.39 (d, *J* = 7.8 Hz, 1H), 4.15–4.10 (m, 2H), 4.04–3.67 (m, 10H), 3.64–3.59 (m, 4H), 3.52–3.45 (m, 3H), 3.24–3.12 (m, 2H), 2.72 (dd, *J* = 12.6, 4.8 Hz, 1H), 2.00 (s, 3H), 1.85–1.64 (m, 3H), 1.38 (d, *J* = 6.0 Hz, 3H). ^{13}C{^{1}H} NMR (150 MHz, D_2O) δ 174.71, 173.00, 158.31, 136.67, 128.78, 128.33, 127.66, 104.59, 101.43, 100.72, 79.74, 74.85, 73.19, 72.32, 72.01, 70.47, 69.33, 68.43, 68.06, 67.46, 66.76, 66.59, 65.73, 63.59, 63.50, 61.14, 59.47, 51.20, 39.97, 37.14, 28.73, 22.20, 18.88. HRMS (ESI) *m*/*z* calculated for $C_{34}H_{49}N_8O_{18}^-$ [M − H]$^-$ 857.3170, found 857.3174.

Leg5,7diN$_3$α2–6Galβ1–3GalNAcαProNHCbz (**16**). A total of 38 mg, 77% yield, white amorphous solid. ^{1}H NMR (400 MHz, D_2O) δ 7.59–7.31 (m, 5H), 5.25–5.01 (m, 2H), 4.85 (d, *J* = 3.6 Hz, 1H), 4.45 (dd, *J* = 15.5, 7.7 Hz, 1H), 4.36–4.26 (m, 1H), 4.24–4.09 (m, 2H), 4.06–3.87 (m, 4H), 3.81–3.64 (m, 7H), 3.62–3.38 (m, 5H), 3.36–3.17 (m, 2H), 2.85–2.60 (m, 1H), 2.01 (s, 3H), 1.94–1.69 (m, 3H), 1.38 (d, *J* = 6.3 Hz, 3H). ^{13}C{^{1}H} NMR (100 MHz, D_2O) δ 174.5, 158.4, 136.7, 128.8, 128.3, 127.5, 104.7, 104.5, 97.1, 77.8, 77.4, 75.9, 74.9, 74.7, 72.5, 72.1, 70.6, 69.4, 69.0, 68.5, 67.6, 66.7, 66.4, 65.4, 63.4, 61.2, 60.9, 59.3, 48.6, 39.2, 37.6, 28.5, 22.0, 18.9. HRMS (ESI) *m*/*z* calculated for $C_{34}H_{49}N_8O_{18}^-$ [M − H]$^-$ 857.3170, found 857.3134.

Leg5,7diN$_3$α2–6Galβ1–3GlcNAcβProNHCbz (**17**). A total of 62 mg, 81% yield, white amorphous solid. ^{1}H NMR (800 MHz, D_2O) δ 7.51–7.37 (m, 5H), 5.10 (d, *J* = 5.0 Hz, 2H), 4.48 (d, *J* = 8.5 Hz, 1H), 4.35 (d, *J* = 7.8 Hz, 1H), 4.15 (dq, *J* = 8.8, 6.3 Hz, 1H), 3.97 (dd, *J* = 12.3, 2.3 Hz, 1H), 3.94–3.88 (m, 3H), 3.81–3.73 (m, 4H), 3.73–3.65 (m, 2H), 3.64–3.58 (m, 2H), 3.56 (dd, *J* = 10.4, 4.0 Hz, 1H), 3.54–3.42 (m, 5H), 3.29–3.08 (m, 2H), 2.69 (dd, *J* = 12.6, 4.8 Hz, 1H), 1.99 (s, 3H), 1.82–1.68 (m, 3H), 1.37 (d, *J* = 6.3 Hz, 3H). ^{13}C{^{1}H} NMR (200 MHz, D_2O) δ 174.6, 173.0, 158.3, 136.6, 128.8, 128.3, 127.6, 103.9, 100.9, 100.5, 84.3, 75.3, 73.5, 72.5, 72.0, 70.5, 69.3, 69.1, 68.4, 67.6, 66.8, 66.5, 65.7, 63.7, 63.5, 61.0, 59.3, 54.2, 39.9, 37.2, 28.7, 22.1, 18.9. HRMS (ESI) *m*/*z* calculated for $C_{34}H_{49}N_8O_{18}^-$ [M − H]$^-$ 857.3170, found 857.3139.

Leg5,7diN$_3$α2–6Galβ1–3GlcNAcαProNHCbz (**18**). A total of 49 mg, 99% yield, white amorphous solid. ^{1}H NMR (400 MHz, D_2O) δ 7.54–7.26 (m, 5H), 5.12 (s, 2H), 4.34 (d, *J* = 7.8 Hz, 1H), 4.22–4.10 (m, 1H), 4.06 (dd, *J* = 10.5, 3.6 Hz, 1H), 3.99–3.65 (m, 11H), 3.63–3.36 (m, 7H), 3.34–3.14 (m, 2H), 2.71 (dd, *J* = 12.7, 4.6 Hz, 1H), 2.01 (s, 3H), 1.90–1.64 (m, 3H), 1.37 (d, *J* = 6.2 Hz, 3H). ^{13}C{^{1}H} NMR (100 MHz, D_2O) δ 174.4, 173.1, 158.3, 136.6, 128.8, 128.3, 127.6, 103.8, 100.9, 96.8, 82.1, 73.5, 72.5, 71.9, 71.5, 70.6, 69.3, 68.9, 68.3, 66.7, 66.4, 65.8, 65.0, 63.7, 63.2, 60.7, 59.3, 52.2, 40.0, 37.5, 28.6, 22.0, 18.9. HRMS (ESI) *m*/*z* calculated for $C_{34}H_{49}N_8O_{18}^-$ [M − H]$^-$ 857.3170, found 857.3138.

3.3. General Procedures for One-Pot Three-Enzyme (OP3E) Preparative-Scale Synthesis of Leg5,7diN$_3$α2–3-Linked Nonulosonosides (**19**–**24**)

Acceptors [30] (LacβProNHCbz **6**, LacNAcβProNHCbz **7**, Galβ1–3GalNAcβProNHCbz **8**, Galβ1–3GalNAcαProNHCbz **9**, Galβ1–3GlcNAcβProNHCbz **10**, or Galβ1–3GlcNAcαProNHCbz **11**) (0.10–0.20 mmol), 6deoxyMan2,4diN$_3$ [9] (**4**, 0.15–0.30 mmol, 1.5 eq.), sodium pyruvate (7.5 eq), and CTP (1.5 eq) were dissolved in water in a 50 mL centrifuge tube containing Tris-HCl buffer (100 mM, pH 8.5) and $MgCl_2$ (20 mM). After adding sialic acid aldolase (1–3 mg), NmCSS (0.5–1.0 mg), and PmST1_M144D (1–4 mg),

water was added to bring the final concentration of the acceptor to 10 mM. The reaction mixture was incubated at 30 °C for 24–36 h. The reaction progress was monitored using TLC (ethyl acetate:methanol:water = 6:1:1, by volume, was used as the developing solvent) and mass spectrometry. The reaction mixture was diluted with the same volume of ethanol and incubated at 4 °C for 30 min. The mixture was then centrifuged and concentrated, which was purified by automated flash chromatography using a C18 column (CH_3CN in H_2O gradient was used as running solvents) to obtain the desired nonulosonosides.

*Leg5,7diN$_3$α2–3Lac*β*ProNHCbz* (**19**). A total of 56 mg, 74% yield, white amorphous solid. ^{1}H NMR (400 MHz, D_2O) δ 7.61–7.33 (m, 5H), 5.11 (s, 2H), 4.50 (d, *J* = 7.8 Hz, 1H), 4.42 (d, *J* = 8.1 Hz, 1H), 4.25–4.09 (m, 2H), 4.07–3.83 (m, 5H), 3.70–3.60 (m, 4H), 3.59–3.48 (m, 5H), 3.47–3.36 (m, 2H), 3.32–3.19 (m, 2H), 2.82–2.62 (m, 2H), 1.86–1.70 (m, 3H), 1.46–1.31 (m, 3H). ^{13}C{^{1}H} NMR (100 MHz, D_2O) δ 171.8, 158.4, 136.6, 128.8, 128.3, 127.6, 102.6, 102.2, 102.1, 78.4, 75.7, 75.1, 74.7, 74.4, 72.8, 72.2, 72.0, 69.3, 67.9, 67.7, 66.7, 65.8, 65.3, 63.5, 61.7, 61.0, 60.3, 59.3, 39.3, 37.3, 28.9, 18.8. HRMS (ESI) *m*/*z* calculated for $C_{32}H_{46}N_7O_{18}^-$ [M − H]$^-$ 816.1905, found 816.1870.

*Leg5,7diN$_3$α2–3LacNAc*β*ProNHCbz* (**20**). A total of 27 mg, 71% yield, white amorphous solid. ^{1}H NMR (600 MHz, D_2O) δ 7.50–7.39 (m, 5H), 5.17–5.08 (m, 2H), 4.54 (d, *J* = 7.9 Hz, 1H), 4.47 (d, *J* = 8.3 Hz, 1H), 4.22–4.14 (m, 1H), 4.04 (dd, *J* = 9.9, 3.0 Hz, 1H), 3.99 (dd, *J* = 12.4, 2.3 Hz, 1H), 3.95–3.88 (m, 2H), 3.84 (dd, *J* = 12.5, 5.1 Hz, 1H), 3.78–3.66 (m, 8H), 3.63–3.52 (m, 4H), 3.45 (dd, *J* = 8.6, 2.2 Hz, 1H), 3.23–3.11 (m, 2H), 2.73 (dd, *J* = 12.7, 4.5 Hz, 1H), 2.02 (s, 3H), 1.91 (t, *J* = 12.2 Hz, 1H), 1.84–1.70 (m, 2H), 1.40 (t, *J* = 6.3 Hz, 3H). ^{13}C{^{1}H} NMR (150 MHz, D_2O) δ 174.5, 172.8, 158.3, 136.6, 128.8, 128.4, 127.6, 102.6, 101.1, 101.0, 78.5, 75.7, 75.1, 74.7, 72.4, 72.2, 69.4, 69.3, 67.9, 67.6, 66.6, 65.3, 63.4, 61.0, 60.1, 59.3, 55.0, 38.8, 37.2, 28.8, 22.1, 18.8. HRMS (ESI) *m*/*z* calculated for $C_{34}H_{49}N_8O_{18}^-$ [M − H]$^-$ 857.3170, found 857.3137.

*Leg5,7diN$_3$α2–3Galβ1–3GalNAc*β*ProNHCbz* (**21**). A total of 23 mg, 96% yield, white amorphous solid. ^{1}H NMR (400 MHz, D_2O) δ 7.55–7.31 (m, 5H), 5.23–5.07 (m, 2H), 4.54–4.36 (m, 2H), 4.21–4.11 (m, 1H), 4.04–3.97 (m, 1H), 3.95–3.88 (m, 2H), 3.86–3.50 (m, 12H), 3.47–3.28 (m, 2H), 3.26–3.10 (m, 1H), 2.92 (d, *J* = 14.7 Hz, 2H), 2.74 (d, *J* = 12.6 Hz, 1H), 2.01 (s, 3H), 1.93–1.72 (m, 3H), 1.39 (d, *J* = 6.2 Hz, 3H). ^{13}C{^{1}H} NMR (200 MHz, D_2O) δ 174.69, 173.39, 158.34, 136.64, 128.77, 128.31, 127.60, 104.82, 104.59, 101.34, 80.20, 75.83, 74.76, 74.71, 72.09, 69.44, 68.87, 67.84, 67.58, 67.47, 66.46, 65.37, 63.30, 60.94, 60.90, 59.28, 51.10, 48.83, 39.18, 37.20, 29.56, 22.20, 18.84. HRMS (ESI) *m*/*z* calculated for $C_{34}H_{49}N_8O_{18}^-$ [M − H]$^-$ 857.3170, found 857.3135.

*Leg5,7diN$_3$α2–3Galβ1–3GalNAc*α*ProNHCbz* (**22**). A total of 36 mg, 77% yield, white amorphous solid. ^{1}H NMR (400 MHz, D_2O) δ 7.50–7.37 (m, 5H), 5.19–5.07 (m, 2H), 4.85 (d, *J* = 3.7 Hz, 1H), 4.47 (d, *J* = 7.9 Hz, 1H), 4.30 (dd, *J* = 11.1, 3.6 Hz, 1H), 4.25–4.11 (m, 2H), 4.06–3.86 (m, 4H), 3.83–3.64 (m, 7H), 3.62–3.37 (m, 5H), 3.27 (q, *J* = 6.9 Hz, 2H), 2.74 (dd, *J* = 12.7, 4.7 Hz, 1H), 2.01 (s, 3H), 1.93–1.74 (m, 3H), 1.39 (d, *J* = 6.3 Hz, 3H). ^{13}C{^{1}H} NMR (100 MHz, D_2O) δ 174.5, 173.4, 158.3, 136.7, 128.8, 128.3, 127.5, 104.5, 100.4, 97.1, 77.8, 75.9, 74.7, 72.1, 70.6, 69.4, 69.0, 68.5, 67.6, 66.7, 66.4, 65.4, 65.1, 63.4, 61.2, 60.9, 48.6, 39.2, 37.6, 28.5, 22.0, 18.9. HRMS (ESI) *m*/*z* calculated for $C_{34}H_{49}N_8O_{18}^-$ [M − H]$^-$ 857.3170, found 857.3141.

*Leg5,7diN$_3$α2–3Galβ1–3GlcNAc*β*ProNHCbz* (**23**). A total of 60 mg, 80% yield, white amorphous solid. ^{1}H NMR (800 MHz, D_2O) δ 7.50–7.35 (m, 5H), 5.13–5.06 (m, 2H), 4.49 (d, *J* = 8.5 Hz, 1H), 4.45 (d, *J* = 7.8 Hz, 1H), 4.19–4.08 (m, 1H), 3.99 (dd, *J* = 9.8, 3.2 Hz, 1H), 3.95–3.87 (m, 3H), 3.85–3.57 (m, 9H), 3.56–3.48 (m, 3H), 3.48–3.39 (m, 2H), 3.25–3.07 (m, 2H), 2.73 (dd, *J* = 12.6, 4.7 Hz, 1H), 2.01 (s, 3H), 1.85 (t, *J* = 12.3 Hz, 1H), 1.74 (p, *J* = 6.3 Hz, 2H), 1.37 (d, *J* = 6.4 Hz, 3H). ^{13}C{^{1}H} NMR (200 MHz, D_2O) δ 174.5, 173.3, 158.3, 136.6, 128.8, 128.3, 127.6, 103.5, 103.5, 100.8, 82.7, 75.9, 75.3, 75.1, 72.0, 69.4, 68.9, 68.7, 67.6, 67.5, 66.7, 66.5, 65.5, 63.3, 60.9, 60.7, 59.3, 54.4, 39.2, 37.2, 28.7, 22.2, 18.9. HRMS (ESI) *m*/*z* calculated for $C_{34}H_{49}N_8O_{18}^-$ [M − H]$^-$ 857.3170, found 857.3142.

*Leg5,7diN$_3$α2–3Galβ1–3GlcNAc*α*ProNHCbz* (**24**). A total of 47 mg, 96% yield, white amorphous solid. ^{1}H NMR (400 MHz, D_2O) δ 7.53–7.32 (m, 5H), 5.13 (s, 2H), 4.48–4.39 (m, 1H), 4.21–4.10 (m, 1H), 4.07 (dd, *J* = 10.6, 3.5 Hz, 1H), 3.99 (dd, *J* = 9.7, 3.0 Hz, 1H), 3.93–3.65

(m, 11H), 3.63–3.37 (m, 6H), 3.35–3.14 (m, 2H), 2.74 (dd, *J* = 12.6, 4.6 Hz, 1H), 2.02 (s, 3H), 1.92–1.72 (m, 3H), 1.38 (d, *J* = 6.2 Hz, 3H). $^{13}C\{^{1}H\}$ NMR (100 MHz, D_2O) δ 174.3, 173.2, 158.4, 136.7, 128.8, 128.3, 127.5, 103.4, 100.6, 96.9, 81.0, 75.9, 75.0, 72.1, 71.5, 69.4, 69.1, 68.7, 67.5, 66.7, 66.5, 65.4, 65.0, 63.3, 60.9, 60.5, 59.3, 52.3, 39.2, 37.4, 28.5, 22.0, 18.9. HRMS (ESI) *m*/*z* calculated for $C_{34}H_{49}N_8O_{18}^-$ $[M-H]^-$ 857.3170, found 857.3132.

*3.4. General Procedures for Synthesizing Leg5,7Ac$_2$-Glycosides (25–37) by Converting the Azido Groups in Leg5,7diN$_3$-Glycosides (***12**–**24***) to NHAc Groups*

To a saturated sodium bicarbonate solution in water in a round bottom flask (100 mL), an azido-containing glycoside selected from **12**–**24** (10–40 mg) was added followed by dropwise addition of 12–24 equivalents of thioacetic acid under argon at room temperature and this was stirred at 70 °C for 20 h. After completion of the reaction, the solvent was removed under vacuum. The mixture was passed through a Bio-Gel P-2 gel filtration column (water was used as an eluent). Then, the product-containing fractions were concentrated and further purified by silica gel chromatography using a mixed solvent (ethyl acetate: methanol: water = 10:1:0.1, by volume) as an eluent, followed by C18 purification (CH_3CN in H_2O gradient was used as running solvents) to obtain pure products.

Leg5,7Ac$_2$α2–6GalNAcαProNHCbz (**25**). A total of 30 mg, 65% yield, white amorphous solid. ^{1}H NMR (400 MHz, D_2O) δ 7.54–7.28 (m, 5H), 5.29–5.03 (m, 2H), 4.20–4.08 (m, 1H), 4.05–3.87 (m, 6H), 3.87–3.64 (m, 5H), 3.62–3.39 (m, 3H), 3.35–3.12 (m, 2H), 2.76 (dd, *J* = 12.6, 4.3 Hz, 1H), 2.01 (s, 3H), 1.97 (s, 3H), 1.95 (s, 3H), 1.81 (p, *J* = 6.3 Hz, 2H), 1.66 (t, *J* = 12.0 Hz, 1H), 1.15 (d, *J* = 6.2 Hz, 3H). $^{13}C\{^{1}H\}$ NMR (100 MHz, D_2O) δ 174.5, 173.9, 173.7, 173.6, 158.3, 136.6, 128.8, 128.3, 127.6, 97.0, 71.5, 69.5, 68.6, 67.6, 67.2, 66.7, 65.5, 64.2, 54.1, 54.0, 52.1, 49.9, 40.4, 37.6, 28.5, 22.1, 22.0, 21.9, 18.1. HRMS (ESI) *m*/*z* calculated for $C_{32}H_{47}N_4O_{15}^-$ $[M-H]^-$ 727.3043, found 727.3006.

Leg5,7Ac$_2$α2–6LacβProNHCbz (**26**). A total of 23 mg, 78% yield, white amorphous solid. ^{1}H NMR (400 MHz, D_2O) δ 7.59–7.27 (m, 5H), 5.12 (s, 2H), 4.55–4.34 (m, 2H), 4.10–3.50 (m, 18H), 3.42–3.19 (m, 3H), 2.74 (dd, *J* = 12.4, 4.7 Hz, 1H), 2.01 (s, 3H), 1.95 (s, 3H), 1.89–1.67 (m, 3H), 1.16 (d, *J* = 6.3 Hz, 3H). $^{13}C\{^{1}H\}$ NMR (100 MHz, D_2O) δ 173.9, 173.7, 173.4, 158.4, 136.6, 128.8, 128.3, 127.6, 103.2, 102.0, 100.3, 79.5, 74.6, 73.6, 72.8, 72.5, 72.4, 71.6, 70.7, 68.8, 68.4, 67.7, 67.1, 66.8, 63.4, 61.0, 60.2, 54.0, 52.1, 40.1, 37.3, 28.9, 22.1, 22.1, 18.1. HRMS (ESI) *m*/*z* calculated for $C_{36}H_{54}N_3O_{20}^-$ $[M-H]^-$ 848.3306, found 848.3253.

Leg5,7Ac$_2$α2–6LacNAcβProNHCbz (**27**). A total of 9 mg, 68% yield, white amorphous solid. ^{1}H NMR (800 MHz, D_2O) δ 7.69–7.29 (m, 5H), 5.19–5.03 (m, 2H), 4.55–4.41 (m, 2H), 4.06–3.76 (m, 9H), 3.75–3.50 (m, 10H), 3.26–3.08 (m, 2H), 2.76–2.65 (m, 1H), 2.03 (s, 3H), 1.97 (s, 3H), 1.92 (s, 3H), 1.85–1.66 (m, 3H), 1.17–1.11 (m, 3H). $^{13}C\{^{1}H\}$ NMR (200 MHz, D_2O) δ 174.5, 173.7, 173.6, 173.4, 158.3, 136.6, 128.8, 128.3, 127.6, 103.3, 100.8, 100.3, 80.0, 74.5, 73.5, 72.4, 72.3, 71.7, 70.7, 68.7, 68.3, 67.6, 67.1, 66.7, 63.1, 60.2, 55.1, 54.0, 52.0, 40.1, 37.2, 28.7, 22.2, 22.1, 22.0, 18.0. HRMS (ESI) *m*/*z* calculated for $C_{38}H_{57}N_4O_{20}^-$ $[M-H]^-$ 889.3572, found 889.3540.

Leg5,7Ac$_2$α2–6Galβ1–3GalNAcβProNHCbz (**28**). A total of 25 mg, 90% yield, white amorphous solid. ^{1}H NMR (800 MHz, D_2O) δ 7.45–7.38 (m, 5H), 5.13–5.08 (m, 2H), 4.43 (d, *J* = 8.0 Hz, 1H), 4.42 (d, *J* = 8.0 Hz, 1H), 4.19 (d, *J* = 3.2 Hz, 1H), 4.02–3.54 (m, 16H), 3.52–3.49 (m, 2H), 3.22–3.12 (m, 2H), 2.74 (dd, *J* = 12.8, 4.8 Hz, 1H), 2.00 (s, 6H), 1.94 (s, 3H), 1.76–1.72 (m, 2H), 1.62 (t, *J* = 4.0 Hz, 1H), 1.74 (s, 2H), 1.62 (t, *J* = 12.1 Hz, 1H), 1.13 (d, *J* = 6.4 Hz, 3H). $^{13}C\{^{1}H\}$ NMR (200 MHz, D_2O) δ 173.91, 173.69, 173.34, 158.34, 136.64, 128.76, 128.31, 127.61, 104.28, 101.43, 100.34, 80.36, 74.68, 73.18, 72.40, 71.63, 70.41, 68.65, 68.50, 67.73, 67.50, 67.01, 66.76, 63.64, 62.83, 61.21, 53.95, 52.10, 51.13, 40.32, 37.19, 28.72, 22.16, 22.12, 22.05, 18.01. HRMS (ESI) *m*/*z* calculated for $C_{38}H_{57}N_4O_{20}^-$ $[M-H]^-$ 889.3572, found 889.3580.

Leg5,7Ac$_2$α2–6Galβ1–3GalNAcαProNHCbz (**29**). A total of 6 mg, 68% yield, white amorphous solid. ^{1}H NMR (800 MHz, D_2O) δ 7.57–7.24 (m, 5H), 5.11 (q, *J* = 12.8 Hz, 2H), 4.42 (d, *J* = 7.7 Hz, 1H), 4.34–4.26 (m, 1H), 4.19–4.12 (m, 1H), 4.06–3.98 (m, 2H), 3.97–3.62 (m, 12H), 3.60–3.43 (m, 4H), 3.32–3.16 (m, 2H), 2.77 (dd, *J* = 12.4, 4.6 Hz, 1H), 1.94 (s, 6H), 1.92 (s, 3H), 1.84–1.75 (m, 2H), 1.71 (t, *J* = 12.1 Hz, 1H), 1.11 (d, *J* = 6.4 Hz, 3H). $^{13}C\{^{1}H\}$ NMR (200 MHz,

D_2O) δ 174.4, 173.9, 173.8, 173.7, 158.4, 136.7, 128.7, 128.3, 127.4, 104.4, 99.4, 97.1, 77.0, 75.6, 74.8, 71.6, 70.6, 68.9, 68.6, 67.3, 66.8, 66.7, 61.2, 60.9, 53.9, 51.9, 48.7, 40.2, 37.4, 28.4, 22.1, 22.0, 21.9, 18.0. HRMS (ESI) *m*/*z* calculated for $C_{38}H_{57}N_4O_{20}^-$ $[M - H]^-$ 889.3572, found 889.3516.

Leg5,7Ac$_2$*α2–6Galβ1–3GlcNAcβProNHCbz* (**30**). A total of 21 mg, 78% yield, white amorphous solid. ^{1}H NMR (800 MHz, D_2O) δ 7.48–7.35 (m, 5H), 5.16–5.06 (m, 2H), 4.50 (d, *J* = 8.5 Hz, 1H), 4.38 (d, *J* = 7.9 Hz, 1H), 4.06–3.96 (m, 3H), 3.95–3.87 (m, 3H), 3.86–3.77 (m, 4H), 3.75–3.68 (m, 2H), 3.66–3.60 (m, 2H), 3.59–3.52 (m, 4H), 3.51–3.46 (m, 1H), 3.25–3.10 (m, 2H), 2.72 (dd, *J* = 12.5, 4.7 Hz, 1H), 2.01 (s, 3H), 1.99 (s, 3H), 1.95 (s, 3H), 1.80–1.70 (m, 3H), 1.15 (d, *J* = 6.3 Hz, 3H).^{13}C{^{1}H} NMR (200 MHz, D_2O) δ 174.6, 173.9, 173.6, 173.4, 158.3, 136.6, 128.8, 128.3, 127.6, 104.0, 100.9, 100.5, 84.4, 75.6, 73.5, 72.5, 71.6, 70.5, 69.0, 68.7, 68.3, 67.6, 67.0, 66.8, 63.2, 60.9, 54.2, 54.0, 52.0, 40.1, 37.2, 28.7, 22.2, 22.1, 18.1. HRMS (ESI) *m*/*z* calculated for $C_{38}H_{57}N_4O_{20}^-$ $[M - H]^-$ 889.3572, found 889.3534.

Leg5,7Ac$_2$*α2–6Galβ1–3GlcNAcαProNHCbz* (**31**). A total of 17 mg, 71% yield, white amorphous solid. ^{1}H NMR (800 MHz, D_2O) δ 7.52–7.31 (m, 5H), 5.22–4.99 (m, 2H), 4.33 (d, *J* = 7.9 Hz, 1H), 4.13–4.05 (m, 1H), 4.04–3.78 (m, 9H), 3.76–3.67 (m, 4H), 3.62–3.43 (m, 6H), 3.33–3.17 (m, 2H), 2.70 (dd, *J* = 12.4, 4.7 Hz, 1H), 1.98 (s, 6H), 1.93 (s, 3H), 1.87–1.77 (m, 2H), 1.77–1.70 (m, 1H), 1.13 (d, *J* = 6.3 Hz, 3H). ^{13}C{^{1}H} NMR (200 MHz, D_2O) δ 174.4, 173.9, 173.6, 173.5, 158.4, 136.6, 128.8, 128.3, 127.4, 103.9, 100.1, 96.8, 82.5, 73.4, 72.5, 71.6, 71.6, 70.5, 68.8, 68.7, 68.2, 67.0, 66.7, 65.0, 63.0, 60.6, 54.0, 52.1, 52.0, 40.1, 37.4, 28.5, 22.1, 21.9, 18.0. HRMS (ESI) *m*/*z* calculated for $C_{38}H_{57}N_4O_{20}^-$ $[M - H]^-$ 889.3572, found 889.3536.

Leg5,7Ac$_2$*α2–3LacβProNHCbz* (**32**). A total of 7 mg, 68% yield, white amorphous solid. ^{1}H NMR (800 MHz, D_2O) δ 7.49–7.35 (m, 5H), 5.10 (s, 2H), 4.48 (d, *J* = 7.9 Hz, 1H), 4.42 (d, *J* = 8.0 Hz, 1H), 4.11–4.05 (m, 1H), 4.00–3.89 (m, 3H), 3.87–3.64 (m, 10H), 3.64–3.59 (m, 2H), 3.59–3.51 (m, 3H), 3.31–3.17 (m, 2H), 2.77 (dd, *J* = 12.4, 4.6 Hz, 1H), 1.97 (d, *J* = 2.0 Hz, 3H), 1.93 (s, 3H), 1.79 (p, *J* = 6.7 Hz, 2H), 1.73 (t, *J* = 12.1 Hz, 1H), 1.14 (d, *J* = 11.5 Hz, 3H). ^{13}C{^{1}H} NMR (200 MHz, D_2O) δ 173.9, 173.7, 169.0, 158.4, 136.6, 128.7, 128.3, 127.6, 102.6, 102.0, 95.1, 78.3, 75.3, 75.1, 74.7, 74.3, 72.7, 71.8, 69.3, 68.7, 67.7, 67.2, 66.8, 66.8, 61.0, 60.1, 58.6, 53.9, 52.0, 40.1, 37.3, 28.8, 22.1, 21.9, 18.0. HRMS (ESI) *m*/*z* calculated for $C_{36}H_{54}N_3O_{20}^-$ $[M - H]^-$ 848.3306, found 848.3271.

Leg5,7Ac$_2$*α2–3LacNAcβProNHCbz* (**33**). A total of 9 mg, 67% yield, white amorphous solid. ^{1}H NMR (800 MHz, D_2O) δ 7.41 (dq, *J* = 17.8, 9.0, 7.9 Hz, 5H), 5.15–5.05 (m, 2H), 4.53–4.48 (m, 1H), 4.44 (dd, *J* = 10.0, 8.0 Hz, 1H), 4.10 (dd, *J* = 9.9, 3.1 Hz, 1H), 4.00–3.92 (m, 3H), 3.90–3.78 (m, 4H), 3.74–3.52 (m, 11H), 3.26–3.07 (m, 2H), 2.77 (dd, *J* = 12.4, 4.6 Hz, 1H), 2.00 (s, 3H), 1.97 (d, *J* = 4.6 Hz, 3H), 1.92 (d, *J* = 2.9 Hz, 3H), 1.76–1.68 (m, 3H), 1.17–1.11 (m, 3H). ^{13}C{^{1}H} NMR (200 MHz, D_2O) δ 174.5, 174.0, 173.7, 173.7, 158.3, 136.6, 128.8, 128.3, 127.6, 103.3, 102.5, 99.5, 78.4, 75.3, 75.1, 74.7, 72.4, 71.8, 69.4, 68.7, 67.6, 67.2, 66.9, 62.4, 61.0, 60.0, 55.0, 53.9, 52.0, 40.0, 37.2, 28.7, 22.1, 22.1, 21.9, 18.0. HRMS (ESI) *m*/*z* calculated for $C_{38}H_{57}N_4O_{20}^-$ $[M - H]^-$ 889.3572, found 889.3540.

Leg5,7Ac$_2$*α2–3Galβ1–3GalNAcβProNHCbz* (**34**). A total of 5 mg, 67% yield, white amorphous solid. ^{1}H NMR (800 MHz, D_2O) δ 7.46–7.36 (m, 5H), 5.18–5.06 (m, 2H), 4.46–4.36 (m, 2H), 4.12 (d, *J* = 3.2 Hz, 1H), 4.06–3.98 (m, 2H), 3.96–3.86 (m, 3H), 3.82–3.53 (m, 13H), 3.28–3.09 (m, 1H), 2.90 (d, *J* = 46.7 Hz, 1H), 2.77 (dd, *J* = 12.4, 4.6 Hz, 1H), 1.96 (s, 3H), 1.92 (s, 6H), 1.85–1.65 (m, 3H), 1.11 (d, *J* = 6.1 Hz, 3H). ^{13}C{^{1}H} NMR (200 MHz, D_2O) δ 173.9, 173.8, 173.7, 172.9, 158.3, 136.7, 128.7, 128.3, 127.5, 104.7, 101.2, 99.3, 75.6, 74.9, 74.8, 72.0, 71.6, 68.8, 68.6, 68.0, 67.4, 67.3, 66.8, 61.0, 60.9, 60.8, 53.9, 51.9, 51.3, 40.2, 37.1, 28.6, 22.2, 22.1, 21.9, 18.0. HRMS (ESI) *m*/*z* calculated for $C_{38}H_{57}N_4O_{20}^-$ $[M - H]^-$ 889.3572, found 889.3536.

Leg5,7Ac$_2$*α2–3Galβ1–3GalNAcαProNHCbz* (**35**). A total of 13 mg, 69% yield, white amorphous solid. ^{1}H NMR (800 MHz, D_2O) δ 7.42 (dd, *J* = 27.7, 7.4 Hz, 5H), 5.17–5.07 (m, 2H), 4.83–4.82 (m, 1H), 4.47 (d, *J* = 7.9 Hz, 1H), 4.32 (dd, *J* = 11.1, 3.8 Hz, 1H), 4.18 (d, *J* = 3.2 Hz, 1H), 4.06–4.00 (m, 2H), 3.98–3.93 (m, 2H), 3.90 (d, *J* = 3.2 Hz, 1H), 3.86–3.79 (m, 2H), 3.77–3.68 (m, 6H), 3.60–3.52 (m, 3H), 3.51–3.43 (m, 1H), 3.33–3.16 (m, 2H), 2.79 (dd, *J* = 12.4, 4.5 Hz, 1H), 1.98 (s, 3H), 1.98 (s, 3H), 1.94 (s, 3H), 1.80 (h, *J* = 6.6 Hz, 2H), 1.73 (t, *J* = 12.1 Hz, 1H), 1.13 (d, *J* = 6.3 Hz, 3H). ^{13}C{^{1}H} NMR (200 MHz, D_2O) δ 174.4, 173.9,

173.7, 158.4, 136.7, 128.8, 128.3, 127.4, 104.4, 99.6, 97.1, 77.0, 75.7, 74.8, 71.7, 71.7, 70.6, 68.9, 68.7, 68.7, 67.3, 66.8, 66.7, 65.0, 61.2, 60.9, 53.9, 51.9, 48.7, 40.2, 37.5, 28.4, 22.1, 22.0, 21.9, 18.1. HRMS (ESI) m/z calculated for $C_{38}H_{57}N_4O_{20}^-$ $[M - H]^-$ 889.3572, found 889.3537.

Leg5,7Ac$_2$α2–3Galβ1–3GlcNAcβProNHCbz (**36**). A total of 15 mg, 75% yield, white amorphous solid. ^{1}H NMR (400 MHz, D_2O) δ 7.54–7.34 (m, 5H), 5.18–5.05 (m, 2H), 4.47 (dd, J = 20.6, 8.1 Hz, 2H), 4.07 (dd, J = 9.9, 3.0 Hz, 1H), 3.99–3.42 (m, 17H), 3.21 (q, J = 7.4 Hz, 3H), 2.80 (dd, J = 12.4, 4.5 Hz, 1H), 2.05–1.96 (m, 6H), 1.95 (s, 3H), 1.85–1.63 (m, 3H), 1.13 (d, J = 6.2 Hz, 3H). ^{13}C{^{1}H} NMR (100 MHz, D_2O) δ 174.3, 173.9, 173.7, 158.3, 136.6, 128.8, 128.3, 127.5, 103.6, 100.9, 100.8, 82.0, 75.7, 75.4, 75.2, 71.6, 68.8, 68.6, 68.6, 67.7, 67.4, 66.8, 61.1, 60.7, 54.5, 53.9, 51.9, 46.7, 40.2, 37.3, 28.7, 22.1, 22.1, 21.9, 18.1. HRMS (ESI) m/z calculated for $C_{38}H_{57}N_4O_{20}^-$ $[M - H]^-$ 889.3572, found 889.3532.

Leg5,7Ac$_2$α2–3Galβ1–3GlcNAcαProNHCbz (**37**). A total of 11 mg, 72% yield, white amorphous solid. ^{1}H NMR (800 MHz, D_2O) δ 7.52–7.31 (m, 5H), 5.25–5.01 (m, 2H), 4.76 (d, J = 3.6 Hz, 1H), 4.45 (d, J = 8.0 Hz, 1H), 4.12–3.99 (m, 2H), 3.97–3.64 (m, 12H), 3.63–3.49 (m, 4H), 3.48–3.40 (m, 1H), 3.33–3.14 (m, 2H), 2.77 (dd, J = 12.4, 4.5 Hz, 1H), 1.97 (s, 3H), 1.95 (s, 3H), 1.92 (s, 3H), 1.84–1.74 (m, 2H), 1.71 (t, J = 12.1 Hz, 1H), 1.11 (d, J = 6.4 Hz, 3H). ^{13}C{^{1}H} NMR (200 MHz, D_2O) δ 174.2, 173.9, 173.7, 158.4, 136.7, 128.7, 128.2, 127.4, 103.3, 99.4, 97.0, 79.8, 75.7, 75.0, 71.6, 71.6, 68.9, 68.6, 68.5, 67.3, 66.8, 66.7, 64.9, 61.0, 60.4, 53.9, 52.5, 51.9, 40.2, 37.3, 28.4, 22.1, 21.9, 21.9, 18.0. HRMS (ESI) m/z calculated for $C_{38}H_{57}N_4O_{20}^-$ $[M - H]^-$ 889.3572, found 889.3537.

3.5. General Procedures for Converting Cbz-Tagged Glycans to Glycosyl Propylamines

To a stirring solution of a Cbz-tagged glycoside selected from **25**–**37** (5–10 mg) in water-methanol solution (3 mL, 1:2 by volume), a catalytic amount of 10% palladium on charcoal was added to a 50 mL round bottom flask. The mixture was stirred under a hydrogen environment for 2–5 h. The solution was passed through a syringe filter. Methanol was removed from the filtrate by blowing air inside a fume hood. The residue was lyophilized and used directly for microarray assays.

3.6. Glycan Microarray Fabrication

Nano-printing of glycans microarray were fabricated as previously described [45,58]. Briefly, arrays (Version VLA1) were fabricated with NanoPrint LM-60 Microarray Printer (Arrayit) on epoxide-derivatized slides (PolyAn 2D) with 16 sub-array blocks on each slide, with each sub-array containing 340 spots arraigned in a 20 × 17 matrix. Glycoconjugates were distributed into 384-well source plates using 4 replicate wells per sample and 8 μL per well. Each glycoconjugate was diluted into 100 μM in an optimized printing buffer (300 mM phosphate buffer, pH 8.4). To monitor printing, ChromPure Human IgG whole molecule (at 20 ng/μL in PBS pH 7.4 + 10% glycerol) and AlexaFlour-555-Hydraside (at 2 ng/μL in 178 mM phosphate buffer, pH 5.5) were used for each sub-array. The arrays were printed with four 946MP3 pins (5 μm tip, 0.25 μL sample channel, ~100 μm spot diameter; Arrayit). The humidity level in the arraying chamber was maintained at about 70% during printing. Printed slides were left on the arrayer deck overnight, allowing humidity to drop to ambient levels (40–45%). Next, slides were packed, vacuum-sealed, and stored at room temperature (RT) until used.

3.7. Glycan Microarray Binding Assays

Slides were developed and analyzed as previously described [58] with some modifications. Slides were rehydrated with dH_2O and incubated for 30 min in a staining dish with 50 °C pre-warmed ethanolamine (0.05 M) in Tris-HCl (0.1 M, pH 9.0), then washed with 50 °C pre-warmed dH_2O. Slides were centrifuged at 200× g for five min then fitted with a ProPlate™ Multi-Array 16-well slide module (Grace Bio-lab) to divide into the sub-arrays (blocks). Slides were washed with PBST (0.1% Tween 20), aspirated, and blocked with 200 μL/sub-array of blocking buffer (PBS pH 7.3 + 1% w/v ovalbumin) for 1 h at RT with gentle shaking. Next, the blocking solution was aspirated and a 100 μL/sub-array

of detection lectins/antibodies diluted in blocking buffer (lectins binding buffer also included divalent cations, as detailed in the ESI glycan microarray data file in Supplementary Materials) were incubated with gentle shaking for 2 h at RT.

For sialidase pretreatment, before blocking, sub-arrays were incubated with either PBS (without sialidase), 10 mU/100 µL *Arthrobacter ureafaciens* sialidase (AUS, EY Laboratories), or 10 mU/100 µL *Clostridium perfringens* neuraminidase (NCP, Rosch, Sigma, St. Louis, MO, USA), for 2 h at 37 °C with gentle shaking. Then, slides were washed twice with PBST (0.1% Tween 20), aspirated, and blocked with 200 µL/sub-array of blocking buffer (PBS pH 7.3 + 1% *w*/*v* ovalbumin) at RT for 1 h with gentle shaking.

For inhibition assays, each IVIG was pre-incubated for 2 h on ice with inhibition solution containing blocking buffer with glycans (2 mM ID#43, ID#51; or 1 mM ID#502, ID#508), glycopeptides (GP at 0.45 mM; produced from mice sera digested with Pronase) [59], 4 mM 2-*O*-methyl-α-Neu5Ac (Ac2Me), or 4 mM 2-*O*-methyl-α-Neu5Gc (Gc2Me) and only then applied to slides for 2 h. Slides were washed 5 times with PBST.

Binding was detected with Cy3-labeled secondary detection reagent diluted in PBS at 200 µL/sub-array at RT for 1 h with gentle shaking (0.4 ng/µL Cy3 AffiniPure goat-anti-human IgG (H + L), 0.375 ng/µL Cy3-anti-chicken IgY, 1.2 ng/µL Cy3-sterptavidin). Slides were washed 4 times with PBST, then with PBS (without Tween-20) for 10 min followed by removal from ProPlate™ Multi-Array slide module and immediately dipping in a staining dish with dH_2O for 10 min with shaking. Slides were then centrifuged at 200× *g* for 5 min and the dry slides were immediately scanned.

3.8. Array Slide Processing

Processed slides were scanned and analyzed as described [45,58] at 10 µm resolution with a Genepix 4000B microarray scanner (Molecular Devices, San Jose, CA, USA) using 350 gain. Image analysis was carried out with Genepix Pro 7.0 analysis software (Molecular Devices). Spots were defined as circular features with a variable radius as determined by the Genepix scanning software. Local background subtraction was performed. RFU from each spot was calculated.

3.9. Statistics

Statistical analyses were performed using GraphPad Prism 10.2.0 and described in context in the Figure legends.

4. Conclusions

We demonstrate here that the chemoenzymatic synthon strategy using 6deoxyMan2,4diN_3 (**4**) as the starting material in OP3E sialylation systems is highly efficient in constructing a comprehensive library of α2–3- and α2–6-linked Leg5,7Ac_2-glycosides via the enzymatic formation of Leg5,7diN_3, CMP-Leg5,7diN_3, and Leg5,7diN_3-glycosides intermediates, followed by chemical conversion of the azido to the acetamido groups. The hydrophobic UV-detectable Cbz group in the sialyltransferase acceptors facilitated product purification from the OP3E systems. Removal of the Cbz group in the ProNHCbz-tagged Leg5,7Ac_2-glycosides produced ProNH_2-tagged Leg5,7Ac_2-glycosides ready for immobilization on the activated glass slide surface. Glycan microarray studies using the Leg5,7Ac_2-glycosides and their structurally related sialoside pairs revealed diverse human IgG antibodies that selectively recognize the α-linked bacterial nonulosonic acid Leg5,7Ac_2. Such broad-spectrum recognition by human IgG antibodies pooled from thousands of donors (IVIG) supports previous encounters of Leg5,7Ac_2-expressing pathogens by the general human population. Overall, these resources and analytical tools are important tools for further in-depth investigation of Leg5,7Ac_2-involved bacterial physiology, virulence, pathogenicity, and host–pathogen interactions.

Supplementary Materials: The following supporting information can be downloaded at: https://www.mdpi.com/article/10.3390/molecules29163980/s1: the ^1H and ^{13}C NMR spectra of products **12**–**37** (PDF) and the glycan microarray data file (EXCEL).

Author Contributions: Conceptualization, A.S.K., H.Y., S.L.B.-A., V.P.-K., and X.C.; data curation, A.S.K., H.Y., and S.L.B.-A.; formal analysis, A.S.K., H.Y., S.L.B.-A., V.P.-K., and X.C.; funding acquisition, V.P.-K. and X.C.; investigation, A.S.K., H.Y., S.L.B.-A., V.P.-K., and X.C.; methodology, A.S.K., H.Y., S.L.B.-A., V.P.-K., and X.C.; project administration, V.P.-K. and X.C.; resources, V.P.-K. and X.C.; supervision, V.P.-K. and X.C.; writing—original draft, A.S.K., H.Y., S.L.B.-A., V.P.-K., and X.C.; writing—review and editing, A.S.K., H.Y., S.L.B.-A., V.P.-K., and X.C. All authors have read and agreed to the published version of the manuscript.

Funding: This work was financially supported by the United States (U.S.) National Institutes of Health (NIH), grant numbers R01AI130684 and R01GM141324 (to X.C.), and by the Israel Science Foundation—Israel Precision Medicine Program (ISF-IPMP no. 3042/22) and by the European Research Council Consolidator Grant ERC-2020-COG-101003021 (to V.P.-K.). The Bruker Avance-800 NMR spectrometer was funded by the U.S. National Science Foundation (NSF), grant number DBI-0722538. The Thermo Scientific Q Exactive HF Orbitrap Mass Spectrometer was purchased with a U.S. NIH, grant number S10OD025271. The contents of this publication are solely the responsibility of the authors and do not necessarily represent the official view of NIH, NSF, or ISF. The funding sponsors had no role in the design of the study; in the collection, analyses, or interpretation of data; in the wiring of the manuscript; and in the decision to publish the results.

Institutional Review Board Statement: Not applicable.

Informed Consent Statement: Not applicable.

Data Availability Statement: The original contributions presented in the study are included in the article/Supplementary Materials, further inquiries can be directed to the corresponding authors.

Conflicts of Interest: The authors declare no conflicts of interest.

References

1. Luetscher, R.N.D.; McKitrick, T.R.; Gao, C.; Mehta, A.Y.; McQuillan, A.M.; Kardish, R.; Boligan, K.F.; Song, X.; Lu, L.; Heimburg-Molinaro, J.; et al. Unique repertoire of anti-carbohydrate antibodies in individual human serum. *Sci. Rep.* **2020**, *10*, 15436. [CrossRef] [PubMed]
2. Geissner, A.; Reinhardt, A.; Rademacher, C.; Johannssen, T.; Monteiro, J.; Lepenies, B.; Thepaut, M.; Fieschi, F.; Mrazkova, J.; Wimmerova, M.; et al. Microbe-focused glycan array screening platform. *Proc. Natl. Acad. Sci. USA* **2019**, *116*, 1958–1967. [CrossRef] [PubMed]
3. Oyelaran, O.; McShane, L.M.; Dodd, L.; Gildersleeve, J.C. Profiling human serum antibodies with a carbohydrate antigen microarray. *J. Proteome Res.* **2009**, *8*, 4301–4310. [CrossRef]
4. Kappler, K.; Hennet, T. Emergence and significance of carbohydrate-specific antibodies. *Genes Immun.* **2020**, *21*, 224–239. [CrossRef]
5. Marglous, S.; Brown, C.E.; Padler-Karavani, V.; Cummings, R.D.; Gildersleeve, J.C. Serum antibody screening using glycan arrays. *Chem. Soc. Rev.* **2024**, *53*, 2603–2642. [CrossRef]
6. Lewis, A.L.; Chen, X.; Schnaar, R.L.; Varki, A. Sialic acids and other nonulosonic acids. In *Essentials of Glycobiology*, 4th ed.; Varki, A., Cummings, R.D., Esko, J.D., Stanley, P., Hart, G.W., Aebi, M., Mohnen, D., Kinoshita, T., Packer, N.H., Prestegard, J.H., et al., Eds.; Cold Spring Harbor Laboratory Press: Cold Spring Harbor, NY, USA, 2022; pp. 185–204.
7. Chen, X. Enabling chemoenzymatic strategies and enzymes for synthesizing sialyl glycans and sialyl glycoconjugates. *Acc. Chem. Res.* **2024**, *57*, 234–246. [CrossRef] [PubMed]
8. Knirel, Y.A.; Shashkov, A.S.; Tsvetkov, Y.E.; Jansson, P.E.; Zahringer, U. 5,7-diamino-3,5,7,9-tetradeoxynon-2-ulosonic acids in bacterial glycopolymers: Chemistry and biochemistry. *Adv. Carbohydr. Chem. Biochem.* **2003**, *58*, 371–417.
9. Santra, A.; Xiao, A.; Yu, H.; Li, W.; Li, Y.; Ngo, L.; McArthur, J.B.; Chen, X. A diazido mannose analogue as a chemoenzymatic synthon for synthesizing di-*N*-acetyllegionaminic acid-containing glycosides. *Angew. Chem. Int. Ed.* **2018**, *57*, 2929–2933. [CrossRef]
10. McArthur, J.B.; Santra, A.; Li, W.; Kooner, A.S.; Liu, Z.; Yu, H.; Chen, X. *L. pneumophila* CMP-5,7-di-*N*-acetyllegionaminic acid synthetase (LpCLS)-involved chemoenzymatic synthesis of sialosides and analogues. *Org. Biomol. Chem.* **2020**, *18*, 738–744. [CrossRef]
11. Tsvetkov, Y.E.; Shashkov, A.S.; Knirel, Y.A.; Zahringer, U. Synthesis and identification in bacterial lipopolysaccharides of 5,7-diacetamido-3,5,7,9-tetradeoxy-D-glycero-D-galacto- and -D-glycero-D-talo-non-2-ulosonic acids. *Carbohydr. Res.* **2001**, *331*, 233–237. [CrossRef] [PubMed]
12. Tsvetkov, Y.E.; Shashkov, A.S.; Knirel, Y.A.; Zahringer, U. Synthesis and NMR spectroscopy of nine stereoisomeric 5,7-diacetamido-3,5,7,9-tetradeoxynon-2-ulosonic acids. *Carbohydr. Res.* **2001**, *335*, 221–243. [CrossRef] [PubMed]
13. McDonald, N.D.; Boyd, E.F. Structural and biosynthetic diversity of nonulosonic acids (NulOs) that decorate surface structures in bacteria. *Trends Microbiol.* **2021**, *29*, 142–157. [CrossRef]

14. Pradhan, K.; Kulkarni, S.S. Synthesis of nonulosonic acids. *Eur. J. Org. Chem.* **2020**, *2020*, 6819–6830. [CrossRef]
15. Matthies, S.; Stallforth, P.; Seeberger, P.H. Total synthesis of legionaminic acid as basis for serological studies. *J. Am. Chem. Soc.* **2015**, *137*, 2848–2851. [CrossRef] [PubMed]
16. Gintner, M.; Yoneda, Y.; Schmolzer, C.; Denner, C.; Kahlig, H.; Schmid, W. A versatile de novo synthesis of legionaminic acid and 4-epi-legionaminic acid starting from D-serine. *Carbohydr. Res.* **2019**, *474*, 34–42. [CrossRef]
17. Siyabalapitiya Arachchige, S.; Crich, D. Syntheses of legionaminic acid, pseudaminic acid, acetaminic acid, 8-epi-acetaminic acid, and 8-epi-legionaminic acid glycosyl donors from *N*-acetylneuraminic acid by side chain exchange. *Org. Lett.* **2022**, *24*, 2998–3002. [CrossRef] [PubMed]
18. Popik, O.; Dhakal, B.; Crich, D. Stereoselective synthesis of the equatorial glycosides of legionaminic acid. *J. Org. Chem.* **2017**, *82*, 6142–6152. [CrossRef] [PubMed]
19. Dhakal, B.; Buda, S.; Crich, D. Stereoselective synthesis of 5-epi-alpha-sialosides related to the pseudaminic acid glycosides. Reassessment of the stereoselectivity of the 5-azido-5-deacetamidosialyl thioglycosides and use of triflate as nucleophile in the Zbiral deamination of sialic acids. *J. Org. Chem.* **2016**, *81*, 10617–10630.
20. Glaze, P.A.; Watson, D.C.; Young, N.M.; Tanner, M.E. Biosynthesis of CMP-*N*,*N*′-diacetyllegionaminic acid from UDP-*N*,*N*′-diacetylbacillosamine in *Legionella pneumophila*. *Biochemistry* **2008**, *47*, 3272–3282. [CrossRef] [PubMed]
21. Schoenhofen, I.C.; Vinogradov, E.; Whitfield, D.M.; Brisson, J.R.; Logan, S.M. The CMP-legionaminic acid pathway in *Campylobacter*: Biosynthesis involving novel GDP-linked precursors. *Glycobiology* **2009**, *19*, 715–725. [CrossRef]
22. Hassan, M.I.; Lundgren, B.R.; Chaumun, M.; Whitfield, D.M.; Clark, B.; Schoenhofen, I.C.; Boddy, C.N. Total biosynthesis of legionaminic acid, a bacterial sialic acid analogue. *Angew. Chem. Int. Ed.* **2016**, *55*, 12018–12021. [CrossRef]
23. Schoenhofen, I.C.; Young, N.M.; Gilbert, M. Biosynthesis of legionaminic scid and its incorporation into glycoconjugates. *Methods Enzymol.* **2017**, *597*, 187–207.
24. Meng, X.; Boons, G.J.; Wosten, M.; Wennekes, T. Metabolic labeling of legionaminic acid in flagellin glycosylation of *Campylobacter jejuni* identifies Maf4 as a putative legionaminyl transferase. *Angew. Chem. Int. Ed.* **2021**, *60*, 24811–24816. [CrossRef] [PubMed]
25. Yu, H.; Chokhawala, H.; Karpel, R.; Yu, H.; Wu, B.; Zhang, J.; Zhang, Y.; Jia, Q.; Chen, X. A multifunctional *Pasteurella multocida* sialyltransferase: A powerful tool for the synthesis of sialoside libraries. *J. Am. Chem. Soc.* **2005**, *127*, 17618–17619. [CrossRef] [PubMed]
26. Watson, D.C.; Leclerc, S.; Wakarchuk, W.W.; Young, N.M. Enzymatic synthesis and properties of glycoconjugates with legionaminic acid as a replacement for neuraminic acid. *Glycobiology* **2011**, *21*, 99–108. [CrossRef]
27. Watson, D.C.; Wakarchuk, W.W.; Leclerc, S.; Schur, M.J.; Schoenhofen, I.C.; Young, N.M.; Gilbert, M. Sialyltransferases with enhanced legionaminic acid transferase activity for the preparation of analogs of sialoglycoconjugates. *Glycobiology* **2015**, *25*, 767–773. [CrossRef]
28. Watson, D.C.; Wakarchuk, W.W.; Gervais, C.; Durocher, Y.; Robotham, A.; Fernandes, S.M.; Schnaar, R.L.; Young, N.M.; Gilbert, M. Preparation of legionaminic acid analogs of sialo-glycoconjugates by means of mammalian sialyltransferases. *Glycoconj. J.* **2015**, *32*, 729–734. [CrossRef] [PubMed]
29. Li, W.; Ghosh, T.; Bai, Y.; Santra, A.; Xiao, A.; Chen, X. A substrate tagging and two-step enzymatic reaction strategy for large-scale synthesis of 2,7-anhydro-sialic acid. *Carbohydr. Res.* **2019**, *479*, 41–47. [CrossRef] [PubMed]
30. Kooner, A.S.; Diaz, S.; Yu, H.; Santra, A.; Varki, A.; Chen, X. Chemoenzymatic synthesis of sialosides containing 7-*N*- or 7,9-di-*N*-acetyl sialic acid as stable *O*-acetyl analogues for probing sialic acid-binding proteins. *J. Org. Chem.* **2021**, *86*, 14381–14397. [CrossRef] [PubMed]
31. Xu, Y.; Fan, Y.; Ye, J.; Wang, F.; Nie, Q.; Wang, L.; Wang, P.G.; Cao, H.; Cheng, J. Successfully engineering a bacterial sialyltransferase for regioselective α2,6-sialylation. *ACS Catal.* **2018**, *8*, 7222–7227. [CrossRef]
32. Sugiarto, G.; Lau, K.; Qu, J.; Li, Y.; Lim, S.; Mu, S.; Ames, J.B.; Fisher, A.J.; Chen, X. A sialyltransferase mutant with decreased donor hydrolysis and reduced sialidase activities for directly sialylating LewisX. *ACS Chem. Biol.* **2012**, *7*, 1232–1240. [CrossRef]
33. Maki, T.; Tsuritani, T.; Yasukata, T. A mild method for the synthesis of carbamate-protected guanidines using the Burgess reagent. *Org. Lett.* **2014**, *16*, 1868–1871. [CrossRef]
34. Song, X.; Xia, B.; Stowell, S.R.; Lasanajak, Y.; Smith, D.F.; Cummings, R.D. Novel fluorescent glycan microarray strategy reveals ligands for galectins. *Chem. Biol.* **2009**, *16*, 36–47. [CrossRef] [PubMed]
35. Blixt, O.; Head, S.; Mondala, T.; Scanlan, C.; Huflejt, M.E.; Alvarez, R.; Bryan, M.C.; Fazio, F.; Calarese, D.; Stevens, J.; et al. Printed covalent glycan array for ligand profiling of diverse glycan binding proteins. *Proc. Natl. Acad. Sci. USA* **2004**, *101*, 17033–17038. [CrossRef]
36. Park, S.; Lee, M.R.; Shin, I. Fabrication of carbohydrate chips and their use to probe protein-carbohydrate interactions. *Nat. Protoc.* **2007**, *2*, 2747–2758. [CrossRef] [PubMed]
37. Park, S.; Lee, M.R.; Shin, I. Construction of carbohydrate microarrays by using one-step, direct immobilizations of diverse unmodified glycans on solid surfaces. *Bioconjug. Chem.* **2009**, *20*, 155–162. [CrossRef] [PubMed]
38. de Boer, A.R.; Hokke, C.H.; Deelder, A.M.; Wuhrer, M. General microarray technique for immobilization and screening of natural glycans. *Anal. Chem.* **2007**, *79*, 8107–8113. [CrossRef]
39. Song, X.; Xia, B.; Lasanajak, Y.; Smith, D.F.; Cummings, R.D. Quantifiable fluorescent glycan microarrays. *Glycoconj. J.* **2008**, *25*, 15–25. [CrossRef]

40. Yu, H.; Chokhawala, H.A.; Varki, A.; Chen, X. Efficient chemoenzymatic synthesis of biotinylated human serum albumin-sialoglycoside conjugates containing *O*-acetylated sialic acids. *Org. Biomol. Chem.* **2007**, *5*, 2458–2463. [CrossRef]
41. Bochner, B.S.; Alvarez, R.A.; Mehta, P.; Bovin, N.V.; Blixt, O.; White, J.R.; Schnaar, R.L. Glycan array screening reveals a candidate ligand for Siglec-8. *J. Biol. Chem.* **2005**, *280*, 4307–4312. [CrossRef]
42. Yu, H.; Huang, S.; Chokhawala, H.; Sun, M.; Zheng, H.; Chen, X. Highly efficient chemoenzymatic synthesis of naturally occurring and non-natural alpha-2,6-linked sialosides: A *P. damsela* alpha-2,6-sialyltransferase with extremely flexible donor-substrate specificity. *Angew. Chem. Int. Ed.* **2006**, *45*, 3938–3944. [CrossRef]
43. Kooner, A.S.; Yu, H.; Chen, X. Synthesis of *N*-glycolylneuraminic scid (Neu5Gc) and its glycosides. *Front. Immunol.* **2019**, *10*, 2004. [CrossRef] [PubMed]
44. Diaz, S.L.; Padler-Karavani, V.; Ghaderi, D.; Hurtado-Ziola, N.; Yu, H.; Chen, X.; Brinkman-Van der Linden, E.C.; Varki, A.; Varki, N.M. Sensitive and specific detection of the non-human sialic scid *N*-glycolylneuraminic acid in human tissues and biotherapeutic products. *PLoS ONE* **2009**, *4*, e4241. [CrossRef] [PubMed]
45. Leviatan Ben-Arye, S.; Yu, H.; Chen, X.; Padler-Karavani, V. Profiling anti-Neu5Gc IgG in human sera with a sialoglycan microarray assay. *J. Vis. Exp.* **2017**, *125*, e56094. [CrossRef]
46. Leviatan Ben-Arye, S.; Schneider, C.; Yu, H.; Bashir, S.; Chen, X.; von Gunten, S.; Padler-Karavani, V. Differential recognition of diet-derived Neu5Gc-neoantigens on glycan microarrays by carbohydrate-specific pooled human IgG and IgA antibodies. *Bioconjug. Chem.* **2019**, *30*, 1565–1574. [CrossRef]
47. Varki, A. Since there are PAMPs and DAMPs, there must be SAMPs? Glycan "self-associated molecular patterns" dampen innate immunity, but pathogens can mimic them. *Glycobiology* **2011**, *21*, 1121–1124. [CrossRef] [PubMed]
48. Kooner, A.S.; Yuan, Y.; Yu, H.; Kang, H.; Klenow, L.; Daniels, R.; Chen, X. Sialosides containing 7-*N*-acetyl sialic acid are selective substrates for neuraminidases from influenza A viruses. *ACS Infect. Dis.* **2023**, *9*, 33–41. [CrossRef]
49. Zebian, N.; Merkx-Jacques, A.; Pittock, P.P.; Houle, S.; Dozois, C.M.; Lajoie, G.A.; Creuzenet, C. Comprehensive analysis of flagellin glycosylation in *Campylobacter jejuni* NCTC 11168 reveals incorporation of legionaminic acid and its importance for host colonization. *Glycobiology* **2016**, *26*, 386–397. [CrossRef]
50. Varki, A.; Gagneux, P. Multifarious roles of sialic acids in immunity. *Ann. N. Y. Acad. Sci.* **2012**, *1253*, 16–36. [CrossRef]
51. Gulati, S.; Schoenhofen, I.C.; Lindhout-Djukic, T.; Lewis, L.A.; Moustafa, I.Y.; Saha, S.; Zheng, B.; Nowak, N.; Rice, P.A.; Varki, A.; et al. Efficacy of antigonococcal CMP-nonulosonate therapeutics require cathelicidins. *J. Infect. Dis.* **2020**, *222*, 1641–1650. [CrossRef]
52. Gulati, S.; Schoenhofen, I.C.; Whitfield, D.M.; Cox, A.D.; Li, J.; St Michael, F.; Vinogradov, E.V.; Stupak, J.; Zheng, B.; Ohnishi, M.; et al. Utilizing CMP-sialic acid analogs to unravel *Neisseria gonorrhoeae* lipooligosaccharide-mediated complement resistance and design novel therapeutics. *PLoS Pathog.* **2015**, *11*, e1005290. [CrossRef] [PubMed]
53. Gulati, S.; Schoenhofen, I.C.; Lindhout-Djukic, T.; Schur, M.J.; Landig, C.S.; Saha, S.; Deng, L.; Lewis, L.A.; Zheng, B.; Varki, A.; et al. Therapeutic CMP-nonulosonates against multidrug-resistant *Neisseria gonorrhoeae*. *J. Immunol.* **2020**, *204*, 3283–3295. [CrossRef] [PubMed]
54. Amon, R.; Grant, O.C.; Leviatan Ben-Arye, S.; Makeneni, S.; Nivedha, A.K.; Marshanski, T.; Norn, C.; Yu, H.; Glushka, J.N.; Fleishman, S.J.; et al. A combined computational-experimental approach to define the structural origin of antibody recognition of sialyl-Tn, a tumor-associated carbohydrate antigen. *Sci. Rep.* **2018**, *8*, 10786. [CrossRef] [PubMed]
55. Borenstein-Katz, A.; Warszawski, S.; Amon, R.; Eilon, M.; Cohen-Dvashi, H.; Leviatan Ben-Arye, S.; Tasnima, N.; Yu, H.; Chen, X.; Padler-Karavani, V.; et al. Biomolecular recognition of the glycan neoantigen CA19-9 by distinct antibodies. *J. Mol. Biol.* **2021**, *433*, 167099. [CrossRef] [PubMed]
56. Li, Y.; Yu, H.; Cao, H.; Lau, K.; Muthana, S.; Tiwari, V.K.; Son, B.; Chen, X. *Pasteurella multocida* sialic acid aldolase: A promising biocatalyst. *Appl. Microbiol. Biotechnol.* **2008**, *79*, 963–970. [CrossRef] [PubMed]
57. Yu, H.; Yu, H.; Karpel, R.; Chen, X. Chemoenzymatic synthesis of CMP-sialic acid derivatives by a one-pot two-enzyme system: Comparison of substrate flexibility of three microbial CMP-sialic acid synthetases. *Bioorg. Med. Chem.* **2004**, *12*, 6427–6435. [CrossRef]
58. Padler-Karavani, V.; Song, X.; Yu, H.; Hurtado-Ziola, N.; Huang, S.; Muthana, S.; Chokhawala, H.A.; Cheng, J.; Verhagen, A.; Langereis, M.A.; et al. Cross-comparison of protein recognition of sialic acid diversity on two novel sialoglycan microarrays. *J. Biol. Chem.* **2012**, *287*, 22593–22608. [CrossRef]
59. Bashir, S.; Leviatan Ben Arye, S.; Reuven, E.M.; Yu, H.; Costa, C.; Galinanes, M.; Bottio, T.; Chen, X.; Padler-Karavani, V. Presentation mode of glycans affect recognition of human serum anti-Neu5Gc IgG antibodies. *Bioconjug. Chem.* **2019**, *30*, 161–168. [CrossRef]

Disclaimer/Publisher's Note: The statements, opinions and data contained in all publications are solely those of the individual author(s) and contributor(s) and not of MDPI and/or the editor(s). MDPI and/or the editor(s) disclaim responsibility for any injury to people or property resulting from any ideas, methods, instructions or products referred to in the content.

biomolecules

MDPI

Article

The Autophagic Activator GHF-201 Can Alleviate Pathology in a Mouse Model and in Patient Fibroblasts of Type III Glycogenosis

Kumudesh Mishra [1], Sahar Sweetat [1], Saja Baraghithy [2], Uri Sprecher [3], Monzer Marisat [3], Sultan Bastu [4], Hava Glickstein [5], Joseph Tam [2], Hanna Rosenmann [1], Miguel Weil [3], Edoardo Malfatti [4] and Or Kakhlon [1,6,*]

1 Department of Neurology, The Agnes Ginges Center for Human Neurogenetics, Hadassah-Hebrew University Medical Center, Jerusalem 9112001, Israel; kumudeshmishra@gmail.com (K.M.); sahar.sweetat@mail.huji.ac.il (S.S.); rosenman@hadassah.org.il (H.R.)
2 Obesity and Metabolism Laboratory, Institute for Drug Research, School of Pharmacy, Faculty of Medicine, The Hebrew University of Jerusalem, Jerusalem 9112001, Israel; saja.baraghithy@mail.huji.ac.il (S.B.); yossi.tam@mail.huji.ac.il (J.T.)
3 The Shmunis School of Biomedicine and Cancer Research, The George S. Wise Faculty for Life Sciences, Sagol School of Neurosciences, Tel Aviv University, Tel Aviv 6997801, Israel; uri8sp@gmail.com (U.S.); monzermar@gmail.com (M.M.); miguelw@tauex.tau.ac.il (M.W.)
4 Centre de Reference de Maladies Neuromusculaires, UPEC—Paris Est University, IMRB INSERM U955, Team Biology of the Neuromuscular System, Faculty of Medicine, APHP Hopital Henri Mondor, 1 Rue Gustave Eiffel, 94010 Creteil, France; sultan.bastu@inserm.fr (S.B.); edoardo.malfatti@aphp.fr (E.M.)
5 Electron Microscopy Unit, The Hebrew University-Hadassah Medical School, Ein Kerem, Jerusalem 9112001, Israel; hava.glickstein@mail.huji.ac.il
6 Faculty of Medicine, Hebrew University of Jerusalem, Jerusalem 9112001, Israel
* Correspondence: ork@hadassah.org.il; Tel.: +972-546-812-380

Abstract: Glycogen storage disease type III (GSDIII) is a hereditary glycogenosis caused by deficiency of the glycogen debranching enzyme (GDE), an enzyme, encoded by *Agl*, enabling glycogen degradation by catalyzing alpha-1,4-oligosaccharide side chain transfer and alpha-1,6-glucose cleavage. GDE deficiency causes accumulation of phosphorylase-limited dextrin, leading to liver disorder followed by fatal myopathy. Here, we tested the capacity of the new autophagosomal activator GHF-201 to alleviate disease burden by clearing pathogenic glycogen surcharge in the GSDIII mouse model $Agl^{-/-}$. We used open field, grip strength, and rotarod tests for evaluating GHF-201's effects on locomotion, a biochemistry panel to quantify hematological biomarkers, indirect calorimetry to quantify in vivo metabolism, transmission electron microscopy to quantify glycogen in muscle, and fibroblast image analysis to determine cellular features affected by GHF-201. GHF-201 was able to improve all locomotion parameters and partially reversed hypoglycemia, hyperlipidemia and liver and muscle malfunction in $Agl^{-/-}$ mice. Treated mice burnt carbohydrates more efficiently and showed significant improvement of aberrant ultrastructural muscle features. In GSDIII patient fibroblasts, GHF-201 restored mitochondrial membrane polarization and corrected lysosomal swelling. In conclusion, GHF-201 is a viable candidate for treating GSDIII as it recovered a wide range of its pathologies in vivo, in vitro, and ex vivo.

Keywords: glycogen; glycogen storage disease type III; pharmacotherapy

1. Introduction

Glycogen is a branched polysaccharide with a molecular weight of nine to ten million Da. The average glycogen molecule contains about 55,000 glucose residues linked by α-1,4 (92%) and α-1,6 (8%) glycosidic bonds [1]. The synthesis of glycogen is primed by glycogenin [2] (even though aberrant forms of glycogen are also formed when glycogenin is suppressed [3]), and catalyzed by glycogen synthase (GYS) and glycogen branching

enzyme (GBE). GYS links glucose residues to each other by α-1,4 glycosidic bonds to form linear chains. GBE, in turn, attaches a short linear stretch of α-1,4-linked glucose units from the outer non-reducing end of a growing glycogen chain into an α-1,6 position of a pre-existing chain, thus generating a branch. Repetitive cycles of elongation and branching generate a large (110–290 nm in liver) [4] spherical molecule with a hydrophilic surface and an increased number of reactive termini, facilitating glycogen synthesis and degradation [5,6]. Glycogen degradation, on the other hand, takes place in the cytosol and in lysosomes. In the cytosol, glycogen is degraded by glycogen phosphorylase (GP), which phosphorylytically releases outer glucose residues in the form of glucose-1-phosphate, and by glycogen debranching enzyme (GDE). GP phosphorylates outer glucose residues and releases each one as glucose-1-hosphate. GP can degrade an outer chain only until four residues from the branch point. Then, GDE is required to complete glycogenolysis. GDE catalyzes two reactions: transferring a three-glucosyl glucan to the non-reducing end of another linear strand (α-1,4-glucanotransferase reaction) and hydrolyzing the α-1-6-glycosidic bond remaining on the branch point, releasing glucose (amylo-α-1,6-glucosidase reaction, *n.b.*, glucose, rather than glucose-1-phosphate, is released [4]). In the lysosomes, glycogen degradation is catalyzed by α-glucosidase.

Glycogen is stored primarily in liver and muscle, where it, respectively, serves as a reservoir for regulating blood glucose levels and as a readily mobilizable energy reserve. Therefore, aberrations in glycogen metabolism, or glycogen storage disorders (GSDs), are primarily hepatic or muscular disorders, with two notable exceptions, APBD and LD, specifically involving the central and peripheral nervous systems. The most common disorder of glycogen metabolism is observed in diabetes [7,8], in which abnormal amounts of insulin or abnormal insulin response result in accumulation or depletion of liver glycogen. However, GSDs are normally associated with hereditary deficiencies in enzymes of glycogen and glucose metabolism causing glycogen accumulation (except for GSD type 0, which is a GYS deficiency and is therefore associated with glycogen insufficiency).

In this work, we focused on GSD type III (GSDIII, Cori disease), the third most prevalent muscle GSD (incidence of 1:100,000) after GSD types V and II [9–11], which is caused by GDE deficiency leading to accumulation of glycogen due to its reduced degradation. Phosphorylase-limit dextrin (PLD), the type of glycogen which accumulates in GSDIII, is structurally abnormal, containing shorter outer branches [12]. While phosphorylase-limit dextrin is sensitive to diastase digestion and does not form polyglucosan bodies [12], it is still associated with large vacuoles and can cause histological damage to myofibrils [13,14]. GSDIII usually starts as a liver disorder characterized by hepatomegaly, hypoglycemia, hyperlipidemia, and hyperketonemia. These result from the limited ability to breakdown glycogen to glucose, leading to excessive use of lipid oxidation as an alternative energy source with ensuing attenuation of lipid uptake by adipocytes and increase in ketone bodies as byproducts of fatty acid oxidation (FAO). Later on, myopathy pursues [15], with occasional cardiomyopathy [16], liver cirrhosis, and hepatocellular adenoma [17].

GSDIII implicates vacuolar myopathy and myofibrillar damage [14,18], also observed in GSDII [19], which shares muscle glycogen over accumulation with GSDIII (albeit lysosomal in GSDII and mostly cytoplasmic in GSDIII). We, therefore, tested the GSDIII curative capacity of GHF-201, a novel, safe compound capable of reversing glycogen accumulation and enhancing autophagy [20,21]. We show that GHF-201 is capable of improving motility and grip strength in an $Agl^{-/-}$ mouse model of GSDIII, where GDE, encoded by the murine *Agl* gene, was knocked out. At the same time, GHF-201 did not modify the deficient motor learning capacities of $Agl^{-/-}$ mice associated with a neurological deficiency not implicated in GSDIII. We further demonstrate that GHF-201 corrected hypoglycemia, hyperlipidemia, and liver and muscle damage, as well as carbohydrate over fat fuel preference. Combined with reduction of glycogen levels and muscle atrophy at the tissue level, and improvement of lysosomal and mitochondrial phenotypes at the cell level (in GSDIII patients' fibroblasts), our results strongly support that GHF-201 has a potential therapeutic capacity for treating GSDIII, either as a standalone, or as part of a combination therapy. At the

moment, GSDIII has no curative alternative and patients are only managed by dietary restrictions [22]. A clinical trial for GSDIII using the UX053 gene therapy-based replacement of GDE (NCT04990388) has been initiated, but was terminated at phase I. While the gene therapy GDE replacement approach is still valid, it can also be improved by add-on therapy based on a mechanistically complementary approach. In that respect, activation of glycogen degradation by autophagy merits appraisal, especially since rapamycin-mediated activation of autophagy was indeed efficacious in a GSDIII dog model [23].

2. Materials and Methods

2.1. In Vivo Studies

In vivo studies were conducted on $Agl^{-/-}$ mice [9] and congenic C57Bl6J mice as littermate wild type controls ($Agl^{-/-}$). n = 6–10 mice/arm were used. Twice a week, 50 µL of 250 mg/kg GHF-201 in 10% DMSO was intramuscularly injected to the gastrocnemius in alternate flanks. A 10% DMSO vehicle was used as a vehicle control. Mice were treated from the age of 3 months to the age of 8 months. Animals' weight was recorded every week. A weight decrease of >10% between biweekly weightings, or >20% from treatment initiation led to removal of the animal from the study. We tested monthly moving distance and cumulative sojourn in the center of an open field, front paw grip strength using a grip strength meter (Columbus Instruments, Columbus, OH, USA), and rotarod performance (latency to fall from a rotating cylinder). The rotating cylinder (UGO Basile S.R.L., Gemonio, Italy) accelerated from 5 to 40 RPM in 99 s. Mice were tested for 3 consecutive trials with a rest period of approximately 10 min between trials.

Blood biochemistry (enzyme activities), triglycerides, and glucose were determined at the Hadassah central laboratory division. Blood was collected from the cheek pouch by submandibular bleeding. Indirect calorimetry and multi-parameter metabolic assessment (metabolic cages) were performed in Promethion Metabolic Phenotyping Systems (Sable Instruments, Las Vegas, NV, USA) as in [20]. Specifically, locomotor activity was assessed in these cages by the number of times an infrared XYZ beam array is disrupted by animal movement, while wheel running was determined by the number of wheel revolutions [24].

2.2. Ultrastructural Electron Microscopy Studies

Gastrocnemius muscle samples were fixed, embedded, sectioned, and analyzed by transmission electron microscope as described in [9]. Area percentage of glycogen dense granules in longitudinal muscle sections (10 sections/animal) was quantified in samples from n = 3 vehicle-treated WT, n = 3 vehicle-treated $Agl^{-/-}$, and n = 3 GHF-201-treated $Agl^{-/-}$ mice.

2.3. Biochemical Glycogen Quantification

Muscle glycogen was quantified biochemically using Merck's Glycogen Assay Kit (Cat. # MAK465) according to the manufacturer instructions. In brief, 10–20 mg of muscle tissues was homogenized on ice in 1 mL of 25 mM citric acid, 2.5 mg/mL NaF, pH 4.2. Samples were spun down (14,000× *g*, 5 min, RT) to clear the debris. Then, 10 µL of cleared supernatant was used for the colorimetric determination of glycogen using the kit. A calibration curve of 0–200 µg/mL glycogen (provided with the kit) was used for glycogen quantification. Water was used as a blank control, to which the same reagents were added. This blank reading was subtracted from the colorimetric readings of all samples and calibration standards.

2.4. High Content Analysis of GSDIII Patient Fibroblasts

Primary skin fibroblasts from 3 patients were procured from Coriell Institute (Camden, NJ, USA) and expanded in DMEM supplemented with 1% Sodium Pyruvate, 1% Penicillin-Streptomycin-Amphotericin B, 10% heat-inactivated fetal calf serum (Biological industries, Beit HaEmek, Israel), and 1% 100× non-essential amino acids solution (NEAA) at 37 °C with 5% CO_2. For live imaging, GSDIII and healthy control (HC) skin fibroblasts were

seeded at 1400 cells per well and cultured at 37 °C and 5% CO_2 with or without GHF-201 (50 μM) for 24 h in specialized microscopy-grade 96-well plates (Cellvis P96-1.5H-N). Cells were then washed in HBSS, supplemented for 20 min with 1.6 mM Hoechst 33342, 0.1 mM LysoTracker Deep Red, 0.05 mM TMRE, and 0.4 mM calcein-AM Green (Thermo-Fisher Scientific, Waltham, MA, USA), and washed again with HBSS. Subsequently, images were acquired using an Operetta G1 system at 20× magnification under environmental control (37 °C and 5% CO_2) conditions. All assay parameters (including the acquisition exposure times, objective, and the analysis parameters) were kept constant for all assay repetitions. Images were analyzed by the Harmony image analysis software version 1.0. Downstream analysis included removal of wells with outlier values using GraphPad Prism (version 10.2.3)'s ROUT method (Q = 10%), feature selection by backward feature elimination, and normalization to HC levels prior to statistical analysis [25]. Multivariate analysis was performed in Python.

2.5. Statistical Analysis

Sample sizes were determined based on the effect sizes of key parameters measured (e.g., open field moving distance), as detailed in [26]. These sample sizes were sufficient to provide the acceptable power of at least 80%. Blinding in in vivo studies was obtained by encoding the animals in the different treatment groups so that the experimenters were blinded to treatment allocation. To obtain randomization, litters from mice born a few days apart were pooled and pups of similar weight were divided into vehicle- and GHF-201-treated arms. Specific statistical tests are mentioned in the relevant text and figure legends.

For the indirect calorimetry and metabolic cage analyses (Figure in Section 3.4), mean differences in metabolic parameters between wild type and vehicle-treated $Agl^{-/-}$ mice, wild type and GHF-201-treated mice and vehicle-treated and GHF-201-treated $Agl^{-/-}$ mice were calculated during light, dark, and overall (light + dark) periods. One Way ANOVA with repeated measures (and Tukey post hoc validation test) was used to determine the statistical significance of these mean differences, which are the output of repeated measures of ANOVA, for each metabolic parameter during the entire time periods analyzed (light, dark, or overall). We show in the left panels the actual time-dependent trends of the respective metabolic parameter in each treatment arm. In the right panels, we show the mean differences between the group trend averages (n = 4 mice in each group) derived from these time trends. For the food and water intake profiles, since they are cumulative, mean differences were calculated based on subtractions of the time periods end values: at 12 h for the light period, at 24 h minus 12 h for the dark period, and at 24 h for the overall periods. The statistical significance of the mean differences is shown by asterisks above the respective bars. The total energy expenditure (TEE) ANCOVA analysis was provided by the NIDDK Mouse Metabolic Phenotyping Centers (MMPC, www.mmpc.org (accessed on 1 July 2024)) using their Energy Expenditure Analysis page (http://www.mmpc.org/shared/regression.aspx (accessed on 1 July 2024)) and supported by grants DK076169 and DK115255.

3. Results

3.1. Animal Weight

GSDIII male mice presented with a higher weight throughout the treatment period as compared to WT mice ($p < 0.0001$, Two Way ANOVA with repeated measures). According to [13], GSDIII mice were lighter than WT mice, while in [27], no significant difference between the weights of GSDIII and WT mice was observed, together suggesting that such a difference might be batch-dependent. GHF-201 treatment did not significantly modify weight in GSDIII mice (Figure 1). Animal weighting was discontinued 138 d after treatment initiation due to an unexplained >10% weight drop between two weightings in all animals.

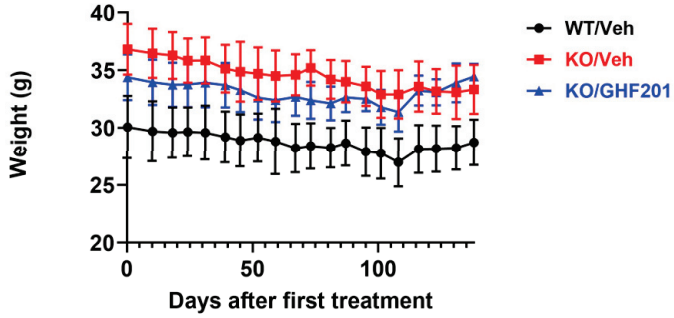


Figure 1. Weight over time in WT mice, $Agl^{-/-}$ (KO) mice injected intramuscularly biweekly with 10% DMSO solvent control, and KO mice injected in the same way with 250 mg/kg GHF-201. n = 8 WT/Veh, n = 6 KO/Veh, and n = 10 KO/GHF-201 mice were used. Throughout the period, KO mice were heavier than WT mice ($p < 0.0001$, Two Way ANOVA with repeated measures). Due to a >10% weight reduction between biweekly weightings, one mouse was removed from the KO/Veh group on day 116 after treatment initiation and one mouse was removed from the KO/GHF201 group on day 52 after treatment initiation.

3.2. Locomotor Studies

We show that GHF-201 improved open field performance at a relatively advanced stage of the disease (last time point when mice were approximately 8 months old). This improvement was demonstrated as increases in both distance traveled (Figure 2A) and sojourn in the center of the open field (Figure 2B), which indicates a more exploratory behavior associated with decreased anxiety. Sojourn in the center was corrected by GHF-201 to WT values at the age of 8 months. Interestingly, while GHF-201 significantly increased grip strength (Figure 2C) and improved open field parameters, it did not increase the latency to fall from a rotating rod in the rotarod test (Two Way ANOVA with repeated measures, $p < 0.95$, $p < 0.95$, $p < 0.97$ at 10, 47, and 108 days post-treatment initiation) and even decreased it 80 days post-treatment initiation (Two Way ANOVA with repeated measures, $p < 0.05$). Latency to fall was decreased in $Agl^{-/-}$ mice as compared to WT at all times post-treatment initiation (Two Way ANOVA with repeated measures, $p < 0.11$ (only a trend), $p < 0.03$, $p < 0.005$, and $p < 0.02$ at 10, 47, 80, and 108 days post-treatment initiation, Figure 2D). Training and motor learning capacity were, respectively, demonstrated by increased latency between runs in each test and by increased overall latency over time. As opposed to untreated and treated $Agl^{-/-}$ mice, which showed no training capacity, WT mice manifested training capacity at 80 days post-treatment initiation. This was determined by comparing the average run latencies (shown in different shades of gray, red, and blue in WT, KO/Veh, and KO/GHF-201, respectively) at each time following treatment initiation using Two Way ANOVA with repeated measures ($p < 0.04$). Motor learning capacity of WT mice was also significantly higher than that of untreated or treated $Agl^{-/-}$ mice ($p < 0.0095$, $R^2 = 0.2687$ for linear correlation of latency v time in WT mice, as compared to ($p < 0.0436$, $R^2 = 0.0732$) and ($p < 0.0691$, $R^2 = 0.0523$) for untreated and treated $Agl^{-/-}$ mice, respectively). Indeed, rotarod measures motor coordination, which is considered a neurological function of the nigrostriatal dopamine system [28,29] not implicated in GSDIII. Motor activity measured by the open field test, on the other hand, is influenced by muscle strength, which was modified by GHF-201 (Figure 2C). There are several works (e.g., [30]) which demonstrate the independence of rotarod and open field results.

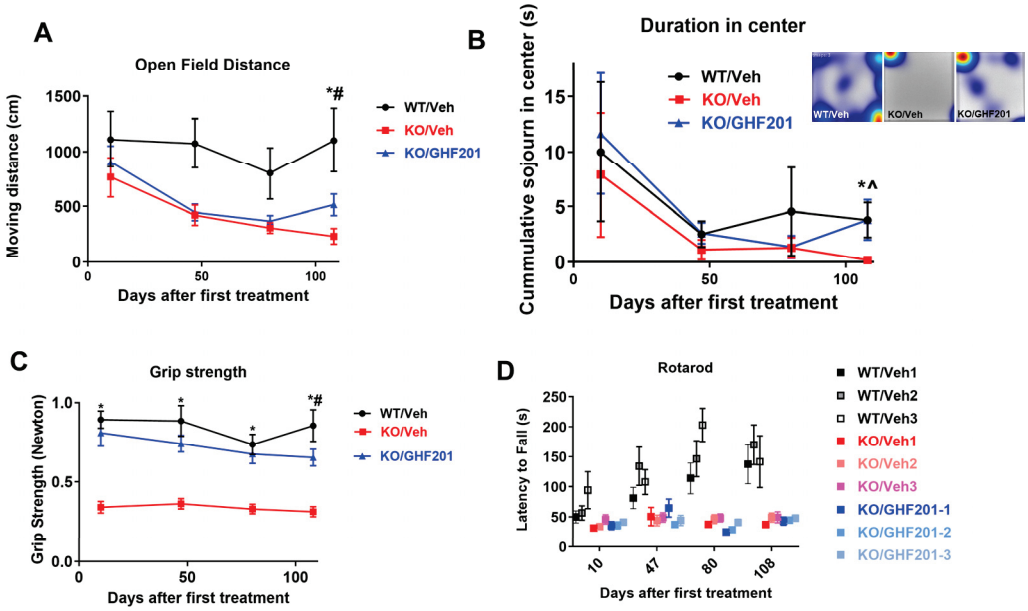


Figure 2. Movement distance (**A**), sojourn in the center of an open field arena (inset representative open field sojourn heatmaps) (**B**), grip strength (**C**), and latency to fall from a rotating rod (**D**) were measured in n = 8 $Agl^{-/-}$ mice treated with 10% DMSO vehicle (KO/Veh), n = 6 wild type mice treated with vehicle (WT/Veh), and n = 10 $Agl^{-/-}$ mice treated with GHF-201 (KO/GHF-201). In (**D**), each rotarod session included three consecutive runs (1–3), separated by 10 min pauses. Two Way ANOVA with repeated measures shows that only in (**C**) GHF-201 treatment values were higher than vehicle-treated values in KO mice throughout the period ($p < 0.05$). Linear regression analysis of overall latency over time (**D**), shows that WT animals developed a significantly higher learning capacity than KO/Veh and KO/GHF-201 mice. Training capacity, shown by increase in latency over runs, was only demonstrated in WT mice 80 days post-treatment initiation. See text for statistical analysis. *, KO/GH201 is significantly different from KO/Veh; *#, KO/GHF-201 is significantly different from both KO/Veh and WT/Veh; *^, KO/GHF-201 is significantly different only from KO/Veh and not from WT/Veh (correction effect). Difference significance determined by multiple *t*-tests with Sidak post hoc correction. All error bars represent s.e.m.

Notably, all behavioral tests had to be discontinued following the 4th test post-treatment initiation. The reason for that was that after the 4th test the weight of all mice was decreased by >10% from the last reading suggesting that GHF-201, increases muscle strength-associated mobility, but not survival, in GSDIII mice.

3.3. Blood Metabolic Panel

We tested whether GHF-201 is able to correct the hypoglycemia, hypertriglyceridemia, and liver and muscle damage as measured by blood examinations [13,31,32]. Such effects are expected from an agent, such as GHF-201, capable of inducing the catabolism of liver glycogen with an ensuing rise in blood glucose and reduction in compensatory lipid flux to the liver. Our blood metabolic panel results show that GHF-201 is able to correct hypoglycemia and hyperlipidemia and partially restore muscle (creatine kinase) and liver (alanine transferase) damage, all of which characteristically accrue with time in the $Agl^{-/-}$ GSDIII mouse model (Figure 3).

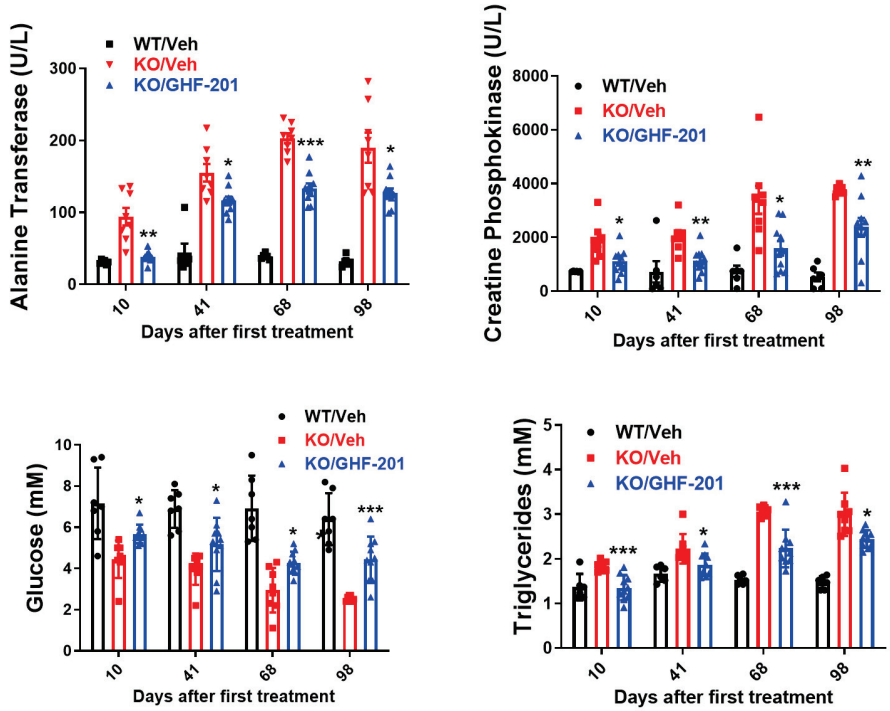


Figure 3. Blood metabolic panel based on n = 8 $Agl^{-/-}$ mice treated with 10% DMSO vehicle (KO/Veh), n = 6 wild type mice treated with vehicle (WT/Veh), and n = 10 $Agl^{-/-}$ mice treated with GHF-201, as indicated. At all time points, GHF-201 significantly reduced alanine transferase and creatine phosphokinase, demonstrating partial restoration of liver and muscle damages, respectively. Additionally, blood glucose was increased, and blood triglycerides were decreased by GHF-201 in treated $Agl^{-/-}$ mice. Statistical significance between KO/Veh and KO/GHF-201 at the different time points was determined by Two Way ANOVA with repeated measures with a Tukey post hoc test according to simple effects within rows (i.e., times). *, $0.01 < p < 0.05$; **, $0.001 < p < 0.01$; ***, $p < 0.001$.

3.4. In Vivo Metabolic Profile

The effect of GHF-201 on various in vivo metabolic parameters was determined by indirect calorimetry. Fuel preference at the whole animal level is determined by the respiratory exchange ratio (RER, the ratio of CO_2 produced to O_2 consumed). Lower RER indicates higher fat burn, while higher RER indicates higher carbohydrate burn. As our results (Figure 4(A1)) show, $Agl^{-/-}$ mice had lower RER values in the light, dark, and overall (positive mean difference in the black and red bar graphs indicates that WT/Veh levels are higher than KO/Veh and KO/GHF-201, respectively; negative mean difference indicates that they are lower). GHF-201 significantly increased RER in treated v. untreated $Agl^{-/-}$ mice in light, dark, and overall (blue bars; positive values indicate KO/Veh > KO/GHF-201, negative values indicate KO/GHF-201 > KO/Veh). However, as compared to WT mice, GHF-201 treated $Agl^{-/-}$ mice still had a significantly reduced RER in all periods (red bars). Total energy expenditure (TEE, Figure 4(A3)) was slightly reduced in $Agl^{-/-}$ mice as compared to WT mice (black bars). Like RER, TEE in $Agl^{-/-}$ mice was also significantly increased by GHF-201 in light and dark conditions and overall (blue bars), with the most significant increase ($p < 0.001$) in the light condition (*cf.* $p < 0.05$ for dark and overall). Compared to WT, TEE in GHF-201-treated $Agl^{-/-}$ mice was increased in the light but remained lower than WT in the dark and overall (red bars). Thus, GHF-201 treatment dramatically increased TEE in $Agl^{-/-}$ mice, where it was slightly reduced as compared to WT. GHF-201 correction of TEE can also be revealed by our ANCOVA analysis (Figure 4(A2),(A4)), performed on light and overall periods, where the TEE effect was the most pronounced, which also accounts for the dependence of TEE on body weight. According to the ANCOVA analysis, GHF-201 corrected weight-adjusted TEE to WT levels: the difference between WT and $Agl^{-/-}$ in light

and overall conditions became insignificant when $Agl^{-/-}$ mice were treated with GHF-201. Importantly, similar to TEE correction to WT level by GHF-201, a significant difference in TEE between vehicle- and GHF-201-treated $Agl^{-/-}$ mice is also revealed by ANCOVA only under the light condition. As opposed to RER and TEE, fat oxidation (Figure 4(A5)) in $Agl^{-/-}$ mice was higher than in WT mice in all periods (black bars). GHF-201 increased fat oxidation in $Agl^{-/-}$ mice only in the light (blue bar) and maintained the higher rate of fat oxidation in $Agl^{-/-}$ as compared to WT mice (red bars). On the other hand, carbohydrate burning was compromised in $Agl^{-/-}$ mice as compared to WT with (red bars) or without (black bars) GHF-201 treatment (Figure 4(A6)). However, GHF-201 increased carbohydrate burning in $Agl^{-/-}$ mice, where it was compromised, strongly suggesting that the compound can increase glycogen catabolism. This is a therapeutic advantage as the accumulated, poorly digested, and malconstructed glycogen in GSDIII is considered a pathogenic factor. Ambulatory activity (Figure 4(B1)) was compromised in $Agl^{-/-}$ mice, as compared to WT, in all periods (black bars). This was corrected in $Agl^{-/-}$ mice by GHF-201 again only in the light (blue bars). Similar to the weight-corrected TEE (Figure 4(A2),(A4)), the ambulatory activity of $Agl^{-/-}$ mice was also rescued to WT level by GHF-201, but again only in the light period (red bar, no significant difference from WT after treatment). While no statistically significant difference between WT and $Agl^{-/-}$ mice was observed for the distance of wheel running (Figure 4(B2), black bars), GHF-201 did increase wheel running distance in $Agl^{-/-}$ mice in the light and overall periods (blue bars). This increase caused wheel running distance in $Agl^{-/-}$ mice to be significantly increased, in the light and overall periods, as compared to WT mice (red bars). Stimulation of wheel running and correction of ambulatory activity in the light (Figure 4B) are in line with open field results (Figure 2A), also acquired in the light, and with the GHF-201-mediated stimulation of carbohydrate catabolism. Together, these results suggest that GHF-201 can improve metabolic efficacy, compromised by the diseased state, at the whole animal level. Compared to WT mice, food intake (Figure 4(C1)) was not significantly modified in $Agl^{-/-}$ mice in the light and was reduced in the dark and overall (black bars). GHF-201 did not exert a significant effect on food intake, possibly excluding an increase in overall food intake which was masked by a large outlier effect of an animal in which GHF-201 reduced, rather than increased, food intake (Figure 4(C1), blue bars). Excluding this outlier, an increase in overall food uptake would have been similar to that observed in the GSDIV mouse model [20]. GHF-201 also did not reverse the reduction in food intake in $Agl^{-/-}$ mice compared to WT mice (red bars). Water uptake, on the other hand, also reduced in all periods in $Agl^{-/-}$ mice compared to WT (Figure 4(C2), black bars), was corrected by GHF-201 in $Agl^{-/-}$ mice in the dark and overall (blue bars). Nevertheless, this correction could not overcome the reduced extent of water intake in $Agl^{-/-}$ mice as compared to WT (red bars). As opposed to food intake, the effect of GHF-201 on water intake was similar in direction and in statistical significance to its effect in GSDIV mice [20]. The GHF-201-mediated increase in water intake was mainly observed in the dark (and, subsequently, overall), where activity and water (and food) consumption are normally increased in mice. A GHF-201-mediated increase in water intake with a parallel increase in fuel burning (Figure 2A) constitutes an improvement in metabolic efficiency. Please note that both food and water intake plots are cumulative and thus diverge from, rather than converge with, one another with time.

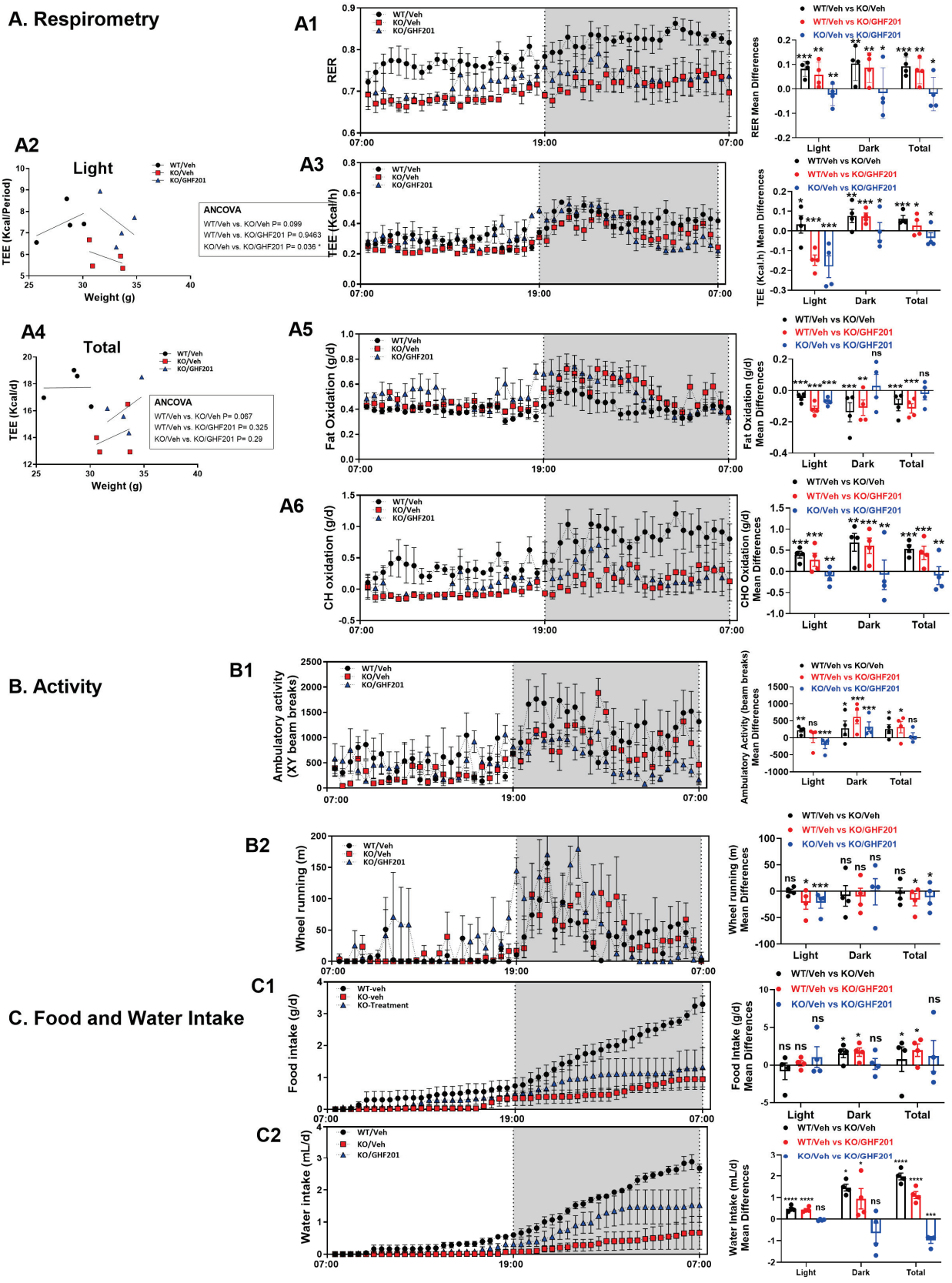


Figure 4. Indirect calorimetry and metabolic cage analysis. Following a 48 h habituation period, mice (n = 4 from each study arm indicated) were monitored over a 24 h period. Data are mean ± SEM from

eight-month-old mice. ((**A**)—Respirometry) As demonstrated by the positive mean differences, in the light, dark, and overall (total), vehicle-treated $Agl^{-/-}$ mice demonstrate lower respiratory exchange ratio (RER, (**A1**)), total energy expenditure (TEE, (**A2**–**A4**)), and carbohydrate oxidation (**A6**). As shown by the negative mean differences, fat oxidation was reduced in $Agl^{-/-}$ mice in light, dark, and overall as compared to WT mice (**A5**). All these parameters were increased or corrected by GHF-201 at all times, except for fat oxidation in the dark and overall (**A4**). ANCOVA results suggest that weight-dependent TEE is reduced in $Agl^{-/-}$ compared to WT mice in both the light condition (**A2**) and overall (**A4**), and that GHF-201 corrects this TEE reduction in $Agl^{-/-}$ mice in the light. ((**B**)—Activity) Ambulatory activity (**B1**) and wheel running (**B2**) were also increased (corrected), or not affected, by GHF-201 as indicated. ((**C**)—Food and Water Intake) Food intake (**C1**) was not significantly affected, and water intake ((**C2**), total cumulative values are shown in the bar graphs) was increased, mainly in the dark period, by GHF-201. Statistical significance of mean differences was determined by One Way ANOVA with repeated measures with a Tukey post hoc test. *, $0.01 < p < 0.05$; **, $0.001 < p < 0.01$; ***, $p < 0.001$; ****, $p < 0.0001$; ns, non-significant.

3.5. Muscle Glycogen Quantification

Blinded quantification by transmission EM (TEM) of gastrocnemius muscle sections showed that in muscle sections derived from GSDIII mice, a higher percentage of the area was occupied by dense glycogen granules as compared to muscle sections derived from wild type mice (Figure 5A). Myofibrils in GSDIII muscle sections were also more dissociated than wild type myofibrils due to the increased glycogen storage (Figure 5B). Both increase in glycogen granule area and myofibril dissociation were significantly corrected (even though not to wild type levels) by the GHF-201 treatment. Additional TEM images are shown in Supplementary Figure S1. These results were corroborated by a biochemical analysis of glycogen content in the same muscle sections (Figure 5C).

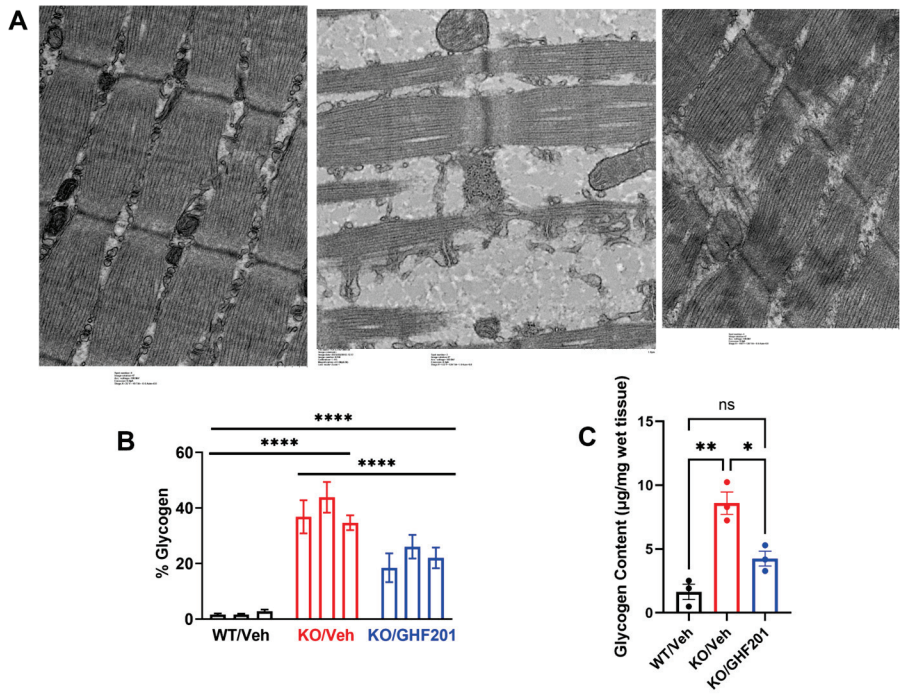


Figure 5. (**A**) Representative transmission electron microscopy images of longitudinal sections of *gastrocnemius* muscle collected from 8-month-old animals treated as indicated. Note granular glycogen material interspersing sarcomeres in the section from untreated $Agl^{-/-}$ mouse. Also note variable width of sarcomeres in $Agl^{-/-}$ mouse sample. These ultrastructural phenotypes were partially corrected in GHF-201-treated $Agl^{-/-}$ mouse. (**B**) Quantification of area percent of glycogen

based on analysis of TEM images from n = 3 animals. ****, significant differences between arms ($p < 0.0001$, Two Way ANOVA (factors are "animal" and "arm") with Tuckey post hoc correction). (**C**) Biochemical quantification of *Gastrocnemius* glycogen. Glycogen levels in muscle tissues collected from n = 3 mice/arm were determined by Merck's glycogen assay kit and statistically analyzed by One Way ANOVA with Tuckey post hoc correction. *, $p < 0.05$; **, $p < 0.01$, ns, $p < 0.08$.

3.6. Glycogen Levels, Lysosomal and Mitochondrial Features of GSDIII Patient-Derived Skin Fibroblasts

Consistent with the results in gastrocnemius muscle, in skin fibroblasts derived from GSDIII patients, GHF-201 also reduced glycogen levels and rendered them similar (not statistically different) to those of HC fibroblasts, as determined by periodic acid-Schiff's reagent (PAS) staining (Figure 6A). This result suggests that the mechanism of action by which GHF-201 alleviated GSDIII symptoms in mice is autolysosomal degradation of glycogen, which is known to be mediated by GHF-201 in GSDIV [20] and GSDIa [21].

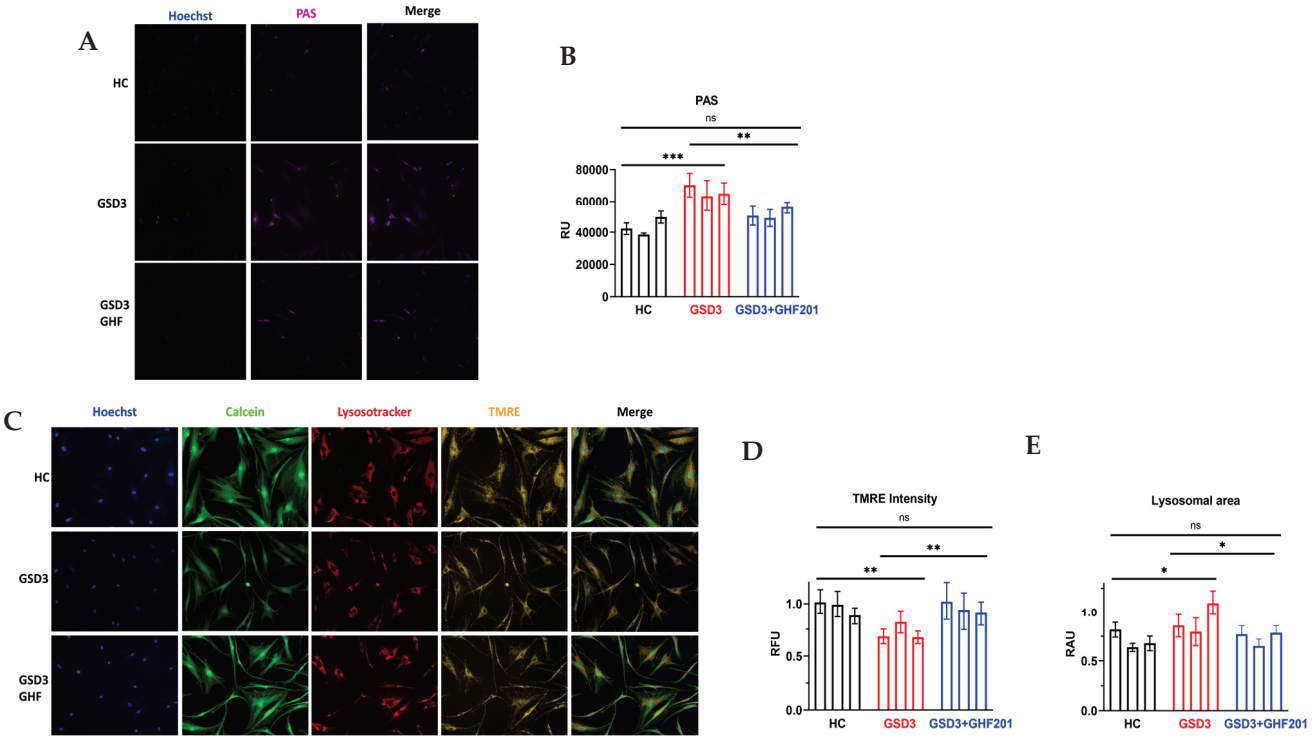


Figure 6. Skin fibroblasts from 3 GSD3 and 3 HC individuals were cultured in 96-well plates for 48 h in starvation medium without FBS and glucose. Subsequently, cells were live-stained with (**A**,**B**) PAS reagent to quantify intracellular glycogen, or (**C**–**E**) a mix of fluorescent dyes which included Hoechst, Calcein-AM, TMRE, and Lysortracker red to, respectively, stain nuclei (blue), cytoplasm (green), respiring mitochondria (yellow), and lysosomes (red). Multiple images from the live-stained cells were automatically obtained by an Operetta G1 image analyzer under environmentally controlled conditions. Shown are representative images and their quantification in relative units. Statistical significance of differences was determined by Two Way ANOVA with Tuckey post hoc correction. *, $p < 0.05$; **, $0.001 < p < 0.01$; ***, $p < 0.001$; ns, not significant.

To confirm GHF-201 mechanism of action at a cellular level, we decided to test its effects on lysosomal and mitochondrial features in fibroblasts derived from GSDIII patients. Since GHF-201 is an autophagic and catabolic activator, we anticipated that its significant effect at a cellular level will be at the lysosomal–mitochondrial axis, as shown, for instance, in GSDII [33]. Our results (Figure 6B) show that under starvation, which induces autophagic flux, GHF-201 reduced the lysosomal area, bringing it close to the area observed

in HC fibroblasts. Reduced lysosomal area was also observed in other systems in healthy as compared to lysosomal impaired cells [34] and is presumably associated with increased autophagic flux and lysosomal function, which can clear overladen lysosomes from their excess content and thus reduce their size, which is increased by the lysosomal swelling this excess content causes. Mitochondrial depolarization was observed in GSDIII patient fibroblasts as compared to HC fibroblasts. This mitochondrial depolarization is probably associated with the limited glycogen degradation and carbohydrate fuel production characteristic of GSDIII (Figure 4A). In accordance with an increase in mitochondrial fueling by enhanced sutophagic catabolism, GHF-201 treatment repolarized mitochondrial membrane potential, bringing it closer to that of HC fibroblasts (Figure 6C).

4. Discussion

The long-term aim of this study was to test the capacity of GHF-201 to alleviate disease symptoms in the $Agl^{-/-}$ mouse model of GSDIII. GHF-201 specifically binds the lysosomal membrane protein LAMP1 [20]. GHF-201 was further able to re-acidify the aberrant alkaline lysosomal pH. In adult GSDIV (APBD) models, GHF-201 ameliorated the diseased state by enhancing lysosomal glycogen catabolism and autophagy.

GSDIII starts with liver involvement followed by storage of glycogen in skeletal muscle, provoking a myopathy. The disease is caused by cytoplasmic glycogen debranching enzyme (GDE) deficiency leading to accumulation of glycogen due to its reduced degradation. Glycogen accumulation in muscle is more extensive in GSDIII as compared to the other myopathy-implicating GSDs GSDII, GSDV, GSDIX, GSDX, and GSDXV [11]. In particular, human muscle biopsies from GSDIII patients show a typical and constant vacuolar myopathy, characterized by multiple and variably sized vacuoles filled with PAS-positive material [9]. Phosphorylase-limit dextrin (PLD), the type of glycogen which accumulates in GSDIII, is structurally abnormal, containing shorter outer branches [12]. While PLD is sensitive to diastase digestion and does not form polyglucosan bodies [12], it is still associated with large vacuoles and can cause histological damage to myofibrils [13,18]. In fact, as also shown by our results (Figure 5), disruption of myofibrillar structure by glycogen vacuoles is more pronounced in GSDIII than in other GSDs with prominent muscular involvement [11].

After the liver disorder, myopathy pursues [15], with occasional cardiomyopathy [16], and at later stages liver cirrhosis, and hepatocellular adenoma [17]. Interestingly, possibly due to higher overall glycogen accumulation, GSDIII manifests with excess glycogen in both cytoplasm and lysosomes, as opposed to GSDII, where excess glycogen is primarily found in lysosomes due to the aberrant function of GAA [35]. The main pathogenic factor in GSDIII, as revealed by ultrastructural analysis of muscle specimens from patients, is autophagosome accumulation. Concordantly, Laforet et al., using electron microscopy, showed the presence of large non-membrane bound sarcoplasmic deposits of normally structured glycogen as well as smaller rounded sac structures lined by a continuous double membrane containing only glycogen, corresponding to autophagosomes. A consistent SQSTM1/p62 decrease and beclin-1 increase in human muscle biopsies suggested autophagic dysregulation [9]. The latter can impede the degradation of dysfunctional organelles and proteins, and, notably, also of glycogen, in a specific pathway mediated by the starch binding domain-containing protein 1 (Stbd1), which tags glycogen for its autophagy, interacting with autophagy machinery and glycogen-related proteins, including GDE, in other domains [36]. Interestingly, among these glycogen-related proteins, GDE has the highest number of Atg8 binding motifs [36], also suggesting an important role of autophagy in GSDIII, which might take place if GDE deficiency impairs the interaction with the autophagy machinery. Moreover, dysfunctional autophagy plays a pivotal role in disrupting muscle homeostasis and causing structural damage to sarcomeres [37]. The tight link between autophagic impairment and GSDIII pathology can, thus, explain the beneficial effects of GHF-201, a general autophagic activator [20], in improving motor function (Figure 2) and skeletal muscle health (Figure 5) in a GSDIII mouse model. Other

possible systemic effects of GHF-201, unrelated to autophagy enhancement, probably do not contribute to the beneficial effect of GHF-201, as it did not influence animal weight gain and histology in the long-term and behavior (Irwin test) in the short-term [20]. Even though the effect of GHF-201 on motor and behavioral features was not tested in WT mice, we assume that the beneficial effect of GHF-201 is specific to $Agl^{-/-}$ mice because PLD accumulation in this strain disrupts muscle structure (Figure 5 and Supplementary Figure S1). Therefore, partial removal of this pathogenic PLD in $Agl^{-/-}$ mice can more noticeably relieve the motor dysfunction caused by the disrupted muscle structure than in WT mice where such a disruption and consequent motor dysfunction do not exist. However, since autophagy and autophagic catabolism are generally considered cell protective and energy producing, GHF-201 might possibly improve animal health in general, even in WT mice.

Our blood biochemistry panel demonstrated that GHF-201 treatment led to improved liver and muscle function and partially corrected blood hypoglycemia and hypertriglyceridemia (Figure 3), also observed in GSDIII patients [38]. Both hypoglycemia and hyperlipidemia are expected outcomes of glycogen surcharge since more glucose is shunted from blood to intracellular glycogen and since high glycogen levels can inhibit the energy sensor AMPK [39–42], leading to activation of acetyl CoA carboxylase, the rate-limiting enzyme of fatty acid synthesis, which is phospho-inhibited by AMPK. Reduction of glycogen levels by GHF-201 (Figure 5) expectedly mitigated this hyperlipidemia. The blood lipid profile can also reflect fuel utilization. As glycogen mobilization is compromised in GSDIII and enhanced by GHF-201, we expected that GSDIII mice use lipid instead of carbohydrate fuel as a compensatory reaction. However, as suggested by the hypertriglyceridemia observed in untreated GSDIII mice (Figure 3), the mice are not capable of this metabolic compensation. Notably, as revealed by both indirect calorimetry (Figure 4) and the blood biochemistry panel (Figure 3), GHF-201 treatment enabled this metabolic compensation by boosting fat burn in the light (Figure 4), which is possibly reflected in the reduction in blood triglyceride levels (Figure 3). A similar effect of GHF-201 was observed in the GSDIV modeling $Gbe^{ys/ys}$ mice [20]. Interestingly, GHF-201-mediated improvement of fat oxidation (Figure 4A), and other in vivo metabolic effects (TEE, (Figure 4A), ambulatory activity (Figure 4B), and wheel running (Figure 2B)) were more pronounced in the light than in the dark. Since mice are nocturnal animals, in which food is mostly consumed in the dark (see also Figure 4C) and digested in the light, it can be conjectured that GHF-201, affecting fuel digestion, or autophagic substrate catabolism, exerts a larger effect in the light. Along these lines, a possible explanation for the GHF201-associated decrease of activity in the dark is that the untimely stimulation of fuel-generating catabolism in the dark (Figure 4(B1)) might lead to fuel excess known to be detrimental as it might lead to mitochondrial fragmentation in pancreatic beta cells [42] and unbalanced reactive oxygen species (ROS) production [43]. However, the fact that GHF-201 increased ambulatory activity in the dark in GSDIV modeling mice [20], while decreasing it in GSDIII modeling mice (Figure 4(B1)), calls for an explanation. One important difference between these two diseases is that in GSDIV patients, and in GSDIV-modeling mice, polyglucosan bodies (PB) formed by brancher deficiency are architecturally different from phosphorylase-limit dextrin in GSDIII formed by debrancher deficiency. The large size and unique amylopectin architecture of PB in GSDIV models causes them to clog axons, which is not the case for the aberrant glycogen (phosphorylase-limit dextrin) in GSDIII. Therefore, PB-clearance from axons and peripheral nerve by GHF-201 in a GSDIV mouse model [20] might enhance mobility by improving nerve–muscle communication. This clearance of the noxious PB from axons and neuromuscular junctions might override the putative detrimental effect of excess fuel in the dark and so might be more important for locomotion and enhance it also in the dark in GSDIV mice, as opposed to GSDIII mice.

In conclusion, we show here that GHF-201, a LAMP-1-targeting small molecule acting as a general activator of autophagic flux, can partially correct aberrant metabolic, motor, and myopathological phenotypes in the $Agl^{-/-}$ mouse model of GDE deficiency, or GSDIII, a disease implicating a particularly high glycogen burden, causing liver and myofibrillar injury.

Supplementary Materials: The following supporting information can be downloaded at https://www.mdpi.com/article/10.3390/biom14080893/s1, Figure S1: An additional representative transmission electron microscopy images of longitudinal sections of gastrocnemius muscle collected from 8-month-old animals treated as indicated.

Author Contributions: Conceptualization, O.K., M.W. and E.M.; Methodology, K.M., S.S., S.B. (Saja Baraghithy), U.S., M.M., S.B. (Sultan Bastu) and H.G.; Writing—original draft preparation, O.K.; Writing—review and editing, M.W. and E.M.; Supervision, J.T., H.R., M.W., E.M. and O.K.; funding acquisition, M.W., E.M. and O.K. All authors have read and agreed to the published version of the manuscript.

Funding: This research was funded by the Association Francaise contre les Myopathies, grant number 23116. The PhD scholarship of US was partly paid by the Yoran Institute of Genome Research and Personalized Medicine and by the Tel Aviv University Prajs-Drimmer Institute for the Development of Anti-Degenerative Drugs.

Institutional Review Board Statement: The animal study protocol was approved by the Institutional Review Board (or Ethics Committee) of THE HEBREW UNIVERSITY OF JERUSALEM (protocol code 16403 and date of approval 30 March 2022).

Informed Consent Statement: Not applicable.

Data Availability Statement: Data is contained within the article. The original contributions presented in the study are included in the article. Further inquiries can be directed to the corresponding authors.

Acknowledgments: The authors wish to thank Eran Perlson from Tel Aviv University for his help in the collection and preparation of the muscle samples and Giuseppe Ronzitti from Genethon, France, for providing the mice used in this study.

Conflicts of Interest: O.K. and M.W. are advisors to the company Golden Heart Flower (GHF) to which GHF-201 is sublicensed. The remaining authors declare that the research was conducted in the absence of any commercial or financial relationships that could be construed as a potential conflict of interest.

References

1. Illingworth, B.; Larner, J.; Cori, G.T. Structure of glycogens and amylopectins. I. Enzymatic determination of chain length. *J. Biol. Chem.* **1952**, *199*, 631–640. [CrossRef]
2. Smythe, C.; Cohen, P. The discovery of glycogenin and the priming mechanism for glycogen biogenesis. *Eur. J. Biochem.* **1991**, *200*, 625–631. [CrossRef] [PubMed]
3. Testoni, G.; Duran, J.; García-Rocha, M.; Vilaplana, F.; Serrano, A.L.; Sebastián, D.; López-Soldado, I.; Sullivan, M.A.; Slebe, F.; Vilaseca, M.; et al. Lack of Glycogenin Causes Glycogen Accumulation and Muscle Function Impairment. *Cell Metab.* **2017**, *26*, 256–266.e254. [CrossRef] [PubMed]
4. Adeva-Andany, M.M.; Gonzalez-Lucan, M.; Donapetry-Garcia, C.; Fernandez-Fernandez, C.; Ameneiros-Rodriguez, E. Glycogen metabolism in humans. *BBA Clin.* **2016**, *5*, 85–100. [CrossRef]
5. Prats, C.; Graham, T.E.; Shearer, J. The dynamic life of the glycogen granule. *J. Biol. Chem.* **2018**, *293*, 7089–7098. [CrossRef] [PubMed]
6. Froese, D.S.; Michaeli, A.; McCorvie, T.J.; Krojer, T.; Sasi, M.; Melaev, E.; Goldblum, A.; Zatsepin, M.; Lossos, A.; Alvarez, R.; et al. Structural basis of glycogen branching enzyme deficiency and pharmacologic rescue by rational peptide design. *Hum. Mol. Genet.* **2015**, *24*, 5667–5676. [CrossRef] [PubMed]
7. Brereton, M.F.; Rohm, M.; Shimomura, K.; Holland, C.; Tornovsky-Babeay, S.; Dadon, D.; Iberl, M.; Chibalina, M.V.; Lee, S.; Glaser, B.; et al. Hyperglycaemia induces metabolic dysfunction and glycogen accumulation in pancreatic β-cells. *Nat. Commun.* **2016**, *7*, 13496. [CrossRef]
8. Ashcroft, F.M.; Rohm, M.; Clark, A.; Brereton, M.F. Is Type 2 Diabetes a Glycogen Storage Disease of Pancreatic β Cells? *Cell Metab.* **2017**, *26*, 17–23. [CrossRef]
9. Laforêt, P.; Inoue, M.; Goillot, E.; Lefeuvre, C.; Cagin, U.; Streichenberger, N.; Leonard-Louis, S.; Brochier, G.; Madelaine, A.; Labasse, C.; et al. Deep morphological analysis of muscle biopsies from type III glycogenesis (GSDIII), debranching enzyme deficiency, revealed stereotyped vacuolar myopathy and autophagy impairment. *Acta Neuropathol. Commun.* **2019**, *7*, 167. [CrossRef]
10. Schreuder, A.; Rossi, A.; Grünert, S.; Derks, T. *Glycogen Storage Disease type III (GeneReviews® [Internet])*; University of Washington: Seattle, WA, USA, 2010.
11. Hannah, W.B.; Derks, T.G.J.; Drumm, M.L.; Grünert, S.C.; Kishnani, P.S.; Vissing, J. Glycogen storage diseases. *Nat. Rev. Dis. Primers* **2023**, *9*, 46. [CrossRef]

12. Kishnani, P.S.; Austin, S.L.; Arn, P.; Bali, D.S.; Boney, A.; Case, L.E.; Chung, W.K.; Desai, D.M.; El-Gharbawy, A.; Haller, R.; et al. Glycogen storage disease type III diagnosis and management guidelines. *Genet. Med.* **2010**, *12*, 446–463. [CrossRef] [PubMed]
13. Vidal, P.; Pagliarani, S.; Colella, P.; Costa Verdera, H.; Jauze, L.; Gjorgjieva, M.; Puzzo, F.; Marmier, S.; Collaud, F.; Simon Sola, M.; et al. Rescue of GSDIII Phenotype with Gene Transfer Requires Liver- and Muscle-Targeted GDE Expression. *Mol. Ther.* **2018**, *26*, 890–901. [CrossRef] [PubMed]
14. DiMauro, S. *Myology*; mcGraw-Hill: New York, NY, USA, 1985; pp. 1535–1558.
15. Decostre, V.; Laforêt, P.; De Antonio, M.; Kachetel, K.; Canal, A.; Ollivier, G.; Nadaj-Pakleza, A.; Petit, F.M.; Wahbi, K.; Fayssoil, A.; et al. Long term longitudinal study of muscle function in patients with glycogen storage disease type IIIa. *Mol. Genet. Metab.* **2017**, *122*, 108–116. [CrossRef]
16. Valayannopoulos, V.; Bajolle, F.; Arnoux, J.B.; Dubois, S.; Sannier, N.; Baussan, C.; Petit, F.; Labrune, P.; Rabier, D.; Ottolenghi, C.; et al. Successful treatment of severe cardiomyopathy in glycogen storage disease type III With D,L-3-hydroxybutyrate, ketogenic and high-protein diet. *Pediatr. Res.* **2011**, *70*, 638–641. [CrossRef] [PubMed]
17. Demo, E.; Frush, D.; Gottfried, M.; Koepke, J.; Boney, A.; Bali, D.; Chen, Y.T.; Kishnani, P.S. Glycogen storage disease type III-hepatocellular carcinoma a long-term complication? *J. Hepatol.* **2007**, *46*, 492–498. [CrossRef]
18. DiMauro, S.; Hartwig, G.B.; Hays, A.; Eastwood, A.B.; Franco, R.; Olarte, M.; Chang, M.; Roses, A.D.; Fetell, M.; Schoenfeldt, R.S.; et al. Debrancher deficiency: Neuromuscular disorder in 5 adults. *Ann. Neurol.* **1979**, *5*, 422–436. [CrossRef] [PubMed]
19. Peng, S.S.; Hwu, W.L.; Lee, N.C.; Tsai, F.J.; Tsai, W.H.; Chien, Y.H. Slow, progressive myopathy in neonatally treated patients with infantile-onset Pompe disease: A muscle magnetic resonance imaging study. *Orphanet J. Rare Dis.* **2016**, *11*, 63. [CrossRef]
20. Kakhlon, O.; Vaknin, H.; Mishra, K.; D'Souza, J.; Marisat, M.; Sprecher, U.; Wald-Altman, S.; Dukhovny, A.; Raviv, Y.; Da'adoosh, B.; et al. Alleviation of a polyglucosan storage disorder by enhancement of autophagic glycogen catabolism. *EMBO Mol. Med.* **2021**, *13*, e14554. [CrossRef]
21. Sprecher, U.; D'Souza, J.; Mishra, K.; Canella Miliano, A.; Mithieux, G.; Rajas, F.; Avraham, S.; Anikster, Y.; Kakhlon, O.; Weil, M. Imprinted cell memory in glycogen storage disorder 1a. *bioRxiv* **2023**. [CrossRef]
22. Koeberl, D.D.; Koch, R.L.; Lim, J.A.; Brooks, E.D.; Arnson, B.D.; Sun, B.; Kishnani, P.S. Gene therapy for glycogen storage diseases. *J. Inherit. Metab. Dis.* **2024**, *47*, 93–118. [CrossRef]
23. Yi, H.; Brooks, E.D.; Thurberg, B.L.; Fyfe, J.C.; Kishnani, P.S.; Sun, B. Correction of glycogen storage disease type III with rapamycin in a canine model. *J. Mol. Med.* **2014**, *92*, 641–650. [CrossRef] [PubMed]
24. Higazi, A.A.; Maraga, E.; Baraghithy, S.; Udi, S.; Azar, S.; Saada, A.; Glaser, B.; Avrahami, D.; Abdeen, S.; Hamdan, Z.; et al. Characterization of metabolic alterations in the lean metabolically unhealthy alpha defensin transgenic mice. *iScience* **2024**, *27*, 108802. [CrossRef] [PubMed]
25. Caicedo, J.C.; Cooper, S.; Heigwer, F.; Warchal, S.; Qiu, P.; Molnar, C.; Vasilevich, A.S.; Barry, J.D.; Bansal, H.S.; Kraus, O.; et al. Data-analysis strategies for image-based cell profiling. *Nat. Methods* **2017**, *14*, 849–863. [CrossRef] [PubMed]
26. Charan, J.; Kantharia, N.D. How to calculate sample size in animal studies? *J. Pharmacol. Pharmacother.* **2013**, *4*, 303–306. [CrossRef]
27. Liu, K.M.; Wu, J.Y.; Chen, Y.T. Mouse model of glycogen storage disease type III. *Mol. Genet. Metab.* **2014**, *111*, 467–476. [CrossRef] [PubMed]
28. Kamel, A.S.; Mohamed, A.F.; Rabie, M.A.; Elsherbiny, M.E.; Ahmed, K.A.; Khattab, M.M.; Abdelkader, N.F. Experimental Evidence for Diiodohydroxyquinoline-Induced Neurotoxicity: Characterization of Age and Gender as Predisposing Factors. *Pharmaceuticals* **2022**, *15*, 251. [CrossRef] [PubMed]
29. Lundblad, M.; Vaudano, E.; Cenci, M.A. Cellular and behavioural effects of the adenosine A2a receptor antagonist KW-6002 in a rat model of l-DOPA-induced dyskinesia. *J. Neurochem.* **2003**, *84*, 1398–1410. [CrossRef] [PubMed]
30. Hassan, M.P.; Abdollahifar, M.A.; Aliaghaei, A.; Tabeie, F.; Vafaei-Nezhad, S.; Norouzian, M.; Abbaszadeh, H.A. Photobiomodulation therapy improved functional recovery and overexpression of interleukins-10 after contusion spinal cord injury in rats. *J. Chem. Neuroanat.* **2021**, *117*, 102010. [CrossRef]
31. Lucchiari, S.; Pagliarani, S.; Salani, S.; Filocamo, M.; Di Rocco, M.; Melis, D.; Rodolico, C.; Musumeci, O.; Toscano, A.; Bresolin, N.; et al. Hepatic and neuromuscular forms of glycogenosis type III: Nine mutations in AGL. *Hum. Mutat.* **2006**, *27*, 600–601. [CrossRef]
32. Lucchiari, S.; Santoro, D.; Pagliarani, S.; Comi, G.P. Clinical, biochemical and genetic features of glycogen debranching enzyme deficiency. *Acta Myol.* **2007**, *26*, 72–74.
33. Lim, J.A.; Li, L.; Kakhlon, O.; Myerowitz, R.; Raben, N. Defects in calcium homeostasis and mitochondria can be reversed in Pompe disease. *Autophagy* **2015**, *11*, 385–402. [CrossRef] [PubMed]
34. de Araujo, M.E.G.; Liebscher, G.; Hess, M.W.; Huber, L.A. Lysosomal size matters. *Traffic* **2020**, *21*, 60–75. [CrossRef] [PubMed]
35. Nascimbeni, A.C.; Fanin, M.; Masiero, E.; Angelini, C.; Sandri, M. The role of autophagy in the pathogenesis of glycogen storage disease type II (GSDII). *Cell Death Differ.* **2012**, *19*, 1698–1708. [CrossRef] [PubMed]
36. Koutsifeli, P.; Varma, U.; Daniels, L.J.; Annandale, M.; Li, X.; Neale, J.P.H.; Hayes, S.; Weeks, K.L.; James, S.; Delbridge, L.M.D.; et al. Glycogen-autophagy: Molecular machinery and cellular mechanisms of glycophagy. *J. Biol. Chem.* **2022**, *298*, 102093. [CrossRef] [PubMed]
37. Margeta, M. Autophagy Defects in Skeletal Myopathies. *Annu. Rev. Pathol.* **2020**, *15*, 261–285. [CrossRef] [PubMed]
38. LaBarbera, M.; Milechman, G.; Dulbecco, F. Premature coronary artery disease in a patient with glycogen storage disease III. *J. Invasive Cardiol.* **2010**, *22*, E156–E158. [PubMed]

39. Mobbs, J.I.; Koay, A.; Di Paolo, A.; Bieri, M.; Petrie, E.J.; Gorman, M.A.; Doughty, L.; Parker, M.W.; Stapleton, D.I.; Griffin, M.D.; et al. Determinants of oligosaccharide specificity of the carbohydrate-binding modules of AMP-activated protein kinase. *Biochem. J.* **2015**, *468*, 245–257. [CrossRef] [PubMed]
40. Li, X.; Wang, L.; Zhou, X.E.; Ke, J.; de Waal, P.W.; Gu, X.; Tan, M.H.; Wang, D.; Wu, D.; Xu, H.E.; et al. Structural basis of AMPK regulation by adenine nucleotides and glycogen. *Cell Res.* **2015**, *25*, 50–66, Erratum in *Cell Res.* **2015**, *25*, 398. [CrossRef] [PubMed]
41. Koay, A.; Woodcroft, B.; Petrie, E.J.; Yue, H.; Emanuelle, S.; Bieri, M.; Bailey, M.F.; Hargreaves, M.; Park, J.T.; Park, K.H.; et al. AMPK beta subunits display isoform specific affinities for carbohydrates. *FEBS Lett.* **2010**, *584*, 3499–3503. [CrossRef]
42. Alan, L.; Scorrano, L. Shaping fuel utilization by mitochondria. *Curr. Biol.* **2022**, *32*, R618–R623. [CrossRef]
43. Fisher-Wellman, K.H.; Gilliam, L.A.A.; Lin, C.T.; Cathey, B.L.; Lark, D.S.; Darrell Neufer, P. Mitochondrial glutathione depletion reveals a novel role for the pyruvate dehydrogenase complex as a key H_2O_2-emitting source under conditions of nutrient overload. *Free Radic. Biol. Med.* **2013**, *65*, 1201–1208. [CrossRef] [PubMed]

Disclaimer/Publisher's Note: The statements, opinions and data contained in all publications are solely those of the individual author(s) and contributor(s) and not of MDPI and/or the editor(s). MDPI and/or the editor(s) disclaim responsibility for any injury to people or property resulting from any ideas, methods, instructions or products referred to in the content.

metabolites

MDPI

Review

Systematic Insights into the Relationship between the Microbiota–Gut–Brain Axis and Stroke with the Focus on Tryptophan Metabolism

Xinyu Shen [1,2] and Xiaoqin Mu [1,2,*]

[1] Genomics Research Center, Key Laboratory of Gut Microbiota and Pharmacogenomics of Heilongjiang Province, College of Pharmacy, Harbin Medical University, Harbin 150081, China; 15543547863@163.com
[2] Translational Medicine Research and Cooperation Center of Northern China, Heilongjiang Academy of Medical Sciences, Harbin 150081, China
* Correspondence: muxiaoqin@ems.hrbmu.edu.cn

Abstract: Stroke, as a serious cerebral vascular disease with high incidence and high rates of disability and mortality, has limited therapeutic options due to the narrow time window. Compelling evidence has highlighted the significance of the gut microbiota and gut–brain axis as critical regulatory factors affecting stroke. Along the microbiota–gut–brain axis, tryptophan metabolism further acquires increasing attention for its intimate association with central nervous system diseases. For the purpose of exploring the potential role of tryptophan metabolism in stroke and providing systematic insights into the intricate connection of the microbiota–gut–brain axis with the pathological procedure of stroke, this review first summarized the practical relationship between microbiota and stroke by compiling the latest case-control research. Then, the microbiota–gut–brain axis, as well as its interaction with stroke, were comprehensively elucidated on the basis of the basic anatomical structure and physiological function. Based on the crosstalk of microbiota–gut–brain, we further focused on the tryptophan metabolism from the three major metabolic pathways, namely, the kynurenine pathway, serotonin pathway, and microbial pathway, within the axis. Moreover, the effects of tryptophan metabolism on stroke were appreciated and elaborated here, which is scarcely found in other reviews. Hopefully, the systematic illustration of the mechanisms and pathways along the microbiota–gut–brain axis will inspire more translational research from metabolic perspectives, along with more attention paid to tryptophan metabolism as a promising pharmaceutical target in order to reduce the risk of stroke, mitigate the stroke progression, and ameliorate the stroke prognosis.

Keywords: stroke; gut microbiota; gut–brain axis; tryptophan metabolism

1. Introduction

As an acute cerebrovascular condition, stroke is one of the most important contributors to long-term disability and mortality, affecting millions of people each year worldwide. Ischemic stroke (IS) and hemorrhage stroke (HS) are the two main types of strokes, among which 87% are ischemic, 10% are intracerebral hemorrhage (ICH), and 3% are subarachnoid hemorrhage (SAH) according to the 2024 American Heart Association statistical update [1,2], implying the structural or functional damage to brain tissue caused by the blockage or rupture of cerebral blood vessels. Recent years have witnessed alarming growth as well as the youthful trend of stroke incidence with the prevalence of unhealthy lifestyle and eating habits. In the US, there is a projection that an additional 3.4 million adults over 18 will suffer a stroke by 2030 [1]. Although the therapy of stroke has improved during the past few decades, including intravenous thrombolysis, intra-arterial thrombectomy, recombinant tissue plasminogen activator therapy, and so on, it is limited due to the narrow therapeutic window, individual differences, as well as the potential risk [3].

In addition, dementia, cognitive impairment [4], anxiety, depression [5], and communication disorder [6] can be observed in a large amount of post-stroke cases. Thus, early prevention and intervention of stroke and understanding potential therapeutic targets are particularly essential.

Numerous studies suggested that intestinal disorders accompanied by gut microbial alteration, such as inflammatory bowel disease, irritable bowel syndrome, and constipation, have complex interactions with stroke [7–10]. Gastrointestinal disorders or gut dysbiosis, on the one hand, often appear as complications in stroke patients; on the other hand, they may increase the risk of stroke [11] or worsen cerebral infarction [12]. The gut environment influences brain function in many ways, involving the central nervous system (CNS), enteric nervous system (ENS), autonomic nervous system (ANS), neuroendocrine system (hypothalamic–pituitary–adrenal axis), and immune system [13]. Likewise, the brain fine-tunes gut activities. The intricate bidirectional communication system between the gastrointestinal tract (GIT) and the brain is called the gut–brain axis (GBA). Since gut microbiota act as an integral regulator in the GBA, the GBA was further extended to the microbiota–gut–brain axis (MGBA) [14].

A key component of the MGBA is tryptophan, an essential amino acid whose metabolism is directly or indirectly regulated by the gut microbiota [15]. Products of tryptophan metabolism, including 5-hydroxytryptamine (serotonin, 5-HT), kynurenines, indole derivatives, etc., exert profound impacts on the pathways related to MGBA [16]. Mounting evidence supports a clear correlation between stroke and Trp metabolism in the MGBA with regard to enzyme activities, metabolite level changes, and related genes [17–19]. Promisingly, tryptophan and its metabolites serve as potential biomarkers as well as therapeutic targets of neurological disorders, including stroke, endorsing high precision of diagnosis and alternative treatments.

In this review, we systematically summarize the mechanism of MGBA and comprehensively discuss the role of MGBA in stroke, with a focus on the correlation between tryptophan metabolism and the pathogenesis and progression of stroke, combining the latest knowledge so as to provide a reference for further exploration of the prevention, treatment, and rehabilitation of stroke.

2. Microbiota–Gut–Brain Axis and Stroke

2.1. Gut Microbiota and Stroke: Epidemiological Relationships

The gut microbiota refers to a community of myriad symbiotic microorganisms that populate the intestinal tract, which harbors over 1000 bacterial species containing more than 100 bacterial phyla [20]. In our bodies, almost 95% of commensal bacteria are dominated by the phyla Firmicutes and Bacteroidetes [21]. As a complex and dynamic metabolic network, the gut microbiota plays a considerable role in the host condition, affecting the immune, inflammation, neural, endocrine, and metabolism processes via GBA.

Emerging evidence elucidated the close relationship between gut dysbiosis and stroke. We looked back on and enumerated 16 case-control studies in the last 5 years (2019–2023) so as to more veritably present such connection (Table A1). By analyzing these case reports, we found that all studies reported differences in gut microbial composition between stroke patients and healthy controls through 16S ribosomal RNA gene sequencing. At the phylum level, the relative abundance of Proteobacteria was increased, while the Firmicutes were mostly reported decreased. At the family level, the amount of Enterobacteriaceae and *Lactobacillaceae* were significantly elevated, while Prevotellaceae were decreased. At the genus level, Lactobacillus, Streptococcus, Akkermansia, and Roseburia were usually upgraded, while Faecalibacterium were reduced. However, the changes in some bacteria, such as Ruminococcaceae, Bacteroidaceae, Coriobacteriaceae, Lachnospiraceae, and Bacteroidetes, remain controversial.

Beyond the altered microbial composition, the gut microbiota itself can be a potential biomarker of the outcome or severity of stroke, verified by the increased Enterobacter, Pyramidobacter, and Lachnospiraceae_UCG_001 in mild ischemic stroke patients, whereas the

increased genera, such as Ruminococcaceae_UCG-002 and Christensenellaceae_R-7_group, were found in severe stroke patients [22]. Xu et al. [12] elaborated that Enterobacteriaceae was the most prevalent pathogen in both an IS cohort and mice with middle cerebral artery occlusion (MCAO). In the study of Jiang et al. [23], a positive correlation between Enterobacteriaceae and the severity of IS was found, with more abundance of Enterobacteriaceae, Faecalibacterium, Lachnospiraceae, and Ruminococcaceae but lower lactic acid bacteria of Lactobacillus in the poor outcome group. Furthermore, when inoculating *E. coli*, a common species of Enterobacteriaceae, it turned out that the genes and serum biomarkers associated with immune and inflation systems apparently upgraded, which confirmed that Enterobacteriaceae is a significant influencing factor of stroke [12]. Zheng et al. [24] elucidated that gut microbiota correlated positively with systemic inflammation in cryptogenic stroke (CS) patients and attributed the high level of lipopolysaccharide (LPS) to the elevated amount of Gram-negative bacteria, such as Escherichia–Shigella and Klebsiella of the Enterobacteriaceae family.

The gut microbiota dysbiosis could potentially lead to IS pathogenesis by modulating the host's traditional risk factors as well [25]; for example, Lactobacillaceae, Enterococcaceae, Streptococcaceae, and Enterobacteriaceae families enriched in IS patients were positively correlated with high-risk factors, including high blood pressure and ApoB/ApoA1 ratio, while negatively correlated with the preventive factor, high-density lipoprotein cholesterol (HDL-C), in the IS patients. Moreover, age, regional, and ethnic variations did make a difference in ischemic stroke when referring to the gut microbiota's taxonomic changes during the disease.

2.2. Mechanisms of the Gut–Brain Axis in Stroke

In this section, we outline the basic anatomical structure and physiology of the gut–brain axis along with the vital impact of microbiota. On that basis, we have illustrated alterations of the MGBA in stroke to provide a comprehensive understanding of the MGBA as well as its association with stroke. To be specific, this section covers four parts of the microbiota–gut–brain axis, including the barrier structure, defense system, neural network, and humoral communication. Albeit being separately recounted as follows, these parts virtually link together closely and interact with each other in the MGBA (Figure 1).

2.2.1. The Barrier Structure of the Microbiota–Gut–Brain Axis

As the gateway to the communication across the MGBA [26], the barrier of MGBA refers to the specifical cellular interfaces, which principally include the blood–brain barrier and gut epithelial barrier.

- **Gut Barrier and Its Association with Stroke**

The gut barrier can be divided into three layers: (1) The mucus layer, mainly comprising mucins secreted by goblet cells, which are also a nutritional source and adhesion sites for microbiome. (2) The gut epithelial barrier, a selectively semipermeable barrier mainly composed of absorptive enterocytes, enteroendocrine cells, goblet cells, Paneth cells, M cells, and stem cells. (3) The gut vascular barrier, which consists of microvascular endothelial cells attached by fibroblasts, enteric glia, and pericytes. All three layers jointly act as a defense for systemic circulation. To reinforce barrier integrity and restrict paracellular transport, tight junctions formed by transmembrane proteins, including claudins, Occludin, and zonula occludens (ZO), as well as adherens junctions, lie in the gut endothelium [27].

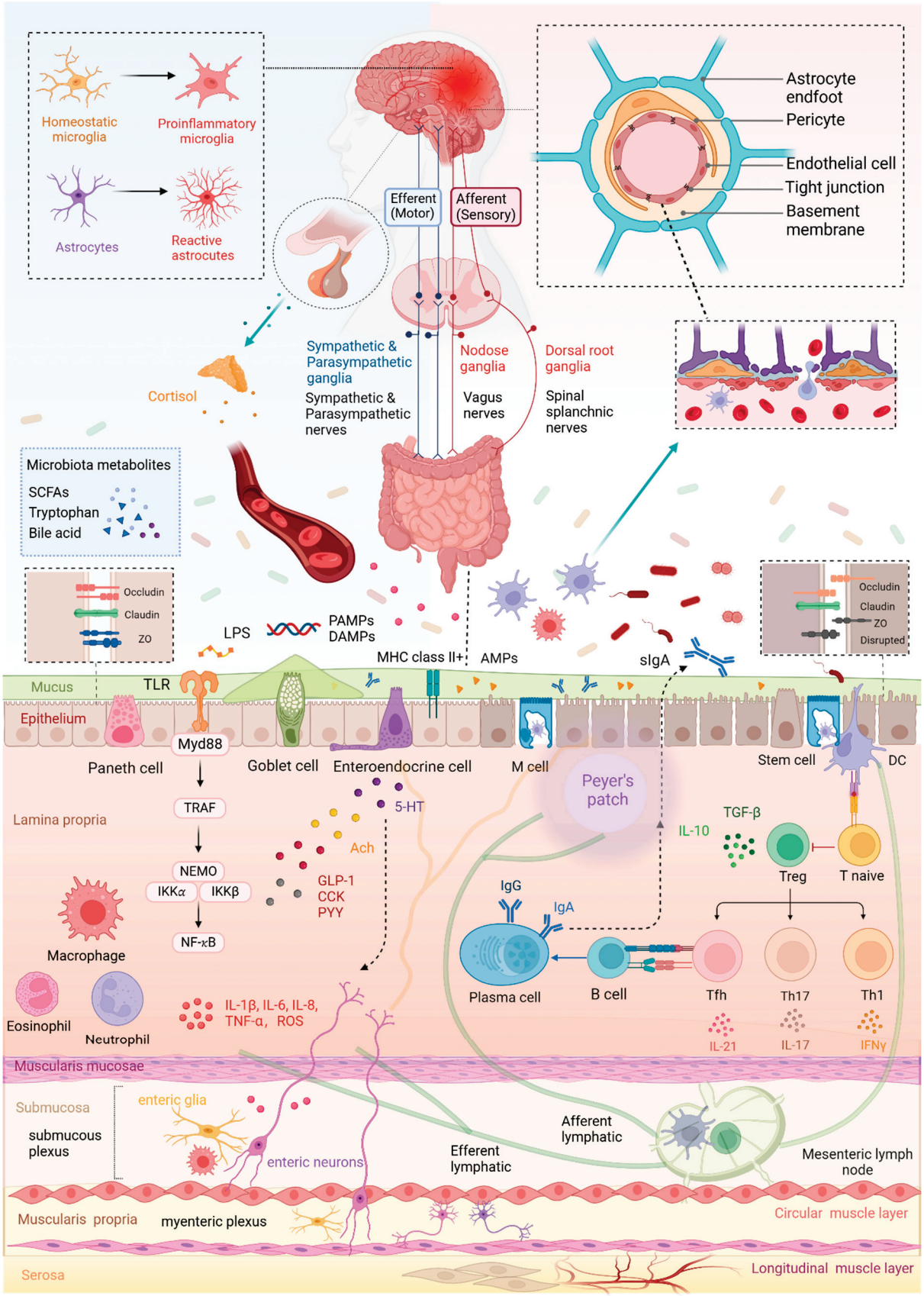


Figure 1. Crosstalk in the microbiota–gut–brain axis associated with stroke. Created with BioRender.com.

Experimental stroke mice exhibited increased gut permeability, especially vascular permeability in the jejunum and ileum, accompanied by impaired gut mucoprotein, claudin production, and goblet cells. Owing the potential mediation to the upregulated noradrenaline effect in the autonomic nervous system, the study employed β-adrenergic receptor blockers, which significantly ameliorated gut permeability and bacterial dissemination [28–30]. A recent study [31] utilizing the MCAO mice model also verified that gut cell death and apoptosis could be reversed by 6-hydroxydopamine, which denervated catecholamine peripheral neurons, and the deficiency of adrenergic receptor ADRB2 alleviated the gut permeability. The upregulated epithelial fructose metabolism gene expression, with hyperplasia of intestinal crypts and goblet cells at 24 h after stroke, was also corroborated, which can be identified as a host compensatory mechanism for the compromised gut barrier. Downregulated tight-junction (TJ) proteins, ZO-1, Occludin, and claudin-1, as well as broken TJ of the intestinal mucosa observed in ischemic stroke mice are simultaneously accompanied by the upregulation of the TNF-α-induced death receptor signaling pathway and inflammation-related proteins NF-κB, iNOS, and MPO, which were suggested to be concerned with intestinal barrier impairment [32].

Gut microbiota can influence the gut barrier by regulating the mucus secretion [33], epithelial cells' turnover [34], antimicrobial peptides' production [35], and gut permeability [36]. In that stroke often causes gut dysbiosis, several studies speculated that gut dysbiosis is a cause of damaged gut barrier in stroke, whereas the study of Kumar et al. [31] indicated that stroke-induced alterations of epithelial cells and goblet cells are independent of microbial dysbiosis, as similar changes were also observed in germ-free (GF) mice. Thus, more studies are expected to unravel the specifical role of gut microbial disruption in gut epithelial permeability related to stroke. Furthermore, the disruption of the intestinal barrier may promote translocation of gut microbiota, such as Enterococcus spp., Escherichia coli, and Morganella morganii [28], and increased plasma LBP and LPS, thus exacerbating systemic inflammation after stroke. Taken together, there is an intricate relationship between stroke, gut microbiota, and gut barrier(Figure 2).

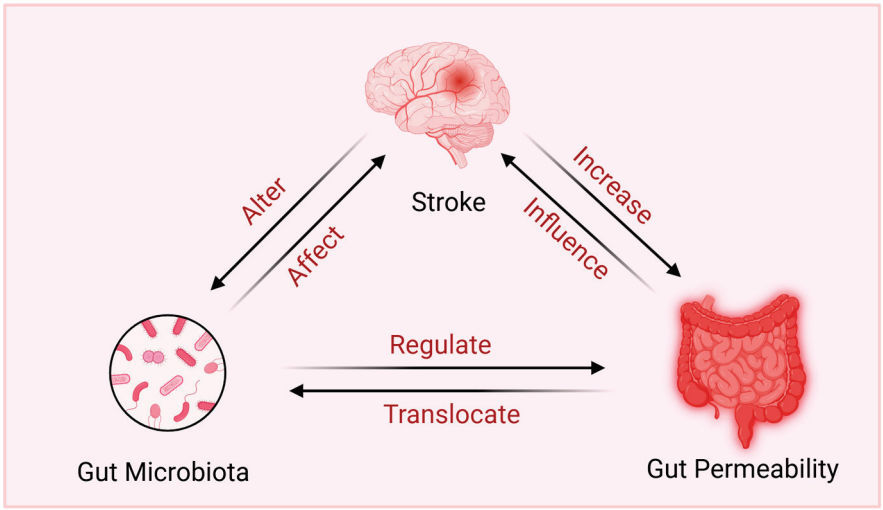


Figure 2. The relationship between stroke, gut microbiota, and gut permeability. Created with BioRender.com.

- **Blood–Brain Barrier Can Be Influenced by the Gut Microbiota**

Extensively located in capillary vessels of the brain and spinal cord parenchyma, the blood–brain barrier (BBB) mainly comprises capillary endothelial cells along with capillary basement membrane, astrocytes end-foot, pericytes, and extracellular matrix, protecting the brain tissue from the harmful substances in the systemic circulation. Similar to the gut barrier, the BBB has tight junctions as well to maintain its function [37]. Studies have reported that when stroke occurs, cerebral ischemia will induce compromised BBB [38],

a key mechanism of brain injury after stroke, which can be caused by oxidative stress, overproduction of free radicals, and iron overload, while the exact molecular mechanisms remain to be explicated.

Previous studies have shown the critical influence of the gut microbiome on the BBB. Germ-free mice exhibited enhanced blood–brain barrier permeability with downgraded tight-junction proteins, Occludin and claudin-5, expression, which can be ameliorated by exposing to the microbiota of pathogen-free mice [39]. Gut dysbiosis mice also displayed decreased TJ proteins in the hippocampus [40] and an impaired cerebral endothelium, as evidenced by three weeks of an antibiotic regimen, which caused endothelial dysfunction in the brain, including an enhanced spontaneous tone as well as blunted L-NAME-mediated constrictions and ATP-mediated dilations, accompanied by lower basal eNOS activity [41]. In another study, the microbiome of spontaneously hypertensive stroke-prone rats disrupted the BBB with enhanced MMP-9 gene expression, and damaged the gut barrier with downregulated E-CAD and Muc-2 gene expression [42]. Under the circumstance of "gut leakiness", which is similar to a broken gate, it is reasonable that more bacteria and their toxic products' interactions with cells and neurons, as well as the diffusion to systemic circulation, were allowed, triggering a vast array of immune responses and inflammation with altered pathways along the GMBA. As a result, BBB permeability is affected by the above alteration, directly or indirectly rendering it more accessible to various pathogens. Thus, it can be found in various studies that changes in the gut and brain barriers are positively correlated and concomitant.

Intriguingly, clear similarities can be found in brain and gut barrier structures, which further facilitate the correlation between the gut and brain along the MGBA and implicate the amenability to be regulated by the common signals, including gut microbiota metabolites, for example, SCFAs, especially butyric acid or sodium butyrate, which exert a protective effect on both gut and brain epithelial integrity [43,44], regulating mucus secretion [45] and redistributing ZO-1, Occludin, and claudin protein expression [46–48].

2.2.2. The Defense System of the Microbiota–Gut–Brain Axis

- **The Immune System in the Gut**

As the gatekeeper [49], when threatened by a noxious substance, the intestinal immune system, the largest defense system in our body, readily delivers various strong immune responses based on its sophisticated structure [50]. At the mucous layer, molecules, including IgA, and antimicrobial peptides (AMPs) can kill bacteria, inhibit pathogens, and engage in the regulation of immune signals. Other components, such as mucin 2, zymogen granule protein 16, and IgG Fc-binding protein, have also been demonstrated as part of the innate immune mucosal defense or messengers to the host immune system [51]. Right next to the mucous layer is epithelial cells, which are equipped with cell junctions, as illustrated before, further contributing to defend against most pathogens. Beneath the epithelium lies the lamina propria, a noncellular connective tissue, which consists of a large number of immune cells [52], including monocytes or macrophages, neutrophils, eosinophils, basophils, mast cells, innate lymphoid cells (ILCs), natural killer (NK) cells, lymphocytes, and dendritic cells (DCs). These cells act to phagocyte and eliminate microorganisms and secrete anti-inflammatory factors, such as interleukin 10 (IL-10) [53], possessing anti-inflammatory effects to maintain gut homeostasis [54]. During the gut dysbiosis or stroke damage, pathogen-associated molecular patterns (PAMPs), such as LPS, peptidoglycan, and lipoteichoic acids [55], and damage-associated molecular patterns (DAMPs), including ATP, mitochondrial DNA, IL-33, etc. [56,57], can be recognized by the pattern-recognition receptors (PRRs), represented by the Toll-like receptors (TLRs) family, expressing on the surface of enterocytes or other immune cells. TLRs then interact with MyD88 through TIR domains and trigger a cascade, which leads to the translocation of NF-κB into the nucleus, regulating the expression of proinflammatory cytokines, including TNF-α, IL-1, and IL-6, in the innate and adaptive immune mediation [58].

Along with the lamina propria, Peyer's patches (PPs), mesenteric lymph nodes (MLNs), and isolated lymphoid follicles comprise the gut-associated lymphoid tissues (GALTs), the largest lymphoid in our body, which assumes the primary immune response in the gut [50,59]. Specifically in adaptive immunity, antigen is sampled by antigen-presenting cells (APCs), such as DCs, after entering through microfold cells in the follicle-associated epithelium (FAE) or through the epithelium where MHC class II+ enterocytes may also act as local APCs. Then, the processed antigens are passed on to Peyer's patches or MLNs to activate CD4+-naive T lymphocytes, which can subsequently differentiate into regulatory T cells or T helper (TH) cells with the expression of integrin α4β7 and the chemokine receptor CCR9, eventually accumulating in the mucosa. B cells mature into plasma cells in the lamina propria, producing IgA to the lumen to bind the antigens, the process of which is influenced by factors such as transforming growth factor-β (TGF-β), IL-10, and signals from T cells as well as DCs [50]. Additionally, some CD8+T cells in lamina propria can be cytotoxic T-lymphocytes (CTL), while some CD4+ and CD8+T cells can be memory cells.

- **The Immune System in the Brain**

In parallel, the responsive immune cells, cytokines, and chemokines, as well as antigens, may also gain access to the bloodstream and enter the brain [60]. After stroke onset, intestinal immune cells, majorly DCs and macrophages, have been found to significantly travel to the central nervous system (CNS), where the trafficking amount is higher than other lymphoid organs [61], which aggravates the brain disease. It was thought that the existence of the BBB and the paucity of specialized antigen-presenting cells render the immune response limited in the CNS [62]. Astrocytes and microglia are two extra types of immune cells, which specifically reside in the CNS parenchyma. Astrocytes are large, ramified glial cells, most abundant in the brain, with the function of immune defense and BBB integrity protection. Microglia, the microphages considered as the earliest cells to sense antigens in the CNS [63], transit to M1/M2 proinflammatory phenotypes [64] and release proinflammatory cytokines under the pathological status, which promote inflammation and, meanwhile, facilitate the interaction with astrocytes.

During the early acute phase after stroke, DAMPs released from damaged cells interact with PRRs to initiate innate immunity, inducing the activation and differentiation of immune cells. Concomitantly, upregulation of adhesion molecules, such as intracellular adhesion molecule 1 (ICAM-1) and p-selectin, contribute to the infiltration of immune cells. The release of inflammatory mediators, including matrix metalloproteinases-9, inducible nitric oxide synthase (iNOS), and reactive oxygen species (ROS), further aggravates cells' apoptosis and the BBB disruption by damaging tight-junction proteins [65,66]. The damaged blood–brain barrier leaves the entrance open for peripheral intestinal immune cells, such as B cells and T cells, where it was reported that over one-fourth of all invading T cells were from intestinal PPs, resulting in the augmentation of neuroinflammatory responses [67].

As the immune response to stroke is a complex and multistage process [68], innate immunity plays a major role in the early acute stage. During the chronic phase, some immune cells, such as B cells, possess a dual effect in the ischemic stroke progression, with benefits related to the secretion of the anti-inflammatory cytokine IL-10, while adverse effects are mediated by autologous immunoglobulins with respect to chronic inflammation [69]. Cerebral ischemia can induce cell-mediated immunity depression, such as diminished early NK and T cell responses with reduced interferons (IFN) production by Th1 cells, all of which was found to be prevented by blocking the sympathetic nervous system [70]. The stroke-induced immunodeficiency related to spontaneously severe bacterial infections primarily contributes to the morbidity, compared to the direct brain lesions.

- **Gut Microbiota Influences the Immune System**

Moreover, microbiota exert a profound impact on gut and brain immunity along the MGBA during stroke [71]. An improved stroke outcome with increased T and B cells was observed in colonized littermates compared to the GF mice [72]. Relevant alterations in the

abundant phyla, such as Actinobacteria, Bacteroidetes, and Firmicutes, will induce T cell priming, including overall increased T helper cells (CD4+) as well as polarized regulatory T cells (Foxp3+), which significantly mediates cerebral protection. Meanwhile, the microbiota influences the level of neutrophil infiltration to affect the ischemic brain. Gut dysbiosis can also cause polarization of proinflammatory Th17 (IL-17+) and Th1 (IFN-1+) cells both in the gut [67] and the ischemic brain, along with the increased Treg cells in the small intestine and less IL-17+ γδ T cells in the meninges. Studies have elucidated that the gut microbiota influences such balance between local intestinal Treg cells and γδT cells by inducing the differentiation of intestinal DCs, ultimately affecting the protective or damaging effects of T cells migrating to the brain after ischemic brain injury. Specifically in the brain, the function and maturation of astrocytes and microglia are regulated by microbiota as well, through the Aryl hydrocarbon receptor (AhR) signaling pathway. As numerous studies have demonstrated the role of the gut microbiota in the development, maturation, and function [73] of peripheral and central immune cells, the influence of dysbiosis under pathological conditions, especially stroke, needs more exploration. Furthermore, metabolites, such as SCFAs, tryptophan (Trp), and bile acid (BA) metabolites, or components, such as LPS and peptidoglycans, of microbiota all significantly influence the immune system [74].

2.2.3. The Neural Network of the Microbiota–Gut–Brain Axis

- **The Enteric Nervous System**

Distinguished from other peripheral organs, the gut possesses an intrinsic complete nervous system, namely the ENS, with extensive regulation of gastrointestinal motility, mucus secretory, gastrointestinal endocrine, epithelial permeability, immunologic, and inflammatory responses [75]. The ENS comprises enteric neurons and enteric glia cells, forming two main plexuses, the submucous (or Meissner's) plexus between the circular muscle layer and the muscularis mucosa, innervating the muscle motor, and the myenteric (or Auerbach's) plexus between the longitudinal and circular muscle, responsible for secretory and absorptive control. Neurons of the ENS can be classified by function into intrinsic primary afferent neurons (IPANs), interneurons, motor neurons, and intestinofugal neurons (IFN), or by morphology, mainly into Dogiel type I and type II neurons [76,77]. In general, primary transmitters in enteric neurons include acetylcholine (Ach), serotonin (5-HT), nitric oxide (NO), substance P, vasoactive intestinal peptide (VIP), and calcitonin gene-related peptide (CGRP). The myenteric neurons are mostly cholinergic or nitrergic, while submucosal neurons are mainly cholinergic neurons or VIP-expressing noncholinergic neurons [76]. Beyond the neurotransmitters, enteric neurons as well as enteric glia may also produce cytokines, such as IL-18, colony stimulatory factor 1 (CSF1), and transforming growth factor-β (TNF-β). Therein, IL-18 is necessary for the AMPs production of goblet cells to defend against pathogens, including Salmonella typhimurium [78]. TNF-β also plays an essential role in muscularis macrophages' development and maintenance, indicating the intimate association between enteric nervous systems and barriers, as well as immune function [79,80].

Loss of enteric neurons has been elucidated in the stroke (pMCAO) model, with central and peripheral galectin-3 release through a TLR4-mediated mechanism involving TAK1 and AMPK [81]. Another study also reported the myenteric neurons' loss with increased VIP-immunoreactive submucous neurons in the ileum of pMCAO mice, which simulated focal cerebral ischemia, whereas global ischemia models exhibited no significant change, implicating that different types of stroke act differently in enteric neuronal survival [82]. A recent study also uncovered that stroke induced decreased neuronal nitric oxide synthase (nNOS) in enteric myenteric neurons, leading to the injured muscle relaxation and slow gut motility. Furthermore, the impairment can be rescued by denervation of the sympathetic nervous system through 6-hydroxydopamine [83].

- **The Connections between the ENS and CNS**

The ENS is closely linked to the CNS through both afferent and efferent pathways [84]. On afferent pathways, where the gastrointestinal tract (GIT) sends sensory information to the brain, the major extrinsic nerves are the vagus nerve (VN) and spinal splanchnic sensory nerves. The vagus nerve, whose cell bodies lie in the nodose ganglia (NG), which project to the brainstem, predominate the upper gut, such as the esophagus and stomach, while spinal splanchnic sensory nerves, whose cell bodies are in the dorsal root ganglia (DRG), which project to the spinal cord dorsal horn and the dorsal column nuclei, generally fall into sympathetic and pelvic pathways responsible for the lower gut. On efferent pathways where the brain delivers the motor information to GIT, the extrinsic nerves are the sympathetic and the parasympathetic nerves. The sympathetic nerves are adrenergic with inhibitory effects, whereas the parasympathetic nerves are cholinergic with excitatory effects in the gut.

As a mixed nerve, the VN contains four principal components, including general visceral efferent, which is parallel with the GIT-distributed part of parasympathetic fibers; thus, when it refers to GIT, the parasympathetic nerves are synonymous with the VN, which has been profoundly studied. The VN connects with ENS, smooth muscle, and mucosa to innervate the gut, readily detecting various signals, including gut hormones, neurotransmitters, as well as bacterial by-products. The neuroprotective effect of VNs and vagus nerve stimulation (VNS) have been found as a promising intervention in cerebral ischemic stroke. VNS can inhibit pyroptosis with suppressed related inflammatory molecules, such as NLRP3, cleaved caspase-1, and reduced pyroptotic cells and membrane pores. It also inhibited Toll-like receptor 4/nuclear factor kappa-B expression and caused a shift from a proinflammatory phenotype in microglia with reduced NOS and TNF α, which is intricately mediated by the α7 nicotinic acetylcholine receptor (α7nAchR) [85,86].

- **Gut Microbiota Influences the Nervous System**

The gut microbiome sends significant signals in the neural network along the MGBA. Studies found that the depletion of microbiota induced activation of the gut sympathetic ganglia, which can be reversed by colonizing with SCF-producing bacteria [87]. Oral inoculation with the microbiota, such as live *Campylobacter jejuni* (*C. jejuni*), could also lead to the activated neurons bilaterally in the vagal ganglia [88], suggesting that peripheral sensory neurons send an early signal to the brain regarding pathogens or gut microbial alteration. Intrinsically, the microbiota closely interacts with the ENS. Antibiotic (Abx)-induced bacterial depletion led to the loss of enteric neurons in both submucosal and myenteric plexuses in the ileum and proximal colon, as well as reduced enteric glia in the ileal myenteric plexus, which could be recovered by microbial restoration. Furthermore, SCFs were verified to stimulate enteric neurogenesis by restoring enteric glia and neurons [89]. A regulatory circuit may also exist in the microbiome, enteric neurons, and other gut cells, including enteroendocrine cells (EECs) and immune cells. EECs can release ENS neurotransmitters, such as Ach and 5-HT, in response to altered microbiota metabolites [54]. Yan et al. revealed a relationship showing that the microbiota affects the neuronal transcriptome and structure, which subsequently tunes the generation of Treg cells lining the enteric neuron projections in the lamina propria [90]. Beyond the SCFs, tryptophan (Trp), and bile acid (BA), gut microbiota also produce and mediate other neuroactive metabolites, such as glutamate, GABA, Ach, 5-HT, and dopamine, affecting neuronal activities [91].

2.2.4. The Humoral Communication of the Microbiota–Gut–Brain Axis

- **Hypothalamic–Pituitary–Adrenal Axis and Its Association with Stroke**

The hypothalamic–pituitary–adrenal (HPA) axis is one of the principal neuroendocrine pathways and a fundamental part of the MGBA. When exposed to stressful stimuli, such as IL-6 and TNF, triggered by a disease such as stroke, the HPA axis is activated, leading to the production of glucocorticoids or cortisol, the primary stress hormones, which exert an anti-inflammatory and immunosuppressive effect on pathological tissue, along with a negative feedback on the hypothalamus and pituitary glands to control the response [92]. However,

chronically elevated levels of glucocorticoids may implicate a pathological condition or underlie a bad prognosis.

A massive response associated with HPA was observed in the early stage of acute stroke, with a continuous high level of cortisol, whereas merely in the initial phase did the concentration of adrenocorticotropic hormone (ACTH) increase [93]. Cortisol levels remained high for at least seven days after stroke, as concluded by a systematic review [94], and exogenous corticosterone contributed to neuronal death with larger infarcts in MCAO mice [95]. It has been reported that post-stroke administration of metyrapone, an inhibitor of glucocorticoid synthesis, decreased the IL-6 level and the infarct size in the ischemic brain [96]. However, glucocorticoid receptor blockade was reported to cause increased blood catecholamine, while the application of prednisolone decreased β2-adrenergic receptor expression on lymphocytes in vitro, possibly reducing the sensitivity to catecholaminergic stimulation following a stroke [97]. ACTH was found to be significantly correlated with the brain lesional volume and functional outcome [93], with the effect of predicting the development of post-stroke depression as a vital and independent biomarker in a three-month follow-up study [98]. Numerous studies have identified a dysregulated HPA axis in stroke patients, and a hyper-activated HPA axis was also demonstrated in diabetic mice after stroke with an augmented inflammatory response [96]. Taken together, these studies show that the HPA axis may be a potential therapeutic target in improving stroke outcomes.

- **Gut Microbiota Influences the HPA Axis**

The gut microbiota is one of important components to activate the HPA axis. A higher HPA axis response to stress was observed in GF mice with plasma ACTH and corticosterone elevation [99]. During the inflammatory condition, bacterial translocation is also able to activate the HPA axis through the disrupted gut and brain barriers. At the genetic level, the microbiota was found to attenuate the expression of Fkbp5, a gene regulating glucocorticoid receptor sensitivity in the pituitary gland, as well as the expression of genes encoding steroidogenesis, such as MC2R and Cyp11a1 in the adrenal gland [100].

- **Gut Hormones**

As important signaling molecules within the GMBA, gut hormones spread throughout the GIT are released by enteroendocrine cells (EECs) to regulate gut motility, appetite, and maintain intestinal homeostasis. Enteroendocrine cells, which only account for 1% of gastrointestinal epithelial cells, secrete various kinds of hormones that act locally on nerve endings, enteric neurons, epithelium, and immune cells or enter the circulation to affect the CNS or other distant sites [101]. There are 12 major types of enteroendocrine cells, including enterochromaffin cells, A cells, and D cells, which secrete more than 20 hormones [102]. The main signals involved in the gut–brain crosstalk are ghrelin, polypeptide YY (PYY), glucagon-like peptide-1 (GLP-1), glucose-dependent insulinotropic polypeptide (GIP), cholecystokinin (CCK), and 5-HT [103]. EECs are equipped with a wide array of sensory receptors, which can detect microbial metabolites, such as SCFAs [104], or bacterial components, such as LPS [105]. These gut hormones may subsequently activate IPANs and extrinsic afferent nerve terminals to influence the functions of the brain [106].

3. Tryptophan Metabolism along the Microbiota–Gut–Brain Axis and Stroke

There is a growing appreciation for tryptophan metabolism along the microbiota–gut–brain axis, which has close associations with stroke. As an essential amino acid, tryptophan mainly originates from the digestion of dietary proteins in the small intestine [107]. Trp is metabolized via three major pathways, with a series of important metabolites in the gut and brain, which experience significant alterations during stroke (Figure 3), exerting a profound effect on the physiological and pathological processes.

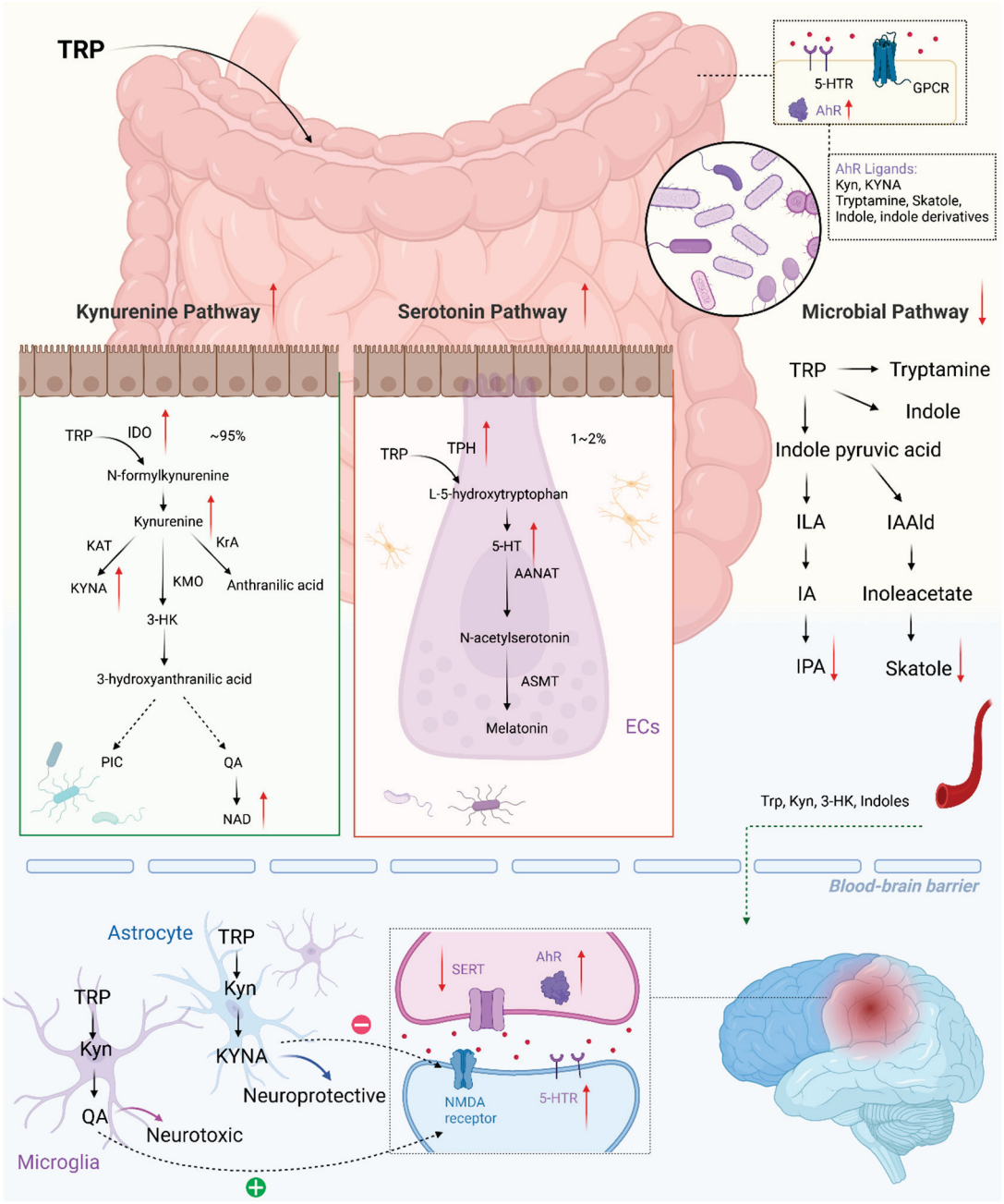


Figure 3. Tryptophan metabolism along the microbiota–gut–brain axis and its main alteration in stroke. Created with BioRender.com.

3.1. Tryptophan Metabolism Pathways along the Microbiota–Gut–Brain Axis

3.1.1. Kynurenine Pathway in the Gut and Brain

The kynurenine pathway (KP) is a key metabolic route that breaks down about 95% of free tryptophan (Trp) [15]. The process is primarily initiated by two crucial rate-limiting enzymes, indoleamine-2,3-dioxygenase (IDO) and tryptophan 2,3-dioxygenase (TDO). IDO is extensively expressed in the body, including the brain and GI tract, with two isoforms, IDO1 and IDO2. IDO1 is pivotal in the immune response and always activated by the inflammatory cytokines, especially interferon (IFN)-γ [108,109], while IDO2 is believed to be basally expressed [110]. TDO, induced by the activation of the HPA axis with increased glucocorticoid, catalyzes 90% of Trp under physiological conditions in the liver and brain [111]. With the aid of the enzyme, Trp is converted to N-formyl kynurenine, which is then catabolized to the pivotal intermediate, kynurenine (Kyn), by formamidase. AhR, a

ligand-activated transcription factor that expresses on various cell types, such as T cells, neutrophils, microglia, and astrocytes, plays a master regulatory role in inflammation and immune function with the release of cytokines, including IL-6, IL-17, and IL-22 [112,113]. Kyn, a biologically active metabolite, acts as a ligand for AhR, with the functions of immunity suppression, inflammation, and carcinogenesis [114,115]. Then, Kyn can be further metabolized into three branches, which are kynurenic acid (KYNA) by kynurenine amino-transferase (KAT), 3–hydroxykynurenine (3-HK) by kynurenine-3-monoxygenase (KMO), and anthranilic acid by kynureninase A (KrA).

KYNA, an endogenous neuroprotective agent [116], can activate AhR and G protein-coupled receptor 35 (GPCR35), the activation of which may induce the inositol trisphosphate production and Ca^{2+} mobilization [117]. The 3-HK can influence the immune function by inhibiting the proliferation of CD8+ T cells and suppressing T cell responses [118,119]. Then, 3-HK converts to 3-hydroxyanthranilic acid, whose catabolism leads to the generation of quinolinic acid (QA) and picolinic acid (PIC). The N-methyl D-aspartate (NMDA) receptor is a ligand-gated cation channel, mediating the glutamate signals, with a critical role in the nervous system [120]. Overexcitation of NMDA receptors was suggested to be of great significance to the etiology of brain damage and neurodegenerative disorders, including stroke [121]. Among the major products of tryptophan, KYNA and PIC act as neuroprotective NMDA receptor antagonists, while QA is considered as a neurotoxic NMDA receptor weak agonist with proinflammatory properties [122]. Under pathophysiological conditions, QA can trigger oxidative stress and apoptosis by forming a complex with iron that contributes to ROS in different cells, including neurons and astrocytes, whose decrement, in turn, leads to lower KYNA production, thus enhancing neurological symptoms and chronic inflammation [123]. Oxidative damages to DNA induced by QA were reported to cause the overactivation of poly (ADP-ribose) polymerase (PARP) [124], an enzyme that repairs damaged DNA after oxidative injury, which would further deplete ATP and NAD [125]. Intriguingly, in mammalian cells, de novo from tryptophan is a significant biosynthesis pathway of NAD [126], which can be generated from QA as the end product of the 3-HK branch mediated by the KMO, also a rate-limiting enzyme sensitive to proinflammatory cytokines. During the inflammatory diseases, KP metabolism, as well as the production of NAD, predominantly increase, implicating the enhanced energy demand in the pathological process. Despite that QA and KYNA cannot cross the BBB, Trp, Kyn, and 3-HK can, which contribute to the accumulation and generation of neurotoxic intermediate products, including 3-HK and QA, in the brain, where microglia mainly produce QA, while astrocytes generate KYNA.

3.1.2. Serotonin Pathway in the Gut and Brain

About 1–2% of ingested Trp is metabolized in the serotonin pathway [127], which is initiated by tryptophan hydroxylase (TPH). There are two isoforms of TPH, including TPH1, which expresses in the enterochromaffin cells (ECs), and TPH2 in the CNS and ENS [111,128]. Most 5-HT is produced by enterochromaffin cells in the gut, while the rest is synthesized by neurons, leading to the distinction between mucosal 5-HT, which was related to intestinal inflammation [129], and neuronal 5-HT, which was found to promote intestinal mucosal epithelial growth and turnover, maintain myenteric neuronal density, and influence gastrointestinal motility [130,131]. Trp serves as the exclusive precursor of 5-HT, a primary monoamine neurotransmitter responsible for central neurotransmission, as well as a regulatory hormone in intestinal development and physiological activities [132–135], depending on the distinct subtypes of 5-HT receptors in various cells and tissues.

The 5-HT receptors, extensively expressed in the CNS, including the hippocampus, hypothalamus, basal ganglia, and cortex [136], are classified into seven principal classes, namely from 5-HT1 to 5-HT7, which all belong to metabotropic G-protein-coupled receptors, except for the ligand-gated ion channel 5-HT3 receptor (5-HT3R) [137]. However, 5-HT3R, which can be found on the terminals of GI vagal afferent neurons, displays an intimate involvement in gut–brain signaling [138]. In response to mechanical or chemical

stimulation in the GI tract, 5-HT is released from ECs and acts locally on 5-HT3 receptors present on vagal afferent fiber, triggering smooth-muscle activity during the physiological and pathophysiological processes, such as distention, nausea, and vomiting [138,139]. Highly exposed to luminal contents, 5-HT4R, widely expressed in the intestinal epithelium as well as the ENS, specifically in myenteric neurons [140], is also vital in GI motility and epithelial secretion. Mucosal administration of 5-HT4R agonists promotes mucus secretion by goblet cells and Cl^- discharge by enterocytes [141]. Stimulation of 5-HT4R led to anti-proinflammatory, neurogenesis, and neuroprotection responses in the gut, and blocking 5-HT production induced loss of myenteric neurons and inhibition of neuronal differentiation from enteric neuronal stem cells [140]. Moreover, the agonist of the 5-HT1A receptor prevented apoptosis of intestinal epithelial cells and enteric glial cells, with reduced mucosal injury [142], and other 5-HT receptors, such as 5-HT1P and 5-HT2A, have also been verified to mediate different signals within the gut toward the CNS [143]. Additionally, the serotonin-selective reuptake transporter (SERT) exists both in the brain and intestinal epithelium, responsible for 5-HT uptake, effectively clearing serotonin from the synaptic gap and managing 5-HT concentrations [111,139]. Despite that intestinal 5-HT cannot cross the BBB, the free tryptophan that enters the circulation through the gut epithelium may cross the BBB to produce 5-HT in the brain, where some 1% of dietary tryptophan is used for the serotonin biosynthesis [132].

Another well-known product in this branch is melatonin (N-acetyl-5-methoxytryptamine), which is converted from serotonin via N-acetylserotonin through arylalkylamine N-acetyltransferase (AANAT) and acetylserotonin O-methyltransferase (ASMT). Melatonin is a hormone secreted by the pineal gland during the night, with a function in the regulation of circadian rhythm and immunity, as well as an antioxidant property [144]. Dysfunctional serotonin signaling has been widely reported in GI disorders combined with psychiatric symptoms [145].

3.1.3. Microbial Pathway

- **The Gut Microbiota's Role in Direct Trp Metabolism**

A small amount of Trp can be directly converted by the gut microbiota, primarily into indole and its derivatives. Accumulating evidence suggests that the homeostasis of microbiota–gut–brain interplay plays a central role in the regulation of Trp metabolism. Superior reviews have summarized various gut bacterial species producing different kinds of tryptophan catabolites [146,147]. Overall, phyla Actinobacteria, Firmicutes, Bacteroidetes, Proteobacteria, and Fusobacteria, as well as genera Clostridium, Burkholderia, Streptomyces, Pseudomonas, and Bacillus, are more common and enriched in tryptophan metabolism according to an in silico analysis based on bacterial genomes and gut microbiome data [148]. Specifically, some permanent-resident microbes of the gut, including the genera Clostridium, Bacteroides, as well as Escherichia coli, can metabolize Trp into indole with the expression of tryptophanase (TnA) [149,150]. Indole, viewed as a signaling molecule, affects several bacteria on quantity, virulence, drug resistance, plasmid stability, and biofilm formation, in turn [150]. It also mediates inflammation in innate immune responses [151], modulates the secretion of gut hormones, such as GLP-1, mechanically through inhibiting the voltage-gated K^+ channel, as well as weakens ATP production with NADH dehydrogenase blockage [152]. Ruminococcus gnavus and Clostridium sporogenes are known to decarboxylate Trp to tryptamine, a β-arylamine neurotransmitter, which induces the release of 5-HT by enteroendocrine cells and binds the 5-HT4 receptor to modulate colonic secretion and promote gut transition [153–155]. Along the microbial pathway, indole, tryptamine, skatole, as well as a series of indole derivatives, including indole-3-acid-acetic (IAA), indole-3-lactic acid (ILA), indole acrylic acid (IA), indole propionic acid (IPA), indole-3-acetaldehyde (IAAld), and indoxyl-3-sulfate (I3S), are ligands of AhR [156]. Typically, Bacteroides, Clostridium, Peptostreptococcus, Lactobacillus, and Bifidobacterium are producers of indole-3-lactic acid (ILA), which was suggested to significantly downregulate the expression of IL-8 in gut epithelial cells and suppress NFκB activation in

macrophages in a dose-dependent manner via activation of the AhR and nuclear factor erythroid 2-related factor 2 (Nrf2) pathway [157]. Research in human peripheral blood mononuclear cells also exhibited the anti-inflammatory and antioxidative effects, with reduced IL-6 and IL-1b and elevated IL-10 levels under the treatment of IA, which is mainly produced by Peptostreptococcus species [158]. During the inflammation induced by LPS, IPA possessed an inhibitory effect on PI3K/AKT/mTOR signaling pathway. In the study, IPA significantly enhanced the intestinal barrier through increasing claudin-1, Occludin, and ZO-1 levels, as well as facilitating the mucin secretion and the goblet cell function [159].

Indoles are known to cross the BBB and exert a profound effect on the brain [160]. Overproduction of indole in the gut increases the cerebral oxindole level. Supplementation with I3S, IPA, IAld, or tryptophanase in antibiotic-treated mice attenuated CNS inflammation via AhR signaling [161]. Equipped with the potent capacity of scavenging hydroxyl radicals and inhibiting superoxide dismutase, IPA protected primary neurons and neuroblastoma cells from oxidative damage and death induced by Aβ or hydrogen peroxide [162]. Oral administration of IPA mitigated ischemic injury, potentially by reducing DNA damage in pyramidal neurons and lipid peroxidation in ischemic hippocampal homogenates [163]. However, some of the effects can be adverse. For example, intraperitoneally administration of indoxyl sulfate can cause its further accumulation in the prefrontal cortical tissues and cerebrospinal fluid, which leads to behavioral changes and neurodegeneration, including anxiety, depression, and cognitive impairment, accompanied by impaired neuronal cell survival and neural stem cell activity, as well as disturbed expression of serotonin, corticosterone, and brain-derived neurotrophic factor (BDNF) [164].

- **Gut Microbiota Influences the Kynurenine and Serotonin Pathways**

Moreover, the gut microbiota influences the tryptophan metabolism indirectly through the kynurenine and serotonin pathways. Gene expression of the kynurenine pathway enzymes, including kynurenine aminotransferase, tryptophan 2, and 3-dioxygenase in the hippocampus, were changed in GF mice [165]. In GF pigs, tryptophan and kynurenine in the large intestine, as well as 5-HT in most organs, were significantly increased, whereas indole metabolites were generally decreased [166]. A recent study revealed relevant features of KP metabolism in Lactobacillus (L.) reuteri, with the emphasis on the qualitative differences between bacterial and mammalian metabolism. They found that kynurenine readily entered the bacterial cells and was preferentially metabolized to KYNA, whose production was positively correlated with the concentration of kynurenine and bacteria [167]. Beyond the *L. reuteri* from the phylum Firmicutes, bacteria expressing KYN pathways also include Bacteroidetes, Actinobacteria, and Proteobacteria phyla [148]. These microbiota-derived LPS were also found to stimulate colonic immune responses with the upregulation of IDO1 in the Kyn pathway, inducing Trp depletion and Kyn accumulation in the circulation [168]. Under the circumstance of inflammation, the available Trp tend to be shunted into KP rather than serotonin, which can be possibly be explained by the overaction of IDO1 [123]. When administered the antibiotics in combination with a ketogenic diet, downregulation of IDO1 and upregulation of hippocampal kynurenic acid was demonstrated [169]. A dextran sulfate sodium (DSS)-induced colitis mice model also showed increased Kyn, as well as a decreased KYNA level, with a significantly elevated Kyn/Trp ratio, and suggested a correlation with several microbial species, including Bacteroides_acidifaciens, Shigella_sonnei, Parabacteroides_distasonis, Ileibacterium_valens, Bacteroides_vulgatus, and Burkholderiales_bacterium_YL45, which may disrupt the IDO in the cortex, and Parabacteroides_distasonis, Ileibacterium_valens, and Burkholderiales_bacterium_YL45, which were indicated to regulate the KYNA level in serum directly or by affecting KAT2 [170].

Furthermore, gut microbiota metabolites are able to influence the KP as well. In a rat model of bilateral common carotid artery occlusion (BCCAO), SCFA supplementation suppressed the conversion of Trp to Kyn and restored 5-HT levels in the hippocampus and gut, inhibiting the inflammatory augmentation [171]. Butyrate treatment ameliorated

serum Kyn accumulation through promoting mitochondrial functions in colonocytes as well as remodeling the gut microbiota in high-fat-diet (HFD) mice [168].

The serotonin pathway is also regulated by the gut microbiota, which plays a key role in promoting 5-HT secretion. Adult GF mice displayed deficient 5-HT concentrations in serum and plasma, with decreased expression of TPH1 in enterochromaffin cells and increased colonic 5-HT transporter SLC6A4, all of which can be reversed by the colonization of indigenous spore-forming microbes (Sp), whose metabolites, such as deoxycholate, a secondary bile acid, also raise 5-HT levels in ECs [172]. In addition, serotonergic neuronal networks were almost absent in GF mice with the alterations of 5-HT4 receptor expression [140]. Activation of 5-HT4R in GF mice may accelerate intestinal transit, concomitant with increased myenteric neurons and innervation of the colonic mucosa [140]. Orally administering gut microbiota from specific pathogen-free mice in GF mice increased 5-HT-positive endocrine cells in the upper GI and colon [173]. Probiotics, such as Bifidobacterium lactis TY-S01, maintained 5-HT in constipated mice with the upregulated mRNA expression of the 5-HT4 receptor [174], and colonization of enteropathogenic Escherichia coli boosted the 5-HT concentration by downregulating the SERT [175]. Besides, frontal cortex 5-HT exhibited negative correlations with the ratio of Firmicutes in total gut microbiota. Treatment with probiotics (fructo- and galacto-oligosaccharide) and prebiotics (Bifidobacterium longum and L. rhamnosus) diminished colonic 5-HT and TPH1 with increased SLC6A4. The decrease in intestinal 5-HT synthesis was then explained for more available tryptophan, possibly converting into 5-HT in the brain through the BBB [176]. Antibiotic-induced gut microbiota intervention was found to significantly increase the 5-HT level and the expression of its receptor 5-HT2A with the upregulation of TPH2 in the hypothalamus [177]. In alcohol-dependent mice, 5-HT content was significantly increased both in intestine and brain tissues after receiving the fecal microbiome from healthy mice [178].

It is believed that BAs activate the bile acid receptor TGR5 on ECs and intrinsic primary afferent neurons to stimulate the release of 5-HT [179], and through the TGR5/TRPA1 pathway, Bacillus subtilis was found to increase 5-HT production from ECs [180]. SFAs, such as butyrate, a positive allosteric modulator of SERT, promoted 5-HT uptake in mouse ileal organoids, and fecal concentrations of both acetate and butyrate were found negatively associated with 5-HT in serum [181]. LPS treatment prenatally increased 5-HT content in serum, the colon, and the medial prefrontal cortex (mPFC) with the increased TPH1, reduced SERT in the colon, and led to a higher serotonin 1B receptor (5-HT1BR) level in the mPFC in autism-like offspring, and they were detected to have lower mRNA expression levels of NAT and ASMT [182].

3.2. Tryptophan Metabolism and Stroke

Among the various abnormalities in metabolism induced by stroke, tryptophan metabolism was the most affected, according to an analysis of untargeted metabonomics in rats with stroke [183]. Furthermore, single-nucleotide polymorphisms of the genes encoding the tryptophan metabolism enzymes, such as TPH1, TPH2, KAT1, KAT2, and IDO1, were found to seriously influence the risk and pathogenesis of stroke [17]. Right before or immediately after a stroke, changes in tryptophan metabolism occurred, which were associated with the inflammatory response and oxidative stress.

Therein, the kynurenine pathway was illustrated to be activated right in the hyperacute phase (<4.5 h) of cerebral ischemia [184]. Along the activated kynurenine pathway after stroke, an increased kynurenine:tryptophan ratio and a highly significant decrease in the ratio of 3-hydroxyanthranilic acid:anthranilic acid were previously found correlated with the infarct volume [185]. IDO1 upregulation was always observed in various inflammatory states, including stroke, when the IDO1 mRNA levels increased at an early phase [19]. TDO has gained attention as well. In one study, L-Kyn levels increased in 3 h right after MCAO, with the predominant upregulation of L-Trp as well as TDO, which accounted for L-Kyn biosynthesis in neurons of the ischemic brain. Then, the Kyn activated the AhR very rapidly, which may be causally involved in brain damage at the crucial period when the

lesion extended following the ischemic occlusion. Therefore, the inhibition of TDO was found to be a promising therapeutic avenue to inhibit the endogenous apoptotic and anti-neuroprotective pathways in ischemic stroke damage [186]. KYNA was demonstrated to act as a neuroprotective/scavenger/antioxidant factor, which counteracted the tissue damage and neuronal loss induced by stroke. From early phases of stroke, an overexpression of KYNA occurred in mammalian astrocytes exclusively in the infarcted regions and continued at least 21 days post-stroke via the utilization of a highly specific monoclonal antibody against KYN in transient MCAO rats [187]. The negative association between the addition of KYNA and the mortality was found in a multicenter prospective cohort study [188].

AHR is activated and overexpressed in neurons of peri-infarct, ischemic core, as well as the cortex regions in experimental MCAO mice, with a damaging role in stroke physiopathology, as revealed by the AhR agonist, which aggravated the stroke outcome. Haploinsufficiency or total deletion of AhR decreased ischemic damage and were neuroprotective. The cAMP response element (CRE)-binding protein (CREB) is a critical neuronal transcription factor, which mediates the expression of survival and antiapoptotic genes, such as neuroprotective BDNF, against ischemic injury. The increased AhR may inhibit the CREB signaling. Administration of the AhR antagonist TMF boosted the cortical levels of CREB as well as BDNF, and decreased numbers of apoptotic cells in the peri-infarct region of MCAO animals, accompanied by the downregulated proapoptotic proteins p53 and Puma as well as increased antiapoptotic Bcl-X [186]. Likewise, during the ICH, AHR overexpressed primarily in neurons in the peri-hematoma zone, which peaked at 48 h from initial insult. Subsequently, the AHR can recruit RhoA/Bax complexes, playing a detrimental role with respect to mitochondria death and free radical accumulation. Pharmacological application of TMF mitigated ROS accumulation and neuronal apoptosis in the ipsilateral hemisphere, with reduced Bax levels, Mito Sox+ cells, proapoptotic protein cleaved caspase-3, and the biomarkers of damage elicited by oxidized lipids, namely 4-HNE protein. In this setting, the kynurenine pathway was initiated immediately after stroke and kynurenine directly contributed to the AHR activation and substantial oxidative stress, with hampered neurobehavioral performance [189].

Of note, the ligands of AHR can be divided into host-derived kynurenine-based ligands, which are upregulated and detrimental after stroke with worsened microglia survival as well as poor prognosis, and microbiota-derived indole-based ligands, such as IAld and IPA, which decrease especially within the first 24 h in both the plasma and the brain after stroke, along with significant reductions in major bacterial populations involved in the regulation of Trp-derived ligands, such as Bifidobacteriales and Lactobacillales [190]. After stroke onset, activation of microglial AHR by microbial Trp-derived ligands was corroborated to suppress the expression of proinflammatory and neurotoxic genes, including TNF, IL6, IL12A, and NOS2, and boost anti-inflammatory IL10 expression. Moreover, the Trp metabolites also led to increased TGFα and downregulated VEGF-B expression via AHR in microglia, which further influenced the proinflammatory gene expression in primary human astrocytes [191]. Post-stroke treatment in GF mice with the cocktail of IPA and IAld beneficially increased microglial AHR expression associated with a higher surface expression of CD11b, MHC-II, and CD80, ameliorating antigen presentation and co-stimulation immune functions in microglia, which resulted in a reduced infarct size and neurological deficits. All these results showed the two sides of the role of AHR depending on its ligands. Herein, a balanced pool of host-derived and microbiota-derived AHR ligands was highlighted, and via post-stroke administration of indoles, stroke outcomes can be improved [190].

Along the microbial pathway, the serum IPA levels were significantly lower in mice with MCAO. And in patients with coronary artery disease (CAD), IPA was the most downregulated metabolite and decreased more evidently in stroke patients. IPA intragastrical supplementation improved stroke outcomes and the MCAO-induced alterations of the gut microbiome structure, leading to a higher abundance of the probiotic Lactobacillus

and Lachnospiraceae_NK4A136_group, which was associated with the enhanced intestinal barrier function and epithelial integrity after IPA treatment. In IPA groups, immune function in MCAO mice was modulated, as proved by the reversing trend of the increased Th17 (CD4+ IL17+) and reduced Treg (CD4+ CD25+ Foxp3+) numbers in the GALT, such as PPs and MLNs, as well as decreasing CD3+ cells and increasing Tregs in the ipsilesional injured brain parenchyma, which further alleviated the neuroinflammation after stroke, with significantly decreased IL1β, IL6, and CCL2 and increased IL10 at both the mRNA and protein levels. The neuroprotective effect of IPA in stroke was further confirmed by the reduction in the activated astrocytes and decreased neuronal apoptosis in the peripheral infarction area. Moreover, the co-cultured experiments in the oxygen–glucose deprivation and reperfusion model revealed that IPA inhibited the A1 phenotype neurotoxic-reactive astrogliosis indirectly via intestinal Tregs [192]. Mechanically, a further study attributed the benefits of IPA to facilitating cholesterol efflux from macrophages to lipid-free apolipoprotein A-I (ApoA-I) through miR-142-5p/ATP-binding cassette transporter A1 (ABCA1) signaling [193]. On the contrary, another study elaborated the hypertensive effect of IPA, and intravenous infusion of IPA in rats increased heart muscle contractility, which can be reflected in the increased stroke volume [194]. In addition, indole-3-lactic acid was found significantly increased at one day after MCAO, but reduced in the chronic phase of stroke, which is potentially related to post-stroke depression [195]. Lower levels of 3-methylindole (skatole) and indoles were discovered in human plasma samples 24 h after IS [196]. In general, higher levels of indole-3-propionate were reported to be correlated with lower all-cause mortality, while indole-3-acetate and indole-3-lactate were positively correlated with fatal cerebral infarction, and indole-3-lactate levels were related to fatal stroke [197].

Higher serotonin levels were associated with the incidence of stroke, including fatal stroke [197]. In the serotonin pathway, TPH1 mRNAs was significantly upregulated in MCAO brains, with increased thrombosis and thromboembolism risk [198], and TPH1 variants were found to be more frequent in heterozygous form in the control group compared to the group of ischemic stroke patients [199], implicating a preventive and therapeutic strategy at the RNA and gene levels. Additionally, an analysis of blood samples collected from AIS patients uncovered that melatonin was significantly increased during the disease, whose synthesis may be provoked by ROS in order to defend against the oxidative injury [200], whereas 5-HT plasma concentrations did not display a distinction [19]. In patients undergoing the hyperacute phase (<4.5 h) of brain ischemia, platelet 5-HT2AR density was higher than in controls, while the platelet density of SERT was significantly lower, which coincides with the analysis of genetic polymorphisms in 834 patients with AIS and TIA, revealing that the presence of the high-expression SERT genotype is linked to a lower risk of ischemic stroke [201]. The patient group also showed temporarily increased urinary 5-HT, which had a role in promoting platelet aggregation, vasoconstriction, and ultimately, a thrombotic process. Nevertheless, these alterations decreased after one day and disappeared at three months from brain ischemia symptoms [184]. Furthermore, 5-HT1AR can also act as a serotonergic target for neuroprotection in cerebral ischemia [202]

4. Conclusions

From metabolic perspectives, emerging insights into the impacting role of the gut microbiota and gut–brain axis in cardiovascular diseases shed light on preventing and intervening in the progression of stroke, which offers a promising opportunity for translational research. A variety of effective and accessible intervention strategies have been clinically verified, encompassing probiotics, prebiotics, synbiotics, antibiotics, and diet or fecal microbiota transplantation. To harness the full potential of these interventions, a comprehensive understanding of the core pathways and mechanisms within the microbiota–gut–brain axis is essential. In this review, we systematically summarized the alterations of gut microbiota in stroke and the interactive influence between stroke and the immune, neural, and humoral pathways within the MGBA.

Tryptophan metabolism is a fundamental part of the MGBA, and its intimate correlation with CNS diseases has been widely reported. Herein, based on the profound and comprehensive perception of the MGBA, we further described the tryptophan metabolism in the kynurenine pathway, serotonin pathway, and microbial pathway. We overviewed the advances on the relationship between stroke and tryptophan metabolism, with the expectation of promoting the potentially diagnostic biomarkers and therapeutic avenues from the perspective of tryptophan metabolism along the MGBA, such as targeting the key metabolic enzymes at gene, mRNA, or protein levels, applying the antagonist or agonist of the crucial receptors, and controlling some critical metabolites. Practically, as the tryptophan index has been selected as one of the biomarkers to clarify the close and independent association between dietary patterns and stroke risk, the possibility of regulating dietary habits, including increased intakes of fresh fruits, vegetables, and fish/seafoods, in order to prevent stroke was highlighted [203]. Some specific healthy dietary patterns, such as the plant-based, Mediterranean, and Dietary Approaches to Stop Hypertension (DASH) diet patterns, are associated with elevated IPA levels as well as reduced stroke risk [204]. In addition, compounds extracted from natural products that have effects on tryptophan metabolism may provide profitable and auspicious alternatives for the treatment of stroke with few side effects and high availability [205,206].

On account of the different types and stages of strokes, sample size limitations, regional and ethnic variations, and different designs and durations, discrepancies did exist among the studies, which are expected to be refined later on. In the future, clear and precise mechanisms of gut–brain communications, how the MGBA affects stroke, and more associations between tryptophan metabolism and stroke are to be deeply explored with the utilization of advantageous technologies, such as metabolomics, proteomics, microbiome sequencing, etc. This will prompt advances in the field, shift from association to causation, and open new lines for more possibilities of clinical translatability and application, which will provide better prevention, diagnosis, and treatment of stroke, as well as ameliorative stroke prognosis and recovery.

Funding: This work was funded by the National Natural Science Foundation of China (NSFC81903631).

Institutional Review Board Statement: Not applicable.

Informed Consent Statement: Not applicable.

Data Availability Statement: No new data were created or analyzed in this study.

Conflicts of Interest: The authors declare no conflicts of interest.

Appendix A

Table A1. Major gut microbiota alterations in clinical stroke in case-control studies in the past five years.

Type of Stroke	Cohort Size	α-Diversity in Stroke	Main Changes in Gut Microbiota in Stroke	Year	Refs.
IS	30 stroke patients and 30 controls	No difference in Ace, Chao1, Simpson, and Shannon	↑*Odoribacter*, *Akkermansia*, *Ruminococcaceae e_UCG_005*, *norank_p_Flavobacteriaceae*, *norank_p_Parcubacteria*, *Victivallis* ↓*Anaerostipes*, *Ruminiclostridium_5*	2019	[22]
IS	31 stroke patients and 9 controls	No difference in Ace, Chao1, Simpson, Shannon, and observed OTUs	↑*Streptococcus * infantis*, *Prevotella * copri* ↓*Blautia obeum*	2019	[207]

Table A1. *Cont.*

Type of Stroke	Cohort Size	α-Diversity in Stroke	Main Changes in Gut Microbiota in Stroke	Year	Refs.
IS	79 stroke patients and 98 controls	No difference in Ace, Chao1, Simpson, Shannon, and observed OTUs	↑Proteobacteria *, Actinobacteria *, *Lactobacillus* *, *Lactococcus* *, *Escherichia/Shigella* *, *Streptococcus* *, *Collinsella* *, *Dorea* * ↓Firmicutes *, Bacteroidetes *, *Faecalibacterium* *, *Subdoligranulum* *, *Eubacterium* *, *Roseburia* *, *Lachnoclostridium* *, *Butyricicoccus* *	2020	[208]
IS, TIA, and HS	349 stroke patients and 51 controls	↓ Shannon, Simpson, and observed OTUs	↑Proteobacteria, *Escherichia/Shigella*, *Peptoniphilus*, *Ezakiella*, *Enterococcus* ↓Firmicutes, Bacteroidetes	2020	[209]
IS	20 stroke patients, 10 post-stroke, and 16 controls	↑Ace, Chao1, and observed OTUs	↑Actinobacteria *, Bacteroidaceae *, Bifidobacteriaceae *, Coriobacteriaceae *, Enterobacteriaceae, Weeksellaceae, Bacillaceae, Paenibaciiaceae, Brucellaceae, Xanthomnadaceae ↓Firmicutes *, Lachnospiraceae *, Ruminococcaceae*, Prevotellaceae*	2020	[210]
IS	28 stroke patients and 28 controls	↓Shannon and phylogenetic diversity	↑Enterobacteriaceae, Ruminococcaceae, Veillonellaceae, Lachnospiraceae ↓Bacteroidaceae, Prevotellaceae	2021	[12]
AIS	140 stroke patients and 92 controls	N/A	↑Lactobacillaceae *, Enterobacteriaceae *, Porphyromonadaceae *, *Akkermansia* * ↓Lachnospiraceae *, *Roseburia* *, *Bacteroides* *, *Faecalibacterium* *, *Blautia* *, *Anaerostipes* *	2021	[211]
AIS and AIS with T2D	150 stroke patients and 55 controls	N/A	↑Enterobacteriaceae *, Proteobacteria, Gammaproteobactera, Deltaproteobacteri, Desulfovibrionaceae, *Dorea* *, *Lactobacillus*, *Megasphaera* ↓*Lachnospira* *, *Coprococcus* *, *Prevotella*, *Faecalibacterium*, *Roseburia*	2021	[212]
IS	82 stroke patients and 82 controls	↑Shannon and observed OTUs	↑Lactobacillaceae *, Enterococcaceae *, Streptococcaceae *, Enterobacteriaceae * ↓Ruminococcaceae, Lachnospiraceae	2022	[25]
ICH	31 stroke patients and 31 controls	No difference in Chao1, Shannon, Simpson, and observed OTUs	↑Bacteroidetes, *Streptococcus*, *Bifidobacterium*, *Akkermansia*, *Lactobacillus*, *Enterococcus* ↓Firmicutes, *Faecalibacterium*, *Clostridium*, *Prevotella*, *Gemmiger*, *Blautia*	2022	[213]
AIS and AIS with PHS	17 stroke patients and 10 controls	↑Chao1 No difference in Ace, Shannon, and Simpson	↑Verrucomicrobia *, Synergistetes *, Actinobacteria, Proteobacteria, *Akkermansia* *, *Olsenella* *, *Escherichia_Shigella*, *Bifidobacterium*, *Ruminococcaceae_UCG_014* ↓Firmicutes, Bacteroidetes, *Megamonas* *, *Prevotella_9*, *Agathobacter*, *Faecalibacterium*	2022	[214]
CS	30 stroke patients and 33 controls	↑Chao1, Shannon, Ace, and observed OTUs	↑Enterobacteriaceae *, Streptococcaceae *, Lactobacillaceae *, *Escherichia–Shigella* *, *Streptococcus* *, *Lactobacillus* *, *Klebsilla* ↓Veillonellaceae *, Faecalibacterium *, Dialister, Roseburia	2022	[24]

Table A1. *Cont.*

Type of Stroke	Cohort Size	α-Diversity in Stroke	Main Changes in Gut Microbiota in Stroke	Year	Refs.
HS and IS	20 stroke patients and 20 controls	↓Chao, Ace, Shannon, Simpson, and observed OTUs	↑Fusobacteriota *, Desulfobacterota *, Akkermansiaceae, Fusobacteriota, Ruminococcaceae, Oscillospirales ↓Acidobacteriota *, *Bacteroides*	2023	[215]
AIS	90 stroke patients and 60 controls	N/A	↑Actinobacteriota, *Bacteroides*, *Parabacteroides* Faecalibacterium ↓Spirochaetes, *Faecallbacterium*, *Prevotella*, *Roseburia*, *Lachnospira*	2023	[23]
IS	10 stroke patients and 21 controls	↓Chao1 No difference in Shannon and Simpson	↑Proteobacteria *, Verrucomicrobiaceae *, Bacteroidaceae *, Streptococcaceae *, Rikenellaceae *, Enterobacteriaceae *, Christensenellacea *, *Phascolarctobacterium*, *Alistipes*, *Sutterella*, *Akkermansia*, *Bacteroides* ↓Coriobacteriaceae *, Actinobacteria, Clostridiaceae, Ruminococcaceae, *Anaerostipes* *, *Clostridiales* *	2023	[196]
AIS and AIS with HHTN	200 stroke patients and 90 controls	No difference in Ace and Shannon	↑Streptococcaceae *, Lactobacillaceae *, Marinifilaceae *, *Lactobacillus* *, *Veillonella* *, *Bacteroides*, *Bifidobacterium*, *Klebsiella* ↓*Escherichia-Shigella* *, *Streptococcus* *, *Anaerostipes* *, *Butyricicoccus* *, *Blautia*, *Faecalibacterium*	2023	[216]

H-type hypertension (HHTN), Type 2 diabetes (T2D), and phlegm-heat syndrome (PHS). Phylum, Class, Family, *Genus*, and *Species* are presented. * Available *p*-value < 0.05. N/A, no available data.

References

1. Martin, S.S.; Aday, A.W.; Almarzooq, Z.I.; Anderson, C.A.M.; Arora, P.; Avery, C.L.; Baker-Smith, C.M.; Barone Gibbs, B.; Beaton, A.Z.; Boehme, A.K.; et al. 2024 Heart Disease and Stroke Statistics: A Report of US and Global Data From the American Heart Association. *Circulation* **2024**, *149*, e347–e913. [CrossRef]
2. Xie, X.; Wang, L.; Dong, S.; Ge, S.; Zhu, T. Immune Regulation of the Gut-Brain Axis and Lung-Brain Axis Involved in Ischemic Stroke. *Neural Regen. Res.* **2024**, *19*, 519–528. [CrossRef]
3. Tsivgoulis, G.; Katsanos, A.H.; Sandset, E.C.; Turc, G.; Nguyen, T.N.; Bivard, A.; Fischer, U.; Khatri, P. Thrombolysis for Acute Ischaemic Stroke: Current Status and Future Perspectives. *Lancet Neurol.* **2023**, *22*, 418–429. [CrossRef] [PubMed]
4. Rost, N.S.; Brodtmann, A.; Pase, M.P.; Van Veluw, S.J.; Biffi, A.; Duering, M.; Hinman, J.D.; Dichgans, M. Post-Stroke Cognitive Impairment and Dementia. *Circ. Res.* **2022**, *130*, 1252–1271. [CrossRef] [PubMed]
5. Schöttke, H.; Giabbiconi, C.-M. Post-Stroke Depression and Post-Stroke Anxiety: Prevalence and Predictors. *Int. Psychogeriatr.* **2015**, *27*, 1805–1812. [CrossRef] [PubMed]
6. Borthwick, S. Communication Impairment in Patients Following Stroke. *Nurs. Stand.* **2012**, *26*, 35–41. [CrossRef] [PubMed]
7. Zhao, L.; Xiong, Q.; Stary, C.M.; Mahgoub, O.K.; Ye, Y.; Gu, L.; Xiong, X.; Zhu, S. Bidirectional Gut-Brain-Microbiota Axis as a Potential Link between Inflammatory Bowel Disease and Ischemic Stroke. *J. Neuroinflamm.* **2018**, *15*, 339. [CrossRef]
8. Sinagra, E.; Pellegatta, G.; Guarnotta, V.; Maida, M.; Rossi, F.; Conoscenti, G.; Pallio, S.; Alloro, R.; Raimondo, D.; Pace, F.; et al. Microbiota Gut–Brain Axis in Ischemic Stroke: A Narrative Review with a Focus about the Relationship with Inflammatory Bowel Disease. *Life* **2021**, *11*, 715. [CrossRef]
9. Tuz, A.A.; Hasenberg, A.; Hermann, D.M.; Gunzer, M.; Singh, V. Ischemic Stroke and Concomitant Gastrointestinal Complications-a Fatal Combination for Patient Recovery. *Front. Immunol.* **2022**, *13*, 1037330. [CrossRef]
10. Song, J.; Chen, W.; Ye, W. Stroke and the Risk of Gastrointestinal Disorders: A Mendelian Randomization Study. *Front. Neurol.* **2023**, *14*, 1131250. [CrossRef]
11. Roth, W.H.; Cai, A.; Zhang, C.; Chen, M.L.; Merkler, A.E.; Kamel, H. Gastrointestinal Disorders and Risk of First-Ever Ischemic Stroke. *Upd. Int. Car.* **2020**, *51*, 3577–3583. [CrossRef] [PubMed]
12. Xu, K.; Gao, X.; Xia, G.; Chen, M.; Zeng, N.; Wang, S.; You, C.; Tian, X.; Di, H.; Tang, W.; et al. Rapid Gut Dysbiosis Induced by Stroke Exacerbates Brain Infarction in Turn. *Gut* **2021**, *70*, 1486–1494. [CrossRef] [PubMed]
13. Carabotti, M.; Scirocco, A.; Maselli, M.A.; Severi, C. The Gut-Brain Axis: Interactions between Enteric Microbiota, Central and Enteric Nervous Systems. *Ann. Gastroenterol.* **2015**, *28*, 203.

14. Cryan, J.F.; O'Riordan, K.J.; Cowan, C.S.M.; Sandhu, K.V.; Bastiaanssen, T.F.S.; Boehme, M.; Codagnone, M.G.; Cussotto, S.; Fulling, C.; Golubeva, A.V.; et al. The Microbiota-Gut-Brain Axis. *Physiol. Rev.* **2019**, *99*, 1877–2013. [CrossRef] [PubMed]
15. Gao, K.; Mu, C.; Farzi, A.; Zhu, W. Tryptophan Metabolism: A Link between the Gut Microbiota and Brain. *Adv. Nutr.* **2020**, *11*, 709–723. [CrossRef] [PubMed]
16. Xue, C.; Li, G.; Zheng, Q.; Gu, X.; Shi, Q.; Su, Y.; Chu, Q.; Yuan, X.; Bao, Z.; Lu, J.; et al. Tryptophan Metabolism in Health and Disease. *Cell Metab.* **2023**, *35*, 1304–1326. [CrossRef]
17. Wigner, P.; Saluk-Bijak, J.; Synowiec, E.; Miller, E.; Sliwinski, T.; Cichon, N.; Bijak, M. Variation of Genes Encoding Tryptophan Catabolites Pathway Enzymes in Stroke. *J. Clin. Med.* **2019**, *8*, 2133. [CrossRef] [PubMed]
18. Shaw, C.; Hess, M.; Weimer, B.C. Microbial-Derived Tryptophan Metabolites and Their Role in Neurological Disease: Anthranilic Acid and Anthranilic Acid Derivatives. *Microorganisms* **2023**, *11*, 1825. [CrossRef]
19. Boros, F.A.; Maszlag-Török, R.; Szűcs, M.; Annus, Á.; Klivényi, P.; Vécsei, L. Relationships of Ischemic Stroke Occurrence and Outcome with Gene Variants Encoding Enzymes of Tryptophan Metabolism. *Biomedicines* **2021**, *9*, 1441. [CrossRef]
20. Quigley, E.M.M. Gut Bacteria in Health and Disease. *Gastroenterol. Hepatol.* **2013**, *9*, 560.
21. MetaHIT Consortium; Qin, J.; Li, R.; Raes, J.; Arumugam, M.; Burgdorf, K.S.; Manichanh, C.; Nielsen, T.; Pons, N.; Levenez, F.; et al. A Human Gut Microbial Gene Catalogue Established by Metagenomic Sequencing. *Nature* **2010**, *464*, 59–65. [CrossRef] [PubMed]
22. Li, N.; Wang, X.; Sun, C.; Wu, X.; Lu, M.; Si, Y.; Ye, X.; Wang, T.; Yu, X.; Zhao, X.; et al. Change of Intestinal Microbiota in Cerebral Ischemic Stroke Patients. *BMC Microbiol.* **2019**, *19*, 191. [CrossRef] [PubMed]
23. Jiang, Z.; Li, L.; Liu, L.; Ding, B.; Yang, Y.; He, F.; Zhang, L.; Wu, Z. Ischemic Stroke and Dysbiosis of Gut Microbiota: Changes to LPS Levels and Effects on Functional Outcomes. *Altern. Ther. Health Med.* **2023**, *29*, 284. [PubMed]
24. Zheng, Q.; Chen, Y.; Zhai, Y.; Meng, L.; Liu, H.; Tian, H.; Feng, R.; Wang, J.; Zhang, R.; Sun, K.; et al. Gut Dysbiosis Is Associated with the Severity of Cryptogenic Stroke and Enhanced Systemic Inflammatory Response. *Front. Immunol.* **2022**, *13*, 836820. [CrossRef]
25. Zhang, N.; Wang, H.; Wang, X.; Tian, M.; Tian, Y.; Li, Q.; Liang, C.; Peng, X.; Ding, J.; Wu, X.; et al. Combination Effect between Gut Microbiota and Traditional Potentially Modifiable Risk Factors for First-Ever Ischemic Stroke in Tujia, Miao and Han Populations in China. *Front. Mol. Neurosci.* **2022**, *15*, 922399. [CrossRef] [PubMed]
26. Aburto, M.R.; Cryan, J.F. Gastrointestinal and Brain Barriers: Unlocking Gates of Communication across the Microbiota–Gut–Brain Axis. *Nat. Rev. Gastroenterol. Hepatol.* **2024**, *21*, 222–247. [CrossRef] [PubMed]
27. Chelakkot, C.; Ghim, J.; Ryu, S.H. Mechanisms Regulating Intestinal Barrier Integrity and Its Pathological Implications. *Exp. Mol. Med.* **2018**, *50*, 1–9. [CrossRef]
28. Stanley, D.; Mason, L.J.; Mackin, K.E.; Srikhanta, Y.N.; Lyras, D.; Prakash, M.D.; Nurgali, K.; Venegas, A.; Hill, M.D.; Moore, R.J.; et al. Translocation and Dissemination of Commensal Bacteria in Post-Stroke Infection. *Nat. Med.* **2016**, *22*, 1277–1284. [CrossRef]
29. Houlden, A.; Goldrick, M.; Brough, D.; Vizi, E.S.; Lénárt, N.; Martinecz, B.; Roberts, I.S.; Denes, A. Brain Injury Induces Specific Changes in the Caecal Microbiota of Mice via Altered Autonomic Activity and Mucoprotein Production. *Brain Behav. Immun.* **2016**, *57*, 10–20. [CrossRef]
30. Amasheh, S.; Fromm, M.; Günzel, D. Claudins of Intestine and Nephron—A Correlation of Molecular Tight Junction Structure and Barrier Function. *Acta Physiol.* **2011**, *201*, 133–140. [CrossRef]
31. Prame Kumar, K.; McKay, L.D.; Nguyen, H.; Kaur, J.; Wilson, J.L.; Suthya, A.R.; McKeown, S.J.; Abud, H.E.; Wong, C.H.Y. Sympathetic-Mediated Intestinal Cell Death Contributes to Gut Barrier Impairment after Stroke. *Transl. Stroke Res.* **2023**. [CrossRef] [PubMed]
32. Ye, D.; Hu, Y.; Zhu, N.; Gu, W.; Long, G.; Tao, E.; Fang, M.; Jiang, M. Exploratory Investigation of Intestinal Structure and Function after Stroke in Mice. *Mediat. Inflamm.* **2021**, *2021*, 1315797. [CrossRef] [PubMed]
33. Johansson, M.E.V.; Larsson, J.M.H.; Hansson, G.C. The Two Mucus Layers of Colon Are Organized by the MUC2 Mucin, Whereas the Outer Layer Is a Legislator of Host–Microbial Interactions. *Proc. Natl. Acad. Sci. USA* **2011**, *108*, 4659–4665. [CrossRef] [PubMed]
34. Arike, L.; Seiman, A.; Van Der Post, S.; Rodriguez Piñeiro, A.M.; Ermund, A.; Schütte, A.; Bäckhed, F.; Johansson, M.E.V.; Hansson, G.C. Protein Turnover in Epithelial Cells and Mucus along the Gastrointestinal Tract Is Coordinated by the Spatial Location and Microbiota. *Cell Rep.* **2020**, *30*, 1077–1087.e3. [CrossRef]
35. Bevins, C.L.; Salzman, N.H. Paneth Cells, Antimicrobial Peptides and Maintenance of Intestinal Homeostasis. *Nat. Rev. Microbiol.* **2011**, *9*, 356–368. [CrossRef]
36. Yu, L.C.-H. Host-Microbial Interactions and Regulation of Intestinal Epithelial Barrier Function: From Physiology to Pathology. *World J. Gastrointest. Pathophysiol.* **2012**, *3*, 27. [CrossRef]
37. Lawther, B.K.; Kumar, S.; Krovvidi, H. Blood–Brain Barrier. *Contin. Educ. Anaesth. Crit. Care Pain* **2011**, *11*, 128–132. [CrossRef]
38. Kim, K.-A.; Kim, D.; Kim, J.-H.; Shin, Y.-J.; Kim, E.-S.; Akram, M.; Kim, E.-H.; Majid, A.; Baek, S.-H.; Bae, O.-N. Autophagy-Mediated Occludin Degradation Contributes to Blood–Brain Barrier Disruption during Ischemia in bEnd.3 Brain Endothelial Cells and Rat Ischemic Stroke Models. *Fluids Barriers CNS* **2020**, *17*, 21. [CrossRef]
39. Braniste, V.; Al-Asmakh, M.; Kowal, C.; Anuar, F.; Abbaspour, A.; Tóth, M.; Korecka, A.; Bakocevic, N.; Ng, L.G.; Kundu, P.; et al. The Gut Microbiota Influences Blood-Brain Barrier Permeability in Mice. *Sci. Transl. Med.* **2014**, *6*, 263ra158. [CrossRef]

40. Fröhlich, E.E.; Farzi, A.; Mayerhofer, R.; Reichmann, F.; Jačan, A.; Wagner, B.; Zinser, E.; Bordag, N.; Magnes, C.; Fröhlich, E.; et al. Cognitive Impairment by Antibiotic-Induced Gut Dysbiosis: Analysis of Gut Microbiota-Brain Communication. *Brain Behav. Immun.* **2016**, *56*, 140–155. [CrossRef]
41. Rustia, A.J.; Paterson, J.S.; Best, G.; Sokoya, E.M. Microbial Disruption in the Gut Promotes Cerebral Endothelial Dysfunction. *Physiol. Rep.* **2021**, *9*, e15100. [CrossRef] [PubMed]
42. Nelson, J.W.; Phillips, S.C.; Ganesh, B.P.; Petrosino, J.F.; Durgan, D.J.; Bryan, R.M. The Gut Microbiome Contributes to Blood-brain Barrier Disruption in Spontaneously Hypertensive Stroke Prone Rats. *FASEB J.* **2021**, *35*, e21201. [CrossRef] [PubMed]
43. Wang, H.; Song, W.; Wu, Q.; Gao, X.; Li, J.; Tan, C.; Zhou, H.; Zhu, J.; He, Y.; Yin, J. Fecal Transplantation from Db/Db Mice Treated with Sodium Butyrate Attenuates Ischemic Stroke Injury. *Microbiol. Spectr.* **2021**, *9*, e00042-21. [CrossRef] [PubMed]
44. Lee, J.; d'Aigle, J.; Atadja, L.; Quaicoe, V.; Honarpisheh, P.; Ganesh, B.P.; Hassan, A.; Graf, J.; Petrosino, J.; Putluri, N.; et al. Gut Microbiota–Derived Short-Chain Fatty Acids Promote Poststroke Recovery in Aged Mice. *Circ. Res.* **2020**, *127*, 453–465. [CrossRef]
45. Peh, A.; Dinakis, E.; Jama, H.; Anderson, D.; Creek, D.J.; Zheng, G.; De Veer, M.; Mackay, C.R.; Zheng, T.; Kemp-Harper, B.K.; et al. Dietary Fibre Reverses Adverse Post-Stroke Outcomes in Mice via Short-Chain Fatty Acids and Its Sensing Receptors GPR41, GPR43 and GPR109A. *bioRxiv* **2023**. [CrossRef]
46. Wang, H.-B.; Wang, P.-Y.; Wang, X.; Wan, Y.-L.; Liu, Y.-C. Butyrate Enhances Intestinal Epithelial Barrier Function via Up-Regulation of Tight Junction Protein Claudin-1 Transcription. *Digest. Dis. Sci.* **2012**, *57*, 3126–3135. [CrossRef] [PubMed]
47. Wang, H.; Song, W.; Gao, X.; Zhu, J.; Li, J.; Wu, Q.; Tan, C.; Zhou, H.; He, Y.; Yin, J. Modulation of the Gut Microbiota of Type 2 Diabetic Mice by Sodium Butyrate Attenuates Ischemic Stroke Injury. *Res. Sq.* **2020**. [CrossRef]
48. Zheng, L.; Kelly, C.J.; Battista, K.D.; Schaefer, R.; Lanis, J.M.; Alexeev, E.E.; Wang, R.X.; Onyiah, J.C.; Kominsky, D.J.; Colgan, S.P. Microbial-Derived Butyrate Promotes Epithelial Barrier Function through IL-10 Receptor–Dependent Repression of Claudin-2. *J. Immunol.* **2017**, *199*, 2976–2984. [CrossRef] [PubMed]
49. Powell, N.; Walker, M.M.; Talley, N.J. The Mucosal Immune System: Master Regulator of Bidirectional Gut–Brain Communications. *Nat. Rev. Gastroenterol. Hepatol.* **2017**, *14*, 143–159. [CrossRef]
50. Mowat, A. McI. Anatomical Basis of Tolerance and Immunity to Intestinal Antigens. *Nat. Rev. Immunol.* **2003**, *3*, 331–341. [CrossRef]
51. Song, C.; Chai, Z.; Chen, S.; Zhang, H.; Zhang, X.; Zhou, Y. Intestinal Mucus Components and Secretion Mechanisms: What We Do and Do Not Know. *Exp. Mol. Med.* **2023**, *55*, 681–691. [CrossRef] [PubMed]
52. Honarpisheh, P.; Bryan, R.M.; McCullough, L.D. Aging Microbiota-Gut-Brain Axis in Stroke Risk and Outcome. *Circ. Res.* **2022**, *130*, 1112–1144. [CrossRef] [PubMed]
53. Kasarello, K.; Cudnoch-Jedrzejewska, A.; Czarzasta, K. Communication of Gut Microbiota and Brain via Immune and Neuroendocrine Signaling. *Front. Microbiol.* **2023**, *14*, 1118529. [CrossRef] [PubMed]
54. Huang, W.; Zhu, L.; Song, W.; Zhang, M.; Teng, L.; Wu, M. Crosstalk between the Gut and Brain in Ischemic Stroke: Mechanistic Insights and Therapeutic Options. *Mediat. Inflamm.* **2022**, *2022*, 6508046. [CrossRef]
55. Eletto, D.; Mentucci, F.; Voli, A.; Petrella, A.; Porta, A.; Tosco, A. Helicobacter Pylori Pathogen-Associated Molecular Patterns: Friends or Foes? *Int. J. Mol. Sci.* **2022**, *23*, 3531. [CrossRef]
56. Roh, J.S.; Sohn, D.H. Damage-Associated Molecular Patterns in Inflammatory Diseases. *Immune Netw.* **2018**, *18*, e27. [CrossRef] [PubMed]
57. Chaudhry, S.; Hafez, A.; Rezai Jahromi, B.; Kinfe, T.; Lamprecht, A.; Niemelä, M.; Muhammad, S. Role of Damage Associated Molecular Pattern Molecules (DAMPs) in Aneurysmal Subarachnoid Hemorrhage (aSAH). *Int. J. Mol. Sci.* **2018**, *19*, 2035. [CrossRef]
58. Fadakar, K.; Dadkhahfar, S.; Esmaeili, A.; Rezaei, N. The Role of Toll-like Receptors (TLRs) in Stroke. *Rev. Neurosci.* **2014**, *25*, 699–712. [CrossRef]
59. Logsdon, A.F.; Erickson, M.A.; Rhea, E.M.; Salameh, T.S.; Banks, W.A. Gut Reactions: How the Blood–Brain Barrier Connects the Microbiome and the Brain. *Exp. Biol. Med.* **2018**, *243*, 159–165. [CrossRef]
60. Zhang, Y.; Wang, Z.; Peng, J.; Gerner, S.T.; Yin, S.; Jiang, Y. Gut Microbiota-Brain Interaction: An Emerging Immunotherapy for Traumatic Brain Injury. *Exp. Neurol.* **2021**, *337*, 113585. [CrossRef]
61. Brea, D.; Poon, C.; Benakis, C.; Lubitz, G.; Murphy, M.; Iadecola, C.; Anrather, J. Stroke Affects Intestinal Immune Cell Trafficking to the Central Nervous System. *Brain Behav. Immun.* **2021**, *96*, 295–302. [CrossRef] [PubMed]
62. Waisman, A.; Liblau, R.S.; Becher, B. Innate and Adaptive Immune Responses in the CNS. *Lancet Neurol.* **2015**, *14*, 945–955. [CrossRef]
63. Reemst, K.; Noctor, S.C.; Lucassen, P.J.; Hol, E.M. The Indispensable Roles of Microglia and Astrocytes during Brain Development. *Front. Hum. Neurosci.* **2016**, *10*, 566. [CrossRef] [PubMed]
64. Li, X.; Chen, G. CNS-Peripheral Immune Interactions in Hemorrhagic Stroke. *J. Cereb. Blood Flow Metab.* **2023**, *43*, 185–197. [CrossRef] [PubMed]
65. Kim, J.Y.; Kawabori, M.; Yenari, M.A. Innate Inflammatory Responses in Stroke: Mechanisms and Potential Therapeutic Targets. *Curr. Med. Chem.* **2014**, *21*, 2076–2097. [CrossRef] [PubMed]
66. Shekhar, S.; Cunningham, M.W.; Pabbidi, M.R.; Wang, S.; Booz, G.W.; Fan, F. Targeting Vascular Inflammation in Ischemic Stroke: Recent Developments on Novel Immunomodulatory Approaches. *Eur. J. Pharmacol.* **2018**, *833*, 531–544. [CrossRef] [PubMed]

67. Singh, V.; Roth, S.; Llovera, G.; Sadler, R.; Garzetti, D.; Stecher, B.; Dichgans, M.; Liesz, A. Microbiota Dysbiosis Controls the Neuroinflammatory Response after Stroke. *J. Neurosci.* **2016**, *36*, 7428–7440. [CrossRef] [PubMed]
68. Iadecola, C.; Buckwalter, M.S.; Anrather, J. Immune Responses to Stroke: Mechanisms, Modulation, and Therapeutic Potential. *J. Clin. Investig.* **2020**, *130*, 2777–2788. [CrossRef]
69. Wu, S.; Tabassum, S.; Payne, C.T.; Hu, H.; Gusdon, A.M.; Choi, H.A.; Ren, X.S. Updates of the Role of B-Cells in Ischemic Stroke. *Front. Cell. Neurosci.* **2024**, *18*, 1340756. [CrossRef]
70. Prass, K.; Meisel, C.; Höflich, C.; Braun, J.; Halle, E.; Wolf, T.; Ruscher, K.; Victorov, I.V.; Priller, J.; Dirnagl, U.; et al. Stroke-Induced Immunodeficiency Promotes Spontaneous Bacterial Infections and Is Mediated by Sympathetic Activation Reversal by Poststroke T Helper Cell Type 1–like Immunostimulation. *J. Exp. Med.* **2003**, *198*, 725–736. [CrossRef]
71. Pu, B.; Zhu, H.; Wei, L.; Gu, L.; Zhang, S.; Jian, Z.; Xiong, X. The Involvement of Immune Cells Between Ischemic Stroke and Gut Microbiota. *Transl. Stroke Res.* **2024**, *15*, 498–517. [CrossRef] [PubMed]
72. Singh, V.; Sadler, R.; Heindl, S.; Llovera, G.; Roth, S.; Benakis, C.; Liesz, A. The Gut Microbiome Primes a Cerebroprotective Immune Response after Stroke. *J. Cereb. Blood Flow Metab.* **2018**, *38*, 1293–1298. [CrossRef] [PubMed]
73. Grant, E.T.; Boudaud, M.; Muller, A.; Macpherson, A.J.; Desai, M.S. Maternal Diet and Gut Microbiome Composition Modulate Early-life Immune Development. *EMBO Mol. Med.* **2023**, *15*, e17241. [CrossRef]
74. Zeng, J.; Yang, K.; Nie, H.; Yuan, L.; Wang, S.; Zeng, L.; Ge, A.; Ge, J. The Mechanism of Intestinal Microbiota Regulating Immunity and Inflammation in Ischemic Stroke and the Role of Natural Botanical Active Ingredients in Regulating Intestinal Microbiota: A Review. *Biomed. Pharmacother.* **2023**, *157*, 114026. [CrossRef]
75. Furness, J.B. The Enteric Nervous System and Neurogastroenterology. *Nat. Rev. Gastroenterol. Hepatol.* **2012**, *9*, 286–294. [CrossRef] [PubMed]
76. Sharkey, K.A.; Mawe, G.M. The Enteric Nervous System. *Physiol. Rev.* **2023**, *103*, 1487–1564. [CrossRef] [PubMed]
77. Spencer, N.J.; Hu, H. Enteric Nervous System: Sensory Transduction, Neural Circuits and Gastrointestinal Motility. *Nat. Rev. Gastroenterol. Hepatol.* **2020**, *17*, 338–351. [CrossRef] [PubMed]
78. Jarret, A.; Jackson, R.; Duizer, C.; Healy, M.E.; Zhao, J.; Rone, J.M.; Bielecki, P.; Sefik, E.; Roulis, M.; Rice, T.; et al. Enteric Nervous System-Derived IL-18 Orchestrates Mucosal Barrier Immunity. *Cell* **2020**, *180*, 50–63.e12. [CrossRef]
79. Muller, P.A.; Koscsó, B.; Rajani, G.M.; Stevanovic, K.; Berres, M.-L.; Hashimoto, D.; Mortha, A.; Leboeuf, M.; Li, X.-M.; Mucida, D.; et al. Crosstalk between Muscularis Macrophages and Enteric Neurons Regulates Gastrointestinal Motility. *Cell* **2014**, *158*, 300–313. [CrossRef]
80. Viola, M.F.; Chavero-Pieres, M.; Modave, E.; Delfini, M.; Stakenborg, N.; Estévez, M.C.; Fabre, N.; Appeltans, I.; Martens, T.; Vandereyken, K.; et al. Dedicated Macrophages Organize and Maintain the Enteric Nervous System. *Nature* **2023**, *618*, 818–826. [CrossRef]
81. Cheng, X.; Boza-Serrano, A.; Turesson, M.F.; Deierborg, T.; Ekblad, E.; Voss, U. Galectin-3 Causes Enteric Neuronal Loss in Mice after Left Sided Permanent Middle Cerebral Artery Occlusion, a Model of Stroke. *Sci. Rep.* **2016**, *6*, 32893. [CrossRef] [PubMed]
82. Cheng, X.; Svensson, M.; Yang, Y.; Deierborg, T.; Ekblad, E.; Voss, U. Focal, but Not Global, Cerebral Ischaemia Causes Loss of Myenteric Neurons and Upregulation of Vasoactive Intestinal Peptide in Mouse Ileum. *Int. J. Exp. Path.* **2018**, *99*, 38–45. [CrossRef] [PubMed]
83. Kumar, K.P.; Wilson, J.L.; Nguyen, H.; McKay, L.D.; Wen, S.W.; Sepehrizadeh, T.; De Veer, M.; Rajasekhar, P.; Carbone, S.E.; Hickey, M.J.; et al. Stroke Alters the Function of Enteric Neurons to Impair Smooth Muscle Relaxation and Dysregulates Gut Transit. *JAHA* **2024**, *13*, e033279. [CrossRef]
84. Goyal, R.K. The Enteric Nervous System. *N. Engl. J. Med.* **1996**, *334*, 1106–1115. [CrossRef] [PubMed]
85. Tang, H.; Li, J.; Zhou, Q.; Li, S.; Xie, C.; Niu, L.; Ma, J.; Li, C. Vagus Nerve Stimulation Alleviated Cerebral Ischemia and Reperfusion Injury in Rats by Inhibiting Pyroptosis via A7 Nicotinic Acetylcholine Receptor. *Cell Death Discov.* **2022**, *8*, 54. [CrossRef] [PubMed]
86. Liu, Y.-L.; Wang, S.-R.; Ma, J.-X.; Yu, L.-H.; Jia, G.-W. Vagus Nerve Stimulation Is a Potential Treatment for Ischemic Stroke. *Neural Regener. Res.* **2023**, *18*, 825. [CrossRef]
87. Muller, P.A.; Schneeberger, M.; Matheis, F.; Wang, P.; Kerner, Z.; Ilanges, A.; Pellegrino, K.; Del Mármol, J.; Castro, T.B.R.; Furuichi, M.; et al. Microbiota Modulate Sympathetic Neurons via a Gut–Brain Circuit. *Nature* **2020**, *583*, 441–446. [CrossRef] [PubMed]
88. Goehler, L.E.; Gaykema, R.P.A.; Opitz, N.; Reddaway, R.; Badr, N.; Lyte, M. Activation in Vagal Afferents and Central Autonomic Pathways: Early Responses to Intestinal Infection with Campylobacter Jejuni. *Brain Behav. Immun.* **2005**, *19*, 334–344. [CrossRef] [PubMed]
89. Vicentini, F.A.; Keenan, C.M.; Wallace, L.E.; Woods, C.; Cavin, J.-B.; Flockton, A.R.; Macklin, W.B.; Belkind-Gerson, J.; Hirota, S.A.; Sharkey, K.A. Intestinal Microbiota Shapes Gut Physiology and Regulates Enteric Neurons and Glia. *Microbiome* **2021**, *9*, 210. [CrossRef]
90. Yan, Y.; Ramanan, D.; Rozenberg, M.; McGovern, K.; Rastelli, D.; Vijaykumar, B.; Yaghi, O.; Voisin, T.; Mosaheb, M.; Chiu, I.; et al. Interleukin-6 Produced by Enteric Neurons Regulates the Number and Phenotype of Microbe-Responsive Regulatory T Cells in the Gut. *Immunity* **2021**, *54*, 499–513.e5. [CrossRef]
91. Chen, Y.; Xu, J.; Chen, Y. Regulation of Neurotransmitters by the Gut Microbiota and Effects on Cognition in Neurological Disorders. *Nutrients* **2021**, *13*, 2099. [CrossRef] [PubMed]

92. Burford, N.; Webster, N.; Cruz-Topete, D. Hypothalamic-Pituitary-Adrenal Axis Modulation of Glucocorticoids in the Cardiovascular System. *Int. J. Mol. Sci.* **2017**, *18*, 2150. [CrossRef] [PubMed]
93. Fassbender, K.; Schmidt, R.; Mössner, R.; Daffertshofer, M.; Hennerici, M. Pattern of Activation of the Hypothalamic-Pituitary-Adrenal Axis in Acute Stroke. Relation to Acute Confusional State, Extent of Brain Damage, and Clinical Outcome. *Stroke* **1994**, *25*, 1105–1108. [CrossRef]
94. Barugh, A.J.; Gray, P.; Shenkin, S.D.; MacLullich, A.M.J.; Mead, G.E. Cortisol Levels and the Severity and Outcomes of Acute Stroke: A Systematic Review. *J. Neurol.* **2014**, *261*, 533–545. [CrossRef] [PubMed]
95. Sugo, N.; Hurn, P.D.; Morahan, M.B.; Hattori, K.; Traystman, R.J.; DeVries, A.C. Social Stress Exacerbates Focal Cerebral Ischemia in Mice. *Stroke* **2002**, *33*, 1660–1664. [CrossRef] [PubMed]
96. Kim, S.; Park, E.S.; Chen, P.R.; Kim, E. Dysregulated Hypothalamic–Pituitary–Adrenal Axis Is Associated With Increased Inflammation and Worse Outcomes After Ischemic Stroke in Diabetic Mice. *Front. Immunol.* **2022**, *13*, 864858. [CrossRef] [PubMed]
97. Mracsko, E.; Liesz, A.; Karcher, S.; Zorn, M.; Bari, F.; Veltkamp, R. Differential Effects of Sympathetic Nervous System and Hypothalamic–Pituitary–Adrenal Axis on Systemic Immune Cells after Severe Experimental Stroke. *Brain Behav. Immun.* **2014**, *41*, 200–209. [CrossRef] [PubMed]
98. Wang, Y.; Wang, H.; Sun, W.; Miao, J.; Liang, W.; Qiu, X.; Lan, Y.; Pan, C.; Li, G.; Zhao, X.; et al. Higher Concentration of Adrenocorticotropic Hormone Predicts Post-Stroke Depression. *Clin. Interv. Aging* **2022**, *17*, 417–427. [CrossRef]
99. Sudo, N.; Chida, Y.; Aiba, Y.; Sonoda, J.; Oyama, N.; Yu, X.; Kubo, C.; Koga, Y. Postnatal Microbial Colonization Programs the Hypothalamic–Pituitary–Adrenal System for Stress Response in Mice. *J. Physiol.* **2004**, *558*, 263–275. [CrossRef]
100. Vodička, M.; Ergang, P.; Hrnčíř, T.; Mikulecká, A.; Kvapilová, P.; Vagnerová, K.; Šestáková, B.; Fajstová, A.; Hermanová, P.; Hudcovic, T.; et al. Microbiota Affects the Expression of Genes Involved in HPA Axis Regulation and Local Metabolism of Glucocorticoids in Chronic Psychosocial Stress. *Brain Behav. Immun.* **2018**, *73*, 615–624. [CrossRef]
101. Rehfeld, J.F. A Centenary of Gastrointestinal Endocrinology. *Horm. Metab. Res.* **2004**, *36*, 735–741. [CrossRef]
102. Furness, J.B.; Rivera, L.R.; Cho, H.-J.; Bravo, D.M.; Callaghan, B. The Gut as a Sensory Organ. *Nat. Rev. Gastroenterol. Hepatol.* **2013**, *10*, 729–740. [CrossRef] [PubMed]
103. Sun, L.-J.; Li, J.-N.; Nie, Y.-Z. Gut Hormones in Microbiota-Gut-Brain Cross-Talk. *Chin. Med. J.* **2020**, *133*, 826–833. [CrossRef] [PubMed]
104. Latorre, R.; Sternini, C.; De Giorgio, R.; Greenwood-Van Meerveld, B. Enteroendocrine Cells: A Review of Their Role in Brain–Gut Communication. *Neurogastroenterol. Motil.* **2016**, *28*, 620–630. [CrossRef] [PubMed]
105. Bogunovic, M.; Davé, S.H.; Tilstra, J.S.; Chang, D.T.W.; Harpaz, N.; Xiong, H.; Mayer, L.F.; Plevy, S.E. Enteroendocrine Cells Express Functional Toll-like Receptors. *Am. J. Physiol.-Gastrointest. Liver Physiol.* **2007**, *292*, G1770–G1783. [CrossRef] [PubMed]
106. Kuwahara, A.; Matsuda, K.; Kuwahara, Y.; Asano, S.; Inui, T.; Marunaka, Y. Microbiota-Gut-Brain Axis: Enteroendocrine Cells and the Enteric Nervous System Form an Interface between the Microbiota and the Central Nervous System. *Biomed. Res.* **2020**, *41*, 199–216. [CrossRef] [PubMed]
107. Comai, S.; Bertazzo, A.; Brughera, M.; Crotti, S. Tryptophan in Health and Disease. In *Advances in Clinical Chemistry*; Elsevier: Amsterdam, The Netherlands, 2020; Volume 95, pp. 165–218. ISBN 978-0-12-821165-6.
108. Yeung, A.W.S.; Terentis, A.C.; King, N.J.C.; Thomas, S.R. Role of Indoleamine 2,3-Dioxygenase in Health and Disease. *Clin. Sci.* **2015**, *129*, 601–672. [CrossRef]
109. Huang, Y.-S.; Ogbechi, J.; Clanchy, F.I.; Williams, R.O.; Stone, T.W. IDO and Kynurenine Metabolites in Peripheral and CNS Disorders. *Front. Immunol.* **2020**, *11*, 388. [CrossRef]
110. Prendergast, G.C.; Metz, R.; Muller, A.J.; Merlo, L.M.F.; Mandik-Nayak, L. IDO2 in Immunomodulation and Autoimmune Disease. *Front. Immunol.* **2014**, *5*, 585. [CrossRef]
111. Roth, W.; Zadeh, K.; Vekariya, R.; Ge, Y.; Mohamadzadeh, M. Tryptophan Metabolism and Gut-Brain Homeostasis. *Int. J. Mol. Sci.* **2021**, *22*, 2973. [CrossRef]
112. Lamas, B.; Natividad, J.M.; Sokol, H. Aryl Hydrocarbon Receptor and Intestinal Immunity. *Mucosal Immunol.* **2018**, *11*, 1024–1038. [CrossRef] [PubMed]
113. Rothhammer, V.; Quintana, F.J. The Aryl Hydrocarbon Receptor: An Environmental Sensor Integrating Immune Responses in Health and Disease. *Nat. Rev. Immunol.* **2019**, *19*, 184–197. [CrossRef]
114. Mrštná, K.; Krčmová, L.K.; Švec, F. Advances in Kynurenine Analysis. *Clin. Chim. Acta* **2023**, *547*, 117441. [CrossRef] [PubMed]
115. Beamer, C.A.; Shepherd, D.M. Role of the Aryl Hydrocarbon Receptor (AhR) in Lung Inflammation. *Semin. Immunopathol.* **2013**, *35*, 693–704. [CrossRef] [PubMed]
116. Lőrinczi, B.; Szatmári, I. KYNA Derivatives with Modified Skeleton; Hydroxyquinolines with Potential Neuroprotective Effect. *Int. J. Mol. Sci.* **2021**, *22*, 11935. [CrossRef] [PubMed]
117. Vécsei, L.; Szalárdy, L.; Fülöp, F.; Toldi, J. Kynurenines in the CNS: Recent Advances and New Questions. *Nat. Rev. Drug Discov.* **2013**, *12*, 64–82. [CrossRef]
118. Lopez, A.; Alegre, E.; Lemaoult, J.; Carosella, E.; Gonzalez, A. Regulatory Role of Tryptophan Degradation Pathway in HLA-G Expression by Human Monocyte-Derived Dendritic Cells. *Mol. Immunol.* **2006**, *43*, 2151–2160. [CrossRef] [PubMed]

119. Weber, W.P.; Feder-Mengus, C.; Chiarugi, A.; Rosenthal, R.; Reschner, A.; Schumacher, R.; Zajac, P.; Misteli, H.; Frey, D.M.; Oertli, D.; et al. Differential Effects of the Tryptophan Metabolite3-hydroxyanthranilic Acid on the Proliferation of Human CD8 $^{+}$ T Cells Induced by TCR Triggering or Homeostatic Cytokines. *Eur. J. Immunol.* **2006**, *36*, 296–304. [CrossRef] [PubMed]
120. Harvey-Girard, E.; Dunn, R.J. Excitatory Amino Acid Receptors of the Electrosensory System: The NR1/NR2B *N*-Methyl-D-Aspartate Receptor. *J. Neurophysiol.* **2003**, *89*, 822–832. [CrossRef]
121. Schwarcz, R.; Stone, T.W. The Kynurenine Pathway and the Brain: Challenges, Controversies and Promises. *Neuropharmacology* **2017**, *112*, 237–247. [CrossRef]
122. Pierozan, P.; Biasibetti, H.; Schmitz, F.; Ávila, H.; Parisi, M.M.; Barbe-Tuana, F.; Wyse, A.T.S.; Pessoa-Pureur, R. Quinolinic Acid Neurotoxicity: Differential Roles of Astrocytes and Microglia via FGF-2-Mediated Signaling in Redox-Linked Cytoskeletal Changes. *Biochim. Biophys. Acta (BBA)-Mol. Cell Res.* **2016**, *1863*, 3001–3014. [CrossRef] [PubMed]
123. Dehhaghi, M.; Panahi, H.K.S.; Kavyani, B.; Heng, B.; Tan, V.; Braidy, N.; Guillemin, G.J. The Role of Kynurenine Pathway and NAD $^{+}$ Metabolism in Myalgic Encephalomyelitis/Chronic Fatigue Syndrome. *Aging Dis.* **2022**, *13*, 698. [CrossRef] [PubMed]
124. Dehhaghi, M.; Tan, V.; Heng, B.; Braidy, N.; Mohammadipanah, F.; Guillemin, G.J. Neuroprotective Effect of Myxobacterial Extracts on Quinolinic Acid-Induced Toxicity in Primary Human Neurons. *Neurotox. Res.* **2019**, *35*, 281–290. [CrossRef] [PubMed]
125. Dehhaghi, M.; Kazemi Shariat Panahi, H.; Braidy, N.; Guillemin, G.J. Herpetosiphon Secondary Metabolites Inhibit Amyloid-β Toxicity in Human Primary Astrocytes. *J. Alzheimers Dis.* **2020**, *76*, 423–433. [CrossRef] [PubMed]
126. Zapata-Pérez, R.; Wanders, R.J.A.; Van Karnebeek, C.D.M.; Houtkooper, R.H. NAD $^{+}$ Homeostasis in Human Health and Disease. *EMBO Mol. Med.* **2021**, *13*, e13943. [CrossRef] [PubMed]
127. Gao, J.; Xu, K.; Liu, H.; Liu, G.; Bai, M.; Peng, C.; Li, T.; Yin, Y. Impact of the Gut Microbiota on Intestinal Immunity Mediated by Tryptophan Metabolism. *Front. Cell. Infect. Microbiol.* **2018**, *8*, 13. [CrossRef]
128. Israelyan, N.; Margolis, K.G. Serotonin as a Link between the Gut-Brain-Microbiome Axis in Autism Spectrum Disorders. *Pharmacol. Res.* **2018**, *132*, 1–6. [CrossRef]
129. Margolis, K.G.; Stevanovic, K.; Li, Z.; Yang, Q.M.; Oravecz, T.; Zambrowicz, B.; Jhaver, K.G.; Diacou, A.; Gershon, M.D. Pharmacological Reduction of Mucosal but Not Neuronal Serotonin Opposes Inflammation in Mouse Intestine. *Gut* **2014**, *63*, 928–937. [CrossRef] [PubMed]
130. Gross, E.R.; Gershon, M.D.; Margolis, K.G.; Gertsberg, Z.V.; Cowles, R.A. Neuronal Serotonin Regulates Growth of the Intestinal Mucosa in Mice. *Gastroenterology* **2012**, *143*, 408–417.e2. [CrossRef]
131. Li, Z.; Chalazonitis, A.; Huang, Y.-Y.; Mann, J.J.; Margolis, K.G.; Yang, Q.M.; Kim, D.O.; Cote, F.; Mallet, J.; Gershon, M.D. Essential Roles of Enteric Neuronal Serotonin in Gastrointestinal Motility and the Development/Survival of Enteric Dopaminergic Neurons. *J. Neurosci.* **2011**, *31*, 8998–9009. [CrossRef]
132. Wolf, D.; Klasen, M.; Eisner, P.; Zepf, F.D.; Zvyagintsev, M.; Palomero-Gallagher, N.; Weber, R.; Eisert, A.; Mathiak, K. Central Serotonin Modulates Neural Responses to Virtual Violent Actions in Emotion Regulation Networks. *Brain Struct. Funct.* **2018**, *223*, 3327–3345. [CrossRef] [PubMed]
133. Ursin, R. Serotonin and Sleep. *Sleep Med. Rev.* **2002**, *6*, 55–67. [CrossRef] [PubMed]
134. Migliarini, S.; Pacini, G.; Pelosi, B.; Lunardi, G.; Pasqualetti, M. Lack of Brain Serotonin Affects Postnatal Development and Serotonergic Neuronal Circuitry Formation. *Mol. Psychiatry* **2013**, *18*, 1106–1118. [CrossRef] [PubMed]
135. Van Kleef, E.S.B.; Gaspar, P.; Bonnin, A. Insights into the Complex Influence of 5-HT Signaling on Thalamocortical Axonal System Development. *Eur. J. Neurosci.* **2012**, *35*, 1563–1572. [CrossRef] [PubMed]
136. Filip, M.; Bader, M. Overview on 5-HT Receptors and Their Role in Physiology and Pathology of the Central Nervous System. *Pharmacol. Rep.* **2009**, *61*, 761–777. [CrossRef] [PubMed]
137. Ciranna, L. Serotonin as a Modulator of Glutamate- and GABA-Mediated Neurotransmission: Implications in Physiological Functions and in Pathology. *Curr. Neuropharmacol.* **2006**, *4*, 101–114. [CrossRef]
138. Browning, K.N. Role of Central Vagal 5-HT3 Receptors in Gastrointestinal Physiology and Pathophysiology. *Front. Neurosci.* **2015**, *9*, 413. [CrossRef] [PubMed]
139. Mawe, G.M.; Hoffman, J.M. Serotonin Signalling in the Gut—Functions, Dysfunctions and Therapeutic Targets. *Nat. Rev. Gastroenterol. Hepatol.* **2013**, *10*, 473–486. [CrossRef] [PubMed]
140. De Vadder, F.; Grasset, E.; Mannerås Holm, L.; Karsenty, G.; Macpherson, A.J.; Olofsson, L.E.; Bäckhed, F. Gut Microbiota Regulates Maturation of the Adult Enteric Nervous System via Enteric Serotonin Networks. *Proc. Natl. Acad. Sci. USA* **2018**, *115*, 6458–6463. [CrossRef] [PubMed]
141. Hoffman, J.M.; Tyler, K.; MacEachern, S.J.; Balemba, O.B.; Johnson, A.C.; Brooks, E.M.; Zhao, H.; Swain, G.M.; Moses, P.L.; Galligan, J.J.; et al. Activation of Colonic Mucosal 5-HT4 Receptors Accelerates Propulsive Motility and Inhibits Visceral Hypersensitivity. *Gastroenterology* **2012**, *142*, 844–854.e4. [CrossRef]
142. Walldorf, J.; Porzner, M.; Neumann, M.; Joodi, G.; Niess, J.H.; Von Boyen, G.; Mäder, K.; Weissbach, J.; Kleger, A.; Seufferlein, T. The Selective 5-HT1A Agonist SR57746A Protects Intestinal Epithelial Cells and Enteric Glia Cells and Promotes Mucosal Recovery in Experimental Colitis. *Inflamm. Bowel Dis.* **2022**, *28*, 423–433. [CrossRef] [PubMed]
143. Mawe, G.M.; Branchek, T.A.; Gershon, M.D. Peripheral Neural Serotonin Receptors: Identification and Characterization with Specific Antagonists and Agonists. *Proc. Natl. Acad. Sci. USA* **1986**, *83*, 9799–9803. [CrossRef] [PubMed]
144. Brzęczek, M.; Słonka, K.; Hyla-Klekot, L. Melatonin—A Pleiotropic Hormone. *Pediatr. Med. Rodz.* **2016**, *12*, 127–133. [CrossRef]

145. Navabi, S.; Gorrepati, V.S.; Yadav, S.; Chintanaboina, J.; Maher, S.; Demuth, P.; Stern, B.; Stuart, A.; Tinsley, A.; Clarke, K.; et al. Influences and Impact of Anxiety and Depression in the Setting of Inflammatory Bowel Disease. *Inflamm. Bowel Dis.* **2018**, *24*, 2303–2308. [CrossRef] [PubMed]
146. Roager, H.M.; Licht, T.R. Microbial Tryptophan Catabolites in Health and Disease. *Nat. Commun.* **2018**, *9*, 3294. [CrossRef] [PubMed]
147. Agus, A.; Planchais, J.; Sokol, H. Gut Microbiota Regulation of Tryptophan Metabolism in Health and Disease. *Cell Host Microbe* **2018**, *23*, 716–724. [CrossRef] [PubMed]
148. Kaur, H.; Bose, C.; Mande, S.S. Tryptophan Metabolism by Gut Microbiome and Gut-Brain-Axis: An in Silico Analysis. *Front. Neurosci.* **2019**, *13*, 1365. [CrossRef] [PubMed]
149. Devlin, A.S.; Marcobal, A.; Dodd, D.; Nayfach, S.; Plummer, N.; Meyer, T.; Pollard, K.S.; Sonnenburg, J.L.; Fischbach, M.A. Modulation of a Circulating Uremic Solute via Rational Genetic Manipulation of the Gut Microbiota. *Cell Host Microbe* **2016**, *20*, 709–715. [CrossRef]
150. Lee, J.-H.; Lee, J. Indole as an Intercellular Signal in Microbial Communities. *FEMS Microbiol. Rev.* **2010**, *34*, 426–444. [CrossRef]
151. Whitfield-Cargile, C.M.; Cohen, N.D.; Chapkin, R.S.; Weeks, B.R.; Davidson, L.A.; Goldsby, J.S.; Hunt, C.L.; Steinmeyer, S.H.; Menon, R.; Suchodolski, J.S.; et al. The Microbiota-Derived Metabolite Indole Decreases Mucosal Inflammation and Injury in a Murine Model of NSAID Enteropathy. *Gut Microbes* **2016**, *7*, 246–261. [CrossRef]
152. Chimerel, C.; Emery, E.; Summers, D.K.; Keyser, U.; Gribble, F.M.; Reimann, F. Bacterial Metabolite Indole Modulates Incretin Secretion from Intestinal Enteroendocrine L Cells. *Cell Rep.* **2014**, *9*, 1202–1208. [CrossRef]
153. Tennoune, N.; Andriamihaja, M.; Blachier, F. Production of Indole and Indole-Related Compounds by the Intestinal Microbiota and Consequences for the Host: The Good, the Bad, and the Ugly. *Microorganisms* **2022**, *10*, 930. [CrossRef] [PubMed]
154. Zhai, L.; Xiao, H.; Lin, C.; Wong, H.L.X.; Lam, Y.Y.; Gong, M.; Wu, G.; Ning, Z.; Huang, C.; Zhang, Y.; et al. Gut Microbiota-Derived Tryptamine and Phenethylamine Impair Insulin Sensitivity in Metabolic Syndrome and Irritable Bowel Syndrome. *Nat. Commun.* **2023**, *14*, 4986. [CrossRef] [PubMed]
155. Williams, B.B.; Van Benschoten, A.H.; Cimermancic, P.; Donia, M.S.; Zimmermann, M.; Taketani, M.; Ishihara, A.; Kashyap, P.C.; Fraser, J.S.; Fischbach, M.A. Discovery and Characterization of Gut Microbiota Decarboxylases That Can Produce the Neurotransmitter Tryptamine. *Cell Host Microbe* **2014**, *16*, 495–503. [CrossRef]
156. Hubbard, T.D.; Murray, I.A.; Perdew, G.H. Indole and Tryptophan Metabolism: Endogenous and Dietary Routes to Ah Receptor Activation. *Drug Metab. Dispos.* **2015**, *43*, 1522–1535. [CrossRef] [PubMed]
157. Ehrlich, A.M.; Pacheco, A.R.; Henrick, B.M.; Taft, D.; Xu, G.; Huda, M.N.; Mishchuk, D.; Goodson, M.L.; Slupsky, C.; Barile, D.; et al. Indole-3-Lactic Acid Associated with Bifidobacterium-Dominated Microbiota Significantly Decreases Inflammation in Intestinal Epithelial Cells. *BMC Microbiol.* **2020**, *20*, 357. [CrossRef]
158. Wlodarska, M.; Luo, C.; Kolde, R.; d'Hennezel, E.; Annand, J.W.; Heim, C.E.; Krastel, P.; Schmitt, E.K.; Omar, A.S.; Creasey, E.A.; et al. Indoleacrylic Acid Produced by Commensal Peptostreptococcus Species Suppresses Inflammation. *Cell Host Microbe* **2017**, *22*, 25–37.e6. [CrossRef]
159. Li, J.; Zhang, L.; Wu, T.; Li, Y.; Zhou, X.; Ruan, Z. Indole-3-Propionic Acid Improved the Intestinal Barrier by Enhancing Epithelial Barrier and Mucus Barrier. *J. Agric. Food Chem.* **2021**, *69*, 1487–1495. [CrossRef] [PubMed]
160. Connell, E.; Le Gall, G.; Pontifex, M.G.; Sami, S.; Cryan, J.F.; Clarke, G.; Müller, M.; Vauzour, D. Microbial-Derived Metabolites as a Risk Factor of Age-Related Cognitive Decline and Dementia. *Mol. Neurodegener.* **2022**, *17*, 43. [CrossRef]
161. Rothhammer, V.; Mascanfroni, I.D.; Bunse, L.; Takenaka, M.C.; Kenison, J.E.; Mayo, L.; Chao, C.-C.; Patel, B.; Yan, R.; Blain, M.; et al. Type I Interferons and Microbial Metabolites of Tryptophan Modulate Astrocyte Activity and Central Nervous System Inflammation via the Aryl Hydrocarbon Receptor. *Nat. Med.* **2016**, *22*, 586–597. [CrossRef]
162. Chyan, Y.-J.; Poeggeler, B.; Omar, R.A.; Chain, D.G.; Frangione, B.; Ghiso, J.; Pappolla, M.A. Potent Neuroprotective Properties against the Alzheimer B-Amyloid by an Endogenous Melatonin-Related Indole Structure, Indole-3-Propionic Acid. *J. Biol. Chem.* **1999**, *274*, 21937–21942. [CrossRef]
163. Hwang, I.K.; Yoo, K.; Li, H.; Park, O.K.; Lee, C.H.; Choi, J.H.; Jeong, Y.; Lee, Y.L.; Kim, Y.; Kwon, Y.; et al. Indole-3-propionic Acid Attenuates Neuronal Damage and Oxidative Stress in the Ischemic Hippocampus. *J. Neurosci. Res.* **2009**, *87*, 2126–2137. [CrossRef] [PubMed]
164. Sun, C.-Y.; Li, J.-R.; Wang, Y.-Y.; Lin, S.-Y.; Ou, Y.-C.; Lin, C.-J.; Wang, J.-D.; Liao, S.-L.; Chen, C.-J. Indoxyl Sulfate Caused Behavioral Abnormality and Neurodegeneration in Mice with Unilateral Nephrectomy. *Aging* **2021**, *13*, 6681–6701. [CrossRef]
165. Moloney, G.M.; O'Leary, O.F.; Salvo-Romero, E.; Desbonnet, L.; Shanahan, F.; Dinan, T.G.; Clarke, G.; Cryan, J.F. Microbial Regulation of Hippocampal miRNA Expression: Implications for Transcription of Kynurenine Pathway Enzymes. *Behav. Brain Res.* **2017**, *334*, 50–54. [CrossRef] [PubMed]
166. Liu, B.; Yu, D.; Sun, J.; Wu, X.; Xin, Z.; Deng, B.; Fan, L.; Fu, J.; Ge, L.; Ren, W. Characterizing the Influence of Gut Microbiota on Host Tryptophan Metabolism with Germ-Free Pigs. *Anim. Nutr.* **2022**, *11*, 190–200. [CrossRef]
167. Schwarcz, R.; Foo, A.; Sathyasaikumar, K.V.; Notarangelo, F.M. The Probiotic Lactobacillus Reuteri Preferentially Synthesizes Kynurenic Acid from Kynurenine. *Int. J. Mol. Sci.* **2024**, *25*, 3679. [CrossRef] [PubMed]
168. Sun, P.; Wang, M.; Liu, Y.-X.; Li, L.; Chai, X.; Zheng, W.; Chen, S.; Zhu, X.; Zhao, S. High-Fat Diet-Disturbed Gut Microbiota-Colonocyte Interactions Contribute to Dysregulating Peripheral Tryptophan-Kynurenine Metabolism. *Microbiome* **2023**, *11*, 154. [CrossRef]

169. Mu, C.; Choudhary, A.; Mayengbam, S.; Barrett, K.T.; Rho, J.M.; Shearer, J.; Scantlebury, M.H. Seizure Modulation by the Gut Microbiota and Tryptophan-Kynurenine Metabolism in an Animal Model of Infantile Spasms. *eBioMedicine* **2022**, *76*, 103833. [CrossRef]
170. Zhao, L.-P.; Wu, J.; Quan, W.; Zhou, Y.; Hong, H.; Niu, G.-Y.; Li, T.; Huang, S.-B.; Qiao, C.-M.; Zhao, W.-J.; et al. DSS-Induced Colitis Activates the Kynurenine Pathway in Serum and Brain by Affecting IDO-1 and Gut Microbiota. *Front. Immunol.* **2023**, *13*, 1089200. [CrossRef] [PubMed]
171. Xiao, W.; Li, J.; Gao, X.; Yang, H.; Su, J.; Weng, R.; Gao, Y.; Ni, W.; Gu, Y. Involvement of the Gut-Brain Axis in Vascular Depression via Tryptophan Metabolism: A Benefit of Short Chain Fatty Acids. *Exp. Neurol.* **2022**, *358*, 114225. [CrossRef]
172. Yano, J.M.; Yu, K.; Donaldson, G.P.; Shastri, G.G.; Ann, P.; Ma, L.; Nagler, C.R.; Ismagilov, R.F.; Mazmanian, S.K.; Hsiao, E.Y. Indigenous Bacteria from the Gut Microbiota Regulate Host Serotonin Biosynthesis. *Cell* **2015**, *161*, 264–276. [CrossRef] [PubMed]
173. Yang, M.; Fukui, H.; Eda, H.; Kitayama, Y.; Hara, K.; Kodani, M.; Tomita, T.; Oshima, T.; Watari, J.; Miwa, H. Involvement of Gut Microbiota in the Association between Gastrointestinal Motility and 5-HT Expression/M2 Macrophage Abundance in the Gastrointestinal Tract. *Mol. Med. Rep.* **2017**, *16*, 3482–3488. [CrossRef] [PubMed]
174. Tang, T.; Wang, J.; Jiang, Y.; Zhu, X.; Zhang, Z.; Wang, Y.; Shu, X.; Deng, Y.; Zhang, F. Bifidobacterium Lactis TY-S01 Prevents Loperamide-Induced Constipation by Modulating Gut Microbiota and Its Metabolites in Mice. *Front. Nutr.* **2022**, *9*, 890314. [CrossRef] [PubMed]
175. Xue, K.; Tao, R.; Wu, Q.; Zhang, L.; Sun, Z.; Yu, X.; Meng, J.; Bao, N.; Zhao, J. Enteropathogenic Escherichia Coli Mediates CoCrMo Particle-Induced Peri-Implant Osteolysis by Increasing Peripheral 5-HT. *Front. Cell. Infect. Microbiol.* **2022**, *11*, 796679. [CrossRef]
176. Li, H.; Wang, P.; Huang, L.; Li, P.; Zhang, D. Effects of Regulating Gut Microbiota on the Serotonin Metabolism in the Chronic Unpredictable Mild Stress Rat Model. *Neurogastroenterol. Motil.* **2019**, *31*, e13677. [CrossRef] [PubMed]
177. Li, S.; Li, X.; Wang, K.; Li, Y.; Nagaoka, K.; Li, C. Gut Microbiota Intervention Attenuates Thermogenesis in Broilers Exposed to High Temperature through Modulation of the Hypothalamic 5-HT Pathway. *J. Anim. Sci. Biotechnol.* **2023**, *14*, 159. [CrossRef] [PubMed]
178. Li, D.; Liang, W.; Zhang, W.; Huang, Z.; Liang, H.; Liu, Q. Fecal Microbiota Transplantation Repairs Intestinal Permeability and Regulates the Expression of 5-HT to Influence Alcohol-Induced Depression-like Behaviors in C57BL/6J Mice. *Front. Microbiol.* **2024**, *14*, 1241309. [CrossRef]
179. Bunnett, N.W. Neuro-humoral Signalling by Bile Acids and the TGR5 Receptor in the Gastrointestinal Tract. *J. Physiol.* **2014**, *592*, 2943–2950. [CrossRef]
180. Chen, Z.; Feng, J.; Hu, S.; Hua, Y.; Ma, S.; Fu, W.; Yang, Q.; Zhang, X. Bacillus Subtilis Promotes the Release of 5-HT to Regulate Intestinal Peristalsis in STC Mice via Bile Acid and Its Receptor TGR5 Pathway. *Dig. Dis. Sci.* **2022**, *67*, 4410–4421. [CrossRef]
181. Cai, J.; Cheung, J.; Cheung, S.W.M.; Chin, K.T.C.; Leung, R.W.K.; Lam, R.S.T.; Sharma, R.; Yiu, J.H.C.; Woo, C.W. Butyrate Acts as a Positive Allosteric Modulator of the 5-HT Transporter to Decrease Availability of 5-HT in the Ileum. *Br. J. Pharmacol.* **2024**, *181*, 1654–1670. [CrossRef]
182. Lin, F.; Wang, X.; Luo, R.; Yuan, B.; Ye, S.; Yang, T.; Xiao, L.; Chen, J. Maternal LPS Exposure Enhances the 5-HT Level in the Prefrontal Cortex of Autism-like Young Offspring. *Brain Sci.* **2023**, *13*, 958. [CrossRef] [PubMed]
183. Huang, D.; Yang, Y.; Song, W.; Jiang, C.; Zhang, Y.; Zhang, A.; Lin, Z.; Ke, X. Untargeted Metabonomic Analysis of a Cerebral Stroke Model in Rats: A Study Based on UPLC–MS/MS. *Front. Neurosci.* **2023**, *17*, 1084813. [CrossRef] [PubMed]
184. Saccaro, L.F.; Pico, F.; Chadenat, M.-L.; Richard, O.; Launay, J.-M.; Bastenaire, B.; Jullien, P.; Lambert, J.; Feuga, V.; Macquet, M.; et al. Platelet, Plasma, Urinary Tryptophan-Serotonin-Kynurenine Axis Markers in Hyperacute Brain Ischemia Patients: A Prospective Study. *Front. Neurol.* **2022**, *12*, 782317. [CrossRef]
185. Darlington, L.G.; Mackay, G.M.; Forrest, C.M.; Stoy, N.; George, C.; Stone, T.W. Altered Kynurenine Metabolism Correlates with Infarct Volume in Stroke. *Eur. J. Neurosci.* **2007**, *26*, 2211–2221. [CrossRef] [PubMed]
186. Cuartero, M.I.; Ballesteros, I.; De La Parra, J.; Harkin, A.L.; Abautret-Daly, A.; Sherwin, E.; Fernández-Salguero, P.; Corbí, Á.L.; Lizasoain, I.; Moro, M.A. L-Kynurenine/Aryl Hydrocarbon Receptor Pathway Mediates Brain Damage After Experimental Stroke. *Circulation* **2014**, *130*, 2040–2051. [CrossRef] [PubMed]
187. Mangas, A.; Yajeya, J.; González, N.; Ruiz, I.; Duleu, S.; Geffard, M.; Coveñas, R. Overexpression of Kynurenic Acid in Stroke: An Endogenous Neuroprotector? *Ann. Anat.-Anat. Anz.* **2017**, *211*, 33–38. [CrossRef]
188. Alme, K.N.; Ulvik, A.; Askim, T.; Assmus, J.; Mollnes, T.E.; Naik, M.; Næss, H.; Saltvedt, I.; Ueland, P.M.; Knapskog, A.B. Neopterin and Kynurenic Acid as Predictors of Stroke Recurrence and Mortality: A Multicentre Prospective Cohort Study on Biomarkers of Inflammation Measured Three Months after Ischemic Stroke. *BMC Neurol.* **2021**, *21*, 476. [CrossRef] [PubMed]
189. Ren, R.; Fang, Y.; Sherchan, P.; Lu, Q.; Lenahan, C.; Zhang, J.H.; Zhang, J.; Tang, J. Kynurenine/Aryl Hydrocarbon Receptor Modulates Mitochondria-Mediated Oxidative Stress and Neuronal Apoptosis in Experimental Intracerebral Hemorrhage. *Antioxid. Redox Signal.* **2022**, *37*, 1111–1129. [CrossRef]
190. Ganesh, B.P.; Peesh, P.; Blasco, M.P.; Hamamy, A.E.; Khan, R.; Guzman, G.; Honarpisheh, P.; Mohan, E.C.; Goodman, G.W.; Nguyen, J.N.; et al. Restoring a Balanced Pool of Host-Derived and Microbiota-Derived Ligands of the Aryl Hydrocarbon Receptor Is Beneficial after Stroke. *Res. Sq.* **2023**. [CrossRef]

191. Rothhammer, V.; Borucki, D.M.; Tjon, E.C.; Takenaka, M.C.; Chao, C.-C.; Ardura-Fabregat, A.; De Lima, K.A.; Gutiérrez-Vázquez, C.; Hewson, P.; Staszewski, O.; et al. Microglial Control of Astrocytes in Response to Microbial Metabolites. *Nature* **2018**, *557*, 724–728. [CrossRef]
192. Xie, Y.; Zou, X.; Han, J.; Zhang, Z.; Feng, Z.; Ouyang, Q.; Hua, S.; Liu, Z.; Li, C.; Cai, Y.; et al. Indole-3-Propionic Acid Alleviates Ischemic Brain Injury in a Mouse Middle Cerebral Artery Occlusion Model. *Exp. Neurol.* **2022**, *353*, 114081. [CrossRef] [PubMed]
193. Xue, H.; Chen, X.; Yu, C.; Deng, Y.; Zhang, Y.; Chen, S.; Chen, X.; Chen, K.; Yang, Y.; Ling, W. Gut Microbially Produced Indole-3-Propionic Acid Inhibits Atherosclerosis by Promoting Reverse Cholesterol Transport and Its Deficiency Is Causally Related to Atherosclerotic Cardiovascular Disease. *Circ. Res.* **2022**, *131*, 404–420. [CrossRef] [PubMed]
194. Konopelski, P.; Chabowski, D.; Aleksandrowicz, M.; Kozniewska, E.; Podsadni, P.; Szczepanska, A.; Ufnal, M. Indole-3-Propionic Acid, a Tryptophan-Derived Bacterial Metabolite, Increases Blood Pressure via Cardiac and Vascular Mechanisms in Rats. *Am. J. Physiol. Regul. Intgr. Comp. Physiol.* **2021**, *321*, R969–R981. [CrossRef]
195. Yoon, N.; Kim, Y.; Kim, S.-D.; Kim, M.; Jung, B.H.; Song, Y.S. Investigation of Long-Term Metabolic Alteration after Stroke in tMCAO (Transient Middle Cerebral Artery Occlusion) Mouse Model Using Metabolomics Approach. *Neurosci. Lett.* **2022**, *774*, 136492. [CrossRef] [PubMed]
196. Marsiglia, R.; Marangelo, C.; Vernocchi, P.; Scanu, M.; Pane, S.; Russo, A.; Guanziroli, E.; Del Chierico, F.; Valeriani, M.; Molteni, F.; et al. Gut Microbiota Ecological and Functional Modulation in Post-Stroke Recovery Patients: An Italian Study. *Microorganisms* **2023**, *12*, 37. [CrossRef] [PubMed]
197. Teunis, C.J.; Stroes, E.S.G.; Boekholdt, S.M.; Wareham, N.J.; Murphy, A.J.; Nieuwdorp, M.; Hazen, S.L.; Hanssen, N.M.J. Tryptophan Metabolites and Incident Cardiovascular Disease: The EPIC-Norfolk Prospective Population Study. *Atherosclerosis* **2023**, *387*, 117344. [CrossRef] [PubMed]
198. Duan, X.; Gan, J.; Xu, F.; Li, L.; Han, L.; Peng, C.; Bao, Q.; Xiao, L.; Peng, D. RNA Sequencing for Gene Expression Profiles in a Rat Model of Middle Cerebral Artery Occlusion. *Biomed. Res. Int.* **2018**, *2018*, 2465481. [CrossRef] [PubMed]
199. Tan, D.-X.; Manchester, L.C.; Sainz, R.M.; Mayo, J.C.; León, J.; Reiter, R.J. Physiological Ischemia/Reperfusion Phenomena and Their Relation to Endogenous Melatonin Production: An Hypothesis. *Endocrine* **2005**, *27*, 149–158. [CrossRef]
200. Hajsl, M.; Hlavackova, A.; Broulikova, K.; Sramek, M.; Maly, M.; Dyr, J.E.; Suttnar, J. Tryptophan Metabolism, Inflammation, and Oxidative Stress in Patients with Neurovascular Disease. *Metabolites* **2020**, *10*, 208. [CrossRef]
201. Mortensen, J.K.; Kraglund, K.L.; Johnsen, S.P.; Mors, O.; Andersen, G.; Buttenschøn, H.N. The Serotonin Transporter Gene Polymorphisms and Risk of Ischemic Stroke. *Cerebrovasc. Dis.* **2018**, *45*, 187–192. [CrossRef]
202. Aguiar, R.P.D.; Newman-Tancredi, A.; Prickaerts, J.; Oliveira, R.M.W.D. The 5-HT1A Receptor as a Serotonergic Target for Neuroprotection in Cerebral Ischemia. *Prog. Neuro-Psychopharmacol. Biol. Psychiatry* **2021**, *109*, 110210. [CrossRef]
203. Liu, D.; Tan, S.; Zhou, Z.; Gu, S.; Zuo, H. Trimethylamine N-Oxide, β-Alanine, Tryptophan Index, and Vitamin B6-Related Dietary Patterns in Association with Stroke Risk. *Nutr. Metab. Cardiovasc. Dis.* **2024**, *34*, 1179–1188. [CrossRef]
204. Bhave, V.M.; Ament, Z.; Patki, A.; Gao, Y.; Kijpaisalratana, N.; Guo, B.; Chaudhary, N.S.; Guarniz, A.G.; Gerszten, R.; Correa, A.; et al. Plasma Metabolites Link Dietary Patterns to Stroke Risk. *Ann. Neurol.* **2023**, *93*, 500–510. [CrossRef]
205. Joshi, B.; Panda, S.K.; Jouneghani, R.S.; Liu, M.; Parajuli, N.; Leyssen, P.; Neyts, J.; Luyten, W. Antibacterial, Antifungal, Antiviral, and Anthelmintic Activities of Medicinal Plants of Nepal Selected Based on Ethnobotanical Evidence. *Evid.-Based. Compl. Alt.* **2020**, *2020*, 1043471. [CrossRef]
206. Li, J.; Zhao, T.; Qiao, H.; Li, Y.; Xia, M.; Wang, X.; Liu, C.; Zheng, T.; Chen, R.; Xie, Y.; et al. Research Progress of Natural Products for the Treatment of Ischemic Stroke. *J. Integr. Neurosci.* **2022**, *21*, 14. [CrossRef] [PubMed]
207. Huang, L.; Wang, T.; Wu, Q.; Dong, X.; Shen, F.; Liu, D.; Qin, X.; Yan, L.; Wan, Q. Analysis of Microbiota in Elderly Patients with Acute Cerebral Infarction. *PeerJ* **2019**, *7*, e6928. [CrossRef] [PubMed]
208. Li, H.; Zhang, X.; Pan, D.; Liu, Y.; Yan, X.; Tang, Y.; Tao, M.; Gong, L.; Zhang, T.; Woods, C.R.; et al. Dysbiosis Characteristics of Gut Microbiota in Cerebral Infarction Patients. *Transl. Neurosci.* **2020**, *11*, 124–133. [CrossRef]
209. Haak, B.W.; Westendorp, W.F.; van Engelen, T.S.; Brands, X.; Brouwer, M.C.; Vermeij, J.D.; Hugenholtz, F.; Verhoeven, A.; Derks, R.J.; Giera, M.; et al. Disruptions of Anaerobic Gut Bacteria Are Associated with Stroke and Post-Stroke Infection: A Prospective Case–Control Study. *Transl. Stroke Res.* **2020**, *12*, 581–592. [CrossRef] [PubMed]
210. Xiang, L.; Lou, Y.; Liu, L.; Liu, Y.; Zhang, W.; Deng, J.; Guan, Y.; She, M.; You, X.; Liu, M.; et al. Gut Microbiotic Features Aiding the Diagnosis of Acute Ischemic Stroke. *Front. Cell. Infect. Microbiol.* **2020**, *10*, 587284. [CrossRef] [PubMed]
211. Tan, C.; Wu, Q.; Wang, H.; Gao, X.; Xu, R.; Cui, Z.; Zhu, J.; Zeng, X.; Zhou, H.; He, Y.; et al. Dysbiosis of Gut Microbiota and Short-chain Fatty Acids in Acute Ischemic Stroke and the Subsequent Risk for Poor Functional Outcomes. *J. Parenter. Enter. Nutr.* **2021**, *45*, 518–529. [CrossRef]
212. Chen, X.; Wu, Q.; Gao, X.; Wang, H.; Zhu, J.; Xia, G.; He, Y.; Song, W.; Xu, K. Gut Microbial Dysbiosis Associated with Type 2 Diabetes Aggravates Acute Ischemic Stroke. *mSystems* **2021**, *6*, e01304-21. [CrossRef]
213. Chen, L.; Wang, S.; Zhang, Y.; Li, Y.; Zhang, X.; Ma, J.; Zou, X.; Yao, T.; Li, S.; Chen, J.; et al. Multi-Omics Reveals Specific Host Metabolism-Microbiome Associations in Intracerebral Hemorrhage. *Front. Cell. Infect. Microbiol.* **2022**, *12*, 999627. [CrossRef]
214. Li, T.; Sun, Q.; Feng, L.; Yan, D.; Wang, B.; Li, M.; Xiong, X.; Ma, D.; Gao, Y. Uncovering the Characteristics of the Gut Microbiota in Patients with Acute Ischemic Stroke and Phlegm-Heat Syndrome. *PLoS ONE* **2022**, *17*, e0276598. [CrossRef]

215. Zhang, X.; Wang, X.; Zhao, H.; Cao, R.; Dang, Y.; Yu, B. Imbalance of Microbacterial Diversity Is Associated with Functional Prognosis of Stroke. *Neural Plast.* **2023**, *2023*, 6297653. [CrossRef]
216. Yu, S.; Chen, J.; Zhao, Y.; Liao, X.; Chen, Q.; Xie, H.; Liu, J.; Sun, J.; Zhi, S. Association Analysis of the Gut Microbiota in Predicting Outcomes for Patients with Acute Ischemic Stroke and H-Type Hypertension. *Front. Neurol.* **2023**, *14*, 1275460. [CrossRef]

Disclaimer/Publisher's Note: The statements, opinions and data contained in all publications are solely those of the individual author(s) and contributor(s) and not of MDPI and/or the editor(s). MDPI and/or the editor(s) disclaim responsibility for any injury to people or property resulting from any ideas, methods, instructions or products referred to in the content.

biomolecules

MDPI

Article

The Rhododendron Chrysanthum Pall.s' Acetylation Modification of Rubisco Enzymes Controls Carbon Cycling to Withstand UV−B Stress

Meiqi Liu, Fushuai Gong, Wang Yu, Kun Cao, Hongwei Xu * and Xiaofu Zhou *

Jilin Provincial Key Laboratory of Plant Resource Science and Green Production, Jilin Normal University, Siping 136000, China

* Correspondence: xuhongwei@jlnu.edu.cn (H.X.); zhouxiaofu@jlnu.edu.cn (X.Z.)

Abstract: Lysine acetylation of proteins plays a critical regulatory function in plants. A few advances have been made in the study of plant acetylproteome. However, until now, there have been few data on *Rhododendron chrysanthum* Pall. (*R. chrysanthum*). We analyzed the molecular mechanisms of photosynthesis and stress resistance in *R. chrysanthum* under UV−B stress. We measured chlorophyll fluorescence parameters of *R. chrysanthum* under UV−B stress and performed a multi−omics analysis. Based on the determination of chlorophyll fluorescence parameters, *R. chrysanthum* Y(NO) (Quantum yield of non−photochemical quenching) increased under UV−B stress, indicating that the plant was damaged and photosynthesis decreased. In the analysis of acetylated proteomics data, acetylated proteins were found to be involved in a variety of biological processes. Notably, acetylated proteins were significantly enriched in the pathways of photosynthesis and carbon fixation, suggesting that lysine acetylation modifications have an important role in these activities. Our findings suggest that *R. chrysanthum* has decreased photosynthesis and impaired photosystems under UV−B stress, but NPQ shows that plants are resistant to UV−B. Acetylation proteomics revealed that up- or down-regulation of acetylation modification levels alters protein expression. Acetylation modification of key enzymes of the Calvin cycle (Rubisco, GAPDH) regulates protein expression, making Rubisco and GAPDH proteins expressed as significantly different proteins, which in turn affects the carbon fixation capacity of *R. chrysanthum*. Thus, Rubisco and GAPDH are significantly differentially expressed after acetylation modification, which affects the carbon fixation capacity and thus makes the plant resistant to UV−B stress. Lysine acetylation modification affects biological processes by regulating the expression of key enzymes in photosynthesis and carbon fixation, making plants resistant to UV−B stress.

Keywords: lysine acetylome; chlorophyll fluorescence; photosynthesis; carbon fixation; *R. chrysanthum*

1. Introduction

Rhododendron chrysanthum Pall. (*R. chrysanthum*) is a rare resource for the study of abiotic stress in plants since it grows permanently in the alpine zone of Changbai Mountain, which has strong radiation and high altitude [1]. *R. chrysanthum* has demonstrated adaptation to UV−B radiation and other abiotic stresses over the course of its lengthy growth and evolution [2].

Among the ultraviolet rays in sunlight that cause the most concern is medium−wave ultraviolet radiation (UV−B, 280–320 nm) [3]. Because of their sessile growth habit, plants are inevitably exposed to UV−B stress. Most plants that are exposed to UV−B radiation will react by producing stress [3]. According to pertinent research, UV−B stress can harm plants in a number of ways, including slowing down their growth, inhibiting photosynthesis, oxidative damage, and rupturing the integrity of vital macromolecules [4–6]. Green plants' rate of photosynthetic activity may be significantly lowered by UV−B stress [7], and

parameters connected to chlorophyll fluorescence are crucial markers of photosynthetic characteristics [8]. The kale (*Brassica oleracea* L.) showed a decrease in Fv/Fm (maximum photochemical efficiency of PSII) and fluorescence transient parameters (RC/CS, ABS/CS, TR_O/CS) with UV−B stress [9]. The maximum photochemical efficiency of PSII, or the ratio of chlorophyll fluorescence parameter Fv/Fm, dramatically dropped in *Olea europaea* (L.) under long-term UV−B stress [10]. Due to its special growing environment, *R. chrysanthum* was used as the experimental material in this study. In order to ascertain the effects of UV−B radiation on photosynthesis and the ideal UV−B radiation dosage for *R. chrysanthum*, we carried out a pertinent study. We also determined the duration of UV−B radiation, which was 48 h, and found that *R. chrysanthum* photosynthesis was inhibited by UV−B but not by UV−A [2]. After UV−B treatment, we also conducted the measurement of chlorophyll fluorescence parameters, and the Fv/Fm and Fv/Fo decreased dramatically, revealing that photo-synthesis was impeded and the photosystem was injured [11].

Proteins' post-translational modifications (PTMs) can alter their activities, subcellular locations, and interaction partners, among other aspects of protein functional stability regulation [12]. One of the most common PTMs in both prokaryotes and eukaryotes is lysine acetylation (Kac) modification [13,14]. After undergoing extensive research, it was discovered that kac was involved in numerous significant processes, including the germination of seeds, the development of organs, blooming, stress response, and leaf senescence [15–20]. During the dormancy release process in poplar, acetylation modification of enzymes in the primary metabolic pathway is an important strategy for breaking the dormancy of bloom buds [21]. The acetylation of essential enzymes for starch biosynthesis to adapt to drought stress is revealed by acetylation proteomics analysis of growing wheat kernels under conditions of water deficit [22]. The OsHYPK-NatA complex plays a crucial role in coordinating rice development and stress responses, primarily through its dynamic regulation of NatA-mediated N-terminal acetylation and global protein turnaround [23]. *Sorghum bicolor* HDAC SbHDT701 enhances acetylation modifications to regulate stress response [24]. LysAc may have a major and previously unknown regulatory role in many nonhistone proteins that are involved in pathways and functions in Arabidopsis and other plants [25]. Some proteins, especially those involved in photosynthesis, glycolysis, and secondary metabolism, may be lysine-acetylated to control particular metabolic processes in tea leaves [26]. Our earlier study revealed that *R. chrysanthum's* ability to photosynthesise was hampered by UV−B radiation, but that UV−B damage to plants could be mitigated by acetylating the PSII protein. This study did not fully explore the photosynthetic carbon cycle process, which is crucial to understanding biological processes [11].

It has been investigated and determined how the *R. chrysanthum* photosystem II protein reacts to UV−B stress. But the examination initially concentrated on physiology, biochemistry, and photosystem aspects [11]. However, plants' ability to sequester carbon is also very significant. Thus, we conducted an acetylation-modified proteomics analysis of *R. chrysanthum* in order to gain a better understanding of the molecular mechanism of UV−B tolerance. This analysis offers important insights for future research on the molecular mechanism of UV−B radiation resistance.

2. Materials and Methods

2.1. Plant Material and Treatment

R. chrysanthum was kept in a climate chamber designed to mimic the conditions of a high mountain environment [2], and in the artificial climate chamber following storage, *R. chrysanthum* was continuously grown and cultured under white fluorescent lights. In the climate chamber, *R. chrysanthum* was cultivated under 50 μmol (photon) m^{-2} s^{-1} white fluorescent lights. And the following conditions were present in the artificial climate chamber: 18 °C for 14 h of light and 16 °C for 10 h of darkness. UV−B and photosynthetically active radiation (PAR) were used in this study. Two groups of *R. chrysanthum* were created: the CG group received a 48-h treatment with PAR, while the BG group received a 48-h treatment with PAR+UV−B. Each group received three biological duplicates (three repetitions for

the CG group and three repetitions for the BG group) to guarantee adequate coverage. PAR radiation was performed by placing a 400 nm filter (Edward, Filter Long 2IN SQ, Barrington, NJ, USA) on the culture flasks (effective irradiance of 50 μmol m^{-2} s^{-1}), and PAR+UV−B radiation was performed by placing a 295 nm filter (Edward, Filter Long 2IN SQ, Barrington, NJ, USA) (effective irradiance of 2.3 W m^{-2}).

2.2. Measurement of Chlorophyll Fluorescence

R. chrysanthum leaves were used to evaluate the induction features of chlorophyll fluorescence using the Imaging-PAM Maxi (HeinzWalz, Effeltrich, Germany). The plants were treated for 20 min in the dark prior to measuring them. We measured the fluorescence parameters. Actual photochemical quantum yield of PSII Y(II); Maximum quantum yield of PSII (Fv'/Fm'); Electron transport rate (ETR), non-photochemical quenching coefficient (NPQ), photochemical quenching coefficient (qL), and quantum yield of uncontrolled energy dissipation of photosystem II Y(NO).

2.3. Quantitative Proteomic Study of Acetylated Modification

2.3.1. Protein Extraction

This experiment's acetylated proteomics were provided by Jingjie PTM Hangzhou Co Inc. BioLab (Hangzhou, China). Using a high−intensity ultrasonic processor (Scientz, Ningbo, China), *R. chrysanthum* was ground and pulverized in liquid nitrogen, transferred to centrifuge tubes, and sonicated three times on ice in a lysis buffer (8 M urea, 2 mM EDTA, 10 mM DTT, and 1% protease inhibitor cocktail). After centrifugation at 5500× *g* for 10 min at 4 °C, the supernatant was centrifuged for 3 min at 4 °C. Proteins in the supernatant were centrifuged for 3 min at 4 °C, and it was then precipitated with 15% TCA for 4 h at −20 °C. The rest of the sediment was washed three times with acetone after chilling in a refrigerator. Finally, the proteins were redissolved in buffer, the buffer consisted of 8 M urea, 100 mM TEAB, pH 8.0. And in order to measure the protein concentration in the supernatant, it was estimated using the 2-D Quantay Analysis Kit (Cytiva 80-6483-56).

2.3.2. Trypsin Digestion

TCA at a concentration of 20% (*m*/*v*) was slowly added to the sample to precipitate the proteins, followed by vortex mixing and incubation at 4 °C for 2 h. The precipitated proteins were collected by centrifugation at 4500× *g* for 5 min at 4 °C. Subsequently, the collected precipitated proteins were washed with pre-cooled acetone three times and allowed to dry for 1 min. The washed and dried proteins were then redissolved in 200 mM TEAB and dispersed by ultrasonication. For the first digestion, trypsin was added at a 1:50 trypsin mass ratio overnight. Subsequently, the peptides were reduced with 5 mM dithiothreitol for 60 min at 37 °C, followed by 11 mM iodoacetamide for 45 min at room temperature and in the dark. Finally, the peptides were desalted, using a Strata X SPE column.

2.3.3. Affinity Enrichment

Tryptic peptides were dissolved in NETN buffer (100 mM NaCl, 1 mM EDTA, 50 mM Tris-HCl, 0.5% NP-40, pH 8.0) to dissolve Kac-modified peptides. Pre-washed antibody beads (PTM-104, 10002D) were then added and incubated with the peptide mixture at 4 °C for an overnight period with gentle shaking. The beads were then washed twice with water and four times with NETN buffer. The use of 0.1% trifluoroacetic acid allowed the bound peptides to be released from the beads. The eluted portions were then mixed and dried under a vacuum. The resultant peptides were desalted using C18 ZipTips (ZTC18S) in accordance with the manufacturer's instructions for LC-MS/MS analysis.

2.3.4. LC-MS/MS Analysis and Database Search

Solvent A (0.1% formic acid, 2% acetonitrile/in water) was used to solubilize the tryptic peptides, which were then loaded directly onto a home-made analytical column (25-cm length, 100 μm i.d.). In a nanoElute UHPLC system (IQLAAAGABHFAPUMZZZ)

running at 350 nL/min, the solvent B gradient increased from 6% to 22% (0.1% formic acid dissolved in acetonitrile) over 42 min, increased from 22% to 30% in 12 min, increased to 80% in 3 min, maintained at 80%, and then hold at 80% for 3 min. Prior to mass spectrometry analysis with timsTOF Pro, the peptides were subjected to Capillary source treatment. Then, 1.75 kV of electrospray voltage was used. At the TOF detector, precursors and fragments were analyzed using MS/MS with a scan range of 100 to 1700 m/z. Parallel accumulation serial fragmentation (PASEF) mode was used to run the timsTOF Pro. Ten PASEF-MS/MS scans were acquired per acquisition cycle, with the fragmentation of precursors with charge states 0 to 5 being the preferred range. A 24 s dynamic exclusion was set. The MaxQuant search engine (v. 1.6.6.0) was used to process the generated MS/MS data. Up to 4 missing cleavage events were made possible by using the cleavage protein trypsin/P. In the first search and the main search, the mass tolerance for precursor ions was set to 20 ppm and 20 ppm, respectively. And the mass tolerance for fragment ions was set as 20 ppm. Protein N-terminal acetylation, oxidation on Met, and acetylation on Lys were designated as variable modifications, while carbamidomethyl on Cys was designated as a fixed modification. FDR was adjusted to <1%.

2.3.5. Bioinformatics Analysis

Firstly, the average quantification of the number of multiple repetitions in the CG and BG groups was first counted separately, and then the ratio of the average of the CG and BG groups was computed. This ratio was used for final quantification. Quantitative values were log-transformed and p-values were calculated from two-tailed Student's t-tests. Significant differences were defined as protein or modified peptide $p < 0.05$, fold change (FC) ≥ 1.5. Functional annotation tools were used to identify enriched clusters of acetylated proteins.

GO enrichment analysis: protein GO annotations are classified into 3 categories: biological process, cellular component, and molecular function. The Fisher's exact test was used to determine the significance of GO enrichment of different changed proteins, and the significance was p-value < 0.05.

KEGG pathway enrichment analysis: for the enrichment analysis of the KEGG pathway, we used the KEGG database. Fisher's exact test was used to determine the significance of KEGG pathway enrichment of different changed proteins, and proteins were considered to be significant at a p-value of less than 0.05.

Protein subcellular localization: in this research, the subcellular localization of proteins is predicted using Wolfpsort(About WoLF PSORT (hgc.jp)) subcellular localization prediction software. Wolfpsort is applied to eukaryotic sequence prediction.

Protein motif analysis: by counting the pattern of amino acid sequences before and after all acetylation modification sites, a trend in the pattern of amino acid sequences within the region of the site where the modification occurs is calculated.

2.4. Modeling Acetylated Proteins Homology

To understand the structure of the protein and the level of acetylation modification sites, we used NCBI BLAST to find and compare homologous sequences. Subsequently, using SWISS-MODEL, a three-dimensional structural model of the protein was generated, labeling the acetylation sites.

2.5. Statistics and Analysis of Data

Chlorophyll fluorescence parameters measured in CG and BG groups were analyzed and plotted using SPSS Statistics 26.

3. Results

3.1. Quantitative Proteomic Analysis of Acetylated Modification in R. chrysanthum

In order to map the sites of lysine acetylation in *R. chrysanthum*, trypsin was used to break down proteins into peptides. *R. chrysanthum* was divided into two groups based

on the treatments: the BG group (*R. chrysanthum* treated with PAR+UV−B for 48 h, three biological replicates) and the CG group (*R. chrysanthum* treated with PAR for 48 h, three biological replicates) groups. Then, an LC-MS/MS analysis was carried out (Supplementary Figure S1B). The majority of the acetylation-containing polypeptides were found to have lengths between 7 and 20, which is consistent with the fundamental principle of trypsin enzymatic digestion (Supplementary Figure S1C). A total of 945 lysine acetylation sites were present in 685 differentially expressed acetylated proteins (DAPs) (Supplementary Table S1). A total of 807 differentially expressed proteins (DEPs) were found using quantitative proteomics analysis; according to fold change >1.5 and $p < 0.05$, 357 of these proteins were downregulated and 450 were upregulated (Supplementary Table S2).

3.2. Plant Carbon Assimilation in R. chrysanthum Is Impacted by Photodamage under UV−B Stress

With the use of chlorophyll fluorescence technology, changes in leaf photosynthesis can be swiftly and precisely reflected. Chlorophyll fluorescence characteristics shift in plants exposed to UV−B stress, which in turn indicates photosynthetic damage. We determined the chlorophyll fluorescence parameters in order to investigate variations in *R. chrysanthum's* photochemical activity. For pictures of chlorophyll fluorescence, see Figure 1. The plant's NPQ is represented by the fluorescence images, which show a decline in *R. chrysanthum's* ability to protect against photodamage (Figure 1A). The plant's photosynthetic activity is reflected in qL, and under UV−B stress, *R. chrysanthum's* photosynthetic activity increases as shown by the fluorescence images (Figure 1B). Additionally, the Y(NO) image shows that the plant has photodamaged (Figure 1C). The (YII) images show a decrease in *R. chrysanthum's* actual photosynthetic rate. (Figure 1D).

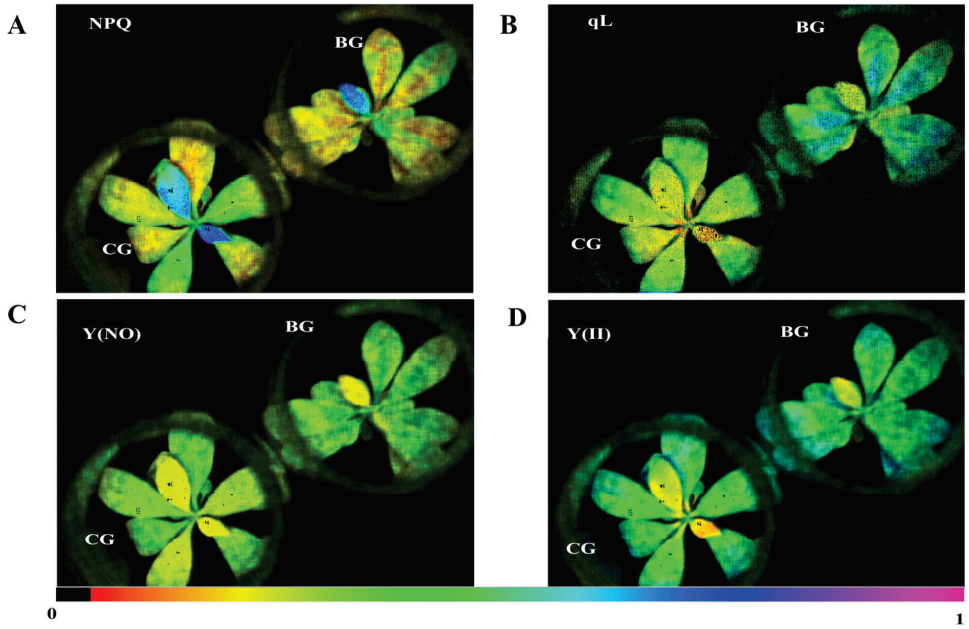


Figure 1. Imaging of real-time fluorescence of *R. chrysanthum* under UV−B stress. (**A**) average nonphotochemical quenching (NPQ); (**B**) photochemical quenching coefficient (qL)-based; (**C**) nonphotochemical quenching quantum yield Y(NO); and (**D**) actual photochemical quantum yield Y(II) for PSII. The color in the color scale of the picture indicates the size of the value, the more reddish the color indicates the smaller the value, and the more purple the color indicates the larger the value.

The rate of Fv′/Fm′ significantly dropped by 9.25% under UV−B stress (Figure 2A, Table 1), suggesting that photoinhibition was taking place and damaging the reaction center of chrysanthemum photosystem II. The real light energy conversion efficiency of leaves over time is represented by Y(II) (Figure 2B, Table 1). However, Y(NO), the quantum yield

of non-photochemical quenching, is a crucial marker of photodamage, and the analysis reveals a notable 15.2% increase in Y(NO) value. The plant damage caused by UV−B radiation was indicated by the significant increase in Y(NO) value (Figure 2C, Table 1). The ability of the plant to transform excess light energy into heat energy is reflected in non-photochemical quenching, which shields the plant from harm. The plant's capacity to disperse heat is indicated by NPQ. The plant's capacity to disperse heat is indicated by NPQ (Figure 2D, Table 1). Photochemical quenching reflects the photosynthetic activity of the plant, while non-photochemical quenching represents the ability of the plant to convert excess light energy into heat. Under UV−B stress, the qL of *R. chrysanthum* increased by 20.4%. This indicates that the photosynthetic activity of *R. chrysanthum* increased under UV−B stress (Figure 2E, Table 1). The rate of electron transfer can serve as an indicator of the photosynthesis's rate of electron transfer. *R. chrysanthum's* electron transfer rate (ETR) values exhibited a declining trend (Figure 2F, Table 1), suggesting that UV−B stress could have an impact on the plant. It is a crucial component of the light response curve and can be used to estimate the rate at which electron transfer energy is converted.

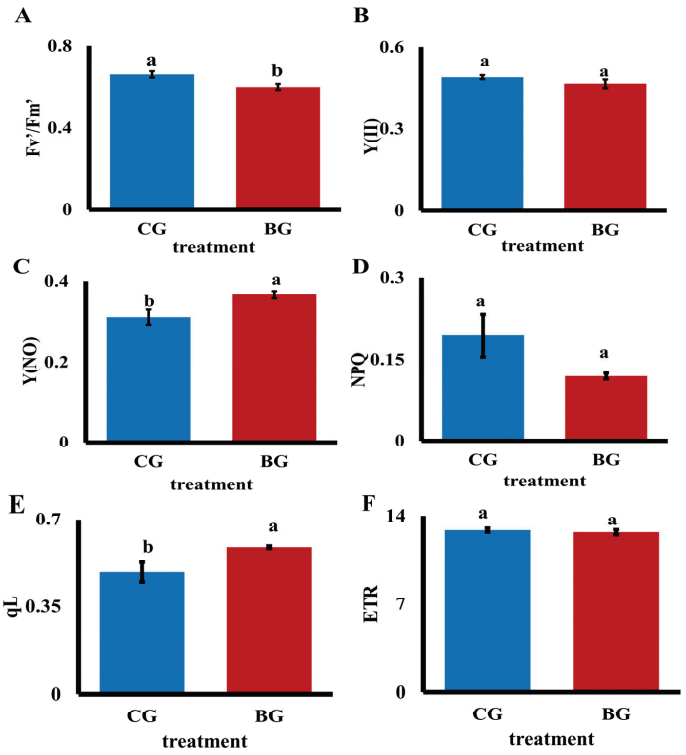


Figure 2. Chlorophyll fluorescence parameters in *R. chrysanthum*. a and b denote significant differences between PAR and PAR+UV−B ($p < 0.05$). (**A**) Maximum quantum yield of PSII (Fv′/Fm′); (**B**) Actual photochemical quantum yield of PSII [Y(II)]; (**C**) Non-photochemical quenching quantum yield [Y(NO)]; (**D**) Non-photochemical quenching coefficient (NPQ); (**E**) Photochemical quenching coefficient (qL); (**F**) Electron transfer rate (ETR). These results are the mean ± standard deviation of three samples.

Table 1. Effect of UV−B stress on chlorophyll fluorescence parameters of *R. chrysanthum*.

Group	Fv′/Fm′	Y(II)	Y(NO)	NPQ	qL	ETR
CG	0.660 ± 0.015a	0.489 ± 0.008a	0.310 ± 0.019b	0.193 ± 0.039a	0.49 ± 0.038b	12.8 ± 0.163a
BG	0.599 ± 0.014b	0.465 ± 0.016a	0.366 ± 0.009a	0.118 ± 0.006a	0.59 ± 0.005a	12.6 ± 0.205a

Note: These results represent the average ± standard deviation of 3 samples. Different lowercase letters suggest significant inter-group differences ($p < 0.05$), whereas identical lower-case characters suggest no relevant difference across groups.

3.3. Analysis of Distribution and Motif of Acetylated Sites in Photosynthetic Carbon Cycle of R. chrysanthum

The number of detected modification sites per protein was estimated in order to evaluate the sites' distribution in the acetylated proteins of *R. chrysanthum*. The findings suggested that 50% of proteins had only 1 site, whereas 30%, 9%, and 11% of proteins had 2, 3, or more modification sites, respectively (Figure 3A). Acetylated proteins are enriched in two processes: photosynthesis and the Calvin cycle. Only 63% of proteins had one acetylation site, whereas 12%, 5%, and 20%, respectively, of proteins had 2, 3, or more modification sites (Figure 3B). The sequence of amino acid distribution around the acetylated lysine was analyzed to comprehend the motifs in *R. chrysanthum*. Using motif-x, a total of 15 significantly enriched acetylation motifs were screened, of which the three motifs "KT", "KY", and "KS" accounted for the largest proportion. (Figure 3C, Supplementary Table S3). These results indicate that the conserved motifs and residues of the proteins in which *R. chrysanthum* undergoes acetylation are more intact and suggest that the lysine residues surrounding the basic residues in *R. chrysanthum* proteins have a greater chance of being acetylated under UV−B stress. The thermogram of compositions of amino acid around the acetylation sites showed that histidine (H) and tyrosine (Y) were apparently excessive from −4 to +4, and others, the cases in point are phenylalanine (F) and serine (S). They were highly enriched at +1 (Figure 3D, Supplementary Table S4).

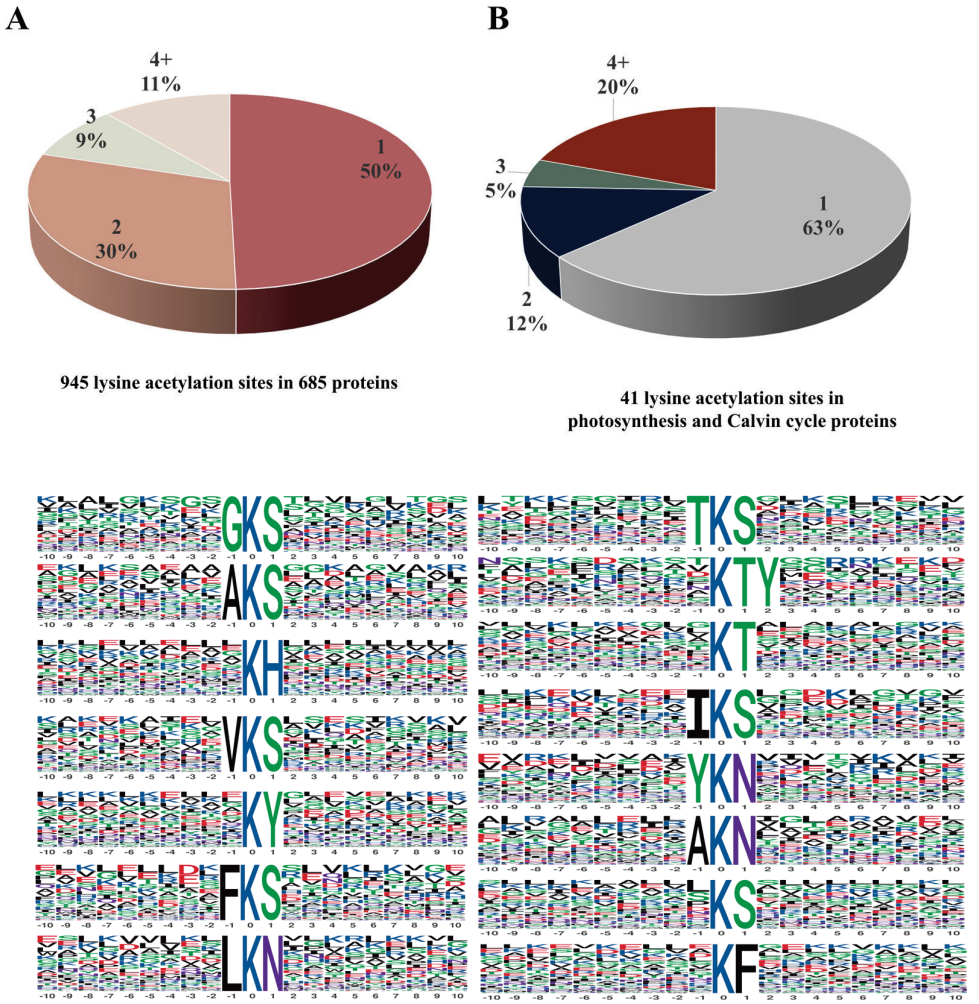


Figure 3. *Cont.*

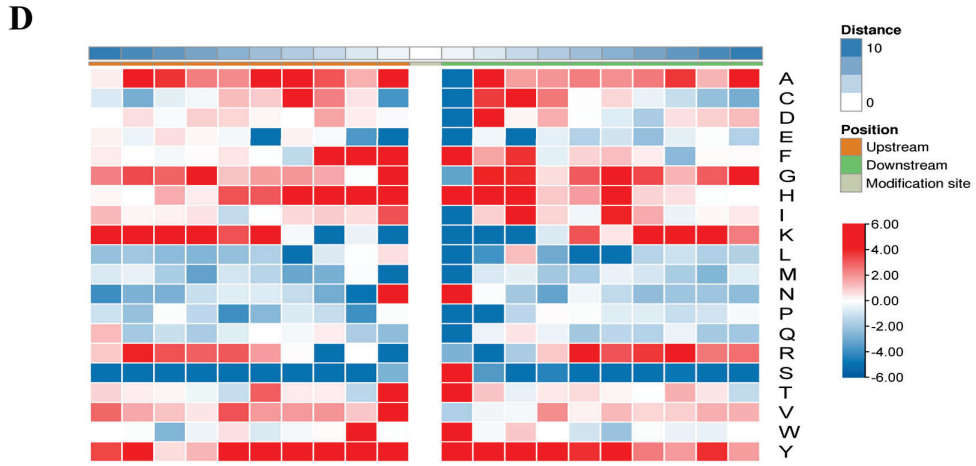


Figure 3. Properties of lysine acetylation sites in photosynthesis of *R. chrysanthum* under UV−B stress. (**A**) The number and proportion of lysine acetylation sites. (**B**) The number and percentage of lysine acetylationproteins sites in photosynthesis and Calvin cycle. (**C**) Sequence probability logos for acetylation site motifs significantly enriched for ± 10 amino acids around the lysine acetylation sites. (**D**) Clustering heatmap of amino acids up-stream and down-stream the acetylation modification site. Red color is that this amino acid is significantly enriched near the modification site, and blue is a significant decrease.

3.4. Analysis of Functional Enrichment of Acetylated Proteins and Sites in Photosynthetic Carbon Cycle of R. chrysanthum

With the aim of further investigating the acetylated proteins, they were divided into 3 main categories: biological process, molecular function, and cellular component (Supplementary Table S5). We carried out GO enrichment (Figure 4A, Supplementary Tables S6–S8). According to the cellular component analysis, *R. chrysanthum*'s acetylation-modified proteins were dramatically enriched in metabolic processes, and proteins enriched in the envelope and chloroplast were more likely to be acetylated (Figure 4A). Acetylation-modified proteins from *R. chrysanthum* were enriched in KEGG metabolic pathways, which allows a better understanding of their general function (Figure 4B, Supplementary Table S9). The findings demonstrated that some proteins in carbon metabolism undergo lysine acetylation (Supplementary Figure S2), the process of photosynthesis (Supplementary Figure S3), as well as carbon fixation in photosynthetic organisms (Supplementary Figure S4). KEGG enrichment showed that 26 acetylated proteins were acetylated in the carbon fixation of photosynthetic organisms, and 53 acetylation sites were identified. Acetylated proteins of *R. chrysanthum* in carbon fixation are localized to chloroplasts, mitochondria, and cytoplasm, as shown by subcellular localization with 17, 1, and 8 (Figure 4C).

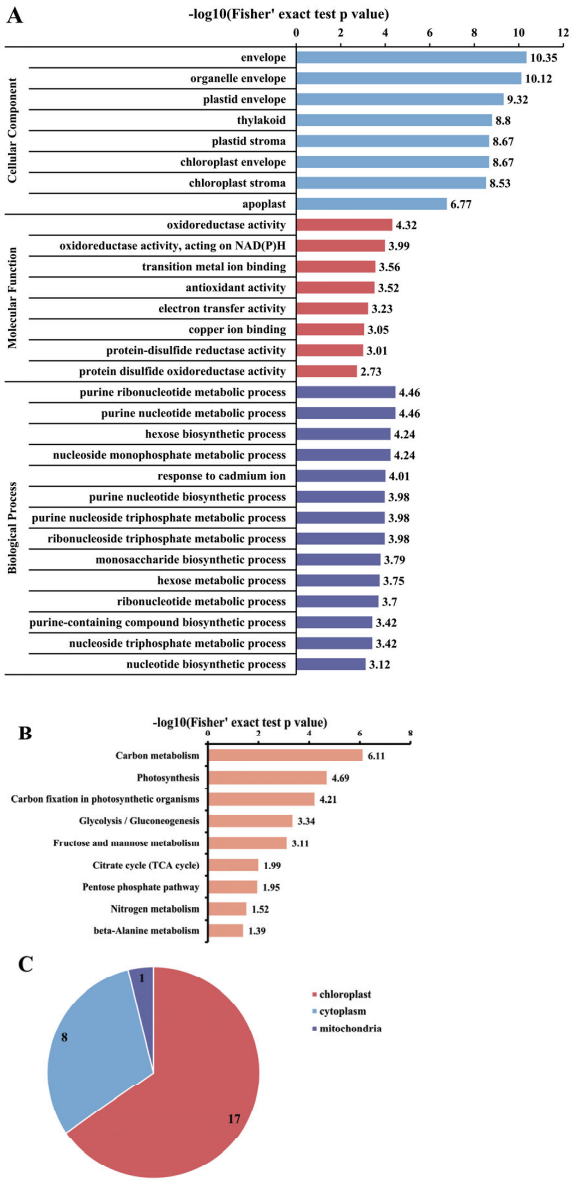


Figure 4. Enrichment analysis of the acetylated proteins in carbon fixation of *R. chrysanthum*. (**A**) The acetylated proteome is analyzed for GO enrichment. (**B**) The acetylated proteome is analyzed for KEGG pathway. (**C**) Subcellular localization of acetylated proteins of carbon fixation.

3.5. Analysis of DEPs and DAPs in Carbon Fixation in Photosynthetic Organisms of R. chrysanthum under UV−B Stress

Based on the outcomes of acetylated proteins' functional enrichment analysis, it was shown that lysine acetylation has a significant role in the pathways of photosynthesis and carbon fixation of plants. We analyzed the proteins in the carbon fixation pathway and found that the enzymes for carbon fixation under UV−B stress underwent acetylation modification with different levels of modification at different sites (Figure 5A). Carbon fixation is a reaction in photosynthesis that does not require the participation of light and involves the conversion of carbon dioxide, as well as other compounds, into glucose through a series of reactions. In the analysis of data from *R. chrysanthum* in the Calvin–Benson cycle, we found up-regulation of acetylation modification levels at the sites of metabolic enzymes Rubisco, PGK, GAPA, GAPDH, ALDO, FBP, SBPase, PRK, and TKT. In CAM, the PPC and maeB enzymes of *R. chrysanthum* were modified by acetylation under UV−B stress, and the level of modification was up-regulated. In the C4-dicarboxylic acid cycle, we also identified the acetylated protein. In this pathway, acetylation-modified MDH1, COT1, GGAT, maeB

and malate dehydrogenase (E1.1.1.39) were recognized, with reduced levels of acetylation modification only at the malate dehydrogenase site (Figure 5A). We further analyzed this by quantitative proteomics and found that the only proteins that underwent acetylation modification were Rubisco and GAPDH enzymes, which showed significant differential expression of the proteins. Rubisco protein expression was up-regulated in *R. chrysanthum* after UV−B stress, which was positively correlated with the level of acetylation modification. GAPDH protein expression was down-regulated and inversely proportional to the acetylation modification level (Figure 5B, Supplementary Table S2). Taken together, these results suggest that proteins undergo acetylation modification and that the level of acetylation modification has an impact on the expression of proteins, which in turn affects the processes of photosynthesis and carbon fixation in plants in response to UV−B stress.

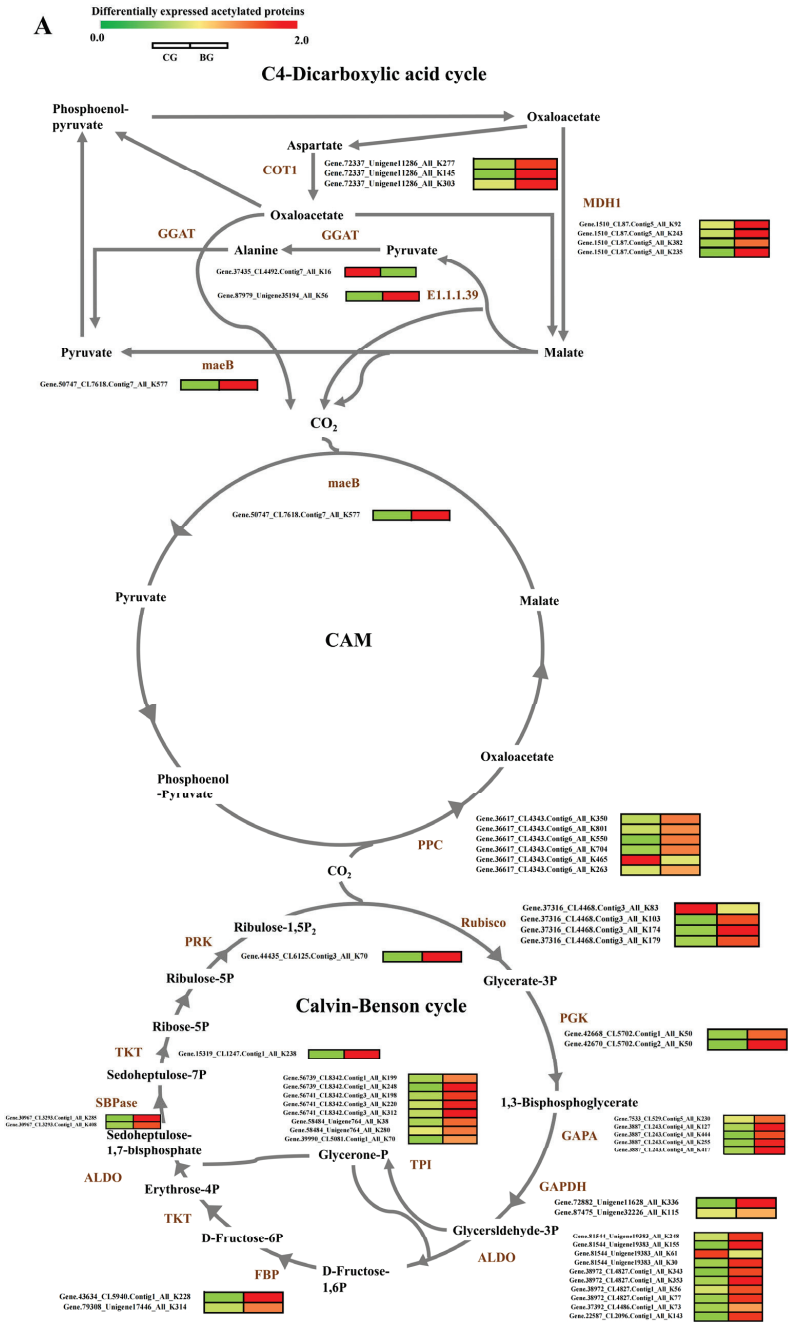


Figure 5. *Cont.*

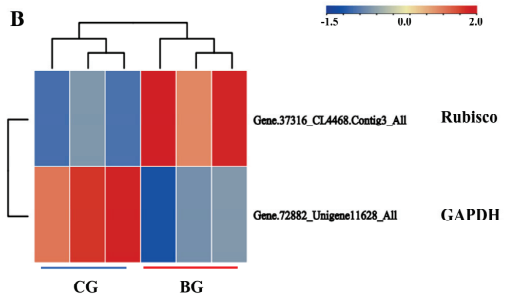


Figure 5. Working scheme of DAPs, sites and DEPs in carbon fixation in photosynthetic organisms in *R. chrysanthum*. (**A**) DAPs involved in carbon fixation in photosynthetic organisms. Rubisco: ribulose bisphosphate carboxylase/oxygenase; PGK: phosphoglycerate kinase; GAPDH: glyceraldehyde 3-phosphate dehydrogenase; GAPA: Glyceraldehyde-3-phosphate dehydrogenase B; ALDO: Fructose-bisphosphate aldolase 3; TPI: triosephosphate isomerase; FBP: fructose-1,6-bisphosphatase; TKT: Transketolase; SBPase: Sedoheputulose-1,7-bisphosphatase; PRK: phosphoribulokinase; PPC: Phosphoenolpyruvate carboxylase; maeB: NADP-dependent malic enzyme; MDH1: Malate dehydrogenase [NADP]; GGAT: Glutamate-glyoxylate aminotransferase 2; COT1: Aspartate aminotransferase; E1.1.1.39: malate dehydrogenase (decarboxylating). (**B**) Clustering heat map of DEPs in carbon fixation in photosynthetic organisms in the *R. chrysanthum* under UV−B stress.

3.6. Protein Structure Analysis of Rubisco and GAPDH Enzymes Undergoing Acetylation Modification in R. chrysanthum under UV−B Stress

The level of protein acetylation in carbon fixation and photosynthesis of *R. chrysanthum* was shown to be higher throughout the entire period of UV−B stress (Supplementary Table S10). By acetylation modification proteomic analysis, we found that acetylation modification occurred mainly for the Rubisco enzyme and the GAPDH enzyme during carbon fixation after UV−B radiation, and significant differences in expression occurred after modification. Therefore, we concluded that these two enzymes play important roles in the carbon fixation process of *R. chrysanthum* under UV−B stress. In order to understand the features and functions of Rubisco and GAPDH proteins at the molecular level, we described the hydrophobic clusters and salt bridges of the proteins. Firstly, we constructed three-dimensional models of the proteins. We used SWISS-MODEL to build statistically acceptable homology models. The acetylation sites were labelled in the 3D structure based on the information on the acetylation sites (Figure 6A). In Rubisco proteins, only the acetylation level of the Lys83 site was down-regulated, and the Lys103, Lys174, and Lys174 sites were up-regulated. In GAPDH proteins, both Lys115 and Lys336 sites were upregulated (Figure 6A(a,b)). The hydrophobic structure was analyzed, and the total area of the largest hydrophobic cluster of the GAPDH protein was 3798.7^2, with a single cluster containing 22 residues. The area of each residue is 42.7^2 and there are 89 interactions between residues (Figure 6B(a), Supplementary Table S11). In Rubisco, the total area of the largest hydrophobic cluster of the Rubisco protein was 1657.1^2, with a single cluster containing 16 residues. The area of each residue is 41.4^2 and there are 40 interactions between residues (Figure 6B(b), Supplementary Table S10). By calculating the charge separation parameters, we can obtain the fraction of charged residues (FCR) of GAPDH as 0.24 and Kappa value (K) as 0.16. The FCR of Rubisco is 0.24 and K is 0.14 (Figure 6C(a,b), Supplementary Table S11).

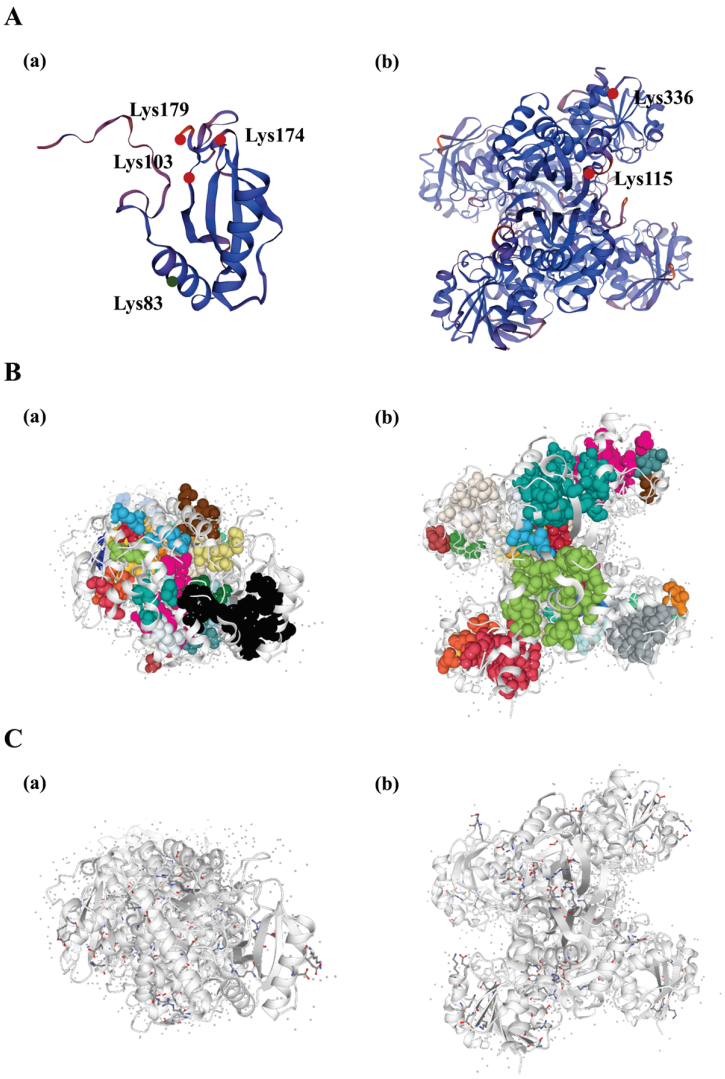


Figure 6. Three-dimensional structure, hydrophobic clusters and salt bridges of acetylation-modifying enzymes for carbon fixation in *R. chrysanthum* under UV−B stress. (**A**) Three-dimensional structure of acetylation-modifying enzymes for carbon fixation. Red is up-regulation of site acetylation modification levels, green is down-regulation of site acetylation modification levels (**B**) Hydrophobic clusters of acetylation-modifying enzymes for carbon fixation; (**C**) Salt bridges of acetylation-modifying enzymes for carbon fixation. (**a**) is Rubisco, (**b**) is GAPDH.

4. Discussion

Lysine acetylation of proteins plays an important regulatory role in plants with different biological functions. So far, acetylated proteins have been reported only in some plants, including *Arabidopsis* [27], wheat [28], poplar [21], rice [29], and pepper [30]. *R. chrysanthum* is a valuable species resource that can withstand UV−B exposure due to its unique growth environment [1]. As a result, we investigated the lysine acetylation proteomics of *R. chrysanthum* under UV−B stress, using *R. chrysanthum* as experimental material. In total, 685 acetylated proteins and 945 modification sites were found using acetylation proteomics analysis. In the natural world, photosynthesis is how plants create the organic materials needed for their own growth and development [30]. However, important enzymes involved in plant carbon fixation are somewhat impacted by abiotic stress, which has an impact on the quantity of CO_2 fixation [31]. In order to identify the mechanism underlying *R. chrysanthum*'s resistance to UV−B light, these acetylated proteins were categorized based

on their GO function and examined with a focus on the acetylation of proteins during carbon fixation.

As the physiological process that provides plants with their energy, photosynthesis is crucial to the functioning of plants. Under UV−B radiation, many plants usually have obvious stress responses, resulting in damage such as inactivation of PSII reaction centers or enhanced photoinhibition [32,33]. Light plays a crucial role in photosynthesis, and the light reaction produces ATP and NADPH to drive the dark reaction. The photosynthetic system of plants utilizes light primarily through photosynthetic pigments in the membranes of the cysts [30]. Photosystem II decomposes H_2O, produces protons and releases O_2 through absorbed light energy. But, UV−B destroys PSII but has no direct effect on PSI. Nevertheless, PSI and PSII drive photosynthetic electron transport sequentially. A study demonstrates that UV−B improves chilling-light-induced PSI photoinhibition and promotes CO_2 assimilation recovery in cucumber (*Cucumis sativus* L.) [34]. Chlorophyll fluorescence parameters are useful indicators of photosynthesis. The analysis of various fluorescence parameters can reveal a number of regulatory processes within photosynthetic mechanisms. Fluorescence parameters such as Fv/Fm and Y(II) are usually reduced in plants under stress conditions [35,36]. In this study, the results of chlorophyll fluorescence parameters of *R. chrysanthum* under UV−B radiation treatment showed that Y(II) was significantly reduced compared to the control (Figure 2). This is consistent with the research results of UV−B radiation on water moss (*Fontinalis antipyretica* Hedw.) [37], indicating that under UV−B radiation stress, the PSII reaction center of plants is significantly damaged, leading to the occurrence of photoinhibition, which in turn affects photosynthetic activity. In addition, to explore the photodamage condition of *R. chrysanthum* under UV−B stress, we analyzed more chlorophyll fluorescence parameters such as NPQ, qL, ETR. Taken together, these results indicate that UV−B can cause some damage to the plant's photosynthetic system, but the plant itself responds to this damage through a series of reactions. To further investigate the molecular mechanisms of plant resistance to UV−B stress, we performed proteomic and acetylation modification analyses.

These amino acids interact and function collectively rather than separately. Since lysine's acetylation modification may have an impact on nearby amino acids, which may also play certain physiological roles in conjunction with lysine, the sequences of lysines undergoing acetylation modification and their neighboring amino acids will be shown in this study (Figure 3). More research is necessary to determine how nearby amino acids are affected by lysine acetylation modification and how lysine acetylation modification functions in conjunction with them. Hydrophobic structures and salt bridges are crucial for preserving the steric structure of proteins (Figure 6). Proteins' three-dimensional structures determine their functions, so in order to better understand how these proteins behave under UV−B stress, their salt-bridge and hydrophobic structures were further characterized after the target's protein structure was established.

Proteins ensure normal plant metabolism, and some proteins (e.g., Rubisco) play an important role in various physiological metabolic processes as biocatalytic enzymes, whose maximum absorption wavelengths fall within the wavelength range of UV−B radiation. Acetylated modification can produce a range of biochemical and physiological reactions [38]. In chloroplasts, in the Calvin cycle, GAPDH plays a crucial role by specifically binding with NADPH [39]. By shaping an invertible multi-enzyme complex with CP12, GAPDH and PRK commonly regulate and control the Calvin cycle [40]. Rubisco, a protein in the chloroplast stroma that catalyzes the carboxylation of ribulose-1,5-bisphosphate for CO_2 fixation, is an important enzyme in the Calvin cycle's first step. In plants, carbon enters the Calvin cycle in the form of carbon dioxide, so enzymes play a crucial role in the Calvin cycle process. In the study, in the Calvin cycle process, the key enzymes were acetylated in *R. chrysanthum* (Figure 5A). This is consistent with previous findings that acetylation modifications of enzymes involved in the Calvin cycle process in the face of abiotic stresses were similarly found in pepper and wheat [28,30]. Interestingly, ribulose-diphosphate carboxylase (Rubisco) contains 4 acetylation sites in *R. chrysanthum* (Supplemental Table S9).

In fact, the carbon fixation of plants is closely related to environmental factors. High UV−B radiation reduced carbon fixation rates in plants [41]. Our results suggest that under UV−B stress, plant photosystems are impaired and photosynthesis is altered, and thus the carbon assimilation process is inevitably affected to some extent. However, the level of acetylation modification affects the expression of plant proteins, which in turn adjusts the alterations that occur in the carbon assimilation process.

In our study, photosynthesis of *R. chrysanthum* was inhibited by UV−B radiation with a significant increase in qL and a significant decrease in NPQ by biochemical analyses, indicating that the photosystem was damaged. The acetylation proteome reveals that the photosynthetic proteins undergo acetylation modification, while the level of key acetylation modification enzymes in the pathway of the carbon cycle shows an upward trend (Figure 7).

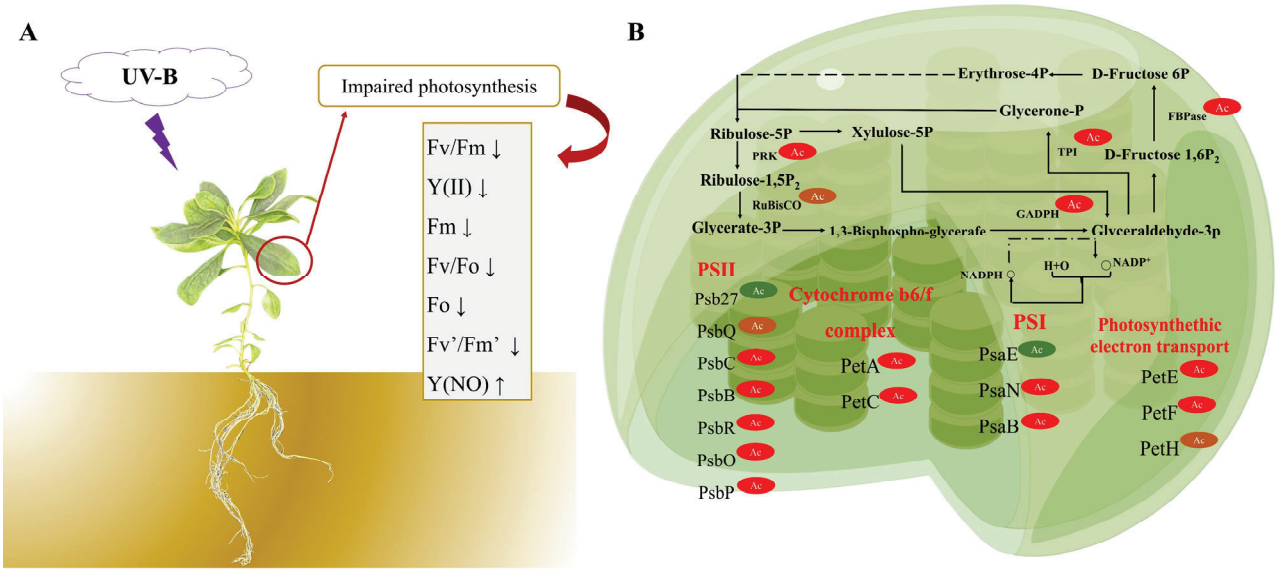


Figure 7. Mechanism diagram of *R. chrysanthum*'s photosynthesis resistance to UV−B stress. (**A**) Altered photosynthesis in *R. chrysanthum* under UV−B stress. (**B**) Schematic diagram of photosynthesis and carbon fixation acetylation of *R. chrysanthum* under UV−B stress. Upward arrows indicate elevated levels, and downward arrows indicate decreased levels.

5. Conclusions

In conclusion, we identified 685 proteins and discovered 945 acetylation modifications at their sites using acetylation proteomics data analysis. Further GO analysis revealed that these proteins are involved in a diverse set of biological processes. According to functional enrichment analysis, acetylated proteins play a role in *R. chrysanthum* photosynthesis and carbon fixation. It was discovered that acetylation modification of key Calvin cycle enzymes (Rubisco, GAPDH) modulates protein expression, causing Rubisco and GAPDH proteins to be expressed in significantly different ways, affecting *R. chrysanthum*'s carbon fixation capacity. As a result of the acetylation modification, Rubisco and GAPDH are significantly differentially expressed, affecting carbon fixation capacity and making the plant resistant to UV−B stress. This study provides valuable information about the plant's response to UV−B and lays the groundwork for future protein post-translational modification research.

Supplementary Materials: The following supporting information can be downloaded at: https://www.mdpi.com/article/10.3390/biom14060732/s1, Figure S1: Identification of lysine acetylation proteome in *Rhododendron chrysanthum*. (A) 4D-label free experimental flowchart. (B) Mass error distribution of whole identified polypeptides. (C) The length distribution of identified peptide; Figure S2. KEGG pathway enrichment analysis of the acetylated proteins in carbon metabolism. The acetylated proteins are in blue; Figure S3. KEGG pathway enrichment analysis of the acetylated proteins in photosynthesis. The acetylated proteins are in blue; Figure S4. KEGG pathway enrichment analysis of the acetylated proteins in carbon fixation in photosynthetic organisms. The acetylated proteins are in blue; Table S1. The identified acetylated sites in *Rhododendron chrysanthum*; Table S2. The identified differentially expressed proteins in *Rhododendron chrysanthum*; Table S3. Peptide motif of *R. chrysanthum*; Table S4. Frequency of the different types of amino acids around the acetylated lysine; Table S5. Go annotation detail of the acetylated proteins in *Rhododendron chrysanthum*; Table S6. Protein GO enrichment in biological process; Table S7. Protein GO enrichment in molecular function; Table S8. Protein GO enrichment in cellular component; Table S9. Protein pathway enrichment; Table S10. Differential acetylated proteins *Rhododendron chrysanthum* under UV−B stress; Table S11. Structural information on hydrophobic clusters and salt bridges in *R. chrysanthum* under UV−B stress.

Author Contributions: Writing—original draft preparation, M.L. and F.G.; writing—review and editing, H.X. and X.Z.; methodology, M.L. and W.Y.; software, K.C. and M.L.; visualization, M.L. and F.G.; supervision, H.X. and X.Z.; project administration, H.X. and X.Z. All authors have read and agreed to the published version of the manuscript.

Funding: This work was supported by the Jilin Provincial Science and Technology Development Program project (Grant numbers: YDZJ202301ZYTS517).

Institutional Review Board Statement: Not applicable.

Informed Consent Statement: Not applicable.

Data Availability Statement: The datasets generated during and/or analysed during the current study are available from the corresponding author on reasonable request.

Acknowledgments: We are grateful to Jingjie PTM Biolab (Hangzhou, China) Co., Ltd. for pro viding mass spectrometry support.

Conflicts of Interest: The authors declare no conflicts of interest.

References

1. Zhou, X.; Chen, S.; Wu, H.; Yang, Y.; Xu, H. Biochemical and proteomics analyses of antioxidant enzymes reveal the potential stress tolerance in *Rhododendron chrysanthum* Pall. *Biol. Direct.* **2017**, *12*, 10. [CrossRef] [PubMed]
2. Lyu, J.; Wang, C.; Liang, D.Y.; Liu, L.; Pandey, L.K.; Xu, H.W.; Zhou, X.F. Sensitivity of wild and domesticated Rhododendron chrysanthum to different light regime (UVA, UVB, and PAR). *Photosynthetica* **2019**, *57*, 841–849. [CrossRef]
3. Bassman, J.H. Ecosystem consequences of enhanced solar ultraviolet radiation: Secondary plant metabolites as mediators of multiple trophic interactions in terrestrial plant communities. *Photochem. Photobiol.* **2004**, *79*, 382–398. [CrossRef]
4. Knox, P.P.; Lukashev, E.P.; Gorokhov, V.V.; Grishanova, N.P.; Paschenko, V.Z. Hybrid complexes of photosynthetic reaction centers and quantum dots in various matrices: Resistance to UV irradiation and heating. *Photosynth. Res.* **2019**, *139*, 295–305. [CrossRef]
5. Widel, M.; Krzywon, A.; Gajda, K.; Skonieczna, M.; Rzeszowska-Wolny, J. Induction of bystander effects by UVA, UVB, and UVC radiation in human fibroblasts and the implication of reactive oxygen species. *Free Radic. Biol. Med.* **2014**, *68*, 278–287. [CrossRef]
6. Hideg, E.; Jansen, M.A.; Strid, A. UV−B exposure, ROS, and stress: Inseparable companions or loosely linked associates? *Trends Plant Sci.* **2013**, *18*, 107–115. [CrossRef] [PubMed]
7. Chen, Y.-E.; Su, Y.-Q.; Zhang, C.-M.; Ma, J.; Mao, H.-T.; Yang, Z.-H.; Yuan, M.; Zhang, Z.-W.; Yuan, S.; Zhang, H.-Y. Comparison of Photosynthetic Characteristics and Antioxidant Systems in Different Wheat Strains. *J. Plant Growth Regul.* **2018**, *37*, 347–359. [CrossRef]
8. Barber, J. Photosystem two. *Biochim. Biophys. Acta Bioenerg.* **1998**, *1365*, 269–277. [CrossRef]
9. Yoon, H.I.; Kim, D.; Son, J.E. Spatial and Temporal Bioactive Compound Contents and Chlorophyll Fluorescence of Kale (*Brassica oleracea* L.) Under UV−B Exposure Near Harvest Time in Controlled Environments. *Photochem. Photobiol.* **2020**, *96*, 845–852. [CrossRef]
10. Piccini, C.; Cai, G.; Dias, M.C.; Romi, M.; Longo, R.; Cantini, C. UV−B Radiation Affects Photosynthesis-Related Processes of Two Italian *Olea europaea* (L.) Varieties Differently. *Plants* **2020**, *9*, 1712. [CrossRef]
11. Liu, M.; Sun, Q.; Cao, K.; Xu, H.; Zhou, X. Acetylated Proteomics of UV−B Stress-Responsive in Photosystem II of *Rhododendron chrysanthum*. *Cells* **2023**, *12*, 478. [CrossRef] [PubMed]

12. UniProt Consortium, T. UniProt: The universal protein knowledgebase. *Nucleic Acids Res.* **2018**, *46*, 2699. [CrossRef] [PubMed]
13. Choudhary, C.; Weinert, B.T.; Nishida, Y.; Verdin, E.; Mann, M. The growing landscape of lysine acetylation links metabolism and cell signalling. *Nat. Rev. Mol. Cell Biol.* **2014**, *15*, 536–550. [CrossRef] [PubMed]
14. Narita, T.; Weinert, B.T.; Choudhary, C. Functions and mechanisms of non-histone protein acetylation. *Nat. Rev. Mol. Cell Biol.* **2019**, *20*, 156–174. [CrossRef] [PubMed]
15. Colville, A.; Alhattab, R.; Hu, M.; Labbé, H.; Xing, T.; Miki, B. Role of HD2 genes in seed germination and early seedling growth in Arabidopsis. *Plant Cell Rep.* **2011**, *30*, 1969–1979. [CrossRef]
16. Kim, W.; Latrasse, D.; Servet, C.; Zhou, D.X. Arabidopsis histone deacetylase HDA9 regulates flowering time through repression of AGL19. *Biochem. Biophys. Res. Commun.* **2013**, *432*, 394–398. [CrossRef] [PubMed]
17. Luo, M.; Wang, Y.Y.; Liu, X.; Yang, S.; Lu, Q.; Cui, Y.; Wu, K. HD2C interacts with HDA6 and is involved in ABA and salt stress response in Arabidopsis. *J. Exp. Bot.* **2012**, *63*, 3297–3306. [CrossRef] [PubMed]
18. Park, H.J.; Baek, D.; Cha, J.Y.; Liao, X.; Kang, S.H.; McClung, C.R.; Lee, S.Y.; Yun, D.J.; Kim, W.Y. HOS15 Interacts with the Histone Deacetylase HDA9 and the Evening Complex to Epigenetically Regulate the Floral Activator GIGANTEA. *Plant Cell* **2019**, *31*, 37–51. [CrossRef] [PubMed]
19. van Zanten, M.; Zöll, C.; Wang, Z.; Philipp, C.; Carles, A.; Li, Y.; Kornet, N.G.; Liu, Y.; Soppe, W.J. HISTONE DEACETYLASE 9 represses seedling traits in Arabidopsis thaliana dry seeds. *Plant J.* **2014**, *80*, 475–488. [CrossRef]
20. Yuan, L.; Chen, X.; Chen, H.; Wu, K.; Huang, S. Histone deacetylases HDA6 and HDA9 coordinately regulate valve cell elongation through affecting auxin signaling in Arabidopsis. *Biochem. Biophys. Res. Commun.* **2019**, *508*, 695–700. [CrossRef]
21. Liao, X.; Li, Y.; Hu, Z.; Lin, Y.; Zheng, B.; Ding, J. Poplar acetylome profiling reveals lysine acetylation dynamics in seasonal bud dormancy release. *Plant Cell Environ.* **2021**, *44*, 1830–1845. [CrossRef] [PubMed]
22. Zhu, G.R.; Yan, X.; Zhu, D.; Deng, X.; Wu, J.S.; Xia, J.; Yan, Y.M. Lysine acetylproteome profiling under water deficit reveals key acetylated proteins involved in wheat grain development and starch biosynthesis. *J. Proteom.* **2018**, *185*, 8–24. [CrossRef] [PubMed]
23. Gong, X.; Huang, Y.; Liang, Y.; Yuan, Y.; Liu, Y.; Han, T.; Li, S.; Gao, H.; Lv, B.; Huang, X.; et al. OsHYPK-mediated protein N-terminal acetylation coordinates plant development and abiotic stress responses in rice. *Mol. Plant* **2022**, *15*, 740–754. [CrossRef]
24. Du, Q.; Qu, Z.; Wang, L.; Jiang, J.; Fu, X.; Fang, Y.; Li, X.; Xie, X. Histone deacetylase SbHDT701 in Sorghum bicolor reveals functions in response to stress factors by enhancing acetylation. *Pestic. Biochem. Physiol.* **2021**, *178*, 104908. [CrossRef] [PubMed]
25. Wu, X.; Oh, M.H.; Schwarz, E.M.; Larue, C.T.; Sivaguru, M.; Imai, B.S.; Yau, P.M.; Ort, D.R.; Huber, S.C. Lysine acetylation is a widespread protein modification for diverse proteins in Arabidopsis. *Plant Physiol.* **2011**, *155*, 1769–1778. [CrossRef] [PubMed]
26. Jiang, J.; Gai, Z.; Wang, Y.; Fan, K.; Sun, L.; Wang, H.; Ding, Z. Comprehensive proteome analyses of lysine acetylation in tea leaves by sensing nitrogen nutrition. *BMC Genom.* **2018**, *19*, 840. [CrossRef]
27. König, A.C.; Hartl, M.; Boersema, P.J.; Mann, M.; Finkemeier, I. The mitochondrial lysine acetylome of *Arabidopsis*. *Mitochondrion* **2014**, *19*, 252–260. [CrossRef] [PubMed]
28. Zhang, Y.; Song, L.; Liang, W.; Mu, P.; Wang, S.; Lin, Q. Comprehensive profiling of lysine acetylproteome analysis reveals diverse functions of lysine acetylation in common wheat. *Sci. Rep.* **2016**, *6*, 21069. [CrossRef]
29. Nallamilli, B.R.; Edelmann, M.J.; Zhong, X.; Tan, F.; Mujahid, H.; Zhang, J.; Nanduri, B.; Peng, Z. Global analysis of lysine acetylation suggests the involvement of protein acetylation in diverse biological processes in rice (*Oryza sativa*). *PLoS ONE* **2014**, *9*, e89283. [CrossRef]
30. Liu, Z.; Song, J.; Miao, W.; Yang, B.; Zhang, Z.; Chen, W.; Tan, F.; Suo, H.; Dai, X.; Zou, X.; et al. Comprehensive Proteome and Lysine Acetylome Analysis Reveals the Widespread Involvement of Acetylation in Cold Resistance of Pepper (*Capsicum annuum* L.). *Front. Plant Sci.* **2021**, *12*, 730489. [CrossRef]
31. Savitch, L.V.; Leonardos, E.D.; Krol, M.; Jansson, S.; Öquist, G. Two different strategies for light utilization in photosynthesis in relation to growth and cold acclimation. *Plant Cell Environ.* **2002**, *25*, 761–771. [CrossRef]
32. Wu, J.-b.; Guan, D.-x.; Yuan, F.-h.; Zhang, X.-j. Research advances on the biological effects of elevated ultraviolet-B radiation on terrestrial plants. *J. For. Res.* **2009**, *20*, 383–390. [CrossRef]
33. Lidon, F.J.C. Micronutrients' accumulation in rice after supplemental UV−B irradiation. *J. Plant Interact.* **2012**, *7*, 19–28. [CrossRef]
34. Zhang, Z.S.; Jin, L.Q.; Li, Y.T.; Tikkanen, M.; Li, Q.M.; Ai, X.Z.; Gao, H.Y. Ultraviolet−B Radiation (UV−B) Relieves Chilling-Light-Induced PSI Photoinhibition And Accelerates The Recovery Of CO_2 Assimilation In Cucumber (*Cucumis sativus* L.) Leaves. *Sci. Rep.* **2016**, *6*, 34455. [CrossRef] [PubMed]
35. Liang, Y.; Chen, H.; Tang, M.J.; Yang, P.F.; Shen, S.H. Responses of Jatropha curcas seedlings to cold stress: Photosynthesis-related proteins and chlorophyll fluorescence characteristics. *Physiol. Plant.* **2007**, *131*, 508–517. [CrossRef]
36. Belkhodja, R.; Morales, F.; Abadia, A.; Gomez-Aparisi, J.; Abadia, J. Chlorophyll Fluorescence as a Possible Tool for Salinity Tolerance Screening in Barley (*Hordeum vulgare* L.). *Plant Physiol.* **1994**, *104*, 667–673. [CrossRef]
37. Martínez-Abaigar, J.; Núñez-Olivera, E.; Beaucourt, N.; García-Álvaro, M.A.; Tomás, R.; Arróniz, M. Different physiological responses of two aquatic bryophytes to enhanced ultraviolet−B radiation. *J. Bryol.* **2003**, *25*, 17–30. [CrossRef]
38. Ifuku, K.; Ido, K.; Sato, F. Molecular functions of PsbP and PsbQ proteins in the photosystem II supercomplex. *J. Photochem. Photobiol. B Biol.* **2011**, *104*, 158–164. [CrossRef] [PubMed]

39. McFarlane, C.R.; Shah, N.R.; Kabasakal, B.V.; Echeverria, B.; Cotton, C.A.R.; Bubeck, D.; Murray, J.W. Structural basis of light-induced redox regulation in the Calvin-Benson cycle in cyanobacteria. *Proc. Natl. Acad. Sci. USA* **2019**, *116*, 20984–20990. [CrossRef]
40. Howard, T.P.; Lloyd, J.C.; Raines, C.A. Inter-species variation in the oligomeric states of the higher plant Calvin cycle enzymes glyceraldehyde-3-phosphate dehydrogenase and phosphoribulokinase. *J. Exp. Bot.* **2011**, *62*, 3799–3805. [CrossRef]
41. Martínez-Lüscher, J.; Morales, F.; Sánchez-Díaz, M.; Delrot, S.; Aguirreolea, J.; Gomès, E.; Pascual, I. Climate change conditions (elevated CO_2 and temperature) and UV−B radiation affect grapevine (*Vitis vinifera* cv. Tempranillo) leaf carbon assimilation, altering fruit ripening rates. *Plant Sci.* **2015**, *236*, 168–176. [CrossRef] [PubMed]

Disclaimer/Publisher's Note: The statements, opinions and data contained in all publications are solely those of the individual author(s) and contributor(s) and not of MDPI and/or the editor(s). MDPI and/or the editor(s) disclaim responsibility for any injury to people or property resulting from any ideas, methods, instructions or products referred to in the content.

molecules

MDPI

Article

Halogenated Boroxine $K_2[B_3O_3F_4OH]$ Modulates Metabolic Phenotype and Autophagy in Human Bladder Carcinoma 5637 Cell Line

Nikolina Elez-Burnjaković [1], Lejla Pojskić [2], Anja Haverić [2], Naida Lojo-Kadrić [2], Maida Hadžić Omanović [2], Ajla Smajlović [2], Svetoslav Kalaydjiev [3], Milka Maksimović [4], Bojan Joksimović [1,*] and Sanin Haverić [2]

[1] Faculty of Medicine Foča, University of East Sarajevo, Studentska 5, 73 300 Foča, Bosnia and Herzegovina; nikolinaa85@hotmail.com
[2] Institute for Genetic Engineering and Biotechnology, University of Sarajevo, Zmaja od Bosne 8, 71 000 Sarajevo, Bosnia and Herzegovina; lejla.pojskic@ingeb.unsa.ba (L.P.); anja.haveric@ingeb.unsa.ba (A.H.); naida.lojo@ingeb.unsa.ba (N.L.-K.); maida.hadzic@ingeb.unsa.ba (M.H.O.); ajla-rizvanovic@hotmail.com (A.S.); sanin.haveric@ingeb.unsa.ba (S.H.)
[3] Agilent Technologies LDA UK Ltd., 5500 Lakeside, Stockport SK8 3GR, UK; svetoslav.kalaydjiev@agilent.com
[4] Faculty of Science, University of Sarajevo, Zmaja od Bosne 33, 71 000 Sarajevo, Bosnia and Herzegovina; mmaksimo@yahoo.co.uk
* Correspondence: bojannjoksimovic@gmail.com; Tel.: +387-65-373-508

Abstract: Halogenated boroxine $K_2[B_3O_3F_4OH]$ (HB), an inorganic derivative of cyclic anhydride of boronic acid, is patented as a boron-containing compound with potential for the treatment of both benign and malignant skin changes. HB has effectively inhibited the growth of several carcinoma cell lines. Because of the growing interest in autophagy induction as a therapeutic approach in bladder carcinoma (BC), we aimed to assess the effects of HB on metabolic phenotype and autophagy levels in 5637 human bladder carcinoma cells (BC). Cytotoxicity was evaluated using the alamar blue assay, and the degree of autophagy was determined microscopically. Mitochondrial respiration and glycolysis were measured simultaneously. The relative expression of autophagy-related genes BECN1, P62, BCL-2, and DRAM1 was determined by real-time PCR. HB affected cell growth, while starvation significantly increased the level of autophagy in the positive control compared to the basal level of autophagy in the untreated negative control. In HB-treated cultures, the degree of autophagy was higher compared to the basal level, and metabolic phenotypes were altered; both glycolysis and oxidative phosphorylation (OXPHOS) were decreased by HB at 0.2 and 0.4 mg/mL. Gene expression was deregulated towards autophagy induction and expansion. In conclusion, HB disrupted the bioenergetic metabolism and reduced the intracellular survival potential of BC cells. Further molecular studies are needed to confirm these findings and investigate their applicative potential.

Keywords: cytotoxicity; autophagy; BC cells; gene expression; metabolic phenotype

1. Introduction

Autophagy is a dynamic process, conserved in all eukaryotes. It is responsible for the degradation of cytoplasmic content and the cell's response to stress, embryonic development, pathogens, and aging. The process is also involved in the pathology of human diseases, such as cancer, diabetes, cardiomyopathy, and neurodegenerative diseases. Among the three types of autophagy, chaperone-mediated autophagy, microautophagy, and macroautophagy, the term autophagy mainly refers to the last one (hereinafter autophagy) [1]. In normal tissues, autophagy is at a low level, and it increases in metabolic stress and in the absence of oxygen and nutrients in tumors. Many cancer types, such as bladder, lung, and colorectal [2,3], as well as melanoma [4], show increased basal autophagy

and are associated with aggressiveness and a poor prognosis [5]. Metastatic tumors are highly "dependent" on autophagy, which provides the metabolic energy needed for growth. However, if extensively or inappropriately activated, autophagy can promote apoptosis (type I) or function as an alternative cell death pathway, which is called autophagic cell death (type II). Autophagy can either promote the death of cancer cells or serve as a survival mechanism against apoptotic or necrotic death induced by various anticancer treatments [6]. Given the contradictory role of autophagy during tumor initiation and progression, the therapeutic use of autophagy depends on the context and must be approached individually.

Bladder carcinoma (BC) is one of the most common malignancies, with an increasing incidence worldwide [7]. The majority of new cases are non-muscle-invasive tumors that are commonly treated by radical resection, radiotherapy, and chemotherapy. However, more than half of the superficial bladder cancers will recur, with 10–40% resulting in metastatic outcomes [8].

The non-muscle-invasive bladder carcinoma cell line 5637 has been used as an in vitro model for high-risk superficial bladder tumors with specific molecular characteristics (Bcl-2 and Bcl-X positive expression and *P53* tumor suppressor mutation) [9]. Loss of p53 tumor suppressor function, due to the P53R280T mutation [10,11], promotes the Warburg effect [11]. P53 is known to reduce the glycolysis rate by increasing the activity of fructose-2,6-bisphosphatase. This mechanism is also involved in the regulatory pathways of apoptosis [12]. This mechanism seems to increase oxidative phosphorylation. Earlier studies have confirmed increased glucose and glutamine uptake, along with pyruvate and alanine production, in 5637 cell lines in vitro [13]. Therefore, 5637 cells show inhibited apoptosis, increased cell proliferation, and chemotherapy resistance. Silencing of the *P53* mutant decreases cell viability [14]. High levels of basal autophagy in 5637 cells are confirmed by LC3 immunofluorescence staining in a nutrient-rich environment. The inhibition of basal autophagy results in apoptotic cell loss [3]. The efficacy of chemotherapy is limited because of drug resistance, while autophagy may account for the failure of chemotherapy treatment in BC. Large proportions of patients with advanced BC are resistant to chemotherapy and are characterized by specific molecular signatures [15]. The cooperative inhibition of autophagy is shown to be a vital strategy against cisplatin resistance in human BC cells [15]. To reduce chemoresistance, efforts should focus on several areas. Multi-omics sequencing and analysis can identify reliable biomarkers for predicting chemosensitivity in bladder cancer and might pinpoint the patient groups that are likely to respond to cytotoxic treatments. Targeting dysregulated pathways in chemotherapy-resistant patients could reverse resistance. Additionally, addressing other tumor microenvironment components, such as immune cells and cancer-associated fibroblasts, is crucial. Precision drug delivery using nanotechnology and antibody–drug conjugates shows promise. These strategies aim to improve response rates and increase overall and progression-free survival [16]. Meanwhile, cisplatin-based adjuvant chemotherapy remains a valid option for muscle-invasive bladder cancer [17].

Therapeutic strategies for BC may cause unfavorable side effects and complications. Therefore, autophagy induction is a promising therapeutic approach [15]. The association of the Warburg effect in cancers with tumor-related autophagy may be relevant for the further development of experimental therapeutics and cancer prevention.

In this work, we investigated the potential of dipotassium trioxohydroxytetrafluorotriborate, $K_2[B_3O_3F_4OH]$, also known as halogenated boroxine (HB), to promote autophagy in BC cell lines. HB is a derivative of the cyclic anhydride of boronic acid [18], containing four fluorine atoms substituted in a six-membered ring. Patented as a prevention and therapeutic agent for various skin changes [19,20], HB has been submitted to numerous in vitro studies [21–25]. It acts as an inhibitor of horseradish peroxidase (HRP) [26], catalase [27], superoxide dismutase [28], and carbonic anhydrases [29]. In the GR-M cell line, HB significantly downregulates the relative expression of *IGF-1*, *hTERT*, and *BCL-2* genes [24,30], suggesting its antitumor activity. At a physiological concentration of Ca^{2+}, HB inhibits the growth of tumor cells without having such an effect on normal cells [31].

The anti-tumor activity of HB in vitro has also been proven against mammary carcinoma (4T1), melanoma (B16F10), and squamous cell carcinoma (SCCVII) [32]. HB significantly inhibits tumor growth in vivo, regardless of the means of application [32]. Temporary mild-to-moderate HB dose-dependent lesions were observed in the kidneys and livers of Wistar rats after single intraperitoneal doses of HB at 25, 35, and 45 mg/kg/body weight (bw) in comparison with the control and 10 mg/kg/bw treatments. Adverse effects were not detected in a single-dose administration lower than 35 mg/kg or in repeated, nine-day dosages with 10 mg/kg/bw [33]. The median lethal dose (LD50) of HB in Sprague Dawley and Wistar rats and BALB/c mice ranges from 63 to 75 mg/kg, meaning that HB shows moderate toxicity [34].

According to the previous findings on the toxic effects of HB, we aimed to test if HB may be used as an autophagy inducer in human BC cells and its potential to modify the Warburg effect.

2. Results

2.1. Cytotoxic Effects of HB on BC Cells

The results of the alamar blue assay revealed BC cell growth inhibition of 47.16% at a 0.05 mg/mL HB concentration. HB concentrations of 0.1 and 0.2 mg/mL reduced cell growth to 65.18% and 64.43%, respectively. The inhibition percentage at 0.4 mg/mL was 53.41%. The association between the HB concentration and the percentage of cell growth inhibition was estimated by a simple linear regression calculation (Figure 1).

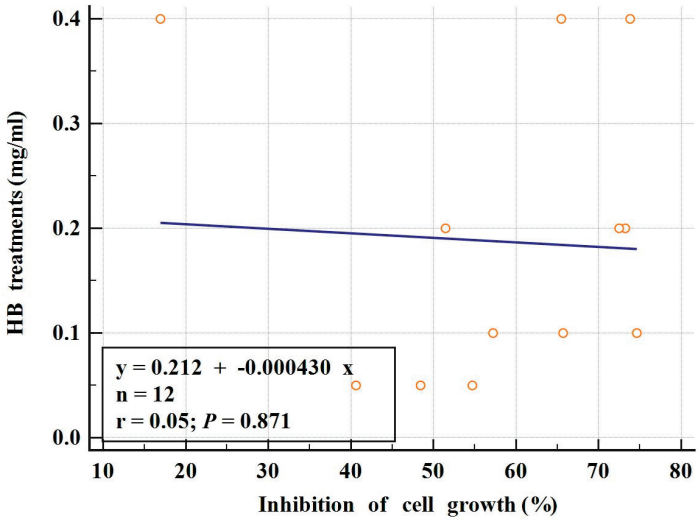


Figure 1. Association between BC cell growth and different HB treatments (simple linear regression; r = 0.05; p = 0.871). Cells were treated for 24 h after initial incubation. Cultures without test substances, set as positive control, and negative control cultures, without cells, were used to calculate the percentage of cell growth inhibition (https://tools.thermofisher.com, accessed on 15 August 2023; the alamarBlue® Assay, Thermo Fisher Scientific, Waltham, MA, USA).

2.2. Evaluation of Autophagy Induction by HB

Autophagosome induction was semi-quantified. Four categories were established according to the estimated number of autophagosome signals per cell. According to the predefined criteria, 200 cells were observed for autophagy markers (signals) for each treatment.

Compared to the negative control, which had a total of 22 cells with autophagy signals, the 0.05 mg/mL HB concentration resulted in 141 cells with autophagy signals, with most cells having 5–10 detected autophagosomes. At 0.1 and 0.2 mg/mL HB treatments, autophagy markers were detected in 166 and 148 cells, respectively. At a 0.1 mg/mL HB concentration, a higher frequency of cells with 5–10 signals was found compared to the 0.2 mg/mL HB treatment, where more cells with coupled signals were detected. At a 0.4 mg/mL HB concentration, 141 cells were positive for autophagy, with the highest

frequency of cells with the coupled signals. Autophagy was successfully induced in the positive control, where 191 cells had different types of autophagy signals.

Different categories of autophagosome induction were observed in all cultures treated with HB in concentrations ranging from 0.05 to 0.4 mg/mL. Autophagy was successfully induced in the positive control, while the negative control showed low levels of basal autophagy according to the detection of autophagosome signals (Figures 2 and 3, Supplementary Materials).

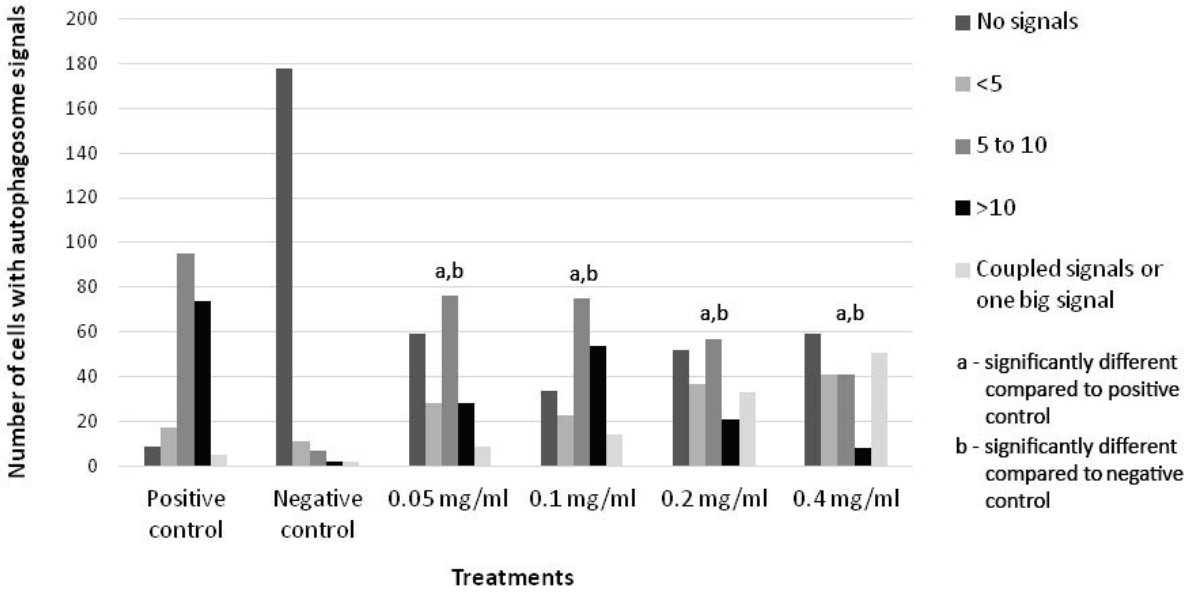


Figure 2. Distribution of frequency of detected autophagosome signals; positive (+) control—starvation-induced autophagy cells; negative (−) control—untreated cells. Four categories were established according to the estimated number of autophagosome signals per cells. According to predefined criteria, 200 cells were observed for autophagy markers (signals) for each treatment. Differences for all treatments and quantification of autophagosome signals were significant ($p < 0.05$).

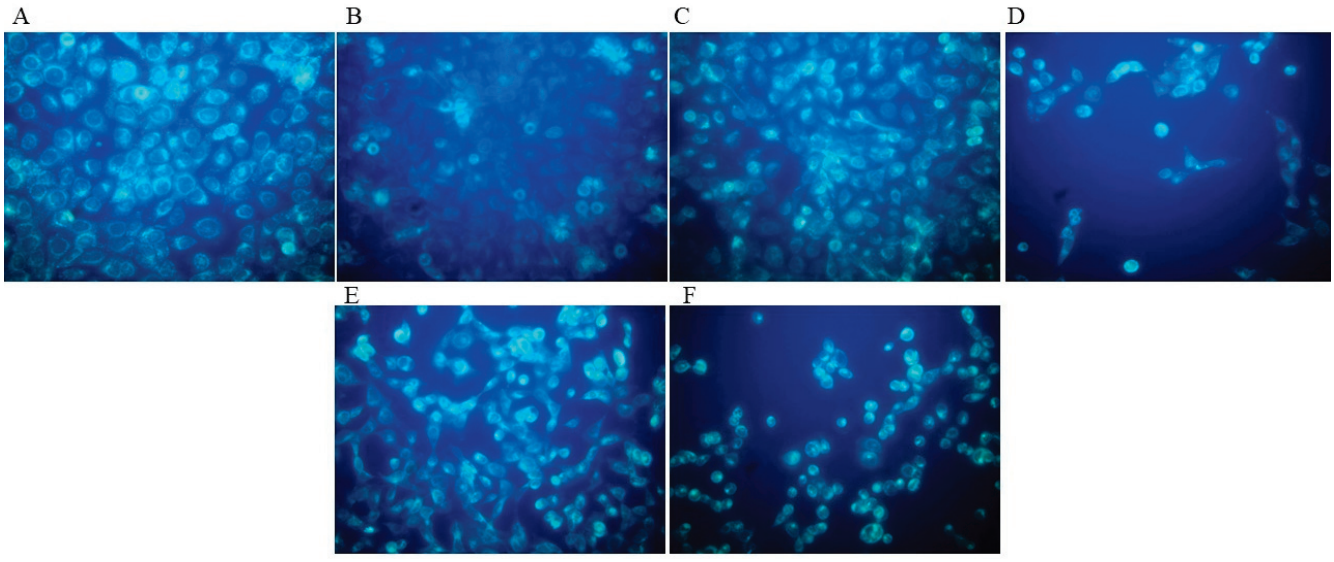


Figure 3. Autophagy detection using Autophagy Assay kit (Sigma-Aldrich, St. Louis, MO, USA). Epifluorescence detection was performed using a BX51 microscope with 400× magnification (Olympus, Tokyo, Japan); the degree of autophagy was photo-documented with a DP50 camera analyzed using View Finder Lite software version 1.0.143c (Olympus, Japan). (**A**)—positive control; (**B**)—negative control; (**C**)—0.05 mg/mL treatment; (**D**)—0.1 mg/mL treatment; (**E**)—0.2 mg/mL treatment; and (**F**)—0.4 mg/mL treatment.

Comparisons of detected autophagosome signals compared to the negative control were statistically significant in 0.05, 0.1, 0.2, and 0.4 mg/mL HB treatments ($p < 0.05$). Comparisons of autophagosome signal ratios, compared to the positive control, were statistically significant at all tested HB concentrations ($p < 0.05$).

2.3. Cellular Energy Phenotype and the Investigation of Metabolic Switching: OCR and ECAR Rates in Response to HB Treatment—Nts

The XF Cell Energy Phenotype test was performed for glycolysis and mitochondrial respiration determination. The oxygen consumption rate (OCR), as a measure of mitochondrial respiration, and the extracellular acidification rate (ECAR), as a measure of glycolysis, were determined in baseline and stressed phenotypes at 0.05, 0.1, 0.2, and 0.4 mg/mL HB concentrations in both positive and negative controls.

Significant differences between basal and stressed OCR values, tested by the Mann–Whitney test, were registered only for the positive control ($p = 0.0002$), with a decrease in the OCR values in a stressed state. ECAR values increased in a stressed state for all treatments. The differences were significant for all HB treatments except for 0.4 mg/mL ($p = 0.12$). There is a clear differentiation in OCR and ECAR values between the negative control, 0.5 and 0.1 mg/mL HB treatments on one side, the highest tested HB concentrations (0.2 and 0.4 mg/mL), and the positive control on the other side (Figure 4).

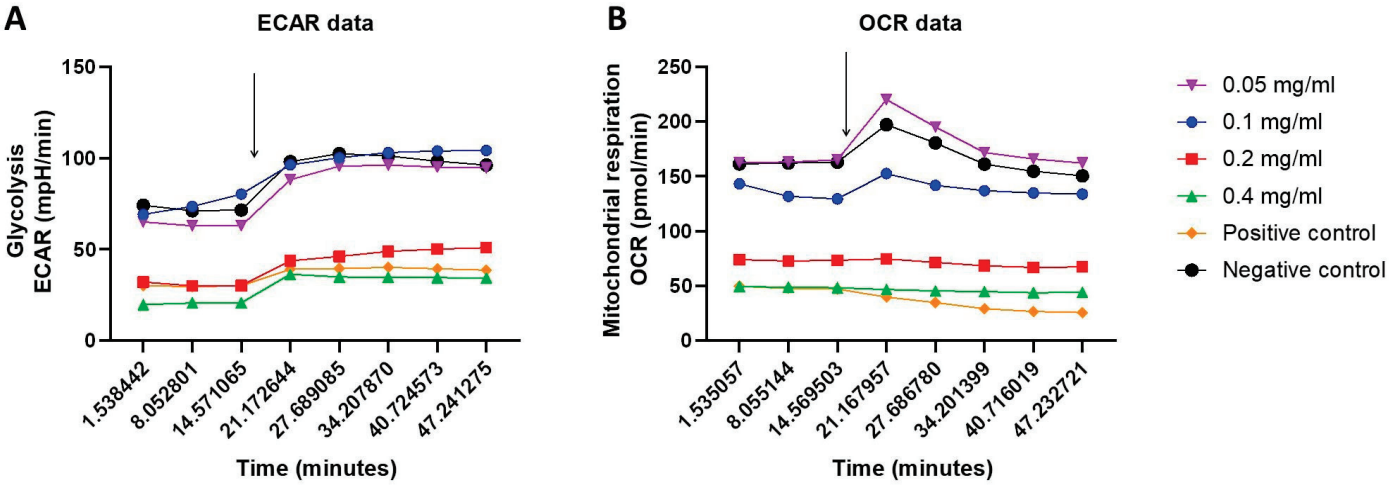


Figure 4. Phenotype Stress Test assessment of basal (three initial measurements) and stressed (five subsequent measurements) metabolic rates in BC cells seeded at 4×10^4/well: (**A**) glycolysis (ECAR) and (**B**) mitochondrial respiration (OCR) were measured on a Seahorse XF HS Mini Analyzer. ECAR—extracellular acidification rate; OCR—oxygen consumption rate. Results are presented as mean values of duplicate measurements.

When baseline and stressed OCR and ECAR values were independently compared, significantly higher values ($p < 0.05$; Kruskal–Wallis test) were found for the negative control, and lower HB concentrations (0.05 and 0.1 mg/mL) were found compared to the positive control and higher HB concentrations (0.2 and 0.4 mg/mL) (Figure 5).

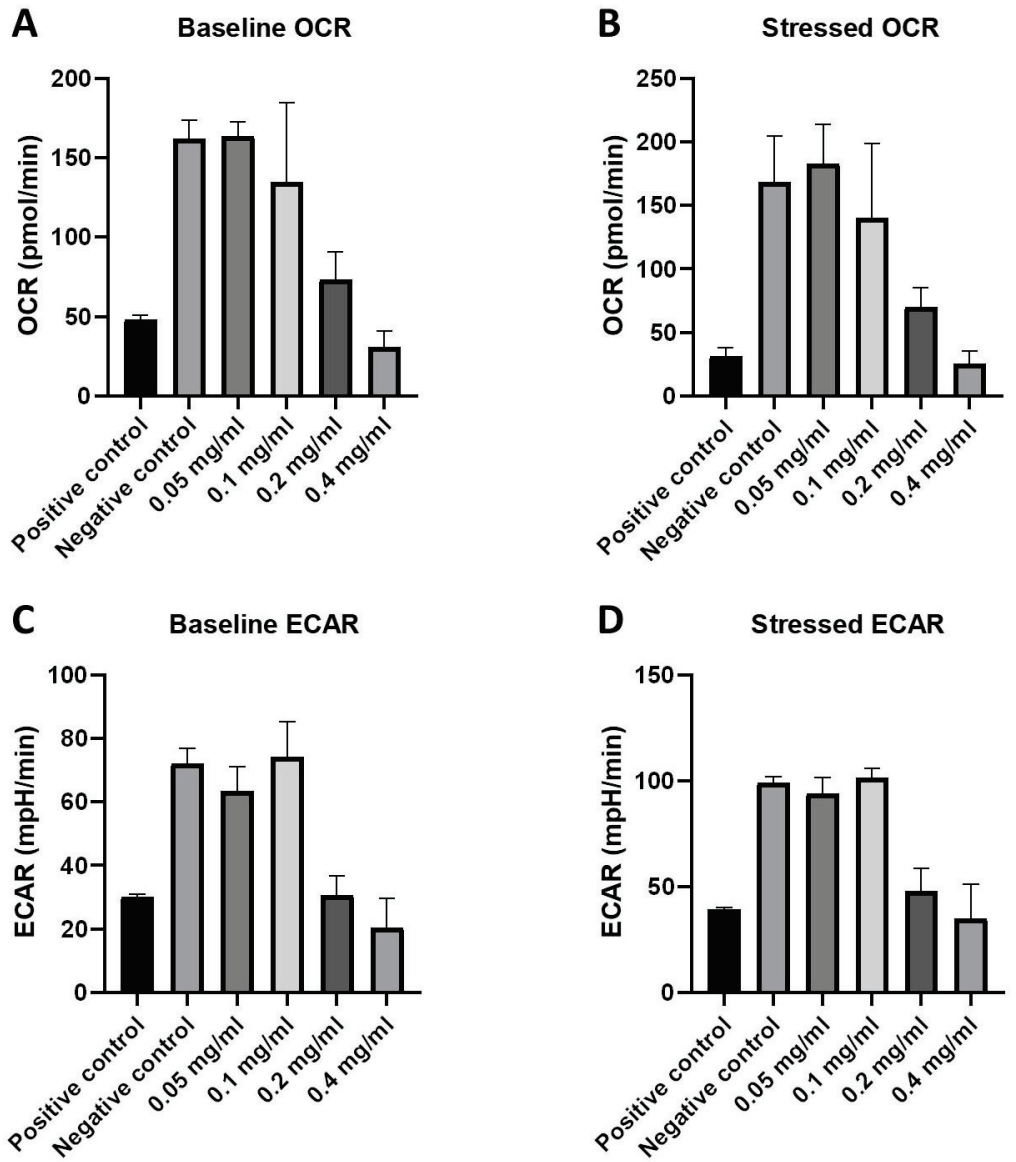


Figure 5. Phenotype Stress Test showing basal and stressed mitochondrial (**A**,**B**) and glycolytic activity (**C**,**D**) of the BC cells. Data are presented as means with SD analyzed by Kruskal–Wallis test, $p < 0.001$. ECAR—extracellular acidification rate; OCR—oxygen consumption rate.

2.4. Deregulation of Autophagy-Associate Genes by HB

The effects of different HB concentrations on cell cycle deregulation were evaluated using a relative gene expression assay for autophagy markers: *BECN-1*, *BCL-2*, *P62*, and *DRAM1*. The normalized gene expression ratios for all evaluated treatments were compared against corresponding values for negative (untreated cells) and positive controls (Figures 6 and 7).

When compared with the negative control, significant upregulation of *P62* was detected for all except for the 0.4 mg/mL HB concentration. *BECN1* was significantly upregulated in all HB treatments, with unsignificant changes at a 0.1 mg/mL HB concentration. Significant downregulation of *DRAM1* was observed in 0.1–0.4 mg/mL HB treatments compared to the positive control, while *BCL-2* was significantly downregulated at 0.1 and 0.4 mg/mL HB treatments compared to the positive control.

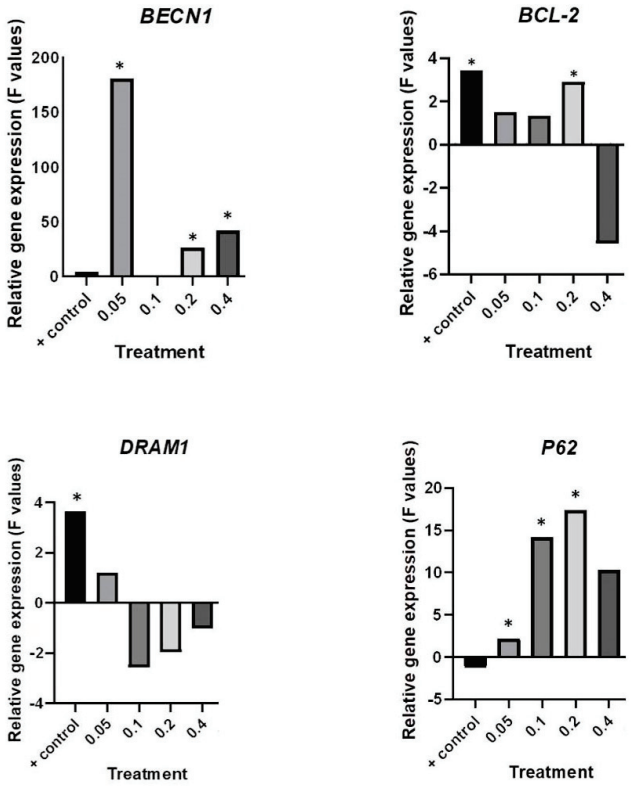


Figure 6. Results of *BECN1*, *BCL-2*, *P62*, and *DRAM1* relative gene expression analysis normalized with the *GAPDH* gene compared with HB-untreated cells (negative control). The F values are shown; * $p < 0.05$.

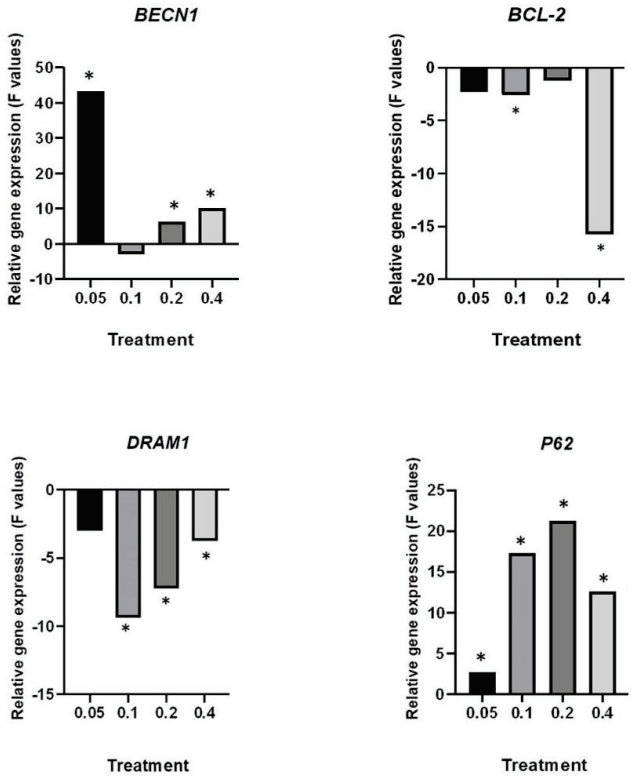


Figure 7. Results of *BECN1*, *BCL-2*, *P62*, and *DRAM1* gene expression analyses normalized with the GAPDH gene were compared with the positive control (starvation-induced autophagy cells). The F values are shown; * $p < 0.05$.

3. Discussion

Previous in vitro studies of the anti-proliferative effects of HB have revealed a selective cytotoxic effect on tumor cells and a weak cytotoxic effect on non-tumor cells [21,24,31,32,35]. In this study, we found dose-dependent HB inhibition of cell proliferation. The lowest tested HB concentration (0.05 mg/mL) slightly inhibited BC cell growth, while concentrations of 0.1, 0.2, and 0.4 mg/mL were highly cytotoxic.

Autophagy is a dynamic and complex process that is regulated by multiple molecules and has a contradictory role in tumor metabolism. In BC cells, high basal and protective autophagy against anticancer treatments [15] facilitates the avoidance of apoptotic cell death. Detected autophagosomes in cells treated with different HB concentrations (0.05–0.4 mg/mL) confirm HB-induced autophagy. The level of HB-induced autophagy was lower than in the positive control, where autophagy was successfully induced by starvation. In the negative control, a lower level of basal autophagy was registered. Therefore, HB effects on autophagy induction in BC cells, together with the inhibition of cell proliferation, indicate its high antitumor potential.

Cells possess two energy-producing pathways: mitochondrial respiration and glycolysis. Using the Seahorse XF HS Mini analyzer (Agilent, Santa Clara, CA, USA), we simultaneously measured both of these pathways in live cells, interrogating key cellular functions. Our data showed that starving BC cells (positive control) and 0.2 and 0.4 mg/mL HB treatments exhibit reduced mitochondrial respiration, indicating compromised or dysfunctional mitochondria, as compared to untreated cells and HB treatments at lower concentrations. Untreated BC cells and those treated with HB at lower concentrations showed high basal and stress glycolysis, indicating the ability to use that metabolic pathway as an energy source. These results suggest that HB disrupts glycolysis and reduces the intracellular survival potential of BC cells. Cancer cell metabolism, characterized by the Warburg effect, results in lactate production by aerobic glycolysis. Lactate production generates an acidic and hypoxic microenvironment, which promotes inflammation, tumorigenesis, invasion, and metastasis. Increased OXPHOS increases the production of reactive oxygen species (ROS) and the activation of c-JUN N-terminal kinases (JNK), resulting in autophagy induction. Hypoxia also induces the expression of a hypoxia-inducing factor (HIF-1α), which leads to the inhibition of the mammalian target of rapamycin (mTOR) and autophagy induction [36,37]. The hybrid glycolysis/OXPHOS metabolic state is suitable for the survival of invasive, aggressive tumors. It offers increased metabolic flexibility in cancer cells, which are able to utilize different nutrients in response to increased energy demands due to high proliferation and maintenance of ROS at a moderate level. It promotes genomic instability, which stimulates tumorigenesis and metastasis, and decreases susceptibility to anticancer therapy [38]. Our data strongly suggest that BC cells have a strong hybrid glycolysis/OXPHOS phenotype, which can be interrupted by HB in specific concentrations.

The HB effects on autophagy induction were considered at the gene transcription level as well. HB decreased *DRAM1* gene expression in comparison with the positive control, and it significantly increased the relative gene expression of *P62* in all applied concentrations. DRAM1 stimulates autophagosome elimination [39]. Knock-down of *DRAM1* inhibits P62 binding to the autophagosome, resulting in a decrease in autophagosome degradation. However, the same authors did not report DRAM1's role in starvation and mTOR-mediated autophagy [40]. Epi-fluorescent analyses of autophagosomes at given concentrations showed the presence of active autophagy, which is supported by increased expression of *BECN1*. Beclin 1 is responsible for the nucleation and maturation of the autophagosomes. The most significant upregulation of *BECN1* was found at 0.05 mg/mL of HB, along with a decreased number of viable cells. An increased frequency of autophagosomes and cells' degradation may also indicate a blocked autophagy flux [41]. This is supported by increased *P62* expression, which indicates higher requirements for the selective labeling of degradation contents.

One of the main mechanisms of autophagy control is the interaction between the autophagy protein beclin 1 and anti-apoptotic members of the Bcl-2 family (BCL-2, BCL-XL,

and MCL-1). Under normal conditions, BCL-2 inhibits beclin 1, and during stress, they separate and further stimulate autophagy. BCL-2 is an anti-apoptotic and anti-autophagy protein [42]. Increased expression of *BCL-2* is present in various types of tumors, including bladder cancer, supporting its tumorigenesis. It is associated with a poor prognosis. In bladder cancer, inhibiting *BCL-2* expression reduces cell proliferation and increases the sensitivity of cells to chemotherapy [43]. Therefore, the regulation of *BCL-2* gene expression is the focus of anti-tumor research. Our results showed a downregulation of *BCL-2* in cells treated with HB at all tested concentrations compared to cells with starvation-induced autophagy. Because a decrease in *BCL-2* expression results in the reduced proliferation of tumor cells [43], HB should be considered a suitable agent for reducing the expression of BCL-2 in bladder tumors. Patterns of relative gene expressions, found in our study, support the hypothesis that the efficiency of HB was associated with the expression of autophagy-specific genes. It has been proven that HB at the same tested concentrations (0.2 and 0.4 mg/mL) reduces BCL-2 expression in UT-7 human leukemia cells [44]. Previously, HB has been shown to reduce *IGF-1* and *hTERT* gene expression [24]. Increased expression of both genes has been related with the poor prognosis in patients with cancer disease [45,46]. The inhibition of telomerase activity and IGF signaling, together with decreased *BCL-2* expression, are possible mechanisms explaining the reduced resistance to cell death. In our study, the results of gene expression and the detection of autophagy showed an increased presence of autophagy. It was previously explained that excessive autophagy can serve as a mechanism of cell death by promoting apoptosis or autophagy cell death due to excessive cell degradation [47]. Although autophagy allows the cell to overcome stress and maintain homeostasis [48], the constant activation of autophagy with a decrease in *BCL-2* expression, observed in BC cells treated with HB, reduced the cell's ability to survive by causing cell death.

This study has revealed HB inhibition of cell growth. A decreased percentage of BC cell growth at higher HB concentrations can be explained by the intricate interplay between extracellular nucleotides affecting the cell cycle and autophagy modulation in response to cell density, ultimately influencing cell proliferation rates [49,50], as the results of this work have suggested that HB induces autophagy in bladder carcinoma (BC) cells. Additionally, HB targeted both aerobic glycolysis and mitochondrial respiration in BC cells in vitro. By causing significant degradation, metabolic disruption, and downregulation of *BCL-2*, HB increases the cells' susceptibility to autophagy.

4. Materials and Methods

4.1. Dipotassium Trioxohydroxytetrafluorotriborate, $K_2[B_3O_3F_4OH]$, Halogenated Boroxine (HB)—Synthesis and Solution Preparation

HB is a water-soluble white powder. It was synthesized in the Laboratory for Physical Chemistry, Department of Chemistry, Faculty of Science, University of Sarajevo, as previously described [21], with 99.99% purity. The $K_2(B_3O_3F_4OH)$ stock solution was prepared by dissolving 20 mg of $K_2(B_3O_3F_4OH)$ in 1 mL of RPMI-1640 culture media.

4.2. Cell Culture Treatment

The human urinary bladder carcinoma (BC) 5637 (ATCC, Manassas, VA, USA; Cat. No. ATCC HTB-9) was obtained through collaboration with ICGEB Trieste (Trieste, Italy). Cells were grown in RPMI-1640 media (Sigma-Aldrich, St. Louis, MO, USA) with 10% fetal bovine serum (FBS) supplemented with L-glutamine and antibiotics in a humidified atmosphere of 5% CO_2 at 37 °C. After the initial 24 h, cell cultures were treated with HB at final concentrations of 0.05, 0.1, 0.2, and 0.4 mg/mL and incubated for an additional 24 h. Untreated tumor cells were used as autophagy negative controls, while for the autophagy positive controls, starvation-induced (serum-free RPMI-1640; Sigma-Aldrich, St. Louis, MO, USA) autophagy cells were used.

4.3. Alamar Blue Assay

Cell proliferation was assessed by an alamar blue assay (Invitrogen, Waltham, MA, USA). Each treatment was carried out in triplicate in the 96-well plate, with 10,000 cells per well seeded. Cells were treated with HB for 24 h after the initial incubation. Alamar blue dye was added in an amount equal to 10% of the culture volume 2 h prior to absorbance measuring. Cultures without test substances were set as positive assay controls, while negative assay controls did not contain cells. Medium was used as a blank. Absorbance was measured at 570 and 620 nm using a Multiscan FC plate reader (Thermo Ficher Scientific, Vantaa, Finland). The percentage of cell growth inhibition was calculated according to manufacturer instructions (https://tools.thermofisher.com, accessed on 15 August 2023; The alamarBlue® Assay).

4.4. Autophagy Detection

The Autophagy Assay kit (Sigma-Aldrich, St. Louis, MO, USA) was used to monitor the degree of autophagy using a fluorescent autophagosome marker that specifically binds to autophagosomes. According to the manufacturer's recommendations, 24 h after incubation of BC cells with HB, epifluorescence detection was performed using a BX51 microscope (Olympus, Japan). The degree of autophagy was photo-documented with a DP50 camera, analyzed using View Finder Lite software (Olympus, Japan), and categorized according to the number of detected signals: no signal; 0–5 signals; 5–10 signals; >10 signals; and coupled signals or one big signal. A total of 200 cells were analyzed per HB treatment or control (Figure 8).

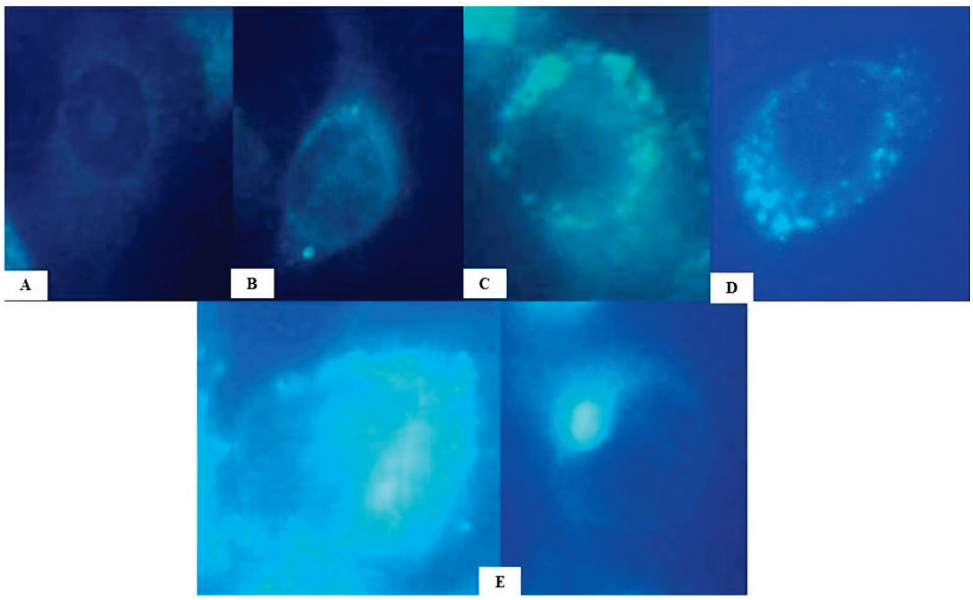


Figure 8. Evaluation of autophagy levels due to the presence and number of signals: no signal (**A**); 0–5 signals (**B**); 5–10 signals (**C**); >10 signals (**D**); and coupled signals or one big signal (**E**). Epifluorescence detection was performed using a BX51 microscope with 1000× magnification (Olympus, Tokyo, Japan).

4.5. Oxygen Consumption Rate and Extracellular Acidification Rate

BC cells were seeded into Seahorse XF cell culture microplates (4×10^4 cells/well) and incubated overnight. After washing the cells with Agilent Seahorse XF Base Medium, the oxygen consumption rate (OCR) and extracellular acidification rate (ECAR) were measured on a Seahorse XF HS Mini Analyzer (Agilent Technologies, Santa Clara, CA, USA). OCR in pmol/min reveals the rate of decrease in oxygen in the assay medium and, as such, is a measure of mitochondrial respiration in the cells. ECAR in mpH/minute illustrates the rate of increase in proton concentration (or decrease in pH) in the assay medium

and reflets changes due to glycolysis. Alterations in metabolic function under basal and "stress" conditions were evaluated using the XFp Cell Energy Phenotype Test Kit (Cat. No. 103275-100; Agilent Technologies), according to the manufacturers' instructions. Briefly, for the measurement of basal metabolic rates, measurements of OCR and ECAR were taken at the starting assay conditions. To evaluate metabolic rates during increased energy demand, "stress" conditions were induced by the addition of a mix of oligomycin (an ATP synthase inhibitor) and the mitochondrial uncoupler carbonyl cyanide 4-[trifluoromethoxy] phenylhydrazone (FCCP). The data were analyzed using Seahorse Analytics software version 3.0.0.41 (Agilent Technologies, Santa Clara, CA, USA).

4.6. q-PCR and Gene Expression Analysis

Five cell populations used in the experiment (untreated BC cells as a negative control and four HB treatments at concentrations of 0.05, 0.1, 0.2, and 0.4 mg/mL) were subsequently analyzed. The total RNA was extracted from harvested cells using an RNA isolation kit (Nucleo Spin RNA, Macherey-Nagel, Düren, Germany). The quantity of isolated RNA was estimated by an RNA fluorometric assay using Qubit 2.0 (Life Technologies, London, UK). For cDNA synthesis, total RNA in a 40 ng/μL concentration was used. High-capacity cDNA Reverse Transcription Kits (Applied Biosystems, Foster City, CA, USA) were used for the generation of cDNA, according to the manufacturer's instructions.

Amplifications of target genes *BECN1* (beclin 1), *P62/SQSTM* (sequestosome 1), *BCL-2* (B-cell lymphoma 2), and *DRAM1* (Damage-Regulated Autophagy Modulator 1) in replicates were performed using ABI 7300 real-time PCR (Applied Biosystems, USA). The primer sequences are given in Table 1.

Table 1. Primer sequences for the target genes.

Gene	Reference Sequence (Fasta Acc Number)	Primers
BECN1	NM_003766.5	Forward: CTCCCGAGGTGAAGAGCATC Reverse: GGGGGATGAATCTGCGAGAG
P62/SQSTM	NM_003900.5	Forward: CCGTGAAGGCCTACCTTCTG Reverse: TCCTCGTCACTGGAAAAGGC
BCL-2	NM_000633.3	Forward: GGGGTCATGTGTGTGGAGAG Reverse: GAAATCAAACAGAGGCCGCA
DRAM1	NM_018370.3	Forward: TTGGTGCAGCCACGATGTAT Reverse: ACACCACAGACAAAGGCCAA

The expression of target genes was monitored and normalized with the housekeeping *GAPDH* gene in REST software, version 2 [51], which was also used to compare gene expression at the transcription level in HB treatments and the control. Subsequently, the expression ratio results of the four investigated transcripts were tested for significance ($p < 0.05$) by a randomization test.

4.7. Statistical Analysis

To determine if HB-induced autophagy is statistically significant compared to untreated samples and starvation-induced autophagy, a Chi square test was applied (PAST 3.15).

Relative gene expression analysis was evaluated using REST-384, version 2, based on a pairwise fixed reallocation randomization test [51]. The test compares the Ct values of the control and the sample (target gene).

To determine OCR and ECAR significance between baseline and stressed conditions for every treatment, a Mann–Whitney test for independent samples was applied. The Kruskal–Wallis test was applied to determine significance between baselines and stressed conditions, followed by a Conover post hoc analysis.

The Pearson correlation coefficient was calculated to correlate ECAR and OCR baselines with the stressed condition. MedCalc 18.9. software was used, and the significance level was set at 0.05.

5. Conclusions

The results of the study suggest autophagy as a cellular and molecular pathway of HB activity in BC cells. This work confirms that HB targets aerobic glycolysis and mitochondrial respiration in BC cells in vitro. Inducing massive degradation, metabolic interruption, and downregulation of *BCL-2* in BC cells HB increases their susceptibility to autophagy. Further studies are needed to elucidate signaling molecules and cellular pathways of HB in autophagy induction in different tumors. The potential of HB based anti-tumor drugs should be additionally investigated.

Supplementary Materials: The following supporting information can be downloaded at: https://www.mdpi.com/article/10.3390/molecules29122919/s1.

Author Contributions: Conceptualization, writing—original draft, formal analysis, N.E.-B.; conceptualization, funding acquisition, supervision, L.P.; data curation, writing—review and editing, A.H.; investigation, methodology, N.L.-K.; investigation, methodology, M.H.O.; methodology, data curation, A.S.; investigation, methodology, S.K.; conceptualization, supervision, M.M.; software, investigation B.J.; conceptualization, supervision, funding acquisition, writing—review and editing, S.H. All authors have read and agreed to the published version of the manuscript.

Funding: This research was funded by the Ministry of Science, Higher Education and Youth of Sarajevo Canton (Project: Cell death types—analysis, detection and classification in human tumor cultures/CELDET, number: 27-02-35-37080-8/23) and Faculty of Medicine Foča, University of East Sarajevo, Bosnia and Herzegovina.

Institutional Review Board Statement: Not applicable.

Informed Consent Statement: Not applicable.

Data Availability Statement: The data presented in this study are available in article.

Acknowledgments: The authors are grateful to Borivoj Galić, who passed away, for a huge contribution to life science and an opportunity to explore his patent, $K_2(B_3O_3F_4OH)$. The authors thank to Nataša Skoko (ICGEB, Trieste, Italy) for a donation of 5637 cell line.

Conflicts of Interest: Author Svetoslav Kalaydjiev was employed by the company Agilent Technologies LDA UK Ltd. The remaining authors declare that the research was conducted in the absence of any commercial or financial relationships that could be construed as a potential conflict of interest.

References

1. Levine, B.; Klionsky, D.J. Development by self-digestion: Molecular mechanisms and biological functions of autophagy. *Dev. Cell* **2004**, *6*, 463–477. [CrossRef]
2. Guo, J.Y.; Chen, H.Y.; Mathew, R.; Fan, J.; Strohecker, A.M.; Karsli-Uzunbas, G.; Kamphorst, J.J.; Chen, G.; Lemons, J.M.; Karantza, V.; et al. Activated Ras requires autophagy to maintain oxidative metabolism and tumourigenesis. *Genes Dev.* **2011**, *25*, 460–470. [CrossRef]
3. Lin, Y.C.; Lin, J.F.; Wen, S.I.; Yang, S.C.; Tsai, T.F.; Chen, H.E.; Chou, K.Y.; Hwang, T.I. Inhibition of High Basal Level of Autophagy Induces Apoptosis in Human Bladder Cancer Cells. *J. Urol.* **2016**, *195*, 1126–1135. [CrossRef]
4. Xie, X.; White, E.P.; Mehnert, J.M. Coordinate autophagy and mTOR pathway inhibition enhances cell death in melanoma. *PLoS ONE* **2013**, *8*, e55096. [CrossRef]
5. Ma, X.H.; Piao, S.; Wang, D.; McAfee, Q.W.; Nathanson, K.L.; Lum, J.J.; Li, L.Z.; Amaravadi, R.K. Measurements of tumour cell autophagy predict invasiveness, resistance to chemotherapy, and survival in melanoma. *Clin. Cancer Res.* **2011**, *17*, 3478–3489. [CrossRef]
6. Goldsmith, J.; Levine, B.; Debnath, J. Autophagy and cancer metabolism. *Methods Enzymol.* **2014**, *542*, 25–57.
7. Antoni, S.; Ferlay, J.; Soerjomataram, I.; Znaor, A.; Jemal, A.; Bray, F. Bladder Cancer Incidence and Mortality: A Global Overview and Recent Trends. *Eur. Urol.* **2017**, *71*, 96–108. [CrossRef]
8. Nishiyama, H.; Habuchi, T.; Watanabe, J.; Teramukai, S.; Tada, H.; Ono, Y.; Ohshima, S.; Fujimoto, K.; Hirao, Y.; Fukushima, M.; et al. Clinical outcome of a large-scale multi-institutional retrospective study for locally advanced bladder cancer: A survey including 1131 patients treated during 1990–2000 in Japan. *Eur. Urol.* **2004**, *45*, 176–181. [CrossRef]

9. Gazzaniga, P.; Silvestri, I.; Gradilone, A.; Scarpa, S.; Morrone, S.; Gandini, O.; Gianni, W.; Frati, L.; Agliano, A.M. Gemcitabine-induced apoptosis in 5637 cell line: An in-vitro model for high-risk superficial bladder cancer. *Anticancer Drugs* **2007**, *18*, 179–185. [CrossRef]
10. Rieger, K.M.; Little, A.F.; Swart, J.M.; Kastrinakis, W.V.; Fitzgerald, J.M.; Hess, D.T.; Libertino, J.A.; Summerhayes, I.C. Human bladder carcinoma cell lines as indicators of oncogenic change relevant to urothelial neoplastic progression. *Br. J. Cancer* **1995**, *72*, 683–690. [CrossRef]
11. Vousden, K.H.; Ryan, K.M. p53 and metabolism. *Nat. Rev. Cancer* **2009**, *9*, 691–700. [CrossRef]
12. Bensaad, K.; Tsuruta, A.; Selak, M.A.; Vidal, M.N.C.; Nakano, K.; Bartrons, R.; Gottlieb, E.; Vousden, K.H. TIGAR, a p53-inducible regulator of glycolysis and apoptosis. *Cell* **2006**, *126*, 107–120. [CrossRef]
13. Whyard, T.; Waltzer, W.C.; Waltzer, D.; Romanov, V. Metabolic alterations in bladder cancer: Applications for cancer imaging. *Exp. Cell Res.* **2016**, *341*, 77–83. [CrossRef]
14. Zhu, H.B.; Yang, K.; Xie, Y.Q.; Lin, Y.W.; Mao, Q.Q.; Xie, L.P. Silencing of mutant p53 by siRNA induces cell cycle arrest and apoptosis in human bladder cancer cells. *World J. Surg. Oncol.* **2013**, *11*, 22. [CrossRef]
15. Lin, J.F.; Lin, Y.C.; Tsai, T.F.; Chen, H.E.; Chou, K.Y.; Hwang, T.I. Cisplatin induces protective autophagy through activation of BECN1 in human bladder cancer cells. *Drug Des. Devel. Ther.* **2017**, *11*, 1517–1533. [CrossRef]
16. Liu, S.; Chen, X.; Lin, T. Emerging strategies for the improvement of chemotherapy in bladder cancer: Current knowledge and future perspectives. *J. Adv. Res.* **2022**, *39*, 187–202. [CrossRef]
17. Advanced Bladder Cancer (ABC) Meta-analysis Collaborators Group. Adjuvant Chemotherapy for Muscle-invasive Bladder Cancer: A Systematic Review and Meta-analysis of Individual Participant Data from Randomised Controlled Trials. *Eur. Urol.* **2022**, *81*, 50–61. [CrossRef]
18. Hall, D.G. *Boronic Acids*; John Wiley and Sons: New York, NY, USA, 2005.
19. Galić, B. Boroxine Composition for Removal of Skin Changes. U.S. Patent US8278289, 2 October 2012.
20. Galić, B. Removal of Skin Changes. European Patent EP1996514, 31 July 2013.
21. Haverić, S.; Haverić, A.; Bajrović, K.; Galić, B.; Maksimović, M. Effects of dipotassium trioxohydroxytetrafluorotriborate ($K_2(B_3O_3F_4OH)$) on genetic material and inhibition of cell division in human cell cultures. *Drug Chem. Toxicol.* **2011**, *34*, 250–254. [CrossRef]
22. Hadžić, M.; Haverić, S.; Haverić, A.; Galić, B. Inhibitory effects of delphinidin and luteolin on genotoxicity induced by $K_2(B_3O_3F_4OH)$ in human lymphocytes in vitro. *Biologia* **2015**, *70*, 553–558. [CrossRef]
23. Haverić, S.; Hadžić, M.; Haverić, A.; Mijanović, M.; Hadžiselimović, R.; Galić, B. Genotoxicity Evaluation of Dipotassium-Trioxohydroxytetrafluorotriborate, $K_2(B_3O_3F_4OH)$, in Human Lymphocyte Cultures and Mice Reticulocytes. *Braz. Arch. Biol. Technol.* **2016**, *59*, e16160195. [CrossRef]
24. Pojskić, L.; Haverić, S.; Lojo-Kadrić, N.; Hadžić, M.; Haverić, A.; Galić, Z.; Galić, B.; Vullo, D.; Supuran, C.T.; Miloš, M. Effects of dipotassium-trioxohydroxytetrafluorotriborate, $K_2(B_3O_3F_4OH)$, on cell viability and gene expression of common human cancer drug targets in a melanoma cell line. *J. Enzym. Inhib. Med. Chem.* **2016**, *31*, 999–1004. [CrossRef]
25. Hadžić, M.; Haverić, S.; Haverić, A.; Lojo-Kadrić, N.; Galić, B.; Ramić, J.; Pojskić, L. Bioflavonoids protect cells against halogenated boroxine-induced genotoxic damage by upregulation of hTERT expression. *Z. Naturforsch. C J. Biosci.* **2019**, *74*, 125–129. [CrossRef]
26. Ostojić, J.; Herenda, S.; Bešić, Z.; Miloš, M.; Galić, B. Advantages of an Electrochemical Method Compared to the Spectrophotometric Kinetic Study of Peroxidase Inhibition by Boroxine Derivative. *Molecules* **2017**, *22*, 1120. [CrossRef]
27. Islamović, S.; Galić, B.; Miloš, M. A study of the inhibition of catalase by dipotassium trioxohydroxytetrafluorotriborate $K_2[B_3O_3F_4OH]$. *J. Enzym. Inhib. Med. Chem.* **2014**, *29*, 744–748. [CrossRef]
28. Herenda, S.; Ostojić, J.; Hasković, E.; Hasković, D.; Miloš, M.; Galić, B. Electrochemical Investigation of the Influence of K2[B3O3F4OH] on the Activity of Immobilized Superoxide Dismutase. *Int. J. Electrochem. Sci.* **2018**, *13*, 3279–3287. [CrossRef]
29. Vullo, D.; Miloš, M.; Galić, B.; Scozzafava, A.; Supuran, C.T. Dipotassium trioxohydroxytetrafluorotriborate $K_2[B_3O_3F_4OH]$, is a potent inhibitor of human carbonic anhydrases. *J. Enzyme Inhib. Med. Chem.* **2015**, *30*, 341–344. [CrossRef]
30. Elez-Burnjaković, N.; Pojskić, L.; Haverić, A.; Lojo-Kadrić, N.; Omanović, M.H.; Ramić, J.; Smajlović, A.; Maksimović, M.; Haverić, S. New in vitro findings about halogenated boroxine cytotoxicity and deregulation of cell death-related genes in GR-M melanoma cells. *Arh. Hig. Rada Toksikol.* **2023**, *74*, 16–21. [CrossRef]
31. Ivanković, S.; Stojković, R.; Maksimović, M.; Galić, B.; Miloš, M. Impact of calcium ion on cytotoxic effect of the boroxine derivative, $K_2(B_3O_3F_4OH)$. *J. Enzym. Inhib. Med. Chem.* **2016**, *31*, 70–74. [CrossRef]
32. Ivanković, S.; Stojković, R.; Galić, Z.; Galić, B.; Ostojić, J.; Marasović, M.; Miloš, M. In vitro and in vivo antitumour activity of the halogenated boroxine dipotassium-trioxohydroxytetrafluorotriborate ($K_2(B_3O_3F_4OH)$). *J. Enzym. Inhib. Med. Chem.* **2015**, *30*, 354–359. [CrossRef]
33. Haverić, A.; Durmić-Pašić, A.; Alić, A.; Mujezinović, I.; Smajlović, A.; Ostojić, J.; Ahatović, A.; Hadžić, M.; Prašović, S.; Haverić, S.; et al. Biochemical and histomorphological findings in Swiss Wistar rats treated with potential boron-containing therapeutic—$K_2(B_3O_3F_4OH)$. *J. Trace Elem. Med. Biol.* **2020**, *62*, 126642. [CrossRef]
34. Haverić, A.; Haverić, S.; Hadžić, M.; Ezić, J.; Ćetković, T.; Galić, B. Moderate Toxicity of Potential Boron-containing Therapeutic, Dipotassium-trioxohydroxytetrafl uorotriborate—$K_2(B_3O_3F_4OH)$ in Rats and Mice. *Braz. J. Pharm. Sci.* **2023**, *59*, e21384. [CrossRef]

35. Liu, J.; Phan, E.; Saračević, O.; Burnett, M.; Lojo-Kadrić, N.; Haverić, A.; Galić, B. In vitro study of the anti-proliferative effects of dipotassium-trioxohydroxytetra fluorotriborate on the H520 non-small cell lung cancer cell line. *Genet. Appl.* **2017**, *1*, 2–7.
36. Gwangwa, M.V.; Joubert, A.M.; Visagie, M.H. Crosstalk between the Warburg effect, redox regulation and autophagy induction in tumourigenesis. *Cell Mol. Biol. Lett.* **2018**, *23*, 20. [CrossRef]
37. Nagelkerke, A.; Sweep, F.C.; Geurts-Moespot, A.; Bussink, J.; Span, P.N. Therapeutic targeting of autophagy in cancer. Part I: Molecular pathways controlling autophagy. *Semin. Cancer Biol.* **2015**, *31*, 89–98. [CrossRef]
38. Jia, D.; Park, J.H.; Jung, K.H.; Levine, H.; Kaipparettu, B.A. Elucidating the Metabolic Plasticity of Cancer: Mitochondrial Reprogramming and Hybrid Metabolic States. *Cells* **2018**, *7*, 21. [CrossRef]
39. Zhang, X.D.; Qi, L.; Wu, J.C.; Qin, Z.H. DRAM1 Regulates Autophagy Flux through Lysosomes. *PLoS ONE* **2013**, *8*, e63245. [CrossRef]
40. Galavotti, S.; Bartesaghi, S.; Faccenda, D.; Shaked-Rabi, M.; Sanzone, S.; McEvoy, A.; Dinsdale, D.; Condorelli, F.; Brandner, S.; Campanella, M.; et al. The autophagy-associated factors DRAM1 and p62 regulate cell migration and invasion in glioblastoma stem cells. *Oncogene* **2013**, *32*, 699–712. [CrossRef]
41. Vats, S.; Manjithaya, R. A reversible autophagy inhibitor blocks autophagosome-lysosome fusion by preventing Stx17 loading onto autophagosomes. *Mol. Biol. Cell* **2019**, *30*, 2283–2295. [CrossRef]
42. Pattingre, S.; Tassa, A.; Qu, X.; Garuti, R.; Liang, X.H.; Mizushima, N.; Packer, M.; Schneider, M.D.; Levine, B. Bcl-2 antiapoptotic proteins inhibit Beclin 1-dependent autophagy. *Cell* **2005**, *122*, 927–939. [CrossRef]
43. Zhou, C.; Ding, J.; Wu, Y. Resveratrol induces apoptosis of bladder cancer cells via miR21 regulation of the Akt/Bcl2 signaling pathway. *Mol. Med. Rep.* **2014**, *9*, 1467–1473. [CrossRef]
44. Hadžić, M.; Pojskić, L.; Lojo-Kadrić, N.; Haverić, A.; Ramić, J.; Galić, B.; Haverić, S. Novel boron-containing compound, halogenated boroxine, induces selective cytotoxicity through apoptosis triggering in UT-7 leukemia. *J. Biochem. Mol. Toxicol.* **2022**, *36*, e23005. [CrossRef]
45. Kucera, R.; Treskova, I.; Vrzalova, J.; Svobodova, S.; Topolcan, O.; Fuchsova, R.; Rousarova, M.; Treska, V.; Kydlicek, T. Evaluation of IGF1 serum levels in malignant melanoma and healthy subjects. *Anticancer. Res.* **2014**, *34*, 5217–5220.
46. Weroha, S.J.; Haluska, P. IGF-1 receptor inhibitors in clinical trials-early lessons. *J. Mammary Gland. Biol. Neoplasia* **2008**, *13*, 471–483. [CrossRef]
47. Shen, H.M.; Codogno, P. Autophagic cell death: Loch Ness monster or endangered species? *Autophagy* **2011**, *7*, 457–465. [CrossRef]
48. Mehrpour, M.; Esclatine, A.; Beau, I.; Codogno, P. Autophagy in health and disease. 1. Regulation and significance of autophagy: An overview. *Am. J. Physiol. Cell Physiol.* **2010**, *298*, 776–785. [CrossRef]
49. Pavel, M.; Renna, M.; Park, S.J.; Menzies, F.M.; Ricketts, T.; Fullgrabe, J.; Ashkenazi, A.; Frake, R.A.; Lombarte, A.C.; Bento, C.F.; et al. Contact inhibition controls cell survival and proliferation via YAP/TAZ-autophagy axis. *Nat. Commun.* **2018**, *9*, 2961. [CrossRef]
50. Sawa, C.; Yofu, S.; Kiriyama, K.; Sutoh, K.; Saito, T.; Kishi, S.; Gunji, M.; Inoue, Y.; Sugi, M.; Shioda, S.; et al. High concentration of extracellular nucleotides suppresses cell growth via delayed cell cycle progression in cancer and noncancer cell lines. *Heliyon* **2021**, *7*, e08318. [CrossRef]
51. Pfaffl, M.W.; Horgan, G.W.; Dempfle, L. Relative expression software tool (REST©) for group-wise comparison and statistical analysis of relative expression results in real-time PCR. *Nucleic Acids Res.* **2002**, *30*, e36. [CrossRef]

Disclaimer/Publisher's Note: The statements, opinions and data contained in all publications are solely those of the individual author(s) and contributor(s) and not of MDPI and/or the editor(s). MDPI and/or the editor(s) disclaim responsibility for any injury to people or property resulting from any ideas, methods, instructions or products referred to in the content.

metabolites

MDPI

Article

Anaplerotic Therapy Using Triheptanoin in Two Brothers Suffering from Aconitase 2 Deficiency

Maximilian Penkl [1,*], Johannes A. Mayr [2], René G. Feichtinger [2], Ralf Reilmann [3], Otfried Debus [4], Manfred Fobker [5], Anja Penkl [1], Janine Reunert [1], Stephan Rust [1] and Thorsten Marquardt [1,*]

[1] Klinik für Kinder- und Jugendmedizin, Universitätsklinikum Münster, Albert-Schweizer-Campus 1, 48149 Muenster, Germany; janine.reunert@ukmuenster.de (J.R.); stephan.rust@ukmuenster.de (S.R.)
[2] Universitätsklinik für Kinder- und Jugendheilkunde, Salzburger Landeskliniken (SALK) and Paracelsus Medical University (PMU), Müllner Hauptstraße 48, 5020 Salzburg, Austria; h.mayr@salk.at (J.A.M.); r.feichtinger@salk.at (R.G.F.)
[3] George-Huntington-Institut, Wilhelm-Schickard-Straße 15, 48149 Muenster, Germany; ralf.reilmann@ghi-muenster.de
[4] Clemenshospital Münster, Klinik für Kinder- und Jugendmedizin, Düesbergweg 124, 48153 Muenster, Germany; o.debus@alexianer.de
[5] Zentrale Einrichtung UKM Labor, Universitätsklinikum Münster, Albert-Schweitzer-Campus 1, 48149 Muenster, Germany; manfred.fobker@ukmuenster.de
* Correspondence: maximilian.penkl@gmail.com (M.P.); marquadt@uni-muenster.de (T.M.)

Abstract: Citric acid cycle deficiencies are extremely rare due to their central role in energy metabolism. The *ACO2* gene encodes the mitochondrial isoform of aconitase (aconitase 2), the second enzyme of the citric acid cycle. Approximately 100 patients with aconitase 2 deficiency have been reported with a variety of symptoms, including intellectual disability, hypotonia, optic nerve atrophy, cortical atrophy, cerebellar atrophy, and seizures. In this study, a homozygous deletion in the *ACO2* gene in two brothers with reduced aconitase 2 activity in fibroblasts has been described with symptoms including truncal hypotonia, optic atrophy, hyperopia, astigmatism, and cerebellar atrophy. In an in vivo trial, triheptanoin was used to bypass the defective aconitase 2 and fill up the citric acid cycle. Motor abilities in both patients improved.

Keywords: *ACO2* mutation; triheptanoin; citric acid cycle; anaplerotic therapy; case report

1. Introduction

The *ACO2* gene is located on chromosome 22q13.2, encoding for the mitochondrial isoform of aconitase (aconitase 2). As the second enzyme of the citric acid cycle (CAC), it is found in the mitochondrial matrix, converting citrate via cis-aconitate to isocitrate (see Figure 1). Besides being part of CAC, aconitase 2 also plays an important role in the maintenance of mitochondrial DNA (mtDNA) [1]. In *ACO2*-deficient cells, the mitochondrial respiratory capacity, the ATP turnover, the cellular ATP level [2], as well as the mtDNA copy number and mtDNA transcription, can be reduced [3]. In yeast, aconitase was found to regulate and maintain mtDNA stability. By direct binding of mtDNA, aconitase can preserve the integrity of mtDNA from the occurrence of point mutations and DNA breaks [4]. In humans, wild-type *ACO2* rescued the mtDNA depletion observed in cells from a patient with missense *ACO2* variants [1]. The maintenance of mtDNA is independent of enzymatic activity in the CAC [5]. Pathogenic variants in *ACO2* present with a neurodegenerative phenotype of variable severity [3,6], as described in over 100 cases [7]. Common symptoms are truncal hypotonia, head bobbing, and variable forms of seizures. Furthermore, patients can have ophthalmologic symptoms like strabismus, nystagmus, optic atrophy, and retinal dystrophy. Symptoms often become apparent within the first year of life [8,9]. In this study, a homozygous deletion in the *ACO2* gene in two brothers was identified. In an in vivo trial, triheptanoin, a synthetic seven-carbon fatty acid triglyceride compound that can be

metabolized to succinyl-CoA, was used as an anaplerotic agent for bypassing the defective enzyme and restoring CAC function.

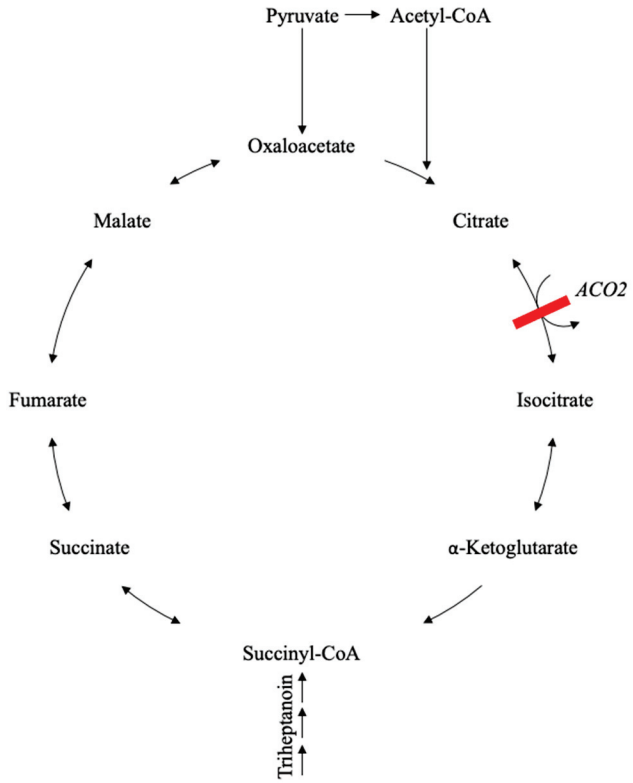


Figure 1. Scheme of the physiological and defective citric acid cycle in aconitase 2 deficiency with an overview of the CAC with its intermediates and bypassing Triheptanoin. The position of the aconitase 2 enzyme in CAC is illustrated as *ACO2*. Blocked pathway by defective *ACO2* marked with a red line. Triheptanoin bypasses aconitase 2 and feeds the CAC as succinyl-CoA.

2. Materials and Methods

2.1. Therapy with Triheptanoin

For compassionate use, triheptanoin was provided by Ultragenyx Pharmaceutical, Novato, CA, USA. Triheptanoin was prepared with banana puree or mashed potatoes. Therapy was slowly increased to 35% of daily calories coming from triheptanoin intake.

2.2. Therapy Monitoring

Standard blood tests were performed, including a complete blood count, urea, creatinine, bilirubin, transaminases, and gamma-glutamyl transferase.

Organic acid excretion in the urine was repeatedly measured for metabolic therapy monitoring.

Motor abilities were quantified by Q-Motor assessments [10], and physical therapy status was assessed with the Hammersmith Functional Motor Scale for spinal muscular atrophy (HFMS) [11] or Children's Hospital of Philadelphia Infant Test of Neuromuscular Disorders (CHOP-intended test) [12], respectively.

2.3. Isolation of Mitochondria from Cell Cultures

Primary human skin fibroblasts were used for the isolation of mitochondria. The medium was removed, and cell pellets were washed once with PBS. Cells were incubated for 3–5 min in a 10 mL trypsin solution for detachment. Cells were transferred quickly into FCS to inactivate trypsin. After centrifugation for 5 min at 1200–1300 units in 50 mL tubes, the supernatant was removed. Cell pellets were washed twice with 1 mL PBS. After centrifugation at 600× *g* at 4 °C for 5 min, cell pellets were weighed. Pellets were

homogenized in 10 × Vol 10 mM Tris pH 7.4 with a potter 8–10 × times at maximum speed. A 1.5 M sucrose solution was immediately added to the suspension to stabilize mitochondria (volume: X = V/5; X = volume sucrose solution; V = volume resuspended cells). The suspension was mixed with a disposable plastic pipette, transferred to an Eppendorf tube, and centrifuged at 600× *g* (=1800 rpm) at 4 °C for 10 min. The supernatant, which contains the mitochondria, was centrifuged at 10,000× *g* at 4 °C for 10 min, after which the supernatant was discarded. The pellet was resuspended in 500 µL SEKT (250 mM sucrose, 2 mM EGTA, 40 mM KCl, and 20 mM Tris. pH 7.4) buffer. After centrifugation of the solution at 10,000× *g* at 4 °C for 10 min, the supernatant was discarded, and the pellet was resuspended in 1 vol of SEKT buffer (if the initial cell pellet has 50 mg, the final volume is 50 µL). The aliquoted pellets were subsequently stored at −70 °C.

2.4. Western Blotting

Isolated mitochondria from primary human skin fibroblasts were used for Western blotting. In brief, mitochondrial lysates were loaded onto a 10% SDS-PAGE gel. Electrophoresis was performed at 150 V for 35 min. Proteins were blotted onto nitrocellulose membranes (Transblot Turbo Pack; Biorad, Hercules, CA, USA) with the Transblot Turbo System from Biorad. Blocking was carried out using the Western blocking reagent (Roche, Basel, Switzerland) for 30 min at room temperature. Membranes were incubated with the following primary antibodies: mouse monoclonal anti-*ACO2* antibody overnight at 4 °C (Abcam, Cambridge, UK; ab110321) and mouse monoclonal anti-VDAC1 antibody 1 h at room temperature (Abcam, ab14734). The secondary antibody from the DAKO Envision kit was used. The Lumi-Light Western blotting substrate (Roche) was used for development.

2.5. Aconitase Activity

In order to determine aconitase activity, a commercially available kit was used (BIOXYTECH Aconitase-340; catalog number 21041). A total of 50 µg of isolated mitochondria from human skin fibroblasts were diluted in assay buffer to a final volume of 250 µL. Subsequently, 250 µL substrate, 250 µL enzyme, and 250 µL NADP were added (final reaction volume: 1 mL). Substrate, enzyme, and NADP are included in the aconitase kit. The solution was sonified for 20 s at low energy. After 15 min of preincubation at 37 °C, the change in absorbance was measured at 340 nm.

2.6. Monitoring of Plasma C7 Fatty Acids

The determination of plasma C8 and C10 fatty acid levels was performed by gas chromatography–mass spectrometry. For this purpose, 100 µL serum was mixed with 10 µL internal standard (20 µg/mL D3-Octanoic acid in methanol), 20 µL 37% HCl/H2O 1:1 (*v*/*v*), 200 µL H2O, 100 µL Methyl-t-butyl ether, and 50 µL n-hexane in a 0.5 mL Eppendorf reaction vessel and centrifuged (3 min, 10,000× *g* rpm). A total of 50 µL of the supernatant was transferred to an autosampler vial with a conical insert, and 1 µL was loaded in splitless mode onto a GC–MS (QP2010 Ultra; Shimadzu, Duisburg, Germany) equipped with a PTV injector and a capillary column (Stabilwax-DA 15 m length, 0.25 mm internal diameter, and 0.25 µm film thickness; Restek GmbH, Bad Homburg, Germany) and an autosampler AS AOC-20s. Measuring time: 58.7 min; injector temperature: 70 °C; column oven temperature program isothermal: 2 min at 40 °C; gradient 12 °C/min to 240 °C; isothermal: 40 min at 240 °C. The carrier gas was helium with a constant flow of 1 mL/min. The transfer line to the ion source was held at 260 °C. The MS detector was set to selected ion monitoring (SIM) mode as *m*/*z* 60 (C8/C10) and *m*/*z* 63 (D3-Octanoic acid, internal standard). An example of a base peak intensity chromatogram of free fatty acids is shown in Figures 2 and 3. LabSolutions software (Version 2.72; Shimadzu, Duisburg, Germany) was used for GC–MS data acquisition and processing.

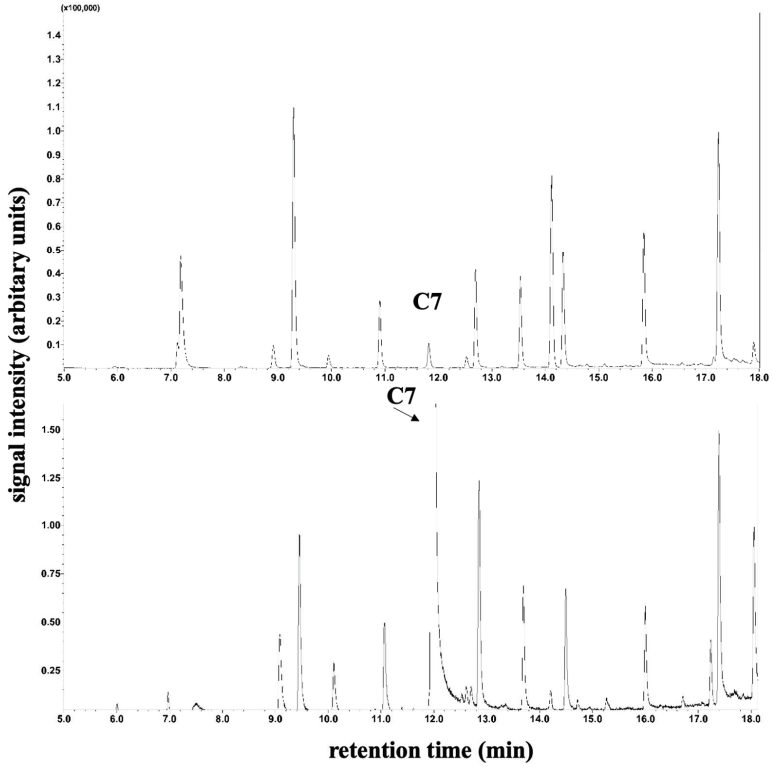


Figure 2. Determination of plasma C7 fatty acids for patient 1. Section of peak intensity chromatogram of plasma medium-chain free fatty acids by gas chromatography–single quadrupole mass spectrometry. The top image shows plasma C7 fatty acids prior to therapy, and the bottom image shows measurements during therapy.

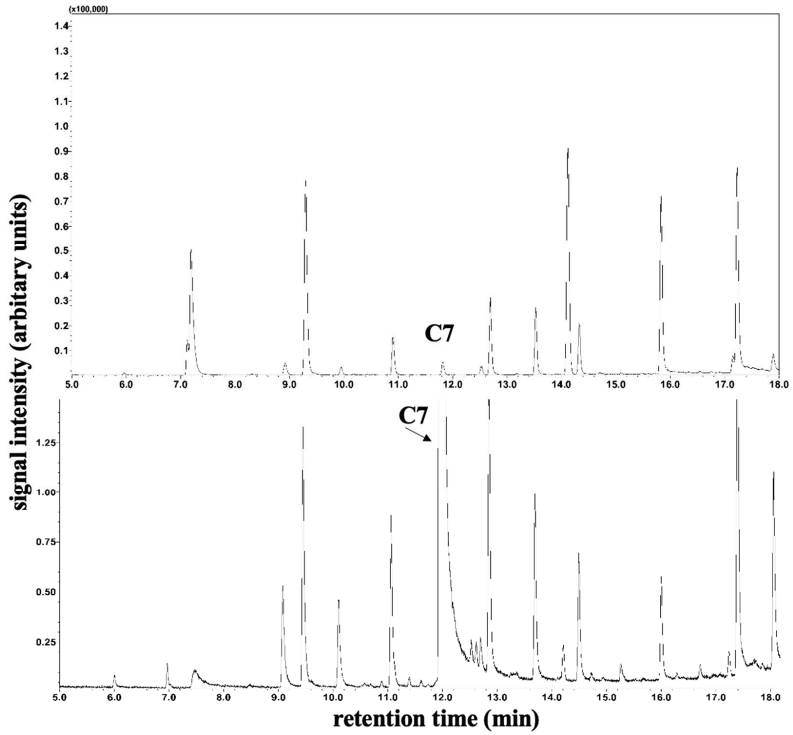


Figure 3. Determination of plasma C7 fatty acids for patient 2. Section of peak intensity chromatogram of plasma medium-chain free fatty acids by gas chromatography–single quadrupole mass spectrometry. The top image shows plasma C7 fatty acids prior to therapy, and the bottom image shows measurements during therapy.

3. Results

3.1. Clinical Report

The patients were born to a consanguineous couple from Yemen. The firstborn boy (patient 1) was born by cesarean section after an uneventful pregnancy with a birth weight of 2840 g, a length of 49 cm, and an occipitofrontal circumference of 35 cm. Apgar scores were 10/10/10.

Hexadactyly was present on both hands and was removed surgically on the third day of life.

Up until a febrile infection at the age of eight months, the development was normal. Simultaneously with the infection, the child became extraordinarily floppy, was unable to stabilize his trunk, and his head showed a head tilt. His targeted movements were atactic, and at rest, his head and body were slightly shaking. Reflexes could not be elicited clearly. His eyes exhibited a slow horizontal nystagmus. Wakefulness and interaction were not disturbed. Seizures were excluded by EEG–liquor, and MRI analysis was normal.

At the age of one year, a motor development slowdown, as well as truncal hypotonia, had progressed—even under physiotherapy. To objectify physical therapy status, 35/66 points on the Hammersmith Functional Motor Scale for spinal muscular atrophy (HFMS) [11] were calculated. In the course, infantile esotropia, downbeat nystagmus, optic atrophy, hyperopia, astigmatism, and cerebellar atrophy were diagnosed. While growing up, poor pronunciation was noticed.

At the age of eight years, a genetic analysis was performed due to the fact that the younger brother (patient 2) displayed similar symptoms.

Patient 2 was born via a planned cesarean section after an uneventful pregnancy with a birth weight of 2810 g, a length of 47 cm, and an occipitofrontal circumference of 34.8 cm. Apgar scores were 10/10/10. Development was normal until the patient was 1 month old. After a febrile infection, the boy displayed the same symptoms as the older brother. In order to objectively measure the boys' physical therapy status, the Children's Hospital of Philadelphia Infant Test of Neuromuscular Disorders (CHOP-intended test) [12] was chosen. Here, 44/64 points were calculated.

3.2. Genetic Analysis

Whole-exome sequencing identified the homozygous variant c.2335_2340delCAACAG, p.Gln779_Gln780del, i.e., deletion of the last two amino acids of the protein, for both brothers in *ACO2* (NM_001098.3). This variant was predicted to be pathogenetic by in silico simulation [13–16].

3.3. Fibroblasts Analysis

Skin fibroblasts were taken and cultured [17] from the older brother in order to quantify the residual enzyme activity and protein level of aconitase 2, with four controls also being measured for comparison purposes. In Western blot, protein levels were reduced (see Figure 4). As seen in Figure 5, aconitase 2 activity was significantly reduced to 40% compared to the four controls.

3.4. Therapy with Triheptanoin

Triheptanoin was started with a low dose and increased to a daily amount of 35% triheptanoin when the caloric intake was reached. During therapy, nausea and vomiting occurred, leading partially to the rejection of the prepared food. Nevertheless, the treatment could still be continued.

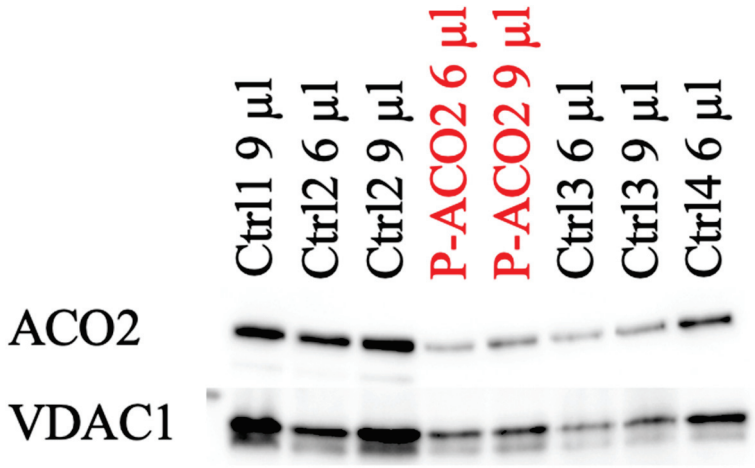


Figure 4. Western blot analysis of the *ACO2* levels of the affected individual and four controls.

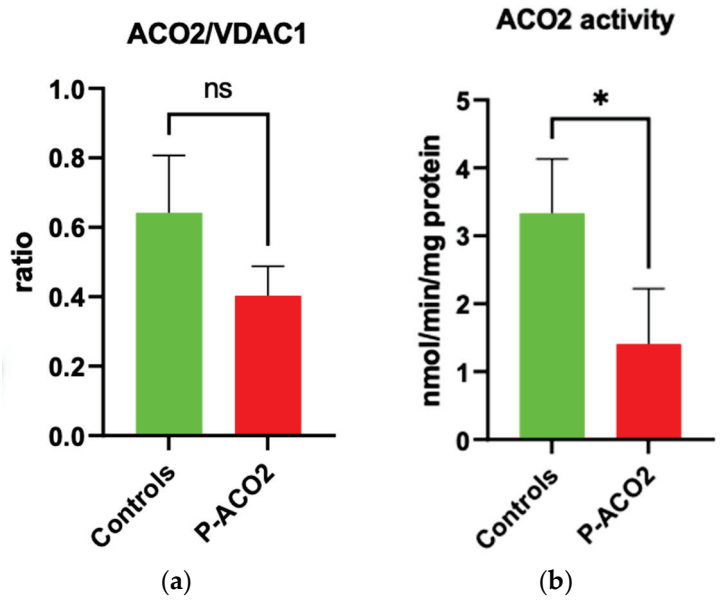


Figure 5. Determination of *ACO2* activity in the affected individual and controls. (**a**) Densitometric analysis of the *ACO2/VDAC1* ratio of the Western blot results. (**b**) Enzymatic activity of *ACO2* in the affected individual and controls. VDAC1 was used as a mitochondrial loading control. A non-parametric Mann–Whitney U test was used for statistical analysis. The enzymatic measurement was repeated twice with the same controls used in Figure 3. For both experiments, isolated mitochondria from human primary skin fibroblasts were used. For the enzymatic determination, 50 µg mitochondria per 1 mL assay volume were taken. Values present mean ± SD. (**a**): $p = 0.28$; (**b**): * $p = 0.0238$.

3.5. Motor Ability Analysis

Depending on the patient's age, either HFMS combined with Q-Motor assessments [10] or a CHOP-intended test was used for the monitoring of motor ability analysis. Prior to therapy, patient 1 scored 35/66 points at HFMS. After two months of therapy, the boy improved to 46/66 points (HFMS) and was able to maintain this level during therapy. Additionally to HFMS, Q-Motor assessments were used for patient 1. The data suggested that speeded tapping performance had improved. With a p-value < 0.05 in the Wilcoxon rank-sum test, the data are significant for the right hand and left foot (see Figures 6 and 7). For patient 2, 44/64 points in the CHOP-intended test were calculated prior to the therapy. After two months of therapy, the boy reached 60/64 points and 56/64 points after six months of therapy (see Figure 6).

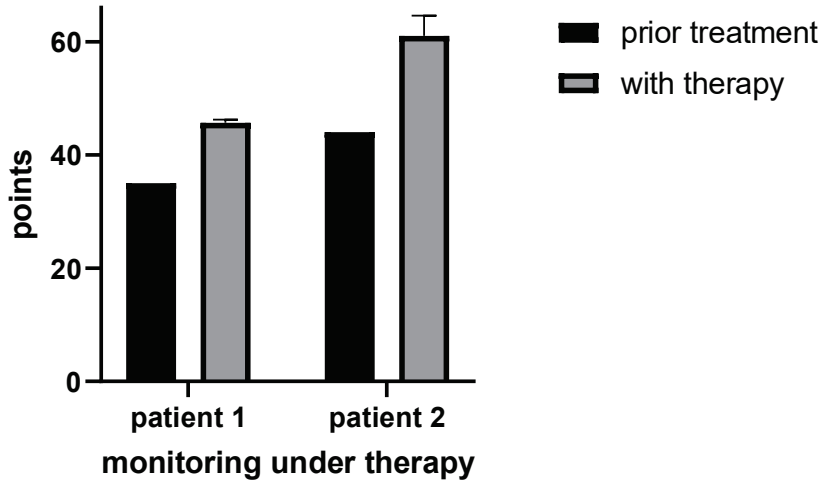


Figure 6. Monitoring of motor ability with HFMS for patient 1 and CHOP for patient 2. Patient 1: Sum of calculated points in HFMS before (n = 1) and during therapy (n = 3). Patient 2: Sum of calculated points in CHOP before (n = 1) and during therapy (n = 3).

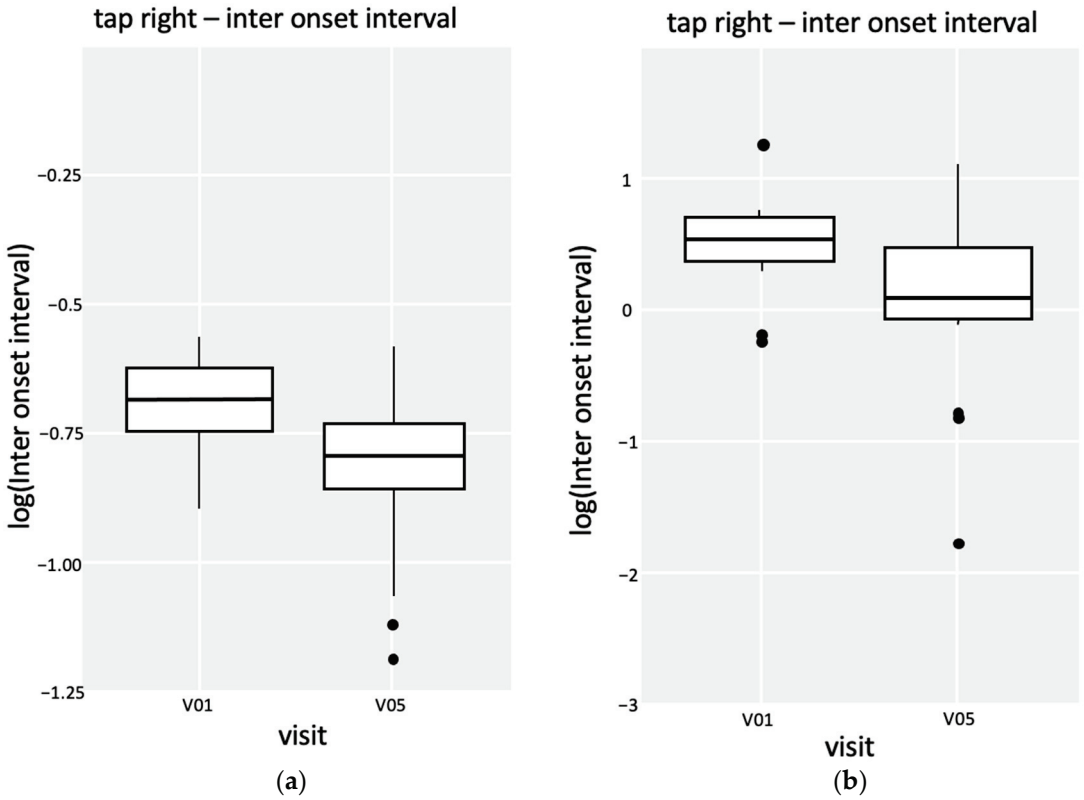


Figure 7. Q-Motor analysis of patient 1 with box plots of speeded tapping tests of the right hand and the left foot. (**a**) Speeded tapping performance of the right hand. The p-value in the Wilcoxon rank sum test is 9.813^{-9}. (**b**) Speeded tapping performance of the left foot. The p-value in the Wilcoxon rank sum test is 0.003691.

3.6. Organic Metabolites

Concurrent with the improvements in HFMS or CHOP-intended tests, respectively, an increase in CAC intermediates in urine organic acid analysis was observed during the therapy phase (see Figures 8 and 9). At the same time, the tremor of patient 1 disappeared, accompanied by improved pronunciation. Improvements in patient 2 were reduced squint-

ing under therapy. On days with high energy demands (e.g., when affected by infection), patient 2 presented with a whole-body tremor again.

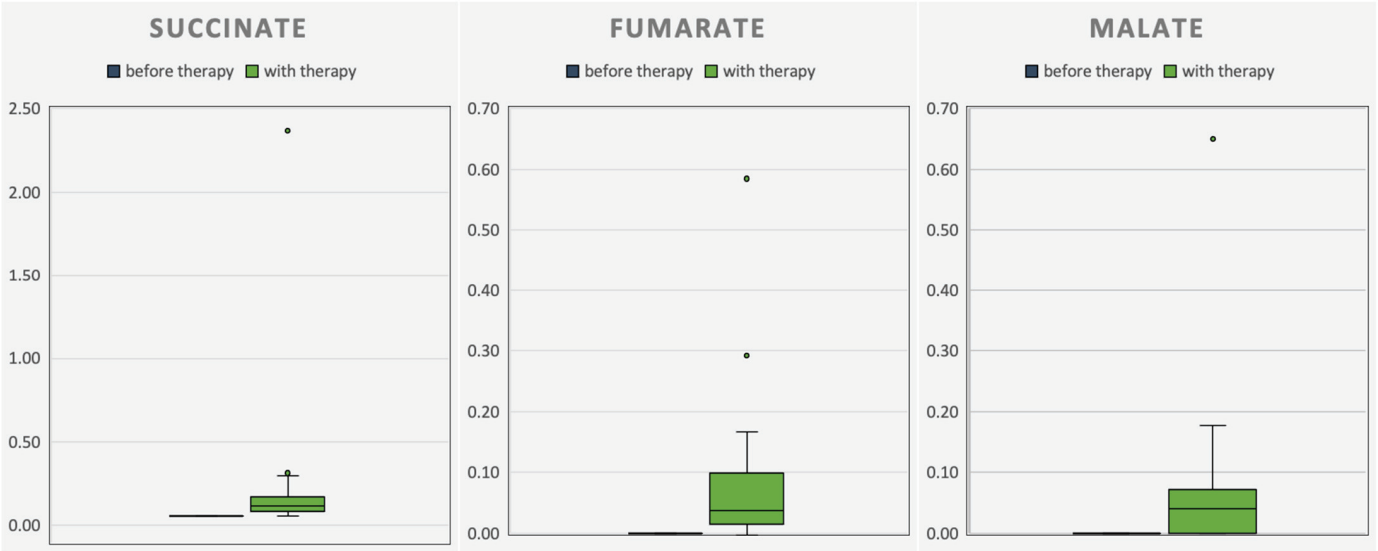


Figure 8. Progression of the measured excretory organic acids succinate, malate, and fumarate in the urine of patient 1. The organic acids fumarate and malate before therapy (blue) were not detectable (n = 5). With therapy (green), a higher excretion of the organic acids was detected (n = 38).

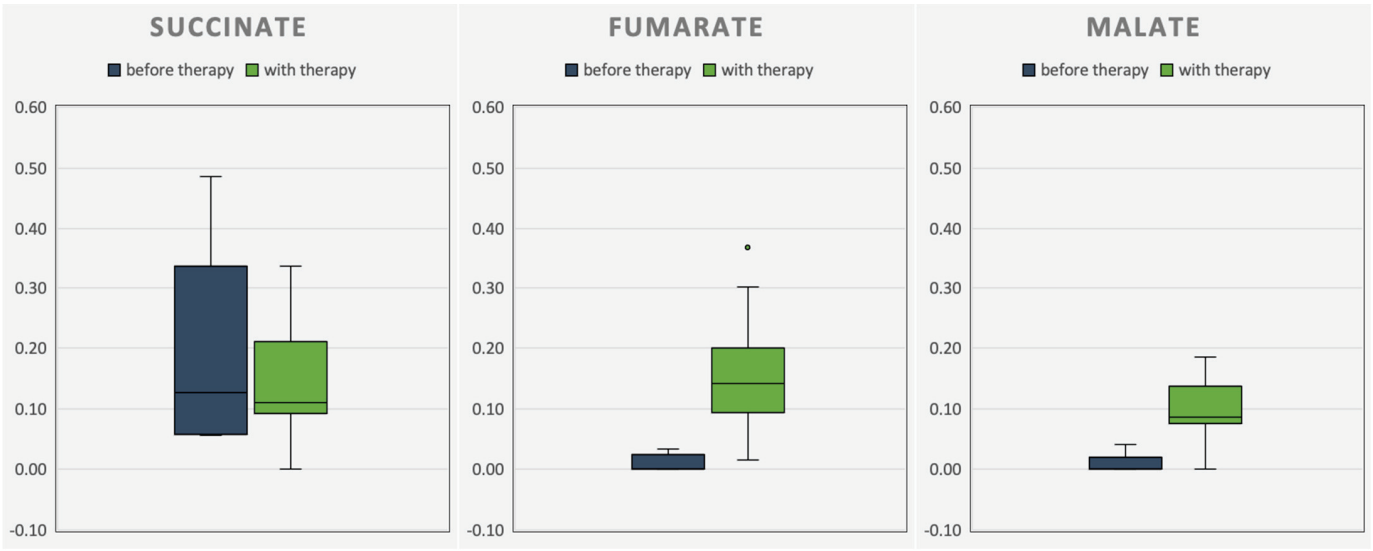


Figure 9. Progression of the measured excretory organic acids succinate, malate, and fumarate in the urine of patient 2. Five samples before therapy (blue; n = 5). With therapy (green), a higher excretion of the organic acids fumarate and malate was detected (n = 38).

3.7. C7 Fatty Acids

According to a modified method of Bartolucci et al. [18], the plasma C7 fatty acids were elevated during therapy compared to the control measured for comparison purposes (see Figures 2 and 3) by gas chromatography–mass spectrometry.

3.8. Follow-Up

After two years of therapy, the patients' parents decided to discontinue triheptanoin therapy because the success in daily life fell below the parents' expectations. During the

follow-up six months after stopping the therapy, patient 1's pronunciation had deteriorated, and there was also again a marked reduction in body tension without therapy.

4. Discussion

The present study provides the first description of triheptanoin in the treatment of aconitase 2 deficiency.

Mutations in *ACO2* have been described in association with early fatal or neurodegenerative diseases. Clinical symptoms range from mildly affected patients with isolated optic atrophy to severely affected patients, including intellectual disability and seizures in early childhood. Also, hypotonia, optic nerve atrophy, cortical atrophy, and cerebellar atrophy are possibly occurring [3,7,9].

Previous studies suggested a correlation between the severity of clinical symptoms and aconitase 2 activity. In these studies, aconitase 2 activity ranged from over 60% to 5% in skin fibroblasts from patients with homozygous or compound heterozygous mutations [1,9,19]. In the case of reduced enzyme activities, a certain tissue specificity must always be considered. The degree of reduction is possibly more pronounced in other, more energy-demanding tissues than in skin fibroblasts.

Patients with higher aconitase 2 activity had a milder clinical phenotype. The same studies could show that aconitase 2 activity did not correlate with aconitase 2 protein levels [1,9,19].

While the protein level of patient 1 decreased (not significantly), there was a reduction in enzyme activity to 40%. Compared to the patients described by Metodiev et al., the phenotype is milder compared to 5% remaining activity but more severe compared to 60% remaining enzyme activity [19]. Additionally, previous investigations found a decreased mitochondrial respiratory capacity, ATP turnover, cellular ATP level, and mtDNA copy number in *ACO2*-deficient cells [1–3].

Assuming that aconitase deficiency results in insufficient energy provision, bypassing the defective aconitase 2 and increasing the mitochondrial respiratory capacity, ATP turnover, and cellular ATP level was the treatment approach. Due to the fact that aconitase 2 converts citrate to isocitrate, which cannot proceed normally in *ACO2*-deficient cells, direct isocitrate supplementation might be beneficial. Indeed, Chen et al. found an increase in cellular ATP levels in *ACO2*-deficient cells compared to controls after isocitrate supplementation in vitro [2]. Preparation of isocitrate is possible, e.g., by using yeast fermentation of sunflower oil [20]. The production of large quantities of isocitrate by this method is costly. Due to a lack of information about isocitrate uptake and metabolism in vivo, an alternative was sought. Physiologically, in CAC, isocitrate is converted to α-ketoglutarate, the next potential target for anaplerotic therapy. Direct α-ketoglutarate supplementation is possible with ornithine α-ketoglutarate; indirect supplementation is possible with a precursor of α-ketoglutarate. Longo et al. tested both ornithine α-ketoglutarate and glutamine as a precursor. They found neither ornithine α-ketoglutarate nor glutamine could increase downstream intermediates of CAC [21].

It was decided to start a trial with triheptanoin for compassionate use because it was described as having good potential in metabolic and neurodegenerative diseases [22–25]. Additionally, the application is easy to handle in homecare and has few side effects at the right dose. Triheptanoin is a synthetic seven-carbon fatty acid triglyceride compound where three C7 fatty acids (heptanoate) are esterified to one glycerol. Triheptanoin comes as an oil, which, when ingested, probably disseminates like other medium-chain triglycerides (MCT) fatty acids [26] via the venous system, mainly to the liver [27–29]. At the target cells, no active transport is required. Heptanoate diffuses through the cell and mitochondrial membrane to enter ß-oxidation by the medium-chain fatty-acid oxidase enzyme. Besides liver cells, heptanoate can be oxidized in mitochondria by most tissues [24].

Through two cycles of ß-oxidation, one molecule of heptanoate is degraded into two molecules of acetyl-CoA and one propionyl-CoA. While acetyl-CoA can enter CAC directly via citrate synthase, propionyl-CoA can be carboxylated and converted to succinyl-CoA via

methylmalonyl-CoA by propionyl-CoA carboxylase, methylmalonyl-CoA epimerase, and methylmalonyl-CoA mutase. Formed succinyl-CoA can then enter CAC as an intermediate and might be used for gluconeogenetic reactions [23,27].

A second opportunity for heptanoate metabolization is to undergo just one cycle of ß-oxidation. The result is one acetyl-CoA and one remaining pentanoyl-CoA. Then, pentanoyl-CoA can be used to generate the C5-ketone bodies β-ketopentanoate and β-hydroxypentanoate. The C5-ketone bodies can cross the blood-brain barrier in order to support the brain. Subsequently, the ketone bodies are converted by the peripheral tissues to acetyl-CoA and anaplerotic propionyl-CoA [23,27]. As shown in Figure 1, triheptanoin feeds the CAC behind aconitase 2 as succinyl-CoA.

Due to the rarity of aconitase 2 deficiency, there is, to date, no specific monitoring test. For the presented patients, problems with motor mobility were the most noticeable and limiting restrictions in their daily routine. To achieve a general overview of treatment response, motor ability with Q-Motor assessments, HFMS, and CHOP-intended tests were monitored. Special monitoring with regard to, e.g., retinal dystrophy was performed in standard care and was not considered within the framework of this investigation paper.

Q-Motor assessments are usually used for neurodegenerative Huntington's disease, which presents with a variety of motor symptoms. Active cooperation of the patient is required in order to perform the tests; therefore, only patient 1 was able to take part in Q-Motor assessments.

Q-Motor assessments provide standardized measurements at different time points to avoid bias induced by examiners or study side effects. Data analysis is free from bias through blinded and automated analysis [10]. For patient 1, there was an indication of improved tapping performance in the right hand and the left foot (see Figure 7). Simultaneously with Q-Motor assessments, physical therapy status with the Hammersmith Functional Motor Scale for spinal muscular atrophy (HFMS) for patient 1 and the CHOP-intended test for patient 2 were measured. HFMS is a functional motor scale for children with spinal muscular atrophy, in particular for those with limited mobility, to provide objective information on motor ability and clinical progression [11].

The CHOP-intended test is also used to evaluate the motor skills of patients with spinal muscular atrophy, but even for infants [12].

During therapy with triheptanoin, motor abilities increased in both patients. The motor abilities of patient 1 increased from 35/66 to 46/66 points (HFMS) after two months of therapy. Patient 2 improved from 44/64 points to 56/64 points (CHOP-intended test). Even though these motor ability tests were not developed specifically for aconitase 2 deficiency and may not accurately capture all aspects of the described symptoms, this work shows that at least some of the symptomatic complex of aconitase 2 deficiency is caused by insufficient energy provision.

5. Conclusions

Pathogenic variants in *ACO2* are rare but can be found by whole-exome sequencing. When *ACO2* activity is reduced, anaplerotic triheptanoin might be beneficial. After ingestion, systemic uptake of triheptanoin has been proven by gas chromatography–mass spectrometry of the patients' plasma. By measuring the elevated levels of the excretory organic acids succinate, malate, and fumarate in the urine (in CAC behind defective *ACO2*), anaplerosis and further metabolization could be shown. Improved motor abilities, verified by Q-Motor assessments, CHOP-intended tests, and HFMS, are attributable to anaplerotic triheptanoin.

Author Contributions: Conceptualization, M.P., A.P., and T.M.; methodology, M.P., J.A.M., R.G.F., R.R., O.D., M.F., A.P., J.R., and S.R.; formal analysis, R.G.F., J.A.M., J.R., A.P., S.R., and R.R.; investigation, M.P., A.P., O.D., and T.M.; writing—original draft preparation, M.P.; writing—review and editing, T.M.; visualization, M.P.; supervision, T.M. All authors have read and agreed to the published version of the manuscript.

Funding: This research was funded by the European Joint Programme on Rare Diseases, project EJPRD19-145 GENOMIT I4695-B, financed by the Austrian Science Fund FWF to JAM.

Institutional Review Board Statement: This study was conducted in accordance with the Declaration of Helsinki and approved by the Ethics Committee of the University Clinic of Münster (UKM), Germany (31 May 2013).

Informed Consent Statement: Informed consent was obtained from all subjects involved in the study. Written, informed consent has been obtained from the patients' parents to publish this paper.

Data Availability Statement: The original contributions presented in the study are included in the article, further inquiries can be directed to the corresponding authors.

Conflicts of Interest: The authors declare no conflicts of interest.

References

1. Sadat, R.; Barca, E.; Masand, R.; Donti, T.R.; Naini, A.; De Vivo, D.C.; DiMauro, S.; Hanchard, N.A.; Graham, B.H. Functional Cellular Analyses Reveal Energy Metabolism Defect and Mitochondrial DNA Depletion in a Case of Mitochondrial Aconitase Deficiency. *Mol. Genet. Metab.* **2016**, *118*, 28–34. [CrossRef] [PubMed]
2. Chen, Y.; Cai, G.H.; Xia, B.; Wang, X.; Zhang, C.C.; Xie, B.C.; Shi, X.C.; Liu, H.; Lu, J.F.; Zhang, R.X.; et al. Mitochondrial Aconitase Controls Adipogenesis through Mediation of Cellular ATP Production. *FASEB J.* **2020**, *34*, 6688–6702. [CrossRef] [PubMed]
3. Neumann, M.A.C.; Grossmann, D.; Schimpf-Linzenbold, S.; Dayan, D.; Stingl, K.; Ben-Menachem, R.; Pines, O.; Massart, F.; Delcambre, S.; Ghelfi, J.; et al. Haploinsufficiency Due to a Novel *ACO2* Deletion Causes Mitochondrial Dysfunction in Fibroblasts from a Patient with Dominant Optic Nerve Atrophy. *Sci. Rep.* **2020**, *10*, 16736. [CrossRef] [PubMed]
4. Ciccarone, F.; Vegliante, R.; Di Leo, L.; Ciriolo, M.R. The TCA Cycle as a Bridge between Oncometabolism and DNA Transactions in Cancer. *Semin. Cancer Biol.* **2017**, *47*, 50–56. [CrossRef] [PubMed]
5. Xin, J.C.; Wang, X.; Kaufman, B.A.; Butow, R.A. Aconitase Couples Metabolic Regulation to Mitochondrial DNA Maintenance. *Science* **2005**, *307*, 714–717. [CrossRef]
6. Guehlouz, K.; Foulonneau, T.; Amati-Bonneau, P.; Charif, M.; Colin, E.; Bris, C.; Desquiret-Dumas, V.; Milea, D.; Gohier, P.; Procaccio, V.; et al. *ACO2* Clinicobiological Dataset with Extensive Phenotype Ontology Annotation. *Sci. Data* **2021**, *8*, 205. [CrossRef] [PubMed]
7. Charif, M.; Gueguen, N.; Ferré, M.; Elkarhat, Z.; Khiati, S.; LeMao, M.; Chevrollier, A.; Desquiret-Dumas, V.; Goudenège, D.; Bris, C.; et al. Dominant *ACO2* Mutations Are a Frequent Cause of Isolated Optic Atrophy. *Brain Commun.* **2021**, *3*, 205. [CrossRef] [PubMed]
8. Sharkia, R.; Wierenga, K.J.; Kessel, A.; Azem, A.; Bertini, E.; Carrozzo, R.; Torraco, A.; Goffrini, P.; Berti, C.C.; McCormick, M.E.; et al. Clinical, Radiological, and Genetic Characteristics of 16 Patients with *ACO2* Gene Defects: Delineation of an Emerging Neurometabolic Syndrome. *J. Inherit. Metab. Dis.* **2019**, *42*, 264–275. [CrossRef] [PubMed]
9. Spiegel, R.; Pines, O.; Ta-Shma, A.; Burak, E.; Shaag, A.; Halvardson, J.; Edvardson, S.; Mahajna, M.; Zenvirt, S.; Saada, A.; et al. Infantile Cerebellar-Retinal Degeneration Associated with a Mutation in Mitochondrial Aconitase, *ACO2*. *Am. J. Hum. Genet.* **2012**, *90*, 518–523. [CrossRef]
10. Reilmann, R.; Schubert, R. *Motor Outcome Measures in Huntington Disease Clinical Trials*; Elsevier B.V.: Amsterdam, The Netherladns, 2017; Volume 144, ISBN 978-0-12-801893-4.
11. Main, M.; Kairon, H.; Mercuri, E.; Muntoni, F. The Hammersmith Functional Motor Scale for Children with Spinal Muscular Atrophy: A Scale to Test Ability and Monitor Progress in Children with Limited Ambulation. *Eur. J. Paediatr. Neurol.* **2003**, *7*, 155–159. [CrossRef]
12. Glanzman, A.M.; Mazzone, E.; Main, M.; Pelliccioni, M.; Wood, J.; Swoboda, K.J.; Scott, C.; Pane, M.; Messina, S.; Bertini, E.; et al. The Children's Hospital of Philadelphia Infant Test of Neuromuscular Disorders (CHOP INTEND): Test Development and Reliability The CHOP INTEND Is a Reliable Measure of Motor Skills in Patients with SMA-I and Neuromuscular Disorders Presenting in Infancy. *Neuromuscul. Disord.* **2010**, *20*, 155–161. [CrossRef] [PubMed]
13. Schwarz, J.M.; Cooper, D.N.; Schuelke, M.; Seelow, D. Mutationtaster2: Mutation Prediction for the Deep-Sequencing Age. *Nat. Methods* **2014**, *11*, 361–362. [CrossRef] [PubMed]
14. Ng, P.C.; Henikoff, S. Predicting Deleterious Amino Acid Substitutions. *Genome Res.* **2001**, *11*, 863–874. [CrossRef]
15. Choi, Y.; Sims, G.E.; Murphy, S.; Miller, J.R.; Chan, A.P. Predicting the Functional Effect of Amino Acid Substitutions and Indels. *PLoS ONE* **2012**, *7*, e46688. [CrossRef]
16. Adzhubei, I.A.; Schmidt, S.; Peshkin, L.; Ramensky, V.E.; Gerasimova, A.; Bork, P.; Kondrashov, A.S.; Sunyaev, S.R. A Method and Server for Predicting Damaging Missense Mutations. *Nat. Methods* **2010**, *7*, 248–249. [CrossRef]
17. Kisiel, M.A.; Klar, A.S. Isolation and Culture of Human Dermal Fibroblasts. In *Skin Tissue Engineering*; Böttcher-Haberzeth, S., Biedermann, T., Eds.; Methods in Molecular Biology; Springer: New York, NY, USA, 2019; Volume 1993, pp. 71–78. ISBN 978-1-4939-9472-4.

18. Bartolucci, G.; Pallecchi, M.; Menicatti, M.; Moracci, L.; Pucciarelli, S.; Agostini, M.; Crotti, S. A Method for Assessing Plasma Free Fatty Acids from C2 to C18 and Its Application for the Early Detection of Colorectal Cancer. *J. Pharm. Biomed. Anal.* **2022**, *215*, 114762. [CrossRef]
19. Metodiev, M.D.; Gerber, S.; Hubert, L.; Delahodde, A.; Chretien, D.; Gérard, X.; Amati-Bonneau, P.; Giacomotto, M.C.; Boddaert, N.; Kaminska, A.; et al. Mutations in the Tricarboxylic Acid Cycle Enzyme, Aconitase 2, Cause Either Isolated or Syndromic Optic Neuropathy with Encephalopathy and Cerebellar Atrophy. *J. Med. Genet.* **2014**, *51*, 834–838. [CrossRef] [PubMed]
20. Heretsch, P.; Thomas, F.; Aurich, A.; Krautscheid, H.; Sicker, D.; Giannis, A. Synthesen Mit Einem Chiralen Baustein Aus Dem Citratzyklus: (2R,3S)-Isocitronensäure Aus Einer Fermentation Mit Sonnenblumenöl. *Angew. Chem.* **2008**, *120*, 1984–1986. [CrossRef]
21. Longo, N.; Price, L.B.; Gappmaier, E.; Cantor, N.L.; Ernst, S.L.; Bailey, C.; Pasquali, M. Anaplerotic Therapy in Propionic Acidemia. *Mol. Genet. Metab.* **2017**, *122*, 51–59. [CrossRef]
22. Wehbe, Z.; Tucci, S. Therapeutic Potential of Triheptanoin in Metabolic and Neurodegenerative Diseases. *J. Inherit. Metab. Dis.* **2019**, *43*, 385–391. [CrossRef]
23. Roe, C.R.; Sweetman, L.; Roe, D.S.; David, F.; Brunengraber, H. Treatment of Cardiomyopathy and Rhabdomyolysis in Long-Chain Fat Oxidation Disorders Using an Anaplerotic Odd-Chain Triglyceride. *J. Clin. Investig.* **2002**, *110*, 259–269. [CrossRef] [PubMed]
24. Mochel, F.; DeLonlay, P.; Touati, G.; Brunengraber, H.; Kinman, R.P.; Rabier, D.; Roe, C.R.; Saudubray, J.M. Pyruvate Carboxylase Deficiency: Clinical and Biochemical Response to Anaplerotic Diet Therapy. *Mol. Genet. Metab.* **2005**, *84*, 305–312. [CrossRef] [PubMed]
25. Schwarzkopf, T.M.; Koch, K.; Klein, J. Reduced Severity of Ischemic Stroke and Improvement of Mitochondrial Function after Dietary Treatment with the Anaplerotic Substance Triheptanoin. *Neuroscience* **2015**, *300*, 201–209. [CrossRef] [PubMed]
26. Lemarié, F.; Beauchamp, E.; Legrand, P.; Rioux, V. Revisiting the Metabolism and Physiological Functions of Caprylic Acid (C8:0) with Special Focus on Ghrelin Octanoylation. *Biochimie* **2016**, *120*, 40–48. [CrossRef] [PubMed]
27. Kinman, R.P.; Kasumov, T.; Jobbins, K.A.; Thomas, K.R.; Adams, J.E.; Brunengraber, L.N.; Kutz, G.; Brewer, W.U.; Roe, C.R.; Brunengraber, H. Parenteral and Enteral Metabolism of Anaplerotic Triheptanoin in Normal Rats. *Am. J. Physiol. Endocrinol. Metab.* **2006**, *291*, 860–866. [CrossRef] [PubMed]
28. Gu, L.; Zhang, G.F.; Kombu, R.S.; Allen, F.; Kutz, G.; Brewer, W.U.; Roe, C.R.; Brunengraber, H. Parenteral and Enteral Metabolism of Anaplerotic Triheptanoin in Normal Rats. II. Effects on Lipolysis, Glucose Production, and Liver Acyl-CoA Profile. *Am. J. Physiol. Endocrinol. Metab.* **2010**, *298*, 362–371. [CrossRef]
29. Aoyama, T.; Nosaka, N.; Kasai, M. Research on the Nutritional Characteristics of Medium-Chain Fatty Acids. *J. Med. Investig.* **2007**, *54*, 385–388. [CrossRef]

Disclaimer/Publisher's Note: The statements, opinions and data contained in all publications are solely those of the individual author(s) and contributor(s) and not of MDPI and/or the editor(s). MDPI and/or the editor(s) disclaim responsibility for any injury to people or property resulting from any ideas, methods, instructions or products referred to in the content.

molecules

MDPI

Article

Hemp Seed Oil Inhibits the Adipogenicity of the Differentiation-Induced Human Mesenchymal Stem Cells through Suppressing the Cannabinoid Type 1 (CB1)

Albatul S. Almousa [1,2,*], Pandurangan Subash-Babu [1,*], Ibrahim O. Alanazi [3,4], Ali A. Alshatwi [1], Huda Alkhalaf [3], Eman Bahattab [3], Atheer Alsiyah [5] and Mohammad Alzahrani [6]

[1] Department of Food Science and Nutrition, College of Food Science and Agriculture, King Saud University, P.O. Box 2460, Riyadh 11451, Saudi Arabia; alshatwi@ksu.edu.sa
[2] Department of Human Nutrition, College of Home Economics, King Khalid University, P.O. Box 3236, Abha 10001, Saudi Arabia
[3] The Healthy Aging Research Institute, King Abdulaziz City for Science and Technology, P.O. Box 6086, Riyadh 11442, Saudi Arabia; iaenazi@kacst.edu.sa (I.O.A.); halkhalaf@kacst.edu.sa (H.A.); ebahattab@kacst.edu.sa (E.B.)
[4] Genome Research Unit, Department of Biochemistry, College of Science, King Saud University, P.O. Box 2460, Riyadh 11451, Saudi Arabia
[5] The Applied Genomics Research Institute, King Abdulaziz City for Science and Technology, P.O. Box 6086, Riyadh 11442, Saudi Arabia; aalsayah@kacst.edu.sa
[6] Institute of Advanced Agricultural and Food Technologies, King Abdulaziz City for Science and Technology, P.O. Box 6086, Riyadh 11442, Saudi Arabia; mzahrani@kacst.edu.sa
* Correspondence: 435203963@students.ksu.edu.sa (A.S.A.); subash@ksu.edu.sa (P.S.-B.)

Abstract: Central and peripheral mechanisms of the endocannabinoid system (ECS) favor energy intake and storage. The ECS, especially cannabidiol (CBD) receptors, controls adipocyte differentiation (hyperplasia) and lipid accumulation (hypertrophy) in adipose tissue. In white adipose tissue, cannabidiol receptor 1 (CB1) stimulation increases lipogenesis and inhibits lipolysis; in brown adipose tissue, it decreases mitochondrial thermogenesis and biogenesis. This study compared the availability of phytocannabinoids [CBD and Δ9-tetrahydrocannabinol (THC)] and polyunsaturated fatty acids [omega 3 (ω3) and omega 6 (ω6)] in different hemp seed oils (HSO). The study also examined the effect of HSO on adipocyte lipid accumulation by suppressing cannabinoid receptors in adipogenesis-stimulated human mesenchymal stem cells (hMSCs). Most importantly, Oil-Red-O′ and Nile red tests showed that HSO induced adipogenic hMSC differentiation without differentiation agents. Additionally, HSO-treated cells showed increased peroxisome proliferator-activated receptor gamma (PPARγ) mRNA expression compared to controls (hMSC). HSO reduced PPARγ mRNA expression after differentiation media (DM) treatment. After treatment with HSO, DM-hMSCs had significantly lower CB1 mRNA and protein expressions than normal hMSCs. HSO treatment also decreased transient receptor potential vanilloid 1 (TRPV1), fatty acid amide hydrolase (FAAH), and monoacylglycerol lipase (MGL) mRNAs in hMSC and DM-hMSCs. HSO treatment significantly decreased CB1, CB2, TRPV1, and G-protein-coupled receptor 55 (GPCR55) protein levels in DM-hMSC compared to hMSC in western blot analysis. In this study, HSO initiated adipogenic differentiation in hMSC without DM, but it suppressed CB1 gene and protein expression, potentially decreasing adipocyte lipid accumulation and lipogenic enzymes.

Keywords: stem cells; cannabidiol; cannabinoid receptor; adipogenesis; lipogenic enzymes

1. Introduction

The endocannabinoid system (ECS) is a complicated cell signaling system that governs many aspects of the body's physiology, including appetite, mood, pain, sensation, and immunological function. Recent developments shed light on how the ECS regulates the

metabolism of adipose tissue. ECS influences various physiological processes related to adipocytes, such as phenotype determination and stimulating preadipocyte proliferation [1]. The primary components of this ECS included endocannabinoids, cannabinoid receptors and non-cannabinoid receptors [2].

The most well-known endocannabinoids are anandamide (AEA) and 2-arachidonoylglycerol (2-AG). Endocannabinoids are produced by the body basis of necessary, serving as signaling molecules that selectively bind to specific receptors. CB1 and CB2 receptors are the two main types of cannabinoids. The CB1 receptor is found primarily in the brain and central nervous system, whereas the CB2 receptor is most frequently located in the Immune system and other body tissues. The CB1 receptor was identified in adipocytes in 2003 marked the initial recognition of ECS specific role in adipocyte physiology [1]. In addition to CB1 and CB2, G-protein-coupled receptor 55 (GPCR55) and transient receptor potential vanilloid 1 (TRPV1) have been recently identified as non-cannabinoid receptors of the ECS [3,4]. Moreover, the ECS primary enzymes involved in this process are fatty acid amide hydrolase (FAAH), which breaks down anandamide, and monoacylglycerol lipase (MGL), which breaks down 2-AG [5].

There are naturally occurring substances that regulate the ECS. For example, the psychoactive Δ9-tetrahydrocannabinol (THC) derived from cannabis mimics endocannabinoid activity and activates ECS [3]. However, the non-psychoactive cannabidiol (CBD) blocks the CB_1 receptor, leading to the downregulation of the ECS [6]. Furthermore, a high intake of omega 3 (ω3) downregulates ECS in adipose tissue, heart, and liver [7], while a high intake of omega 6 (ω6) upregulates ECS, suggesting an inverse relationship between ECS tone and ω3 levels and a positive relationship between ECS tone and ω6 levels in the body. Hemp seeds, derived from the *Cannabis sativa* L. plant, have been a crucial source of food, fiber, and medicine for centuries [8]. Hemp seeds contain elevated levels of the natural CBD and a trace level of THC [9]. Additionally, hemp seed contains major essential fatty acids, including ω3 and ω6, representing the optimal ratio of ω3:ω6 (1:3) [8].

Distinct dietary bioactive compounds can impact various stages of the cell cycle. Human mesenchymal stem cells (hMSCs) may experience differentiation to new cell types, including adipocytes, in response to natural products [10]. Hemp seeds represent most compounds that alter the ECS, including polyunsaturated fatty acids (ω3 and ω6), THC, and CBD. Nevertheless, the increasing recreational use of hemp seed makes comprehending how this compound affects the ECS balance essential. Therefore, we hypothesize that hemp seed oil may have a regulatory effect on the ECS, controlling adipogenesis, fat accumulation, and hMSC differentiation to the preadipocyte stage. This research will focus on different aspects of hemp seed oil (HSO). Initially, the hemp seed oil was extracted using shell (S) and no-shell (NS) seeds with different extraction methods, and the phytoconstituents were compared to cold-pressed oil. Furthermore, we studied its ability on adipogenic differentiation among hMSCs, and the involvement of the ECS system downstream gene and protein signaling cascade molecules expression levels have been analyzed. Our results may lead to the involvement of hemp seed and its derivatives in the alteration of the ECS system and its association with lipid metabolism during the early stages of adipocyte differentiation.

2. Results

2.1. Soxhlet Extraction Method Produces More Oil and Cold-Pressed Hemp Seed Oil Has the Optimal Ratios to Carry out the Research

Due to inconsistencies in the scientific literature regarding the chemical components of hemp seeds [11], we sought to test the products used in this study to establish a more coherent understanding of the seeds and select the optimal product for the research. To this end, HSO was extracted from shelled (S) and no-shell (NS) hemp seeds following three different extraction techniques [dynamic maceration (DyM), Soxhlet (Sox), and cannabinoids extracting method (CEM)] using methanol to chloroform (3:1) solution (10 g/experiment). Extracted oils were then compared to the ready-to-use cold-pressed hemp seed oil using GC–MS and HPLC to identify the composition of lipids and cannabinoids. Table 1

shows the oil yield of each extraction method and its average ± SD. Sox extraction had the most oil yield, with an average of 3.8 mL compared to 3 mL from DyM experiments and 2.75 mL from the CEM experiments. Also, it is well noted that Sox extraction from NS hemp seeds significantly yielded more oil than DyM and CEM, S hemp seeds extraction (p-value ≤ 0.002) (Table 1).

Table 1. Hemp seed oil yield following different extraction methods.

Type of Seed	Extraction Method	Average (mL)	Average (mL) by Extraction Method
S	DyM	2.4 ± 0.39	DyM
	Sox	3.3 ± 0.50	3 mL
	CEM	2.5 ± 0.25	Sox
NS	DyM	3.6 ± 0.52 [d]	3.8 mL
	Sox	4.3 ± 0.19 [a,b,c]	CEM
	CEM	3 ± 0.12	2.75 mL

Oil was extracted from 10 g of seeds. Each value is mean ± SD Sox (NS): [a]—p = 0.002 compared to DM (S), [b]—p = 0.002 compared to CEM (S), [c]—p = 0.024 compared to CEM (NS). DM (NS): [d]—p = 0.038 compared to DM (S). DyM: dynamic maceration; Sox: Soxhlet; CEM: cannabinoid extraction method; S: shilled hemp seed; NS: not-shilled hemp seed.

GC–MS results showed that Soxhlet (Sox) experiments yield the highest amount of ω3 and ω6 compared to DyM and CEM. In addition, long-chain saturated fatty acids (LCSFA), including palmitic acid and stearic acid, were present among all extraction methods; however, Sox extraction presented both acids. Meanwhile, DyM presented 1.79% stearic acid from S hemp seeds only. On the other hand, CEM presented palmitic acid only, and it was higher in S hemp seeds compared to NS hemp seeds. Additionally, CEM yields a remarkably high amount of ω6 (60.71%) compared to a meager amount of ω3 (0.695%). Regarding CBD and THC, they were not detected by GC–MS in all samples. Table 2 displays the compounds detected by GC–MS and their percentage.

Table 2. Hemp seed extracted oil GC–MS analysis.

Oil Content	DyM		Sox		CEM		HSO
	S	NS	S	NS	S	NS	Cold-Pressed
ω3	30.65%	14.46%	28.78%	34.08% *	1.24%	0.69%	13.36%
ω6	41.98%	20.4%	64.74% *	55.02%	54.06%	60.71%	25.09%
Vitamin E	0	0	0	0	0	2.65% *	0
Palmitic acid	0	0	4.13%	6.78%	7.68% *	5.71%	5.02%
Stearic acid	1.79%	0	0.89%	2.20% *	0	0	1.87%
Pentadecanoic acid	0	0	0	0	0	0	3.80% *

* The highest among all extraction methods.

HPLC results showed a trace amount of CBD but not THC in all samples. The highest amount of CBD was found in the cold-pressed HSO (0.327 ppm) compared to Sox (S) (0.162 ppm) and Sox (NS) (0.144 ppm). Table 3 displays the amount of CBD detected by HPLC and their concentration (ppm). GC–MS chromatograms of Sox extraction of NS hemp seeds, Sox extraction of S hemp seed oil, and HPLC chromatogram of HSO (Sox extraction) are presented in Figure S1. The observed results confirmed that cold-pressed techniques possess the favorable ratio of ω3 and ω6 fatty acid, and the availability of highest CBD compared to the Sox, DyM, and CEM methods of extraction. So, further studies were carried out using cold-pressed oil.

Next, to examine the cytotoxic effect of HSO on hMSC, we seeded hMSCs at 5×10^4 cells/well in a 96-well plate and incubated for 24 h. HSO was emulsified using tween-20 at various concentrations (0.5%, 1%, 1.5%, 2%, 2.5%, 3%, 3.5%), then mixed with medium. Later, cells were treated with MTS in accordance with the directions given by the manufacturer after 72 h. A microplate reader was used to measure the absorbance at 570 nm. MTS assay

indicated that the lower range of HSO was not toxic. A higher concentration of the HSO was required to kill the hMSCs. As shown in Figure 1, the IC_{50} value for HSO-treated cells was (1.922% ± 0.342). Ultimately, two physiobiological doses of HSO (0.1% and 0.05%) were carried out through all experiments.

Table 3. CBD concentration in hemp seed extracted oils using HPLC.

DyM		Sox		CEM		HSO
S	NS	S	NS	S	NS	Cold-Pressed
0.131	0.141	0.162	0.144	0.101	0.109	0.327 *

* The highest among all extraction methods.

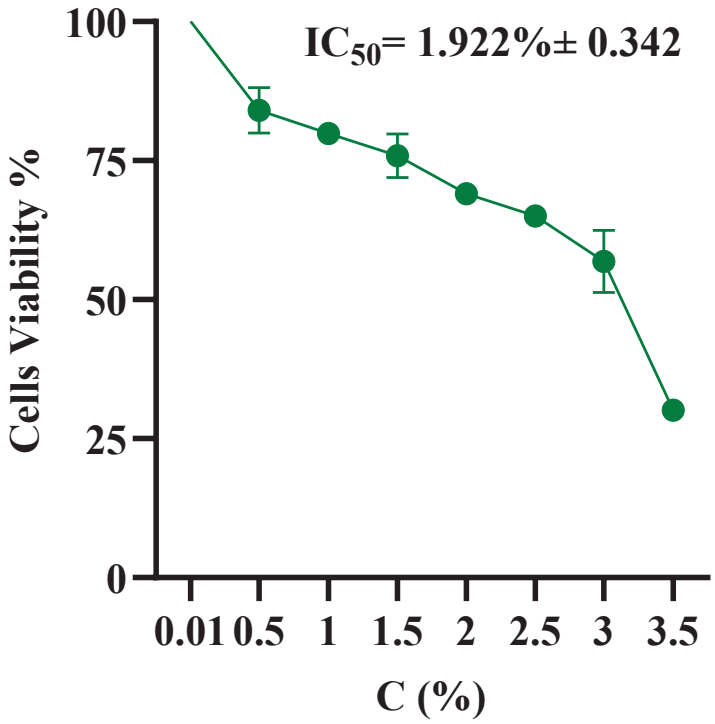


Figure 1. The IC_{50} of hMSC after 72 h incubation with HSO at various concentrations.

2.2. HSO, CBD, and THC Differentiate hMSC into Adipocyte

Since active ECS favors adipogenesis, we thought to study the effect of two doses of HSO on hMSC and compare the results with CBD (ECS antagonists) and THC (ECS agonists) with and without differentiation media. Thus, hMSCs were seeded in 24-well plates and allowed to reach 70% confluence. Then, cells were treated with media containing treatment only (TO) or media containing differentiation agents (DM) + treatment for 72 h. Both the groups were treated with 0.05% HSO, 0.1% HSO, 1 µM of CBD, or 1 µM THC. To confirm the adipogenic differentiation among hMSCs, we first performed an Oil Red O (ORO) and Nile red staining. As appears in Figure 2a,b (ORO) and Figure 2c,d (NR), HSO (in a dose-dependent manner), CBD, and THC started the adipogenic differentiation on hMSC with or without DM. Subsequently, the intracellular lipid content was measured by quantifying the absorbance of the released Oil Red O bound at 620 nm after adding 400 µL of 100% isopropanol overnight. As seen in Figure 2e, the ORO bound test showed that all treatment groups were significantly higher in their lipid content compared to their controls (hMSC for TO and DM-hMSC for DM).

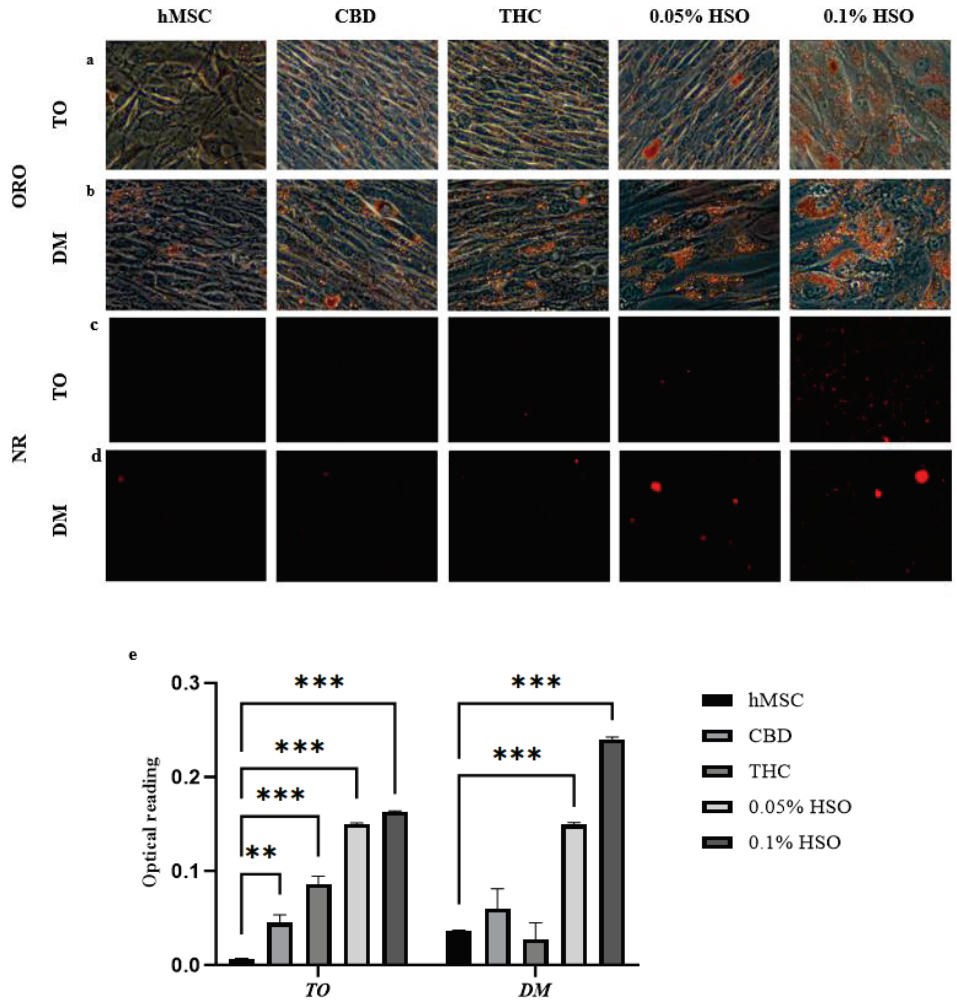


Figure 2. The morphological changes in hMSC after 72 h incubation with CBD, THC, 0.05% HSO, or 0.1% HSO in either Differentiation Media (DM) or Treatment Only (TO) using (**a**,**b**) ORO stain, (**c**,**d**) fluorescence dye—Nile Red at 50µm scale. (**e**) Intracellular lipid content represented by ORO density using 100% absolute isopropanol; the mean ± SD are shown; ANOVA as ** $p \leq 0.01$, *** $p \leq 0.001$.

Second, we sought to confirm the Oil Red O by quantifying the transcription levels of fat accumulation and adipogenic genes: peroxisome proliferator-activated receptor gamma (PPARγ) and CCAAT/enhancer-binding protein alpha (CEBPα). Subsequently, cells were harvested, cDNA was prepared and utilized for quantitative reverse transcription-polymerase chain reaction (qRT-PCR) analysis. Results showed that expression levels of these genes differed significantly between TO and DM (Figure 3). As far as PPARγ expression is concerned, Figure S1 shows the $2^{-\Delta\Delta Ct2}$ (fold change) between each group compared to the control group (hMSC). Although there was a very minimal increase among all TO groups, it was significantly higher than the control group when compared with DM groups (Figure S2). However, because the fold change of the TO groups was minimal, whereas the fold change of the DM groups was enormous in comparison to the control (hMSC), we decided to compare the results to the DM control to determine whether adding the treatments to the DM affected the results significantly. As Figure 3 shows, adding THC to the DM has increased PPARγ expression significantly by 0.573-fold ± 0.132 compared to the DM control ($p \leq 0.001$); meanwhile, adding 0.1% HSO treatment to the DM has decreased PPARγ expression significantly by 0.177-fold ± 0.130 compared to the DM control ($p \leq 0.01$). Similarly, the fold change of the CEBPα mRNA expression among DM groups was higher than TO when compared to the control hMSCs (Figure S1). Also, comparing all

groups to the DM control showed that all DM treatments except THC have significantly increased the expression of CEBPα mRNA. Meanwhile, a significant decrease was seen among all TO groups ($p \leq 0.05$) (Figure 3). Interestingly, Figure S2 shows that comparing the groups (TO and DM) separately from each other resulted in the following: among the TO groups, all treatments groups (CBD, THC, 0.05% HSO and 0.1% HSO) have decreased the expression of CEBPα mRNA significantly, and the most decrease was observed among the THC treatment group by 0.9095-fold $\pm$ 0.345 ($p \leq 0.001$). However, among the DM groups, adding treatments to the DM has increased the expression of CEBPα mRNA except for the THC treatment that decreased the expression, suggesting that THC might have a direct effect on the expression of CEBPα mRNA (Figure S2).

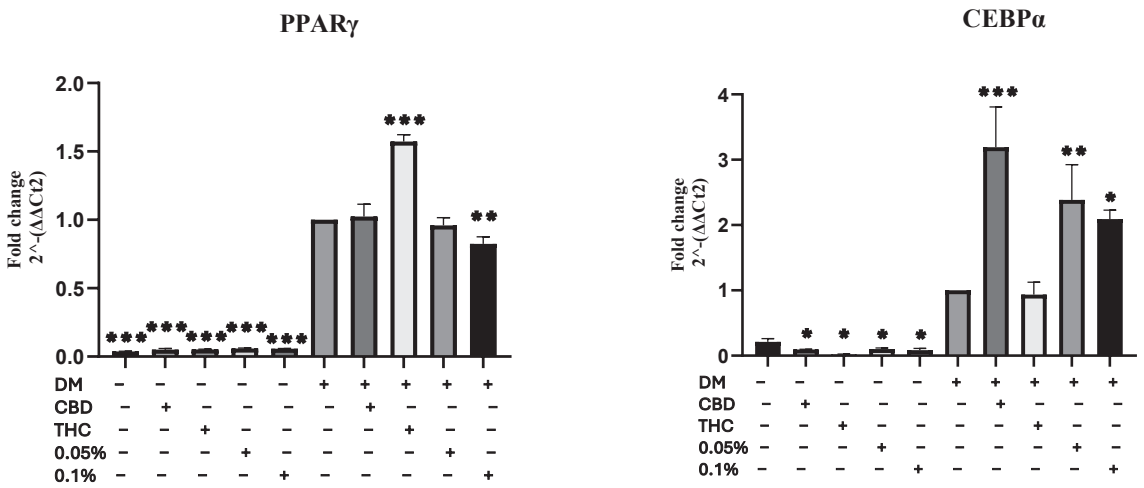


Figure 3. Gene expression. mRNA levels of adipogenic gene (PPARγ and CEBPα) were investigated by quantitative RT-PCR after 72 h of culturing in CBD, THC, 0.05% HSO, or 0.1% HSO treatments with/without DM; the mean $\pm$ SD are shown compared to the DM control; ANOVA as * $p \leq 0.05$, ** $p \leq 0.01$, *** $p \leq 0.001$.

2.3. HSO, CBD, and THC Treatments Regulated the ECS

Since HSO and its active compounds (CBD and THC) initiated the adipogenic differentiation, we sought to examine whether this effect was related to the activation of the ECS. Thus, we studied the trends of EC receptors (CB1, CB2, TRPV1, GPCR 55) and degrading enzymes (FAAH and MGL) in terms of their mRNAs expression upon treatment with TO or DM. As shown in Figure 4, CB1 mRNA expression compared to the control (hMSC) was significantly downregulated in all groups except for TO-CBD, and TO-0.1% HSO was decreased but not significantly. Meanwhile, CB2 mRNA expression was significantly upregulated upon the treatment with CBD in both TO and DM groups by 0.631 $\pm$ 0.212 ($p \leq 0.05$) and 0.915 $\pm$ 0.008 ($p \leq 0.01$), respectively. It is possible that CBD is a direct activator of CB2. On the other hand, THC treatment has decreased the CB2 mRNA expression in both groups (TO and DM) but not significantly. Generally, a similar pattern can be noted in the CB2 mRNA expression when comparing the TO groups to the DM groups (Figure 4). Regarding TRPV1 mRNA expression, we found that adding DM has downregulated the expression significantly in all DM groups, except DM-0.1% HSO was not significant. However, TO-0.1% HSO along with TO-CBD has significantly increased the expression of TRPV1 mRNA ($p \leq 0.01$). In terms of GPCR55 mRNA, adding DM has increased the GPCR55 mRNA expression in all DM groups but was only significant among DM control, DM-CBD, and DM-0.05% HSO ($p \leq 0.01$, $p \leq 0.001$, and $p \leq 0.01$, respectively). Interestingly, TO-CBD has also increased the expression of GPCR55 mRNA but not significantly, whereas TO-0.1% HSO has significantly increased the expression of GPCR55 mRNA ($p \leq 0.001$). As far as the EC enzymes FAAH and MGL are concerned, we found that adding DM has significantly decreased FAAH mRNA in all groups ($p \leq 0.001$)

and significantly decreased MGL mRNA in all groups except for the DM-THC group, where it was significantly increased ($p \leq 0.001$). Interestingly, THC treatment has significantly increased both enzymes compared to their controls. THC treatment has increased the expression of MGL mRNA significantly ($p \leq 0.001$) in the TO group. Furthermore, THC treatment in the TO has increased the expression of FAAH mRNA significantly ($p \leq 0.05$), suggesting that there might be a direct relationship between THC treatment and EC-degrading enzymes (FAAH and MGL).

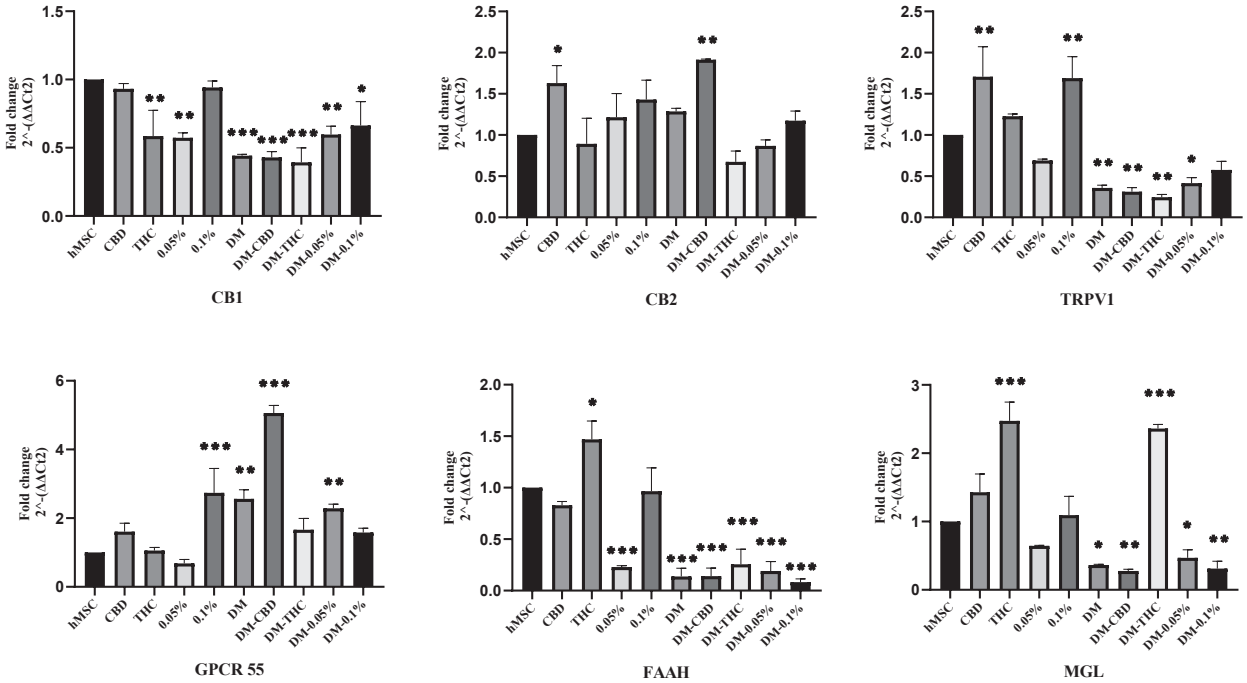


Figure 4. Gene expression. mRNA levels of ECS genes (CB1, CB2, TRPV1, GPCR55, FAAH, and MGL) were investigated by quantitative RT-PCR after 72 h of culturing with CBD, THC, 0.05% HSO, or 0.1% HSO treatment with/out DM; the mean ± SD are shown; ANOVA compared to hMSC as * $p \leq 0.05$, ** $p \leq 0.01$, *** $p \leq 0.001$.

Next, we sought to study the protein expression trends of the EC receptors (CB1, CB2, TRPV1, GPCR55). To this end, cells were harvested, and immunoblotting was performed on whole-cell lysates followed by blot quantification using densitometry scanning. As Figure 4 shows, protein expression of CB1 has confirmed the CB1 mRNA expression and was significantly decreased in all groups ($p \leq 0.001$), and the highest decrease was among the DM-treated groups. As far as CB2 protein expression is concerned, it was significantly decreased in all DM-treated groups, except DM-0.1% HSO was not significant; meanwhile, it was slightly but not significantly increased in all TO groups. It is noteworthy that CB2 protein expression was upregulated upon the treatment of 0.1% HSO when comparing each treated group to their controls. Figure 5d shows that TRPV1 protein expression has upregulated in the CBD- and THC-treated groups in the TO and DM; meanwhile, it was downregulated after the oil treatment (0.05% HSO and 0.1% HSO) in both TO and DM groups. In contrast to the mRNA result, we found that the protein level of TRPV1 in DM, DM-CBD, and DM-THC was significantly higher than the control ($p \leq 0.001$). This could be due to the stableness and degradation resistance of the resulting protein even with low levels of mRNA. In addition, some proteins have longer half-lives than their mRNA, despite the rapid degradation of their mRNA [12]. As far as GPCR 55 protein levels are concerned, Figure 5e shows that the expression was notably and significantly decreased in all DM-treated groups compared to the control ($p \leq 0.001$). However, the expression of GPCR55 in DM-THC, DM-0.05% HSO, and DM-0.1% HSO was increased compared to their

control (DM control). In addition, GPCR 55 protein expression was significantly increased in the TO-0.05% HSO and TO-CBD ($p \leq 0.001$).

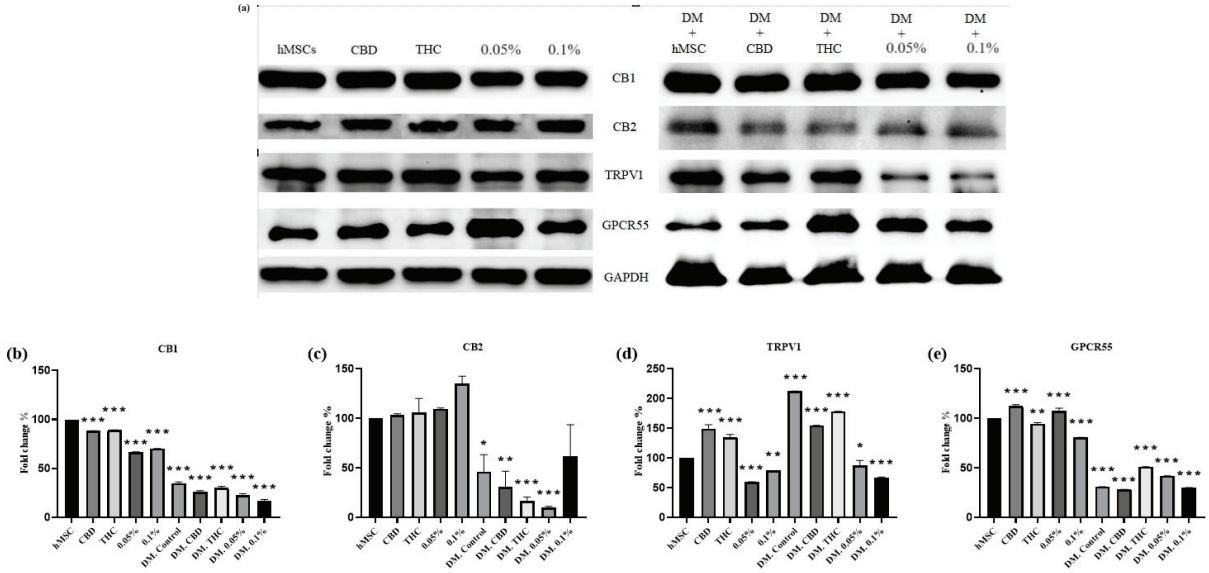


Figure 5. Western blotting of ECS receptors on hMSCs and treatments with or without DM (**a**). Densitometry analysis of CB1, CB2, TRPV1, and GPCR55 are shown in (**b**–**e**), respectively. The means ± SD are shown; ANOVA as * $p \leq 0.05$, ** $p \leq 0.01$, *** $p \leq 0.001$.

3. Discussion

In this investigation, we aimed to identify the role of active ECS in the effects of HSO on adipogenesis in hMSCs. Cold-pressed HSO used in this study contained around a 0.5:1 ratio of ω3:ω6 and 0.327 ppm CBD. CBD (1 μM) and THC (1 μM) treatments were used for comparison. Our present study confirmed for the first time that HSO was able to initiate adipocyte differentiation among hMSCs without the differentiation media (DM) in a dose-dependent manner (Figure 2). Additionally, HSO treatment increased the size of adipocytes in DM-treated cells (Figure 2). This might be due to the high lipid accumulation in DM-treated cells. Similarly, based on ORO results in Figure 2, we found that CBD and THC treatments in TO and DM have initiated the adipogenic differentiation compared to the control (hMSC). However, THC treatment in the DM-treated cells have decreased intracellular lipid content compared to its control (DM control) (Figure 2e). This could be attributed to the fact that the acid form of THC (THCA) creates fewer and smaller lipid droplets than rosiglitazone in hMSCs [13,14] and, as previously stated, that most of the CBD and THC were appropriately stored in hemp seed oil in the form of acidic precursor [15,16]. Furthermore, as PPAR-γ and CEBP-α are two master transcription factors that govern the differentiation and proliferation of adipocytes [17], we confirmed that the adipogenic gene CEBP-α expression level has been significantly downregulated in HSO-, CBD-, and THC-treated hMSCs compared to its control (hMSC) (Figure S2a); however, adding DM increased the CEBP-α gene expression significantly in HSO- and CBD-treated maturing adipocytes (DM-cells) compared to its control (DM-hMSC) (Figure S2b). Interestingly, we found that THC treatment has downregulated the expression of the CEBP-α mRNA in both TO- and DM-treated cells (Figure S2), suggesting a direct relationship between THC treatment and CEBP-α mRNA expression. However, THC treatment has significantly increased the expression of PPAR-γ mRNA in both TO- and DM-treated cells when compared to the control in each group (Figure S2). It is also noteworthy that all treatments in TO (HSO, CBD, and THC) have increased the expression of PPAR-γ mRNA compared to their control (hMSC). However, in the DM-treated cells, HSO treatment has decreased the PPAR-γ mRNA expression compared to the DM control (Figure S2). Both HSO treatments (0.1% HSO and 0.05% HSO) in the DM-treated cells have decreased the

expression of PPAR-γ mRNA—in a dose-dependent manner—by 0.04-fold ± 0.053 and 0.176-fold ± 0.057, respectively (Table S2). This suggests that HSO might have a controlling role of lipid accumulation and adipogenesis. In addition, the ability of CBD administration to activate PPAR-γ mRNA and drive adipogenesis in both mice and hMSCs has been validated and identified such that CBD's impact might be attributed to its tendency to stimulate lipogenesis without the balance of lipolysis [18]. CBD in our study has similarly increased the expression of PPAR-γ mRNA significantly ($p > 0.05$) when in hMSCs; however, adding CBD to DM has maintained the same expression levels compared to the DM control.

We also studied the EC receptors' and enzymes' involvement in hMSC adipocyte differentiation with and without differentiation media. Upon discovery of cannabinoid receptor-1 (CB1) and its role in peripheral organs, many studies led to the discovery that CB1 receptors are directly involved in the physiological processes of energy homeostasis in adipocytes and many tissues [19,20]. CB1 receptor agonist in adipocytes and chronic activation in white adipose tissue have been found with impaired mitochondrial functions and decreased mitochondrial biogenesis [20]. In contrast, Roche et al. [19] found that activation of the CB1 receptor with the endocannabinoid 2-AG has increased the intracytoplasmic cyclic adenosine monophosphate (cAMP), which may lead to increased lipolysis and decreased lipid accumulation. Another study found that CB1 antagonist stimulates the expression of mitochondrial biogenesis enzymes, including Krebs cycle, and increased the oxidative phosphorylation potential [20]. In the current study, all treatments—especially HSO—significantly decreased CB1 mRNA expression and protein expression in all groups ($p \leq 0.001$); meanwhile, DM-treated cells showing the highest reduction. The adipogenic effect of HSO on hMSCs is evident by ORO and PPAR-γ mRNA expression—in an early stage—but might not be mediated by EC CB1 receptor. Bajzer et al. [21] confirmed that persistent CB1 antagonism has been linked to increased energy consumption, lipolysis, mitochondrial biogenesis, and activation of thermogenesis. Further, inhibition of adipocyte CB1 potentially influences lipid homeostasis in a positive way and the production of adipokines, which facilitate the lipolysis or inhibit lipid accumulation and hypertrophy [1,22].

As far as cannabinoid receptor-2 (CB2) is concerned, it was previously linked to immune system cells only. However, Roche et al. [19] were able to discover the biological functions of CB2 receptor in human pre-adipocytes and mature adipose tissue; the activation of adipocyte CB2 receptor inhibits cyclic adenosine monophosphate (cAMP) synthesis, which may lead to decreased lipolysis. In the present study, we found that CBD treatment showed strong affinity towards CB2 compared to THC. CBD treatment has significantly increased the CB2 mRNA expression in both TO- and DM-treated cells ($p \leq 0.05$, $p \leq 0.01$, respectively). On the other hand, THC treatment has decreased the CB2 mRNA expression in both TO- and DM-treated cells (not significantly). Furthermore, the CB2 protein levels have been slightly elevated in both CBD and THC treatments in the TO; however, when added to DM-treated cells, both treatments have decreased the CB2 protein levels significantly ($p \leq 0.01$, $p \leq 0.001$, respectively). Meanwhile, HSO treatment, especially 0.1% HSO, has slightly elevated the expression of CB2 mRNA in both TO- and DM-treated cells, and held this elevation even at protein level, suggesting that there are other substances in HSO that activate the CB2 receptor besides CBD, such as arachidonic acid, an ω6 PUFA that is a precursor for AEA.

Another EC receptor is TRPV1; AEA and other endocannabinoids are natural ligands for TRPV1 [23,24], and it is produced when intracellular Ca^{2+} levels increase [3]. In addition, a cross talk between CB1 and TRPV1 has been demonstrated by several studies [25–28]. CB1 has been demonstrated to either enhance or reduce TRPV1 channel activity [26]. In the present study, we found similar expression trends between TRPV1 and CB1 (Figure 4), as CBD and 0.1% HSO held the highest expression of CB1 compared to other treatment groups, it also increased the expression of TRPV1 mRNA significantly ($p \leq 0.01$). Similarly, as DM has decreased the expression of CB1 in all treatment groups significantly, it also decreased the TRPV1 mRNA expression significantly, except for 0.1% HSO it was not sig-

nificant. However, this was not the case when it comes to TRPV1 protein expression, where DM-treated cells (DM control), DM-CBD, and DM-THC have significantly increased the TRPV1 protein expression. Meanwhile, HSO treatments (0.05% HSO and 0.1% HSO) have decreased its expression significantly in both TO and DM. It appears that the interaction between CB1 and TRPV1 is dependent on the amount of circulating AEA. Research has shown that TRPV1 may be activated by supplementing high dosages of AEA (1–10 M) [28,29]. In contrast, low doses of AEA (3–30 nM) decrease TRPV1 expression [30,31]. Therefore, the enzymatic production and breakdown of endogenous cannabinoids may be crucial determinants of TRPV1 activity in tissues that co-express TRPV1 and CB1 [25].

The enzymes FAAH and MGL are degrading enzymes of the intracellular endocannabinoids AEA and 2-AG, produced in response to high levels of the endocannabinoid to retain hemostasis of the active ECS [20,32]. In the present study, we found that FAAH mRNA expression was downregulated in all groups except TO-THC treatment. Significant reduction of FAAH mRNA was noted among all DM-treated groups ($p \leq 0.001$). Similar findings were observed on MGL mRNA expression. DM-treated groups have significantly reduced its expression except DM-THC, which significantly increased the expression of MGL mRNA ($p \leq 0.001$). Also, THC treatment in the TO has significantly upregulated both FAAH and MGL mRNAs ($p \leq 0.05$, $p \leq 0.001$, respectively), while CBD and HSO treatments have upregulated MGL mRNA and downregulated FAAH mRNA expression but not significantly. Furthermore, since FAAH is expressed on demand upon high levels of anandamide to retain homeostasis of the active ECS [33], our present study suggests that the ECS might not be highly activated in the differentiation process of hMSC to adipocyte. Also, the balance ratio of ω3 to ω6 in the HSO might have a role in maintaining lower endocannabinoids (AEA and 2-AG) and consequently lower the expression levels of FAAH and MGL, which are associated with low lipid accumulation. In this context, an in vitro study has demonstrated that ω3 polyunsaturated fatty acids (PUFA) have the potential to reduce the amounts of AEA and 2-AG in differentiated adipocytes from mice [34]. Conversely, arachidonic acid (ω6, PUFA) has been seen to elevate endocannabinoid levels [35].

l-α-lysophosphatidylinositol (LPI) is known as a regulator of the intracellular Ca^{2+} accumulation, and it is believed to be the only endogenous ligand of G-protein-coupled receptor-55 (GPCR55) that is presumed to be a cannabinoid receptor [36]. In addition, a positive association between obesity, type 2 diabetes, and GPCR55 expression in visceral adipose tissue (VAT) has been identified [37]. Consistently, obese patients have been identified with higher plasma levels of LPI than lean subjects [36]. In our study, we observed that all groups subjected to DM treatment exhibited a notable upregulation in the expression of GPCR55 mRNA. However, a contrasting trend was observed in the levels of GPCR55 protein, as DM treatment resulted in a significant decrease in its expression across all groups ($p \leq 0.001$). Similar findings were noted in TO-HSO (both doses 0.05% HSO and 0.1% HSO), where TO-0.1% HSO has significantly increased GPCR55 mRNA but significantly reduced the protein levels, whereas TO-0.05% HSO decreased GPCR55 mRNA but significantly increased its protein expression.

Generally, the observed discrepancy between the findings of our research and those of previous studies might perhaps be attributed to variances in the level of maturation or cell type. In our current study, endpoint measures were conducted three days after initiating adipocyte differentiation in hMSCs and treatment, whereas other investigations employed distinct cell types or conducted in vivo experiments, or achieved a fully developed state of adipocyte, often after a differentiation period of 14 days.

4. Materials and Methods

4.1. Plant Products and Chemicals

Raw hemp seeds (shelled-S and not shelled-NS-Canadian source) and cold-pressed hemp seed oil (HSO) (Moreno Valley, CA, USA) were bought from iHerb (Irvine, CA, USA). Liquid Cannabidiol (CBD) and Δ^9-tetrahydrocannabinol (THC) standards were obtained from RESTEK® (Bellefonte, PA, USA). Powder CBD was obtained from Abcam

(ab120448) (Cambridge, UK). Methanol, acetonitrile, chloroform, formic acid, acetone, and isopropanol HPLC grade were supplied thankfully by the King Saud University (KSU) chemical warehouse.

4.2. Instrument

Gas Chromatography–Mass Spectrometry (GC–MS) was utilized for the analysis of extracts to determine the chemical components present and their respective concentrations. The column utilized was a DB-5MS with dimensions of 30 m in length, 0.250 mm in diameter, and 0.25 μm in thickness. The flow rate was 3 mL/min, pressure set at 10.42 psi, operating in splitless mode, with an injection volume of 3 μL. The oven temperature was 60 °C for 3 min, then increased to 100 °C at a rate of 3 °C per minute, followed by reaching 200 °C in 1 min at the same rate, and finally reaching 300 °C in 1 min at a rate of 5 °C per minute. GC–MS data were interpreted using FAME and NIST libraries. The chromatogram threshold in all experiments was set at 17.

High-Performance Liquid Chromatography: Ultraviolet/Diode Array Detector (HPLC-UV/DAD): HPLC-UV/DAD (Shimadzu, Colombia, MD, USA) was used to identify and quantify chemical compounds using a standard for each analyte (CBD and THC). Hypersil® column (100 × 4.6 mm, Thermo Scientific, Waltham, MA, USA) with a particle size of 5 μm ODS was used. The temperature was set at 30 °C, and injection volume was 10 microliters. Mobile phase solutions were A: 70% acetonitrile and B: 30% formic acid (0.1%). Samples and standards were prepared following Brighenti et al. [38]. The ratio of samples to isopropanol was 20 μL:4 mL, then vortexed for 30 s, and 2 mL was taken into an HPLC vial.

4.3. Extraction Method

Three extraction techniques (dynamic maceration-DyM, Soxhlet-Sox, and cannabinoids extraction method-CEM) were followed using methanol/chloroform solution (M/C, 3:1). DyM extraction: a modified method of Brighenti et al. [38] was followed, shelled-(S) and no-shell-(NS) hemp seeds (HS) were grounded for 30 s each. An amount of 10 g of extract(s) as initial weight was added with 40 mL of the solvent and placed on a magnetic stirrer for 4 h at room temperature. The solution was filtered using No. 1 Whatman™ filter papers (Maidstone, UK, 125 mm), and the residue was extracted twice with another 40 mL of the solvent, followed by 20 mL for 1 h 30 min and 30 min, respectively, and was placed on magnetic stirring. Finally, the filtrate was evaporated under a vacuum, and the crude extract was collected. Soxhlet-Sox extraction: a modified method of Devi and Khanam [39] was followed. An amount of 10 g of S or NS hemp seed powder was weighed and placed in a thimble (Whatman™ cellulose extraction thimbles 25 mm × 100 mm). Then, 100 mL of solvent was added to keep the solvent and HS ratio at 1:10 g/mL. The procedure was carried out for 6 h, the mixture was evaporated under a vacuum, and the crude extract was collected. CEM extraction: a modified method of Mandrioli et al. [40] was followed, whereby 10 g of S or NS hemp seed powder was mixed with 100 mL of solvent. The oscillator node was placed inside the beaker touching solvent (Physical Field) at 350 hertz and amplitude of 10 vpp and "Sin" wave shape for 30 min. Then, the beaker was placed in a sonic bath for 30 min. The process was repeated on the oscillator for 20 min and a sonic bath for 20 min. The mixture was then filtered into the evaporator flask using No. 1 Whatman™ filter papers (125 mm). Then, the mixture evaporated, and crude oil was collected. All extraction methods were performed in triplicate.

An evaporator was used at 55 °C throughout the experiments, along with a vacuum to collect the solvent-free crude extract. Then, crude extracts were collected in centrifuge tubes for further purification process. Firstly, liquid–liquid extraction (LLE) was utilized, 2 mL of crude extract was placed in a centrifuge tube along with 2 mL of H_2O and 2 mL of methanol, centrifuged at 5000 rpm for 5 min, then 1.5 mL of the solvent layer was taken into an Eppendorf tube. Secondly, a syringe filter (PTFE-0.45 μm- Thermo Scientific, Waltham, MA, USA) was used, followed by another syringe filter (Nylon-0.45 μm- Thermo Scientific,

Waltham, MA, USA), then brought to dryness using a stream of nitrogen. Finally, the residue was diluted in acetone for analysis.

4.4. Cell Culture

The hMSCs were obtained from the American Type Culture Collections (ATCC) in Manassas, VA, USA. Early passage of hMSCs (≤passage 3) were cultured in Dulbecco's Modified Eagle's Medium (DMEM, Gibco, Waltham, MA, USA). The cells were cultured in a medium containing 10% fetal bovine serum (FBS, Gibco™, Grand Island, NY, USA) and 1% penicillin–streptomycin (Gibco™, NY, USA) at 37 °C in a humidified environment with 5% CO_2. At 70% confluency, cells were maintained in either DMEM + treatment only (5 groups: control/DMEM only, CBD, THC, 0.05% HSO, and 0.1% HSO for 72 h or in a differentiation media containing Dexamethasone (1 μM), IBMX (0.5 μM), Rosiglitazone (1 μM), recombinant human insulin (167 nM) for 72 h [41] along with treatments (5 groups: DM-hMSC, DM-CBD, DM-THC, DM-0.05% HSO, and DM-0.1% HSO) for 72 h. HSO was dissolved in 1% tween-20 to ensure homogenization. CBD and THC were dissolved in methanol. Finally, condition media of DM groups were collected for further use.

4.5. Cell Viability Assay

Human mesenchymal stem cells (hMSCs) were placed in a 96-well plate with a concentration of 1×10^4 cells per well and left to incubate for 24 h. Cells were exposed to varying amounts of hemp seed oil (HSO) (0.5%, 1%, 1.5%, 2%, 2.5%, and 3%) for 72 h. HSO was dissolved in 1% tween-20 and emulsified using a sonication device at 30 °C and 40 RPM for 5 min to ensure homogenization. hMSC treated with 0.5% tween-20 was used as a control. Then, cells were treated with MTS in accordance with the directions given by the manufacturer after 72 h. A microplate reader (SPECTROstar® Nano—BMG Labtech, Ortenberg, Germany) was used to measure the absorbance at 570 nm. Three replicate wells were used for each data point throughout the experiments. Ultimately, two physiobiological doses of HSO (0.05%) and (0.1%) were used along with (1 μM) of CBD and THC for comparison.

4.6. Oil Red O and Nile Red Staining

hMSC were seeded in a 24-well plate and allowed to reach 70% confluence. Cells were treated with HSO, CBD, and THC. After 72 h of treatment, growth media was removed, and cells were gently washed using phosphate-buffered saline (PBS). Subsequently, the cells were fixed with a 10% formalin solution for a duration of 1 h at room temperature, then washed three times with deionized water. Oil Red O (ORO) solution (4:6 water to 6% Oil Red O dye in isopropanol) was applied to the cells for 10 min, then unbound Oil Red O was removed by washing with PBS. The stained lipid droplets were captured using a light microscope (ZEISS, Axiocam 506 color, Jena, Germany). Finally, bound ORO were extracted with 100% isopropanol (400 μL/well) overnight, and the concentration of intracellular ORO was assessed, which is directly proportional to lipid accumulation. The absorbance at 620 nm was measured in duplicate wells using a microplate reader.

For Nile Red (NR) staining, media from the experimental cells were discarded and washed with PBS, further NR staining was added to each well. Then, the cells were incubated at room temperature for 10 min, then washed with deionized water to remove the unbound dye before imaging. The stained lipid droplets were captured using the green filter of an inverted florescence microscope (ZEISS, Axiocam 506 color).

4.7. RNA Extraction and Real-Time Polymerase Chain Reaction (RT-PCR)

hMSCs were seeded in a 24-well plate and allowed to reach 70% confluence. Cells were treated with HSO, CBD, and THC for 72 h; then, total RNA was extracted from hMSC using Qiagen, RNEASY MINI KIT (Qiagen, Inc., Tulsa, OK, USA). After that, the concentration and purity of the extracted RNA were measured using Quickdrop (SpectraMax, QuickDrop, Framingham, MA, USA). Then, 1 μg RNA was converted to cDNA using a

High-Capacity cDNA Reverse Transcription Kit (Thermo Fisher Scientific, Vilnius, Lithuania). The QuantStudio 3 (Thermo Fisher Scientific, Waltham, MA, USA), along with SYBR® green Universal Master Mix (Life Technologies Ltd., Paisley, UK), were used to quantify the transcription levels of specific genes (PPARγ, CEBPα, CB1, CB2, TRPV1, GPCR55, FAAH, MGL). For each sample, PCR reactions were repeated twice, and the transcription levels of each gene were standardized to GAPDH (primer sequences are presented in Table S3).

4.8. Immunoblot Analysis

Cell lysates were prepared using RIPA lysis buffer and Halt™ Protease inhibitor (PI) (Thermo Fisher Scientific, USA) at a 1:25 ratio (PI:RIPA). Cell lysates were homogenized for an hour on ice, then centrifuged at 14,000 rpm for 30 min at 4 °C. The Bradford assay (Bio-Rad Protein Assay kit, Hercules, CA, USA) was used to measure protein concentration. A total protein concentration was set at 35 μg/μL for all samples. The sample buffer was prepared at a 1:19 ratio of β-mercaptoethanol:2x-laemmli-sample-buffer. Then, a 1:1 ratio of samples to sample buffer was mixed and heated at 95 °C for 5 min before uploading to the 10% SDS-polyacrylamide gel electrophoresis (PAGE). Gels were transferred to 0.2 μm polyvinylidene difluoride blotting membrane (PVDF, Amersham™ Hybond™, Cytiva, München, Germany) after electrophoresis, then blocked for 1 h with 5% skimmed milk. Next, TBST 1X buffer (50 mL of TBS 20X + 950 mL DW + 1 mL of Tween 20) was used to rinse the membrane three times. Then, the membrane was incubated overnight at 4 °C with primary monoclonal antibodies anti-CB_1 (rabbit, 1:4000), primary polyclonal antibodies anti-CB_2 (rabbit, 1:200), primary polyclonal antibodies anti-$TRPV_1$ (rabbit, 1:500), and primary polyclonal antibodies anti-GPCR55 (rabbit, 1:166) (Abcam). After that, the membrane was incubated for 2 h at room temperature with primary monoclonal antibodies anti-GAPDH (mouse, 1:10,000). The membrane was washed three times and then incubated for 1 h with anti-(rabbit/mouse) IgG secondary antibody horseradish peroxidase-conjugated (1:1000, Abcam) in 5% skim milk.

Finally, images were taken using the ChemiDoc™ Touch Imaging System (Bio-Rad, USA) after incubating the membrane in the Clarity Western ECL Substrate kit (Bio-Rad, USA). Image lab 6.1 software was used to quantify band intensities.

4.9. Statistical Analysis

The mean and standard deviation (SD) of at least duplicate experiments are used to represent all data. In addition, one-way ANOVA was used to examine the statistical significance among multiple groups, followed by the Dunnett test for multiple comparisons using GraphPad Prism 9.4.1 (Windows, GraphPad Software, San Diego, CA, USA) https://www.graphpad.com (accessed on 13 September 2022). Statistical significances were indicated as p-values ≤ 0.05.

5. Conclusions

The endocannabinoid system (ECS) is essential in promoting fat storage in animals through many mechanisms. EC tone in hMSC—including receptors and enzymes—was investigated following treatment with HSO (0.05% HSO and 0.1% HSO), CBD, and THC with and without DM during the early stages of adipogenesis. The agonism and antagonism of CB1 pose a direct effect on adipocytes and regulate energy intake and expenditure through central and peripheral pathways. In the present study, HSO effectively downregulated the CB1 mRNA, and protein expression further reduced the endogenous ligand TRPV1. Endogenous CB1 inhibition neutralizes or reduced the FAAH and MGL expressions, which play a major role in the endocannabinoid AEA and AA degradation. Although HSO independently has the capacity to initiate the adipogenic differentiation among hMSCs and upregulation of adipogenic gene PPAR-γ, HSO inhibits CB1, TRPV1, and PPAR-γ when differentiation was induced by DM. That indicates that HSO alone might have the ability to initiate the differentiation; however, it reduces the lipid accumulation and energy metabolism when differentiation is induced by DM compared to CBD or THC alone. There-

fore, hemp seed might be considered as a natural agent for CB1 inhibition, to overcome adipocyte lipogenesis and obesity. Finally, we recommend an in vivo study to confirm whether HSO will continue to inhibit CB1 and define the adipocyte maturation.

Supplementary Materials: The following supporting information can be downloaded at: https://www.mdpi.com/article/10.3390/molecules29071568/s1, Figure S1: GC–MS chromatograms: (a) Sox extraction of NS hemp seeds. (b) Sox extraction of S hemp seed oil. (c) HPLC chromatogram of HSO (cold-pressed); Figure S2: Gene expression. mRNA levels of adipogenic gene (PPARγ and CEBPα) were investigated by quantitative RT-PCR after 72 h of culturing with CBD, THC, 0.05% HSO, or 0.1% HSO treatments without DM (a), or with DM (b); the mean ± SD are shown compared to their controls; ANOVA as * $p \leq 0.05$, ** $p \leq 0.01$, *** $p \leq 0.001$; Table S1: Mean fold change ($2^{-\Delta\Delta Ct2}$) of PPARγ and CEBPα mRNAs expression compared to the control (hMSC); Table S2: Mean fold change ($2^{-\Delta\Delta Ct2}$) of PPARγ and CEBPα mRNAs expression compared to the control (DM-hMSC) and Table S3: Sequences of the primers used for qRT-PCR.

Author Contributions: Conceptualization, A.S.A. and A.A.A.; data curation, A.S.A. and P.S.-B.; formal analysis, A.S.A.; funding acquisition, A.A.A.; investigation, A.S.A., E.B., A.A. and M.A.; methodology, P.S.-B., I.O.A. and H.A.; project administration, P.S.-B.; resources, A.A.A. and H.A.; software, A.S.A., P.S.-B., E.B., A.A. and M.A.; supervision, P.S.-B., I.O.A., A.A.A. and H.A.; validation, P.S.-B., I.O.A. and H.A.; visualization, A.S.A., E.B., A.A. and M.A.; writing—original draft, A.S.A. and P.S.-B.; writing—review and editing, P.S.-B., I.O.A. and H.A. All authors have read and agreed to the published version of the manuscript.

Funding: This research was funded by the Researchers Supporting Project number (RSP2024R178), King Saud University, Riyadh, Saudi Arabia.

Institutional Review Board Statement: Ethical review and approval were waived for this study as it exclusively involved the use of established human cell lines. The use of these cell lines does not involve human subjects directly, and therefore, IRB approval was not required. All experiments were conducted following standard laboratory protocols and in accordance with institutional guidelines.

Informed Consent Statement: Not applicable.

Data Availability Statement: The data presented in this study are openly available in FigShare at [https://doi.org/10.6084/m9.figshare.25218842.v1 (accessed on 1 March 2024)].

Conflicts of Interest: The authors declare no conflicts of interest. The funders had no role in the design of the study; in the collection, analyses, or interpretation of data; in the writing of the manuscript; or in the decision to publish the results.

References

1. Matias, I.; Belluomo, I.; Cota, D. The fat side of the endocannabinoid system: Role of endocannabinoids in the adipocyte. *Cannabis Cannabinoid Res.* **2016**, *1*, 176–185. [CrossRef]
2. Bermudez-Silva, F.J.; Viveros, M.P.; McPartland, J.M.; Rodriguez de Fonseca, F. The endocannabinoid system, eating behavior and energy homeostasis: The end or a new beginning? *Pharmacol. Biochem. Behav.* **2010**, *95*, 375–382. [CrossRef] [PubMed]
3. Silvestri, C.; Di Marzo, V. The endocannabinoid system in energy homeostasis and the etiopathology of metabolic disorders. *Cell Metab.* **2013**, *17*, 475–490. [CrossRef] [PubMed]
4. Tudurí, E.; Imbernon, M.; Hernández-Bautista, R.J.; Tojo, M.; Fernø, J.; Diéguez, C.; Nogueiras, R. GPR55: A new promising target for metabolism? *J. Mol. Endocrinol.* **2017**, *58*, R191–R202. [CrossRef]
5. Bennetzen, M.F.; Wellner, N.; Ahmed, S.S.; Ahmed, S.M.; Diep, T.A.; Hansen, H.S.; Richelsen, B.; Pedersen, S.B. Investigations of the human endocannabinoid system in two subcutaneous adipose tissue depots in lean subjects and in obese subjects before and after weight loss. *Int. J. Obes.* **2011**, *35*, 1377–1384. [CrossRef]
6. De Petrocellis, L.; Ligresti, A.; Moriello, A.S.; Allarà, M.; Bisogno, T.; Petrosino, S.; Stott, C.G.; Di Marzo, V. Effects of cannabinoids and cannabinoid-enriched Cannabis extracts on TRP channels and endocannabinoid metabolic enzymes. *Br. J. Pharmacol.* **2011**, *163*, 1479–1494. [CrossRef] [PubMed]
7. Batetta, B.; Griinari, M.; Carta, G.; Murru, E.; Ligresti, A.; Cordeddu, L.; Giordano, E.; Sanna, F.; Bisogno, T.; Uda, S.; et al. Endocannabinoids may mediate the ability of (n-3) fatty acids to reduce ectopic fat and inflammatory mediators in obese Zucker rats. *J. Nutr.* **2009**, *139*, 1495–1501. [CrossRef] [PubMed]
8. Callaway, J.C. Hempseed as a nutritional resource: An overview. *Euphytica* **2004**, *140*, 65–72. [CrossRef]
9. NHA. Hemp Resources—Hemp Facts and Statistics. The National Hemp Association. Available online: https://nationalhempassociation.org/hemp-resources/#Hemp%20Facts%20and%20Statistics (accessed on 8 February 2024).

10. Subash-Babu, P.; Alshatwi, A.A. Aloe-emodin inhibits adipocyte differentiation and maturation during in vitro human mesenchymal stem cell adipogenesis. *J. Biochem. Mol. Toxicol.* **2012**, *26*, 291–300. [CrossRef]
11. Mead, A. The legal status of cannabis (marijuana) and cannabidiol (CBD) under U.S. law. *Epilepsy Behav.* **2017**, *70*, 288–291. [CrossRef]
12. Greenbaum, D.; Colangelo, C.; Williams, K.; Gerstein, M. Comparing protein abundance and mRNA expression levels on a genomic scale. *Genome Biol.* **2003**, *4*, 117. [CrossRef] [PubMed]
13. Villarroel-Vicente, C.; Gutiérrez-Palomo, S.; Ferri, J.; Cortes, D.; Cabedo, N. Natural products and analogs as preventive agents for metabolic syndrome via peroxisome proliferator-activated receptors: An overview. *Eur. J. Med. Chem.* **2021**, *221*, 113535. [CrossRef] [PubMed]
14. Palomares, B.; Ruiz-Pino, F.; Garrido-Rodriguez, M.; Eugenia Prados, M.; Sánchez-Garrido, M.A.; Velasco, I.; Vazquez, M.J.; Nadal, X.; Ferreiro-Vera, C.; Morrugares, R.; et al. Tetrahydrocannabinolic acid A (THCA-A) reduces adiposity and prevents metabolic disease caused by diet-induced obesity. *Biochem. Pharmacol.* **2020**, *171*, 113693. [CrossRef] [PubMed]
15. Cardenia, V.; Toschi, T.G.; Scappini, S.; Rubino, R.C.; Rodriguez-Estrada, M.T. Development and validation of a Fast gas chromatography/mass spectrometry method for the determination of cannabinoids in *Cannabis sativa* L. *J. Food Drug Anal.* **2018**, *26*, 1283–1292. [CrossRef] [PubMed]
16. Pellegrini, M.; Marchei, E.; Pacifici, R.; Pichini, S. A rapid and simple procedure for the determination of cannabinoids in hemp food products by gas chromatography-mass spectrometry. *J. Pharm. Biomed. Anal.* **2005**, *36*, 939–946. [CrossRef]
17. Oosterveer, M.H.; Koolman, A.H.; de Boer, P.T.; Bos, T.; Bleeker, A.; van Dijk, T.H.; Bloks, V.W.; Kuipers, F.; Sauer, P.J.; van Dijk, G. Resistance to diet-induced adiposity in cannabinoid receptor-1 deficient mice is not due to impaired adipocyte function. *Nutr. Metab.* **2011**, *8*, 93. [CrossRef]
18. Chang, R.C.; Thangavelu, C.S.; Joloya, E.M.; Kuo, A.; Li, Z.; Blumberg, B. Cannabidiol promotes adipogenesis of human and mouse mesenchymal stem cells via PPARγ by inducing lipogenesis but not lipolysis. *Biochem. Pharmacol.* **2022**, *197*, 114910. [CrossRef]
19. Roche, R.; Hoareau, L.; Bes-Houtmann, S.; Gonthier, M.-P.; Laborde, C.; Baron, J.-F.; Haffaf, Y.; Cesari, M.; Festy, F. Presence of the cannabinoid receptors, CB1 and CB2, in human omental and subcutaneous adipocytes. *Histochem. Cell Biol.* **2006**, *126*, 177–187. [CrossRef]
20. Tedesco, L.; Valerio, A.; Cervino, C.; Cardile, A.; Pagano, C.; Vettor, R.; Pasquali, R.; Carruba, M.O.; Marsicano, G.; Lutz, B.; et al. Cannabinoid type 1 receptor blockade promotes mitochondrial biogenesis through endothelial nitric oxide synthase expression in white adipocytes. *Diabetes* **2008**, *57*, 2028–2036. [CrossRef]
21. Bajzer, M.; Olivieri, M.; Haas, M.K.; Pfluger, P.T.; Magrisso, I.J.; Foster, M.T.; Tschöp, M.H.; Krawczewski-Carhuatanta, K.A.; Cota, D.; Obici, S. Cannabinoid receptor 1 (CB1) antagonism enhances glucose utilisation and activates brown adipose tissue in diet-induced obese mice. *Diabetologia* **2011**, *54*, 3121–3131. [CrossRef]
22. Rakotoarivelo, V.; Sihag, J.; Flamand, N. Role of the endocannabinoid system in the adipose tissue with focus on energy metabolism. *Cells* **2021**, *10*, 1279. [CrossRef] [PubMed]
23. Caterina, M.J.; Julius, D. The vanilloid receptor: A molecular gateway to the pain pathway. *Annu. Rev. Neurosci.* **2001**, *24*, 487–517. [CrossRef] [PubMed]
24. Premkumar, L.S.; Sikand, P. TRPV1: A target for next generation analgesics. *Curr. Neuropharmacol.* **2008**, *6*, 151–163. [CrossRef]
25. Christie, S.; Wittert, G.A.; Li, H.; Page, A.J. Involvement of TRPV1 channels in energy homeostasis. *Front. Endocrinol.* **2018**, *9*, 420. [CrossRef] [PubMed]
26. Hermann, H.; De Petrocellis, L.; Bisogno, T.; Schiano Moriello, A.; Lutz, B.; Di Marzo, V. Dual effect of cannabinoid CB 1 receptor stimulation on a vanilloid VR1 receptor-mediated response. *Cell. Mol. Life Sci.* **2003**, *60*, 607–616. [CrossRef] [PubMed]
27. Matsuda, L.A.; Lolait, S.J.; Brownstein, M.J.; Young, A.C.; Bonner, T.I. Structure of a cannabinoid receptor and functional expression of the cloned cDNA. *Nature* **1990**, *346*, 561–564. [CrossRef] [PubMed]
28. Premkumar, L.S.; Ahern, G.P. Induction of vanilloid receptor channel activity by protein kinase C. *Nature* **2000**, *408*, 985–990. [CrossRef] [PubMed]
29. Vellani, V.; Mapplebeck, S.; Moriondo, A.; Davis, J.B.; McNaughton, P.A. Protein kinase C activation potentiates gating of the vanilloid receptor VR1 by capsaicin, protons, heat and anandamide. *J. Physiol.* **2001**, *534*, 813–825. [CrossRef]
30. Mahmud, A.; Santha, P.; Paule, C.C.; Nagy, I. Cannabinoid 1 receptor activation inhibits transient receptor potential vanilloid type 1 receptor-mediated cationic influx into rat cultured primary sensory neurons. *Neuroscience* **2009**, *162*, 1202–1211. [CrossRef]
31. Sántha, P.; Jenes, Á.; Somogyi, C.; Nagy, I. The endogenous cannabinoid anandamide inhibits transient receptor potential vanilloid type 1 receptor-mediated currents in rat cultured primary sensory neurons. *Acta Physiol. Hung.* **2010**, *97*, 149–158. [CrossRef]
32. Della Pietra, A.; Giniatullin, R.; Savinainen, J.R. Distinct activity of endocannabinoid-hydrolyzing enzymes MAGL and FAAH in key regions of peripheral and central nervous system implicated in migraine. *Int. J. Mol. Sci.* **2021**, *22*, 1204. [CrossRef] [PubMed]
33. Di Marzo, V.; Maccarrone, M. FAAH and anandamide: Is 2-AG really the odd one out? *Trends Pharmacol. Sci.* **2008**, *29*, 229–233. [CrossRef] [PubMed]
34. Matias, I.; Carta, G.; Murru, E.; Petrosino, S.; Banni, S.; Marzo, V.D. Effect of polyunsaturated fatty acids on endocannabinoid and N-acyl-ethanolamine levels in mouse adipocytes. *Biochim. Biophys. Acta Mol. Cell Biol. Lipids* **2008**, *1781*, 52–60. [CrossRef]
35. Koolman, A.H. *The Role of the Endocannabinoid System in the Regulation of Energy Balance*; University of Groningen: Groningen, The Netherlands, 2010.

36. Moreno-Navarrete, J.M.; Catalán, V.; Whyte, L.; Díaz-Arteaga, A.; Vázquez-Martínez, R.; Rotellar, F.; Guzmán, R.; Gómez-Ambrosi, J.; Pulido, M.R.; Russell, W.R.; et al. The L-α-lysophosphatidylinositol/GPR55 system and its potential role in human obesity. *Diabetes* **2012**, *61*, 281–291. [CrossRef]
37. Choi, J.W.; Lee, C.-W.; Chun, J. Biological roles of lysophospholipid receptors revealed by genetic null mice: An update. *Biochim. Biophys. Acta* **2008**, *1781*, 531–539. [CrossRef] [PubMed]
38. Brighenti, V.; Pellati, F.; Steinbach, M.; Maran, D.; Benvenuti, S. Development of a new extraction technique and HPLC method for the analysis of non-psychoactive cannabinoids in fibre-type *Cannabis sativa* L. (hemp). *J. Pharm. Biomed. Anal.* **2017**, *143*, 228–236. [CrossRef] [PubMed]
39. Devi, V.; Khanam, S. Comparative study of different extraction processes for hemp (*Cannabis sativa*) seed oil considering physical, chemical and industrial-scale economic aspects. *J. Clean. Prod.* **2019**, *207*, 645–657. [CrossRef]
40. Mandrioli, M.; Tura, M.; Scotti, S.; Gallina Toschi, T. Fast detection of 10 cannabinoids by RP-HPLC-UV method in *Cannabis sativa* L. *Molecules* **2019**, *24*, 2113. [CrossRef]
41. PromoCell. Preadipocyte/Adipocyte Media Instruction Manual. PromoCell. Available online: https://promocell.com/wp-content/uploads/product-information/manual/C-27436.pdf (accessed on 8 February 2024).

Disclaimer/Publisher's Note: The statements, opinions and data contained in all publications are solely those of the individual author(s) and contributor(s) and not of MDPI and/or the editor(s). MDPI and/or the editor(s) disclaim responsibility for any injury to people or property resulting from any ideas, methods, instructions or products referred to in the content.

International Journal of
Molecular Sciences

MDPI

Article

Dietary Methionine Restriction Improves Gut Health and Alters the Plasma Metabolomic Profile in Rats by Modulating the Composition of the Gut Microbiota

Mei Yang [1,2,†], Qian Xie [1,2,†], Yintao Xiao [1,2], Minglong Xia [1,2], Jiashun Chen [1,2], Bi-E Tan [1,2,*] and Yulong Yin [2,3,*]

[1] Key Laboratory of Hunan Province for the Products Quality Regulation of Livestock and Poultry, College of Animal Science and Technology, Hunan Agricultural University, Changsha 410128, China; aym1223@163.com (M.Y.)
[2] Yuelushan Laboratory, Changsha 410128, China
[3] Key Laboratory of Agro-Ecological Processes in Subtropical Region, National Engineering Laboratory for Pollution Control and Waste Utilization in Livestock and Poultry Production, Institute of Subtropical Agriculture, Chinese Academy of Sciences, Changsha 410125, China
* Correspondence: bietan@hunau.edu.cn (B.-E.T.); yinyulong@isa.ac.cn (Y.Y.)
† These authors contributed equally to this work.

Abstract: Dietary methionine restriction (MetR) offers an integrated set of beneficial health effects, including delaying aging, extending health span, preventing fat accumulation, and reducing oxidative stress. This study aimed to investigate whether MetR exerts entero-protective effects by modulating intestinal flora, and the effect of MetR on plasma metabolites in rats. Rats were fed diets containing 0.86% methionine (CON group) and 0.17% methionine (MetR group) for 6 weeks. Several indicators of inflammation, gut microbiota, plasma metabolites, and intestinal barrier function were measured. 16S rRNA gene sequencing was used to analyze the cecal microbiota. The MetR diet reduced the plasma and colonic inflammatory factor levels. The MetR diet significantly improved intestinal barrier function by increasing the mRNA expression of tight junction proteins, such as zonula occludens (*ZO*)-1, claudin-3, and claudin-5. In addition, MetR significantly increased the levels of short-chain fatty acids (SCFAs) by increasing the abundance of SCFAs-producing *Erysipclotxichaceae* and *Clostridium_sensu_stricto_1* and decreasing the abundance of pro-inflammatory bacteria *Proteobacteria* and *Escherichia-Shigella*. Furthermore, MetR reduced the plasma levels of taurochenodeoxycholate-7-sulfate, taurocholic acid, and tauro-ursodeoxycholic acid. Correlation analysis identified that colonic acetate, total colonic SCFAs, 8-acetylegelolide, collettiside I, 6-methyladenine, and cholic acid glucuronide showed a significant positive correlation with *Clostridium_sensu_stricto_1* abundance but a significant negative correlation with *Escherichia-Shigella* and *Enterococcus* abundance. MetR improved gut health and altered the plasma metabolic profile by regulating the gut microbiota in rats.

Keywords: methionine restriction; intestinal barrier; *ZO-1*; SCFAs; BAs

1. Introduction

Nutrition exerts profound effects on health, and dietary interventions are commonly used to treat metabolic disorders. Methionine is a sulfur-containing essential amino acid that is required for normal growth and development [1]. Methionine restriction (MetR) is gaining popularity due to its several health benefits, including improved stress resistance, increased longevity, and inhibition of fat deposition in experimental animals [2,3]. More specifically, both 80 and 40% MetR diets are associated with lifespan extension and metabolic health from yeast to rodents, which may be partially mediated through a reduction in oxidative stress [4]. MetR improves hepatic steatosis and delays the development of non-alcoholic steatohepatitis through antioxidant effects and alteration in lipid composition in obese mice [5,6]. In a recent study, MetR reduced liver fat content by regulating fatty acid oxidation and lipid catabolism in high-fat-fed mice [7].

The diverse and dynamic microbial community contributes to maintaining healthy gut homeostasis [8]. The integrity of the intestinal barrier, which is supported by the gut microbiota, is essential for maintaining the stability of the body [9]. Disruption and depletion of the gut microbiota may therefore affect the gut barrier and cause persistent systemic inflammation [10]. Microbiome–host interactions and microbial metabolites are associated with the capacity to produce inflammatory factors [11]. As end products of carbohydrates fermented by the gut microbiota, short-chain fatty acids (SCFAs) are involved in ameliorating host metabolic syndromes [12].

Research has highlighted the role of metabolites in mediating the interaction between the gut microbiota and the host diet. For example, bile acids (BAs) play a critical role in modulating host inflammation and the gut barrier [12,13]. In addition to their well-established role in lipid metabolism and maintaining cholesterol homeostasis, BAs also act as signaling molecules that reshape the composition of the gut microbiota through BA receptors, such as the farnesoid X receptor (FXR), which are involved in entero-protection in order to inhibit bacterial overgrowth and mucosal injury in the ileum [14].

Although previous studies have speculated that MetR exerts beneficial effects on the gut by improving epithelial barrier function in normal rats [15], the role and mechanism of the gut microbiota, and especially its metabolites, on gut health in dietary MetR intervention require further research. Therefore, we hypothesized that MetR plays a role in gut health and investigate whether the effects of MetR on plasma metabolomics are related to the modulation of the gut microbiota composition. The aim of this study was to analyze the effect of MetR diet on gut health in rats using 16S rRNA sequencing combined with plasma metabolomics. We sought to identify plasma metabolites that were associated with the MetR dietary supplements, including taurine-conjugated BAs. We also determined inflammatory cytokines, intestinal tight junction proteins, and SCFAs to investigate the effects of MetR on the plasma metabolome and to identify underlying mechanisms for maintaining gut health. The present study may contribute to the provision of new therapeutic strategies from the perspective of gut microbiota.

2. Results

2.1. Effects of MetR on Plasma LpS, D-Lactate, DAO, and Cytokine Levels

The plasma level of D-lactate was significantly reduced in rats in the MetR group compared to those in the CON group ($p < 0.05$) (Figure 1B). In addition, the LPS and DAO level in the plasma were not significantly different between the CON group and MetR group ($p > 0.05$, Figure 1A,C). Furthermore, MetR significantly decreased the TNF-α level relative to the control rat ($p < 0.05$) (Figure 1D). There were no significant differences in the plasma levels of IL-1β, IL-2, IL-4, IL-6, and IL-12 between the MetR and CON groups ($p > 0.05$, Figure 1D).

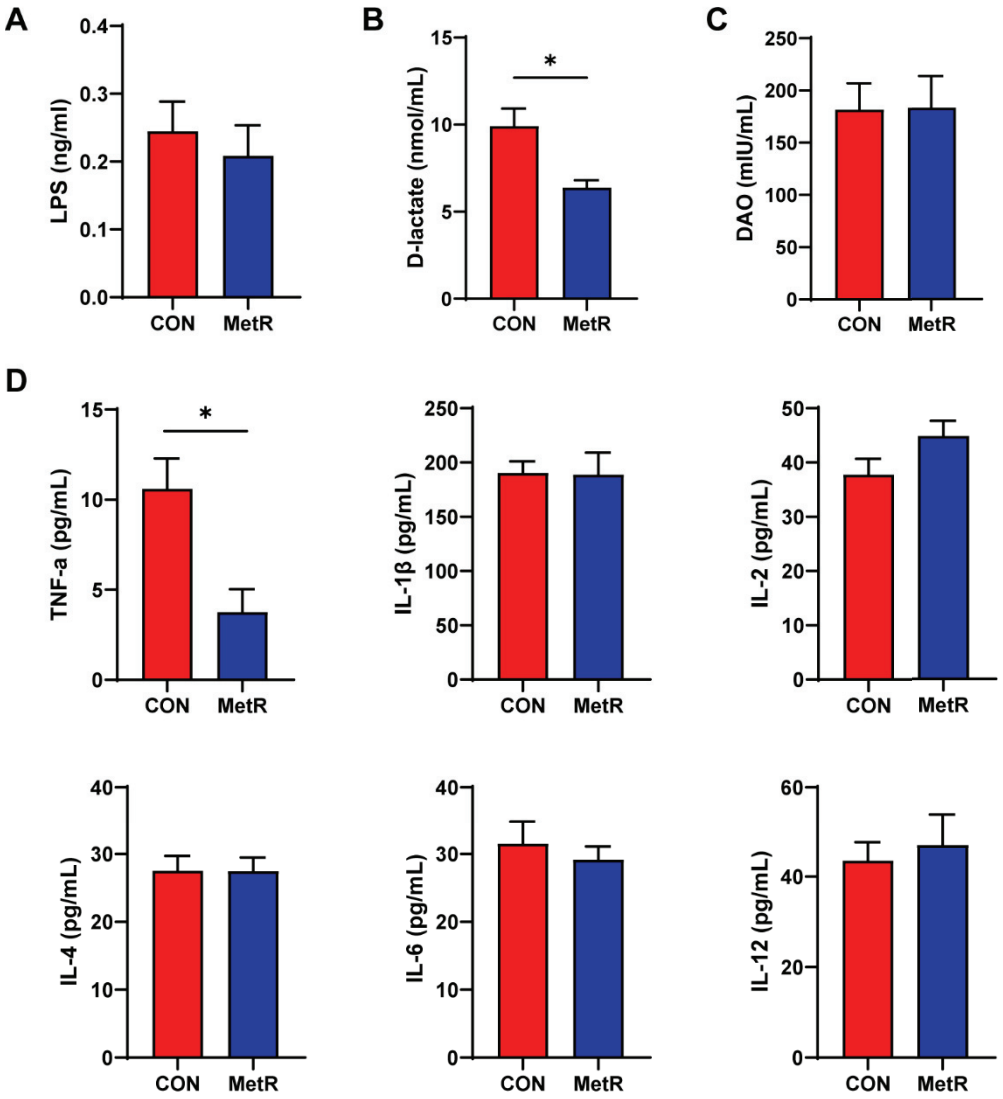


Figure 1. The plasma (**A**) LPS, (**B**) DAO, (**C**) D-lactate, (**D**) TNF-α, IL-1β, IL-2, IL-4, IL-6, and IL-12 levels in the rat. Data are expressed as the mean ± SEM for $n = 10$, * $p < 0.05$ versus CON.

2.2. Effects of MetR on Colonic Cytokine Levels, Barrier Function, and the Morphological Structure of the Colon

The cytokine levels in the colon are shown in Figure 2A. The levels of TNF-α, IL-2, IL-6, and IL-12 were significantly decreased in the MetR group compared to the CON group ($p < 0.05$). The qRT–PCR analysis revealed an increase in the abundance of zonula occludens (*ZO*)-1, claudin-3, and claudin-5 in colonic samples from rats in the MetR group relative to those in the CON group ($p < 0.05$) (Figure 2B). However, no significant changes in the mRNA expression of occludin and claudin-1 were observed in the colon of rats in the MetR group. Representative photo-micrographs of the H and E-stained and PAS-stained colon tissues are shown in Figure 3A. Goblet cell in MetR group was significantly higher than that in CON group ($p < 0.05$) (Figure 3B). Similarly, MetR significantly upregulated the protein expression of *ZO-1* compared to the CON group ($p < 0.05$) (Figure 3C,D).

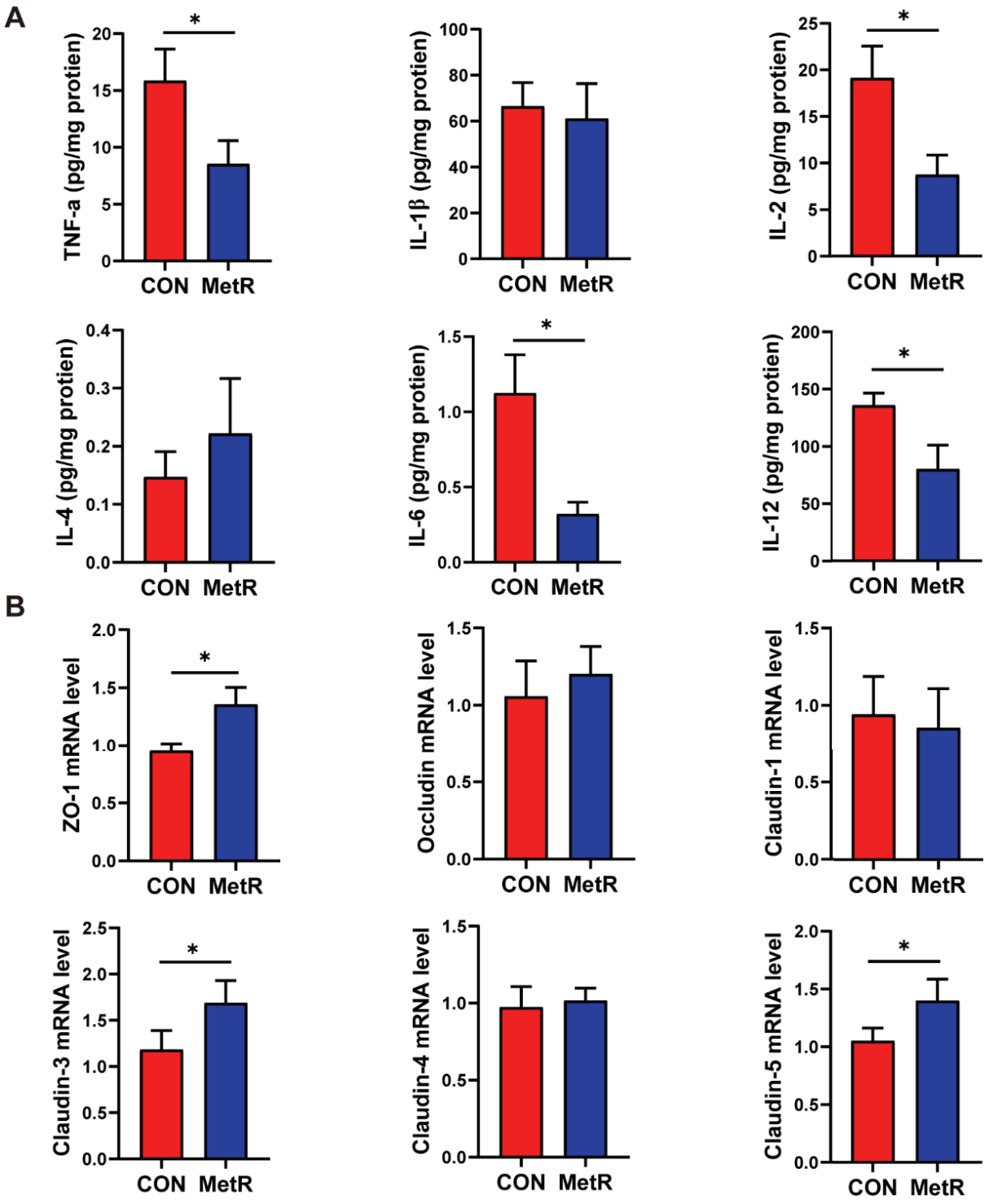


Figure 2. (**A**) Inflammatory factors and (**B**) mRNA expression levels of markers of tight junction proteins on the colon tissue. Data are expressed as the mean ± SEM for $n = 10$, * $p < 0.05$ versus CON.

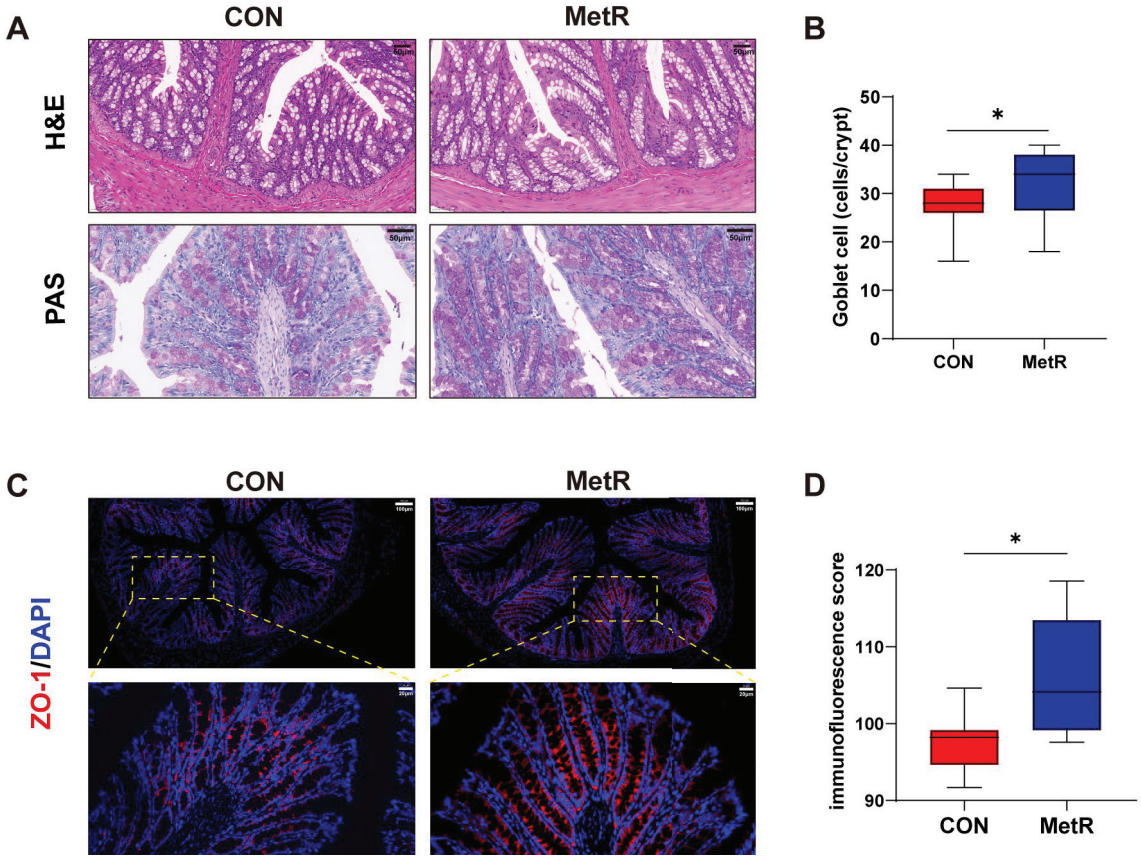


Figure 3. (**A**) Representative images of colon H and E and PAS staining. (**B**) The goblet cell numbers per crypt. (**C**) Representative immunofluorescence images of colonic sections stained with ZO-1 antibody. The dashed rectangle shows the image below with higher magnification. (**D**) Immunofluorescence score. Data are expressed as the mean ± SEM for $n = 10$, * $p < 0.05$ versus CON.

2.3. Effects of MetR on Cecal Microbiota

The results of the common alpha-diversity analysis (Sob index, Shannon index, Simpson index, Ace index, Chao index, and Coverage index) are shown in Figure 4A. The Simpson index of rats in the MetR group was significantly decreased relative to that of rats in the CON group ($p < 0.05$, Figure 4A). Moreover, MetR administration tended to restore the reduction of the ACE index, but the increase did not reach statistical difference ($p > 0.05$, Figure 4A). We found 296 common OTUs among two groups, while the number of OTUs, about 153, shared by MetR group was higher than that in CON group, with only 41 OTUs (Figure 4C). The Bray-Curtis distance-based PCoA and cluster tree revealed that the CON and MetR group exhibited a distinct clustering of microbiota composition (Figure 4B,D).

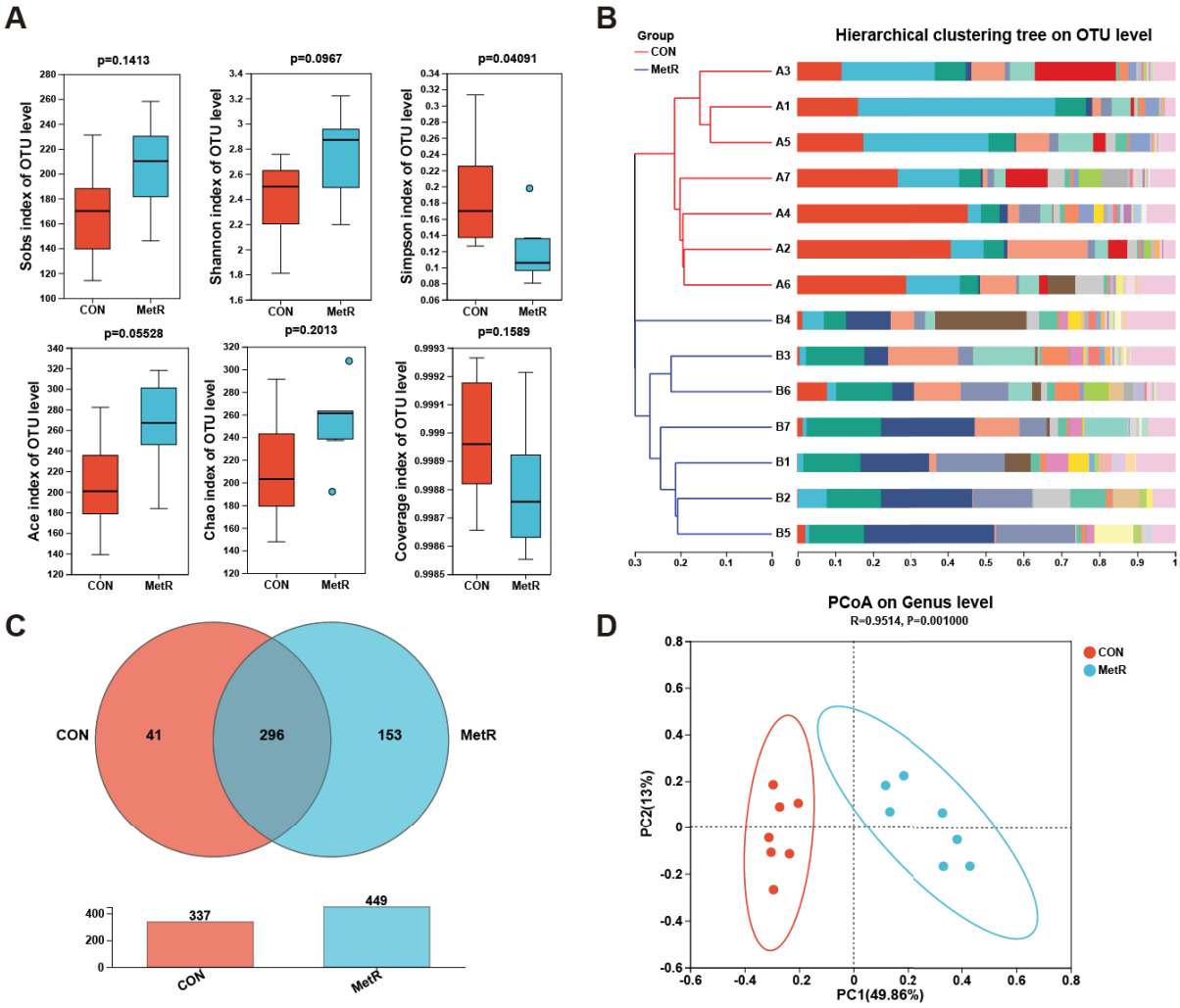


Figure 4. (**A**) Community diversity and richness among CON and MetR group. (**B**) Different colors in the figure represent samples in different groups. The degree of similarity between samples is reflected by the level of aggregation in the graph. (**C**) Venn diagram showing shared and unique OTUs among the two groups. (**D**) PCoA of the bacterial community structure among CON and MetR group. PCoA score plots showed significantly separated clusters between CON and MetR group. Data are expressed as the mean ± SEM for $n = 7$.

The bacterial sequences of cecal contents from the two experimental groups were examined at the phylum level. Based on the relative abundance of gut microbiota, the top five phyla are displayed (Figure 5A). The phylum level analysis showed that MetR feeding resulted in a significant decrease in the relative abundance of *Proteobacteria* and a significant increase in that of *Firmicutes* ($p < 0.05$). To further investigate the differences, an order-level analysis was performed. As shown in Figure 5B, the MetR diet markedly decreased the relative abundance of *Enterobacteriaceae* and *Enterococcaceae* but increased the relative abundance of *Erysipclotxichaceae* ($p < 0.05$). In addition, the MetR diet significantly decreased the relative abundance of *Escherichia-Shigella* and *Enterococcus* but increased the relative abundance of *Clostridium_sensu_stricto_1* at the genus level ($p < 0.05$) (Figure 5C).

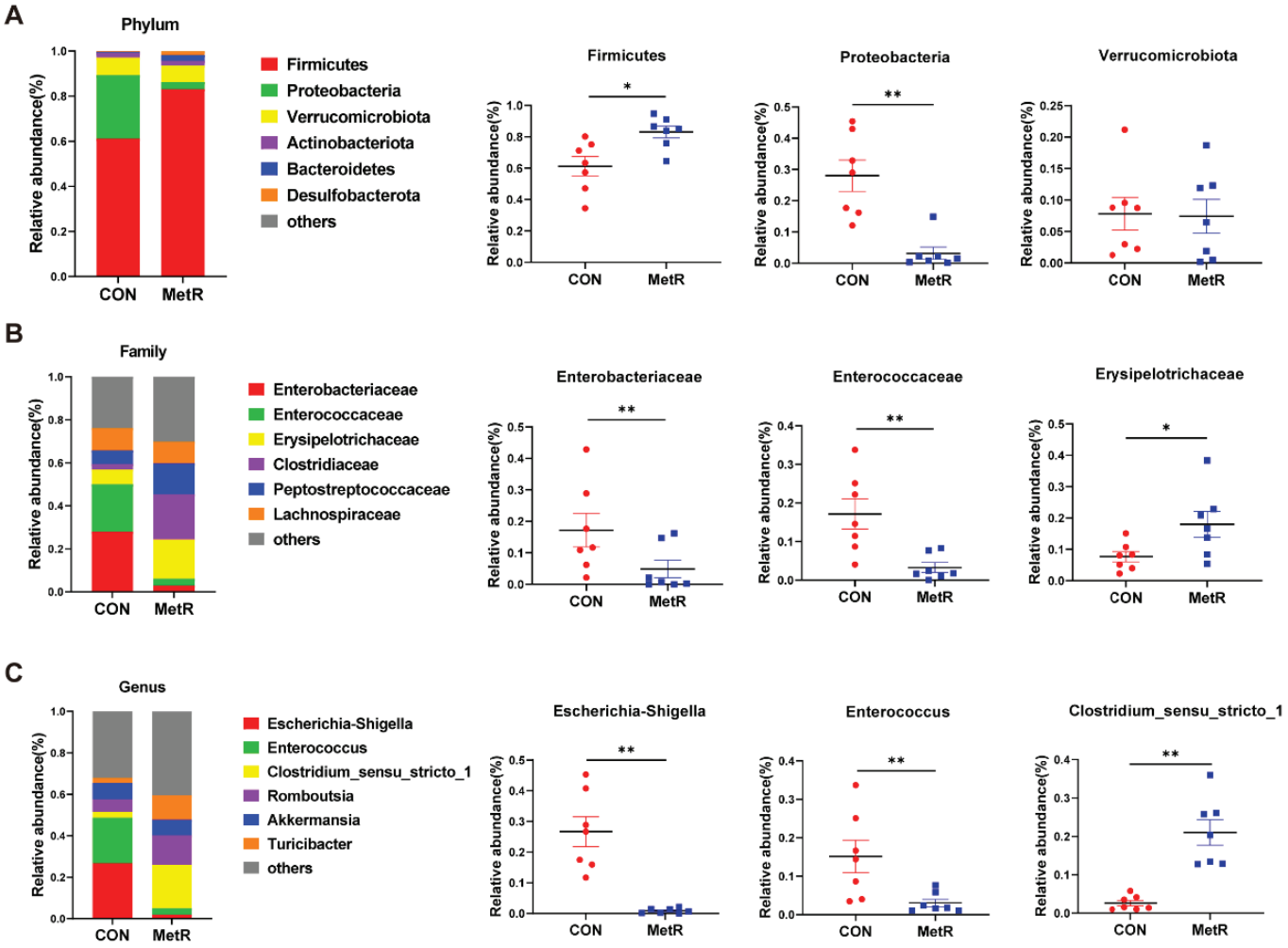


Figure 5. Microbial composition at the (**A**) phylum level, (**B**) family level, and (**C**) genus level. Each bar represents the relative abundance of each bacterial taxa of rats. Data are expressed as the mean ± SEM for $n = 7$, * $p < 0.05$, ** $p < 0.01$ versus CON.

2.4. Effects of MetR on Gut Microbiota and Cecal, Colon, and Fecal SCFA Levels

The abundances of Kyoto Encyclopedia of Genes and Genome (KEGG) pathways in each group were predicted using PICRUSt ($p < 0.01$, Figure 6A). Notably, the biosynthesis of amino acids and secondary metabolites was significantly enriched in tissues from rats in the MetR group relative to rats in the CON group (Figure 6A). In addition, other metabolic pathways, such as ABC transporters and microbial metabolism in different environments, were significantly upregulated in the CON group but downregulated in the MetR group. Figure 6B shows the levels of SCFAs in cecal, colonic, and fecal contents. The concentrations of acetate and total SCFA were significantly higher in the MetR group than in the CON group ($p < 0.05$). In particular, the concentrations of propionate and valerate in the colonic contents showed a notable increase in the MetR group compared to the CON group ($p < 0.05$, Figure 6B).

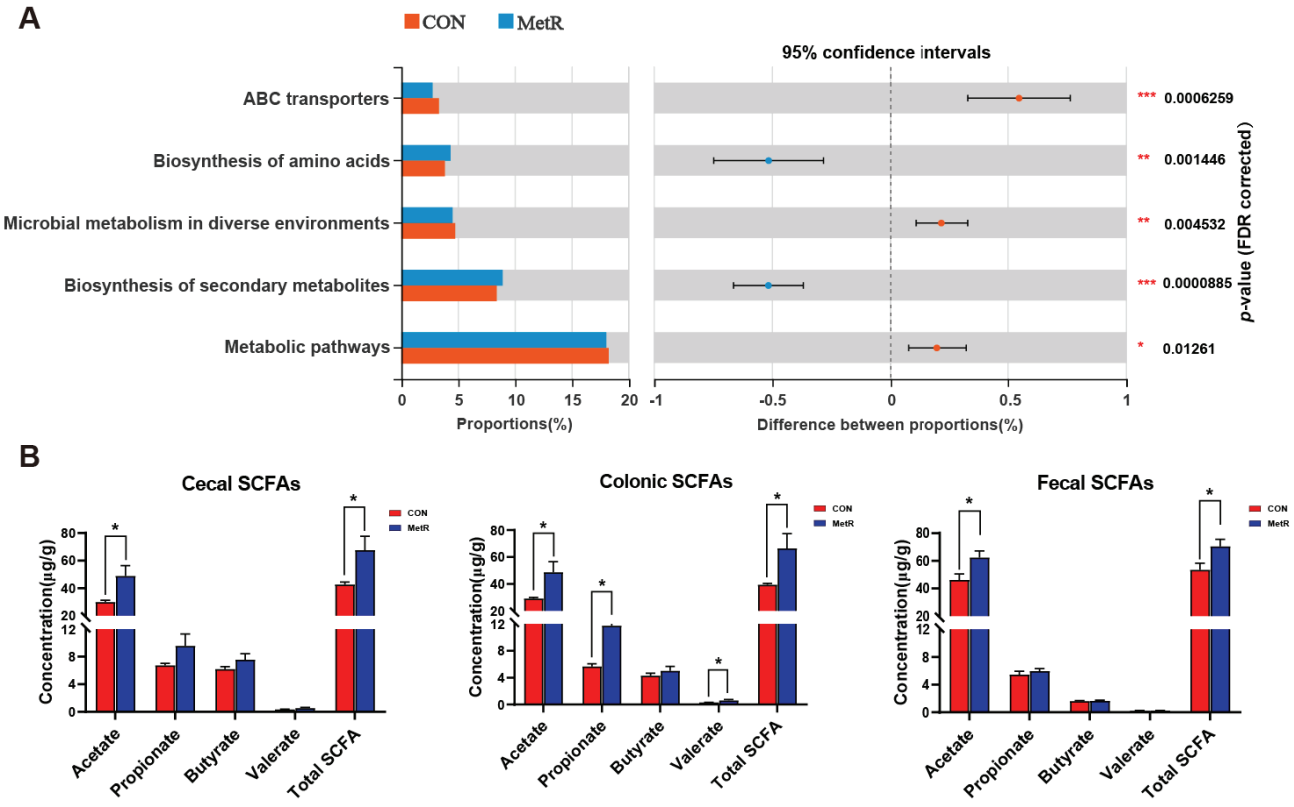


Figure 6. (**A**) Inferred metabolic functions of cecum microbiota by PICRUSt analysis among the two groups. (**B**) Concentrations of SCFAs in cecal content, colon content and fecal content. Data are expressed as the mean ± SEM for $n = 10$, * $p < 0.05$, ** $p < 0.01$, *** $p < 0.001$ versus CON.

2.5. Effects of MetR on Plasma Metabolome

A total of 149 metabolites were identified in the rat plasma, among which 61 were upregulated and 88 were downregulated (Figure 7A). A supervised OPLS-DA model (R2 = 0.996, Q2 = 0.916, $p < 0.05$) showed a robust separation of the diet groups as visualized by the score plot (Figure 7B). The KEGG databases were used to establish the metabolic pathways, which included glycine, serine, and threonine metabolism, primary bile acid biosynthesis, and bile secretion (Figure 7C). A total of 30 metabolites had VIP > 1, suggesting that they contribute to the discrimination of the groups (Figure 8A). The levels of 8-acetylegelolide, collettiside I, cholic acid glucuronide, 6-methyladenine, and cholic acid glucuronide were significantly increased in the MetR group relative to the CON group ($p < 0.01$, Figure 8B). In addition, the levels of taurochenodeoxycholate-7-sulfate, taurocholic acid (TCA), tauro-ursodeoxycholic acid (TUDCA), and 10-acetyl-3,7-dihydroxyphenoxazine were markedly reduced in the MetR group relative to the CON group ($p < 0.01$, Figure 8B).

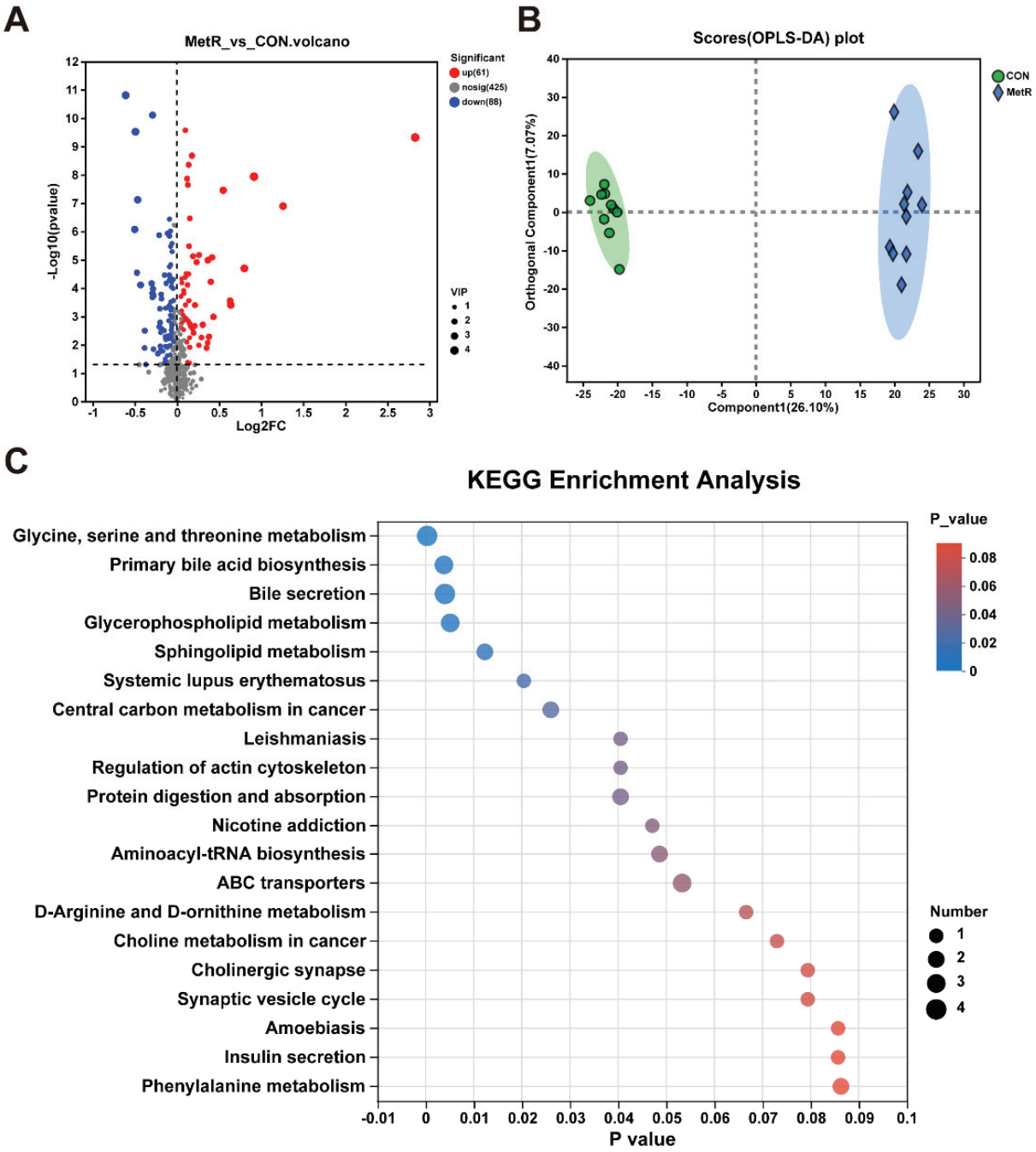


Figure 7. (**A**) Volcano plot for the CON and MetR groups, where each point represents a metabolite. Differentially expressed metabolites in combined CON and MetR (|log2 (Fold Change)| > 1 and nominal $p < 0.05$). Red dots represent upregulated metabolites; blue dots represent downregulated metabolites; and gray dots indicate non-significant differences. (**B**) Scatter plot of scores from OPLS-DA of the CON and MetR groups. (**C**) KEGG pathways enriched in the MetR group compared to the CON group.

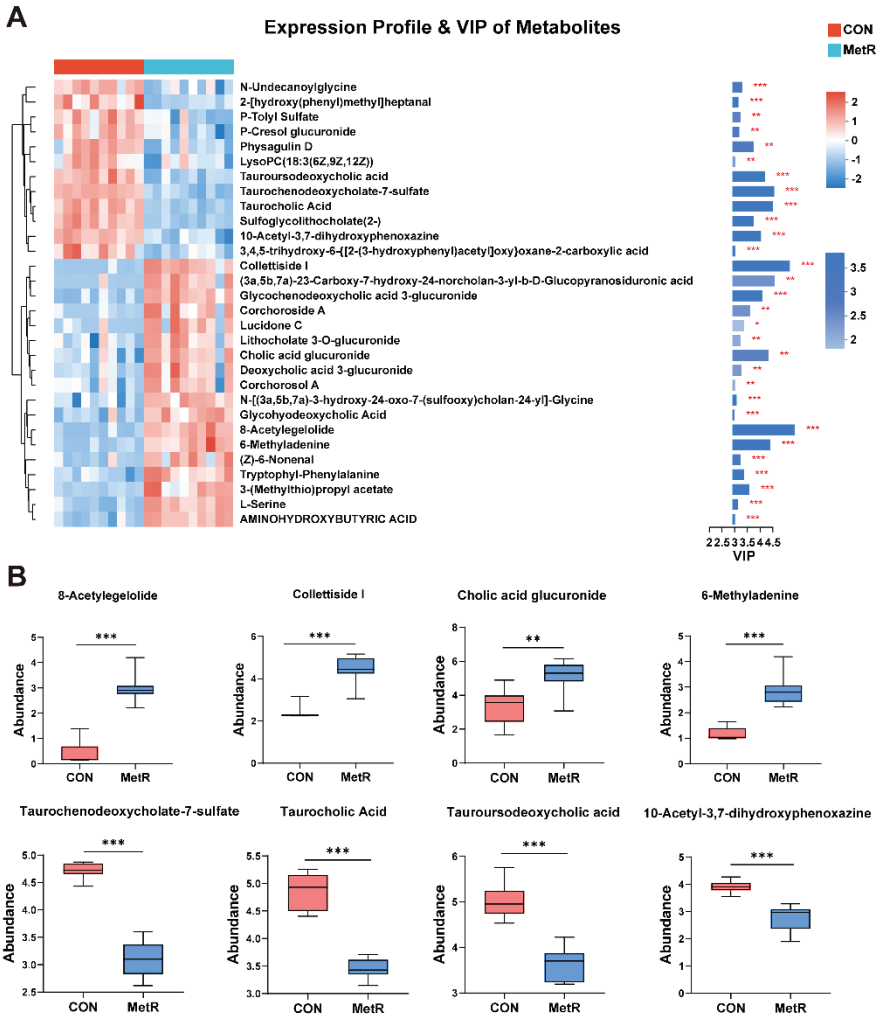


Figure 8. (**A**) Heatmap showing normalized values of 30 metabolites that were differentially abundant among the CON and MetR groups. The normalized abundance values are depicted from red to green, where red represents the highest abundance and green represents the lowest abundance. The dendrogram shows the distances of the metabolites based on their relative abundances. (**B**) The identified and change trend of the potential biomarkers of rat intervened by Wilcox test, unpaired. Data are expressed as the mean ± SEM for $n = 10$, * $p < 0.05$, ** $p < 0.01$, *** $p < 0.001$ versus CON.

2.6. Spearman's Correlation Analysis between Plasma Metabolites, Colonic SCFAs, and Gut Microbiota

The correlations between plasma metabolites, colonic SCFAs and gut microbiota were evaluated by Spearman's correlation analysis (Figure 9). The levels of colonic acetate, total colonic SCFA, 8-acetylegelolide, collettiside I, 6-methyladenine, and cholic acid glucuronide were positively correlated with the abundance of *Clostridium_sensu_stricto_1* but negatively correlated with the abundance of *Escherichia-Shigella* and *Enterococcus*. Furthermore, the levels of taurochenodeoxycholate-7-sulfate, TCA, TUDCA, and 10-acetyl-3,7-dihydroxyphenoxazine were positively correlated with the abundance of *Escherichia-Shigella* and *Enterococcus* but positively correlated with the abundance of *Clostridium_sensu_stricto_1* and *Turicibacter*.

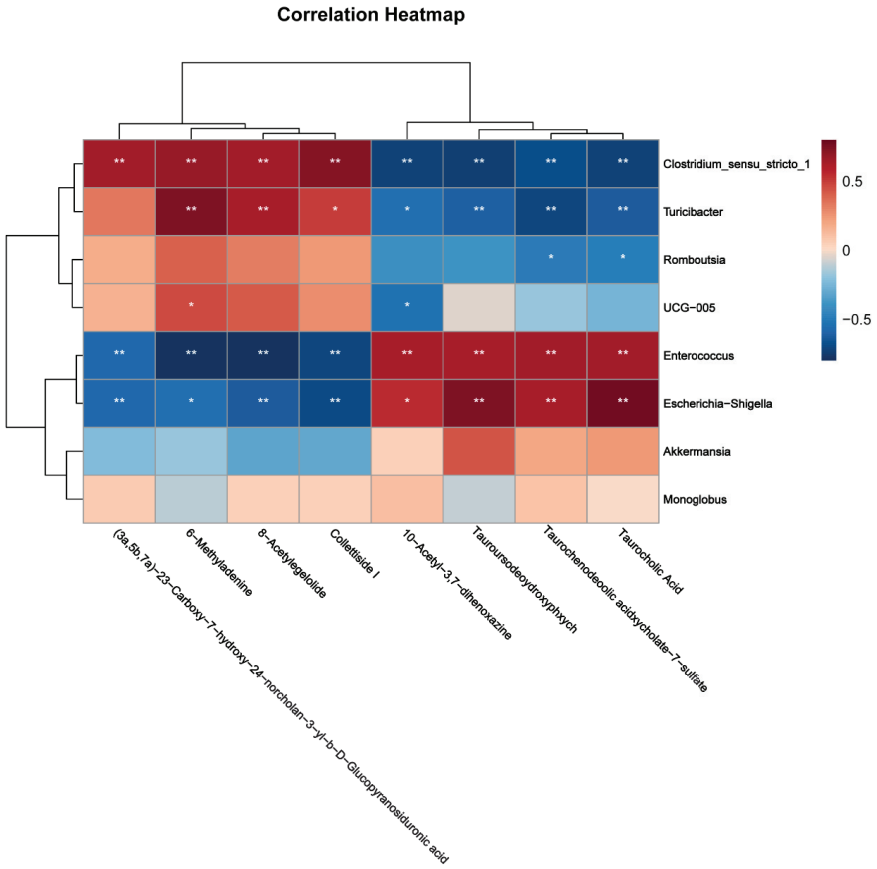


Figure 9. Heat map of the relationship between plasma metabolites, colonic SCFAs and gut microbiota. Red squares represent significant positive correlations (R > 0.5, $p < 0.05$), blue squares represent significant negative correlations (R < −0.5, $p < 0.05$), and white squares represent non-significant correlations. * $p < 0.05$, ** $p < 0.01$.

3. Discussion

There is overwhelming evidence consistently demonstrating that the MetR diet has many beneficial health effects, including reducing hepatic steatosis [6], ameliorating fat accumulation [16], preventing systemic inflammation [17], and regulating energy and protein homeostasis [7] in high-fat-fed mice. Dietary MetR prevents cognitive impairment in D-galactose-induced aging mice and extends lifespan in progeroid mice [3,18]. In this study, MetR diet increased the abundance of *Clostridium_sensu_stricto_1*, resulting in a considerable upregulation of SCFAs and downregulation of the plasma taurine-conjugated bile acids, like TCA and TUDCA. Moreover, SCFAs facilitated health benefits in the rats, including decreasing systemic inflammation and enhancing the integrity of the gut barrier.

Dietary MetR has been used as a research model for preventing and treating obesity-related metabolic diseases. The gut epithelial barrier is an essential barrier between the environment and the internal milieu of the body, limiting the passage of pathogens and toxins [19]. The disruption of the integrity of the gut barrier allows the passage of bacterial products, leading to the production of pro-inflammatory cytokines [20]. In the current study, we found that MetR reduced the levels of serum and colonic pro-inflammatory factors in rats. This finding may be related to the enhancement of tight junction proteins by MetR. The gut microbiota plays a critical role in gut growth, nutrient absorption, and host health [21]. Higher Simpson index values indicate lower community diversity [22]. The MetR group had the richest microbiota species diversity compared to the CON group, as evidenced by the reduced Simpson indices. Our results indicate that MetR selectively decreased the abundance of *Proteobacteria*. Several studies have shown that *Proteobacteria* are closely correlated with inflammatory bowel disease [23,24]. The integrity of the

gut barrier plays a critical role in maintaining gut homeostasis by ensuring a complex crosstalk between gut microbes and the host [25]. Previous studies have shown that pro-inflammatory cytokines facilitate intestinal barrier damage and invasion of pathogens [26]. Ren et al. [27] showed that MetR can improve gut barrier function in aged mice by alleviating the oscillations of inflammation-related microbes. In general, an increase in the relative abundance of *Enterobacteriaceae* causes inflammatory damage to the gut epithelium barrier [28]. Our data showed that the levels of colonic D-lactate, TNF-α, IL-2, IL-6, and IL-12 in the MetR group were significantly lower than those in the CON group. Consistent with this result, MetR decreased the abundance of *Enterobacteriaceae*, *Enterococcaceae*, and *Escherichia-Shigella*; this also corresponded with an increase in *ZO-1*, claudin-3, and claudin-5 mRNA expression [29,30].

SCFAs are important energy sources for intestinal epithelial cells, allowing them to modulate the gut barrier function and host metabolism [12]. The present work revealed that MetR effectively elevated the concentration of SCFAs (acetate, propionate, and valerate) and improved enteral homeostasis. *Erysipclotxichaceae, Bacteroides, Lactobacillus*, and *Clostridium_sensu_stricto_1* consist of microbes that produce SCFAs, which are beneficial for preventing inflammation [31,32]. Moreover, *Proteobacteria* and *Escherichia-Shigella* are associated with microbiota inflammatory properties [33,34]. In this study, we found that MetR selectively increased the abundance of representative SCFAs producers (*Erysipclotxichaceae* and *Clostridium_sensu_stricto_1*), along with enhanced levels of SCFAs in the cecal, colonic, and fecal contents [35,36], indicating that MetR maintained intestinal homeostasis by promoting the growth of beneficial gut bacteria. What is more interesting is that colonic acetate and total SCFAs levels were found to positively correlate with relative *Clostridium_sensu_stricto_1* abundance. This is consistent with a previous study in which MetR increased the abundance of SCFA-producing bacteria, decreased the abundance of inflammation-related bacteria, and improved the intestinal mucosal immune barrier in a time-dependent manner [16]. Furthermore, PICRUSt indicates MetR may have mediated amino acid and secondary metabolite biosynthesis in the gut microbiota. These results suggested that MetR supplementation effectively increased the abundance of SCFA-producing bacteria and increased amino acid biosynthesis in the gut microbiota.

The metabolomic profiling revealed that eight plasma metabolites associated with the MetR diet were mainly involved in glycine–serine–threonine metabolism, primary BA biosynthesis, and bile secretion. This is consistent with the findings of Aon et al. (2020), who reported that glycine–serine–threonine metabolism influences longevity and related life-sustaining mechanisms [37]. Furthermore, BAs promote health and longevity in various organisms [38]. In our study, the levels of taurochenodeoxycholate-7-sulfate, TCA, and TUDCA were reduced and negatively correlated with the abundance of *Clostridium_sensu_stricto_1*. Excess taurine-conjugated BAs in the serum, particularly TCA, TUDCA, and tauro-chenodeoxycholic acid (TCDCA), may exacerbate the progression of non-alcoholic steatohepatitis and the severity of drug-induced liver injury [39–41]; this supports our observations in this study, indicating that the reduction in the levels of taurine-conjugated BAs might represent a means by which MetR exerts its hepato-protective effect. Moreover, TCA and TCDCA downregulate the expression of hepatic FXR and are positively associated with pro-inflammatory cytokines, such as TNF-α [42,43], supporting our observation in this study. It has been reported that bile salt hydrolase-producing bacteria such as *Clostridium_sensu_stricto_1* and *Bacteroidetes* hydrolyze taurine- and glycine-conjugated BAs to unconjugated free forms, which can be further converted to secondary BAs [40,44]. Therefore, the increased abundance of *Clostridium_sensu_stricto_1* and *Bacteroidetes* in the cecal contents may account for the depleted taurine-conjugated BAs in the MetR-fed rats.

However, the exact mechanism by which MetR affects serum BAs levels and improves gut health remains to be elucidated.

4. Methods and Materials

4.1. Animal Experiment

The animal protocols were carried out under the guidelines of animal care and were approved by the Institutional Animal Care and Use Committee of Hunan Agricultural University (approval number: CACAHU 2022-0426). Seven-week-old male Sprague–Dawley rats were purchased from Tianqin Biotechnology (Changsha, China) and were individually housed in a conventional animal facility that was maintained at 22 ± 2 °C and 55 ± 10% relative humidity with a 12-h light/dark photoperiod. After one week of acclimation, all the rats were randomly divided into two experimental diet groups: (1) the control group fed with the normal diet (CON, 0.86% methionine); (2) methionine-restricted diet group (MetR, 0.17% methionine). The composition and nutritional value of the diets are presented in Table S1 as previously described [15,45,46].

4.2. Sample Collection and Preparation

After six weeks of experimental administration, blood samples were collected from the retro-orbital of each rat under fasting conditions and centrifuged at 3500× *g* at 4 °C for 10 min. The separated plasma was then stored in a refrigerator at −80 °C. The contents of the cecum of each rat were removed, snap-frozen in liquid nitrogen, and stored at −80 °C for subsequent 16S rRNA gene sequencing analysis. The contents of the colon and the fresh feces were collected for analysis.

4.3. Enzyme-Linked Immunosorbent Assay (ELISA)

The levels of lipopolysaccharide (LPS) and D-lactate in rat plasma were determined using the ELISA kit (Jiangsu Meimian Industrial Co., Ltd., Yancheng, China). The concentrations of tumor necrosis factor-alpha (TNF-α), interleukin-1 beta (IL-1β), interleukin-2 (IL-2), interleukin-4 (IL-4), interleukin-6 (IL-6), and interleukin-12 (IL-12) were quantified using enzyme-linked immunosorbent assay kits (CSB-E11987r, CSB-E08055r, CSB-E08055r, CSB-E04635r, CSB-E04635r, CSB-E07364r, CUSABIO, Wuhan, China, https://www.cusabio.com/, 4 June 2022) according to the manufacturer's instructions. The protein concentration of the colon tissues was measured using the Omni-Easy™Instant BCA Protein Assay Kit (ZJ102, Epizyme Biotech; Shanghai; China).

4.4. Gene Expression

Total RNA was isolated from colon tissues using RNAiso Plus (Cat # 9109, Takara Biomedical Technology (Beijing) Co., Ltd., Beijing, China) according to the manufacturer's instructions. The concentration of each RNA sample was determined using Nanodrop One (Thermo Fisher Scientific, Waltham, MA, USA). Genomic DNA contamination was removed by incubating with the Evo *M-MLV* RT Kit with gDNA Clean for qPCR (AG11705) before reverse transcription. RT-qPCR was conducted using SYBR Green Premix Pro Taq HS qPCR Kit (AG11701, Accurate Biotechnology (Hunan) Co., Ltd., Changsha, China) by real-time PCR instrument (LightCycler480II, Roche, Germany). The relative expression levels of the target genes were calculated using the $2^{-\Delta\Delta Ct}$ method. GAPDH was used as the reference gene.

4.5. Histological Analysis

Colon tissues were fixed in 4% paraformaldehyde for 24 h, dehydrated using a gradient of ethanol and xylene, and finally embedded in paraffin. A microtome (Leica, RM2016, Vizna, Germany) was then used to make 4 μm sections that were subsequently dewaxed in xylene. The dewaxed sections were then rehydrated by lowering the concentration of ethanol before being stained with hematoxylin and eosin (H and E). Finally, the sections were dehydrated with gradient ethanol before dehydration with xylene. Carnoy's colonic tissues were stained with PAS according to the manufacturer's instructions (Servicebio, Wuhan, China). The sections were briefly stained with PAS dye solution for 10 to 15 min and then rinsed with distilled water. The slides were dehydrated with absolute ethyl

alcohol and xylene before image acquisition on an inverted fluorescence microscope (Axio Vert A1, Zeiss, Germany).

4.6. Immunofluorescence

Paraffin sections of colon tissue of 4 μm thickness were subjected to antigen extraction with citrate buffer (pH 6.0). Tissue sections were then incubated overnight at 4 °C with primary antibodies (Abcam, UK) against ZO-1 (1:200, ab221547). Next, sections were incubated with Alexa Fluor 488 conjugated secondary antibodies (1:100, Invitrogen, Life Technologies, Carlsbad, CA, USA) for 50 min at 37 °C. Samples were observed under an inverted fluorescence microscope (Axio Vert A1, Zeiss, Germany).

4.7. 16S rRNA Gene Sequencing Analysis

Microbial genomic DNA from cecal contents was extracted using the E.Z.N.A.® Soil DNA Kit (Omega Bio-tek, Norcross, GA, USA) according to the manufacturer's instructions. Total bacterial concentrations in each sample were measured using a qPCR assay that targets the V3–V4 hypervariable region of the 16S rRNA gene from the cecal microbiota was amplified using a forward primer (338F: 5′-ACTCCTACGGGAGGCAGCAG-3′) and a reverse primer (806R: 5′-GGACTACHVGGGTWTCTAAT-3′). The sequencing libraries of bacterial 16S rRNA genes were produced using NEXTFLEX® Rapid DNA-Seq Kit (Bio Scientific, Phoenix, AZ, USA) for high throughput sequencing. The sequencing was carried out at Majorbio Bio-Pharm Technology Co., Ltd. (Shanghai, China) on an Illumina MiSeq PE300 platform. The original DNA fragments were quality filtered and merged using fastp (version 0.20.0) and Flash (version 1.2.11). The sequence reads were classified into operational taxonomic units (OTUs) at 97% identity using Uparse (version 7.1). The RDP classifier (version 2.2) was used to classify and annotate each sequence, and a comparison was conducted against the Silva 16S rRNA database (v138) using a threshold of 70%.

4.8. Plasma Metabolomics Analysis

A 50-μL aliquot of plasma in an Eppendorf tube was mixed with a pre-cooled methanol/water solution (4:1, v/v). The mixture was vortexed for 5 min and centrifuged at 12,000× g at 4 °C for 10 min, after which the supernatant was carefully transferred into a new Eppendorf tube and thoroughly dried using a vacuum centrifugal concentrator (SPD130P1, Thermo Fisher, Waltham, MA, USA). A volume of 200 μL of acetonitrile: water (1:1) was added to completely dissolve the dried supernatant. After centrifugation at 12,000× g at 4 °C for 5 min, the sample was carefully transferred into sample vials for combined ultra-high liquid chromatography–mass spectrometry (Q-Exactive Plus, Thermo Fisher, USA). The EZinfo 2.0 software was used to perform orthogonal partial least squares discriminant analysis (OPLS-DA) by analyzing each ion. All metabolite variables were scaled using the Pareto method before conducting the OPLS-DA. The model validity was evaluated using model parameters R2 and Q2, which provide information on the interpretability and predictability of the model, respectively, and avoid the risk of over-fitting. Metabolites with variable importance in the projection (VIP) > 1 and $p < 0.05$ were considered statistically significant.

4.9. SCFAs

Colonic, cecal, and fecal content samples (1 g) were mixed with ultrapure water via processes of homogenization and centrifugation. The supernatant was collected in a 10 mL Eppendorf tube, mixed with 25% metaphosphate at a ratio of 9:1 (v/v) and filtered through a 0.22 μm membrane filter. The SCFAs (acetate, propionate, butyrate, and valerate) were quantified using gas chromatography (8890, Agilent, Santa Clara, CA, USA).

4.10. Statistical Analysis

Data were analyzed using the IBM SPSS 23.0 statistical software (SPSS Inc., Chicago, IL, USA). Differences between means were tested using Student's t-test. Beta-diversity

containing principal co-ordinates analysis (PCoA) with a Bray-Curtis diversity distance matrix were performed using R software (version 3.3.1). The different relative abundance of bacteria within groups was calculated by Wilcoxon rank-sum test. The Spearman correlation coefficients were generated using GraphPad Prism (version 9.5.0). All data are presented as mean ± SEM. $p < 0.05$ was considered statistically significant.

5. Conclusions

These results indicated that MetR treatment increased the concentration of intestinal SCFAs by remodeling the gut microbiota, as shown by the increased relative abundance of *Erysipclotxichaceae* and *Clostridium_sensu_stricto_1* and the decreased relative abundance of *Proteobacteria, Enterobacteriaceae*, *Enterococcaceae*, and *Escherichia-Shigella* in the cecum. The results indicate that MetR has the potential to enhance the integrity of the gut barrier and reduce the levels of taurine-conjugated BAs. These alterations in plasma metabolite levels have contributed to the beneficial effects of MetR. Therefore, MetR improved gut health and modified plasma BA levels and conjugation by regulating the gut microbiota in rats. These findings offer valuable insights that can guide the implementation of nutritional strategies aimed at promoting gut health and longevity.

Supplementary Materials: The following supporting information can be downloaded at: https://www.mdpi.com/article/10.3390/ijms25073657/s1.

Author Contributions: M.Y. and Q.X.: Conceptualization, Writing—original draft. Y.X.: Formal analysis, Methodology. M.X.: Methodology, Data curation. J.C.: Conceptualization, Project administration. B.-E.T.: Conceptualization, Supervision, Funding acquisition. Y.Y.: Conceptualization, Supervision, Writing—review and editing, Funding acquisition. All authors have read and agreed to the published version of the manuscript.

Funding: This work was supported by the National Key R&D Program (2021YFD1301004, 2021YFD1301005, 2021YFD1300401), National Natural Science Foundation of China (U20A2054, 32072745, 32102571, 32130099), Natural Science Foundation of Hunan Province (2024JJ1004) the earmarked fund for CARS (CARS-35), the Science and Technology Major Project of Yunnan Province (202202AE090032).

Institutional Review Board Statement: The animal protocols were carried out the guidelines of animal care and were approved by the Institutional Animal Care and Use Committee of Hunan Agricultural University (approval number: CACAHU 2022-0426. date of approval: 20 May 2022).

Informed Consent Statement: Not applicable.

Data Availability Statement: Data will be made available on request. Sequencing data generated in this study were deposited in Sequence Read Archive (SRA) with the SRA accession numbers PRJNA1065593.

Conflicts of Interest: The authors declare no conflicts of interest.

Abbreviations

MetR, Methionine restriction; LPS, lipopolysaccharide; DAO, diamine oxidase; TNF-α, tumor Necrosis Factor Alpha; IL-1β, interleukin-1 Inhibitors; IL-2, interleukin-2; IL-4, interleukin-4; IL-6, interleukin-6; IL-12, interleukin-12; ZO-1, zonula occludens-1; H and E, hematoxylin and eosin; SCFAs, short-chain fatty acids; OPLS-DA, orthogonal partial least squares discriminant analysis; VIP, variable importance in the projection; TCA, taurocholic acid; TUDCA, tauro-ursodeoxycholic acid; TCDCA, tauro-chenodeoxycholic acid; BA, bile acid.

References

1. Gao, X.; Sanderson, S.M.; Dai, Z.; Reid, M.A.; Cooper, D.E.; Lu, M.; Richie, J.P., Jr.; Ciccarella, A.; Calcagnotto, A.; Mikhael, P.G.; et al. Dietary methionine influences therapy in mouse cancer models and alters human metabolism. *Nature* **2019**, *572*, 397–401. [CrossRef]
2. Han, L.; Wu, G.; Feng, C.; Yang, Y.; Li, B.; Ge, Y.; Jiang, Y.; Shi, Y.; Le, G. Dietary methionine restriction improves the impairment of cardiac function in middle-aged obese mice. *Food Funct.* **2020**, *11*, 1764–1778. [CrossRef]

3. Bárcena, C.; Quirós, P.M.; Durand, S.; Mayoral, P.; Rodríguez, F.; Caravia, X.M.; Mariño, G.; Garabaya, C.; Fernández-García, M.T.; Kroemer, G.; et al. Methionine Restriction Extends Lifespan in Progeroid Mice and Alters Lipid and Bile Acid Metabolism. *Cell Rep.* **2018**, *24*, 2392–2403. [CrossRef]
4. Kitada, M.; Ogura, Y.; Monno, I.; Xu, J.; Koya, D. Effect of Methionine Restriction on Aging: Its Relationship to Oxidative Stress. *Biomedicines* **2021**, *9*, 130. [CrossRef]
5. Mladenović, D.; Radosavljević, T.; Hrnčić, D.; Rasic-Markovic, A.; Stanojlović, O. The effects of dietary methionine restriction on the function and metabolic reprogramming in the liver and brain—Implications for longevity. *Rev. Neurosci.* **2019**, *30*, 581–593. [CrossRef]
6. Yang, Y.; Wang, Y.; Sun, J.; Zhang, J.; Guo, H.; Shi, Y.; Cheng, X.; Tang, X.; Le, G. Dietary methionine restriction reduces hepatic steatosis and oxidative stress in high-fat-fed mice by promoting H_2S production. *Food Funct.* **2019**, *10*, 61–77. [CrossRef]
7. Yang, Y.; Zhang, J.; Wu, G.; Sun, J.; Wang, Y.; Guo, H.; Shi, Y.; Cheng, X.; Tang, X.; Le, G. Dietary methionine restriction regulated energy and protein homeostasis by improving thyroid function in high fat diet mice. *Food Funct.* **2018**, *9*, 3718–3731. [CrossRef]
8. Gasaly, N.; de Vos, P.; Hermoso, M.A. Impact of Bacterial Metabolites on Gut Barrier Function and Host Immunity: A Focus on Bacterial Metabolism and Its Relevance for Intestinal Inflammation. *Front. Immunol.* **2021**, *12*, 658354. [CrossRef]
9. Martel, J.; Chang, S.H.; Ko, Y.F.; Hwang, T.L.; Young, J.D.; Ojcius, D.M. Gut barrier disruption and chronic disease. *Trends Endocrinol. Metab. TEM* **2022**, *33*, 247–265. [CrossRef]
10. Banerjee, S.; Sindberg, G.; Wang, F.; Meng, J.; Sharma, U.; Zhang, L.; Dauer, P.; Chen, C.; Dalluge, J.; Johnson, T.; et al. Opioid-induced gut microbial disruption and bile dysregulation leads to gut barrier compromise and sustained systemic inflammation. *Mucosal Immunol.* **2016**, *9*, 1418–1428. [CrossRef]
11. Schirmer, M.; Smeekens, S.P.; Vlamakis, H.; Jaeger, M.; Oosting, M.; Franzosa, E.A.; Ter Horst, R.; Jansen, T.; Jacobs, L.; Bonder, M.J.; et al. Linking the Human Gut Microbiome to Inflammatory Cytokine Production Capacity. *Cell* **2016**, *167*, 1125–1136.e1128. [CrossRef]
12. Martin-Gallausiaux, C.; Marinelli, L.; Blottière, H.M.; Larraufie, P.; Lapaque, N. SCFA: Mechanisms and functional importance in the gut. *Proc. Nutr. Soc.* **2021**, *80*, 37–49. [CrossRef]
13. Akhtar, M.; Chen, Y.; Ma, Z.; Zhang, X.; Shi, D.; Khan, J.A.; Liu, H. Gut microbiota-derived short chain fatty acids are potential mediators in gut inflammation. *Anim. Nutr. (Zhongguo Xu Mu Shou Yi Xue Hui)* **2022**, *8*, 350–360. [CrossRef]
14. Ma, J.; Hong, Y.; Zheng, N.; Xie, G.; Lyu, Y.; Gu, Y.; Xi, C.; Chen, L.; Wu, G.; Li, Y.; et al. Gut microbiota remodeling reverses aging-associated inflammation and dysregulation of systemic bile acid homeostasis in mice sex-specifically. *Gut Microbes* **2020**, *11*, 1450–1474. [CrossRef]
15. Ramalingam, A.; Wang, X.; Gabello, M.; Valenzano, M.C.; Soler, A.P.; Ko, A.; Morin, P.J.; Mullin, J.M. Dietary methionine restriction improves colon tight junction barrier function and alters claudin expression pattern. *Am. J. Physiol. Cell Physiol.* **2010**, *299*, C1028–C1035. [CrossRef]
16. Wu, G.; Shi, Y.; Han, L.; Feng, C.; Ge, Y.; Yu, Y.; Tang, X.; Cheng, X.; Sun, J.; Le, G.W. Dietary Methionine Restriction Ameliorated Fat Accumulation, Systemic Inflammation, and Increased Energy Metabolism by Altering Gut Microbiota in Middle-Aged Mice Administered Different Fat Diets. *J. Agric. Food Chem.* **2020**, *68*, 7745–7756. [CrossRef]
17. Yang, Y.; Zhang, Y.; Xu, Y.; Luo, T.; Ge, Y.; Jiang, Y.; Shi, Y.; Sun, J.; Le, G. Dietary methionine restriction improves the gut microbiota and reduces intestinal permeability and inflammation in high-fat-fed mice. *Food Funct.* **2019**, *10*, 5952–5968. [CrossRef]
18. Xu, Y.; Yang, Y.; Li, B.; Xie, Y.; Shi, Y.; Le, G. Dietary methionine restriction improves gut microbiota composition and prevents cognitive impairment in D-galactose-induced aging mice. *Food Funct.* **2022**, *13*, 12896–12914. [CrossRef]
19. Barbara, G.; Barbaro, M.R.; Fuschi, D.; Palombo, M.; Falangone, F.; Cremon, C.; Marasco, G.; Stanghellini, V. Inflammatory and Microbiota-Related Regulation of the Intestinal Epithelial Barrier. *Front. Nutr.* **2021**, *8*, 718356. [CrossRef]
20. Bischoff, S.C.; Barbara, G.; Buurman, W.; Ockhuizen, T.; Schulzke, J.D.; Serino, M.; Tilg, H.; Watson, A.; Wells, J.M. Intestinal permeability--a new target for disease prevention and therapy. *BMC Gastroenterol.* **2014**, *14*, 189. [CrossRef]
21. Kuziel, G.A.; Rakoff-Nahoum, S. The gut microbiome. *Curr. Biol. CB* **2022**, *32*, R257–R264. [CrossRef] [PubMed]
22. Xue, Y.; Jin, T.; Gao, C.; Li, C.; Zhou, T.; Wan, D.; Yang, M. Effects of biodegradable film mulching on bacterial diversity in soils. *Arch. Microbiol.* **2022**, *204*, 195. [CrossRef]
23. Zhao, C.; Hu, X.; Bao, L.; Wu, K.; Zhao, Y.; Xiang, K.; Li, S.; Wang, Y.; Qiu, M.; Feng, L.; et al. Gut dysbiosis induces the development of mastitis through a reduction in host anti-inflammatory enzyme activity by endotoxemia. *Microbiome* **2022**, *10*, 205. [CrossRef]
24. Yang, M.; Gu, Y.; Li, L.; Liu, T.; Song, X.; Sun, Y.; Cao, X.; Wang, B.; Jiang, K.; Cao, H. Bile Acid-Gut Microbiota Axis in Inflammatory Bowel Disease: From Bench to Bedside. *Nutrients* **2021**, *13*, 3143. [CrossRef]
25. Stolfi, C.; Maresca, C.; Monteleone, G.; Laudisi, F. Implication of Intestinal Barrier Dysfunction in Gut Dysbiosis and Diseases. *Biomedicines* **2022**, *10*, 289. [CrossRef]
26. Kaminsky, L.W.; Al-Sadi, R.; Ma, T.Y. IL-1β and the Intestinal Epithelial Tight Junction Barrier. *Front. Immunol.* **2021**, *12*, 767456. [CrossRef] [PubMed]
27. Ren, B.; Wang, L.; Mulati, A.; Liu, Y.; Liu, Z.; Liu, X. Methionine Restriction Improves Gut Barrier Function by Reshaping Diurnal Rhythms of Inflammation-Related Microbes in Aged Mice. *Front. Nutr.* **2021**, *8*, 746592. [CrossRef] [PubMed]
28. Zhai, Z.; Zhang, F.; Cao, R.; Ni, X.; Xin, Z.; Deng, J.; Wu, G.; Ren, W.; Yin, Y.; Deng, B. Cecropin A Alleviates Inflammation Through Modulating the Gut Microbiota of C57BL/6 Mice With DSS-Induced IBD. *Front. Microbiol.* **2019**, *10*, 1595. [CrossRef]

29. Jang, H.M.; Kim, J.K.; Joo, M.K.; Shin, Y.J.; Lee, K.E.; Lee, C.K.; Kim, H.J.; Kim, D.H. Enterococcus faecium and Pediococcus acidilactici deteriorate Enterobacteriaceae-induced depression and colitis in mice. *Sci. Rep.* **2022**, *12*, 9389. [CrossRef]
30. Li, S.; Guo, J.; Liu, R.; Zhang, F.; Wen, S.; Liu, Y.; Ren, W.; Zhang, X.; Shang, Y.; Gao, M.; et al. Predominance of Escherichia-Shigella in Gut Microbiome and Its Potential Correlation with Elevated Level of Plasma Tumor Necrosis Factor Alpha in Patients with Tuberculous Meningitis. *Microbiol. Spectr.* **2022**, *10*, e0192622. [CrossRef]
31. Liu, S.; Li, E.; Sun, Z.; Fu, D.; Duan, G.; Jiang, M.; Yu, Y.; Mei, L.; Yang, P.; Tang, Y.; et al. Altered gut microbiota and short chain fatty acids in Chinese children with autism spectrum disorder. *Sci. Rep.* **2019**, *9*, 287. [CrossRef]
32. Gao, X.; Du, L.; Randell, E.; Zhang, H.; Li, K.; Li, D. Effect of different phosphatidylcholines on high fat diet-induced insulin resistance in mice. *Food Funct.* **2021**, *12*, 1516–1528. [CrossRef] [PubMed]
33. Baltazar-Díaz, T.A.; González-Hernández, L.A.; Aldana-Ledesma, J.M.; Peña-Rodríguez, M.; Vega-Magaña, A.N.; Zepeda-Morales, A.S.M.; López-Roa, R.I.; Del Toro-Arreola, S.; Martínez-López, E.; Salazar-Montes, A.M.; et al. Escherichia/Shigella, SCFAs, and Metabolic Pathways-The Triad That Orchestrates Intestinal Dysbiosis in Patients with Decompensated Alcoholic Cirrhosis from Western Mexico. *Microorganisms* **2022**, *10*, 1231. [CrossRef] [PubMed]
34. Han, L.; Li, T.; Du, M.; Chang, R.; Zhan, B.; Mao, X. Beneficial Effects of Potentilla discolor Bunge Water Extract on Inflammatory Cytokines Release and Gut Microbiota in High-Fat Diet and Streptozotocin-Induced Type 2 Diabetic Mice. *Nutrients* **2019**, *11*, 670. [CrossRef] [PubMed]
35. Firrman, J.; Liu, L.; Mahalak, K.; Tanes, C.; Bittinger, K.; Tu, V.; Bobokalonov, J.; Mattei, L.; Zhang, H.; Van den Abbeele, P. The impact of environmental pH on the gut microbiota community structure and short chain fatty acid production. *FEMS Microbiol. Ecol.* **2022**, *98*, fiac038. [CrossRef] [PubMed]
36. Soriano-Lerma, A.; García-Burgos, M.; Alférez, M.J.M.; Pérez-Carrasco, V.; Sanchez-Martin, V.; Linde-Rodríguez, Á.; Ortiz-González, M.; Soriano, M.; García-Salcedo, J.A.; López-Aliaga, I. Gut microbiome-short-chain fatty acids interplay in the context of iron deficiency anaemia. *Eur. J. Nutr.* **2022**, *61*, 399–412. [CrossRef] [PubMed]
37. Aon, M.A.; Bernier, M.; Mitchell, S.J.; Di Germanio, C.; Mattison, J.A.; Ehrlich, M.R.; Colman, R.J.; Anderson, R.M.; de Cabo, R. Untangling Determinants of Enhanced Health and Lifespan through a Multi-omics Approach in Mice. *Cell Metab.* **2020**, *32*, 100–116.e104. [CrossRef] [PubMed]
38. Bárcena, C.; Valdés-Mas, R.; Mayoral, P.; Garabaya, C.; Durand, S.; Rodríguez, F.; Fernández-García, M.T.; Salazar, N.; Nogacka, A.M.; Garatachea, N.; et al. Healthspan and lifespan extension by fecal microbiota transplantation into progeroid mice. *Nat. Med.* **2019**, *25*, 1234–1242. [CrossRef]
39. Li, X.; Zhao, W.; Xiao, M.; Yu, L.; Chen, Q.; Hu, X.; Zhao, Y.; Xiong, L.; Chen, X.; Wang, X.; et al. Penthorum chinense Pursh. extract attenuates non-alcholic fatty liver disease by regulating gut microbiota and bile acid metabolism in mice. *J. Ethnopharmacol.* **2022**, *294*, 115333. [CrossRef]
40. Zhang, X.; Coker, O.O.; Chu, E.S.; Fu, K.; Lau, H.C.H.; Wang, Y.X.; Chan, A.W.H.; Wei, H.; Yang, X.; Sung, J.J.Y.; et al. Dietary cholesterol drives fatty liver-associated liver cancer by modulating gut microbiota and metabolites. *Gut* **2021**, *70*, 761–774. [CrossRef]
41. Tian, Q.; Yang, R.; Wang, Y.; Liu, J.; Wee, A.; Saxena, R.; Wang, L.; Li, M.; Liu, L.; Shan, S.; et al. A High Serum Level of Taurocholic Acid Is Correlated With the Severity and Resolution of Drug-induced Liver Injury. *Clin. Gastroenterol. Hepatol. Off. Clin. Pract. J. Am. Gastroenterol. Assoc.* **2021**, *19*, 1009–1019.e1011. [CrossRef] [PubMed]
42. Jia, W.; Xie, G.; Jia, W. Bile acid-microbiota crosstalk in gastrointestinal inflammation and carcinogenesis. *Nat. Rev. Gastroenterol. Hepatol.* **2018**, *15*, 111–128. [CrossRef]
43. Wang, L.; Ren, B.; Zhang, Q.; Chu, C.; Zhao, Z.; Wu, J.; Zhao, W.; Liu, Z.; Liu, X. Methionine restriction alleviates high-fat diet-induced obesity: Involvement of diurnal metabolism of lipids and bile acids. *Biochim. Biophys. Acta. Mol. Basis Dis.* **2020**, *1866*, 165908. [CrossRef]
44. Shen, B.; Zhou, C.; Gu, T.; Shen, Z.; Guo, Y.; Dai, W.; Liu, Y.; Zhang, J.; Lu, L.; Dong, H. Kuhuang alleviates liver fibrosis by modulating gut microbiota-mediated hepatic IFN signaling and bile acid synthesis. *Front. Pharmacol.* **2022**, *13*, 1080226. [CrossRef]
45. Maddineni, S.; Nichenametla, S.; Sinha, R.; Wilson, R.P.; Richie, J.P., Jr. Methionine restriction affects oxidative stress and glutathione-related redox pathways in the rat. *Exp. Biol. Med.* **2013**, *238*, 392–399. [CrossRef] [PubMed]
46. Tamanna, N.; Kroeker, K.; Braun, K.; Banh, S.; Treberg, J.R. The effect of short-term methionine restriction on glutathione synthetic capacity and antioxidant responses at the whole tissue and mitochondrial level in the rat liver. *Exp. Gerontol.* **2019**, *127*, 110712. [CrossRef] [PubMed]

Disclaimer/Publisher's Note: The statements, opinions and data contained in all publications are solely those of the individual author(s) and contributor(s) and not of MDPI and/or the editor(s). MDPI and/or the editor(s) disclaim responsibility for any injury to people or property resulting from any ideas, methods, instructions or products referred to in the content.

biomolecules

MDPI

Article

Overexpression of *S30* Ribosomal Protein Leads to Transcriptional and Metabolic Changes That Affect Plant Development and Responses to Stress

Alin Finkelshtein [1], Hala Khamesa-Israelov [1] and Daniel A. Chamovitz [2,*]

[1] School of Plant Sciences and Food Security, Tel Aviv University, Ramat Aviv 69978, Israel
[2] The Department of Life Sciences, Ben-Gurion University of the Negev, Be'er Sheva 84105, Israel
* Correspondence: dchamovitz@bgu.ac.il

Abstract: ICT1 is an *Arabidopsis thaliana* line that overexpresses the gene encoding the S30 ribosomal subunit, leading to tolerance to exogenous indole-3-carbinol. Indole-3-carbinol (I3C) is a protective chemical formed as a breakdown of I3M in cruciferous vegetables. The overexpression of S30 in ICT1 results in transcriptional changes that prime the plant for the I3C, or biotic insult. Emerging evidence suggests that ribosomal proteins play important extra-ribosomal roles in various biochemical and developmental processes, such as transcription and stress resistance. In an attempt to elucidate the mechanism leading to I3C and stress resistance in ICT1, and using a multi-pronged approach employing transcriptomics, metabolomics, phenomics, and physiological studies, we show that overexpression of S30 leads to specific transcriptional alterations, which lead to both changes in metabolites connected to biotic and oxidative stress tolerance and, surprisingly, to photomorphogenesis.

Keywords: ribosome; indole-3-carbinol; metabolomics; photomorphogenesis; plant development; stress resistance

1. Introduction

ICT1 is an *Arabidopsis thaliana* line that overexpresses the gene encoding the *S30* ribosomal subunit, leading to tolerance to exogenous indole-3-carbinol (I3C) [1]. I3C is formed from the breakdown of indole-3-methylglucosinolate (I3M), the predominant indole glucosinolate [2], by a reaction primarily catalyzed by myrosinase [3,4], though the formation of I3M can also occur in the absence of myrosinase [5]. In Arabidopsis, I3C serves as a signaling molecule that modulates the auxin response by antagonizing auxin binding to the TIR1 receptor and other mechanisms [6–8]. Hence, exogenous I3C at high concentrations inhibits *Arabidopsis* growth and development [7].

While ICT1 was specifically tolerant to I3C and not to other toxic molecules, it was also tolerant to bacterial and fungal pathogens, as well as to oxidative stress [1]. The overexpression of *S30* in ICT1 results in transcriptional changes that prime the plant for the I3C, or biotic insult. For example, the genes involved in responses to biotic stress, immune responses, and stress responses are expressed constitutively, priming the plant to respond more quickly [1].

The ribosome, a two-subunit ribonucleoprotein complex, plays a pivotal role in protein synthesis but also has emerging roles in transcriptional regulation. In *Arabidopsis thaliana*, the large 60S subunit consists of 48 ribosomal proteins (RPs), while the small 40S subunit contains 32 RPs, including *S30* [9]. *S30* is required for ribosome assembly and protein synthesis by promoting the interaction between the tRNA anticodon stem-loop and the 18S rRNA 530 loop [10].

Mounting evidence indicates that differences in RP expression can impact functions unrelated to ribosome assembly or protein synthesis. For example, mutations and differential expression in ribosomal genes have been found to play a role in regulating normal

development and responding to environmental stresses [11–14]. In an attempt to elucidate the mechanism leading to I3C and stress resistance in ICT1, and using a multi-pronged approach employing transcriptomics, metabolomics, phenomics, and physiological studies, we show that overexpression of *S30* leads to specific transcriptional alterations, which lead to both changes in metabolites connected to biotic and oxidative stress tolerance and, surprisingly, to photomorphogenesis.

2. Materials and Methods

2.1. Plant Material and Growth Assays

The *Arabidopsis* lines used in this work were all WT ecotype Columbia-0 backgrounds. Transgenic and mutant lines were previously reported: ICT1 [1], $S30^{t\text{-}DNA}$ (Salk_087911.4) [15], *tgg1/2* double mutant [16], and *cyp79B2/B3* double mutant [17]. Seeds were cultivated in Petri plates using medium containing 0.8% agar (Acumedia, Lansing, MI, USA, 7178A), half-strength Murashige and Skoog salts (MS) (Sigma, Yokohama, Japan, M5519), and 1% sucrose (Bio Lab, Rockville, MD, USA, 19220591, pH 5.7. The Petri plates were placed in chambers at 21 °C under light/dark conditions of 16 h white light at 75 lmol m^2 sec^{-1} and 8 h darkness, at 55% relative humidity. For root phenotype experiments, plates were placed vertically in the chambers. All treatments were conducted under the same day-time conditions. For experiments that included ICT1, at least 3 independent lines of ICT1 were used in each; the results are the average of all lines.

Hydroponic growth: For treatments with I3C, plants were grown hydroponically in tall petri dishes with liquid MS. ~60 seedlings were in each plate for two weeks in normal conditions (long day, 21 °C, humidity 55%). All lines were exposed for two hours to either 0.05% DMSO or 400 μM I3C (diluted in 0.05% DMSO). All samples were collected at the same time to eliminate circadian clock effects and washed three times with fresh DDW. Moreover, 10 seedlings for each sample were pooled, frozen in liquid nitrogen, and lyophilized. Indole-3-carbinol (I3C) (Sigma I7256)was dissolved in 0.05% DMSO (Merck, Rahway, NJ, USA, 1.02931) to produce a 1 M solution and stored in the dark at −20 °C.

2.2. Yield

ICT1 and WT lines were grown in pots in optimal conditions until full ripening. Seeds were collected separately from each plant and weighted. The weight was transformed into the number of seeds with the aid of a calibration curve. The average weight and number of seeds per plant were calculated.

2.3. LC-MS-MS

Sample preparation: Seedlings were grown hydroponically. Dry samples were powdered with 2 stainless-steel balls in a beat beater (1 min, MM400, Retsch, Haan, Germany). One mg of each sample was extracted with 80% methanol (Bio Lab, 1368060200) in 0.2% formic acid (500 uL), containing ethylparaben (1 ng/mL) as an internal standard (IS), by shaking (20,000 rpm, 65 °C, 15 min, Thermomixer C, Eppendorf, Hamburg, Germany). Then, the mixtures were centrifuged (14,000× *g*, 10 min), and supernatants were collected and placed in LC-MS vials. Standard curve mixtures of 0.001–10 ug/mL of I3C and DIM were prepared in 80% methanol/0.2% formic acid, containing 1 ug/mL of ethylparaben as IS.

Standards: Indole-3-carbinol (I3C) I7256, 3,3′-diindolylmethane (DIM) D9568, and ethylparaben PHR1011 (internal standard, IS) were purchased from Sigma/Merck.

LC-MS-MS analysis was performed on the Acquity UPLC system and the triple quadrupole Xevo TQ-S (both Waters). TargetLynx (Waters, Milford, MA, USA) was applied for quantitation based on standard curves.

LC parameters: Acquity BEH C18 column (2.1 × 100 mm, 1.7 μm; Waters) at 35 °C. Gradient with mobile phases A—0.01% aqueous formic acid and B—0.01% formic acid in acetonitrile: 0 min, 20%B; 3 min, 100%B; 4 min, 100%B; 4.5 min, 20%B; 7 min, 20%

B. Injection volume: 2.0 µL; flow rate: 0.3 mL/min. Retention times: 2.25 min for I3C, 2.96 min for DIM, and 2.18 min for IS.

MS/MS parameters: Electrospray ionization in positive-ion mode; desolvation temperature, 400 °C; desolvation gas flow, 600 L/hr; cone gas flow, 150 L/hr; nebulizer pressure, 7 Bar; capillary voltage, 3.56 kV; cone voltage, 44 V; with argon 0.10 mg/min as the collision gas. The MRM transitions are: 130.1 > 77.0 and 130.1 > 103.1 with collision energy (CE) 22 V in both I3C and DIM; 167.1 > 95.0 and 167.1 > 139.1, with CE 13 and 10 V, respectively, for IS.

2.4. LC-MS

Sample preparation: seedlings were grown in MS plates, with ~60 seeds in each plate, vertically standing for 16 days in normal conditions.

With and without I3C treatment, ICT1 and WT were grown hydroponically. Each tube contains 100 mg of wet weight.

Metabolic profiling of the semipolar phase was performed using the Waters ACQUITY UPLC system coupled to a Vion IMS QTof mass spectrometer (Waters Corp., MA, USA). The chromatographic separation was performed on an ACQUITY UPLC BEH C18 column (2.1 × 100 mm, i.d., 1.7 µm) (Waters Corp., MA, USA). The mobile phase A consisted of 95% water (UPLC grade) and 5% acetonitrile, with 0.1% formic acid; the mobile phase B consisted of 100% acetonitrile with 0.1% formic acid. The column was maintained at 35 °C, and the flow rate of the mobile phase was 0.3 mL*min^{-1}. Mobile phase A was initially run at 100%, and it was gradually reduced to 72% at 22 min, following a decrease to 60% at 22.5 min and 0% at 23 min. Then, mobile phase B was run at 100% until 26.5 min, and mobile phase A was set to 100% at 27 min. Finally, the column was equilibrated at 100% A for 28 min. MS parameters were as follows: the source and de-solvation temperatures were maintained at 120 °C and 350 °C, respectively. The capillary voltage was set to 2 kV, and the cone voltage was set to 40 V. Nitrogen was used as de-solvation gas and cone gas at a flow rate of 700 L*h^{-1} and 50 L*h^{-1}, respectively. The mass spectrometer was operated in full-scan HDMSE negative ionization over a mass range of 50–2000 Da. For the high energy scan function, a collision energy ramp of 20–80 eV was applied; for the low energy scan function, 5 eV was applied. Leucine-enkephalin was used as a lock-mass reference standard.

Semipolar compound identification and data analysis: LC-MS data were analyzed and processed with UNIFI (Version 1.9.4, Waters Corp., MA, USA). The putative identification of the different semipolar species was performed by comparing the accurate mass, fragmentation pattern, and ion mobility (CCS) values of theoretical structures in an in-house-generated library. The data were normalized using internal standards and sample weights.

2.5. Photomorphogenesis

WT and six independent ICT1 lines (1, 2, 28, 33, 478, and 8098) were used for the experiment. Seeds were exposed to 5 h of light, covered with aluminum foil, and grown at 21 °C for ten days. Hypocotyl length, cotyledon opening %, and angle were measured.

2.6. Abiotic Stresses

All lines were grown for two weeks and then exposed to the following conditions: 1. Salt stress: pots were irrigated with a 200 mM NaCl solution; 2. Constitutive heat (28 °C) for 3 days; 3. Intermittent high heat (44 °C) two hours a day for a week; 4. Drought: plants were irrigated with half the normal volume of water (1.5 lit/64 pots of soil); 5. UV stress: single exposure to UVb 5000 ERG for 1 min; 6. Cold stress: 4 °C during the night for a week. Untreated samples were used as controls. Plants were monitored for plant area, roundness, water content, and photosynthesis (QY max, Fv/Fm_Lss, NPQ_Lss, and RFD_Lss) using a Plant Screen^{TM} Phenotyping System (Photon Systems Instruments (PSI),

Drasov, Czech Republic). Seedlings grown in MS were transferred to PSI standard pots (one seedling per pot), and imaging was performed on days 14–31 with a 3–4-day interval.

2.7. Statistics

All the experiments were repeated at least three times. The variance between the groups that were statistically compared was similar. The samples were analyzed using a *t*-test. We considered $p < 0.05$ to be significant.

PCA is a dimension reduction analysis that transforms the original data into a new set of uncorrelated variables (principal components (PC)) that capture the maximum variance in the data. To see how many PCs can explain the most variance, we use the scree plot. In a scree plot, the point where the eigenvalues start to level off or show a bend is often referred to as the "elbow" of the plot. The number of principal components before this bend is typically considered for retention. In our case, six PCs are the most significant ones. Thus, we have chosen the combinations between them that give the best separation between samples for visualization.

3. Results

3.1. Tolerance to Exogenous I3C in ICT1 Likely Arises from Reduced Endogenous Levels of I3C

To elucidate the mechanisms leading to I3C tolerance in ICT1, we took several approaches. To investigate if the tolerance of ICT1 mutants to I3C can be attributed to reduced uptake of extracellular I3C, we conducted I3C uptake assays using LC-MS-MS. The lines used for the assay were: ICT1, WT, *S30*$^{\text{t-DNA}}$, *tgg1/2* (myrosinase-deficient), and *cyp79B2/B3* (deficient in indolic GLS synthesis).

In control samples treated with dimethyl sulfoxide (DMSO), the measured I3C content represents I3C endogenously produced by the plant. We observed similar concentrations of endogenous I3C levels in WT and *tgg1/2* and reduced concentrations in ICT1, while no detectable I3C was observed in the *cyp79B2/B3* double mutant (Figure 1a). The similar concentrations in WT and *tgg1/2* indicate that in an undamaged plant, endogenous I3C is hydrolyzed by a non-enzymatic breakdown, consistent with previously shown myrosinase-dependent and independent I3C hydrolysis pathways [5]. The reduction in endogenous levels of I3C in ICT1 correlates with the downregulation of several glucosinolate (GLS) biosynthetic genes in ICT1 (Figure 1b). The fact that *cyp79B2/B3* and ICT1 have reduced I3C levels supports the idea that downregulation of GLS genes contributes to the lower abundance of I3C in ICT1. Interestingly, while GLS synthesis is down-regulated in ICT1, this line has increased expression of the myrosinase-encoding *tgg* genes (Figure S1). Conversely, the uptake of exogenous I3C by ICT1 mutants was found to be twice as high as in WT plants (Figure 1a). Therefore, tolerance to exogenous I3C in ICT1 is not due to defects in I3C uptake.

We next tested whether the increased degradation of I3C contributes to ICT1′s tolerance of I3C. I3C is a highly unstable metabolite that forms various oligomers (Figure S2), such as the formation of 3,3′-diindolylmethane (DIM) [18]. As depicted in Figure 1c, I3C-treated samples exhibited approximately 3-times higher levels of DIM compared to I3C alone, indicating that a significant portion of absorbed I3C was indeed degraded to DIM.

As endogenous I3C levels are reduced in ICT1, and as *cyp79B2/B3* (Figure 1a) contains no I3C, we thus hypothesized that *cyp79B2/B3*, like ICT1, would also be tolerant to I3C. Using the root growth assay, as seen in Figure 2, *cyp79B2/B3* is indeed tolerant to exogenous I3C. Thus, the explanation for the tolerance to exogenous I3C in both lines is that the tolerance likely arises from reduced endogenous levels of I3C.

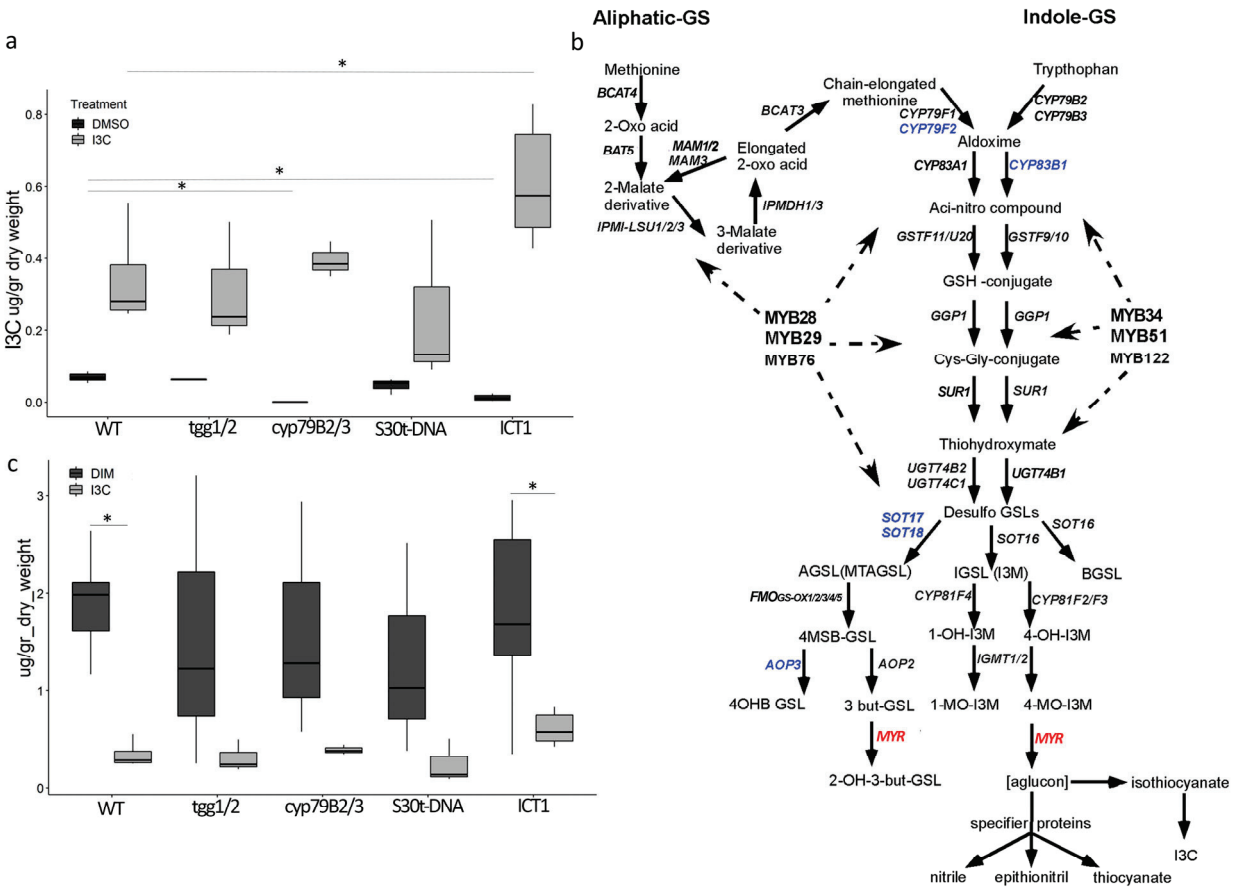


Figure 1. Uptake of exogenous I3C. LC-MS-MS results. (**a**) Total I3C content (mg/g dry weight) for each line. Each sample was treated with either 1 M DMSO or I3C 400 µM (in 1 M DMSO) for 2 h. (**b**) Glucosinolate pathway: genes marked in blue are down-regulated, and genes marked in red are up-regulated in ICT1. (**c**) Total DIM and I3C content following treatment with I3C (mg/g dry weight) for each line. * p value < 0.009 t-test. $3 > n > 6$.

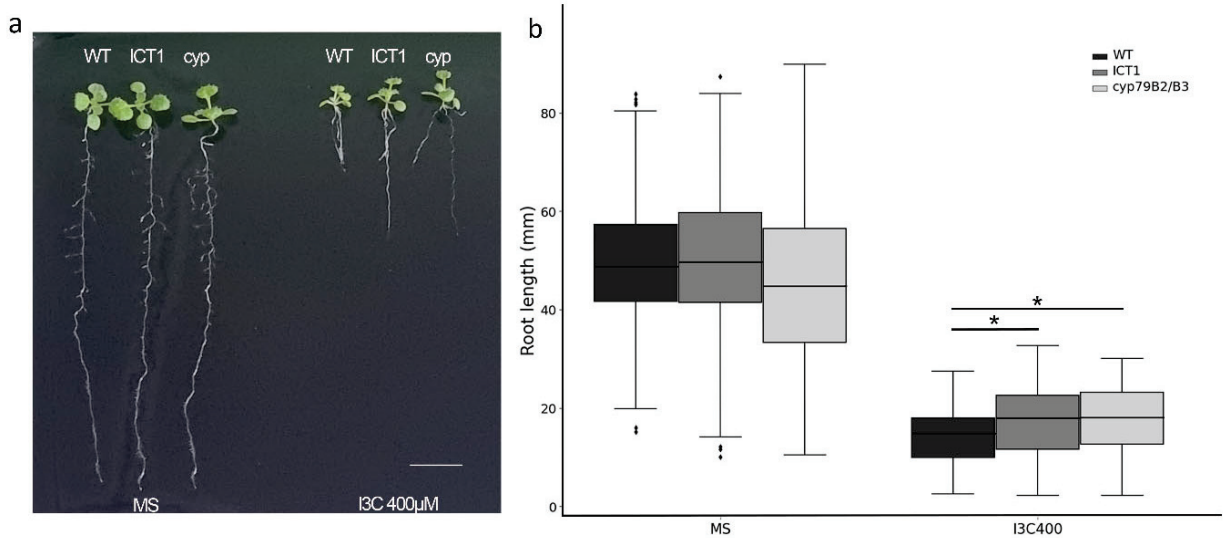


Figure 2. cyp79B2/B3 is tolerant of I3C. (**a**). Phenotypes of WT, ICT1, and cyp79B2/B3 on MS and I3C 400 µM after 14 days. Scale bar = 1 cm. (**b**) The average root length on MS and 400 µM I3C. t-test * p value < 0.05. $127 < n < 258$. The dots over the whiskers are the outliers.

3.2. ICT1 Displays Unique Metabolomic Profiles That Correlate with Known Phenotypes

As our previous transcriptomic study revealed differences in expression of specific metabolic pathways, we sought to determine if these differences corresponded to metabolomic changes, which led us to conduct a metabolomic profiling experiment. Specifically, we investigated the profiles of GLS metabolites (GLS) and non-GLS secondary metabolites (SM) in ICT1 compared to WT and *cyp79B2/B3*. Supplementary Table S1 presents the complete list of metabolites and abundances. The principal component analysis of this data clearly differentiates between the three lines in both SM and GLS content (Figure 3a,b). In the comparison between ICT1 and WT, we identified 39 SM that are significantly different, 24 with lower relative abundance in ICT1 and 15 with higher relative abundance (Table S1). Among the 15 prevalent SMs in ICT1, some are associated with ICT1 phenotypes (Figure 3c). Notably, our previous study demonstrated that ICT1 exhibited tolerance to both oxidative and biotic stress [1]. The tolerance to oxidative stress correlates with an increase in four specific secondary metabolites—quercitrin, linarin, citric acid, and 4-O-p-coumaroylquinic acid—each known to be effective against oxidative stress [19–23]. Tolerance to both bacteria and fungi correlates with five secondary metabolites—salicylic acid, kaempferol-7-O-glucoside, linarin, quercitrin, and ascorbigen, each of which shows strong antipathogen activities [23–29].

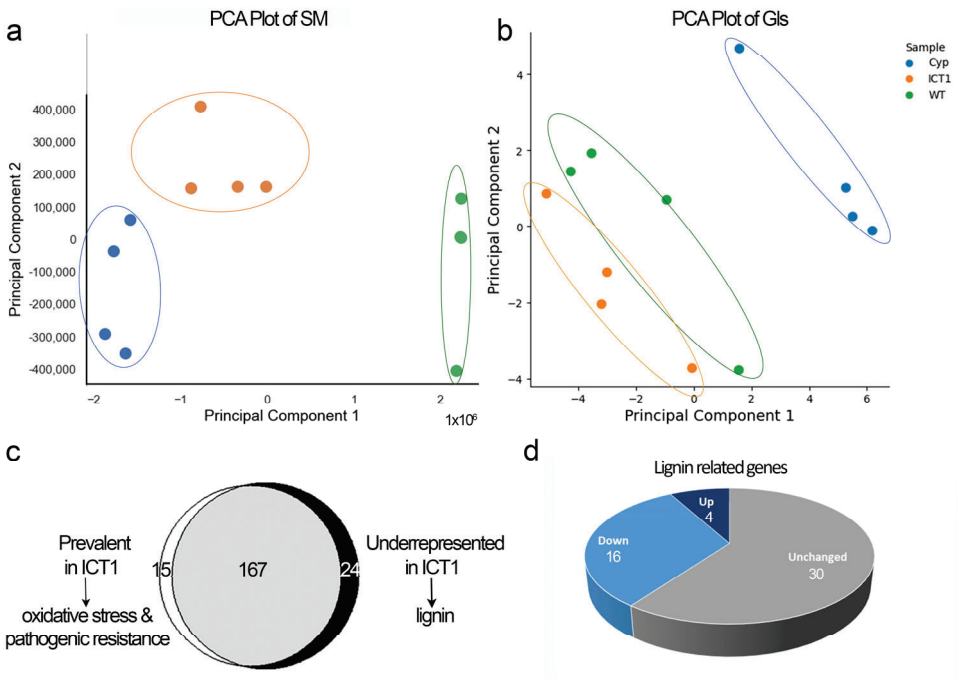


Figure 3. Secondary metabolites (SM) and glucosinolates (GLS) profiles. (**a**,**b**) Principal component analysis of the metabolite profiles of WT, ICT1, and *cyp*79B2/B3 for SM (**a**) and GLS (**b**). Each dot in PCA represents a biological replicate. In the case of SM, two dots in the WT sample overlap. (**c**) Out of 206 SM identified, 15 were overrepresented in ICT1, while 24 were underrepresented. In the overrepresented group, there are four SMs related to oxidative tolerance and eight related to pathogen tolerance. In the underrepresented group, the majority are lignin-related metabolites. (**d**) Out of 50 genes indicated in lignin synthesis, 16 (32%) are downregulated in ICT1 vs. WT [1]. The numbers of lignin-related genes are indicated on the pie chart.

Furthermore, we observed three prevalent glucosinolates in ICT1: glucobrassicin, a significant indole glucosinolate serving as a precursor for active indoles; 6-hydroxyindole-3-carboxylate hexoside isomer 1; and 2-hydroxy-2-methylpropyl glucosinolate/4-hydroxybutyl glucosinolate. Indolic glucosinolates are well-known determinants for pest and disease resistance in plants [30–32]. Consequently, the overexpression of *S30* in ICT1 results in a

higher relative abundance of metabolites associated with oxidative stress and pathogen tolerance, which correlates biochemically with the observed corresponding phenotypes.

Among the secondary metabolites with reduced content in ICT1, 62.5% are lignin related (Table S1). This reduction correlates with transcriptome results [1], which showed a down-regulation in 16 out of 50 lignin biosynthetic genes (Figure 3d).

3.3. I3C Treatment Impacts the Metabolic Profiles of WT More Than That of ICT1

We further tested the differences in metabolic profiles between WT and ICT1 before and after treatment with I3C (Table S2). Using principal component analysis, we see a clear differentiation between WT vs. ICT1 for both SM and GLS profiles, whether treated or untreated with I3C. In other words, the overexpression of 30S clearly influences the metabolic profiles of ICT1, differentiating it from WT. Following treatment of WT with I3C, the metabolic profiles of both SM and GLS are clearly separated, indicating that the I3C treatment leads to clear changes in the metabolic profiles of WT. The situation for ICT1 was, though, different. Treatment of ICT1 with I3C did not cause a significant shift in SM profile, which correlates with tolerance to I3C in this mutant (Figure 4a). In other words, just as ICT1 exhibits tolerance to I3C-induced inhibition of root growth, it also exhibits tolerance to I3C-induced changes in SM profiles.

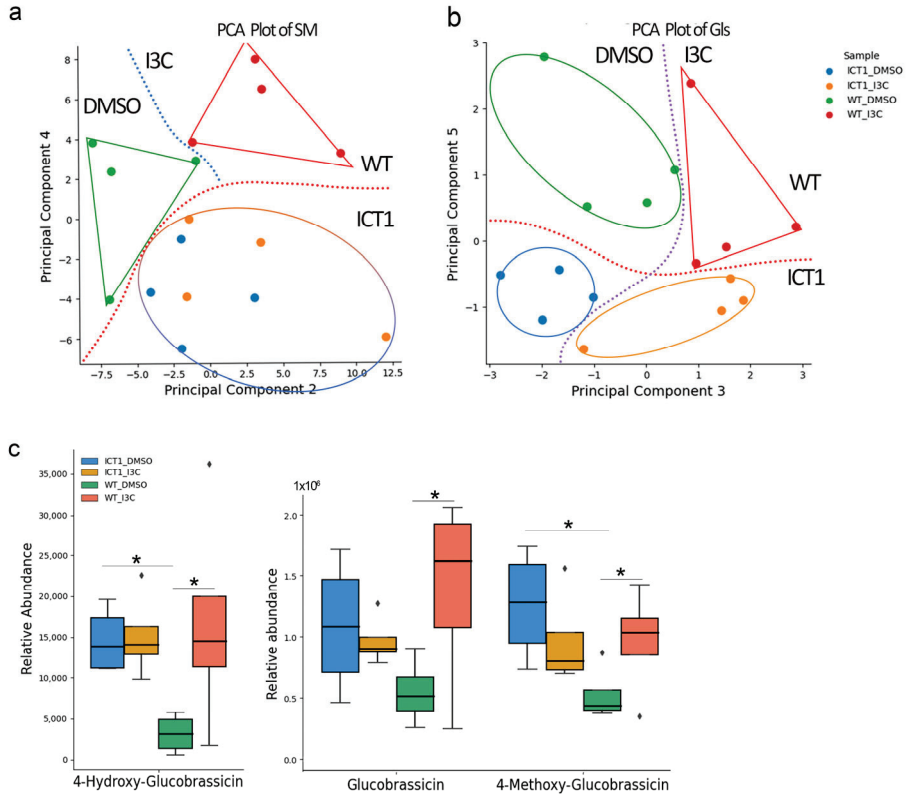


Figure 4. Metabolomic analysis of WT and ICT1 before and following I3C treatment. PCA plots of (**a**) secondary metabolites (SM) and (**b**) glucosinolates (GLS). The red lines differentiate between WT and ICT1. The blue and purple lines differentiate between I3C-treated and untreated. (**c**). Relative abundance of indolic GLS upstream of I3C. Following exposure to exogenous I3C, the levels of these three metabolites increase in WT while remaining constant in ICT1. * *t*-test p value < 0.05, $n = 4$.

However, the GLS profiles of ICT1 are influenced by I3C treatment (Figure 4b). However, we discovered that for three specific GLS, the I3C treatment has no effect on their levels in ICT1, while having increased levels in WT. These glucosinolates, glucobrassicin, 4-hydroxy glucobrassicin, and 4-methoxy glucobrassicin, are upstream of I3C production. The fact that they are induced by I3C treatment in WT but not in ICT1 also correlates with the tolerance in ICT1 (Figure 4c).

3.4. ICT1 Displays Constitutive Photomorphogenic Phenotypes

Further inspection of the transcriptome [1] revealed a group of genes related to skotomorphogenesis that are mis-regulated in ICT1, with 30 genes including Csn8 and LSH6 [33] being downregulated and 18 genes including SOB7, PCH1, CIP1, and PHOT2 [34–36] being upregulated (Figure S3). To test if ICT1 is affected by skotomorphogenesis, WT and six independent ICT1 lines were grown in the dark, and phenotypes were measured after 10 days. While in WT the cotyledons were closed and the hypocotyl was long, all ICT1 lines presented a constitutive photomorphogenesis (cop) phenotype of open cotyledons and short hypocotyl (Figure 5a–d). Thus, the misregulation of skotomorphogenesis-related genes in ICT1 suggests that ICT1 is defective in the regulation of photomorphogenesis.

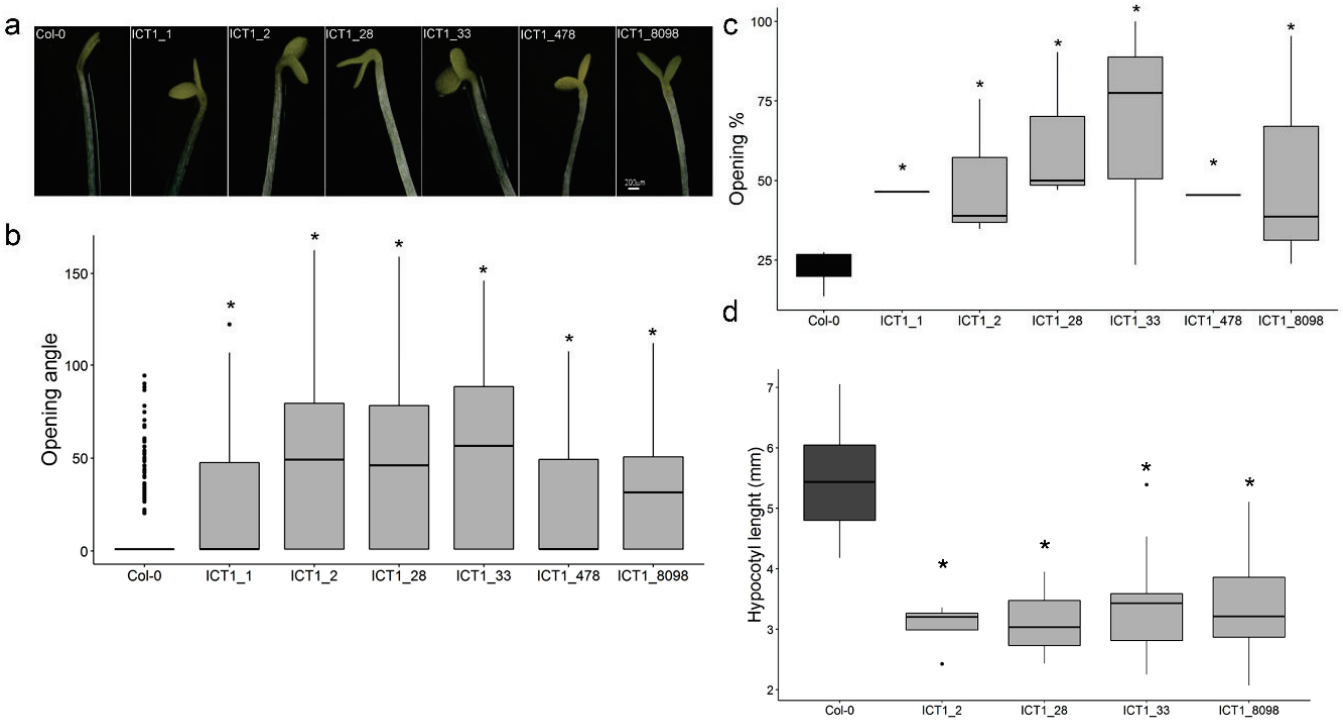


Figure 5. ICT1 shows a constitutive photomorphogenesic phenotype. (**a**) Representative photographs of cotyledons of 14-day-old, dark-grown WT and ICT1. Scale bar = 200 μm. (**b**–**d**) Quantitative measurements of angle of cotyledon opening (**b**), percentage of open cotyledons (**c**), and hypocotyl lengths (**d**). n = 55–187. * t-test p value < 0.05.

3.5. ICT1 Does Not Have Wide Resistance to Abiotic Stresses

Since ICT1 is primed in stress response pathways and showed resistance to oxidative and biotic stress [1], we wanted to see if ICT1 has a wide range of abiotic stress resistance. To test this, six additional abiotic stresses were tested: (1) salt stress; (2) constitutive 3 days of heat; (3) high heat (44 °C) 2 h a day for a week; (4) drought; (5) UV stress; and (6) cold stress. Untreated samples were used as controls. To test if the stress caused phenotypical changes in the plants such as rosette area, leaf roundness, water content, and photosynthesis (QY max, Fv/Fm_Lss, NPQ_Lss, and RFD_Lss), we have scanned all lines by phenomics from day 14 up to day 31 with a 3–4-day interval. Not only was ICT1 not tolerant to any of these stresses, it was hypersensitive to cold treatment (Figure 6). Thus, based on these results, ICT1 did not present wide resistance to abiotic stresses, further supporting the specificity of resistance to specific biotic and abiotic challenges.

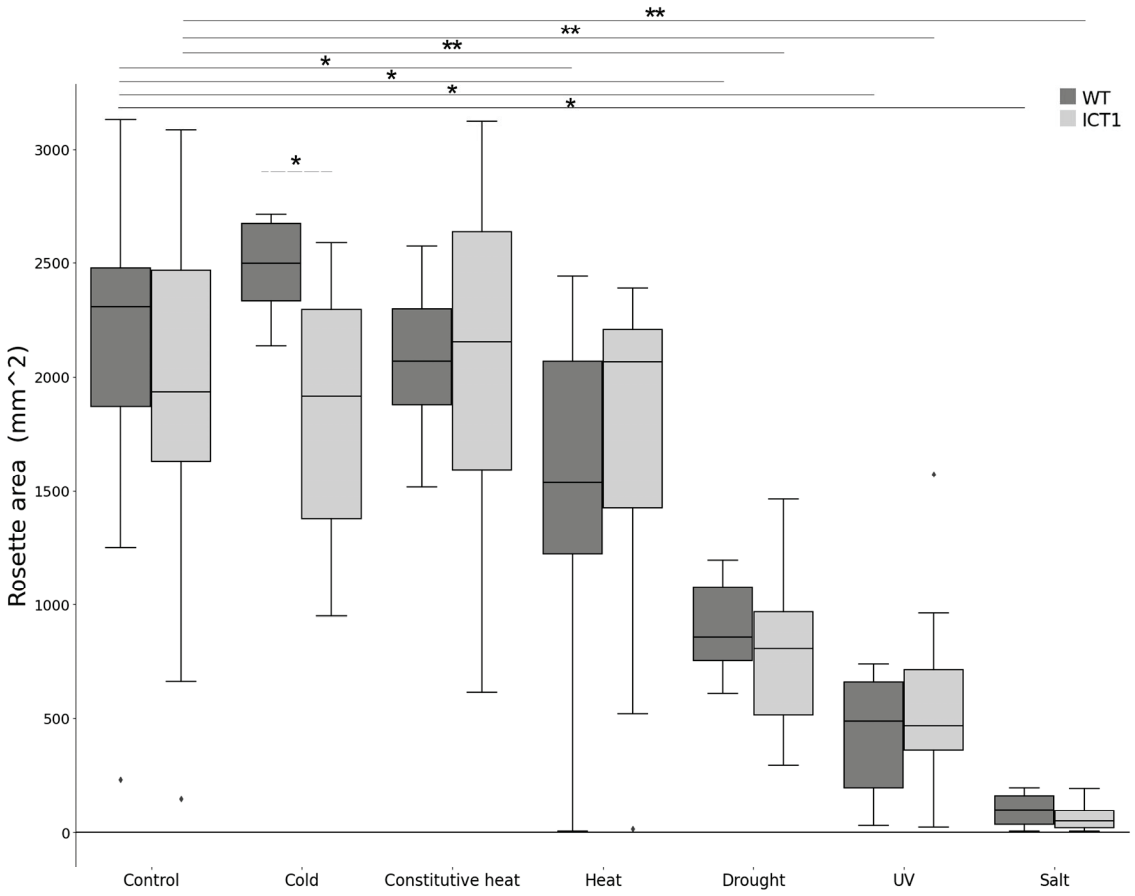


Figure 6. Differences in the rosette area following abiotic stresses. Rosette area following stresses: salt stress, constitutive 3 days of heat (28 °C), high heat (44 °C) 2 h a day for a week, drought, UV stress, and cold stress. Untreated samples were used as controls. *t*-test p value < 0.05 * WT, ** ICT1.

4. Discussion

Tolerance or resistance to specific toxic molecules can arise through several mechanisms, including but not limited to target site mutation [37], increased activity of efflux pumps that actively remove the specific molecule from inside the cell [38], reduced uptake of the molecule [39,40], and detoxification or degradation of the specific molecule [41–44]. We have shown here that tolerance to exogenously applied I3C in ICT1 is not due to defects in the uptake of exogenous I3C or increased degradation, but is likely due to reduced levels of endogenous I3C.

This conclusion is supported by our analysis of both ICT1 and the *cyp*79B2/B3 double mutant. *Cyp*79B2/B3 is deficient in GLS synthesis due to the knockout of two enzymes at the beginning of the indolic GLS pathway [17]. We showed that several genes involved in the GLS pathway are down-regulated in ICT1 (Figure 1b) (based on the transcriptome [1]). This deficiency in GLS synthesis in *cyp*79B2/B3 and the reduction in GLS synthesis in ICT1 lead to a lack or reduction of endogenous I3C levels in each line, respectively. Thus, as we found that *cyp*79B2/B3 is, like ICT1, also tolerant to exogenous I3C (Figure 2), we concluded that the tolerance to I3C in these lines results from reduced levels of endogenous I3C.

However, this reduction in I3C levels is likely not the only contributor to the I3C tolerant phenotype. As we previously showed, over-expression of *S30* in ICT1 leads to transcriptional priming, which primes the plant for the I3C treatment [1]. We further showed here that these specific transcriptional changes lead to both changes in metabolite profiles and development.

I3C is produced by the hydrolysis of indol-3-ylmethylglucosinolate (I3M-GS) in the presence of myrosinase [45]. As the glucosinolates and myrosinases are stored in different

compartments, tissue rupture is necessary to bring them into contact [46]. Thus, I3C is produced mainly during pathogen attacks or mechanical damage [7]. Endogenous I3C found in the healthy, undamaged plant is a result of the non-enzymatic breakdown of I3M [5]. This is supported by similar levels of I3C in both WT and *tgg1/2* myrosinase-deficient mutants (Figure 1a). Interestingly, ICT1 overexpresses all functional myrosinase-encoding *Tgg* genes (Figure S1). This is likely a compensatory mechanism for the reduction in expression of GLS biosynthetic genes and consequent reduction in I3M levels.

We want to emphasize that the tolerance/resistance phenotypes detected for ICT1 are highly specific and correlate with specific transcriptional changes. In our original study, we showed that ICT1 also exhibited tolerance to oxidative stress and fungal and bacterial pathogens and that this tolerance was due to changes in gene expression patterns that primed the plants for response to the various treatments [1]. We showed here that these resistances are specific, as ICT1 was not tolerant to salt, heat, drought, UV, or cold stresses. Perhaps not unsurprisingly, we also did not detect transcriptional priming for these stress response pathways (based on the transcriptome [1]). Thus, just as we earlier showed that the tolerance in ICT1 is specific to I3C treatment and not a general tolerance response to all indoles/glucosinolates or other toxic molecules, the environmental tolerances identified were also specific to oxidative stress and pathogens and not to stresses in general. Thus, the overexpression of *S30* leads to specific transcriptional changes that lead to tolerance to abiotic and oxidative stresses, not a general overall stress response. It is important to notice that these specific tolerances carry with them a yield penalty (Figure S4).

The results from metabolic profiling coupled with transcriptome analysis (based on transcriptome [1]) further supported the hypothesis that overexpression of *S30* leads to changes in gene expression that influence specific metabolic pathways, which then lead to specific resistance phenotypes. Among the secondary metabolites enriched in ICT1, we notice metabolites associated with resistance to oxidative stress and pathogen resistance. These include quercitrin, linarin, citric acid, and 4-O-p-coumaroylquinic acid, each known to be effective against oxidative stress [19–23], and salicylic acid, kaempferol-7-O-glucoside, linarin, quercitrin, ascorbigen, and three glucosinolates, including glucobrassicin, each of which show strong antipathogen activities [23–32]. Thus, the overexpression of *S30* in ICT1 results in a higher relative abundance of metabolites associated with oxidative stress and pathogen tolerance, which provides a biochemical explanation for the observed corresponding phenotypes.

Genes related to lignin biosynthesis were also downregulated in ICT1 (Figure 3d) (based on the transcriptome [1]), and unsurprisingly, we identified a reduction in a number of lignin-related secondary metabolites (Table S1). Lignin is one of the most important secondary metabolites, which is produced by the phenylalanine/tyrosine metabolic pathway in plant cells [47,48]. However, this reduction did not correlate with any of the phenotypes tested, and indeed, a reduction in lignin would be thought to lead to an increase in pathogen or drought sensitivity. ICT1 could be a tool for further analyzing the role of lignin in plant development.

The most unexpected finding for us was that overexpression of the ribosomal gene *S30* in ICT1 affects light-mediated plant development. The misregulation of key genes (based on the transcriptome [1]), such as the down-regulation of COP9 signalosome subunit 8 (*Csn8*, also known as *Cop9*) and light-sensitive hypocotyls 6 (*LSH6*), and the up-regulation of a number of positive regulators of light signaling, including *Cop1-interating protein 1* (CIP1, [49]), photoperiodic control of hypocotyl 1 (*Pch1*), suppressor of PHYB-4 7 (*SOB7*), and phototropin 2 (PHOT2) (Figure 5), led us to test if ICT1 has a phenotype related to photomorphogenesis. Indeed, ICT1 has a constitutive photomorphogenic phenotype in the dark, including short hypocotyls and open and expanded cotyledons (Figure 6), similar, for example, to mutations in the Cop9 signalosome [33] or overexpression of positive regulators of photomorphogenesis [50]. Considering that the overexpression of *S30* interacts with I3C responses, this finding of a cop phenotype for a plant resistant to I3C is not that unexpected. Indeed, a number of studies have connected the Cop9 signalosome with hormonal as well

as environmental responses [51,52], and treatment with I3C induces transcriptional changes in *Arabidopsis* similar to mutations in the CSN.

While our motivation was to further identify the mechanism of I3C tolerance in ICT1, we keep meeting the surprising findings that overexpression of a single ribosomal subunit, *S30*, triggers the misregulation of specific gene families. How this subunit mediates these responses is unclear. Indeed, the function of many individual ribosomal subunits is unclear, and in this case, we do not know if the over-expressed protein solely incorporates into the ribosome or has some mode of action in a form independent of the ribosome. Unfortunately, attempts at using antibodies or tagged proteins to answer this question were inconclusive.

Our results add to mounting evidence that differences in RP expression can impact functions unrelated to ribosome assembly or protein synthesis. For example, the constitutive expression of *L6* in rice has been linked to enhanced tolerance to salt stress (NaCl 150–200 mM) [53], while the downregulation of *S6* in cotton has resulted in reduced levels of salicylic acid and jasmonic acid, rendering cotton plants more susceptible to *V. dahliae*. On the other hand, overexpression of *S6* in *Arabidopsis thaliana* has imparted resistance to *V. dahliae* [54]. Studies employing *S. cerevisiae* also provide evidence that RP effect transcription as over-production of specific ribosomal proteins repress mutations of RNA Pol III in *S. cerevisiae* [55,56]. These and other studies indicate that individual ribosomal proteins have extra-ribosomal functions in addition to those in the translation machinery [57–60]. Future studies must elucidate the mechanism by which *S30* influences transcription.

Supplementary Materials: The following supporting information can be downloaded at: https://www.mdpi.com/article/10.3390/biom14030319/s1. Figure S1: Expression of *Tgg* functional genes in ICT1 vs. WT; Figure S2: I3C hydrolysis products; Table S1: Secondary metabolites significantly different between ICT1 and WT; Table S2: A list of significantly differing metabolites following I3C treatment; Figure S3: Transcript levels of Skoto/photo morphogenesis-related genes in ICT1 vs. WT; Figure S4: Reduced yield in ICT1.s [1,5,61–63].

Author Contributions: Conceptualization, A.F. and D.A.C.; methodology, A.F.; validation, A.F. and H.K.-I.; formal analysis, A.F. and H.K.-I.; investigation, A.F.; resources, D.A.C.; data analysis, A.F.; writing—original draft preparation, A.F. and D.A.C.; writing—review and editing, A.F. and D.A.C.; visualization, A.F.; supervision, D.A.C.; project administration, D.A.C.; funding acquisition, D.A.C. All authors have read and agreed to the published version of the manuscript.

Funding: This research was funded by the Israeli Scientific Foundation (ISF), No. 1041/18.

Institutional Review Board Statement: Not applicable.

Informed Consent Statement: Not applicable.

Data Availability Statement: The information about the transcriptomic data can be found in [1].

Conflicts of Interest: The authors declare no conflicts of interest.

Nomenclature

Glucosinolates (GLS); ribosomal proteins (RP); secondary metabolites (SM); relative abundance (RA).

References

1. Finkelshtein, A.; Khamesa, H.; Tuan, L.A.; Rabanim, M.; Chamovitz, D.A. Overexpression of the ribosomal *S30* subunit leads to indole-3-carbinol tolerance in *Arabidopsis thaliana*. *Plant J.* **2021**, *105*, 668–677. [CrossRef] [PubMed]
2. Wittstock, U.; Burow, M. Glucosinolate breakdown in Arabidopsis: Mechanism, regulation and biological significance. *Arab. Book* **2010**, *8*, e0134. [CrossRef]
3. Andréasson, E.; Bolt Jørgensen, L.; Höglund, A.S.; Rask, L.; Meijer, J. Different myrosinase and idioblast distribution in *Arabidopsis* and *Brassica napus*. *Plant Physiol.* **2001**, *127*, 1750–1763. [CrossRef] [PubMed]
4. Koroleva, O.A.; Gibson, T.M.; Cramer, R.; Stain, C. Glucosinolate-accumulating S-cells in *Arabidopsis* leaves and flower stalks undergo programmed cell death at early stages of differentiation. *Plant J.* **2010**, *64*, 456–469. [CrossRef] [PubMed]

5. Kim, J.H.; Lee, B.W.; Schroeder, F.C.; Jander, G. Identification of indole glucosinolate breakdown products with antifeedant effects on *Myzus persicae* (green peach aphid). *Plant J.* **2008**, *54*, 1015–1026. [CrossRef] [PubMed]
6. Katz, E.; Nisani, S.; Sela, M.; Behar, H.; Chamovitz, D.A. The effect of indole-3-carbinol on PIN1 and PIN2 in *Arabidopsis* roots. *Plant Signal. Behav.* **2015**, *10*, e1062200. [CrossRef] [PubMed]
7. Katz, E.; Nisani, S.; Yadav, B.S.; Woldemariam, M.G.; Shai, B.; Obolski, U.; Ehrlich, M.; Shani, E.; Jander, G.; Chamovitz, D.A. The glucosinolate breakdown product indole-3-carbinol acts as an auxin antagonist in roots of *Arabidopsis thaliana*. *Plant J.* **2015**, *82*, 547–555. [CrossRef]
8. Katz, E.; Chamovitz, D.A. Wounding of *Arabidopsis* leaves induces indole-3-carbinol-dependent autophagy in roots of *Arabidopsis thaliana*. *Plant J.* **2017**, *91*, 779–787. [CrossRef]
9. Barakat, A.; Szick-Miranda, K.; Chang, I.-F.; Guyot, R.; Blanc, G.; Cooke, R.; Delseny, M.; Bailey-Serres, J. The Organization of Cytoplasmic Ribosomal Protein Genes in the *Arabidopsis* Genome. *Plant Physiol.* **2001**, *127*, 398. [CrossRef]
10. Feng, Z.; Zhang, L.; Wu, Y.; Wang, L.; Xu, M.; Yang, M.; Li, Y.; Wei, G.; Chou, M. The *Rpf84* gene, encoding a ribosomal large subunit protein, RPL22, regulates symbiotic nodulation in *Robinia pseudoacacia*. *Planta* **2019**, *250*, 1897–1910. [CrossRef]
11. Nagaraj, S.; Senthil-Kumar, M.; Ramu, V.S.; Wang, K.; Mysore, K.S. Plant Ribosomal Proteins, RPL12 and RPL19, Play a Role in Nonhost Disease Resistance against Bacterial Pathogens. *Front. Plant Sci.* **2015**, *6*, 1192. [CrossRef]
12. Zhang, J.; Yuan, H.; Yang, Y.; Fish, T.; Lyi, S.M.; Thannhauser, T.W.; Zhang, L.; Li, L. Plastid ribosomal protein S5 is involved in photosynthesis, plant development, and cold stress tolerance in Arabidopsis. *J. Exp. Bot.* **2016**, *67*, 2731–2744. [CrossRef] [PubMed]
13. Ramu, V.S.; Dawane, A.; Lee, S.; Oh, S.; Lee, H.K.; Sun, L.; Senthil-Kumar, M.; Mysore, K.S. Ribosomal protein QM/RPL10 positively regulates defence and protein translation mechanisms during nonhost disease resistance. *Mol. Plant Pathol.* **2020**, *21*, 1481–1494. [CrossRef] [PubMed]
14. Zhang, H.; Pei, Y.; He, Q.; Zhu, W.; Jahangir, M.; Haq, S.U.; Khan, A.; Chen, R. Salicylic acid-related ribosomal protein CaSLP improves drought and *Pst.DC3000* tolerance in pepper. *Mol. Hortic.* **2023**, *3*, 6. [CrossRef]
15. Sessions, A.; Burke, E.; Presting, G.; Aux, G.; McElver, J.; Patton, D.; Dietrich, B.; Ho, P.; Bacwaden, J.; Ko, C.; et al. A High-Throughput *Arabidopsis* Reverse Genetics System. *Plant Cell* **2002**, *14*, 2985–2994. [CrossRef] [PubMed]
16. Barth, C.; Jander, G. Arabidopsis myrosinases *TGG1* and *TGG2* have redundant function in glucosinolate breakdown and insect defense. *Plant J.* **2006**, *46*, 549–562. [CrossRef]
17. Zhao, Y.; Hull, A.K.; Gupta, N.R.; Goss, K.A.; Alonso, J.; Ecker, J.R.; Normanly, J.; Chory, J.; Celenza, J.L. Trp-dependent auxin biosynthesis in *Arabidopsis*: Involvement of cytochrome P450s *CYP*79B2 and *CYP*79B3. *Genes Dev.* **2002**, *16*, 3100–3112. [CrossRef]
18. Stresser, D.M.; Bjeldanes, L.F.; Bailey, G.S.; Williams, D.E. The anticarcinogen 3,3′-diindolylmethane is an inhibitor of cytochrome P-450. *J. Biochem. Toxicol.* **1995**, *10*, 191–201. [CrossRef]
19. Ganzon, J.G.; Chen, L.-G.; Wang, C.-C. 4-O-Caffeoylquinic acid as an antioxidant marker for mulberry leaves rich in phenolic compounds. *J. Food Drug Anal.* **2018**, *26*, 985–993. [CrossRef]
20. Mallhi, Z.I.; Rizwan, M.; Mansha, A.; Ali, Q.; Asim, S.; Ali, S.; Hussain, A.; Alrokayan, S.H.; Khan, H.A.; Alam, P.; et al. Citric Acid Enhances Plant Growth, Photosynthesis, and Phytoextraction of Lead by Alleviating the Oxidative Stress in Castor Beans. *Plants* **2019**, *8*, 525. [CrossRef]
21. Mottaghipisheh, J.; Taghrir, H.; Boveiri Dehsheikh, A.; Zomorodian, K.; Irajie, C.; Mahmoodi Sourestani, M.; Iraji, A. Linarin, a Glycosylated Flavonoid, with Potential Therapeutic Attributes: A Comprehensive Review. *Pharmaceuticals* **2021**, *14*, 1104. [CrossRef] [PubMed]
22. Tahjib-Ul-Arif, M.; Zahan, M.I.; Karim, M.M.; Imran, S.; Hunter, C.T.; Islam, M.S.; Mia, M.A.; Hannan, M.A.; Rhaman, M.S.; Hossain, M.A. Citric acid-mediated abiotic stress tolerance in plants. *Int. J. Mol. Sci.* **2021**, *22*, 7235. [CrossRef] [PubMed]
23. Chen, J.; Li, G.; Sun, C.; Peng, F.; Yu, L.; Chen, Y.; Tan, Y.; Cao, X.; Tang, Y.; Xie, X.; et al. Chemistry, pharmacokinetics, pharmacological activities, and toxicity of Quercitrin. *Phytother. Res.* **2022**, *36*, 1545–1575. [CrossRef] [PubMed]
24. Vlot, A.C.; Dempsey, D.M.A.; Klessig, D.F. Salicylic acid, a multifaceted hormone to combat disease. *Annu. Rev. Phytopathol.* **2009**, *47*, 177–206. [CrossRef] [PubMed]
25. An, C.; Mou, Z. Salicylic Acid and its Function in Plant Immunity. *J. Integr. Plant Biol.* **2011**, *53*, 412–428. [CrossRef] [PubMed]
26. Kátay, G.; Tyihák, E.; Kátay, E. Effect of ascorbigen and 1′-methylascorbigen on disease resistance of bean plants to *Uromyces phaseoli*. *Nat. Prod. Commun.* **2011**, *6*, 1934578X1100600508. [CrossRef]
27. Singh, D.; Sharma, S.; Rani, R.; Mishra, S.; Sharma, R. Kaempferol-7-O-glucoside and their antimicrobial screening isolate from Cassia renigera Wall. *Int. J. Pharm. Clin. Res.* **2011**, *3*, 30–34.
28. Klessig, D.F.; Choi, H.W.; Dempsey, D.M.A. Systemic Acquired Resistance and Salicylic Acid: Past, Present, and Future. *Mol. Plant-Microbe Interact.* **2018**, *31*, 871–888. [CrossRef]
29. Davoodi, M.; Nejad-Ebrahimi, S.; Rustaiyan, A.; Esmaeili, D. The chemical composition and antibacterial activity of a methanolic extract of *Satureja khuzistanica*. *Braz. J. Pharm. Sci.* **2022**, *58*, e19233. [CrossRef]
30. Bednarek, P.; Pislewska-Bednarek, M.; Svatos, A.; Schneider, B.; Doubsky, J.; Mansurova, M.; Humphry, M.; Consonni, C.; Panstruga, R.; Sanchez-Vallet, A.; et al. A glucosinolate metabolism pathway in living plant cells mediates broad-spectrum antifungal defense. *Science* **2009**, *323*, 101–106. [CrossRef]

31. Prince, D.C.; Rallapalli, G.; Xu, D.; Schoonbeek, H.J.; Çevik, V.; Asai, S.; Kemen, E.; Cruz-Mireles, N.; Kemen, A.; Belhaj, K.; et al. *Albugo*-imposed changes to tryptophan-derived antimicrobial metabolite biosynthesis may contribute to suppression of non-host resistance to *Phytophthora infestans* in *Arabidopsis thaliana*. *BMC Biol.* **2017**, *15*, 20. [CrossRef] [PubMed]
32. Nguyen, V.P.T.; Stewart, J.; Lopez, M.; Ioannou, I.; Allais, F. Glucosinolates: Natural Occurrence, Biosynthesis, Accessibility, Isolation, Structures, and Biological Activities. *Molecules* **2020**, *25*, 4537. [CrossRef] [PubMed]
33. Qin, N.; Xu, D.; Li, J.; Deng, X.W. COP9 signalosome: Discovery, conservation, activity, and function. *J. Integr. Plant Biol.* **2020**, *62*, 90–103. [CrossRef] [PubMed]
34. Turk, E.M.; Fujioka, S.; Seto, H.; Shimada, Y.; Takatsuto, S.; Yoshida, S.; Wang, H.; Torres, Q.I.; Ward, J.M.; Murthy, G.; et al. *BAS1* and *SOB7* act redundantly to modulate *Arabidopsis* photomorphogenesis via unique brassinosteroid inactivation mechanisms. *Plant J. Cell Mol. Biol.* **2005**, *42*, 23–34. [CrossRef] [PubMed]
35. Huang, H.; Yoo, C.Y.; Bindbeutel, R.; Goldsworthy, J.; Tielking, A.; Alvarez, S.; Naldrett, M.J.; Evans, B.S.; Chen, M.; Nusinow, D.A. PCH1 integrates circadian and light-signaling pathways to control photoperiod-responsive growth in Arabidopsis. *eLife* **2016**, *5*, e13292. [CrossRef] [PubMed]
36. Zhao, X.; Zhao, Q.; Xu, C.; Wang, J.; Zhu, J.; Shang, B.; Zhang, X. Phot2-regulated relocation of NPH3 mediates phototropic response to high-intensity blue light in *Arabidopsis thaliana*. *J. Integr. Plant Biol.* **2018**, *60*, 562–577. [CrossRef] [PubMed]
37. Murphy, B.P.; Tranel, P.J. Target-Site Mutations Conferring Herbicide Resistance. *Plants* **2019**, *8*, 382. [CrossRef]
38. Pasqua, M.; Grossi, M.; Zennaro, A.; Fanelli, G.; Micheli, G.; Barras, F.; Colonna, B.; Prosseda, G. The Varied Role of Efflux Pumps of the MFS Family in the Interplay of Bacteria with Animal and Plant Cells. *Microorganisms* **2019**, *7*, 285. [CrossRef]
39. Vila-Aiub, M.M.; Balbi, M.C.; Distéfano, A.J.; Fernández, L.; Hopp, E.; Yu, Q.; Powles, S.B. Glyphosate resistance in perennial *Sorghum halepense* (Johnsongrass), endowed by reduced glyphosate translocation and leaf uptake. *Pest. Manag. Sci.* **2012**, *68*, 430–436. [CrossRef]
40. Hu, X.; Wang, S.; Zhang, H.; Zhang, H.; Feng, S.; Qiao, K.; Lv, F.; Gong, S.; Zhou, A. Plant cadmium resistance 6 from *Salix linearistipularis* (SlPCR6) affects cadmium and copper uptake in roots of transgenic *Populus*. *Ecotoxicol. Environ. Saf.* **2022**, *245*, 114116. [CrossRef]
41. Singh, B.K.; Walker, A. Microbial degradation of organophosphorus compounds. *FEMS Microbiol. Rev.* **2006**, *30*, 428–471. [CrossRef] [PubMed]
42. Drawz, S.M.; Bonomo, R.A. Three decades of beta-lactamase inhibitors. *Clin. Microbiol. Rev.* **2010**, *23*, 160–201. [CrossRef] [PubMed]
43. Xia, J.; Guo, Z.; Yang, Z.; Han, H.; Wang, S.; Xu, H.; Yang, X.; Yang, F.; Wu, Q.; Xie, W.; et al. Whitefly hijacks a plant detoxification gene that neutralizes plant toxins. *Cell* **2021**, *184*, 3588. [CrossRef] [PubMed]
44. Tang, Z.; Wang, H.Q.; Chen, J.; Chang, J.D.; Zhao, F.J. Molecular mechanisms underlying the toxicity and detoxification of trace metals and metalloids in plants. *J. Integr. Plant Biol.* **2023**, *65*, 570–593. [CrossRef] [PubMed]
45. Singh, A.A.; Patil, M.P.; Kang, M.-J.; Niyonizigiye, I.; Kim, G.-D. Biomedical application of Indole-3-carbinol: A mini-review. *Phytochem. Lett.* **2021**, *41*, 49–54. [CrossRef]
46. Kliebenstein, D.J.; Kroymann, J.; Mitchell-Olds, T. The glucosinolate-myrosinase system in an ecological and evolutionary context. *Curr. Opin. Plant Biol.* **2005**, *8*, 264–271. [CrossRef] [PubMed]
47. Liu, Q.; Luo, L.; Zheng, L. Lignins: Biosynthesis and Biological Functions in Plants. *Int. J. Mol. Sci.* **2018**, *19*, 335. [CrossRef]
48. Vanholme, R.; De Meester, B.; Ralph, J.; Boerjan, W. Lignin biosynthesis and its integration into metabolism. *Curr. Opin. Biotechnol.* **2019**, *56*, 230–239. [CrossRef]
49. Kang, H.; Zhang, T.-T.; Fu, L.-L.; Yao, Y.-X.; You, C.-X.; Wang, X.-F.; Hao, Y.-J. The apple MdCOP1-interacting protein 1 negatively regulates hypocotyl elongation and anthocyanin biosynthesis. *BMC Plant Biol.* **2021**, *21*, 15. [CrossRef]
50. Myers, Z.A.; Kumimoto, R.W.; Siriwardana, C.L.; Gayler, K.K.; Risinger, J.R.; Pezzetta, D.; Holt Iii, B.F. NUCLEAR FACTOR Y, Subunit C (NF-YC) Transcription Factors Are Positive Regulators of Photomorphogenesis in *Arabidopsis thaliana*. *PLoS Genet.* **2016**, *12*, e1006333. [CrossRef]
51. Singh, A.K.; Chamovitz, D.A. Role of Cop9 Signalosome Subunits in the Environmental and Hormonal Balance of Plant. *Biomolecules* **2019**, *9*, 224. [CrossRef] [PubMed]
52. Singh, A.K.; Yadav, B.S.; Dhanapal, S.; Berliner, M.; Finkelshtein, A.; Chamovitz, D.A. CSN5A Subunit of COP9 Signalosome Temporally Buffers Response to Heat in Arabidopsis. *Biomolecules* **2019**, *9*, 805. [CrossRef] [PubMed]
53. Moin, M.; Saha, A.; Bakshi, A.; Madhav, M.S.; Kirti, P.B. Constitutive expression of Ribosomal Protein L6 modulates salt tolerance in rice transgenic plants. *Gene* **2021**, *789*, 145670. [CrossRef] [PubMed]
54. Zhu, D.; Zhang, X.; Zhou, J.; Wu, Y.; Zhang, X.; Feng, Z.; Wei, F.; Zhao, L.; Zhang, Y.; Shi, Y.; et al. Genome-Wide Analysis of Ribosomal Protein GhRPS6 and Its Role in Cotton Verticillium Wilt Resistance. *Int. J. Mol. Sci.* **2021**, *22*, 1795. [CrossRef] [PubMed]
55. Hermann-Le Denmat, S.; Sipiczki, M.; Thuriaux, P. Suppression of yeast RNA polymerase III mutations by the *URP2* gene encoding a protein homologous to the mammalian ribosomal protein S20. *J. Mol. Biol.* **1994**, *240*, 1–7. [PubMed]
56. Dieci, G.; Ruotolo, R.; Braglia, P.; Carles, C.; Carpentieri, A.; Amoresano, A.; Ottonello, S. Positive modulation of RNA polymerase III transcription by ribosomal proteins. *Biochem. Biophys. Res. Commun.* **2009**, *379*, 489–493. [CrossRef] [PubMed]
57. Tchórzewski, M.; Boldyreff, B.; Grankowski, N. Extraribosomal function of the acidic ribosomal P1-protein YP1alpha from Saccharomyces cerevisiae. *Acta Biochim. Pol.* **1999**, *46*, 901–910. [CrossRef]

58. Tu, W.Y.; Huang, Y.C.; Liu, L.F.; Chang, L.H.; Tam, M.F. Rpl12p affects the transcription of the *PHO* pathway high-affinity inorganic phosphate transporters and repressible phosphatases. *Yeast* **2011**, *28*, 481–493. [CrossRef]
59. Prakash, C.; Pandey, M.; Talwar, S.; Singh, Y.; Kanojiya, S.; Pandey, A.K.; Kumar, N. Extra-ribosomal functions of *Mtb* RpsB in imparting stress resilience and drug tolerance to mycobacteria. *Biochimie* **2020**, *177*, 87–97. [CrossRef] [PubMed]
60. Kour, R.; Kim, J.; Roy, A.; Richardson, B.; Cameron, M.J.; Knott, J.G.; Mazumder, B. Loss of function of ribosomal protein L13a blocks blastocyst formation and reveals a potential nuclear role in gene expression. *FASEB J.* **2023**, *37*, e23275. [CrossRef]
61. Aggarwal, B.B.; Ichikawa, H. Molecular Targets and Anticancer Potential of Indole-3-Carbinol and Its Derivatives. *Cell Cycle* **2005**, *4*, 1201–1215. [CrossRef] [PubMed]
62. Katz, E.; Nisani, S.; Chamovitz, D.A. Indole-3-carbinol: A plant hormone combatting cancer. *F1000Research* **2018**, *7*, 689. [CrossRef] [PubMed]
63. Centofanti, F.; Buono, A.; Verboni, M.; Tomino, C.; Lucarini, S.; Duranti, A.; Pandolfi, P.P.; Novelli, G. Synthetic Methodologies and Therapeutic Potential of Indole-3-Carbinol (I3C) and Its Derivatives. *Pharmaceuticals* **2023**, *16*, 240. [CrossRef]

Disclaimer/Publisher's Note: The statements, opinions and data contained in all publications are solely those of the individual author(s) and contributor(s) and not of MDPI and/or the editor(s). MDPI and/or the editor(s) disclaim responsibility for any injury to people or property resulting from any ideas, methods, instructions or products referred to in the content.

metabolites

MDPI

Article

Optimization of Fermentation Process for New Anti-Inflammatory Glycosylceramide Metabolite from *Aspergillus* sp.

Yung-Husan Chen [1,2,*], Qiaoqiao Zhu [1,2], Jingyi Li [1,2], Rong Yang [1,2], Jingwen Zhang [1,2], Minxin You [1,2], Lianzhong Luo [1,2] and Bingye Yang [1,2,*]

[1] Xiamen Key Laboratory of Natural Products Resources of Marine Medicine, Xiamen Medical College, Xiamen 361023, China; zhuqq@stu.njmu.edu.cn (Q.Z.); 202005440053@xmmc.edu.cn (J.L.); 201400080002@xmmc.edu.cn (R.Y.); 202102460027@xmmc.edu.cn (J.Z.); 202205480025@xmmc.edu.cn (M.Y.); llz@xmmc.edu.cn (L.L.)

[2] Fujian Provincial University Marine Biomedical Resources Engineering Research Center, Xiamen Medical College, Xiamen 361023, China

* Correspondence: cyxuan@xmmc.edu.cn (Y.-H.C.); yby@xmmc.edu.cn (B.Y.)

Abstract: A novel ceramide compound, named Aspercerebroside A (AcA), was successfully isolated from the ethyl acetate layer of the marine symbiotic fungus *Aspergillus* sp. AcA exhibited notable anti-inflammatory activity by effectively inhibiting the production of nitric oxide (NO) in RAW 264.7 cells at concentrations of 30 μg/mL and 40 μg/mL, offering a promising avenue for the treatment of inflammatory diseases. To optimize the yield of glycosylceramide (AcA), a series of techniques, including single-factor experiments, orthogonal experiments, and response surface optimization, were systematically employed to fine-tune the composition of the fermentation medium. Initially, the optimal carbon source (sucrose), nitrogen source (yeast extract powder), and the most suitable medium salinity (14 ppt) were identified through single-factor experiments. Subsequently, orthogonal experiments, employing an orthogonal table for planning and analyzing multifactor experiments, were conducted. Finally, a mathematical model, established using a Box–Behnken design, comprehensively analyzed the interactions between the various factors to determine the optimal composition of the fermentation medium. According to the model's prediction, when the sucrose concentration was set at 37.47 g/L, yeast extract powder concentration at 19.66 g/L, and medium salinity at 13.31 ppt, the predicted concentration of glycosylceramide was 171.084 μg/mL. The experimental results confirmed the model's accuracy, with the actual average concentration of glycosylceramide under these conditions measured at 171.670 μg/mL, aligning closely with the predicted value.

Keywords: *Aspergillus* sp.; glycosylceramid; orthogonal experiments; fermentation optimization; response surface optimization

1. Introduction

As valuable sources of novel pharmaceuticals and bioactive compounds, secondary metabolites have been generated by various species within the *Aspergillus* genus, and their prominence has been steadily increasing. Among the common marine fungi belonging to the *Aspergillus* genus are *Aspergillus* nidulans, *Aspergillus* oryzae, *Aspergillus* versicolor, *Aspergillus* nidurans, *Aspergillus* carneus, *Aspergillus* wentii, and others [1,2]. These fungal cells have the capacity to produce a diverse array of secondary metabolites, including alkaloids, polyketides, terpenes, peptides, and a variety of other categories [3].

Chemical analysis has revealed that ceramides consist of long-chain bases (LCBs) and long-chain fatty acid amides (FABs), linked together by an amide bond [4]. Biological analysis has shown that ceramides and their glycosylated counterparts, cerebrosides, can exhibit a wide range of biological activities, including cytotoxicity, antifungal properties,

immunostimulation, and immunosuppressive effects [5]. These ceramides and cerebrosides have been extracted from various marine invertebrates, including starfish, sea anemones, sponges, corals, ascidians, and bryozoans, and from some terrestrial plants as well.

Glycosylceramides have progressively found applications in various aspects of daily life. Their potential properties for cancer prevention, immunostimulation, and anticancer effects have been demonstrated. Consequently, they have been employed as functional foods or pharmaceuticals to enhance human physiological well-being. Clinical research has highlighted age-related declines in glycosylceramide levels. In particular, glycosylceramide supplementation has shown the potential to effectively slow down the aging process of facial skin and hand skin [6,7].

Glycosylceramides were discovered to play a pivotal role as structural precursors for various sphingolipids in previous studies. They could be modified to produce hydrophilic head groups, resulting in a range of compounds, including glycosphingolipids, sphingomyelins, and glycosylceramides. These substances, identified as critical constituents of biological membranes, contributed to the formation of diverse complex sphingolipids, gangliosides, and cerebrosides within the hydrophobic backbone of the body [8]. Glycosylceramides are typically localized in specific regions of cell membranes, where membrane integrity was preserved, and they become involved in cell signaling through influencing receptor oligomerization, signal amplification, or modification of cell signals. Moreover, owing to their hydrophobic nature, glycosylceramides have been identified as essential components of the skin's stratum corneum membrane, where they aid in the establishment of the skin's permeability barrier and play a pivotal role in skin hydration [9].

The research highlights the significant role played by long-chain fatty acid amides (FABs) in skin barrier function, particularly in the formation of lipid envelopes within keratinocytes [10]. Reduced sweating ability is often experienced by individuals with atopic dermatitis (AD) due to epidermal barrier dysfunction, resulting in a marked reduction in glycosylceramides esterified with linoleic acid (LA) within the stratum corneum. This leads to sweat duct blockage and prolonged sweating latency. The elevation of glycosylceramide levels in the stratum corneum has been shown to ameliorate epidermal barrier dysfunction, reduce sweating latency, and enhance stratum corneum function [11,12].

Glycosylceramides, serving as novel and highly effective moisturizers, have found extensive application in skincare products. They effectively mitigate moisture and lipid loss in the epidermis and dermis by stabilizing glycosylceramides on cell membranes, thereby delivering exceptional moisturization [13]. Additionally, they enhance skin elasticity, resistance, and slow the aging process of the skin [14]. However, due to their unique molecular structure, glycosylceramides possess a high melting point and low solubility, making them unsuitable for direct use as components in skincare products [15]. To address this challenge, numerous cosmetics companies are actively researching and developing innovative raw materials such as glycosylceramide liposomes and glycosylceramide encapsulates. These glycosylceramide-based skincare products have gained popularity among consumers.

In this study, a fungus was isolated from *Dendronephthya* sp. on Xiongdiyu Island, Dongshan Island, Zhangzhou City, Fujian Province, and was preliminarily identified as *Aspergillus* sp. From the ethyl acetate extract of this fungus, a glycosylceramide compound named AcA was isolated. Through spectroscopy and chemical analysis, it was discovered that AcA inhibited the production of nitric oxide (NO) in RAW 264.7 macrophage cells stimulated by lipopolysaccharide (LPS) at concentrations of 30 μg/mL and 40 μg/mL, demonstrating its anti-inflammatory properties. Building upon single-factor experiments, the Design-expert 8.0.6.1 software was utilized to establish a mathematical model based on the Box–Behnken design to optimize the fermentation medium composition of this fungus. On the basis of the results, response surface methodology (RSM) was applied to optimize the optimized glycosylceramide condition. The objective was to enhance the content of glycosylceramide, particularly AcA, in the secondary metabolites of this fungal strain, thus laying the experimental groundwork for large-scale industrial fermentation production of glycosylceramides. Through the successful optimization of the fermentation medium

for AcA production by Aspergillus sp., an extract rich in glycosylceramides from marine filamentous fungi was obtained.

2. Materials and Methods

2.1. Chemicals and Equipment

The chemicals and reagents used in this study included methanol, acetic acid, ethyl acetate, glucose, sucrose, glycerol, and soluble starch (purchased from Xilong Scientific Co., Ltd., Guangzhou, China); chromatographic methanol (purchased from Guangzhou Tongyuan Chemical Technology Co., Ltd., Guangzhou, China); marine saltwater (provided by Jiangxi Yantong Technology Co., Ltd., Ningdu, China); N-acetylglucosamine (purchased from Shanghai Maclin Biochemical Technology Co., Ltd., Shanghai, China); peptone, yeast extract powder, potato glucose broth dry medium, and potato glucose agar dry medium (purchased from Guangdong Huanke Microbial Science and Technology Co., Ltd., Guangzhou, China); silica gel (200–300 mesh, Qingdao Marine Chemical Co., Ltd., Qingdao, China); Sephadex LH-20 gel (purchased from Nanjing Yuanbaofeng Medical Technology Co., Ltd., Nanjing, China); a laminar flow cabinet (model SW-CJ-2FD, Suzhou Antai Air Technology Co., Ltd., Suzhou, China); an autoclave sterilizer (model GR85DR, Zhengzhou Instrument Co., Ltd., Zhengzhou, China); a biochemical incubator (model SPX-250B-Z, Shanghai Boyuan Industrial Co., Ltd. Medical Equipment Factory, Shanghai, China); an orbital shaker (model ZQZY-CGF8, Shanghai Zhichu Instrument Co., Ltd., Shanghai, China); an ultrasonic cleaning machine (model DS-080S, Dongsen Washing Technology Co., Ltd., Zhengzhou, China); an Abbott salinometer (Wuhan Zhongxia Medical College undergraduate thesis design Hongtu measurement instrument Co., Ltd., Wuhan, China); a rotary evaporator (model RE212-B, Shanghai Guigu Technology Development Co., Ltd.); and an Agilent 1260 high-performance liquid chromatography system (Agilent Technologies, Inc., Santa Clara, CA, USA). Ultraviolet (UV) spectra were obtained using a Shimadzu UV-1800 UV/vis spectrophotometer. IR data were acquired by a Bruker TENSOR27 spectrophotometer. High resolution ESIMS and MS/MS experiments were carried out on a Q-Exactive (Thermo Scientific, Waltham, MA, USA) mass spectrometer. NMR spectra were determined on a BRUKER AVANCE III 500 MHz NMR spectrometer at 298.0 K equipped with 5 mm probes (500 MHz for ^{1}H and 125 MHz for ^{13}C NMR, Bruker BioSpin, Billerica, MA, USA). The ^{1}H and ^{13}C NMR spectrum were referenced to the solvent peaks for DMSO-d6. HPLC purification was performed on a PURIFLASH® 4250 equipped with QuikSep-DAC50 series DAC-50 dynamic axial compression column system (YMC-Triart C18 S-10 μm particles, H&E Co., Ltd., Beijing, China). All solvents were purchased from Merck KGaA (Darmstadt, Germany), if not mentioned.

2.2. LC-ESI-MS/MS Analysis

One μL of AcA content was injected into the LCESI-MS/MS system (LC system: Waters CapLC; MS system: nanoACQUITY/QExactive). The flow rate of the LC system was 6 μL/min through the column system (Waters Atlantis dC18″, 3 μm, 75 μm × 50 μm column) and the flow rate eventually was reduced to 0.3 μL/min by the splitter before entering into chromatographic column system. The solvent gradient system consisted of 5–100% methanol. The solvent increased from 5% to 100% in 4 min and then equilibrated for 1 min.

Mass spectrometry was performed in +ESI ionization mode with voltage of 4.50 kV and desolvation temperature of 290 °C. Triple quadrupole detection was controlled at an accelerating voltage of 9.1 kV, cone voltage of 100 V, and impact energy of 10 eV. The scanning range of mass spectrometry was monitored between *m/z* 600 and 800. The selected reaction model (SRM) mode was used to quantify the AcA contents. The ion chromatography peak area of the product ion was compared with the standard, and then the contents of AcA in the *Aspergillus* sp. extracts were calculated. The mass spectrometer tuning and calibration standard was [Glu]-Fibrinopeptide B (Sigma Chemicals, Kewdale, WA, USA).

2.3. Strain and Fermentation Conditions

The marine fungus *Aspergillus* sp., isolated from the waters of Dongshan Island, Zhangzhou City, Fujian Province, is currently preserved in the Guangdong Microbial Culture Collection Center (registration number GDMCC61933). Seed culture media included potato dextrose agar dry medium (PDA) and potato dextrose broth dry medium (PDB). Fermentation media comprised carbon source single-factor fermentation medium, nitrogen source single-factor fermentation medium, and response surface-optimized fermentation medium.

2.4. Strain Propagation

Propagation of the strain involved transferring a 1 cm^2 single colony from a successfully passaged culture onto potato dextrose agar dry medium (PDA) and incubating at room temperature for 1–2 months under sealed conditions.

2.5. Organic Solvent Extraction

Sterile extraction was carried out using a mixed solvent A (ethyl acetate: methanol: acetic acid = 80:15:5). Repeated extraction was performed to obtain secondary metabolites, and rotary evaporation was used to concentrate the extract, resulting in a weight of M0 (134.59 g).

A mixed solvent B (ethyl acetate: water = 1:1) was used for liquid–liquid extraction of the concentrated extract, retaining the ethyl acetate layer. Rotary evaporation was then employed to obtain a weight of M (52.11 g).

2.6. Silica Gel Column Chromatography

The ethyl acetate layer concentrate (DS142-1) was passed through a normal-phase silica gel column (200–300 mesh) using the following elution conditions: 100% petroleum ether → petroleum ether: ethyl acetate = 90:1 → petroleum ether: ethyl acetate = 50:1 → petroleum ether: ethyl acetate = 30:1 → petroleum ether: ethyl acetate = 10:1 → petroleum ether: ethyl acetate = 5:1 → petroleum ether: ethyl acetate = 3:1 → petroleum ether: ethyl acetate = 1:1 → 100% petroleum ether → 100% methanol. This yielded 18 components.

A portion of DS142-1-18-2 (2.1719 g) was passed through a normal-phase flash column (300–400 mesh silica gel) using the elution conditions: dichloromethane: methanol = 36:1 → dichloromethane: methanol = 32:1 → dichloromethane: methanol = 30:1 → dichloromethane: methanol = 20:1 → 100% methanol. This resulted in five components: DS142-1-18-1 (20.1 mg), DS142-1-18-2 (17.5 mg), DS142-1-18-3 (1.0511 g), DS142-1-18-4 (200 mg), DS142-1-18-5 (880 mg).

DS142-1-18-2-3 was subjected to liquid-phase analysis and purification using a Welch Ultimate® XB-C18 column (5 μm, 10 × 250 mm) with 100% methanol as the eluent, monitored at 210 nm and 254 nm, and a flow rate of 2 mL/min. This process yielded compound 1 (2.3 mg).

2.6.1. Optimization of Culture and Fermentation Conditions

Seed Cultivation: The frozen strain suspension stored at −80 °C was gradually thawed, and a small amount of the thawed culture was spread and activated on solid PDA medium within a laminar flow hood. After incubating at 25 °C for 72 h, spores from the activated strain were collected. These spores were then inoculated into 250 mL triangular flasks containing 100 mL of PDB liquid culture medium and incubated on a light-shaking incubator at 180 rpm for 24 h to obtain the seed culture.

Seed Culture Medium Fermentation Conditions: Salt concentration in the culture medium: 15 ppt; pH: 7.2–7.4; temperature: 25 °C; shaking speed: 180 rpm; fermentation time: 24 h.

Optimization of Culture Medium Fermentation Conditions: pH: 7.2–7.4; temperature: 25 °C; shaking speed: 150 rpm; fermentation time: 72 h.

2.6.2. Sample Extraction

The fermentation broth was filtered and separated using four layers of gauze to obtain mycelial balls and clear liquid. The clear liquid was subjected to extraction with an equal

volume of ethyl acetate, while the mycelial balls were subjected to ultrasound-assisted extraction 2–3 times using a mixed solution system of ethyl acetate: methanol: acetic acid = 80:15:5. After filtering and separating the mycelial balls and the extract, the extract was further extracted with ethyl acetate twice, and the combined ethyl acetate extracts were concentrated using rotary evaporation to obtain the crude extract. The weight of the crude extract was accurately measured and recorded.

Dry loading was performed using 1–1.5 times the mass of diatomaceous earth as an adsorbent, and 1–2 mL of methanol was used to dissolve the sample. The two components were mixed thoroughly to ensure that diatomaceous earth fully adsorbed the sample. After the organic reagents evaporated, the sample was dried at 45 °C for 3 h in an oven. Subsequently, a C18 SPE reverse-phase solid-phase extraction column was used for initial separation, retaining the extract under 100% methanol elution conditions. After rotary evaporation, 1 mL of methanol was used for ultrasonic dissolution, and the sample was filtered through a 0.22 μm filter membrane to obtain the final sample for HPLC analysis.

2.6.3. Determination of Glycosylceramides Content

Chromatographic Detection Conditions: Ultimate XB-C18 column: 4.6 × 250 mm, 5 μm; mobile phase: ultrapure water–methanol, flow rate: 0.8 mL/min; detection wavelength: 210 nm; injection volume: 8 μL; temperature: 26 °C; methanol elution for 20 min.

Construction of Standard Curve: Precisely weigh 10 mg of glycosylceramide standard into a 10 mL volumetric flask, dissolve it in methanol, shake it well, and bring it to a standard solution of 1 mg/mL. Subsequently, prepare a series of glycosylceramide standard solutions with concentrations of 200 μg/mL, 100 μg/mL, 75 μg/mL, 50 μg/mL, 25 μg/mL, and 10 μg/mL from the stock solution, and analyze them in triplicate using HPLC. Finally, construct a linear standard curve with peak area as the independent variable and glycosylceramides concentration as the dependent variable. The equation for the standard curve is $y = 3.5932x - 3.6172$, $R^2 = 0.9996$, where x represents peak area and y represents glycosylceramides concentration.

2.6.4. Determination of NO Content

An in vitro NO production inhibition experiment was conducted following a method reported in the literature [16]. The experiment was divided into four groups: normal group, LPS group, Ac A group (30 ug/mL, 40 ug/mL. RAW 264.7 cells (5×10^6 cells in a 96-well plate) were incubated for 6 h in a humidified incubator (37 °C, 5% CO_2). After incubation, the culture medium for the normal group was replaced with serum-containing medium. The LPS group was treated with LPS (0.2 ug/mL), and the two Ac A groups were treated with Ac A (30 ug/mL and 40 ug/mL) and LPS (0.2 ug/mL), respectively, followed by a 24 h incubation. Equivalent supernatants from RAW 264.7 cell cultures were collected and subjected to NO activity assays using a NO production inhibition assay kit (Cat NO S00215, Beyotime Biotechnology, Nantong, China).

2.6.5. Single-Factor Impact Experiments

Effect of Different Carbon Sources on glycosylceramides Production: Different carbon sources (glucose/sucrose/soluble starch/glycerol) at a concentration of 40 g/L were used as carbon sources in the fermentation medium, with 10 g/L of peptone as the nitrogen source for single-factor experiments. Each experimental group was repeated in triplicate. After fermentation, glycosylceramides were extracted from the metabolic products and analyzed by HPLC. The concentration of glycosylceramides under different carbon source conditions was determined using the standard curve. Significant differences in glycosylceramides production under different carbon source conditions were analyzed using SPSS software (analysis method: LSD, $p < 0.01$).

Effect of Different Nitrogen Sources on glycosylceramides Production: Different nitrogen sources (peptone/yeast extract/N-acetylglucosamine) at a concentration of 10 g/L were used as nitrogen sources in the fermentation medium, with 40 g/L of sucrose as the

carbon source for single-factor impact experiments. Each experimental group was repeated in triplicate. After fermentation, glycosylceramides in the metabolic products were qualitatively and quantitatively determined by HPLC. The concentration of glycosylceramides under different nitrogen source conditions was determined using the standard curve. SPSS software was used to analyze the results (analysis method: LSD, as mentioned earlier), and the nitrogen source that resulted in the highest glycosylceramides content was identified.

Effect of Different Medium Salinities on glycosylceramides Production: Using 40 g/L sucrose as the carbon source and 10 g/L yeast extract as the nitrogen source, the salinity of the fermentation medium was varied to 6 ppt, 14 ppt, 22 ppt, and 30 ppt to investigate the effect of different medium salinities on glycosylceramide production by the strain. Each salinity condition was repeated in triplicate. After fermentation, combining the qualitative and quantitative results obtained by HPLC with the standard curve, the optimal medium salinity for glycosylceramide production by the strain was determined using SPSS-22.0 software.

2.6.6. Orthogonal Experimental Design

Based on the results of the single-factor experiments for various influencing factors and their levels, *Aspergillus* sp. was cultured in a fermentation medium containing 45 g/L sucrose, 8 g/L yeast extract, and an appropriate amount of marine salt. An orthogonal table L9 (34) was used according to the selected influencing factors and the number of levels.

2.6.7. Response Surface Analysis for Optimization of Fermentation Medium

Using the selected factors of sucrose, yeast extract, and medium salinity, with glycosylceramides production as the response value, a three-factor, three-level experiment was established using the Box–Behnken design in the response surface design software Design-expert 8.0.6.1. This was performed to optimize the fermentation medium formula for *Aspergillus* sp. The factors and levels for the response surface experiments are listed in Table 1.

Table 1. Factors and levels for response surface experiments.

Factor	Level		
	−1	**0**	**1**
Soluble starch g/L	35	40	45
Yeast extract g/L	8	14	20
Culture-medium salinity ppt	6	14	22

2.6.8. Model Validation

The optimal culture medium formula for *Aspergillus* sp. from marine filamentous fungi, as determined by the Box–Behnken design method, was experimentally validated to assess the reliability of the model and analyze the final optimization results.

3. Results

3.1. Structural Analysis

The crude extracts from *Aspergillus* sp. were separated by a silica gel column and purified with Sephadex LH-20 and high-performance liquid chromatography to obtain AcA. The structure of the isolated compound was established by analyzing its spectroscopic data including UV, IR, 1D (^{1}H and ^{13}C), and 2D NMR (^{1}H-^{1} H COSY, HMQC, HMBC, NOESY) and HR-ESI-MS] and comparing the obtained data with what was reported in refs [17–20].

AcA was isolated as a colorless amorphous powder. The HR-ESI-MS (positive ion mode) m/z: 768.56 $[M+H]^{+}$ and the ^{13}C-NMR data suggested a molecular formula

of $C_{44}H_{81}NO_9$. The infrared spectrum of AcA showed absorption bands of hydroxy (3310 cm^{-1}) and carbonyl amide (1626 cm^{-1} and 1532 cm^{-1}) functional groups. The ^1H and ^{13}C-NMR spectra of AcA (Table 2) showed characteristic signals of glycoside derivatives (also known as cerebroside). These signals included anomeric protons at δ_H 4.11 (d; J = 7.75), carbon oxides (sugar portion) of H-1″ and δ_C 61.06–76.88, carbonyl carbons of H-1′ and δ_C 172.01, C-1′ (amide bond) and terminal methyl protons of δ_H 0.85 (t; J = 6.875), and methylene protons of δ_H 1.23–3.97 (m) (long-chain hydrocarbons). The glucose ^{13}C-NMR signals were δ_C 61.06 (C-6″), 70.01 (C-4″), 73.39 (C-2″), 76.54 (C-3″), 76.88 (C-5″), 103.50 (C-1″). The trans geometry of the C-8 double bond was established by the chemical shifts of the methyl groups attached to the C-9, which was δ_C 15.72 (C-18).

Table 2. ^1H and ^{13}C NMR Data for 1 (500, 125 MHz,DMSO-d6, TMS, δ ppm).

No.	δ_C	δ_H (J in Hz)	No.	δ_C	δ_H (J in Hz)
1″	103.50	4.11, ^1H, d(7.75)	1	68.60	3.97, m
2″	73.39	2.96, ^1H, m			3.51, dd(10.4,3.8)
3″	76.54	3.14, m	2	52.90	3.78, m
4″	70.01	3.04, m	3	70.51	3.97, m
5″	76.88	3.08, m	4	130.91	5.36, ^1H, dd(15.4,6.7)
6″	61.06	3.66, brdd(10.1,6.1)	5	130.91	5.67, ^1H, dt(15.4,6.7)
1′	172.01	—	6	27.37	1.94, m
2′	71.91	4.30, brt(4.78) t	7	32.13	1.94, m
3′	129.05	5.43, ^1H, dd(15.4,5.4)	8	123.5	5.09, ^1H, brt(6.1)
4′	130.91	5.45, ^1H, dt(15.4,5.4)	9	134.91	—
5′	31.63	1.94, m	10	39.10	1.94, m
6′-15′	29.00	1.24, m	11	27.29	1.23, m
16′	31.28	1.24, m	12–14	29.05	1.23, m
17′	22.08	1.24, m	15	28.69	1.23, m
18′	13.92	0.85, 3H, t(6.875)	16	22.08	1.23, m
NH	—	7.38, d(9.2)	17	13.92	0.85, ^3H, t(6.875)
OH-2′	—	5.77, d(5)	18	15.72	1.54, ^3H, s
OH-2″	—	4.98, d(4.6)	OH-3	—	4.97, d(4.2)
OH-4″	—	4.94, d(4.6)	OH-3″	—	4.92, d(5.0)
			OH-6″	—	4.52, t(5.9)

The length of the sphingoid long-chain base (LCB) and the amide-linked long-chain fatty acid base (FAB) were suggested as 17 and 20 carbons, respectively. The fragment ions at m/z 310.76 $[FAB+H]^+$ confirmed the length of the amide-linked long-chain fatty acid (FAB). Moreover, the fragment ions at m/z 280.26$[LCB+H]^+$ revealed the length of the sphingoid long-chain base (LCB) (as depicted in Figure S3). Based on the above data, the structure of AcA was defined as (2R,3E)-N-((2S,3R,4E,8E)-3-hydroxy-9-methyl-1-(β-D-glucopyranosyloxy) 2-hydroxyheptadeca-4,8-dien-2-yl))icos-3-enamide and was named Aspercerebroside A (as depicted in Figure 1).

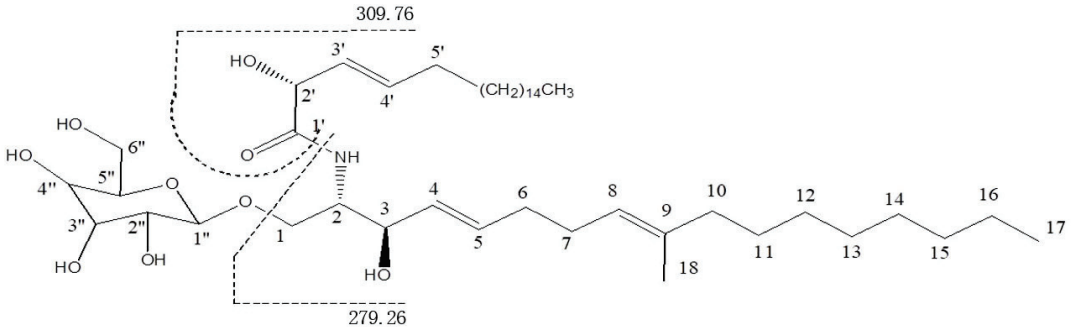


Figure 1. The chemical structural formula of Aspercerebroside A.

3.2. NO Production Assay

The inhibitory activity of the obtained aspercerebroside A on nitric oxide (NO) production was evaluated using an LPS-stimulated RAW 264.7 cell model. The NO release inhibition assay demonstrated that this compound exhibits significant anti-inflammatory effects at concentrations of 30 μg/mL and 40 μg/mL in Figure 2.

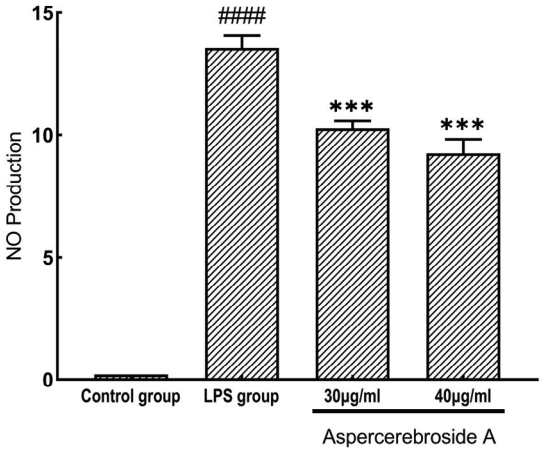


Figure 2. Inhibition of NO production by aspercerebroside A at concentrations of 30 μg/mL and 40 μg/mL in RAW 264.7 cells. Values represent the mean ± SD of three independent experiments. *** $p < 0.001$ (significant difference between the Aspercerebroside A treatment group and the LPS group). #### $p < 0.001$ (significant difference within the control group).

3.3. Single-Factor Experiments

3.3.1. Influence of Carbon Source Types on Glycosylceramide Production

Carbon sources are essential nutrients in microbial culture media. They provide the carbon skeleton for cell growth and the synthesis of cellular products, as well as the energy required for cellular activities. As shown in Figure 3, when sucrose is used as the carbon source in the fermentation medium for *Aspergillus* sp., the glycosylceramide production is the highest, with a yield of 89.32 μg/mL. Soluble starch, glucose, and glycerol have a similar impact on glycosylceramide production, which may be related to the enzymatic system utilized by this strain in glycosylceramide biosynthesis. Therefore, based on the experimental results, sucrose was selected as the optimal carbon source for the fermentation medium.

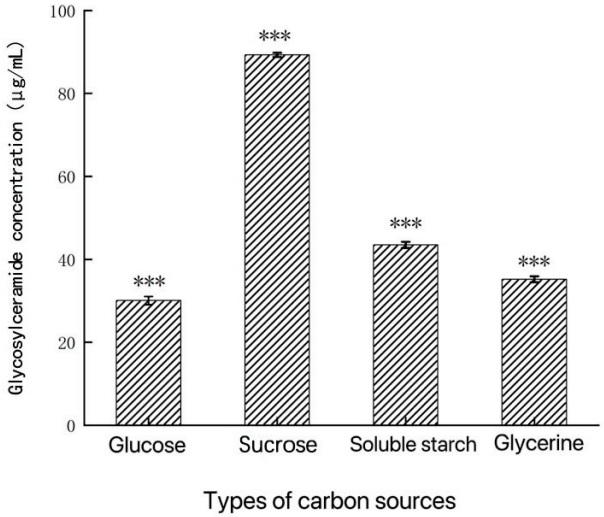


Figure 3. Influences of different carbon sources on glycosylceramide production from *Aspergillus* sp. ***: $p < 0.001$ (significant difference within the control group).

As shown in Figure 4, with the increase in sucrose concentration, glycosylceramide production first increased and then decreased. At 40 g/L, the maximum glycosylceramide production was 121 μg/mL. With the continuous increase in sucrose concentration, glycosylceramide production began to decline, which may have had a blocking effect.

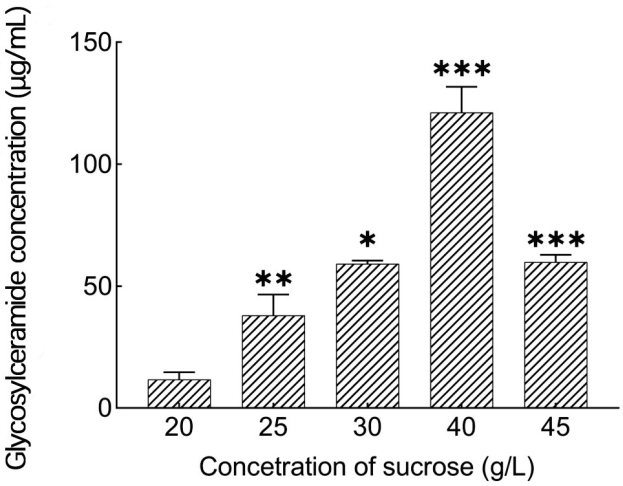


Figure 4. Influences of sucrose concentration on glycosylceramide production from *Aspergillus* sp. *: $p < 0.05$, **: $p < 0.01$, ***: $p < 0.001$ (significant difference within the control group).

3.3.2. Influence of Nitrogen Source Types on Glycosylceramide Production

Nitrogen sources are essential components in the composition of living organisms. Their primary function is to provide the necessary nitrogen elements for the synthesis of amino acids, proteins, nucleic acids, and other essential compounds. As shown in Figure 5, in the single-factor experiments with different nitrogen sources, when yeast extract was used as the nitrogen source, the glycosylceramide production was the highest, reaching 136.80 μg/mL. Next was peptones, and then the lowest production was observed with N-acetylglucosamine as the nitrogen source. Therefore, yeast extract was selected as the nitrogen source for the culture medium based on these results.

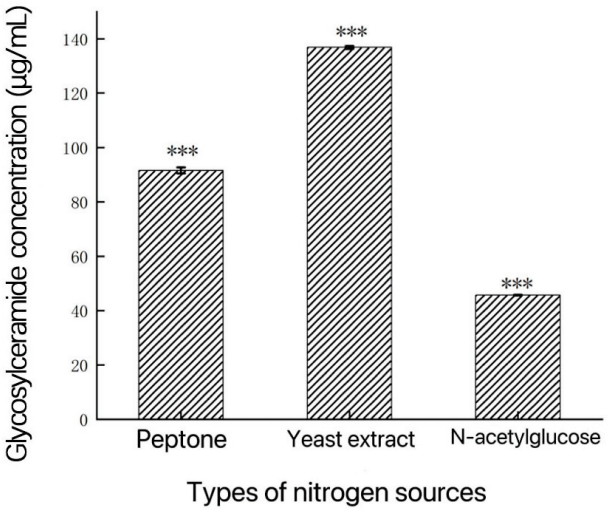


Figure 5. Influences of different nitrogen sources on glycosylceramide production from *Aspergillus* sp. ***: $p < 0.001$ (significant difference within the control group).

As shown in Figure 6, Yeast extract powder has the greatest influence on glycosylceramide yield. When the concentration of yeast extract powder is 14 g/L, the glycosylceramide yield is the highest. When the concentration of yeast extract powder continues

to increase, the glycosylceramide yield is inhibited and begins to decline, Therefore, the optimal concentration is 14 g/L.

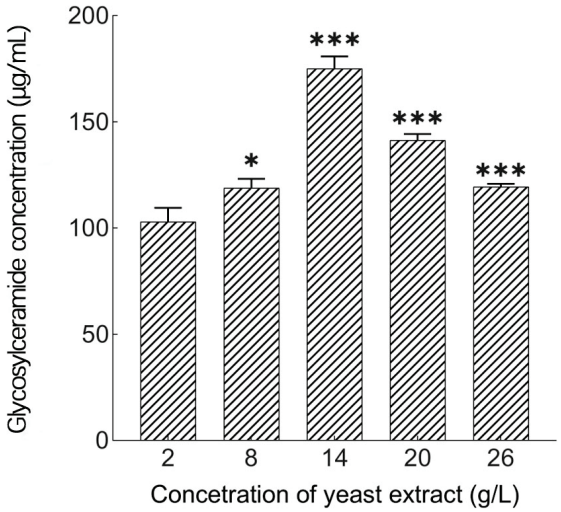


Figure 6. Influences of yeast extract concentration on glycosylceramide production from *Aspergillus* sp. *: $p < 0.05$, ***: $p < 0.001$ (significant difference within the control group).

3.3.3. Influence of Culture Medium Salinity on Glycosylceramide Production

Marine microorganisms face a unique environment characterized by high salinity, which differs from that of terrestrial microorganisms. The addition of ecological sea salt to the culture medium not only helps replicate the components of seawater but also provides essential inorganic salts for microbial growth. Changes in culture medium salinity may affect the concentration of glycosylceramides in the secondary metabolites of *Aspergillus*. sp. As shown in Figure 7, when the culture medium salinity was 14 ppt, the marine *Aspergillus* fungus produced the maximum amount of glycosylceramides, reaching 245.46 μg/mL. However, as the salinity of the culture medium increased beyond this point, the concentration of glycosylceramides gradually decreased. When the culture medium salinity reached 30 ppt, the glycosylceramide concentration was at its minimum, at only 11.47 μg/mL.

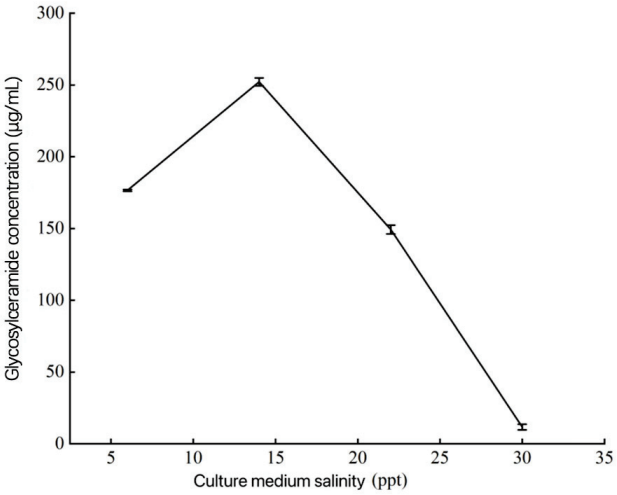


Figure 7. Influences of different nitrogen sources on glycosylceramide production from *Aspergillus* sp.

3.4. Orthogonal Array Experiment

Based on the single-factor results of various influencing factors and their levels, *Aspergillus* sp. was cultured in a fermentation medium containing 45 g/L sucrose, 8 g/L yeast

extract, and an appropriate amount of ecological sea salt. An orthogonal array L9 (34) was used according to the selected influencing factors and their levels. The influencing factors and their levels to be investigated are shown in Table 3. The orthogonal experimental table L9 (34) and the experimental results are presented in Table 4, while the variance analysis data processing can be found in Table 5.

Table 3. Experimental factors of SPSS design and their levels.

Level	A (Initial pH Value)	B (Initial Salinity/ppt)	C (Temperature/°C)	D (Time/d)
1	6.2~6.4	6	20	3
2	7.2~7.4	14	25	4
3	8.2~8.4	22	30	5

Table 4. SPSS design table and experimental results.

Number	A (Initial pH Value)	B (Initial Salinity/ppt)	C (Temperature/°C)	D (Time/d)	Glycosylceramide Concentration Group 1 (μg/mL)	Glycosylceramide Concentration Group 2 (μg/mL)	Glycosylceramide Concentration Group 1 (μg/mL)
1	1	1	1	1	28.62	27.06	21.44
2	1	2	3	2	193.07	177.85	187.81
3	1	3	2	3	201.87	229	211.22
4	2	1	3	3	209.74	178.74	185.28
5	2	2	2	1	73.62	83.87	76.82
6	2	3	1	2	74.82	90.04	114.03
7	3	1	2	2	169.61	139.41	171.84
8	3	2	1	3	122.38	139.19	141.14
9	3	3	3	1	177.40	178.04	215.03
K1	1277.94	1131.96	758.72	881.9			
K2	1087.18	1195.75	1279.11	1318.48			
K3	1454.04	1491.45	1703.18	1618.78			
K1/9	141.99	125.77	84.3	97.99			
K2/9	120.80	132.86	142.12	146.5			
K3/9	161.56	165.72	189.24	179.86			
R	40.76	39.94	104.94	81.88			

Table 5. Analysis of variance.

Source of Variance	Type III Square Sum	Df	the Average Square	F Value	Significance
A	7480.994	2	3740.497	18.178	$p < 0.05$
B	8175.582	2	4087.791	19.866	$p < 0.05$
C	50,737.610	2	25,368.805	123.287	$p < 0.05$
D	30,510.160	2	15,255.080	74.137	$p < 0.05$
Error	3703.852	18	205.770		

F0.05(2,18) = 3.555, F0.01(2,18) = 6.01.

From the intuitive analysis in Table 4 using the range analysis method, it can be seen that the most significant factor affecting the production of aspercerebroside A by marine-derived *Aspergillus* sp. is temperature, and the optimal combination for aspercerebroside A production is A3B3C3D3. The K values refer to the sum of the experimental data Y for each factor at every level. For instance, in this experiment, K1 for factor A represents the sum of the nervonic acid yield for all experimental groups at pH levels ranging from 6.2 to 6.4. R value stands for the range of factors, reflecting the degree of variation among different levels. By analyzing its magnitude, it is possible to make an initial ranking of the selected factors based on their differences. K1, K2, and K3 are the sum values corresponding to different factor levels. K1/9, K2/9, and K3/9 are the means of these sum values. The R value is calculated by subtracting the smallest mean value from the largest mean value.

Table 5, utilizing the variance analysis method, shows that the order of influence on aspercerebroside A production is temperature > time > initial salinity > initial pH value. All four factors have a highly significant impact on aspercerebroside A yield. Based on the analysis of the results, the discrepancy between the order of influence of initial salinity and initial pH value observed in the range analysis and variance analysis may be due to the closeness of their effects on aspercerebroside A production. Moreover, range analysis cannot estimate the inevitable errors that occur during experiments and the measurement of the results. Therefore, the results are considered more reliable based on variance analysis.

To validate these orthogonal results, marine-derived *Aspergillus* sp. was cultured under the optimized fermentation conditions from the best combination. The aspercerebroside A content obtained from this experiment was 436.86 μg/mL.

3.4.1. Response Surface Optimization Results and Analysis

Using the sucrose concentration, yeast extract concentration, and initial salinity as independent variables, a three-factor, three-level response surface experiment was conducted through the Box–Behnken design method to analyze the interactive effects among various influencing factors. The response surface results are shown in Table 6.

Table 6. Response surface design test and results.

Test Number	Level			Glycosylceramide Concentration (μg/mL)
	Sucrose Concentration (A)	Concentration of Yeast Extract Powder (B)	Salinity of Medium (C)	
1	0	−1	−1	155.6
2	0	0	0	168.4
3	1	−1	0	157.9
4	1	0	1	162.2
5	1	0	−1	160.1
6	0	1	−1	165.8
7	0	−1	1	157.7
8	−1	0	1	161.9
9	−1	−1	0	159.1
10	0	1	1	164.9
11	1	1	0	166.8
12	0	0	0	169.1
13	0	0	0	167.1
14	0	0	0	168.8
15	−1	1	0	171.3
16	−1	0	−1	163.2
17	0	0	0	169.3

The regression equation for the neuralamide concentration (Y) in relation to sucrose concentration (A), yeast extract concentration (B), and initial salinity (C), as obtained through data analysis using the Design-Expert 8.0.6.1 software, is as follows:

$$Y = 168.54 - 1.14A + 4.81B + 0.25C - 0.83AB + 0.70AC - 0.75BC - 1.96A^2 - 2.81B^2 - 4.73C^2$$

3.4.2. Variance Analysis

From Table 7, it can be observed that the *p*-value of the model is less than 0.0001, indicating that the regression equation model is highly significant. The lack-of-fit *p*-value is 0.4638, which is greater than 0.05, suggesting that errors due to random factors do not significantly affect the experimental results. The model's determination coefficient (R^2) is 0.9851, indicating that 98.51% of the response variation in neuralamide concentration is explained by the selected variables. The adjusted R^2 (R^2adj) is 0.9960, signifying that the model can explain 99.60% of the variation in neuralamide concentration response. Overall,

the established model fits well and can be used to predict the concentration of neuralamide in fermentation production.

Table 7. Regression model analysis of variance.

Source of Variation	Quadratic Sum	Degree of Freedom	Mean Square	F-Value	*p*-Value
Model	360.73	9	40.08	51.53	<0.0001
Concentration of sucrose (A)	10.35	1	10.35	13.31	0.0082
Concentration of yeast extract (B)	185.28	1	185.28	238.22	<0.0001
Salinity of medium (C)	0.50	1	0.50	0.64	0.4490
AB	2.72	1	2.72	3.50	0.1035
AC	1.96	1	1.96	2.52	0.1564
BC	2.25	1	2.25	2.89	0.1328
A^2	16.13	1	16.13	20.74	0.0026
B^2	33.19	1	33.19	42.67	0.0003
C^2	94.30	1	94.30	121.24	<0.0001
Residual error	5.44	7	0.78		
Out of fit term	2.39	3	0.80	1.05	0.4638
Net error	3.05	4	0.76		
Total deviation	366.18	16			
R^2 = 0.9851			R^2adj = 0.9960		

Note: $p < 0.01$ indicates a very significant difference; $p < 0.05$ indicates a significant difference.

The analysis of variance (ANOVA) reveals that the first-order terms A and B have highly significant differences, indicating that the sucrose concentration and yeast extract concentration both have a highly significant impact on the concentration of neuralamide produced by the strain. The second-order terms A^2, B^2, and C^2 exhibit highly significant differences, suggesting that the relationship between neuralamide concentration and sucrose concentration, yeast extract concentration, and initial salinity is not linear. The interaction terms AB, AC, and BC all have *p*-values greater than 0.05, indicating that the pairwise interactions between the three factors are not significant. Based on the F-values, the order of significance of the three selected variables in influencing the neuralamide production concentration is as follows: yeast extract concentration (B) > sucrose concentration (A) > initial salinity (C).

3.4.3. RSM Analysis

The interaction between sucrose concentration and yeast extract concentration is depicted in Figure 8. These figures include a contour plot and a response surface plot, with the culture medium salinity being held constant at 14 ppt. The contour plot predominantly showcases an elliptical shape, underscoring the substantial interaction between sucrose concentration and yeast extract concentration in their collective impact on glycosylceramide concentration. In the 3D surface plot, it becomes apparent that the surface representing sucrose concentration undergoes more gradual changes when compared to the surface representing yeast extract concentration. This observation suggests that the yeast extract concentration exerts a more pronounced influence on glycosylceramide concentration within the strain.

Furthermore, Figure 9 displays the contour plot and response surface plot for the interaction between sucrose concentration and initial salinity when yeast extract concentration is fixed at 14 g/L. The contour plot is elliptical in shape, indicating a significant interaction between sucrose concentration and initial salinity on neuralamide concentration. In the 3D surface plot, the initial salinity surface changes more gradually compared to the sucrose concentration surface, implying that sucrose concentration has a greater influence on the neuralamide concentration produced by the strain.

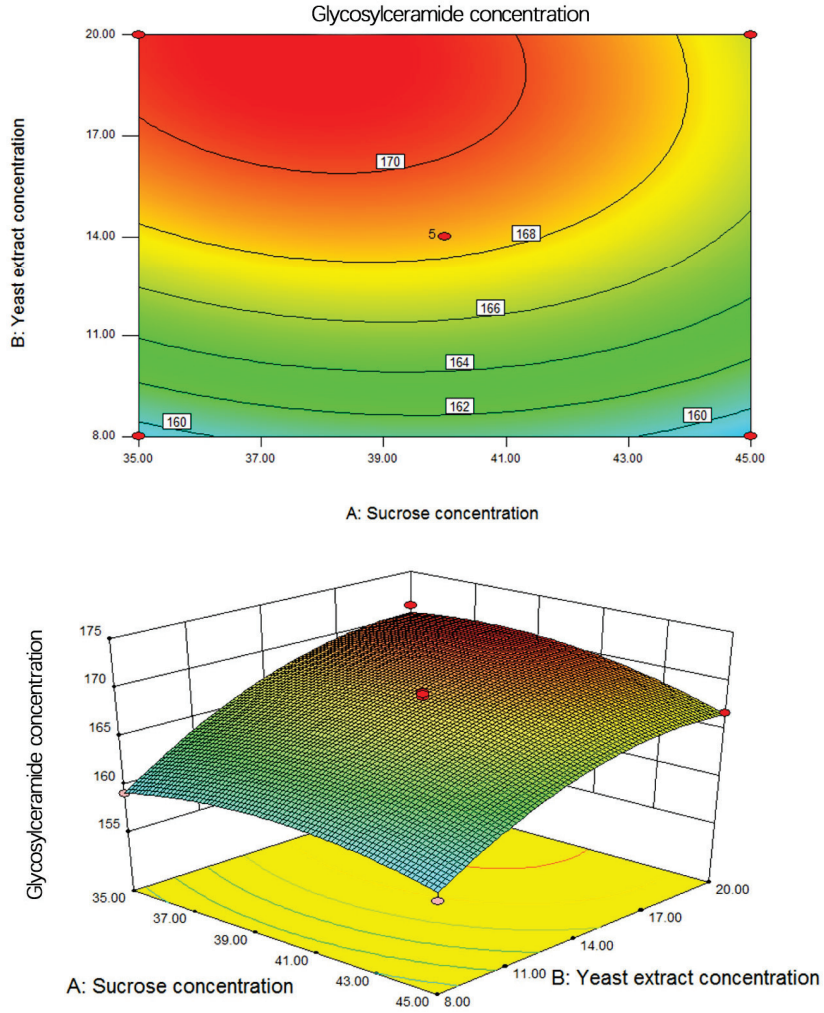


Figure 8. Contour and response surface diagram of sucrose concentration and yeast extract powder concentration on glycosylceramide concentration.

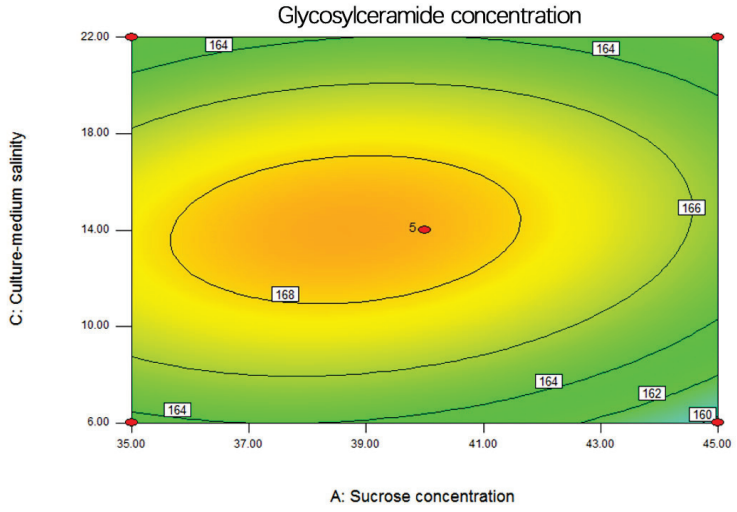


Figure 9. *Cont*.

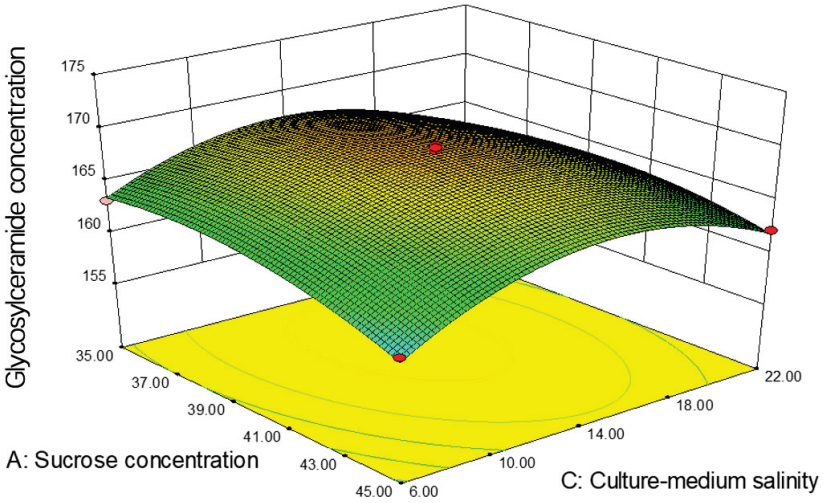


Figure 9. Contour and response surface diagram of sucrose concentration and culture-medium salinity on glycosylceramide concentration.

The influence on neuralamide concentration is influenced by the strain. Figure 10 depicts a contour plot and a response surface plot illustrating the interaction between the yeast extract concentration and initial salinity, with the sucrose concentration fixed at 40 g/L. The contour plot displays an overall elliptical shape, indicating a strong interaction between yeast extract concentration and initial salinity concerning neuralamide concentration. In the 3D surface plot, the surface representing yeast extract concentration changes more significantly compared to the initial salinity surface, suggesting that the yeast extract concentration has a notably greater impact on the glycosylceramide production of the strain than sucrose concentration.

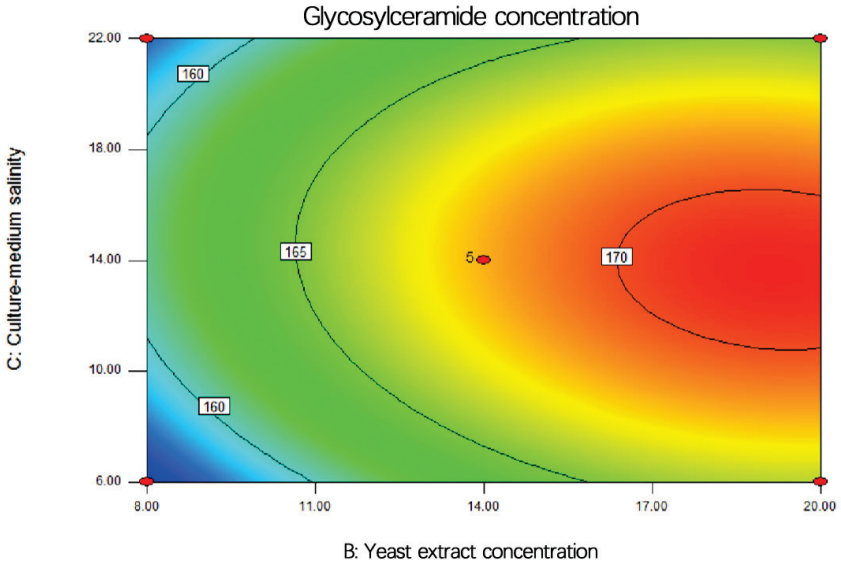


Figure 10. *Cont.*

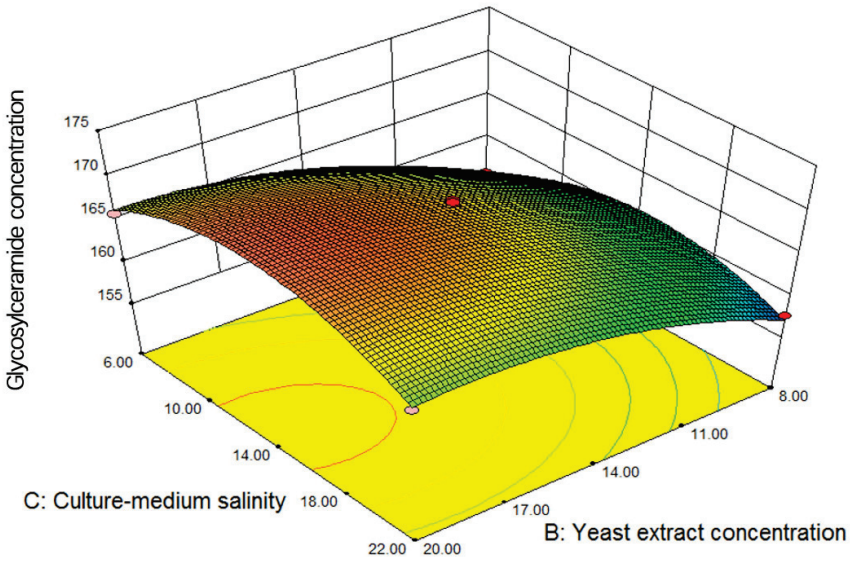


Figure 10. Contour and response surface diagram of yeast extract powder concentration and culture-medium salinity on glycosylceramide concentration.

3.5. Verification Experiment Results

Based on the response surface analysis, the predicted optimal culture medium formula for producing glycosylceramides with *Aspergillus* sp. was determined as follows: a sucrose concentration of 37.47 g/L, yeast extract concentration of 19.66 g/L, and a culture medium salinity of 13.31 ppt. Under these conditions, the glycosylceramide concentration was predicted to be 171.084 μg/mL. In practical experiments, the model parameters were adjusted to a sucrose concentration of 37.5 g/L, yeast extract concentration of 19.7 g/L, and culture medium salinity of 13.3 ppt. Three parallel repeated experiments were conducted, resulting in glycosylceramide concentrations of 172.421 μg/mL, 171.976 μg/mL, and 170.612 μg/mL, with an average value of 171.670 μg/mL. These results closely aligned with the predicted values, indicating a strong model fit and high model credibility.

4. Discussion

It is worth noting that within *Aspergillus* sp., glycosylceramide compounds falling under the glycosylceramide class have been isolated [21]. These compounds exhibit similarities to AcA, sharing a molecular weight range between 760 and 780 [22]. This similarity indicates a resemblance between these glycosylceramide variants and underscores their association with aspercerebroside A within the glycosylceramide category. Such findings further emphasize the existence of analogous glycosylceramide compounds in the *Aspergillus* sp. genus, aligning with our identification of glycosylceramide (AcA) and supporting its classification within the broader glycosylceramide spectrum.

In marine environments, microorganisms harbor abundant resources, and yet the production of potentially valuable metabolites often demonstrates low yields during initial fermentation. Hence, the optimization of microbial fermentation processes has become pivotal to enhance metabolite production and fully exploit marine microbial resources. Typically, optimizing microbial fermentation conditions involves a blend of statistical and mathematical modeling techniques, as evidenced in previous studies. For instance, Wang Cong et al. [23] successfully optimized fermentation conditions for enhancing lincomycin D production by Streptomyces parvulus OUCMDZ-2554, resulting in a remarkable 3.6-fold increase in yield. Similarly, Dong Yanjuan et al. [24] optimized the fermentation conditions for elevating xylanase production by strain YS1069, achieving a remarkable five-fold increase in xylanase activity.

However, studies focusing on enhancing glycosylceramide fermentation yields have been relatively limited. Prior research primarily centered on the applications and extraction

methods of glycosylceramides, such as elevating glycosylceramide production through Ganoderma lucidum fermentation or preparing glycosylceramides through emulsion fermentation. This study bridges a gap in this domain by augmenting glycosylceramide production through the optimization of culture medium specifically designed for marine-derived microorganisms.

During the optimization of conditions by selecting the initial pH value and initial salinity as variables, it was observed that the initially fixed salinity of the culture medium would fluctuate due to subsequent pH adjustments. Throughout the fermentation process, both salinity and pH dynamically changed. Comprehensive monitoring of salinity and acidity throughout the fermentation might identify the most suitable conditions for synthesizing glycosylceramides. The experimental findings revealed that at a temperature of 20 °C, the strain's growth was notably inhibited compared to the standard temperature (25 °C), whereas at 30 °C, the growth accelerated significantly. Temperature was identified as a critical factor influencing glycosylceramide production, suggesting the potential to increase temperature moderately to enhance the strain's metabolic capacity.

Simultaneously, throughout fermentation, time displayed a direct correlation with glycosylceramide accumulation. Identifying an optimal fermentation timepoint combined with an appropriate temperature could significantly enhance fermentation capability, optimizing the cost-effectiveness of glycosylceramide production. In summary, optimizing the fermentation of the marine-derived fungus Aspergillus sp. can be achieved by enhancing its own development and nutrient synthesis through adjustments in suitable culture medium components such as inorganic salts, the number of carbon and nitrogen source types, as well as regulating the fermentation liquid's pH acidity and salinity and altering the fermentation temperature, duration, inoculum size, and speed to investigate their impact on metabolite production and content. Further exploration of the interaction between these factors could refine the fermentation conditions for optimal glycosylceramide synthesis.

5. Conclusions

This investigation explored the anti-inflammatory potential of AcA using LPS-induced RAW 264.7 cells, revealing significant inhibitory effects of Compound 1 on nitric oxide (NO) production in RAW 264.7 cells, particularly at concentrations of 30 μg/mL and 40 μg/mL. This discovery holds crucial importance in identifying potent active components derived from marine fungi.

In this study, a comprehensive investigation was conducted to determine the fermentation parameters for *Aspergillus* sp. derived from marine fungi. Initially, single-factor impact experiments were employed to explore the range and trends of carbon sources, nitrogen sources, initial pH values, salinity, temperature, and time fluctuations during fermentation. Subsequently, an orthogonal study was conducted, focusing on four influencing factors—initial pH value, initial salinity, temperature, and time—at three suitable levels, resulting in the optimal fermentation combination of A3B3C3D3. Experimental validation confirmed that the most suitable fermentation conditions for Aspergillus sp. were as follows: 45 g/L sucrose, 8 g/L yeast extract, initial salinity of 22 ppt (using ecological mineral salts to adjust fermentation medium), initial pH range of 8.2 to 8.4, and cultivation at 30 °C for 5 days, resulting in a glycosylceramide content of 436.86 μg/mL. Additionally, these optimized fermentation conditions resulting in a glycosylceramide content represent a significant finding in this research. Glycosylceramide production under such precise and enhanced conditions, previously sparsely discussed in the existing literature, emphasizes the novelty and importance of this study's outcomes.

Furthermore, employing a combination of single-factor impact experiments and response surface optimization led to the successful determination of the optimal culture medium formulation for glycosylceramide production by Aspergillus sp. derived from marine fungi. This formulation consisted of 37.5 g/L sucrose, 19.7 g/L yeast extract, and a culture medium salinity of 13.3 ppt. Experimental validation demonstrated a close align-

ment between actual and predicted production values, affirming the high reliability of the established regression model.

In conclusion, The discovery of these specific fermentation parameters offers a valuable contribution to the field, particularly in elucidating optimal conditions for glycosylceramide biosynthesis in *Aspergillus* sp. derived from marine fungi. It not only expands the limited literature discussing these specific fermentation conditions but also paves the way for potential applications in industrial-scale glycosylceramide production.

Supplementary Materials: The following supporting information can be downloaded at: https://www.mdpi.com/article/10.3390/metabo14020099/s1. Figure S1: ^{1}H NMR spectrum of 1, Figure S2: ^{13}C NMR spectrum of 1, Figure S3: mass spectrum of 1, Figure S4: fungal culture on YM medium, Figure S5: glycosylceramide standard curve, Figure S6: influences of different carbon sources, Figure S7: influences of different nitrogen sources, Figure S8: influences of different nitrogen sources, Table S1: response surface design test and results, Table S2: regression model analysis of variance, Figure S9: contour and response surface diagram of sucrose concentration and yeast extract powder concentration, Figure S10: contour and response surface diagram of sucrose concentration and culture-medium salinity, Figure S11: contour and response surface diagram of yeast extract powder concentration and culture-medium salinity, Figure S12: contour and response surface diagram of sucrose concentration and yeast extract powder concentration on glycosylceramide concentration, Figure S13: contour and response surface diagram of sucrose concentration and culture-medium salinity on glycosylceramide concentration, Figure S14: contour and response surface diagram of yeast extract powder concentration and culture-medium salinity on glycosylceramide concentration.

Author Contributions: Conceptualization, Y.-H.C. and B.Y. methodology, Q.Z.; software, J.L.; formal analysis, R.Y.; investigation Q.Z. and B.Y.; resources, L.L.; data curation, Q.Z. and R.Y.; writing—original draft preparation, J.Z.; writing—review and editing, M.Y.; visualization, Y.-H.C.; supervision, Y.-H.C.; project administration, B.Y.; funding acquisition, Y.-H.C. and B.Y. All authors have read and agreed to the published version of the manuscript.

Funding: This research was funded by the Xiamen Natural Science Foundation, grant number 3502Z20227311, Technology Innovation Program of Xiamen Ocean and Fisheries Development Special Funds, number 23YYZP004QCB28, 2023 Natural Science Foundation of Fujian Province Grant No. 2023 J011651 and the Science and Technology Program of Fujian province, number 2023J011659.

Institutional Review Board Statement: Not applicable.

Informed Consent Statement: Not applicable.

Data Availability Statement: All data are available in the manuscript and in the Supplementary Information.

Conflicts of Interest: The authors declare no conflicts of interest.

References

1. Lin, S.F.; Jiang, H.; Fu, Q.Q.; Huang, S.J.; Tang, L.Y.; Li, A.; Liu, M.Q. Effects of Pulsed Light on Mycelium Growth and Conidiation in *Aspergillus oryzae*. *Fermentation* **2023**, *9*, 674. [CrossRef]
2. Ghazawi, K.F.; Fatani, S.A.; Mohamed, S.G.A.; Mohamed, G.A.; Ibrahim, S.R.M. *Aspergillus nidulans*—Natural Metabolites Powerhouse: Structures, Biosynthesis, Bioactivities, and Biotechnological Potential. *Fermentation* **2023**, *9*, 325. [CrossRef]
3. Zhuravleva, O.I.; Afiyatullov, S.S.; Denisenko, V.A.; Svetlana, P.E.; Natalya, N.S.; Pavel, S.D.; Natalya, Y.K. Secondary metabolites from a marine-derived fungus *Aspergillus carneus Blochwitz*. *Phytochemistry* **2012**, *80*, 123–131. [CrossRef] [PubMed]
4. Jin, W.; Rinehart, K.L.; Jares-Erijman, E.A. Ophidiacerebrosides: Cytotoxic glycosphingolipids containing a novel sphingosine from a sea star. *J. Org. Chem.* **1994**, *59*, 144–147. [CrossRef]
5. Tan, R.X.; Chen, J.H. The cerebrosides. *Nat. Prod. Rep.* **2003**, *20*, 509. [CrossRef] [PubMed]
6. Rossi, C.; Ferrante, R.; Valentinuzzi, S.; Zucchelli, M.; Buccolini, C.; Di Rado, S.; Trotta, D.; Stuppia, L.; Federici, L.; Aricò, M. Noninvasive DBS-Based Approaches to Assist Clinical Diagnosis and Treatment Monitoring of Gaucher Disease. *Biomedicines* **2023**, *11*, 2672. [CrossRef] [PubMed]
7. Pu, Y.F.; Zhang, W.M.; Zhong, G. Functions and Applications of Ceramides. *Cereals Oils* **2005**, *7*, 14–16.
8. Bruno, M.C.; Manuel, P.; Liana, C.S. Ceramide: A simple sphingolipid with unique biophysical properties. *Prog. Lipid Res.* **2014**, *54*, 53–67.
9. Wei, J.; Zhang, W.M.; Zhong, G. Function of ceramides in skin and application in cosmetic. *Cereals Oils* **2007**, *1*, 21–24.

10. Bakar, J.; Michael-Jubeli, R.; Libong, D.; Baillet-Guffroy, A.; Tfayli, A. Stratum corneum ceramide profiles in vitro, ex vivo, and in vivo: Characterization of the α-hydroxy double esterified ceramides. *Anal. Bioanal. Chem.* **2022**, *414*, 3675–3685. [CrossRef]
11. Stelmasiewicz, M.; Świątek, Ł.; Ludwiczuk, A. Chemical and Biological Studies of Endophytes Isolated from *Marchantia polymorpha*. *Molecules* **2023**, *28*, 2202. [CrossRef]
12. Hu, Z.; Yu, C.S. Research Progress on Skin Barrier Function. *Chin. Clin. Physician J. (Electron. Ed.)* **2013**, *7*, 3101–3103.
13. Shindo, S.; Murota, H.; Seki, T.; Mori, K.; Kaizu, K.; Nishizaka, T.; Takagi, Y.; Katayama, I. Effects of a moisturizer containing pseudo-ceramide and a eucalyptus extract on sweating function in adult atopic dermatitis: A double-blind, randomized, controlled left-right comparison clinical trial. *J. Cosmet. Dermatol.* **2022**, *21*, 4503–4509. [CrossRef] [PubMed]
14. Cheawchanlertfa, P.; Chitcharoen, S.; Raethong, N.; Liu, Q.; Chumnanpuen, P.; Soommat, P.; Song, Y.; Koffas, M.; Laoteng, K.; Vongsangnak, W. Enhancing Genome-Scale Model by Integrative Exometabolome and Transcriptome: Unveiling Carbon Assimilation towards Sphingolipid Biosynthetic Capability of *Cordyceps militaris*. *J. Fungi* **2022**, *8*, 887. [CrossRef] [PubMed]
15. Bi, S.Y.; Liu, W. Influence of Ceramides on Skin Barrier Function in Atopic Dermatitis. *Chin. J. Med. Aesthet. Cosmetol.* **2015**, *21*, 317–318.
16. Wang, H.C.; He, C.F. Research Status and Application of Ceramides in the Skin. *China Surfactant Deterg. Cosmet.* **2019**, *49*, 51–57.
17. Wang, W.L.; Wang, Y.; Tao, H.W.; Tao, H.W.; Peng, X.P.; Liu, P.P.; Zhu, W.M. Cerebrosides of the Halotolerant Fungus *Alternaria raphani* Isolated from a Sea Salt Field. *J. Nat. Prod.* **2009**, *72*, 1695–1698. [CrossRef]
18. Wu, S.; Chen, Y.; Miao, C. Secondary metabolites of endophytic fungus *Xylaria* sp. YC-10 of *Azadirachta indica*. *Chem. Nat. Compd.* **2011**, *47*, 858–861. [CrossRef]
19. Hamed, A.; Abdel-Razek, A.S.; Araby, M.; Abu-Elghait, M.; EI-Hosari, D.G.; Frese, M.; Soliman, H.S.M.; Stammler, H.G.; Sewald, N.; Shaaban, M. Meleagrin from marine fungus *Emericella dentata* Nq45: Crystal structure and diverse biological activity studies. *Nat. Prod. Res.* **2021**, *35*, 3830–3838. [CrossRef]
20. Boulis, A.G.; Hamed, A.A.; El-awady, M.E.; Mohanmed, A.R.; Shaaban, M. Diverse bioactive metabolites from *Penicillium* sp. MMA derived from the red sea: Structure identification and biological activity studies. *Arch. Microbiol.* **2020**, *202*, 1985–1996. [CrossRef]
21. Kitagaki, H. Medical application of substances derived from non-pathogenic fungi *Aspergillus oryzae* and A. luchuensis-containing *koji*. *J. Fungi* **2021**, *7*, 243–258. [CrossRef] [PubMed]
22. Toledo, M.S.; Levery, S.B.; Straus, A.H.; Suzuki, E.; Momany, M.; Glushka, J.; Takahashi, H.K. Characterization of sphingolipids from mycopathogens: Factors correlating with expression of 2-hydroxy fatty acyl (E)-Δ3-unsaturation in cerebrosides of Paracoccidioides brasiliensis and *Aspergillus fumigatus*. *Biochemistry* **1999**, *38*, 7294–7306. [CrossRef]
23. Wang, C.; Liu, P.P.; Wang, Y.; Sun, K.L.; Zhu, W. Optimization of Fermentation Conditions for the Production of Lincomycin D by Marine-Derived Actinomycete *Streptomyces parvulus* OUCMDZ-2554. *Chin. J. Mar. Drugs* **2014**, *33*, 34–42.
24. Dong, Y.J.; Hao, J.H.; Zheng, H.F.; Sun, Y. Optimization of Enzyme Production Conditions by the Strain YS1069. *Prog. Fish. Sci.* **2016**, *37*, 154–159.

Disclaimer/Publisher's Note: The statements, opinions and data contained in all publications are solely those of the individual author(s) and contributor(s) and not of MDPI and/or the editor(s). MDPI and/or the editor(s) disclaim responsibility for any injury to people or property resulting from any ideas, methods, instructions or products referred to in the content.

molecules

MDPI

Review

G-Quadruplexes in Human Telomere: Structures, Properties, and Applications

Yan Xu [1,*] and Makoto Komiyama [2,*]

[1] Division of Chemistry, Department of Medical Sciences, Faculty of Medicine, University of Miyazaki, 5200 Kihara, Kiyotake, Miyazaki 889-1692, Japan
[2] Research Center for Advanced Science and Technology (RCAST), The University of Tokyo, 4-6-1 Komaba, Meguro, Tokyo 153-8904, Japan
* Correspondence: xuyan@med.miyazaki-u.ac.jp (Y.X.); komiyama.makoto@emer.rcast.u-tokyo.ac.jp (M.K.)

Abstract: G-quadruplexes, intricate four-stranded structures composed of G-tetrads formed by four guanine bases, are prevalent in both DNA and RNA. Notably, these structures play pivotal roles in human telomeres, contributing to essential cellular functions. Additionally, the existence of DNA:RNA hybrid G-quadruplexes adds a layer of complexity to their structural diversity. This review provides a comprehensive overview of recent advancements in unraveling the intricacies of DNA and RNA G-quadruplexes within human telomeres. Detailed insights into their structural features are presented, encompassing the latest developments in chemical approaches designed to probe these G-quadruplex structures. Furthermore, this review explores the applications of G-quadruplex structures in targeting human telomeres. Finally, the manuscript outlines the imminent challenges in this evolving field, setting the stage for future investigations.

Keywords: DNA G-quadruplex; RNA G-quadruplex; DNA:RNA hybrid G-quadruplex

1. Introduction

The term telomere is derived from two Greek words: telos (meaning "end") and meros (meaning "part"). Human telomeric DNA consists of a duplex region composed of TTAGGG repeats, which terminates with a G-rich single-stranded overhang of 100–200 nucleotide (nt) length. Though telomeres are crucial for many cellular functions, they are subject to progressive decreases in length at each round of DNA replication. It has been demonstrated by many studies that human telomere DNA plays important roles in cancer and aging [1,2]. Telomeres provide the machinery to protect chromosomes from such detriments. The protective function of telomeres might depend on their state, e.g., whether they have "capping" or "uncapping" structures. Telomere DNA sequences can form G-quadruplexes with various folding topologies, as demonstrated by many structural studies [1]. As shown in Figure 1a, four guanine bases are bound to a tetrad through Hoogsteen hydrogen bondings, and these guanine tetrads stack each other into G-quadruplexes. Metal cations (e.g., Na^+ and K^+) are usually bound to the center of guanine tetrad to stabilize the whole structures. G-quadruplexes are promising for numerous approaches that were developed to target telomeres [3–5]. Several ligands for G-quadruplexes were developed, and their interactions were investigated in detail. For a long time, telomere DNA was believed not to be transcribed into RNA. However, more recent findings showed that telomere DNA is in fact transcribed into RNA (referred to as telomere RNA) in cells [6,7]. These telomere RNAs exist in human cells with heterogeneous length. It was proposed that telomere RNA is associated with the end chromosome, and reveals a new level of protection of chromosomal ends [8–10]. Valuable insight into biological processes such as cancer and aging has been provided.

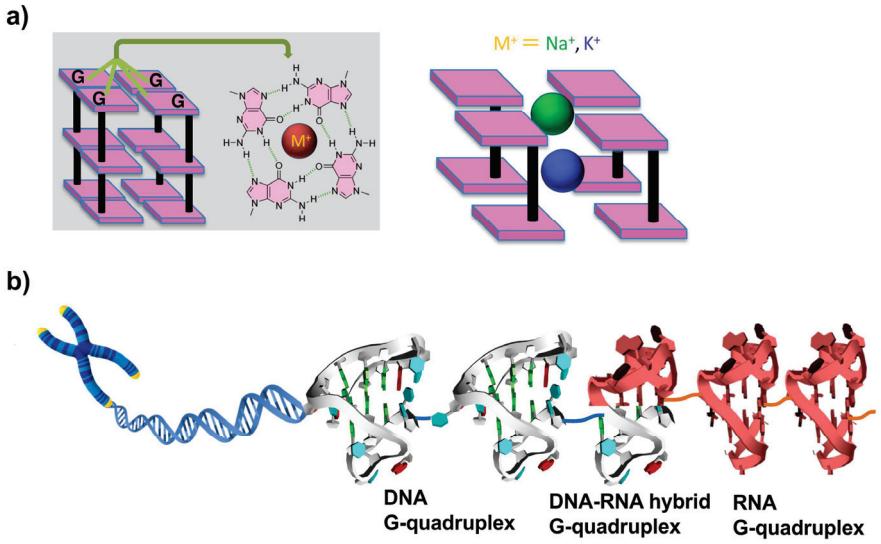


Figure 1. (**a**) Structures of G tetrads and G-quadruplexes. Cations with larger ionic radii, such as K^+ (depicted in blue), are positioned between the tetrads. In contrast, smaller cations, such as Na^+ (illustrated in green), can coordinate within the plane of the tetrads or assume an intermediate position. (**b**) Superhelix structure formed at the ends of chromosomes from telomeric DNA G-quadruplexes, DNA:RNA G-quadruplexes, and RNA G-quadruplexes. As the result, this essential portion is sufficiently protected and further functionalized.

Recently, telomere RNA was suggested to form G-quadruplexes which perform complicated functions [11–14]. With the use of probes provided by chemical approaches, telomere DNA and RNA G-quadruplex structures were detected in vitro and also in human cells [15–17]. Moreover, an DNA:RNA hybrid G-quadruplex is formed from telomeric DNA and telomeric RNA [18–22]. These results indicate that DNA G-quadruplexes, DNA:RNA hybrid G-quadruplexes, and RNA G-quadruplexes can be key players to protect the terminus of telomere (Figure 1b).

In order to deeply understand the biology of telomere, precise information on the structures of G-quadruplexes and their physicochemical properties is essential. Accordingly, the present review focuses on the structural information of DNA G-quadruplexes, RNA G-quadruplexes, and DNA:RNA hybrid G-quadruplexes in human telomere. Various chemical approaches to probe human telomere G-quadruplex structures, as well as applications of G-quadruplex structures to target human telomere, are also described. Lastly, the future aspects of these unique noncanonical structures are discussed.

2. DNA G-Quadruplexes in Human Telomere

The telomeres of human chromosome ends are composed of telomeric repeats of 5′-TTAGGG-3′ sequence. Through many structural studies on the human telomere, a large number of G-quadruplexes of different structures have been already identified, as depicted in Figure 2 [23–32]. These structural differences are primarily based on the syn/anti conformations of guanine residues and the relative orientation of the G-quartet core [33]. Thus, the topologies of DNA G-quadruplex are drastically dependent on the sequences and lengths of telomere DNA, the types of linking loops, and the nature of the associated metal cations.

For example, in NaCl solution, a 22-mer telomeric DNA d[AGGG(TTAGGG)$_3$] forms an antiparallel G-quadruplex with anti/syn guanines (Figure 2a) [34]. One loop is diagonal, and two other loops are lateral. In KCl solution, however, this sequence forms the mixtures of hybrid-1 and hybrid-2 G-quadruplexes, in which the loop types are external, lateral, and lateral (Figure 2c,d) [35–38]. In the crystal grown in the presence of K^+ ion, the same sequence adopts a completely different parallel G-quadruplex conformation having three external linking loops (Figure 2b) [39]. On the other hand, another telomeric sequence

d[GGG(TTAGGG)$_3$T] forms in KCl solution an antiparallel G-quadruplex with only two G-tetrad layers (Figure 2e) [40–42]. More recently, d[(GGGTTA)$_2$GGGTTTGGG] sequence was reported to take another antiparallel structure, so-called "chair" with lateral loops (Figure 2f) [43]. Circular dichroism (CD) spectroscopy is very useful to distinguish G-quadruplex structures in terms of fundamental characteristic bands [44]. For example, the CD spectrum of human telomeric sequence d[AGGG(TTAGGG)$_3$] in 100 mM Na^+ solution exhibits a 295 nm positive band and a 265 nm negative band, which is characteristic of an antiparallel G-quartet structure [35]. In a 100 mM K^+ ion solution, however, this sequence shows a stronger positive CD band at 290 nm, with weak negative peaks near 255 and 235 nm, indicating that a mixture of hybrid G-quadruplexes is formed under these conditions.

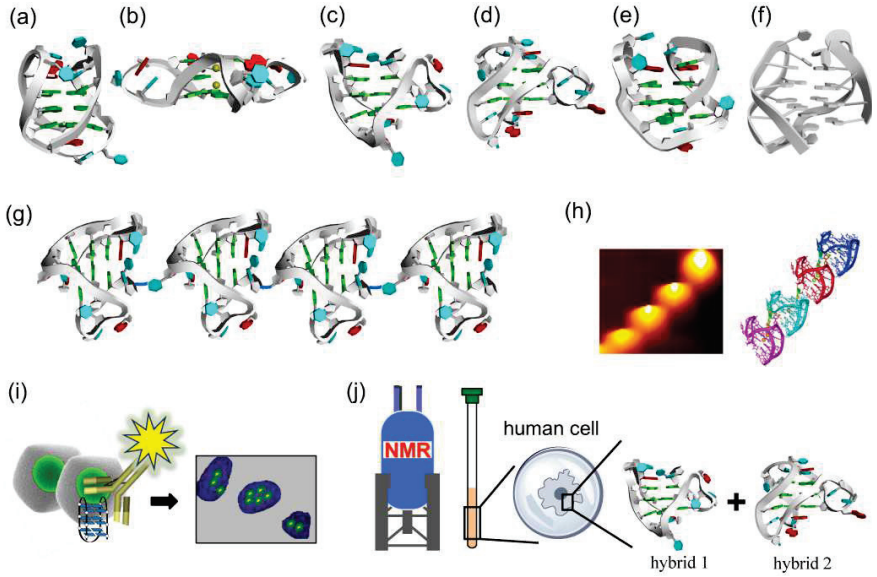


Figure 2. Variety of conformations of DNA G-quadruplexes observed under different conditions. (**a**) Antiparallel G-quadruplex from d[AGGG(TTAGGG)$_3$] formed in Na^+ solution. (**b**) A crystal structure from d[AGGG(TTAGGG)$_3$] in the presence of K^+ ions. (**c**,**d**) Hybrid-1 type and hybrid-2 type G-quadruplexes from d[AGGG(TTAGGG)$_3$] prepared in K^+ solution. (**e**) Antiparallel G-quadruplex of d[GGG(TTAGGG)$_3$T] with only two G-tetrad layers in K^+ solution. (**f**) Chair antiparallel conformation from d[(GGGTTA)$_2$GGGTTTGGG] in K^+ solution. (**g**,**h**) Higher order G-quadruplex observed by AFM. (**i**) Visualization of DNA G-quadruplex structures in cells by immunostaining with the use of structure-specific antibody. (**j**) In-cell ^{19}F NMR of d[AGGG(TTAGGG)$_3$] in Hela cells.

For the analysis of the structures of G-quadruplexes from still longer telomeric sequence, atomic force microscope (AFM) was employed (Figure 2g,h) [45]. In the AFM image, a telomere DNA (around 100-nucleotide length) forms a higher-order assembly of G-quadruplex, in which adjacent G-quadruplex conformation units are arranged in end-to-end structure. These G-quadruplex units stack each other into higher-order packing structures. Some small molecules and antibodies were also used to investigate the DNA G-quadruplexes in living cells (Figure 2i) [46,47].

The topology of G-quadruplex of telomeric DNA in living human cells has not yet been sufficiently clarified. To shed light on this problem, in-cell ^{19}F NMR experiments were performed in the environment close to the inside of human cells. ^{19}F NMR spectroscopy is suitable for this purpose, since it is characterized by (i) simplicity of spectra, (ii) high sensitivity of chemical shift to the environment, and (iii) absence of natural background signals in cells. For example, 3,5-bis(trifluoromethyl)phenyl moiety was connected to the 5′-end of telomeric DNA sequence (d[AGGG(TTAGGG)$_3$]), and this ^{19}F-labelled DNA was injected into human cells. According to in-cell ^{19}F NMR, this telomeric DNA forms the mixture of hybrid-1 and hybrid-2 G-quadruplexes in the human cells (Figure 2j) [48,49].

In *Xenopus laevis* oocytes, a hybrid-2 type G-quadruplex is formed [50]. The two-tetrad G-quadruplex in Figure 2e was further examined by ^{19}F NMR spectroscopy. Only one ^{19}F NMR signal was observed both in K^+ solution and in HeLa cells [48]. These results provide valuable information on the understanding of the structures of human telomeric DNA in living human cells and also on the design new drugs that target telomeric DNA.

Many fluorescent probes to detect DNA G-quadruplexes have been reported, and employed to image living cells [51–57]. In 2015, naturally occurring alkaloid epiberberine was found to emit fluorescence upon the binding with DNA G-quadruplex [58]. Later, various fluorescent probes were developed [59–62], and used to construct quadruplex-based analytical sensing platforms. Among these probes, a tripodal cationic fluorescent probe was featured by notable differences in fluorescence lifetime between G-quadruplexes and other DNA topologies [63]. Furthermore, its fluorescence quantum yield was greatly increased upon G-quadruplex binding. These two features allowed a clearcut differentiation of DNA G-quadruplexes from background signals in cell imaging, and a quantitative analysis was accomplished in terms of photon counts. According to NMR spectroscopy, this probe interacts with G-quadruplexes using three arms through π–π stacking. An artificial protein of 6.7 kD is useful to detect G-quadruplexes in living cells with the ChIP-Seq technique [64]. In this protein probe, two identical G4-binding domains (23-amino acid residues each) are connected with linker peptide to bind G-quadruplexes with sufficient strength. Small molecular ligands, which distinguish different conformations of G-quadruplexes each other, were also reported [65–67].

It is noteworthy that small molecules targeting G-quadruplexes are also important as potent drugs for therapy of cancer and other diseases [68–79]. For example, a small molecule, phenyl-ethenyl-quinoline, specifically binds G-quadruplex in oncogene MYC promoter, and is promising as a lead compound of anticancer drug [80]. This compound consists of phenyl and quinoline moieties linked via rather flexible ethenyl bridge, and has +1 charge on the methylated N1 atom. In addition to its direct interaction with the G-quadruplex core, this molecule additionally interacts with the 3′- and the 5′-flanking residues of target G-quadruplex that are immediately adjacent to the G-core. These interactions help this binder to distinguish the MYC promoter G-quadruplex from other G4 structures, as proposed previously [81]. Important roles of structured water in these G-quadruplex-small molecule interactions have been also indicated [82].

3. RNA G-Quadruplexes in Human Telomere

Telomere DNA is transcribed into telomeric RNA (UUAGGG repeat) which shows various biological functions [6,7]. Importantly, RNA G-quadruplexes in most cases take parallel conformation. For example, a 12-mer telomeric RNA r(UAGGGUUAGGGU) forms a parallel dimer G-quadruplex in Na^+ solution, as determined by ^{1}H-NMR (Figure 3a) [83]. Both in K^+ solution and in K^+-stabilized crystal, this 12-mer RNA also forms a G-quadruplex of the same topology [12,14]. This feature is highly in contrast with the results for DNA G-quadruplexes, in which the structures enormously depend on the conditions (Figure 2). Stereochemical constraints inherent to RNA should be one of the governing factors for this difference. Very interestingly, the formation of parallel G-quadruplex from four strands of r(UAGGGU) is accompanied by simultaneous formation of a U-tetrad [13]. As shown in Figure 3b, this U-tetrad (in red), formed through Hoogsteen bindings of four uridines at the 3′-end of each RNA strand, sits on the parallel G-quadruplex structure (in green). It is noteworthy that this U-tetrad dramatically stabilizes the whole structure of RNA assembly. In cells, this kind of U-tetrad could be also formed, and promote the functions of human telomere. In many biological regulations by RNA G-quadruplex, specific proteins bind to this noncanonical structure. For example, heterogeneous nuclear ribonucleoprotein A1 (hnRNPA1) cooperates with RNA G-quadruplex to facilitate telomere capping [84–86]. The loops of G-quadruplex are primarily responsible for the interactions with hnRNPA1.

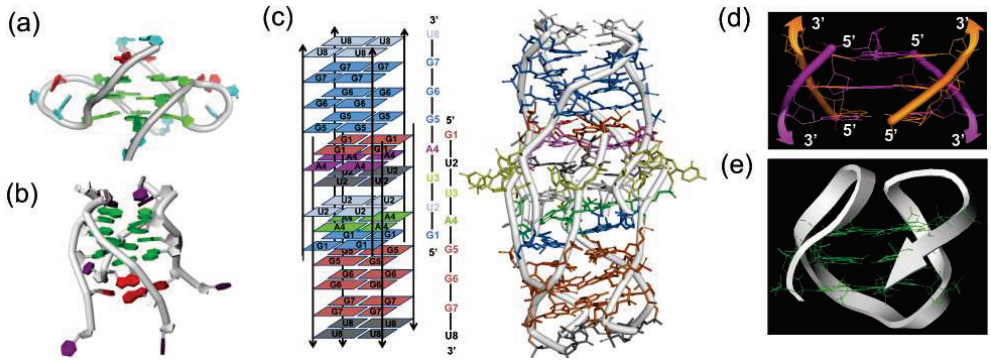


Figure 3. (**a**) Dimeric parallel telomeric RNA G-quadruplex from r(UAGGGUUAGGGU). (**b**) Tetramolecular RNA G-quadruplex from r(UAGGGU) possessing a novel U-tetrad on the bottom (in red). (**c**) RNA G-quadruplex having 14 tetrads, in which an eight-stranded helix part intercalates at the center. (**d**) Antiparallel RNA G-quadruplex from the fragments having 8-bromoguanosine. (**e**) Antiparallel RNA G-quadruplex formed by a 22-mer telomeric RNA.

Until very recently, it was believed that almost all natural RNAs form only parallel G-quadruplexes [87,88]. However, it was evidenced that an antiparallel G-quadruplex is formed in Na^+ solution from a 22-mer RNA of telomere sequence (Figure 3e) [89]. An antiparallel G-quadruplex was also obtained in K^+ solution, when 6-mer RNA (r(UAGGGU)) was modified with 8^{Br}rG (Figure 3d) [90]. On the other hand, 8-mer telomere RNA GUUAGGGU forms an unusual RNA architecture which involves 14 tetrads such as A-, U- and G-tetrad (Figure 3c) [91]. A central scaffold with eight stranded helices intercalates two symmetry subunit G-quadruplexes. This conformation is stable and is retained even under denaturing conditions. Apparently, the structures of RNA G-quadruplexes are more complicated than expected before [92].

Formation of RNA G-quadruplexes in vivo was first proposed in terms of the dimerization of two genomic RNA copies of HIV through RNA-RNA interactions [93]. This dimerization was dramatically stabilized by K^+ cation. This result, as well as other evidence, indicated the formation of an intermolecular RNA G-quadruplex, in which four guanine bases are assembled to tetrad as already known in DNA G-quadruplexes [87,94–96]. Later, RNA G-quadruplexes were found in many biological systems, and their essential roles were evidenced in many bioprocesses: regulation of mRNA translation [97–103], telomere homeostasis [104], mRNA splicing [105–107], and others [106,108]. Of course, their relevance to diseases is apparent [109,110]. In RNA viruses, G-quadruplexes in their genomes control viral replication, transcription, and other processes. For example, there exist many G-quadruplex folding sequences in the open reading frame regions of SARS-CoV-2 (the virus of COVID-19) [111], which caused a terrible pandemic from 2019 to 2023. Direct interaction of one of these G-quadruplexes with viral helicase, which is inevitable enzyme for the viral functions, was proposed.

In order to detect the formation of RNA G-quadruplex in cells, a light-switching probe was fabricated by incorporating pyrenes into both the 5′- and the 3′-ends of r(GGGUUAGGG) (Figure 4a) [17]. When G-quadruplex is formed from this RNA, the two pyrene chromophores are placed in close proximity to form their exciplexes. As the results, the maximum of fluorescence emission shifts from 400 nm (blue emission) to 480 nm (green emission). The system is employable for in-cell detection, as depicted in fluorescence microscopy images in the bottom. Furthermore, ^{19}F NMR was successfully used to investigate the structure of telomeric RNA in cells (Figure 4b) [112–117]. Telomeric RNA r(UAGGGUUAGGU) was labeled with 3,5-bis(trifluoromethyl)phenyl moiety, and injected into *Xenopus laevis* oocytes [112]. A new ^{19}F-NMR signal was observed (the bottom spectrum), and assigned to stacking assembly of two G-quadruplex units with the use of the reference spectrum obtained in vitro (the top).

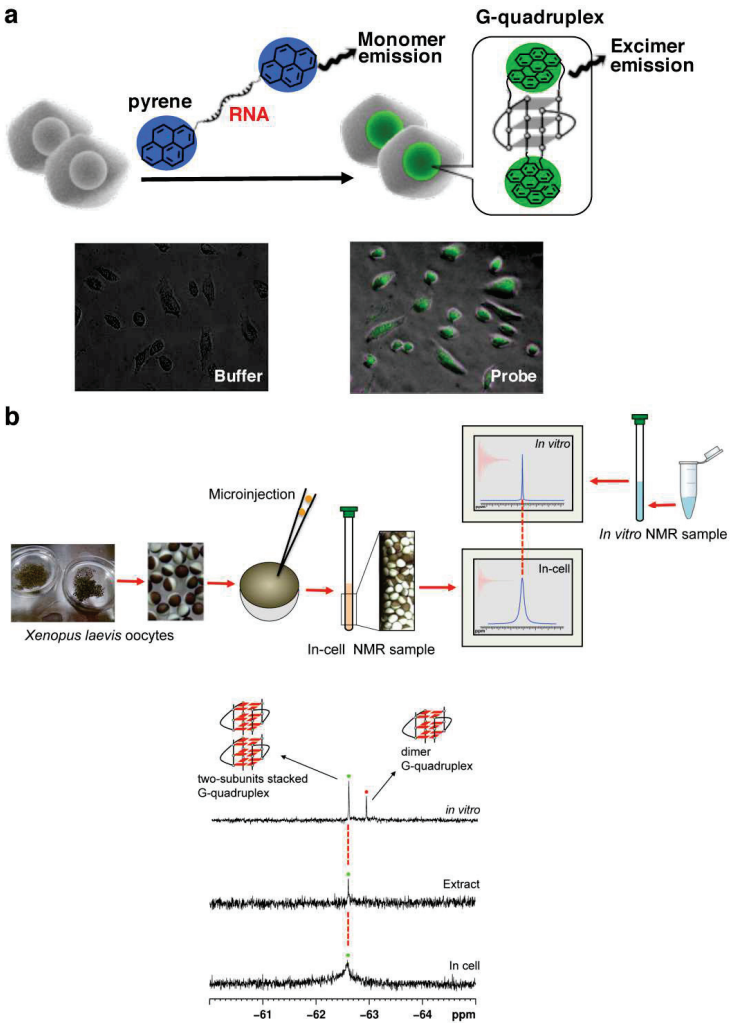


Figure 4. (**a**) A pyrene probe used to detect in-cell formation of G-quadruplex from telomeric RNA (r(GGGUUAGGG)). Fluorescence microscopy images of living cells with or without the probe are shown below. (**b**) In-cell ^{19}F NMR experiment in *Xenopus* oocytes. The spectra of (**top**) RNA telomeric G-quadruplex in vitro and (**bottom**) in *Xenopus* oocytes.

Alternatively, RNA G-quadruplexes were detected in cells by using a coumarin-hemicyanine fluorophore (QUMA-1), which was prepared through the condensation of a coumarin aldehyde and an N-methylated quinoline derivative [118]. Its fluorescence emission at 660 nm is only weak in buffer, but is significantly enhanced by RNA G-quadruplexes. This enhancement is specific to G-quadruplexes, and either single-stranded RNA or double-stranded RNA hardly affects the emission intensity. This red-emitting fluorescent probe was successfully employed for selective, continuous, and real-time visualization of RNA G-quadruplexes in living cells. It was proposed that the tight binding of the probe to RNA G-quadruplexes restricts the rotation around the methine bridge between the coumarin and the N-methylated quinoline moiety, and locks the probe in its fluorescently active conformation. In another probe PyroTASQ, four guanines are attached to a pyrene as fluorescent chromophore [119]. The intrinsic fluorescence from this probe is minimal, since the emission from the pyrene chromophore is quenched by their own guanines through intramolecular photo-induced electron transfer. Upon binding with G-quadruplex, however, this probe achieves a conformational switch to assemble its four guanines into an intramolecular G-quartet, which stacks on the analyte G-quadruplex. As a result, the electrons in the guanines are redistributed to suppress the fluorescence quenching, and the emission from the pyrene is restored. These two fluorescent probes are

highly promising to sensitively detect G-quadruplexes in vivo and in vitro, since they light up only with the coexistence of G-quadruplexes and are otherwise virtually silent.

Diastereomerically pure Fe(II) metametallohelices strongly bind the G-quadruplex of human telomeric repeat-containing RNA (TERRA rG4), and stabilize this non-canonical structure [120]. Accordingly, DNA synthesis on RNA template containing four repeats of human telomeric sequence is inhibited by them. As tailor-made binders, unique aptamers towards TERRA rG4 were prepared using unnatural L-RNA units (mirror image of natural D-RNA nucleotides) [121]. Strong and specific binding of TERRA rG4 by the aptamer was evidenced. Notably, they recognized the target TERRA rG4 very strictly, and never bound other forms of constructs. Neither simple RNA hairpin nor telomeric DNA G-quadruplex was bound, and still more importantly, even other rG4s (hTERC, NRAS, miRNA149, and others) were not bound either. Cationic porphyrins (CPs) bearing an alkyl chain was used for photodynamic therapy of cancer [122]. The porphyrin derivatives preferentially bind to the RNA G-quadruplex formed in mRNA, and destroys this mRNA upon photoirradiation.

4. DNA:RNA Hybrid G-Quadruplexes in Human Telomere

The discovery of telomere RNA soon raised a crucial question of how telomeric RNA is specifically associated with telomeric DNA to accomplish various functions (chromosome-end regulation, protection, and others). An association between telomere RNA and telomere DNA through the formation of an intermolecular DNA:RNA G-quadruplex may be an answer to this problem. However, it is technically difficult to study the DNA:RNA hybrid G-quadruplex structure by traditional methods, such as NMR spectroscopy and X-ray crystallography, since the DNA G-quadruplex, RNA G-quadruplex, and DNA:RNA hybrid G-quadruplex may coexist as a mixture in solution. Thus, concrete evidence for the formation of DNA:RNA G-quadruplex is hard to obtain. Accordingly, the experiments in Figure 5a,b were designed to trap DNA:RNA hybrid G-quadruplex by click reaction and produce a snapshot of the inter-converting structures that are present in complicated solutions. Human telomeric DNA and RNA are modified with either an alkyne or an azide, and mixed each other. The detection of "azide-alkyne cycloaddition" product between the DNA and the RNA is used as the evidence for the formation of DNA:RNA hybrid G-quadruplex. In Figure 5a, an alkyne is bound to the 5′-end of RNA, and an azide is bound to the 5′-end of DNA [19]. Thus, only when the DNA:RNA hybrid G-quadruplex is formed in the reaction mixture, the alkyne and the azide are placed nearby and the click reaction between them should efficiently proceed [123]. In fact, it was clearly shown by gel-electrophoresis that DNA:RNA hybrid G-quadruplex is formed from telomere DNA and telomeric RNA in aqueous K^+ solutions [19,20,45,123]. Furthermore, this method was applied to in-cell reactions, where the DNA was labelled with an azide-bearing profluorophore (7-azidocoumarin), and incorporated into human cells together with the alkyne-bearing RNA. Direct evidence for the formation of DNA:RNA hybrid G-quadruplexes in cells was provided as fluorescent signals in the bottom images in Figure 5b [20,21,123]. Consistently, no fluorescent signals were detected in the absence of Cu catalysts for the click reactions (upper images).

With the use of ^{19}F NMR spectrum, the formation of DNA:RNA hybrid G-quadruplex in living human cells was also assessed and strongly confirmed [22]. In Figure 5c, a ^{19}F-labelled 12-mer G-rich RNA was mixed with 12-mer G-rich DNA in 1:3 ratio. Among two major peaks, the signal at −62.61 ppm was assigned to the DNA:RNA hybrid G-quadruplex (HQ). As shown in the top spectrum, this signal was clearly observed in living human cells, confirming the formation of this DNA:RNA hybrid G-quadruplex. Concurrently, the RNA G-quadruplex (RQ) was also formed.

Telomere RNA plays a crucial role in the "capping" of telomeres through the formation of telomeric DNA:RNA G-quadruplexes [20,124–126]. This argument is supported by insights from a single-molecule FRET study examining the folding patterns of telomere DNA in conjunction with telomere RNA. Notably, telomere RNA exhibits a preference for the formation of DNA:RNA hybrid G-quadruplexes at the 3′ end of telomeric DNA.

Furthermore, DNA G-quadruplexes is unfolded by a complementary C-rich sequence, but this effect is not observed for DNA:RNA hybrid G-quadruplexes. These findings underscore previous arguments that these hybrid G-quadruplexes protect the 3′ end of the telomeric DNA overhang, which is critical for the interaction with telomerase and other telomere-associated proteins. Unique contribution of RNA in reinforcing the structural integrity of telomeres has been evidenced. According to bioinformatic analysis, putative DNA:RNA hybrid G-quadruplex-forming sequences are abundant on both sides of the transcription start sites in the genome of warm-blooded animals [125]. Their formation is dependent on the negative supercoiling generated by RNA polymerases. Genome-wide occurrence of DNA:RNA hybrid G-quadruplexes has been also indicated [126]. The biological roles of DNA:RNA hybrid G-quadruplexes are gradually getting clearer.

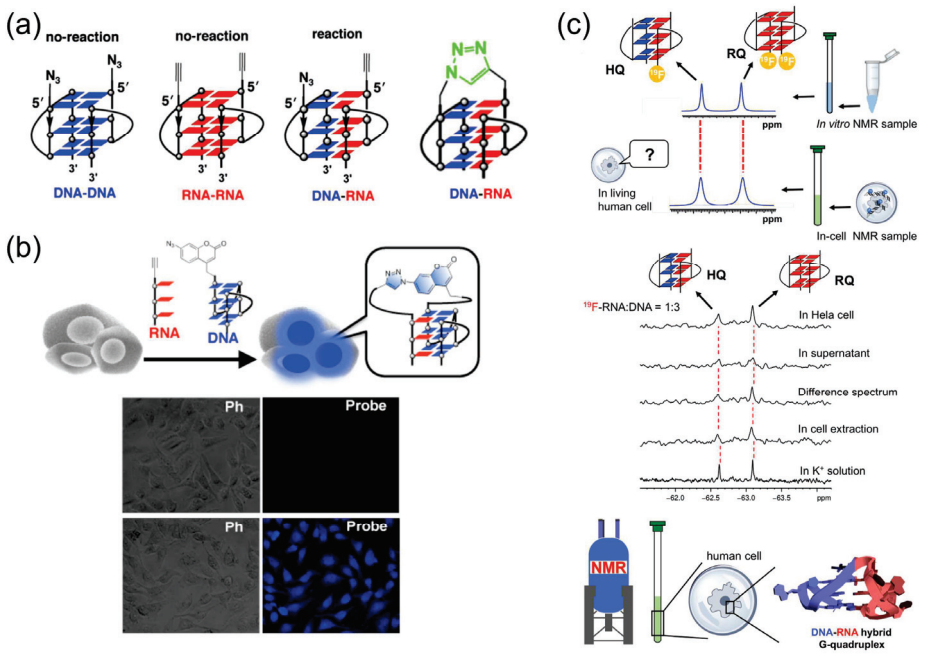


Figure 5. (**a**) Formation of DNA:RNA hybrid G-quadruplex promotes a click reaction to differentiate this hybrid G-quadruplex from DNA G-quadruplex and RNA G-quadruplex. (**b**) Fluorescence images with and without the probe in cells. Formation of DNA:RNA hybrid G-quadruplex in cells was confirmed. Upper images; without Cu catalyst for the click reaction. Bottom images; with Cu catalyst. Ph; phase-contrast imaging. (**c**) ^{19}F NMR showing the formation of DNA:RNA hybrid G-quadruplex in human cells.

5. Binding Proteins of Telomere DNA and RNA G-Quadruplexes

Notably, POT1 has been demonstrated to unravel intramolecular G-quadruplexes to facilitate its binding to telomeric DNA [127,128]. The unfolding of G-quadruplexes by POT1 also impacts the capacity of telomeric sequences to undergo extension by telomerase, at least in vitro [1]. Initially, it was shown with telomerase from three distinct species of ciliated protozoa that oligonucleotides adopting antiparallel intramolecular G-quadruplex structures do not serve as favorable substrates for telomerase [129,130]. The antiparallel and hybrid G-quadruplex structures assumed by a 4-repeat oligonucleotide in K^+ solution have been also demonstrated to be ineffective substrates for telomerase [129–134]. These G-quadruplex conformations [133,134] inhibit the binding of telomerase to the DNA, leading to a non-processive attempted extension of the DNA by telomerase [129]. POT1 can reinstate the capability of telomerase to engage with these substrates by unfolding the G-quadruplex and capturing the DNA in a linear form with a protruding tail [127]. The dynamic interplay of G-quadruplex folding and their unfolding by POT1 may thus serve as a regulatory mechanism, governing the access of telomerase to the telomere.

HnRNPA1 is an RNA binding protein which is involved in the telomere maintenance machinery. The binding of hnRNPA1 to telomere RNA with structure-dependence can regulate human telomere function. In Figure 6, the interactions of G-quadruplex RNA with hnRNPA1 were analyzed by gel electrophoresis in which RNA G-quadruplexes of different structures were employed [85,86]. It was demonstrated that the loops of G-quadruplex RNA are very important for interaction with hnRNPA1. Furthermore, a macrocyclic heptaoxazole molecule, 7OTD, and its fluorescent derivative, Cy5−7OTD, have been developed to bind to telomere RNA G-quadruplex and visualize its complex formation with hnRNPA1 [85]. In Figure 7a, the green band is for telomere RNA G-quadruplex. The red band of smaller mobility, observed after the addition of Cy5−7OTD, is assigned to the interaction of RNA G-quadruplex with Cy5−7OTD. Upon further addition of hnRNPA1, a new band appeared in the upper part of the gel, due to its binding with the RNA G-quadruplex. Furthermore, Cy5−7OTD was employed in Figure 7b to analyze the interactions of RNA telomere G-quadruplex with hnRNPA1 in cells. By incubating HeLa cells with this probe, the telomere RNA G-quadruplex was detected as red signals in fluorescence microscopy. On the other hand, hnRNPA1 in the cells was visualized by green fluorescence from anti-hnRNPA1 antibody-based probe. Quite importantly, the green fluorescence of hnRNPA1 and the red fluorescent foci of the RNA G-quadruplex notably overlapped each other. Consistently, the intensity of the red signal was reduced by RNase treatment, confirming that this signal came from the Cy5−7OTD bound to the RNA G-quadruplex.

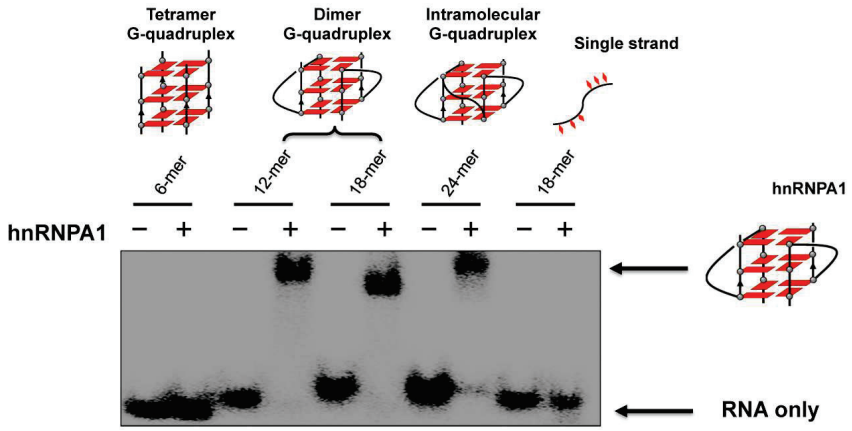


Figure 6. Binding of hnRNPA1 to telomere RNA G-quadruplexes of various structures. Only the RNA G-quadruplexes involving loops (the dimer and the intramolecular G-quadruplexes) bind hnRNPA1, and neither the tetramer RNA G-quadruplex without loops nor single-stranded RNA binds the protein.

The C-terminal region of TLS, a human telomere-binding protein, engages in the formation of a ternary complex with G-quadruplex DNA and RNA from human telomeres in vitro, specifically within the Arg-Gly-Gly domain [135]. Notably, TLS exhibits binding affinity to G-quadruplex telomere DNA within double-stranded regions and G-quadruplex RNA. This dual interaction plays a crucial role in regulating histone modifications associated with telomeres, influencing overall telomere length. The findings propose that the G-quadruplex serves as a scaffold for TLS, orchestrating the modulation of telomere length through histone modifications. In parallel, the N-terminal Gly/Arg-rich (GAR) domain of TRF2 demonstrates recognition capabilities for G-quadruplex RNA [136]. The G-quadruplex structure within telomere RNA emerges as a pivotal recognition element for the TRF2 GAR domain. The interaction between TRF2 GAR and telomere RNA is deemed essential for maintaining telomere stability, underlining its significance in the intricate regulatory mechanisms governing telomeric function.

Alternative lengthening of telomeres (ALT), a telomerase-independent mechanism for maintaining telomeres, is orchestrated primarily through break-induced replication

(BIR) [137,138]. The human protein RAD52 plays a key role in promoting ALT by facilitating the formation of D-loops. However, it is noteworthy that ALT can also occur via a RAD52-independent BIR pathway. In the absence of RAD52, telomere RNA contributes significantly to ALT activity by forming dynamic telomeric R-loops. These R-loops, in turn, augment the presence of G-quadruplex structures at telomeres. The increased G-quadruplex formation enhances ALT, even in cases where telomeric RNA is depleted. This observation suggests that G-quadruplexes operate downstream of R-loops, playing a pivotal role in promoting break-induced replication and contributing to the ALT process.

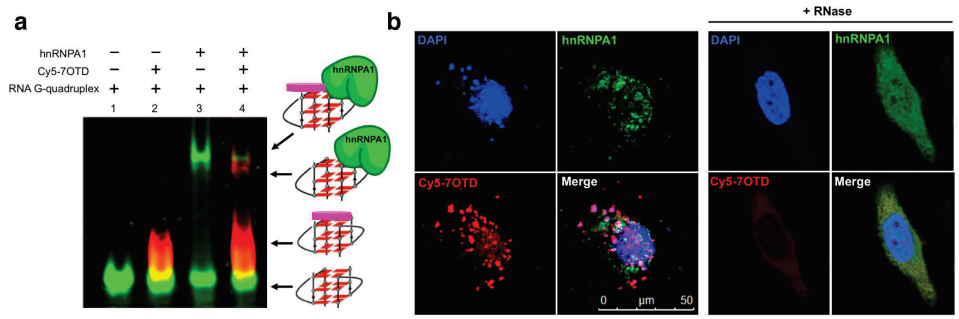


Figure 7. Analysis of the binding of hnRNP1 with RNA G-quadruplex using Cy5−7OTD. (**a**) Gel electrophoresis on the binding. Lane 1, RNA G-quadruplex visualized with fluorescein in green; lane 2, RNA G-quadruplex with Cy5−7OTD in red; lane 3, the mixture of RNA G-quadruplex and hnRNPA1 visualized by fluorescein in green; lane 4, the complex formation of RNA G-quadruplex with hnRNPA1 colored in red by Cy5− 7OTD. (**b**) Microscopy images of human cells incubated with Cy5−7OTD (red) and then with antibody of hnRNPA1 (green). DNA was stained by DAPI (blue fluorescence). In the merged panel, colocalization of RNA G-quadruplex (red) and hnRNPA1 (green) is apparent. As expected, the signals of RNA G-quadruplex were notably weakened when the cells were treated by RNase.

Telomeric RNA exhibits the ability to adopt a G-quadruplex structure and engage in interactions with the chromatin remodeler ATRX [139]. In this interaction, telomere RNA acts as a regulator, preventing ATRX from binding to subtelomeric regions. Instead, it facilitates the promotion of G-quadruplex formation in proximity to transcription start sites (TSS) that are distant from telomeres. Upon depletion of telomere RNA, there is an observed increase in ATRX binding at TSS, leading to the unwinding of G-quadruplex DNA and subsequent repression of gene expression. This unveils an epigenetic regulatory mechanism by which telomere RNA serves to sequester ATRX, thereby preserving DNA G-quadruplex structures and influencing gene expression patterns.

6. Applications of G-Quadruplexes

Unique structural restraints of G-quadruplexes are effectively employed as scaffolds for specific biological and/or chemical reactions. Freedoms of structural design of the systems are highly advantageous for these applications. In terms of the formation of DNA G-quadruplex, a chemical method to selectively cleave human telomere DNA was developed [83]. In Figure 8a, 16-mer DNA of three-repeat human telomere sequence (^{Br}GGGTTA^{Br}G^{Br}GGTTAGGGT) binds to a telomere DNA substrate through the formation of dimeric G-quadruplex. To the 5′-end of this 16-mer DNA, an ethylenediamine-*N*,*N*,*N*′,*N*′-tetrakis(methylenephosphonic acid) (EDTP) as metal-binding group is conjugated. Upon the addition of $Ce^{IV}(NH_4)_2(NO_3)_6$, Ce^{IV} ion (a catalyst for DNA hydrolysis) is bound to the EDTP, and placed near the phosphodiester linkage(s) in the telomere DNA substrate. As a result, only telomere DNA is picked up from reaction mixtures through G-quadruplex formation, and cleaved through hydrolytic pathway.

A similar strategy was employed to design a photo-controllable inhibitor of telomerase, which is vigorously expressed in cancer cells (Figure 8b) [140]. To the 5′-end of 6-mer DNA (TA^{Br}GGGT), a photosensitive dye psoralen (green colored) was conjugated. This photo-

crosslinking reagent is a linear furanocoumarin, and selectively reacts with pyrimidine bases (T and C) for crosslinking. This psoralen-conjugated 6-mer DNA binds to telomere DNA through the formation of intermolecular G-quadruplex. Upon photo-irradiation, the psoralen crosslinked the telomere DNA with the 6-mer DNA. As the result, the duplication of telomere DNA by telomerase was sterically inhibited, triggering the death of cancer cells. These two results apparently show that G-quadruplex formation serves as an efficient approach to target human telomere for its effective transformation.

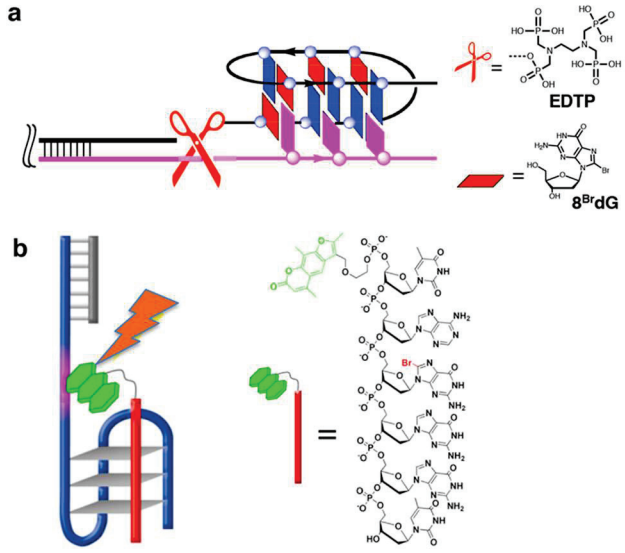


Figure 8. (**a**) Telomere DNA specific cleavage by G-quadruplex formation. The structures of ligand EDTP and 8^{Br}dG are shown. (**b**) Photochemical inhibition of telomerase by targeting human telomere DNA with a 6-mer DNA (red bar) through G-quadruplex formation. The 6-mer DNA bears a psoralen (green) at the 5′-end.

Alternatively, the formation of an intermolecular G-quadruplex presents a novel mechanism to regulate the efficiency of translation [141]. A G-rich sequence (5′-GGGCCCGGG-3′) was introduced to the 5′-UTR of mRNA, and a telomere related G-rich RNA (5′-GGGUUAGGG-3′) was employed as on-off controller of translation. An enhanced green fluorescent protein reporter (EGFP1) was employed. Without the addition of the short telomere RNA, the 5′-UTR of mRNA was in the normal state, and EGFP1 protein was efficiently expressed to emit green fluorescence. Upon the addition of the telomere short RNA. However, EGFP1 was hardly expressed. Apparently, the mRNA translation was inhibited by the formation of RNA G-quadruplex between the short telomere RNA and the G-rich sequence in the 5′-UTR. The short telomere RNA successfully worked as an on-off controller of translation.

7. Future Prospects and Conclusions

Telomere biology has come a long way in the past 70 years, from the observation that chromosomes require protection to the award of the 2009 Nobel Prize for the discovery of telomerase and the effects of telomere shortening on cells. Functional telomeres have been experimentally implicated in a number of molecular cell processes. Molecular components of telomeres, including terminal double- and single-stranded telomeric DNA, protein complex shelterin, and telomerase form physical states which are associated with functional capping and uncapping. In this decade in particular, structural information of DNA G-quadruplexes and RNA G-quadruplexes has been rapidly accumulated, deepening our understanding on the biological roles of telomeres. Pre-clinical experiments suggested that telomere is an encouraging target for cancer therapy. The findings of telomere RNA molecules open new doors to a better understanding of the complicated functions of telomeres. These telomere RNAs are bound by a complicated set of proteins [142]. Furthermore,

telomeric RNA G-quadruplex and DNA G-quadruplex show homogeneous dimerization and mutual association. Telomere RNA, a newly emerging player, may be useful for cancer treatment, since these RNA molecules accompanies malignant transformation. Thus, telomere RNA G-quadruplex structures should be also a valuable target for anticancer agents [1]. Stabilization of telomere RNA G-quadruplex structures by small molecules can lead to telomerase inhibition. All of these results confirm that there are crucial needs to revisit the structural and functional mechanisms of telomeres.

The current status of our understanding on telomere science is schematically depicted in Figure 9. Telomere DNA, telomere RNA, and related-proteins construct TDRP body (telomeric DNA, RNA and proteins body), such as P bodies for mRNA surveillance, mRNA decay, RNA-mediated silencing and translational control [143]. Telomere capping is promoted by the binding of POT1 protein to single-strand telomere DNA [84]. Many evidences show that telomere RNAs are associated with various elements in the telomere. Through the formation of telomeric DNA:RNA G-quadruplexes, telomere RNA interacts with telomeric DNA for the "capping" of telomere. Moreover, telomeric RNA is a structural component of the telomere nucleoprotein complex, and is also bound to the telomere through interactions with Shelterin components such as TRF1 and TRF2. Three domains of TRF2 interact with telomeric RNA including the amino-terminal basic domain (GAR) [144]. Telomeric RNA further interacts with the ORC1 region that associates with TRF2 GAR. Interestingly, the TRF2 GAR has a relatively high affinity towards G-rich RNA capable of forming G-quadruplex structures, indicating that the recognition mainly depends on G-quadruplex structure, rather than a specific sequence [85]. Telomeric RNA promotes POT1 binding to telomeric DNA by removing hnRNPA1 [84]. Thus, the accumulation of telomeric RNA is helpful for the formation of TDRP body and promotes telomere capping. It was also shown that acridine ligands notably change the UUA loop conformation of RNA G-quadruplex [145]. The resultant stabilization of G-quadruplexes should facilitate the formation of TDRP bodies, in which higher-order telomere structures are satisfactorily capped to accomplish homeostatic functions.

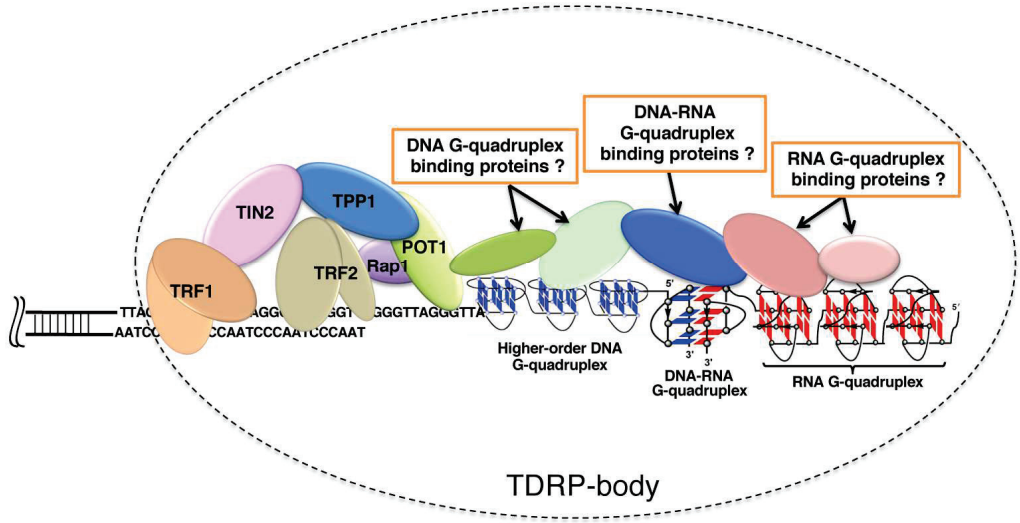


Figure 9. A schematic view of human telomere end: telomere DNA, telomere RNA, and related-proteins in the TDRP body. Proteins can recognize DNA telomere G-quadruplex, RNA telomere G-quadruplex and hybrid DNA:RNA G-quadruplex. The TDRP body at the ends of chromosomes provides a protective structure. Note that some of the contents could be speculative, and have not necessarily been firmly established.

Furthermore, it should be noted that newly discovered telomere RNA may provide a solution to "the end replication problem" in which a protruding single-stranded 3′-DNA end causes a progressive shortening of telomeric DNA at each round of DNA replication [146,147]. In normal cells, telomere RNA can act as a template for telomere elongation

synthesis by reverse transcriptase. Support for this hypothesis comes from the finding that telomere RNAs are significantly downregulated in various types of human cancers, compared to normal tissues. In normal cells, the reverse transcription pathway is involved in the maintenance of telomere length, whereas telomerase is mainly responsible for telomere length maintenance in cancer cells.

Funding: This research received no external funding.

Conflicts of Interest: The authors declare no conflicts of interest.

References

1. Xu, Y. Chemistry in Human Telomere Biology: Structure, Function and Targeting of Telomere DNA/RNA. *Chem. Soc. Rev.* **2011**, *40*, 2719–2740. [CrossRef] [PubMed]
2. Hurley, L.H. DNA and its associated processes as targets for cancer therapy. *Nat. Rev. Cancer* **2002**, *2*, 188–200. [CrossRef] [PubMed]
3. Monchaud, D.; Teulade-Fichou, M.P. A hitchhiker's guide to G-quadruplex ligands. *Org. Biomol. Chem.* **2008**, *6*, 627–636. [CrossRef] [PubMed]
4. Georgiades, S.N.; Abd Karim, N.H.; Suntharalingam, K.; Vilar, R. Interaction of metal complexes with G-quadruplex DNA. *Angew. Chem. Int. Ed.* **2010**, *49*, 4020–4034. [CrossRef]
5. Ou, T.M.; Lu, Y.J.; Tan, J.H.; Huang, Z.S.; Wong, K.Y.; Gu, L.Q. G-quadruplexes: Targets in anticancer drug design. *ChemMedChem* **2008**, *3*, 690–713. [CrossRef]
6. Azzalin, C.M.; Reichenbach, P.; Khoriauli, L.; Giulotto, E.; Lingner, J. Telomeric repeat containing RNA and RNA surveillance factors at mammalian chromosome ends. *Science* **2007**, *318*, 798–801. [CrossRef]
7. Schoeftner, S.; Blasco, M.A. Developmentally regulated transcription of mammalian telomeres by DNA-dependent RNA polymerase II. *Nat. Cell Biol.* **2008**, *10*, 228–236. [CrossRef]
8. Luke, B.; Lingner, J. TERRA: Telomeric repeat-containing RNA. *EMBO J.* **2009**, *28*, 2503–2510. [CrossRef]
9. Schoeftner, S.; Blasco, M.A. A 'higher order' of telomere regulation: Telomere heterochromatin and telomeric RNAs. *EMBO J.* **2009**, *28*, 2323–2336. [CrossRef]
10. Feuerhahn, S.; Iglesias, N.; Panza, A.; Porro, A.; Lingner, L. TERRA biogenesis, turnover and implications for function. *FEBS Lett.* **2010**, *84*, 3812–3818. [CrossRef]
11. Xu, Y.; Kaminaga, K.; Komiyama, M. G-Quadruplex Formation by Human Telomeric Repeats-Containing RNA in Na^+ Solution. *J. Am. Chem. Soc.* **2008**, *130*, 11179–11184. [CrossRef]
12. Martadinata, H.; Phan, A.T. Structure of propeller-type parallel-stranded RNA G-quadruplexes, formed by human telomeric RNA sequences in K^+ solution. *J. Am. Chem. Soc.* **2009**, *131*, 2570–2578. [CrossRef] [PubMed]
13. Xu, Y.; Ishizuka, T.; Kimura, T.; Komiyama, M. A U-tetrad stabilizes human telomeric RNA G-quadruplex structure. *J. Am. Chem. Soc.* **2010**, *132*, 7231–7233. [CrossRef] [PubMed]
14. Collie, G.W.; Haider, S.M.; Neidle, S.; Parkinson, G.N. A crystallographic and modelling study of a human telomeric RNA (TERRA) quadruplex. *Nucleic Acids Res.* **2010**, *38*, 5569–5580. [CrossRef]
15. Xu, Y.; Sugiyama, H. Highly efficient photochemical 2'-deoxyribonolactone formation at the diagonal loop of a 5-iodouracil-containing antiparallel G-quartet. *J. Am. Chem. Soc.* **2004**, *126*, 6274–6279. [CrossRef] [PubMed]
16. Shrestha, P.; Jonchhe, S.; Emura, T.; Hidaka, K.; Endo, M.; Sugiyama, H.; Mao, H. Confined space facilitates G-quadruplex formation. *Nat. Nanotechnol.* **2017**, *12*, 582–588. [CrossRef] [PubMed]
17. Xu, Y.; Suzuki, Y.; Ito, K.; Komiyama, M. Telomeric repeat-containing RNA structure in living cells. *Proc. Natl. Acad. Sci. USA* **2010**, *107*, 14579–14584. [CrossRef]
18. Xu, Y.; Kimura, T.; Komiyama, M. Human telomere RNA and DNA form an intermolecular G-quadruplex. *Nucleic Acids Symp. Ser.* **2008**, *52*, 169–170. [CrossRef]
19. Xu, Y.; Suzuki, Y.; Komiyama, M. Click chemistry as an approach to probing G-quadruplex structure. *Angew. Chem. Int. Ed.* **2009**, *48*, 3281–3284. [CrossRef]
20. Xu, Y.; Ishizuka, T.; Yang, J.; Ito, K.; Katada, H.; Komiyama, M.; Hayashi, T. Oligonucleotide models of telomeric DNA and RNA form a hybrid G-quadruplex structure as a potential component of telomeres. *J. Biol. Chem.* **2012**, *287*, 41787–41796. [CrossRef]
21. Xu, Y. Recent progress in human telomere RNA structure and function. *Bioorg. Med. Chem. Lett.* **2018**, *28*, 2577–2584. [CrossRef] [PubMed]
22. Bao, H.L.; Xu, Y. Telomeric DNA-RNA-hybrid G-quadruplex exists in environmental conditions of HeLa cells. *Chem. Commun.* **2020**, *56*, 6547–6550. [CrossRef] [PubMed]
23. Guschlbauer, W.; Chantot, J.F.; Thiele, D. 4-Stranded nucleic-acid structures 25 years later -From guanosine gels to telomer DNA. *J. Biomol. Struct. Dyn.* **1990**, *8*, 491–511. [CrossRef] [PubMed]
24. Williamson, J.R. G-Quartet Structures in Telomeric DNA. *Annu. Rev. Biophys. Biomol. Struct.* **1994**, *23*, 703–730. [CrossRef] [PubMed]
25. Simonsson, T. G-quadruplex DNA structures--variations on a theme. *Biol. Chem.* **2001**, *382*, 621–628. [CrossRef] [PubMed]

26. Lane, A.N.; Chaires, J.B.; Gray, R.D.; Trent, J.O. Stability and kinetics of G-quadruplex structures. *Nucleic Acids Res.* **2008**, *36*, 5482–5515. [CrossRef] [PubMed]
27. Gilbert, D.E.; Feigon, J. Multistranded DNA structures. *Curr. Opin. Struct. Biol.* **1999**, *9*, 305–314. [CrossRef]
28. Phan, A.T.; Kuryavyi, V.; Patel, D.J. DNA architecture: From G to Z. *Curr. Opin. Struct. Biol.* **2006**, *16*, 288–298. [CrossRef]
29. Burge, S.; Parkinson, G.N.; Hazel, P.; Todd, A.K.; Neidle, S. Quadruplex DNA: Sequence, topology and structure. *Nucleic Acids Res.* **2006**, *34*, 5402–5415. [CrossRef]
30. Huppert, J.L. Four-stranded nucleic acids: Structure, function and targeting of G-quadruplexes. *Chem. Soc. Rev.* **2008**, *37*, 1375–1384. [CrossRef]
31. Mergny, J.L.; De Cian, A.; Ghelab, A.; Sacca, B.; Lacroix, L. Kinetics of tetramolecular quadruplexes. *Nucleic Acids Res.* **2005**, *33*, 81–94. [CrossRef]
32. Phan, A.T. Human telomeric G-quadruplex: Structures of DNA and RNA sequences. *FEBS J.* **2010**, *277*, 1107–1117. [CrossRef]
33. Williamson, J.R. Guanine quartets. *Curr. Opin. Struct. Biol.* **1993**, *3*, 357–362. [CrossRef]
34. Wang, Y.; Patel, D.J. Solution Structure of the Human Telomeric Repeat d[$AG_3(T_2AG_3)_3$] G-Tetraplex. *Structure* **1993**, *1*, 263–282. [CrossRef]
35. Xu, Y.; Noguchi, Y.; Sugiyama, H. The New Models of the Human Telomere d[$AGGG(TTAGGG)_3$] in K^+ Solution. *Bioorg. Med. Chem.* **2006**, *14*, 5584–5591. [CrossRef]
36. Ambrus, A.; Chen, D.; Dai, J.; Bialis, T.; Jones, R.A.; Yang, D. Human Telomeric Sequence Forms a Hybrid-Type Intramolecular G-quadruplex Structure with Mixed Parallel/Antiparallel Strands in Potassium Solution. *Nucleic Acids Res.* **2006**, *34*, 2723–2735. [CrossRef]
37. Luu, K.N.; Phan, A.T.; Kuryavyi, V.; Lacroix, L.; Patel, D.J. Structure of the Human Telomere in K^+ Solution: An Intramolecular (3 + 1) G-quadruplex Scaffold. *J. Am. Chem. Soc.* **2006**, *128*, 9963–9970. [CrossRef]
38. Dai, J.; Carver, M.; Punchihewa, C.; Jones, R.A.; Yang, D. Structure of the Hybrid-2 Type Intramolecular Human Telomeric G-quadruplex in K^+ Solution: Insights into Structure Polymorphism of the Human Telomeric Sequence. *Nucleic Acids Res.* **2007**, *35*, 4927–4940. [CrossRef]
39. Parkinson, G.N.; Lee, M.P.; Neidle, S. Crystal Structure of Parallel Quadruplexes from Human Telomeric DNA. *Nature* **2002**, *417*, 876–880. [CrossRef] [PubMed]
40. Zhang, Z.; Dai, J.; Veliath, E.; Jones, R.A.; Yang, D. Structure of a two-G-tetrad intramolecular G-quadruplex formed by a variant human telomeric sequence in K^+ solution: Insights into the interconversion of human telomeric G-quadruplex structures. *Nucleic Acids Res.* **2010**, *38*, 1009–1021. [CrossRef] [PubMed]
41. Lim, K.W.; Amrane, S.; Bouaziz, S.; Xu, W.; Mu, Y.; Patel, D.J.; Luu, K.N.; Phan, A.T. Structure of the human telomere in K^+ solution: A stable basket-type G-quadruplex with only two G-tetrad layers. *J. Am. Chem. Soc.* **2009**, *131*, 4301–4309. [CrossRef] [PubMed]
42. Hansel, R.; Lohr, F.; Trantirek, L.; Dotsch, V. High-resolution insight into G-overhang architecture. *J. Am. Chem. Soc.* **2013**, *135*, 2816–2824. [CrossRef]
43. Liu, C.; Zhou, B.; Geng, Y.; Yan Tam, D.; Feng, R.; Miao, H.; Xu, N.; Shi, X.; You, Y.; Hong, Y.; et al. A chair-type G-quadruplex structure formed by a human telomeric variant DNA in K^+ solution. *Chem. Sci.* **2019**, *10*, 218–226. [CrossRef]
44. Shiekh, S.; Kodikara, S.G.; Balci, H. Structure, Topology, and Stability of Multiple G-quadruplexes in Long Telomeric Overhangs. *J. Mol. Biol.* **2023**, *434*, 168205. [CrossRef]
45. Xu, Y.; Ishizuka, T.; Kurabayashi, K.; Komiyama, M. Consecutive Formation of G-Quadruplexes in Human Telomeric-Overhang DNA: A Protective Capping Structure for Telomere Ends. *Angew. Chem. Int. Ed.* **2009**, *48*, 7833–7836. [CrossRef]
46. Biffi, G.; Tannahill, D.; McCafferty, J.; Balasubramanian, S. Quantitative Visualization of DNA G-quadruplex Structures in Human Cells. *Nat. Chem.* **2013**, *5*, 182–186. [CrossRef]
47. Zhang, S.; Sun, H.; Wang, L.; Liu, Y.; Chen, H.; Li, Q.; Guan, A.; Liu, M.; Tang, Y. Real-Time Monitoring of DNA G-quadruplexes in Living Cells with a Small-Molecule Fluorescent Probe. *Nucleic Acids Res.* **2018**, *46*, 7522–7532. [CrossRef]
48. Bao, H.L.; Liu, H.S.; Xu, Y. Hybrid-type and two-tetrad antiparallel telomere DNA G-quadruplex structures in living human cells. *Nucleic Acids Res.* **2019**, *47*, 4940–4947. [CrossRef] [PubMed]
49. Wu, G.; Chen, L.; Liu, W.; Yang, D. Molecular Recognition of the Hybrid-Type G-Quadruplexes in Human Telomeres. *Molecules* **2019**, *24*, 1578. [CrossRef] [PubMed]
50. Manna, S.; Sarkar, D.; Srivatsan, S.G. A Dual-App Nucleoside Probe Provides Structural Insights into the Human Telomeric Overhang in Live Cells. *J. Am. Chem. Soc.* **2018**, *140*, 12622–12633. [CrossRef]
51. Ma, D.; Zhang, Z.; Wang, M.; Lu, L.; Zhong, H.; Leung, C. Recent Developments in G-Quadruplex Probes. *Chem. Biol.* **2015**, *22*, 812–828. [CrossRef] [PubMed]
52. Xu, J.; Jiang, R.; He, H.; Ma, C.; Tang, Z. Recent advances on G-quadruplex for biosensing, bioimaging and cancer therapy. *Trends Anal. Chem.* **2021**, *139*, 116257. [CrossRef]
53. Chen, L.; Dickerhoff, J.; Sakai, S.; Yang, D. DNA G-Quadruplex in Human Telomeres and Oncogene Promoters: Structures, Functions, and Small Molecule Targeting. *Acc. Chem. Res.* **2022**, *55*, 2628–2646. [CrossRef] [PubMed]
54. Yuan, J.H.; Shao, W.; Chen, S.B.; Huang, Z.S.; Tan, J.H. Recent advances in fluorescent probes for G-quadruplex nucleic acids. *Biochem. Biophys. Res. Commun.* **2020**, *531*, 18–24. [CrossRef] [PubMed]

55. Raguseo, F.; Chowdhury, S.; Minard, A.; Antonio, M.D. Chemical-biology approaches to probe DNA and RNA G-quadruplex structures in the genome. *Chem. Commun.* **2020**, *56*, 1317–1324. [CrossRef] [PubMed]
56. Iida, K.; Suzuki, N.; Sasaki, A.; Ishida, S.; Arai, T. Development of a novel light-up probe for detection of G-quadruplexes in stress granules. *Sci. Rep.* **2022**, *12*, 12892. [CrossRef] [PubMed]
57. Holden, L.; Gkika, K.S.; Burke, C.S.; Long, C.; Keyes, T.E. Selective, Disruptive Luminescent Ru(II) Polypyridyl Probes of G-Quadruplex. *Inorg. Chem.* **2023**, *62*, 2213–2227. [CrossRef] [PubMed]
58. Zhang, L.; Liu, H.; Shao, Y.; Lin, C.; Jia, H.; Chen, G.; Yang, D.; Wang, Y. Selective Lighting Up of Epiberberine Alkaloid Fluorescence by Fluorophore-Switching Aptamer and Stoichiometric Targeting of Human Telomeric DNA G-Quadruplex Multimer. *Anal. Chem.* **2015**, *87*, 730–737. [CrossRef]
59. Chang, C.C.; Wu, J.Y.; Chien, C.W.; Wu, W.S.; Liu, H.; Kang, C.C.; Yu, L.J.; Chang, T.C. A Fluorescent Carbazole Derivative: High Sensitivity for Quadruplex DNA. *Anal. Chem.* **2003**, *75*, 6177–6183. [CrossRef]
60. Chang, C.C.; Kuo, I.C.; Ling, I.F.; Chen, C.T.; Chen, H.C.; Lou, P.J.; Lin, J.J.; Chang, T.C. Detection of Quadruplex DNA Structures in Human Telomeres by a Fluorescent Carbazole Derivative. *Anal. Chem.* **2004**, *76*, 4490–4494. [CrossRef]
61. Chang, C.C.; Chu, J.F.; Kao, F.J.; Chiu, Y.C.; Lou, P.J.; Chen, H.C.; Chang, T.C. Verification of Antiparallel G-Quadruplex Structure in Human Telomeres by Using Two-Photon Excitation Fluorescence Lifetime Imaging Microscopy of the 3,6-Bis(1-Methyl-4-Vinylpyridinium)Carbazole Diiodide Molecule. *Anal. Chem.* **2006**, *78*, 2810–2815. [CrossRef] [PubMed]
62. Liu, W.; Lin, C.; Wu, G.; Dai, J.; Chang, T.-C.; Yang, D. Structures of 1:1 and 2:1 Complexes of BMVC and MYC Promoter G-Quadruplex Reveal a Mechanism of Ligand Conformation Adjustment for G4-Recognition. *Nucleic Acids Res.* **2019**, *47*, 11931–11942. [CrossRef] [PubMed]
63. Liu, L.; Liu, W.; Wang, K.; Zhu, B.; Xia, X.; Ji, L.; Mao, Z. Quantitative Detection of G-Quadruplex DNA in Live Cells Based on Photon Counts and Complex Structure Discrimination. *Angew. Chem. Int. Ed.* **2020**, *59*, 9719–9726. [CrossRef] [PubMed]
64. Zheng, K.W.; Zhang, J.Y.; He, Y.D.; Gong, J.Y.; Wen, C.J.; Chen, J.N.; Hao, Y.H.; Zhao, Y.; Tan, Z. Detection of genomic G-quadruplexes in living cells using a small artificial protein. *Nucleic Acids Res.* **2020**, *48*, 11706–11720. [CrossRef] [PubMed]
65. Biver, T. Discriminating between Parallel, Anti-Parallel and Hybrid G-Quadruplexes: Mechanistic Details on Their Binding to Small Molecules. *Molecules* **2022**, *27*, 4165. [CrossRef] [PubMed]
66. Ma, Y.; Iida, K.; Nagasawa, K. Topologies of G-quadruplex: Biological functions and regulation by ligands. *Biochem. Biophys. Res. Commun.* **2020**, *531*, 3–17. [CrossRef] [PubMed]
67. Nagatsugi, F.; Onizuka, K. Functional G-Quadruplex Binding Molecules. *Chem. Lett.* **2020**, *49*, 771–780. [CrossRef]
68. Sun, D.; Thompson, B.; Cathers, B.E.; Salazar, M.; Kerwin, S.M.; Trent, J.O.; Jenkins, T.C.; Neidle, S.; Hurley, L.H. Inhibition of Human Telomerase by a G-Quadruplex-Interactive Compound. *J. Med. Chem.* **1997**, *40*, 2113–2116. [CrossRef]
69. Neidle, S.; Parkinson, G. Telomere Maintenance as a Target for Anticancer Drug Discovery. *Nat. Rev. Drug Discov.* **2002**, *1*, 383–393. [CrossRef]
70. Yang, D.; Okamoto, K. Structural Insights into G-Quadruplexes: Towards New Anticancer Drugs. *Future Med. Chem.* **2010**, *2*, 619–646. [CrossRef]
71. Wang, K.B.; Elsayed, M.S.A.; Wu, G.; Deng, N.; Cushman, M.; Yang, D. Indenoisoquinoline Topoisomerase Inhibitors Strongly Bind and Stabilize the MYC Promoter G-Quadruplex and Downregulate MYC. *J. Am. Chem. Soc.* **2019**, *141*, 11059–11070. [CrossRef] [PubMed]
72. Monsen, R.C. Higher-order G-quadruplexes in promoters are untapped drug targets. *Front. Chem.* **2023**, *11*, 1211512. [CrossRef] [PubMed]
73. Shu, H.; Zhang, R.; Xiao, K.; Yang, J.; Sun, X. G-Quadruplex-Binding Proteins: Promising Targets for Drug Design. *Biomolecules* **2022**, *12*, 648. [CrossRef] [PubMed]
74. Kosiol, N.; Juranek, S.; Brossart, P.; Heine, A.; Paeschke, K. G-quadruplexes: A promising target for cancer therapy. *Mol. Cancer* **2021**, *20*, 40. [CrossRef] [PubMed]
75. Teng, F.Y.; Jiang, Z.Z.; Guo, M.; Tan, X.Z.; Chen, F.; Xi, X.G.; Xu, Y. G-quadruplex DNA: A novel target for drug design. *Cell. Mol. Life Sci.* **2021**, *78*, 6557–6583. [CrossRef] [PubMed]
76. Zou, M.; Li, J.Y.; Zhang, M.J.; Li, J.H.; Huang, J.T.; You, P.D.; Liu, S.W.; Zhou, C.Q. G-quadruplex binder pyridostatin as an effective multi-target ZIKV inhibitor. *Int. J. Biol. Macromol.* **2021**, *190*, 178–188. [CrossRef]
77. Hu, X.X.; Wang, S.Q.; Gan, S.Q.; Liu, L.; Zhong, M.Q.; Jia, M.H.; Jiang, F.; Xu, Y.; Xiao, C.D.; Shen, X.C. A Small Ligand That Selectively Binds to the G-quadruplex at the Human Vascular Endothelial Growth Factor Internal Ribosomal Entry Site and Represses the Translation. *Front. Chem.* **2021**, *9*, 781198. [CrossRef]
78. Miglietta, G.; Marinello, J.; Russo, M.; Capranico, G. Ligands stimulating antitumour immunity as the next G-quadruplex challenge. *Mol. Cancer* **2022**, *21*, 180. [CrossRef]
79. Dhamodharan, V.; Pradeepkumar, P.I. Specific Recognition of Promoter G-Quadruplex DNAs by Small Molecule Ligands and Light-up Probes. *ACS Chem. Biol.* **2019**, *14*, 2102–2114. [CrossRef]
80. Dickerhoff, J.; Dai, J.; Yang, D. Structural recognition of the MYC promoter G-quadruplex by a quinoline derivative: Insights into molecular targeting of parallel G-quadruplexes. *Nucleic Acids Res.* **2021**, *49*, 5905–5915. [CrossRef]
81. Calabrese, D.R.; Chen, X.; Leon, E.C.; Gaikwad, S.M.; Phyo, Z.; Hewitt, W.M.; Alden, S.; Hilimire, T.A.; He, F.; Michalowski, A.M.; et al. Chemical and structural studies provide a mechanistic basis for recognition of the MYC G-quadruplex. *Nat. Commun.* **2018**, *9*, 4229. [CrossRef] [PubMed]

82. Neidle, S. Structured Waters Mediate Small Molecule Binding to G-Quadruplex Nucleic Acids. *Pharmaceuticals* **2022**, *15*, 7. [CrossRef] [PubMed]
83. Xu, Y.; Suzuki, Y.; Lönnberg, T.; Komiyama, M. Human telomeric DNA sequence-specific cleaving by G-quadruplex formation. *J. Am. Chem. Soc.* **2009**, *131*, 2871–2874. [CrossRef] [PubMed]
84. Flynn, R.L.; Centore, R.C.; O'Sullivan, R.J.; Rai, R.; Tse, A.; Songyang, Z.; Chang, S.; Karlseder, J.; Zou, L. TERRA and HnRNPA1 Orchestrate an RPA-to-POT1 Switch on Telomeric Single-Stranded DNA. *Nature* **2011**, *471*, 532–536. [CrossRef] [PubMed]
85. Liu, X.; Ishizuka, T.; Bao, H.L.; Wada, K.; Takeda, Y.; Iida, K.; Nagasawa, K.; Yang, D.; Xu, Y. Structure-dependent Binding of hnRNPA1 to Telomere RNA. *J. Am. Chem. Soc.* **2017**, *139*, 7533–7539. [CrossRef] [PubMed]
86. Liu, X.; Xu, Y. HnRNPA1 Specifically Recognizes the Base of Nucleotide at the Loop of RNA G-Quadruplex. *Molecules* **2018**, *23*, 237. [CrossRef] [PubMed]
87. Agarwala, P.; Pandey, S.; Maiti, S. The tale of RNA G-quadruplex. *Org. Biomol. Chem.* **2015**, *13*, 5570–5585. [CrossRef]
88. Mendoza, O.; Porrini, M.; Salgado, G.F.; Gabelica, V.; Mergny, J.L. Orienting Tetramolecular G-Quadruplex Formation: The Quest for the Elusive RNA Antiparallel Quadruplex. *Chem. Eur. J.* **2015**, *21*, 6732–6739. [CrossRef]
89. Xiao, C.-D.; Shibata, T.; Yamamoto, Y.; Xu, Y. An intramolecular antiparallel G-quadruplex formed by human telomere RNA. *Chem. Commun.* **2018**, *54*, 3944–3946. [CrossRef]
90. Xiao, C.-D.; Ishizuka, T.; Xu, Y. Antiparallel RNA G-quadruplex Formed by Human Telomere RNA Containing 8-Bromoguanosine. *Sci. Rep.* **2017**, *7*, 6695. [CrossRef]
91. Xiao, C.-D.; Ishizuka, T.; Zhu, X.-Q.; Li, Y.; Sugiyama, H.; Xu, Y. Unusual Topological RNA Architecture with an Eight-Stranded Helical Fragment Containing A-, G-, and U-Tetrads. *J. Am. Chem. Soc.* **2017**, *139*, 2565–2568. [CrossRef] [PubMed]
92. Banco, M.T.; Ferré-D'amaeré, A.R. The emerging structural complexity of G-quadruplex RNAs. *RNA* **2021**, *27*, 390–402. [CrossRef] [PubMed]
93. Sundquist, W.I.; Heaphy, S. Evidence for interstrand quadruplex formation in the dimerization of human immunodeficiency virus 1 genomic RNA. *Proc. Natl. Acad. Sci. USA* **1993**, *90*, 3393–3397. [CrossRef] [PubMed]
94. Marquet, R.; Paillart, J.C.; Skripkin, E.; Ehresmann, C.; Ehresmann, B. Dimerization of human immunodeficiency virus type 1 RNA involves sequences located upstream of the splice donor site. *Nucleic Acids Res.* **1994**, *22*, 145–151. [CrossRef] [PubMed]
95. Piekna-Przybylska, D.; Sharma, G.; Bambara, R.A. Mechanism of HIV-1 RNA Dimerization in the Central Region of the Genome and Significance for Viral Evolution. *J. Biol. Chem.* **2013**, *288*, 24140–24150. [CrossRef] [PubMed]
96. Shen, W.; Gao, L.; Balakrishnan, M.; Bambara, R.A. A Recombination Hot Spot in HIV-1 Contains Guanosine Runs That Can Form a G-quartet Structure and Promote Strand Transfer in Vitro. *J. Biol. Chem.* **2009**, *284*, 33883–33893. [CrossRef] [PubMed]
97. Gomez, D.; Guédin, A.; Mergny, J.-L.; Salles, B.; Riou, J.-F.; Teulade-Fichou, M.-P.; Calsou, P. A G-quadruplex structure within the 5′-UTR of TRF2 mRNA represses translation in human cells. *Nucleic Acids Res.* **2010**, *38*, 7187–7198. [CrossRef]
98. Norseen, J.; Johnson, F.B.; Lieberman, P.M. Role for G-Quadruplex RNA Binding by Epstein-Barr Virus Nuclear Antigen 1 in DNA Replication and Metaphase Chromosome Attachment. *J. Virol.* **2009**, *83*, 10336–10346. [CrossRef]
99. Wang, Q.; Liu, J.-q.; Chen, Z.; Zheng, K.-w.; Chen, C.-y.; Hao, Y.-h.; Tan, Z. G-quadruplex formation at the 3′ end of telomere DNA inhibits its extension by telomerase, polymerase and unwinding by helicase. *Nucleic Acids Res.* **2011**, *39*, 6229–6237. [CrossRef]
100. Arora, A.; Dutkiewicz, M.; Scaria, V.; Hariharan, M.; Maiti, S.; Kurreck, J. Inhibition of translation in living eukaryotic cells by an RNA G-quadruplex motif. *RNA* **2008**, *14*, 1290–1296. [CrossRef]
101. Patel, D.J.; Phan, A.T.; Kuryavy, V. Human telomere, oncogenic promoter and 5′-UTR G-quadruplexes: Diverse higher order DNA and RNA targets for cancer therapeutics. *Nucleic Acids Res.* **2007**, *35*, 7429–7455. [CrossRef] [PubMed]
102. Mullen, M.A.; Olson, K.J.; Dallaire, P.; Major, F.; Assmann, S.M.; Bevilacqua, P.C. RNA G-Quadruplexes in the model plant species *Arabidopsis thaliana*: Prevalence and possible functional roles. *Nucleic Acids Res.* **2010**, *38*, 8149–8163. [CrossRef] [PubMed]
103. Morris, M.J.; Basu, S. An unusually stable G-quadruplex within the 5′-UTR of the MT3 matrix metalloproteinase mRNA represses translation in eukaryotic cells. *Biochemistry* **2009**, *48*, 5313–5319. [CrossRef] [PubMed]
104. Gros, J.; Guédin, A.; Mergny, J.-L.; Lacroix, L. G-Quadruplex formation interferes with P1 helix formation in the RNA component of telomerase hTERC. *ChemBioChem* **2008**, *9*, 2075–2079. [CrossRef] [PubMed]
105. Ribeiro, M.M.; Teixeira, G.S.; Martins, L.; Marques, M.R.; de Souza, A.P.; Line, S.R.P. G-quadruplex formation enhances splicing efficiency of *PAX9* intron 1. *Hum. Genet.* **2015**, *134*, 37–44. [CrossRef]
106. Huang, H.; Zhang, J.; Harvey, S.E.; Hu, X.; Cheng, C. RNA G-quadruplex secondary structure promotes alternative splicing via the RNA-binding protein hnRNPF. *Genes Dev.* **2023**, *31*, 2296–2309. [CrossRef]
107. Jara-Espejo, M.; Fleming, A.M.; Burrows, C.J. Potential G-Quadruplex Forming Sequences and N^6-Methyladenosine Colocalize at Human Pre-mRNA Intron Splice Sites. *ACS Chem. Biol.* **2020**, *15*, 1292–1300. [CrossRef]
108. Georgakopoulos-Soares, I.; Parada, G.E.; Wong, H.Y.; Medhi, R.; Furlan, G.; Munita, R.; Miska, E.A.; Kwok, C.K.; Hemberg, M. Alternative splicing modulation by G-quadruplexes. *Nat. Commun.* **2022**, *13*, 2404. [CrossRef]
109. Asamitsu, S.; Yabuki, Y.; Ikenoshita, S.; Kawakubo, K.; Kawasaki, M.; Usuki, S.; Nakayama, Y.; Adachi, K.; Kugoh, H.; Ishii, K.; et al. CGG repeat RNA G-quadruplexes interact with FMRpolyG to cause neuronal dysfunction in fragile X-related tremor/ataxia syndrome. *Sci. Adv.* **2021**, *7*, eabd9440. [CrossRef]
110. Mcrae, E.K.S.; Dupas, S.J.; Booy, E.P.; Piragasam, R.S.; Fahlman, R.P.; Mckenna, S.A. An RNA guanine quadruplex regulated pathway to TRAIL-sensitization by DDX21. *RNA* **2020**, *26*, 44–57. [CrossRef]

111. Ji, D.; Juhas, M.; Tsang, C.M.; Kwok, C.K.; Li, Y.; Zhang, Y. Discovery of G-quadruplex-forming sequences in SARS-CoV-2. *Brief. Bioinform.* **2021**, *22*, 1150–1160. [CrossRef] [PubMed]
112. Bao, H.L.; Ishizuka, T.; Sakamoto, T.; Fujimoto, K.; Uechi, T.; Kenmochi, N.; Xu, Y. Investigation of higher-order RNA G-quadruplex structures in vitro and in living cells by ^{19}F NMR spectroscopy. *Nucleic Acids Res.* **2017**, *45*, 5501–5511. [CrossRef] [PubMed]
113. Ishizuka, T.; Zhao, P.Y.; Bao, H.L.; Xu, Y. A Multi-functional Guanine Derivative for Studying DNA G-quadruplex Structure. *Analyst* **2017**, *142*, 4083–4088. [CrossRef] [PubMed]
114. Ishizuka, T.; Yamashita, A.; Asada, Y.; Xu, Y. Studying DNA G-quadruplex aptamer by ^{19}F NMR. *ACS Omega* **2017**, *2*, 8843–8848. [CrossRef] [PubMed]
115. Bao, H.L.; Ishizuka, T.; Iwanami, A.; Oyoshi, T.; Xu, Y. A Simple and Sensitive ^{19}F NMR Approach for Studying the Interaction of RNA G-Quadruplex with Ligand Molecule and Protein. *ChemistrySelect* **2017**, *2*, 4170–4175. [CrossRef]
116. Bao, H.L.; Xu, Y. Investigation of higher-order RNA G-quadruplex structures in vitro and in living cells by ^{19}F NMR spectroscopy. *Nat. Protoc.* **2018**, *13*, 652–665. [CrossRef] [PubMed]
117. Bao, H.L.; Ishizuka, T.; Yamashita, A.; Furukoji, E.; Asada, Y.; Xu, Y. Improving thermodynamic stability and anticoagulant activity of thrombin binding aptamer by incorporation of 8-trifluoromethyl-2′-deoxyguanosine. *J. Med. Chem.* **2021**, *1*, 711–718. [CrossRef]
118. Chen, X.; Chen, S.; Jing Dai, J.; Yuan, J.; Ou, T.; Huang, Z.; Tan, J. Tracking the Dynamic Folding and Unfolding of RNAG-Quadruplexes in Live Cells. *Angew. Chem. Int. Ed.* **2018**, *57*, 4702–4706. [CrossRef]
119. Laguerre, A.; Stefan, L.; Larrouy, M.; Genest, D.; Novotna, J.; Pirrotta, M.; Monchaud, D. Twice-As-Smart Synthetic G-Quartet: PyroTASQ Is Both a Smart Quadruplex Ligand and a Smart Fluorescent Probe. *J. Am. Chem. Soc.* **2014**, *136*, 12406–12414. [CrossRef]
120. Malina, J.; Scott, P.; Brabec, V. Stabilization of human telomeric RNA G-quadruplex by the water-compatible optically pure and biologically-active metallohelices. *Sci. Rep.* **2020**, *10*, 14543. [CrossRef]
121. Chan, C.Y.; Kwok, C.K. Specific Binding of a d-RNA G-Quadruplex Structure with an l-RNA Aptamer. *Angew. Chem. Int. Ed.* **2020**, *59*, 5293–5297. [CrossRef] [PubMed]
122. Ferino, A.; Nicoletto, G.; D'Este, F.; Zorzet, S.; Lago, S.; Richter, S.N.; Tikhomirov, A.; Shchekotikhin, A.; Xodo, L.E. Photodynamic Therapy for ras-Driven Cancers: Targeting G-Quadruplex RNA Structures with Bifunctional Alkyl-Modified Porphyrins. *J. Med. Chem.* **2020**, *63*, 1245–1260. [CrossRef] [PubMed]
123. Xu, Y.; Suzuki, Y.; Ishizuka, T.; Xiao, C.-D.; Liu, X.; Xiao, C.-D.; Komiyama, M. Finding a Human Telomere DNA-RNA Hybrid G-Quadruplex Formed by Human Telomeric 6-mer RNA and 16-mer DNA using Click Chemistry: A Protective Structure for Telomere End. *Bioorg. Med. Chem.* **2014**, *22*, 4419–4421. [CrossRef]
124. Choi, B.E.; Lee, H.T. DNA-RNA hybrid G-quadruplex tends to form near the 3′ end of telomere overhang. *Biophys. J.* **2022**, *121*, 2962–2980. [CrossRef] [PubMed]
125. Zhang, J.; Xia, Y.; Hao, Y.; Tan, Z. DNA:RNA hybrid G-quadruplex formation upstream of transcription start site. *Sci. Rep.* **2020**, *10*, 7429. [CrossRef]
126. Ren, C.; Duan, R.; Hao, Y.; Tan, Z. Genome-Wide Formation of DNA:RNA Hybrid G-Quadruplexes in Live Yeast Cells. *bioRxiv* **2023**. [CrossRef]
127. Zaug, A.J.; Podell, E.R.; Cech, T.R. Human POT1 disrupts telomeric G-quadruplexes allowing telomerase extension in vitro. *Proc. Natl. Acad. Sci. USA* **2005**, *102*, 10864–10869. [CrossRef]
128. Wang, H.; Nora, G.J.; Ghodke, H.; Opresko, P. Single molecule studies of physiologically relevant telomereic tails reveals Pot1 mechanism for promoting G-quadruplex unfolding. *J. Biol. Chem.* **2011**, *286*, 7479–7489. [CrossRef]
129. Zahler, A.M.; Williamson, J.R.; Cech, T.R.; Prescott, D.M. Inhibition of telomerase by G-quartet DNA structures. *Nature* **1991**, *350*, 718–720. [CrossRef]
130. Oganesian, L.; Moon, I.K.; Bryan, T.M.; Jarstfer, M.B. Extension of G-quadruplex DNA by ciliate telomerase. *EMBO J.* **2006**, *25*, 1148–1159. [CrossRef]
131. Moye, A.L.; Porter, K.C.; Cohen, S.B.; Phan, T.; Zyner, K.G.; Sasaki, N.; Lovrecz, G.O.; Beck, J.L.; Bryan, T.M. Telomeric G-quadruplexes are a substrate and site of localization for human telomerase. *Nat. Commun.* **2015**, *6*, 7643. [CrossRef] [PubMed]
132. De Cian, A.; Cristofari, G.; Reichenbach, P.; De Lemos, E.; Monchaud, D.; Teulade-Fichou, M.P.; Shin-Ya, K.; Lacroix, L.; Lingner, J.; Mergny, J.L. Reevaluation of telomerase inhibition by quadruplex ligands and their mechanisms of action. *Proc. Natl. Acad. Sci. USA* **2007**, *104*, 17347–17352. [CrossRef]
133. Hwang, H.; Kreig, A.; Calvert, J.; Lormand, J.; Kwon, Y.; Daley, J.M.; Sung, P.; Opresko, P.L.; Myong, S. Telomeric overhang length determines structural dynamics and accessibility to telomerase and ALT-associated proteins. *Structure* **2014**, *22*, 842–853. [CrossRef] [PubMed]
134. Lee, H.T.; Bose, A.; Lee, C.Y.; Opresko, P.L.; Myong, S. Molecular mechanisms by which oxidative DNA damage promotes telomerase activity. *Nucleic Acids Res.* **2017**, *45*, 11752–11765. [CrossRef] [PubMed]
135. Takahama, K.; Takada, A.; Shota Tada, S.; Shimizu, M.; Sayama, K.; Kurokawa, R.; Oyoshi, T. Regulation of Telomere Length by G-Quadruplex Telomere DNA and TERRA-Binding Protein TLS/FUS. *Chem. Biol.* **2013**, *20*, 341–550. [CrossRef] [PubMed]

136. Mei, Y.; Deng, Z.; Vladimirova, O.; Gulve, N.; Johnson, F.B.; Drosopoulos, W.C.; Schildkraut, C.L.; Lieberman, P.M. TERRA G-quadruplex RNA interaction with TRF2 GAR domain is required for telomere integrity. *Sci. Rep.* **2021**, *11*, 3509. [CrossRef] [PubMed]
137. Yang, S.Y.; Emily Chang, E.Y.C.; Lim, J.; Kwan, H.H.; Monchaud, D.; Yip, S.; Stirling, P.C.; Wong, J.M.Y. G-quadruplexes mark alternative lengthening of telomeres. *NAR Cancer* **2021**, *3*, zcab031. [CrossRef]
138. Yadav, T.; Zhang, J.M.; Ouyang, J.; Leung, W.; Simoneau, A.; Zou, L. TERRA and RAD51AP1 promote alternative lengthening of telomeres through an R- to D-loop switch. *Mol. Cell* **2022**, *82*, 3985–4000. [CrossRef]
139. Tsai, R.X.; Fang, K.C.; Yang, P.C.; Hsieh, Y.H.; Chiang, I.T.; Chen, Y.; Lee, H.G.; Lee, J.T.; Chu, H.C. TERRA regulates DNA G-quadruplex formation and ATRX recruitment to chromatin. *Nucleic Acids Res.* **2022**, *50*, 12217–12234. [CrossRef]
140. Xu, Y.; Ito, K.; Komiyama, M. A 6-mer photocontrolled oligonucleotide as an effective telomerase inhibitor. *J. Am. Chem. Soc.* **2010**, *132*, 631–637. [CrossRef]
141. Ito, K.; Go, S.; Komiyama, M.; Xu, Y. Inhibition of Translation by Small RNA-Stabilized mRNA Structures in Human Cells. *J. Am. Chem. Soc.* **2011**, *133*, 19153–19159. [CrossRef] [PubMed]
142. de Silanes, I.L.; d'Alcontres, M.S.; Blasco, M.A. TERRA transcripts are bound by a complex array of RNA-binding proteins. *Nat. Commun.* **2010**, *1*, 33. [CrossRef] [PubMed]
143. Eulalio, A.; Behm-Ansmant, I.; Izaurralde, E. P bodies: At the crossroads of post-transcriptional pathways. *Nat. Rev. Mol. Cell Biol.* **2007**, *8*, 9–22. [CrossRef] [PubMed]
144. Deng, Z.; Norseen, J.; Wiedmer, A.; Riethman, H.P.; Lieberman, M. TERRA RNA Binding to TRF2 Facilitates Heterochromatin Formation and ORC Recruitment at Telomeres. *Mol. Cell* **2009**, *35*, 403–413. [CrossRef]
145. Collie, G.W.; Sparapani, S.; Parkinson, G.N.; Neidle, S. Structural Basis of Telomeric RNA Quadruplex−Acridine Ligand Recognition. *J. Am. Chem. Soc.* **2011**, *133*, 2721–2728. [CrossRef]
146. Wynford-Thomas, D.; Kipling, D. The end-replication problem. *Nature* **1997**, *389*, 551–552. [CrossRef]
147. Bonnell, E.; Pasquier, E.; Wellinger, R.J. Telomere Replication: Solving Multiple End Replication Problems. *Front. Cell Dev. Biol.* **2021**, *9*, 668171. [CrossRef]

Disclaimer/Publisher's Note: The statements, opinions and data contained in all publications are solely those of the individual author(s) and contributor(s) and not of MDPI and/or the editor(s). MDPI and/or the editor(s) disclaim responsibility for any injury to people or property resulting from any ideas, methods, instructions or products referred to in the content.

molecules

MDPI

Article

Absorption, Distribution, Metabolism, and Excretion of [^{14}C]BS1801, a Selenium-Containing Drug Candidate, in Rats

Cheng Yang [1,2], Mingzhen Xue [3], Yifei He [2], Hanwei Yin [4], Chen Yang [2], Dafang Zhong [2], Huihui Zeng [4,*], Yuandong Zheng [2,*] and Xingxing Diao [1,2,*]

1 School of Chinese Materia Medica, Nanjing University of Chinese Medicine, Nanjing 210023, China; yc2550983083@163.com
2 Shanghai Institute of Materia Medica, Chinese Academy of Sciences, Shanghai 201210, China; s20-heyifei@simm.ac.cn (Y.H.); yangchen@simm.ac.cn (C.Y.); dfzhong@simm.ac.cn (D.Z.)
3 Jiangsu Key Laboratory for Functional Substances of Chinese Medicine, Nanjing University of Chinese Medicine, Nanjing 210023, China; xuemingzhen@foxmail.com
4 Shanghai Yuanxi Pharmaceutical Technology Co., Ltd., Shanghai 201203, China; yinhanwei@yxmedicine.com
* Correspondence: zenghh@bjmu.edu.cn (H.Z.); ydzheng@simm.ac.cn (Y.Z.); xxdiao@simm.ac.cn (X.D.)

Abstract: BS1801 is a selenium-containing drug candidate with potential for treating liver and lung fibrosis. To fully elucidate the biotransformation of BS1801 in animals and provide sufficient preclinical drug metabolism data for human mass balance study, the metabolism of BS1801 in rats was investigated. We used radiolabeling techniques to investigate the mass balance, tissue distribution, and metabolite identification of BS1801 in Sprague–Dawley/Long–Evans rats after a single oral dose of 100 mg/kg (100 μCi/kg) [^{14}C]BS1801: 1. The mean recovery of radioactive substances in urine and feces was 93.39% within 168 h postdose, and feces were the main excretion route. 2. Additionally, less than 1.00% of the dose was recovered from either urine or bile. 3. BS1801-related components were widely distributed throughout the body. 4. Fifteen metabolites were identified in rat plasma, urine, feces, and bile, and BS1801 was detected only in feces. 5. BS1801-M484, the methylation product obtained via a N–Se bond reduction in BS1801, was the most abundant drug-related component in plasma. The main metabolic pathways of BS1801 were reduction, amide hydrolysis, oxidation, and methylation. Overall, BS1801 was distributed throughout the body, and excreted mainly as an intact BS1801 form through feces. No differences were observed between male and female rats in distribution, metabolism, and excretion of BS1801.

Keywords: [^{14}C]BS1801; BS1801 (butaselen); tissue distribution; metabolism; mass balance; selenium

1. Introduction

The thioredoxin (Trx) system, which consists of Trx, thioredoxin reductase (TrxR), and nicotinamide adenine dinucleotide phosphate (NADPH), is a key antioxidant system that defends against oxidative stress by regulating the protein dithiol/disulfide balance through its disulfide reductase activity [1]. TrxR/Trx is involved in the development of various diseases, especially cancer [2,3]. In addition, the Trx system is essential for normal cellular function, so it is necessary to develop its inhibitors as a therapeutic strategy [4]. TrxR is a selenocysteine-containing enzyme responsible for maintaining redox homeostasis in cells and plays a key role in regulating diverse cellular redox signaling pathways [5]. However, few pharmaceutical companies have been actively involved in the development of TrxR enzyme inhibitors, and the inhibitors described in the literature and patents fall into the following main categories: metal complexes, Michael receptors, sulfur/selenium (Se)-containing compounds, and others [4]. Nevertheless, most of the disclosed inhibitors were developed based on the modification of the selenocysteine residue (the selenol group) of TrxR, which has an overall similar but relatively stronger response (nucleophilicity and metal-binding property) than

that of its counterpart cysteine residue (the thiol group) [2,4,6]. Importantly, the concentration of thiols in cells is much higher than that of selenols, so the abundance of thiols compensates for their low reactivity; as a result, the inhibitor may undergo cross-reactivity with thiols [4]. Therefore, inhibitors of TrxR should be further developed.

In recent years, Se-containing compounds have attracted increasing attention. Se is an essential trace element for many biological functions and a component of selenoproteins [7]. It is generally believed that Se has multiple positive effects on human health [8,9]. A study summarizing more than 100 Se-containing compounds found that Se-containing compounds exhibit a variety of anticancer, antioxidant, and antifibrotic activities and that incorporating Se atoms into small molecules significantly increases their biological activity [6]. Different structures of Se derivatives have different efficacy [6,7]. Compared with the toxicity and adverse reactions of inorganic selenium compounds, organic selenium derivatives have attracted more attention, and many organic selenium compounds have been found to have strong anti-tumor activity [6,10,11]. Selenium-containing drugs are effective chemopreventive and chemotherapeutic agents for cancer [6,12]. Se is also ingested in the form of dietary supplements [13]. Additionally, the presence of Se affects the pharmacokinetics, metabolism, and detection of drugs. Se contains six stable isotopes with different abundances, which form characteristic peak clusters and facilitate the identification of compounds containing Se.

Ebselen (2-phenyl-1,2-benzisoselenazol-3(2H)-one), a nontoxic organoselenium compound discovered in the 1980s, was used to prevent and treat a variety of diseases because of its wide range of targets and ability to modulate a variety of biological processes [9,14,15]. The treatment of stroke in 1997 was not approved in Japan due to insufficient efficacy data [14]. However, researchers have not stopped exploring the compound, and it is currently in clinical stage III [16]. BBSKE (1,2-[bis(1,2-benzisoselenazolone-3 (2H)-ketone)]-ethane) is a heterocyclic organoselenium compound that has been reported to exhibit antitumor effects and is a novel antitumor agent [17]. Ebselen and BBSKE had a high binding rate with plasma proteins, resulting in their inability to perform pharmacokinetic studies by directly quantifying the parent drug. Several studies quantified the plasma metabolites (selenol derivatives) of ebselen or BBSKE via different sample pretreatment methods or the LC–MS method combined with other methods to assess their pharmacokinetics [18–20].

BS1801 (butaselen), a selenium-containing drug candidate, is a novel TrxR inhibitor developed by Shanghai Yuanxi Pharmaceutical Technology Co., Ltd. It is a structural analog of ebselen and BBSKE, all of which contain Se. Ebselen exerts its effects by mimicking glutathione peroxidase activity, whereas BS1801 and BBSKE exert their effects by inhibiting TrxR activity [21–23]. Although ebselen has been included in a number of clinical trials in the United States and Asia, there is no specific prospect of clinical application [24]. Studies on BBSKE have focused more on its anticancer activity, while the current drug candidate BS1801 has been proposed for the clinical treatment of fibrosis and is currently in phase I clinical trials [17,25,26].

To our knowledge, there are only two studies on the metabolism and pharmacokinetics related to BS1801. In the first study, the covalent binding product of BS1801 and human serum albumin was described, as well as the mechanism of its reduction and methylation [27]. In another study, M2 (BS1801-M484) was identified as the major metabolite of BS1801 in human plasma via mass spectrometry response and UV absorption peak area, and the pharmacokinetics of M2 were evaluated [25]. However, the mass spectrometry and UV response do not accurately reflect the abundance of metabolites since they are susceptible to structural modifications of metabolites.

Among the available studies, there were no accurate data to investigate the proportion of metabolites in BS1801, so the safety of major metabolites cannot be evaluated. At the same time, there was a lack of tissue distribution and mass balance data for BS1801 in vivo. Since the concentration of the drug in the target organ is directly related to the efficacy and toxicity, tissue distribution must be investigated in animals to further advance the research progress of BS1801 for eventual marketing [28]. A mass balance study of radiolabeled BS1801 in humans is also needed. In the draft *Clinical Pharmacology Considerations for*

Human Radiolabeled Mass Balance Studies published by the US FDA in May 2022, it was noted that the dose of human radioactive administration should be estimated based on animal research data [29]. Therefore, the radiolabeled mass balance study in animals must be performed before human-radiolabeled mass balance study.

In this study, the distribution, metabolism, and excretion of [^{14}C]BS1801(Figure 1) in rats were studied. We evaluated the overall metabolism of BS1801 in rats, providing a strong basis for human mass balance study and promoting clinical research.

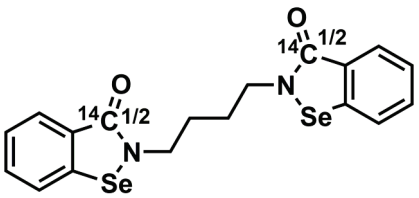


Figure 1. Chemical structure of [^{14}C]BS1801.

2. Results

2.1. Mass Balance

The mean radioactive recovery in urine and feces was 93.39% in SD rats after a single oral administration from 0 to 168 h. Among them, feces was the main excretion route, and the cumulative excretion of radioactive substances accounted for 92.77% of the dose, while urine accounted for only 0.62%. The mean radioactive recovery in urine and feces within 0–48 h was 91.57% after administration. The cumulative radioactive recoveries of urine and feces are provided in Figure 2A (detailed data are provided in Supplemental Table S2).

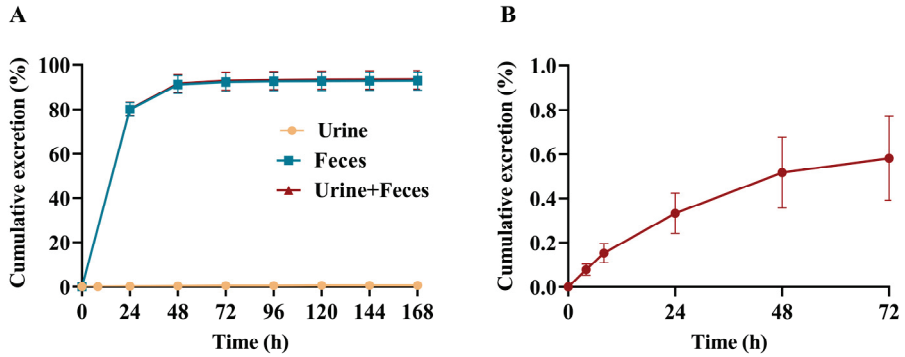


Figure 2. Mean cumulative excretion of total radioactivity (3 male and 3 female SD rats) in urine and feces (**A**) and bile (**B**) in SD rats after a single oral dose of 100 mg/kg (100 μCi/kg) [^{14}C]BS1801.

The recovery of radioactivity in bile within 72 h after a single intragastric administration in SD rats undergoing BDC was 0.58% (Figure 2B and detailed data are provided in Supplemental Table S2). The drug excreted through the feces consisted mainly of the part absorbed via the bile and the unabsorbed part, and it was clear from the biliary excretion data that BS1801 in feces was predominantly unabsorbed.

2.2. Tissue Distribution

All tissues of twenty-four LE rats (3 male and 3 female at each time point) were collected at 2, 10, 48, and 96 h after intragastric administration. The drug-related substances in male rats were mainly concentrated in the liver, stomach, large intestine, and eyes (Figure 3A). The ratios of $AUC_{0–96h}$ in these tissues to plasma $AUC_{0–96h}$ were 11.80, 10.60, 7.48, and 5.35, respectively (Supplemental Table S3). In female rats, drug-related substances were mainly concentrated in the large intestine and liver, and the $AUC_{0–96h}$ ratios of these tissues to the plasma $AUC_{0–96h}$ were 16.82 and 6.59, respectively (Figure 3B and Supplemental Table S3). The ratios of other tissues $AUC_{0–96h}$ to plasma $AUC_{0–96h}$ were lower than 5.00 postdose in all rats (Supplemental Table S3).

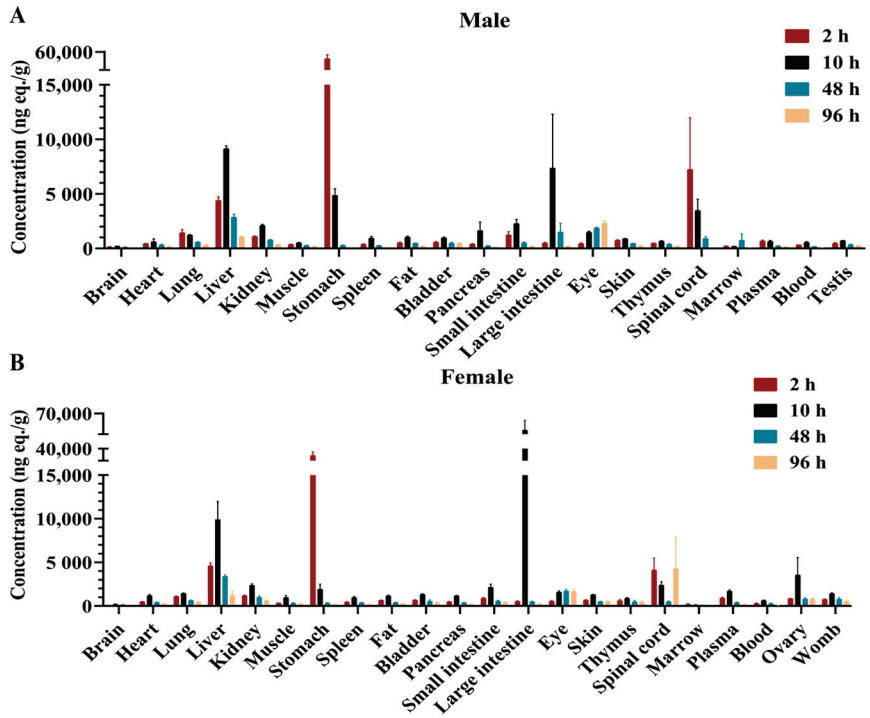


Figure 3. Tissue concentration–time distribution in male (**A**) and female (**B**) LE rats after a single oral dose of 100 mg/kg (100 μCi/kg) [^{14}C]BS1801.

In male LE rats, the T_{max} was 2 or 10 h for all tissues except the eyes and marrow. In female LE rats, the T_{max} was 2 or 10 h for all tissues except the eyes and spinal cord (Figure 3A,B).

The average ratio of blood $AUC_{0–96h}$ to plasma $AUC_{0–96h}$ was 0.73 in male rats post-dose, while that of female rats was 0.45 (Supplemental Table S3), indicating that the drug-related substances preferred to not be distributed in blood cells.

2.3. Metabolite Identification

Figure 4 presents radio-chromatograms of pooled plasma (0–72 h), urine (0–96 h), feces (0–48 h), and bile (0–48 h) for male and female rats. A total of twelve metabolites in male rats and thirteen metabolites in female rats were identified after drug administration. Supplemental Table S4 summarizes the proposed metabolic pathways, elemental composition, determined m/z ($[M + H]^+$), mass error (ppm), and characteristic fragment ions for BS1801 and its metabolites.

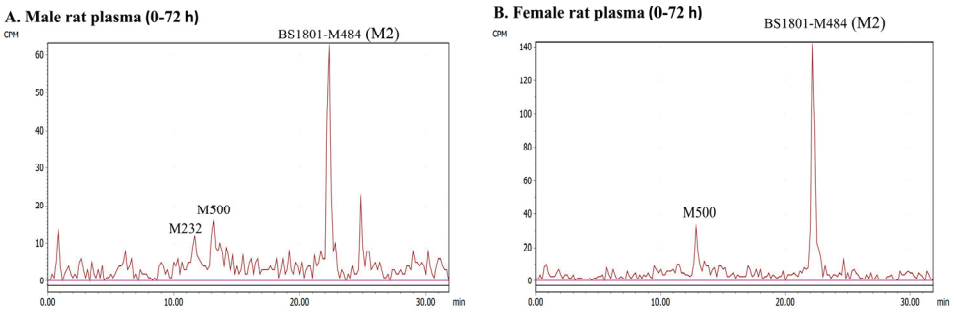


Figure 4. *Cont.*

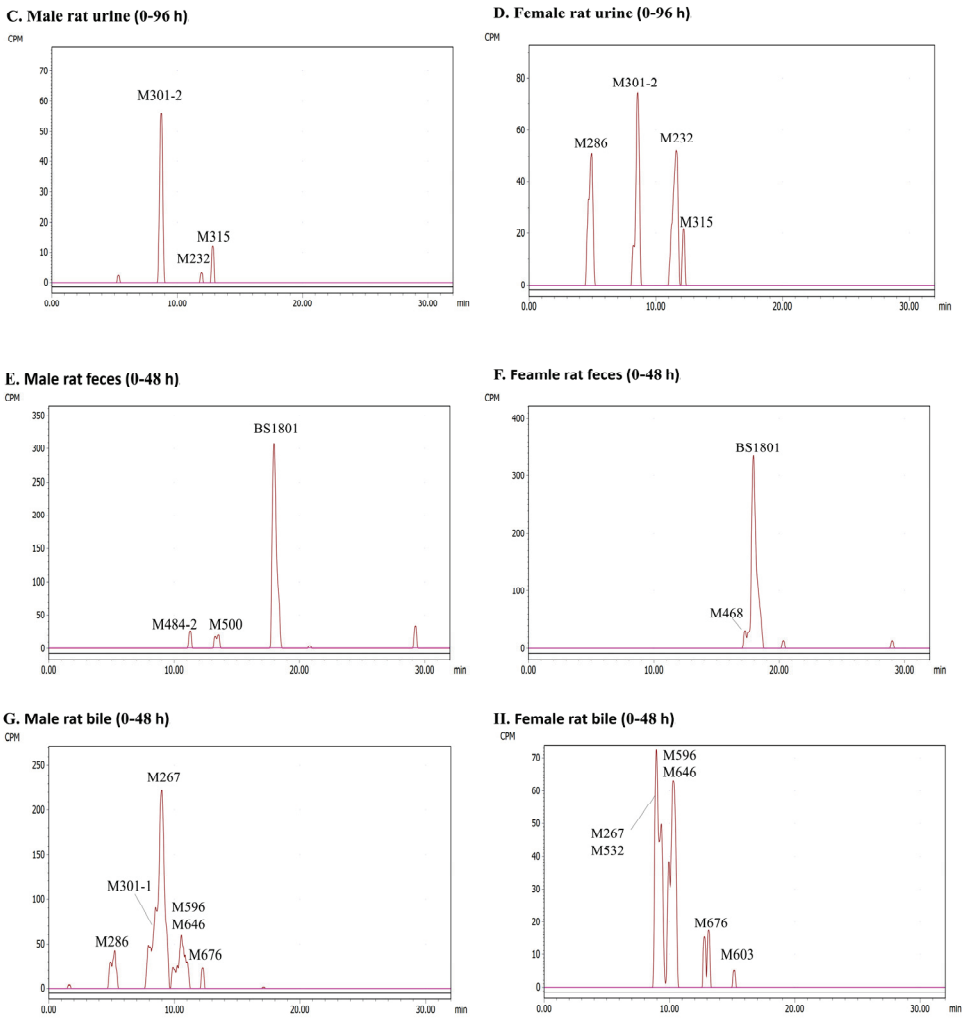


Figure 4. Representative radio-chromatograms of metabolites of BS1801 after a single oral dose of 100 mg/kg (100 μCi/kg) [^{14}C]BS1801 in male and female SD rats. (**A**) Male rat plasma (0–72 h); (**B**) female rat plasma (0–72 h); (**C**) male rat urine (0–96 h); (**D**) female rat urine (0–96 h); (**E**) male rat feces (0–48 h); (**F**) female rat feces (0–48 h); (**G**) male rat bile (0–48 h); (**H**) female rat bile (0–48 h).

2.3.1. HR-MS Analysis of BS1801 and M2 Reference Standards

BS1801. Under the experimental conditions of this study, BS1801 ($C_{18}H_{16}N_2O_2Se_2$) eluted at 17.65 min, and the molecular ion ($[M + H]^+$) obtained in the full-scan MS was *m*/*z* 452.9617. The major fragment ions of BS1801 were *m*/*z* 254.0079, 211.9608, 199.9608, and 184.9501. The fragment ions *m*/*z* 254.0079 and 199.9608 were mainly produced by C–N bond cleavage. The C–C bond breakage produced a fragment ion *m*/*z* 211.9608. The fragment ion *m*/*z* 184.9501 was produced by the amide bond breakage and N–Se bond breakage (Figure 5A).

M2. M2 was the product of BS1801 reduction and further methylation, and its retention time was 22.28 min. M2 yielded a molecular ion ($[M + H]^+$) *m*/*z* 485.0242 and its major fragment ions *m*/*z* 270.0392, 198.9656, 183.9418, and 72.0815 in full-scan MS. The cleavage of the C–N bond produced a fragment ion *m*/*z* 270.0392, and the cleavage of the amide bond produced a fragment ion *m*/*z* 198.9656. Amide bond breakage and the loss of $CH_3\cdot$ radical produced the fragment ion *m*/*z* 183.9418. The fragment ion *m*/*z* 72.0815 was produced by C–N bond breakage (Figure 5B).

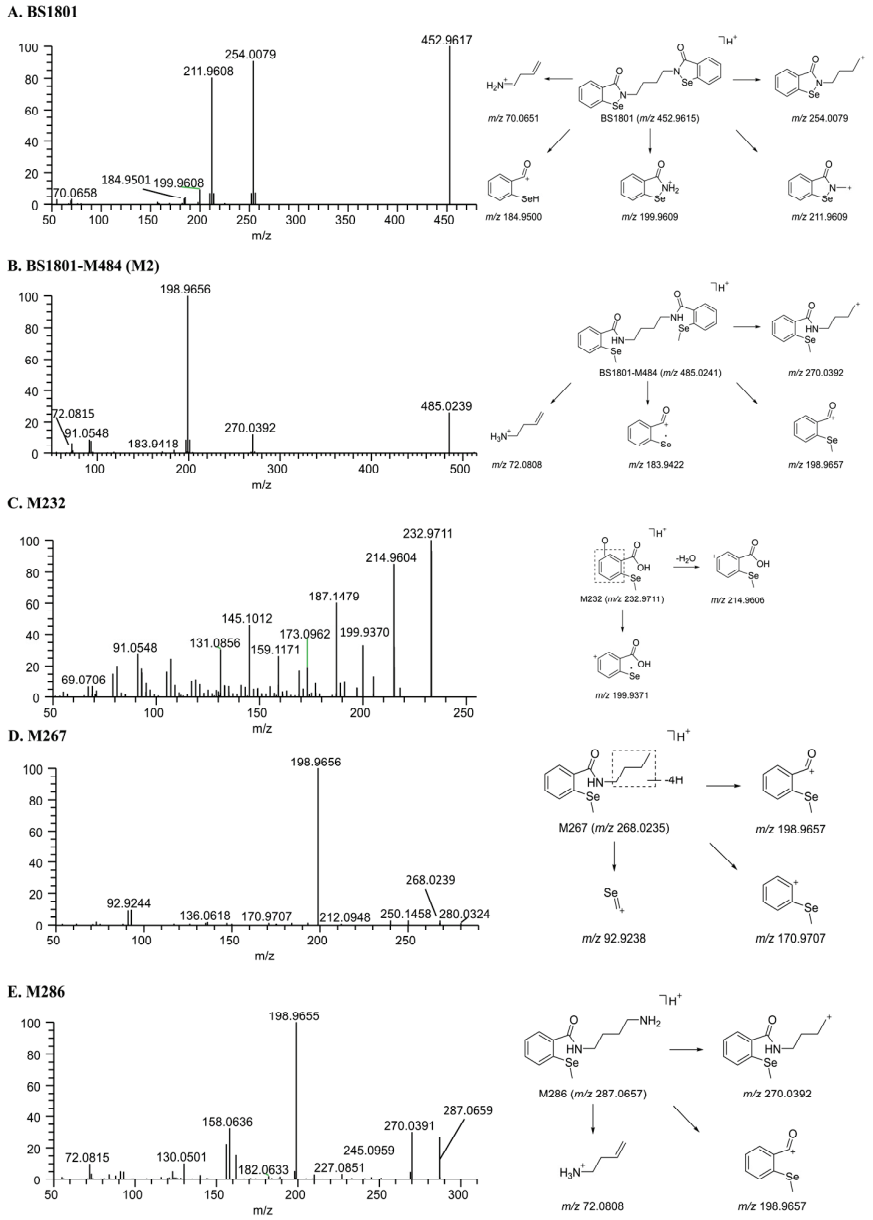


Figure 5. Mass spectra of metabolites and their proposed fragmentation profiles. (**A**) BS1801; (**B**) BS1801-M484 (M2); (**C**) M232; (**D**) M267; (**E**) M286.

2.3.2. Plasma

BS1801 was not detected in $AUC_{0–72h}$ pooled male rat plasma. Three metabolites were identified via HR-MS and radio-chromatographic peaks. Among them, M2 accounted for 65.41% of the total radioactivity and was the most abundant metabolite. M500 and M232 accounted for 20.07% and 11.59% of the total radioactivity, respectively. In female rats, BS1801 was also undetected in plasma. Only two metabolites, M2 and M500, were detected, accounting for 81.33% and 14.00% of the total plasma radioactivity, respectively (Figure 4, and Supplemental Table S5).

2.3.3. Urine

The cumulative excretion of radioactive substances in urine was only 0.62% of the dose, as shown in the mass balance study. A total of three radioactive chromatographic peaks were identified in 0–96 h pooled male rat urine sample, and the parent drug BS1801 was not detected. M232, M301-2, and M315 accounted for 0.018%, 0.41%, and 0.068% of the dose, respectively. Four radioactive peaks were identified in 0–96 h pooled female rat urine

sample, and BS1801 was not detected. M232, M286, M301-2, and M315 accounted for 0.23%, 0.20%, 0.21%, and 0.046% of the dose, respectively (Figure 4, and Supplemental Table S5).

2.3.4. Feces

According to the mass balance study, feces was the main excretion route. The cumulative excretion of radioactive substances in male rats feces accounted for 92.32% of the dose, and BS1801 accounted for 76.97% of the dose. Two metabolites were identified by combining HR-MS and radio-chromatographic peaks. Among them, M500 was the major metabolite, accounting for 5.73% of the dose; M484-2 was the minor metabolite, accounting for 4.00% of the dose. The cumulative excretion of radioactive substances in the feces of female rats accounted for 93.22% of the dose, and BS1801 accounted for 81.89% of the dose. Only the metabolite M468 was identified by combining HR-MS and radio-chromatographic peaks, accounting for 7.77% of the dose (Figure 4, and Supplemental Table S5).

2.3.5. Bile

The cumulative excretion of radioactive substances in bile accounted for only 0.58% of the dose. Six metabolites were identified using HR-MS and radio-chromatographic peaks in pooled 0–48 h male rat bile. Among them, M267 was the major metabolite, accounting for 0.46% of the dose. M301-1 was the second abundant metabolite, accounting for 0.22% of the dose. Co-eluting metabolites M596 and M646 accounted for 0.18% of the dose. The contents of M286 and M676 were less than 0.1% of the dose. Six metabolites were also identified in pooled female rat bile. Among them, M267 and M532 co-eluted; M596 and M646 also co-eluted. The contents of all metabolites in bile were less than 0.1% of the dose (Figure 4, and Supplemental Table S5).

2.3.6. Description of Metabolites

BS1801 and M2. The structures of BS1801 and M2 were confirmed by comparison with the retention time and LC–MS/MS spectra of the reference standards.

M232. The metabolite of M232 (m/z 232.9713) was composed of $C_8H_8O_3Se$, which was produced by the amide hydrolysis of M484-2. Its main fragment ions were m/z 214.9604 and 199.9370. The fragment ion m/z 214.9604 was 18.0109 Da (H_2O) smaller than M232, which was obtained by the neutral loss of water from the precursor ion. The fragment ion m/z 199.9370 was produced by further losing $CH_3\cdot$ radical from the precursor ion m/z 214.9604 (Figure 5C).

M267. The elemental composition of M267 (m/z 268.0237) was $C_{12}H_{13}NOSe$. The precise molecular weight of M267 was the same as that of M286 minus an NH_5, corresponding to deamination and dehydrogenation. The main product ions were m/z 198.9656, 170.9707, and 92.9244. Among them, the product ion m/z 198.9656 was the same as the product ion m/z M286. This supports the inferred structure of M267 (Figure 5D).

M286. The elemental composition of M286 (m/z 287.0660) was $C_{12}H_{18}N_2OSe$, which was produced by *N*-dealkylation and methylation of BS1801. The main fragment ions were m/z 270.0391, 198.9655, and 72.0815. Among them, the fragment ion m/z 270.0391 was produced by the neutral loss of NH_3; fragment ion m/z 198.9655 was produced by amide bond cleavage (Figure 5E).

M301-1 and M301-2. M301-1 and M301-2 were produced by oxidative deamination and further oxidation of M286. The $[M + H]^+$ of M301-1 and M301-2 ($C_{12}H_{15}NO_3Se$) were m/z 302.0290, which was identical to the theoretical value. The main fragment ion m/z 198.9655 (the same as the fragment ions of M286) was produced by amide bond breakage, and the fragment ion m/z 183.9421 was produced by amide bond cleavage and losing $CH_3\cdot$ radical. The fragment ion m/z 86.0602 supported the modification site of M301-1. The fragment ions of M301-2 were similar to those of M301-1 (Figure 6A).

M315. Metabolite M315 (m/z 316.0447) was composed of $C_{13}H_{17}NO_3Se$, which was produced by M301 methylation. M315 produced the same fragment ions as M301 at m/z 198.9656 and 183.9426. The fragment ion m/z 284.0182 was the fragment of M315 after the

neutral loss of methanol. These results indicated that M315 was a methylated product of M301 (Figure 6B).

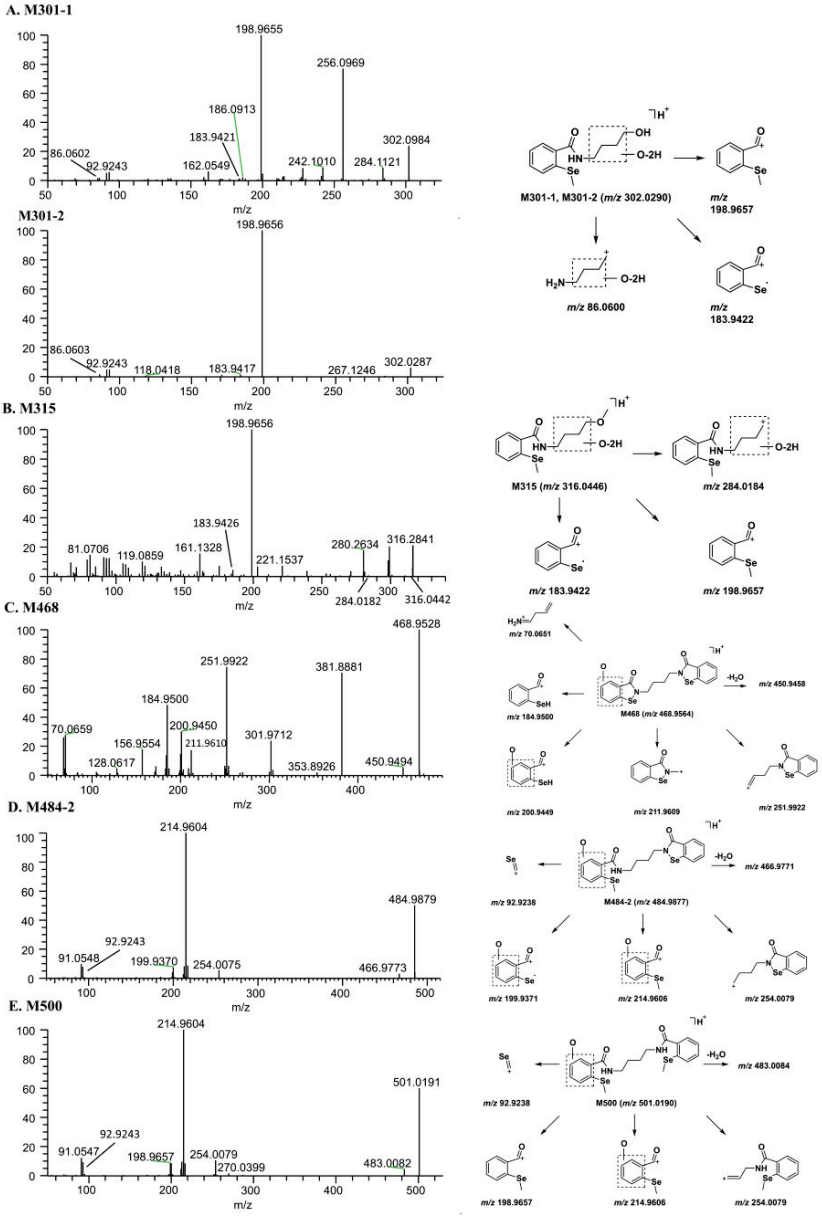


Figure 6. Mass spectra of metabolites and their proposed fragmentation profiles. (**A**) M301-1 and M301-2; (**B**) M315; (**C**) M468; (**D**) M484-2; (**E**) M500.

M468. M468 ($C_{18}H_{16}N_2O_3Se_2$), with $[M + H]^+$ at m/z 468.9552, was 15.9945 Da (O) larger than that of BS1801, suggesting that M468 was produced by the mono-oxidation of BS1801. Its major product ions m/z 211.9610, 184.9500, and 70.0659 were identical to those of BS1801. The product ion m/z 450.9494 was obtained by the neutral loss of water from the precursor ion. The difference between the product ions m/z 200.9450 and 184.9500 was 15.9950 Da (O), so it was inferred that the oxidation site was on the benzene ring (Figure 6C).

M484-2. The $[M + H]^+$ of M484-2, m/z 484.9880, was 16.0328 Da (CH_4) larger than that of M468. Its elemental composition was $C_{19}H_{20}N_2O_3Se_2$. Therefore, it was inferred that M484-2 was the product of Se methylation of M468. The fragment ion m/z 254.0075 was produced by C–N bond cleavage. Amide bond cleavage produced a fragment ion m/z 214.9604, and further losing $CH_3\cdot$ radical produced a fragment ion m/z 199.9370. The fragment ion m/z 466.9773 was obtained from the neutral loss of water from M484-2 (Figure 6D).

M500. The $[M + H]^+$ of M500, m/z 501.0192, was 15.9950 Da (O) larger than that of M2. According to the precise molecular weight, the molecular formula of M500 was $C_{20}H_{24}N_2O_3Se_2$, indicating that it was derived from the mono-oxidation of M2. The main product ions of M500 were m/z 483.0082, 254.0079, 214.9604, 198.9657, and 92.9243. The product ion m/z 483.0082 was obtained by the neutral loss of water from the precursor ion. The product ion m/z 198.9657 was similar to the product ion of M2 and was 15.9947 Da (O) smaller than the product ion m/z 214.9604, indicating that the oxidation site was on the benzene ring (Figure 6E).

M532. The $[M + H]^+$ of M532 ($C_{20}H_{24}N_2O_5Se_2$) was m/z 533.0091, which was produced by the di-oxidation of M500. The neutral loss of water from M532 produced fragment ion m/z 514.9987, and the further loss of water produced fragment ion m/z 496.9887. The breakage of the amide bond produced fragment ion m/z 230.9554, the further removal of one oxygen atom produced ion m/z 214.9605, and the removal of two oxygen atoms produced ion m/z 198.9656 (Figure 7A).

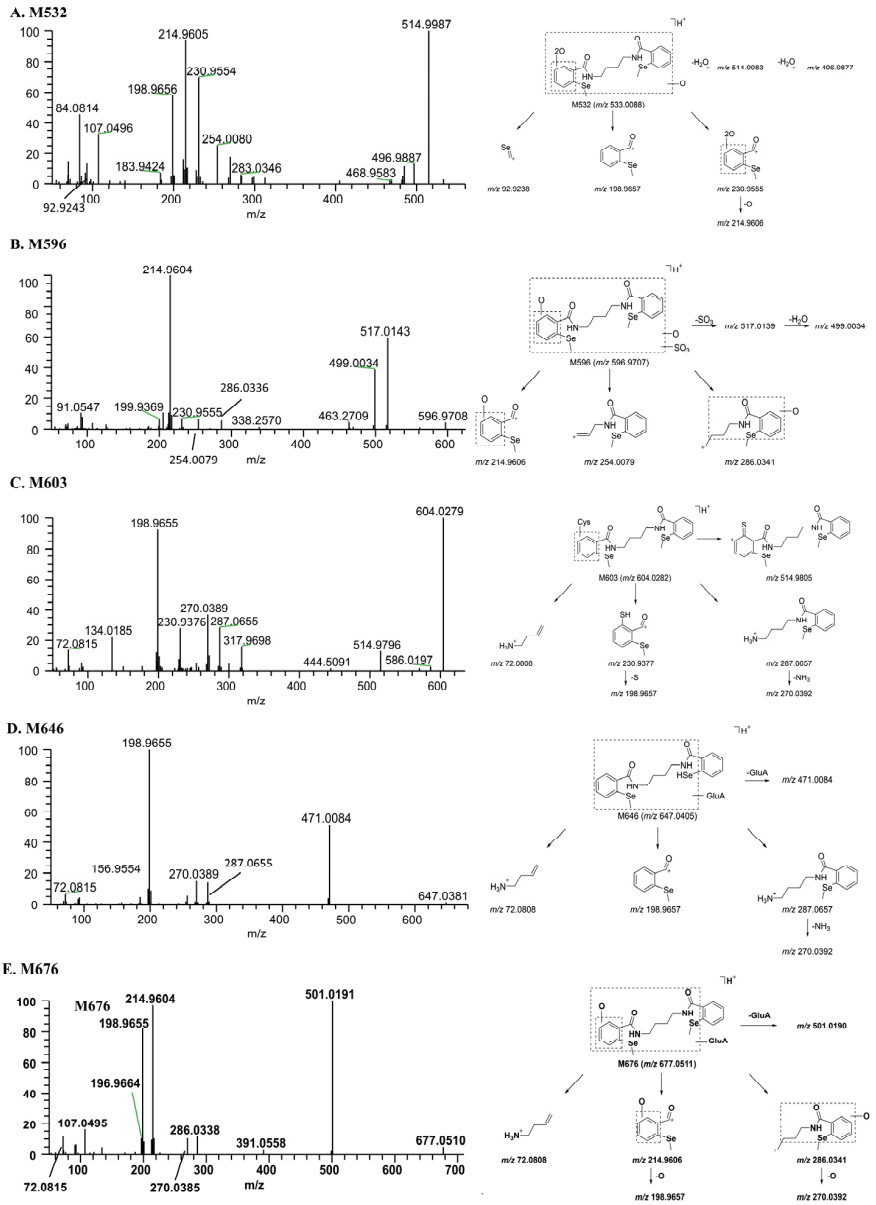


Figure 7. Mass spectra of metabolites and their proposed fragmentation profiles. (**A**) M532; (**B**) M596; (**C**) M603; (**D**) M646; (**E**) M676. Cys, cysteine conjugation; GluA, glucuronidation; SO_3, sulfation.

M596. The elemental composition of M596 (*m*/*z* 596.9709) was $C_{20}H_{24}N_2O_7Se_2S$. M596 had one more SO_4 than M500, indicating sulfation and oxidation. Its major product ions were *m*/*z* 517.0143 (the loss of SO_3), 499.0034 (the loss of SO_3 and water), 286.0336 (C–N bond breakage), 254.0079, and 214.9604. Among them, the product ions *m*/*z* 254.0079, and 214.9604 were identical to those of M500. However, the specific conjugation and oxidation sites were not determined (Figure 7B).

M603. The $[M + H]^+$ of M603 ($C_{23}H_{29}N_3O_4Se_2S$) was *m*/*z* 604.0291. Compared with M2, M603 was $C_3H_5NO_2S$ more than M2, corresponding to cysteine. The product ions *m*/*z* 270.0389, 198.9655, and 72.0815 of M603 were the same as those of M2. The product ion *m*/*z* 230.9376 was 31.9720 Da (S) more than the product ion *m*/*z* 198.9656 of M2; therefore, the binding site of M603 to cysteine was located on the benzene ring. The product ion *m*/*z* 514.9796 further supported the proposed structure of M603 (Figure 7C).

M646. The elemental composition of M646 (*m*/*z* 647.0406) was $C_{25}H_{30}N_2O_8Se_2$. It was the product of BS1801 reduction, methylation, and glucuronidation. The fragment ion *m*/*z* 471.0084 was produced by the neutral loss of glucuronic acid. The breakage of the amide bond on one side yielded the product ions *m*/*z* 287.0655 and 198.9655. The neutral loss of NH_3 (17.0266 Da) from the ion *m*/*z* 287.0655 generated the product ion *m*/*z* 270.0389 (Figure 7D).

M676. M676 (*m*/*z* 677.0506) had an elemental composition of $C_{26}H_{32}N_2O_9Se_2$, which was $C_6H_8O_6$ more than M500. After the neutral loss of a molecule of glucuronic acid ($C_6H_8O_6$), M676 yielded product ion *m*/*z* 501.0191. When one side of the C–N or amide bond was broken, product ions *m*/*z* 286.0338 or 214.9604 were obtained; the further loss of an O atom yielded product ions *m*/*z* 270.0385 and 198.9655, respectively. The product ions *m*/*z* 214.9604 and 198.9655 were identical to M500 (Figure 7E).

The main metabolic pathways of BS1801 are shown in Figure 8.

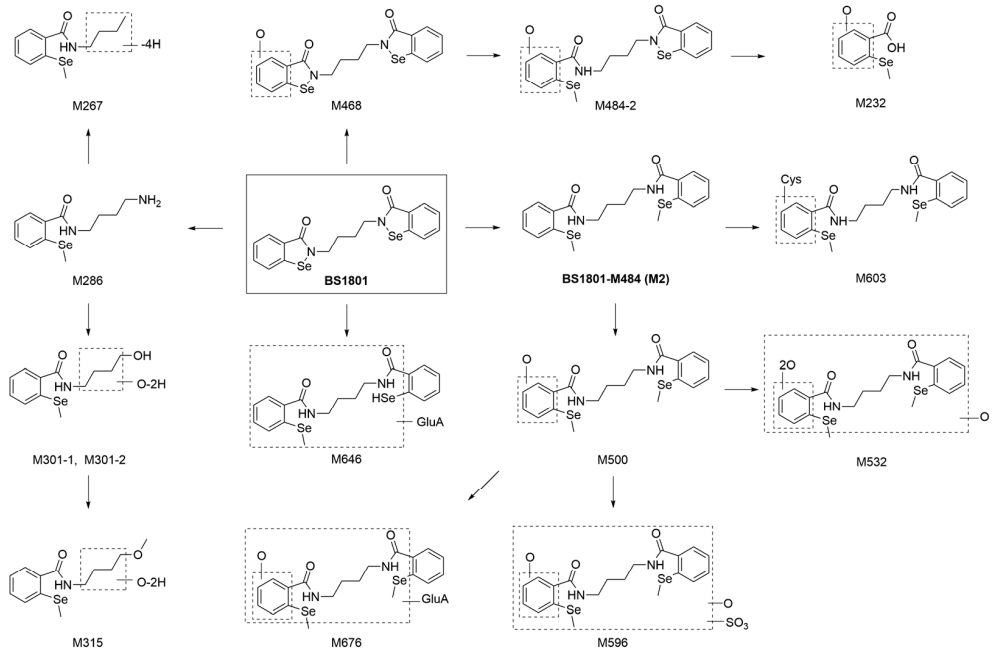


Figure 8. Metabolic pathway of BS1801 in rat. Cys, cysteine conjugation; GluA, glucuronidation; SO_3, sulfation. Bold means reference standards available.

3. Discussion

This study investigated the mass balance, tissue distribution, and metabolism of BS1801 in rats after a single oral dose of 100 mg/kg (100 μCi/kg) [^{14}C]BS1801. BS1801 and its metabolites were identified in plasma, urine, feces, and bile via an accurate mass determination and diagnostic MS fragment ions.

In mass balance studies, the results measured with radiolabeling techniques are much more accurate than those measured with non-radiolabeled compounds [30]. In this study, 91.57% of the radioactivity was excreted within 48 h after oral administration of [^{14}C]BS1801, indicating that [^{14}C]BS1801 was rapidly excreted in rats. The mean cumulative radioactivity recovery in urine and feces was 93.39% within 168 h after administration, of which 92.77% was in feces, and only 0.62% was in urine, suggesting that feces was the main excretion route. The average cumulative radioactive recovery in bile was 0.58% of the dose. The radioactive recovery in either urine or bile was less than 1% of the dose; thus, we inferred that BS1801 was not well absorbed in rats (Supplemental Table S2). However, previous studies have shown that it has very good pharmacological effect, which may indicate that a small amount of BS1801 can exert a strong therapeutic effect [26]. Therefore, further research is needed to investigate whether BS1801 absorption may be improved by altering the dosage form, etc., which can minimize the administered dose. Drug-related substances were widely distributed after the intragastric administration of [^{14}C]BS1801, and radioactivity was detected in all collected tissues. However, the overall distribution of radioactivity concentrations was low, which may be attributed to its low absorption. In male LE rats, high radioactivity concentration was detected mainly in the liver, stomach, large intestine, and eyes; in female LE rats, high radioactivity concentration was detected mainly in the large intestine and liver (Figure 3A,B). The relatively high concentration levels in the liver are favorable for the targeted treatment of liver fibrosis. The ratio of $AUC_{0–96h}$ of brain to that of plasma was the lowest in all analyzed tissues, which may be due to the blood–brain barrier limiting the entry of BS1801 into the brain. The results of mass balance and tissue distribution of [^{14}C]BS1801 in rats provide a basis for human dosimetry.

It is well known that high-resolution mass spectrometry is commonly used to quantitatively analyze compounds, but quantifying metabolite content is also crucial [31]. This study used high-resolution mass spectrometry combined with radio-chromatography to qualitatively and quantitatively analyze the metabolites associated with BS1801 simultaneously, which can provide the ratio of metabolites to dose. This will help us identify major metabolites that need further attention. This is the greatest advantage of radiolabeling technology, which can reflect the metabolite content and reveal the biotransformation pathway. Based on the high radioactive recovery of BS1801, a total of 15 metabolites were identified in plasma, urine, feces, and bile. The major metabolic pathways of BS1801 were reduction, amide hydrolysis, oxidation, and methylation, and the minor metabolic pathways were glucuronidation and sulfation (Figure 8). BS1801 was not detected in plasma, urine, and bile but was observed only in feces. Unchanged BS1801 was the major component in rat feces, accounting for more than 75.00% of the dose. M2, a product of methylation following reduction in the N–Se bond, was the major metabolite in plasma, accounting for 65.41% and 81.33% of plasma total radioactivity in male and female SD rats, respectively (Supplemental Table S5). This result is consistent with the findings obtained for unradiolabeled BS1801 in humans [25]. However, the metabolite of M2 was only present in plasma and was completely converted to other metabolites before excretion. In this study, M500 accounted for 20.07% and 14.00% of the plasma total radioactivity in male and female rats, respectively (Supplemental Table S5). This is inconsistent with a previous study in which the exposure of other metabolites was less than 5% of M2 [25]. This may result from several reasons, such as species differences or MS signal changes from metabolic modifications. Notably, it is likely that the MS response and UV peak area do not accurately reflect the metabolite content due to the influence of metabolic modifications. Additionally, we could not quantify each metabolite by using reference standards. In contrast, radiolabeling technology exhibits a unique advantage due to quantitative radioactivity unaffected by metabolite structure. M232 was a newly identified metabolite in the plasma of male rats, accounting for 11.59% of the total plasma radioactivity (Supplemental Table S5). Considering that M500 and M232 accounted for more than 10% of total radioactivity in plasma, we need to pay attention to their exposure in future human study. The advantages of the radiolabeling technique were

demonstrated by comparing the results with those obtained by non-radiolabeled human plasma. Because the method can more accurately quantify the content of metabolites, some metabolites that are easily overlooked but need attention or safety assessment can be found.

BS1801 is further modified from the structure of ebselen and BBSKE. It has been reported that ebselen and BBSKE have high binding rates with albumin [19,32]. However, it is worth mentioning that when BS1801 plasma pooling was performed for protein precipitation, the recoveries of radioactivity in the supernatants of male and female rats were 105.85% and 91.23%, respectively, which demonstrated that the bottom-layer precipitation was almost free of BS1801 and its related metabolites. It has been reported that BS1801 can bind to human serum albumin rapidly and thoroughly, but the covalent binding is unstable; thus, the compound can be reduced and eventually metabolized to BS1801-M484 (M2) [25]. This explains why the bottom-layer protein precipitates in our study contain almost no radioactive substances. According to the free drug hypothesis, after compounds bind to plasma proteins, only free compounds are used for hepatic uptake through active transport or passive diffusion, and only free drugs can reach target tissues to interact with the target [29,33,34]. The properties of BS1801 covalently bound to albumin and eventually metabolized to the free product M2 are more conducive to drug efficacy. The pharmacokinetic/pharmacodynamic modeling (PK/PD modeling) of BS1801 needs to be further explored.

4. Materials and Methods

4.1. Chemicals and Reagents

BS1801 (99.5% content) and the related reference standard M2 (97.7% content) were provided by Shanghai Yuanxi Pharmaceutical Technology Co., Ltd. (Shanghai, China). [^{14}C]BS1801 (Figure 1, 99.71% content) was provided by Wuxi Beta Co., Ltd. (Wuxi, China). The liquid scintillation solution was purchased from Zhejiang Dingxin (Shaoxing, China). The alkaline liquid scintillation cocktail was obtained from RDC^{TM} (Hilladale, NJ, USA). Acetonitrile and methanol of high-performance liquid chromatography (HPLC) grade were purchased from Sigma (St. Louis, MO, USA). Formic acid was purchased from Rhawn Chemical Reagent Co., Ltd. (Shanghai, China). Ammonium acetate was purchased from Sinopharm (Shanghai, China). Ultrapure water was obtained from a Milli-Q integral water purification system (Millipore, Molsheim, France). All other reagents used were HPLC grade or analytical grade.

4.2. Animals

Sprague–Dawley (SD, *Rattus norvegicus*) rats (6–8 weeks, 200–300 g) and Long–Evans (LE, *Rattus norvegicus*) rats (6–8 weeks, 160–220 g) were purchased from Zhejiang Charles River Laboratory Animals Co., Ltd. (Jiaxing, China). The animal use license number of Shanghai Institute of Materia Medica, Chinese Academy of Sciences is SYXK (Hu) 2020-0042. The ethics committee approval number for this study is 2022-07-DXX-06, and it was valid from July 2022 to July 2023. Healthy eligible rats were housed in cages containing toys for 2–5 days in a 12 h day/night constant-temperature laboratory with free access to food and water after receipt in cages with no more than 5 rats per cage. The rats were fasted for 12 h prior to drug administration. The Animal Ethics Committee of the Shanghai Institute of Materia Medica, Chinese Academy of Science (Shanghai, China) approved the study protocol. The study design is shown in Supplementary Table S1.

4.3. Dosing Solutions and Oral Administration

BS1801 and [^{14}C]BS1801 were prepared in 0.5% sodium carboxymethyl cellulose solution at a target concentration of 10 mg/mL (10 μCi/mL). The radioactivity of [^{14}C]BS1801 was measured using a liquid scintillation counter (LSC) (Hidex, Turku, Finland) before and after administration, and a single dose of 10 mL/kg was administered orally.

4.4. Plasma Samples for Metabolite Identification

Three SD rats of each sex were used to obtain plasma samples. Approximately 200 μL of blood was collected from the jugular vein of six SD rats in a centrifuge tube containing heparin sodium before and 0.5, 2, 4, 6, 10, 12, 24, 48, 72, and 96 h after administration, followed by centrifugation (3500× *g*, 5 min, 4 °C), to obtain plasma. All samples were stored at −20 °C for analysis.

4.5. Mass Balance

Three male and three female SD rats were housed individually in metabolic cages. Urine samples were collected from each rat at predose and 0–8, 8–24, 24–48, 48–72, 72–96, 96–120, 120–144, and 144–168 h postdose. When each urine sample was collected, the metabolic cage was flushed with a small amount of water for 0–72 h and methanol/water (50:50, *v*:*v*) for 72–168 h, and the flushing solution was added to the urine sample for the corresponding period. Fecal samples were also collected at predose and 0–24, 24–48, 48–72, 72–96, 96–120, 120–144, and 144–168 h postdose. Urine and fecal samples were weighed and recorded during each collection period. All samples were stored at −20 °C for testing.

Bile duct cannulation (BDC) was performed in 3 male and 3 female SD rats before drug administration. After the operation, the wounds were wiped with iodophor for 2 days, and painkillers were administered appropriately. The state of the rats was observed daily, and the drug was administered only when no abnormality was observed within 2 days. Bile was collected before and 0–4, 4–8, 8–24, 24–48, and 48–72 h after dosing. The weights of the bile samples were recorded, and the samples were stored at −20 °C until testing.

4.6. Tissue Distribution

Twenty-four LE rats (12 of each sex) were used for tissue distribution studies. Three male and three female rats were sacrificed through abdominal aortic bleeding at 2, 10, 48, and 96 h after administration. Approximately 1/5 of the blood was stored frozen at −20 °C, and the remaining blood was centrifuged (3500× *g*, 5 min, 4 °C) to obtain plasma. The brain, heart, lung, liver, stomach wall, spleen, kidney, muscle, pigmented fat, ovary, womb, testis, bladder wall, pancreas, small intestine wall, large intestine wall, eye, pigmented skin, thymus, spinal cord, and marrow were also collected. The tissues were washed with saline, dried, and stored at −20 °C until testing.

4.7. Sample Preparation for Radioactivity Analysis

4.7.1. Urine, Bile, and Plasma Samples

Samples of urine (100 μL), bile (30 μL), and plasma (100 μL from the tissue distribution study) were weighed and added to 15 mL scintillation solution. Among them, urine and bile samples were duplicated, and plasma samples were in singlicate. The radioactivity was measured directly via LSC.

4.7.2. Feces, Blood, and Tissue Samples

Approximately three times the weight of methanol/water (50:50, *v*:*v*) was added to each fecal sample and homogenized with a homogenizer (SKGZ, Shanghai Biheng, Shanghai, China). Approximately 0.2~0.3 g of the fecal homogenate was weighed in a combustion boat, and dried overnight. Blood samples (100 μL) and tissue samples (approximately 0.1 g) were weighed into burning boats. After the samples were completely dried, they were combusted using a Biological Sample Oxidizer (OTCS-11/1, Shanghai Yixing, Shanghai, China). The $^{14}CO_2$ generated was captured with 15 mL alkaline scintillation solution; then, the radioactivity was measured using LSC.

4.8. Metabolite Radio-Profiling and Characterization

4.8.1. Sample Preparation

The plasma samples (predose and 0.5, 2, 4, 6, 10, 12, 24, 48, and 72 h postdose) were pooled according to the AUC-pooling principle [35,36]. Then, 3 mL of methanol/water

(50:50, *v*:*v*) was slowly added to the pooled plasma (1 mL), followed by vortexing for 1 min and sonication for 10 min twice. Then, the upper extract and the lower precipitate were separated by centrifugation (5000 rpm, 10 min). The supernatant was transferred to another new centrifuge tube. Then, 1 mL of water was added to the precipitate, vortexed for 1 min, and sonicated for 10 min. Then, 2 mL of methanol/acetonitrile (50:50, *v*:*v*) was added to the mixture, two vortexes were performed for 1 min, and the mixture was ultrasonicated for 10 min, followed by centrifugation (5000 rpm, 10 min). The two-times supernatant extracts were combined and dried under a nitrogen stream and finally redissolved with acetonitrile/water (20:80, *v*:*v*). The recoveries of extraction and reconstitution processes were measured via LSC.

Urine samples were pooled based on equal percentage according to the volume of urine from 0–8, 8–24, 24–48, 48–72, and 72–96 h, and the corresponding volumes of urine samples were mixed with the same gender. The pooled urine was vortexed and centrifuged (5000 rpm, 10 min). After centrifugation, the supernatant was dried under a nitrogen stream and then redissolved in acetonitrile/water (20:80, *v*:*v*). The bile samples at 0–4, 4–8, 8–24, and 24–48 h were pooled according to the same process as for urine.

The feces samples were pooled based on equal percentage according to the feces weight at 0–24 and 24–48 h for the same sex. The pooled fecal homogenate (1 g) was extracted by using the same method as for the plasma. The supernatant was then evaporated under a nitrogen stream and redissolved in 300 μL acetonitrile/water (20:80, *v*:*v*).

4.8.2. UHPLC-β-RAM/UV/QE MS Analysis

An ACQUITY UPLC BEH Pheny column (100 × 2.1 mm, 1.7 μm) with a Phenomenex KrudKatcher Ultra HPLC In-Line Filter guard column (2 μm, Depth Filter × 0.004 in ID) was used to perform metabolite radio-profiling and characterization on the Vanquish UHPLC system, which was combined with a QExactive Plus mass spectrometer (Thermo, Waltham, MA, USA) containing an electrospray ionization (ESI) source. The column temperature was 40 °C, and the flow rate was 0.45 mL/min. The mobile phases contained 5 mM ammonium acetate with 0.1% formic acid in water (A) and acetonitrile (B). The gradient elution procedure was as follows: 0 min, 5% B; 2 min, 10% B; 27 min, 40% B; 28 min, 95% B; 31 min, 95% B; 32 min, 5% B; and 35 min, 5% B. The eluent was monitored using a photodiode array detection with a full range of wavelengths. The mass spectrometer was operated in positive (+ESI) mode with a m/z 100–1500 Da scanning range. The optimized MS parameters were as follows: sheath gas, 35 L/min; auxiliary gas, 10 L/min; capillary temperature, 320 °C; and spray voltage, 3.8 kV. Data acquisition was performed using Xcalibur 4.1 software (Thermo, Waltham, MA, USA), and data analysis was accomplished using Compound Discoverer software 3.3 SP2 (Thermo, Waltham, MA, USA).

The extracted plasma, urine, feces, and bile samples were separated via UHPLC and detected using an online/offline radioactivity detector to obtain the corresponding radioactive metabolite profiles. Due to low radioactivity of plasma, the UHPLC eluent was collected using a UHPLC fraction collector (Thermo, Waltham, MA, USA) over time (10 s/well) on Deepwell LumaPlateTM 96-well plates. After evaporation via a vacuum centrifuge concentrator, the radioactivity was determined with an offline Sense Beta detector (1 min/well, Hidex, Turku, Finland). For the urine, feces, and bile samples, the UHPLC eluent was analyzed using an online radioactivity detector β-RAM. Radioactive metabolite profiling was integrated to obtain the radio-chromatogram with Laura 6.0.5.101 software (Lablogic, Sheffield, UK). The percentage of each metabolite in urine, feces, and bile (%dose) and the ratio of metabolites in the plasma (% area under the curve, %AUC) were calculated.

5. Conclusions

In brief, this study investigated the distribution, metabolism, and excretion of [^{14}C]BS1801 in rats. The mean recovery of radioactive substances in urine and feces was 93.39% in SD rats within 168 h postdose, and feces was the main excretion route with the cumulative

excretion of radioactive substances accounting for 92.77% of the dose. Additionally, less than 1.00% of the dose was recovered from either urine or bile. The main excretion period of [^{14}C]BS1801 after administration was within 48 h, during which the mean radioactive dose recovery in urine and feces reached 91.57%. Drug-related substances were mainly distributed in the liver, stomach, large intestine, and eyes, and high concentrations in the liver facilitate targeted liver fibrosis therapy. A total of fifteen metabolites of BS1801 were detected in rats, and the main metabolic pathways were reduction, amide hydrolysis, oxidation, and methylation. Consistent with most thiol metabolites, the Se site was susceptible to methylation. BS1801-M484, the methylation product obtained by reduction in the N–Se bond in BS1801, was the most abundant drug-related component, and its radioactivity accounted for 65.41% and 81.33% of the pooled $AUC_{0–72h}$ plasma in male and female rats, respectively. In conclusion, these data are expected to provide a strong basis for further clinical studies.

Supplementary Materials: The following are available online at https://www.mdpi.com/article/10.3390/molecules28248102/s1, Table S1: Study design. Table S2: Mean cumulative dose recovery in urine, feces, urine + feces, and bile following a single oral administration of [^{14}C]BS1801 at the dose of 100 mg/kg (100 μCi/kg) to SD rats. Table S3: $AUC_{0–96h}$ of radioactivity in tissues and plasma of rats, and their ratio to plasma following a single oral administration of [^{14}C]BS1801 at the dose of 100 mg/kg (100 μCi/kg). Table S4: Information of BS1801and its metabolites detected in rat plasma, urine, feces, and bile by using UHPLC-Q Exactive Plus MS. Table S5: The distribution of radioactivity from BS1801 and its major metabolites in rat plasma, urine, feces, and bile and the percent of dose in urine and feces (%).

Author Contributions: Data curation, C.Y. (Cheng Yang) and Y.H.; Formal analysis, C.Y. (Cheng Yang); Funding acquisition, H.Z.; Investigation, C.Y. (Cheng Yang), M.X., Y.H. and C.Y. (Chen Yang); Methodology, H.Y., H.Z. and Y.Z.; Project administration, X.D.; Resources, X.D.; Supervision, H.Y., D.Z., Y.Z. and X.D.; Writing—original draft, C.Y. (Cheng Yang); Writing—review and editing, X.D. All authors have read and agreed to the published version of the manuscript.

Funding: This study was sponsored by Shanghai Yuanxi Medicine Corp. This work was also supported by grants from the National Natural Science Foundation of China (NO. 82104275), the National Key R&D Program of China (NO. 2022YFF1202600), the National Natural Science Foundation of China (NO. 82373938), and the Key Technologies R&D Program of Guangdong Province (NO. 2023B1111030004).

Institutional Review Board Statement: The animal study protocol was approved by the Animal Ethics Committee of the Shanghai Institute of Materia Medica, Chinese Academy of Sciences for studies involving animals. The ethics committee approval number for this study is 2022-07-DXX-06, and it was approved in July 2022.

Informed Consent Statement: Not applicable.

Data Availability Statement: The research data used to support the findings of this study are included in the article.

Conflicts of Interest: Hanwei Yin and Huihui Zeng are employees of the Shanghai Yuanxi Pharmaceutical Technology Co., Ltd. The other authors declare that they have no competing interests.

References

1. Lu, J.; Holmgren, A. The thioredoxin antioxidant system. *Free Radic. Biol. Med.* **2014**, *66*, 75–87. [CrossRef] [PubMed]
2. Zhang, J.; Li, X.; Han, X.; Liu, R.; Fang, J. Targeting the Thioredoxin System for Cancer Therapy. *Trends Pharmacol. Sci.* **2017**, *38*, 794–808. [CrossRef]
3. Ghareeb, H.; Metanis, N. The Thioredoxin System: A Promising Target for Cancer Drug Development. *Chem. Eur. J.* **2020**, *26*, 10175–10184. [CrossRef]
4. Zhang, B.; Zhang, J.; Peng, S.; Liu, R.; Li, X.; Hou, Y.; Han, X.; Fang, J. Thioredoxin reductase inhibitors: A patent review. *Expert Opin. Ther. Pat.* **2017**, *27*, 547–556. [CrossRef]
5. Chupakhin, E.; Krasavin, M. Thioredoxin reductase inhibitors: Updated patent review (2017-present). *Expert Opin. Ther. Pat.* **2021**, *31*, 745–758. [CrossRef]
6. Chuai, H.; Zhang, S.Q.; Bai, H.; Li, J.; Wang, Y.; Sun, J.; Wen, E.; Zhang, J.; Xin, M. Small molecule selenium-containing compounds: Recent development and therapeutic applications. *Eur. J. Med. Chem.* **2021**, *223*, 113621. [CrossRef] [PubMed]

7. Ye, R.H.; Huang, J.Q.; Wang, Z.X.; Chen, Y.X.; Dong, Y.L. Trace Element Selenium Effectively Alleviates Intestinal Diseases. *Int. J. Mol. Sci.* **2021**, *22*, 11708. [CrossRef]
8. Steinbrenner, H.; Speckmann, B.; Klotz, L.O. Selenoproteins: Antioxidant selenoenzymes and beyond. *Arch. Biochem. Biophys.* **2016**, *595*, 113–119. [CrossRef]
9. Barchielli, G.; Capperucci, A.; Tanini, D. The Role of Selenium in Pathologies: An Updated Review. *Antioxidants* **2022**, *11*, 251. [CrossRef]
10. Gandin, V.; Khalkar, P.; Braude, J.; Fernandes, A.P. Organic selenium compounds as potential chemotherapeutic agents for improved cancer treatment. *Free Radic. Biol. Med.* **2018**, *127*, 80–97. [CrossRef]
11. Jariwalla, R.J.; Gangapurkar, B.; Nakamura, D. Differential sensitivity of various human tumour-derived cell types to apoptosis by organic derivatives of selenium. *Br. J. Nutr.* **2008**, *101*, 182–189. [CrossRef] [PubMed]
12. Ip, C.; Dong, Y.; Ganther, H.E. New concepts in selenium chemoprevention. *Cancer Metastasis Rev.* **2002**, *21*, 281–289. [CrossRef]
13. Rayman, M.P. Selenium and human health. *Lancet* **2012**, *379*, 1256–1268. [CrossRef] [PubMed]
14. Parnham, M.J.; Sies, H. The early research and development of ebselen. *Biochem. Pharmacol.* **2013**, *86*, 1248–1253. [CrossRef]
15. Wang, J.; Wang, P.; Dong, C.; Zhao, Y.; Zhou, J.; Yuan, C.; Zou, L. Mechanisms of ebselen as a therapeutic and its pharmacology applications. *Future Med. Chem.* **2020**, *12*, 2141–2160. [CrossRef] [PubMed]
16. Sound Pharmaceuticals lnc. Ebselen. 2022. Available online: https://data.pharmacodia.com/drug#/main/drugInfo (accessed on 12 September 2023).
17. Lan, L.; Zhao, F.; Wang, Y.; Zeng, H. The mechanism of apoptosis induced by a novel thioredoxin reductase inhibitor in A549 cells: Possible involvement of nuclear factor-kappaB-dependent pathway. *Eur. J Pharmacol.* **2007**, *555*, 83–92. [CrossRef]
18. Zheng, W.; He, R.; Boada, R.; Subirana, M.A.; Ginman, T.; Ottosson, H.; Valiente, M.; Zhao, Y.; Hassan, M. A general covalent binding model between cytotoxic selenocompounds and albumin revealed by mass spectrometry and X-ray absorption spectroscopy. *Sci. Rep.* **2020**, *10*, 1274. [CrossRef]
19. Zhou, H.Y.; Dou, G.F.; Meng, Z.Y.; Lou, Y.Q.; Zhang, G.L. High performance liquid chromatographic determination of 1,2-[bis(1,2-benzisoselenazolone-3(2H)-ketone)]-ethane (BBSKE), a novel organoselenium compound, in dog plasma using pre-column derivatization and its application in pharmacokinetic study. *J. Chromatogr. B* **2007**, *852*, 617–624. [CrossRef]
20. Zhou, H.Y.; Dou, G.F.; Meng, Z.Y.; Lou, Y.Q.; Zhang, G.L. Development of a rapid and sensitive liquid chromatography/tandem mass spectrometry method for the determination of 1,2-[bis(1,2-benzisoselenazolone-3(2H)-ketone)]-ethane (BBSKE), a novel anti-cancer agent in rat plasma. *Biomed. Chromatogr.* **2008**, *22*, 1123–1129. [CrossRef]
21. Sies, H. Ebselen, a Selenoorganic Compound as Glutathione-Peroxidase Mimic. *Free Radic. Biol. Med.* **1993**, *14*, 313–323. [CrossRef]
22. Zheng, X.; Ma, W.; Sun, R.; Yin, H.; Lin, F.; Liu, Y.; Xu, W.; Zeng, H. Butaselen prevents hepatocarcinogenesis and progression through inhibiting thioredoxin reductase activity. *Redox. Biol.* **2018**, *14*, 237–249. [CrossRef]
23. Zheng, X.Q.; Chen, Y.F.; Bai, M.; Liu, Y.X.; Xu, B.Y.; Sun, R.X.; Zeng, H.H. The antimetastatic effect and underlying mechanisms of thioredoxin reductase inhibitor ethaselen. *Free Radic. Biol. Med.* **2019**, *131*, 7–17. [CrossRef] [PubMed]
24. Santi, C.; Scimmi, C.; Sancineto, L. Ebselen and Analogues: Pharmacological Properties and Synthetic Strategies for Their Preparation. *Molecules* **2021**, *26*, 4230. [CrossRef] [PubMed]
25. Tian, Q.; Jiang, J.; Yin, H.; Ma, J.; Deng, G.; Zhou, J.; Zhong, D. Quantification of the major circulating metabolite of BS1801, an ebselen analog, in human plasma. *J. Pharm. Biomed. Anal.* **2022**, *212*, 114638. [CrossRef]
26. Chen, Y.; Yin, H.; Sun, J.; Zhang, G.; Zhang, Y.; Zeng, H. TrxR/Trx inhibitor butaselen ameliorates pulmonary fibrosis by suppressing NF-κB/TGF-β1/Smads signaling. *Biomed. Pharmacother.* **2023**, *169*, 115822. [CrossRef] [PubMed]
27. Tian, Q.; Jiang, J.; Yin, H.; Zhang, Y.; Li, Y.; Wu, P.; Peng, C.; Wang, Z.; Zhou, J.; Zeng, H.; et al. Investigating the Metabolic Mechanisms of Butaselen, An Ebselen Analog. *Curr. Drug Metab.* **2022**, *23*, 928–939. [CrossRef] [PubMed]
28. Lu, J.J.; Pan, Q.Q.; Zhou, J.Q.; Weng, Y.; Chen, K.L.; Shi, L.; Zhu, G.X.; Chen, C.L.; Li, L.; Geng, M.Y.; et al. Pharmacokinetics, distribution, and excretion of sodium oligomannate, a recently approved anti-Alzheimer's disease drug in China. *J. Pharm. Anal.* **2022**, *12*, 145–155. [CrossRef]
29. Schulz, J.A.; Stresser, D.M.; Kalvass, J.C. Plasma protein-mediated uptake and contradictions to the free drug hypothesis: A critical review. *Drug Metab. Rev.* **2023**, *55*, 205–238. [CrossRef]
30. Zheng, Y.D.; Zhang, H.; Zhan, Y.; Bian, Y.C.; Ma, S.; Gan, H.X.; Lai, X.J.; Liu, Y.Q.; Gong, Y.C.; Liu, X.F.; et al. Pharmacokinetics, mass balance, and metabolism of [(14)C]vicagrel, a novel irreversible P2Y12 inhibitor in humans. *Acta Pharmacol. Sin.* **2021**, *42*, 1535–1546. [CrossRef]
31. Wang, L.; Li, S.; Li, J.; Cheng, Z.; Feng, Y.; Ouyang, H.; Du, Z.; Jiang, H. Comprehensive metabolic profiling of Alismatis Rhizoma triterpenes in rats based on characteristic ions and a triterpene database. *J. Pharm. Anal.* **2021**, *11*, 96–107. [CrossRef]
32. Wagner, G.; Schuch, G.; Akerboom, T.P.; Sies, H. Transport of ebselen in plasma and its transfer to binding sites in the hepatocyte. *Biochem. Pharmacol.* **1994**, *48*, 1137–1144. [CrossRef]
33. Tillement, J.P.; Urien, S.; Chaumet-Riffaud, P.; Riant, P.; Bree, F.; Morin, D.; Albengres, E.; Barre, J. Blood binding and tissue uptake of drugs. Recent advances and perspectives. *Fundam. Clin. Pharmacol.* **1988**, *2*, 223–238. [CrossRef] [PubMed]
34. Hammarlund-Udenaes, M. Active-site concentrations of chemicals—Are they a better predictor of effect than plasma/organ/tissue concentrations? *Basic Clin. Pharmacol. Toxicol.* **2010**, *106*, 215–220. [CrossRef] [PubMed]
35. Hop, C.E.C.A.; Wang, Z.; Chen, Q.; Kwei, G. Plasma-Pooling Methods To Increase Throughput for in Vivo Pharmacokinetic Screening. *J. Pharm. Sci.* **1998**, *87*, 901–903. [CrossRef] [PubMed]

36. Hamilton, R.A.; Garnett, W.R.; Kline, B.J. Determination of mean valproic acid serum level by assay of a single pooled sample. *Clin. Pharmacol. Ther.* **1981**, *29*, 408–413. [CrossRef]

Disclaimer/Publisher's Note: The statements, opinions and data contained in all publications are solely those of the individual author(s) and contributor(s) and not of MDPI and/or the editor(s). MDPI and/or the editor(s) disclaim responsibility for any injury to people or property resulting from any ideas, methods, instructions or products referred to in the content.

biomolecules

MDPI

Article

Rhododendron chrysanthum's Primary Metabolites Are Converted to Phenolics More Quickly When Exposed to UV-B Radiation

Fushuai Gong, Wang Yu, Qingpan Zeng, Jiawei Dong, Kun Cao, Hongwei Xu and Xiaofu Zhou *

Jilin Provincial Key Laboratory of Plant Resource Science and Green Production, Jilin Normal University, Siping 136000, China
* Correspondence: zhouxiaofu@jlnu.edu.cn

Abstract: The plant defense system is immediately triggered by UV-B irradiation, particularly the production of metabolites and enzymes involved in the UV-B response. Although substantial research on UV-B-related molecular responses in *Arabidopsis* has been conducted, comparatively few studies have examined the precise consequences of direct UV-B treatment on *R. chrysanthum*. The ultra-high-performance liquid chromatography tandem mass spectrometry (UPLC-MS/MS) methodology and TMT quantitative proteomics are used in this study to describe the metabolic response of *R. chrysanthum* to UV-B radiation and annotate the response mechanism of the primary metabolism and phenolic metabolism of *R. chrysanthum*. The outcomes demonstrated that following UV-B radiation, the primary metabolites (L-phenylalanine and D-lactose*) underwent considerable changes to varying degrees. This gives a solid theoretical foundation for investigating the use of precursor substances, such as phenylalanine, to aid plants in overcoming abiotic stressors. The external application of ABA produced a considerable increase in the phenolic content and improved the plants' resistance to UV-B damage. Our hypothesis is that externally applied ABA may work in concert with UV-B to facilitate the transformation of primary metabolites into phenolic compounds. This hypothesis offers a framework for investigating how ABA can increase a plant's phenolic content in order to help the plant withstand abiotic stressors. Overall, this study revealed alterations and mechanisms of primary and secondary metabolic strategies in response to UV-B radiation.

Keywords: UV-B radiation; *Rhododendron chrysanthum*; primary metabolite; phenolic compounds; ultra-performance liquid chromatography tandem mass spectrometry (UPLC-MS/MS); ABA

1. Introduction

China's Changbai Mountain are home to the medicinal properties ornamental shrub *R. chrysanthum*. The predominant abiotic stressor in the Changbai Mountains is UV-B radiation because of the area's unique alpine habitat, which includes cold temperatures, a thin atmosphere, and intense sun radiation. As a result, *R. chrysanthum* is a unique plant resource for the investigation of plant adaptability, and our earlier research has enough physiological support for the plant's great tolerance to UV-B exposure.

UV-B radiation (280–315 nm) was a natural component of sunlight before the 1980s and 1990s, when a surge in the atmosphere's hydrochlorofluorocarbon caused a severe thinning of the stratospheric ozone layer and a corresponding rapid rise in the amount of UV-B light reaching the Earth's surface [1,2]. Obviously, this has a detrimental effect on farming and the vegetation in the natural ecosystem [3]. Even while UV-B only makes up a little portion of the energy, it has a lot of energy on its own [4]. Induced by the UV resistance motif 8 (UVR8)-dependent UV-B signaling pathway, UV-B-responsive genes encourage the formation of phenolic substances such as hydroxycinnamic acid, Kaempferol-3-hexoside rhamnose, and luteolin (5,7,3′,4′-Tetrahydroxyflavone) [5–7]. Numerous studies have looked at the long-term impact of UV-B radiation on plants, but few have concentrated on

the short-term consequences. Studies on the impact of short-term UV-B exposure may aid in the understanding of the UV-induced pathways of signaling as well as the modifications in compounds and enzymes that occur immediately in reaction to UV irradiation. In light of this hypothesis, it is critical to comprehend how *R. chrysanthum* metabolites adjust to increased UV-B exposure.

Phenolic compounds make up the biggest class of secondary metabolites found in plants. In addition to aiding in the creation of cell walls, these substances shield plants against diseases and UV radiation [8]. Phenolics, particularly flavonoids, are the secondary metabolites that are most important for UV protection out of the more than 8000 that exist. According to Marco Santin et al., UV-B radiation triggers the downstream activation of several phenylpropane biosynthetic and regulatory genes, which causes the levels of particular phenolic compounds to significantly increase [9]. Depending on their chemical makeup, phenolic compounds can be categorized into three classes and show a variety of structural variations in nature. Specifically, there are three types of phenolic compounds: (1) those with a C6C1 carbon dioxide in the framework such as 4-hydroxybenzoic acid and 2,5-Dihydroxybenzoic acid; (2) those with C6C3 carbon bones, such as caffeic acid, p-coumaric acid, and ferulic acid; and (3) those with a C6C3C6 carbon skeleton (flavonoids are the typical C6C3C6) [10,11]. Higher plants produce secondary metabolites through the shikimate pathway, which is also the pathway by which phenolic compounds are often generated. Phosphoenolpyruvate and erythrose 4-phosphate are the starting points of the route, whereas chorismite is its last stop [12,13]. A vital metabolite produced by the chorion is phenylalanine [14]. In plant metabolism, phenylalanine is regarded as a universal precursor of the molecules C6C1-, C6C3-, and C6C3C6 and their polymers. The phenolic compound buildup, which is controlled by abiotic stressors, has received a lot of attention in studies. A possible explanation for the large carbon flux through the phenylalanine metabolic network is the vast range of physiological functions of these substances and their significance for plant growth, development, defense, and environmental reactions [15]. There are many phenolic chemicals in *R. chrysanthum* that can be studied.

Abscisic acid (ABA), a plant hormone, is crucial for numerous physiological processes, including seed germination, dormancy, growth, and adaptation to biotic and abiotic stressors. By controlling the processes of starch breakdown, source pool transfer, and leaf senescence, ABA may encourage bud dormancy. Additionally, ABA shields plants from dry stress by encouraging the build-up of proline. It was demonstrated that *TaFDL2-1A* enhances transgenic wheat's resistance to drought by positively regulating ABA production, ABA responsiveness, and ROS scavenging [16].

Metabolomics is a rapidly developing field that plays a critical role in understanding the complicated primary and secondary metabolite variations in higher plants [17]. Modern biology is increasingly adopting and recognizing metabolomics techniques. Nuclear magnetic resonance spectroscopy (NMR), gas chromatography–mass spectrometry (GC-MS), and liquid chromatography–mass spectrometry (LC-MS) are typical analytical methods used in plant metabolomics research [18,19]. Due to recent advancements in UPLC-MS techniques, which offer greater and fewer run durations than traditional HPLC-MS techniques, metabolite analysis has become more reliable [20]. UV-B stabilizes health-promoting bioactive chemicals that are necessary for the bread-making process [21]. Additionally, the analysis of flavonoids using ultra-high-performance liquid chromatography revealed that UVR8-mediated flavonoid induction is a UV-B tolerance feature that is conserved in terrestrial plants and could be an early adaptation to life on Earth [22].

UV-B light activates a number of phenolic compound biosynthesis enzymes, including chalcone synthase (CHS, E.C. 2.3.1.74) and phenylalanine deaminase (PAL, E.C. 4.3.1.25) [23]. The enzymes PAL, cinnamate 4-hydroxylase (C4H, E.C. 1.14.13.11), and 4-coumarate coenzyme A ligase (4CL, E.C. 6.2.1.12) are engaged in the upstream phenylalanine route, which provides precursors for the downstream flavonoid metabolism pathway as well as the flavonol metabolism pathway.

In general, plants' primary defense against harmful UV-B radiation is to encourage the creation of UV-absorbing substances such phenolic compounds, flavonoids, and hydroxycinnamates [24]. The mechanisms of *R. chrysanthum*'s metabolic reactions to UV-B light are poorly understood. We investigated the impact of short-duration UV-B rays on the formation of both primary and phenolic compounds specific for primary and phenolic metabolites in *R. chrysanthum* using ultra-performance liquid chromatography–mass spectrometry (UPLC-MS) metabolomics in order to investigate in depth the reactions and mechanisms of how metabolic reprogramming reaches a new homeostasis after UV-B light.

2. Materials and Methods

2.1. Plant Material, Growing Conditions, and Treatments

Three of the nine (n = 3) genetically identical *R. chrysanthum* seedlings that were chosen were separated into three groups as an array of biological duplicates. Before receiving UV-B therapy, all seedlings were cultivated in a sophisticated artificial climate room (http://www.nbsaifu.cn/about_about/gsjj9f6.html accessed on 15 July 2023; Ningbo Saifu Experimental Instrument Co., Ningbo, China) at a temperature of 25 °C/25 °C (day/night) and a photoperiod of 14 h/10 h (day/night). One batch of seedlings was grown in a media that also contained exogenous ABA, whereas the remainder of the two groups were both cultured in regular *R. chrysanthum* medium. After four months of growth, all three groups of seedlings were at once moved to an artificial climate chamber used for this experiment that replicated an alpine environment (18 °C (light for 14 h)/16 °C (dark for 10 h)) with white light radiation of 50 mol (photons) $m^{-2}s^{-1}$ and 60% relative humidity. Group M of seedlings grown on regular *R. chrysanthum* media were the only ones to receive PAR light. Group N of seedlings grown on regular *R. chrysanthum* medium were only exposed to UV-B light [25]. For group Q, seedlings grown in media with exogenous ABA application likewise only received UV-B light. The three groups' seedlings underwent two days of artificial climate chamber incubation with 8 h of light per day.

In a simulated climate room, UV-B light (UV-B) (295–315 nm) and PAR (400–700 nm) were applied to three sets of seedlings [26]. UV intensity measurements were made by Sentry Optronics Corp. in China. The culture flasks were specifically covered during the UV-B treatment using a 295 nm long-pass filter (Filter Long 2IN SQ Filter, Edmund, NJ, USA). Above the culture flasks, 400 nm long-pass filters were installed for the PAR treatments (Edmund). According to the transmission function of the long-pass filter, the samples actually received an irradiance of 50 mol (photons) m^{-2} s^{-1} of PAR and 2.3 W m^{-2} UV-B, respectively.

2.2. Identification and Quantification of Primary Metabolites and Secondary Metabolites by UPLC-MS/MS

The following steps were followed when conducting the metabolomic analysis with Metware Biotech Inc. in Wuhan, China: At −20 °C, 1200 µL of an aqueous solution of 70% methanol was used to extract 50 mg of crushed, lyophilized powder. The supernatant was aspirated and put through a 0.22 µm membrane after being centrifuged at 12,000 rpm for 3 min. The metabolites in samples of *R. chrysanthum* were broadly quantified using a liquid chromatography–electrospray ionization tandem mass spectrometry (LC-ESI-MS/MS) technology. Following the established techniques previously described, Wuhan METWARE Biotechnology Co., Ltd. in Wuhan (Wuhan, China) employed an LC-ESI-MS/MS system (UPLC, gasket-packed UFLC CBM30A, Shimadzu, Kyoto, Japan; MS, 6500 QTRAP, Applied Biosystems, Norwalk, CT, USA), and analyses were performed on all sample extracts [27,28]. Ultrapure water with a formic acid content of 0.1% and acetonitrile with a formic acid content of 0.1% were the two mobile phases A and B, respectively. According to the gradient program, phase B was raised from 5% to 95% in 9 min, held for 1 min, and then immediately lowered to 5% and adjusted for 14 min. The column temperature was 40 °C, the mobile phase flow rate was 0.35 mL/min, and the injection volume was 2 µL.

By using electrospray ionization (ESI), metabolites were ionized. They were recognized using the Metware database's secondary fragment ion spectra. By using triple quadrupole mass spectrometry, the identified metabolites were measured through multiple reaction monitoring. The relative content of metabolites was calculated using peak regions. Variable importance (VIP) in projection scores with orthogonal partial least squares discriminant analysis (OPLS-DA) > 1 and |fold change| > 1.2 were regarded as differential metabolites (DMs). Based on the KEGG database, metabolites were enhanced and categorized.

2.3. Analysis of Metabolite Data

The statistics function prcomp in R (www.r-project.org, accessed on 15 July 2023) was used to perform unsupervised PCA (principal component analysis). Prior to unsupervised PCA, the data were unit-variance-scaled. Using the program MetaboAnalyst 5.0 (https://www.metaboanalyst.ca/, accessed on 17 July 2023), metabolite correlation network diagrams were created for the metabolites in the samples. Utilizing the KEGG Compound database (http://www.kegg.jp/kegg/compound/, accessed on 20 July 2023), identified metabolites were annotated. The annotated metabolites were then linked to the KEGG Pathway database (http://www.kegg.jp/kegg/pathway.html, accessed on 25 July 2023). The *p*-values for the hypergeometric test were used to establish the importance of the pathways where significantly regulated metabolites had been mapped.

2.4. Identification and Quantification of Proteins by Liquid Chromatography–Mass Spectrometry Analysis

In order to execute the proteome analysis, the following procedures were followed: protein extraction, trypsin digestion, Tandem Mass Tag (TMT) tagging, peptide fractionation, LC-MS/MS analysis, protein annotation, and functional enrichment [29].

2.5. Statistical Analysis

R (http://cran.r-project.org/, accessed on 2 July 2023) and IBM SPSS statistical software (https://www.ibm.com/analytics/spss-statistics, IBM SPSS Statistics 26, accessed on 5 July 2023) were used for the statistical analysis. Results show letters to indicate the levels of significance. A one-way analysis of variance (ANOVA) and a Pearson correlation test with an 80% threshold of significance were used to evaluate the data.

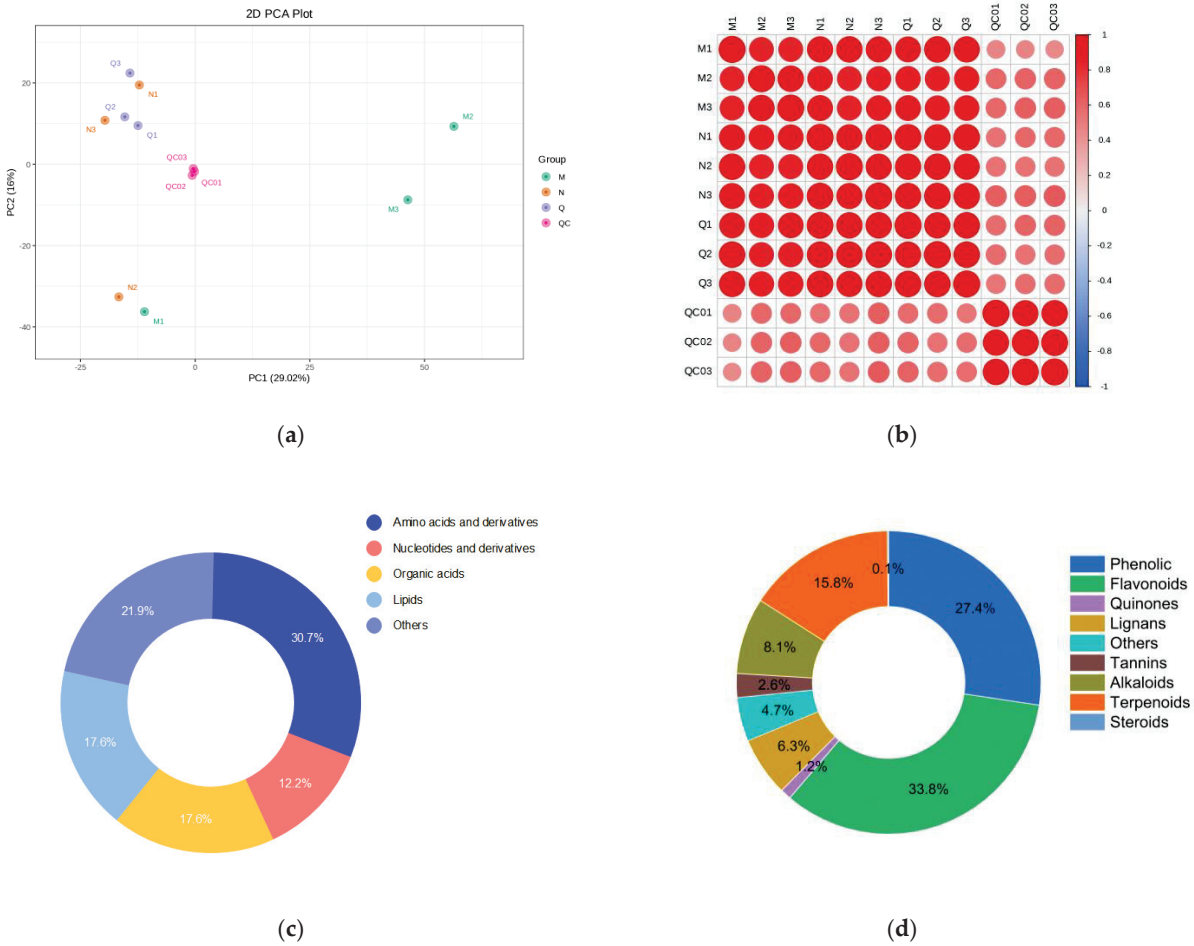
3. Results

3.1. The Primary Metabolism Reprogramming in the Presence of UV-B Stress

The repeatability of various experimental materials under UV-B exposure was ensured by inserting quality control (QC) samples into every 10 test samples during the identification of metabolites using the UPLC-MS/MS method [30]. The curves of the total ion current for metabolite detection showed high overlap when the total ion current plots (TIC plots) of various QC samples were analyzed by mass spectrometry detection (Supplementary Figures S1 and S2). This means that the retention times and peak intensities were consistent, indicating that mass spectrometry had better signal stability when detecting the same sample at various times.

To comprehend the general metabolic variations and variability between groups among the samples, Principal Component Analysis (PCA) was carried out on the specimens, including the QC samples. PCA determines whether there are variations among metabolomes by separating metabolome trends into groups. Insignificant differences were found between UV-B pressure treatment specimens of the same materials in PCA of the control, experimental, and QC samples; however, there was a clear pattern of segregation between the various groups (Figure 1a). The Pearson correlation coefficient (PCC) R was employed as an evaluation metric for the correlation of the three biological replicates. Heat maps of the correlation between the three biological replicates and the QC samples were also created. The data showed a strong positive association among the three biological replicates (Figure 1b).

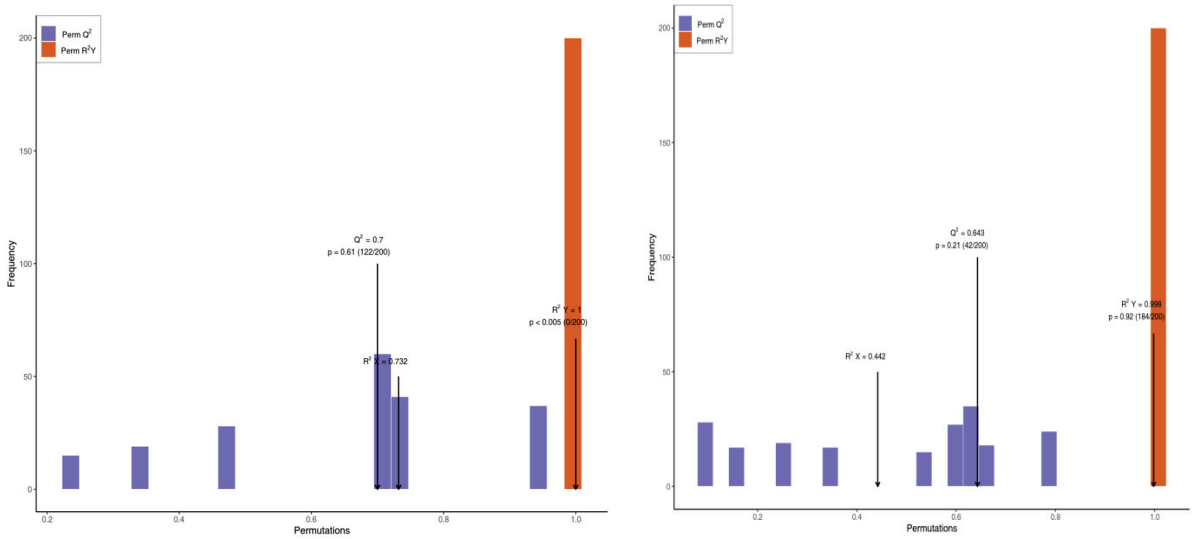
The MetWare Database (MWDB), multiple reaction monitoring (MRM), and the Kyoto Encyclopedia of Genes and Genomes (KEGG) Compound Database were used in the qualitative and quantitative mass spectrometry analysis of the metabolites in each UV-B stress sample. Comprehensive targeted metabolic analysis yielded a total of 2148 metabolites, of which 615 were primary metabolites, comprising organic acids, lipids, amino acids and their derivatives, nucleotides and their derivatives, and other classes (Figure 1c). The majority of amino acids and their derivatives, such as L-phenylalanine, L-tyrosine*, etc., were upregulated in the MN group as well as in the NQ group. Of these, phenylalanine attenuates the adverse effects of abiotic stresses. While nucleotides and their derivatives were upregulated in the MN group but did not show any significant changes in the NQ group, the majority of lipid metabolites did not exhibit any appreciable changes. The same trend was also observed in the organic acids, such as 3-Dehydroshikimic acid and L-Tartaric acid. The 3-Dehydroshikimic acid substantially altered in response to UV-B exposure, indicating that it functions as a crucial intermediary product influencing the metabolic pathways involved in the biosynthesis of aromatic amino acids. The majority of the saccharides, including D-Lactose* and DMelezitose O-rhamnoside, among other classes, were downregulated in the MN group but not significantly altered or upregulated in the NQ group; 1359 different secondary metabolites were found, such as phenolic acids, flavonoids, quinones, lignans and coumarins, ellagitannins, alkaloids, terpenoids, steroids, and others (Figure 1d). Significant changes were observed in the phenolic acids and flavonoids. For example, phenolic acid metabolites such as 4-O-Galloylquinic acid, chlorogenic acid (3-O-Caffeoylquinic acid), methyl caffeate, etc. were upregulated in the MN group and also tended to be upregulated in the NQ group.



(**a**) (**b**)

(**c**) (**d**)

Figure 1. *Cont.*



(**e**) (**f**)

Figure 1. UV-B-treated as well as externally applied ABA UV-B-treated samples and quality control (QC) samples were examined in different groups and categorized for primary and secondary metabolites. (**a**) Comparing control, UV-B-treated, and quality control (QC) samples using principal component analysis (PCA); (**b**) comparison of control, UV-B-treated, and quality control (QC) data with those from various groups; (**c**) classification and proportions of primary metabolites; (**d**) classification and proportions of secondary metabolites; (**e**,**f**) the variables that led to differences between groups were monitored and calculated using the OPLS-DA model. The explanatory rates of the X and Y matrices are denoted by R^2X and R^2Y, respectively. Q^2Y represents the model's ability to forecast. The model is more stable and reliable the closer its value is near one. Additionally, $Q^2Y > 0.5$ and $Q^2Y > 0.9$ are regarded as valid and outstanding models, respectively.

A supervised OPLS-DA model was also used to compare metabolite levels and pinpoint the factors that contributed to group disparities. The OPLS-DA model was used to compute the differences between M and N ($R^2X = 0.732$, $R^2Y = 1$, $Q^2 = 0.7$) (Figure 1e) and between N and Q ($R^2X = 0.442$, $R^2Y = 0.998$, $Q^2 = 0.643$) (Figure 1f). Both comparisons had Q^2 values that were more than 0.5, showing that the two models were steady and had distinct metabolic phenotypes in response to UV-B exposure. These findings imply that the metabolite composition of *R. chrysanthum* is significantly altered by UV-B stress.

A total of 56 significantly modified metabolites were found between N and Q (39 upregulated, 17 downregulated) (Figure 2a,c), and 203 were found between M and N (126 upregulated, 77 downregulated) (Figure 2a,b) using the thresholds of $|\log2\text{Fold Change}| \geq 1.2$ and VIP (variable importance in project, VIP) > 1. Under UV-B stress, groups M and N as well as groups N and Q only co-influenced eighteen DMs, with seventeen of these co-influencing compounds located in the upper Venn diagram (Figure 2e), including S-methyl-L-cysteine and 6-O-methylguanine, and just one in the lower Venn diagram (Figure 2f), namely, Nystose. This is due to the fact that the differentially expressed metabolites that are most frequently impacted in both Venn diagrams are those metabolites whose expression levels varied between the two groups (Figure 2d). Our study focused on the DMs of these two trends, where the first trend's DMs were those that responded favorably to UV-B stress and the second trend's DMs were those that responded adversely to UV-B stress. The differential compounds of the two trends were classified as core DMs. Amino acids and their derivatives, which are the main primary metabolites of plants and, as monomers, are crucial to the synthesis of proteins, are the most varied group of core differential metabolites. The categorization and expression data for the 18 core DMs are shown in Figure 2g, together with information about the core DMs (Supplementary Table S1), Table 1 shows information on the first seven core DMs.

3.2. Dynamics of Phenolic Compounds under UV-B Radiation

The screening parameters for secondary metabolites matched those for primary metabolites. The MN group of secondary metabolites had a total of 392 DMs that were upregulated and 88 which were downregulated, while the NQ group had 180 DMs that were upregulated and 136 that were downregulated (Figure 3a). According to the VIP value, Figure 3b,c show the first 15 metabolites were up- and downregulated in the MN group and the NQ group, respectively. In addition, following UV-B stress and ABA addition, cluster analysis revealed three distinct metabolite trends (Figure 3d). Naturally, we focused more on the sixth cluster. There, we discovered that the DMs that were clustered to the sixth cluster showed a growing trend in the MN group, indicating that these metabolites are crucial in the response to UV-B stress, and continued to show an upward trend in the NQ group, showing that the outwardly applied ABA helps the *R. chrysanthum* to withstand UV-B stress. The majority of the secondary DMs in cluster VI are phenolic substances. As a result, we suggest that variations in phenolic content may help to improve the fluidity of membranes and promote the protective effects of reactive oxygen species (ROS) when exposed to UV-B stress. There were statistical differences between groups in the quantity of phenolic chemicals (Figure 3e). It was discovered that *R. chrysanthum* was able to withstand UV-B stress thanks to the external application of ABA, which also caused phenolic abundance to grow greatly following UV-B stress.

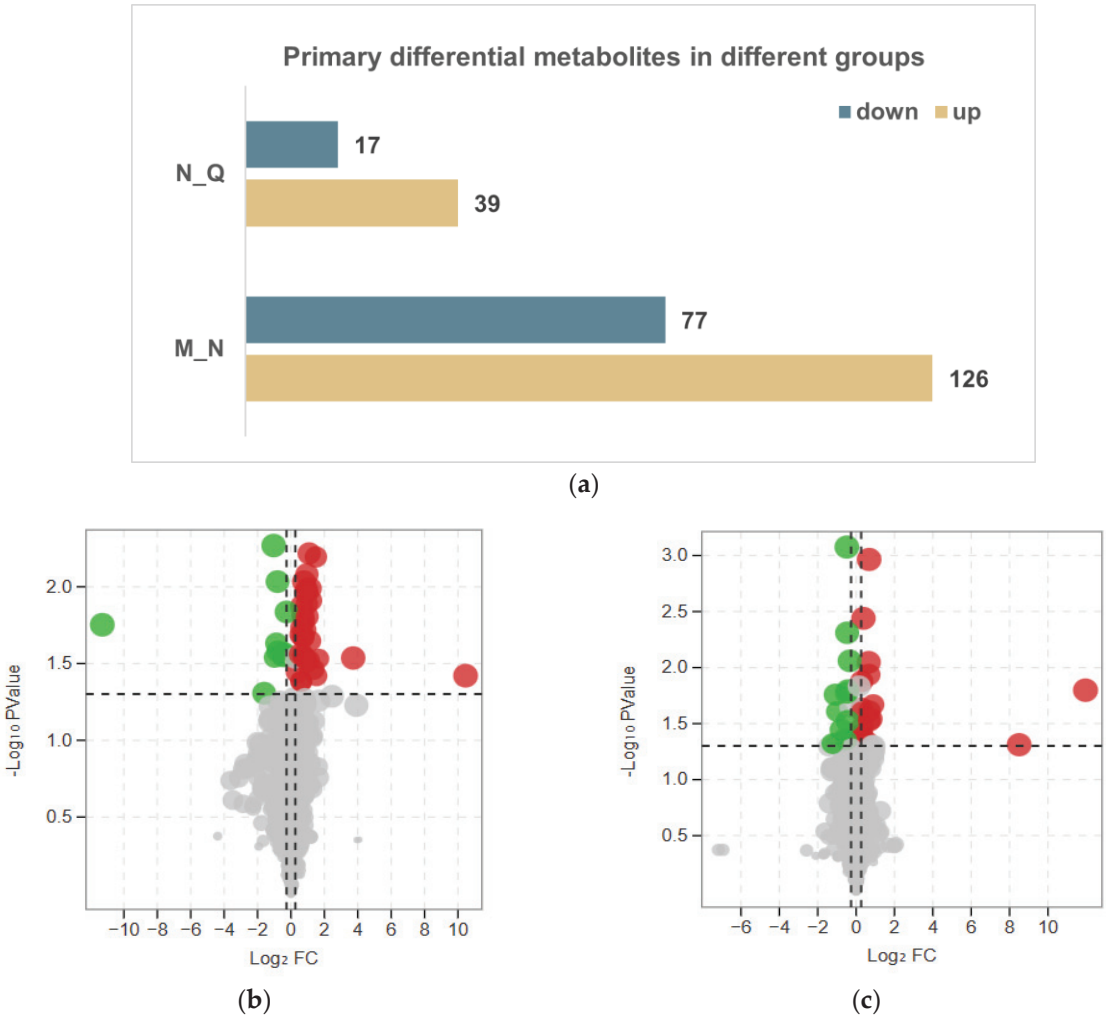


Figure 2. *Cont.*

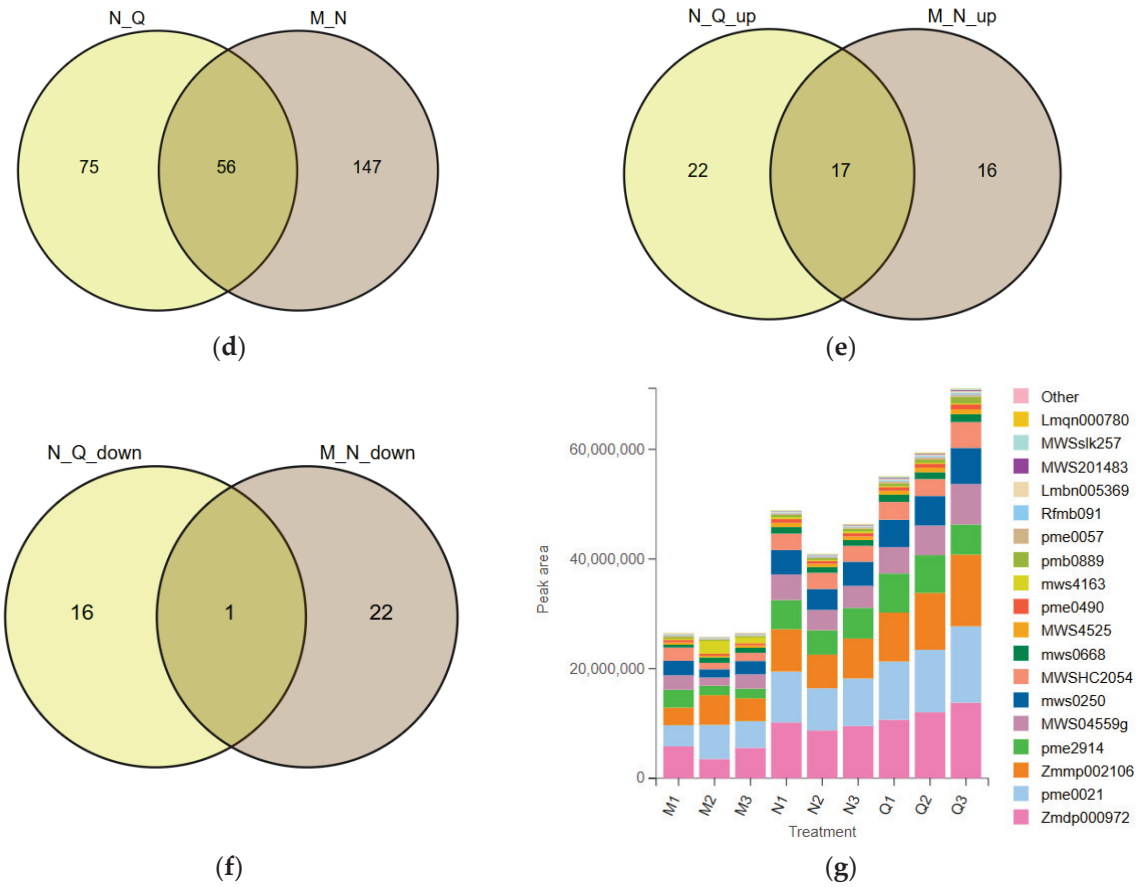


Figure 2. Analysis of the primary DMs in *R. chrysanthum* following UV-B exposure and UV-B exposure with externally administered ABA. (**a**) Statistic differences in metabolites across groups; (**b**,**c**) DMs of the M−N and N−Q groups are displayed on volcano plots, respectively. In the volcano plot, red circles represent up-regulated substances and green circles represent down-regulated substances, horizontal dashed lines indicate screening $p < 0.05$, vertical dashed lines screening |fold change| > 1.2; (**d**–**f**) Venn diagrams for DMs, upregulated DMs, and downregulated DMs are shown for the M−N and N−Q groups, respectively; (**g**) The three MNQ groups' core DMs are shown in bar graphs.

The ratio of the phenolic content in *R. chrysanthum* after UV-B radiation only to the phenolic content in *R. chrysanthum* without UV-B radiation as well as the ratio of the phenolic content in *R. chrysanthum* after UV-B radiation with externally applied ABA to the phenolic content in *R. chrysanthum* after UV-B radiation with no ABA applied were greater than one (Figure 4a–c). In other words, phenolics contribute to *R. chrysanthum*'s ability to fend off UV-B harm. The plant's ability to withstand UV-B stress was also improved by the effective promotion of stomatal closure by ABA when administered externally. Additionally, the abundance changes of all C6C3C6 backbone phenolics were less pronounced in the MN group than in the NQ group, indicating that this group of phenolics likely contributes significantly to *R. chrysanthum*'s UV-B protection (Figure 4c).

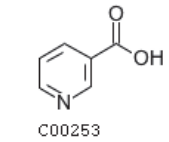
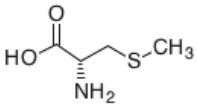
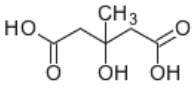
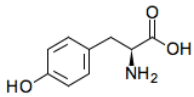
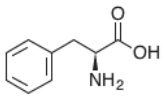
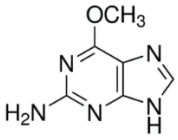
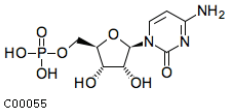
3.3. Network Diagram and Correlation Analysis of R. chrysanthum's Main and Phenolic Metabolite Relationships

A metabolite interaction network was carried out to further investigate how the primary and phenolic metabolites in the *R. chrysanthum* responded to UV-B exposure. To supervise the network's simplification, the Degree Filter was set to 2.0 and the Betweenness Filter was set to 1.0. Adenine is a significant "hub" in the network since it has the greatest degree and the most connections to other nodes (84). The purine metabolism pathway

is the one that is reportedly damaged, according to the network diagram. With a degree of 71, L-phenylalanine is also a more significant "hub" in the network, influencing pathways such as the biosynthesis of phenylalanine, tyrosine, and tryptophan as well as the metabolic pathway of phenylalanine. Both of these pathways have *p*-values of 0.01, and L-phenylalanine is labeled in the figure with its structural formula. L-tyrosine's degree is also relatively large, 63, and plays an important role in the network, affecting pathways. In addition to the biosynthesis of phenylalanine, tyrosine, and tryptophan, there is also the tyrosine metabolic pathway, which is labeled as the L-tyrosine structural formula in the figure. Many plant secondary metabolites, such as rhodiolosides, betalains, and tocopherols (vitamin E), are derived from tyrosine.

For each category of phenolic core DMs and each category of primary core DMs in M, N, and Q, Pearson's pairwise correlation coefficient values were obtained. Significant correlations were defined as those with a *p*-value of 0.05 or below and a relationship analysis threshold of 0.8.

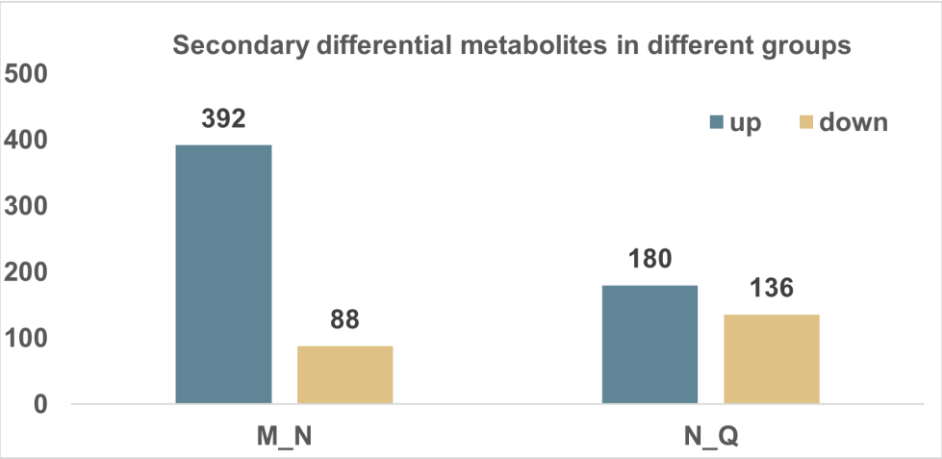
Table 1. The first seven key core DMs' VIP and *p*-value changes in different components under UV-B circumstances of stress.

Index	Structural Formula	Compounds	VIP (MN)	*p*-Value (MN)	VIP (NQ)	*p*-Value (NQ)
pme0490	 C00253	Nicotinic acid (Vitamin B3)	1.707	0.021	1.290	0.182
Zmdp000972	 C22040	S-methyl-L-cysteine	1.683	0.010	1.610	0.078
pme2914	 C03761	3-hydroxy-3-methylpentane-1,5-dioic acid	1.676	0.012	1.425	0.097
mws0250	 C00082	L-tyrosine*	1.655	0.013	1.627	0.079
pme0021	 C00079	L-phenylalanine	1.655	0.017	1.694	0.057
MWS4525		6-O-methylguanine	1.602	0.029	1.268	0.166
MWSslk257	 C00055	Cytidine 5′-monophosphate(Cytidylic acid)	1.595	0.112	1.268	0.192

In the correlation analysis between amino acids and their derivatives and phenolic acids, there were 57 positive correlations and no negative correlations (Figure 5b). For instance, L-phenylalanine showed a positive correlation with ferulic acid-4-O-glucoside, 3-O-Feruloylquinic acid-O-glucoside, and particularly with Trans-5-O-(p-Coumaroyl) shikimate, as well as significantly positive correlations with chlorogenic acid (3-O-Caffeoylquinic acid)

and correlation coefficients of 0.95 and 0.90, respectively. It was demonstrated (Figure 5c) that there were 40 positive correlations and, once more, no negative correlations in the correlation study of amino acids and their derivatives with flavonoids. For instance, L-tyrosine* showed a strong association with 5,7,3′-Trihydroxy-4,6,5′-trimethoxyxanthone, luteolin-7-O-glucuronid e-5-O-rhamnoside, and especially with dihydromyricetin (ampelopsin), which had a correlation value of 0.86. There were 10 positive associations and no negative correlations in the correlation study of amino acids and their derivatives with lignans, alkaloids, and terpenoids (Figure 5d). For instance, N-(2-hydroxy-4-methoxyphenyl) acetamide was strongly positively associated with L-hom ocysteine, Dimethylfraxetin, Dehydrodiconiferyl alcohol, and others, with a correlation coefficient of 0.96. Combining these three correlation analyses, it was discovered that amino acids and their derivatives significantly correlated with phenolic acid compounds, and the interaction network was more complex. This finding suggests that amino acids and their derivatives, along with phenolic acids, play significant roles in the *R. chrysanthum*'s defense against UV-B stress and that the two classes of compounds can be used as markers for assessing the *R. chrysanthum*.

Again, only 25 positive correlations and no negative correlations were found in the correlation analysis of nucleotides and their derivatives with phenolic acids (Figure 5e). For instance, with correlation values of 0.92 and 0.88, respectively, adenine strongly positively linked with 2-phenylethanol, and xanthosine significantly positively associated with Trans-5-O-(p-Coumaroyl) shikimate. Only 22 positive correlations between nucleotides and their derivatives and flavonoids were found in the correlation study (Figure 5f). For instance, adenine and dihydromyricetin (ampelopsin) had a correlation of 0.91, which was significantly positive. In addition, 6-O-methylguanine and dihydromyricetin (ampelopsin) exhibited positive correlations with adenine and 13(S)-HODE, respectively. There were only seven positive connections and no negative correlations in the correlation study of nucleotides and their derivatives with lignans, alkaloids, and terpenoids (Figure 5g). For instance, adenine and N-(2-hydroxy-4-methoxyphenyl) acetamide had a correlation coefficient of 0.94 that was significantly positive. Combining the results of the three correlation analyses, it was discovered that nucleotides and their derivatives had the strongest link with phenolic acids and interacted with the most compounds, followed by flavonoids.



(**a**)

Figure 3. *Cont*.

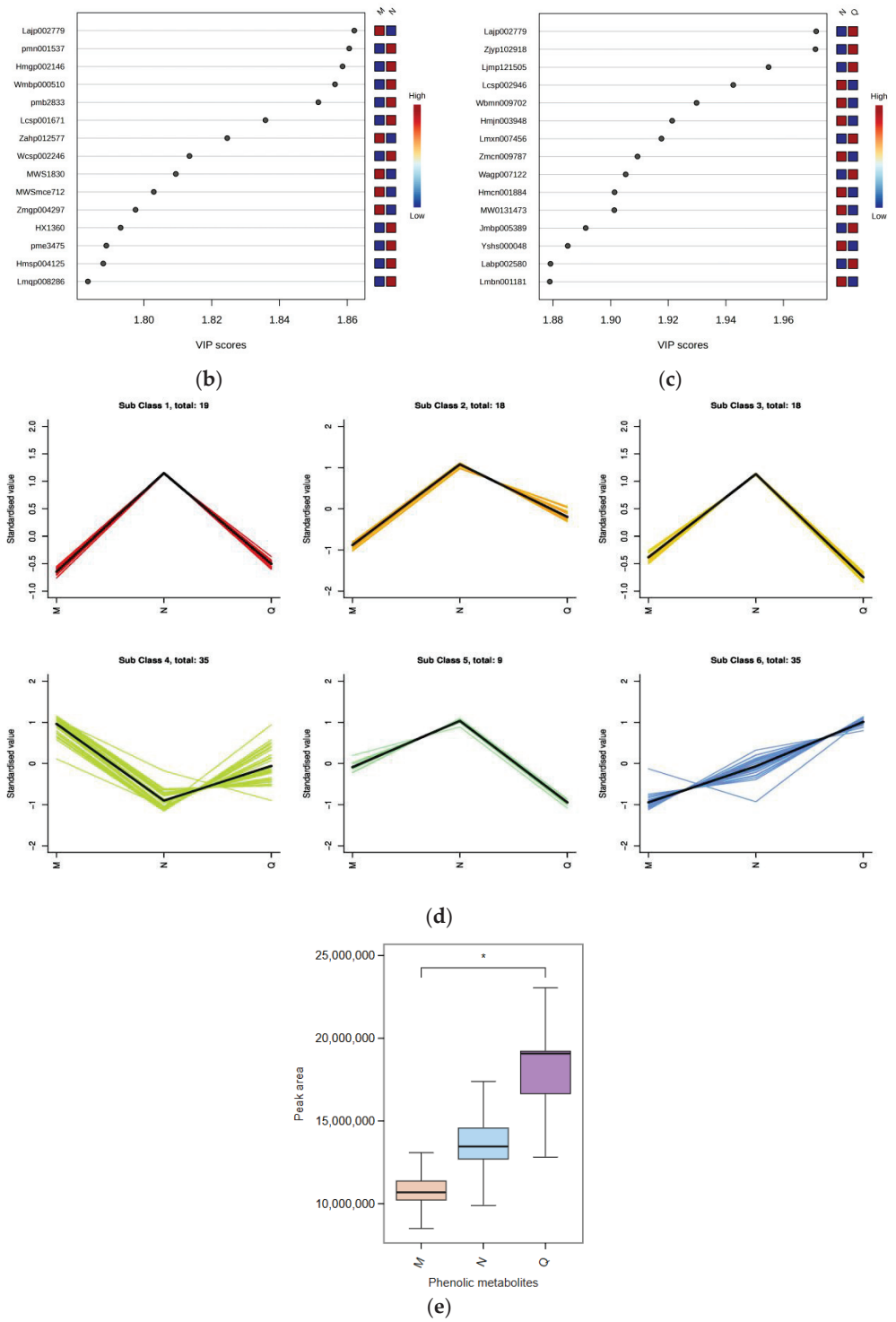


Figure 3. Secondary *R. chrysanthum* metabolites in reaction to UV-B light and UV-B radiation with externally administered ABA. (**a**) Comparative metabolite histogram statistics between different categories. (**b**,**c**) For the M−N and N−Q groups, respectively, the top 15 different metabolites ranked by VIP value of secondary differential compounds are displayed, with red representing high levels and green indicating low levels; (**d**) analyses of metabolites using the K-means clustering technique; (**e**) trends in phenolic metabolite abundance with UV-B therapy and exposure to UV-B rays with externally administered ABA are shown in a boxed line graph, * indicates $p < 0.05$.

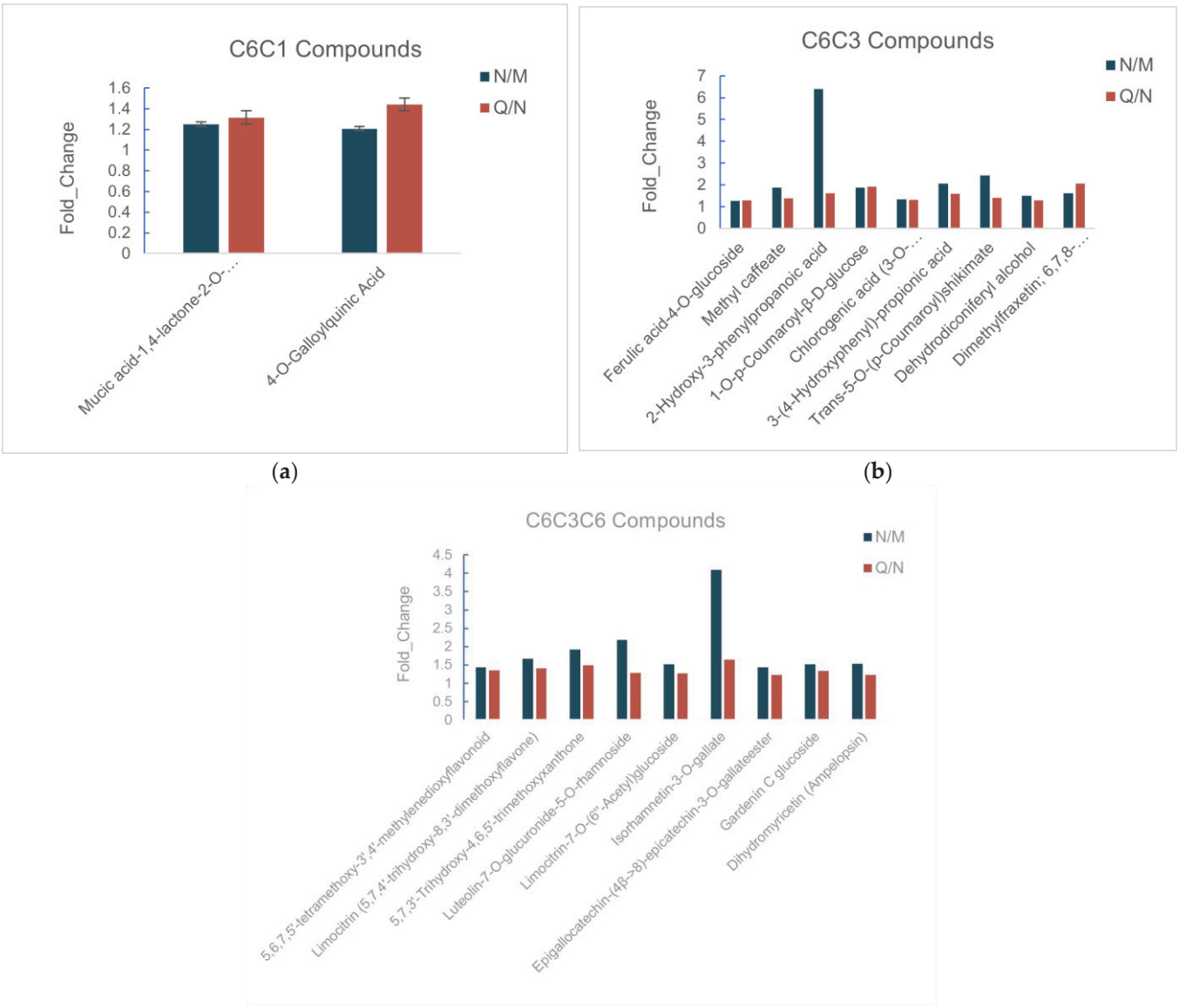


Figure 4. Statistics of phenolic and flavonoid abundance under the effects of UV-B and UV-B treatment with externally administered ABA. The proportion of each substance's expression is set as the vertical coordinate. (**a**) C6C1-carbon skeleton phenols; (**b**) phenolics with the carbon skeleton C6C3; (**c**) phenolics with the carbon skeleton C6C3C6.

Thirty-three correlations were found in the correlation analysis of vitamins, lipids, sugars, and phenolic acids (Figure 5h), twenty-nine of which were positive and four of which were negative. For instance, Nystose and methyl caffeate were negatively connected, while 13(S)-HODE and Elaidolinolenic Acid were positively correlated. Additionally, there was a substantial positive link between chlorogenic acid (3-O-caffeoylquinic acid) and nicotinic acid (Vitamin B3), with correlation coefficients of 0.88 and 0.90, respectively. Twenty-six correlations were found in the correlation analysis of vitamins, lipids, sugars, and flavonoids (Figure 5i), of which twenty-two were positive and four were negative. Specifically, dihydromyricetin (ampelopsin) and nicotinic acid (Vitamin B3) revealed a substantial positive link with a correlation of 0.94. Nicotinic acid (Vitamin B3) was positively correlated with 13(S)-HODE, Nystose was negatively correlated with luteolin-7-O-glucuronide-5-O-rhamnoside, etc. Only seven associations, four of which were positive and three of which were negative, were discovered when vitamins, lipids, and carbohydrates were correlated

with lignans, alkaloids, and terpenoids (Figure 5j). It was found that 13(S)-HODE and N-(2-hydroxy-4-methoxyphenyl) acetamide had positive and negative correlations, respectively. With a correlation coefficient of 0.95, N-(2-hydroxy-4-methoxyphenyl) acetamide in particular showed a highly positive link with nicotinic acid (Vitamin B3). These three correlation analyses combined showed that there were more metabolite interactions between vitamins, lipids, and sugars in correlation with phenolic acids to help *R. chrysanthum* resist UV-B stress, indicating that phenolic acid compounds can be used as markers for *R. chrysanthum*'s reaction to UV-B stress.

When viewed collectively, the nine correlation analyses demonstrate the critical role that amino acids and their derivatives play in the network of correlation analyses as well as the complex interactions that phenolic compounds, including phenolic acids and flavonoids, exhibit with other compounds in this network. Additionally, it was shown that only sugars, lipids, and vitamins had negative correlations with other substances, which may be connected to Nystose's decreased expression in response to UV-B radiation. Together, our findings imply that in response to extreme UV-B exposure, *R. chrysanthum* mobilizes more complicated metabolite relationships to cooperate.

3.4. Building a Comprehensive Picture of the Primary and Phenolic Metabolite Networks of the R. chrysanthum

Simplified primary and phenolic compound metabolic pathways were employed to demonstrate the *R. chrysanthum*'s metabolic response to UV-B radiation in order to more clearly illustrate the linkages between the data mentioned above. Heat maps are used to display the expression levels of the relevant enzymes in the proteome in an effort to completely reveal the enzymes associated with the L-phenylalanine and flavonoid biosynthesis pathways as well as in the monolignol biosynthesis pathway (Figure 6a). Metabolite abundance and the levels of metabolite-related enzyme expression in metabolic pathways are intricately connected. Some amino acids, such as S-methyl-L-cysteine, L-phenylalanine, and L-tyrosine*, considerably elevated in response to UV-B radiation for primary metabolites. Moreover, following UV-B treatment, the concentrations of acids implicated in the tricarboxylic acid (TCA) cycle, such as fumarate, malate, and succinate, were elevated. In terms of the phenolic components, Trans-5-O-(p-Coumaroyl) shikimate and naringenin chalcone were the primary phenolic acids and flavonoids that were upregulated in *R. chrysanthum*. Furthermore, the shikimate acid pathway uses L-phenylalanine as a crucial node in the synthesis of phenolic compounds, which may explain why most phenolic compounds rise in concentration when exposed to UV-B light. The boxed line graphs show how the expression of L-phenylalanine, naringenin chalcone, and Trans-5-O-(p-Coumaroyl) shikimate changes in response to UV-B stress. Significant changes in the expression of L-phenylalanine and naringenin chalcone can be observed, indicating a potential protective effect of *R. chrysanthum* against UV-B stress.

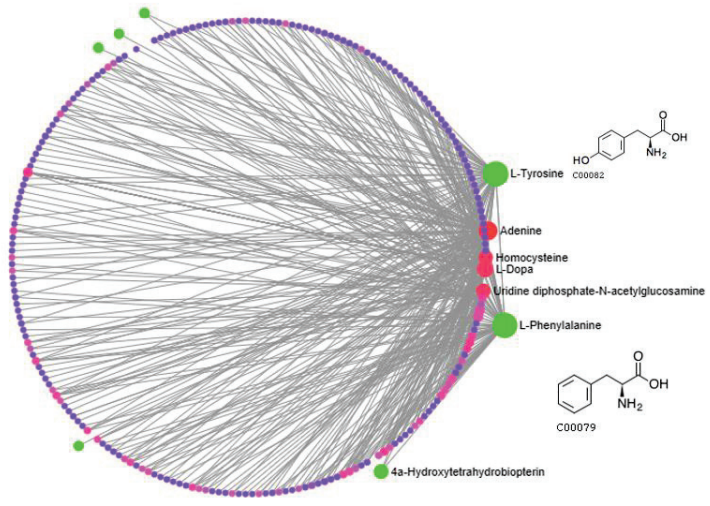
3.5. Enrichment Pathway Analysis and Correlation between R. chrysanthum Proteomics and Metabolomics in Response to UV-B Stress

KEGG enrichment analysis of the 11 identified enzymes was performed on a total of eight metabolic pathways (Figure 7a,b). These included flavonoid biosynthesis; circadian rhythm of plant, propane, piperidine and pyridine alkaloids biosynthesis; secondary metabolites biosynthesis; metabolic pathways, flavonoids, and flavonoids biosynthesis; phenyl metabolic pathway, piperidine, and pyridine alkaloids biosynthesis; secondary metabolites biosynthesis; metabolic pathways, flavonoids, and flavonols biosynthesis; phenylalanine, tyrosine, and tryptophan biosynthesis; and amino acid biosynthesis. According to the results, L-phenylalanine, naringenin chalcone, and Trans-5-O-(p-Coumaroyl) shikimate increased in response to UV-B stress while cinnamic acid, p-Coumaric acid, and naringenin (5,7,4′-Trihydroxyflavanone) * were continually depleted. Among these, Trans-5-O-(p-Coumaroyl) shikimate, naringenin chalcone, and L-phenylalanine displayed considerably higher levels and are important nodes in the UV-B stress regulation network.

Pearson correlation studies were carried out (Figure 7c) to further evaluate the links between important enzymes and essential DMs. The hub of the entire network, CHS and CHI, exhibits a favorable connection with metabolites. The 2-hydroxy-3-phenylpropanoic acid, isorhamnetin-3-O-gallate, and 3-O-Feruloylquinic acid-O-glucosid all showed strong positive associations with CHS1 and CHS, with the least significant correlation coefficient being 0.88 and the most significant correlation coefficient being as high as 0.99. With correlation coefficients around 0.9, CHI and CHI3 demonstrated valuable positive relationships with 3-O-Feruloylquinic acid-O-glucosid, 2-hydroxy-3-phenylpropanoic acid, and L-phenylalanine. Two metabolites, 1-O-p-Coumaroyl-D-glucose and 3-hydroxy-3-methylpentane-1,5-dioic acid, are under the control of F3H. Additionally, PPA-AT favorably regulated 1-O-p-Coumaroyl-D-glucose and 2-hydroxy-3-phenylpropanoic acid. These six metabolites belonged to amino acids and their derivatives, phenolic acids, and flavonoids, indicating that CHS, CHI, F3H, and PPA-AT collectively affected primary metabolites as well as phenolic compounds against UV-B stress in the *R. chrysanthum*. This further affected phenylpropane biosynthesis and controlled the primary as well as phenolic compound metabolic pathways. The information about 11 important enzymes is shown in Table 2.

Table 2. Information about 11 important enzymes under UV-B stress.

Protein Accession	KEGG KO No.	KEGG Gene	M/N Ratio
Gene.41041_CL5299.Contig1_All	K00475	F3H; naringenin 3-dioxygenase [EC:1.14.11.9]	0.573
Gene.13909_CL1098.Contig2_All	K00660	CHS; chalcone synthase [EC:2.3.1.74]	0.48
Gene.75412_Unigene13888_All	K00660	CHS; chalcone synthase [EC:2.3.1.74]	0.546
Gene.13913_CL1098.Contig3_All	K00660	CHS; chalcone synthase [EC:2.3.1.74]	0.557
Gene.22273_CL2057.Contig1_All	K01850	E5.4.99.5; chorismate mutase [EC:5.4.99.5]	0.727
Gene.77444_Unigene15688_All	K01859	E5.5.1.6; chalcone isomerase [EC:5.5.1.6]	0.781
Gene.9527_CL706.Contig2_All	K01859	E5.5.1.6; chalcone isomerase [EC:5.5.1.6]	0.865



(**a**)

Figure 5. *Cont.*

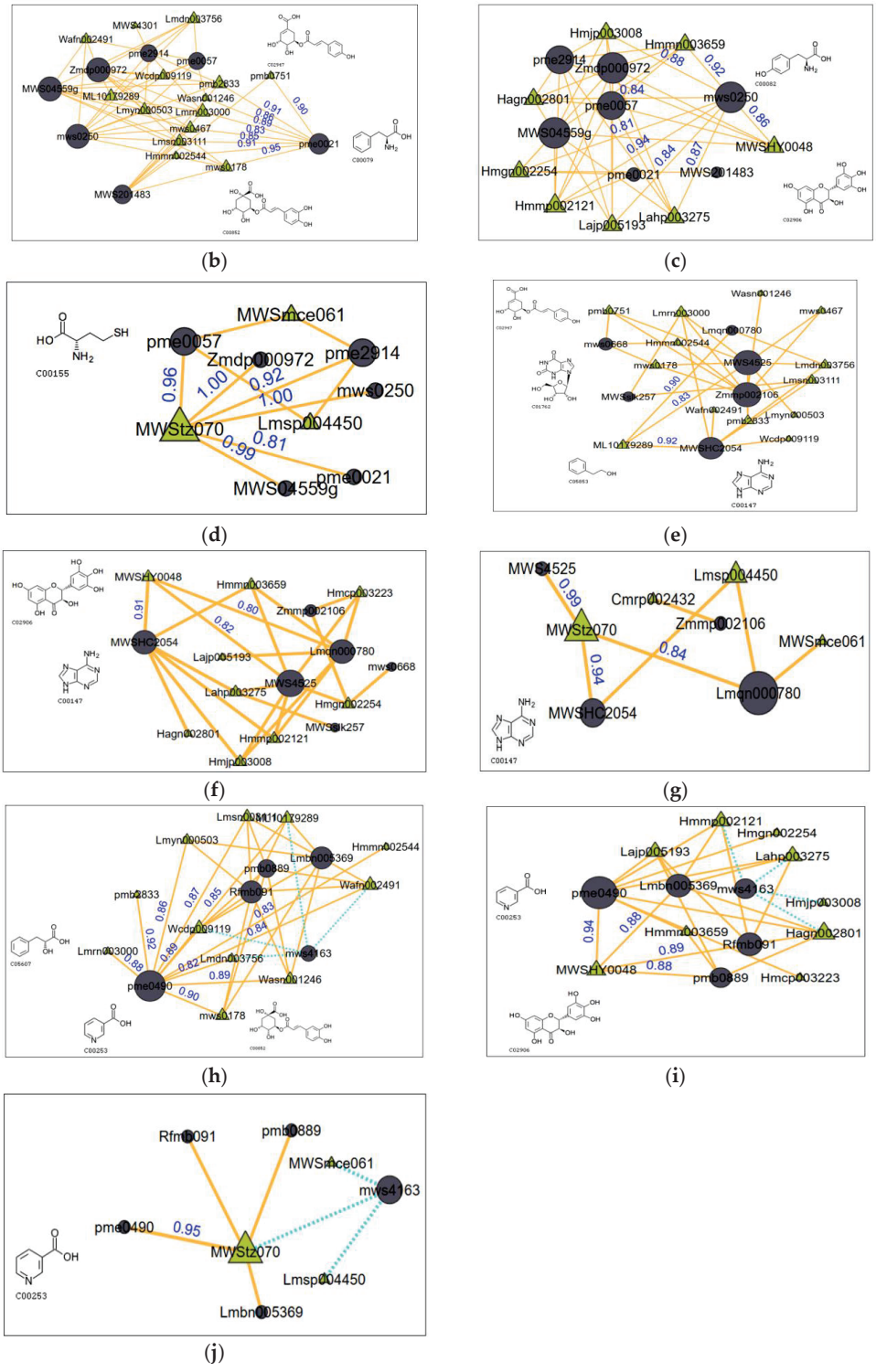


Figure 5. Network analysis and correlation of different primary and secondary metabolites linked to *R. chrysanthum*'s reaction to UV-B stress are shown. (**a**) Degrees are the number of connections to other points, and green is used to highlight the substances that are the focus of the study. (**b**–**d**) Correlation analysis of amino acids and their derivatives with phenolic acids, flavonoids, and lignans, alkaloids, and terpenoids, respectively. (**e**–**g**) Correlation analysis of nucleotides and their derivatives with phenolic acids, flavonoids, and lignans, alkaloids, terpenoids, respectively. (**h**–**j**) Correlation analysis of sugars, vitamins, and free fatty acids with phenolic acids, flavonoids, and lignans, alkaloids, and terpenoids, respectively.

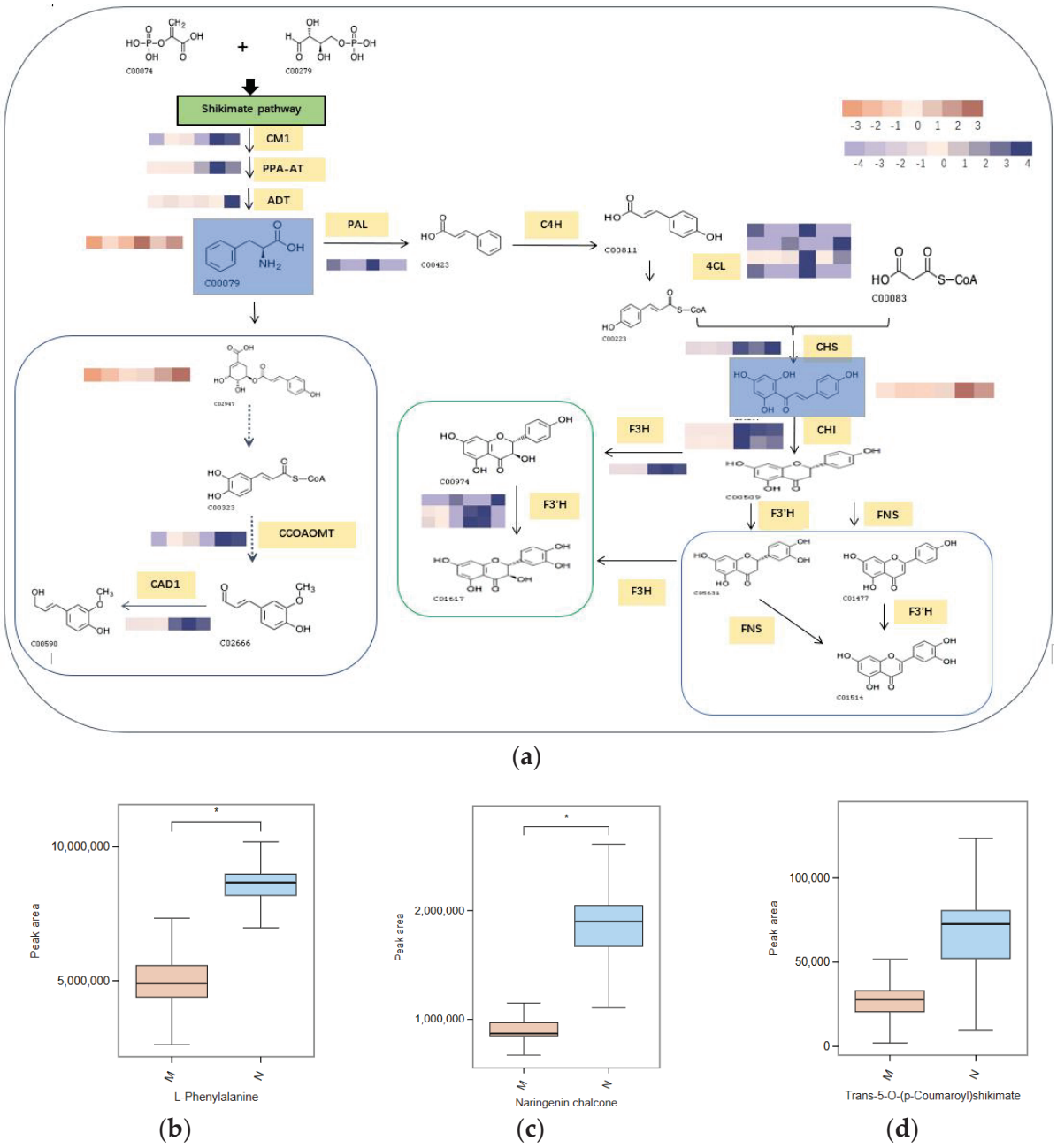
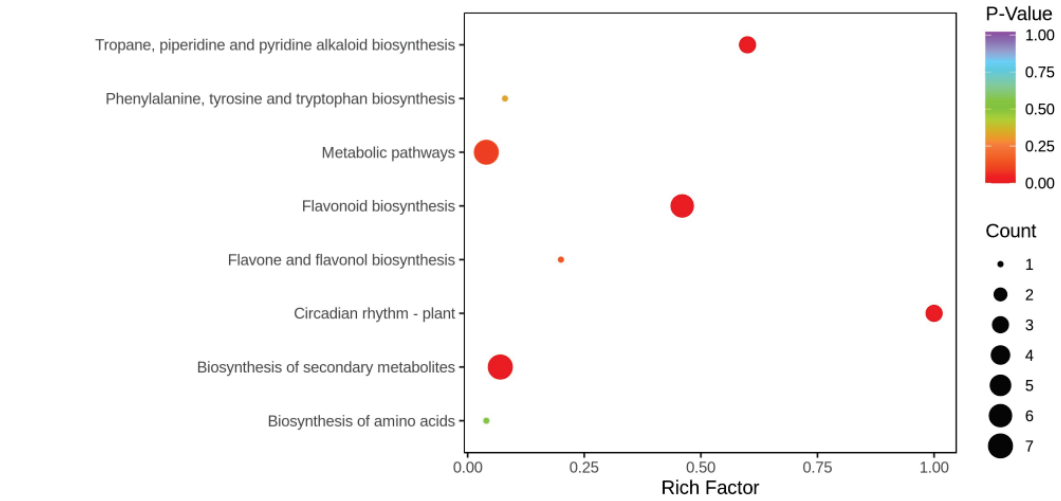
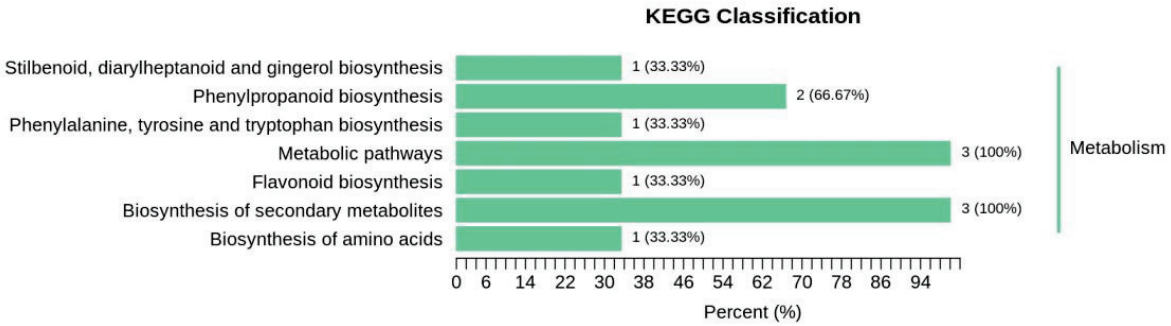


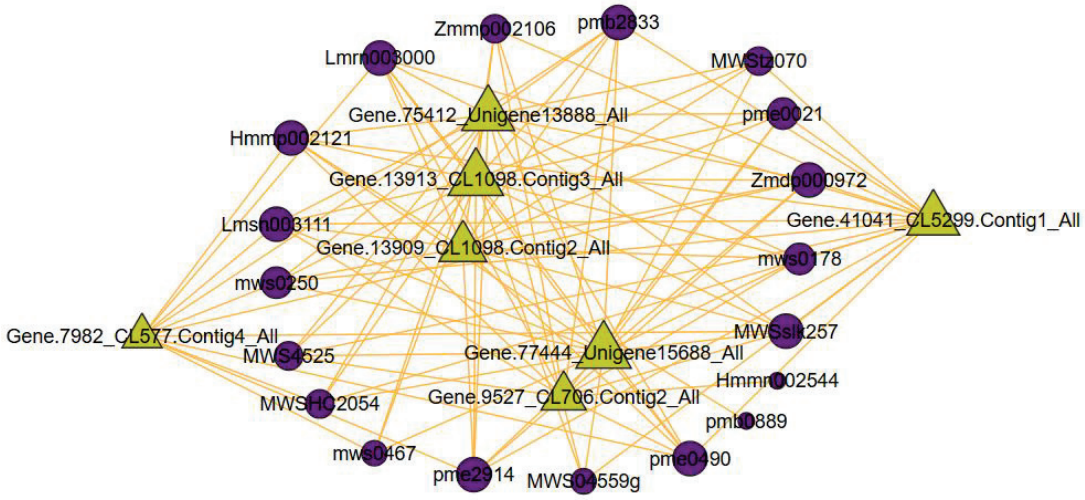
Figure 6. Visualization of dynamic pathways of primary and phenolic metabolites. (**a**) Yellow fills indicate enzymes that cause changes in the pathway, while green fills indicate metabolites with significant changes in the pathway. The flavanone metabolic pathway is represented by pink boxes, the flavonol metabolic pathway by green boxes, and the monolignol metabolic pathway by blue boxes. In the heat map, the color pink denotes that UV-B duress has almost no impact on the enzyme, the color light purple denotes that UV-B radiation inhibits the enzyme's activity, and the color dark purple denotes that UV-B radiation increases the enzyme's activity; likewise, a metabolite's light brown hue suggests that UV-B radiation is downregulating it, whereas a metabolite's dark brown color indicates that UV-B radiation is upregulating it. (**b**–**d**) L-phenylalanine, naringenin chalcone, and Trans-5-O-(p-Coumaroyl) shikimate all show significant alterations. Significant difference (* $p < 0.05$).



(**a**)



(**b**)



(**c**)

Figure 7. Key enzymes involved in *R. chrysanthum*'s reaction to UV-B exposure were analyzed using the KEGG pathway method, and correlations between key enzymes and metabolites were examined. (**a**,**b**) Key enzymes' KEGG bubble and bar graphs; (**c**) links between proteins and metabolomes. Proteins are represented by triangles, metabolites by circles, and positive relationships by solid yellow lines.

4. Discussion

Numerous responses of plants to elevated UV-B radiation have an impact on plant development, growth, and the accumulation of secondary metabolites [31]. According to

the UPLC-MS/MS detection platform, the abundance and characterization of metabolites were investigated in this study, and *R. chrysanthum*'s response to UV-B stress was examined at the level of both primary and secondary metabolites. These analyses together revealed alterations to the metabolic profiles of various metabolites of the *R. chrysanthum* under UV-B stress and explored the reprogramming of primary and secondary metabolic responses to UV-B. In order to validate the changes in the expression of important metabolites in the pathway in response to UV-B stress, we also examined protein expression under UV-B stress based on LC-MS/MS and evaluated changes in the abundance of the key enzymes of L-phenylalanine, tyrosine, and tryptophan; the flavonol metabolism pathway, the flavonoid metabolism pathway, and the monolignol biosynthesis pathway, as well as changes in the pathways of enzyme action through the proteome.

Based on UPLC-MS/MS metabolomics, we examined specific variations in the principal metabolites of *R. chrysanthum* under UV-B radiation. Growth requires energy from sugar, and glucose is a significant soluble sugar and signaling molecule that clearly plays a fundamental role in plant stress [32]. Following UV-B radiation, the *R. chrysanthum*'s decreased glucose levels may be linked to a more pronounced transition from carbon absorption to carbon storage [31]. Additionally, larger concentrations of monosaccharides from the pentose phosphate pathway (PPP), such as D-erythrose-4-phosphate, were found in the UV-B-treated group, which may be due to the PPP pathway's higher respiratory frequency in the *R. chrysanthum*. Through the glycolytic pathway and the TCA cycle, carbohydrates like sucrose can be oxidized, and since glycolysis can result in an increase in ATP content, the plant's capacity to adapt to its surroundings under abiotic stress circumstances is unavoidably improved [33]. The fundamental metabolites that plants primarily produce are amino acids, which are crucial for protecting them from abiotic stressors and, more critically, serving as precursors to secondary metabolites that increase plant resistance to UV-B radiation. This research uses L-phenylalanine as an example, which exhibits a substantial rise under UV-B stress. The flavonoid pathway is indirectly impacted by the activity of pathways involving phenylpropanoid substances linked with amino acid metabolism, as has been shown in prior investigations, and the same results have been drawn in this paper [34].

The amount of flavanols and flavonols in *R. chrysanthum* increased in response to UV-B radiation, according to the dynamic response pattern of the phenolic compounds. According to physiological research, phenolics play a role in UV-B protection [35]. Within the phenolics, flavonoids and flavonols shield the cells as they collect in the *R. chrysanthum*'s epidermis, acting as filters and absorbing the majority of UV-B radiation [36,37]. Ryan et al. reported that UV radiation caused the production of flavonols with a significant amount of hydroxylation in the *Petunia* and the *Arabidopsis thaliana*. They hypothesized that flavonols might act on an as-yet-uncharacterized role in the UV stress reaction due to their UV-absorbing qualities and that the hydroxylation of flavonols may have a positive impact on antioxidant capacity [38]. Thus, under UV-B radiation, the biggest increases in the concentrations of flavonoid and flavonol substances such as luteolin (5,7,3′,4′-Tetrahydroxyflavone) and quercetin-3-O-rhamnoside (quercitrin) were seen. Additionally, it was found that C6C3C6 carbon compounds were accumulating at a faster rate than C6C3 carbon compounds like cinnamic acid and ferulic acid, which were shown to be accumulating at a slower rate. The greater UV-B absorption and antioxidant activity of C3C6C3 carbon compounds compared to C3C6 carbon compounds (Figure 4a–c) may be the cause of this event, which led to the incorporation of C6C3C6 carbon components at the expense of C3C6 carbon compounds.

For the *R. chrysanthum*, interaction network diagrams were created for the primary and phenolic metabolites, and correlation analysis diagrams were examined between each of the primary core difference metabolites and the secondary phenolic metabolites in order to better understand the differences in the specificity of metabolites identified between the UV-B-treated and control groups (Figure 5). The network diagram was mainly enriched with phenylalanine, tyrosine, and tryptophan biosynthesis as well as

phenylalanine biosynthesis pathways, suggesting the significance of L-phenylalanine in the *R. chrysanthum*'s defense against UV-B stress; and the absence of phenolics-annotated pathways may be due to the fact that some of the detected phenolics were not annotated to the KEGG data, which can be further explored in future studies. A diagram of the primary and phenolic metabolite pathways was created (Figure 6) to help further clarify the mechanisms of primary as well as phenolic metabolites against UV-B damage. UV-B light causes a rise in TCA cycle intermediates such as fumarate, a key regulator of carbon and nitrogen interactions. After plants mobilize their stored carbon reserves to boost flux along the phenylpropane pathway, it appears highly likely that fumarate will be elevated under UV-B light [39]. The same conclusion was obtained in our experiments. Shikimic acid is the initiator of secondary metabolism in higher plants, linking sugar metabolism to polyphenol metabolism, and is an essential pathway for the biosynthesis of aromatic compounds. In plants, phenylalanine is recognized as a general precursor of C6C1-, C6C3-, and C6C3C6 compounds and their polymers such as tannins and lignin [40]. Thus, taken as a whole, these data imply that in response to UV-B, there is an "initiating" mechanism at the primary metabolic level in plant cells that involves the reprogramming of metabolism to effectively transfer carbon to aromatic amino acid precursors of the phenylpropane pathway [41]. Tryptophan and phenylalanine compete for chorismate to synthesize alkaloids and phenols, respectively [31]. Phenylalanine accumulated greater under UV-B radiation, according to the findings. This demonstrates that the increase in phenolic compounds during UV-B radiation, which is caused by the movement of carbon in primary metabolism, is the result of metabolic reprogramming. Phenylalanine, a critical node in phenolic metabolism, dramatically increased under UV-B radiation.

Proteomics was used to validate the aforementioned inferences made from metabolomics (Figure 7a–c). On the one hand, qualitative and quantitative analyses of the key enzymes in the metabolic pathway showed that the changes between the key enzymes in the pathway and the key metabolites showed consistency; specifically, the key enzymes in the metabolic pathway were significantly increased in the *R. chrysanthum* against UV-B stress, which in turn affected the increase in the expression of the related metabolites and the response of the entire pathway to UV-B stress. The findings of a correlation analysis of 11 major enzymes from mid-species with the core DMs, on the other hand, showed that the proteome and metabolome responded consistently to UV-B stress.

We also discovered that after applying ABA externally and then applying UV-B radiation, alterations in significant primary metabolites and phenolics were considerably more pronounced than they were after the standard UV-B radiation treatment. In contrast to flavonoids, which are secondary metabolites with antioxidant activity and UV absorbers, ABA enhances UV-B stress acclimation by promoting ROS scavenging, according to earlier investigations [42]. The results of the present study's results, which had a much greater flavonoid content, imply that externally administered ABA may work in concert with UV-B to encourage the conversion of primary metabolites to phenolic compounds.

5. Conclusions

Using ultra-performance liquid chromatography tandem mass spectrometry (UPLC-MS/MS) technology, we were able to determine the metabolic profiles and explore the particular metabolic pathways of *R. chrysanthum* in response to short-duration UV-B radiation. Our findings indicate that plant cells reprogrammed the L-phenylalanine biosynthesis pathway to undergo a more intensive shift from carbon absorption to carbon accumulation as a main metabolic level mechanism in response to UV-B exposure. This gives phenylalanine, a precursor substance, a solid theoretical foundation for research on its potential to assist plants in coping with abiotic stressors. Simultaneously, alterations in pertinent metabolites and enzymes within the flavonoid and monolignol biosynthesis pathways were initiated at the secondary metabolic level. In phenolics, C6C1 carbon compounds (phenolic acids) and C6C3C6 carbon compounds (flavonoids and flavonols) were upregulated at the expense of C6C3 carbon compounds in order to withstand UV-B stress. Furthermore,

we discovered that *R. chrysanthum*'s resistance to UV-B was markedly improved and that phenolic abundance increased significantly following the external application of ABA; in other words, external application of ABA may encourage the conversion of primary metabolites to phenolics in concert with UV-B, thereby strengthening the plant's capacity for both UV-B uptake and antioxidant defense. In addition to offering insights for future research on the mechanism by which externally applied ABA can mitigate UV-B damage in the *R. chrysanthum*, this study advances our knowledge of how primary and secondary metabolites in this plant respond to UV-B stress.

Supplementary Materials: The following supporting information can be downloaded at: https://www.mdpi.com/article/10.3390/biom13121700/s1, Figure S1: Total ion flow diagram in positive ion mode; Figure S2: Total ion flow map in negative ion mode; Table S1: Information on 18 core differential metabolites.

Author Contributions: Writing—original draft preparation, F.G. and W.Y.; writing—review and editing, K.C., H.X. and X.Z.; methodology, F.G. and Q.Z.; software, F.G. and J.D.; visualization, F.G. and W.Y.; supervision, K.C. and X.Z.; project administration, H.X. and X.Z. All authors have read and agreed to the published version of the manuscript.

Funding: This work was supported by the Jilin Provincial Science and Technology Development Program project (Grant numbers: YDZJ202301ZYTS517).

Institutional Review Board Statement: Not applicable.

Informed Consent Statement: Not applicable.

Data Availability Statement: The datasets generated during and/or analyzed during the current study are available from the corresponding author on reasonable request.

Acknowledgments: We are grateful to Jingjie PTM Biolab (Hangzhou, China) Co., Ltd. for providing mass spectrometry support.

Conflicts of Interest: The authors declare no conflict of interest.

References

1. Hossaini, R.; Chipperfield, M.P.; Montzka, S.A.; Leeson, A.A.; Dhomse, S.S.; Pyle, J.A. The increasing threat to stratospheric ozone from dichloromethane. *Nat. Commun.* **2017**, *8*, 15962. [CrossRef]
2. Neale, R.E.; Barnes, P.W.; Robson, T.M.; Neale, P.J.; Williamson, C.E.; Zepp, R.G.; Wilson, S.R.; Madronich, S.; Andrady, A.L.; Heikkilä, A.M.; et al. Environmental effects of stratospheric ozone depletion, UV radiation, and interactions with climate change: UNEP Environmental Effects Assessment Panel, Update 2020. *Photochem. Photobiol. Sci.* **2021**, *20*, 1–67. [CrossRef]
3. Bornman, J.F.; Barnes, P.W.; Robinson, S.A.; Ballaré, C.L.; Flint, S.D.; Caldwell, M.M. Solar ultraviolet radiation and ozone depletion-driven climate change: Effects on terrestrial ecosystems. *Photochem. Photobiol. Sci.* **2015**, *14*, 88–107. [CrossRef]
4. Parihar, P.; Singh, S.; Singh, R.; Singh, V.P.; Prasad, S.M. Changing scenario in plant UV-B research:UV-B from a generic stressor to a specific regulator. *J. Photochem. Photobiol. B* **2015**, *153*, 334–343. [CrossRef]
5. Jenkins, G.I. Signal Transduction in Responses to UV-B Radiation. *Annu. Rev. Plant Biol.* **2009**, *60*, 407–431. [CrossRef]
6. Neugart, S.; Fiol, M.; Schreiner, M.; Rohn, S.; Zrenner, R.; Kroh, L.W.; Krumbein, A. Interaction of Moderate UV-B Exposure and Temperature on the Formation of Structurally Different Flavonol Glycosides and Hydroxycinnamic Acid Derivatives in Kale (*Brassica oleracea* var. sabellica). *J. Agric. Food. Chem.* **2014**, *62*, 4054–4062. [CrossRef] [PubMed]
7. Wargent, J.J.; Moore, J.P.; Roland Ennos, A.; Paul, N.D. Ultraviolet Radiation as a Limiting Factor in Leaf Expansion and Development. *Photochem. Photobiol.* **2009**, *85*, 279–286. [CrossRef] [PubMed]
8. Frolov, A.; Henning, A.; Böttcher, C.; Tissier, A.; Strack, D. An UPLC-MS/MS Method for the Simultaneous Identification and Quantitation of Cell Wall Phenolics in *Brassica napus* Seeds. *J. Agric. Food. Chem.* **2013**, *61*, 1219–1227. [CrossRef]
9. Santin, M.; Simoni, S.; Vangelisti, A.; Giordani, T.; Cavallini, A.; Mannucci, A.; Ranieri, A.; Castagna, A. Transcriptomic Analysis on the Peel of UV-B-Exposed Peach Fruit Reveals an Upregulation of Phenolic- and UVR8-Related Pathways. *Plants* **2023**, *12*, 1818. [CrossRef]
10. Gómez-Caravaca, A.M.; López-Cobo, A.; Verardo, V.; Segura-Carretero, A.; Fernández-Gutiérrez, A. HPLC-DAD-q-TOF-MS as a powerful platform for the determination of phenolic and other polar compounds in the edible part of mango and its by-products (peel, seed, and seed husk). *Electrophoresis* **2016**, *37*, 1072–1084. [CrossRef]
11. Abad-García, B.; Berrueta, L.A.; Garmón-Lobato, S.; Gallo, B.; Vicente, F. A general analytical strategy for the characterization of phenolic compounds in fruit juices by high-performance liquid chromatography with diode array detection coupled to electrospray ionization and triple quadrupole mass spectrometry. *J. Chromatogr. A* **2009**, *1216*, 5398–5415. [CrossRef]

12. Maeda, H.; Dudareva, N. The Shikimate Pathway and Aromatic Amino Acid Biosynthesis in Plants. *Annu. Rev. Plant Biol.* **2012**, *63*, 73–105. [CrossRef]
13. Herrmann, K.M.; Weaver, L.M. The Shikimate Pathway. *Annu. Rev. Plant Physiol. Plant Mol. Biol.* **1999**, *50*, 473–503. [CrossRef]
14. Babst, B.A.; Harding, S.A.; Tsai, C.-J. Biosynthesis of Phenolic Glycosides from Phenylpropanoid and Benzenoid Precursors in *Populus*. *J. Chem. Ecol.* **2010**, *36*, 286–297. [CrossRef]
15. Marković, S.; Tošović, J. Application of Time-Dependent Density Functional and Natural Bond Orbital Theories to the UV–vis Absorption Spectra of Some Phenolic Compounds. *J. Phys. Chem. A* **2015**, *119*, 9352–9362. [CrossRef]
16. Wang, B.; Li, L.; Liu, M.; Peng, D.; Wei, A.; Hou, B.; Lei, Y.; Li, X. *TaFDL2-1A* confers drought stress tolerance by promoting ABA biosynthesis, ABA responses, and ROS scavenging in transgenic wheat. *Plant J.* **2022**, *112*, 722–737. [CrossRef]
17. Razzaq, A.; Sadia, B.; Raza, A.; Khalid Hameed, M.; Saleem, F. Metabolomics: A Way Forward for Crop Improvement. *Metabolites* **2019**, *9*, 303. [CrossRef]
18. Obata, T.; Fernie, A.R. The use of metabolomics to dissect plant responses to abiotic stresses. *Cell. Mol. Life Sci.* **2012**, *69*, 3225–3243. [CrossRef]
19. Fiehn, O. Combining Genomics, Metabolome Analysis, and Biochemical Modelling to Understand Metabolic Networks. *Comp. Funct. Genom.* **2001**, *2*, 914970. [CrossRef]
20. Rogachev, I.; Aharoni, A. UPLC-MS-based metabolite analysis in tomato. *Methods Mol. Biol.* **2012**, *860*, 129–144. [CrossRef] [PubMed]
21. Klopsch, R.; Baldermann, S.; Voss, A.; Rohn, S.; Schreiner, M.; Neugart, S. Narrow-Banded UVB Affects the Stability of Secondary Plant Metabolites in Kale (*Brassica oleracea* var. sabellica) and Pea (Pisum sativum) Leaves Being Added to Lentil Flour Fortified Bread: A Novel Approach for Producing Functional Foods. *Foods* **2019**, *8*, 427. [CrossRef]
22. Clayton, W.A.; Albert, N.W.; Thrimawithana, A.H.; McGhie, T.K.; Deroles, S.C.; Schwinn, K.E.; Warren, B.A.; McLachlan, A.R.G.; Bowman, J.L.; Jordan, B.R.; et al. UVR8-mediated induction of flavonoid biosynthesis for UVB tolerance is conserved between the liverwort *Marchantia polymorpha* and flowering plants. *Plant J.* **2018**, *96*, 503–517. [CrossRef]
23. Logemann, E.; Tavernaro, A.; Schulz, W.; Somssich, I.E.; Hahlbrock, K. UV light selectively coinduces supply pathways from primary metabolism and flavonoid secondary product formation in parsley. *Proc. Natl. Acad. Sci. USA* **2000**, *97*, 1903–1907. [CrossRef]
24. Hahlbrock, K.; Scheel, D. Physiology and Molecular Biology of Phenylpropanoid Metabolism. *Annu. Rev. Plant Physiol. Plant Mol. Biol.* **1989**, *40*, 347–369. [CrossRef]
25. Maher, M.; Ahmad, H.; Nishawy, E.; Li, Y.; Luo, J. Novel Transcriptome Study and Detection of Metabolic Variations in UV-B-Treated Date Palm (*Phoenix dactylifera* cv. Khalas). *Int. J. Mol. Sci.* **2021**, *22*, 2564. [CrossRef]
26. Liu, Y.; Fan, H.; Dong, J.; Chen, J.; Xu, H.; Zhou, X. Phosphoproteomics of cold stress-responsive mechanisms in *Rhododendron chrysanthum*. *Mol. Biol. Rep.* **2022**, *49*, 303–312. [CrossRef] [PubMed]
27. Giovannoni, J. Tomato Multiomics Reveals Consequences of Crop Domestication and Improvement. *Cell* **2018**, *172*, 6–8. [CrossRef]
28. Chen, W.; Gong, L.; Guo, Z.; Wang, W.; Zhang, H.; Liu, X.; Yu, S.; Xiong, L.; Luo, J. A Novel Integrated Method for Large-Scale Detection, Identification, and Quantification of Widely Targeted Metabolites: Application in the Study of Rice Metabolomics. *Mol. Plant* **2013**, *6*, 1769–1780. [CrossRef]
29. Zhou, X.; Chen, S.; Wu, H.; Yang, Y.; Xu, H. Biochemical and proteomics analyses of antioxidant enzymes reveal the potential stress tolerance in *Rhododendron chrysanthum* Pall. *Biol. Direct* **2017**, *12*, 10. [CrossRef]
30. Li, Q.; Song, J. Analysis of widely targeted metabolites of the euhalophyte *Suaeda salsa* under saline conditions provides new insights into salt tolerance and nutritional value in halophytic species. *BMC Plant Biol.* **2019**, *19*, 388. [CrossRef]
31. Liu, Y.; Liu, J.; Abozeid, A.; Wu, K.X.; Guo, X.R.; Mu, L.Q.; Tang, Z.H. UV-B Radiation Largely Promoted the Transformation of Primary Metabolites to Phenols in *Astragalus mongholicus* Seedlings. *Biomolecules* **2020**, *10*, 504. [CrossRef]
32. Yoon, J.; Cho, L.-H.; Tun, W.; Jeon, J.-S.; An, G. Sucrose signaling in higher plants. *Plant Sci.* **2021**, *302*, 110703. [CrossRef]
33. Mookerjee, S.A.; Gerencser, A.A.; Nicholls, D.G.; Brand, M.D. Quantifying intracellular rates of glycolytic and oxidative ATP production and consumption using extracellular flux measurements. *J. Biol. Chem.* **2017**, *292*, 7189–7207. [CrossRef]
34. Sun, Q.; Liu, M.; Cao, K.; Xu, H.; Zhou, X. UV-B Irradiation to Amino Acids and Carbohydrate Metabolism in *Rhododendron chrysanthum* Leaves by Coupling Deep Transcriptome and Metabolome Analysis. *Plants* **2022**, *11*, 2730. [CrossRef]
35. Peer, W.A.; Murphy, A.S. Flavonoids and auxin transport: Modulators or regulators? *Trends Plant Sci.* **2007**, *12*, 556–563. [CrossRef]
36. Ryan, K.G.; Swinny, E.E.; Markham, K.R.; Winefield, C. Flavonoid gene expression and UV photoprotection in transgenic and mutant *Petunia* leaves. *Phytochemistry* **2002**, *59*, 23–32. [CrossRef] [PubMed]
37. Taylor, L.P.; Grotewold, E. Flavonoids as developmental regulators. *Curr. Opin. Plant Biol.* **2005**, *8*, 317–323. [CrossRef]
38. Ryan, K.G.; Swinny, E.E.; Winefield, C.; Markham, K.R. Flavonoids and UV Photoprotection in Arabidopsis Mutants. *Z. Für Naturforschung C* **2001**, *56*, 745–754. [CrossRef]
39. Gibon, Y.; Pyl, E.-T.; Sulpice, R.; Lunn, J.E.; HÖHne, M.; GÜNther, M.; Stitt, M. Adjustment of growth, starch turnover, protein content and central metabolism to a decrease of the carbon supply when *Arabidopsis* is grown in very short photoperiods. *Plant Cell Environ.* **2009**, *32*, 859–874. [CrossRef]
40. Robbins, M.P. Biochemistry of plant secondary metabolism. Annual Plant Reviews, Volume 2. Edited by Michael Wink. *Eur. J. Plant Pathol.* **2000**, *106*, 487. [CrossRef]

41. Kusano, M.; Fukushima, A.; Redestig, H.; Saito, K. Metabolomic approaches toward understanding nitrogen metabolism in plants. *J. Exp. Bot.* **2011**, *62*, 1439–1453. [CrossRef]
42. Hewage, K.A.H.; Yang, J.-F.; Wang, D.; Hao, G.-F.; Yang, G.-F.; Zhu, J.-K. Chemical Manipulation of Abscisic Acid Signaling: A New Approach to Abiotic and Biotic Stress Management in Agriculture. *Adv. Sci.* **2020**, *7*, 2001265. [CrossRef]

Disclaimer/Publisher's Note: The statements, opinions and data contained in all publications are solely those of the individual author(s) and contributor(s) and not of MDPI and/or the editor(s). MDPI and/or the editor(s) disclaim responsibility for any injury to people or property resulting from any ideas, methods, instructions or products referred to in the content.

metabolites

MDPI

Article

Unravelling Effects of Rosemary (*Rosmarinus officinalis* L.) Extract on Hepatic Fat Accumulation and Plasma Lipid Profile in Rats Fed a High-Fat Western-Style Diet

Sidsel Madsen [1], Steffen Yde Bak [2], Christian Clement Yde [2], Henrik Max Jensen [2], Tine Ahrendt Knudsen [2], Cecilie Bæch-Laursen [3], Jens Juul Holst [3], Christoffer Laustsen [4] and Mette Skou Hedemann [1,*]

[1] Department of Animal and Veterinary Sciences, Aarhus University, Blichers Allé 20, DK-8830 Tjele, Denmark
[2] IFF—Nutrition Biosciences Aps, Edwin Rahrs Vej 38, DK-8220 Brabrand, Denmark; steffen.yde.bak@iff.com (S.Y.B.); christian-clement.yde@iff.com (C.C.Y.); henrik.max.jensen@iff.com (H.M.J.); tine.ahrendt.knudsen@iff.com (T.A.K.)
[3] Department of Biomedical Sciences and Novo Nordisk Foundation, Center for Basic Metabolic Research, Faculty of Health and Medical Sciences, University of Copenhagen, Blegdamsvej 3, DK-2200 Copenhagen, Denmark; cecilie.b@sund.ku.dk (C.B.-L.); jjholst@sund.ku.dk (J.J.H.)
[4] The MR Research Centre, Department of Clinical Medicine, Aarhus University, Palle Juul-Jensens Boulevard 99, DK-8200 Aarhus, Denmark; cl@clin.au.dk
* Correspondence: mette.hedemann@anivet.au.dk

Abstract: The objective of the study was to investigate the preventive effect on obesity-related conditions of rosemary (*Rosmarinus officinalis* L.) extract (RE) in young, healthy rats fed a high-fat Western-style diet to complement the existing knowledge gap concerning the anti-obesity effects of RE in vivo. Sprague Dawley rats (71.3 ± 0.46 g) were fed a high-fat Western-style diet (WD) or WD containing either 1 g/kg feed or 4 g/kg feed RE for six weeks. A group fed standard chow served as a negative control. The treatments did not affect body weight; however, the liver fat percentage was reduced in rats fed RE, and NMR analyses of liver tissue indicated that total cholesterol and triglycerides in the liver were reduced. In plasma, HDL cholesterol was increased while triglycerides were decreased. Rats fed high RE had significantly increased fasting plasma concentrations of Glucagon-like peptide-1 (GLP-1). Proteomics analyses of liver tissue showed that RE increased enzymes involved in fatty acid oxidation, possibly associated with the higher fasting GLP-1 levels, which may explain the improvement of the overall lipid profile and hepatic fat accumulation. Furthermore, high levels of succinic acid in the cecal content of RE-treated animals suggested a modulation of the microbiota composition. In conclusion, our results suggest that RE may alleviate the effects of consuming a high-fat diet through increased GLP-1 secretion and changes in microbiota composition.

Keywords: obesity; metabolomics; proteomics; polyphenol; *Rosmarinus officinalis*

1. Introduction

Worldwide, the prevalence of obesity has increased markedly over the last decades, and obesity is now defined as a pandemic. Obesity is linked to a sedentary lifestyle combined with a high intake of energy-dense food products and is associated with an increased risk of numerous comorbidities including type 2 diabetes, certain cancers, cardiovascular diseases, asthma, gallbladder disease, osteoarthritis, and chronic back pain, resulting in higher overall mortality [1].

In recent years, the interest in natural, bioactive compounds with anti-obesity effects has increased. Polyphenols are a group of compounds found in many fruits, vegetables, and cereals [2]. Polyphenols have been studied in relation to human health, and regular consumption is thought to be associated with a decreased risk of several chronic diseases [3,4]. Obesity is one of the conditions, where polyphenols appear to have a preventive effect.

Different polyphenols have shown the ability to modulate hormonal appetite regulation [5], inhibit the activity of digestive enzymes [6], inhibit fatty acid synthesis [7], or increase fatty acid oxidation [8], all of which are considered expedient in attenuating the development of obesity.

Rosemary (*Rosmarinus officinalis* L.) is an aromatic, evergreen plant containing high concentrations of polyphenols, with carnosic acid and rosmarinic acid being the most abundant bioactive compounds [9]. In medical use, rosemary has been shown to be beneficial in several conditions, including obesity, metabolic syndrome, and type 2 diabetes, and potential mechanisms of action include an ability to limit absorption of lipids [10] and inhibit hepatic fat accumulation and adipocyte hypertrophy [11].

Recent in vitro studies showed that rosemary extract (RE) stimulated the secretion of the satiety-inducing hormone Glucagon-like peptide-1 (GLP-1) from immortalized GLP-1 producing cell lines [12]. GLP-1 is a peptide hormone secreted from intestinal L-cells in response to nutrients in the intestinal lumen. Following secretion, GLP-1 is rapidly inactivated by enzymes in plasma and on cell surfaces, resulting in a half-life of intact GLP-1 of only one to two minutes in humans [13]. Upon entering the blood-stream, GLP-1 is circulated to several target organs, where its metabolic functions include stimulation of insulin secretion, induction of satiety, inhibition of hepatic gluconeogenesis, stimulation of glycogen synthesis and glucose oxidation in muscle tissue, and stimulation of free fatty acid (FFA) synthesis and glucose uptake in adipose tissue, although these effects may be secondary to the actions on the endocrine pancreas or the effects on body weight [14–17].

Dyslipidemia is often seen in obese patients and includes reduced levels of circulating high-density lipoproteins (HDL) and enhanced levels of low-density lipoproteins (LDL) and triglycerides [18]. Obesity is associated with liver diseases, such as non-alcoholic fatty liver disease (NAFLD). NAFLD is characterized by excessive intrahepatic triglyceride levels and may be accompanied by excessive levels of FFAs and cholesterol in the plasma. It is often associated with alterations in whole-body metabolic homeostasis [19]. Consumption of polyphenols has been associated with the prevention and treatment of NAFLD [20], and the mechanisms may involve the effects of microbial gut metabolites as well as stimulation of gut-derived hormones [21].

We hypothesized that RE reduces feed intake in rats and inhibits diet-induced weight gain through increased fasting GLP-1 levels. The study was carried out in young, non-obese rats with the aim to investigate if daily consumption of a high-fat diet with RE over a period of six weeks influenced weight gain. We studied metabolic parameters related to obesity and used untargeted metabolomics and proteomics to decipher the mode of action.

2. Materials and Methods

2.1. Plant Material and Extract

The RE (IFF-Nutrient Bioscience ApS, Brabrand, Denmark) used in the present experiment was a dried powder from a water/ethanol extract of rosemary leaves, containing min. 65% carnosic acid and min. 70% carnosic acid + carnosol.

2.2. Animals

In vivo study: The study included 64 male Sprague Dawley rats obtained from Taconic Biosciences (Ejby, Denmark) with a starting weight of 71.34 g (±0.46 SEM). The rats were divided into pairs of two rats (32 pairs) and the pairs were divided into four experimental groups (8 pairs per group). Each group was fed one of four pelleted experimental diets; standard rodent chow (Altromin 1324, Altromin GmbH, Lage, Germany) (ST), Western-style diet (D12079B; 40% fat, 43% carbohydrates, 17% protein; Research Diets, New Brunswick, NJ, USA) (WD), WD supplemented with 100 mg rosemary extract (RE) pr. 100 g feed (WD+low-RE), or WD supplemented with 400 mg RE pr. 100 g feed (WD+high-RE). The dose of RE added was based on a previous experiment where reduced weight gain was observed in mice fed a high-fat diet supplemented with RE [22]. The rats were expected to eat 10–20 g feed/day which corresponds to daily intakes of 40–80 mg of RE in rats fed the

highest level of RE. The chemical composition of the diets was determined as previously described [23] and is shown in Supplementary Table S1.

Animals were housed in pairs in clear plastic boxes (38 × 60 cm) bedded with shavings and followed a 12:12 h light-dark cycle, at 25 °C and 60% humidity, with ad libitum access to water and feed during the entire experiment. Rats were individually marked to enable measurement of individual body weight (BW). BW gain and feed intake were measured twice weekly (see supplementary methods). The experiment was conducted over 46 days.

2.3. Sample Collection

At the end of the experiment, and after six hours of food deprivation to allow for the normalization of metabolic markers, all rats were euthanized by an intraperitoneal injection of 0.5 mL pentobarbital (200 mg/mL) with lidocaine (20 mg/mL). From each box, one rat was euthanized and kept intact at −20 °C for whole body composition analysis, while the second rat in the box was used for tissue and blood collection. When death was ensured, blood was collected from the heart into EDTA-coated tubes containing 1% (*V*/*V*) dipeptidylpeptidase-4 (DPP-4) inhibitor (Merck KGaA, Darmstad, Germany). Blood samples were immediately centrifuged at 2000× *g* for 12 min at 4 °C before plasma was stored at −80 °C until further analysis. The abdominal cavity was opened, and the liver was dissected out, weighed, and snap-frozen in liquid nitrogen. Samples were collected from three segments of the small intestine (5 cm distal to the pylorus sphincter, a mid-section, and 5 cm proximal to the ileocaecal valve). The samples were washed thoroughly in saline before being placed in RNAlater®(ThermoFisher Scientific, Waltham, MA, USA), and further treated according to the manufacturer's protocol. All tissue samples were stored at −80 °C until further analysis. The caecum was dissected free and cecal tissue and content were weighed. Content was collected and stored at −80 °C until further analysis.

2.4. Studies on Isolated Perfused Rat Small Intestine

Male Wistar rats (~250 g) were obtained from Janvier (Saint Berthevin Cedex, France) and housed with ad libitum access to standard chow and water, following a 12:12 h light:dark cycle. Rats were acclimatized for a least a week before the experiments. On the day of the experiment, rats were transferred to our perfusion facility and anesthetized, and the entire small intestine was isolated and perfused as described in detail in the supplementary methods and elsewhere [24,25].

2.5. Total Body Fat Content

Body composition data were acquired using a 9.4T pre-clinical MR scanner (Agilent, Yarnton, UK) equipped with a 72 mm proton volume coil (RAPID Biomedical GmbH, Rimpar, Germany). Full body proton NMR spectra from each animal were Fourier Transformed and spectrally analyzed by fitting the water and the fat peaks using a general linear model approach that was developed in-house (MATLAB, The MathWorks, Inc., Natick, MA, USA). Subsequently, the fitted peak areas were used to calculate the fat percentage by division by the water component and fat component signal areas.

2.6. Fasting Total GLP-1 Plasma Concentrations

Fasting total GLP-1 concentrations were measured using an in-house radioimmunoassay, as previously described [26], based on an antiserum directed against the amidated C-terminus of GLP-1. The antibody reacts equally with intact amidated GLP-1 (7–36 amide), the primary metabolite (9–36 amide), and truncated sequences produced by mid-site cleavage (e.g., by NEP 24.11). Therefore, the concentrations represent the total GLP-1 concentration. I125-labeled GLP-1 7-36NH2 (a kind gift from Novo Nordisk A/S) was used as a tracer. The experimental detection limit was 1 pmol/L, and the coefficient of variation was <6% at 20 pM.

2.7. RNA Extraction and Gene Expression

Total RNA was extracted from the whole wall of the small intestine using a NucleoSpin RNA kit (Macherey-Nagel GmbH & Co., Ltd., KG, Duren, Germany), in accordance with the manufacturer's protocol. RNA concentration and purity were evaluated using a NanoDrop spectrophotometer (ND-1000, NanoDrop Technologies, Wilmington, DE, USA). A High-Capacity cDNA Reverse Transcriptase Kit (Life Technologies, Taastrup, Denmark) was used for cDNA synthesis. The qPCR of glyceraldehyde-3-phosphate dehydrogenase (GAPDH), β-actin, and proglucagon (GCG) genes was run in 384-well plates with a 1:4 ratio of cDNA and TaqMan Master Mix (Applied Biosystems, Foster, CA, USA), according to the manufacturer's protocol. The analyses were performed in triplicates for the housekeeping genes and in duplicates for the target genes, under standard amplification conditions determined for the Applied Biosystem ViiA 7 Real-Time PCR system (Life Technologies, Taastrup, Denmark). Expression levels were first normalized to the expression level in the most proximal sample in the respective rats, and values were then normalized to the control group fed the standard diet. For the interaction between the treatment and the tissue, normalization to the most proximal segment for the standard diet treatment was used.

2.8. Plasma Metabolic Markers

Plasma cholesterol, HDL, LDL, and triglycerides were quantified by standard procedures (Siemens Diagnostics® Clinical Methods for ADVIA 1800). FFAs were determined using the Wako, NEFA C ACS-ACOD assay method. All analyses were performed using an autoanalyzer, ADVIA 1800 Chemistry System (Siemens Medical Solutions, Tarrytown, NY 10591, USA).

2.9. Analysis of Hepatic Fat Percentage

Liver samples were homogenized in twice the amount of methanol (w/v) using an Ultra-Turrax homogenizer (IKA Labortechnik, Staufen, Germany) while placed in an ice bath. Of this homogenate, 600 mg was mixed with 1.0 mL water, 1.5 mL methanol, and 1.0 mL chloroform, before being shaken for one minute. Water (1.0 mL) and chloroform (2.0 mL) were added to the mixture, following shaking for one minute. Phase separation was accelerated by centrifugation at 2000× g for 5 min. The lower chloroform phase (2 mL) was collected and dried, and the residue was weighed for determination of fat content.

2.10. Proteomics Analysis of Liver Tissue

Approximately 100–200 mg of tissue was excised from the left lateral lobe. Frozen tissue was covered with 1 mL lysis buffer (5% SDS in 100 mM triethylammonium bicarbonate, TEAB, pH 7.5). Tissue homogenization was done using a ball mill at 25 Hz for 10 min (Retsch GmbH, Haan, Germany). Homogenates were centrifuged for 10 min at 14,000× g. The supernatants were heated to 95 °C for 10 min to fully denature proteins. DNA was sheared using a Bioruptor Pico (Diagenode Diagnostics, Liege, Belgium) high-energy water bath sonicator system using 10 cycles of 30 s sonication followed by a 30 s break. The temperature was set to 5 °C throughout the entire process. Protein concentrations were estimated in triplicates using a BCA micro assay kit (Thermo Scientific Pierce, Rockford, IL, USA).

Liver lysates were digested into peptides using the S-trap™ micro digestion protocol [27] using a trypsin-to-protein ratio of 1:30. Peptide elutes were dried down and resuspended in 50 µL 0.1% TFA. Concentrations of the peptides were estimated using a micro-BCA™ protein assay kit (Thermo Scientific Pierce, Rockford, IL, USA) and samples were adjusted to equal concentrations. A QC sample (mixture of all samples) was prepared by taking 10 µL from all samples and mixing well. Data acquisition and analysis were performed as described in the supplementary methods.

Data Acquisition: Nano LC−MS/MS analyses were performed using an UltiMate™ 3000 RSLCnano System (Thermo Fisher Scientific, Waltham, MA, USA) interfaced to a Q Exactive™ HF Hybrid Quadrupole-Orbitrap™ Mass Spectrometer (Thermo Fisher Scientific, Waltham,

MA, USA). Samples were dissolved in 0.1% TFA and loaded onto a 20 mm nanoViper Trap Column (Acclaim™ PepMap™ 100 C18, 3µm particle size, and an i.d. 0.075mm) connected to a 400 mm analytical column (PepSep, ReproSil 3 µm C18 beads, pore diameter 120Å and an i.d. 0.075 mm). Separation was performed at a flow rate of 300 nL/min using a 40 min gradient of 0−41% Solvent B (100% ACN, 0.1% FA) into the Nanospray Flex Ion Source (Thermo Scientific). The Q Exactive HF instrument was operated in a data-dependent MS/MS using HCD fragmentation. The peptide masses were measured by the Orbitrap (MS scans were obtained with a resolution of 60,000 (FWHM) at m/z 200). The top 12 most intense ions were selected and subjected to fragmentation. Ions were isolated by the quadrupole using a 1.2 Da width isolation window. Fragment spectra were recorded in the Orbitrap with a resolution of 30,000 (FWHM) at m/z 200. Dynamic exclusion was enabled with an exclusion duration of 30 s, and an exclusion mass tolerance width of ±10 ppm relative to masses on the list. Samples were analyzed in a randomized order with a QC sample after every fifth sample and with five QC samples at the beginning of the sample sequence.

Data analysis: The LC−MS/MS data were processed (smoothing, background subtraction, and centroiding) using Proteome Discoverer (Version 2.2, Thermo Scientific). The processed LC−MS/MS data were subjected to database searching against a UniProt Rattus Norvegicus database containing 29,944 sequences using an in-house Mascot server. Trypsin was chosen as an enzyme with a maximum of two missed cleavages allowed. S-Carbamidomethyl cysteine was defined as a fixed modification and oxidation of methionine as a variable modification. The MS/MS results were searched with a peptide ion mass tolerance of ±10 ppm and a fragment ion mass tolerance of ±0.8 Da. A percolator [28] was used for calculating the false discovery rate. Only peptides that were identified as rank 1 peptides and with a confidence value of 1% ($q < 0.01$) were considered for further analysis.

All raw files were imported into Expressionist v.12.0.9 (Genedata, Basel, Schwitzerland) for data analysis. Imported files were noise filtered using a chemical noise subtraction. Data were RT aligned using a pairwise alignment, filtered, and smoothed before peak detection, based on volumes. Detected peaks were isotopically clustered and singletons were filtered out. Peak clusters were matched with Proteome Discoverer identifications and peptides were grouped based on protein identifications. Proteins were quantified based on the three most intense peptides' Hi-3 [29]. Quantitative results were exported into Analyst v.12.0.9 (Genedata) for normalization, statistical filtering, and testing. Principle Component Analysis was performed using the GeneData Analyst module. A total of 1570 proteins were identified and quantified and within these, 999 proteins were quantified with a minimum of two peptides per protein. The average finding percentage of the 999 proteins throughout all 44 runs was 99.3%, giving an almost complete data matrix. Data were normalized using an intensity drift normalization, where intensities from QC samples are used to correct for drift in the LC-MS/MS performance. Using an ANOVA, we found 247 proteins significantly changing between one of the four diets with an overall FDR of 5%. Regulated proteins were manually annotated.

2.11. NMR Spectroscopy

A dual-phase methanol/chloroform/water (1:1:1) extraction protocol was performed on the left lateral lobe liver samples (weight 259 ± 94 mg), as previously described [30]. The NMR measurements were performed on a 600 MHz Bruker Avance III spectrometer operating at a frequency of 600.13 MHz for 1H nucleus (Bruker Biospins, Rheinstetten, Germany) and equipped with a 5mm TCI CryoProbe. Polar extracts: 1H NMR spectra were recorded at 298 K using a 1D Noesy pulse sequence with pre-saturation. A total of 256 scans collected into 64 K data points were acquired with a spectral width of 20.02 ppm, a recycle delay of 5 s, and an acquisition time of 2.73 s. Non-polar extracts: 1H NMR spectra were obtained at 298 K using a single pulse sequence with a 30° flip angle. A total of 128 scans collected into 64K data points were acquired with a spectral width of 20.02 ppm, a recycle delay of 3 s, and an acquisition time of 2.73 s. The anomeric glycogen H-1 signal at 5.4 ppm in the polar extracts was manually quantified and normalized to the weight of the liver for each rat.

Hepatic lipid signals in the non-polar phase were mainly tentatively assigned according to Fathi et al. [31]. Prior to data analysis, the residual water signal was excluded from the "Polar" spectra, and all 1H NMR spectra were normalized to the weight of each sample. Baseline correction by distribution-based classification [32], alignment using icoshift version 1.3.1 [33], and binning according to an optimized bucketing algorithm [34] were performed for both data sets. Multivariate data analysis was applied using Principal Component Analysis (PCA) on Pareto-scaled data using PLS Toolbox 8.7 (eigenvector Research, USA) in Matlab R2018b (The MathWorks, Inc., Natick, MA, USA) to detect clustering behavior.

2.12. Metabolomic Analysis of Plasma and Cecal Contents

LC-MS was used to analyze the plasma and cecal metabolome in an untargeted approach. Plasma samples (150 µL) were placed in the wells of a 96-well plate and deproteinized with 450 µL ACN containing internal standards (*p*-chlorophenylalanine and glycocholic acid (Glycine-1 13C), final concentration 0.01 mg/mL) and processed as previously described [35]. Cecal contents were freeze-dried and milled prior to analysis. Cecal content (50 mg) was mixed with 500 µL 80% ACN with added internal standards as described above. The samples were vortexed for 20 min at room temperature and centrifuged for 10 min at 10,000× *g* and 4 °C. The supernatant was transferred to a 96-square well, 0.45 µM polypropylene filter plate and aspirated into a new plate. The filtered supernatant was treated as described for the plasma samples. UPLC-MS analysis was performed using a Dionex UltiMate 3000 (Dionex, Sunnyvale, CA, USA) ultra-high pressure liquid chromatography system coupled with an Impact HD Quadrupole Time-of-Flight (QTOF) mass spectrometer (Bruker Daltonics GmbH, Bremen, Germany) operating in positive electrospray ionization mode (ESI+) and negative electrospray ionization mode (ESI-) using the instrumental parameters previously described [35,36]. The chromatographic behavior of the samples, pre-processing, and identification of metabolites was assessed as previously described [35].

2.13. SCFA Analysis

Short-chain fatty acid (SCFA) concentrations were measured as previously described [37], with some modifications as described in the supplementary methods.

2.14. Statistical Analyses

Differences in fasting plasma GLP-1 concentrations, metabolic markers in plasma, total and hepatic fat accumulation, weight, and SCFA were assessed by One-way ANOVA with Tukey multiple-comparison correction. Differences in the presence of liver proteins were assessed by One-way ANOVA using Storey-Tibshriani correction. $p < 0.05$ was considered statistically significant whereas a *p*-value between 0.05 and 0.10 was considered as an indication of a trend towards significance.

Gene expression data were analyzed using a normal mixed model:

$$Yij = \mu + \alpha i + \upsilon j + \varepsilon ij,$$

where Yij is the gene expression; µ is the overall mean; αi is the effect of treatment (i = ST, WD, WD+low-RE, WD+high-RE); υj is the random effect of a block (j = 1, 2); and εij is the residual error component. The data are presented as least square means with a 95% confidence interval. Effects were considered significant when $p < 0.05$, whereas $0.05 \leq p \leq 0.10$ represented a tendency.

For perfusion studies, GLP-1 total outputs were calculated by multiplying perfusion flow (7.5 mL/min) with the GLP-1 concentration in the perfusion effluents (measured in pmol/L). Hormone outputs (fmol/min) are presented as means ± SEM. To test for the statistical significance of responses, total GLP-1 outputs were calculated by summing up the outputs during the entire period of stimulus administrations (15 min intra-luminal/intra-vascular RE administration) and were compared to respective total GLP-1 outputs at baseline conditions. Baseline outputs were calculated over a similar number of samples with half of the samples taken immediately before stimulus administration and the other

half coming from the terminal part of the subsequent baseline period. Statistical calculations were performed using GraphPad Prism 7 software (La Jolla, CA, USA), employing One-way ANOVA for repeated measurements followed by the Bonferroni multiple comparison test or student *t*-test as indicated in the figure legends. $p < 0.05$ was considered significant. Prior to testing, the D'Agostino-Pearson omnibus normality test was performed to confirm the Gaussian distribution of the data.

3. Results

3.1. Body Weight and Feed Intake

As presented in Figure 1A, during the six-week experimental period, a clear effect of time ($p < 0.0001$) was observed for body weight, while no overall effect of treatments was observed ($p = 0.10$). The treatments influenced the 24-h feed intake significantly ($p = 0.006$; Figure 1B). When determining the daily weight gain pr. energy intake (g/kcal), an overall effect of treatment was observed ($p < 0.0001$; Figure 1C). When comparing this for the different treatments, a significant difference was seen on days 3–17; however, no overall effect of treatment was observed after day 13.

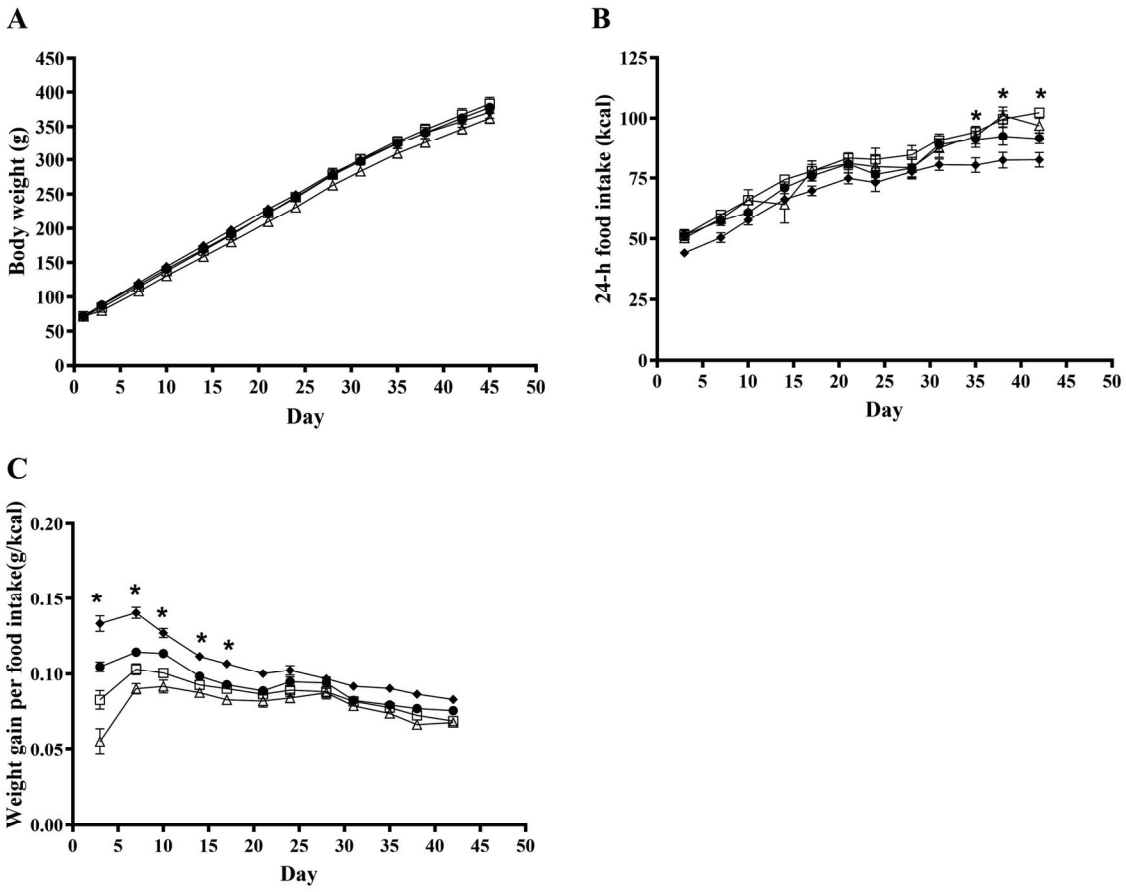


Figure 1. Effects of rosemary extract on body weight, $n = 16$ (**A**), 24-h feed intake, $n = 8$ (**B**), and weight gain per energy intake, $n = 8$ (**C**), in rats fed a ST (♦), WD (●), WD+low-RE (□), or WD+high-RE (Δ) over 46 days. Results are presented as mean ± SEM. * indicates a significant difference ($p < 0.05$) between two or more treatments: (**B**) ST and WD+low-RE differ significantly at days 35, 38, and 42, and ST and WD+high-RE differ significantly at day 38. (**C**) All four treatments differ at day 3. In addition, WD and WD+high-RE differ at day 7, and ST and WD+high-RE differ at days 7, 10, 14, and 17. ST, standard diet; WD, Western-style diet; WD+low-RE, WD supplemented with low concentration of rosemary extract; WD+high-RE, WD supplemented with high concentration of rosemary extract.

3.2. Liver Weight and Fat Accumulation in the Liver and Whole Body

Mean total body fat percentages (Figure 2A) following six weeks of treatment were 14.1% (ST), 17.3% (WD), 18.9% (WD+low-RE), and 15.0% (WD+high-RE), and no difference between the treatments was observed ($p = 0.18$). Rats treated with WD had significantly higher liver fat percentages compared to ST treatment ($p < 0.0001$). Treatment with WD+high-RE strongly decreased the fat mass in the liver (Figure 2B), with an average reduction of 46% compared to the WD. The mean weights of wet liver tissue (Figure 2C), expressed as a percentage of total body weight, were 3.99% (ST), 4.50% (WD), 5.26% (WD+low-RE), and 5.16% (WD+high-RE). ST treatment resulted in the lowest relative liver weight, it increased when feeding WD, and the addition of RE to the diet increased the relative liver weight further.

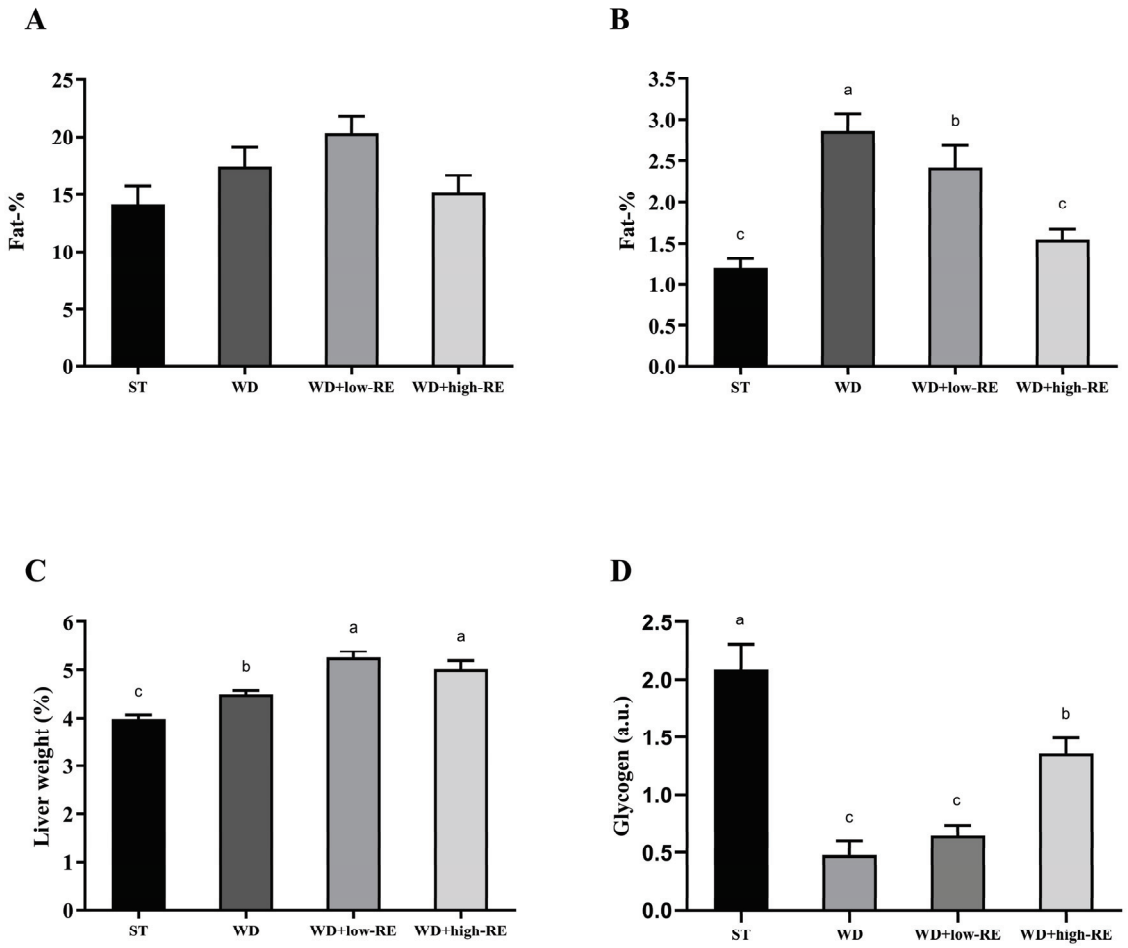


Figure 2. Effects of rosemary extract on (**A**) total body fat percentage, (**B**) liver fat percentage, (**C**) liver weight as a percentage of total body weight, and (**D**) hepatic glycogen (a.u) in rats fed a standard diet (ST), Western-style diet (WD), or a WD supplemented with either low (WD+low-RE) or high (WD+high-RE) concentrations of rosemary extract, measured at day 46. $n = 8$. Results are presented as mean ± SEM. Means without common letters differ significantly ($p < 0.05$).

3.3. Plasma Metabolic Markers

An overall effect of treatment was observed for total cholesterol ($p = 0.0008$; Figure 3A). Thus, feeding WD, WD+low-RE, and WD+high-RE caused a significantly higher level of total plasma cholesterol, compared to ST, but no significant differences were observed between the three. For mean plasma levels of LDL-cholesterol (Figure 3B), only WD+low-RE treatment resulted in a significantly higher level than ST, whereas WD+high-RE was similar to ST and WD was intermediate. Analysis of mean plasma levels of HDL-cholesterol

(Figure 3C) showed that WD+low-RE and WD+high-RE treatment caused significantly higher plasma HDL levels than ST treatment. An effect of treatment on the plasma level of triglycerides was observed (p = 0.0002; Figure 3D). The mean plasma levels of plasma triglycerides were significantly higher with WD and WD+low-RE compared to the ST, whereas levels were intermediate in rats fed WD+high-RE. Plasma FFA levels (Figure 3E) were significantly higher for WD compared to ST (p = 0.005), whereas WD-low-RE and WD+high-RE were intermediate.

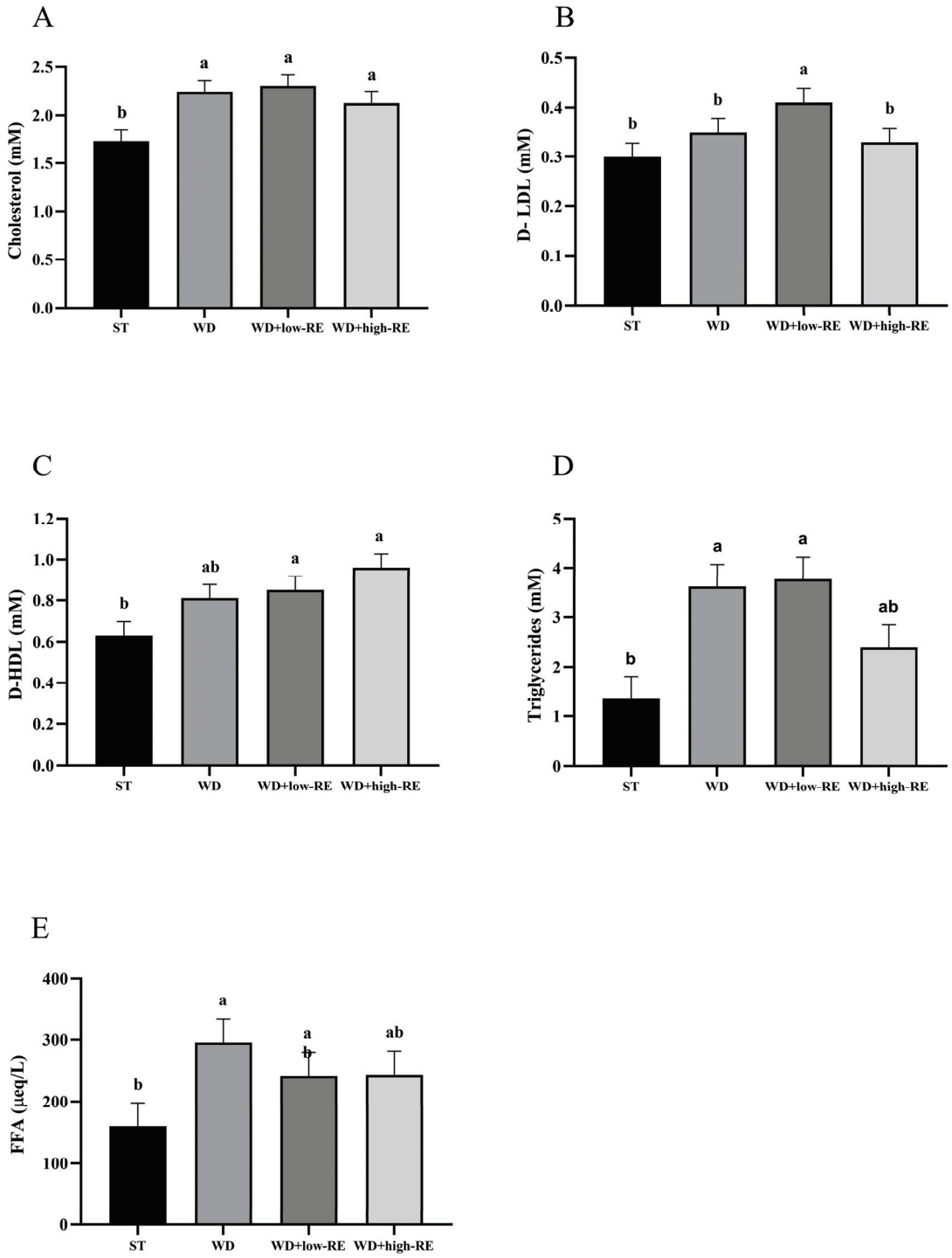


Figure 3. Effects of rosemary extract on plasma levels of (**A**) total cholesterol (mM), (**B**) low-density lipoprotein (D-LDL) (mM), (**C**) high-density lipoprotein (D-HDL) (mM), (**D**) triglycerides (mM), and

(**E**) free fatty acids (FFA) (μeq/L) in rats fed a standard diet (ST), Western-style diet (WD), or a WD supplemented with either low (WD+low-RE) or high (WD+high-RE) concentrations of rosemary extract. Measured at day 46. $n = 8$. Results are presented as mean ± SEM. Means without common letters differ significantly ($p < 0.05$).

3.4. Fasting GLP-1 Plasma Concentrations and Proglucagon Expression

An effect of treatment was observed for the fasting plasma GLP-1 concentration ($p = 0.01$, Figure 4A). Thus, fasting GLP-1 plasma concentrations were increased by WD+high-RE treatment compared to ST and WD treatment, but concentrations were not different from the WD+low-RE group and also did not differ from ST and WD.

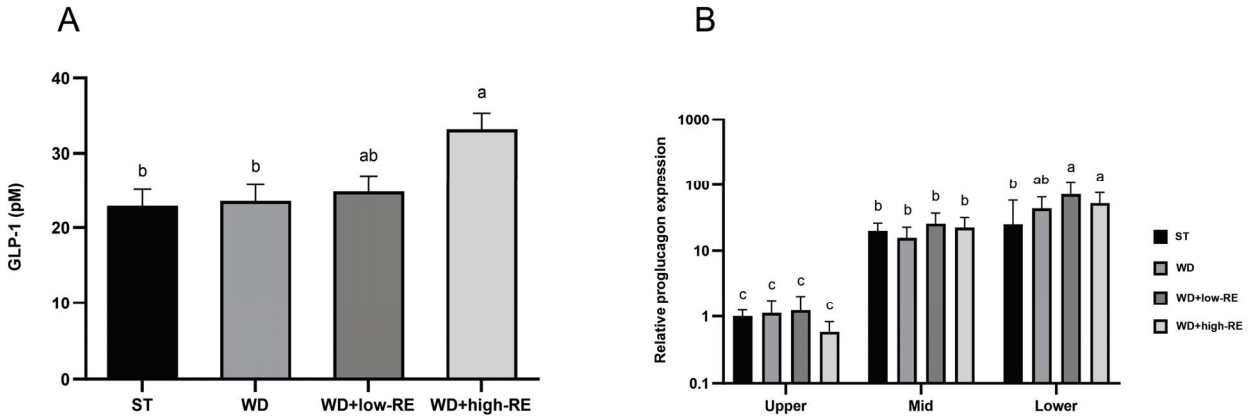


Figure 4. Effects of rosemary extract on (**A**) fasting levels of glucagon-like peptide-1 (GLP-1) (pM) and (**B**) relative proglucagon expression for the interaction between segment and treatment, normalized to ST treatment in upper small intestine (SI) in rats fed a standard diet (ST), Western-style diet (WD), or a WD supplemented with either low (WD+low-RE) or high (WD+high-RE) concentrations of rosemary extract. Measured at day 46. $n = 8$. Results on GLP-1 are presented as mean ± SEM and results on relative proglucagon expression are presented as means with 95% confidence intervals. Means without common letters differ significantly ($p < 0.05$).

An interaction between treatment and segment was observed for relative proglucagon expression ($p = 0.03$; Figure 4B). The interactive effect was observed in the lower SI where the relative expression was higher in rats fed WD+low-RE and WD+high-RE compared to rats fed ST. For segment-specific changes in relative proglucagon gene expression, the mid-part and the distal part of the small intestine were 21-fold and 48-fold higher than the proximal part, respectively.

3.5. Acute Effects of RE on GLP-1 Secretion from Isolated Perfused Rat Small Intestine

The baseline GLP-1 output was (mean ± SEM) 171 ± 11.2 fmol/min. GLP-1 output was neither affected by intra-luminal RE infusion ($p > 0.99$ between total output at 15 min baseline and 15 min stimulation), nor by intra-arterial RE infusion ($p = 0.97$ between preceding total baseline output and 15 min of stimulation) (n = 6, Figure 5). Confirming responsiveness of the perfused preparation, intra-arterial taurodeoxycholic acid (100 μM, a conjugated secondary bile acid) instantly and reversibly increased secretion by a factor of 2–3 during 15 min of stimulation ($p < 0.05$ compared to preceding output at baseline).

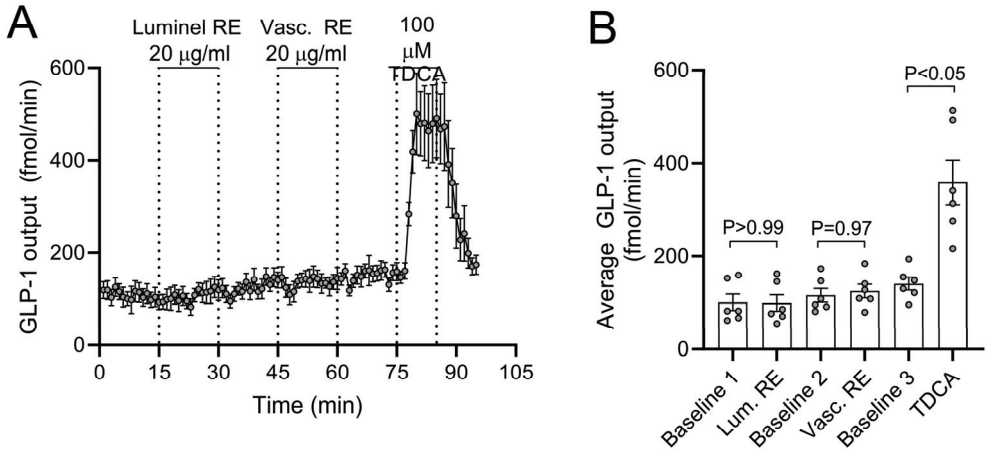


Figure 5. Luminal and vascular rosemary extract (RE)-stimulated glucagon-like peptide-1 (GLP-1) secretion. (**A**) GLP-1 output and (**B**) average GLP-1 output are shown as means ± SEM in response to two subsequent stimulations with 20 μg/mL RE. Intra-luminal infusion of 100μM taurodeoxycholice acid (TDCA) was included at the end of all experiments as a positive control.

3.6. Proteomic Analysis of Liver Tissue

In this study, we used label-free LC-MS/MS-based proteomics. A principal components analysis (PCA) score plot of the liver proteins is shown in Figure 6. Principal component (PC) 2 shows the second largest variation (10.5%) in the dataset and, in this case, separates the different diets.

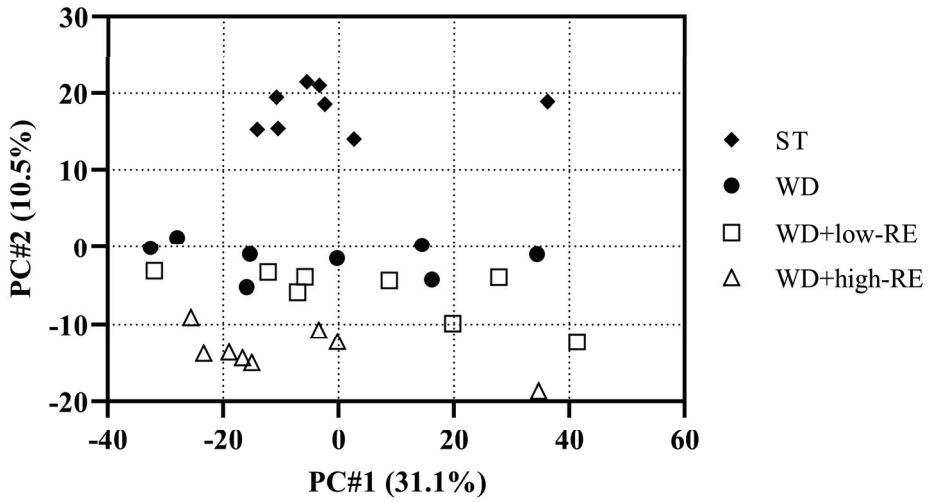


Figure 6. Principal components analysis score plot of liver proteins of rats fed ST (♦), WD (●), WD+low-RE (□), or WD+high-RE (Δ), over 46 days. ST, standard diet; WD, Western-style diet; WD+low-RE, WD supplemented with a low concentration of rosemary extract; WD+high-RE, WD supplemented with a high concentration of rosemary extract.

A number of proteins involved in lipid metabolism and oxidation of lipids were found to be affected in WD-fed animals compared to ST-fed animals. The proteins found related to fatty acid metabolism and oxidation and regulated in comparison to the ST diet are shown in Table 1. Interestingly, a number of these proteins are regulated differentially in response to the RE supplement. The hydroxyacyl-coenzyme A dehydrogenase and all-trans-retinol 13,14-reductase (RETSAT) were upregulated by WD whereas, in rats supplemented with RE, these proteins were not significantly altered compared to ST.

Table 1. Gene and protein name of quantified proteins involved in fatty acid metabolism. Fold changes between the different diets in relation to rats fed a standard diet (ST), Western-style diet (WD), or a WD supplemented with either low (low-RE) or high (high-RE) concentrations of rosemary extract, measured at day 46. n = 8.

Protein Name	Gene	WD/ST	WD+Low-RE/ ST	WD+High-RE/ ST
Arylacetamide deacetylase	*AADAC*	1.7	1.6	1.7
ATP-binding cassette sub-family D member 3	*ABCD3*	1.2	1.3	1.5
Short/branched chain specific acyl-CoA dehydrogenase, mitochondrial	*ACADS*	0.5	0.6	0.5
Aldehyde oxidase 1	*AOX1*	1.2	1.2	1.3
CDGSH iron-sulfur domain-containing protein 1	*CISD1*	0.9	0.8	0.8
2,4-dienoyl-CoA reductase, mitochondrial	*DECR1*	2.0	1.6	1.8
Enoyl-CoA delta isomerase 1, mitochondrial	*ECI1*	2.1	1.8	2.2
Hydroxyacyl-coenzyme A dehydrogenase, mitochondrial	*HADH*	1.3	1.0	1.0
Trifunctional enzyme subunit alpha, mitochondrial	*HADHA*	1.4	1.3	1.5
Trifunctional enzyme subunit beta, mitochondrial	*HADHB*	1.3	1.0	1.3
Hydroxymethylglutaryl-CoA synthase, mitochondrial	*HMGCS2*	1.4	1.2	1.2
Corticosteroid 11-beta-dehydrogenase isozyme 1	*HSD11B1*	0.5	0.3	0.5
Estradiol 17-beta-dehydrogenase 2	*HSD17B2*	1.2	1.4	1.6
MICOS complex subunit Mic60 (Fragment)	*IMMT*	0.8	1.2	1.7
Enoyl-[acyl-carrier-protein] reductase, mitochondrial	*MECR*	1.6	2.2	4.1
Macrophage migration inhibitory factor	*MIF*	1.1	1.3	1.6
5′-AMP-activated protein kinase catalytic subunit alpha-2	*PRKAA2*	1.4	1.2	1.5
All-trans-retinol 13,14-reductase	*RETSAT*	2.4	1.4	1.2
Stearoyl-coenzyme A desaturase 1	*SCD1*	9.8	10.1	7.6

The mitochondrial protein Enoyl-[acyl-carrier-protein] reductase and the protein macrophage migration inhibitory factor (MIF) increased in the WD+high-RE diet compared to ST, whereas WD only enhanced the abundance slightly. Changes were also observed in the mitochondrial protein MICOS complex subunit Mic60 which increased by 1.7-fold in the WD+high-RE diet compared to ST. Stearoyl-CoA desaturase 1 (SCD1) was found to be the most regulated protein in response to WD as the protein was 9.8-fold upregulated in the WD samples compared to ST samples. In WD+high-RE treatment, this increase was slightly lower at 7.6-fold.

Several members of UDP-glucuronosyltransferases and glutathione reductases and glutathione S-transferases belonging to the Xenobiotic pathway phase II response were also found to be regulated in response to a high-RE diet (Table S2).

3.7. NMR Analysis of Liver Tissue

A PCA model on the non-polar liver extracts resulted in a clear separation of the treatments along PC1 (Figure 7A). The WD+low-RE treatment could not be separated from WD in PC1, whereas WD+high-RE showed a shift towards the lipid profile of the ST-fed rats. The PC1 loadings for the hepatic free and total cholesterol could be ranked according to treatments: WD and WD+low-RE > WD+high-RE > ST (Figure 7B). The same pattern was also shown for glycerol backbone signals, which could indicate less hepatic triglyceride in WD+high-RE rats compared to WD rats. The PC1 loadings in Figure 7B of the fatty acyl chain signals have in general both positive and negative loadings for the same functional group (e.g., (CH2)2 at 1.24–1.37 ppm). This could be seen as minor differences in the lipid signals when comparing different treatments. Moreover, the unsaturated fatty acid broad peak from 5.23 to 5.38 ppm shows mainly negatively valued loadings, which means that livers from WD+high-RE rats have a higher prevalence of unsaturated fatty acids than livers from WD and WD+low-RE rats.

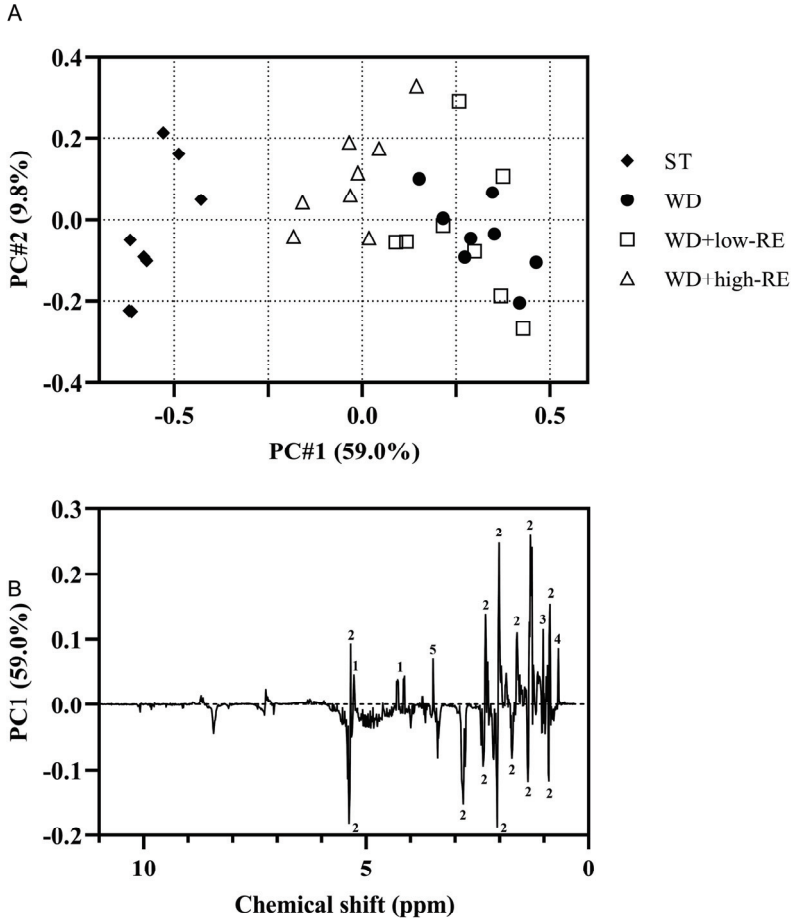


Figure 7. (**A**): Principal components analysis score plot of the non-polar extracts from the liver of rats fed ST (⧫), WD (●), WD+low-RE (□), or WD+high-RE (Δ), over 46 days. ST, standard diet; WD, Western-style diet; WD+low-RE, WD supplemented with a low concentration of rosemary extract; WD+high-RE, WD supplemented with a high concentration of rosemary extract. (**B**): PC1 loadings plot of non-polar extracts. Assignments: 1, glycerol backbone; 2, fatty acyl chain; 3, free cholesterol; 4, total cholesterol; 5, residual methanol.

The hepatic glycogen levels were quantified in the polar liver extracts by NMR spectroscopy (Figure 2D). A significant treatment effect was found for glycogen hepatic levels with elevated levels in ST and WD+high-RE compared to WD and WD+low-RE rats.

3.8. LC-MS Metabolomics of Plasma and Caecum Content

The PCA scores plot of cecal digesta samples analyzed in negative mode revealed four separated clusters based on treatment (Figure 8A). Likewise, the PCA score plot of plasma (Figure 8B) in negative mode showed a clear separation between rats fed ST and WD. The separation between WD and WD with added RE was less clear; however, a ranking of the samples was evident.

In cecal content, the ST-treated rats differed from WD-, WD+low-RE-, and WD+high-RE-treated rats by having high levels of metabolites linked to whole grain intake, e.g., enterolactone and dihydroferulic acid (Figure S2, Tables S2 and S3). Moreover, ST-treated rats had higher levels of certain lipid metabolites, indicating different lipid sources in ST and WD. In general, the treatment with WD, WD+low-RE, and WD+high-RE caused high levels of putatively identified bile acid (BA) metabolites (Figure S3). However, for many of these BA metabolites, the concentration was decreasing with the increase in RE concentration. Cholic acid, a primary BA, appears to be the only identified BA metabolite increasing with RE

concentration. Many metabolites were seen increasing with RE concentration, most of which were connected to rosemary. These include carnosol, carnosic acid, and glucuronides of these.

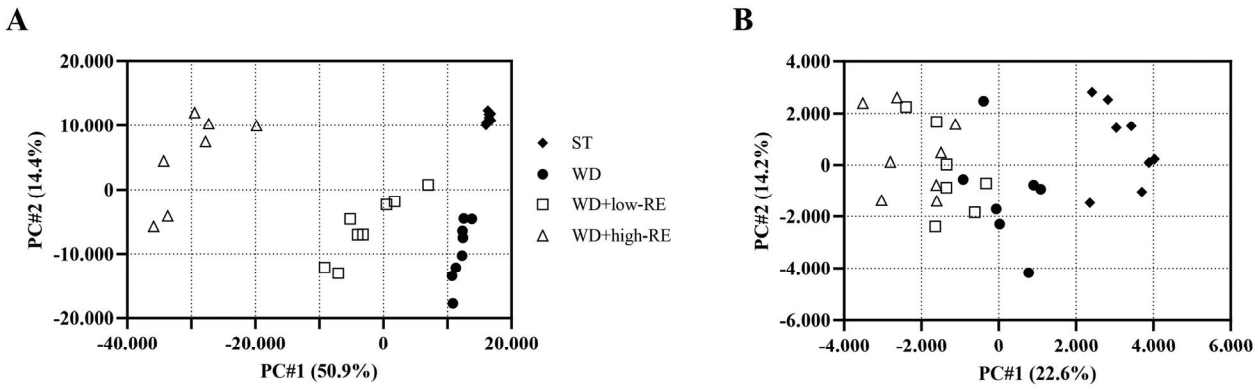


Figure 8. Principal components analysis score plot of the metabolome, acquired in negative mode, of cecal content (**A**) and plasma (**B**) of rats fed ST (♦), WD (●), WD+low-RE (□), or WD+high-RE (Δ), over 46 days. ST, standard diet; WD, Western-style diet; WD+low-RE, WD supplemented with a low concentration of rosemary extract; WD+high-RE, WD supplemented with a high concentration of rosemary extract.

In plasma, many RE-derived metabolites, including carnosol, carnosic acid, and rosmadial, were found in WD+low-RE- and WD+high-RE-treated rats, with a clear positive correlation to concentration in the diets (Figure S6, Tables S4 and S5). Furthermore, lysophosphatidylcholines comprised a major part of the metabolites differing in the plasma metabolome of rats fed the experimental diets.

3.9. Short-Chain Fatty Acids

ST-fed rats had significantly ($p < 0.0001$) more content in the caecum than rats fed WD, who on the other hand had less cecal content than rats fed WD supplemented with RE (Table 2). The total amount of carboxylic acids in the caecum was significantly higher ($p < 0.0001$) in ST-treated rats compared to treatment with WD, WD+low-RE, and WD+high-RE. The same trend was seen in the pool size of acetic, propionic, and butyric acid. In contrast, the pool size of succinic acid was significantly lower in ST- and WD-treated rats compared to treatment with WD+low-RE and WD+high-RE.

Table 2. Weight of cecal content and pool size of total and individual carboxylic acids in caecum content in rats fed a standard diet (ST), Western-style diet (WD), or a WD supplemented with either low (low-RE) or high (high-RE) concentrations of rosemary extract, measured at day 46. $n = 8$. Mean values with 95% confidence intervals.

	ST	WD	WD+Low-RE	WD+High-RE	*p*-Value
Cecal content (g)	4.64 [a] [3.69–5.83]	1.79 [c] [1.42–2.25]	2.44 [b] [1.94–3.07]	2.62 [b] [2.01–3.41]	<0.0001
Carboxylic acids, pool size (μmol)					
Total carboxylic acids	555 [a] [445–692]	84 [c] [67–104]	125 [b] [100–155]	128 [b] [96–169]	<0.0001
Acetic acid	302 [a] [241–379]	52.3 [b] [41.7–65.5]	69.0 [b] [55.1–86.5]	69.5 [b] [52.3–92.5]	<0.0001
Propionic acid	58.9 [a] [44.7–77.5]	13.2 [b] [10.0–17.3]	15.5 [b] [11.8–20.4]	12.7 [b] [9.0–18.0]	<0.0001
Butyric acid	165 [a] [128–214]	6.75 [b] [5.21–8.74]	3.15 [c] [2.43–4.08]	1.72 [d] [1.27–2.32]	<0.0001
Succinic acid	4.03 [b] [2.09–7.75]	2.45 [b] [1.41–4.26]	31.6 [a] [18.9–53.1]	21.8 [a] [12.0–39.7]	<0.0001

[a, b, c, d] Mean values within a row with unlike superscript letter were significantly different ($p < 0.05$).

4. Discussion

Over the six-week intervention, we did not observe an effect on body weight after supplementing a Western-style diet high in fat with RE, despite an elevated fasting total GLP-1 concentration, and hence our hypothesis was rejected. In a previous study [10], daily administration of carnosic acid (20 mg/kg BW/day), a polyphenol found in high concentrations in rosemary, to six-week-old mice fed a high-fat diet ad libitum for 14 days was sufficient to reduce weight gain significantly. For comparison, the WD+high-RE rats consumed up to approximately 150 mg RE per kg body weight per day, corresponding to 98 mg of carnosic acid per kg body weight per day. Thus, the lack of effect of the treatment on body weight in the present experiment is not likely to be due to insufficient dosing. Furthermore, adult, obese mice on a high-fat diet supplemented with 200 mg/kg body weight of RE had a significantly lower weight gain after 35 days of treatment compared to those who did not receive RE [38]. The lack of effect on BW observed in the present study may be explained by the choice of animal and strain. In a study with rats with a start weight of approximately 100 g, feeding the rats either a standard chow or a high-fat diet did not induce any diet-related differences in body weight over a period of six weeks in Sprague Dawley rats, while in Long-Evans rats, the animals exposed to a high-fat diet gained significantly more weight [39]. In addition, for outbred Sprague Dawley rats fed a diet high in fat and energy, only about half will develop obesity, while the other half is resistant to diet-induced obesity and will gain weight at the same pace as standard chow-fed controls [40].

We showed that feeding WD+high-RE for six weeks significantly increased fasting total GLP-1 plasma concentrations. This is not supported by our studies on isolated perfused rat small intestine, where intra-luminal or intra-arterial RE infusion did not stimulate the secretion of intestinal GLP-1. However, our previous in vitro studies showed augmented secretion of GLP-1 from STC-1 and HuTu-80 cells when stimulated with RE [12]. The discrepancy between the long-term and acute effects of RE on GLP-1 secretion points towards an adaptive effect of RE, as previously seen for nutritional modulation of GLP-1 secretion [41]. It is well documented that RE is a potent inhibitor of the primary enzyme catalyzing GLP-1 degradation, DPP-4 [42]. Our metabolomics data demonstrated that several RE-derived metabolites, including carnosol, carnosic acid, and rosmadial, were present in plasma which could possibly lead to inhibition of DPP-4 and thereby a higher concentration of active GLP-1. Confirmation of this would require measurement of active GLP-1. We observed a higher proglucagon gene expression after treatment with WD+low-RE and WD+high-RE, but this does not correlate with the increased fasting levels after WD+high-RE only. The expression increased progressively from the proximal duodenum to the distal ileum, which corresponds to the tissue concentrations of GLP-1 in rats [43], in agreement with the distribution of GLP-1-secreting cells.

GLP-1 has been associated with an increased activity of peroxisome proliferator-activated receptor (PPAR)-α, and PPARγ [44] and polyphenols have been shown to modulate PPARα expression when added to high-fat diets [45]. PPARα and PPARγ are both known to downregulate the expression of SCD1 and RETSAT [44,46,47]. Our proteomics data show upregulation of SCD1 in the WD compared to ST, which is in accordance with previous studies, showing that SCD1 activity is upregulated in diets high in saturated fatty acids [48]. Interestingly, this upregulation was significantly lower in WD+high-RE compared to WD. High SCD1 activity is associated with hypertriglyceridemia and reduced levels of HDL cholesterol [49]. Consequently, a reduction in the upregulation of the high-fat diet-induced SCD1 expression by RE may contribute to lower concentrations of TG through SCD1. Our data also show RETSAT to be upregulated by WD, but this protein was no longer significantly upregulated when the rats received RE supplements. In humans, hepatic RETSAT expression correlates with serum TGs and steatosis, and depletion of RETSAT in obese mice lowers hepatic and circulating TGs [50]. Consequently, the effect of RE on RETSAT may contribute to the reduction in TG. Several studies have associated lower expression of SCD1 and RETSAT with a favorable lipid profile in plasma and liver

tissue, such as decreased plasma triglycerides and increased plasma HDL, lower total liver fat, triglycerides, and cholesterol in the liver, and a higher proportion of unsaturated fatty acids in the liver [47,49,51,52]. The levels of MIF in the liver were increased by RE. MIF has a hepatoprotective role in in vivo models of NAFLD [53]. Hence, it is possible that RE contributed to lower hepatic fat accumulation through its upregulation of MIF.

The observed increase in fasting GLP-1 concentrations might cause an increase in fatty acid β-oxidation and a decrease in fatty acid synthesis, resulting in the reduction in relative fat mass in the liver. Animal studies have reported a decrease in hepatic fat accumulation upon treatment with the GLP-1 receptor agonist exenatide [54,55]. It has also been concluded that rats on a high-fat diet treated with exenatide have increased levels of transcripts of factors involved in fatty acid β-oxidation, resulting in a reduction in total hepatic lipid accumulation [56]. Others have found an increased plasma GLP-1 concentration to be associated with a reduction in mRNA and protein expression of transcription factors required for cholesterol biosynthesis and enzymes that catalyze fatty acid synthesis [57]. Repeating our study protocol in animals deficient in GLP-1 signaling will be required to ultimately test this hypothesis.

Our data showed that rats consuming a high-fat diet for six weeks increased hepatic fat percentage by 2.4-fold, but RE inhibited the accumulation of fat in the liver, resulting in a fat percentage only 1.29-fold higher than ST for WD+high-RE. This finding agrees with that of others who have found polyphenol-rich extracts capable of attenuating steatosis in human and animal models [58,59]. The observations on fat in liver tissue are consistent with our NMR data, where the lipid profile of the liver showed that consumption of a Western-style diet for six weeks resulted in higher levels of cholesterol and triglycerides, and that the present fatty acids were more often saturated fatty acids than in a standard diet. Interestingly, by supplementing the diet with high-RE, the overall lipid profile in the liver shifted to resemble a mix of standard and Western-style diets, with less free and total cholesterol, less triglycerides, and more unsaturated fatty acids than the Western-style diet. This is consistent with previous studies in mice showing that RE can reduce triglyceride levels in the liver by 39% [38]. The rats fed WD supplemented with RE had a relatively increased liver weight. This is most probably associated with the enzyme induction seen due to the xenobiotic metabolism taking place in the liver [60]. This is supported by the increase in several proteins involved in metabolic detoxification pathways, as well as the observed glucuronidation of RE-derived metabolites.

In our study, we did not see any differences in total body fat mass between ST and the other treatments, even though they were based on a high-fat diet. Interestingly, our WD+high-RE treated rats showed decreased levels of plasma triglycerides and increased levels of HDL, demonstrating a positive effect of continuous consumption of rosemary extract. This contradicts the study by Harach et el. [38], where a RE concentration corresponding to half of the concentration in our WD+high-RE did not lower the plasma triglyceride concentration, although hepatic triglyceride concentration was reduced. We observed higher total cholesterol in plasma in rats fed a diet based on high fat but did not see an effect of RE. A meta-analysis that included 750 participants evaluated the effect of polyphenol-rich cinnamon on blood lipid concentrations and concluded that supplementation with this polyphenol source reduced plasma triglycerides and total cholesterol but did not have any effect on LDL and HDL [61]. In another study, 25 healthy participants received a polyphenol-rich pine bark extract for six weeks, resulting in decreased LDL and increased HDL [62].

Our metabolomics data showed that the concentration of numerous putative BA metabolites in cecal content was inversely proportional to the RE concentration. In contrast to the present study, several studies have shown that polyphenols induce increases in BA excretion [63]. In the present study, the excretion of cholic acid, a primary BA, was increased with increasing addition of RE to the diet. However, the excretion of deoxycholic acid, a secondary BA, and numerous putative BA metabolites were decreased with increasing RE in the diet. Dietary fat stimulates the secretion of BA into the intestinal lumen which promotes changes in the microbiota that increases the conversion of primary to secondary

BA [64]. In the present study, this effect was counteracted by the addition of RE which is in agreement with previous studies [65,66], and it has been suggested that polyphenols may regulate the profile and concentration of BA [65] through modulation of the profile of the microflora [67].

Changing the diet from ST to WD and supplementing the high-fat diet with RE caused noticeable changes in the pool of carboxylic acids found in the cecal content, indicating that the microbiota composition was modulated. The considerably lower microbial activity observed when feeding WD is due to the lower content of substrate (dietary fiber) for the microflora in WD. However, the pool of succinic acid increased approximately 10-fold when adding RE to WD and this is in accordance with a previous study showing that the addition of some polyphenols to a high-fat diet increased the concentration of succinic acid in cecal content [68]. It has been shown that RE increases *Prevotella* groups [69], and *Prevotella copri* has been recognized as a succinate producer [70]. Succinate contributes to improved plasma glucose through the activation of intestinal gluconeogenesis [71] and increased glycogen storage in the liver [72], as also seen in our study.

5. Conclusions

We did not observe an increase in body weight or total body fat percentage in young, healthy rats during the experimental period when the animals were fed a high-fat diet. However, the treatment with the high-fat diet-induced dyslipidemia manifested as a higher hepatic fat percentage, higher cholesterol and triglyceride concentrations in the plasma and liver, and higher LDL in plasma which was ameliorated when supplementing 4 g RE per kg feed to the diet. Furthermore, RE increased plasma HDL. Our proteomics data suggest this is accomplished through the upregulation of proteins involved in fatty acid metabolism. Altogether, our study strongly indicates that RE improves the lipid profile in animals before the onset of classical signs of obesity, perhaps associated with an increase in fasting GLP-1 or possibly through the upregulation of PPARα and PPARγ. The study indicates that the effect of RE is exerted both via bioavailable metabolites that exert their effect systemically and through gut microbiota-associated metabotypes.

Supplementary Materials: The following supporting information can be downloaded at: https://www.mdpi.com/article/10.3390/metabo13090974/s1, Supplementary methods; Figure S1: Heat maps of metabolites discriminating between the ST and the WD diet identified and annotated in cecal content of rats and being dominant in the (A) ST diet or (B) WD diet, respectively; Figure S2: Heat maps of metabolites discriminating between the WD and the WD+high-RE diet identified and annotated in caecal content of rats and being dominant in the (A) WD diet or (B) WD+high-RE diet, respectively; Figure S3: Heat maps of metabolites discriminating between the ST and the WD diet identified and annotated in plasma of rats and being dominant in the (a) ST diet or (b) WD diet, respectively; Figure S4: Heat maps of metabolites discriminating between the WD and the WD+high-RE diet identified and annotated in plasma of rats and being dominant in the (a) WD diet or (b) WD+high-RE diet, respectively; Table S1: Ingredient composition and chemical composition1 of standard diet (ST), Western style diet (WD), or a WD supplemented with either low (low-RE) or high (high-RE) concentrations of rosemary extract; Supplementary Table S2. Gene and protein name of quantified proteins involved in metabolic detoxification pathways; Supplementary Table S3. List of metabolic features discriminating between rats fed ST and WD in caecal content; Supplementary Table S4. List of metabolic features discriminating between rats fed WD and WD+high-RE in caecal content; Supplementary Table S5. List of metabolic features discriminating between rats fed ST and WD in plasma; Supplementary Table S6. List of metabolic features discriminating between rats fed WD and WD+high-RE in plasma.

Author Contributions: Conceptualization: S.M., H.M.J. and M.S.H.; Data curation: S.M., C.C.Y., S.Y.B., C.B.-L., C.L. and M.S.H.; Formal analysis: S.M., C.C.Y., S.Y.B. and M.S.H.; Funding acquisition; T.A.K., H.M.J. and M.S.H.; Investigation: S.M. and M.S.H.; Methodology: S.M., C.C.Y., S.Y.B., M.S.H., C.B.-L., J.J.H. and C.L.; Project administration: T.A.K.; Supervision: M.S.H.; Writing—original draft: S.M.; Writing—review & editing: all authors. All authors have read and agreed to the published version of the manuscript.

Funding: This research was funded by Innovation Found Denmark, grant number 5158-00011B.

Institutional Review Board Statement: The study on the 64 intact rats was conducted with permission from the Danish Animal Experiments Inspectorate (2018-15-0201-01454). The study complied with the guidelines of the Danish Ministry of Justice, Act no. 474 af 15 May 2014, concerning the care and use of animals in research as stipulated in the executive order no. 12 of 7 January 2016, and under consideration of the Arrive Guidelines [73]. The intestinal perfusion studies were conducted with permission from the Danish Animal Experiments Inspectorate (Perfusions: 2018-15-0201-01397) and the local ethical committee in accordance with the guidelines of Danish legislation governing animal experimentation (1987) and the National Institutes of Health (publication number 85-23) and the European Convention for the Protection of Vertebrate Animals used for Experimental and other Scientific Purposes (Council of Europe No 123, Strasbourg 1985).

Informed Consent Statement: Not applicable.

Data Availability Statement: None of the data were deposited in an official repository. The data that support the study findings are available from the authors upon request.

Acknowledgments: Karin Kvorning Jensen and Emilie Sommerlund, Department of Animal and Veterinary Sciences, Aarhus University are gratefully acknowledged for rearing and handling of the animals. Kasper V. Poulsen, Anette M. Pedersen, and Thomas Rebsdorf are gratefully acknowledged for their excellent technical assistance.

Conflicts of Interest: The authors declare no conflict of interest.

References

1. Guh, D.P.; Zhang, W.; Bansback, N.; Amarsi, Z.; Birmingham, C.L.; Anis, A.H. The incidence of co-morbidities related to obesity and overweight: A systematic review and meta-analysis. *BMC Public Health* **2009**, *9*, 88. [CrossRef] [PubMed]
2. Williamson, G. The role of polyphenols in modern nutrition. *Nutr. Bull.* **2017**, *42*, 226–235. [CrossRef] [PubMed]
3. Arts, I.C.W.; Hollman, P.C.H. Polyphenols and disease risk in epidemiologic studies. *Am. J. Clin. Nutr.* **2005**, *81*, 317s–325s. [CrossRef]
4. Scalbert, A.; Manach, C.; Morand, C.; Remesy, C.; Jimenez, L. Dietary polyphenols and the prevention of diseases. *Crit. Rev. Food Sci. Nutr.* **2005**, *45*, 287–306. [CrossRef] [PubMed]
5. Panickar, K.S. Effects of dietary polyphenols on neuroregulatory factors and pathways that mediate food intake and energy regulation in obesity. *Mol. Nutr. Food Res.* **2013**, *57*, 34–47. [CrossRef] [PubMed]
6. Gu, Y.Y.; Hurst, W.J.; Stuart, D.A.; Lambert, J.D. Inhibition of Key Digestive Enzymes by Cocoa Extracts and Procyanidins. *J. Agric. Food Chem.* **2011**, *59*, 5305–5311. [CrossRef] [PubMed]
7. Matsui, N.; Ito, R.; Nishimura, E.; Yoshikawa, M.; Kato, M.; Kamei, M.; Shibata, H.; Matsumoto, I.; Abe, K.; Hashizume, S. Ingested cocoa can prevent high-fat diet-induced obesity by regulating the expression of genes for fatty acid metabolism. *Nutrition* **2005**, *21*, 594–601. [CrossRef] [PubMed]
8. Shimoda, H.; Tanaka, J.; Kikuchi, M.; Fukuda, T.; Ito, H.; Hatano, T.; Yoshidao, T. Effect of Polyphenol-Rich Extract from Walnut on Diet-Induced Hypertriglyceridemia in Mice via Enhancement of Fatty Acid Oxidation in the Liver. *J. Agric. Food Chem.* **2009**, *57*, 1786–1792. [CrossRef]
9. Erkan, N.; Ayranci, G.; Ayranci, E. Antioxidant activities of rosemary (*Rosmarinus Officinalis* L.) extract, blackseed (*Nigella sativa* L.) essential oil, carnosic acid, rosmarinic acid and sesamol. *Food Chem.* **2008**, *110*, 76–82. [CrossRef]
10. Ibarra, A.; Cases, J.; Roller, M.; Chiralt-Boix, A.; Coussaert, A.; Ripoll, C. Carnosic acid-rich rosemary (*Rosmarinus officinalis* L.) leaf extract limits weight gain and improves cholesterol levels and glycaemia in mice on a high-fat diet. *Br. J. Nutr.* **2011**, *106*, 1182–1189. [CrossRef]
11. Ninomiya, K.; Matsuda, H.; Shimoda, H.; Nishida, N.; Kasajima, N.; Yoshino, T.; Morikawa, T.; Yoshikawa, M. Carnosic acid, a new class of lipid absorption inhibitor from sage. *Bioorg. Med. Chem. Lett.* **2004**, *14*, 1943–1946. [CrossRef] [PubMed]
12. Yue, Y.; Madsen, S.; Hedemann, M.S.; Knudsen, K.E.B.; Sparsø, F.V.; Laursen, A.; Jensen, H.M.; Knudsen, T.A.; Purup, S. Effect of food ingredients on glucagon-like peptide-1 secretion in STC-1 and HuTu-80 cells. *Int. J. Food Sci. Technol.* **2019**, *54*, 3149–3155. [CrossRef]
13. Vilsbøll, T.; Christensen, M.; Junker, A.E.; Knop, F.K.; Gluud, L.L. Effects of glucagon-like peptide-1 receptor agonists on weight loss: Systematic review and meta-analyses of randomised controlled trials. *BMJ* **2012**, *344*, d7771. [CrossRef] [PubMed]
14. Gribble, F.M.; Reimann, F. Metabolic Messengers: Glucagon-like peptide 1. *Nat. Metab.* **2021**, *3*, 142–148. [CrossRef] [PubMed]
15. Knauf, C.; Cani, P.D.; Perrin, C.; Iglesias, M.A.; Maury, J.F.; Bernard, E.; Benhamed, F.; Gremeaux, T.; Drucker, D.J.; Kahn, C.R.; et al. Brain glucagon-like peptide-1 increases insulin secretion and muscle insulin resistance to favor hepatic glycogen storage. *J. Clin. Investig.* **2005**, *115*, 3554–3563. [CrossRef] [PubMed]
16. Green, C.J.; Henriksen, T.I.; Pedersen, B.K.; Solomon, T.P.J. Glucagon like peptide-1-induced glucose metabolism in differentiated human muscle satellite cells is attenuated by hyperglycemia. *PLoS ONE* **2012**, *7*, e44284. [CrossRef] [PubMed]

17. Farr, S.; Taher, J.; Adeli, K. Glucagon-like peptide-1 as a key regulator of lipid and lipoprotein metabolism in fasting and postprandial states. *Cardiovasc. Hematol. Disord. Drug Targets* **2014**, *14*, 126–136. [CrossRef] [PubMed]
18. Howard, B.V.; Ruotolo, G.; Robbins, D.C. Obesity and dyslipidemia. *Endocrinol. Metab. Clin. North Am.* **2003**, *32*, 855–867. [CrossRef]
19. Fabbrini, E.; Sullivan, S.; Klein, S. Obesity and nonalcoholic fatty liver disease: Biochemical, metabolic, and clinical implications. *Hepatology* **2010**, *51*, 679–689. [CrossRef]
20. Abenavoli, L.; Larussa, T.; Corea, A.; Procopio, A.C.; Boccuto, L.; Dallio, M.; Federico, A.; Luzza, F. Dietary Polyphenols and Non-Alcoholic Fatty Liver Disease. *Nutrients* **2021**, *13*, 494. [CrossRef]
21. Wang, Z.; Zeng, M.; Wang, Z.; Qin, F.; Chen, J.; He, Z. Dietary Polyphenols to Combat Nonalcoholic Fatty Liver Disease via the Gut–Brain–Liver Axis: A Review of Possible Mechanisms. *J. Agric. Food Chem.* **2021**, *69*, 3585–3600. [CrossRef] [PubMed]
22. Zhao, Y.; Sedighi, R.; Wang, P.; Chen, H.; Zhu, Y.; Sang, S. Carnosic Acid as a Major Bioactive Component in Rosemary Extract Ameliorates High-Fat-Diet-Induced Obesity and Metabolic Syndrome in Mice. *J. Agric. Food Chem.* **2015**, *63*, 4843–4852. [CrossRef] [PubMed]
23. Hedemann, M.S.; Hermansen, K.; Pedersen, S.; Bach Knudsen, K.E. Resistant Starch but Not Enzymatically Modified Waxy Maize Delays Development of Diabetes in Zucker Diabetic Fatty Rats. *J. Nutr.* **2017**, *147*, 825–834. [CrossRef] [PubMed]
24. Kuhre, R.E.; Frost, C.R.; Svendsen, B.; Holst, J.J. Molecular Mechanisms of Glucose-Stimulated GLP-1 Secretion From Perfused Rat Small Intestine. *Diabetes* **2015**, *64*, 370–382. [CrossRef] [PubMed]
25. Kuhre, R.E.; Holst, J.J. Mechanisms Underlying Gut Hormone Secretion Using the Isolated Perfused Rat Small Intestine. *J. Vis. Exp.* **2019**, *144*, e58533. [CrossRef]
26. Ørskov, C.; Rabenhøj, L.; Wettergren, A.; Kofod, H.; Holst, J.J. Tissue and plasma concentrations of amidated and glycine-extended glucagon-like peptide I in humans. *Diabetes* **1994**, *43*, 535–539. [CrossRef] [PubMed]
27. Zougman, A.; Selby, P.J.; Banks, R.E. Suspension trapping (STrap) sample preparation method for bottom-up proteomics analysis. *Proteomics* **2014**, *14*, 1006-1000. [CrossRef]
28. Käll, L.; Canterbury, J.D.; Weston, J.; Noble, W.S.; MacCoss, M.J. Semi-supervised learning for peptide identification from shotgun proteomics datasets. *Nat. Methods* **2007**, *4*, 923–925. [CrossRef]
29. Silva, J.C.; Gorenstein, M.V.; Li, G.-Z.; Vissers, J.P.C.; Geromanos, S.J. Absolute Quantification of Proteins by LCMSE: A Virtue of Parallel ms Acquisition *S. *Mol. Cell. Proteom.* **2006**, *5*, 144–156. [CrossRef]
30. Yde, C.C.; Clausen, M.R.; Ditlev, D.B.; Lillefosse, H.; Madsen, L.; Kristiansen, K.; Liaset, B.; Bertram, H.C. Multi-block PCA and multi-compartmental study of the metabolic responses to intake of hydrolysed versus intact casein in C57BL/6J mice by NMR-based metabolomics. *Metabolomics* **2014**, *10*, 938–949. [CrossRef]
31. Fathi, F.; Brun, A.; Rott, K.H.; Falco Cobra, P.; Tonelli, M.; Eghbalnia, H.R.; Caviedes-Vidal, E.; Karasov, W.H.; Markley, J.L. NMR-Based Identification of Metabolites in Polar and Non-Polar Extracts of Avian Liver. *Metabolites* **2017**, *7*, 61. [CrossRef] [PubMed]
32. Wang, K.-C.; Wang, S.-Y.; Kuo, C.-h.; Tseng, Y.J. Distribution-Based Classification Method for Baseline Correction of Metabolomic 1D Proton Nuclear Magnetic Resonance Spectra. *Anal. Chem.* **2013**, *85*, 1231–1239. [CrossRef] [PubMed]
33. Savorani, F.; Tomasi, G.; Engelsen, S.B. icoshift: A versatile tool for the rapid alignment of 1D NMR spectra. *J. Magn. Reson.* **2010**, *202*, 190–202. [CrossRef] [PubMed]
34. Sousa, S.A.A.; Magalhães, A.; Ferreira, M.M.C. Optimized bucketing for NMR spectra: Three case studies. *Chemom. Intell. Lab. Syst.* **2013**, *122*, 93–102. [CrossRef]
35. Curtasu, M.V.; Tafintseva, V.; Bendiks, Z.A.; Marco, M.L.; Kohler, A.; Xu, Y.; Nørskov, N.P.; Nygaard Lærke, H.; Bach Knudsen, K.E.; Hedemann, M.S. Obesity-Related Metabolome and Gut Microbiota Profiles of Juvenile Göttingen Minipigs—Long-Term Intake of Fructose and Resistant Starch. *Metabolites* **2020**, *10*, 456. [CrossRef]
36. Curtasu, M.V.; Knudsen, K.E.B.; Callesen, H.; Purup, S.; Stagsted, J.; Hedemann, M.S. Obesity Development in a Miniature Yucatan Pig Model: A Multi-compartmental Metabolomics Study on Cloned and Normal Pigs Fed Restricted or Ad Libitum High-Energy Diets. *J. Proteome Res.* **2019**, *18*, 30–47. [CrossRef] [PubMed]
37. Jensen, M.T.; Cox, R.P.; Jensen, B.B. Microbial-Production of Skatole in the Hind Gut of Pigs Given Different Diets and Its Relation to Skatole Deposition in Backfat. *Anim. Sci.* **1995**, *61*, 293–304. [CrossRef]
38. Harach, T.; Aprikian, O.; Monnard, I.; Moulin, J.; Membrez, M.; Beolor, J.C.; Raab, T.; Mace, K.; Darimont, C. Rosemary (*Rosmarinus officinalis* L.) Leaf Extract Limits Weight Gain and Liver Steatosis in Mice Fed a High-Fat Diet. *Planta Med.* **2010**, *76*, 566–571. [CrossRef]
39. Song, Z.B.; Xie, W.R.; Chen, S.S.; Strong, J.A.; Print, M.S.; Wang, J.I.; Shareef, A.F.; Ulrich-Lai, Y.M.; Zhang, J.M. High-fat diet increases pain behaviors in rats with or without obesity. *Sci. Rep.* **2017**, *7*, 10350. [CrossRef]
40. Levin, B.E.; DunnMeynell, A.A.; Balkan, B.; Keesey, R.E. Selective breeding for diet-induced obesity and resistance in Sprague-Dawley rats. *Am. J. Physiol-Regul. Integr. Comp. Physiol.* **1997**, *273*, R725–R730. [CrossRef]
41. Bodnaruc, A.M.; Prud'homme, D.; Blanchet, R.; Giroux, I. Nutritional modulation of endogenous glucagon-like peptide-1 secretion: A review. *Nutr. Metab.* **2016**, *13*, 92. [CrossRef] [PubMed]
42. Bower, A.M.; Hernandez, L.M.R.; Berhow, M.A.; de Mejia, E.G. Bioactive Compounds from Culinary Herbs Inhibit a Molecular Target for Type 2 Diabetes Management, Dipeptidyl Peptidase IV. *J. Agric. Food Chem.* **2014**, *62*, 6147–6158. [CrossRef] [PubMed]

43. Wewer Albrechtsen, N.J.; Kuhre, R.E.; Toräng, S.; Holst, J.J. The intestinal distribution pattern of appetite- and glucose regulatory peptides in mice, rats and pigs. *BMC Res. Notes* **2016**, *9*, 1–6. [CrossRef] [PubMed]
44. Patel, V.; Joharapurkar, A.; Kshirsagar, S.; Sutariya, B.; Patel, M.; Patel, H.; Pandey, D.; Patel, D.; Bahekar, R.; Jain, M. Central administration of coagonist of GLP-1 and glucagon receptors improves dyslipidemia. *Biomed. Pharmacother.* **2018**, *98*, 364–371. [CrossRef] [PubMed]
45. Domínguez-Avila, J.A.; González-Aguilar, G.A.; Alvarez-Parrilla, E.; De la Rosa, L.A. Modulation of PPAR Expression and Activity in Response to Polyphenolic Compounds in High Fat Diets. *Int. J. Mol. Sci.* **2016**, *17*, 1002. [CrossRef] [PubMed]
46. Yao-Borengasser, A.; Rassouli, N.; Varma, V.; Bodles, A.M.; Rasouli, N.; Unal, R.; Phanavanh, B.; Ranganathan, G.; McGehee, R.E., Jr.; Kern, P.A. Stearoyl-coenzyme A desaturase 1 gene expression increases after pioglitazone treatment and is associated with peroxisomal proliferator-activated receptor-gamma responsiveness. *J. Clin. Endocrinol. Metab.* **2008**, *93*, 4431–4439. [CrossRef] [PubMed]
47. Schupp, M.; Lefterova, M.I.; Janke, J.; Leitner, K.; Cristancho, A.G.; Mullican, S.E.; Qatanani, M.; Szwergold, N.; Steger, D.J.; Curtin, J.C.; et al. Retinol saturase promotes adipogenesis and is downregulated in obesity. *Proc. Natl. Acad. Sci. USA* **2009**, *106*, 1105–1110. [CrossRef] [PubMed]
48. Sampath, H.; Miyazaki, M.; Dobrzyn, A.; Ntambi, J. Stearoyl CoA desaturase-1 mediates the pro-lipogenic effects of dietary saturated fat. *FASEB J.* **2007**, *21*, A109. [CrossRef]
49. Chu, K.; Miyazaki, M.; Man, W.C.; Ntambi, J.M. Stearoyl-coenzyme A desaturase 1 deficiency protects against hypertriglyceridemia and increases plasma high-density lipoprotein cholesterol induced by liver X receptor activation. *Mol. Cell. Biol.* **2006**, *26*, 6786–6798. [CrossRef]
50. Heidenreich, S.; Witte, N.; Weber, P.; Goehring, I.; Tolkachov, A.; von Loeffelholz, C.; Docke, S.; Bauer, M.; Stockmann, M.; Pfeiffer, A.F.H.; et al. Retinol saturase coordinates liver metabolism by regulating ChREBP activity. *Nat. Commun.* **2017**, *8*, 384. [CrossRef]
51. Silbernagel, G.; Kovarova, M.; Cegan, A.; Machann, J.; Schick, F.; Lehmann, R.; Haring, H.U.; Stefan, N.; Schleicher, E.; Fritsche, A.; et al. High hepatic SCD1 activity is associated with low liver fat content in healthy subjects under a lipogenic diet. *J. Clin. Endocrinol. Metab.* **2012**, *97*, E2288–E2292. [CrossRef] [PubMed]
52. Miyazaki, M.; Kim, Y.C.; Gray-Keller, M.P.; Attie, A.D.; Ntambi, J.M. The biosynthesis of hepatic cholesterol esters and triglycerides is impaired in mice with a disruption of the gene for stearoyl-CoA desaturase 1. *J. Biol. Chem.* **2000**, *275*, 30132–30138. [CrossRef] [PubMed]
53. Heinrichs, D.; Berres, M.L.; Coeuru, M.; Knauel, M.; Nellen, A.; Fischer, P.; Philippeit, C.; Bucala, R.; Trautwein, C.; Wasmuth, H.E.; et al. Protective role of macrophage migration inhibitory factor in nonalcoholic steatohepatitis. *FASEB J.* **2014**, *28*, 5136–5147. [CrossRef] [PubMed]
54. Ding, X.K.; Saxena, N.K.; Lin, S.B.; Gupta, N.; Anania, F.A. Exendin-4, a glucagon-like protein-1 (GLP-1) receptor agonist, reverses hepatic steatosis in ob/ob mice. *Hepatology* **2006**, *43*, 173–181. [CrossRef] [PubMed]
55. Trevaskis, J.L.; Griffin, P.S.; Wittmer, C.; Neuschwander-Tetri, B.A.; Brunt, E.M.; Dolman, C.S.; Erickson, M.R.; Napora, J.; Parkes, D.G.; Roth, J.D. Glucagon-like peptide-1 receptor agonism improves metabolic, biochemical, and histopathological indices of nonalcoholic steatohepatitis in mice. *Am. J. Physiol-Gastrointest. Liver Physiol.* **2012**, *302*, G762–G772. [CrossRef] [PubMed]
56. Svegliati-Baroni, G.; Saccomanno, S.; Rychlicki, C.; Agostinelli, L.; De Minicis, S.; Candelaresi, C.; Faraci, G.; Pacetti, D.; Vivarelli, M.; Nicolini, D.; et al. Glucagon-like peptide-1 receptor activation stimulates hepatic lipid oxidation and restores hepatic signalling alteration induced by a high-fat diet in nonalcoholic steatohepatitis. *Liver Int* **2011**, *31*, 1285–1297. [CrossRef] [PubMed]
57. Khound, R.; Taher, J.; Baker, C.; Adeli, K.; Su, Q. GLP-1 Elicits an Intrinsic Gut-Liver Metabolic Signal to Ameliorate Diet-Induced VLDL Overproduction and Insulin Resistance. *Arterioscler. Thromb. Vasc. Biol.* **2017**, *37*, 2252–2259. [CrossRef]
58. Chang, H.C.; Peng, C.H.; Yeh, D.M.; Kao, E.S.; Wang, C.J. Hibiscus sabdariffa extract inhibits obesity and fat accumulation, and improves liver steatosis in humans. *Food Funct.* **2014**, *5*, 734–739. [CrossRef]
59. Gan, L.; Meng, Z.J.; Xiong, R.B.; Guo, J.Q.; Lu, X.C.; Zheng, Z.W.; Deng, Y.P.; Luo, B.D.; Zou, F.; Li, H. Green tea polyphenol epigallocatechin-3-gallate ameliorates insulin resistance in non-alcoholic fatty liver disease mice. *Acta Pharmacol. Sin.* **2015**, *36*, 597–605. [CrossRef]
60. Maronpot, R.R.; Yoshizawa, K.; Nyska, A.; Harada, T.; Flake, G.; Mueller, G.; Singh, B.; Ward, J.M. Hepatic Enzyme Induction: Histopathology. *Toxicol. Pathol.* **2010**, *38*, 776–795. [CrossRef]
61. Maierean, S.M.; Serban, M.C.; Sahebkar, A.; Ursoniu, S.; Serban, A.; Penson, P.; Banach, M.; Meta-anal, L.B.P. The effects of cinnamon supplementation on blood lipid concentrations: A systematic review and meta-analysis. *J. Clin. Lipidol.* **2017**, *11*, 1393–1406. [CrossRef] [PubMed]
62. Devaraj, S.; Vega-Lopez, S.; Kaul, N.; Schonlau, F.; Rohdewald, P.; Jialal, I. Supplementation with a pine bark extract rich in polyphenols increases plasma antioxidant capacity and alters the plasma lipoprotein profile. *Lipids* **2002**, *37*, 931–934. [CrossRef] [PubMed]
63. Chambers, K.F.; Day, P.E.; Aboufarrag, H.T.; Kroon, P.A. Polyphenol Effects on Cholesterol Metabolism via Bile Acid Biosynthesis, CYP7A1: A Review. *Nutrients* **2019**, *11*, 2588. [CrossRef] [PubMed]
64. Ridlon, J.M.; Kang, D.-J.; Hylemon, P.B. Bile salt biotransformations by human intestinal bacteria. *J. Lipid Res.* **2006**, *47*, 241–259. [CrossRef]

65. Fotschki, B.; Juśkiewicz, J.; Jurgoński, A.; Rigby, N.; Sójka, M.; Kołodziejczyk, K.; Mackie, A.; Zduńczyk, Z. Raspberry pomace alters cecal microbial activity and reduces secondary bile acids in rats fed a high-fat diet. *J. Nutr. Biochem.* **2017**, *46*, 13–20. [CrossRef] [PubMed]
66. Holscher, H.D.; Guetterman, H.M.; Swanson, K.S.; An, R.; Matthan, N.R.; Lichtenstein, A.H.; Novotny, J.A.; Baer, D.J. Walnut Consumption Alters the Gastrointestinal Microbiota, Microbially Derived Secondary Bile Acids, and Health Markers in Healthy Adults: A Randomized Controlled Trial. *J. Nutr.* **2018**, *148*, 861–867. [CrossRef] [PubMed]
67. Han, Y.; Haraguchi, T.; Iwanaga, S.; Tomotake, H.; Okazaki, Y.; Mineo, S.; Moriyama, A.; Inoue, J.; Kato, N. Consumption of Some Polyphenols Reduces Fecal Deoxycholic Acid and Lithocholic Acid, the Secondary Bile Acids of Risk Factors of Colon Cancer. *J. Agric. Food Chem.* **2009**, *57*, 8587–8590. [CrossRef]
68. Haraguchi, T.; Kayashima, T.; Okazaki, Y.; Inoue, J.; Mineo, S.; Matsubara, K.; Sakaguchi, E.; Yanaka, N.; Kato, N. Cecal Succinate Elevated by Some Dietary Polyphenols May Inhibit Colon Cancer Cell Proliferation and Angiogenesis. *J. Agric. Food Chem.* **2014**, *62*, 5589–5594. [CrossRef]
69. Romo-Vaquero, M.; Selma, M.-V.; Larrosa, M.; Obiol, M.; García-Villalba, R.; González-Barrio, R.; Issaly, N.; Flanagan, J.; Roller, M.; Tomás-Barberán, F.A.; et al. A rosemary extract rich in carnosic acid selectively modulates caecum microbiota and inhibits β-glucosidase activity, altering fiber and short chain fatty acids fecal excretion in lean and obese female rats. *PLoS ONE* **2014**, *9*, e94687. [CrossRef]
70. Fernández-Veledo, S.; Vendrell, J. Gut microbiota-derived succinate: Friend or foe in human metabolic diseases? *Rev. Endocr. Metab. Disord.* **2019**, *20*, 439–447. [CrossRef]
71. De Vadder, F.; Kovatcheva-Datchary, P.; Zitoun, C.; Duchampt, A.; Bäckhed, F.; Mithieux, G. Microbiota-Produced Succinate Improves Glucose Homeostasis via Intestinal Gluconeogenesis. *Cell Metab.* **2016**, *24*, 151–157. [CrossRef]
72. Kovatcheva-Datchary, P.; Nilsson, A.; Akrami, R.; Lee, Y.S.; De Vadder, F.; Arora, T.; Hallen, A.; Martens, E.; Björck, I.; Bäckhed, F. Dietary Fiber-Induced Improvement in Glucose Metabolism Is Associated with Increased Abundance of Prevotella. *Cell Metab.* **2015**, *22*, 971–982. [CrossRef]
73. Percie du Sert, N.; Ahluwalia, A.; Alam, S.; Avey, M.T.; Baker, M.; Browne, W.J.; Clark, A.; Cuthill, I.C.; Dirnagl, U.; Emerson, M.; et al. Reporting animal research: Explanation and elaboration for the ARRIVE guidelines 2.0. *PLoS Biol.* **2020**, *18*, e3000411. [CrossRef]

Disclaimer/Publisher's Note: The statements, opinions and data contained in all publications are solely those of the individual author(s) and contributor(s) and not of MDPI and/or the editor(s). MDPI and/or the editor(s) disclaim responsibility for any injury to people or property resulting from any ideas, methods, instructions or products referred to in the content.

molecules

MDPI

Article

Novel Quinazoline Derivative Induces Differentiation of Keratinocytes and Enhances Skin Barrier Functions against Th2 Cytokine-Mediated Signaling

Yukyung Park [1,†], Huddar Srigouri [2,†] and Dongwon Kim [1,3,*]

[1] Department of Energy and Biotechnology, Graduate School, Dongseo University, Busan 47011, Republic of Korea
[2] Drug Information Platform Center, Korea Research Institute of Chemical Technology, Daejeon 34114, Republic of Korea; srigouri@krict.re.kr
[3] Department of Bio-Pharmaceutical Engineering, College of Bio-Health Convergence, Dongseo University, Busan 47011, Republic of Korea
* Correspondence: dwkim@dongseo.ac.kr; Tel.: +82-051-320-1972
† These authors contributed equally to this work.

Abstract: Atopic dermatitis (AD) is a common inflammatory skin disease characterized by pruritic lesions and skin barrier dysfunction. In this study, we evaluated the effect of a quinazoline derivative, SH-340, on TSLP expression and signaling in human primary keratinocytes. Our results demonstrated that SH-340 significantly increased factors for differentiation and skin barrier function including KRT1, KRT2, KRT10, IVL, LOR, CLDN1, OVOL1, and FLG, whereas it inhibited TSLP expression in a dose-dependent manner, both at the mRNA and protein levels. Furthermore, SH-340 was found to inhibit the phosphorylation of STAT6, a downstream signaling molecule of IL-4 and IL-13, in keratinocytes. These findings suggest that SH-340 may suppress TSLP expression by inhibiting the IL-4/IL-13-STAT6 signaling pathway. Finally, SH-340 may potentially contribute to both the alleviation of inflammation and the restoration of skin barrier function.

Keywords: atopic dermatitis; quinazoline; filaggrin; TSLP; STAT6

1. Introduction

Quinazolines are a class of heterocyclic compounds that have been extensively studied in the field of medicinal chemistry due to their wide range of biological activities. These compounds have been found to exhibit a variety of pharmacological activities, including anticancer, antimicrobial, and anti-inflammatory activities [1,2]. Previous studies support the biological activities of quinazolines in skin research. Studies have demonstrated that quinazolines show potent anti-inflammatory effects by inhibiting pro-inflammatory cytokines such as tumor necrosis factor-alpha (TNF-α), interleukin (IL)-1 beta, and IL-6 [3]. In addition, quinazolines inhibit the proliferation of skin cells and modulate the immune response in the skin [4,5]. Additionally, quinazolines have shown promising effects in promoting wound healing by stimulating fibroblast proliferation, collagen synthesis, and angiogenesis [6]. Furthermore, quinazolines have shown notable antioxidant activity, effectively scavenging reactive oxygen species (ROS) and protecting skin cells from oxidative stress-induced damage [7]. Some quinazoline derivatives have potential antimicrobial effects against common skin pathogens including *Staphylococcus aureus* [5,8]. Collectively, these findings highlight the significant potential of quinazolines in various aspects of skin research associated with inflammation modulation, wound healing, antioxidant protection, and antimicrobial applications.

Atopic dermatitis (AD) is characterized by chronic inflammation and a defective skin barrier, which allows for the penetration of irritants and allergens [9–11]. In AD patients, the skin barrier is weakened due to defects in the filaggrin (FLG) gene, which

codes for a protein that helps to maintain the structural integrity of the stratum corneum, the outermost layer of the skin [10,12]. Overall, the regulation of the FLG gene involves a complex interplay of signaling mechanisms, transcription factors, cytokines, and genetic variations [11–13]. Accumulating evidence strongly supports that T help type 2 (Th2)-mediated cytokines (IL-4 and IL-13) have been implicated in the regulation of FLG gene expression by activating JAK (Janus kinase)-STAT signaling pathway [10]. Thus, current therapeutic strategies for AD aim to restore and maintain skin barrier function by inducing FLG expression, as well as reducing inflammation and pruritus. JAK inhibitors work by blocking the activity of JAKs, which leads to the activation of immune cells and the production of pro-inflammatory cytokines.

Several JAK inhibitors are currently being investigated for the treatment of AD, including baricitinib, upadacitinib, and abrocitinib [14,15]. Clinical studies have demonstrated that these JAK inhibitors can improve the signs and symptoms of AD, including reducing itching, redness, and skin lesions [16,17]. Recently, a quinazoline derivative called JTE-052 (delgocitinib) has been shown to reduce inflammation and improve skin barrier function in a mouse model of atopic dermatitis [18]. JTE-052 was found to inhibit the production of pro-inflammatory cytokines and chemokines such as TNF-α, IL-1β, IL-6, and CCL17 in the skin. It also decreased the infiltration of inflammatory cells such as eosinophils and mast cells into the skin. In addition, JTE-052 was found to increase the expression of proteins that are involved in maintaining the integrity of the skin barrier, such as loricrin (LOR), involucrin (IVL), and FLG.

Despite the existence of a quinazoline-based drug for AD, the development of new quinazoline derivatives with improved efficacy and fewer side effects is required to enhance the existing treatments for AD. Given the limited efficacy of current treatments for atopic dermatitis, we wanted to explore novel compounds to develop more effective and targeted therapies. Here, we synthesized a quinazoline derivative SH-340, the synthesis method is shown in Figure 1, refs. [19–23] N-(3-chloro-4-fluorophenyl)-7-((4-methyl piperazin-1-yl)methyl)-7,8-dihydro [1,4]dioxino [2,3-g]quinazolin-4-amine), and investigated biological activities in human primary keratinocytes using in vitro AD model.

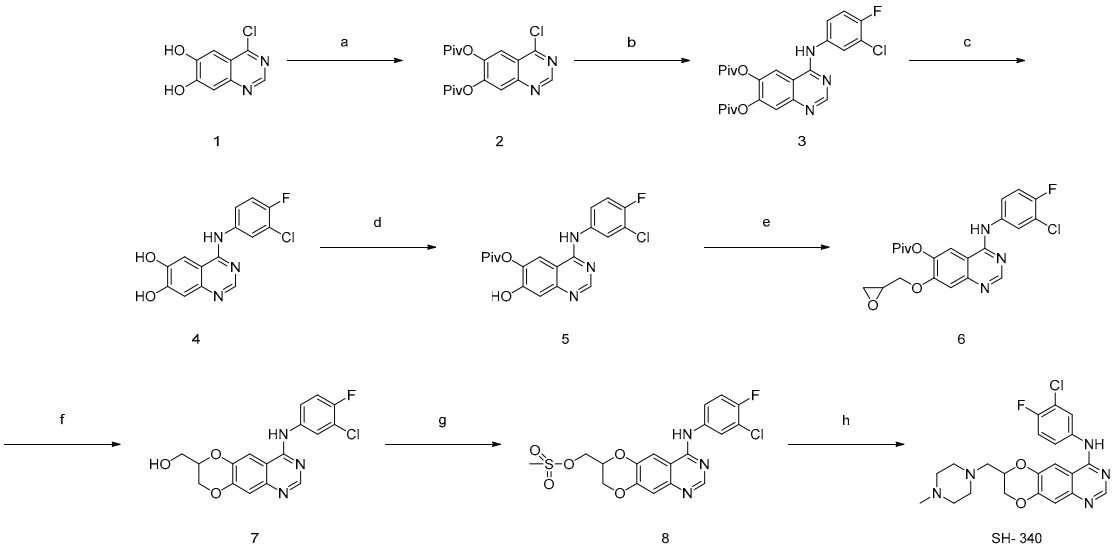


Figure 1. Chemical structure and synthesis of SH-340. 1. Reagents and condition: (**a**) Piv-Cl, TEA, DCM, −10 °C to r.t; (**b**) 3-chloro-4-fluoroaniline, IPA reflux 12 h; (**c**) 7N NH_3 in MeOH, 0–23 °C 12 h; (**d**) Piv-Cl, Et_3N, THF −40 °C 2 h, (regioselective acylation gives 5 major product) (**e**) oxiran-2-ylmethyl 4-nitrobenzenesulfonate, K_2CO_3, DMF, 0 °C-rt, 12 h; (**f**) K_2CO_3, MeOH 12 h, rt; (**g**) Et_3N, MsCl, THF 0–23 °C, 16 h; and (**h**) 1-methylpiperazine, Et_3N, DMF 85 °C 24 h.

2. Results

2.1. Synthesis and Functionalization of Novel Quinazoline Compound SH-340 via Multi-Step Reactions

Commercially purchased diol (1) was subsequently protected with pivaloyl groups. We found that the use of pivaloyl groups over acetyl-protecting groups was essential in aiding the purification of the subsequent chloride (2), and the substitution of aromatic halides with nitrogen nucleophiles, 3-chloro-2-fluoroaniline, was achieved in excellent yield in i-PrOH at reflux. Deprotection of (3) via ammonolysis afforded the stable diol (4), Finally, regioselective protection of (5) was achieved using pivaloyl chloride in the presence of TEA at −40 °C to afford the key intermediate, and its regiochemistry was discussed in chemical synthesis 4.5; compound (5) was treated with oxiran-2-yl-methyl-3-nitrobenzenesulfonate to give corresponding epoxide (6), which transforms the ring opening of epoxides, leads to cyclization, and gives free hydroxy group (7); mesylation of the resultant free hydroxy group with MsCl/TEA gives (8); and subsequent displacement of mesylate with 1-methylpiperazine affords desired novel quinazoline compound SH-340.

2.2. SH-340 Inhibits Proliferation of Keratinocytes

To determine the appropriate concentration of primary keratinocytes, we initially checked the cytotoxicity of SH-340 (Figure 2) at different concentrations. Cell viability results show that SH-340 has significant cytotoxicity from 0.5 to 25 μM (Figure 2C). Although keratinocytes cultured in keratinocyte growth media (KGM) maintain their stemness, they are allowed to differentiate in the basal media (KBM) without growth factors. When normal human epidermal keratinocytes (NHEKs) were treated with SH-340, we found that their growth is slow and the morphology shows a differentiated cell type with the increased cell size (Figure 2A,B). Given that the cytotoxicity assay measures the metabolic activities of mitochondria, our results indicate that SH-340 may inhibit proliferation and induce differentiation.

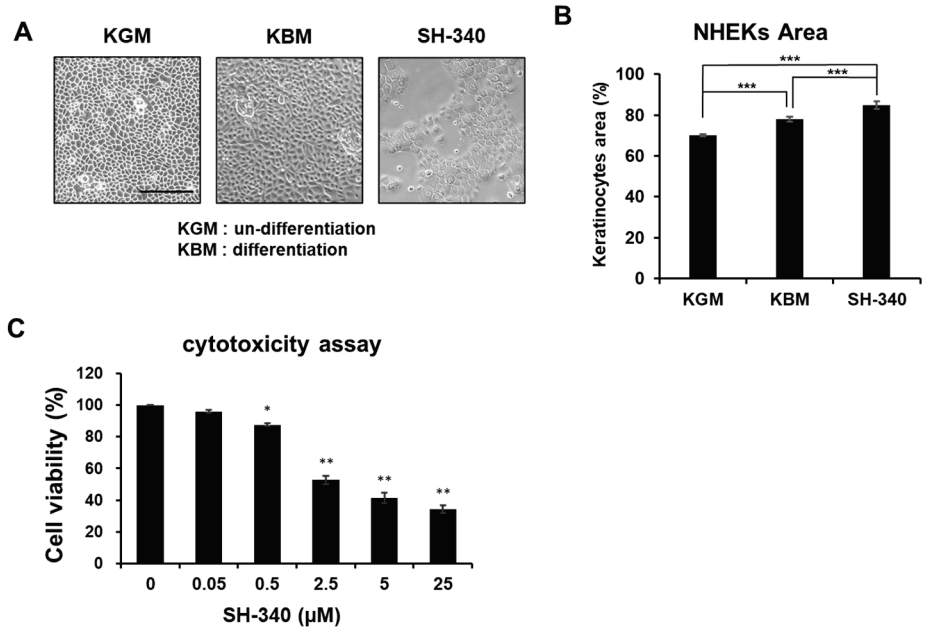


Figure 2. SH-340 inhibits the proliferation of keratinocytes. The morphology (**A**) and quantified cell area (**B**) of keratinocytes cultured in KGM, KBM, and KBM+SH-340 (0.5 μM). (**C**) Cell viability at different concentrations of SH-340. KGM indicates undifferentiated keratinocytes cultured in keratinocyte growth media, and KBM indicates differentiated keratinocytes cultured in keratinocyte basal media without growth factors. Scale bar: 250 μm. DMSO 1%: apoptotic positive control. (n = 3, *** $p < 0.001$, ** $p < 0.01$, * $p < 0.05$).

2.3. SH-340 Induces Differentiation of Keratinocytes

To examine whether SH-340 stimulates the differentiation of keratinocytes, we checked differentiated markers in NHEKs. NHEKs treated with SH-340 (0.5 μM) show remarkably increased gene expression of differentiation markers such as KRT1, KRT2, KRT2, and Ovo Like Transcriptional Repressor 1 (OVOL1) (Figure 3A). We also checked the expression of IVL, LOR, and Cloudin1 (CLDN1), and FLG is increased by SH-340 (Figure 2A). We confirmed that the protein expression of KRT1, KRT10, and FLG is increased in a dose-dependent manner in NHEK treated with SH-340 (Figure 3B). These results suggest that SH-340 is a potent material that can improve skin barrier function by effectively inducing NHEK differentiation.

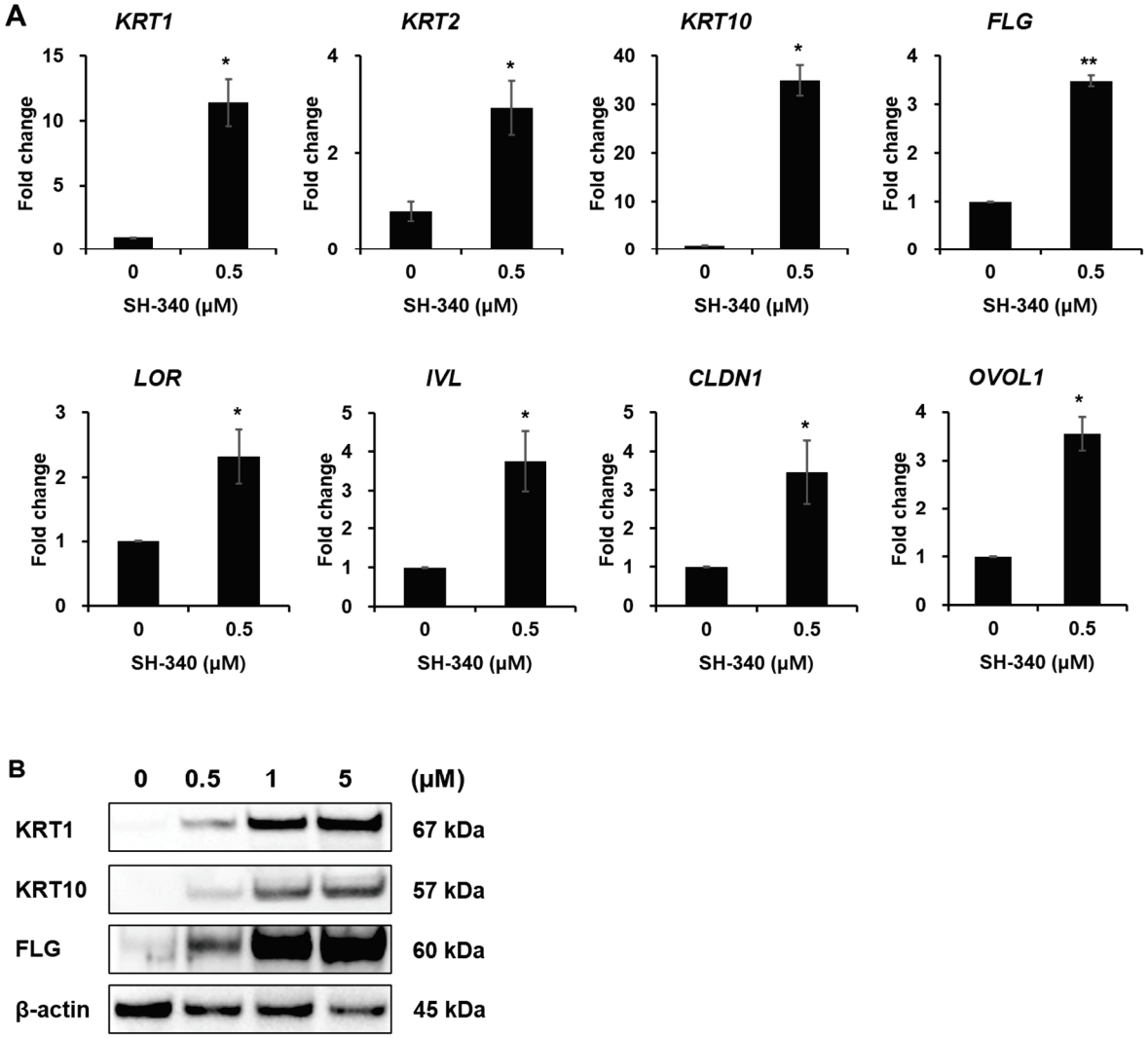


Figure 3. SH-340 induces the differentiation of keratinocytes. (**A**) Quantified real-time PCR results of gene expression for keratinocyte differentiation. (**B**) Western blot analysis of KRT1, KRT10, and FLG in keratinocytes treated with different concentrations of SH-340. β-actin was used as a loading control (n = 4–5, ** $p < 0.01$, * $p < 0.05$).

2.4. SH-340 Inhibits IL-4/IL-13-Induced STAT6 Signaling

AD is characterized by overexpression of Th2 cytokines interleukin-4 (IL-4) and IL-13, which leads to defective keratinocyte differentiation [24]. Strong research evidence proved that Th2-mediated IL-4/IL-13 inhibits gene expression of FLG by activating the JAK-STAT pathway, resulting in disruption of the skin barrier [14,25]. Thus, we attempted to verify if SH-340 regulates the IL-4/IL-13-induced signaling pathway. We identified that SH-340 induces KRT1, KRT10, and FLG protein expression (Figure 4A). Moreover, SH-340

significantly restores their expression in the presence of IL-4/IL-13 (Figure 4A). Moreover, SH-340 showed a 45% inhibition of IL-4/IL-13-induced STAT6 phosphorylation in NHEKs (Figure 4B,C). Thus, these results indicate that SH-340 has the potential to counteract the negative effects of IL-4 and IL-13 on keratinocyte differentiation and skin barrier function.

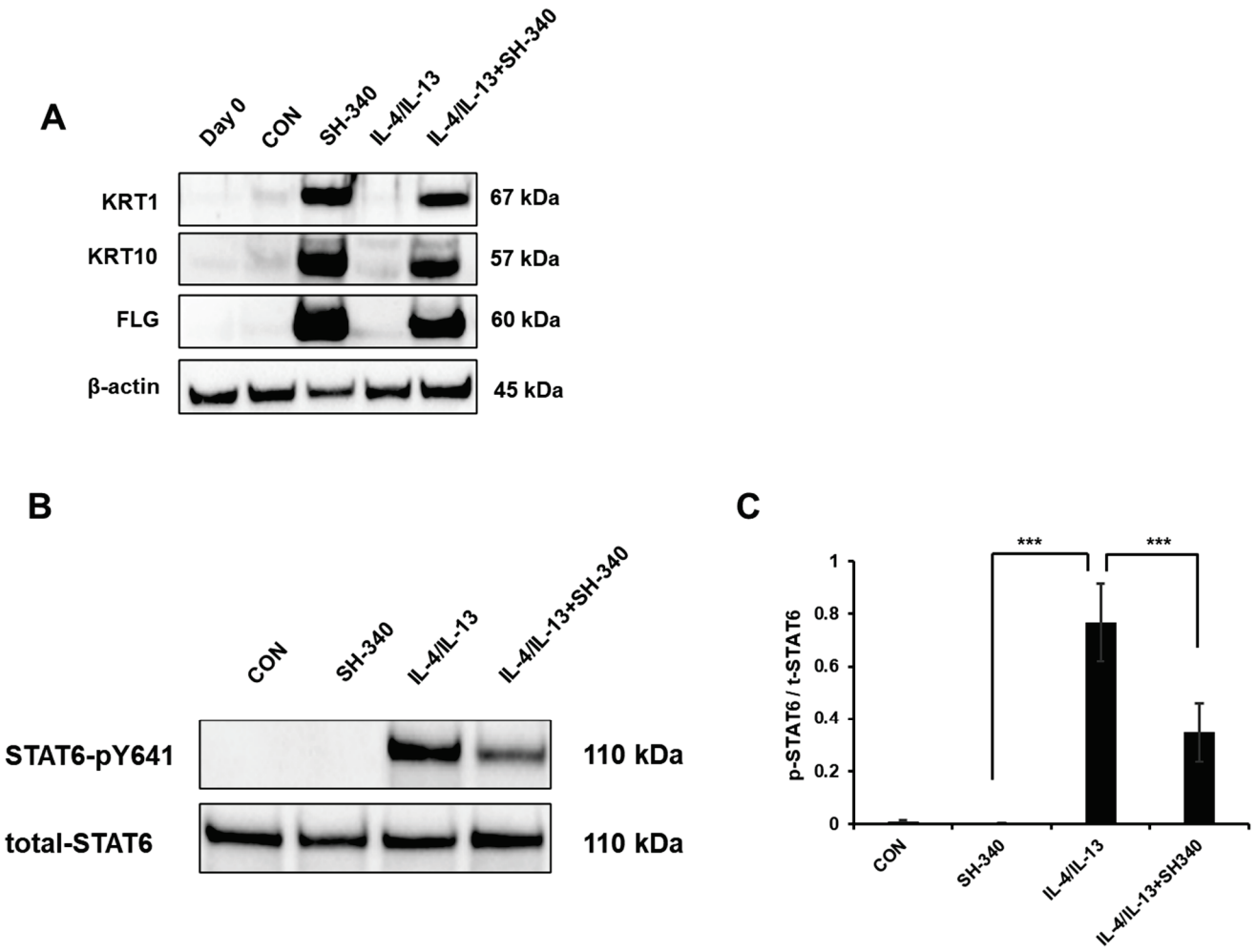


Figure 4. SH-340 inhibits Th2 cytokine-mediated signaling. (**A**) SH-340 restores KRT1, KRT10, and FLG expression in keratinocytes with IL-4 and IL-13. (**B**) Analysis of STAT6 phosphorylation in keratinocytes. SH-340 inhibits and significantly inhibits STAT6 phosphorylation induced by IL-4 and IL-13. (**C**) Quantified results of STAT6 phosphorylation ($n = 6$, *** $p < 0.001$).

2.5. SH-340 Inhibits TSLP Expression in NHEK

The presence of IL-4 and IL-13 in skin lesions of atopic dermatitis is associated with the stimulation of thymic stromal lymphopoietin (TSLP) production in keratinocytes upon exposure to external substances [26]. Previous studies demonstrated that toll-like receptor 3 (TLR3) activation induces the expression of TSLP in human keratinocytes [27]. In addition, damaged tissues release non-coding double-stranded RNAs (dsRNAs) to activate TLR3, resulting in enhanced wound healing and tissue regeneration [28,29]. Given the repeated scratching that occurs in the skin of patients with AD, we were interested in investigating whether exposure of keratinocytes to a synthetic dsRNA (polyinosinic-polycytidylic acid; poly I:C), IL-4, and IL-13 can lead to the production of TSLP. Compared to the control group, poly I:C induced TSLP expression in keratinocytes (Figure 5). Moreover, keratinocytes exposed to poly I:C, IL-4, and IL-13 produce TSLP more than poly I:C alone (Figure 5). However, SH-340 significantly suppressed TSLP production in keratinocytes treated with poly I:C, IL-4, and IL-13 (Figure 5), suggesting that SH-340 may have the potential to alleviate pruritus caused by AD.

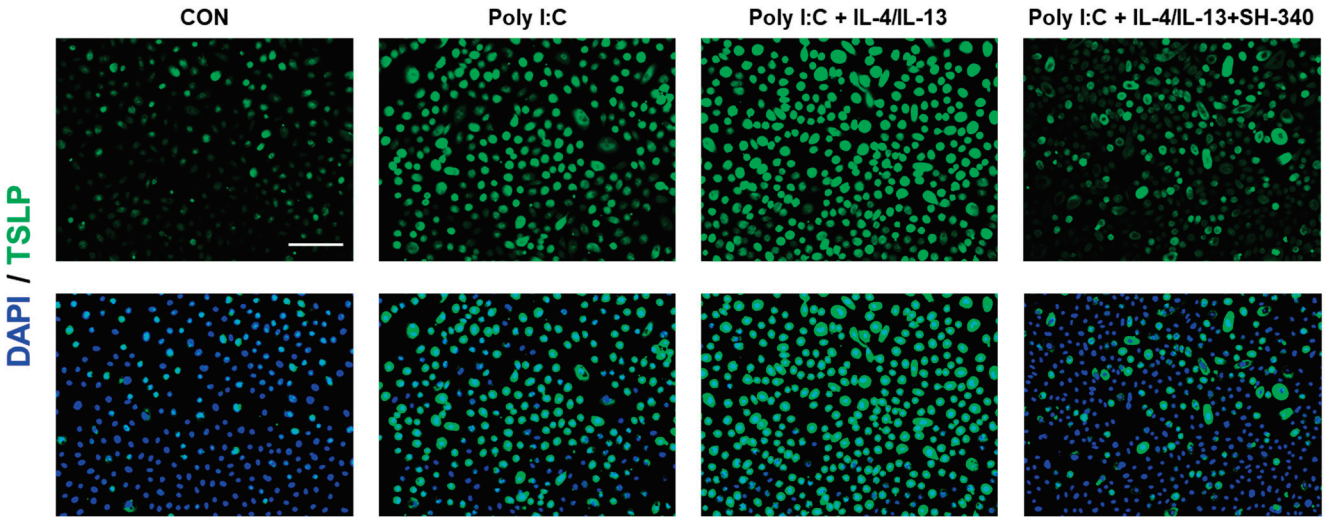


Figure 5. SH-340 inhibits TSLP expression induced by poly I:C or poly I:C with IL-4/IL-13 treatment. Green indicates TSLP-positive keratinocytes. Blue indicates nuclear counterstaining. The scale bar is 125 μm (n = 3).

3. Discussion

Quinazoline derivatives have been studied and used in various research areas, including cancer research, neuropharmacology, inflammatory diseases, and infectious diseases. Especially, JTE-052 is a quinazoline-based drug currently being studied for the treatment of inflammatory skin diseases such as AD [18]. JTE-052 is a potent JAK inhibitor, which has been extensively studied in the context of various inflammatory disorders. Despite the existence of a few quinazoline-based drugs for AD, there are some significant reasons why we still need to study and develop quinazoline derivatives, for example, limited efficacy or safety concerns. Thus, studying and understanding the mechanisms of action of quinazoline derivatives could help researchers identify new targets and develop novel treatments for various diseases. Here, we investigated a new quinazoline molecule, SH-340, to demonstrate its potential as a therapeutic agent for AD. First, SH-340 at 0.5 μM inhibits proliferation and induces differentiation, although a high concentration of SH-340 (from 2.5 μM) showed cytotoxicity. When keratinocytes transition from basal cells to more differentiated cells, they normally change morphology, gene expression, and protein production [30,31]. The increase in cell size during keratinocyte differentiation is accompanied by the synthesis and deposition of structural proteins, which contribute to the development of a protective skin barrier. SH-340 inhibits proliferation and increases cell size, which indicates that keratinocytes may undergo a differentiation process in the presence of SH-340. We also confirmed this by analyzing differentiation factors and found that SH-340 induces keratinocyte differentiation by increasing the gene expression for initial and terminal differentiation and skin barrier functions. Second, SH-340 inhibits IL-4/IL-13-induced STAT6 signaling, which plays a key role in the pathogenesis of AD. Third, we found that SH-340 inhibits TSLP expression in NHEK, suggesting that it may attenuate the symptoms of AD by reducing the activation of dendritic cells and Th2 cells.

The potent inhibition of TSLP by SH-340 represents a significant breakthrough in immunological and therapeutic research. Since TSLP plays a pivotal role in initiating and perpetuating allergic responses, it can be a crucial target for allergic diseases such as asthma, eczema, and allergic rhinitis. The discovery that SH-340 can effectively inhibit TSLP opens up new avenues for designing innovative treatments that could attenuate allergic reactions. From a scientific standpoint, this finding deepens our comprehension of the intricate pathways underlying allergic responses, potentially paving the way for further insights into immunomodulation strategies. Clinically, SH-340's ability to suppress TSLP suggests a potential breakthrough in treating a range of allergic diseases, offering a novel

therapeutic angle that could complement or even surpass existing approaches. Although JTE-052's JAK inhibitory activity positions it as a promising therapeutic agent in various inflammatory conditions, by targeting JAKs, key mediators of cytokine signaling, JTE-052 broadly affects multiple cytokine pathways, leading to the suppression of a wide range of inflammatory responses. However, when considering its impact on TSLP, the downstream consequences of JAK inhibition need to be evaluated. While TSLP expression is influenced by JAK-STAT signaling, JTE-052 has not been studied to demonstrate its effect on TSLP inhibition. Thus, the specific regulation of the IL-4/IL-13-STAT6 pathway by SH-340 offers a targeted approach to addressing TSLP-associated inflammation. By focusing on this specific pathway, SH-340′s inhibition of TSLP expression represents a precise strategy for curbing the initial triggers of AD. This targeted approach not only reduces the risk of unintended downstream effects on unrelated cytokine networks but also highlights the importance of TSLP in the context of AD. Furthermore, as TSLP influences autoimmune diseases and certain skin conditions, SH-340 might hold promise in addressing these disorders. Moreover, the compound's mechanism of action could be harnessed for enhancing the efficacy of cancer immunotherapies by modulating immune responses. This versatility positions SH-340 as a versatile tool for exploring new therapeutic directions across diverse medical fields, making it a significant asset in drug development and clinical research.

Taken together, our results suggest that SH-340 has potential as a novel therapeutic agent for the treatment of AD. By targeting keratinocyte differentiation, skin barrier functions, and TSLP expression, SH-340 may offer a multi-faceted approach to the treatment of AD, which could address both the inflammatory and barrier dysfunction aspects of the disease. Despite these results, the effect of SH-340 on enhancing skin barrier function is reported for the first time in this study, and the exact mechanism is not yet known. Therefore, further studies are needed to fully elucidate the mechanism of action of SH-340 and to evaluate its efficacy and safety in vivo.

4. Materials and Methods

4.1. Chemical Synthesis

General methods reagents, solvents, and starting products were acquired from commercial sources. When indicated, the reaction products were purified by "flash" chromatography on silica gel (35–70 μm) with the indicated solvent system. HRMS analysis was conducted in EI mode, 70 eV, resolution 5000 using a JEOL JMS-700 high-resolution mass spectrometer (MS), LC-Ms were analyzed by ESI^+ represented as m/z $(M + H)^+$, NMR spectra were recorded in $CDCl_3$ at 300 MHz, 400 MHz, 500 MHz (1H), and 101 MHz (13C), and chemical shifts are reported in δ values downfield from TMS or relative to residual chloroform (7.26 ppm, 77.0 ppm) or residual DMSO (2.50 ppm) as an internal standard. Data are reported in the following manner: chemical shift, multiplicity, coupling constant (J) in hertz (Hz), and integrated intensity and assignment (when possible). Multiplicities are reported using the following abbreviations: s, singlet; d, doublet; dd, doublet of doublets; t, triplet; q, quadruplet; m, multiplet; br s, broad signal; and app, apparent. Assignments and stereochemical determinations are given only when they are derived from definitive dimensional NMR experiments (g-HSQC) (Supplementary Materials).

*4.2. Synthesis of 4-Chloroquinazoline-6,7-diyl bis(2,2-dimethylpropanoate) (***2***)*

To a stirred suspension of commercially available 4-chloroquinazoline-6,7-diol (2.0 g, 10.17 mmol) and TEA (4.9 mL, 35.59 mmol) in dichloromethane (20 mL), trimethylacetyl chloride (Pivolyl chloride) (2.7 mL, 22.38 mmol) was added dropwise. The resulting suspension was stirred at room temperature for 2 h, distilled of excess DCM, diluted with EtOAc (500 mL), and washed with water (5 × 20 mL). The organic phase was concentrated to dryness and the residue triturated with water, and the resulting precipitate was collected by filtration, washed with water (5 × 20 mL), and dried to a constant weight to afford the title compound (2.6 g, 91%), LCMS: ESI^+ m/z 364.82 $(M + H)^+$, ^1H NMR (300 MHz, Chloroform-*d*) δ 9.05 (s, 1H), 8.06 (s, 1H), 7.91 (s, 1H), 1.43 (d, J = 4.0 Hz, 18H).

*4.3. Synthesis of 4-((3-Chloro-4-fluorophenyl)amino)quinazoline-6,7-diyl bis(2,2-dimethyl propanoate) (**3**)*

A mixture of 4-chloroquinazoline-6,7-diyl bis(2,2-dimethylpropanoate) (1 g, 2.741 mmol) in *i*-PrOH (10.9 mL) was treated with 3-chloro-4-fluoroaniline (1.5 eq) and stirred at 95 °C for 12 h. When TLC showed completion of the reaction, it cooled to room temperature and evaporated to dryness. And the residue was suspended several times in diethyl ether; solidification was done and obtained a pure yellow solid compound after filtration. Obtained yield (1.2 g, 93%) LCMS: ESI$^+$ *m*/*z* 474.5 (M + H)$^+$, ^{1}H NMR (300 MHz, Methanol-d_4) δ 8.89 (s, 1H), 8.64 (s, 1H), 8.00 (dd, *J* = 6.6, 2.6 Hz, 1H), 7.88 (s, 1H), 7.71 (ddd, *J* = 8.9, 4.2, 2.7 Hz, 1H), 7.41 (t, *J* = 8.9 Hz, 1H), 1.44 (d, *J* = 9.0 Hz, 18H).

*4.4. Synthesis of 4-((3-Chloro-4-fluorophenyl)amino)quinazoline-6,7-diol (**4**)*

A stirred slurry of (1.0 g, 2.11 mmol) was treated at 0 °C, with 7 M solution of NH_3 in MeOH (7 mL); the mixture was stirred at 0 °C for 15 min, and then at 23 °C for 4.5 h. The mixture was evaporated, and the residue was suspended in water (40 mL), stirred overnight, and filtered. The residue was washed with water (50 mL), DCM (4 × 50 mL), Et_2O (2 × 50 mL), and dried in a desiccator to afford the title compound (0.587 g, 91%), LCMS: ESI$^+$ *m*/*z* 306.7 (M + H)$^+$, ^{1}H NMR (300 MHz, DMSO-d_6) δ 9.54 (s, 1H), 8.43 (s, 1H), 8.21 (dd, *J* = 6.9, 2.5 Hz, 1H), 7.87–7.72 (m, 1H), 7.41 (t, *J* = 9.1 Hz, 1H), 7.12 (s, 1H).

*4.5. Synthesis of 4-((3-Chloro-4-fluorophenyl)amino)-7-hydroxyquinazolin-6-yl pivalate (**5**)*

A stirred suspension of 4-((3-chloro-4-fluorophenyl)amino)quinazoline-6,7-diol (1.4 g, 4.57 mmol) in DMF (15 mL) was treated with Et_3N (1.9 mL, 13.71 mmol), cooled to −40 °C, and treated dropwise with Piv_2O (0.672 mL, 5.5 mmol). The mixture was stirred at −40 °C for 1 h, after which the cooling bath was removed, and stirring was continued for 2.5 h. The reaction mixture was diluted with DCM (50 mL), washed with 10% citric acid (2 × 10 mL), dried over (Na_2SO_4), filtered, and evaporated flash column (DCM: EtOAc 1:1) to afford solid (beige–yellow solid). Yield obtained (0.510 g, 30%) LCMS: ESI$^+$ *m*/*z* 390.9 (M + H)$^+$, ^{1}H NMR (500 MHz, DMSO-d_6) δ 11.04 (s, 1H), 9.66 (s, 1H), 8.54 (s, 1H), 8.20 (d, *J* = 5.5 Hz, 2H), 7.82 (dq, *J* = 9.7, 3.4, 2.9 Hz, 1H), 7.44 (t, *J* = 9.1 Hz, 1H), 7.18 (s, 1H), 1.38 (s, 9H).

The regiochemistry of the 6-OPiv-7-OH intermediate 6 was determined by NMR experiments. In comparison, to the parent bis-phenol 4, the proton at C-5 shifted 0.5 ppm downfield (as opposed to the C-8 proton which did not move) and a NOE was observed between the C-5 proton and the aniline N–H.

*4.6. Synthesis of 4-((3-Chloro-4-fluorophenyl)amino)-7-(oxiran-2-ylmethoxy)quinazolin-6-yl pivalate (**6**)*

For the synthesis, the following instructions should be followed: Dissolve 4-((3-chloro-4-fluorophenyl)amino)-7-hydroxyquinazolin-6-yl pivalate (0.180 g, 0.461 mmol) in N, N-dimethylformamide (2 mL) then add K_2CO_3 at 0 °C and stir for 10 min, then add oxiran-2-ylmethyl 4-nitrobenzenesulfonate (1.1 eq) and stir at 0 °C, for 30 min more, and bring RM to room temperature; continue stirring for 6 h. When TLC shows completion of the reaction, extract RM with EtOAc (50 mL) and wash with water (3 × 20 mL), then wash with a brine solution to remove excess DMF. This organic phase was concentrated and used in the next step without purification. Obtained yield, 0.140 mg, 68%. LCMS: ESI$^+$ *m*/*z* 446.9 (M + H)$^+$, ^{1}H NMR (400 MHz, Methanol-d_4) δ 8.53 (s, 1H), 8.10 (s, 1H), 8.06 (dd, *J* = 6.7, 2.5 Hz, 1H), 7.69 (dt, *J* = 8.8, 3.3 Hz, 1H), 7.29–7.22 (m, 2H), 4.52 (dd, *J* = 11.2, 2.1 Hz, 1H), 4.00 (dd, *J* = 11.2, 6.6 Hz, 1H), 3.37 (dd, *J* = 6.5, 4.0 Hz, 1H), 2.91 (t, *J* = 4.6 Hz, 1H), 2.78 (dd, *J* = 4.9, 2.6 Hz, 1H), 1.45 (s, 9H).

*4.7. Synthesis of (4-((3-Chloro-4-fluorophenyl)amino)-7,8-dihydro-[1,4]dioxino[2,3-g]quinazolin-7-yl) methanol (**7**)*

For the synthesis, the following instructions should be followed: Dissolve 4-((3-chloro-4-fluorophenyl)amino)-7-(oxiran-2-ylmethoxy)quinazolin-6-yl pivalate (0.230 g, 0.515 mmol) in MeOH (5 mL) then add K_2CO_3 (0.142 g, 1.0 mmol) and stir at rt for 12 h. When TLC

shows completion of the reaction, evaporate RM to dryness, add H_2O, adjust pH to 7 by NH_4Cl, extract RM with EtOAc (50 mL) and wash with water (3 × 20 mL), and evaporate organic layer to dryness. There is no need to purify, by column, it can be directly used for the next step. Obtained yield (140 mg, 75%). LCMS: ESI^+ m/z 362.85 $(M + H)^+$.

*4.8. Synthesis of (4-((3-Chloro-4-fluorophenyl)amino)-7,8-dihydro-[1,4]dioxino[2,3-g]quinazolin-7-yl) methyl methanesulfonate (***8***)*

A solution of (4-((3-chloro-4-fluorophenyl)amino)-7,8-dihydro-[1,4]dioxino[2,3-g] quinazolin-7-yl)methanol (0.160 g, 0.442 mmol) in THF (10 mL) was treated with Et_3N (1.5 eq), cooled to 0 °C, and treated dropwise with MsCl (1.3 eq). The mixture was stirred at rt for 16 h, cooled to 0 °C, treated with $NaHCO_3$ (pH-7), extracted with EtOAc (50 mL), and washed with water (3 × 20 mL). The organic layer was evaporated to dryness. There was no need to purify, by column, it was directly used for the next step. Obtained yield (215 mg, 100%) LCMS: ESI^+ m/z 440.1 $(M + H)^+$.

4.9. Synthesis of N-(3-Chloro-4-fluorophenyl)-7-((4-methylpiperazin-1-yl)methyl)-7,8-dihydro-[1,4]dioxino[2,3-g]quinazolin-4-amine (SH-340)

Nucleophilic substitution of quinazolinyl mesylates with secondary amines: A mixture of quinazolinyl mesylate (150 mg, 0.341 mmol) in DMF (5 mL) was treated with 1-methylpiperazine (<10 eq) and Et_3N (<10 eq), and the mixture was stirred at 85 °C for 24 h; the mixture was cooled to rt, residue was dissolved in EtOAc (50 mL) and washed with water (3 × 20 mL), excess DMF was removed by brine wash, the organic layer evaporated, and purification was conducted by 10% Mc: MeOH. Obtained yield (82 mg, 54%) LCMS: ESI^+ m/z 444.5 $(M + H)^+$ HRMS exact mass observed m/z 443.1523 with int 100%, ^1H NMR (300 MHz, Chloroform-*d*) δ 8.63 (s, 1H), 8.02 (dd, *J* = 6.5, 2.4 Hz, 1H), 7.62–7.54 (m, 1H), 7.48 (s, 1H), 7.35 (s, 1H), 7.15 (t, *J* = 8.8 Hz, 1H), 4.48–4.38 (m, 2H), 4.13 (dd, *J* = 11.7, 8.0 Hz, 1H), 2.73 (ddt, *J* = 24.0, 15.8, 8.3 Hz, 10H), 2.42 (s, 3H). ^{13}C NMR (101 MHz, $CDCl_3$) δ 171.95, 156.27, 153.44, 149.04, 146.45, 143.61, 135.33, 123.77, 121.31, 121.24, 116.68, 116.46, 113.95, 110.14, 106.36, 71.61, 67.05, 62.59, 58.81, 58.14, 55.08, 54.98, 54.67, 53.57, 51.01, 46.02, 45.85, 45.56, 45.18, 41.68, 41.47.

4.10. Culture of Human Keratinocytes

Normal human epidermal keratinocytes (NHEK) were commercially provided from Lonza. NHEKs were grown in KGM media by adding 1 mL of KGM SingleQuots™ supplements to 500 mL of KGM basal medium as per the manufacturer's instructions. One vial of NHEKs frozen stock was thawed in a 37 °C water bath. Once thawed, the cells were transferred to a 15 mL conical tube containing 10 mL of KGM. After centrifugation at 3000 rpm for 5 min, the supernatant was removed and the cell pellet was resuspended in 2 mL of KGM. NHEKs were plated in a sterile culture flask at a density of 2×10^5 cells/cm^2 and incubated in a humidified CO_2 incubator at 37 °C and 5% CO_2. Media was replaced with fresh KGM every other day. Once NHEKs reached about 70–80% confluency, they were split using 0.025% trypsin-EDTA solution for a subculture. For all experiments, cells were used in passages 3–6.

4.11. Cytotoxicity Assay

The cytotoxicity of the extract was evaluated using the Cell Counting Kit-8 (CCK-8, Dojindo, Kumamoto, Japan) assay. Normal human epidermal keratinocytes (NHEK) were seeded at a density of 1×10^4 cells/well in a 96-well plate and cultured for 24 h. After replacing the medium, the cells were treated with various concentrations (1, 2, 5, and 10 μg/mL) of the extract and incubated for 48 h in standard cell culture conditions. Next, the culture medium was supplemented with the CCK-8 solution, and the cells were further incubated for 3 h in a CO_2 incubator. Absorbance readings were taken at 450 nm using an

INNO-M microplate spectrophotometer (LTEK). The cell viability at each concentration was determined using the provided equation.

$$Cell\ Viability\ (\%) = \frac{A_{sample}}{A_{control}} \times 100$$

4.12. RNA Isolation and qRT-PCR

NHEKs were seeded at a concentration of 7×10^4 cells/well in a 12-well plate and incubated for 24 h. After the incubation period, the cells were treated with the extract at a concentration of 1 μg/mL and further incubated for 72 h. Total RNA was extracted from the cells using the Quick-RNA Micro Prep Kit (ZYMO Research, Irvine, CA, USA), following the instructions provided by the manufacturer. The concentration and purity of the isolated RNA were assessed using a Jenway Genova Nano spectrophotometer (Cole-Parmer Ltd., Vernon Hills, IL, USA). For cDNA synthesis, the high-capacity cDNA Kit (ThermoFisher Scientific, Waltham, MA, USA) was utilized, with 1–2 μg of total RNA being used as the starting material for the reaction. For real-time quantitative polymerase chain reaction (qRT-PCR), the synthesized cDNA was prepared using a QuantStudio 3 instrument (Applied Biosystems, Carlsbad, CA, USA) and TaqMan Fast Advanced Master Mix (ThermoFisher Scientific). Specific target probes (ThermoFisher Scientific) were used, including KRT1 (Hs00196158_m1), KRT2 (Hs00166294_m1), KRT9 (Hs00413861_m1), IVL (Hs00846307_s1), FLG (Hs00856927_g1), CLDN1 (Hs00221623_m1), and TSLP (Hs00263639_m1). To normalize the results, the ribosomal protein lateral stalk subunit P0 (RPLP0, Hs00420895) was used as a loading control. The qRT-PCR conditions involved an initial incubation at 50 °C for 5 min, followed by denaturation at 95 °C for 20 s, annealing at 95 °C for 3 s, and extension at 60 °C for 20 s. A total of 40 cycles were performed. The amplified gene expression was quantitatively analyzed using the ddCt method [32] with the assistance of QuantStudio™ Design & Analysis Software (version 1.5.1; Applied Biosystems).

4.13. Western Blot

NHEKs were plated in a 6-well plate at a density of 1×10^5 cells/well and incubated for 24 h. Following the incubation period, the cells were treated with SH-340 (0.5 μM), Recombinant Human IL-4 (10 ng/mL), and IL-13 (10 ng/mL) obtained from PeproTech (Cranbury, NJ, USA) for 96 h. Subsequently, the cells were collected using a scraper, and protein lysates were prepared using RIPA lysis buffer (ThermoFisher Scientific) supplemented with protease inhibitors (GenDepot, Katy, TX, USA) and phosphatase inhibitors (GenDepot). Proteins were first extracted using RIPA buffer (#89900, ThermoFisher Scientific). NHEKs were first homogenized in ice-cold RIPA buffer containing protease and phosphatase inhibitors by sonication with 125 W and 20 kHz conditions 10 times in 2 s. The lysates were then incubated on ice for 30 min to allow complete cell lysis. After centrifugation at the maximum speed for 10 min at 4 °C, the supernatant containing the extracted proteins was collected and stored at −80 °C until further use. The protein concentration was determined using a BCA (bicinchoninic acid) assay (#23225, ThermoFisher Scientific) followed by the manual. For the experiment, protein samples were separated by electrophoresis on a polyacrylamide gel (10%) (#1610158, Bio-Rad). The separated proteins were then transferred onto the PVDF membrane (#10600021, Cytiva, Marlborough, MA, USA). The membrane was then blocked with non-fat dry milk in TBS including 0.1% Tween 20 (TBS-T) to prevent non-specific binding of the primary antibody. The primary antibody (KRT1: #sc-376224, KRT10: #sc-23877, FLG: #sc-80609, Santacruz biotechnology) was then incubated with the membrane overnight at 4 °C. After washing the membrane using TBS-T three times, a secondary antibody conjugated with horseradish peroxidase (HRP) (#31430, Invitrogen, Carlsbad, CA, USA) was added, and the membrane was incubated for 1 h at room temperature. The presence of TSLP was visualized by adding a chemiluminescent substrate using a chemiluminescent imaging system. The intensity of the signal can be

quantified using densitometry. Beta-actin (#sc-47778, Santacruz biotechnology) was used as a reference protein to normalize the levels of the protein of interest.

4.14. Measuring of STAT6 Phosphorylation

Cells were plated in a 6-well plate with a density of 2×10^5 cells/well and incubated for 24 h. Following the incubation, the cells were exposed to varying concentrations of SH-340 (0.5 μM) for a duration of 2 h. After the pre-treatment, the cells were subjected to IL-4 and IL-13 at a concentration of 10 ng/mL for 30 min to induce phosphorylation. Phosphorylation levels were assessed using Western blotting, employing phospho-STAT6 antibody (1:2000, BD Biosciences, San Jose, CA, USA) and total STAT6 antibody (1:2000, Cell Signaling, Danvers, MA, USA) through the same technique.

4.15. Immunostaining

To detect thymic stromal lymphopoietin (TSLP) in NHEKs, cells were seeded onto chamber slides (#154461PK, ThermoFisher Scientific). Then cells were fixed with 4% paraformaldehyde for 10 min and permeabilized with PBS including 0.4% Triton X-100 for 15 min. After washing with PBS three times, cells were blocked with PBS containing 10% normal goat serum for 1 h at room temperature. After blocking, cells were incubated with a primary TSLP antibody (1:100 dilution; Rabbit polyclonal, Cat# A13134, ABclonal, Woburn, MA, USA) in a blocking buffer overnight at 4 °C. The cells were then washed with PBS and incubated with a fluorescently labeled secondary antibody (goat anti-rabbit IgG, 1:1000 dilution, RSA1245, BioActs, Incheon, South Korea) for 1 h at room temperature. The cells were then counterstained with a nuclear stain, such as 4′,6-diamidino-2-phenylindole (DAPI) (ab104139, Abcam, Boston, MA, USA), and mounted on glass slides with a mounting medium. The cells were visualized using a fluorescence microscope (EVOS M5000 Imaging System, Invitrogen) and images were stored as JPEG files.

4.16. Analysis of Cell Size

To analyze the average cell size, six random regions were selected from the cell images of each group, and the area of the cell was measured using Image J software. The average values of the measured areas from three images per group were calculated, and statistical analysis was performed using Student's *t*-test.

4.17. Statistics

The experiments were conducted at least three times, and the findings were presented as the mean ± standard error of the mean (SEM). Statistical significance was evaluated using Student's *t*-test for comparing two groups and one-way ANOVA for comparing more than two groups with a significance level of $p < 0.05$.

5. Conclusions

In summary, the quinazoline derivatives SH-340 shows promising potential as a therapeutic for AD. Its ability to address keratinocyte differentiation, skin barrier functions, and TSLP inhibition holds implications not only for AD but also for broader allergic diseases like asthma and eczema. Additionally, SH-340's innovative TSLP modulation offers a targeted approach to curb AD triggers without affecting unrelated pathways. Its versatility extends to autoimmune diseases and cancer immunotherapies, positioning SH-340 as a versatile tool in diverse medical fields. However, further investigation is needed to unravel its mechanisms fully, validate efficacy, and ensure safety. This study underscores SH-340's transformative potential in dermatology and beyond, redefining AD treatment and immunotherapeutic strategies.

Supplementary Materials: The following supporting information can be downloaded at: https://www.mdpi.com/article/10.3390/molecules28166119/s1, Figure S1: LC-MS analysis data, Figure S2: SH340 HRMS analysis report, Figure S3: SH-340 1H-NMR (300 MHz Chloroform), Figure S4: SH-340 13C-NMR (300 MHz Chloroform); Table S1: SH-340 LC-MS: Analytical equipment and conditions.

Author Contributions: Conceptualization, D.K.; methodology, D.K., Y.P. and H.S.; validation, Y.P. and H.S.; formal analysis, Y.P. and H.S.; investigation, Y.P. and H.S.; data curation, D.K., Y.P. and H.S.; writing—original draft preparation, Y.P. and H.S.; writing—review and editing, D.K., Y.P. and H.S.; visualization, Y.P. and H.S.; supervision, D.K.; project administration, D.K.; funding acquisition, D.K. All authors have read and agreed to the published version of the manuscript.

Funding: This study received support from the National Research Foundation of Korea (Grant No. 2020R1C1C1005206).

Institutional Review Board Statement: Not applicable.

Informed Consent Statement: Not applicable.

Data Availability Statement: Not applicable.

Acknowledgments: The chemical library used in this study was kindly provided by Korea Chemical Bank (www.chembank.org (accessed on 1 June 2021)) of Korea Research Institute of Chemical Technology.

Conflicts of Interest: The authors declare no conflict of interest.

Sample Availability: Not applicable.

References

1. Alsibaee, A.M.; Al-Yousef, H.M.; Al-Salem, H.S. Quinazolinones, the winning horse in drug discovery. *Molecules* **2023**, *28*, 978. [CrossRef] [PubMed]
2. Li, Z.; Zhao, L.; Bian, Y.; Li, Y.; Qu, J.; Song, F. The antibacterial activity of quinazoline and quinazolinone hybrids. *Curr. Top. Med. Chem.* **2022**, *22*, 1035–1044. [CrossRef] [PubMed]
3. Lv, L.; Maimaitiming, M.; Huang, Y.; Yang, J.; Chen, S.; Sun, Y.; Zhang, X.; Li, X.; Xue, C.; Wang, P.; et al. Discovery of quinazolin-4(3h)-one derivatives as novel ache inhibitors with anti-inflammatory activities. *Eur. J. Med. Chem.* **2023**, *254*, 115346. [CrossRef]
4. Powell, T.J.; Ben-Bassat, H.; Klein, B.Y.; Chen, H.; Shenoy, N.; Mccollough, J.; Narog, B.; Gazit, A.; Harzstark, Z.; Chaouat, M.; et al. Growth inhibition of psoriatic keratinocytes by quinazoline tyrosine kinase inhibitors. *Br. J. Dermatol.* **1999**, *141*, 802–810. [CrossRef] [PubMed]
5. Bouley, R.; Ding, D.; Peng, Z.; Bastian, M.; Lastochkin, E.; Song, W.; Suckow, M.A.; Schroeder, V.A.; Wolter, W.R.; Mobashery, S.; et al. Structure–activity relationship for the 4(3h)-quinazolinone antibacterials. *J. Med. Chem.* **2016**, *59*, 5011–5021. [CrossRef] [PubMed]
6. Bagheri, E.; Saremi, K.; Hajiaghaalipour, F.; Faraj, L.F.; Ali, M.H.; Abdulla, A.M.; Khaing, L.S.; Salehen, N.A. Synthesis of novel derivatives of quinazoline schiff base compound promotes epithelial wound healing. *Curr. Pharm. Des.* **2018**, *24*, 1395–1404. [CrossRef] [PubMed]
7. Perveen, S.; Saad, M.S.; Khan, M.K.; Choudhary, I.M. Antioxidant and ros inhibitory activities of heterocyclic 2-aryl-4(3h)-quinazolinone derivatives. *Lett. Drug Des. Discov.* **2021**, *18*, 806–815. [CrossRef]
8. Malasala, S.; Ahmad, M.N.; Akunuri, R.; Shukla, M.; Kaul, G.; Dasgupta, A.; Madhavi, Y.V.; Chopra, S.; Nanduri, S. Synthesis and evaluation of new quinazoline-benzimidazole hybrids as potent anti-microbial agents against multidrug resistant staphylococcus aureus and mycobacterium tuberculosis. *Eur. J. Med. Chem.* **2021**, *212*, 112996. [CrossRef]
9. Mortlock, R.D.; Ma, E.C.; Cohen, J.M.; Damsky, W. Assessment of treatment-relevant immune biomarkers in psoriasis and atopic dermatitis: Toward personalized medicine in dermatology. *J. Investig. Dermatol.* **2023**, *143*, 1412–1422. [CrossRef]
10. Drislane, C.; Irvine, A.D. The role of filaggrin in atopic dermatitis and allergic disease. *Ann. Allergy Asthma Immunol.* **2020**, *124*, 36–43. [CrossRef]
11. Ong, P.Y. New insights in the pathogenesis of atopic dermatitis. *Pediatr. Res.* **2014**, *75*, 171–175. [CrossRef] [PubMed]
12. Cohen, I.; Birnbaum, R.Y.; Leibson, K.; Taube, R.; Sivan, S.; Birk, O.S. Znf750 is expressed in differentiated keratinocytes and regulates epidermal late differentiation genes. *PLoS ONE* **2012**, *7*, e42628. [CrossRef] [PubMed]
13. Furue, M. Regulation of filaggrin, loricrin, and involucrin by il-4, il-13, il-17a, il-22, ahr, and nrf2: Pathogenic implications in atopic dermatitis. *Int. J. Mol. Sci.* **2020**, *21*, 5382. [CrossRef] [PubMed]
14. Huang, I.H.; Chung, W.H.; Wu, P.C.; Chen, C.B. Jak-stat signaling pathway in the pathogenesis of atopic dermatitis: An updated review. *Front. Immunol.* **2022**, *13*, 1068260. [CrossRef]
15. Renert-Yuval, Y.; Guttman-Yassky, E. New treatments for atopic dermatitis targeting beyond il-4/il-13 cytokines. *Ann. Allergy Asthma Immunol.* **2020**, *124*, 28–35. [CrossRef] [PubMed]

16. Paller, A.S.; Ladizinski, B.; Mendes-Bastos, P.; Siegfried, E.; Soong, W.; Prajapati, V.H.; Lio, P.; Thyssen, J.P.; Simpson, E.L.; Platt, A.M.; et al. Efficacy and safety of upadacitinib treatment in adolescents with moderate-to-severe atopic dermatitis: Analysis of the measure up 1, measure up 2, and ad up randomized clinical trials. *JAMA Dermatol.* **2023**, *159*, 526–535. [CrossRef]
17. Blauvelt, A.; Szepietowski, J.C.; Papp, K.; Simpson, E.L.; Silverberg, J.I.; Kim, B.S.; Kwatra, S.G.; Kuligowski, M.E.; Venturanza, M.E.; Wei, S.; et al. Itch-free state in patients with atopic dermatitis treated with ruxolitinib cream: A pooled analysis from two randomized phase 3 studies. *J. Am. Acad. Dermatol.* **2023**, *88*, 651–653. [CrossRef] [PubMed]
18. Amano, W.; Nakajima, S.; Kunugi, H.; Numata, Y.; Kitoh, A.; Egawa, G.; Dainichi, T.; Honda, T.; Otsuka, A.; Kimoto, Y.; et al. The janus kinase inhibitor jte-052 improves skin barrier function through suppressing signal transducer and activator of transcription 3 signaling. *J. Allergy Clin. Immunol.* **2015**, *136*, 667–677.e7. [CrossRef]
19. Lee, J.Y.; Park, Y.K.; Seo, S.H.; Yang, B.S.; Park, H.; Lee, Y.S. 7-substituted-[1,4]dioxano[2,3-g]quinazolines as inhibitors of epidermal growth factor receptor kinase. *Arch. Pharm.* **2002**, *335*, 487–494. [CrossRef]
20. Hassan, H.M.A.; Denetiu, I.; Khan, S.A.; Rehan, M.; Sakkaf, K.; Gauthaman, K. Synthesis and biological evaluation of novel triazolyl 4-anilinoquinazolines as anticancer agents. *Med. Chem. Res.* **2019**, *28*, 1766–1772. [CrossRef]
21. Vollono, L.; Falconi, M.; Gaziano, R.; Iacovelli, F.; Dika, E.; Terracciano, C.; Bianchi, L.; Campione, E. Potential of curcumin in skin disorders. *Nutrients* **2019**, *11*, 2169. [PubMed]
22. Harris, C.S.; Hennequin, L.F.; Willerval, O. Three-point variation of a gefinitib quinazoline core. *Tetrahedron Lett.* **2009**, *50*, 1600–1602. [CrossRef]
23. Harris, C.S.; Hennequin, L.F.; Kettle, J.G.; Willerval, O.A. Selective alkylation of a 6,7-dihydroxyquinazoline. *Tetrahedron Lett.* **2005**, *46*, 7715–7719. [CrossRef]
24. Gittler, J.K.; Shemer, A.; Suárez-Fariñas, M.; Fuentes-Duculan, J.; Gulewicz, K.J.; Wang, C.Q.; Mitsui, H.; Cardinale, I.; de Guzman Strong, C.; Krueger, J.G.; et al. Progressive activation of t(h)2/t(h)22 cytokines and selective epidermal proteins characterizes acute and chronic atopic dermatitis. *J. Allergy Clin. Immunol.* **2012**, *130*, 1344–1354. [CrossRef] [PubMed]
25. Hu, X.; Li, J.; Fu, M.; Zhao, X.; Wang, W. The jak/stat signaling pathway: From bench to clinic. *Signal Transduct. Target. Ther.* **2021**, *6*, 402. [CrossRef] [PubMed]
26. Soumelis, V.; Reche, P.A.; Kanzler, H.; Yuan, W.; Edward, G.; Homey, B.; Gilliet, M.; Ho, S.; Antonenko, S.; Lauerma, A.; et al. Human epithelial cells trigger dendritic cell mediated allergic inflammation by producing tslp. *Nat. Immunol.* **2002**, *3*, 673–680. [CrossRef] [PubMed]
27. Vu, A.T.; Chen, X.; Xie, Y.; Kamijo, S.; Ushio, H.; Kawasaki, J.; Hara, M.; Ikeda, S.; Okumura, K.; Ogawa, H.; et al. Extracellular double-stranded rna induces tslp via an endosomal acidification- and nf-κb-dependent pathway in human keratinocytes. *J. Investig. Dermatol.* **2011**, *131*, 2205–2212. [CrossRef] [PubMed]
28. Kim, D.; Chen, R.; Sheu, M.; Kim, N.; Kim, S.; Islam, N.; Wier, E.M.; Wang, G.; Li, A.; Park, A.; et al. Noncoding dsrna induces retinoic acid synthesis to stimulate hair follicle regeneration via tlr3. *Nat. Commun.* **2019**, *10*, 2811. [CrossRef]
29. Nelson, A.M.; Reddy, S.K.; Ratliff, T.S.; Hossain, M.Z.; Katseff, A.S.; Zhu, A.S.; Chang, E.; Resnik, S.R.; Page, C.; Kim, D.; et al. Dsrna released by tissue damage activates tlr3 to drive skin regeneration. *Cell Stem Cell* **2015**, *17*, 139–151. [CrossRef]
30. Ali, D.; Alhattab, D.; Jafar, H.; Alzubide, M.; Sharar, N.; Bdour, S.; Awidi, A. Differential marker expression between keratinocyte stem cells and their progeny generated from a single colony. *Int. J. Mol. Sci.* **2021**, *22*, 10810. [CrossRef]
31. Finnegan, A.; Cho, R.J.; Luu, A.; Harirchian, P.; Lee, J.; Cheng, J.B.; Song, J.S. Single-cell transcriptomics reveals spatial and temporal turnover of keratinocyte differentiation regulators. *Front. Genet.* **2019**, *10*, 775. [CrossRef]
32. Livak, K.J.; Schmittgen, T.D. Analysis of relative gene expression data using real-time quantitative pcr and the 2(-delta delta c(t)) method. *Methods* **2001**, *25*, 402–408. [CrossRef]

Disclaimer/Publisher's Note: The statements, opinions and data contained in all publications are solely those of the individual author(s) and contributor(s) and not of MDPI and/or the editor(s). MDPI and/or the editor(s) disclaim responsibility for any injury to people or property resulting from any ideas, methods, instructions or products referred to in the content.

molecules

MDPI

Review

Research Progress of Takeda G Protein-Coupled Receptor 5 in Metabolic Syndrome

Xianmei Gou [1], Lin Qin [1], Di Wu [1], Jian Xie [1], Yanliu Lu [1,2], Qianru Zhang [1,*] and Yuqi He [1,*]

[1] Guizhou Engineering Research Center of Industrial Key-Technology for Dendrobium Nobile, Zunyi Medical University, Zunyi 563000, China; gxm8777@outlook.com (X.G.)
[2] Joint International Research Laboratory of Ethnomedicine of Ministry of Education, Zunyi Medical University, Zunyi 563000, China
* Correspondence: zhangqianru@zmu.edu.cn (Q.Z.); yqhe2016@zmu.edu.cn (Y.H.)

Abstract: Bile acids are acknowledged as signaling molecules involved in metabolic syndrome. The Takeda G protein-coupled receptor 5 (TGR5) functions as a significant bile acid receptor. The accumulated evidence suggests that TGR5 involves lipid homeostasis, glucose metabolism, and inflammation regulation. In line with this, recent preclinical studies also demonstrate that TGR5 plays a significant role in the generation and progression of metabolic syndrome, encompassing type 2 diabetes mellitus, obesity, atherosclerosis, and non-alcoholic fatty liver disease (NAFLD). In this review, we discuss the role of TGR5 in metabolic syndrome, illustrating the underlying mechanisms and therapeutic targets.

Keywords: bile acids; TGR5; Takeda G protein-coupled receptor 5; metabolic syndrome

1. Introduction

Metabolic syndrome (MS) refers to a group of metabolic dysregulations characterized by central obesity, hyperglycemia, insulin resistance, and hypertension. Individuals with MS have an increased risk of cardiovascular diseases and type 2 diabetes mellitus (T2DM) [1,2]. MS has become an increasing global public health problem, with the worldwide prevalence of metabolic syndrome predicted to encompass one-fourth of the world's population, equating to an excess of one billion people worldwide being affected by metabolic syndrome [3,4]. It is most significant for lowering blood glucose and lipid levels of MS individuals in the therapeutic and preventive aspects of cardiovascular diseases.

Takeda G protein-coupled receptor 5 (TGR5, GPBAR1, M-BAR, or GPR131) is a bile acid membrane receptor and a member of the G protein-coupled receptor subfamily. TGR5 can influence bile acid composition and enterohepatic circulation [5]. Accumulated evidence has demonstrated that TGR5 plays special roles in lipid and glucose metabolism, energy homeostasis, and immune and anti-inflammatory regulation [6–9]. TGR5 is widely expressed in the liver, intestine, pancreas, central nervous system, and immune cells [10]. TGR5 activation by bile acids can influence lipid, glucose, and energy metabolism (Figure 1). Hepatic TGR5 acts as a suppressor of lipid accumulation in the liver by regulating the bile acids composition and enterohepatic circulation [11,12]. Mouse models with MS have illustrated that the activation of TGR5 could promote insulin secretion and insulin sensitivity [13,14]. TGR5 is also involved in neuronal regulation in the central system to influence food intake and body weight [15]. Studies using tissue-specific mice have revealed that TGR5 could increase energy expenditure in skeletal muscle and adipose tissue [16,17]. TGR5 also involves in the pathogenesis of atherosclerosis by regulating the secretion of vasodilators and vasoconstrictors [18,19] (Figure 1).

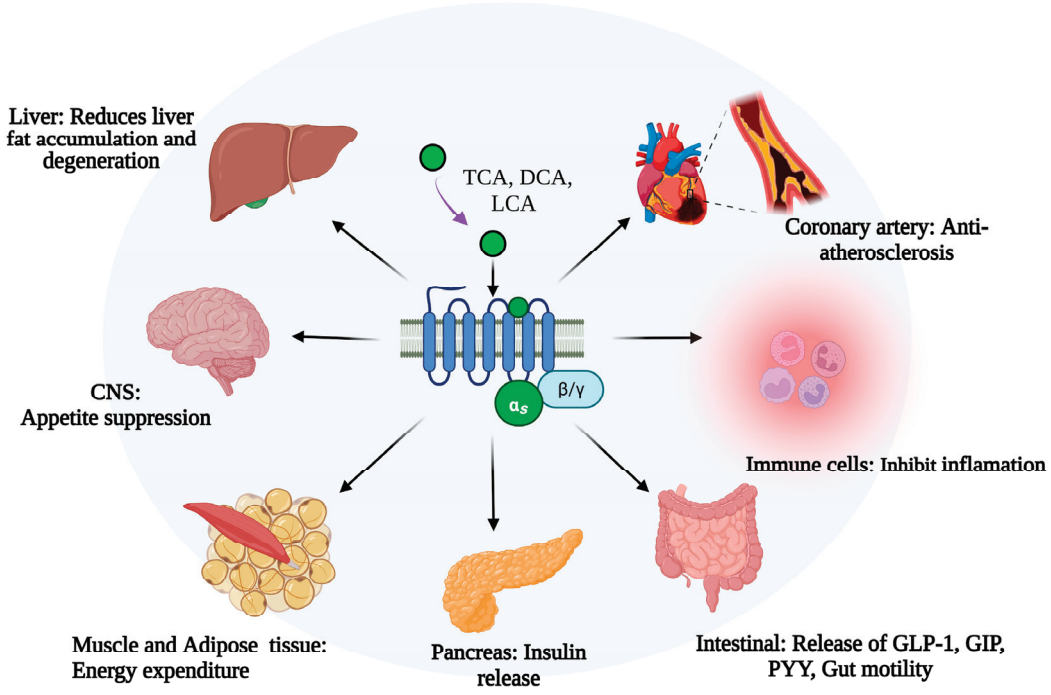


Figure 1. The role of TGR5 in metabolic syndrome in different cells and tissues. TCA, taurocholic acid; DCA, deoxycholic acid; LCA, Lithocholic acid; CNS, center nervous system; NAFLD, non-alcoholic fatty liver disease; NASH, non-alcoholic steatohepatitis; GLP-1, glucagon-like peptide-1; GIP, gastric inhibitory polypeptide; PYY, Peptide YY. This figure was created by Biorender (https://app.biorender.com/, accessed on 9 June 2023).

Bile acids (BAs) have been acknowledged as pivotal signal factors involving diverse biological functions including metabolic homeostasis and the immune response, mainly through activating two bile acid receptors: TGR5 and farnesoid X receptor (FXR). Recently, hundreds of research articles about TGR5 and MS have been collected in SCIE and PubMed up to 2023. However, the approved drugs targeting TGR5 for the treatment of MS are still limited. This review aims to map the underlying mechanisms of TGR5 and its potential as a drug target in the treatment of MS.

2. TGR5

The encoded sequence of the TGR5 gene is evolutionarily conserved in humans, rats, and other mammals and is located on human chromosome 2q35 and mouse chromosome 1c3 [6,20]. TGR5 gene expression is densely found in human tissues and cells, including the brain, liver, endocrine glands, skeletal muscles, spleen, lymph nodes, lung, placenta, nerve cells, and adipocytes. In the liver, TGR5 is highly expressed in bile duct cells, activated liver stem cells, sinusoidal endothelial cells, Kupffer cells, and NKT cells [10,21].

There are seven transmembrane domains (TMH1-7) of TGR5, including three extracellular loops that bind to ligands (ECL1-3) and three intracellular loops responsible for transmitting signals (ICL1-3) [22]. TGR5 is activated by bile acids in the order of LCA > DCA > CDCA > CA [23]. Bile acids and TRG5 agonists interact with TGR5 in the binding pocket and deliver a G-protein complex with α_s, β, and γ subunits [24]. GDP is subsequently released from the G protein complex and replaced by GTP, inducing the separation of G-protein α_s with β-γ dimers. G-protein α_s activates intracellular adenylyl cyclase (AC), resulting in ATP to cAMP conversion and protein kinase A (PKA) activation, which further induce downstream signaling involving bile acid synthesis, insulin sensitivity, atherosclerosis development, energy expenditure, and inflammation [25,26].

3. TGR5 and Bile Acids

BAs, including primary and secondary types, are synthesized from cholesterol and other precursors within hepatocytes. BAs have been acknowledged as metabolic messengers that could regulate their own metabolism and immune system by targeting FXR and TGR5 [27,28]. A disruption of the bile acids pool component has been described in MS, including T2DM, insulin-resistant, and non-alcoholic hepatitis [29–31]. Cholesterol 12α hydroxylase (CYP8B1) is an important enzyme in the synthesis of bile acids, particularly with the amount of 12α-hydroxy bile acids. TGR5 activation decreases the expression of CYP8B1 and reduces the ratio of 12α-hydroxylated bile acids to non-12α-hydroxylated bile acids in the bile acid pool. Mcgavgan et al. [11] found that reduced circulating bile acid profile hydrophobicity was related to a TGR5-dependent expression of the CYP8B1 protein. Meanwhile, the TGR5 agonist (INT-777) could downregulate hepatic Cyp8b1 expression [32]. The levels of Cyp8b1 and hydrophobic bile acids, especially 12α-hydroxy bile acids, have been upregulated in tgr5$^{-/-}$ mice and significantly reduced in tgr5$^{+/+}$ mice [33,34]. Thus, selective under-regulation of the expression level of hepatic Cyp8b1 may be a mechanism by which TGR5 regulates the bile acid profiles (Figure 2).

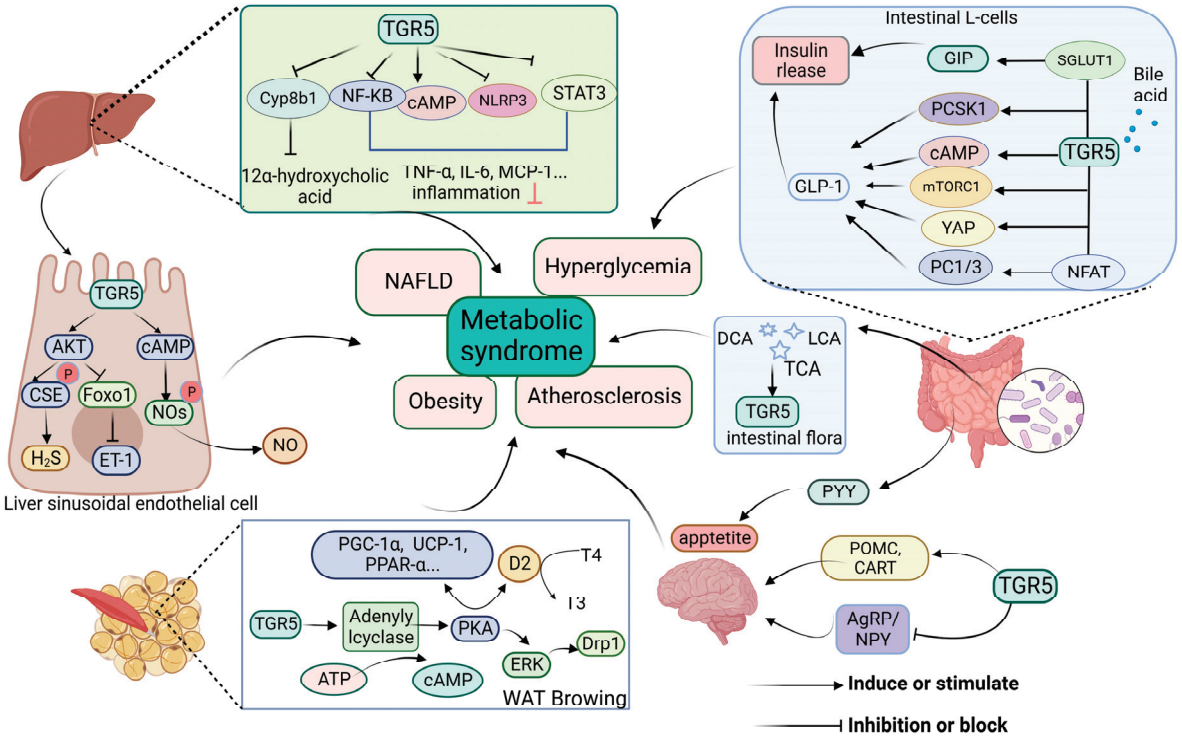


Figure 2. Review on the mechanisms of TGR5 in metabolic syndrome. TGR5 signaling is involved in the regulation of bile acid synthesis, vascular factor function [11,18], amelioration of inflammatory diseases by inhibiting inflammation [30,35,36], modulation of endocrine peptide release to ameliorate glucose disorders [17,37,38], appetite suppression, and promotion of energy expenditure [39,40]. TGR5 is also indirectly activated by regulating intestinal flora [41,42]. TGR5, takeda G protein-coupled receptor 5; TCA, taurocholic acid; DCA, deoxycholic acid; LCA, lithocholic acid; CYP8B1, cholesterol 12α hydroxylase; cAMP, cyclic adenosine monophosphate; PKA, protein kinase A; GLP-1, glucagon-like peptide-1; PC1/3, prohormone convertase 1/3; PCSK1, proprotein convertase subtilisin/kexin type 1; mTOR, mammalian target of rapamycin; NFAT, nuclear factor of activated T cells; YAP, yes associated protein; GIP, gastric inhibitory polypeptide; SGLT1, sodium glucose cotransporter 1; PYY, peptide YY; TNF-α, tumor necrosis factor-α; IL-6, interleukin-6; NLRP3, NOD-like receptor domain associated protein 3; WAT, white adipose tissue; ERK, extracellular regulated protein kinases; Drp1,

dynamin-related protein 1; D2, deiodinase 2; T4, thyroxine; T3, 3,5,3′-triiodothyronine; Ucp1, uncoupling protein 1; PGC-1α, PPAR-γ coactivator-1α; POMC, pro-opiomelanocortin; CART, cocaine-amphetamine-regulated transcript; YAgRP/NPY, neuropeptide Y/agouti-related peptide; MCP-1, monocyte chemoattractant protein-1; NOS, nitric oxide synthase; NO, nitric oxide; STAT3, signal transducer and activator of transcription 3; CSE, cystathionine γ-lyase; FoxO1, forkhead box protein O1; ET-1, endothelin-1. This figure was created by Biorender (https://app.biorender.com/, accessed on 11 June 2023).

4. TGR5 and T2DM

TGR5 is an essential receptor in maintaining the balance of glucose levels in the body and controlling insulin sensitivity. It was suggested that TGR5$^{-/-}$ mice display impaired glucose tolerance and insulin resistance compared to their WT counterparts, whereas TGR5-overexpressing mice showed good tolerance to glucose [9]. Meanwhile, the administration of TGR5 agonists was shown to modulate glucose levels in high-fat diet (HFD) mice, further demonstrating that TGR5 plays an active role in the disease process of T2DM [43].

4.1. Promote GLP-1 Secretion

Several studies suggest that TGR5 activation elevates glucagon-like peptide-1 (GLP-1) secretory capacity and expands the L-cell population (Figure 2). The intestinal L cells are the main synthesizing and releasing cells of GLP-1, and TGR5 sits in the basal layer of L cells [44]. GLP-1 is an important peptide hormone that binds to the GLP-1 receptor in pancreatic β cells; its functions include stimulating insulin release, delaying gastric emptying, enhancing satiety, and inhibiting glucagon secretion [45].

On the one hand, TGR5 was found to induce GLP-1 production and regulate glucose metabolism through different metabolic pathways. In STC-1 cells, handling of bile acid-activated TGR5 stimulated GLP-1 secretion through the cAMP pathway [13]. Prohormone convertase 1/3 (PC1/3), processing and modifying GLP-1, is an important enzyme for the production and secretion of GLP-1. It has been found that altered intestinal bile acid composition induced an elevation of the TGR5 agonist, taurocholic acid (TCA), which stimulated the nuclear factor of activated T cells (NFAT). Then, PC1/3 binds to NFAT binding, promotes PC1/3 gene expression, and induces GLP-1 secretion, thereby improving glucose tolerance [46]. Meanwhile, proprotein convertase subtilisin/kexin type 1 (PCSK1) encoding the PC1/3 is important for GLP-1 synthesis and can affect its secretion. It was shown that the administration of oligofructose (OFS) to wild-type mice improved glucose tolerance compared to TGR5$^{-/-}$ mice. The mechanism was as follows: OFS altered the composition of the intestinal BAs, particularly 6α-hydroxy bile acids, increased TGR5 activity, and promoted PCSK1 expression and, subsequently, GLP-1 release [47]. mTORC1 is a complex of mammalian target of rapamycin (mTOR). Several studies have shown that ileal TGR5–mTOR1 signaling engages in GLP-1 secretion in L cells. The cellular experiment showed that deoxycholic acid (DCA) activated the TGR5–mTOR1 signaling pathway, phosphorylated mTOR, S6, and S6 kinases (S6Ks), and induced GLP-1 synthesis and release. However, the effect of DCA-induced GLP-1 synthesis is abolished when siRNA is knocked down of mTORC1 or TGR5 [48].

On the other hand, TGR5 could expand the L-cell population indirectly to increase GLP-1 production. Ginsenoside K has been found to activate TGR5 by elevating lithocholic acid (LCA) and DCA content. This, in turn, activates the RhoA/ROCK/YAP signaling pathway, increasing the abundance of L-cells, and ultimately enhancing GLP-1 release [49]. When TGR5 is knocked down, yes-associated protein (YAP) exhibits low expression and loses its glucose regulatory function [50]. Therefore, TGR5 is a promising target for use against T2DM.

FXR and TGR5 are essential receptors in the feedback of bile acids synthesis and en-terohepatic circulation [51]. Moreover, these two receptors are co-expressed in the ileum and colon [52]. In intestinal endocrine L cells, FXR and TGR5 could stimulate GLP-1 secretion, which contributes to increasing insulin secretion to improve insulin sensitivity,

respectively. A study using FXR/TGR5-knockout mice has illustrated that FXR and TGR5 may coordinately regulate GLP-1 production and secretion [53]. Further research on the roles of FXR and TGR5 in metabolic syndrome is still needed.

4.2. Promote GIP Secretion

A glucose-dependent gastric inhibitory polypeptide (GIP) increases insulin secretion and maintains glucose homeostasis in the intestine (Figure 2). Upon food ingestion, intestinal cells release GIP into the bloodstream, where it binds to the GIP receptor (GIPR) on pancreatic β-cells. This activation of GIPR leads to increased cAMP levels and proinsulin gene transcription, which ultimately promotes insulin secretion and regulates the survival and reproduction of insulin-independent pancreatic β cells [37]. Zhu et al. [54] found that saponins derived from *Camellia Sinensis* seeds could stimulate GIP secretion in mouse and STC-1 cells via sodium glucose cotransporter 1 (SGLT1) and TGR5. However, TGR5 siRNA was able to counteract the increase in GIP expression, revealing that TGR5 participates in the regulation of GIP expression for the first time. Furthermore, network pharmacology analysis showed that PCSK1 was related to SGLT1, TGR5, and GIP [54]. Interestingly, the downregulation of PCSK1 inhibits GIP and GLP-1 production in STC-1 cells [55]. Thus, the TGR5–PCSK1 axis is likely critical for the simultaneous induction of GLP-1 and GIP secretion, and in vivo experiments are still needed to verify the involved mechanisms further. The TGR5–GIP signaling pathway offers a promising avenue for creating novel hypoglycemic medications.

4.3. Promote PYY Secretion

Peptide YY (PYY) is a gastrointestinal hormone released by L cells in the ileum and colon. PYY could slow gastric emptying, delay gastrointestinal transport, and suppress appetite through the hypothalamic circuits [56]. Bile acids promote the secretion of PYY by activating the TGR5 receptor in L cells (Figure 2). In vitro studies have shown that the TGR5 agonist DCA induces the release of PYY in a dose-dependent manner [23]. However, this effect was not observed in TGR5 knockout mice [57]. In a clinical study, the administration of DCA and TCA can simulate a rapid and noticeable increase in plasma PYY. In contrast, applying bile acids with a low binding affinity to TGR5 cannot induce PYY secretion significantly [58]. Of mechanistic relevance was the demonstration that activation of TGR5 stimulates the production of Gα and cAMP to release PYY via the Epac/PLC-ε-CA^{2+} pathway in a cAMP-dependent manner [59]. The findings above demonstrate that TGR5 signaling is associated with bile acid-induced PYY secretion.

4.4. Increase Glucose Metabolism in Skeletal Muscle

TGR5 is highly expressed in skeletal muscle, the largest organ of glucose handling in humans. Skeletal muscle also increases glucose clearance and improves insulin resistance to regulate body glucose homeostasis, in addition to promoting energy metabolism (Figure 2). One TGR5 agonist, known as 4-Phenoxynicotinamide (MN6), could enhance insulin-stimulated glucose transport via the cAMP/PKA pathway, thereby ameliorating insulin resistance and glucose tolerance in skeletal muscle in HFD mice and C2C12 myotubes [60]. Furthermore, TGR5 has been proven to alleviate glucose homeostasis and age-related glucose disorders in skeletal muscle. Sasaki et al. [17] found that the activation of the glycolytic pathway in skeletal muscle-specific TGR5 transgenic mice led to increased glucose utilization and clearance in HFD mice. Moreover, observation shows that old transgenic mice exhibit increased the glucose clearance and strength of the skeletal muscles. More importantly, the activation of TGR5 increases a higher muscle mass, which is beneficial in improving diabetes. Sasaki et al. [21] showed that exercise-induced unfolded protein response (UPR) and activating transcription factor 6α (ATF6α) increase the expression of TGR5, which, in turn, promotes the differentiation of skeletal muscle cells and muscle hypertrophy in mice. Moreover, Sund et al. [61] found that TGR5 strengthens skeletal muscle regeneration and myogenic process through the AKT/mTOR/FoXO3 signaling pathway

in C2C12 cells. This research reveals that activating TGR5 in skeletal muscle effectively improves glucose metabolism disorder, opening new avenues for drug development to treat diabetes.

4.5. Inhibit Inflammation

Chronic inflammation is a crucial initiating factor of insulin resistance. TGR5 signaling becomes a promising approach for treating T2DM by interfering with the inflammatory response (Figure 2). Several studies have shown a high expression of TGR5 in monocytes, macrophages, and immune organs such as the spleen. The bile acid–TGR5 pathway inhibits the secretion of various cytokines, including tumor necrosis factor-α (TNF-α) and interleukin (IL)-1α, IL-1β, IL-6, and IL-8 [62].

In Kupffer cells, TGR5 activation reduces cytokine expression induced by LPS and inhibits NF-κB-dependent inflammatory responses, improving glucose tolerance [63]. According to a study, activation of TGR5 reduces chemokines expression in macrophages via the AKT–mTOR pathway [64]. This pathway involves the phosphorylation of AKT and mTORC1, which induces the expression of 4E-binding proteins (4E-BP) and CCAAT/enhancer binding protein beta (C/EBPβ) isoform liver-inhibitory protein (LIP). Therefore, the TGR5–AKT–mTOR-LIP pathway is a newly discovered pathway for macrophages to promote anti-diabetic effects [64]. Moreover, abnormal glucose metabolism is closely associated with regulating NOD-like receptor domain-associated protein 3 (NLRP3) inflammatory vesicles. TGR5 activation induces PKA kinase, leading to the ubiquitination of NLRP3. Therefore, the TGR5–cAMP–PKA axis inhibits the formation of NLRP3 inflammatory vesicles to attenuate inflammatory response, glucose tolerance, and insulin resistance induced by a high-fat diet [65]. It also estimated that the inflammation and insulin resistance of chimeric mice simultaneous upregulated after that specifically removing TGR5 from macrophages and bone marrow [26]. According to these studies, TGR5 signaling could prevent hepatic insulin resistance development and progression, ultimately improving systemic glucose levels.

5. TGR5 and Obesity

5.1. Promote Energy Consumption and Fat Browning

Obesity is mainly induced by an imbalance between energy intake and expenditure, ultimately resulting in increased fat storage in adipose tissue. Adipose tissue can be divided into white adipose tissue (WAT) and brown adipose tissue (BAT). WAT primarily stores energy, while BAT contains more mitochondria and plays a key role in energy consumption. Therefore, an increase in BAT is conducive to improving obesity. TGR5 is a crucial target for regulating mitochondrial function and promoting adipose tissue remodeling (Figure 2).

BAs haven been acknowledged as metabolic regulators affecting energy expenditure via TGR5 stimulation. In brown adipose tissue and skeletal muscle, the interaction of BA and TGR5 promotes the activation of type 2 deiodinase (Dio2), which induces the expression of the crucial metabolic genes including uncoupling protein 1 (UCP1) and peroxisome proliferator-activated receptor-gamma coactivator-1 alpha (PGC-1α) in mitochondria [66–68]. Dio2 converts inactive thyroxine (T4) to active 3,5,3′-triiodothyronine (T3), inducing the activation of UCP1 [16,69]. Mitochondrial UCP1 diverts the electron gradient through proton leak and induces uncoupled respiration [70,71]. PGC–1α co-activates proliferator-activated receptor γ (PPARγ) and fine-tunes mitochondrial biogenesis, oxidative metabolism, and thermogenesis [72]. The thermogenic activity of BA supplementation was disappeared in Tgr5-knockout mice that were fed a high-fat diet [73]. BA–TGR5–Dio2 signaling promotes thermogenic activity instead of ATP production. In addition, an in-vivo study demonstrated administration of TGR5-activated bile acid, which can transform white adipose tissue into beige adipose tissue and promote mitochondrial fission via the extracellular regulated protein kinases/dynamin-related protein 1 (ERK/DRP1) pathway [70].

5.2. Increase Intestinal Peristalsis

TGR5 is involved in bile acids-induced intestinal peristalsis and significantly prevents central obesity caused by constipation. Studies have demonstrated that TGR5 agonists can enhance the intestinal motility of mice, while the absence of TGR5 results in a longer colonic transit time and decreased frequency of defecation in mice [50]. Activated TGR5 could stimulate the secretions of peristaltic mediators, including 5-hydroxytryptamine (5-HT) and calcitonin gene-related peptide (CGRP) in enterochromaffin cells (ECs), while the effect was lost in TGR5$^{-/-}$ mice [74]. In vitro and in vivo experiments have demonstrated that TGR5 activation can enhance the production of 5-HT from EC cells. This improvement in constipation is achieved by activating the transient receptor potential ankyrin 1 (TRPA1) and the PLC-γ1/PIP2 signaling pathway [75].

5.3. Regulate Hypothalamic Neurons

TGR5 signaling in the hypothalamus is an important factor in protecting against obesity caused by HFD. Hypothalamic bile acid level is reduced in diet-induced obese (DIO) mice compared to the control group [15]. However, when DIO mice are administered with bile acids or central TGR5 agonists, their body weight and fat mass are reduced by activating the sympathetic nervous system, thereby regulating energy homeostasis. Conversely, when hypothalamic TGR5 expression in the medio basal hypothalamus is downregulated or deleted, it contributes to obesity by weakening sympathetic nerve activity [15]. Together, hypothalamic TGR5 is an important receptor for anti-obesity via the supplementation of bile acid, which provides a basis for the development of BA–TGR5 as a pathway for anti-obesity drugs.

Findings from a study of the central neurons involved in TGR5 regulation of food intake to improve obesity (Figure 2). TGR5 not only promotes the expression of anorexia neurons to increase satiety signals but also inhibits the expression of hunger-signaling neurons to suppress hunger signals, thereby reversing obesity. A study has shown that DCA and cholecystokinin octapeptide (CCK8) act synergistically to stimulate pro-opiomelanocortin (POMC) and cocaine–amphetamine-regulated transcript (CART) neurons via the TGR5 receptor of the valgus nerve. Then, it delivers satiety signals to the hypothalamus, reducing food intake [76]. Chen et al. [77] investigated the mechanism of bile acids releasing POMC in mouse hypothalamus GT1-7 cells. The results showed that phosphorylation of the signal transducer and activator of transcription 3 (p-STAT3), phosphorylation of threonine kinase (p-AKT), suppressor of cytokine signaling (SOCS3), and TGR5 expression were significantly increased. This led to the conclusion that bile acid may regulate anorexigenic neuropeptides through p-AKT and p-STAT3–SOCS3 signaling. In the other study, TGR5 activation inhibits the secretion of hypothalamic appetite-promoting neuropeptide Y/agouti-related peptide (AgRP/NPY) neurons via the Rho/ROCK/Actin-remodeling pathway, which, in turn, suppresses hunger signaling to reduce food intake. In contrast, the deletion of TGR5 results in a notable rise in food consumption and encourages the onset of obesity [78]. In addition to POMC, CART, and AgRP/NPY neurons, other neurons still play a role in regulating body weight through TGR5 and related mechanisms. Further exploration is needed to understand their involvement fully.

6. TGR5 and Atherosclerosis

6.1. Regulate Inflammation

The development and progression of atherosclerosis are promoted by dyslipidemia and chronic inflammation, with TGR5 being associated with the pathogenesis of atherosclerosis. When macrophages remove the modified forms of LDL-C from the vascular wall, it eventually forms foam cells and produces local inflammatory factors and chemokines, causing chronic inflammation in the vascular wall and promoting lipid accumulation in the cells [24]. It has been shown that activation of TGR5 blunts the production of a cluster of differentiation 36 (CD36), scavenger receptor A (SR-A), monocyte chemoattractant protein-1 (MCP-1), and chemokine ligand-5 (CCL5) through the cAMP–NF-κB signaling

pathway [79], which reduces the uptake of oxidized LDL (Ox-LDL) and the formation of foam cells, thereby inhibiting the progression of atherosclerosis. In the atherosclerosis model of $LDL^{-/-}$ mice, activation of TGR5 reduces atheromatous plaques by inhibiting inflammation and lipid accumulation. However, when the Tgr5 gene was knocked out, there was no inhibitory effect on atherosclerosis [79]. This suggests that the activation of TGR5 plays a crucial role in preventing atherosclerosis by modulating the immune system.

6.2. Promote NO Release

Nitric oxide (NO) is an essential molecule in preventing atherosclerosis. It has multiple beneficial effects, including vasodilation and increased blood flow. Moreover, NO reduces the adhesion of monocytes to vascular endothelial cells, thus preventing the formation of atheromatous plaque. Activation of TGR5 may offer a novel therapeutic strategy for treating atherosclerosis. When bile acid binds to TGR5 and triggers the expression of cAMP in liver sinusoidal endothelial cells, this process results in an elevation of intracellular Ca^{2+} levels, leading to the activation of nitric oxide synthase (NOS) phosphorylation and subsequent release of nitric oxide (NO) (Figure 2) [80].

TGR5 is activated by endogenous bile acids, with TCA being the most effective, followed by LCA, DCA, chenodeoxycholic acid (CDCA), and cholic acids (CA). A study revealed that individuals with atherosclerosis had significantly lower levels of LCA in their serum. This reduction level of LCA could impede TGR5 on anti-inflammatory in macrophages, leading to increasing plaque formation. Thus, LCA may be a marker for the clinic diagnosis of coronary atherosclerosis [19].

7. TGR5 and NAFLD

Prior research has demonstrated that TGR5 protects against several liver diseases. Non-alcoholic fatty liver disease (NAFLD) is a common complication of obesity and T2DM. NAFLD has the potential to advance to non-alcoholic steatohepatitis (NASH), liver fibrosis, hepatocellular injury, cirrhosis, and hepatocellular carcinoma, because of lipid buildup in the liver (Figure 2). The TGR5 receptor may play a role in the regulation of NAFLD/NASH, as indicated by a notable decrease in TGR5 expression observed in the liver tissues of both NASH patients and NASH animals [35,65]. Meanwhile, $TGR5^{-/-}$ HFD mice showed lipid accumulation and increased hepatic fat energy [11]. Furthermore, the impact of TGR5 on lipid accumulation may vary depending on the gender of the individual. Research conducted by Vassileva et al. [9] on DIO mice revealed that male $Tgr5^{-/-}$ mice showed higher levels of hepatic steatosis than female $Tgr5^{-/-}$ mice, highlighting the regulatory role of TGR5 in this process.

7.1. Improve Insulin Resistance

The development of NAFLD is significantly influenced by insulin resistance in both the liver and adipose tissue [81]. The TGR5 signaling pathway is critical in regulating intestinal GLP-1 secretion and improving insulin resistance. According to Lambert et al. [82], GLP-1 has been shown to improve insulin sensitivity and reduce hepatic glucose production in the animal model of NAFLD, which inhibits the development of liver steatosis, NASH, and liver fibrosis. A clinical study has further demonstrated that treatment with liraglutide, a GLP-1 agonist, can hinder the histological deterioration of NAFLD. This is achieved by reducing body weight and fasting blood glucose, increasing insulin sensitivity and inhibiting de novo lipogenesis and inflammation [83]. In addition, activation of TGR5 releases Glucagon-like peptide-2 (GLP-2), which possesses anti-inflammatory properties and accelerates liver regeneration after partial hepatectomy [84,85]. Thus TGR5 is expected to be a novel target that improves NAFLD/NASH via increasing the release of GLP-1 as well as GLP-2.

7.2. Inhibit Inflammation

Monocytes and macrophages are important sources of inflammatory factors in the liver, playing a crucial role in the development of NASH and hepatocellular carcinoma [86]. The TGR5 receptor improves NASH in various immune cells by inhibiting inflammation (Figure 2).

Activation of TGR5 in macrophages has been shown to effectively inhibit inflammatory responses through the toll-like receptor 4 (TLR4)/NF-κB pathway [87]. Additionally, TGR5 activation reduces the binding activity of NF–κB–p65 DNA, inhibiting the NF–κB pathway and decreasing TNF-α secretion in CD14 macrophages both in vitro and in vivo [88]. Moreover, TGR5 agonists increase the phosphorylation of PKA and induce ubiquitination of NLRP3 inflammasome, which inhibits NLRP3-mediated M1 macrophage polarization, thereby alleviating liver steatosis and inflammation in NASH [89]. Activation of TGR5 has been observed to inhibit lipopolysaccharide (LPS)-induced inflammatory factors production in Kupffer cells and THP-1 cells of TGR5 overexpressed. Additionally, TGR5 activation has been found to reduce phosphorylated level of the signal transducer and activator of transcription 3 (STAT3), resulting in a hepatoprotective effect [90]. Conversely, LPS-induced $TGR5^{-/-}$ mice show severe liver injury, hepatocyte apoptosis, and inflammation and cause elevated serum alanine and aspartate aminotransferase [91]. The above studies show that TGR5 signaling pathways inhibit the occurrence and development of NASH by regulating inflammatory factors, providing a new idea for the treatment of NASH.

7.3. Ameliorate Effect on Fibrin

TGR5 agonists ameliorate liver fibrosis by inducing apoptosis, inhibiting inflammation, and improving blood circulation.

LCA has been identified as the effective natural agonist of TGR5, which plays a crucial role in regulating metabolism and inhibiting inflammation. A recent study has investigated the effects of LCA on immune cells and hematopoietic stem cells (HSCs) in liver fibrosis. According to the findings, LCA could hinder the activity of transforming growth factor beta (TGF-β) and glycolysis while enhancing oxidative phosphorylation. This leads to the differentiation of macrophages towards the M2 type and prevents their differentiation into the M1 type [92]. Meanwhile, LCA increases the recruitment of NK cells and decreases NKT cell activation, ameliorating liver fibrosis in mice induced by carbon tetrachloride (CCL4) [92]. BAR501, a TGR5 agonist, has been shown to reverse liver and vascular damage in mouse models of NASH in a TGR5-dependent manner. BAR501 treatment induces the browning of white adipose tissue and inhibits the development of aortic intima–media thickness [93]. Additionally, it reduces the expression of specific inflammatory genes and adhesion molecules in the aorta, such as IL-6, TNF-a, vascular cell adhesion molecule (VCAM), intercellular adhesion molecule-1 (ICAM-1), and endothelial selection [93].

The activation of TGR5 in liver sinusoidal endothelial cells (LSECs) promotes vasodilators secretion and inhibition of vasoconstrictors release (Figure 2). The former is achieved through the induction of endothelial nitric oxide synthase (eNOS) phosphorylation, which increases nitric oxide (NO) production [18]. Similarly, TGR5 activation increases cystathionine γ-lyase (CSE) activity via Akt-induced serine phosphorylation, increasing H_2S production. Moreover, the activation of Akt leads to the reduced transcription of forkhead box protein O1 (FoxO1), inhibiting the expression of vasoconstrictor endothelin-1 (ET-1) [94]. These findings indicate that increased TGR5 signaling has the potential to improve liver function by decreasing lipid buildup in the liver, reducing fibrosis and inflammation.

8. Gut Microbiota Regulates TGR5

The interaction between gut flora and the TGR5 receptor has become a current research hotspot. Accumulating evidence shows that gut flora indirectly activates the TGR5 pathway by metabolizing the composition of the bile acid profile, facilitating the effect on a series of MS. In contrast, TGR5 deficiency causes gut microbiota imbalance and aggravates liver injury.

Studies have demonstrated that knocking out hypoxia-inducible factor 2α (HIF-2α) in mice can effectively reduce obesity by decreasing gut lactate levels (Figure 2). This reduction leads to a decrease in the frequency of *Bacteroides vulgatus* and an increase in the abundance of *Ruminococcus torques*. These changes result in higher TCA and DCA and TGR5 activation levels. Activation of TGR5 enhances the thermogenic capacity of white adipose tissue by increasing the expression of UCP-1 and creatine kinase mitochondrial 2 (CKMT2) [44]. A recent study has shown that flaxseed can alleviate NASH by reducing the abundance of *Firmicutes* and increasing the abundance of *Bifidobacterium* and *Actinobacteria*. Additionally, it can increase the proportion of LCA and DCA, which can inhibit liver inflammation and protect against HFD-induced hepatic steatosis via the TGR5–NF–κB signaling pathway [95]. Dietary supplementation with probiotics can enhance insulin sensitivity and stimulate adipose tissue browning, ultimately resulting in weight loss. The mechanism increases the abundance of *Bacteroides* that further induce the TGR5–GLP-1 pathway and inhibit intestinal dipeptidyl peptidase-4 (DDP4) [96]. Meanwhile, a clinical study has also shown that probiotics consumption improves metabolic parameters such as lowering cholesterol, improving intestinal function and increasing insulin sensitivity in obese and T2DM patients [41].

9. TGR5 Agonists

TGR5 activation could improve insulin resistance, increase adipose tissue thermogenesis and energy expenditure, and inhibit inflammation. However, the approved drug targeting TGR5 is limited in the treatment of MS. Bile acid analogs and non-bile acid regulators exhibit therapeutic potential for the treatment of metabolic disorders, including obesity, diabetes, and NAFLD. Ursodeoxycholic acid (UDCA) is a secondary bile acid used as a first-line drug in the treatment of primary biliary cholangitis [97]. A clinical study has shown that administering low doses of UDCA can enhance GLP-1 secretion through TGR5 signaling in diabetic patients. A combination of sitagliptin and UDCA is in phase-IV clinical trials [98]. The steroid agonist 6α-ethyl-23(S)-methylcholic acid (INT-777), specific to TGR5, has been found to promote thermogenesis and energy metabolism in adipose tissue [99]. Furthermore, it also stimulates the secretion of GLP-1 and inhibits macrophage-mediated inflammation and lipid accumulation [32], which can lead to improved insulin sensitivity and reduced hepatic steatosis [100]. Recent studies have shown that INT-777 inhibits neuroinflammation and improves nerve injury [101,102]. Meanwhile, in vivo studies using mouse model with NAFLD also validated the hypoglycemic effects of INT-777 [103].

RDX8940 is a highly effective and selective TGR5 agonist, which could promote the secretion of GLP-1, GLP-2, and PYY in mouse intestinal L cells with minimal systemic side effects. Unlike other agonists, it does not inhibit gallbladder emptying in mice, and it is also non-toxic to the heart, liver, and pancreas. Furthermore, RDX8940 improves hepatic steatosis and insulin sensitivity in insulin-resistant mouse models, which has the potential to treat NASH and NAFLD [14]. A-Ionone is an aromatic diterpenoid compound with the same TGR5-activating effect as CDCA and is used in food and cosmetics with a high safety coefficient. The administration of 0.2% α-Ionone to mice fed with HFD led to a significant rise in the expression of thermogenic genes, such as PGC-1α, UCP-1, and Dio2, in their brown adipose tissue. It inhibits weight gain in DIO mice by activating TGR5 compared to normal HFD mice. It is suggested that α-Ionone has shown potential as a TGR5 agonist for preventing obesity [104]. To improve TGR5 agonists for treating metabolic diseases, Zhao et al. [105] developed a new series of 1-benzyl–1H-imidazole–5-carboxyamide derivatives. The most potent compounds, 19d and 19e, activated TGR5 better than the control drugs INT-777 and LCA while exhibiting good FXR selectivity. In vivo studies also showed significant hypoglycemic effects.

Nevertheless, systemic TGR5 activation can cause some unpleasant adverse effects including excessive gallbladder filling and insufficient emptying [106,107]. TGR5 agonists have also been associated with "bile-acid-related" itching and analgesia [108]. Animal

studies have illustrated that structurally diverse TGR5 agonists reduce vascular tone and blood pressure, resulting in reflex tachycardia and inotropy [109].

10. Conclusions

In summary, TGR5 activation influences glucolipid metabolism, energy metabolism, inflammatory response, and endogenous signaling molecules expression through multiple signal transduction pathways. It has excellent potential effects in treating T2DM, obesity, atherosclerosis, and NAFLD, which is a key direction and hot area for drug research and development at home and abroad. However, the activity of TGR5 has been demonstrated in animal and cellular assays and needs to be further validated and observed in clinical trials. A comprehensive understanding of the potential mechanisms of TGR5 in metabolic syndrome can serve as a theoretical foundation and reference value for future TGR5-specific targeting in the treatment of metabolic syndrome.

Author Contributions: Conceptualization, Q.Z., L.Q. and X.G.; writing—original draft preparation, X.G.; writing—review and editing, L.Q. and D.W.; visualization, J.X. and Y.L.; funding acquisition, Y.H. All authors have read and agreed to the published version of the manuscript.

Funding: The study was funded by the National Nature Science Foundation of China (82260843, 82060649, 82160740); Zunyi City of China (ZSKHHZ [2021]290, QKHPTRC [2020]-16); and the Guizhou Engineering Research Center of Industrial Key-technology for Dendrobium Nobile (QJJ [2022]048, QJJ [2022]006).

Institutional Review Board Statement: Not applicable.

Informed Consent Statement: Not applicable.

Data Availability Statement: Not applicable.

Conflicts of Interest: The authors declare there are no competing interest.

Sample Availability: Not applicable.

References

1. Hu, C.; Jia, W. Multi-omics profiling: The way toward precision medicine in metabolic diseases. *J. Mol. Cell Biol.* **2021**, *13*, 576–593. [CrossRef] [PubMed]
2. Ambroselli, D.; Masciulli, F.; Romano, E.; Catanzaro, G.; Besharat, Z.M.; Massari, M.C.; Ferretti, E.; Migliaccio, S.; Izzo, L.; Ritieni, A.; et al. New Advances in Metabolic Syndrome, from Prevention to Treatment: The Role of Diet and Food. *Nutrients* **2023**, *15*, 640. [CrossRef] [PubMed]
3. Saklayen, M.G. The Global Epidemic of the Metabolic Syndrome. *Curr. Hypertens. Rep.* **2018**, *20*, 1–8. [CrossRef] [PubMed]
4. Vrdoljak, J.; Kumric, M.; Vilovic, M.; Martinovic, D.; Rogosic, V.; Borovac, J.A.; Kurir, T.T.; Bozic, J. Can Fasting Curb the Metabolic Syndrome Epidemic? *Nutrients* **2022**, *14*, 456. [CrossRef] [PubMed]
5. Chiang, J.Y.L. Bile Acid Metabolism and Signaling. *Compr. Physiol.* **2013**, *3*, 1191–1212. [CrossRef]
6. Duboc, H.; Taché, Y.; Hofmann, A.F. The bile acid TGR5 membrane receptor: From basic research to clinical application. *Dig. Liver Dis.* **2014**, *46*, 302–312. [CrossRef]
7. van Nierop, F.S.; Scheltema, M.J.; Eggink, H.M.; Pols, T.W.; Sonne, D.P.; Knop, F.K.; Soeters, M.R. Clinical relevance of the bile acid receptor TGR5 in metabolism. *Lancet Diabetes Endocrinol.* **2016**, *5*, 224–233. [CrossRef]
8. Ferrell, J.M.; Pathak, P.; Boehme, S.; Gilliland, T.; Chiang, J.Y.L. Deficiency of Both Farnesoid X Receptor and Takeda G Protein–Coupled Receptor 5 Exacerbated Liver Fibrosis in Mice. *Hepatology* **2019**, *70*, 955–970. [CrossRef]
9. Vassileva, G.; Hu, W.; Hoos, L.; Tetzloff, G.; Yang, S.; Liu, L.; Kang, L.; Davis, H.R.; Hedrick, J.A.; Lan, H.; et al. Gender-dependent effect of Gpbar1 genetic deletion on the metabolic profiles of diet-induced obese mice. *J. Endocrinol.* **2010**, *205*, 225–232. [CrossRef]
10. Holter, M.M.; Chirikjian, M.K.; Govani, V.N.; Cummings, B.P. TGR5 Signaling in Hepatic Metabolic Health. *Nutrients* **2020**, *12*, 2598. [CrossRef]
11. McGavigan, A.K.; Garibay, D.; Henseler, Z.M.; Chen, J.; Bettaieb, A.; Haj, F.G.; Ley, R.E.; Chouinard, M.L.; Cummings, B.P. TGR5 contributes to glucoregulatory improvements after vertical sleeve gastrectomy in mice. *Gut* **2015**, *66*, 226–234. [CrossRef] [PubMed]
12. Chevre, R.; Castaño, D.; Chua, T.; Corlianò, M.; Patankar, J.V.; Sng, L.; Sim, L.; Juin, T.L.; Carissimo, G.; Ng, L.F.P.; et al. Therapeutic modulation of the bile acid pool by *Cyp8b1* knockdown protects against nonalcoholic fatty liver disease in mice. *FASEB J.* **2018**, *32*, 3792–3802. [CrossRef] [PubMed]
13. Maczewsky, J.; Kaiser, J.; Gresch, A.; Gerst, F.; Düfer, M.; Krippeit-Drews, P.; Drews, G. TGR5 Activation Promotes Stimulus-Secretion Coupling of Pancreatic β-Cells via a PKA-Dependent Pathway. *Diabetes* **2018**, *68*, 324–336. [CrossRef] [PubMed]

14. Finn, P.D.; Rodriguez, D.; Kohler, J.; Jiang, Z.; Wan, S.; Blanco, E.; King, A.J.; Chen, T.; Bell, N.; Dragoli, D.; et al. Intestinal TGR5 agonism improves hepatic steatosis and insulin sensitivity in Western diet-fed mice. *Am. J. Physiol. Liver Physiol.* **2019**, *316*, G412–G424. [CrossRef]
15. Castellanos-Jankiewicz, A.; Guzmán-Quevedo, O.; Fénelon, V.S.; Zizzari, P.; Quarta, C.; Bellocchio, L.; Tailleux, A.; Charton, J.; Fernandois, D.; Henricsson, M.; et al. Hypothalamic bile acid-TGR5 signaling protects from obesity. *Cell Metab.* **2021**, *33*, 1483–1492.e10. [CrossRef]
16. Drigo, R.A.; Fonseca, T.L.; Werneck-De-Castro, J.P.S.; Bianco, A.C. Role of the type 2 iodothyronine deiodinase (D2) in the control of thyroid hormone signaling. *Biochim. Biophys. Acta* **2013**, *1830*, 3956–3964. [CrossRef]
17. Sasaki, T.; Watanabe, Y.; Kuboyama, A.; Oikawa, A.; Shimizu, M.; Yamauchi, Y.; Sato, R. Muscle-specific TGR5 overexpression improves glucose clearance in glucose-intolerant mice. *J. Biol. Chem.* **2021**, *296*, 100131. [CrossRef]
18. Kida, T.; Tsubosaka, Y.; Hori, M.; Ozaki, H.; Murata, T. Bile Acid Receptor TGR5 Agonism Induces NO Production and Reduces Monocyte Adhesion in Vascular Endothelial Cells. *Arter. Thromb. Vasc. Biol.* **2013**, *33*, 1663–1669. [CrossRef]
19. Duboc, H.; Aelion, H.; Rainteau, D.; Rajca, S.; Sokol, H.; Humbert, L.; Farabos, D.; Coffin, B.; Weber, S.; Porcher, R.; et al. Crosstalk between the hepatologist and the cardiologist: A future place for the lithocholic acid as a coronary atheroma risk factor? *Hepatology* **2012**, *56*, 2426. [CrossRef]
20. Tiwari, A.; Maiti, P. TGR5: An emerging bile acid G-protein-coupled receptor target for the potential treatment of metabolic disorders. *Drug Discov. Today* **2009**, *14*, 523–530. [CrossRef]
21. Sasaki, T.; Kuboyama, A.; Mita, M.; Murata, S.; Shimizu, M.; Inoue, J.; Mori, K.; Sato, R. The exercise-inducible bile acid receptor Tgr5 improves skeletal muscle function in mice. *J. Biol. Chem.* **2018**, *293*, 10322–10332. [CrossRef]
22. Hov, J.R.; Keitel, V.; Laerdahl, J.K.; Spomer, L.; Ellinghaus, E.; ElSharawy, A.; Melum, E.; Boberg, K.M.; Manke, T.; Balschun, T.; et al. Mutational Characterization of the Bile Acid Receptor TGR5 in Primary Sclerosing Cholangitis. *PLoS ONE* **2010**, *5*, e12403. [CrossRef]
23. Kuhre, R.E.; Wewer Albrechtsen, N.J.; Larsen, O.; Jepsen, S.L.; Balk-Møller, E.; Andersen, D.B.; Deacon, C.F.; Schoonjans, K.; Reimann, F.; Gribble, F.M.; et al. Bile acids are important direct and indirect regulators of the secretion of appetite- and metabolism-regulating hormones from the gut and pancreas. *Mol. Metab.* **2018**, *11*, 84–95. [CrossRef]
24. Kawamata, Y.; Fujii, R.; Hosoya, M.; Harada, M.; Yoshida, H.; Miwa, M.; Fukusumi, S.; Habata, Y.; Itoh, T.; Shintani, Y.; et al. A G Protein-coupled Receptor Responsive to Bile Acids. *J. Biol. Chem.* **2003**, *278*, 9435–9440. [CrossRef] [PubMed]
25. Qi, Y.C.; Li, P.F. Progress in the study of TGR5 receptor-mediated signaling pathway. *Chin. J. Pharmacol.* **2020**, *36*, 153–157.
26. Herbert, M.R.; Siegel, D.L.; Staszewski, L.; Cayanan, C.; Banerjee, U.; Dhamija, S.; Anderson, J.; Fan, A.; Wang, L.; Rix, P.; et al. Synthesis and SAR of 2-aryl-3-aminomethylquinolines as agonists of the bile acid receptor TGR5. *Bioorg. Med. Chem. Lett.* **2010**, *20*, 5718–5721. [CrossRef] [PubMed]
27. Perino, A.; Demagny, H.; Velazquez-Villegas, L.A.; Schoonjans, K. Molecular physiology of bile acid signaling in health, disease, and aging. *Physiol. Rev.* **2021**, *101*, 683–731. [CrossRef]
28. Wang, X.X.; Xie, C.; Libby, A.E.; Ranjit, S.; Levi, J.; Myakala, K.; Bhasin, K.; Jones, B.A.; Orlicky, D.J.; Takahashi, S.; et al. The role of FXR and TGR5 in reversing and preventing progression of Western diet–induced hepatic steatosis, inflammation, and fibrosis in mice. *J. Biol. Chem.* **2022**, *298*, 102530. [CrossRef] [PubMed]
29. Li, T.; Francl, J.M.; Boehme, S.; Ochoa, A.; Zhang, Y.; Klaassen, C.D.; Erickson, S.K.; Chiang, J.Y. Glucose and insulin induction of bile acid synthesis: Mechanisms and implication in diabetes and obesity. *J Biol Chem.* **2012**, *287*, 1861–1873. [CrossRef] [PubMed]
30. Xie, G.; Jiang, R.; Wang, X.; Liu, P.; Zhao, A.; Wu, Y.; Huang, F.; Liu, Z.; Rajani, C.; Zheng, X.; et al. Conjugated secondary 12α-hydroxylated bile acids promote liver fibrogenesis. *Ebiomedicine* **2021**, *66*, 103290. [CrossRef]
31. Ticho, A.L.; Malhotra, P.; Dudeja, P.K.; Gill, R.K.; Alrefai, W.A. Intestinal Absorption of Bile Acids in Health and Disease. *Compr. Physiol.* **2019**, *10*, 21–56. [CrossRef]
32. Pathak, P.; Liu, H.; Boehme, S.; Xie, C.; Krausz, K.W.; Gonzalez, F.; Chiang, J.Y.L. Farnesoid X receptor induces Takeda G-protein receptor 5 cross-talk to regulate bile acid synthesis and hepatic metabolism. *J. Biol. Chem.* **2017**, *292*, 11055–11069. [CrossRef]
33. Xie, C.; Huang, W.; Young, R.L.; Jones, K.L.; Horowitz, M.; Rayner, C.K.; Wu, T. Role of Bile Acids in the Regulation of Food Intake, and Their Dysregulation in Metabolic Disease. *Nutrients* **2021**, *13*, 1104. [CrossRef]
34. Donepudi, A.C.; Boehme, S.; Li, F.; Chiang, J.Y. G-protein-coupled bile acid receptor plays a key role in bile acid metabolism and fasting-induced hepatic steatosis in mice. *Hepatology* **2017**, *65*, 813–827. [CrossRef]
35. Gillard, J.; Clerbaux, L.-A.; Nachit, M.; Sempoux, C.; Staels, B.; Bindels, L.B.; Tailleux, A.; Leclercq, I.A. Bile acids contribute to the development of non-alcoholic steatohepatitis in mice. *JHEP Rep.* **2022**, *4*, 100387. [CrossRef]
36. Qi, Y.; Duan, G.; Wei, D.; Zhao, C.; Ma, Y. The Bile Acid Membrane Receptor TGR5 in Cancer: Friend or Foe? *Molecules* **2022**, *27*, 5292. [CrossRef]
37. Scheen, A.J. Dual GIP/GLP-1 receptor agonists: New advances for treating type-2 diabetes. *Ann. D'endocrinologie* **2023**, *84*, 316–321. [CrossRef]
38. Ballantyne, G.H.; Longo, W.E.; Savoca, P.E.; Adrian, T.E.; Vukasin, A.P.; Bilchik, A.J.; Sussman, J.; Modlin, I.M. Deoxycholate-stimulated release of peptide YY from the isolated perfused rabbit left colon. *Am. J. Physiol. Liver Physiol.* **1989**, *257*, G715–G724. [CrossRef]
39. Saito, M.; Matsushita, M.; Yoneshiro, T.; Okamatsu-Ogura, Y. Brown Adipose Tissue, Diet-Induced Thermogenesis, and Thermogenic Food Ingredients: From Mice to Men. *Front. Endocrinol.* **2020**, *11*, 222. [CrossRef]

40. Svensson, P.-A.; Olsson, M.; Andersson-Assarsson, J.C.; Taube, M.; Pereira, M.J.; Froguel, P.; Jacobson, P. The TGR5 gene is expressed in human subcutaneous adipose tissue and is associated with obesity, weight loss and resting metabolic rate. *Biochem. Biophys. Res. Commun.* **2013**, *433*, 563–566. [CrossRef]
41. Depommier, C.; Everard, A.; Druart, C.; Plovier, H.; Van Hul, M.; Vieira-Silva, S.; Falony, G.; Raes, J.; Maiter, D.; Delzenne, N.M.; et al. Supplementation with Akkermansia muciniphila in overweight and obese human volunteers: A proof-of-concept exploratory study. *Nat. Med.* **2019**, *25*, 1096–1103. [CrossRef]
42. Wu, Q.; Liang, X.; Wang, K.; Lin, J.; Wang, X.; Wang, P.; Zhang, Y.; Nie, Q.; Liu, H.; Zhang, Z.; et al. Intestinal hypoxia-inducible factor 2α regulates lactate levels to shape the gut microbiome and alter thermogenesis. *Cell Metab.* **2021**, *33*, 1988–2003.e7. [CrossRef] [PubMed]
43. Shen, H.; Ding, L.; Baig, M.; Tian, J.; Wang, Y.; Huang, W. Improving glucose and lipids metabolism: Drug development based on bile acid related targets. *Cell Stress* **2021**, *5*, 1–18. [CrossRef] [PubMed]
44. Bouzas, C.; Pastor, R.; Garcia, S.; Monserrat-Mesquida, M.; Martínez-González, M.; Salas-Salvadó, J.; Corella, D.; Goday, A.; Martínez, J.A.; Alonso-Gómez, M.; et al. Comparative effects of glucagon-like peptide-1 receptors agonists, 4-dipeptidyl peptidase inhibitors, and metformin on metabolic syndrome. *Biomed. Pharmacother.* **2023**, *161*, 114561. [CrossRef] [PubMed]
45. Christiansen, C.B.; Trammell, S.A.J.; Wewer Albrechtsen, N.J.; Schoonjans, K.; Albrechtsen, R.; Gillum, M.; Kuhre, R.E.; Holst, J.J. Bile acids drive colonic secretion of glucagon-like-peptide 1 and peptide-YY in rodents. *Am. J. Physiol. Liver Physiol.* **2019**, *316*, G574–G584. [CrossRef]
46. Morimoto, K.; Watanabe, M.; Sugizaki, T.; Irie, J.-I.; Itoh, H. Intestinal Bile Acid Composition Modulates Prohormone Convertase 1/3 (PC1/3) Expression and Consequent GLP-1 Production in Male Mice. *Endocrinology* **2016**, *157*, 1071–1081. [CrossRef]
47. Makki, K.; Brolin, H.; Petersen, N.; Henricsson, M.; Christensen, D.P.; Khan, M.T.; Wahlström, A.; Bergh, P.-O.; Tremaroli, V.; Schoonjans, K.; et al. 6α-hydroxylated bile acids mediate TGR5 signalling to improve glucose metabolism upon dietary fiber supplementation in mice. *Gut* **2022**, *72*, 314–324. [CrossRef]
48. Zhai, H.; Li, Z.; Peng, M.; Huang, Z.; Qin, T.; Chen, L.; Li, H.; Zhang, H.; Zhang, W.; Xu, G. Takeda G Protein-Coupled Receptor 5-Mechanistic Target of Rapamycin Complex 1 Signaling Contributes to the Increment of Glucagon-Like Peptide-1 Production after Roux-en-Y Gastric Bypass. *Ebiomedicine* **2018**, *32*, 201–214. [CrossRef]
49. Tian, F.; Xu, W.; Chen, L.; Chen, T.; Feng, X.; Chen, J.; Wei, D.; Huang, Q. Ginsenoside compound K increases glucagon-like peptide-1 release and L-cell abundance in db/db mice through TGR5/YAP signaling. *Int. Immunopharmacol.* **2022**, *113*, 109405. [CrossRef]
50. Sorrentino, G.; Perino, A.; Yildiz, E.; El Alam, G.; Sleiman, M.B.; Gioiello, A.; Pellicciari, R.; Schoonjans, K. Bile Acids Signal via TGR5 to Activate Intestinal Stem Cells and Epithelial Regeneration. *Gastroenterology* **2020**, *159*, 956–968.e8. [CrossRef]
51. Chen, M.-J.; Liu, C.; Wan, Y.; Yang, L.; Jiang, S.; Qian, D.-W.; Duan, J.-A. Enterohepatic circulation of bile acids and their emerging roles on glucolipid metabolism. *Steroids* **2020**, *165*, 108757. [CrossRef]
52. Chiang, J.Y.; Pathak, P.; Liu, H.; Donepudi, A.; Ferrell, J.; Boehme, S. Intestinal Farnesoid X Receptor and Takeda G Protein Couple Receptor 5 Signaling in Metabolic Regulation. *Dig. Dis.* **2017**, *35*, 241–245. [CrossRef]
53. Zhai, Z.; Niu, K.; Liu, H.; Lin, C.; Tu, Y.; Liu, Y.; Cai, L.; Ouyang, K.; Liu, J. Policosanol alleviates hepatic lipid accumulation by regulating bile acids metabolism in C57BL6/mice through AMPK–FXR–TGR5 cross-talk. *J. Food Sci.* **2021**, *86*, 5466–5478. [CrossRef]
54. Zhu, H.; Wang, K.; Chen, S.; Kang, J.; Guo, N.; Chen, H.; Liu, J.; Wu, Y.; He, P.; Tu, Y.; et al. Saponins from *Camellia sinensis* Seeds Stimulate GIP Secretion in Mice and STC-1 Cells via SGLT1 and TGR. *Nutrients* **2022**, *14*, 3413. [CrossRef]
55. Zhang, Y.; Huang, S.; Li, P.; Chen, Q.; Li, Y.; Zhou, Y.; Wang, L.; Kang, M.; Zhang, B.; Yang, B.; et al. Pancreatic cancer-derived exosomes suppress the production of GIP and GLP-1 from STC-1 cells in vitro by down-regulating the PCSK1/3. *Cancer Lett.* **2018**, *431*, 190–200. [CrossRef]
56. Wu, Y.; He, H.; Cheng, Z.; Bai, Y.; Ma, X. The Role of Neuropeptide Y and Peptide YY in the Development of Obesity via Gut-brain Axis. *Curr. Protein Pept. Sci.* **2019**, *20*, 750–758. [CrossRef]
57. Yang, H.; Liu, H.; Jiao, Y.W.; Qian, J. Roux-en-Y Gastrointestinal Bypass Promotes Activation of TGR5 and Peptide YY. *Endocr. Metab. Immune Disord. Drug Targets* **2020**, *20*, 1262–1267. [CrossRef]
58. Guida, C.; Stephen, S.; Watson, M.; Dempster, N.; Larraufie, P.; Marjot, T.; Cargill, T.; Rickers, L.; Pavlides, M.; Tomlinson, J.; et al. PYY plays a key role in the resolution of diabetes following bariatric surgery in humans. *Ebiomedicine* **2019**, *40*, 67–76. [CrossRef]
59. Bala, V.; Rajagopal, S.; Kumar, D.P.; Nalli, A.D.; Mahavadi, S.; Sanyal, A.J.; Grider, J.R.; Murthy, K.S. Release of GLP-1 and PYY in response to the activation of G protein-coupled bile acid receptor TGR5 is mediated by Epac/PLC-Îµ pathway and modulated by endogenous H2S. *Front. Physiol.* **2014**, *5*, 420. [CrossRef]
60. Huang, S.; Ma, S.; Ning, M.; Yang, W.; Ye, Y.; Zhang, L.; Shen, J.; Leng, Y. TGR5 agonist ameliorates insulin resistance in skeletal muscles and improves glucose homeostasis in diabetic mice. *Metabolism* **2019**, *99*, 45–56. [CrossRef]
61. Sun, L.; Li, F.; Tan, W.; Zhao, W.; Li, Y.; Zhu, X.; Gao, P.; Shu, G.; Wang, S.; Jiang, Q.; et al. Lithocholic acid promotes skeletal muscle regeneration through the TGR5 receptor. *Acta Biochim. Biophys. Sin.* **2023**, *55*, 51–61. [CrossRef]
62. Sahakyan, G.; Vejux, A.; Sahakyan, N. The Role of Oxidative Stress-Mediated Inflammation in the Development of T2DM-Induced Diabetic Nephropathy: Possible Preventive Action of Tannins and Other Oligomeric Polyphenols. *Molecules* **2022**, *27*, 9035. [CrossRef]

63. Xiao, H.; Sun, X.; Liu, R.; Chen, Z.; Lin, Z.; Yang, Y.; Zhang, M.; Liu, P.; Quan, S.; Huang, H. Gentiopicroside activates the bile acid receptor Gpbar1 (TGR5) to repress NF-kappaB pathway and ameliorate diabetic nephropathy. *Pharmacol. Res.* **2019**, *151*, 104559. [CrossRef]
64. Perino, A.; Pols, T.W.H.; Nomura, M.; Stein, S.; Pellicciari, R.; Schoonjans, K. TGR5 reduces macrophage migration through mTOR-induced C/EBPβ differential translation. *J. Clin. Investig.* **2014**, *124*, 5424–5436. [CrossRef]
65. Guo, C.; Xie, S.; Chi, Z.; Zhang, J.; Liu, Y.; Zhang, L.; Zheng, M.; Zhang, X.; Xia, D.; Ke, Y.; et al. Bile Acids Control Inflammation and Metabolic Disorder through Inhibition of NLRP3 Inflammasome. *Immunity* **2016**, *45*, 802–816. [CrossRef]
66. Watanabe, M.; Houten, S.M.; Mataki, C.; Christoffolete, M.A.; Kim, B.W.; Sato, H.; Messaddeq, N.; Harney, J.W.; Ezaki, O.; Kodama, T.; et al. Bile acids induce energy expenditure by promoting intracellular thyroid hormone activation. *Nature* **2006**, *439*, 484–489. [CrossRef]
67. de Jesus, L.A.; Carvalho, S.D.; Ribeiro, M.O.; Schneider, M.; Kim, S.-W.; Harney, J.W.; Larsen, P.R.; Bianco, A.C. The type 2 iodothyronine deiodinase is essential for adaptive thermogenesis in brown adipose tissue. *J. Clin. Investig.* **2001**, *108*, 1379–1385. [CrossRef]
68. Gereben, B.; Zavacki, A.M.; Ribich, S.; Kim, B.W.; Huang, S.A.; Simonides, W.S.; Zeld, A.; Bianco, A.C. Cellular and Molecular Basis of Deiodinase-Regulated Thyroid Hormone Signaling. *Endocr. Rev.* **2008**, *29*, 898–938. [CrossRef]
69. Fonseca, T.L.; Russo, S.C.; Luongo, C.; Salvatore, D.; Bianco, A.C. Inactivation of Type 3 Deiodinase Results in Life-long Changes in the Brown Adipose Tissue Transcriptome in the Male Mouse. *Endocrinology* **2022**, *5*, 1–10. [CrossRef]
70. Velazquez-Villegas, L.A.; Perino, A.; Lemos, V.; Zietak, M.; Nomura, M.; Pols, T.W.H.; Schoonjans, K. TGR5 signalling promotes mitochondrial fission and beige remodelling of white adipose tissue. *Nat. Commun.* **2018**, *9*, 1–13. [CrossRef]
71. Krauss, S.; Zhang, C.-Y.; Lowell, B.B. The mitochondrial uncoupling-protein homologues. *Nat. Rev. Mol. Cell Biol.* **2005**, *6*, 248–261. [CrossRef]
72. Jeong, J.H.; Cho, S.; Pak, Y.K. Sterol-independent repression of low density lipoprotein receptor promoter by peroxisome proliferator activated receptor γ coactivator-1α (PGC-1α). *Exp. Mol. Med.* **2009**, *41*, 406–416. [CrossRef]
73. Fan, M.; Wang, Y.; Jin, L.; Fang, Z.; Peng, J.; Tu, J.; Liu, Y.; Zhang, E.; Xu, S.; Liu, X.; et al. Bile Acid–Mediated Activation of Brown Fat Protects From Alcohol-Induced Steatosis and Liver Injury in Mice. *Cell. Mol. Gastroenterol. Hepatol.* **2021**, *13*, 809–826. [CrossRef]
74. Lund, M.L.; Egerod, K.L.; Engelstoft, M.S.; Dmytriyeva, O.; Theodorsson, E.; Patel, B.A.; Schwartz, T.W. Enterochromaffin 5-HT cells—A major target for GLP-1 and gut microbial metabolites. *Mol. Metab.* **2018**, *11*, 70–83. [CrossRef]
75. Zhan, Y.; Wen, Y.; Zhang, L.-L.; Shen, X.-L.; Chen, X.-H.; Wu, X.-H.; Tang, X.-G. Paeoniflorin Improved Constipation in the Loperamide-Induced Rat Model via TGR5/TRPA1 Signaling-Mediated 5-Hydroxytryptamine Secretion. *Evid.-Based Complement Altern. Med.* **2021**, *2021*, 6076293. [CrossRef]
76. Wu, X.; Li, J.-Y.; Lee, A.; Lu, Y.-X.; Zhou, S.-Y.; Owyang, C. Satiety induced by bile acids is mediated via vagal afferent pathways. *J. Clin. Investig.* **2020**, *5*, e132400. [CrossRef] [PubMed]
77. Chen, C.; Zhou, Y.; Huang, R.; Wang, M.; Li, Y.; Li, J. Bile acids regulate anorexigenic neuropeptide through p-STAT3-SOCS3 signaling in mouse hypothalamic cells. *Nan Fang Yi Ke Da Xue Xue Bao* **2020**, *40*, 1001–1007. [PubMed]
78. Perino, A.; Velázquez-Villegas, L.A.; Bresciani, N.; Sun, Y.; Huang, Q.; Fénelon, V.S.; Castellanos-Jankiewicz, A.; Zizzari, P.; Bruschetta, G.; Jin, S.; et al. Central anorexigenic actions of bile acids are mediated by TGR. *Nat. Metab.* **2021**, *3*, 595–603. [CrossRef] [PubMed]
79. Pols, T.W.; Nomura, M.; Harach, T.; Sasso, G.L.; Oosterveer, M.H.; Thomas, C.; Rizzo, G.; Gioiello, A.; Adorini, L.; Pellicciari, R.; et al. TGR5 Activation Inhibits Atherosclerosis by Reducing Macrophage Inflammation and Lipid Loading. *Cell Metab.* **2011**, *14*, 747–757. [CrossRef]
80. Guizoni, D.M.; Vettorazzi, J.F.; Carneiro, E.M.; Davel, A.P. Modulation of endothelium-derived nitric oxide production and activity by taurine and taurine-conjugated bile acids. *Nitric Oxide* **2019**, *94*, 48–53. [CrossRef]
81. Hashimoto, E.; Taniai, M.; Tokushige, K. Characteristics and diagnosis of NAFLD/NASH. *J. Gastroenterol. Hepatol.* **2013**, *28*, 64–70. [CrossRef] [PubMed]
82. Lambert, J.E.; Ramos-Roman, M.A.; Browning, J.D.; Parks, E.J. Increased De Novo Lipogenesis Is a Distinct Characteristic of Individuals With Nonalcoholic Fatty Liver Disease. *Gastroenterology* **2014**, *146*, 726–735. [CrossRef]
83. Cegla, J. Liraglutide safety and efficacy in patients with non-alcoholic steatohepatitis (LEAN): A multicentre, double-blind, randomized, placebo-controlled phase 2 study. *Ann. Clin. Biochem. Int. J. Biochem. Lab. Med.* **2016**, *53*, 518. [CrossRef] [PubMed]
84. El-Jamal, N.; Erdual, E.; Neunlist, M.; Koriche, D.; Dubuquoy, C.; Maggiotto, F.; Chevalier, J.; Berrebi, D.; Dubuquoy, L.; Boulanger, E.; et al. Glugacon-like peptide-2: Broad receptor expression, limited therapeutic effect on intestinal inflammation and novel role in liver regeneration. *Am. J. Physiol. Gastrointest. Liver Physiol.* **2014**, *307*, G274–G285. [CrossRef]
85. Ivory, C.P.A.; Wallace, L.E.; McCafferty, D.-M.; Sigalet, D.L. Interleukin-10-independent anti-inflammatory actions of glucagon-like peptide. *Am. J. Physiol. Liver Physiol.* **2008**, *295*, G1202–G1210. [CrossRef]
86. Baffy, G. Kupffer cells in non-alcoholic fatty liver disease: The emerging view. *J. Hepatol.* **2009**, *51*, 212–223. [CrossRef]
87. Mobraten, K.; Haugbro, T.; Karlstrom, E.; Kleiveland, C.R.; Lea, T. Activation of the bile acid receptor TGR5 enhances LPS-induced inflammatory responses in a human monocytic cell line. *J. Recept. Signal Transduct.* **2015**, *35*, 402–409. [CrossRef]
88. Yang, H.; Luo, F.; Wei, Y.; Jiao, Y.; Qian, J.; Chen, S.; Gong, Y.; Tang, L. TGR5 protects against cholestatic liver disease via suppressing the NF-κB pathway and activating the Nrf2/HO-1 pathway. *Ann. Transl. Med.* **2021**, *9*, 1158. [CrossRef]

89. Shi, Y.; Su, W.; Zhang, L.; Shi, C.; Zhou, J.; Wang, P.; Wang, H.; Shi, X.; Wei, S.; Wang, Q.; et al. TGR5 Regulates Macrophage Inflammation in Nonalcoholic Steatohepatitis by Modulating NLRP3 Inflammasome Activation. *Front. Immunol.* **2020**, *11*, 609060. [CrossRef]
90. Zhao, L.; Zhang, H.; Liu, X.; Xue, S.; Chen, D.; Zou, J.; Jiang, H. TGR5 deficiency activates antitumor immunity in non-small cell lung cancer via restraining M2 macrophage polarization. *Acta Pharm. Sin. B* **2022**, *12*, 787–800. [CrossRef]
91. Rao, J.; Yang, C.; Yang, S.; Lu, H.; Hu, Y.; Lu, L.; Cheng, F.; Wang, X. Deficiency of TGR5 exacerbates immune-mediated cholestatic hepatic injury by stabilizing the β-catenin destruction complex. *Int. Immunol.* **2020**, *32*, 321–334. [CrossRef] [PubMed]
92. Shao, J.; Ge, T.; Tang, C.; Wang, G.; Pang, L.; Chen, Z. Synergistic anti-inflammatory effect of gut microbiota and lithocholic acid on liver fibrosis. *Inflamm. Res.* **2022**, *71*, 1389–1401. [CrossRef]
93. Carino, A.; Marchianò, S.; Biagioli, M.; Bucci, M.; Vellecco, V.; Brancaleone, V.; Fiorucci, C.; Zampella, A.; Monti, M.C.; Distrutti, E.; et al. Agonism for the bile acid receptor GPBAR1 reverses liver and vascular damage in a mouse model of steatohepatitis. *FASEB J.* **2019**, *33*, 2809–2822. [CrossRef]
94. Häussinger, D.; Keitel, V. Role of TGR5 (GPBAR1) in Liver Disease. *Semin. Liver Dis.* **2018**, *38*, 333–339. [CrossRef]
95. Yang, C.; Wan, M.; Xu, D.; Pan, D.; Xia, H.; Yang, L.; Sun, G. Flaxseed Powder Attenuates Non-Alcoholic Steatohepatitis via Modulation of Gut Microbiota and Bile Acid Metabolism through Gut–Liver Axis. *Int. J. Mol. Sci.* **2021**, *22*, 10858. [CrossRef]
96. Yang, J.-Y.; Lee, Y.-S.; Kim, Y.; Lee, S.-H.; Ryu, S.; Fukuda, S.; Hase, K.; Yang, C.-S.; Lim, H.; Kim, M.-S.; et al. Gut commensal Bacteroides acidifaciens prevents obesity and improves insulin sensitivity in mice. *Mucosal Immunol.* **2017**, *10*, 104–116. [CrossRef] [PubMed]
97. Suraweera, D.; Rahal, H.; Jimenez, M.; Viramontes, M.; Choi, G.; Saab, S. Treatment of primary biliary cholangitis ursodeoxycholic acid non-responders: A systematic review. *Liver Int.* **2017**, *37*, 1877–1886. [CrossRef] [PubMed]
98. Murakami, M.; Une, N.; Nishizawa, M.; Suzuki, S.; Ito, H.; Horiuchi, T. Incretin secretion stimulated by ursodeoxycholic acid in healthy subjects. *Springerplus* **2013**, *2*, 20. [CrossRef] [PubMed]
99. Pellicciari, R.; Gioiello, A.; Macchiarulo, A.; Thomas, C.; Rosatelli, E.; Natalini, B.; Sardella, R.; Pruzanski, M.; Roda, A.; Pastorini, E.; et al. Discovery of 6α-Ethyl-23(*S*)-methylcholic Acid (*S*-EMCA, INT-777) as a Potent and Selective Agonist for the TGR5 Receptor, a Novel Target for Diabesity. *J. Med. Chem.* **2009**, *52*, 7958–7961. [CrossRef]
100. Thomas, C.; Gioiello, A.; Noriega, L.; Strehle, A.; Oury, J.; Rizzo, G.; Macchiarulo, A.; Yamamoto, H.; Mataki, C.; Pruzanski, M.; et al. TGR5-Mediated Bile Acid Sensing Controls Glucose Homeostasis. *Cell Metab.* **2009**, *10*, 167–177. [CrossRef]
101. Liu, X.; Guan, J.; Wu, Z.; Xu, L.; Sun, C. The TGR5 Agonist INT-777 Promotes Peripheral Nerve Regeneration by Activating cAMP-dependent Protein Kinase A in Schwann Cells. *Mol. Neurobiol.* **2023**, *60*, 1901–1913. [CrossRef]
102. Huang, R.; Gao, Y.; Chen, J.; Duan, Q.; He, P.; Zhang, J.; Huang, H.; Zhang, Q.; Ma, G.; Zhang, Y.; et al. TGR5 Agonist INT-777 Alleviates Inflammatory Neurodegeneration in Parkinson's Disease Mouse Model by Modulating Mitochondrial Dynamics in Microglia. *Neuroscience* **2022**, *490*, 100–119. [CrossRef]
103. de Oliveira, M.C.; Gilglioni, E.H.; de Boer, B.A.; Runge, J.H.; de Waart, D.R.; Salgueiro, C.L.; Ishii-Iwamoto, E.L.; Elferink, R.P.O.; Gaemers, I.C. Bile acid receptor agonists INT747 and INT777 decrease oestrogen deficiency-related postmenopausal obesity and hepatic steatosis in mice. *Biochim. Biophys. Acta* **2016**, *1862*, 2054–2062. [CrossRef]
104. Sasaki, T.; Ikari, N.; Hashimoto, S.; Sato, R. Identification of α-ionone, nootkatone, and their derivatives as TGR5 agonists. *Biochem. Biophys. Res. Commun.* **2023**, *653*, 147–152. [CrossRef] [PubMed]
105. Zhao, S.; Li, X.; Wang, L.; Peng, W.; Ye, W.; Li, W.; Wang, Y.-D.; Chen, W.-D. Design, synthesis and evaluation of 1-benzyl-1H-imidazole-5-carboxamide derivatives as potent TGR5 agonists. *Bioorganic Med. Chem.* **2020**, *32*, 115972. [CrossRef] [PubMed]
106. Vassileva, G.; Golovko, A.; Markowitz, L.; Abbondanzo, S.J.; Zeng, M.; Yang, S.; Hoos, L.; Tetzloff, G.; Levitan, D.; Murgolo, N.J.; et al. Targeted deletion of Gpbar1 protects mice from cholesterol gallstone formation. *Biochem. J.* **2006**, *398*, 423–430. [CrossRef]
107. Piotrowski, D.W.; Futatsugi, K.; Warmus, J.S.; Orr, S.T.M.; Freeman-Cook, K.D.; Londregan, A.T.; Wei, L.; Jennings, S.M.; Herr, M.; Coffey, S.B.; et al. Identification of Tetrahydropyrido[4,3-*d*]pyrimidine Amides as a New Class of Orally Bioavailable TGR5 Agonists. *ACS Med. Chem. Lett.* **2012**, *4*, 63–68. [CrossRef]
108. Alemi, F.; Kwon, E.; Poole, D.P.; Lieu, T.; Lyo, V.; Cattaruzza, F.; Cevikbas, F.; Steinhoff, M.; Nassini, R.; Materazzi, S.; et al. The TGR5 receptor mediates bile acid–induced itch and analgesia. *J. Clin. Investig.* **2013**, *123*, 1513–1530. [CrossRef] [PubMed]
109. Fryer, R.M.; Ng, K.J.; Mazurek, S.G.N.; Patnaude, L.; Skow, D.J.; Muthukumarana, A.; Gilpin, K.E.; Dinallo, R.M.; Kuzmich, D.; Lord, J.; et al. G Protein–Coupled Bile Acid Receptor 1 Stimulation Mediates Arterial Vasodilation through a $K_{Ca}1.1$ (BK_{Ca})–Dependent Mechanism. *Experiment* **2014**, *348*, 421–431. [CrossRef] [PubMed]

Disclaimer/Publisher's Note: The statements, opinions and data contained in all publications are solely those of the individual author(s) and contributor(s) and not of MDPI and/or the editor(s). MDPI and/or the editor(s) disclaim responsibility for any injury to people or property resulting from any ideas, methods, instructions or products referred to in the content.

metabolites

MDPI

Article

Mucosal Metabolomic Signatures in Chronic Colitis: Novel Insights into the Pathophysiology of Inflammatory Bowel Disease

Nathan Calzadilla [1], Aisha Qazi [2], Anchal Sharma [2], Kai Mongan [2], Shane Comiskey [2], Jahnavi Manne [2], Alvin G. Youkhana [2], Sonam Khanna [2], Seema Saksena [2,3], Pradeep K. Dudeja [2,3], Waddah A. Alrefai [2,3] and Ravinder K. Gill [2,3,*]

[1] Department of Biomedical Engineering, University of Illinois Chicago, Chicago, IL 60612, USA; ncalza3@uic.edu
[2] Division of Gastroenterology & Hepatology, University of Illinois Chicago, Chicago, IL 60612, USA; aqazi7@uic.edu (A.Q.); anchals@uic.edu (A.S.); kmongan@neomed.edu (K.M.); shanec@uic.edu (S.C.); jmanne2@uic.edu (J.M.); ayoukh4@uic.edu (A.G.Y.); skhann5@uic.edu (S.K.); saksena@uic.edu (S.S.); pkdudeja@uic.edu (P.K.D.); walrefai@uic.edu (W.A.A.)
[3] Jesse Brown VA Medical Center, Chicago, IL 60612, USA
* Correspondence: rgill@uic.edu; Tel.: +1-(312)-569-7463

Abstract: Inflammatory bowel diseases (IBD) involve complex interactions among genetic factors, aberrant immune activation, and gut microbial dysbiosis. While metabolomic studies have focused on feces and serum, fewer investigations have examined the intestinal mucosa despite its crucial role in metabolite absorption and transport. The goals of this study were twofold: to test the hypothesis that gut microbial dysbiosis from chronic intestinal inflammation leads to mucosal metabolic alterations suitable for therapeutic targeting, and to address gaps in metabolomic studies of intestinal inflammation that have overlooked the mucosal metabolome. The chronic DSS colitis was induced for five weeks in 7–9-week-old wild-type C57BL/6J male mice followed by microbial profiling with targeted 16srRNA sequencing service. Mucosal metabolite measurements were performed by Metabolon (Morrisville, NC). The data were analyzed using the bioinformatic tools Pathview, MetOrigin, and Metaboanalyst. The novel findings demonstrated increases in several host- and microbe-derived purine, pyrimidine, endocannabinoid, and ceramide metabolites in colitis. Origin analysis revealed that microbial-related tryptophan metabolites kynurenine, anthranilate, 5-hydroxyindoleacetate, and C-glycosyltryptophan were significantly increased in colon mucosa during chronic inflammation and strongly correlated with disease activity. These findings offer new insights into the pathophysiology of IBD and provide novel potential targets for microbial-based therapeutics.

Keywords: chronic colitis; mucosal inflammation; host–microbe interactions; mucosal metabolomics

1. Introduction

Inflammatory bowel diseases (IBD) are chronic, debilitating illnesses with two major subtypes: ulcerative colitis and Crohn's disease. Between 1990 and 2017, the number of affected individuals rose from 3.7 million to 6.8 million, with the highest prevalence rates in North America [1]. In addition to diarrhea, abdominal pain, ulcers, and rectal bleeding, IBD carries an increased risk of colon cancer along with several extraintestinal manifestations [2]. Ulcerative colitis is characterized by mucosal inflammation localized to the colon, while Crohn's disease is characterized by full thickness inflammation anywhere along the gastrointestinal tract with skip lesions [3]. While there are many therapeutic options, treatment is complex, not curative, and carries significant side effects [4]. Moreover, patients with refractory disease often require surgery and possibly parenteral nutrition. Further complicating the clinical picture are the various factors in the pathophysiology of

IBD, including host genetic factors, intestinal barrier disruption, immune dysregulation, gut microbial dysbiosis, and altered metabolite pools [5]. This has led to several groups utilizing metabolomic and integrated omic tools to better understand the pathophysiology and progression of IBD [6–15].

For instance, meta-analysis of gene expression data in IBD patients revealed that ileal and colonic disease have distinct molecular patterns that are not adequately considered with clinical diagnosis and management [16]. These approaches have also been successfully applied to predict patient responses to anti-integrin therapy for the implementation of more efficacious combinatorial treatments [17]. Several studies have also performed microbiota profiling and metabolomics in the serum and feces of IBD patients to detect novel disease signatures [18,19]. Furthermore, human studies provide tremendous value in their translational potential, but due to the myriad of confounding variables in clinical studies, it is much more difficult to reach mechanistic conclusions. Therefore, animal models of IBD are often used to mimic human disease and supplement human studies [20]. Additionally, animal models allow for more uniformity and the ability to capture a disease process at a specific timepoint. For instance, one such study performed untargeted mucosal and serum metabolomics in a model of acute DSS colitis and found that alterations in tryptophan metabolism affected AhR-mediated IL-10 signaling [21]. Moreover, these high throughput approaches have also been used to identify novel drivers of intestinal inflammation such as proteins involved in the actin cytoskeleton and beneficial dietary compounds from human studies with further investigation using animal models to gain mechanistic insight [22,23]. However, there is a need for such studies in additional models that are more reflective of the chronically relapsing and remitting nature of IBD.

Here we performed untargeted colonic mucosal metabolomic profiling in a murine model of chronic DSS colitis that resembles IBD. The objectives of this study were to understand gut microbial changes during chronic colitis, identify differentially altered microbial metabolites, and uncover altered pathways during chronic intestinal inflammation for future study. This study was driven by the hypothesis that chronic colonic inflammation drives unique changes in the mucosal metabolome reflective of IBD due to inflammation-induced gut microbial dysbiosis and disturbed intestinal architecture.

2. Materials and Methods

2.1. Animals

All animal studies were performed in accordance with institutional guidelines and regulations and approved by the Animal Care Committees of the University of Illinois at Chicago and the Jesse Brown Veterans Affairs Medical Center (Approval Code: ACC 21-078). Wild-type C57/BL6 mice were purchased from Jackson Laboratory (Bar Harbour, ME, USA). Autoclaved polypropylene cages with corncob bedding were used to house the mice. The mice were provided free access to food and water (Teklad Irradiated LM-485 Mouse/Rat Diet 7912, Envigo, Indianapolis, IN, USA) under a 12 h light/dark cycle. Male mice aged 7–9 weeks were provided either water alone (control group) or water supplemented with 2.5% *w*/*v* dextran sulfate sodium (DSS) (colitis group) for 5 weeks to induce chronic colitis. DSS was administered to mice for three cycles (one week/cycle), alternating with water only between the cycles (DSS was administered during weeks 1, 3, and 5, while water was administered during weeks 2 and 4) [24].

2.2. Metabolomic Analysis

Samples were processed and analyzed by Metabolon Inc. (Durham, NC, USA) as previously described [25]. Additional details are provided below.

2.2.1. Sample Preparation

Hamilton Company's automated MicroLab STAR® system was used to prepare samples. For quality control purposes, several recovery standards were added prior to the first step in the extraction process. Proteins were precipitated with methanol for 2 min

with vigorous shaking, followed by centrifugation for 5 min at 700× *g* to dissociate small molecules bound to protein or trapped in the precipitated protein matrix and recover chemically diverse metabolites (Glen Mills GenoGrinder 2000). The resulting extract was divided into five fractions: two for analysis using two separate reverse phases (RP)/UPLC-MS/MS methods with positive ion mode electrospray ionization (ESI), one for analysis using RP/UPLC-MS/MS with negative ion mode ESI, one for analysis using HILIC/UPLC-MS/MS with negative ion mode ESI, and one for backup. To remove the organic solvent, samples were briefly placed on a TurboVap® (Zymark; Hopkinton, MA, USA). Before preparing for analysis, the sample extracts were dried overnight under nitrogen gas [25].

2.2.2. Ultrahigh Performance Liquid Chromatography–Tandem Mass Spectroscopy (UPLC-MS/MS)

Waters ACQUITY ultra-performance liquid chromatography (UPLC) and a Thermo Scientific Q-Exactive high resolution/accurate mass spectrometer interfaced with a heated electrospray ionization (HESI-II) source and Orbitrap mass analyzer operated at 35,000 mass resolution were used in all methods. The sample extract was dried before being reconstituted in solvents suitable for each of the four methods. To ensure injection and chromatographic consistency, each reconstitution solvent contained a series of standards at fixed concentrations. One aliquot was analyzed under acidic positive ion conditions, which were chromatographically tailored for more hydrophilic substances. In this procedure, the extract was gradient eluted from a C18 column (Waters UPLC BEH C18-2.1 × 100 mm, 1.7 m) using water and methanol containing 0.05% perfluoropentanoic acid (PFPA) and 0.1% formic acid (FA). Another aliquot was examined under acidic positive ion conditions that had been chromatographically tuned for more hydrophobic substances. The extract was gradient-eluted from the same aforementioned C18 column using methanol, acetonitrile, water, 0.05% PFPA, and 0.01% FA and was operated at a higher total organic content in this method. A separate dedicated C18 column was used to evaluate another aliquot under basic negative ion optimized conditions. The basic extracts were gradient-eluted from the column with methanol and water containing 6.5 mM ammonium bicarbonate at pH 8. After being eluted from an HILIC column (Waters UPLC BEH Amide 2.1 × 150 mm, 1.7 m) using a gradient of water and acetonitrile with 10 mM ammonium formate, pH 10.8, the fourth aliquot was subjected to negative ionization analysis. Dynamic exclusion was used to alternate between the MS analysis and data-dependent MSn scans. The scan range varied slightly between methods, but it was between 70 and 1000 m/z. The raw data files were archived and extracted in the manner described below [25].

2.2.3. Compound Identification and Metabolite Quantification

Using Metabolon's equipment and software (Durham, NC, USA), raw data were retrieved, peaks were found, and quality control was performed. Compounds were discovered by comparing them to purified standards in the library. The library was built on authenticated standards and included retention time/index (RI), mass-to-charge ratio (m/z), and chromatographic data (including MS/MS spectrum data). Compound identification was based on the retention index within a limited RI window of the proposed identification, an accurate mass match to the library within 10 ppm, and the MS/MS forward and reverse scores between experimental data and authenticated standards. Peaks were measured using the area-under-the-curve method and normalized to total protein as determined using the Bradford assay [25].

2.3. Bioinformatic Analysis

Heatmaps were generated for statistically significant differential metabolites using ComplexHeatMap in R [26,27]. Origin analysis was performed utilizing the online MetOrigin interface [28]. Briefly, a list of significantly altered metabolites with Kyoto Encyclopedia of Genes and Genomes (KEGG) and Human Metabolome Database (HMBD) IDs

were uploaded, and we proceeded with simple analysis. Enrichment analysis and sPLSDA analysis were performed using Metaboanalyst [29].

2.4. Myeloperoxidase Activity

With some minor modifications, the Krawisz [30] method was used to measure myeloperoxidase activity (MPO) in the distal colon. MPO activity is expressed as units per milligram of tissue after being normalized to the amount of tissue.

2.5. Hematoxylin and Eosin Staining

The intestines were sampled, and they were quickly rinsed in PBS. The tissues were immediately snap-frozen in liquid nitrogen after being embedded in OCT media. Hematoxylin and eosin (H&E) staining was performed according to the manufacturer's protocol (ScyTek Laboratories, Logan, UT, USA) on longitudinal sections that were 5 μm thick, as previously described [31].

2.6. Microbial Sampling and 16S rRNA Sequencing

Cecal contents were collected and immediately snap-frozen in liquid nitrogen. Samples were sent to Zymo Research (Irvine, CA, USA) for 16S rRNA sequencing. Amplicon sequence variant (ASV) analysis was performed with DADA2. Linear discriminant analysis (LDA) was performed with bioBakery [32,33].

2.7. Statistical Analysis

For metabolite abundances, Welch's two-sample *t*-test was used to assess the significance and set at a level of $p < 0.05$. A false discovery rate (FDR) method was also applied with a set $q < 0.1$. Welch's two-sample *t*-test was used to assess significance for all other comparisons.

3. Results

3.1. Gut Microbial Dysbiosis Is Associated with Chronic DSS Treatment

Mucosal inflammation is a key feature in IBD [34]. Optimal treatment options focusing on complete healing of the mucosa are warranted. To understand the key mucosal alterations occurring during chronic intestinal inflammation, we utilized the chronic DSS colitis to model the relapsing and remitting nature of human IBD. Wild-type mice were administered alternating cycles of 2.5% DSS in drinking water and water alone for five weeks to induce chronic colitis (Figure 1A). We first assessed the severity of experimentally induced inflammation. As shown in Figure 1B and Supplementary Figure S1, colon length was significantly decreased in the group treated with DSS, suggestive of intestinal inflammation. The average colon length decreased from 6.3 cm to 5.0 cm during chronic DSS treatment ($p < 0.0001$). Additionally, the colon weight-to-length ratio, a marker used to determine diarrhea, was significantly increased in the group treated with chronic DSS ($p < 0.0001$) (Figure 1C). Given that another key aspect of colitis is neutrophil infiltration, the severity of inflammation was further determined by measuring myeloperoxidase (MPO) activity in colonic mucosa from the distal colon. Figure 1D showed that the average MPO activity increased from 0.495 units/mg of tissue to 6.163 units/mg of tissue ($p = 0.0333$). Further, qPCR demonstrated increases in the mRNA expression of proinflammatory cytokines IL-1β ($p = 0.0067$) (Figure 1E) and CXCL1 ($p = 0.0224$) (Figure 1F). Finally, representative histological analysis revealed architectural distortion, active inflammation, and a greater than 25% ulcerated area in the distal colon during chronic DSS colitis compared to controls (Figure 1G).

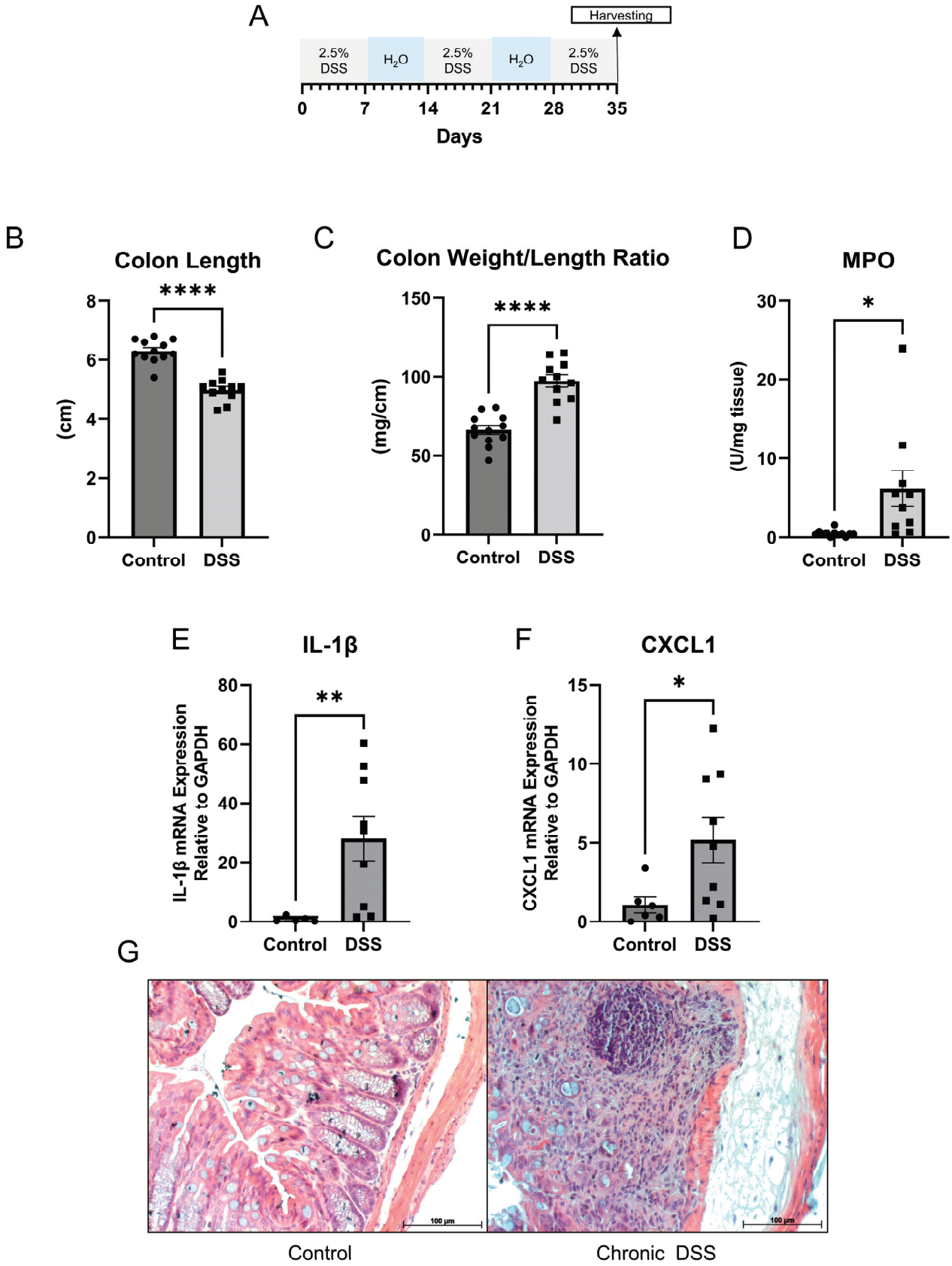


Figure 1. (**A**) Schematic for study design. (**B**) Colon length (cm) (**C**) Colon weight/length ratio (mg/cm) (**D**) Myeloperoxidase (MPO) activity units per mg of tissue (control $n = 12$; dextran sulfate sodium (DSS) $n = 11$). (**E**,**F**) Quantitative PCR for IL-1β and CXCL1 in distal colon mucosa (control $n = 5$; DSS $n = 9$). (**G**) Representative hematoxylin and eosin staining of control and chronic DSS mice. (Welch *t*-test; * $p < 0.05$, ** $p < 0.01$, **** $p < 0.0001$).

Gut microbial dysbiosis, another hallmark of chronic colitis, was further examined [35]. 16S rRNA sequencing was performed on the cecal contents, followed by LEfSe analysis to identify differentially altered microbes. The cladogram depicted in Figure 2A shows the various taxonomic levels of microbes associated with chronic colitis and control groups and their taxonomic relationship to each other from LEfSe (linear discriminant analysis effect size) analysis. A tabular summary of these taxa are depicted with their effect size and *p*-value in Supplemental Table S1. Additionally, changes observed in this study that are consistent with IBD are depicted in Supplemental Table S2 [36–42]. Figure 2B depicts the top 20 taxa associated with the control and DSS groups, and Supplemental Figures S2 and S3 depict all taxa. Of note, the phyla Verrucomicrobia, Bacteroidetes, and Actinobacteria were significantly associated with chronic DSS colitis. Furthermore, alpha diversity was assessed using several indices, including the total number of observed species, Chao1, Fisher, Shannon Diversity, and Simpson index. Overall, the data demonstrated a loss of alpha diversity within samples of mice with chronic colitis (Figure 2D). Specifically, the overall species observed dropped from 226.7 in the control group to 189.5 in the colitis group ($p = 0.0001$). Additionally, the Chao1, Fisher, Simpson, and Shannon diversity indices, which consider both the number of species and the abundance of each species, decreased from 226.8 in the control group to 189.5 during chronic colitis ($p = 0.0001$), 35.84 to 29.03 ($p = 0.0001$), 0.9819 to 0.9696 ($p = 0.0002$), and 6.629 to 6.117 ($p < 0.0001$), respectively. As expected, chronic colitis led to both a decrease in the overall number of species and the distribution of species. Furthermore, beta diversity was assessed using the weighted UniFrac method [43], which accounts for the presence of organisms, their abundance, and their taxonomic relationship to each other. The analysis showed that each sample's microbial communities clustered according to their treatment group (Figure 2E). Furthermore, a hallmark of microbial changes in IBD is a loss of short-chain fatty acid-producing bacteria [44]. There was a decrease in the relative abundance of the genus *Roseburia* ($p < 0.001$) (Figure 2C) and several *Roseburia* species (Supplemental Figure S4), which were identified as biomarkers for the control groups through LEfSe analysis. There have also been reported increases in the genus Lactobacillus in IBD cohorts [37], which were also found in the chronic DSS samples (Figure 2C, $p = 0.0070$). Further, we found increases in *Turicibacter sanguinis* ($p < 0.001$) and *Erysipelatoclostridium* species ($p < 0.001$), which also correspond well with previous reports on human cohorts with IBD (Figure 2C) [36]. Overall, our findings showed that chronic DSS treatment in mice resulted in chronic colitis phenotype with associated dysbiosis, providing an adequate model to further explore the mucosal changes that occur in the colon during on-again, off-again inflammatory insults.

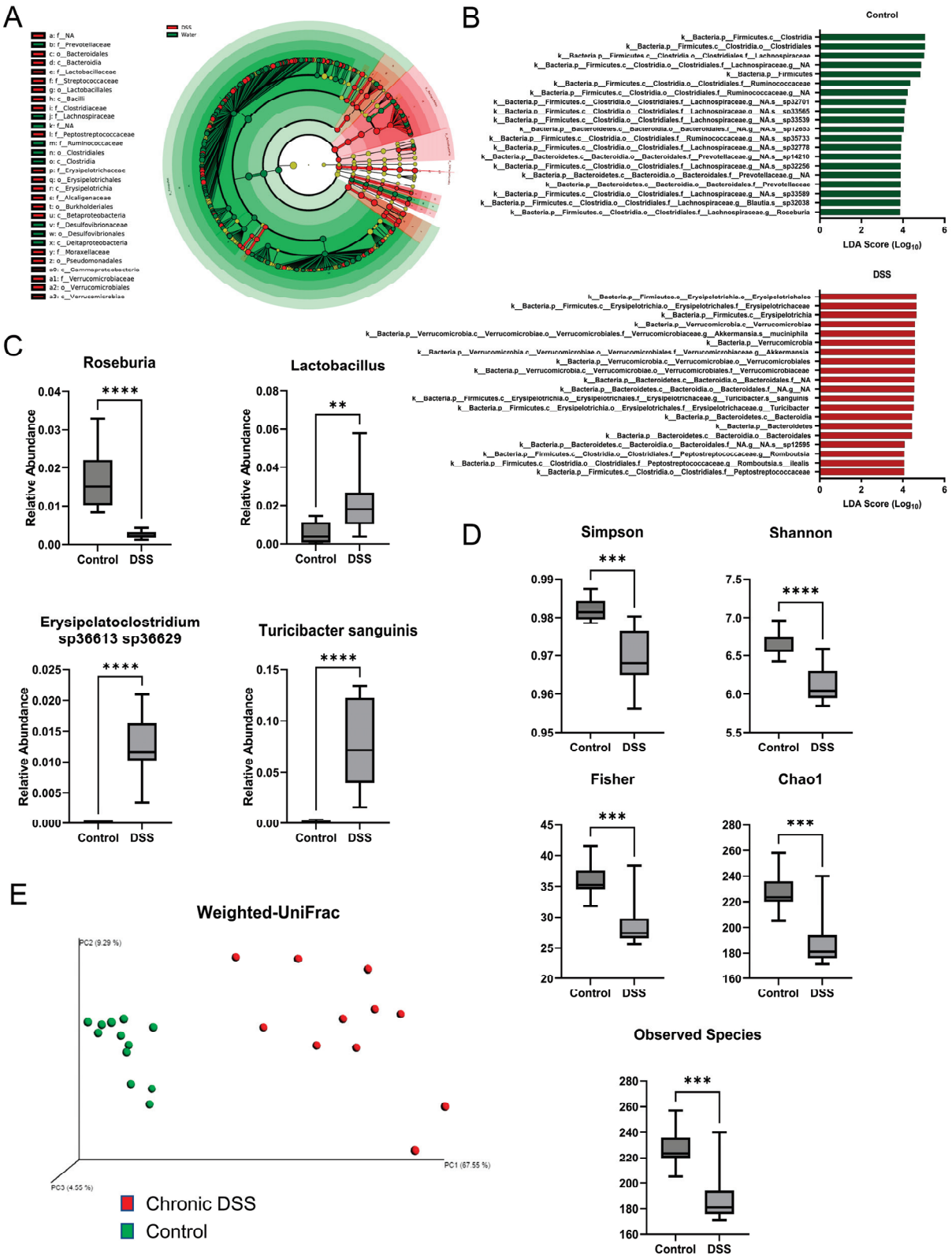


Figure 2. (**A**) Cladogram highlighting taxa associated with control water and dextran sulfate sodium (DSS) treatments based on linear discriminant analysis effect size. (**B**) Top 20 taxa associated with control group based on linear discriminant analysis effect size (LEfSe) analysis (**top**) and top 20 taxa associated with DSS group based on LEfSe analysis (**bottom**). (**C**) Boxplots of relative abundances for various taxa associated with inflammatory bowel diseases (IBD) ($p < 0.05$, Welch *t*-test; control $n = 12$; DSS $n = 11$). (**D**) Boxplots for alpha diversity measures. (**E**) Weighted UniFrac beta diversity plot. (Welch *t*-test; ** $p < 0.01$, *** $p < 0.001$, **** $p < 0.0001$).

3.2. Chronic Colitis Leads to Distinct Metabolomic Profile in the Colonic Mucosa

Given that functional changes in the gut microbiome are manifested through metabolic alterations, untargeted metabolomic analysis was next performed to take an unbiased approach to discovering novel changes in the intestinal mucosa during chronic inflammation. The analysis revealed a unique metabolic signature in the colon mucosa after chronic colitis. Overall, there were 314 differentially altered metabolites ($p < 0.05$, $q < 0.1$), with 80 being decreased and 234 metabolites increased in the colonic mucosa of mice with chronic colitis (Figure 3A, Supplemental Figure S5). Of the 314, the largest proportion of altered metabolites was involved in lipid metabolism, with the next largest group involved in amino acid metabolism. The same trend was observed for both the increased and decreased metabolites when compared to the control (Figure 3B). Additionally, sparse partial least squares discriminant analysis (sPLSDA) revealed two distinct clusters when comparing the colon mucosa metabolome of control mice to those with chronic colitis (Figure 3C). This assessment was followed up using enrichment analysis, which considers how many metabolites are altered within a given Kyoto Encyclopedia of Genes and Genomes (KEGG) pathway (Figure 3D). Of note, several nucleotide and amino acid metabolism pathways were among the most enriched.

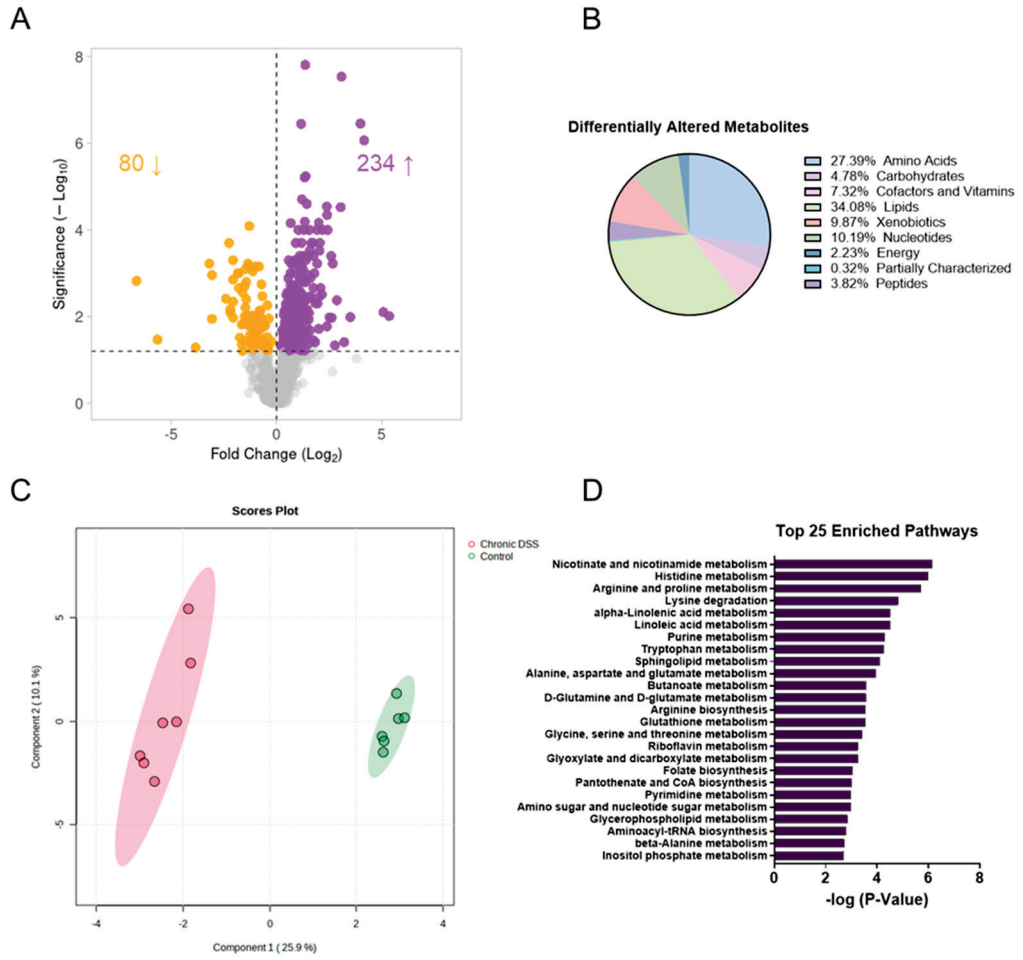


Figure 3. (**A**) Volcano plot (the log2 of the fold change of metabolites in wild-type (WT) dextran sulfate sodium (DSS) compared to WT was plotted against the −log10 of the *p*-value) where the up-facing arrow indicates the number of significantly metabolites increased in abundance and the down-facing arrow indicates the number of decreased and (**B**) pie chart showing the proportion of differentially altered metabolites by metabolite subtype. (**C**) Sparse partial least squares discriminant analysis (sPLSDA) plots generated in Metaboanalyst using the Statistical Analysis function. (**D**) Top 25 enriched pathways in mucosa of control vs. DSS treated mice.

3.3. Chronic Colitis Leads to Increased Mucosal Localization of Inflammatory Metabolites and Impaired Enterohepatic Circulation

Our investigations revealed striking differences in the mucosal abundances of several metabolites that are implicated in inflammatory processes such as polyamines, amino acid metabolites, eicosanoids, and TCA cycle intermediates. Figure 4A highlights the distributions of the significantly altered inflammatory mediators in the mucosa during chronic DSS colitis. It is worth highlighting the vast increase in mucosal itaconate levels of nearly 18-fold ($p < 0.001$) during chronic inflammation, as it has been shown to have anti-inflammatory properties in models for sepsis, autoimmune disease, and reperfusion injury [45]. Furthermore, kynurenine, a tryptophan metabolite known to be upregulated during inflammation, was increased nearly 16-fold ($p < 0.001$) in the mucosa after chronic DSS treatment. Additionally, our data revealed several interesting changes in metabolites involved in enterohepatic circulation (Figure 4B). For instance, the secondary bile acids deoxycholate and lithocholate, which are directly influenced by gut microbiota, are significantly decreased during chronic colitis ($p < 0.05$). Moreover, heme and its degradation products bilirubin, biliverdin, and protoporphyrin IX were significantly increased in the chronically inflamed mucosa, suggesting increased synthesis and/or absorption of erythrocyte byproducts.

3.4. Contribution of Microbial Mucosal Metabolomic Profile during Chronic Colitis

An unbiased approach was utilized to examine the potential link between gut microbial dysbiosis and the altered metabolic profile in the colonic mucosa. The bioinformatic tool Met-Origin was utilized to aid in classifying metabolites as related to microbes or co-metabolized by both the host and microbes. This analysis revealed a multitude of metabolites that were altered, at least in part, through changes in gut microbial composition (Figure 5). Our analysis showed 23 microbial-related metabolites differentially altered in chronic colitis (Figure 5A). Interestingly, fucose was increased in the colon mucosa of mice with chronic colitis. Additionally, several differentially altered metabolites were significantly associated with disease severity assessed by MPO levels (Figure 5B, Supplemental Figure S6). Our analysis revealed that in addition to several co-metabolized nucleotides highlighted in Figure 5, there were increases in heme-related metabolites protoporphyrin IX and biliverdin in the colonic mucosa of mice with chronic colitis (Figure 5C) that are also highlighted in Figure 4B in more detail. This may suggest increased heme breakdown and compensatory synthesis in response to chronic intestinal inflammation. Ultimately, this analysis allows for a better understanding of the contribution of gut microbial dysbiosis to the metabolomic alterations in the mucosa of mice with chronic colitis.

3.5. Chronic Colitis Alters Mucosal Dietary, Nucleotide, Amino Acid, and Lipid Metabolism

Food and plant components: Differentially altered metabolites were subsequently organized by their metabolic pathway. For instance, there were several alterations in dietary and plant-derived metabolites in the colonic mucosa of mice with chronic colitis (Figure 6A). Stachydrine and ergothioneine, for instance, are both increased in the mucosa during chronic colitis. Given that these are dietary metabolites, our findings suggest altered colonic nutrient absorption in response to inflammation. Our analysis also revealed alterations in several nucleotide metabolism pathways.

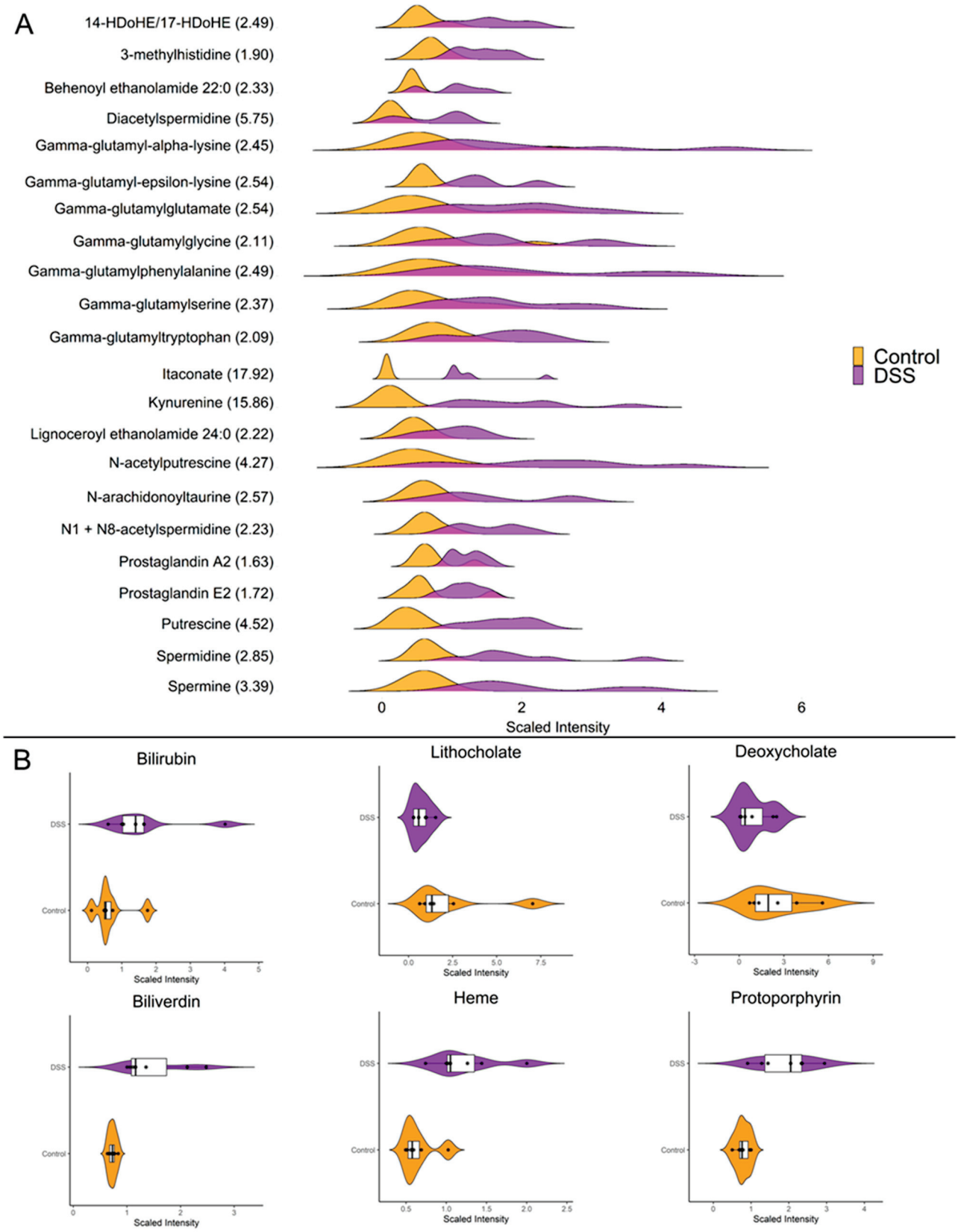


Figure 4. (**A**) Ridgeline plot showing the distributions of differentially altered metabolites with known roles as inflammatory mediators ($p < 0.05$, q < 0.01, Welch *t*-test; control $n = 6$; DSS $n = 7$). The values within parenthesis indicate the fold change between DSS and control. (**B**) Raincloud plots showing abundance and distributions of differentially altered enterohepatic metabolites ($p < 0.05$, q < 0.01, Welch *t*-test; control $n = 6$; DSS $n = 7$).

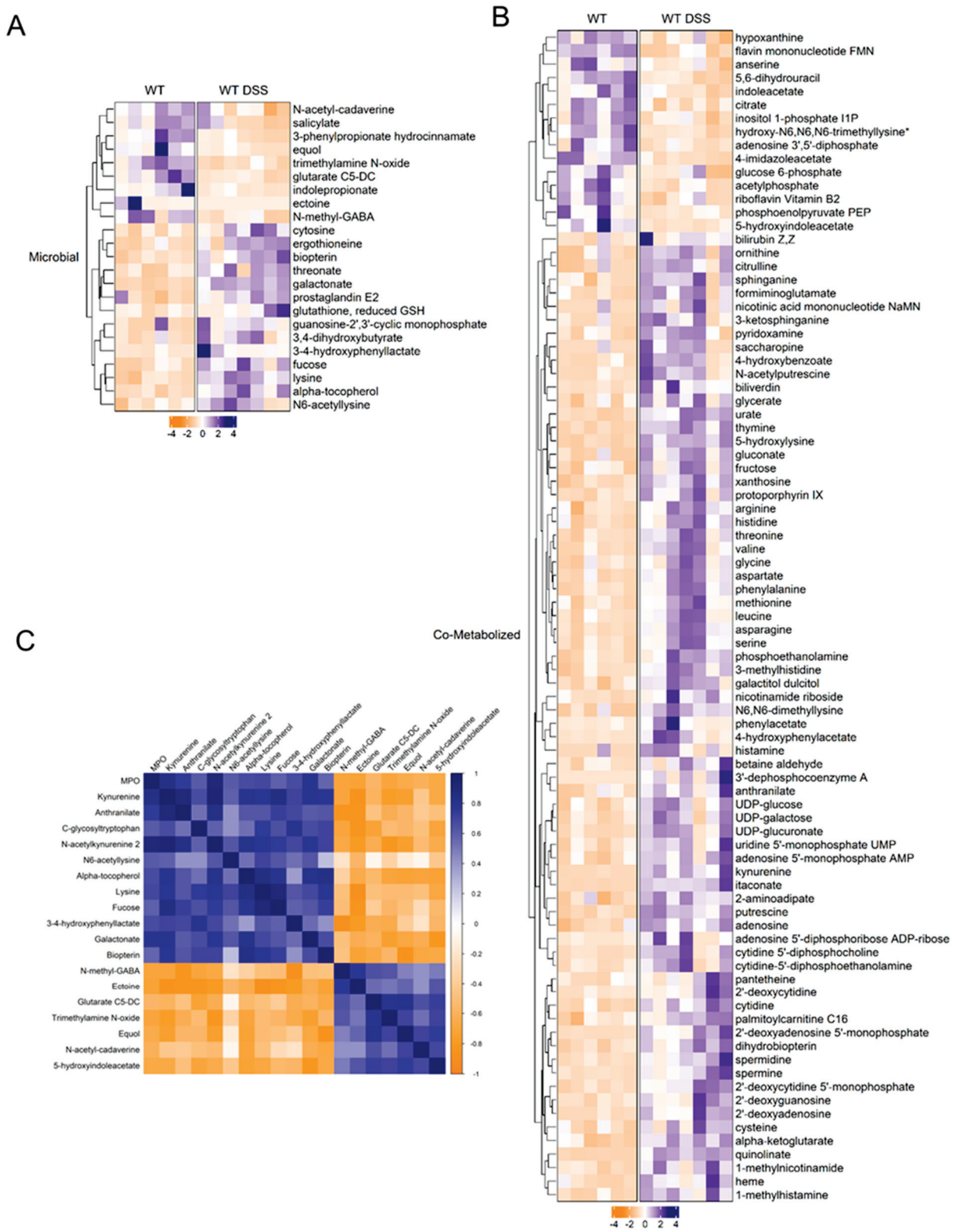


Figure 5. (**A**) Heatmap of microbial-related and (**B**) co-metabolized differentially altered metabolites between control and chronic colitis mice ($p < 0.05$, q < 0.1, Welch *t*-test; control $n = 6$; DSS $n = 7$. (**C**) Correlation plot showing Spearman correlation coefficients between microbial metabolites and MPO activity that were statistically significant ($p < 0.05$). * indicates compounds with lack of reference standard acquisition but their identity is based upon orthogonal information.

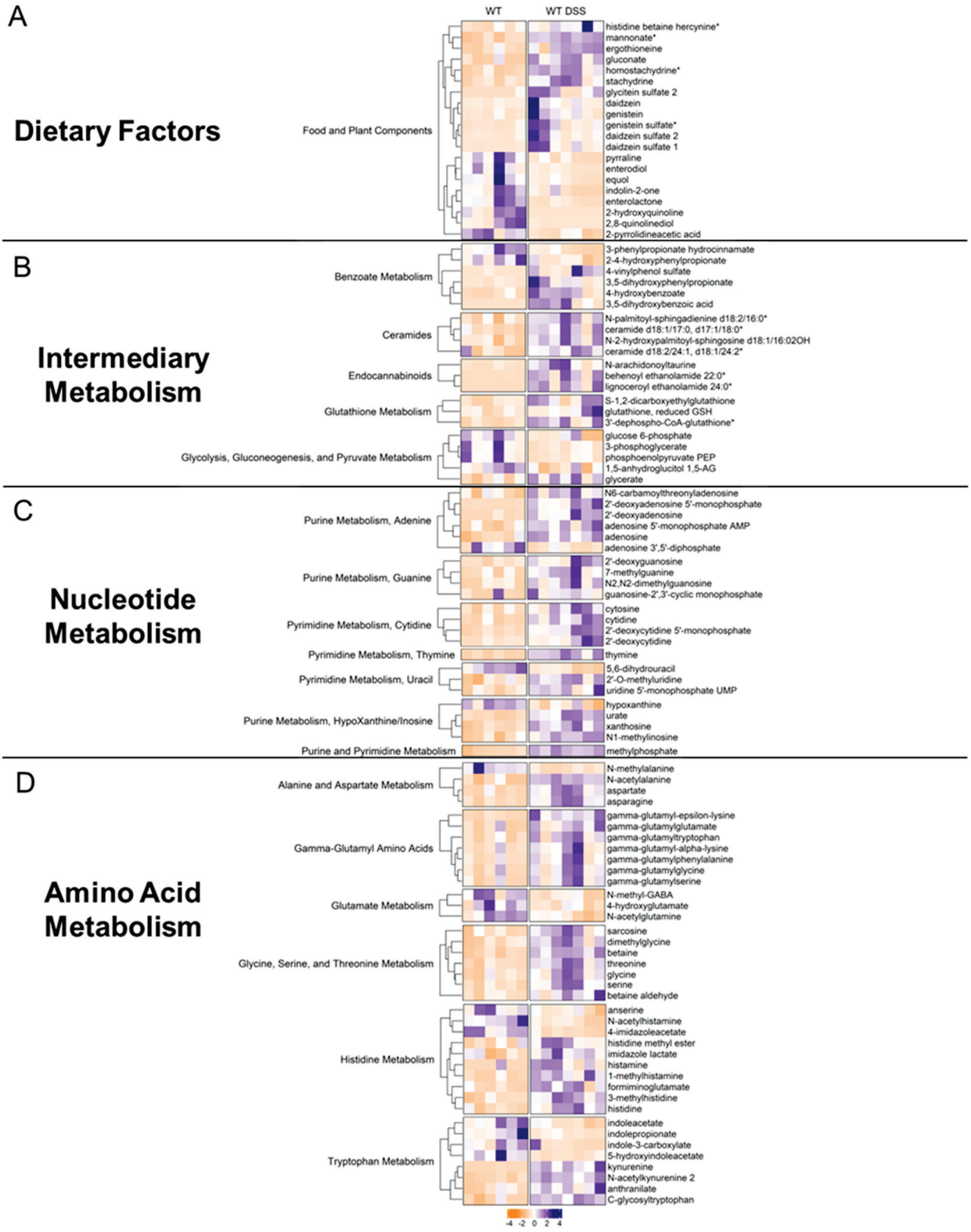


Figure 6. Heatmaps of differentially altered metabolites ($p < 0.05$, q < 0.1, Welch *t*-test) in (**A**) dietary factors, (**B**) intermediary metabolism, (**C**) nucleotide metabolism, and (**D**) amino acid metabolism. Heatmap was scaled from −4 to 4 (control = 6; DSS $n = 7$). * indicates compounds with lack of reference standard acquisition but their identity is based upon orthogonal information.

Intermediary metabolism: Several interesting increases in other classes of metabolites were also found. For instance, endocannabinoids (Figure 6B), a class of compounds newly

emerging as a possible therapeutic target in IBD, showed general increases in the mucosa of mice with chronic colitis. Other interesting findings included increases in ceramides. Furthermore, the mucosa of mice with chronic colitis demonstrated decreased glycolytic intermediates such as glucose 6-phosphate, phosphoenolpyruvate, and 3-phosphoglycerate, suggesting decreased glycolytic activity (Supplemental Figure S7).

Nucleotide metabolism: Generally, there were increases in metabolites involved in adenine, guanine, cytidine, thymine, uracil, and inosine metabolism (Figure 6C, Supplemental Figure S8) in the colon mucosa of chronic colitis mice, suggesting increased nucleotide production due to increased epithelial cell turnover. For instance, adenosine was increased in the mucosa during chronic colitis. Interestingly, adenosine receptor agonists have been shown to mitigate the effects of DSS-induced colitis through NF-κB signaling. Another interesting finding was the increase in methylated nucleotide metabolites such as N1-methylinosine, 2′-O-methyluridine, and N2, N2-dimethylguanosine, suggesting changes in genetic regulation.

Amino acid metabolism: Our data showed that gamma-glutamyl amino acids were increased during chronic colitis (Figure 6D, Supplemental Figure S9). Interestingly, decreases in microbial indole tryptophan metabolites and increases in co-metabolized kynurenine were also found, revealing alterations in tryptophan metabolism within intestinal mucosa during inflammation. Increases in the amino acids glycine, serine, threonine, histidine, aspartate, and asparagine were also identified, suggesting altered transport and/or metabolism in the intestinal mucosa during chronic inflammation. This analysis revealed several findings corroborated in human cohorts of IBD and other IBD models while also describing novel metabolomic findings in the colonic mucosa during chronic colitis.

4. Discussion

In this study, it was hypothesized that chronic colonic inflammation results in a unique microbially influenced mucosal metabolomic profile, providing new insight into the pathophysiology of inflammatory bowel diseases (IBD). This study investigated the gut microbial composition and mucosal metabolome of mice with induced chronic colitis. This work found that chronic colitis resulted in increased myeloperoxidase activity in the colon, as well as increased levels of proinflammatory cytokines IL-1β and CXCL1. Gut microbial analysis revealed expected losses in alpha diversity, two distinct beta diversity clusters, and microbial composition changes consistent with IBD patients. Furthermore, mucosal metabolomics revealed 328 differentially altered metabolites with several enriched metabolic pathways. These changes were alterations in microbial-related metabolites, food and plant components, nucleotides, amino acids, and lipids.

4.1. Facts and Perspectives

Gut microbial dysbiosis is a critical factor in the pathophysiology of IBD [35]. In this regard, several groups have investigated changes in the gut microbiome in IBD patients and in animal models for IBD with one characteristic feature being a loss of alpha diversity [46,47], a measure for the total number of species as well as the abundance of such species, which were observed in the present study. Additionally, beta diversity, which has also been consistently affected by IBD [47], was also found to be affected by induced chronic colitis in the current study. Furthermore, several characteristic microbial changes have been highlighted in the chosen disease model that have also been reported in IBD patients. The genus Roseburia was identified as a characteristic feature of untreated control mice and was significantly decreased in abundance in mice with chronic colitis. Roseburia are known to produce short-chain fatty acids, which have been shown to decrease in abundance in IBD, and administration of Roseburia intestinalis supernatant has been shown to alleviate induce colitis [48–50]. Although there was not a statistically significant decrease in the mucosal levels of the SCFA butyrate, there was a trend towards a decrease in the chronically inflamed mucosa. This could be due to SCFAs serving as the key fuel for colonocytes and thus being rapidly metabolized. There was also an increase in the genus

Lactobacillus, Turicibacter sanguinis, and an Erysipleatoclostridium species, which have also been observed in IBD patients [36,37,39].

While it was not surprising to observe distinct mucosal metabolic profiles during chronic colitis, there were several findings that have been corroborated in IBD patients parallel to novel discoveries that can be used for further mechanistic inquiries. For example, decreases in indole metabolites such as indoleacetate, indolepropionate (IPA), and indole-3-carboxylate have been shown in the serum of subjects with ulcerative colitis with IPA serving as a marker for disease remission [51]. Interestingly, our data show that the decreases in these indole metabolites are occuring in the intestinal mucosa during inflammation. This suggests that the decreases in the serum of those with IBD is due to decreased microbial production and not increased transport in mucosal epithelial or immune cells. Collectively, these findings can be exploited for the benefit of patients with IBD through microbial-based therapy with cocktails of microbes capable of synthesizing beneficial indole metabolites from tryptophan. Regarding dietary factors, increases in ergothioneine and stachydrine were found in the inflamed mucosa. Stachydrine has been shown to have anti-inflammatory properties in primary human chondrocytes isolated from subjects with osteoarthritis that were treated with IL-1β [52]. Ergothioneine was previously shown to also demonstrate protective effects against DSS-induced colitis by decreasing MPO activity levels and improving intestinal barrier function [53]. Taken together, our findings suggest a compensatory increase in the absorption of anti-inflammatory metabolites stachydrine and ergothioneine in response to mucosal inflammation. This suggests that increasing epithelial absorption of stachydrine and ergothioneine could be used as a potential therapeutic approach in IBD, possibly by increasing the activity of the ergothioneine transporter [54]. Increases in mucosal ceramides, which have been associated with increased inflammation in the mucosa of subjects with IBD, were found [55]. It was also found that the microbial-derived metabolite fucose, a sugar known to participate in the formation of Lewis antigens, was increased in the colon mucosa of mice with chronic colitis. This is particularly notable, as Lewis antigens have been associated with ulcerative colitis [56]. In fact, IgG and IgM reactivity has been shown to be increased towards fucosylated oligosaccharides in the serum of patients with Crohn's disease, implicating fucose-carrying Bacteroides species in intestinal inflammation [57]. In fact, our analysis identified the order Bacteroidales as a key distinguishing feature for mice with chronic colitis. Considering these findings, therapeutics targeting fucose degradation could serve as a novel strategy for inflammation in IBD.

The present study also identified several altered metabolic pathways in response to chronic colitis. There were decreased levels of glycolytic intermediates, which is important to note, as a previous study found that patients with IBD had antibodies that recognized several glycolytic enzymes as antigens [58]. One such enzyme was phosphoglycerate mutase, the enzyme responsible for conversion of glycerate-3P to glycerate-2P. Our rendering of the KEGG glycolysis pathway demonstrated decreased levels of glycerate-2P in the intestinal mucosa during chronic colitis, highlighting the need to further explore the implications of disrupted glycolysis. Our data also highlight novel increases in endocannabinoids in the colon mucosa during chronic inflammation. This is an important finding, as the role of the endocannabinoid system in IBD is an emerging area of interest [59]. Moreover, this work found increases in several ceramides, a class of sphingolipids, which are emerging as a new area of investigation in IBD [55]. Ultimately, this study provides a comprehensive report of alterations in mucosal metabolism during chronic inflammation in a relevant model that highlights microbial contributions, novel pathways for future investigation, and identifies newer therapeutic targets for intestinal inflammation.

This work characterized the gut microbial alterations associated with chronic inflammation and further elucidated the impacts of those changes by analyzing differentially altered microbial-related metabolites. For instance, these studies revealed increases in heme degradation products protoporphyrin IX and biliverdin within the chronically inflamed colon mucosa. Simultaneously, we found that *Turicibacter sanguinis*, a bacterial

species that synthesizes biliverdin through heme oxygenase [60], and the family of bacteria *Erysipelotrichaceae,* which are known to utilize protoporphyrin IX as a substrate [61], were both increased in the intestinal lumens of mice with chronic colitis. Our study yielded significant findings indicating elevated levels of various purine, pyrimidine, endocannabinoid, and ceramide metabolites derived from both the host and the gut microbiota in colitis with the potential to both serve as disease biomarkers and as areas of future mechanistic investigation. Notably, our analysis of the origin of these metabolites revealed a microbial contribution, particularly in the case of tryptophan metabolites, including kynurenine, anthranilate, 5-hydroxyindoleacetate, and C-glycosyltryptophan. These microbial-related tryptophan metabolites displayed substantial increases within the colon mucosa during chronic inflammation and exhibited strong correlations with disease activity. Consequently, these findings provide opportunity to develop targeted therapies for harnessing the beneficial metabolites through engineered microbes that can break the proinflammatory metabolites or shunt them towards the synthesis of beneficial compounds. For example, kynurenine aminotransferase-expressing microbes can be utilized to convert increased kynurenine into kynurenate [62]. These findings provide valuable insights into the underlying pathophysiology of IBD and present promising new targets for the development of microbial-based therapeutics.

4.2. Strengths of the Study

This study utilized a preclinical translational model for IBD in the form of chronic DSS colitis that mimics remitting and relapsing inflammation observed in human disease. Furthermore, while several metabolomic studies in IBD have focused on less invasive biological compartments such as serum and feces, the present study rigorously examined the mucosal metabolome—an understudied tissue compartment. Moreover, this work utilized a discovery approach with the integration of gut microbiota and mucosal metabolites. This resulted in the identification of differentially altered microbial metabolites resulting from gut microbial dysbiosis that can be utilized as potential biomarkers and targeted with microbial-based therapeutics. The limitations of our study include that metabolomic profiling and microbial sequencing were performed on two distinct sets of mice. However, the approaches utilized in this work were able to identify microbial contributions to microbial-related metabolic changes with MetOrigin. Furthermore, our study used only male mice and should be repeated in female mice at various stages of their estrous cycles, with those stages taken under consideration as a variable. While there are not strong differences in the incidence of IBD between males and females, there are some slight differences that require future study [63]. For instance, females tend to have a higher risk of CD while males tend to have a higher risk of UC. Future studies can focus on further exploring the mechanistic processes involved in the disruption of identified metabolic pathways by separating the mucosa into epithelial cell fractions and lamina propria fractions to better understand which changes are coming from epithelial cells or immune cells specifically.

5. Conclusions

In summary, our studies provide a comprehensive view into the metabolomic alterations in the intestinal mucosa during chronic inflammation that adds to the growing number of studies utilizing metabolomics to gain new insight into disease [64,65]. This study identified novel mucosal metabolites that could be used as potential inflammatory biomarkers and that should warrant further investigation such as disturbances in glycolytic metabolism, endocannabinoids, and ceramides. Finally, this work identified several potential therapeutic targets: increasing microbial production of indole metabolites, shunting kynurenine pathway, targeting fucose degradation, and increasing epithelial cell ergothioneine and stachydrine influx.

Supplementary Materials: The following supporting information can be downloaded at: https://www.mdpi.com/article/10.3390/metabo13070873/s1, Figure S1: Representative colon pictures; Figure S2: LEfSe analysis of taxa for control mice; Figure S3: LEfSe analysis of taxa for chronic DSS mice; Figure S4: Relative abundance of *Roseburia* species; Figure S5: Differentially altered mucosal metabolites; Figure S6: Associations between microbial metabolites and MPO; Figure S7: Metabolic alterations in glycolysis/gluconeogenesis; Figure S8: Metabolic alterations in pyrimidine and purine metabolism; Figure S9: Metabolic alterations in amino acid metabolism; Table S1: Notable changes in gut microbiota determine by LEfSe; Table S2: Overlapping microbiota changes with human IBD; Data S1: Gut microbial composition across samples; Data S2: Colon mucosa metabolomics.

Author Contributions: Conceptualization, W.A.A. and R.K.G.; Formal analysis, N.C.; Funding acquisition, N.C., S.S., P.K.D., W.A.A. and R.K.G.; Investigation, N.C., A.Q., A.S., K.M., S.C., J.M., A.G.Y. and S.K.; Methodology, N.C., A.Q. and A.S.; Writing—original draft, N.C.; Writing—review and editing, N.C., S.S., P.K.D., W.A.A. and R.K.G. All authors have read and agreed to the published version of the manuscript.

Funding: These studies were supported by the NIDDK grants R01 DK098170 (RKG); the Crohn's and Colitis Foundation CCFA 581138 (RKG), and the Department of Veterans Affairs I01BX000152 (WAA), I01BX002867 (SS), VA Merit Award I01BX002011 (PKD), VA Senior Research Career Scientist Award 1IK6BX005242 (PKD), VA BCCMA Award I01BX005862 (PKD), NIH NIDDK grant R01 DK092441 and R01 DK054016 (PKD), and F30AA030222 (NC), the Veterans Affairs Research Career Scientist Award 1IK6BX005243 (WAA).

Institutional Review Board Statement: All animal studies were performed in accordance with institutional guidelines and regulations and approved by the Animal Care Committees of the University of Illinois at Chicago and the Jesse Brown Veterans Affairs Medical Center (Approval Code: ACC 21-078).

Informed Consent Statement: Not applicable.

Data Availability Statement: All data is publicly available as part of supplemental data.

Conflicts of Interest: The authors declare no conflict of interest.

References

1. Kaplan, G.G.; Ng, S.C. Understanding and Preventing the Global Increase of Inflammatory Bowel Disease. *Gastroenterology* **2017**, *152*, 313–321.e2. [CrossRef] [PubMed]
2. Guan, Q. A Comprehensive Review and Update on the Pathogenesis of Inflammatory Bowel Disease. *J. Immunol. Res.* **2019**, *2019*, 7247238. [CrossRef] [PubMed]
3. Gohil, K.; Carramusa, B. Ulcerative Colitis and Crohn's Disease. *P T* **2014**, *39*, 576–577. [PubMed]
4. Al-Bawardy, B.; Shivashankar, R.; Proctor, D.D. Novel and Emerging Therapies for Inflammatory Bowel Disease. *Front. Pharmacol.* **2021**, *12*, 651415. [CrossRef]
5. Chang, J.T. Pathophysiology of Inflammatory Bowel Diseases. *N. Engl. J. Med.* **2020**, *383*, 2652–2664. [CrossRef]
6. Lloyd-Price, J.; Arze, C.; Ananthakrishnan, A.N.; Schirmer, M.; Avila-Pacheco, J.; Poon, T.W.; Andrews, E.; Ajami, N.J.; Bonham, K.S.; Brislawn, C.J.; et al. Multi-Omics of the Gut Microbial Ecosystem in Inflammatory Bowel Diseases. *Nature* **2019**, *569*, 655–662. [CrossRef]
7. Franzosa, E.A.; Sirota-Madi, A.; Avila-Pacheco, J.; Fornelos, N.; Haiser, H.J.; Reinker, S.; Vatanen, T.; Hall, A.B.; Mallick, H.; McIver, L.J.; et al. Gut Microbiome Structure and Metabolic Activity in Inflammatory Bowel Disease. *Nat. Microbiol.* **2019**, *4*, 293–305. [CrossRef]
8. Zheng, L.; Wen, X.-L.; Duan, S.-L. Role of Metabolites Derived from Gut Microbiota in Inflammatory Bowel Disease. *World J. Clin. Cases* **2022**, *10*, 2660–2677. [CrossRef]
9. Aldars-García, L.; Gisbert, J.P.; Chaparro, M. Metabolomics Insights into Inflammatory Bowel Disease: A Comprehensive Review. *Pharmaceuticals* **2021**, *14*, 1190. [CrossRef]
10. Kolho, K.-L.; Pessia, A.; Jaakkola, T.; de Vos, W.M.; Velagapudi, V. Faecal and Serum Metabolomics in Paediatric Inflammatory Bowel Disease. *J. Crohn's Colitis* **2017**, *11*, 321–334. [CrossRef]
11. Le Gall, G.; Noor, S.O.; Ridgway, K.; Scovell, L.; Jamieson, C.; Johnson, I.T.; Colquhoun, I.J.; Kemsley, E.K.; Narbad, A. Metabolomics of Fecal Extracts Detects Altered Metabolic Activity of Gut Microbiota in Ulcerative Colitis and Irritable Bowel Syndrome. *J. Proteome Res.* **2011**, *10*, 4208–4218. [CrossRef]
12. Bjerrum, J.T.; Wang, Y.; Hao, F.; Coskun, M.; Ludwig, C.; Günther, U.; Nielsen, O.H. Metabonomics of Human Fecal Extracts Characterize Ulcerative Colitis, Crohn's Disease and Healthy Individuals. *Metabolomics* **2015**, *11*, 122–133. [CrossRef]

13. Manzella, C.R.; Jayawardena, D.; Pagani, W.; Li, Y.; Alrefai, W.A.; Bauer, J.; Jung, B.; Weber, C.R.; Gill, R.K. Serum Serotonin Differentiates Between Disease Activity States in Crohn's Patients. *Inflamm. Bowel Dis.* **2020**, *26*, 1607–1618. [CrossRef] [PubMed]
14. De Preter, V.; Machiels, K.; Joossens, M.; Arijs, I.; Matthys, C.; Vermeire, S.; Rutgeerts, P.; Verbeke, K. Faecal Metabolite Profiling Identifies Medium-Chain Fatty Acids as Discriminating Compounds in IBD. *Gut* **2015**, *64*, 447–458. [CrossRef] [PubMed]
15. Jansson, J.; Willing, B.; Lucio, M.; Fekete, A.; Dicksved, J.; Halfvarson, J.; Tysk, C.; Schmitt-Kopplin, P. Metabolomics Reveals Metabolic Biomarkers of Crohn's Disease. *PLoS ONE* **2009**, *4*, e6386. [CrossRef] [PubMed]
16. Perez, K.; Ngollo, M.; Rabinowitz, K.; Hammoudi, N.; Seksik, P.; Xavier, R.J.; Daly, M.J.; Dotan, I.; Le Bourhis, L.; Allez, M. Meta-Analysis of IBD Gut Samples Gene Expression Identifies Specific Markers of Ileal and Colonic Diseases. *Inflamm. Bowel Dis.* **2022**, *28*, 775–782. [CrossRef]
17. Abreu, M.T.; Davies, J.M.; Quintero, M.A.; Delmas, A.; Diaz, S.; Martinez, C.D.; Venables, T.; Reich, A.; Crynen, G.; Deshpande, A.R.; et al. Transcriptional Behavior of Regulatory T Cells Predicts IBD Patient Responses to Vedolizumab Therapy. *Inflamm. Bowel Dis.* **2022**, *28*, 1800–1812. [CrossRef] [PubMed]
18. Gallagher, K.; Catesson, A.; Griffin, J.L.; Holmes, E.; Williams, H.R.T. Metabolomic Analysis in Inflammatory Bowel Disease: A Systematic Review. *J. Crohn's Colitis* **2021**, *15*, 813–826. [CrossRef]
19. Aldars-García, L.; Chaparro, M.; Gisbert, J.P. Systematic Review: The Gut Microbiome and Its Potential Clinical Application in Inflammatory Bowel Disease. *Microorganisms* **2021**, *9*, 977. [CrossRef]
20. Baydi, Z.; Limami, Y.; Khalki, L.; Zaid, N.; Naya, A.; Mtairag, E.M.; Oudghiri, M.; Zaid, Y. An Update of Research Animal Models of Inflammatory Bowel Disease. *Sci. World J.* **2021**, *2021*, 7479540. [CrossRef]
21. Lanis, J.M.; Alexeev, E.E.; Curtis, V.F.; Kitzenberg, D.A.; Kao, D.J.; Battista, K.D.; Gerich, M.E.; Glover, L.E.; Kominsky, D.J.; Colgan, S.P. Tryptophan Metabolite Activation of the Aryl Hydrocarbon Receptor Regulates IL-10 Receptor Expression on Intestinal Epithelia. *Mucosal. Immunol.* **2017**, *10*, 1133–1144. [CrossRef]
22. Chen, Y.; Mai, Q.; Chen, Z.; Lin, T.; Cai, Y.; Han, J.; Wang, Y.; Zhang, M.; Tan, S.; Wu, Z.; et al. Dietary Palmitoleic Acid Reprograms Gut Microbiota and Improves Biological Therapy against Colitis. *Gut Microbes* **2023**, *15*, 2211501. [CrossRef]
23. Kang, S.; Kim, J.; Park, A.; Koh, M.; Shin, W.; Park, G.; Lee, T.A.; Kim, H.J.; Han, H.; Kim, Y.; et al. TRIM40 Is a Pathogenic Driver of Inflammatory Bowel Disease Subverting Intestinal Barrier Integrity. *Nat. Commun.* **2023**, *14*, 700. [CrossRef] [PubMed]
24. Chassaing, B.; Aitken, J.D.; Malleshappa, M.; Vijay-Kumar, M. Dextran Sulfate Sodium (DSS)-Induced Colitis in Mice. *Curr. Protoc. Immunol.* **2014**, *104*, 15.25.1–15.25.14. [CrossRef]
25. Guo, L.; Milburn, M.V.; Ryals, J.A.; Lonergan, S.C.; Mitchell, M.W.; Wulff, J.E.; Alexander, D.C.; Evans, A.M.; Bridgewater, B.; Miller, L.; et al. Plasma Metabolomic Profiles Enhance Precision Medicine for Volunteers of Normal Health. *Proc. Natl. Acad. Sci. USA* **2015**, *112*, E4901–E4910. [CrossRef] [PubMed]
26. Gu, Z. Complex Heatmap Visualization. *iMeta* **2022**, *1*, e43. [CrossRef]
27. Gu, Z.; Eils, R.; Schlesner, M. Complex Heatmaps Reveal Patterns and Correlations in Multidimensional Genomic Data. *Bioinformatics* **2016**, *32*, 2847–2849. [CrossRef] [PubMed]
28. Yu, G.; Xu, C.; Zhang, D.; Ju, F.; Ni, Y. MetOrigin: Discriminating the Origins of Microbial Metabolites for Integrative Analysis of the Gut Microbiome and Metabolome. *iMeta* **2022**, *1*, e10. [CrossRef]
29. Xia, J.; Psychogios, N.; Young, N.; Wishart, D.S. MetaboAnalyst: A Web Server for Metabolomic Data Analysis and Interpretation. *Nucleic Acids Res.* **2009**, *37*, W652–W660. [CrossRef]
30. Krawisz, J.E.; Sharon, P.; Stenson, W.F. Quantitative Assay for Acute Intestinal Inflammation Based on Myeloperoxidase Activity. Assessment of Inflammation in Rat and Hamster Models. *Gastroenterology* **1984**, *87*, 1344–1350. [CrossRef]
31. Kumar, A.; Anbazhagan, A.N.; Coffing, H.; Chatterjee, I.; Priyamvada, S.; Gujral, T.; Saksena, S.; Gill, R.K.; Alrefai, W.A.; Borthakur, A.; et al. Lactobacillus Acidophilus Counteracts Inhibition of NHE3 and DRA Expression and Alleviates Diarrheal Phenotype in Mice Infected with Citrobacter Rodentium. *Am. J. Physiol. Gastrointest. Liver Physiol.* **2016**, *311*, G817–G826. [CrossRef] [PubMed]
32. McIver, L.J.; Abu-Ali, G.; Franzosa, E.A.; Schwager, R.; Morgan, X.C.; Waldron, L.; Segata, N.; Huttenhower, C. BioBakery: A Meta'omic Analysis Environment. *Bioinformatics* **2018**, *34*, 1235–1237. [CrossRef] [PubMed]
33. Beghini, F.; McIver, L.J.; Blanco-Míguez, A.; Dubois, L.; Asnicar, F.; Maharjan, S.; Mailyan, A.; Manghi, P.; Scholz, M.; Thomas, A.M.; et al. Integrating Taxonomic, Functional, and Strain-Level Profiling of Diverse Microbial Communities with BioBakery 3. *eLife* **2021**, *10*, e65088. [CrossRef] [PubMed]
34. Ahmad, R.; Sorrell, M.F.; Batra, S.K.; Dhawan, P.; Singh, A.B. Gut Permeability and Mucosal Inflammation: Bad, Good or Context Dependent. *Mucosal. Immunol.* **2017**, *10*, 307–317. [CrossRef]
35. Santana, P.T.; Rosas, S.L.B.; Ribeiro, B.E.; Marinho, Y.; de Souza, H.S.P. Dysbiosis in Inflammatory Bowel Disease: Pathogenic Role and Potential Therapeutic Targets. *Int. J. Mol. Sci.* **2022**, *23*, 3464. [CrossRef]
36. Qiu, Z.; Yang, H.; Rong, L.; Ding, W.; Chen, J.; Zhong, L. Targeted Metagenome Based Analyses Show Gut Microbial Diversity of Inflammatory Bowel Disease Patients. *Indian J. Microbiol.* **2017**, *57*, 307–315. [CrossRef]
37. Wang, W.; Chen, L.; Zhou, R.; Wang, X.; Song, L.; Huang, S.; Wang, G.; Xia, B. Increased Proportions of Bifidobacterium and the Lactobacillus Group and Loss of Butyrate-Producing Bacteria in Inflammatory Bowel Disease. *J. Clin. Microbiol.* **2014**, *52*, 398–406. [CrossRef]
38. Glover, J.S.; Browning, B.D.; Ticer, T.D.; Engevik, A.C.; Engevik, M.A. Acinetobacter Calcoaceticus Is Well Adapted to Withstand Intestinal Stressors and Modulate the Gut Epithelium. *Front. Physiol.* **2022**, *13*, 880024. [CrossRef]

39. Facchin, S.; Vitulo, N.; Calgaro, M.; Buda, A.; Romualdi, C.; Pohl, D.; Perini, B.; Lorenzon, G.; Marinelli, C.; D'Incà, R.; et al. Microbiota Changes Induced by Microencapsulated Sodium Butyrate in Patients with Inflammatory Bowel Disease. *Neurogastroenterol. Motil.* **2020**, *32*, e13914. [CrossRef]
40. Dahal, R.H.; Kim, S.; Kim, Y.K.; Kim, E.S.; Kim, J. Insight into Gut Dysbiosis of Patients with Inflammatory Bowel Disease and Ischemic Colitis. *Front. Microbiol.* **2023**, *14*, 1174832. [CrossRef]
41. Sasaki, K.; Inoue, J.; Sasaki, D.; Hoshi, N.; Shirai, T.; Fukuda, I.; Azuma, T.; Kondo, A.; Osawa, R. Construction of a Model Culture System of Human Colonic Microbiota to Detect Decreased Lachnospiraceae Abundance and Butyrogenesis in the Feces of Ulcerative Colitis Patients. *Biotechnol. J.* **2019**, *14*, e1800555. [CrossRef] [PubMed]
42. Liu, S.; Zhao, W.; Lan, P.; Mou, X. The Microbiome in Inflammatory Bowel Diseases: From Pathogenesis to Therapy. *Protein Cell* **2021**, *12*, 331–345. [CrossRef] [PubMed]
43. Chang, Q.; Luan, Y.; Sun, F. Variance Adjusted Weighted UniFrac: A Powerful Beta Diversity Measure for Comparing Communities Based on Phylogeny. *BMC Bioinform.* **2011**, *12*, 118. [CrossRef] [PubMed]
44. Parada Venegas, D.; De la Fuente, M.K.; Landskron, G.; González, M.J.; Quera, R.; Dijkstra, G.; Harmsen, H.J.M.; Faber, K.N.; Hermoso, M.A. Short Chain Fatty Acids (SCFAs)-Mediated Gut Epithelial and Immune Regulation and Its Relevance for Inflammatory Bowel Diseases. *Front. Immunol.* **2019**, *10*, 277. [CrossRef]
45. Peace, C.G.; O'Neill, L.A. The Role of Itaconate in Host Defense and Inflammation. *J. Clin. Investig.* **2022**, *132*, e148548. [CrossRef]
46. Clooney, A.G.; Eckenberger, J.; Laserna-Mendieta, E.; Sexton, K.A.; Bernstein, M.T.; Vagianos, K.; Sargent, M.; Ryan, F.J.; Moran, C.; Sheehan, D.; et al. Ranking Microbiome Variance in Inflammatory Bowel Disease: A Large Longitudinal Intercontinental Study. *Gut* **2021**, *70*, 499–510. [CrossRef]
47. Abdel-Rahman, L.I.H.; Morgan, X.C. Searching for a Consensus Among Inflammatory Bowel Disease Studies: A Systematic Meta-Analysis. *Inflamm. Bowel Dis.* **2023**, *29*, 125–139. [CrossRef]
48. Nie, K.; Ma, K.; Luo, W.; Shen, Z.; Yang, Z.; Xiao, M.; Tong, T.; Yang, Y.; Wang, X. Roseburia Intestinalis: A Beneficial Gut Organism from the Discoveries in Genus and Species. *Front. Cell. Infect. Microbiol.* **2021**, *11*, 757718. [CrossRef]
49. Luo, W.; Shen, Z.; Deng, M.; Li, X.; Tan, B.; Xiao, M.; Wu, S.; Yang, Z.; Zhu, C.; Tian, L.; et al. Roseburia Intestinalis Supernatant Ameliorates Colitis Induced in Mice by Regulating the Immune Response. *Mol. Med. Rep.* **2019**, *20*, 1007–1016. [CrossRef]
50. Tilg, H.; Danese, S. Roseburia Hominis: A Novel Guilty Player in Ulcerative Colitis Pathogenesis? *Gut* **2014**, *63*, 1204–1205. [CrossRef]
51. Alexeev, E.E.; Lanis, J.M.; Kao, D.J.; Campbell, E.L.; Kelly, C.J.; Battista, K.D.; Gerich, M.E.; Jenkins, B.R.; Walk, S.T.; Kominsky, D.J.; et al. Microbiota-Derived Indole Metabolites Promote Human and Murine Intestinal Homeostasis through Regulation of Interleukin-10 Receptor. *Am. J. Pathol.* **2018**, *188*, 1183–1194. [CrossRef] [PubMed]
52. Wu, H.; Zhang, M.; Li, W.; Zhu, S.; Zhang, D. Stachydrine Attenuates IL-1β-Induced Inflammatory Response in Osteoarthritis Chondrocytes through the NF-KB Signaling Pathway. *Chem. Biol. Interact.* **2020**, *326*, 109136. [CrossRef] [PubMed]
53. Gao, Y.; Zhou, B.; Zhang, H.; Chen, L.; Wang, X.; Chen, H.; Zhou, L. L-Ergothioneine Exhibits Protective Effects against Dextran Sulfate Sodium-Induced Colitis in Mice. *ACS Omega* **2022**, *7*, 21554–21565. [CrossRef]
54. Gründemann, D.; Harlfinger, S.; Golz, S.; Geerts, A.; Lazar, A.; Berkels, R.; Jung, N.; Rubbert, A.; Schömig, E. Discovery of the Ergothioneine Transporter. *Proc. Natl. Acad. Sci. USA* **2005**, *102*, 5256–5261. [CrossRef] [PubMed]
55. Bryan, P.-F.; Karla, C.; Edgar Alejandro, M.-T.; Sara Elva, E.-P.; Gemma, F.; Luz, C. Sphingolipids as Mediators in the Crosstalk between Microbiota and Intestinal Cells: Implications for Inflammatory Bowel Disease. *Mediat. Inflamm.* **2016**, *2016*, 9890141. [CrossRef]
56. Hu, D.; Zhang, D.; Zheng, S.; Guo, M.; Lin, X.; Jiang, Y. Association of Ulcerative Colitis with FUT2 and FUT3 Polymorphisms in Patients from Southeast China. *PLoS ONE* **2016**, *11*, e0146557. [CrossRef]
57. Kappler, K.; Lasanajak, Y.; Smith, D.F.; Opitz, L.; Hennet, T. Increased Antibody Response to Fucosylated Oligosaccharides and Fucose-Carrying Bacteroides Species in Crohn's Disease. *Front. Microbiol.* **2020**, *11*, 1553. [CrossRef]
58. Vermeulen, N.; Vermeire, S.; Arijs, I.; Michiels, G.; Ballet, V.; Derua, R.; Waelkens, E.; Van Lommel, L.; Schuit, F.; Rutgeerts, P.; et al. Seroreactivity against Glycolytic Enzymes in Inflammatory Bowel Disease. *Inflamm. Bowel Dis.* **2011**, *17*, 557–564. [CrossRef]
59. Hryhorowicz, S.; Kaczmarek-Ryś, M.; Zielińska, A.; Scott, R.J.; Słomski, R.; Pławski, A. Endocannabinoid System as a Promising Therapeutic Target in Inflammatory Bowel Disease—A Systematic Review. *Front. Immunol.* **2021**, *12*, 790803. [CrossRef]
60. Maki, J.J.; Nielsen, D.W.; Looft, T. Complete Genome Sequence and Annotation for Turicibacter Sanguinis MOL361T (DSM 14220). *Microbiol Resour Announc* **2020**, *9*, e00475-20. [CrossRef]
61. Lim, S.; Rhee, M.-S.; Chang, D.-H.; Kim, B.-C. Whole-Genome Sequence of Erysipelothrix Larvae LV19T (=KCTC 33523T), a Useful Strain for Arsenic Detoxification, from the Larval Gut of the Rhinoceros Beetle, Trypoxylus Dichotomus. *J. Biotechnol.* **2016**, *223*, 40–41. [CrossRef] [PubMed]
62. Chen, L.-M.; Bao, C.-H.; Wu, Y.; Liang, S.-H.; Wang, D.; Wu, L.-Y.; Huang, Y.; Liu, H.-R.; Wu, H.-G. Tryptophan-Kynurenine Metabolism: A Link between the Gut and Brain for Depression in Inflammatory Bowel Disease. *J. Neuroinflamm.* **2021**, *18*, 135. [CrossRef] [PubMed]
63. Rustgi, S.D.; Kayal, M.; Shah, S.C. Sex-Based Differences in Inflammatory Bowel Diseases: A Review. *Therap. Adv. Gastroenterol.* **2020**, *13*, 1756284820915043. [CrossRef]

64. Sochal, M.; Ditmer, M.; Binienda, A.; Gabryelska, A.; Białasiewicz, P.; Talar-Wojnarowska, R.; Fichna, J.; Małecka-Wojciesko, E. Relation between Selected Sleep Parameters, Depression, Anti-Tumor Necrosis Factor Therapy, and the Brain-Derived Neurotrophic Factor Pathway in Inflammatory Bowel Disease. *Metabolites* **2023**, *13*, 450. [CrossRef]
65. Jo, J.-K.; Seo, S.-H.; Park, S.-E.; Kim, H.-W.; Kim, E.-J.; Kim, J.-S.; Pyo, J.-Y.; Cho, K.-M.; Kwon, S.-J.; Park, D.-H.; et al. Gut Microbiome and Metabolome Profiles Associated with High-Fat Diet in Mice. *Metabolites* **2021**, *11*, 482. [CrossRef] [PubMed]

Disclaimer/Publisher's Note: The statements, opinions and data contained in all publications are solely those of the individual author(s) and contributor(s) and not of MDPI and/or the editor(s). MDPI and/or the editor(s) disclaim responsibility for any injury to people or property resulting from any ideas, methods, instructions or products referred to in the content.

cells

MDPI

Article

Identification of Small Molecules Affecting the Secretion of Therapeutic Antibodies with the Retention Using Selective Hook (RUSH) System

Mathilde Coulet [1,2,3], Sylvie Lachkar [2,3], Marion Leduc [2,3], Marc Trombe [1], Zelia Gouveia [4], Franck Perez [4], Oliver Kepp [2,3], Guido Kroemer [2,3,5,*,†] and Stéphane Basmaciogullari [1,*,†]

1 Sanofi R&D, 94400 Vitry-sur-Seine, France
2 Metabolomics and Cell Biology Platforms, Gustave Roussy Cancer Center, 94800 Villejuif, France
3 Centre de Recherche des Cordeliers, Equipe Labellisée par la Ligue Contre le Cancer, Université de Paris Cité, Sorbonne Université, Inserm U1138, Institut Universitaire de France, 75006 Paris, France
4 Institut Curie, PSL Research University, Sorbonne Université, CNRS, UMR 144, 26 rue d'Ulm, 75005 Paris, France
5 Department of Biology, Institut du Cancer Paris CARPEM, Hôpital Européen Georges Pompidou, AP-HP, 75015 Paris, France
* Correspondence: kroemer@orange.fr (G.K.); stephane.basmaciogullari@sanofi.com (S.B.)
† These authors contributed equally to this work.

Abstract: Unlocking cell secretion capacity is of paramount interest for the pharmaceutical industry focused on biologics. Here, we leveraged retention using a selective hook (RUSH) system for the identification of human osteosarcoma U2OS cell secretion modulators, through automated, high-throughput screening of small compound libraries. We created a U2OS cell line which co-expresses a variant of streptavidin addressed to the lumen-facing membrane of the endoplasmic reticulum (ER) and a recombinant anti-PD-L1 antibody. The heavy chain of the antibody was modified at its C-terminus, to which a furin cleavage site, a green fluorescent protein (GFP), and a streptavidin binding peptide (SBP) were added. We show that the U2OS cell line stably expresses the streptavidin hook and the recombinant antibody bait, which is retained in the ER through the streptavidin–SBP interaction. We further document that the addition of biotin to the culture medium triggers the antibody release from the ER, its trafficking through the Golgi where the GFP-SBP moiety is clipped off, and eventually its release in the extra cellular space, with specific antigen-binding properties. The use of this clone in screening campaigns led to the identification of lycorine as a secretion enhancer, and nigericin and tyrphostin AG-879 as secretion inhibitors. Altogether, our data support the utility of this approach for the identification of agents that could be used to improve recombinant production yields and also for a better understanding of the regulatory mechanism at work in the conventional secretion pathway.

Keywords: RUSH assay; antibody; high-throughput screening; protein secretion

1. Introduction

Secretion is a fundamental cell-biology process that enables the release of molecules in the extracellular environment. This capacity is necessary to fulfill a multitude of needs, and the released molecules can play roles in growth, chemotactism, homeostasis, immunity, and cell–cell signaling, to mention a few [1]. Eukaryotic cells have a functional network of interconnected organelles, enabling the synthesis and the controlled transport of a variety of proteins along multiple routes. In particular, the conventional secretory pathway allows for the exocytosis of proteins synthetized in the endoplasmic reticulum (ER) to the extracellular environment. Upon completion of mRNA translation and protein translocation to the lumen of the ER, the newly formed proteins are sorted in specialized membrane structures that bud coat protein complex II (COPII)-coated vesicles. These vesicles are transported

along the microtubule network towards the Golgi apparatus, where fusion with the *cis*-Golgi takes place, involving the interaction of soluble N-ethylmaleimide-sensitive-factor attachment receptors (SNAREs) present on both the vesicles and *cis*-Golgi membranes. Proteins undergo additional post-translational modifications as they reach the *trans*-Golgi face from which the clathrin-coated vesicles bud. These vesicles transport their payload to the plasma membrane, where SNARE-mediated fusion occurs, and the proteins are eventually released into the extracellular space [2]. In addition to the structural components that make the trafficking of vesicles from the ER to the plasma membrane possible, many regulatory mechanisms act as quality control during this process, such as the unfolded protein response (UPR) within the ER, where misfolded proteins are diverted from the secretory pathway, in order to ensure the secretion of functional proteins. Defects in protein folding and secretion can lead to various pathologies, such as cancer, and neurodegenerative, metabolic, and inflammatory diseases, highlighting the importance of better understanding the underlying cellular mechanisms, which would pave the way for the identification of novel therapeutic molecules [3–6].

An understanding of the secretion mechanisms is also of paramount interest for the pharmaceutical industry, which has started a transition from the all-chemical era to biologics. Indeed, the proportion of drugs made from living organisms has greatly increased in the past decades, today representing one quarter of all approved therapies; half of them being for therapeutic antibodies [7]. Such antibodies are produced after transfection of suitable cells with specific heavy and light chain-encoding vectors, cell culture upscaling, and antibody purification from the cell culture supernatant [7]. Several directions have been investigated with the final goal of optimizing titers of recombinant proteins, and these include cell host selection, vector design, and medium formulation, together with upstream and downstream process optimization. Small-scale experiments are thus conducted in development labs, before intermediate and final upscaling of the production process in bioreactors for clinical or commercial manufacturing [8]. Besides these canonical optimization efforts, little has been reported in the engineering literature regarding the secretion mechanism itself, from the protein assembly in the ER down to its secretion in the extracellular environment [9]. The identification of modulators of protein secretion is an efficient strategy for enriching the available knowledge on the key elements of the secretory pathway. Among the inhibitors reported in the literature, several small molecules have enabled highlighting the role of the cytoskeleton in protein secretion. Brefeldin A is known for its capacity to impact the anterograde transport of vesicles from the ER to the Golgi, while nocodazole causes depolymerization of microtubules, and cytochalasin B destabilizes the actin network [10,11]. In addition, monensin was shown to block the transport of the protein within the Golgi apparatus [12]. All of these compounds significantly decrease protein secretion and have made it possible to study the key molecular mechanisms of the conventional secretory pathway. Other approaches have also allowed the identification of practices or compounds capable of increasing protein secretion. For example, cell cycle arrest has been correlated with enhanced protein production. Although the exact mechanisms remain to be understood, this strategy is used in the industry to increase production yields. Cell cycle arrest can be achieved through genetic engineering, such as in cell cycle regulatory gene over-expression; through the induction of the hypothermic response; or through the use of small molecules, such as sodium butyrate [13,14]. The importance of chaperone proteins for the correct folding of nascent proteins and secretion has also been widely documented, and their over-expression obtained through genetic manipulation resulted in enhanced protein secretion in several studies [2,15,16]. For example, targeting the UPR via the upregulation of genes involved in this pathway or using ER stress-inducing small molecules resulted in increased cell-specific productivity, confirming the importance of this response [17]. Finally, the conventional secretory pathway was successfully activated through strategies involving the proteins required for the correct addressing of vesicles, such as SNAREs [18], ceramide transferase protein (CERT) [19], and Munc18b [2], or proteins participating in the dynamics of the

cytoskeleton, including cofilin [20], actin alpha cardiac muscle 1 (ACTC1), and guanosine triphosphate GTPase-activating protein (TAGAP) [21,22].

In line with these studies, we aimed to identify new modulators of protein secretion by leveraging retention using a selective hook (RUSH) system in a medium-throughput drug library screening approach. The RUSH system was first described by Boncompain et al. [23] and is based on the retention of the protein of interest in a specific subcellular location, until its triggered release in the secretory pathway. This model is particularly useful in a kinetics-based screening approach, where events need to be synchronized. In this work, the RUSH system was adapted to study the secretion of a modified anti-PDL1 antibody and the screening of small compound libraries. A GFP moiety was added to the C-terminal portion of the antibody heavy chain, to allow secretion monitoring with video microscopy. In addition, a furin-cleavable sequence was inserted between the Fc domain of the antibody and the GFP moiety. This ensured the processing of the fusion protein by Golgi-resident furins [24] and the release of a native antibody in the extracellular space that was directly usable in functional assays. Our screen identified inhibitors and activators of antibody secretion, which were further validated in an antigen binding assay.

2. Materials and Methods

2.1. Cell Culture, Chemicals, and Antibodies

Human osteosarcoma U2OS cells obtained from the Kroemer lab were maintained at 37 °C in a humidified incubator with 5% CO_2 in Dulbecco's modified Eagle medium (DMEM) supplemented with 10% fetal bovine serum (FBS), 1% penicillin-streptomycin, and 1% HEPES (Gibco, Carlsbad, CA, USA). CHO-K1 (CCL-61) cells were obtained from the ATCC and cultured at 37 °C in a humidified incubator with 5% CO_2 in F-12 Ham's nutrient mixture (Sigma, Saint-Louis, MO, USA) supplemented with 10% FBS and 2 mM L-Glutamine (Gibco). PD-L1-expressing CHO cells (Sanofi property) were cultured in similar conditions in medium supplemented with 7.5 µg/mL puromycin (Gibco). Prestwick, the BML-2840 ICCB Known Bioactives, and the Autophagy Compounds libraries were purchased from Prestwick Chemicals (Illkirch, France), Enzo Life Sciences (Farmingdale, NY, USA), and TargetMol (Boston, MA, USA), respectively. Anti-streptavidin (Santa Cruz Biotechnology, Dallas, TX, USA), anti-calreticulin (Abcam, Cambridge, UK), anti-SBP (Santa Cruz Biotechnology), anti- human heavy and light IgG chains (Invitrogen), and the anti-GFP (Cell Signaling, Danvers, MA, USA) antibodies were used at 1:500, 1:200, 1:500, 1:5000, and 1:1000 dilutions, respectively, in Western blotting and immunofluorescence experiments. The reference anti-human PD-L1 antibody used in FACS experiments was produced at Sanofi labs from cells transfected with plasmid constructs based on the published Atezolizumab heavy and light chain sequences available on the IMGT website (imgt.org, accessed on 12 May 2023) [25]. The secondary Alexa Fluor 568- and 488-conjugated anti-mouse and rabbit IgG antibodies (Life Technologies, Carlsbad, CA, USA) were used at 1:1000 and 1:500 dilutions, respectively, in immunofluorescence and FACS experiments. The secondary HRP-conjugated goat anti-mouse and rabbit IgG (Southern Biotech, Birmingham, AL, USA) antibodies were used at a 1:5000 dilution in the Western blotting experiments. The anti-human kappa light chain antibody (Thermo Fisher Scientific, Waltham, MA, USA) was used at a 1:4000 dilution in ELISA.

2.2. Constructs Used for the RUSH Antibody Secretion System

The streptavidin-KDEL plasmid was described in Zhao et al. [26]. The amino acid sequences of the heavy and light chains of the anti-PD-L1 Atezolizumab antibody available on IMGT were used to generate nucleic acid sequences adapted to expression in human cells. Sequences encoding a furin-cleavable site (AVSKERSKRSP), a linker $(G_4S)_2$, enhanced green fluorescent protein (eGPF), and a streptavidin binding protein (SBP) were added in that order to the 3′ end of the anti-PD-L1 heavy chain coding sequence. Anti-PD-L1 heavy and light chain constructs were manufactured by GeneArt (Ratisbonne, Germany) and provided in a shuttle vector. The heavy and light chain sequences were then cloned

into the multiple cloning sites 2 and 1, respectively, of the pVITRO1 plasmid (Invivogen, San Diego, CA, USA) using a NEBuilder assembly kit (New England Biolabs, Ipswich, MA, USA). The integrity of the construct, hereafter referred to as anti-PD-L1 IgG RUSH plasmid, was confirmed by sequencing (Eurofins, Luxemburg).

2.3. Establishment of the RUSH-Antibody Cell Line

U2OS cells were transfected with the streptavidin-KDEL plasmid using Lipofectamine 2000 (Thermo Fisher Scientific) and selected in medium supplemented with G418 (400 μg/mL, Gibco-Invitrogen) for 2 weeks. Limiting dilution in 96-well plates was used for single cell isolation from the selected pool. Clones were amplified and selected based on streptavidin immunofluorescence. Clone #BD6 showing the highest streptavidin expression was further expanded in medium supplemented with G418 (200 μg/mL) and transfected with the anti-PD-L1 IgG RUSH plasmid using Lipofectamine 2000 and selected in medium supplemented with G418 (200 μg/mL) and hygromycin (100 μg/mL, Santa Cruz Biotechnology) for 2 weeks. Limiting dilution in 96-well plates was used for single cell isolation from clone #BD6-derived selected pool. Clones were amplified and selected based on GFP fluorescence, and clone #7 was selected for further characterization and screening campaigns.

2.4. Immunofluorescence

U2OS cells were seeded in black 96-well imaging plates (Greiner bio one, Kremsmünster, Austria). After 24 h, the medium was removed, cells were rinsed with 37 °C pre-heated PBS and fixed in PBS supplemented with 4% paraformaldehyde (PFA, Sigma) and 1 μg/mL Hoechst (Life Technologies, Carlsbad, CA, USA) for 20 min under agitation at room temperature (RT). Cells were rinsed with PBS before addition of a 5% FBS/0.3% Triton X-100/PBS permeabilizing solution for 30 min under agitation at RT. Cells were rinsed with PBS and incubated overnight under agitation at 4 °C with the primary antibody in 1% BSA/PBS. Cells were washed with PBS and incubated for 45 min under agitation at RT with the secondary antibody in 1% BSA/PBS. Finally, cells were washed and processed for image acquisition using a IXM XL BioImager (Molecular Devices, Sunnyvale, CA, USA).

2.5. Antibody Expression and Secretion Characterization by Western Blot

U2OS clone #7 cells were seeded in T-175 flasks and kept for 24 h at 37 °C in a humidified incubator with 5% CO_2. The next day, the supernatant was removed; cells were rinsed with 37 °C pre-heated PBS; and new serum-free medium containing no biotin, 40 μM biotin, or 40 μM biotin together with 100 μM of furin inhibitor I (Sigma) was added to the flask for 4 h. At the end of the incubation time, cells were harvested and lysed in RIPA buffer (Thermo Fisher Scientific) supplemented with protease and phosphatase inhibitors (Roche, Basel, Switzerland). Additionally, cell culture supernatants were collected and concentrated ~100-fold in a Amicon 50 kDa filter unit (Sigma) according to the manufacturer's instructions. Cell lysate and concentrated supernatant protein concentrations were determined using a BCA™ protein assay kit (Thermo Fisher Scientific). Next, 10 μg of total protein content from lysates and supernatants was resolved on NuPAGE™ 4–12% Bis-Tris gels (Invitrogen, Carlsbad, CA, USA) under reducing conditions and transferred to a nitrocellulose membrane (BioRad, Hercules, CA, USA) using a BioRad system. The membranes were blocked for 1 h with 0.01% Tween-20/5% non-fat dry milk/TBS, and the primary antibodies were added overnight under agitation at 4 °C. The membranes were rinsed with 0.01% Tween-20/5% non-fat dry milk/TBS and incubated for 1 h with secondary antibodies under agitation at 4 °C. The membranes were then washed 3 times for 5 min with 0.01% Tween-20/TBS, and the peroxidase activity was evaluated with Amersham ECL Primer Western Blotting Detection Reagent (GE Healthcare, Little Chalfont, UK) on ImageQuant LAS4000 (GE Healthcare).

2.6. Flow Cytometric Validation of Antibody Reactivity

U2OS clone #7 cell culture supernatants were prepared as described above and used to assess the binding of the RUSH antibody to PD-L1-expressing cells through flow cytometry. Three million CHO-K1 and CHO PD-L1 cells were harvested, rinsed with PBS, and incubated for 30 min at 4 °C under agitation in the dark with either 150 µL of the recombinant Atezolizumab prepared in Sanofi research labs or concentrated U2OS clone #7 cell culture supernatant. Cells were then rinsed with PBS and secondarily stained for 30 min at 4 °C under agitation in the dark with an Alexa Fluor 647-coupled anti-human IgG antibody, before flow cytometry analysis of 100 µL solution on a MACSQuant (Miltenyi Biotec, Bergisch Gladbach, Germany).

2.7. High-Throughput Compound Screening for Modulators of Protein Secretion

U2OS clone #7 cells were seeded in black 384-well imaging plates (Greiner bio one), at 2000 cells/well, and incubated for 24 h at 37 °C in a humidified incubator with 5% CO_2. Cells were treated on the next day with compounds from either the Prestwick library at 20 µM or 10 µM, the ICCB Known Bioactives library at $1/100^e$ or $1/1000^e$, or the autophagy compound library at 10 µM or 1 µM for 4 h. At the end of the incubation time, biotin was added at 40 µM for 1 h (untreated cells and DMSO-treated cells were used as a control). Cells were then fixed as described above and processed for subsequent automated image acquisition using a robot-assisted IXM XL BioImager (Molecular Devices, Sunnyvale, CA, USA) equipped with a Sola light source (Lumencor, Beaverton, OR, USA), adapted excitation and emission filters (Semrock, Rochester, NY, USA), and a 16-bit monochrome sCMOS PCO.edge 5.5 camera (PCO, Kelheim, Germany). A 20 X PlanAPO objective (Nikon, Tokyo, Japan) was used to acquire a minimum of 4 view fields in each well. The acquired images were processed using the open-access R software (https://www.r-project.org, accessed on 12 May 2023) with the use of the freely available packages EBImage (available on the Bioconductor repository https://www.bioconductor.org, accessed on 12 May 2023) and RBioFormats (https://github.com/aoles/RBioFormats, accessed on 12 May 2023), and the custom packages MetaxpR. (https://github.com/asauvat/MetaxpR, accessed on 12 May 2023) and MorphR (https://github.com/kroemerlab/MorphR, accessed on 12 May 2023). Nuclei were first detected using the Hoechst 33342 signal and used as a marker to detect cytoplasmic areas based on GFP signal, allowing for the evaluation of cytoplasmic GFP intensity. Data were subsequently extracted and statistically evaluated using R (https://www.r-project.org, accessed on 12 May 2023). Data were normalized using negative and positive controls, reduced, and transformed into a Z-score. The experiments were repeated manually at low scale with selected drugs, to confirm their effects on secretion; in this second set of assays, U2OS clone #7 cells incubated with secretion inhibitors were fixed and stained with Hoechst as described above, for imaging and viability determination based on cell counts.

2.8. ELISA

U2OS clone #7 cells were seeded in 6-well plates and kept for 24 h at 37 °C in a humidified incubator with 5% CO_2. The next day, the supernatants were removed, cells were rinsed with 37 °C pre-heated PBS, and new medium containing the chemical treatment was added for 4 h. At the end of the incubation time, no biotin or 40 µM biotin was added to the flask for 30 min (inhibitory selected molecules) or 1 h (activator selected molecules). Then supernatants were collected and used for the ELISA assay, as follows: MaxiSorp 96-well plates (Thermo Fisher Scientific) were coated with 0.5 µg/mL hFc-human-PD-L1 (R&D Systems, Minneapolis, MN, USA) in PBS for 5.5 h at RT. Coating solution was then removed and 2% BSA/PBS blocking solution was added overnight at 4 °C. The next day, wells were washed 3 times with 0.5% BSA/0.05% Tween-20/PBS solution. Supernatants were added after a 1/3 dilution in 0.5% BSA/0.05% Tween-20/PBS, for 2.3 h at RT. Wells were washed 3 times with 0.5% BSA/0.05% Tween-20/PBS solution. Anti-human kappa light chain HRP-coupled antibody was added diluted in 0.5% BSA/0.05% Tween-20/PBS

at 1/4000^{e} for 2.3 h at RT. Wells were washed 3 times with 0.5% BSA/0.05% Tween-20/PBS solution, before incubation with a substrate reagents pack (R&D Systems) for 15 min in the dark. Then, 50 µL of STOP solution (R&D Systems) was added to each well and the absorbance in each well was measured at 450 nm, and 635 nm for background subtraction, using a VICTOR^{TM} X4 (PerkinElmer, Waltham, MA, USA).

2.9. Statistics

Unless otherwise specified, data are reported as the mean ± SD of two replicates in a minimum of three independent experiments. Statistical significance was assessed using a one-sided Mann–Whitney U-test.

3. Results

3.1. Design of an Antibody RUSH System

The RUSH system is composed of a hook that is streptavidin and a bait that is a protein fused to a streptavidin-binding peptide (SBP). When these two molecules are co-expressed, the bait is sequestered by the hook, due to the high-affinity streptavidin/SBP interaction (K_d in the range of 10^{-8} to 10^{-9} Mol) [27], and released upon addition of biotin, which outcompetes SBP due to its higher affinity for streptavidin (K_d in the range 10^{-14} Mol) [28]. Here, we adapted this cell-based assay to monitor the secretion kinetics of an antibody (the bait) and screen small compound libraries to identify secretion modulators. As antibodies are secreted through the conventional pathway, the streptavidin hook was fused to a KDEL peptide to ensure its retention in the endoplasmic reticulum (ER) through the interaction with the KDEL receptors present in the ER [29]. The antibody was also modified to fit the purpose of the assay. A polycistronic vector was used that encodes both the heavy and light (kappa) chains of a human PD-L1-specific antibody [30]. The C-terminus of the heavy chain was fused to a $(Gly_4Ser)_2$ linker, a furin-cleavable site, the green fluorescent protein (GFP), and SBP (Figure 1B). We reasoned that the fusion molecule (hereafter called RUSH antibody) would assemble into mature homodimers upon protein synthesis and remain in the ER due to its interaction with the streptavidin KDEL hook, until addition of biotin would trigger its release and maturation in the Golgi through its trafficking to the extracellular space (Figure 1A).

The hook and bait expressing clone was obtained using U2OS cell transfection with the hook-encoding construct and the selection a clone with high hook expression levels, in order to ensure efficient retention of the bait and minimize leakiness in the absence of biotin. As shown in Figure 1C, Clone #BD6 staining with streptavidin-specific antibodies revealed the colocalization of the hook with the prototypic ER-sessile protein calreticulin [31]. Clone #BD6 was further transfected with the RUSH antibody encoding vector, followed by single cell cloning and the selection of the hook/bait clone used in this study (clone #7). This clone was selected based on two criteria: (i) a bright GFP-dependent fluorescent signal, indicating high abundance of the RUSH antibody; and (ii) discrete localization of the GFP signal in the perinuclear area, indicating ER retention (Figure 2A). Fluorescence video-microscopic observation of cells from clone #7 revealed that GFP remained in the same subcellular compartment over the 2 h of acquisition. On the contrary, the addition of biotin resulted in the relocation of the GFP signal towards discrete puncta that corresponded to the Golgi apparatus within 40 to 120 min, with a complete cytoplasmic GFP signal decay within 4 h, most likely due to the release of the fusion protein into the extracellular space (Figure 2A). The GFP signal co-localized with streptavidin at baseline and the addition of biotin did not modify this pattern, confirming the retention of the hook in the ER, regardless of the presence or absence of biotin in the medium. However, the GFP/streptavidin co-localization was lost 4 h after addition of biotin (Figure 2B). These results confirmed the expression of the bait and its retention in the ER through the hook, and suggest its progressive release in the extracellular space upon addition of biotin.

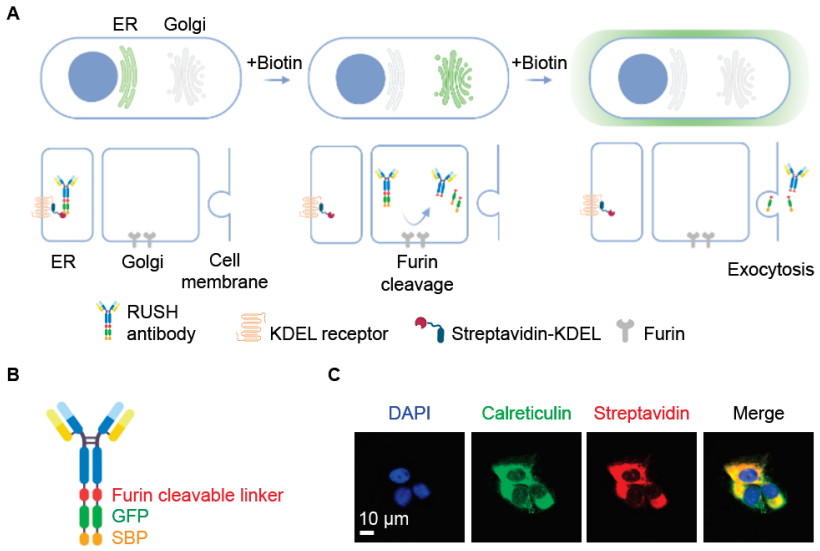


Figure 1. Design of the RUSH antibody secretion system (**A**) Principle of the RUSH assay for antibody secretion. The fusion protein (in this case, the antibody fused to the streptavidin binding domain, SBD, separated by a linker that contains a furin cleavage site) is retained in the ER lumen via the interaction of SBP with a streptavidin-KDEL hook. Upon addition of biotin, the interaction between the hook and the fusion protein is competitively disrupted, and the fusion protein is hence free to follow the classical secretory pathway to the Golgi, where the resident furin protease cleaves the linker between SBD and the antibody. The resulting parts are then secreted in the extracellular environment. The GFP moiety enables following the process with fluorescence microscopy. (**B**) Schematic representation of the custom anti-PD-L1 RUSH antibody, a fusion protein composed of an anti-PD-L1 IgG modified in its C-terminal end by the addition of a furin cleavable linker, a GFP, and an SBP sequence. (**C**) Immunostaining of fixed cells showing the colocalization of the streptavidin-KDEL hook with calreticulin in the ER. Pearson's correlation coefficient (PCC) = 0.69. Surface overlap coefficient (SOC) = 0.45.

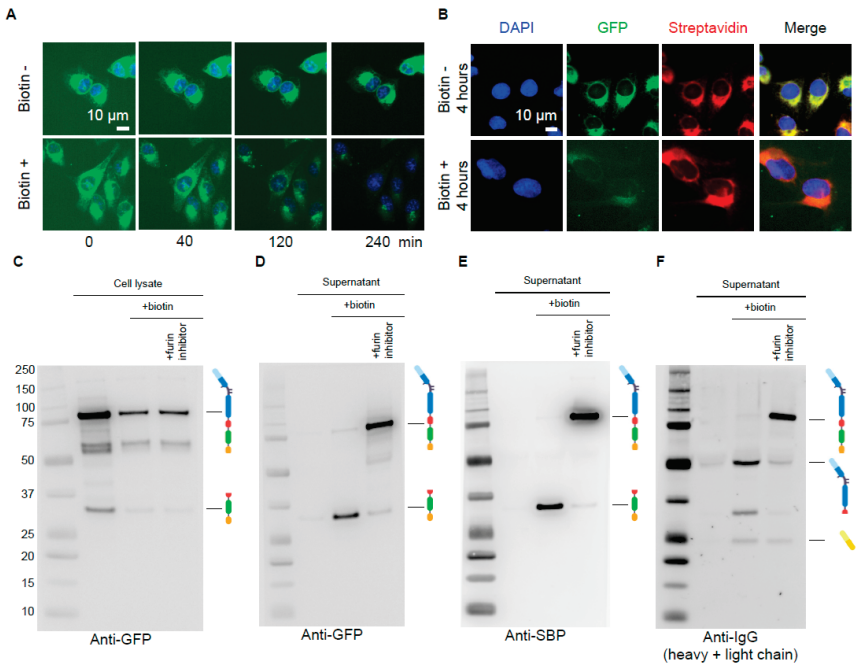


Figure 2. Characterization of the anti-PD-L1 antibody RUSH system (**A**) Time lapse microscopy of clone #7 cells incubated in the absence or in presence of 40 µM biotin, fixed and stained with DAPI.

The secretion rate could be deducted from the decreasing intracellular GFP intensity upon addition of biotin to the cell cultures. (**B**) Immunostaining of fixed cells incubated for 4 h in the absence or in the presence of biotin showing the colocalization of the streptavidin-KDEL hook with the GFP-tagged antibody in the absence of biotin and the loss of colocalization 4 h post biotin addition. PCC = 0.51 in the absence of biotin, and PCC = 0.29 in the presence of biotin. (**C**–**F**) Western blot of cell lysates (**C**) or concentrated supernatants (**D**–**F**) of clone #7 incubated for 4 h in the absence of biotin, in the presence of 40 μM biotin, or in the presence of 40 μM biotin together with 100 μM furin inhibitor I. Membranes were probed with the indicated antibodies to detect proteins that contain the GFP moiety (**C**,**D**), the SBP moiety (**E**), or epitopes from the immunoglobulin heavy and light chains (**F**). Molecular mass standards (in kDa) are indicated on the left, in panel (**D**). The structures of the proteins detected by immunoblot are indicated based on the scheme shown in Figure 1B (blue, antibody heavy chain; yellow, antibody light chain; green, GFP; orange, SBP; red shape, linker with furin cleavage site; truncated red shape, linker residues left after cleavage by furin). Results are representative of at least three independent experiments.

3.2. Biochemical Validation of the Antibody RUSH System

In the next step, we proceeded to the biochemical validation of clone #7, before its use in a screening campaign. For this aim, we characterized the molecular species synthesized and released by clone #7 cultured with or without biotin and a furin protease inhibitor. As can be seen in Figure 2C, the GFP-specific antibodies used in the Western blotting experiments revealed the presence of a major molecular species of ~80 kDa and two minor species of ~55 and ~35 kDa in the lysate of cells grown in the absence of biotin. The 80 kDa mass was compatible with the full-length heavy chain of the RUSH antibody (theoretical mass of 84 kDa), while the 35 kDa mass was compatible with the GFP-SBP C-terminal fragment of the heavy chain, which was released upon cleavage by furin (theoretical mass of 32 kDa). A similar analysis performed on the cell culture supernatant with GFP, SBP, and human IgG- specific antibodies only revealed trace amounts of recombinant protein in the absence of biotin (Figure 2D–F). This is consistent with the minor processing observed in cell lysates and therefore the efficient retention of the RUSH antibody in pre-Golgi intracellular compartments, as documented through the immunofluorescence (Figure 2A,B).

When cells were cultured in the presence of biotin, the Western blotting pattern in the cell lysate was unchanged, except that the intensity of the signal was lower, which was concomitant with the detection of recombinant species in the cell culture supernatant (Figure 2C–F). This demonstrates that the intracytoplasmic GFP decay observed via immunofluorescence in Figure 2A,B was a direct consequence of the protein release in the extracellular space. Moreover, the molecular masses of the material detected in the supernatant suggest an almost full processing of the released RUSH antibody. This was further confirmed by the comparable patterns obtained in cell lysates and in the cell culture supernatant when cells were grown in the presence of furin inhibitor. It can therefore be concluded that the RUSH antibody was released through the Golgi network and processed upon addition of biotin.

Taken together, these findings demonstrated that clone #7 allowed for biotin-stimulated release, as well as for the furin-dependent proteolytic maturation, of the RUSH antibody.

3.3. Immunological Validation of the Antibody RUSH System

Besides the mechanistic validation of clone #7, in terms of the antibody production, retention, maturation, and release upon addition of biotin, we also addressed the PD-L1 binding properties of the secreted RUSH antibody. We further investigated the RUSH antibody binding properties to PD-L1 in its native conformation when it was presented at the plasma membrane. For this aim, clone #7 was incubated with biotin and the cell culture supernatant was assayed for binding on PD-L1^{pos} and PD-L1^{neg} CHO cells by FACS. As can be seen in Figure 3A,B, native recombinant anti-PD-L1 binding to PD-L1^{pos} (CHO-PDL1) but not PD-L1^{neg} CHO (CHO-K1) cells was documented, which validated the use of such a system for further characterization of the RUSH antibody. Similarly, the

supernatant of clone #7 cultured in the presence of biotin demonstrated binding activity to CHO-PDL1 cells but not to CHO-K1 cells (Figure 3C,D), indicating that the released RUSH antibody conserved its antigen-binding properties, despite the presence of extra ammino-acids at its C-terminus, left after processing with furins. Of note, PD-L1 binding was also detectable in the supernatant of clone #7 cultured in the presence of biotin and a furin protease inhibitor (Figure 3E,F). In these conditions, binding was detected through both the secondary staining antibody and the GFP moiety of the unprocessed RUSH antibody, which was not detectable with the native antibody (Figure 3B) and only very slightly detected in the case of the supernatant of clone #7 cultured with biotin only (Figure 3D). Altogether, these observations indicate that clone #7 was fit for both screening campaigns and further antibody characterization in PD-L1-binding assays.

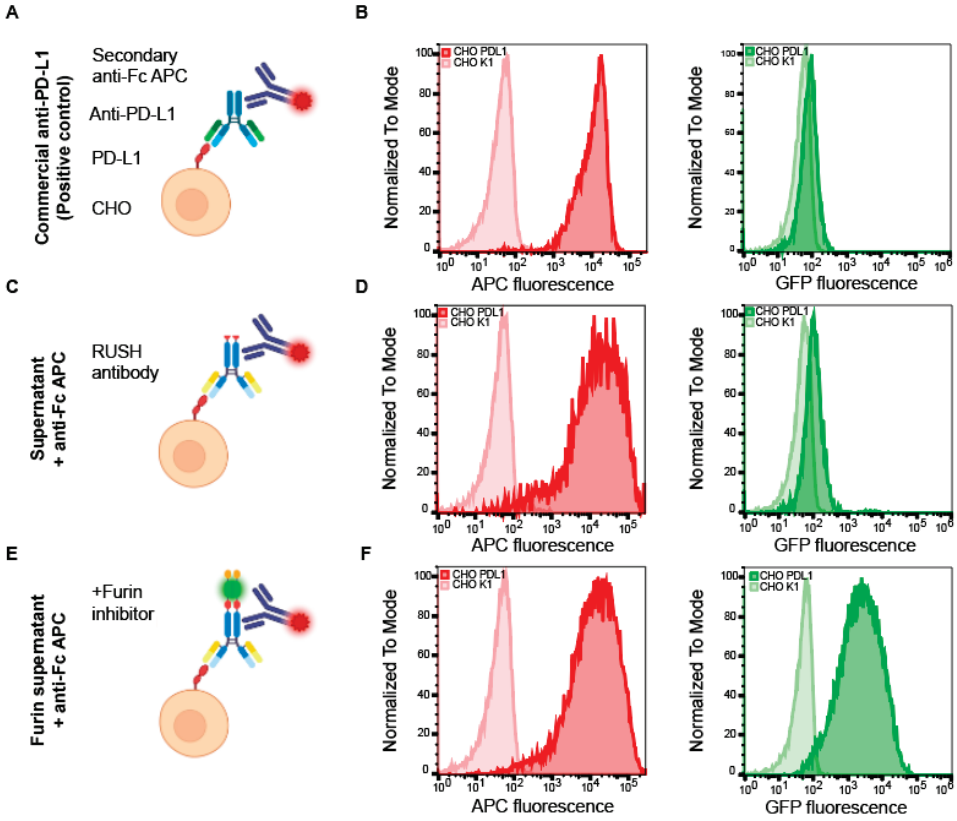


Figure 3. Characterization of the binding capacity of the anti-PD-L1 RUSH antibody released through the biotin-activated RUSH system. (**A**,**C**,**E**) Schematic representation of the antibody binding to PD-L1^{pos} cells and detection by flow cytometry. (**B**) FACS histogram plot of native recombinant and purified anti-PD-L1 antibody. (**D**,**F**) FACS histogram plots of processed and unprocessed RUSH anti-PD-L1 antibody released by clone #7 in the presence of biotin and in the absence or presence of furin inhibitor, respectively. Dark colors, binding to PD-L1^{pos} CHO cells (CHO-PDL1); light colors, binding to PD-L1^{neg} parental CHO cells (CHO-K1). Antibody binding was detected by means of an indirect immunofluorescence assay with a secondary anti-Fc APC conjugated (red) or by direct measurement of GFP fluorescence.

3.4. Pharmacological Screen for Modulators of Biotin-Induced Antibody Release

We next sought to use clone #7 in screening campaigns for the identification of drugs capable of enhancing or inhibiting antibody secretion. For this, clone #7 was cultured in 384 well plates and treated for 4 h with drugs from chemical libraries, followed by the addition of biotin for 1 h and the determination of the intra-cytoplasmic GFP signal (Figure 4A). Cell counting was facilitated by nuclear counterstaining with Hoechst 33324, in order to assess the viability and distinguish drug effects on the secretion kinetics from direct cytotoxicity, and to select relevant drugs for further characterization. Two independent

screening campaigns were performed, to test a total of 2300 drugs at 2 different concentrations (i.e., a low concentration and a 10-fold higher concentration, referred to as "low" and "high" doses, as described in the Section 2).

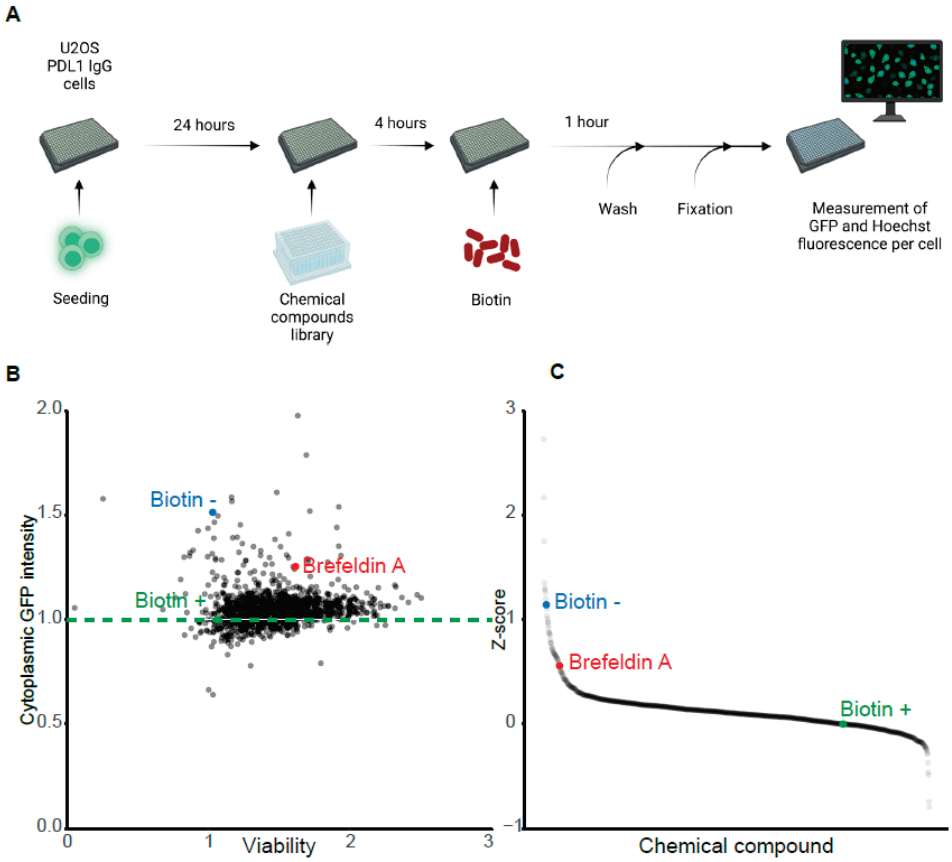


Figure 4. High-throughput screening of chemical compound libraries for the identification of modulators of protein secretion. (**A**) Screening workflow. U2OS clone #7 was plated in 384-well plates and incubated for 24 h, before treatment with each compound of the Prestwick, ICCB Known Bioactives, or autophagy compounds at two concentrations: low and high (with a 10-fold difference). Biotin was added after 4 h, and cells were washed and fixed 1 h after addition of biotin and processed for automated image acquisition of the intracellular Hoechst 33324 and GFP fluorescence. (**B**) Dot plot representation of drugs based on their impact on GFP release (cytoplasmic GFP signal) and nucleus integrity (viability). (**C**) Z-score ranking of the cytoplasmic GFP intensity after treatment. The results of the Prestwick library screening at a low drug concentration were plotted. Brefeldin A was used as a positive control for the inhibition of secretion. The compounds causing a cytoplasmic GFP intensity below that observed for the biotin-only treated cells were potential enhancers of protein secretion. Drugs that induced a GFP fluorescence level higher than that measured in the presence of biotin only were potential inhibitors of protein secretion.

The biotin-induced decrease of the cellular GFP signal was influenced by a minority of compounds from various chemical libraries, as indicated through the plotting of primary data (Figure 4B) or Z-score analyses (Figure 4C). As an internal control, brefeldin A, which is an inhibitor of conventional Golgi-dependent protein secretion [32], inhibited the biotin-induced decrease of the GFP signal (Figure 4B,C). Plotting of the Z-scores obtained at the low and high concentrations for each compound (Figure 5A,B) led to the identification of several compounds that consistently decreased the fluorescent signal, therefore acting as secretion activators. In order to select candidates to be further characterized, the 20 best activators identified at either the low or high concentration were identified, and among these, activators working at both concentrations were shortlisted. In the Prestwick library,

balsalazide sodium (no longer commercially available), methenamine, pyrithyldione, cycloheximide, digoxigenin, verteporfin, and ropinirole fulfilled these criteria (Figure 5A). Verteporfin was eliminated due to its phototoxicity that leads to GFP bleaching [33]. In a combined screen involving compounds contained in two additional libraries (ICCB Known Bioactives and TargetMol Autophagy), several additional compounds (anisomycin, emetine, and pinocembrine) were active at both low and high concentrations. Additionally, although lycorine was not among the 20 most active compounds at high concentration, it was more efficient than any other compound at low concentration and was therefore selected (Figure 5B).

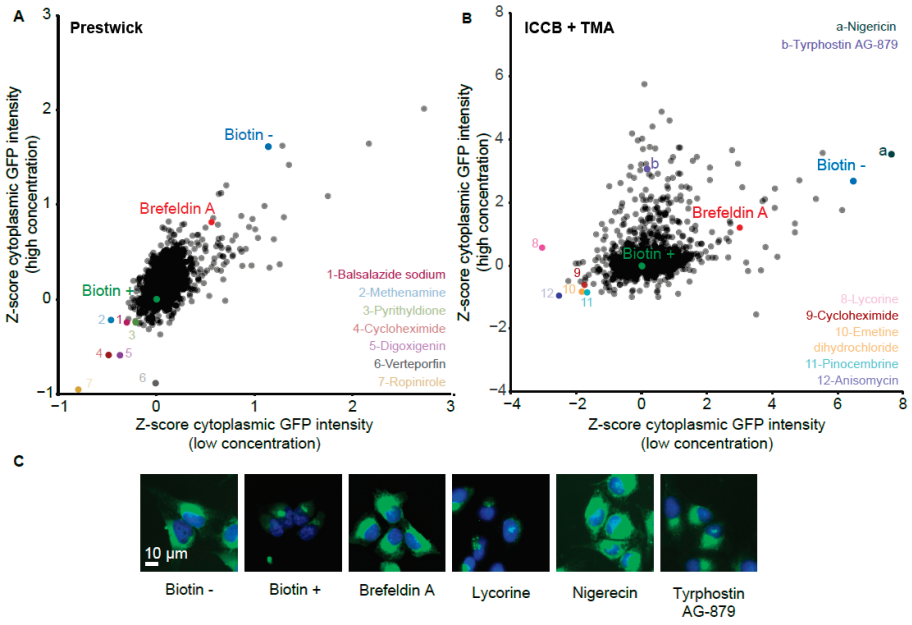


Figure 5. Selection of potential modulators of protein secretion. (**A**,**B**) Dot plot representation of drug efficiency based on the Z-scores measured at low and high drug concentration ((**A**) Prestwick library; (**B**) ICCB Known Bioactives and TargetMol Autophagy libraries). Compounds selected for further characterization are listed and highlighted in color. (**C**) Clone #7 was treated with the indicated compounds, fixed and analyzed as described in Figure 4A legend.

Several drugs were also identified that inhibited the biotin-induced cytoplasmic GFP signal decay, therefore acting as potential secretion inhibitors, among which nigericin and tyrphostin AG-879 were selected for further characterization (Figure 5B) because they had not been identified previously by Zhao et al. [26].

3.5. Validation of Stimulators and Inhibitors of Biotin-Induced Antibody Release

Medium- and high-throughput screenings often yield false positive and negative hits, calling for independent validation in low-throughput experiments with orthogonal technologies. In a first round of experiments, we evaluated the effects of shortlisted compounds with potential antibody secretion enhancer activity. The compounds identified in the screening campaigns were retested on clone #7 at a low concentration (Figure 6A) or a ten-fold higher concentration (Figure 6B) for their ability to increase antibody secretion. This experiment showed that all selected hits were active at the highest concentration, which confirmed the results of the screening (Figure 6B). We further characterized these hits in an PD-L1 binding ELISA. In this system, sodium butyrate induced a two-fold increase of RUSH antibody release upon biotin addition, as expected from its effect on protein expression [34,35]. Among the drugs tested, only lycorine (tested at both 1 and 50 µM) was considered to be active, although its effect was milder than that of sodium butyrate, while all the other compounds failed to display any antibody secretion stimulatory activity (Figure 6B).

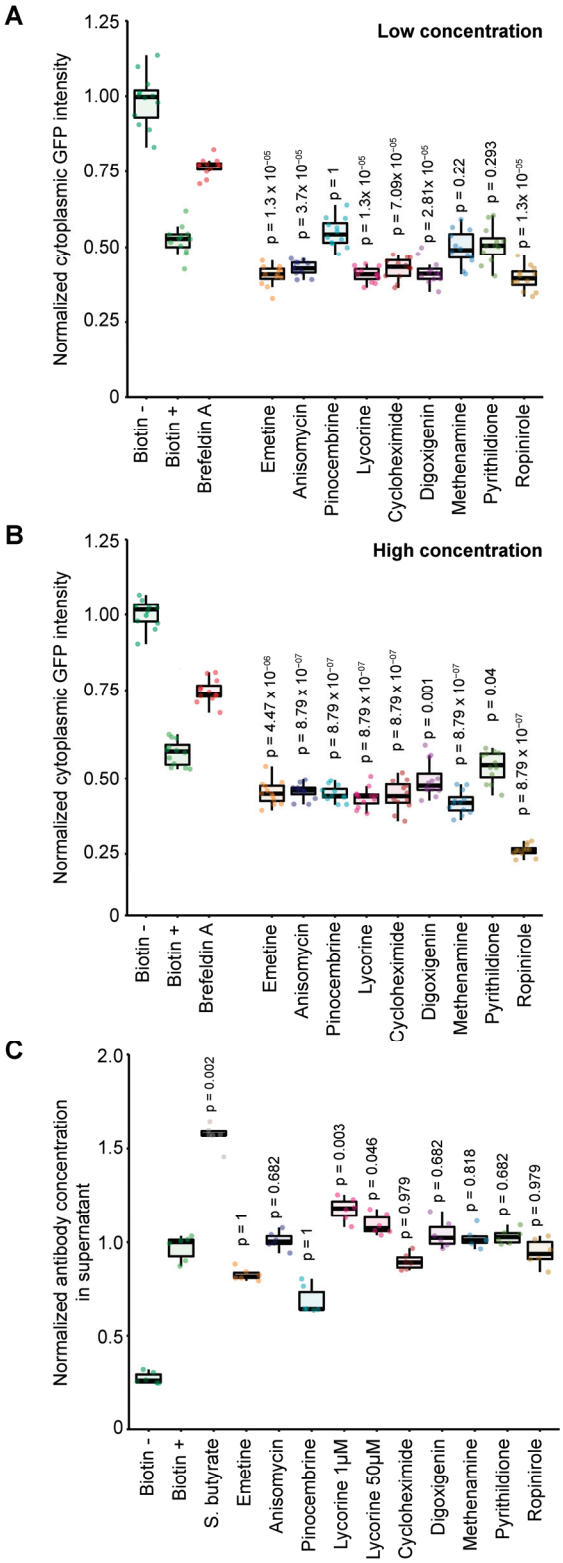


Figure 6. Validation of enhancers of protein secretion. (**A**,**B**) Clone #7 cells were treated with the indicated compounds and analyzed as indicated in the legend of Figure 4A. Drugs were used at low (**A**) or high concentration (**B**), as indicated in the text, and the post-treatment intracytoplasmic fluorescence was normalized to that measured in mock-treated cells (no biotin). (**C**) ELISA assay on immobilized PD-L1. Clone #7 cells were treated with the indicated compounds, and supernatants were assayed for PD-L1 binding. Sodium butyrate was used as a protein secretion enhancer positive control.

Similarly, potential secretion inhibitors identified during the screening campaigns were also tested in an ad hoc assay. Both nigericin and tyrphostin AG-879 (used at 50 µg/mL) turned out to be as potent as brefeldin A in suppressing antibody secretion (Figure 7A), without affecting cellular viability (Figure 7B). Cell imaging further confirmed the secretion activator effect of lycorine and the inhibitory effect of nigericin and tyrphostin AG-879 (Figure 5C).

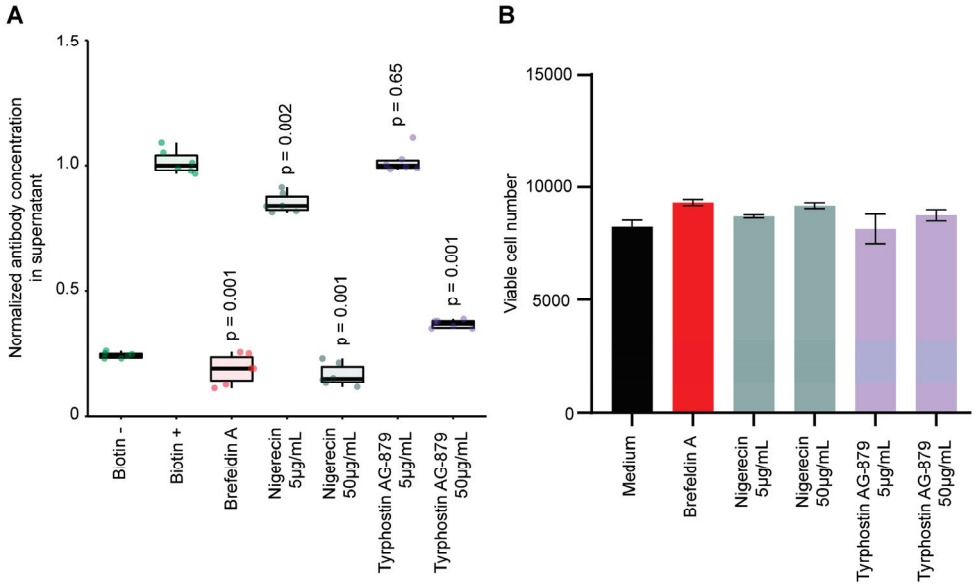


Figure 7. Validation of inhibitors of protein secretion. (**A**) ELISA assay on immobilized PD-L1. Clone #7 cells were treated with the indicated compounds and supernatants were assayed for PD-L1 binding. Brefeldin A was used as a protein secretion inhibitor positive control. (**B**) Cells treated in A were subjected to a toxicity assay. Hoechst 33324 fluorescence was measured, which enabled counting the adherent living cells in each well.

4. Discussion

In the present study, we provide evidence that the RUSH system can be adapted to the controlled release of functional antibodies (exemplified by the immunotherapeutic anti-PD-L1 antibody Atezolizumab) from cultured U2OS cells via the addition of biotin. Using this antibody compatible RUSH system, small chemical compounds libraries were successfully screened using a high-throughput fluorescence imaging system, for the identification of modulators of conventional antibody secretion. Here, we report one novel activator and two novel inhibitors of antibody secretion validated using enzyme-linked immunosorbent assay (ELISA) antibody titration.

The RUSH system offers a cost-effective, high-throughput, high-content, and screening-compatible alternative to complementary assays such as ELISA. Thus, expressed in firmly adherent human osteosarcoma U2OS cells, the RUSH system becomes a valuable tool for the image-based kinetic assessment of protein trafficking. Of note, U2OS cells are neither antibody producing nor specialized secretory cells, which necessitates validation in physiologically relevant systems. In previous publications, variations of the RUSH system were generated by fusing different proteins, such as calreticulin [36], giantin [37], transferrin receptor [38], and tumor necrosis factor [37] to SBP and a reporter protein, either GFP, which can be directly visualized by fluorescence microscopy, or other non-fluorescent proteins tracked by alternative methods. The particularity of these model cargos is their monomeric nature, and no large homo-dimeric proteins such as antibodies have ever been studied in the RUSH system, in order to document whether secretion can be triggered and whether antibodies maintain antigen-binding properties upon release after long-term immobilization in the ER lumen. These questions needed to be addressed

prior to using the RUSH system for the identification of antibody secretion modulators in screening campaigns.

Setting up a RUSH system requires the addition of SBP to the antibody for reversible ER targeting and a fluorescent protein (e.g., GFP) for automatized video microscopy monitoring of antibody secretion. As highlighted by Haas et al. and Luria et al., this represents a challenge for antibodies, since immunoglobulins and GFP do not normally originate from the same cellular compartment, and the addition of foreign sequences to antibodies has been shown to interfere with their secretion and functionality [39,40]. The mechanism of IgG heavy and light chain assembly prior to mature antibody secretion poses another challenge. Indeed, while antibody heavy chains require assembly with light chains for secretion, a free light chain might be secreted. We therefore opted to retain the RUSH antibody through its heavy chain, in order to confidently monitor the secretion of fully assembled antibodies [41–44]. With these constraints considered, the RUSH machinery was added to the C-terminus of the anti-PD-L1 heavy chain. A furin cleavage site was also added between the heavy chain and the RUSH construct for the removal of the SBP and GFP sequences past the Golgi network, which might have affected the functions of the antibody otherwise.

Our data showed the efficient detection and retention of the antibody-GFP fusion in the ER of clone #7, and its release and maturation upon addition of biotin in the cell culture medium. ELISA and cell-based assays also demonstrated the specific binding of the released antibody to its PD-L1 target. The fact that the majority of secreted molecules were processed by furins suggests that the secretory machinery of clone #7 was not saturated, which makes this system relevant for the identification of secretion modulators. Of note, the uncleaved full-length antibody retained its specificity and was detectable through its GFP moiety. This has also been described by others and confirms the potential interest of such constructs for live imaging of cells, organs, or organisms [40].

Using this antibody-compatible RUSH system, we screened chemical libraries to identify small molecules that would modulate antibody secretion. The conditions were adapted to identify inhibitors of protein secretion and compare the results with previous screening campaigns performed with a distinct cargo [26], but also with activators. Among the 31 inhibitory compounds of the Prestwick library identified by Zhao et al., 13 were also identified in our screen, due to their ability to increase intracytoplasmic GFP intensity either at high or low concentration, suggesting consistency between the two approaches, despite the use of different clones and cargos. Among the two unique compounds that caused the retention of the RUSH antibody in the cytoplasm, tyrphostin AG-879, which is characterized as a tyrosine kinase inhibitor (IC_{50} = 10 μM), could be validated as an inhibitor of antibody secretion when it was used at a concentration of 50 μg/mL. The identification of a kinase inhibitor is consistent with the involvement of various kinases that act on the Golgi and that are responsible for protein maturation, secretion, and triage to the degradation pathways [45]. This is also consistent with the need for phosphorylation of effectors of the secretory pathway, such as the eukaryotic initiation factor 2 (eiF2), resulting in the decrease of the UPR and hence of the secretory capacity of the cells [46]. Nigericin was also confirmed as a secretion inhibitor when used at a concentration of 50 μg/mL (but not 5 μg/mL). This potassium ionophore might interfere with bioenergetic functions, pH regulation, and ion homeostasis, and induce pleiotropic cellular effects, leading to a decreased secretion potential [47].

Our screening campaigns also led to the identification of candidate molecules that might increase antibody secretion in the biotin-stimulated RUSH system, because they decreased the intracytoplasmic GFP fluorescence signal, among which eight compounds (anisomycin, cycloheximide, digoxigenin, lycorine, methenamine, ropinirole, pinocembrine, and pyrithyldione) were selected for further characterization by ELISA. This assay measures the RUSH antibody binding to its immobilized PD-L1 target and was used to measure antibody titers in cells treated with candidate molecules. Unexpectedly, among these eight compounds that consistently decreased intracytoplasmic GFP fluorescence, which

was interpreted as accelerated antibody release, only lycorine was shown to increase RUSH antibody titers in treated cell culture supernatant. These discrepancies might be attributable to the nature of the read out of both assays, with one being the measurement of intracytoplasmic GFP fluorescence intensity decrease and the second being the antibody titration in the cell culture supernatant. As a possible explanation, compounds selected based on the screening results might have had an unsuspected negative impact on the affinity of the RUSH antibody/antigen interaction, therefore masking their direct impact on antibody secretion. On the contrary, the fact that lycorine was validated in both assays and in several independent experiments strongly supports its stimulatory effect on antibody secretion in our system.

Lycorine likely has multiple effects on cell biology, with several cellular targets and a proposed utility for rather diverse indications, including cancer [48], fungal infection [49], and Alzheimer's disease [50]; however, no effect on secretion has been published to the best of our knowledge. Further investigations will be required to decipher its mode of action as an activator, as well as that of the inhibitors identified in this work.

In future applications, the screening approach presented in this study could be upscaled to larger pharmacological screening campaigns at the industrial level, for the discovery of novel molecules with secretion modulatory effects. Potential clinical applications would involve the direct use of the identified compounds to modulate protein secretion in related diseases, or the identification of their cellular target for subsequent development of therapeutic solutions [5]. In an industrial context, the RUSH system adapted to producer cell lines in liquid culture could be seen as a tool to control the secretion of recombinant therapeutics proteins of interest with toxic properties once secreted in the culture supernatant, resulting in cell growth inhibition or even cell death. This would represent a valuable alternative to the inducible transcription systems that were initially explored for the decoupling of cell growth and product formation, which proved challenging to develop [51].

5. Conclusions

Overall, while the addition of lycorine in bioreactors might hamper drug substance purification in industrial processes, deciphering its mechanism of action would be of great interest. A direct action of lycorine on cellular targets through genetic engineering could unlock the secretory potential of cell hosts. Such hosts would bring added value to the field of recombinant therapeutic protein production and to the pharmaceutical industry.

Author Contributions: Conceptualization, M.C., O.K., S.B. and G.K.; investigation, M.C., S.L. and M.L. software, M.L.; resources, M.T., Z.G. and F.P.; writing—original draft preparation, M.C., S.B. and G.K.; writing—review and editing, M.C., O.K., S.B. and G.K.; supervision, O.K., S.B. and G.K. All authors have read and agreed to the published version of the manuscript.

Funding: This work was primarily supported by a research contract involving Sanofi and Institut Gustave Roussy. M.C. is supported by a grant from the French ANRT agency (CIFRE No 2020/0106). O.K. receives funding from the Institut National du Cancer (INCa) and the DIM ELICIT initiative of the Ile de France. GK is supported by the Ligue contre le Cancer (équipe labellisée); Agence National de la Recherche (ANR)—Projets blancs; AMMICa US23/CNRS UMS3655; Association pour la recherche sur le cancer (ARC); Cancéropôle Ile-de-France; European Research Council Advanced Investigator Grand "ICD-Cancer", Fondation pour la Recherche Médicale (FRM); a donation by Elior; Equipex Onco-Pheno-Screen; European Joint Programme on Rare Diseases (EJPRD); European Research Council (ICD-Cancer), European Union Horizon 2020 Projects Oncobiome and Crimson; Fondation Carrefour; Institut National du Cancer (INCa); Institut Universitaire de France; LabEx Immuno-Oncology (ANR-18-IDEX-0001); a Cancer Research ASPIRE Award from the Mark Foundation; the RHU Immunolife; Seerave Foundation; SIRIC Stratified Oncology Cell DNA Repair and Tumor Immune Elimination (SOCRATE); and SIRIC Cancer Research and Personalized Medicine (CARPEM). This study contributes to the IdEx Université de Paris ANR-18-IDEX-0001. The work in FP lab was supported by LabEx CelTisPhyBio (ANR-10-LBX-0038 part of the IDEX PSL no. ANR-10-IDEX-0001-02, by the ANR grants ANR-22-CE14-0066-01, ANR-20-CE14-0017-02,

ANR-19-CE13-0006-03, ANR-19-CE13-0002-03) and by the Fondation pour la Recherche Médicale (EQU201903007925).

Institutional Review Board Statement: Not applicable. This study did not involve humans or animals.

Informed Consent Statement: Not applicable. This study did not involve humans.

Data Availability Statement: The data presented in this study are available on request from the corresponding authors. The data are not publicly available since they are being used for filing a patent.

Acknowledgments: We acknowledge Christine DeMaria and Henry Lin at Sanofi for a critical review of the manuscript. Figures 1A,B, 2C–F, 3A,C,E and 4A were created with BioRender.com, accessed on 31 March 2023.

Conflicts of Interest: G.K. received research support from Sanofi. M.C., M.T. and S.B. are full-time employees of Sanofi and may hold shares and/or stock options in the company. Outside of this work, G.K. has held research contracts with Daiichi Sankyo, Eleor, Kaleido, Lytix Pharma, PharmaMar, Osasuna Therapeutics, Samsara Therapeutics, Tollys, and Vascage. G.K. is on the Board of Directors of the Bristol Myers Squibb Foundation France. G.K. is a scientific co-founder of everImmune, Osasuna Therapeutics, Samsara Therapeutics, and Therafast Bio. G.K. is in the scientific advisory boards of Hevolution, Institut Servier, and Longevity Vision Funds. G.K. is the inventor of patents covering therapeutic targeting of aging, cancer, cystic fibrosis, and metabolic disorders. G.K.'s wife, Laurence Zitvogel, has held research contracts with Glaxo Smyth Kline, Incyte, Lytix, Kaleido, Innovate Pharma, Daiichi Sankyo, Pilege, Merus, Transgene, 9 m, Tusk, and Roche; was on the on the Board of Directors of Transgene; is a cofounder of everImmune; and holds patents covering the treatment of cancer and the therapeutic manipulation of the microbiota. G.K.'s brother, Romano Kroemer, was an employee of Sanofi and now consults for Boehringer-Ingelheim. O.K. is a scientific co-founder of Samsara Therapeutics. Z.G. and F.P. were employed by the start-up Honing Biosciences until May 2023. Sanofi and Inserm have filed a patent application (not yet published) covering the methods for secretion modulation reported here. M.C., O.K., S.B. and G.K. are inventors.

References

1. Viotti, C. ER to Golgi-Dependent Protein Secretion: The Conventional Pathway. *Methods Mol. Biol.* **2016**, *1459*, 3–29. [CrossRef]
2. Torres, M.; Hussain, H.; Dickson, A.J. The secretory pathway—The key for unlocking the potential of Chinese hamster ovary cell factories for manufacturing therapeutic proteins. *Crit. Rev. Biotechnol.* **2022**, *43*, 628–645. [CrossRef]
3. Jena, B.P. Molecular machinery and mechanism of cell secretion. *Exp. Biol. Med.* **2005**, *230*, 307–319. [CrossRef] [PubMed]
4. Luesch, H.; Paavilainen, V.O. Natural products as modulators of eukaryotic protein secretion. *Nat. Prod. Rep.* **2020**, *37*, 717–736. [CrossRef] [PubMed]
5. Wang, M.; Kaufman, R.J. Protein misfolding in the endoplasmic reticulum as a conduit to human disease. *Nature* **2016**, *529*, 326–335. [CrossRef]
6. Dejeans, N.; Manié, S.; Hetz, C.; Bard, F.; Hupp, T.; Agostinis, P.; Samali, A.; Chevet, E. Addicted to secrete—Novel concepts and targets in cancer therapy. *Trends Mol. Med.* **2014**, *20*, 242–250. [CrossRef]
7. Walsh, G.; Walsh, E. Biopharmaceutical benchmarks 2022. *Nat. Biotechnol.* **2022**, *40*, 1722–1760. [CrossRef] [PubMed]
8. Wurm, F.M. Production of recombinant protein therapeutics in cultivated mammalian cells. *Nat. Biotechnol.* **2004**, *22*, 1393–1398. [CrossRef]
9. Chiu, M.L.; Goulet, D.R.; Teplyakov, A.; Gilliland, G.L. Antibody Structure and Function: The Basis for Engineering Therapeutics. *Antibodies* **2019**, *8*, 55. [CrossRef]
10. Pelham, H.R. Multiple targets for brefeldin A. *Cell* **1991**, *67*, 449–451. [CrossRef]
11. Badr, C.E.; Hewett, J.W.; Breakefield, X.O.; Tannous, B.A. A highly sensitive assay for monitoring the secretory pathway and ER stress. *PLoS ONE* **2007**, *2*, e571. [CrossRef]
12. Aowicki, D.; Huczyński, A. Structure and antimicrobial properties of monensin A and its derivatives: Summary of the achievements. *BioMed Res. Int.* **2013**, *2013*, 742149. [CrossRef]
13. Fussenegger, M.; Mazur, X.; Bailey, J.E. A novel cytostatic process enhances the productivity of Chinese hamster ovary cells. *Biotechnol. Bioeng.* **1997**, *55*, 927–939. [CrossRef]
14. Sunley, K.; Butler, M. Strategies for the enhancement of recombinant protein production from mammalian cells by growth arrest. *Biotechnol. Adv.* **2010**, *28*, 385–394. [CrossRef] [PubMed]
15. Chung, J.Y.; Lim, S.W.; Hong, Y.J.; Hwang, S.O.; Lee, G.M. Effect of doxycycline-regulated calnexin and calreticulin expression on specific thrombopoietin productivity of recombinant Chinese hamster ovary cells. *Biotechnol. Bioeng.* **2004**, *85*, 539–546. [CrossRef]

16. Berger, A.; Le Fourn, V.; Masternak, J.; Regamey, A.; Bodenmann, I.; Girod, P.A.; Mermod, N. Overexpression of transcription factor Foxa1 and target genes remediate therapeutic protein production bottlenecks in Chinese hamster ovary cells. *Biotechnol. Bioeng.* **2020**, *117*, 1101–1116. [CrossRef]
17. Chandrawanshi, V.; Kulkarni, R.; Prabhu, A.; Mehra, S. Enhancing titers and productivity of rCHO clones with a combination of an optimized fed-batch process and ER-stress adaptation. *J. Biotechnol.* **2020**, *311*, 49–58. [CrossRef] [PubMed]
18. Peng, R.W.; Abellan, E.; Fussenegger, M. Differential effect of exocytic SNAREs on the production of recombinant proteins in mammalian cells. *Biotechnol. Bioeng.* **2011**, *108*, 611–620. [CrossRef]
19. Rahimpour, A.; Vaziri, B.; Moazzami, R.; Nematollahi, L.; Barkhordari, F.; Kokabee, L.; Adeli, A.; Mahboudi, F. Engineering the cellular protein secretory pathway for enhancement of recombinant tissue plasminogen activator expression in Chinese hamster ovary cells: Effects of CERT and XBP1s genes. *J. Microbiol. Biotechnol.* **2013**, *23*, 1116–1122. [CrossRef]
20. Hammond, S.; Lee, K.H. RNA interference of cofilin in Chinese hamster ovary cells improves recombinant protein productivity. *Biotechnol. Bioeng.* **2012**, *109*, 528–535. [CrossRef]
21. Pourcel, L.; Buron, F.; Garcia, F.; Delaloix, M.S.; Le Fourn, V.; Girod, P.A.; Mermod, N. Transient vitamin B5 starving improves mammalian cell homeostasis and protein production. *Metab. Eng.* **2020**, *60*, 77–86. [CrossRef]
22. Pourcel, L.; Buron, F.; Arib, G.; Le Fourn, V.; Regamey, A.; Bodenmann, I.; Girod, P.A.; Mermod, N. Influence of cytoskeleton organization on recombinant protein expression by CHO cells. *Biotechnol. Bioeng.* **2020**, *117*, 1117–1126. [CrossRef]
23. Boncompain, G.; Divoux, S.; Gareil, N.; de Forges, H.; Lescure, A.; Latreche, L.; Mercanti, V.; Jollivet, F.; Raposo, G.; Perez, F. Synchronization of secretory protein traffic in populations of cells. *Nat. Methods* **2012**, *9*, 493–498. [CrossRef]
24. Shapiro, J.; Sciaky, N.; Lee, J.; Bosshart, H.; Angeletti, R.H.; Bonifacino, J.S. Localization of endogenous furin in cultured cell lines. *J. Histochem. Cytochem. Off. J. Histochem. Soc.* **1997**, *45*, 3–12. [CrossRef]
25. Lefranc, M.P.; Ehrenmann, F.; Kossida, S.; Giudicelli, V.; Duroux, P. Use of IMGT(®) Databases and Tools for Antibody Engineering and Humanization. *Methods Mol. Biol.* **2018**, *1827*, 35–69. [CrossRef] [PubMed]
26. Zhao, L.; Liu, P.; Boncompain, G.; Loos, F.; Lachkar, S.; Bezu, L.; Chen, G.; Zhou, H.; Perez, F.; Kepp, O.; et al. Identification of pharmacological inhibitors of conventional protein secretion. *Sci. Rep.* **2018**, *8*, 14966. [CrossRef] [PubMed]
27. Barrette-Ng, I.H.; Wu, S.C.; Tjia, W.M.; Wong, S.L.; Ng, K.K. The structure of the SBP-Tag-streptavidin complex reveals a novel helical scaffold bridging binding pockets on separate subunits. *Acta Crystallographica. Sect. D Biol. Crystallogr.* **2013**, *69*, 879–887. [CrossRef]
28. Delgadillo, R.F.; Mueser, T.C.; Zaleta-Rivera, K.; Carnes, K.A.; González-Valdez, J.; Parkhurst, L.J. Detailed characterization of the solution kinetics and thermodynamics of biotin, biocytin and HABA binding to avidin and streptavidin. *PLoS ONE* **2019**, *14*, e0204194. [CrossRef] [PubMed]
29. Capitani, M.; Sallese, M. The KDEL receptor: New functions for an old protein. *FEBS Lett.* **2009**, *583*, 3863–3871. [CrossRef] [PubMed]
30. Zhang, F.; Qi, X.; Wang, X.; Wei, D.; Wu, J.; Feng, L.; Cai, H.; Wang, Y.; Zeng, N.; Xu, T.; et al. Structural basis of the therapeutic anti-PD-L1 antibody atezolizumab. *Oncotarget* **2017**, *8*, 90215–90224. [CrossRef]
31. Nomura, R.; Orii, M.; Senda, T. Calreticulin-2 is localized in the lumen of the endoplasmic reticulum but is not a Ca^{2+}-binding protein. *Histochem. Cell Biol.* **2011**, *135*, 531–538. [CrossRef]
32. Misumi, Y.; Misumi, Y.; Miki, K.; Takatsuki, A.; Tamura, G.; Ikehara, Y. Novel blockade by brefeldin A of intracellular transport of secretory proteins in cultured rat hepatocytes. *J. Biol. Chem.* **1986**, *261*, 11398–11403. [CrossRef] [PubMed]
33. Coulet, M.; (Sanofi R&D, Vitry-sur-Seine, France). Personal communication, 2023.
34. Jiang, Z.; Sharfstein, S.T. Sodium butyrate stimulates monoclonal antibody over-expression in CHO cells by improving gene accessibility. *Biotechnol. Bioeng.* **2008**, *100*, 189–194. [CrossRef]
35. Mimura, Y.; Lund, J.; Church, S.; Dong, S.; Li, J.; Goodall, M.; Jefferis, R. Butyrate increases production of human chimeric IgG in CHO-K1 cells whilst maintaining function and glycoform profile. *J. Immunol. Methods* **2001**, *247*, 205–216. [CrossRef] [PubMed]
36. Liu, P.; Zhao, L.; Loos, F.; Marty, C.; Xie, W.; Martins, I.; Lachkar, S.; Qu, B.; Waeckel-Énée, E.; Plo, I.; et al. Immunosuppression by Mutated Calreticulin Released from Malignant Cells. *Mol. Cell* **2020**, *77*, 748–760.e9. [CrossRef]
37. Fourriere, L.; Divoux, S.; Roceri, M.; Perez, F.; Boncompain, G. Microtubule-independent secretion requires functional maturation of Golgi elements. *J. Cell Sci.* **2016**, *129*, 3238–3250. [CrossRef] [PubMed]
38. Deffieu, M.S.; Cesonyte, I.; Delalande, F.; Boncompain, G.; Dorobantu, C.; Song, E.; Lucansky, V.; Hirschler, A.; Cianferani, S.; Perez, F.; et al. Rab7-harboring vesicles are carriers of the transferrin receptor through the biosynthetic secretory pathway. *Sci. Adv.* **2021**, *7*, eaba7803. [CrossRef]
39. Haas, A.K.; Mayer, K.; Brinkmann, U. Generation of fluorescent IgG fusion proteins in mammalian cells. *Methods Mol. Biol.* **2012**, *901*, 265–276. [CrossRef] [PubMed]
40. Luria, Y.; Raichlin, D.; Benhar, I. Fluorescent IgG fusion proteins made in *E. coli*. *MAbs* **2012**, *4*, 373–384. [CrossRef]
41. Leitzgen, K.; Knittler, M.R.; Haas, I.G. Assembly of immunoglobulin light chains as a prerequisite for secretion. A model for oligomerization-dependent subunit folding. *J. Biol. Chem.* **1997**, *272*, 3117–3123. [CrossRef] [PubMed]
42. Hammond, C.; Helenius, A. Quality control in the secretory pathway. *Curr. Opin. Cell Biol.* **1995**, *7*, 523–529. [CrossRef] [PubMed]
43. Dul, J.L.; Aviel, S.; Melnick, J.; Argon, Y. Ig light chains are secreted predominantly as monomers. *J. Immunol.* **1996**, *157*, 2969–2975. [CrossRef] [PubMed]

44. Hopper, J.E.; Papagiannes, E. Evidence by radioimmunoassay that mitogen-activated human blood mononuclear cells secrete significant amounts of light chain Ig unassociated with heavy chain. *Cell. Immunol.* **1986**, *101*, 122–131. [CrossRef]
45. Sreelatha, A.; Kinch, L.N.; Tagliabracci, V.S. The secretory pathway kinases. *Biochim. Et Biophys. Acta* **2015**, *1854*, 1687–1693. [CrossRef]
46. Harding, H.P.; Zhang, Y.; Zeng, H.; Novoa, I.; Lu, P.D.; Calfon, M.; Sadri, N.; Yun, C.; Popko, B.; Paules, R.; et al. An integrated stress response regulates amino acid metabolism and resistance to oxidative stress. *Mol. Cell* **2003**, *11*, 619–633. [CrossRef]
47. Gao, G.; Liu, F.; Xu, Z.; Wan, D.; Han, Y.; Kuang, Y.; Wang, Q.; Zhi, Q. Evidence of nigericin as a potential therapeutic candidate for cancers: A review. *Biomed. Pharmacother.* **2021**, *137*, 111262. [CrossRef] [PubMed]
48. Roy, M.; Liang, L.; Xiao, X.; Feng, P.; Ye, M.; Liu, J. Lycorine: A prospective natural lead for anticancer drug discovery. *Biomed. Pharmacother.* **2018**, *107*, 615–624. [CrossRef]
49. Zhao, S.; Guo, Y.; Wang, Q.; An, B. Antifungal effects of lycorine on Botrytis cinerea and possible mechanisms. *Biotechnol. Lett.* **2021**, *43*, 1503–1512. [CrossRef]
50. Kola, A.; Lamponi, S.; Currò, F.; Valensin, D. A Comparative Study between Lycorine and Galantamine Abilities to Interact with AMYLOID β and Reduce In Vitro Neurotoxicity. *Int. J. Mol. Sci.* **2023**, *24*, 2500. [CrossRef]
51. Li, F.; Vijayasankaran, N.; Shen, A.Y.; Kiss, R.; Amanullah, A. Cell culture processes for monoclonal antibody production. *MAbs* **2010**, *2*, 466–479. [CrossRef]

Disclaimer/Publisher's Note: The statements, opinions and data contained in all publications are solely those of the individual author(s) and contributor(s) and not of MDPI and/or the editor(s). MDPI and/or the editor(s) disclaim responsibility for any injury to people or property resulting from any ideas, methods, instructions or products referred to in the content.

cells

MDPI

Article

Ginsentide TP1 Protects Hypoxia-Induced Dysfunction and ER Stress-Linked Apoptosis

Bamaprasad Dutta [1], Shining Loo [1,2], Antony Kam [1,3], Siu Kwan Sze [1,4] and James P. Tam [1,*]

[1] School of Biological Sciences, Nanyang Technological University, Singapore 637551, Singapore; bama0001@e.ntu.edu.sg (B.D.); shining.loo@xjtlu.edu.cn (S.L.); antony.kam@xjtlu.edu.cn (A.K.); nsze@brocku.ca (S.K.S.)
[2] Academy of Pharmacy, Xi'an Jiaotong-Liverpool University, Suzhou 215123, China
[3] Department of Biological Sciences, Xi'an Jiaotong-Liverpool University, Suzhou 215123, China
[4] Department of Health Sciences, Brock University, Niagara Region, St. Catharines, ON L2S 3A1, Canada
* Correspondence: jptam@ntu.edu.sg; Tel.: +65-6316-2833

Abstract: Hypoxia-induced vascular endothelial dysfunction (VED) is a significant contributor to several severe human diseases, including heart disease, stroke, dementia, and cancer. However, current treatment options for VED are limited due to the lack of understanding of the underlying disease mechanisms and therapeutic leads. We recently discovered a heat-stable microprotein in ginseng, called ginsentide TP1, that has been shown to reduce vascular dysfunction in cardiovascular disease models. In this study, we use a combination of functional assays and quantitative pulsed SILAC proteomics to identify new proteins synthesized in hypoxia and to show that ginsentide TP1 provides protection for human endothelial cells against hypoxia and ER stress. Consistent with the reported findings, we also found that hypoxia activates various pathways related to endothelium activation and monocyte adhesion, which in turn, impairs nitric oxide (NO) synthase activity, reduces the bioavailability of NO, and increases the production of reactive oxygen species that contribute to VED. Additionally, hypoxia triggers endoplasmic reticulum stress and initiates apoptotic signaling pathways associated with cardiovascular pathology. Treatment with ginsentide TP1 reduced surface adhesion molecule expression, prevented activation of the endothelium and leukocyte adhesion, restored protein hemostasis, and reduced ER stress to protect against hypoxia-induced cell death. Ginsentide TP1 also restored NO signaling and bioavailability, reduced oxidative stress, and protected endothelial cells from endothelium dysfunction. In conclusion, this study shows that the molecular pathogenesis of VED induced by hypoxia can be mitigated by treatment with ginsentide TP1, which could be one of the key bioactive compounds responsible for the "cure-all" effect of ginseng. This research may lead to the development of new therapies for cardiovascular disorders.

Keywords: vascular endothelial dysfunction; hypoxia; ginsentide; ER stress; unfolded protein response; antioxidation; anti-inflammation; anti-apoptosis; pulsed SILAC; quantitative proteomics

1. Introduction

Hypoxia-induced vascular endothelial dysfunction (VED) plays a key role in the pathogenesis of multiple human disorders, including heart disease, stroke, dementia, and diabetic complications; however, the molecular mediators of VED largely remain unknown. Clinical data suggest that hypoxia induced by sleep apnea or high-altitude conditions is strongly associated with VED and may increase the risk of cardiovascular disorders and heart failure [1–6]. Models of pulmonary vasoconstriction studied under low-oxygen conditions also suggest that hypoxia strongly influences the endothelium via connexin-40-mediated effects on the endothelial membrane potential [7]. However, hypoxia also modulates the functions of P2X and P2Y cell surface receptors, which stimulate the release of nitric oxide (NO) and hyperpolarizing factors [8]. In addition, VED restricts blood flow and oxygen supply to tissues and endothelium, forming a vicious cycle and amplifying

the hypoxia-induced VED. Acting through these underlying mechanisms, hypoxia can trigger proinflammatory endothelial responses, including the upregulation of cell adhesion molecules that increase macrophage infiltration [9], which is a known risk factor for adverse cardiovascular events [1,4–6]. Therapeutic targeting of hypoxia-VED will break this vicious cycle and limit the progression of vascular pathology underlying major human diseases.

Under normal physiological conditions, NO generation maintains the quiescent state of the endothelium [10]. In contrast, disrupting NO signaling triggers endothelial activation and the expression of cytokines, chemokines, and adhesion molecules that promote leukocyte adhesion and inflammation [10,11]. During oxidative stress, NO reacts with superoxide anions to generate peroxynitrite, which reduces the function of endothelial nitric oxide synthases (eNOSs) and limits the production of NO to promote VED [10,12,13]. Hypoxia also induces endoplasmic reticulum (ER) stress, which triggers proapoptotic signaling pathways that are implicated in cardiovascular disease [14,15]. In contrast, the inhibition of ER stress-induced endothelial apoptosis is known to prevent VED and reduce the cardiovascular complications of diabetes [16]. Therefore, ER stress represents a critical component of VED and a priority target for therapeutic interventions; however, methods for limiting ER stress in the hypoxic endothelium have not been identified.

Ginseng plants belong to the *Panax* (panacea) genus and were named for their "cure-all" medicinal effects. For many centuries, ginseng has been used as a herbal medicine to treat various disorders, including heart disease and diabetes [17,18]. Currently, identified bioactive compounds are primarily derived from small-molecule metabolites. Moreover, the molecular basis underlying the beneficial effects of ginseng on VED in human patients has not been clarified. Studies conducted in our laboratory led to the identification of a novel family of cysteine-rich peptides (CRPs) or microproteins from ginseng plants designated as ginsentides [19]. To date, 14 ginsentides (TP1–14) have been identified from three common and medicinally valuable ginseng species, i.e., *Panax ginseng*, *Panax notoginseng*, and *Panax quinquefolius*. [19]. All ginsentides are 31–33 amino acids long and contain a conserved 8-cysteine motif and four disulfide linkages [19]. The prototypic member ginsentide TP1 (hereafter given as TP1) is the most abundant CRP found in *P. ginseng* and *P. notoginseng*. The 31-residue TP1 is both cysteine- and glycine-rich (Figure 1A). The eight cysteine residues in TP1 form novel disulfide connectivity of Cys I–IV, II–VI, III–VII, and V–VIII, resulting in a pseudocyclic knot in which the first and last residues are cystine forming disulfides with a knotted and multicyclic structure (Figure 1A,B) [19]. This unique disulfide connectivity provides the structural rigidity to TP1 and braces it into a hyperstable and compact microprotein that is resistant to heat, acid, and both exopeptidase and endopeptidase degradation [19–22].

TP1 and other members of ginsentides (TP2–14) form a new CRP family. They contain eight cysteine residues and a cysteine motif similar to heveins found in *Hevea brasiliensis* and hevein-like peptides, but they can be distinguished from heveins by a distinctly different disulfide connectivity, biosynthesis, and the absence of a chitin-binding domain which is essential for the host-defense functions of heveins and hevein-like peptides [19–24]. Recently, we showed that ginsentides TP1, TP3, and TP8 modulate multiple biological systems to exert potent effects on vascular biology [25].

Here, we show that TP1 protects endothelial cells (ECs) from hypoxia-induced and stress-linked dysfunctions underlying VED pathogens by synthesizing new proteins critical to their adaptive responses; we used pulsed SILAC (pSILAC) quantitative proteomics to pulse/chase de novo protein synthesis in ECs subjected to low-oxygen stress with or without TP1. Guided by the pSILAC results, we further investigated how TP1 protects ECs from hypoxia stress using functional assays. Using these approaches, we show that TP1 protects human ECs from hypoxia-induced VED by preventing ER stress-mediated apoptotic signaling and by increasing cell survival. We also compared TP1 with ginsenosides, a family of well-studied bioactive metabolites from ginseng. Our findings showed that ginsenosides did not exert protective effects against hypoxia-induced VED when compared to the novel ginsentides.

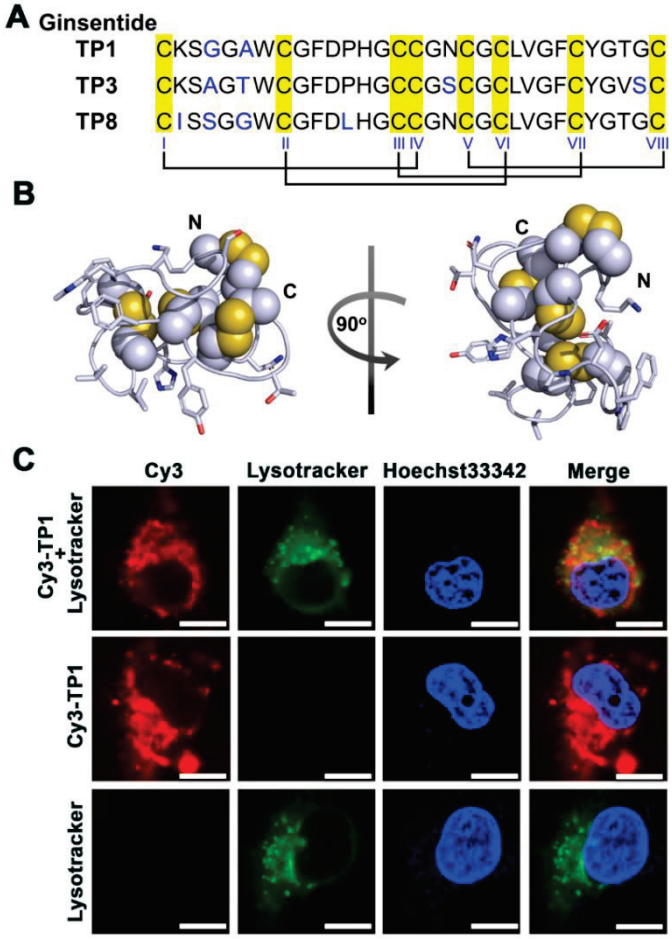


Figure 1. Ginsentides: cysteine- and glycine-rich cell-penetrating peptides from ginseng. (**A**) Primary sequence and disulfide connectivity (Cys I–IV, Cys II–VI, Cys III–VII, and Cys V–VIII) of ginsentides TP1, TP3, and TP8. (**B**) Cartoon representation of the structure of the pseudocyclic TP1 (PDB code: 2ML7). The unusual disulfide connectivity between cysteine residues forms a pseudocyclic knot, in which the first and last residues are cysteines. (**C**) Images of HUVEC-CS cells after incubation with 1 μM Cy3–TP1, captured using live-cell confocal microscopy at 37 °C. Cy3–TP1 is shown in red, whereas lysosomes and nuclei are counterstained with LysoTracker (green) and Hoechst 33342 (blue), respectively. Scale bar: 5 μm.

2. Materials and Methods

2.1. Reagents

All chemicals and reagents were purchased from Sigma-Aldrich (St. Louis, MO, USA) unless otherwise indicated. Antibodies against GAPDH (6C5) and actin (C-2) were purchased from Santa Cruz Biotechnology (Santa Cruz, CA, USA), whereas anti-LC3B (L7543) antibody was purchased from Sigma-Aldrich. Anti-eNOS (D9A5L), anti-phospho-eNOS (Ser1177), anti-integrin αV (D2N5H), anti-integrin β1 (D6S1W), anti-integrin β3, HRP-linked anti-mouse IgG, and HRP-linked anti-rabbit IgG antibodies were obtained from Cell Signaling Technology (Danvers, MA, USA). Clarity Max Western ECL Blotting Substrate (1705062) was purchased from Bio-Rad Laboratories (Milan, Italy). The cell lines, including HUVEC-CS (ATCC CRL-2873), H9c2 (ATCC CRL-1446), C2C12 (ATCC CRL-1772), A7r5 (ATCC CRL-1444) and THP-1 (ATCC TIB-202) were acquired from ATCC.

2.2. Extraction and Purification of TP1 and Other Ginsentides

Peptide extraction was performed using the method described by Tam et al. [19]. Briefly, dried *P. ginseng* flowers were pulverized and blended with Milli-Q water (100 g/L). The extract was then centrifuged, and the obtained supernatant was filtered through a

0.22 μm membrane (Thermo Fisher Scientific, Waltham, MA, USA). Purification was performed using multiple rounds of reversed-phase high-performance liquid chromatography (RP-HPLC), which was conducted using a C18 column (250 × 22 mm; 5 μm particle size; Phenomenex, Torrance, CA, USA) at a flow rate of 5 mL/min with a linear gradient of 1%/min of 10–80% buffer B [0.1% trifluoroacetic acid (TFA) in acetonitrile (ACN)] and buffer A (0.1% TFA in HPLC water). Final purification was performed via analytical RP-HPLC using a C18 column (250 × 4.6 mm; 5 μm particle size; Phenomenex) at a flow rate of 1 mL/min using the same gradient. MALDI-TOF mass spectrometry was used to identify the peptide-containing fractions. Ginsentide TP3 and TP8 were isolated from dried *P. ginseng* seeds and dried *P. quinquefolius* flowers, respectively, and purified using the same method.

2.3. Cell Culture

HUVEC-CS cells, rat cardiomyoblast cells (H9c2), rat aorta thoracic/smooth muscle cells (A7r5), and mouse myoblast cells (C2C12) were maintained in DMEM supplemented with 10% FBS at 37 °C in 5% CO_2. THP1 cells were maintained in an RPMI medium supplemented with 10% FBS at 37 °C in 5% CO_2.

2.4. Confocal Microscopic-Based Cellular Uptake Analyses

Cy3–TP1 was used to study the cellular uptake of TP1 in HUVEC-CS cells. To visualize the intracellular distribution of Cy3–TP1, cells were grown on an 8-well chamber slide (Ibidi, Gräfelfing, Germany) overnight before they were incubated with 1 μM Cy3–TP1 at 37 °C for 1 h and counterstained with LysoTracker and Hoechst 333241. Postincubation, the medium was drained, and the cells were washed gently with PBS. Fresh medium was added prior to imaging. Slides were observed and imaged using a Zeiss LSM 710 confocal microscope.

2.5. Pulsed SILAC Labeling

For pSILAC labeling, 2×10^6 HUVEC-CS cells were seeded onto 10 cm Petri dishes and cultured overnight at 37 °C in 5% CO_2. The supernatant was aspirated the following day and replaced with SILAC medium containing $^{13}C_6$ L-arginine and $^{13}C_6$ and $^{15}N_2$ L-lysine together with 10% SILAC-compatible dialyzed FBS. The cells were then supplemented with 20 μM TP1 or PBS vehicle control, after which the dishes were transferred into hypoxia chambers from which the air was removed by flashing the chambers with hypoxic gas (95% N_2, 5% CO_2, and <0.1% O_2) for 10 min at a constant flow rate of 15 L/min. The chambers were then sealed and incubated at 37 °C for 24 h. Control cells were instead maintained under standard culture conditions (i.e., normoxia: 21% O_2 and 5% CO_2) at 37 °C for the 24 h incubation period. Subsequently, the cells were trypsinized and washed three times with ice-cold PBS before they were stored at −80 °C until they were used in proteomic experiments. The entire experimental protocol was performed in triplicate, as summarized in Figure S2B.

2.6. Protein Extraction and Tryptic Digestion

The cell pellets obtained from each experimental condition were suspended in lysis buffer (8 M urea in 100 mM ammonium bicarbonate supplemented with a protease inhibitor cocktail) and sonicated at 30% amplitude for 30 s. The cell lysates were clarified via centrifugation at 20,000× *g* for 10 min, and the protein content of the lysates was quantified using the Bradford protein assay. For each sample, 500 μg of protein was diluted with 100 mM ammonium bicarbonate buffer to decrease the urea concentration to <1 M. The samples were then reduced using 10 mM dithiothreitol at 37 °C for 2 h, after which they were alkylated with 55 mM iodoacetamide at room temperature for 45 min in the dark. Finally, the samples were digested via incubation with trypsin (with an enzyme:protein ratio of 1:50) overnight at 37 °C, after which the reaction was stopped by adding formic acid to a final

concentration of 0.5%. Tryptic peptides were then desalted using Sep-Pak C18 cartridges (Waters, Milford, MA, USA), vacuum dried, and stored for HPLC fractionation.

2.7. Reverse-Phase Chromatography Fractionation and Liquid Chromatography with Tandem Mass Spectrometry

Tryptic peptides were fractionated using reverse-phase chromatography separation performed at pH 8. Briefly, the desalted tryptic peptides were reconstituted in buffer A (0.02% NH_4OH in water) and fractionated using an X-Bridge C18 column (4.6 × 200 mm; 5 μm particle size; 130 Å pore size; Waters) at a flow rate of 1 mL/min in an HPLC unit (Prominence, Shimadzu, Kyoto, Japan). The gradient was as follows: 100–95% buffer A for 3 min; 5–35% buffer B (80% ACN and 0.02% NH_4OH) for 40 min; 35–70% buffer B for 12 min; and 70% buffer B for 5 min. The 280 nm wavelength was selected for chromatogram recording, and 64 fractions were collected within a 65 min period. The collected fractions were combined into 13 pools using a concatenated pooling strategy, after which they were dried via vacuum centrifugation. The samples were then subjected to liquid chromatography with tandem mass spectrometry (LC–MS/MS) analysis using a Q Exactive mass spectrometer coupled with an online Dionex Ultimate 3000 RSLC nano-LC system (Thermo Fisher Scientific). Peptide samples were separated using a Dionex EASY-spray column (PepMap C18; 3 μm; 100 Å) and sprayed through an EASY nanospray source at a voltage of 1.5 kV. The range 350–1600 m/z was used for the full MS scan with a resolution of 70,000 at m/z 200. The maximum ion accumulation time was set to 100 ms, and dynamic exclusion was set to 30 s. The top 10 ions above a threshold of 1000 counts were selected for high-energy collision dissociation fragmentation using 28% normalized collision energy with a maximum ion accumulation time of 120 ms as a fragmentation parameter. The other parameters were set as follows: an AGC setting of 1×10^6 for the full MS scan and 2×10^5 for the MS2 scan, an isolation width of 2 Da for the MS2 scan, the exclusion of single and unassigned charged ions from the MS/MS scan, and an underfill ratio of 0.1%. All raw data were acquired using Xcaliber 2.2 (Thermo Scientific, Waltham, MA, USA). Samples from triplicate experiments were run as technical duplicates.

2.8. Mass Spectrometric Data Analysis and Bioinformatics

Protein identification and quantification were performed using MaxQuant version 1.5.2.8 (Max Planck Institute of Biochemistry, Planegg, Germany). The parameters used were as follows: carbamidomethyl at cysteine as a static modification; N-term acetyl, methionine oxidation, and asparagine and glutamine deamidation as dynamic modifications; trypsin/P and a maximum of two missed cleavages as digestion parameters; and a 30-ppm precursor mass and 0.5 Da fragment mass tolerance. The UniProt Knowledgebase of human proteins (downloaded on 25 July 2016, including 70,849 sequences and 23,964,784 residues) was used as a search database with a false discovery rate cutoff of <0.01% both at the peptide and protein levels. For SILAC quantification, Arg6 and Lys8 were set as labeling residues. Searched data were extracted in text format for further analysis. Technical duplicates were searched in combination, and statistical analysis was conducted on data collected in triplicate experiments. The online bioinformatics tool GOrilla was used for bioinformatics analyses [26].

2.9. LDH Assay

A LDH release–based cytotoxicity assay was conducted using a CytoSelect LDH Cytotoxicity Assay Kit (CBA-241, Cell Biolabs, Inc., San Diego, CA, USA). Briefly, HUVEC-CS cells were cultured with or without 100 μM TP1 for 24 h at 37 °C in 5% CO_2. PBS was used as vehicle control, and 1% Triton X-100 was used as a positive control, i.e., as a cell death and membrane-damaging agent. The culture medium was collected, transferred, and mixed with the LDH assay reagent at a ratio of 9:1. The reaction mixture was then incubated at 37 °C for 2 h. Quantification was performed calorimetrically using a wavelength of

450 nm. The assay was conducted in triplicate, and statistical analyses and graphing were performed using GraphPad Prism (version 6.01).

2.10. MTT Assay

Cells were cultured in DMEM with or without 20 μM TP1 (or dose maintained) under normoxic and hypoxic conditions for 24 h, after which MTT reagent (final concentration of 0.5 mg/mL) was added, and the cells were incubated for a further 2 h at 37 °C. The culture medium was then aspirated, and formazan crystals were dissolved in dimethyl sulfoxide to conduct colorimetric quantification at 570 nm using a microplate reader (Tecan Magellan, Männedorf, Switzerland) with a reference wavelength of 630 nm. Experiments were conducted in triplicate, and the resultant data were used for statistical analysis. For ginsentide TP3 and TP8 and ginsenoside Rb1 and Rg1 treatments, cells were treated with 20 μM of the respective compounds for 24 h under normoxic and hypoxic conditions, respectively, with PBS used as vehicle control. Cell viability was assessed using a MTT assay, as described.

2.11. Monocyte–Epithelium Adhesion Assay

HUVEC-CS cells were seeded in 6-well plates and grown as a monolayer in DMEM supplemented with 20 μM TP1 (or the PBS control) under normoxic or hypoxic conditions for 24 h. The ginsenosides Rb1 and Rg1 were used as reference controls at 20 μM. THP-1 cells were cultured in RPMI medium supplemented with 10% FBS. Immediately prior to their use in adhesion assays, the THP-1 cells were harvested, washed three times with PBS, and labeled with 10 μM carboxyfluorescein succinimidyl ester (CFSE) for 10 min at 37 °C. The cell culture medium was aspirated from the HUVEC-CS monolayers, which were then washed with a serum-free RPMI medium. CFSE-labeled THP1 cells were then seeded onto the HUVEC-CS monolayer at a density of 2×10^5 cells/well in serum-free RPMI medium and incubated for 90 min at 37 °C. After incubation, the culture medium was drained, and the HUVEC-CS monolayer was washed three times with PBS to remove nonadherent leukocytes. Images of adherent leukocytes were then captured using the green fluorescence channel of a Nikon ECLIPSE Ti-S inverted microscope system (Nikon, Yokosuka, Kanagawa, Japan). Cells were quantified via cell counting, and statistical analyses were performed using data collected in triplicate experiments.

2.12. NO Detection

Intercellular NO levels were measured using a diaminofluorescein-2 diacetate (DAF-2DA)–based assay. ECs were cultured under various experimental conditions for 24 h before the assay began. For hypoxic cultures, the cells were also treated with 100 μM $CoCl_2$. First, the culture medium was aspirated, after which the cells were washed with Hank's Balanced Salt Solution. The cells were incubated with 1 μM DAF-2DA for 60 min at 37 °C, after which the medium was refreshed, and images of labeled cells were captured using the green fluorescence channel of the Nikon ECLIPSE Ti-S inverted microscope system. Fluorescence intensity was quantified by analyzing the labeled cells via ImageJ. The experiment was performed in triplicate.

2.13. Western Blot Analysis

First, 35 μg of each protein sample was resolved on a 10% acrylamide gel and transferred onto a PVDF membrane. Immunoblotting was then performed using anti-protein antibodies, and detection was achieved using an ECL system (Millipore, Burlington, MA, USA).

2.14. Cell Cycle Analysis

Cells cultured under different experimental conditions were harvested via trypsinization and washed with ice-cold multivalent cation-free PBS. The cells were then fixed in ethanol at −20 °C for 24 h and stained with 0.5 mg/mL propidium iodide for 15 min

at 37 °C. DNA content was measured using a BD FACSCalibur flow cytometer (BD Biosciences, San Jose, CA, USA), and data analysis was performed using Weasel (version 3.3.2).

2.15. qRT-PCR

RNA was extracted from cells using RNA isolation kits (Macherey-Nagel, Duren, Germany) according to the 'manufacturer's protocol. RevertAid H Minus First Strand cDNA Synthesis Kits (Thermo Fisher Scientific) were used to synthesize first strand cDNA from 2 μg of total RNA. The primer sequences used in this study are listed in Supplementary Table S1. The primers used to assess ER stress pathway–related genes were designed as described by Oslowski et al. [27]. Real-time PCR amplification was performed using a CFX Connect Real-Time PCR Detection System (Bio-Rad Laboratories, Singapore) with KAPA SYBR FAST qPCR Kits (KAPA Biosystems, Boston, MA, USA). The cycling temperatures were as follows: enzyme activation at 95 °C for 3 min; denaturation at 95 °C for 10 s; annealing and extension at 60 °C for 30 s. Data were normalized against the expression level of 18S ribosomal RNA in each sample. The experiment was performed in triplicate.

2.16. Apoptosis Detection

Apoptotic cells were detected using an Annexin V Apoptosis Detection Kit with PI (BioLegend Inc., San Diego, CA, USA). HUVEC-CS cells were cultured in DMEM with or without 20 μM TP1 under normoxic or hypoxic conditions for 24 h. In some experiments, the apoptosis of HUVEC-CS cells was induced using 0.2 μg/mL doxorubicin treatment for 24 h. After incubation, the cells were stained with FITC-conjugated annexin V and propidium iodide according to the manufacturer's protocol. Apoptotic cells were quantified using the BD FACSCalibur flow cytometry system (BD Biosciences).

2.17. ROS Detection

Intracellular ROS activity was measured using a DCFDA-based fluorogenic assay. Briefly, ECs were grown as a monolayer for 24 h under various experimental conditions, washed with serum-free medium, and stained with 1 μM DCFDA for 60 min at 37 °C. The dye-containing medium was then replaced with a fresh medium, and images of DCFDA-labeled cells were captured using the green fluorescence channel of the Nikon ECLIPSE Ti-S inverted microscope system. Quantification of fluorescence intensity was performed by analyzing labeled cells in ImageJ. Statistical analyses were performed using data from triplicate experiments.

2.18. Immunostaining

Thioflavin-T staining was used to detect UPR activity. Cells were grown on coverslips under various experimental conditions for 24 h, washed with PBS, and fixed with 4% paraformaldehyde for 20 min at room temperature. The fixed cells were then permeabilized for 5 min with 0.2% Triton X-100 at room temperature, stained with 1 μg/mL DAPI for 5 min, and counterstained with 5 μM thioflavin-T for 10 min. Coverslips were then mounted on glass slides with Clarion mounting medium, and images were captured using the Nikon ECLIPSE Ti-S inverted microscope system. Quantification of fluorescence intensity was performed by analyzing labeled cells in ImageJ. The experiment was performed in triplicate.

2.19. Aggregated Protein Isolation

Cells were cultured with or without TP1 under normoxic or hypoxic conditions for 24 h, after which aggregated proteins were isolated from 10×10^6 cells per condition. Briefly, cells were lysed in lysis buffer [50 mM Tris–HCl (pH 7.6), 150 mM NaCl, 1 mM EDTA, 1% NP-40, 0.1% SDS, 0.5% SDC, and protease inhibitor cocktail] with sonication at 4 °C. Cell debris was removed via centrifugation at 3000× *g*. Aggregated proteins were isolated from precleared lysates via ultracentrifugation at 112,000× *g* and 4 °C for 1 h. Aggregates were washed once with lysis buffer and dissolved in a modified lysis buffer

containing 5% ammonium hydroxide. Bradford quantification was used to measure the protein content. The experiment was performed in triplicate.

2.20. Statistical Analyses

Statistical analysis was performed using GraphPad Version 6.01 software (GraphPad Software, Inc., La Jolla, CA, USA). All data used for the analysis were obtained from individual experimental triplicates or as specified in the experiments. For data analysis, a one-way analysis of variance (ANOVA) with a Newman–Keuls posthoc test was conducted. Additionally, a two-way ANOVA with Šidák's multiple comparisons test was considered for the groups with two independent variables. The data are presented as the mean ± standard deviation (SD) or standard error of the mean (SEM). A significance level of $p < 0.05$ was considered statistically significant.

3. Results

3.1. TP1 Is a Hyperstable Nontoxic and Non-Membranolytic Cell-Penetrating Peptide

TP1 is a positively charged and hydrophobic peptide. To determine whether it interacts with intracellular proteins to protect against hypoxia-induced dysfunction, we site-specifically labeled TP1 with Cy3 at its lysine side chain. The cellular uptake of Cy3-labeled TP1 (Cy3–TP1) in live cells was observed using confocal microscopy to minimize artifacts in localizing labeled peptides under fluorescence microscopy [28]. The live-cell images of human umbilical vein/vascular endothelium (HUVEC-CS) cells after incubation with 1 μM Cy3–TP1 for 1 h revealed that Cy3–TP1 was internalized and distributed throughout the cytoplasm, whereas LysoTracker counterstaining showed that Cy3–TP1 also accumulated in lysosomes (Figure 1C) due its internalization through energy-dependent endocytosis as observed in our previous studies [25].

To investigate the toxicity of TP1, we used a lactate dehydrogenase (LDH) release assay and an MTT assay–based cell viability assay to assess multiple cell lines, including HUVEC-CS, H9c2, A7r5, and C2C12 cells. The LDH release assay revealed that treatment with TP1 up to 100 μM produced no significant cytotoxicity or cell-membrane-damaging effects on HUVEC-CS cells (Figure S2A). In agreement with the LDH assay results, the MTT-based cell viability assay also indicated that HUVEC-CS cell viability was not altered following TP1 treatment up to 100 μM (Figure S2B–D). The MTT-based cell viability assay also confirmed the nontoxic effect of TP1 at the effective dosage of 20 μM in multiple cell lines used in subsequent assays (Figure S2D). In addition, the MTT-based assay indicated that TP1 has no significant effect on cell proliferation, which was validated via a flowcytometry–based cell cycle assessment (Figure S2C). In agreement with our previous in vivo toxicity study, which did not show acute toxicity effects, e.g., cytotoxic, hemolytic, and immunogenic effects [19], the present results reflect the comparable nontoxic effect of TP1. Thus, we conclude that TP1 does not exert membranolytic, cytotoxic, or mitogenic effects at a dosage of up to 100 μM. The dose–response of TP1 was investigated within a range of 0–60 μM (Figure S2E), and a dose of 20 μM was chosen for subsequent studies.

3.2. TP1 Alters Hypoxia-Modulated Endothelial Proteome

To study hypoxia-induced pathophysiology in ECs, we used a pSILAC proteomic method to pulse/chase the incorporation of stable isotope-labeled lysine and arginine into newly synthesized proteins [29]. Briefly, HUVEC-CS cells were cultured for 24 h in SILAC medium containing $^{13}C_6$ L-arginine and $^{13}C_6$ and $^{15}N_2$ L-lysine in the presence or absence of 20 μM TP1 [or the phosphate-buffered saline (PBS)–only control] under normal oxygenation or hypoxic conditions (Figure S3A,B). After a 24 h incubation, the cells were lysed, and their protein content was extracted for LC-MS/MS proteomic analysis, in which 7614 proteins were identified with high confidence (3 experimental replicates and a false discovery rate of <1%), including 7101 proteins identified based on more than one component peptide (Supplementary dataset). According to Pearson's correlation analysis, a linear relationship ($R^2 > 0.9$) existed between replicates (Figure S4), indicating

the high reproducibility and reliability of the experiments. All statistical analyses were conducted using data from triplicate experiments, *p*-values were calculated using 'Student's heteroscedastic *t*-test with a two-tailed distribution, and volcano plots were used to determine data distribution and cutoff levels (Figure S5A–C). In total, 2802 proteins were significantly enriched under hypoxia, either in the presence or absence of TP1, and the relative abundance of the newly synthesized proteins was subjected to hierarchical clustering (Figure 2A). Cutoffs for differential protein synthesis were determined using $\log_2$ ratio distributions: ratio values of <0.76 [log2 (Ratio) < −0.4] and >1.32 [log2 (Ratio) > 0.4] for reduced and induced proteins, respectively (Figure S5A–C). Using these cutoff values, we found that 148 and 431 proteins were induced and suppressed, respectively, under hypoxic conditions compared to normoxic conditions. We also found that TP1 treatment induced and repressed a further 39 and 172 distinct proteins, respectively, during hypoxia.

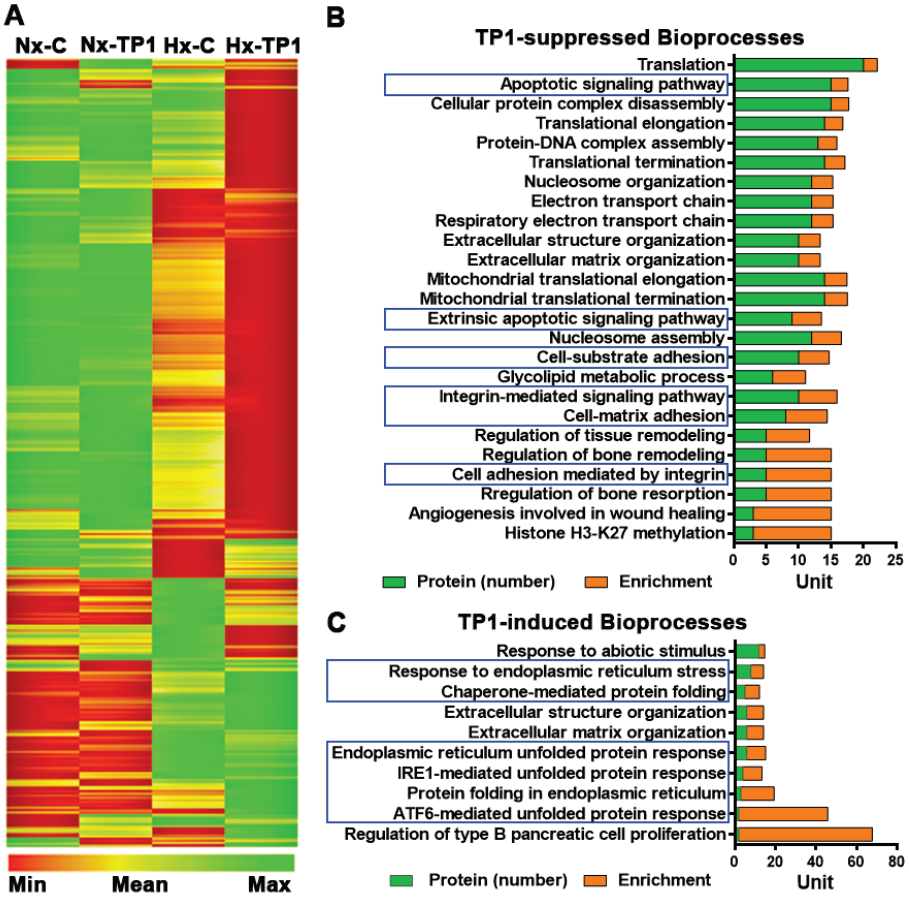


Figure 2. TP1-mediated differential protein synthesis in HUVEC-CS cells under normoxic and hypoxic conditions. (**A**) Heat map representing the relative abundance of newly synthesized proteins under the indicated experimental conditions. HUVEC-CS cells were treated with 20 µM TP1 for 24 h under normoxic or hypoxic conditions, respectively, and PBS was used as the vehicle control. A SILAC-based protein labeling approach was used to label the newly synthesized proteins, which were later quantified using a LC-MS/MS-based quantitative proteomic technique. Cluster analysis of the identified proteins was performed using the online bioinformatics tool Gene Pattern (http://genepattern.broadinstitute.org, accessed on 20 November 2017) with hierarchical clustering and Pearson's correlation options. Vehicle control under normoxic (Nx-C) or hypoxic (Hx-C) conditions and TP1 treatment under normoxic (Nx-TP1) or hypoxic (Hx-TP1) conditions are shown. (**B**,**C**) Bioinformatics analysis of TP1-regulated bioprocesses in hypoxic HUVEC-CS cells. Figures represent TP1-suppressed bioprocesses (**B**) and TP1-induced bioprocesses (**C**) during 24 h of hypoxic stress.

3.3. TP1 Limits Hypoxia-Induced Endothelial Activation and THP-1 Cell Adhesion

We performed functional analyses of the proteins modulated by low-oxygen stress with or without TP1 treatment. Data analysis performed using the online bioinformatics tool GOrilla (http://cbl-gorilla.cs.technion.ac.il, accessed on 30 December 2016) [26] revealed that hypoxia induced the expression of exocytosis regulators, key mediators of leukocyte activation/inflammatory responses and various metabolic intermediaries (Figure S6A–C). Importantly, TP1-treatment significantly reduced the synthesis of proteins involved in VED pathogenesis, including integrin-mediated cell adhesion molecules, cell-matrix/substrate adhesion regulators, and apoptotic signaling pathways (Figure 2B). Additionally, hypoxia stimulates endothelial activation and promotes inflammatory responses, which are significantly reduced by treatment with TP1. Indeed, TP1 treatment also induced the synthesis of proteins associated with cellular responses to ER stress, including the ATF6-mediated unfolded protein response (UPR), IRE1-mediated UPR, and chaperone-mediated protein folding (Figure 2B,C). Taken together, TP1 decreases hypoxia-induced ER stress in the human endothelium.

Bioinformatics analysis of our pSILAC data indicated that hypoxia stress-activated inflammatory response pathways were active in ECs (Figure S6A–C), leading to leukocyte activation and recruitment. Therefore, we used quantitative PCR to determine the expression patterns of leukocyte adhesion receptors during hypoxia. Our finding showed that the expression level of *ICAM1* mRNA increased 9-fold and the expression of *ALCAM*, *L1CAM*, and *VCAM1* mRNAs was also substantially upregulated (Figure 3A). Analysis of proteomic data showed that ICAM1 protein synthesis was upregulated in hypoxic ECs relative to normoxic cells (Figure 3B). In addition, cell adhesion assays using THP-1 human monocytic cells showed that THP-1 binding to hypoxic HUVEC-CS cells increased 2-fold (Figure 3C,D). Proteomic data analysis also revealed that TP1 treatment significantly decreased the expression of ICAM1 and ALCAM at the mRNA and protein levels in hypoxic ECs (Figure 3A,B) and reduced the transcription of L1CAM and VCAM1 (Figure 3A). Integrins are key signaling molecules involved in the regulation of various bioprocesses such as the activation of inflammatory responses [30]. The activation of integrin subsets, including αvβ3 and α5β1, is considered to trigger inflammatory responses through the activation of proinflammatory gene expression [31–33]. In the present study, we found that integrin-subtype-β3 synthesis was induced by hypoxia (Figure S7A), which also significantly upregulated total integrin levels, including the levels of integrin subtypes α_v, β_1, and β_3 in ECs (Figure S7B,C). Proteomic data analysis revealed that TP1-treatment suppressed the synthesis of critical integrin subtypes in hypoxic ECs (Figure S7B,C) and significantly downregulated the total expression levels of integrin subtypes α_v, β_1 and β_3 in hypoxic ECs (Figure S7B,C). Therefore, the TP1-mediated suppression of integrin expression might prevent the activation of integrin subtypes, including αvβ3 and α5β1, which could result in the deactivation of proinflammatory gene expression [31–33], including the expression of *ALCAM*, *ICAM1*, *L1CAM*, and *VCAM1*, in hypoxic ECs. Accordingly, THP1 cell adhesion to hypoxic ECs was decreased 2.9-fold following TP1 treatment (Figure 3C,D), suggesting the high potential of TP1 affecting VED pathogenesis in vitro. In contrast, treatment with two major bioactive ginseng metabolites, ginsenosides Rb1 and Rg1, did not affect hypoxia-mediated proinflammatory gene activation (Figure 3A), nor did these ginseng metabolites prevent hypoxia-induced leukocyte adhesion to ECs (Figure 3C,D). Thus, unlike TP1, ginsenosides Rb1 and Rg1 do not have any protective impacts against hypoxia-induced endothelium activation.

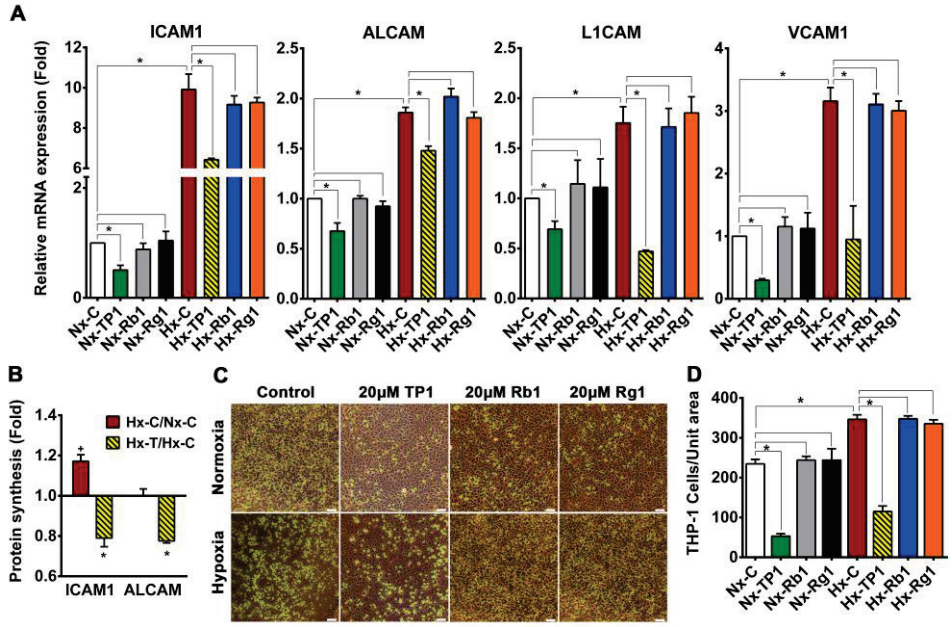


Figure 3. Ginsentide TP1 inhibits THP-1 cell adhesion to human vascular endothelial cells. (**A**) Relative mRNA expression of adhesion receptors in control and treated HUVEC-CS cells cultured under normoxic or hypoxic conditions. Data means ± SEM, and statistical significance was determined using triplicate biological replicates. Vehicle control cells were cultured for 24 h under normoxic (Nx-C) or hypoxic (Hx-C) conditions and TP1/Rb1/Rg1-treated cells were cultured for 24 h under normoxic (Nx-TP1/Nx-Rb1/Nx-Rg1) or hypoxic (Hx-TP1/Hx-Rb1/Hx-Rg1) conditions, respectively. * $p < 0.05$. (**B**) Fold-change in the newly synthesized cell surface adhesion receptors ICAM1 and ALCAM under hypoxic conditions relative to normoxic conditions (Hx-C/Nx-C) or in TP1-treated hypoxic cells compared with vehicle-treated hypoxic cells (Hx-TP1/Hx-C). Data are means ± standard error of the mean (SEM), and statistical significance was calculated based on triplicate experiments. + $p < 0.05$ respect to Nx-C and * $p < 0.05$ respect to Hx-C. (**C**) Differential binding of human monocytic THP1 cells to a HUVEC-CS monolayer cultured under normoxic or hypoxic conditions in the presence of TP1/Rb1/Rg1 or the PBS vehicle-only control. Carboxyfluorescein succinimidyl ester (CFSE)-labeled THP-1 cells are shown in green. Scale bar: 100 μm. (**D**) THP-1 adhesion was quantified via cell counting, and statistical significance was determined using triplicate experiments.

3.4. TP1 Promotes EC Survival by Antagonizing Apoptotic Signaling during Hypoxia

Given our findings that TP1 protects ECs against hypoxia-induced oxidative stress and ER stress, we assessed whether TP1 increases cell viability under hypoxic conditions. Briefly, ECs were cultured in Dulbecco's modified Eagle medium (DMEM) containing 10% fetal bovine serum (FBS) with or without TP1 and then incubated in a normoxic or hypoxic environment for 24 h before cell survival was determined using an MTT assay. These experiments revealed that TP1 treatment increased EC viability by 20% under hypoxic conditions (Figure 4A,B). Importantly, comparable protective effects were also observed in other TP1-treated cell types, including rat heart myoblast H9c2 cells (32%), rat aorta thoracic/smooth muscle A7r5 cells (31%), and mouse myoblast C2C12 cells (19%) (Figure 4A). We also tested two other ginsentide members, TP3 (*P. ginseng* seed) and TP8 (*P. quinquefolius* flower), which differ from TP1 by one and three amino acid residues, respectively (Figure 1A). Like TP1, TP3, and TP8 also exerted similar protective effects against hypoxic cell death in ECs (Figure 4B). Collectively, these results suggest that TP1 and its closely related homologs TP3 and TP8 provide various cell types with protection against hypoxia-induced death.

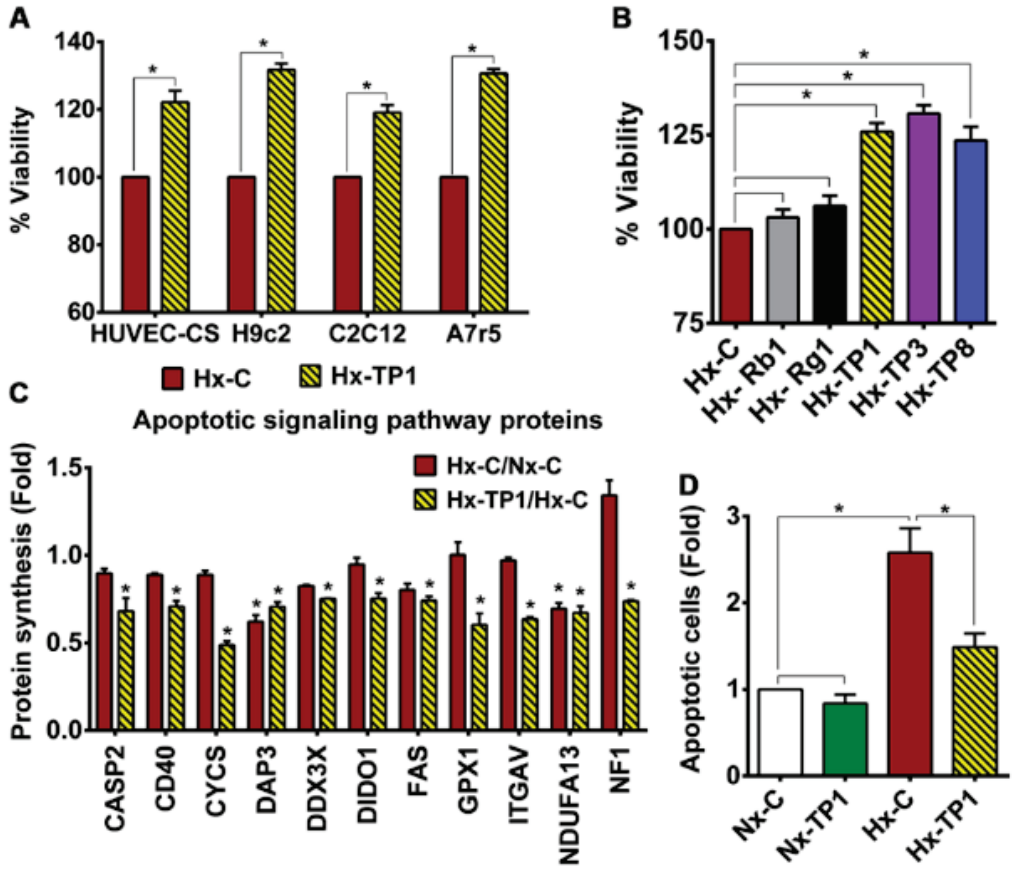


Figure 4. Ginsentide TP1 prevents hypoxic stress-mediated cell death. (**A**) Viability of hypoxic cells measured using an MTT assay after treatment with TP1 or vehicle control. Relative survival is expressed as mean values and statistical significance was calculated using three independent experimental replicates. (**B**) Effects of ginsentides, i.e., TP1, TP3, and TP8, and ginsenosides, i.e., Rb1 and Rg1, on the viability of hypoxic HUVEC-CS cells. Viability was measured using an MTT assay after treatment with 20 μM ginsenoside (Rb1 or Rg1), 20 μM ginsentide (TP1, TP3, or TP8), or PBS (vehicle control). Relative survival is expressed as mean values ± standard error of the mean (SEM) from three independent experimental replicates. * $p < 0.05$. (**C**) Relative change in the expression of apoptotic signaling pathway proteins after 24 h of hypoxic culture in the presence of TP1. Statistical significance was calculated using data from triplicate experiments. (**D**) Effect of TP1 on hypoxia-induced apoptosis in HUVEC-CS cells. Relative quantification was based on annexin V and propidium Iodide (PI) staining used to identify apoptotic cells. Statistical significance was calculated using three independent experimental replicates. Data are means ± SEM for triplicate experiments. * $p < 0.05$.

Hypoxia is known to induce cell cycle arrest in the G0/G1 phase and impair mitochondrial function, leading to the apoptosis of ECs and progression to VED [34]. Our proteomic data analysis showed that TP1 could suppress the synthesis of apoptosis signaling proteins in hypoxic ECs (Figure 4C); therefore, we investigated the antiapoptotic effects of TP1 via the flow cytometric analysis of annexin V and propidium iodide (PI) staining. We observed a marked increase in the proportion of apoptotic and necrotic HUVEC-CS cells cultured under hypoxic conditions; however, treatment with TP1 was sufficient to abolish this increase (Figure 4D and Figure S8A,B). TP1 also conferred significant protection against cell death in an alternative doxorubicin-induced apoptosis model (Figure S8C,D). This result is significant because doxorubicin is a leading drug against certain types of cancer, and TP1 exerts antiapoptotic effects to prevent doxorubicin-induced cell death during hypoxia.

We also investigated the effects of ginsenosides on the viability of ECs during hypoxic stress but found no significant effects of Rb1 or Rg1 treatment on cell survivability

(Figure 4B). Thus, unlike the tested ginsentides, we found these two ginsenosides have no protective effects against hypoxia-mediated cell death.

3.5. TP1 Treatment Rescues ECs from Hypoxia-Induced ER Stress

The disruption of ER homeostasis during hypoxia leads to the accumulation of misfolded/unfolded proteins in the ER lumen, resulting in ER stress. Hypoxia-induced ER stress initiates the unfolded protein response (UPR), which promotes cellular adaptation to stress conditions and promotes the apoptosis of cells that fail to restore normal function [35,36]. To better understand the mechanism underlying the promotion of hypoxic cell survival by TP1, we measured the mRNA expression levels of the UPR marker XBP1. We found that the spliced isoform was upregulated 20-fold in hypoxic HUVEC-CS cells compared to normoxic HUVEC-CS cells (Figure S9). Under these conditions, according to our proteomic data analysis, TP1 induced the synthesis of several ER stress sensor (ATF6/IRE1)–regulated downstream proadoptive UPR genes, including those encoding chaperone proteins and autophagy proteins, in hypoxic ECs (Figure 5A,B). Consistent with these proteomic findings, we also detected the upregulation of spliced-XPB1 mRNA in TP1-treated hypoxic ECs (Figure S9) as well as the enhanced expression of ATF6 transcripts and multiple downstream UPR genes, e.g., *BiP* (*HSPA5*), *GRP94* (*HSP90B1*), and *EDEM* (Figure 5C). Our quantitative reverse transcription–polymerase chain reaction (qRT-PCR) analyses also indicated that TP1-treatment significantly downregulated the expression of multiple genes in the PERK–eIF2a–ATF4 apoptosis pathway, including *ATF4*, *CHOP*, *DR5*, and *TRB3*, in hypoxic cells (Figure 5D). Conversely, this qRT–PCR analysis showed that the reference compounds, ginsenosides Rb1 and Rg1, had no significant effect on the mRNA expression of ER stress-related genes (Figure S10A,B).

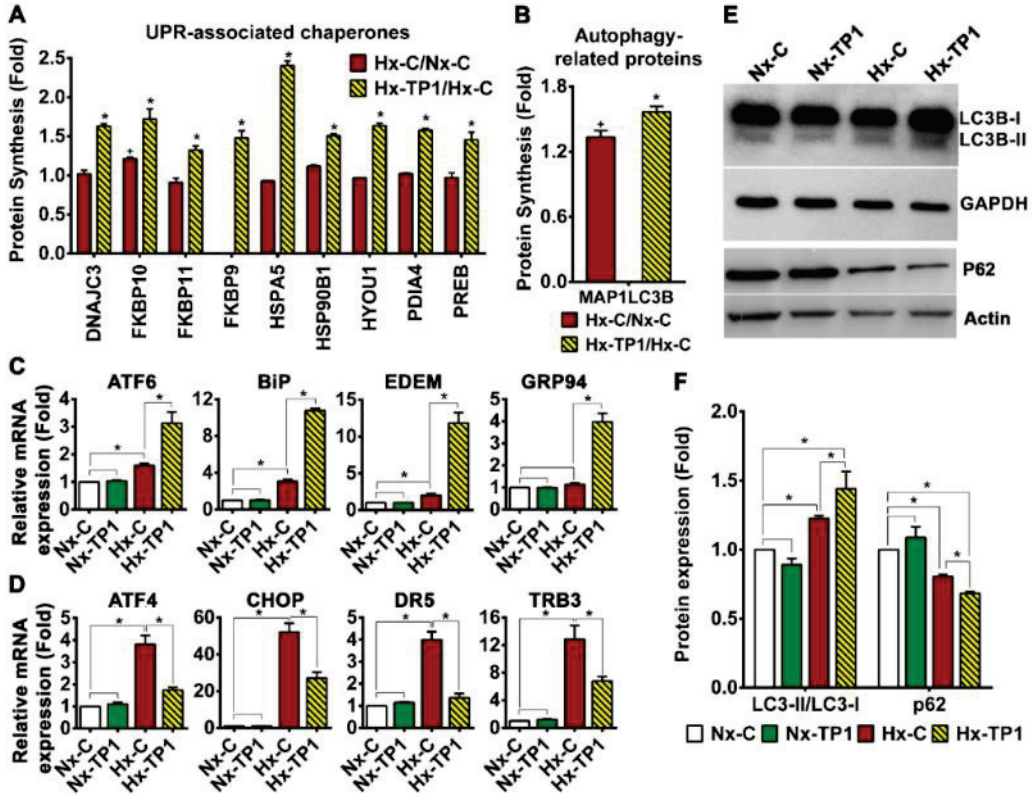


Figure 5. Ginsentide TP1 rescues endothelial cells from hypoxia-induced ER stress. (**A**,**B**) Relative expression levels of UPR-associated chaperone proteins (**A**) and autophagy-related proteins (**B**) under hypoxic conditions compared with normoxic conditions (Hx-C/Nx-C) or in TP1-treated hypoxic cells relative to PBS-treated hypoxic cells (Hx-TP1/Hx-C). Data are means ± standard error of the mean (SEM), and statistical significance was calculated using triplicate experiments. Significance

+ $p < 0.05$ respect to Nx-C and * $p < 0.05$ respect to Hx-C. (**C**,**D**) Relative mRNA expression of ER stress-related genes in HUVEC-CS cells cultured under various conditions. Data are means ± SEM, and statistical significance was calculated using triplicate biological replicates. (**E**) Western blot images of autophagy markers, including LC3B-I and II and P62, under the indicated experimental conditions. (**F**) Relative quantification of the LC3B-II/LC3B-I ratio and relative expression of P62 under the given experimental conditions (quantified based on Western blot band intensity). Data are means ± SEM, and statistical significance was calculated using triplicate biological replicates. Vehicle control cells were cultured for 24 h under normoxic (Nx-C) or hypoxic (Hx-C) conditions and TP1-treated cells were cultured for 24 h under normoxic (Nx-TP1) or hypoxic (Hx-TP1) conditions. * $p < 0.05$.

Autophagy is an essential cell process, a principal component of the integrated stress response [37], and part of the ER stress-mediated proadoptive UPR response [35,36]. Indeed, Western blot analysis revealed that the ratio of LC3B-II/LC3B-I increased significantly upon TP1 treatment under hypoxic conditions (Figure 5E,F), indicating an increase in autophagosome formation [37]. TP1-treatment also increased P62 degradation in hypoxic ECs and resulted in a lower level of P62 in these cells (Figure 5E,F), further confirming the activation of autophagy. Overall, our Western blot results indicated that TP1-induced selective autophagy occurred in ginsentide-treated hypoxic cells. Thus, TP1 promotes the clearance of accumulated proteins and suppresses apoptotic signaling to prevent the ER-stress-induced death of hypoxic cells. Indeed, when we measured protein aggregation using thioflavin-T staining and fluorescence microscopic analysis, we found a 1.6-fold increase in protein accumulation in hypoxic HUVEC-CS cells, which was effectively reversed by TP1 treatment (Figure 6A,B). The protective effect of TP1 against hypoxia was also confirmed using alternative cell lines, i.e., H9c2, A7r5, and C2C12, in which the reduction in thioflavin-T staining upon TP1-treatment was comparable to that in HUVEC-CS cells (Figure S11A,B). Consistent with the fluorescence-based analyses, the ultracentrifugation and quantitation of protein aggregates confirmed that protein accumulation in HUVEC-CS cells during hypoxic stress was markedly reduced by TP1 treatment, suggesting that TP1 is an efficient stimulator of the UPR (Figure 6C).

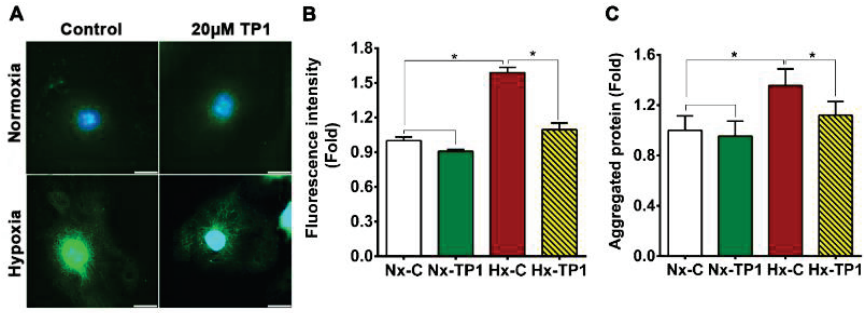


Figure 6. TP1-mediated recovery of ER/protein homeostasis in hypoxic endothelial cells. (**A**) Thioflavin-T (ThT) staining of protein aggregates in HUVEC-CS cells cultured under the indicated conditions. Aggregated proteins were stained with ThT (green), and nuclei were counterstained with DAPI (blue). Scale bar: 20 μm. (**B**) Relative quantification of protein aggregation in cells subjected to the indicated experimental conditions. Protein aggregation was quantified by calculating the average fluorescence intensity of >100 individual cells, and statistical analysis was performed using four experimental replicates. (**C**) Relative abundance of aggregated proteins isolated from HUVEC-CS cells cultured under different conditions. Data are means ± standard error of the mean, and statistical significance was calculated using triplicate experiments. Vehicle control cells were cultured for 24 h under normoxic (Nx-C) or hypoxic (Hx-C) conditions and TP1-treated cells were cultured for 24 h under normoxic (Nx-TP1) or hypoxic (Hx-TP1) conditions. * $p < 0.05$.

3.6. TP1 Restores NO Production and Reduces Reactive Oxygen Species Generation in Hypoxic ECs

Under normal physiological conditions, NO maintains the quiescent state of the endothelium, while disruption of NO signaling can trigger the endothelial expression of

mediators that promote leukocyte adhesion and inflammation [38]. Under oxidative stress conditions, the reaction of NO with superoxide anions generates peroxynitrite, which significantly impairs NO production by nitric oxide synthases, thereby promoting endothelial activation and progression to VED [38–40]. Given our finding that TP1 limits endothelial activation under hypoxic conditions, we assessed whether TP1 acts via effects on the generation of NO and reactive oxygen species (ROS). Using a fluorogenic staining approach, i.e., a 2′,7′-dichlorofluorescein diacetate (DCFDA) assay, we found that intracellular ROS levels were higher in hypoxic ECs than normoxic cells; however, TP1-treatment reduced ROS levels 1.4-fold in hypoxic ECs (Figure 7A,B). Similarly, a 1.3-fold reduction in intracellular NO was detected in hypoxic ECs, but this deficit was effectively reversed by TP1 treatment (Figure 7B). Accordingly, when the expression of eNOS was assessed using Western blotting, protein levels that were reduced under hypoxic conditions were partially restored by TP1 treatment (Figure 7C). Consistent with these data, hypoxic stress was found to induce a 1.3-fold decrease in eNOS phosphorylation at residue Ser^{1177}, which is known to modify enzyme activity under both physiological and pathological conditions [41,42]; however, TP1-treatment reversed this deficiency in eNOS phosphorylation (Figure 7C). Taken together, our data indicate that TP1 limits ROS generation and maintains NO bioavailability to prevent endothelial activation under hypoxic conditions. Bioactive ginsenosides are known to counteract redox regulation, promote NO production, and prevent ROS generation; thus, they protect cells against oxidative damage [25,43–45]. Consistent with these reported effects, we found that treatment with the ginsenosides Rb1 and Rg1 reduced the intracellular ROS levels of both normoxic and hypoxic ECs, comparable with the impact of TP1 treatment (Figure S12A,B).

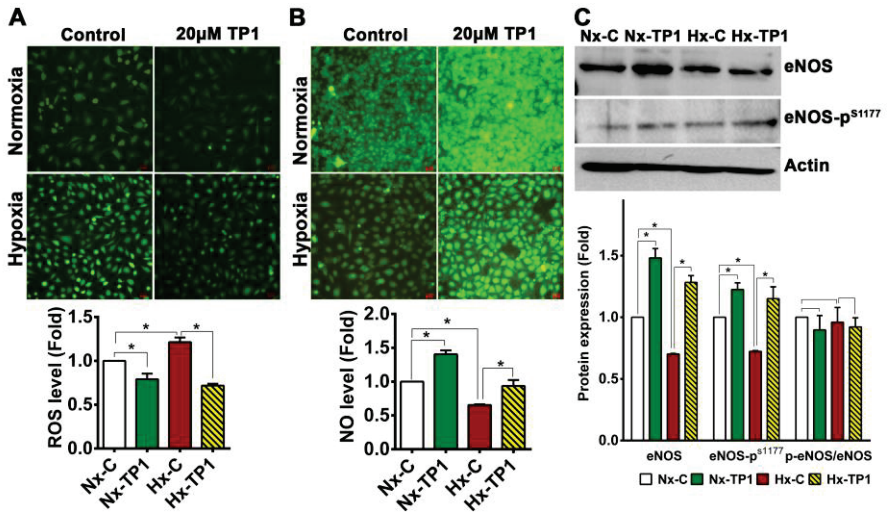


Figure 7. Ginsentide TP1 reduces intracellular reactive oxygen species (ROS) generation and restores nitric oxide (NO) generation in endothelial cells. (**A**) Effect of TP1 on ROS levels in HUVEC-CS cells cultured under different experimental conditions. ROS activity was measured by (DCFDA)-based fluorogenic assay. Scale bar: 25 μm. Relative quantification was performed using the relative fluorescence intensity. Statistical significance was calculated using five biological replicates. (**B**) HUVEC-CS cells were cultured with or without TP1 for 24 h under normoxic or hypoxic conditions, and NO levels were measured via DAF-2DA staining. Scale bar: 25 μm. Relative quantification of NO was based on the fluorescence intensity in each image, and statistical significance was calculated using four biological replicates. (**C**) Relative expression of eNOS and Ser^{1177}-phosphorylated eNOS (eNOS-p^{S1177}) under the indicated experimental conditions (quantified based on Western blot band intensity). Data are shown as means ± standard error of the mean, and statistical significance was calculated using biological triplicates. Vehicle control cells were cultured for 24 h under normoxic (Nx-C) or hypoxic (Hx-C) conditions and TP1-treated cells were cultured for 24 h under normoxic (Nx-TP1) or hypoxic (Hx-TP1) conditions. * $p < 0.05$.

4. Discussion

Ginseng, the most valuable herb in traditional medicines, is prescribed to treat a wide range of disorders, including cardiovascular disease [17,18,46]. Thus far, ginsenosides, which belong to the small-molecule metabolites of the triterpene saponin family, have received the most attention as the active compounds to account for the ethnomedicinal effects of ginseng [46,47]. Despite an abundance of ginseng research, ginsenosides alone cannot adequately explain the "cure-all" effect of ginseng in its ethnomedicinal uses [46,47]. Recently, we reported that the cell-penetrating cystine-dense microprotein TP1 coordinates multiple systems to exert anti-stress and cardiovascular benefits [25]. This report shows that ginsentide TP1 differing from the two key ginsenosides, Rb1 and Rg1, plays an important adaptogenic role in maintaining protein homeostasis in hypoxic cells and suppressing ER-stress-induced apoptosis.

Ginsentides have two distinct advantages over most unconstrained peptide biologics of comparable size. First, ginsentides, containing about 25% cysteine, are highly cystine-braced, rendering them structurally compact and highly resistant to proteolytic degradation. Second, ginsentide TP1, the representative and most abundant ginsentide, is a cell-penetrating peptide and can target intracellular protein–protein interactions. Additionally, TP1 does not exhibit any toxic or membrane-damaging effects. In comparison, ginsenosides have poor bioavailability, thereby limiting their clinical applications [48]. TP1's cell-penetrating property can also be found in certain highly cystine-braced microproteins, such as the plant-derived 8C-hevein-like peptides [20–24,28]. Thus, hyperstability and cell-penetrating properties of ginsentides are desirable attributes for drug development.

The vascular endothelium is comprised of a monolayer of cells that maintain hemostasis by regulating vascular tone, cell adhesion, smooth muscle proliferation, and tissue inflammation. The dysregulation of these mechanisms leads to VED, which can result in systemic inflammatory pathology, adverse thrombotic events, and vascular tissue remodeling. A link between hypoxia and VED has been established, as well as their consequences in relation to cardiovascular disorders [1–6]. Because preventing hypoxia-linked VED will be beneficial for treating cardiovascular disorders, we established a pulsed SILAC–based quantitative proteomic approach to determine the effects of TP1 on hypoxia-linked VED. We profiled the newly synthesized proteome of normoxic and hypoxic endothelium cells with or without TP1 treatment and analyzed the differentially expressed newly synthesized proteins. Our findings showed that hypoxia and TP1 treatment alter the expression profile of newly synthesized proteins in endothelium cells. Gene ontology analysis revealed that hypoxia promotes the expression of endothelium dysfunction–linked pathway proteins. In addition, TP1 treatment reduced the expression of VED pathogenesis-linked pathway proteins, including integrins, cell adhesion molecules, and apoptotic signaling proteins. In this regard, we showed that pulsed SILAC-based quantitative proteomics is useful in the functional characterization of cell-penetrating and cystine-dense microproteins such as ginsentides.

Hypoxia promotes inflammatory signaling [9] in ECs, resulting in the increased surface expression of adhesion molecules, including ICAM1 and VCAM1, which promote leukocyte/platelet binding and progression to VED [49,50]. Integrin complexes, including $\alpha v\beta 3$, are involved in the regulation of surface adhesion molecules [31–33] and the TP1-mediated suppression of integrin αv, $\beta 1$, and $\beta 3$ expression, which lead to decreased surface molecule expression levels in hypoxic ECs and reduced THP-1 cell adhesion to these cells. In the present study, hypoxic ECs enhanced the expression of adhesion molecules and increased leukocyte binding by 2-fold. In contrast, hypoxic ECs treated with TP1 exhibited reduced adhesion molecule expression at both the mRNA and protein levels. Accordingly, leukocyte binding to hypoxic ECs decreased 2.9-fold in the presence of TP1, indicating the potent effects of ginsentides on the activation of the endothelium [51,52]. In contrast, ginsenosides Rb1 and Rg1, two bioactive components of ginseng, displayed no notable effects on the surface molecule expression and THP-1 cell adhesion of ECs.

Cellular stress, including hypoxia, can cause defects in protein folding that lead to protein aggregation in the ER lumen and induce ER stress [53,54], which is a crucial component of endothelial dysfunction and cardiovascular disease [15,55,56]. The eNOS/NO pathway plays a critical role in maintaining the intracellular redox balance and protecting against ER stress in ECs [57]. Hence, the disruption of this pathway results in oxidative stress and proinflammatory responses that promote VED [15,58]. One mechanism underlying the protection of hypoxic cells against ER stress is the evolutionarily conserved UPR, which first attempts to restore protein homeostasis and later triggers apoptosis if recovery is unsuccessful [35,36,59]. The UPR plays a vital role in determining the fate of stressed cells. In the current study, hypoxic HUVEC-CS cells exhibited the 18-fold upregulation of spliced XBP1 mRNA, an archetypal marker of UPR activation [60]. Indeed, low-oxygen conditions also promoted the accumulation of unfolded proteins in multiple cell types, including ECs, myocytes, cardiomyocytes, and vascular smooth muscle cells, and the significant upregulation of the cell death signaling genes *ATF4*, *CHOP*, *DR5*, and *TRB3*. However, treatment with TP1 increased the hypoxic EC expression of anti-aggregation ERED genes and molecular chaperones that support protein folding, including *DNAJC3*, *HSP90B1*, *HSPA5*, and *HYOU1*, which help restore protein homeostasis and reduce ER stress in hypoxic ECs. In addition, TP1 promoted selective autophagy as a part of the proadaptive UPR response [36,37], thereby enhancing protein clearance and restoring protein homeostasis in hypoxic ECs. Our proteomic results revealed that the expression of apoptosis signaling proteins and cell death rates were significantly reduced following TP1 treatment in hypoxic ECs, myocytes, cardiomyocytes, and vascular smooth muscle cells. Taken together, our data indicate that TP1 exerts potent effects on the UPR pathway and reduces ER-stress-induced apoptotic signaling, thereby increasing overall EC survival under hypoxic conditions (Figure 8). The ability of TP1 to protect ECs from stress-induced apoptosis could be exploited clinically to treat various human disorders, particularly hypoxia-associated cardiovascular disorders.

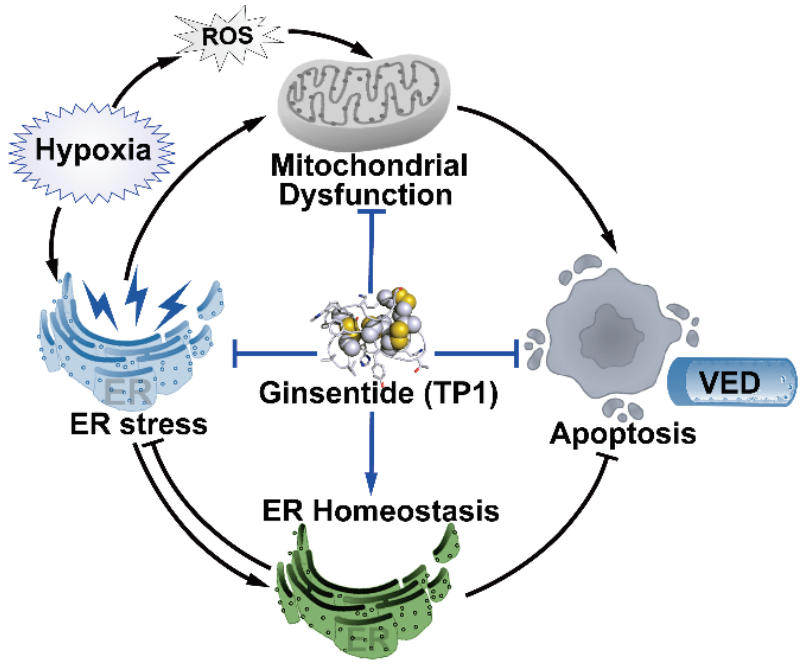


Figure 8. Proposed model for TP1-mediated protective effects against hypoxic stress in the endothelium. Endoplasmic reticulum (ER) stress initiates the unfolded protein response (UPR) as a part of the integrated stress response. UPR promotes both cellular adaptations to stress conditions and the apoptosis of cells that fail to restore normal function. Adaptive UPR prevents ER stress by restoring ER/protein homeostasis. In contrast, prolonged ER stress induces mitochondrial dysfunction and promotes apoptotic cell death. Hypoxia-induced ER stress in endothelium cells initiates proadaptive responses. Prolonged hypoxia leads to prolonged ER stress, which is proposed to cause the failure

of proadaptive responses and ensure apoptotic cell death, leading to endothelium dysfunction. Ginsentide TP1 is thought to minimize the effect of ER stress in hypoxic endothelial cells by restoring ER/protein homeostasis via the activation of proadaptive responses and suppression of apoptotic cell death.

Hypoxia has been shown to impair the activity of the NO biosynthetic enzyme eNOS via multiple mechanisms, including the subduction of protein phosphorylation at Ser^{1177} [41,42,61,62], which leads to the disruption of NO-mediated protective pathways and endothelial activation by redox signaling [61,63]. Loss of eNOS function reduces NO production and increases superoxide radical generation in hypoxic ECs, leading to endothelium activation. However, in the present study, we found a significant decrease in eNOS expression and NO levels, in parallel with elevated ROS production, in hypoxic ECs. Importantly, TP1 treatment reversed this hypoxia-induced effect in hypoxic ECs, increasing eNOS expression and phosphorylation at Ser^{1177}, which led to the recovery of NO synthesis. The TP1-mediated restoration of the redox balance in hypoxic cells via the eNOS/NO pathway may prevent endothelium dysfunction [25,51,52]. Notably, the tested ginsenosides Rb1 and Rg1 exerted a comparable effect [25], i.e., they restored the redox balance by increasing the NO level and reducing the ROS load in hypoxic ECs.

5. Conclusions

Hypoxia impairs essential cellular functions to promote endothelial cell activation and progression to VED. Low oxygen conditions also induce ER stress, which activates apoptotic signaling in hypoxic endothelial cells and multiple other cell lineages affected by cardiovascular pathology. Ginsentide TP1 rescues protein homeostasis in hypoxic cells and suppresses ER-stress-induced apoptotic signals to improve the survival of multiple cardiovascular cell types. TP1 also restores NO bioavailability and reduces intercellular ROS in hypoxic endothelial cells via restorative effects on the NO/eNOS pathway, which also protects against hypoxia-induced VED. Our results provide strong support that ginsentides are unexplored microproteins responsible for the ethnomedicinal benefits of ginseng in cardiovascular diseases. Additionally, ginsentides could provide therapeutic leads useful in treating patients at risk of VED and associated cardiovascular complications. However, to ascertain the efficacy of TP1 as a therapeutic, further in vivo studies would be necessary.

Supplementary Materials: The following supporting information can be downloaded at: https://www.mdpi.com/article/10.3390/cells12101401/s1, Supplementary Data S1: Figure S1: HPLC and mass spectrometry profiles of purified ginsentide TP1 extracted from *Panax ginseng* flowers; Figure S2: Toxicity and dose–response curve of ginsentide TP1; Figure S3: Schematic representation of the experimental workflow of pulsed SILAC labelling and proteomics; Figure S4: Linear regression plots representing the correlation among triplicate experiments under different experimental; Figure S5: Statistical analysis of proteomic data; Figure S6: Hypoxia-induced biological processes in endothelial cells (ECs); Figure S7: Ginsentide TP1 suppresses integrin expression in hypoxic endothelial cells; Figure S8: TP1 prevents apoptosis in HUVEC-CS; Figure S9: Effect of TP1 on the hypoxia-induced unfolded protein response (UPR) in endothelial cells; Figure S10: Effects of ginsenosides on hypoxia-induced ER stress-related gene expression in ECs; Figure S11: TP1-mediated recovery of ER/protein homeostasis in hypoxic cardiovascular cell types; Figure S12: Effect of ginsenoside treatment on the intracellular ROS load in ECs; Table S1: List of genes and corresponding primers used in quantitative RT–PCR. Supplementary Data S2: Table S2: List of all proteins identified; and Table S3: List of proteins identified with multiple peptides.

Author Contributions: B.D. involved in designing and performing experiments, analyzing data, and writing the manuscript; S.L. and A.K. performed peptide extraction, purification, and confocal microscopic-based cellular uptake studies; S.K.S. conceived and oversaw the proteomics analysis and edited the manuscript; J.P.T. conceived the idea and supervised and edited the manuscript. All authors have read and agreed to the published version of the manuscript.

Funding: This study was supported in part by the Nanyang Technological University Internal 702 Funding to Synzymes and Natural Products (SYNC) and the AcRF Tier 3 funding (MOE2016703 T3-1-003).

Institutional Review Board Statement: Not applicable.

Informed Consent Statement: Not applicable.

Data Availability Statement: The mass spectrometry proteomics raw data files, along with the Proteome Discoverer search data file (including protein summary), have been deposited to the ProteomeXchange Consortium (http://proteomecentral.proteomexchange.org, accessed on 18 January 2023) via the jPOSTrepo (Japan ProteOme STandard Repository) partner repository [64] with the dataset identifier PXD039938 for ProteomeXchange and JPST001996 for jPOST. The data preview page access URL is https://repository.jpostdb.org/preview/32803372563e3629fe4684 (Access key 8294).

Conflicts of Interest: The authors declare that they have no potential conflict of interest.

References

1. Hoyos, C.M.; Melehan, K.L.; Liu, P.Y.; Grunstein, R.R.; Phillips, C.L. Does obstructive sleep apnea cause endothelial dysfunction? A critical review of the literature. *Sleep Med. Rev.* **2015**, *20*, 15–26. [CrossRef] [PubMed]
2. Wilkins, M.R.; Ghofrani, H.A.; Weissmann, N.; Aldashev, A.; Zhao, L. Pathophysiology and treatment of high-altitude pulmonary vascular disease. *Circulation* **2015**, *131*, 582–590. [CrossRef] [PubMed]
3. Costanzo, M.R.; Khayat, R.; Ponikowski, P.; Augostini, R.; Stellbrink, C.; Mianulli, M.; Abraham, W.T. Mechanisms and clinical consequences of untreated central sleep apnea in heart failure. *J. Am. Coll. Cardiol.* **2015**, *65*, 72–84. [CrossRef] [PubMed]
4. Chen, J.; Lin, S.; Zeng, Y. An Update on Obstructive Sleep Apnea for Atherosclerosis: Mechanism, Diagnosis, and Treatment. *Front. Cardiovasc. Med.* **2021**, *8*, 647071. [CrossRef]
5. Haranczyk, M.; Konieczynska, M.; Plazak, W. Endothelial dysfunction in obstructive sleep apnea patients. *Sleep Breath* **2022**, *26*, 231–242. [CrossRef]
6. Peracaula, M.; Torres, D.; Poyatos, P.; Luque, N.; Rojas, E.; Obrador, A.; Orriols, R.; Tura-Ceide, O. Endothelial Dysfunction and Cardiovascular Risk in Obstructive Sleep Apnea: A Review Article. *Life* **2022**, *12*, 537. [CrossRef]
7. Wang, L.; Yin, J.; Nickles, H.T.; Ranke, H.; Tabuchi, A.; Hoffmann, J.; Tabeling, C.; Barbosa-Sicard, E.; Chanson, M.; Kwak, B.R.; et al. Hypoxic pulmonary vasoconstriction requires connexin 40-mediated endothelial signal conduction. *J. Clin. Investig.* **2012**, *122*, 4218–4230. [CrossRef]
8. Burnstock, G.; Ralevic, V. Purinergic signaling and blood vessels in health and disease. *Pharmacol. Rev.* **2014**, *66*, 102–192. [CrossRef]
9. Erlinge, D.; Burnstock, G. P2 receptors in cardiovascular regulation and disease. *Purinergic Signal.* **2008**, *4*, 1–20. [CrossRef]
10. Cai, H.; Harrison, D.G. Endothelial dysfunction in cardiovascular diseases: The role of oxidant stress. *Circ. Res.* **2000**, *87*, 840–844. [CrossRef]
11. Pober, J.S. Endothelial activation: Intracellular signaling pathways. *Arthritis Res. Ther.* **2002**, *4* (Suppl. S3), S109. [CrossRef] [PubMed]
12. Handy, D.E.; Loscalzo, J. Responses to reductive stress in the cardiovascular system. *Free. Radic. Biol. Med.* **2017**, *109*, 114–124. [CrossRef] [PubMed]
13. Szocs, K. Endothelial dysfunction and reactive oxygen species production in ischemia/reperfusion and nitrate tolerance. *Gen. Physiol. Biophys.* **2004**, *23*, 265–295. [PubMed]
14. Bourdier, G.; Flore, P.; Sanchez, H.; Pepin, J.L.; Belaidi, E.; Arnaud, C. High-intensity training reduces intermittent hypoxia-induced ER stress and myocardial infarct size. *Am. J. Physiol. Heart Circ. Physiol.* **2016**, *310*, H279–H289. [CrossRef]
15. Battson, M.L.; Lee, D.M.; Gentile, C.L. Endoplasmic reticulum stress and the development of endothelial dysfunction. *Am. J. Physiol. Heart Circ. Physiol.* **2017**, *312*, H355–H367. [CrossRef]
16. Choi, Y.Y.; Kim, S.; Han, J.H.; Nam, D.H.; Park, K.M.; Kim, S.Y.; Woo, C.H. CHOP deficiency inhibits methylglyoxal-induced endothelial dysfunction. *Biochem. Biophys. Res. Commun.* **2016**, *480*, 362–368. [CrossRef]
17. Wee, J.J.; Mee Park, K.; Chung, A.S. Biological Activities of Ginseng and Its Application to Human Health. In *Herbal Medicine: Biomolecular and Clinical Aspects*, 2nd ed.; Benzie, I.F.F., Wachtel-Galor, S., Eds.; CRC Press/Taylor & Francis LLC: Boca Raton, FL, USA, 2011.
18. Wang, H.; Peng, D.; Xie, J. Ginseng leaf-stem: Bioactive constituents and pharmacological functions. *Chin. Med.* **2009**, *4*, 20. [CrossRef]
19. Tam, J.P.; Nguyen, G.K.T.; Loo, S.; Wang, S.; Yang, D.; Kam, A. Ginsentides: Cysteine and Glycine-rich Peptides from the Ginseng Family with Unusual Disulfide Connectivity. *Sci. Rep.* **2018**, *8*, 16201. [CrossRef]
20. Dutta, B.; Huang, J.; To, J.; Tam, J.P. LIR Motif-Containing Hyperdisulfide beta-Ginkgotide is Cytoprotective, Adaptogenic, and Scaffold-Ready. *Molecules* **2019**, *24*, 2417. [CrossRef]

21. Loo, S.; Kam, A.; Li, B.B.; Feng, N.; Wang, X.; Tam, J.P. Discovery of Hyperstable Noncanonical Plant-Derived Epidermal Growth Factor Receptor Agonist and Analogs. *J. Med. Chem.* **2021**, *64*, 7746–7759. [CrossRef]
22. Tam, J.P.; Wang, S.; Wong, K.H.; Tan, W.L. Antimicrobial Peptides from Plants. *Pharmaceuticals* **2015**, *8*, 711–757. [CrossRef] [PubMed]
23. Loo, S.; Tay, S.V.; Kam, A.; Lee, W.; Tam, J.P. Hololectin Interdomain Linker Determines Asparaginyl Endopeptidase-Mediated Maturation of Antifungal Hevein-Like Peptides in Oats. *Front. Plant Sci.* **2022**, *13*, 899740. [CrossRef] [PubMed]
24. Loo, S.; Tay, S.V.; Kam, A.; Tang, F.; Fan, J.S.; Yang, D.; Tam, J.P. Anti-Fungal Hevein-like Peptides Biosynthesized from Quinoa Cleavable Hololectins. *Molecules* **2021**, *26*, 5909. [CrossRef]
25. Loo, S.; Kam, A.; Dutta, B.; Zhang, X.; Feng, N.; Sze, S.K.; Liu, C.-F.; Wang, X.; Tam, J.P. Decoding the Cure-all Effects of Ginseng. *bioRxiv* **2023**. [CrossRef]
26. Eden, E.; Navon, R.; Steinfeld, I.; Lipson, D.; Yakhini, Z. GOrilla: A tool for discovery and visualization of enriched GO terms in ranked gene lists. *BMC Bioinform.* **2009**, *10*, 48. [CrossRef] [PubMed]
27. Oslowski, C.M.; Urano, F. Measuring ER stress and the unfolded protein response using mammalian tissue culture system. *Methods Enzym.* **2011**, *490*, 71–92. [CrossRef]
28. Kam, A.; Loo, S.; Dutta, B.; Sze, S.K.; Tam, J.P. Plant-derived mitochondria-targeting cysteine-rich peptide modulates cellular bioenergetics. *J. Biol. Chem.* **2019**, *294*, 4000–4011. [CrossRef] [PubMed]
29. Park, J.E.; Tse, S.W.; Xue, G.; Assisi, C.; Maqueda, A.S.; Ramon, G.P.X.; Low, J.K.; Kon, O.L.; Tay, C.Y.; Tam, J.P.; et al. Pulsed SILAC-based proteomic analysis unveils hypoxia- and serum starvation-induced de novo protein synthesis with PHD finger protein 14 (PHF14) as a hypoxia sensitive epigenetic regulator in cell cycle progression. *Oncotarget* **2019**, *10*, 2136–2150. [CrossRef]
30. Finney, A.C.; Stokes, K.Y.; Pattillo, C.B.; Orr, A.W. Integrin signaling in atherosclerosis. *Cell. Mol. Life Sci. CMLS* **2017**, *74*, 2263–2282. [CrossRef]
31. Chen, J.; Green, J.; Yurdagul, A., Jr.; Albert, P.; McInnis, M.C.; Orr, A.W. alphavbeta3 Integrins Mediate Flow-Induced NF-kappaB Activation, Proinflammatory Gene Expression, and Early Atherogenic Inflammation. *Am. J. Pathol.* **2015**, *185*, 2575–2589. [CrossRef]
32. Akbar, N.; Digby, J.E.; Cahill, T.J.; Tavare, A.N.; Corbin, A.L.; Saluja, S.; Dawkins, S.; Edgar, L.; Rawlings, N.; Ziberna, K.; et al. Endothelium-derived extracellular vesicles promote splenic monocyte mobilization in myocardial infarction. *JCI Insight* **2017**, *2*, e93344. [CrossRef] [PubMed]
33. Roebuck, K.A.; Finnegan, A. Regulation of intercellular adhesion molecule-1 (CD54) gene expression. *J. Leukoc. Biol.* **1999**, *66*, 876–888. [CrossRef] [PubMed]
34. Tang, X.; Luo, Y.X.; Chen, H.Z.; Liu, D.P. Mitochondria, endothelial cell function, and vascular diseases. *Front. Physiol.* **2014**, *5*, 175. [CrossRef] [PubMed]
35. Xu, C.; Bailly-Maitre, B.; Reed, J.C. Endoplasmic reticulum stress: Cell life and death decisions. *J. Clin. Investig.* **2005**, *115*, 2656–2664. [CrossRef]
36. Rozpedek, W.; Pytel, D.; Mucha, B.; Leszczynska, H.; Diehl, J.A.; Majsterek, I. The Role of the PERK/eIF2alpha/ATF4/CHOP Signaling Pathway in Tumor Progression During Endoplasmic Reticulum Stress. *Curr. Mol. Med.* **2016**, *16*, 533–544. [CrossRef]
37. Kroemer, G.; Marino, G.; Levine, B. Autophagy and the integrated stress response. *Mol. Cell* **2010**, *40*, 280–293. [CrossRef]
38. Tousoulis, D.; Kampoli, A.M.; Tentolouris, C.; Papageorgiou, N.; Stefanadis, C. The role of nitric oxide on endothelial function. *Curr. Vasc. Pharmacol.* **2012**, *10*, 4–18. [CrossRef]
39. Montezano, A.C.; Touyz, R.M. Reactive oxygen species and endothelial function-role of nitric oxide synthase uncoupling and Nox family nicotinamide adenine dinucleotide phosphate oxidases. *Basic Clin. Pharmacol. Toxicol.* **2012**, *110*, 87–94. [CrossRef]
40. Norouzirad, R.; Gonzalez-Muniesa, P.; Ghasemi, A. Hypoxia in Obesity and Diabetes: Potential Therapeutic Effects of Hyperoxia and Nitrate. *Oxid. Med. Cell. Longev.* **2017**, *2017*, 5350267. [CrossRef]
41. Michell, B.J.; Griffiths, J.E.; Mitchelhill, K.I.; Rodriguez-Crespo, I.; Tiganis, T.; Bozinovski, S.; de Montellano, P.R.; Kemp, B.E.; Pearson, R.B. The Akt kinase signals directly to endothelial nitric oxide synthase. *Curr. Biol.* **1999**, *9*, 845–848. [CrossRef]
42. Kolluru, G.K.; Siamwala, J.H.; Chatterjee, S. eNOS phosphorylation in health and disease. *Biochimie* **2010**, *92*, 1186–1198. [CrossRef]
43. Mohanan, P.; Subramaniyam, S.; Mathiyalagan, R.; Yang, D.C. Molecular signaling of ginsenosides Rb1, Rg1, and Rg3 and their mode of actions. *J. Ginseng Res.* **2018**, *42*, 123–132. [CrossRef] [PubMed]
44. Xu, M.; Ma, Q.; Fan, C.; Chen, X.; Zhang, H.; Tang, M. Ginsenosides Rb1 and Rg1 Protect Primary Cultured Astrocytes against Oxygen-Glucose Deprivation/Reoxygenation-Induced Injury via Improving Mitochondrial Function. *Int. J. Mol. Sci.* **2019**, *20*, 6086. [CrossRef] [PubMed]
45. Rajput, S.A.; Shaukat, A.; Rajput, I.R.; Kamboh, A.A.; Iqbal, Z.; Saeed, M.; Akhtar, R.W.; Shah, S.A.H.; Raza, M.A.; El Askary, A.; et al. Ginsenoside Rb1 prevents deoxynivalenol-induced immune injury via alleviating oxidative stress and apoptosis in mice. *Ecotoxicol. Environ. Saf.* **2021**, *220*, 112333. [CrossRef] [PubMed]
46. Ratan, Z.A.; Haidere, M.F.; Hong, Y.H.; Park, S.H.; Lee, J.O.; Lee, J.; Cho, J.Y. Pharmacological potential of ginseng and its major component ginsenosides. *J. Ginseng Res.* **2021**, *45*, 199–210. [CrossRef]
47. Choi, S.H.; Jung, S.W.; Lee, B.H.; Kim, H.J.; Hwang, S.H.; Kim, H.K.; Nah, S.Y. Ginseng pharmacology: A new paradigm based on gintonin-lysophosphatidic acid receptor interactions. *Front. Pharmacol.* **2015**, *6*, 245. [CrossRef]
48. Leung, K.W.; Wong, A.S. Pharmacology of ginsenosides: A literature review. *Chin. Med.* **2010**, *5*, 20. [CrossRef]

49. Schaefer, A.; van Duijn, T.J.; Majolee, J.; Burridge, K.; Hordijk, P.L. Endothelial CD2AP Binds the Receptor ICAM-1 To Control Mechanosignaling, Leukocyte Adhesion, and the Route of Leukocyte Diapedesis In Vitro. *J. Immunol.* **2017**, *198*, 4823–4836. [CrossRef]
50. Anbarasan, C.; Bavanilatha, M.; Latchumanadhas, K.; Ajit Mullasari, S. ICAM-1 molecular mechanism and genome wide SNP's association studies. *Indian Heart J.* **2015**, *67*, 282–287. [CrossRef]
51. De Caterina, R.; Libby, P.; Peng, H.B.; Thannickal, V.J.; Rajavashisth, T.B.; Gimbrone, M.A., Jr.; Shin, W.S.; Liao, J.K. Nitric oxide decreases cytokine-induced endothelial activation. Nitric oxide selectively reduces endothelial expression of adhesion molecules and proinflammatory cytokines. *J. Clin. Investig.* **1995**, *96*, 60–68. [CrossRef]
52. Li, S.; Xu, J.; Yao, W.; Li, H.; Liu, Q.; Xiao, F.; Irwin, M.G.; Xia, Z.; Ruan, W. Sevoflurane pretreatment attenuates TNF-alpha-induced human endothelial cell dysfunction through activating eNOS/NO pathway. *Biochem. Biophys. Res. Commun.* **2015**, *460*, 879–886. [CrossRef] [PubMed]
53. Badiola, N.; Penas, C.; Minano-Molina, A.; Barneda-Zahonero, B.; Fado, R.; Sanchez-Opazo, G.; Comella, J.X.; Sabria, J.; Zhu, C.; Blomgren, K.; et al. Induction of ER stress in response to oxygen-glucose deprivation of cortical cultures involves the activation of the PERK and IRE-1 pathways and of caspase-12. *Cell Death Dis.* **2011**, *2*, e149. [CrossRef] [PubMed]
54. Thuerauf, D.J.; Marcinko, M.; Gude, N.; Rubio, M.; Sussman, M.A.; Glembotski, C.C. Activation of the unfolded protein response in infarcted mouse heart and hypoxic cultured cardiac myocytes. *Circ. Res.* **2006**, *99*, 275–282. [CrossRef] [PubMed]
55. Minamino, T.; Kitakaze, M. ER stress in cardiovascular disease. *J. Mol. Cell. Cardiol.* **2010**, *48*, 1105–1110. [CrossRef] [PubMed]
56. Cimellaro, A.; Perticone, M.; Fiorentino, T.V.; Sciacqua, A.; Hribal, M.L. Role of endoplasmic reticulum stress in endothelial dysfunction. *Nutr. Metab. Cardiovasc. Dis. NMCD* **2016**, *26*, 863–871. [CrossRef]
57. Takaki, A.; Morikawa, K.; Tsutsui, M.; Murayama, Y.; Tekes, E.; Yamagishi, H.; Ohashi, J.; Yada, T.; Yanagihara, N.; Shimokawa, H. Crucial role of nitric oxide synthases system in endothelium-dependent hyperpolarization in mice. *J. Exp. Med.* **2008**, *205*, 2053–2063. [CrossRef]
58. Wu, S.; Gao, X.; Yang, S.; Meng, M.; Yang, X.; Ge, B. The role of endoplasmic reticulum stress in endothelial dysfunction induced by homocysteine thiolactone. *Fundam. Clin. Pharmacol.* **2015**, *29*, 252–259. [CrossRef]
59. Oslowski, C.M.; Urano, F. The binary switch between life and death of endoplasmic reticulum-stressed beta cells. *Curr. Opin. Endocrinol. Diabetes Obes.* **2010**, *17*, 107–112. [CrossRef]
60. Chen, X.; Iliopoulos, D.; Zhang, Q.; Tang, Q.; Greenblatt, M.B.; Hatziapostolou, M.; Lim, E.; Tam, W.L.; Ni, M.; Chen, Y.; et al. XBP1 promotes triple-negative breast cancer by controlling the HIF1alpha pathway. *Nature* **2014**, *508*, 103–107. [CrossRef]
61. De Pascali, F.; Hemann, C.; Samons, K.; Chen, C.A.; Zweier, J.L. Hypoxia and reoxygenation induce endothelial nitric oxide synthase uncoupling in endothelial cells through tetrahydrobiopterin depletion and S-glutathionylation. *Biochemistry* **2014**, *53*, 3679–3688. [CrossRef]
62. Fish, J.E.; Yan, M.S.; Matouk, C.C.; St Bernard, R.; Ho, J.J.; Gavryushova, A.; Srivastava, D.; Marsden, P.A. Hypoxic repression of endothelial nitric-oxide synthase transcription is coupled with eviction of promoter histones. *J. Biol. Chem.* **2010**, *285*, 810–826. [CrossRef] [PubMed]
63. Widmer, R.J.; Lerman, A. Endothelial dysfunction and cardiovascular disease. *Glob. Cardiol. Sci. Pract.* **2014**, *2014*, 291–308. [CrossRef] [PubMed]
64. Okuda, S.; Watanabe, Y.; Moriya, Y.; Kawano, S.; Yamamoto, T.; Matsumoto, M.; Takami, T.; Kobayashi, D.; Araki, N.; Yoshizawa, A.C.; et al. jPOSTrepo: An international standard data repository for proteomes. *Nucleic Acids Res.* **2017**, *45*, D1107–D1111. [CrossRef] [PubMed]

Disclaimer/Publisher's Note: The statements, opinions and data contained in all publications are solely those of the individual author(s) and contributor(s) and not of MDPI and/or the editor(s). MDPI and/or the editor(s) disclaim responsibility for any injury to people or property resulting from any ideas, methods, instructions or products referred to in the content.

MDPI AG
Grosspeteranlage 5
4052 Basel
Switzerland
Tel.: +41 61 683 77 34

MDPI Books Editorial Office
E-mail: books@mdpi.com
www.mdpi.com/books



Disclaimer/Publisher's Note: The title and front matter of this reprint are at the discretion of the Topic Editors. The publisher is not responsible for their content or any associated concerns. The statements, opinions and data contained in all individual articles are solely those of the individual Editors and contributors and not of MDPI. MDPI disclaims responsibility for any injury to people or property resulting from any ideas, methods, instructions or products referred to in the content.





Academic Open
Access Publishing

mdpi.com

ISBN 978-3-7258-6571-0